

ISBN: 978-4-909106049 C3051

GEOMATE Proceedings



11-13 November 2020
RMIT University, Melbourne, Australia



Edited by
Zakaria Hossain
John V. Smith

GEOMATE 2020 MELBOURNE, AUSTRALIA 11-13 NOVEMBER, 2020
GEOTECHNIQUE, CONSTRUCTION MATERIALS AND ENVIRONMENT

PROCEEDINGS OF THE EIGHTH INTERNATIONAL CONFERENCE – GEOMATE 2020
GEOTECHNIQUE, CONSTRUCTION MATERIALS AND ENVIRONMENT, MELBOURNE,
AUSTRALIA 11-13 NOVEMBER, 2020

Geotechnique, Construction Materials and Environment

Edited by

Prof. Zakaria Hossain

*Department of Environmental Science and Technology
Graduate School of Bioresources
Mie University, Japan*

Dr. John V. Smith

*School of Civil and Infrastructure Engineering
RMIT University, Australia*



THE GEOMATE INTERNATIONAL SOCIETY

Copyright @ 2020 by The GEOMATE International Society

All rights reserved. In principle, no part of this publication or the information contained herein may be reproduced in any form or by any means, translated in any language, stored in any data base or retrieval system, or transmitted in any form or by any means without prior permission in writing from the publisher.

Disclaimer: The editors and the publisher have tried their best effort to ensure the integrity and the quality of this publication and information herein. However, they give no warranty of any kind, expressed or implied with regard to the material contained in this book, and will not be liable in any event for the consequences of its use.

Published by:
The GEOMATE International Society
Tsu city, Mie, Japan
E-mail: society@geomate.org
<http://www.geomate.org/>

ISBN Number: 978-4-909106049 C3051

Table of Contents

	Preface	xii
	Organization	xiii
	<i>Technical Papers</i>	1
<i>ID</i>	<i>Geotechnique</i>	2
GX128	ELASTIC BEHAVIOURS OF A CEMENTED LATERITIC SOIL FOR A ROAD BASE Sawanya Dararat, Warat Kongkitkul, Thitikorn Posribink and Pornkasem Jongpradist	3
GX132	INFLUENCES OF SEEPAGE FLOW HISTORIES ON DETERIORATION WITHIN EMBANKMENTS Koji Nakashima and Katsuyuki Kawai	9
GX134	RELATIONSHIP BETWEEN THE PRODUCTION CONDITIONS OF SOLIDIFIED CRUSHED SOIL AND THE PHYSICAL PROPERTIES AND STRENGTH OF THE PRODUCT Atsuko Sato and Osamu Hatakeyama	15
GX141	PREDICTION METHOD OF SLIP SURFACE DEPTH FOR SLOPE HEALTH MONITORING BASED ON VOLUMETRIC WATER CONTENT Keigo Koizumi, Sota Tsukabe, Mitsuru Komatsu, Kazuhiro Oda and Shinichi Ito	21
GX142	FUNDAMENTAL STUDY ON INSTALLATION POSITION OF SENSORS FOR ON-SITE MONITORING FOCUSING ON SLOPE FAILURE Haruki Iwamoto, Keigo Koizumi, Mitsuru Komatsu and Hiroshi Tsutsumi	27
GX159	A METHOD FOR REAL-TIME EVALUATION OF THE PROPERTIES OF COMPACTED SOIL FROM ACCELERATION RESPONSE OF COMPACTION ROLLER Hiroyuki Nagai, Yoshiaki Kikuchi, Sou Ihara, Shohei Noda, Taichi Hyodo and Fumio Tatsuoka	33
GX162	MECHANICAL STRENGTH OF PEAT SOIL TREATED BY FIBER INCORPORATED MICROBIAL CEMENTATION Meiqi Chen, Sivakumar Gowthaman, Kazunori Nakashima and Satoru Kawasaki	41
GX168	HYDRAULIC CONDUCTIVITY CHARACTERISTICS OF A FINE-GRAINED SOIL POTENTIAL FOR LANDFILL LINER APPLICATION Jonathan M. Tiongson and Mary Ann Q. Adajar	47
Gx169	GEOTECHNICAL CHARACTERIZATION OF ALLUVIAL SOIL AS AN ALTERNATIVE ROADWAY CONSTRUCTION MATERIAL Emerzon S. Torres and Mary Ann Q. Adajar	53
GX172	RESISTANCE FORCE AND GROUND BEHAVIOR IN THRUST PROTECTION FOR BURIED PIPES USING GEOGRID GABION Hiroyuki Araki and Daiki Hirakawa	59

GX179	A STUDY ON SOIL RESISTIVITY MEASUREMENT USING READILY INSTALLABLE ELECTRODES MOUNTED ON DRIVING-PIPES Hidetake Matsui, Tadafumi Fujiwara, Hiroyasu Ishii and Yoh Takahata	65
GX181	THE CONTRIBUTION OF PILES TO THE AVOIDANCE OF THE RAINFALL-INDUCED SLOPE FAILURE Yujia Wang, John V. Smith and Majid Nazem	71
GX183	SIMULATING EARTHQUAKE-INDUCED SLOPE FAILURES USING A SOLID-FLUID COUPLING MODEL BASED ON THE SMOOTHED PARTICLE HYDRODYNAMICS FRAMEWORK Yusuke Ono	77
GX184	EVALUATION ON THE PERFORMANCE OF MICP TREATED SLOPE SOIL UNDER ACID RAIN ENVIRONMENT Sivakumar Gowthaman, Arash Mohsenzadeh, Kazunori Nakashima, Hiromi Nakamura and Satoru Kawasaki	82
GX185	ESTIMATION OF SUBSURFACE STRUCTURE AND GROUND MOTION CHARACTERISTICS IN THE DAMAGED AREAS DUE TO THE 2016 CENTRAL TOTTORI PREFECTURE EARTHQUAKE, JAPAN Isamu Nishimura, Tatsuya Noguchi and Takao Kagawa	88
GX186	EVALUATION OF SCENIC HEALING AT VIEWPOINTS IN PARKS CONSIDERING DIFFERENCES IN MIGRATION BEHAVIOR Kazuki Ito, Kazunari Tanaka	94
GX189	ANALYSIS OF EMBANKMENT STRESSES PRODUCED DURING CONSTRUCTION AND IN-SERVICE PHASES CONSIDERING EMBANKMENT GEOMETRIES Shin-ichi KANAZAWA and Haruna IGARASHI	100
GX190	DEVELOPMENT OF THE GROUND INJECTION METHOD USING GEO-POLYMER MATERIAL Satoshi Tashiro, Naoaki Suemasa, Takamitsu Sasaki and Koichi Nagao	106
GX192	EVALUATION OF EARTHQUAKE-INDUCED SLOPE FAILURE HAZARD USING THE ANALYTIC HIERARCHY PROCESS METHOD Masanori Kohno and Yusuke Ono	112
GX194	ESTIMATION OF SUBSURFACE STRUCTURE BASED ON MICROTREMOR AND SEISMIC OBSERVATION IN THE DAMAGED AREA DUE TO 2018 HOKKAIDO EASTERN IBURI EARTHQUAKE, HOKKAIDO, JAPAN Tatsuya Noguchi, Isamu Nishimura, Yusuke Ono and Masanori Kohno	118
GX200	STUDY ON COLLAPSE MECHANISM OF RIVER LEVEE DUE TO EXTERNAL WATER LEVEL FLUCTUATION Hayato Suzuki, Shin-ichi Kanazawa, Yudai Tonoki	124
GX201	STRESS ANALYSIS OF RIVER EMBANKMENT CONSIDERING EXTERNAL WATER LEVEL FLUCTUATION Tsubasa Ichijo, Shin-ichi Kanazawa	130
GX202	ANALYTICAL STUDY ON QUALITY EVALUATION OF EMBANKMENT STRUCTURE WITH A VIEW TO LONGER LIFE Emika Nakamura, Shin-ichi Kanazawa	136
GX206	NUMERICAL INVESTIGATION ON PILE BEHAVIOR DUE TO THE RISING GROUNDWATER EFFECT Harutus Phoban, Uma Seeboonruang and Prateep Lueprasert	142
GX223	COUPLED ANALYSIS CONSIDERING DENSITY CHANGE OF UNSATURATED SOIL Daiki Yamashita and Shin-ichi Kanazawa	147
GX224	MUTUAL RELATIONSHIP BETWEEN SUFFUSION AND SHEAR BEHAVIOR IN TRIAXIAL COMPRESSION APPARATUS Taichi Ishimaru, Motoyuki Suzuki and Tomoki Wakamatsu	153
GX227	INVESTIGATION OF TIME-SERIES EXTENSOMETER DATA IN A CONCRETE LINED MINE SHAFT Jordan Tyler Kalyvas, John Victor Smith and Gang Ren	159

GX229	LIMIT ANALYSIS OF THE FUNDAO TAILINGS DAM SLOPE FAILURE IN BRAZIL 2015 Juan Hernandez Espinoza, John V. Smith and Majid Nazem	164
GX235	EXPERIMENT REGARDING MONTMORILLONITE CONTENT AND STRENGTH PROPERTIES IN BENTONITE UNDER THE INFLUENCE OF HEAT Rie Suzuki, Shin-ichi Kanazawa, Masaki Yanai and Yoshino Osamu	170
GX252	A VALIDATION OF SHALLOW SLOPE FAILURE MONITORING METHOD BASED ON THE FIELD SOIL MOISTURE OBSERVATIONS Mitsuru Komatsu and Keigo Koizumi	176
GX253	A STUDY ON MIGRATION OF KAOLIN CLAY SUSPENSION IN THE PORES USED FOR REDUCING SAND LAYER PERMEABILITY Keisuke Takahashi, Mitsuru Komatsu, Toru Iwata, and Kouji Takimoto	182
GX254	A REVIEW ON THE UNDERSTANDING OF THE PROPERTIES OF GRANULATED BENTONITE MIXTURES IN THE RADIOACTIVE WASTE DISPOSAL CONCEPTS Mazhar Nazir, Ken Kawamoto and Toshihiro Sakaki	188
GX261	THE NEW ADVANCED PROTOTYPE OF AIRBORNE VISUAL CONTROL OF A GROUND ROBOT Oleg Kupervasser, Hennadii Kutomanov, Vitalii Sarychev, and Roman Yavich	194
GX272	INVESTIGATION OF OPEN-PIT MINE DRAINAGE FEATURES Cristhiana Perdigão, Ashley Dyson, Mohammadjavad Yaghoubi and Thomas Baumgartl	200
GX274	A COMPREHENSIVE LEACHATE STUDY OF FIRED-CLAY BRICKS INCORPORATING CIGARETTE BUTTS Halenur Kurmus and Abbas Mohajerani	205
GX277	EFFECT OF FINES CONTENT ON LIQUEFACTION CHARACTERISTICS Wen LIU, Shoji KAMAO and Kei YOKOYAMA	211
GX288	STUDY ON ROTATION ANGLE ESTIMATION METHOD OF UPLIFT FOUNDATION CONSIDERING PLASTICITY REGION Yasuhide Mochida and Makoto Minemoto	217
GX298	THE EFFECT OF CEMENT ADDITIVE TO IMPROVE STRENGTH OF GRATI SOFT SOIL Yulvi Zaika, Harimurti, Adista Fahara, Nisa Safira, Wahid Darmawan	223
GX310	LABORATORY MODEL TEST ON CONTACT EROSION BETWEEN SAND AND SILTY CLAY LAYERS Pradeep Pokhrel, Jiro Kuwano	229
GX314	UNIAXIAL COMPRESSION TEST OF BENTONITE UNDER VARIOUS CONDITIONS Masaki Yanai, Shinichi Kanazawa, Rie Suzuki and Osamu Yoshino	235
GX324	STUDY ON SOIL-BENTONITE VERTICAL CUTOFF WALLS WITH EARTHQUAKE-PROOF PERFORMANCE Koji Watanabe, Shinya Matsushita, Daisuke Ueno and Masaaki Hasegawa	241
GX328	FUNDAMENTAL STUDY ON TRENCH STABILITY OF DIAPHRAGM WALL Yuki Sasaki, Koji Watanabe, Makoto Arakawa and Tadahisa Yamamoto	247
GX331	A PRACTICAL APPROACH TO DETERMINE THE TEMPERATURE CORRECTION FOR EC-5 MOISTURE SENSORS EMBEDDED IN VERTOSOL Rajitha Shehan Udukumburage, Chaminda Gallage and Les Dawes	253
GX344	EXISTENCE OF SILT SEAM LAYER TRIGGERNG FLOW LIQUEFACTION ON THE PALU MW 7.5 EARTHQUAKE 2018 Dandung Sri Harninto and Widjoyo A. Prakoso	259

GX345	EXPERIMENTAL RESEARCH ON THE INFLUENCE OF DISTANCE BETWEEN CFG PILES ON THE FOUNDATION TREATMENT RESULT IN VIETNAM Doanh Phu Bui, Tung Hoang, Phuong Viet Nguyen, Duc Viet Ngo and Cuong Phu Cao	267
GX347	DESIGNING GABION STRUCTURES UNDER MULTI CRITERIA OBJECTIVES WITH GOAL PROGRAMMING Vuttichai Chatpattananan, Tanadol Kongsomboon, and Vatanavongs Ratanavaraha	273
GX350	INTRODUCTION OF ARTIFICIAL INTELLIGENCE SYSTEM FOR SUPPORTING SOIL CLASSIFICATION Shinya Inazumi, Kazuhiko Kojima, Hiroyuki Hashida and Ken-ichi Shishido	280
GX353	UNSATURATED SHEAR STRENGTH OF EXPANSIVE SOILS FROM NATURAL SLOPES IN QUEENSLAND Tharindu Abeykoon, Chaminda Gallage and Jessica Trofimovs	284
GX362	A LABORATORY METHOD FOR ACCURATE CALIBRATION OF STRAIN-GAUGE TYPE SOIL PRESSURE TRANSDUCERS Chamara Prasad Gunasekara Jayalath and Chaminda Gallage	290
GX383	NUMERICAL SIMULATION OF INHIBITORY EFFECT OF SUBSIDENCE FOR THE LEANING PAGODA BY GROUND IMPROVEMENT Yuko Ishida, Hajime Ito and Ryoichi Fukagawa	295
GX384	APPLICATION OF ABAQUS PROGRAM TO INVESTIGATE THE EFFECT OF VARIATION IN SUBGRADE LAYER PROPERTIES ON THE DAMAGE OF FLEXIBLE PAVEMENT STRUCTURE Saad Farhan Ibrahim AlAbdullah, Maryam Hussain Hassan, Suha Aldahwi	301
GX395	DEVELOPMENT OF A COMBINATION OF A ROTARY PENETRATION TYPE SAMPLER Katsuya Iwai, Naoaki Suemasa and Tsuyoshi Tanaka	309
GX398	BASE-ROCK ELEVATION MEASUREMENT USING SINGLE AND ARRAY MICROTREMOR INVESTIGATION Windu Partono, Sukamta, Frida Kistiani, Undayani Cita Sari and Kuku Cahya Adi Putra	315
GX416	OUTFLOW CHARACTERISTICS OF FINE PARTICLES IN TWO KINDS OF WATER-PASSING EXPERIMENTS USING A COLUMN Tomoki Wakamatsu, Motoyuki Suzuki and Taichi Ishimaru	321
GX429	APPLICATION OF COMPUTER VISION TECHNIQUE IN RAPID SOIL CLASSIFICATION Aw, Y.J.E., Koh, J.W., Chew, S.H., Tan, S.E.D., Cheng, L.M., Yim, H.M.A., Ang, L.J.L. and Chua K.E.,	327
GX434	UTILISATION OF RECYCLED MATERIALS IN STABILISATION OF EXPANSIVE SOILS: A REVIEW Jiasheng Zhu, Mohammad Saberian, Haiyun Luo, Junkai Gong, Manlin Liu, Gang Ren and Jie Li	333
GX435	OPTIMUM UTILIZATION OF RICE HUSK ASH WASTE FOR GROUND IMPROVEMENT Najmun Nahar and Zakaria Hossain	339
ID	<i>Construction Materials</i>	345
GX147	FIELD EXPERIMENTS TO INVESTIGATE PULL-OUT MECHANISM OF FLIP-TYPE GROUND ANCHORS INSTALLED IN CLAY SOIL Shota Yoshida, Tatsunori Matsumoto, Mimu Yoshida	346
GX130	FINITE DIFFERENCE APPROXIMATION FOR SOLVING TRANSIENT HEAT CONDUCTION EQUATION OF THE CAST IRON Dalal Adnan Maturi	352
GX180	DEVELOPMENT OF ARTIFICIAL BEACHROCK USING WATERMELON SEEDS AS A SOURCE OF UREASE Md. Al Imran, Kazunori Nakashima, Niki Evelpidou and Satoru Kawasaki	356

GX220	STUDY ON STRUCTURAL EFFECTIVENESS OF A BUILDINGS STRUCTURE BY USING A CFRTP Yasuhide Mochida, Kouhei Kasahara	362
GX282	UTILIZATION GGBFS AS CEMENT SUBSTITUTION TO REDUCE PRODUCTION COST OF CONSTRUCTION PROJECT Ranti Hidayawanti, Yusnita Rahayu, Soetjipto Soewono, Fahdun Ibnu Wachid and Rony Panca Adi Widodo	369
GX260	POSSIBLE RECYCLING OF WASTE GLASS IN SUSTAINABLE FIRED CLAY BRICKS: A REVIEW Yuecheng Xin, Abbas Mohajerani, Halenur Kurmus, John V. Smith	376
GX263	DYNAMIC PROPERTIES OF RIGID POLYURETHANE FOAM IN CYCLIC TRIAXIAL TESTS Atsushi Koyama, Daisuke Suetsugu and Yoshinori Fukubayashi	382
GX264	EVALUATION OF FROST DAMAGE RESISTANCE OF LPC-FA COMBINED CONCRETE CURED FOR A LONG TIME Shogo KAWAMORITA, Kazuhito NIWASE	388
GX267	IMPROVEMENT OF INITIAL STRENGTH OF LPC-FA CONCRETE BY USING C-S-H-TYPE ACCELERATOR Takuya KUDO and Kazuhito NIWASE	394
GX279	POSSIBLE RECYCLING OPTIONS FOR WASTE MATERIALS IN CERAMIC TILES Qibin Yuan, Abbas Mohajerani, Halenur Kurmus, John V. Smith	400
GX281	EFFECTS OF SIZE AND GRADING, TYPE AND QUALITY OF AGGREGATES ON MECHANICAL PROPERTIES OF UNBOUND ROADBED MATERIALS: A LITERATURE REVIEW Hong Nam Thai, Akira Kato, Hoang Giang Nguyen, Tien Dung Nguyen, Ton Kien Tong,	406
GX258	RECYCLING OF CIGARETTE BUTTS IN STONE MASTIC ASPHALT Md Tareq Rahman, Abbas Mohajerani and Filippo Giustozzi	413
GX292	A STUDY ON COMPRESSIVE STRENGTH AND EFFECTIVE DIFFUSION COEFFICIENT OF SOLIDIFIED BODY WITH HIGH ZEOLITE MIXING RATE Ryo Takano and Kazuhito Niwase	419
GX375	INVESTIGATING COMPRESSIVE, PULLOUT AND TENSILE STRENGTH OF CONCRETE CONTAINING POLYPROPYLENE Md Jahidul Islam, Niaz Md Ashraful haque and Anika Tahsin	425
GX433	SOLAR PANEL FOUNDATIONS ON SLOPING LAND AND OFFSHORE ~ A REVIEW Alex Otieno Owino, Jamie Ure Ovia, Jim Shiau, Zakaria Hossain	432
ID	<i>Environment</i>	443
GX126	THE DYNAMICS OF LAND COVER CHANGE AND CAUSAL FACTORS IN THE KURANJI WATERSHED Teguh Haria Aditia Putra, Bambang Istijono, Aprisal, Bujang Rusman and Taufika Ophiyandri	444
GX133	CONVERSION OF WASTE STONE-FINE SLURRY INTO GEOPOLYMER CEMENT WITH ADDITION OF COAL FLY ASH Takaaki Wajima and Say Buntan	450
GX135	SALINITY PREDICTION USING DYNAMIC PARAMETER OF THAILAND'S BANG KRACHAO Uma Seeboonruang, Pinit Tanachaichoksirikun and Uba Sirikaew	456
GX153	SOIL PARAMETERS IN DIFFERENT LAND USE TYPES IN CU LAO DUNG, VIETNAM Duong Minh Truyen, Truong Hoang Dan, Duong Van Ni and Ly Van Loi	463

GX157	PREPARATION OF FLUORIDE ADSORBENT FROM ZIRCON SAND USING MECHANOCHEMICAL TREATMENT, AND ITS APPLICATION FOR FLUORIDE REMOVAL Nagisa Minami and Takaaki Wajima	467
GX174	COMPARISON OF THE NATIONAL PARK MANAGEMENT SYSTEM IN THE UNITED STATES AND JAPAN Takashi Kuchii, Atsushi Nakashima	473
GX175	DIVERSITY OF NATURE CONSERVATION SYSTEM IN EACH REGION AND CHALLENGE OF CREATING GLOBAL NATURE CONSERVATION SYSTEM Takashi Kuchii, Hiroko Kuchii and Atsushi Nakashima	480
GX188	THE ENVIRONMENTAL PARAMETERS CONTROLLING THE HABITAT OF INVASIVE ALIEN SPECIES, SPARTINA ALTERNIFLORA IDENTIFIED BY PREDICTIVE MODELING Michiko Masuda, Testuya Morioka and Fumitake Nishimura	486
GX197	PARADIGM SHIFT IN NATURAL RESOURCES AND ENERGY POLICIES Hisatoshi Tanaka, Atsushi Nakashima and Nabil Maghrebi	492
GX199	TECHNOLOGICAL INNOVATION AND ESG INVESTMENT IN THE JAPANESE ENERGY SECTOR Hisatoshi Tanaka, Atsushi Nakashima and Nabil Maghrebi	497
GX212	DESALINATION BEHAVIOR OF NATURAL ZEOLITE IN SEAWATER Fumika Sekihata, and Takaaki Wajima	502
GX219	ESTUARY ZONATION BOUNDARY BASED ON SEA SURFACE SALINITY DISTRIBUTION IN CILETUH BAY, WEST JAVA S. Supriatna, Iqbal Putut Ash Shidiq, Dennisa M. Tunjung	508
GX239	EFFECTS OF RIPARIAN WORKS ON ICHTHYOFAUNA IN THE NACHI RIVER, JAPAN Taiki Mizumachi, Kentarou Hirashima and Atsushi Nakashima	514
GX262	EARLY FOREST RESTORATION ON THE CLOSED SKI SLOPE IS ENHANCED BY NATURAL REGENERATION AND ARTIFICIAL THINNING Tetsuo Shirota, Chizuru Iwasaki, Tetsuo Okano, and Shinjiro Oya	520
GX266	THE ADEQUACY OF HOUSEHOLDS SANITATION LEVEL IN THE CITY OF JAKARTA: A MICRODATA ANALYSIS FROM SUSENAS 2017 Noviyati Valentina Sidabutar and Chotib	525
GX280	SPATIAL PATTERN OF EARTHQUAKE PRONE AREAS OF BANTUL REGENCY, INDONESIA Susiloningtyas, D, Della Ayu Lestari, Hengki Tasman, Tuty Handayani, Annacletus Ari Dartoyo	531
GX315	INFLUENCE OF LIGHT ON MICROBIAL RIVER WATER ECOSYSTEM AND ITS SELF-PURIFICATION POTENTIAL Fumitake Nishimura, Yuki Koike and Michiko Masuda	537
GX319	ABILITY AND WILLINGNESS TO PAY FOR WASTE WATER MANAGEMENT MAINTENANCE SERVICES (IPAL) Marselina Djayasinga, Tsra Subianto, Tri Joko Prasetyo	543
GX330	LIFE CYCLE ASSESSMENT APPROACH FOR PREDICTING GREENHOUSE GAS EMISSION FROM COLUMN, BEAM AND PLATE IN A REAL ESTATE CONSTRUCTION Yatnanta Padma Devia, Indradi Wijatmiko, Bernadus Martino, and Annisa Nur Rakhmawati	550
GX335	TRENDS IN THE USE OF STREET TREES IN JAPAN Masaaki Furuno, Taizo Uchida, Daisuke Hayasaka, Xue Jun Huan and Teruo Arase	557
GX361	THE RELATIONSHIP BETWEEN LAND USE AND TRANSPORT PERFORMANCE: A CASE STUDY OF PADANG, INDONESIA Aleksander Purba, Nikko Yulianda, Shahnaz Nabila Fuady	563

GX388	THE UTILIZATION OF BIOGAS SLUDGE TO LEAD ZERO WASTE SYSTEM IN BIOGAS IMPLEMENTATION: THE EFFECT OF VOLUME ON CARBON DIOXIDE AND METHANE CONTENT Ambar Pertiwinigrum, Margaretha Arnita Wuri, Widyawati Luhur Pambudi and Lies Mira	570
GX404	ENVIRONMENTAL IMPACT ANALYSIS IN HOTEL SECTOR: A CASE STUDY IN THAILAND Jarotwan Koiwanit and Viachaslau Filimonau	574
GX425	TOWARD SUSTAINABLE COMMUNITIES: A COMPREHENSIVE ENVIRONMENTAL IMPACT ASSESSMENT OF BUILDING Nantamol Limphitakphong and Orathai Chavalparit	580
GX437	EXPERIMENTAL INVESTIGATION OF PHYSICAL PROPERTIES OF PEATS IN WESTERN PROVINCE, SRI LANKA A.M.Z. Zimar, M.C.M. Nasvi, D. Robert, S.Jayakody, J.R.R.N.Jayarathne and John V. Smith	586
GX176	SPATIAL MODELLING OF LARVA GLASS EEL AT CILETUH BAY, WEST JAVA, INDONESIA Illa Annisa, S. Supriatna, and Iqbal Putut Ash Shidiq	592
GX177	NUMERICAL SIMULATION OF THREE-DIMENSIONAL FLOW AND LOCAL SCOUR AROUND A CYLINDER INDUCED BY TSUNAMI RUN-UP Yuki Kajikawa and Masamitsu Kuroiwa	599
GX195	ON RELATIONSHIP BETWEEN MONUMENT AND THE STATION BUILDING Kaho HASEGAWA, Kazunari TANAKA	605
GX198	STUDY ON THE MEANING OF "QUAINT" SPACE Yoshiki Shirafuji, Kenta Aoki, Koji Inoue, Dr. Kazunari Tanaka	609
GX226	SPATIAL CHARACTERISTICS OF FACTORS INFLUENCING THE OCCURRENCE AND SCALE OF MULTIPLE SLOPE FAILURES Takashi Wada, Ryo Kodani, Hiroshi Miwa	612
GX268	SPATIAL ENTRAPMENT OF WOMEN WORKERS IN METROPOLITAN AREAS Putri Halimah, Chotib	618
GX293	DAMAGE PREDICTION OF THE STEEL GIRDER ARCH BRIDGE MODEL BASED ON ARTIFICIAL NEURAL NETWORK METHOD Widya Apriani, Reni Suryanita, Yohannes Firzal, and Fadrizal Lubis	624
GX325	OPTIMUM LOCATION OF LAST-MINED STOPE IN SILL PILLAR RECOVERY WITH INFLUENCE OF BACKFILLING: A CASE STUDY Derek B. Apel	630
GX341	MEASURING ACCESS TO SUSTAINABLE TRANSPORT OPTIONS FOR THE ELDERLY Kaniz Fatima, Sara Moridpour, Chris De Gruyter and Tayebbeh Saghapour	635
GX348	QUANTIFICATION OF SLOPE DEFORMATION USING LASER POINT CLOUD DATA BY MOBILE MAPPING SYSTEM Naoto Samori, Satoshi Nishiyama, Koki Sakita, Michinari Fuziki and Naoya Ono	641
GX354	MEASURING THE ACCESSIBILITY TO TRANSIT STATION: A CASE STUDY OF TANJUNG KARANG, LAMPUNG INDONESIA Aleksander Purba Diti Artanti Utami Putri, Rahayu Sulistyorini, Shahnaz Nabila Fuady, and Lusmeilia Afriani	647
GX370	SEISMIC RESPONSE OF ABUTMENTS IN A REAL BRIDGE MODEL Desy Setyowulan, Toshitaka Yamao, Eko Andi Suryo Eva Arifi, and Devi Nuralinah	653
GX374	PREDICTION OF AERODYNAMIC COEFFICIENTS FOR OFFSHORE TURBINE BLADE UNDER THE VARIATION OF WIND VELOCITIES Eaindra Soe, Yasothorn Sapsathiarn and Jetsadaporn Priyadumkol	658

GX409	NUMERICAL ANALYSIS OF INVASION PATTERNS DURING DRAINAGE PROCESS IN A SIMPLIFIED PORE NETWORK MODEL Yuto Takeuchi, Junichiro Takeuchi and Masayuki Fujihara	664
GX410	A US\$6.07 BILLION JAKARTA - BANDUNG HIGH - SPEED RAIL: CHALLENGES AMID COVID-19 PANDEMIC Aleksander Purba	670
GX423	APPLYING DECENTRALIZED CONSENSUS: A CASE STUDY OF CARBON TRADING Pasu Poonpakdee and Jarotwan Koiwanit	676
GX321	EVALUATING EFFECTS OF MIXING PROPORTION ON WATER RETENTION CURVE AND PORE SIZE DISTRIBUTION OF RECYCLED CONCRETE AGGREGATES BLENDED WITH AUTOCLAVED AERATED CONCRETE GRAINS PHAM Van Nam, Akira KATO, NGUYEN Hoang Giang, NGUYEN Van Tuan, PHAN Quang Minh, and Ken KAWAMOTO	681
GX247	A COMPARATIVE STUDY OF CONVENTIONAL EXTENDED AERATION AND MODERN MEMBRANE BIOREACTOR METHODS OF SEWAGE TREATMENT FROM THE ENVIRONMENTAL AND FINANCIAL PERSPECTIVES Mohamed Fetouh, Rabee Rustum and Adebayo J. Adeloje	686
GX278	RESEARCH ON HOUSING RESTORATION COSTS AND DISASTER RISK MANAGEMENT FOR URBAN EARTHQUAKES Norikazu Sakaba and Harumi Yashiro	692
GX129	INVESTIGATION OF THE INFLUENCE OF RECYCLED RUBBER PARTICLES ON CEMENT PASTE PROPERTIES Mohamed Atef, NahedA.Azab, Mohamed Hazem Abdellatif and Ghada Bassioni	700
GX436	IMPROVEMENT OF SOIL STRENGTH USING RICE HUSK ASH Jamie Ure Ovia, Najmun Nahar, Alex Otieno Owino, Noma Tamaki and Zakaria Hossain	706
GX360	SURFACE SHAPE MEASUREMENT AND EVALUATION OF MECHANICAL STABILITY BY DEM SIMULATION FOR DAMAGED TRADITIONAL STONEWALLS Satoshi Sugimoto, Maho Yamaguchi and Minoru Yamanaka	710

Preface

On behalf of the GEOMATE 2020 Organizing Committee, we would like to welcome you in attending the International Conference on Geotechnique, Construction Materials and Environment held at the RMIT University, Australia in conjunction with School of Civil and Infrastructure Engineering, RMIT University, Australia, The GEOMATE International Society, Useful Plant Spread Society, Glorious International, AOI Engineering, HOJUN, JCK, CosmoWinds and Beppu Construction, Japan.

On Friday 11 March 2011, at 14:46 Japan Standard Time, the northeast of Japan was struck and severely damaged by a series of powerful earthquakes which also caused a major tsunami. This conference was first dedicated to the tragic victims of the Tohoku-Kanto earthquake and tsunami disasters. The Geomate 2020 conference covers three major themes with 17 specific themes including:

- | | |
|---|---|
| • Advances in Composite Materials | • Ecology and Land Development |
| • Computational Mechanics | • Water Resources Planning |
| • Foundation and Retaining Walls | • Environmental Management |
| • Slope Stability | • Public Health and Rehabilitation |
| • Soil Dynamics | • Earthquake and Tsunami Issues |
| • Soil-Structure Interaction | • Safety and Reliability |
| • Pavement Technology | • Geo-Hazard Mitigation |
| • Tunnels and Anchors | • Case History and Practical Experience |
| • Site Investigation and Rehabilitation | |

Due to COVID-19, this year we have received less number of paper submissions from different countries. The participated countries are Australia, Bangladesh, Canada, Indonesia, Israel, Japan, Philippines, Saudi Arabia, Singapore, Thailand, United Arab Emirates, and Vietnam. The technical papers were selected from the vast number of contributions submitted after a review of the abstracts. The final papers in the proceedings have been peer reviewed rigorously and revised as necessary by the authors. It relies on the solid cooperation of numerous people to organize a conference of this size. Hence, we appreciate everyone who supports as well as participate in this joint conferences.

Last but not least, we would like to express our gratitude to all the authors, session chairs, reviewers, participants, institutions and companies for their contribution to GEOMATE 2020. We hope you enjoy the conference and find this experience inspiring and helpful in your professional field. We look forward to seeing you at our upcoming conference next year.

Best regards,

Prof. Zakaria Hossain,
Mie University, Japan
Chairman (General)



Dr. Dr. John V. Smith
RMIT University, Australia
Chairman (Program)

Organization

Conference Honorary Chairmen:

Emeritus Professor Dr. Sohji Inoue, Mie University, Japan
Emeritus Professor Dr. Teruo Nakai, Nagoya Institute of Technology, Japan
Emeritus Professor Dr. Fusao Oka, Kyoto University, Japan
Prof. Dr. Bajang B.K. Huat, UPM, Malaysia

Scientific Committees:

Conference Chairmen:

A/Prof. Dr. John V. Smith, RMIT Univ. Australia (Program)
Prof. Dr. Zakaria Hossain, Mie University, Japan (General)

Conference Organizing Committee:

A/Prof. Dr. John V. Smith, RMIT Univ. Australia (Program)
Prof. Dr. Zakaria Hossain, Mie University, Japan (Chair)
A/Prof. Dr. Annan Zhou, RMIT University Australia (Co-Chair)
Prof. Dr. M Ibn Ibrahimy, Prof., Int. Islamic Univ. (Co-Chair)
Prof. Dr. Toshinori Sakai, Mie University, Japan (Co-Chair)
Prof. Dr. Takamitsu Kajisa, Mie University, Japan (Co-Chair)
Dr. Vivi Anggraini, Lecturer, Monash Uni Malaysia (Co-Chair)
Dr. Masaaki Kondo, Mie University, Japan (Co-Chair)

National & International Advisory Committee:

Dr. Fumio Tatsuoka, Prof., Tokyo University of Science, Japan
Dr. Junichiro Takeuchi, Prof., Kyoto University, Japan
Dr. Kingshuk Roy, Prof., Nihon University, Japan
Dr. Sai Vanapalli, Prof., University of Ottawa, Canada
Dr. Musharraf Zaman, Prof. Univ. of Oklahoma, USA
Dr. Rafiqul Tarefder, Prof. University of New Mexico, USA
Dr. M. Bouassida, Prof., National Sch. of Engg. of Tunis
Dr. L.R. Austriaco, Prof., Angles Univ. Found., Philippines
Dr. A.S.M. Abdul Awal, Prof., UTHM, Malaysia
Dr. M. Ibn Ibrahimy, Prof., Int. Islamic Univ., Malaysia
Dr. Bujang B.K. Huat, Prof., Univ. Putra Malaysia
Dr. Nemy Banthia, Prof., Univ. of British Columbia, Canada
Dr. Ian Jefferson, Prof., Univ. of Birmingham, UK
Dr. John Bolander, Prof., Univ. of California, USA
Dr. Shamsul Chowdhury, Prof., Roosevelt Univ., USA
Dr. Isabel Pinto, Prof., University of Coimbra, Portugal
Dr. Mark Jaksa, Prof., University of Adelaide, Australia
Dr. Hj. Ramli Bin Hj. Nazir, A/Prof., UTM, Malaysia
Dr. M.S. Hossain, Prof., International Islamic Univ. Bangladesh

Dr. Suksun Horpibulsuk, Prof. Suranaree Uni of Tech, Thailand
Dr. Muzamir Hasan, Director, CERRM, Univ. Malaysia Pahang
Dr. Afshin Asadi, S/Lecturer, Int. College of Auckland, New Zealand

International Technical Program Committee:

Prof. Sai Vanapalli, University of Ottawa, Canada
Prof. Alaa Masoud, Tanta University, Egypt
Prof. Aly Ahmed, Beni-Suef University, Egypt
Prof. Aminaton Marto, Universiti Teknologi Malaysia, Malaysia
Prof. Bandari Shankar, Osmania University, India
Prof. Bashir Ahmed Mir, National Institute of Technology, India
Prof. Hamidi Abdul, Aziz, Universiti Sains Malaysia (USM), Malaysia
Prof. Hussein Elarabi, University of Khartoum, Sudan
Prof. M. Shohidullah Miah, International Univ. of Business Agriculture &Tech., Bangladesh
Prof. Michele, Casagrande, Pontifical University Catholic of Rio De Janeiro, Brazil
Prof. Radim Cajka, Technical University of Ostrava, Czech Republic
Prof. Rajaraman Jambunathan, AMET University, India
Prof. Reshma Chandran T., Global Institute of Architecture, India
Prof. Roslan Hashim, University of Malaya, Malaysia
Prof. Seyed Naser Moghaddas Tafreshi, K.N. Toosi University of Technology, Iran
Prof. Valeriy Perminov, Tomsk Polytechnic University, Russia
Prof. Quanmei Gong, Tongji University, China
A/ Prof. Abdoullah Namdar, Sichuan University, China
A/ Prof. Abdul Naser Abdul Ghani, Universiti Sains Malaysia, Malaysia
A/ Prof. Alaeddinne Eljamassi, Islamic University of Gaza, Palestine
A/ Prof. Alina Paranina, Herzen State Pedagogical University of Russia, Russia
A/ Prof. Ashraf Elmoustafa, Ain Shams Univeristy, Egypt
A/ Prof. Bindu C S, Cochin University of Science & Technology, India
A/ Prof. Chee-Ming Chan, Universiti Tun Hussein Onn Malaysia, Malaysia
A/ Prof. Chidanand Naik, Anjuman Institute of Technology and Management, India
A/ Prof. Dahlia Hafez, Cairo University, Egypt
A/ Prof. Deepa G Nair, Isfahan University of Technology, India
A/ Prof. Dolrerdee Hormdee, Khon Kaen University, Thailand
A/ Prof. Farhad Behnamfar, Isfahan University of Technology, Iran
A/ Prof. Gabriela B. Cazacu, Geotech Dobrogea, Romania
A/ Prof. Hadi Khabbaz, University of Technology, Sydney (UTS), Australia
A/ Prof. Homayoon Ganji, Herat Univercity Badghis, Afghanistan
A/ Prof. Hudson Jackson, US Coast Guard Academy, United States
A/ Prof. Inazumi Shinya, National Institute of Technology, Akashi, Japan
A/ Prof. John Smith, RMIT University, Australia
A/ Prof. Kasinathan Muthukkumaran, National Institute of Technology, India
A/ Prof. Lindrianasari Lindrianasari, Universitas Lampung, Indonesia
A/ Prof. Mahdi Karkush, Baghdad University, Iraq
A/ Prof. Mohamed Redha Menani, Batna University, Algeria
A/ Prof. Navid Khayat, Ahvaz Branch, Islamic Azad University, Iran
A/ Prof. Salam, Bash AlMaliky, AlMustansiriya University, Iraq
A/ Prof. Shailesh Kumar Jha, Indian Institute of Technology, India
A/Prof. Teodor Lucian Grigorie, University of Craiova, Romania
A/Prof. Paresch Dalal, Shri Vitthalrao Shankarrao Naik Arts, Commerce and Science College, India
A/Prof. Muhammad Qasim, Abdul Wali Khan University Mardan, Pakistan
A/Prof. R. S. Ajin, GeoVin Solutions Pvt. Ltd., India
Dr. Abdul Karim M. Zein, University of Khartoum, Sudan
Dr. Abdull Halim Abdul, Universiti Teknologi MARA, Malaysia
Dr. Afshin Asadi, University Putra Malaysia, Malaysia
Dr. Ahmad Safuan A Rashid, Univeristi Teknologi Malaysia, Malaysia
Dr. Ahmad Safuan Bin A Rashid, Univeristi Teknologi Malaysia, Malaysia
Dr. Akindele Okewale, Federal University of Petroleum Resources, Nigeria

Dr. Akinola Johnson Olarewaju, Federal Polytechnic Ilaro, Nigeria
 Dr. Ali Sobhanmanesh, Universiti Teknologi Malaysia (UTM), Malaysia
 Dr. Alireza Bahiraie, Semnan University, Iran
 Dr. Allan Manalo, Centre of Excellence in Engineered Fibre Composites, Australia
 Dr. Aniza Ibrahim, National Defence University of Malaysia, Malaysia
 Dr. Arif Ali Baig Moghal, King Saud University, Saudi Arabia
 Dr. Aslan S. Hokmabadi, University of Technology, Sydney (UTS), Australia
 Dr. Ather Ashraf, PUCIT, Old Campus Punjab University, Pakistan
 Dr. Atsuko Sato, Cical Engineering Research Institute for Cold Region, Japan
 Dr. Ben-Hur Silva, Military Institute of Engineering, United States
 Dr. Choy Soon Tan, Univeristi Teknologi Malaysia, Malaysia
 Dr. David Thorpe, University of Southern Queensland, Australia
 Dr. Delsye Ching Lee Teo, Universiti Malaysia Sarawak, Malaysia
 Dr. Domenico Lombardi, University of Manchester, United Kingdom
 Dr. Ehsan, Jorat Newcastle University, United Kingdom
 Dr. Ganesh Kumar Shanmugam, National Institute of Ocean Technology, India
 Dr. Helsin Wang, Institute of Bridge Engineering, Taiwan
 Dr. Hossein Moayedi, Kermanshah University of Technology, Iran
 Dr. Hossein MolaAbasi, Babol University of Technology, Iran
 Dr. James Hambleton, University of Newcastle, Australia
 Dr. James Hambleton, University of Newcastle, Australia
 Dr. Janaka Kumara, Tokyo University of Science, Japan
 Dr. Jirayut, Suebsuk Rajamangala University of Technology Isan, Thailand
 Dr. Juhung Lee, Korea Institute of Civil Engineering and Building Technology, South Korea
 Dr. Jun Sugawara, Advision - WorleyParsons Group, Australia
 Dr. Lamia Touiti Bouebdellah, Ecole Nationale d'Ingénieurs de Gabes, Tunisia
 Dr. Luky Handoko, Universitas Atma Jaya Yogyakarta, Indonesia
 Dr. M. Mohammad Ali, California Public Utilities Commission, United States
 Dr. Marfiah Ab.Wahid, Universiti Teknologi Mara, Malaysia
 Dr. Maryam Naeimi, Semnan University, Iran
 Dr. Mehdi Mokhberi, Islamic Azad University, Shiraz, Iran
 Dr. Mohd Hairy Ibrahim, Sultan Idris Education University, Malaysia
 Dr. Neelima Satyam, International Institute of Information Technology, India
 Dr. Nor Zurairahetty Mohd Yunus, Univeristi Teknologi Malaysia, Malaysia
 Dr. Siavash Zamiran, Southern Illinois University Carbondale, United States
 Dr. Subha Vishnudas, Cochin University of Science and Technology, India
 Dr. Sunggi Jin, SK E&C, South Korea
 Dr. Sunil Pusadkar, Govt. College of Engineering, Amravati, India
 Dr. Teresa Lopez-Lara, Universidad Autonoma De Queretaro, Mexico
 Dr. Usama Juniansyah Fauzi, University of Tokyo, Japan
 Dr. Yusep Muslih Purwana, Sebelas Maret University, Indonesia
 Dr. Ana Almerich-Chulia, Universitat Politecnica de Valencia, Spain
 Dr. Khor Shing Fhan, Universiti Malaysia Perlis, Malaysia
 Dr. Afshin Asadi, International College of Auckland, New Zealand

Conference Correspondence:

Prof. Dr. Zakaria Hossain, Conference Chairman,
 Dept. of Env. Sci. & Tech., Mie University, Japan,
 E-mail: conference@geomate.org
 Tel & Fax: +81-59-231-9578

Editorial Committee and Executive Committee:

A/Prof. Dr. John V. Smith, RMIT Univ. Australia
 Prof. Zakaria Hossain, Prof. Mie University, Japan

Technical Papers

Geotechnique

ELASTIC BEHAVIOURS OF A CEMENTED LATERITIC SOIL FOR A ROAD BASE

Sawanya Dararat¹, Warat Kongkitkul², Thitikorn Posribink³ and Pornkasem Jongpradist⁴

^{1,2,4} Department of Civil Engineering, Faculty of Engineering, King Mongkut's University of Technology Thonburi, Thailand; ³ Bureau of Maintenance, Department of Rural Roads, Ministry of Transport, Thailand

ABSTRACT

Cemented soils are widely used as a base course material for flexible pavement structures in Thailand. In the current design approach, the compressive strength of cemented soil cured for 7 days is taken into account as the only design strength parameter. The strains mobilized in the layers of pavement structure are not taken account for determination of the lifetime. In order to utilize the cemented soil more efficiently, its elastic (or resilient) behaviour should be investigated and understood. In this study, a series of triaxial compression (TC) tests, in which the specimen's axial deformation was measured locally so as to reliably determine the quasi-elastic Young's modulus (E_{eq}) at various stress states, were performed on a cemented lateritic soil cured for 7 days. It was found that the E_{eq} value exhibits a hypo-elastic stress state-dependent behaviour, which can be explained by the k - θ model as for the resilient modulus (M_r) used in the mechanistic-empirical design of a pavement structure. In addition, the E_{eq} value also increases with increasing cement content (C). Thus, the E_{eq} value can be expressed as a function of k , θ and C .

Keywords: Triaxial compression, Elastic modulus, Cement, Lateritic soil, Pavement structure

INTRODUCTION

For a pavement structure, most of base layer materials are usually compacted crushed rock, which is an unbound granular type. However, pavement construction in Thailand encounters the problem of material deficiency for a long time, especially crushed rock products used for granular base layer. In many cases, the material sources are located far away from the construction site, which results in a high construction cost. In addition, the production of crushed rock aggregate involves drilling, blasting, crushing and road haulage, all of which create dust, causing environmental problems. Although the lateritic soil is local natural material abundantly found in many areas in Thailand, it is poor in engineering properties such as high plasticity, low strength, high permeability, and a tendency to retain moisture content [1]–[3]. Lateritic soils, especially fine-grained lateritic soils, are not suitable for as the road base layer. Cement stabilization with the lateritic soil has been widely employed to improve the mechanical properties [4], [5] such that it is strong enough to serve as a road base or subbase layer.

The conventional design method of pavement structure in Thailand is based on empirical rules from behaviour observed during service of the pavement structure or of the experimental sections. For the cement-treated soil, it must satisfy the minimum requirement in terms of unconfined compressive strength (q_u). Moreover, in the construction practice, the q_u value is the only strength parameter of cemented soil used for quality control. Department of

Highways (DOH), Thailand and Department of Rural Roads (DRR), Thailand specify the minimum value of q_u for soil cement base of not less than 1717 kPa. The thickness of this soil cement base, typically 20 cm, is also specified. However, this design method does not take the deformation behaviours responded from the traffic loading into consideration.

Development of more rational design methods becomes necessary. Analytical or mechanistic design has been developed and is popular among a number of pavement engineers since 1940 and 1960s, respectively. This design uses fundamental material behaviour (linear or nonlinear-elastic, plastic, viscoelastic, etc.), and theoretical model of each pavement material to predict the response of stresses, strains and deflections due to the traffic loads. Using resilient modulus (M_r) as a key parameter in the design has been widely recommended in many design guides [6]–[8]. Generally, the M_r is determined from repeated load triaxial apparatus for simulating wheel load [9]. Because the M_r is a stiffness of a material responded after many cycles of traffic loading have been applied until there is no irrecoverable deformation developed (therefore, resilient), it is significantly the same as the elastic stiffness. On the other hand, triaxial compression tests, in which small strain-amplitude cyclic loadings were applied, were performed to determine the quasi-elastic Young's modulus (E_{eq}) of geomaterial [10], [11]. In addition, it was shown that the determination of E_{eq} by triaxial compression test can be alternatively used in place of M_r [12].

This study aims to analyse the elastic modulus of

cemented lateritic soil and to report its dependency with the stress state and cement content so that a better understanding of the material can be achieved.

MATERIAL AND APPARATUS

Test Materials

A lateritic soil, which did not satisfy the requirements (i.e., gradation, plastic index, and %CBR) for use as a subbase material of ordinary pavement structure specified in DOH and DRR standards, was used in this study. This lateritic soil contains the amount of fines more than the limit indicated in the standards (finer than sieve No.200 over 20%) as shown in Fig. 1. A series of modified Proctor compaction tests (ASTM D1557) were conducted to determine the maximum dry density (MDD) and the optimum moisture content (OMC). Then, CBR tests (ASTM D1883) on specimens prepared with the water content at OMC were performed to determine %CBR for various values of dry density (ρ_d). Table 1 lists its physical and compaction properties. The %CBR at 95% of MDD is equal to 4.26%. This value is significantly lower than the minimum value specified in the standards (DH-S 205/1989 and DRR-S 202/2014) for use as subbase material (i.e., %CBR= 25%).

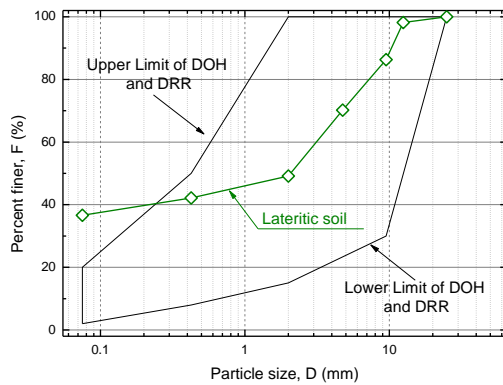


Fig. 1 Gradation characteristics of the lateritic soil in comparison with DOH and DRR standards.

Apparatus

A compression machine, consisting of a reaction frame and a precise gear loading system, was used in the present study. The loading system is driven by a computer-controlled servo-motor and is able to perform load reversal with practically no backlash, which is a very important feature for performing precise cyclic loading test [13]. By controlling the displacement to accuracy of less than 1 μ m in an

automated way, it becomes possible: i) to smoothly switch between displacement and load control loading phases and between sustained loading or stress relaxation stage and a constant strain rate loading or unloading phases; ii) to apply monotonic loading with a very precise controlled displacement rate; and iii) to apply very small amplitude unload/reload cycles to evaluate the elastic properties of test material during otherwise constant strain rate monotonic loading. This gear loading system has a capacity of 50 kN.

Table 1. Physical and index properties of the lateritic soil

Properties	Lateritic soil
Specific gravity, G_s	2.89
Liquid limit, LL (%)	31.3
Plastic limit, PI (%)	14.7
Optimum water content, OMC (%) [*]	10.79
Maximum dry density, MMD (g/cm ³) [*]	2.099
CBR at 95% of MMD (%)	4.26

^{*}Modified Proctor compaction test (ASTM D1557)

TEST METHODS

Specimen Preparation

The lateritic soil has been treated with Portland cement type I to improve the mechanical performance for using as a material for base in the pavement structure. The cement content (C) was varied at 1, 2%, 3%, 4%, and 5% by dry weight of the lateritic soil, and then after being compacting in mould, the specimens were cured for 7 days. This curing period is for verification in the construction process, also specified in the DOH and DRR standards (DH-S 204/1990 and DRR-S 244/2013). The cement-treated lateritic soil specimens were wrapped with the plastic film in order to avoid loss of moisture after disassembling the mould and were kept in an incubator for 7 days. For all the tests, the specimens are cylindrical. They are 150 mm high and 70 mm in diameter. Specimens were prepared to achieve the dry density equal to maximum dry density (MDD). The values of water content and wet density of a specimen were controlled not to vary by more than $\pm 1\%$ of OMC and $\pm 3\%$ of the target value, respectively.

Test Procedure

A specimen is set on the pedestal and a membrane is put on it. An axial load cell used in triaxial compression (TC) tests performed in the present study was connected in series with the cap inside the

chamber so that its reading was free from friction that may be mobilised at the bearing house on top of the chamber. Prior to mould disassembly, suction of -20 kPa was temporarily applied to the specimen via the drainage lines connected to the cap and the pedestal so that the membrane was adhered firmly with the specimen's side surface. Then, a pair of local deformation transducers (LDTs) were installed on the pseudo-hinges firmly glued on the membrane at the opposite diametrical sides, and three clip gauges (CGs) were placed at the height of 1/5, 1/2 and 4/5 of the specimen's initial height, as shown in Fig. 2. These LDTs and CGs were calibrated with a micrometre head mounted with a cross slide roller table. In this paper, the axial strain and the radial strain in TC tests are the averages of readings from two LDTs and three CGs, respectively. In addition, the specimen's axial deformation was also measured externally with a LVDT, which was necessary when the measuring range of LDT was exceeded.

The TC test was performed by applying small strain-amplitude cyclic loadings (CLs) at various $q:p$ stress states to determine quasi-elastic Young's modulus (E_{eq}). In these TC tests, the E_{eq} value were determined from local axial deformation measured by a pair of local deformation transducers (LDTs, [14]), so the E_{eq} is free from bedding error. These $q:p$ stress states are in accordance with AASHTO T307-99 standard [9]. The loading pattern for the TC was presented by Dararat et al. [12]. That is, the sample is first isotropically confined with different values of cell pressure (σ_3). Then it is continuous monotonic loading (ML) sheared by axial compression to a target deviator stress (q) value, while the cell pressure is kept constant to achieve a target $q:p$ stress state. After that, sustained loading (SL) is performed for 30 min, holding the stress state at the target, while the sample is allowed to deform (i.e., creep). Next, cyclic loadings (CL), of which the stress-amplitude is equal to 30 kPa, are performed for 10 cycles for evaluating the E_{eq} value. Then, ML shearing is performed to the next target q value, at which 30-min SL and then CLs for 10 cycles are repeated. After finishing CLs at the largest target q value, q is reduced to zero, and then the cell pressure is increased to the next target value under isotropic condition. Then, similar shearing processes as of the first target cell pressure are repeated. In this TC test, the specimen's response was measured at 15 $q:p$ stress states by varying five different confining pressures and deviator stress. More details of this TC apparatus and test procedures can be found at Dararat et al. [12].

TEST METHODS

Stress-Strain Relationship

As the elastic modulus is the parameter that is of interest in this study, the behaviours at small strain

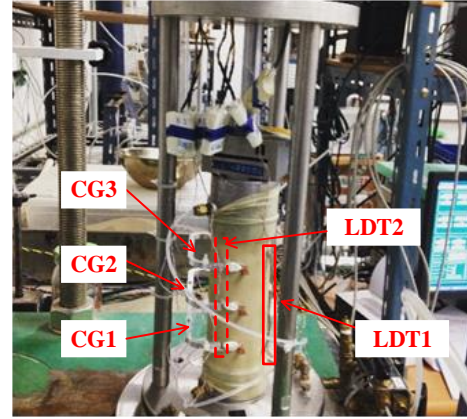


Fig. 2 Installations of LDTs and CGs for measurements of axial and radial deformations free from any bedding errors.

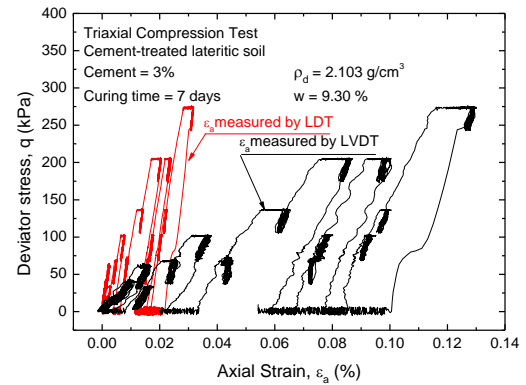


Fig. 3 Relationships between deviator stress (q) and axial strain (ϵ_a) obtained from small-strain amplitude cyclic loading test on cement-treated lateritic soil with $C = 3\%$.

level must be reliably measured, and therefore the local strain measurement was employed by using LDTs. Figure 3 shows the relationship between deviator stress (q) and axial strain (ϵ_a) from the TC test employing continuous monotonic loading test, intervened by 30-min sustained loadings, after which ten small-strain amplitude unload-reload cycles were performed, with a constant strain rate of 0.0277 %/min, on lateritic soil treated with 3% cement. In addition, Fig. 4 shows a zoomed-up portion of Fig. 3, and only axial strain measured by using a pair of LDTs ($\epsilon_{a,LDT}$) is presented.

These figures show that at the same deviator stress (q) the value of axial strain (ϵ_a) measured by LVDT is always greater than that measured by a pair of LDTs, which is due to the measuring errors consisting of system compliances and bedding errors. The axial strain measured by using a pair of LDTs ($\epsilon_{a,LDT}$), are found to give a sound basis for axial strains measurement at small strains. Moreover, from Fig. 4,

it can be readily seen that the q - $\varepsilon_{a,LDT}$ loops during the respective unload-reload cycles are very small, which are consistent with the fact that the residual axial strain developed by these cycles is very small. Therefore, the behaviour during small unload-reload cycles is highly linear-elastic.

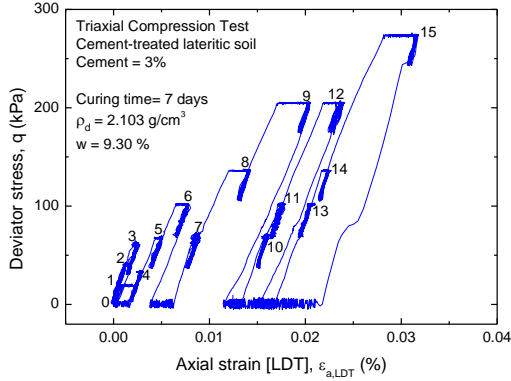


Fig. 4 Close-up of q - $\varepsilon_{a,LDT}$ relationship obtained from small-strain amplitude cyclic loading test on cement-treated lateritic soil with $C = 3\%$.

Quasi-Elastic Young's Modulus (E_{eq})

Figure 5 shows the unloading q - $\varepsilon_{a,LDT}$ branches for the loop nos. 6-10, by small unload-reload cycles at the sequence no. 5, at which $q = 68.9$ kPa and $p = 57.5$ kPa, obtained from the TC tests on lateritic soil treated with cements with the cement contents of 1%, 2%, 3%, 4%, and 5%, respectively. It is obvious that the q - $\varepsilon_{a,LDT}$ branches exhibit highly linear-elastic behaviour for the whole vertical deviator stress amplitude (30 kPa). Thus, the E_{eq} was determined

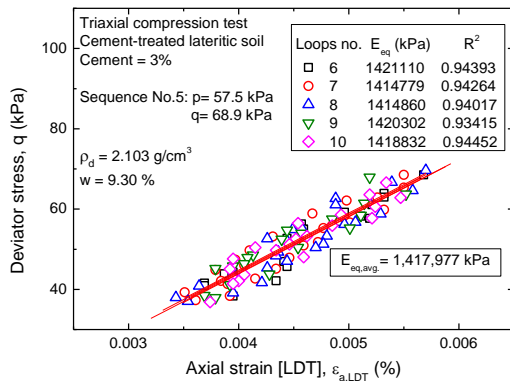


Fig. 5 Relationships between deviator stress (q) and axial strain measured by LDTs ($\varepsilon_{a,LDT}$) during unloading branches to determine the quasi-elastic Young's modulus (E_{eq}) on lateritic soil treated with 3% cement.

from a linear relation fit to the unloading branches presented in Fig. 5. Each E_{eq} value can be defined with a degree of confidence, as confirmed by the values of coefficient of determination (R^2 -value) shown in the figure. For each sample, the E_{eq} value is mostly constant among loop nos. 6-10, implying that the behaviour during these unloading branches is significantly linear-elastic. The E_{eq} at the other $q:p$ stress states (shown in Fig. 4) were determined in the same way as of Fig. 5. It is worth noting that as axial strain value is measured locally, and hence free from bedding error, the E_{eq} value defined as shown in Fig. 5 is of the true value.

Figure 6 shows relationships between the average E_{eq} and the bulk stress (θ) in a full-log plot for lateritic soil treated with cement with cement contents of 1%, 2%, 3%, 4%, and 5%. The θ value is normalised by the reference pressure (P_a) of 100 kPa. The E_{eq} value increases significantly with an increase in the bulk stress ratio (θ/P_a) value. That is, the E_{eq} of cement-treated lateritic soil is also of hypo-elastic type. Dependency of E_{eq} with θ can be mathematically expressed by Eq. 1.

$$E_{eq} = E_0 \left(\frac{\theta}{P_a} \right)^m \quad (1)$$

where E_0 is the value of E_{eq} when $\theta = P_a = 100$ kPa; and m is constant. The lines were best-fitted to the test data points shown in Fig. 6(a). The values of E_0 and m for respective test samples are shown in Fig. 6(a). The functional forms of E_{eq} in Eq. 1 is similar to the k -Theta (k - θ) model [15].

Considering at the m value, it could be seen that the m values obtained from test samples with different cement contents are quite similar. This implies that the characteristics of increasing E_{eq} with the bulk stress for different C values are very similar. For this reason, averaging the m values was attempted and the averaged m value (m_{avg}) of 0.271 was obtained with an exemption that the value of sample for cement content equal to 1% was excluded. Then, regression analysis was re-performed for different cement content values using Eq. 1, but with the fixed value of $m = m_{avg}$ as shown in Fig. 6(b). The new values of E_0 and m determined from the regression analysis with the fixed value of $m = m_{avg}$ are also shown in Fig. 6(b). Although the data are scattered to some extent, especially for the sample with 1% cement as seen from Fig. 6(b), the E_{eq} value can be defined with a degree of confidence, as confirmed by the coefficient of determination (R^2 -value) value shown in the figure.

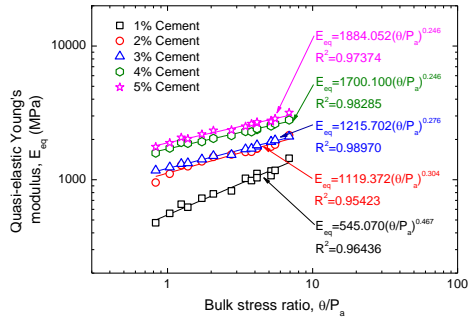
The E_0 values by regression analysis with the common average m value are plotted against the C value in full-logarithmic scale as shown in Fig. 7. It seems that the E_0 is rather a function of C . Relationship between E_0 and C can be fitted using the mathematical form expressed in Eq. 2.

$$E_0 = E_{0,C} C^n \quad (2)$$

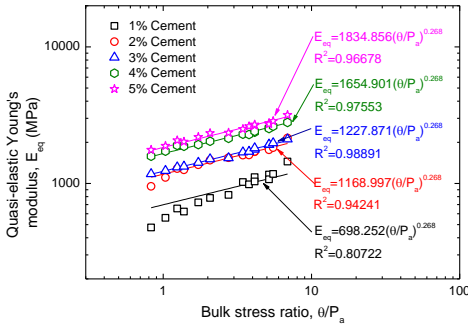
where $E_{0,C}$ is the value of E_0 when $C=1\%$ (equal to 764.309 MPa); n is constant (equal to 0.582). The values of $E_{0,C}$ and n for the cement-treated lateritic soil for different cement contents are shown in Fig. 7. By combining Eq. 1 with Eq. 2, E_{eq} of cement-treated lateritic soil can be mathematically expressed as follows.

$$E_{eq} = E_{0,C} C^n \left(\frac{\theta}{P_a} \right)^m \quad (3)$$

where $E_{0,C}$ is the value of E_0 when $C=1\%$ (equal to 716.519 MPa); n is constant (equal to 0.582); and P_a is the reference pressure (equal to 100 kPa). Fig. 8 shows the comparison between predicted (by substituting the θ and C into Eq. 3) and the measured E_{eq} values for cement-treated lateritic soil. It can be seen that Eq. 3 gives very satisfactory prediction results as with a good agreement shown in Fig. 8.



(a)



(b)

Fig. 6 Relationships between quasi-elastic Young's modulus (E_{eq}) and bulk stress ratio (θ/P_a) for lateritic soil treated with various cement contents using: (a) respective m ; and (b) common average m .

CONCLUSIONS

From the test results and analyses performed in this study, the following conclusions can be derived:

- 1) The compressive strength and stiffness of cement-treated lateritic soil significantly increase with an increase in the cement content (C).
- 2) The triaxial compression test (TC) employing by the small strain-amplitude cyclic loadings can be used to evaluate the true quasi-elastic Young's modulus (E_{eq}) for cement treated lateritic soil by using the local displacement transducers (LDTs) to locally measure the axial strain. The E_{eq} value of test samples exhibited significant dependency on the bulk stress (θ) and the C value.
- 3) The equation to estimate E_{eq} value from this study can be used as the M_r in the solution to design and analysis of pavement structure.

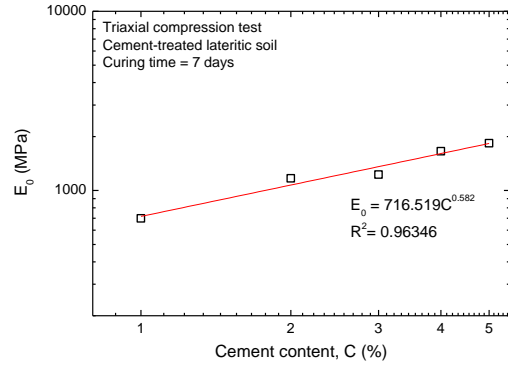


Fig. 7 Dependency of the E_0 value with the cement content (C).

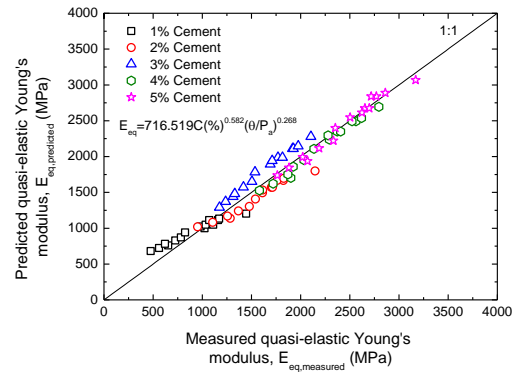


Fig. 8 Comparison between the predicted and measured values of E_{eq} .

ACKNOWLEDGMENTS

The authors are grateful to Thailand Research Fund (TRF) and King Mongkut's University of Technology Thonburi (KMUTT) for the financial support granted to this research via the Royal Golden Jubilee Ph.D. Program under the contract number PHD/0187/2556.

REFERENCES

- [1] Gidigas, M. (Ed.), *Laterite soil engineering: pedogenesis and engineering principles*, Vol.9, Amsterdam, Netherlands, Elsevier, 2012.
- [2] Eluozo, S. N. and Nwaobakata, C., Predictive models to determine the behavior of plastic and liquid limit of lateritic soil for road construction at Egbema: Imo state of Nigeria, *International Journal of Engineering & Technology*, Vol. 2, No. 1, 2013, p. 25.
- [3] Lawane, A., Vinai, R., Pantet, A., Thomassin, J. H. and Messan, A., Hygrothermal features of laterite dimension stones for sub-Saharan residential building construction, *Journal of Materials in Civil Engineering*, Vol. 26, No. 7, 2014.
- [4] Millogo, Y., Hajjaji, M., Ouedraogo, R. and Gomina, M., Cement-lateritic gravels mixtures: Microstructure and strength characteristics, *Construction and Building Materials*, Vol. 22, No. 10, 2008, pp. 2078–2086.
- [5] Oyediran, I. A. and Kalejaiye, M., Effect of increasing cement content on strength and compaction parameters of some lateritic soils from southwestern Nigeria, *Electronic Journal of Geotechnical Engineering*, Vol. 16, 2011, pp. 1501–1514.
- [6] AASHTO, *Mechanistic-Empirical Pavement design guide: A Manual of Practice*, Washington, D.C., AASHTO, 2008.
- [7] ARA, *Guide for mechanistic-empirical design of new and rehabilitated pavement structures*, Final report, NCHRP Project 1-37A, Washington, D.C., Transportation Research Board of the National Academies, 2004.
- [8] Austroads, *Pavement design - A guide to the structural design of road pavements*, Sydney, Austroads, 2004.
- [9] AASHTO T307-99, *Standard method of test for determining the resilient modulus of soil and aggregate materials*, Washington, D.C., AASHTO, 2012.
- [10] Hoque, E. and Tatsuoka, F., Anisotropy in elastic deformation of granular materials, *Soils and Foundations*, Vol. 38, No. 1, 1998, pp. 163–179.
- [11] Kongkitkul, W., Musika, N., Tongnuapad, C., Jongpradist, P. and Youwai, S., Anisotropy in compressive strength and elastic stiffness of normal and polymer-modified asphalts, *Soils and Foundations*, Vol. 54, No. 2, 2014, pp. 94–108.
- [12] Dararat, S., Kongkitkul, W., Arangjelovski, G. and Ling, H.I., Estimation of stress state-dependent elastic modulus of pavement structure materials using one-dimensional loading test, *Road Materials and Pavement Design*, 2019. (Published online: 27 May 2019)
- [13] Santucci de Magistris, F., Koseki, J., Amaya, M., Hamaya, S., Sato, T. and Tatsuoka, F., A triaxial testing system to evaluate stress-strain behaviour of soils for wide range of strain and strain rate, *Geotechnical Testing Journal*, Vol. 22, No. 1, 1999, pp. 44–6.
- [14] Goto, S., Tatsuoka, F., Shibuya, S., Kim, Y.-S. and Sato, T., A simple gauge for local small strain measurements in the laboratory, *Soils and Foundations*, Vol. 31, No. 1, 1991, pp. 169–180.
- [15] Hicks, R.G. and Monismith, C.L., Factors influencing the resilient response of granular materials, *Highway Research Record*, Vol. 345, 1971, pp. 15–31.

INFLUENCES OF SEEPAGE FLOW HISTORIES ON DETERIORATION WITHIN EMBANKMENTS

Koji Nakashima¹ and Katsuyuki Kawai¹

¹Department of Civil and Environmental Engineering, Kindai University, Japan

ABSTRACT

Embankment structures are important to protect against flooding damage. Suffusion, in which fine particles within the soil are transported and washed away following the seepage flow, intensifies the instability of embankment structures. Therefore, it is possible that some embankment structures that repeatedly experienced flooding and rainfall penetration have been deteriorated. However, there is little research investigating the relation between seepage flow histories and deterioration within the embankments. In this study, small-scale modeling tests duplicating a river levee were conducted under different seepage flow histories: (i) short term-critical ground water level, (ii) continuous-high ground water level and (iii) repeated-high ground water level. The work in this paper investigates changes in “drainage flow rate”, “height of ground water level” and “particle size distribution” during the seepage tests, and evaluates the effects of seepage flow histories on them. Soils gradually showed lower permeability under the first seepage experience in each cases. In the case of relatively longer flooding duration, the drainage flow rate is gradually increased. Fine particles were eroded, regardless of the seepage flow histories; “the number of fluctuations” and “height” of ground water level could particularly be a trigger of suffusion.

Keywords: Seepage, Embankment, Suffusion, Particle size distribution

1. INTRODUCTION

Soils are often used for the construction of embankment structures, such as levees and earth dams, and they protect neighborhoods from flooding.

In recent years in Japan, increased daily precipitation tends to accompany global warming, which frequently causes flooding events and an embankment failure. For example, a river levee along the Yabe River failed following heavy rains in Northern Kyusyu, in 2012. A piping development was assumed as a cause of the failure (Zhang and Maeda, 2015; Saito et al., 2015; Ueno et al., 2017). In 2015, a river levee along the Kinu River failed due to overtopping and seepage of water during heavy rain (Yasuda et al., 2016). Furthermore, in 2017, many embankment structures were failed due to flooding, such as a river levee along the Oda River.

Most embankments are constructed from the

various natural soil materials extracted from the local area, and they are repeatedly elevated using additional material. Therefore, the embankment is assumed to have uncertain homogeneity in terms of such as particle properties, density, permeability and strength. Suffusion is one of the causes of internal erosion, in which fine particles within the soils are transported and washed away following the seepage flow from the surface of the embankment. Figure 1 illustrates the deterioration problems of concern for a river levee under seepage. Once fine particles wash away, the area could become a water path for localized flow. Moreover, clogging due to transported fine particles increases the possibility of water level rises. High ground water levels raised during flooding events due to conditions such as continuous rain or torrential rain intensify the occurrence of suffusion, whereby the deterioration of embankment may lead to devastating failure. Hence, it is thought that there are many working embankment structures which have been progressively deteriorating and have been having a potential for failure.

Various laboratory experiments and analytical studies have previously been performed regarding internal erosion, and they have revealed the causes of soils instability, such as particle properties, hydraulic conditions and stress conditions (Horikoshi and Takahashi, 2015). However, there is very little research investigating the relation between seepage flow history and deterioration within the embankments due to suffusion.

In this research, small-scale modeling tests duplicating a river levee were conducted under different seepage flow histories. For the test conditions, different seepage histories were applied to investigate their influences on the deterioration of

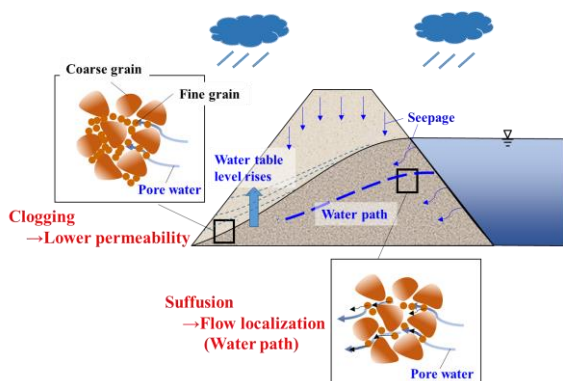


Fig. 1 Deterioration problems of concern for
a river levee under seepage

soils within the embankment. As an evaluation of deterioration, the work in this paper focuses on changes in “drainage flow rate”, “height of ground water level” and “particle size distribution” during the seepage flow tests.

2. EXPERIMENTAL STUDY

2.1 Experimental Material

The experimental material, which incorporated fine and coarse grain fractions, was prepared by mixing No.4 and No.8 silica sands. The combined particle size distribution curves are shown in Figure 2. Kenny and Lau (1985) proposed the criterion that classifies the stability of soils against internal erosion. The criterion can be defined by two parameters, H and F , which are obtained from particle size distribution curve, as illustrated in Figure 3. According to the criterion, the experimental material has $(H/F)_{\min}$ of 0.55 (<1.0), which can be interpreted as having a potential for instability due to internal erosion, as shown in Figure 4. The material properties are also presented in Table 1.

Constant head permeability tests were conducted for 3 days in advance. Figure 5 shows the fluctuation of the coefficient of permeability k during the permeability test. For comparison, the result of a stable soil mixture with a $(H/F)_{\min}$ of 1.84 (>1.3) is also shown in the figure. It is worth mentioning that decreasing of the coefficient of permeability can be observed.

2.2 Model Preparation

Figure 6 illustrates details of the model configuration. The embankment model was constructed by compaction. A 0.075mm mesh filter was fixed in a perforated metal plate to allow the washing away of fine particles. The plate was then installed into the test box. Water was added to the test material to a moisture content of $w=10\%$, and unsaturated soil material was prepared. Five layers of the material were gently compacted into the test box at a relative density of $D_r=80\%$. After compaction, the excess materials were then excavated using pallet knives, and the embankment model was sculpted. The embankment model had the following geometry: height of 185mm, crest width of 60mm, base width of 330mm, and a slope of 1:2. Three manometers were equipped to the bottom of the base materials through the test box. Figure 7 shows an overview of the test equipment. An observation camera used to capture the pictures for digital image correlation (DIC) analysis was set in front of the model.

2.3 Test Procedures

The seepage tests were conducted by supplying

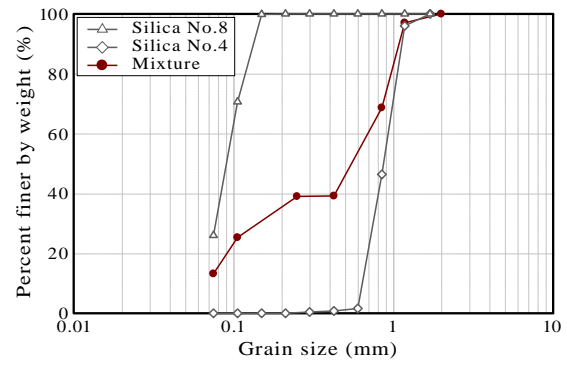


Fig. 2 Particle size distribution curve

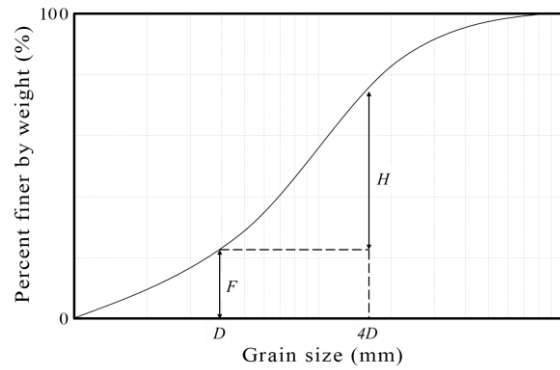


Fig. 3 Definition of parameters H and F

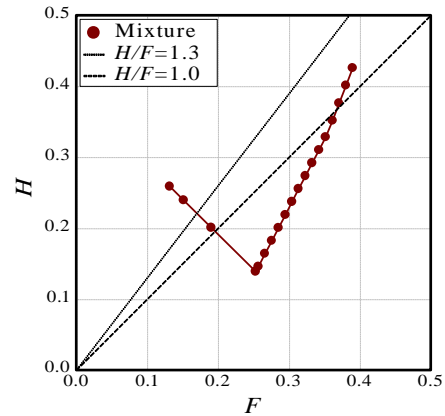


Fig. 4 H/F relation

Table. 1 Material properties

Specific gravity of soil particles G_s	Fines content F_c (%)	Mean diameter D_{50} (mm)	Uniformity coefficient U_c	$(H/F)_{\min}$
2.67	13.2	0.58	16.7	0.55

water from the back of the embankment, as shown in Figure 6. Water circulation using a pump enabled a constant water level at the upper tank and the back of the embankment.

In this study, three seepage histories were set as the test conditions, as shown in Figure 8. Case 1 is the

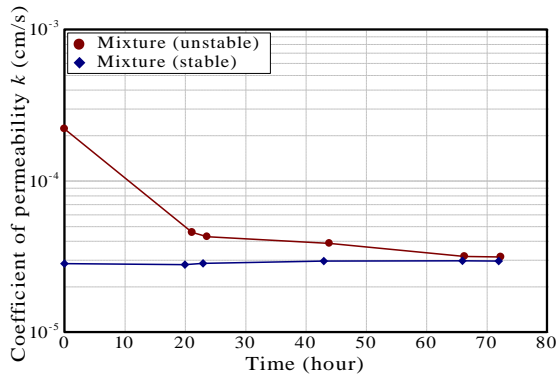


Fig. 5 Fluctuation of coefficient of permeability

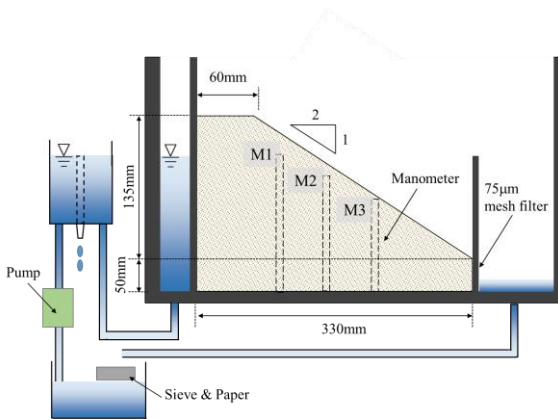


Fig. 6 Model configuration

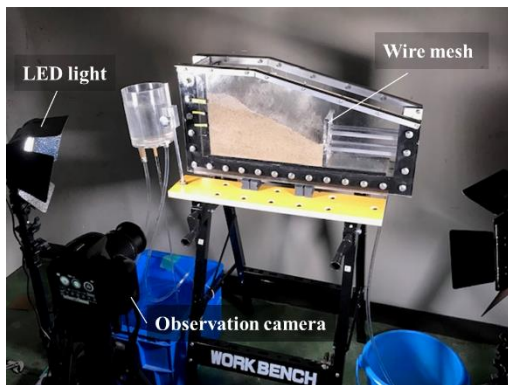


Fig. 7 Overview of test equipment

condition which simulates short term-critical ground water level (90% of the embankment height) caused by concentrated heavy rain. Case 2 simulates continuous-high ground water level (70% of the embankment height), such as seen in the rainy season. Case 3 simulates repeated-high ground water level rises (70% of the embankment height). In each cases, a ground water level at 50% of the embankment height is assumed as the usual groundwater, and

	Top water level: percentage of embankment height (Duration)			
Case 1	50% (24h)	→ 90% (6h)	→ 50% (24h)	
Case 2	50% (24h)	→ 70% (120h)		
Case 3	50% (24h)	→ 70% (24h)	→ 50% (48h)	→ 70% (48h)

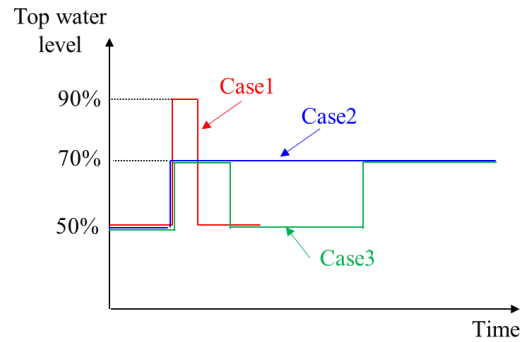


Fig. 8 Seepage test condition

seepage for 24 hours was previously carried out.

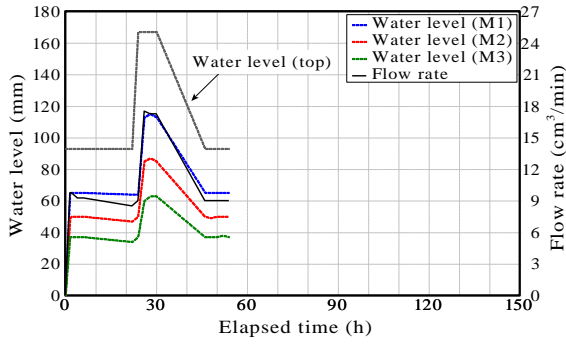
Leaking water from the toe of the embankment model was collected, and the flow rates were calculated. The water level within the embankment was investigated by measuring the manometer's water level.

After the seepage tests, the soil materials at different locations were sampled, and sieve analysis was then conducted.

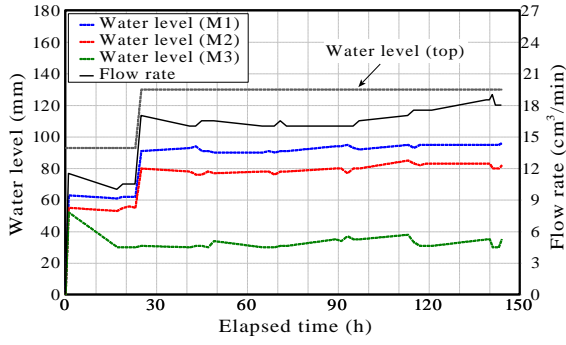
3. TEST RESULTS

3.1 Ground Water Table and Flow Rate

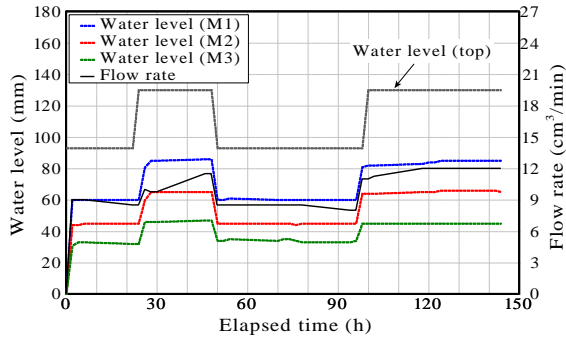
Figure 9 shows the results of the ground water level for each manometers and drainage flow rate during the seepage tests. As seen in the figure, the result of the first 24 hours duration, when the top water level was 50% of the embankment height, shows a gradual decrease of drainage flow rate in each tests. A decreasing a magnitude of the coefficient of permeability was confirmed from the constant permeability test, as mentioned before. It is more likely that soil structures easily change, and that some areas of the embankment could be clogged due to fine particle transportation following seepage flow in the first seepage experience. The permeability of the soils, therefore, tends to decrease. The embankment model was compacted in the same manner, nevertheless, the decreasing trends of flow rate are different for each cases. Figure 10 shows the displacement contours for first 24 hours. Matlab and GeoPIV (White et al., 2003) were used to compute the DIC analysis. For Case 2, larger displacement can be seen compared with other cases. This result especially exhibits compaction of the embankment at



(a) Case 1



(b) Case 2

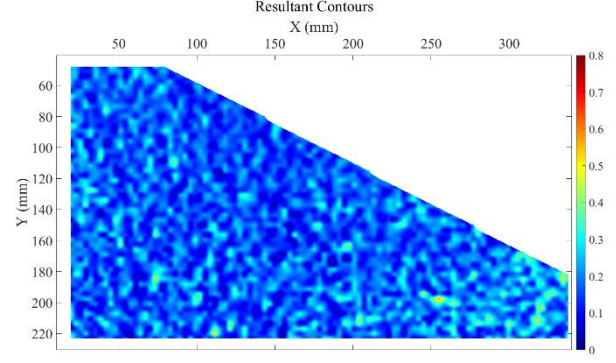


(c) Case 3

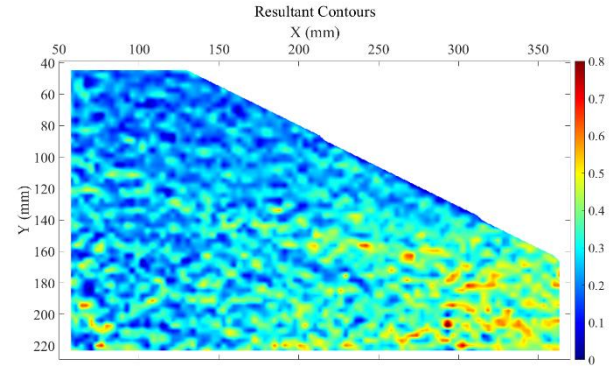
Fig. 9 Time histories of ground water level and drainage flow rate

the toe. It is likely that clogging caused by the compression at the toe induced the decreasing permeability. It is assumed that differences in deformation are caused by non-uniformity in the model construction. However, this clearly implies that non-uniformity during construction of an embankment structure greatly affects permeability and deformation behavior.

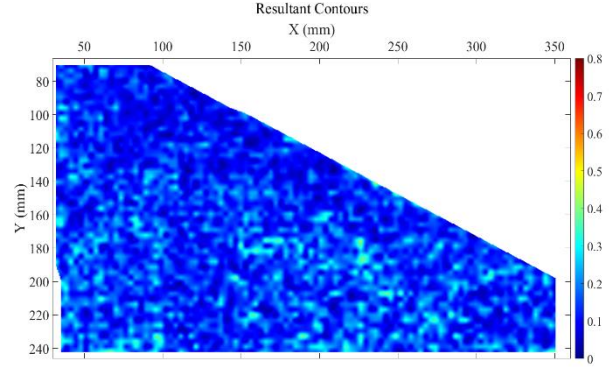
The results of Case 2 and Case 3 show that the manometer water levels respond in an accordance with flooding; whereas, the drainage flow rate gradually increases after flooding. This is probably because a water path gradually formed, and water was locally transported. After the second flooding event for Case 2, the gradient of increasing drainage flow rate is flatter, compared with the first flooding. For Case 1, it is assumed that a delay of increasing flow



(a) Case 1



(b) Case 2



(c) Case 3

Fig. 10 Displacement contours for first 24h

rate cannot be seen because the flooding duration is relatively shorter than those of the other two cases. Devastating failure was not observed in any of the cases.

The expended energy E_{flow} , which is the time integration of the instantaneous power dissipated by the water seepage for the test duration, is represented as follows (Marot et al., 2016);

$$E_{\text{flow}}(t) = \sum_0^t Q \gamma_w \Delta h \Delta t \quad (1)$$

where, Q (m^3/s) is the flow rate of water; γ_w (kN/m^2) is the unit weight of water; Δh is the difference of water level between the upstream section and the downstream section; and Δt is the time for a certain duration. In this study, Δh is defined as the difference

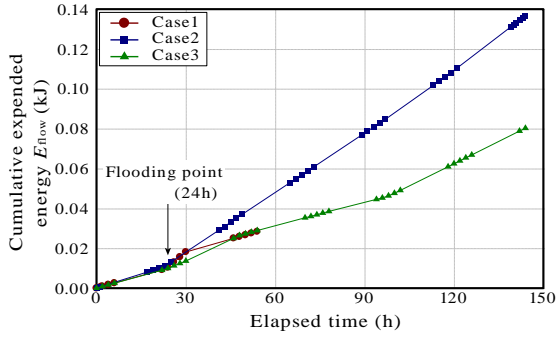


Fig. 11 Time histories of cumulative expended energy

between the top water level and the water level of the toe h_{toe} . h_{toe} can be calculated by Eq.(2);

$$h_{toe} = \sqrt{l^2 + h_{top}^2} - l \quad (2)$$

where, h_{top} is the top water level and l is the base width. Figure 11 represents the time histories of cumulative expended energy during the seepage tests. As shown by the result of the first 24 hours duration, the expended energy of each test is almost the same. The cumulative expended energy at the terminate point of Case 1 agrees with the magnitude of Case 3 at that time. Larger cumulative expended energy at the terminate point can be seen in Case 2 compared with the other cases.

3.2 Particle Size Distribution

The tested materials were extracted at different locations in the embankment model, as illustrated in Figure 12. Figure 13 shows the particle size distribution curves after the seepage tests. It can be observed that finer particles were washed away in each case. A decreasing rate of 0.075mm percentage by weight after the test is summarized in table 2. Assuming that the decreasing rate corresponds to the magnitude of suffusion, in Case 1 and Case 3, it is confirmed that greater fine particles are washed away compared with Case 2. A correlation between the location where the materials were extracted and the decreasing rate was not observed.

3.3 Discussion

It was expected that one of the reason why the flow rate gradually increases after flooding is due to the formation water paths following the transportation and washing away of fines. Especially in cases where the ground water level repeatedly changes, such as in Case 3, structural changes are possible due to the fluctuation of pore water pressure within the soil, whereby the permeable area regularly changes. As a result, suffusion is significantly observed in Case 3. In addition, in cases where the

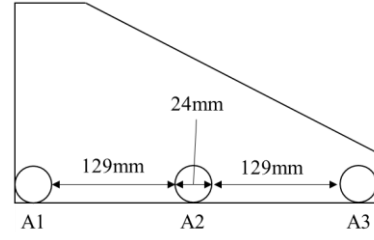
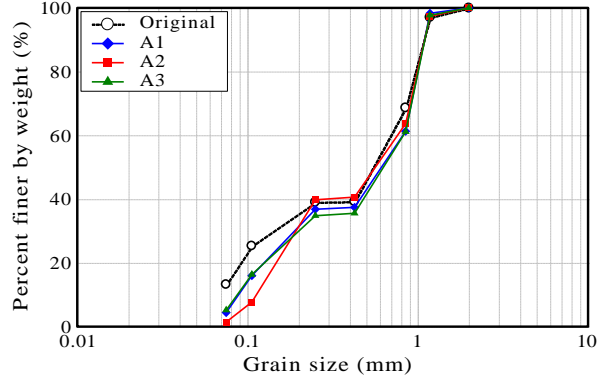
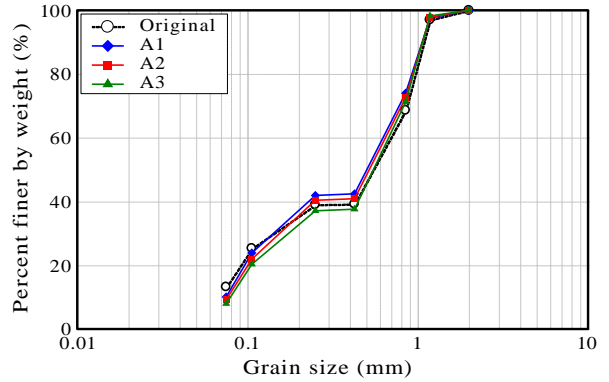


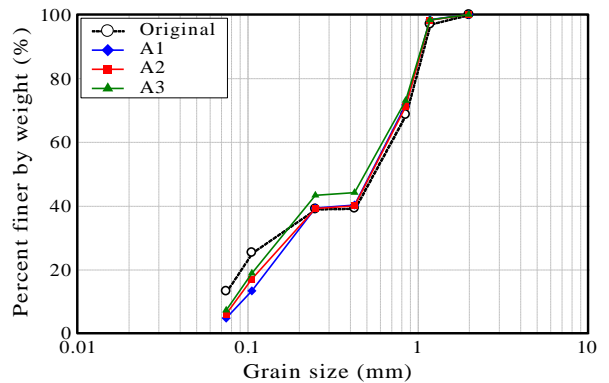
Fig. 12 Sampled location



(a) Case 1



(b) Case 2



(c) Case 3

Fig. 13 Particle size distribution after test

Table. 2 Decreasing rate of 0.075mm particles

	A1	A2	A3
Case 1	57%	90%	67%
Case 2	39%	30%	23%
Case 3	79%	72%	81%

ground water level rapidly rises, such as Case 1, it was expected that the pore water pressure would vary rapidly, and hence the possibility of suffusion would increase.

According to the one-dimensional seepage flow tests of the elemental specimens, the mass of fine particles that wash away, generally increases in accordance with the magnitude of expended energy (Marot et al., 2016; Le et al., 2018). As observed in Fig.10 and Table.2, the results in this study do not follow such trends. This is probably because the compression of the embankment model occurred with the first seepage, and the non-permeable area was maintained after flooding. Additionally, wherever there is less fluctuation of ground water levels, such as in Case 2, the flow of water becomes locally concentrated in the same area, whereby less fine particle loss can be observed against greater drainage flow rate.

It was expected that “the number of fluctuations” and “height” of ground water level could certainly be a trigger of suffusion. However, the event of fine particles washing away has less effects on the deformation of the embankment. As seen in the DIC results, the rising of the ground water table due to the clogging of the embankment toe intensifies the possibility of deformation.

4. CONCLUSION

In this paper, small-scale modeling tests duplicating a river levee were carried out under different seepage flow histories. The test material for constructing the embankment model was prepared based on the Kenny’s criterion. The following conclusions were drawn;

- 1) Whenever soils experience the first seepage, permeability tends to decrease. It is interpreted that the soil structure easily changes and that some areas could become clogged due to fine particle transportation following seepage flow.
- 2) In the case of respectively longer flooding duration, it is assumed that a water path could gradually form, and water is locally transported, whereby the flow rate gradually increases.

3) Loss of finer particles could be observed in each case, and the magnitude of the suffusion was evaluated by a decreasing rate of 0.075mm particles. The relation between the cumulative expended energy during the seepage tests and the loss of fine particles could not be confirmed.

The results indicate that “the number of fluctuations” and “height” of ground water level could certainly be a trigger of suffusion. However, the rising of the ground water table raising due to clogging of the embankment toe has larger effects on the possibility of deformation.

REFERENCES

- [1] Horikoshi, K., Takahashi, A., Suffusion-induced change in spatial distribution of fine fractions in embankment subjected to seepage flow, *Soils and Foundations*, 55(5), 2015, pp.1293-1304.
- [2] Kenny, T.C., Lau, D., Internal instability of granular filters. *Canadian Geotechnical Journal*, 22(2), 1985, pp.215-225.
- [3] Le, V.Z., Marot, D., Rochim, A., Bendahmane, F., Nguyen, H., Suffusion susceptibility investigation by energy-based method and statistical analysis, *Canadian Geotechnical Journal*, 55, 2018, pp.57-68.
- [4] Marot, D., Rochim, A., Nguyen, H.H., Bendahmane, F., Sibille, L., Assessing the susceptibility of gap-graded soils to internal erosion: proposition of a new experimental methodology, *Natural Hazards*, 83, 2016, pp.365-388.
- [5] Saito, H., Maeda, K., Izumi, N., Li, Z., Water leak-piping behaviors of river levees with different foundation ground properties under loading duration of high water level, *Advances in River Engineering*, 21, 2015, pp.349-354 (in Japanese).
- [6] Ueno, T., Sasaoka, S., Mori, H., Nakamura, K., Fukushima, M., Suwa, Y., Analysis of soil condition related to piping development in river levee based on model experiment, *Advances in River Engineering*, 23, 2017, pp.405-410 (in Japanese).
- [7] White, D., Take, W., Bolton, M., Soil Deformation Measurement Using Particle Image Velocimetry (PIV) and Photogrammetry, *Géotechnique*, 53(7), 2003, pp.619-631.
- [8] Yasuda, S., Shimizu, Y., Deguchi, K., Investigation of the mechanism of the 2015 failure of a dike on Kinu River, *Soils and Foundations*, 56(4), 2016, pp.581-592.
- [9] Zhang, W. and Maeda, K., SPH simulations for slope and levee failure under heavy rainfall considering the effect of air phase, *Computer Methods and Recent Advances in Geomechanics*, 2015, pp.1465-1470.

RELATIONSHIP BETWEEN THE PRODUCTION CONDITIONS OF SOLIDIFIED CRUSHED SOIL AND THE PHYSICAL PROPERTIES AND STRENGTH OF THE PRODUCT

Atsuko Sato¹ and Osamu Hatakeyama¹

¹ Civil Engineering Research Institute for Cold Region Public Works Research Institute

ABSTRACT

When surplus soil generated in construction is too soft for reuse as a construction material, one method for improving it is to add a solidifier. By this method expect to achieve improvement; however, an embankment constructed using such improved soil may have a strength that exceeds the required value. As a method for controlling the development of excess strength, mixing a solidifier into the soft soil and then crushing the mixture during solidification and investigated the physical properties and strength of the resulting soil. Constructed a full-scale embankment using crushed solidified soil on soft ground and investigated the deformation of that embankment. The result found that it was possible to control the increase in the strength of the solidified soil by crushing it and that an embankment constructed on soft ground from crushed solidified soil deformed following the deformation of the soft ground.

Keywords: Solidified crushed soil, Production conditions, Physical properties, Strength

INTRODUCTION

Soil that is generated during road and river excavation is too soft for reuse in embankment construction can be improved by solidification using solidifiers such as cement or lime [1]. Be able to improve soft soil by using this method; however, the strength of an embankment constructed using this type of improved soil may exceed the required value. If the strength of an embankment constructed using the solidified soil is exceedingly high due to solidification, it may be difficult to re-excavate the embankment when installing median strips or guardrails. High strength embankments may fail when they are constructed on soft ground and are not able to accommodate the behavior of the soft ground. For these reasons, the crushed solidified soil was investigated, which is produced by mixing a solidifier in soft soil and then crushing it in the middle of the solidification, as a material whose strength development is possible to control even when a solidifier is mixed [2] [3]. Also the strength and compaction characteristics of the solidified crushed soil affect the type, amount of the solidifier, and the leaving time from the mixing of the solidified material to the crushing. Investigated the physical properties and strength of crushed solidified soil produced using volcanic ash depending on the amount of solidifier, time for leaving still before crushing, and the curing time. Furthermore, two full-scale embankments were constructed on soft ground and investigated their deformation. The original soil for these embankments was clay. One embankment was constructed using solidified soil, and the other was constructed using the crushed solidified soil. This

paper summarizes the investigation results.

CRUSHED SOLIDIFIED SOIL

The crushed solidified soil is a soil material produced by mixing a solidifier in an original soil that requires solidification and crushing it after a certain length of time. The crushed solidified soil can be used in construction that involves compaction. The strength characteristics of the compacted crushed solidified soil differ depending on the time between solidification and crushing. When the time before crushing is short, the solidification process has not been completed, and the constructability is inferior because the strength development is low at compaction. The solidification ability of this type of crushed solidified soil is still maintained after compaction. Therefore, the strength develops further after curing for a certain length of time, during which the solidification reaction progresses. When the time before crushing is long, crushing is done for soil that has already developed a certain degree of strength; therefore, the constructability is good. The residual ability to develop solidification in the crushed soil is smaller than that of the soil with a shorter time before crushing, and the increase in the strength after compaction is small.

The terms used in this report are defined as shown in Figure 1.

Solidified soil: A mixture of the solidifier and the soil subject to improvement (original soil).

Leaving time: The time between the mixing of the solidifier in the original soil and the crushing.

Crushed solidified soil: A soil material produced by

crushing the solidified soil.

Curing time: The time between the production of a specimen and the strength test for solidified soil and crushed solidified soil.

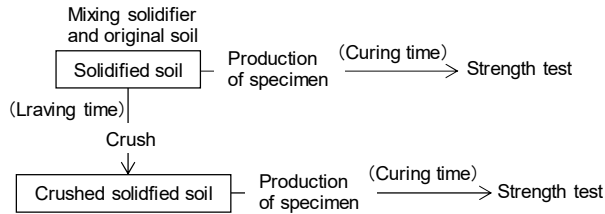


Fig. 1 Defined of term.

SOIL TEST METHOD

Table-1 shows the basic physical properties of original soil No.1, which was used in testing the physical properties and strength of the crushed solidified soil, and No. 2, which was used for constructing full-scale embankments. Original soil No. 1 used for the physical properties and strength tests was volcanic ash sand and had a high cone index. The original soil used for constructing full-scale embankments was clay with a high liquid limit, whose cone index was very low, and construction machines were not able to travel on it [4].

Physical properties and strength tests

The tests for physical properties and strength were done at the Tomakomai Construction Test Field of the Civil Engineering Research Institute for Cold Region. The wet weight of original soil No. 1, which was put in a container of 1m³, was measured. Portland blast-furnace slag cement B was added to the original soil. The ratios of the added soil improvement material for the specimens were 5%, 10%, and 15% in the dry weight ratio. Each specimen was mixed for about 10 minutes in the backhoe bucket. An embankment of 50

cm in height and 1 m in crest width was constructed for each specimen. The embankment was formed by pressing the soil with the backhoe bucket. These embankments were left at the open test field under natural weather conditions. The test specimens for each solidified soil was produced by using the backhoe bucket and the backhoe breaker and breaking the part of the embankment into crushed solidified soil of about 10 mm in grain size on the 11th, 53rd, 109th, and 259th days. A compaction test was conducted on solidified crushed soil. The tests for the specimen of each age were done in a laboratory immediately after preparing the specimens so as to avoid further progress in the solidification of the specimens.

To clarify the time-dependent changes in the strength of the compacted crushed solidified soil specimens, the specimens for the unconfined compression test (5 cm in diameter and 10 cm in height) [5] and those for the impact acceleration test (15 cm in diameter and 12.5 cm in height) [6] were produced. The impact acceleration is measured using a steel weight with a built-in accelerometer, which was dropped in a free-fall condition. This method of measurement is applied at construction sites as a quality control technique by the Hokkaido Regional Development Bureau of the Ministry of Land, Infrastructure, Transport and Tourism.

As a result of previous studies [7], it was found that the solidified crushed soil has different compaction curves depending on the standing time and the amount of solidifying material mixed. For this reason, the density of the specimen was determined by compacting with standard proctor energy for each standing time and each amount of the solidifying material to be mixed, with reference to Cement Association's specimen manufacturing method [8]. The unconfined compressive strength and impact acceleration were measured according to the age of

Table 1 Basic physical properties of original soil (The Japanese Geotechnical Society, JGS)

Sample No.	1	2	
Purpose of test	physical properties/ Strength	Full-scale embankment	Standard number
Soil particle density ρ_s (g/cm ³)	2.693	2.587	JGS 0111-2009
Natural water content w_n (%)	55.97	88.6	JGS 0121-2009
Grain size 2mm-(%)	3.6	0.0	
75 μ m-2mm(%)	64.9	0.1	JGS 0131-2009
characteristics -75m(%)	31.5	99.9	
Liquid limit w_L (%)	90.5	115.4	
Plastic limit w_P (%)	62.0	39.4	JGS 0141-2009
Ground material classification	SV	CH	JGS 0051-2009
Cone index q_c (kN/m ²)	1500	90	JGS 0716-2009
Maximum dry density ρ_{dmax} (g/cm ³)	0.961	-	JGS 0711-2009
Optimum moisture content w_{opt} (%)	51.7	-	(A-c)

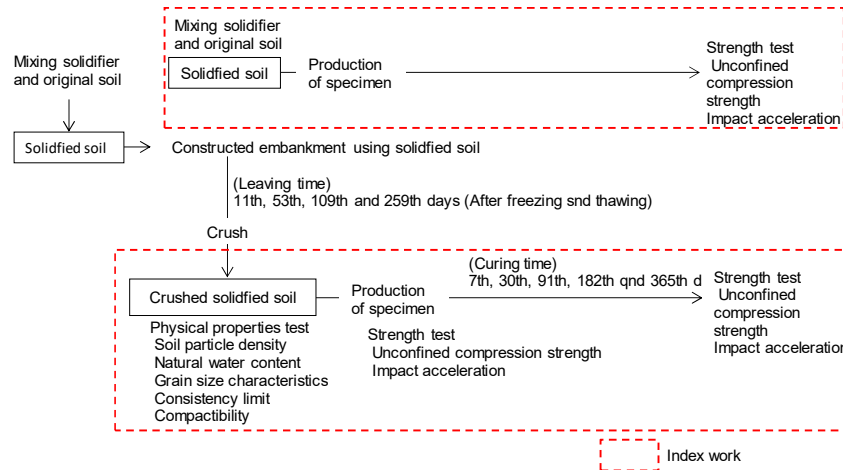


Fig. 2 Flows of the test procedures.

each specimen. Measurements were done on the day of the specimen production, i.e., on the 7th, 30th, 90th, 180th, and 365th days. Three specimens were used for the unconfined compressive strength test, and one specimen was used for the impact acceleration test. The unconfined compressive strength and the compressive strength of the solidified soil produced by mixing the original soil and the solidifier, which had a mixing ratio similar to that for the soil solidified on site, were measured using the same curing durations as those for the crushed solidified soil specimens. The flows of the test procedures are shown in Figure-2.

The full-scale embankment test

The river embankment constructed on soft ground settles after construction. Such embankment has to deform following the deformation of the ground. If the deformation of the embankment on the soft ground does not follow the deformation of the ground, gaps may be created between the embankment and the ground or cracks may occur in the embankment, which may result in water leakage. Therefore, the material of the embankment has to behave flexibly following the deformation of the ground. This characteristic is also required for the crushed solidified soil when it is used as the material for an embankment on soft ground. Two full-scale embankments were constructed on soft ground using solidified soil for one embankment and crushed solidified soil for the other embankment and

investigated these two embankments regarding the deformation characteristics caused by the settlement of the ground. The information on the ground around the embankments is shown in Table-2. The ground was of alternate strata of peat and clay. The water content ratios of the upper layers were high. In the past, an embankment of 2.8 m in height was constructed and found that this embankment had subsidence of 70 cm in one year.

The full-scale embankment construction test was done by constructing one embankment using the solidified soil and the other using the crushed solidified soil. The material was prepared using original soil No. 2 and a cement solidifier, which is considered as a solidifier with early strength development and a small increase in the strength development after the initial strength development (hereinafter, this solidifier will be called “ETR3”). The target strength value for the improvement of solidified soil and crushed solidified soil was a cone index of $q_c = 400 \text{ kN/m}^2$ at the construction of the embankment. The test done before the construction of the embankments were found, to obtain the target strength for the solidified soil and the crushed solidified soil, it was necessary to use 200 kg/m^3 and 95 kg/m^3 of ETR3, respectively. The embankment of the solidified soil was constructed during the period from September 24 to October 2, 2018, and the embankment of the crushed solidified soil with a leaving time of 28 days was constructed during the period from October 16 to 25, 2018. As shown in Figure-3, the dimensions of the embankments are 3 m in height, 20 m in length, and 5 m in crest width. The

Table 2 Ground information around the full-scale embankment construction site

Soil layer symbol	Soil layer name	Thickness (m)	Ignition loss $L_i(\%)$	water content $w_n(\%)$
Ap1	Peat	1.4	48	414
Acp	Clay mixed with peat	1.0	26	263
Ap2	Peat	2.5	54	396
Acs	Sandy clay	2.4	-	42

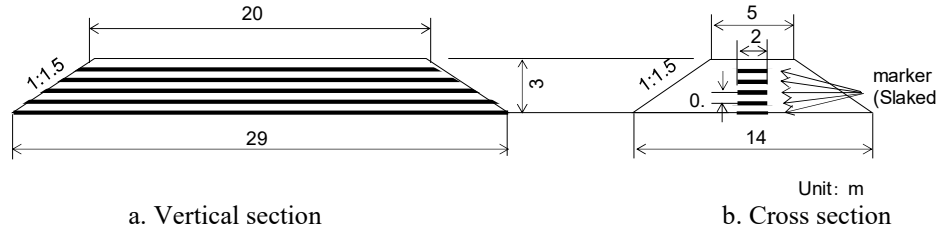


Fig. 3 Defined of term.

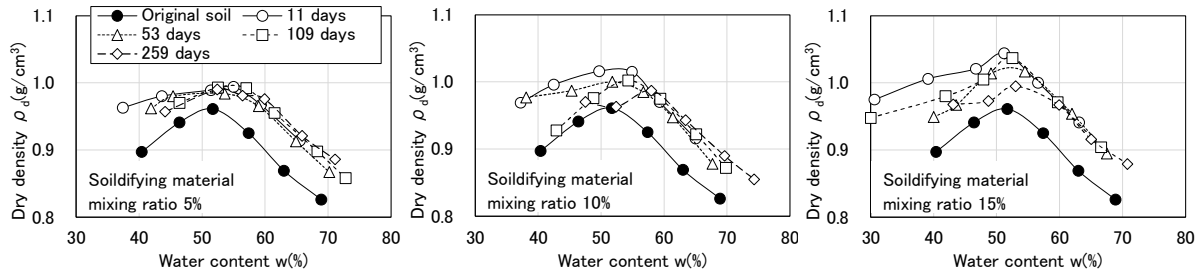


Fig. 4 Compaction curves for the crushed solidified soil.

slope gradient was 1:1.5. To clarify the deformation of the embankment when it is excavated, markers were set in the embankment during the construction. For the markers, 1-cm thick lime layers with 60cm intervals in the depth direction were installed in an area of 2 m in width along the longitudinal center of the embankment. The construction machine used was a 4t-combined-roller which had a steel wheel (roller) at either of the front or the rear side and tires on the other side. Four runs of rolling compaction were done for each layer. In constructing embankments, that were worked in a short time to avoid damaging the ground. Up to the height of 1.8 m, 3 layers in one day were constructed, and after that, one layer per day was constructed. The two embankments were constructed 20 m apart between the toe ends to avoid interference from the other embankment's settlement. On August 29, 2019, which was about one year after the construction of the two embankments, the embankments were excavated in the longitudinal direction and investigated the deformation.

TEST RESULTS

The physical properties and strength

Compaction characteristics

The compaction curves for the crushed solidified soil specimens with solidifier mixing ratios of 5%, 10%, and 15% are shown in Figure-4. All the compaction curves for the crushed solidified soil specimens are above that for the original soil specimen. The maximum dry density became higher for the crushed solidified soil than that for the original soil. For the crushed solidified soil specimens with a solidifier mixing ratio of 5%, the maximum dry density changed very little with the changes in the

leaving time; however, the maximum dry density changed considerably depending on the leaving time for the specimens with solidifier mixing ratios of 10% and 15%. By continue of investigation to collect more data and clarify the tendency in the changes in the maximum dry density according to the solidifier mixing ratio and the leaving time.

The strength of the specimens immediately after production

The relationship between the leaving time and the unconfined compressive strength of the specimens immediately after production is shown in Figure-5. The relationship between the leaving time and the impact acceleration of the specimens immediately after production is shown in Figure-6. The longer the leaving time, the lower the unconfined compressive strength was. The impact acceleration was slightly higher for the longer leaving time. From this result, it was considered that the quality of the soil specimen changes from that of cohesive soil to that of sandy soil, and the quality of sandy soil became dominant with longer leaving times. The cohesion of the unconfined crushed solidified soil specimen was lower with longer leaving time, and the uniaxial compressive strength of the specimen became lower with longer leaving time. In the impact acceleration test for the confined specimen, the angle of shear resistance of the specimen became greater with longer leaving time, and the impact acceleration of the specimen became greater with longer leaving time.

The curing time and the strength

The relationship between the unconfined compressive strength and the curing time is shown in Figure-7. Excluding the crushed solidified soil with a

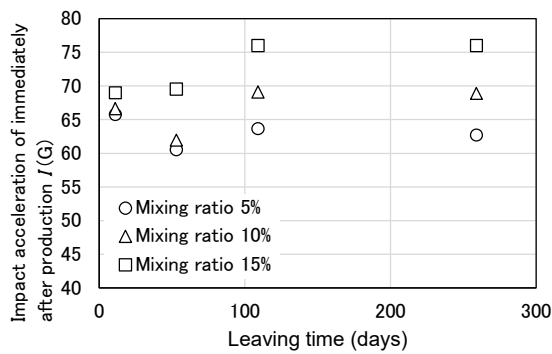


Fig. 5 Relationship between leaving time, and impact acceleration immediately after production

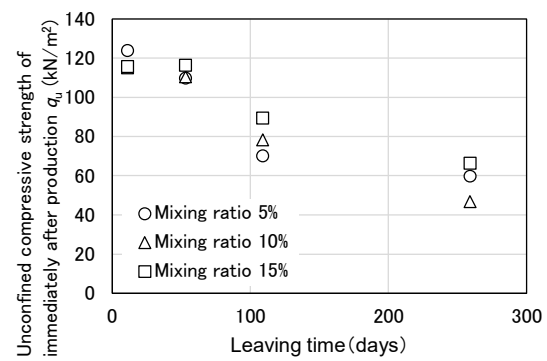


Fig. 6 Relationship between leaving time, and unconfined compressive strength of immediately after production

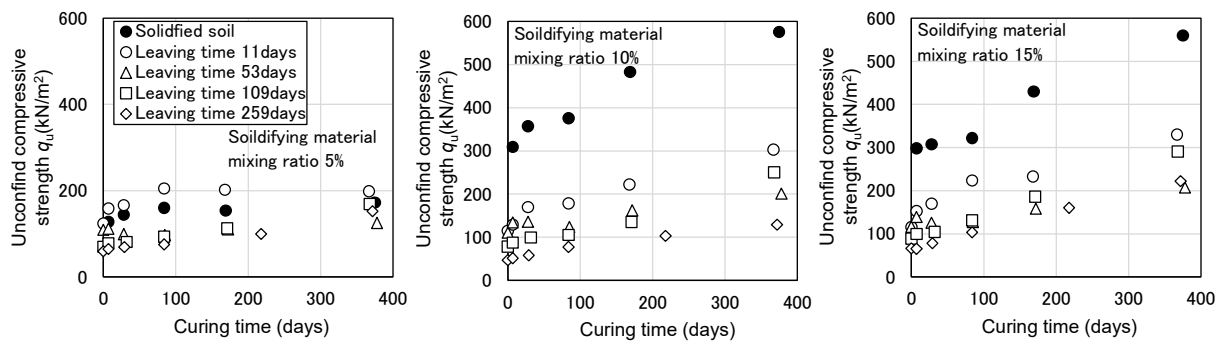


Fig. 7 Relationship between curing time and unconfined compressive strength

solidifier mixing ratio of 5% and a leaving time of 11 days, the unconfined compressive strengths of the crushed solidified soil specimens were lower than those of the solidified soil, regardless of the solidifier mixing ratio and curing time. The unconfined compressive strength increases very slightly after the curing time of 84 days for the crushed solidified soil with the solidifier mixing ratio of 5%. However, for the specimens with the solidifier mixing ratios of 10% and 15%, the unconfined compressive strength tended to increase with the curing time. The degree of increase in the unconfined compressive strength of the crushed solidified soil for the specimen with a leaving time of 259 days was great. The increases in

the unconfined compressive strength of the crushed solidified soil specimens with longer leaving times tended to be smaller than those of the specimen with shorter leaving times. In light of this, it can be concluded that the unconfined compressive strength of the crushed solidified soil with a low solidifier mixing ratio or a long leaving time does not considerably increase. The relationship between the curing time and the impact acceleration showed a similar tendency as that observed between the curing time and the unconfined compressive strength.

The full-scale embankment test

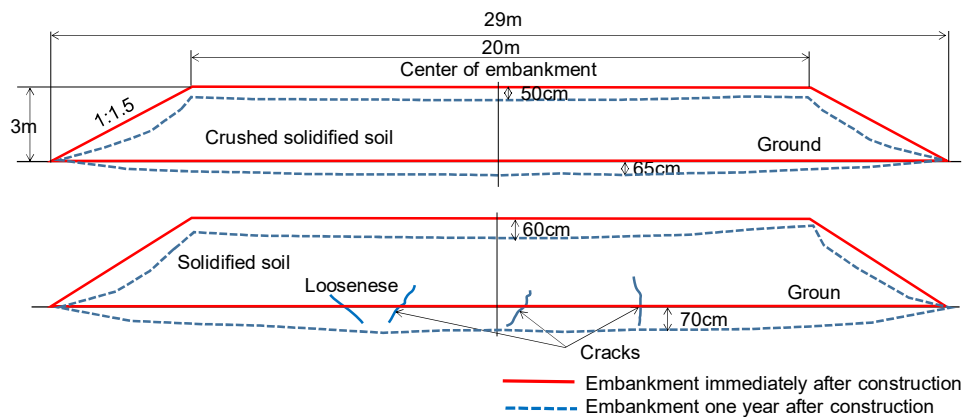


Fig. 8 Deformation of embankment.

The excavated cross-section of the embankment constructed using the crushed solidified soil is shown in Figure-8. Deformation was observed in the entire body of the embankment constructed using the solidified soil and that of the embankment constructed using the crushed solidified soil. The deformation of the embankment on soft ground is large at the center of the embankment, and it is reported that the entire embankment is deformed [9]. About 60 cm to 70 cm of settlement was seen at the center of both of the embankments. It was found that the embankment constructed using the crushed solidified soil was entirely homogeneous in soil quality and had no cracks. The embankment constructed using the solidified soil had three cracked areas and one loose area near the bottom surface. At these three locations, 2.0 m to 2.5 m long and 1 cm to 2 cm wide cracks developed upward from the bottom of the embankment were found. At the one location, the embankment toe failed from the loosening of the soil near the location of the installed settlement plate. Based on these findings, the cracks had formed in the embankment constructed using the solidified soil because the embankment was not able to follow the deformation of the soft ground were clarified; however, the embankment constructed using the crushed solidified soil followed the deformation of the soft ground similar to the embankments constructed using common soil materials.

SUMMARY

By using the original soil containing volcanic ash and that containing clay with a high liquid limit, the relationship between the production conditions and the physical properties and strength of the crushed solidified soil and the settlement characteristics of the embankment constructed using the crushed solidified soil on soft ground were investigated. the mix proportion and leaving time for producing crushed solidified soil which does not develop excess strength were could not determine; however, the following on the crushed solidified soil were found.

[1] The physical properties of the crushed solidified soil, including compaction characteristics, differed from those of the original soil. The compaction curves showed that the maximum dry density of the crushed solidified soil was higher than that of the original soil and that the higher the mixing ratio of the solidifier, the higher the maximum dry density became. When constructing an embankment using the crushed solidified soil, it is necessary to perform quality control by obtaining the compaction curve for each specimen.

[2] The unconfined compressive strength of the compacted crushed solidified soil immediately after the specimen preparation tended to be smaller with longer leaving times. The impact acceleration became

greater with longer leaving times; however, the increase in the impact acceleration became negligible after a certain length of leaving time. The unconfined compressive strength and the impact acceleration of the compacted crushed solidified soil increase with the curing time. The unconfined compressive strength of the crushed solidified soil with a large amount of solidifier became higher with the curing time, even for the material with the leaving time of 259 days. The strength development of the crushed solidified soil was smaller than that of the solidified soil. Excess strength development was able to be controlled.

[3] When an embankment was constructed on soft ground using the solidified soil, the embankment was not able to accommodate the deformation of the soft ground and cracks developed; however, cracks did not develop in the embankment constructed using the crushed solidified soil. The crushed solidified soil is able to be used for the material to construct embankments on soft ground was concluded.

REFERENCES

- [1] Civil Engineering Research Institute for Cold Region: The Manual of Measures against Unsuitable Soil in Hokkaido, 2013.
- [2] Atsuko Sato, Jun'ichi Nishikawa and Hatsuo Kitano, Strength characteristics of solidified-crushed soil, Proceedings of the 32th Japan National Conference on Geotechnical Engineering, 1997, pp.2423-2424.
- [3] Atsuko Sato, Osamu Hatakeyama, Hirotsugu Kouoka, Yutaka Inazawa, Tomonori Nagata, Hideaki Takahashi and Kiyome Hatakeyama, Preparation conditions and geotechnical characteristics of solidified crushed soil, Japanese Geotechnical Society, Hokkaido Branch, Technical Report No. 60, 2020, pp. 93-100.
- [4] Japan Road Association, Road Construction Summary, 2009, p.287
- [5] Japanese Geotechnical Society, Japanese Standards and Explanations of Laboratory Tests of Geomaterials, 2009, pp. 226-258.
- [6] Hokkaido Regional Development Bureau, Road Design Guidelines, 2019.
- [7] Atsuko Sato and Naoyuki Kuji, Leaving time and geotechnical properties of crushed solidified soil, Symposium of ground Improvement No.13, 2018, pp.415-418.
- [8] Japan Cement Association, Strength test method for improved products by cement-based solidifying material, 2006.
- [9] PWRI Cold Region PWRI, Peat Soft Ground Countermeasure Manual, Annnn B., Unpublished Work but Accepted, Vol., Issue, Year, 2017.

PREDICTION METHOD OF SLIP SURFACE DEPTH FOR SLOPE HEALTH MONITORING BASED ON VOLUMETRIC WATER CONTENT

Keigo Koizumi¹, Sota Tsukabe², Mitsuru Komatsu³, Kazuhiro Oda⁴ and Shinichi Ito⁵

¹Graduate School of Engineering, Osaka University, Japan; ²Faculty of Engineering, Osaka University, Japan; ³Graduate School of Environmental and Life Science, Okayama University, Japan; ⁴Faculty of Engineering, Osaka Sangyo University, Japan; ⁵Graduate School of Science and Engineering, Kagoshima University, Japan

ABSTRACT

This research proposes a method to install a sensor at an appropriate position for monitoring slope soundness against heavy rainfall. The frequency of natural disasters caused by climate change has increased in recent years. In particular, rainfall-induced slope failures owing to localized heavy rain have increased; accordingly, countermeasures have been implemented on an urgent issue in Japan. As current nonstructural measures, there are various regulation standards, such as hourly rainfall, continuous rainfall, and Soil Water Index; however, it is difficult to evaluate the risk of slope failures individually. In contrast, studies are evaluating individual slope stability by monitoring rainwater infiltration, pore water pressure, and other parameters in the slope or by detecting slope deformation. These studies focused on sandy slopes, and the value of N_d can be used to estimate the depth of the slip surface, which is one of the main factors of slope failures. However, N_d is an index value that shows the rigidity and hardness of the ground. Therefore, it is not possible to directly estimate whether the water level forms or not only based on the information of N_d . Therefore, to accurately analyze the slip surface, a method for evaluating water permeability and water retention in the slope is required. Herein, we proposed a method to predict the depth of the slip surface, considering the rate of decrease of the volumetric water content in the soil. Then, its applicability was confirmed by using numerical analysis and verified on an actual slope. As a result, we indicated that the slip surface could be predicted using the proposed prediction method in the actual slope.

Keywords: Slope failure, Volumetric water content, Slip surface depth, Slope health monitoring

INTRODUCTION

In recent years, the frequency of natural disasters associated with climate change in Japan has increased. In particular, the annual frequency of slope disasters is increasing, and implementing appropriate countermeasures is a major problem. Based on current nonstructural measures, criteria such as hourly rainfall, continuous rainfall, and Soil Water Index are set using rainfall data as an index; however, these criteria cannot be considered for evaluating the risk of slope failures individually. This is because slope failure occurs due to the combination of factors that indicate topographical and geological characteristics and incentives such as rain and earthquakes. However, this warning criterion based on rainfall information does not become a criterion considering slope angle and physical properties of soil as a predisposing factor. In contrast, several studies have evaluated the health of individual slopes by monitoring rainwater infiltration and deformation behaviors in the slope. For example, by focusing on slope deformation, methods to forecast the failure time based on the creep-rupture life or velocity of surface displacement [1], [2] and to predict the pre-failure stages based on the tilting rate of tilt sensors [3], [4] have been proposed. Further, methods to

predict slope failure based on the pore water pressure or groundwater level [5], [6] and to evaluate the health of slopes based on the volumetric water content [7]–[9] have been proposed. These studies have focused on the shallow slope failure. When the sensors for monitoring the slope stability are installed, only the value of N_d which is the index obtained by handy dynamic cone penetration test can be used to estimate the depth of the slip surface [10]. N_d is an index value that represents the degree of rigidity and hardness of the ground; however, it cannot be used to estimate whether a saturated zone has formed at the slip surface. Therefore, for accurately estimating the slip surface, N_d and the index for evaluating permeability and water retention of the ground are required. The purpose of this study is to propose a method to install a sensor at an appropriate position for monitoring slope soundness against heavy rainfall. In this study, the existence of the slip surface and its depth were analyzed by evaluating permeability and water retentivity in the slope based on the volumetric water content, which we are currently monitoring.

The slip surface described in this study is defined as the boundary layer where a saturation zone is formed. Therefore, it has not been discussed whether the defined slip surface is consistent with the actual slip surface.

PREDICTION METHOD OF SLIP SURFACE DEPTH

This study describes a method to estimate the slip surface based on the temporal change of volumetric water content in the slope of sandy soil. First, a case where a slip surface is formed in a shallow layer is considered. When there is a soil layer with poor water permeability in the shallow layer, it is considered that the water level is formed by the stagnation of the infiltration surface in the upper layer of the slip surface because water cannot drain out to the lower layer. Figure 1 shows the rate of decrease in the volumetric water content at each depth after rainfall to a certain time period with and without slip surfaces. In the case of “with slip surface,” though the water of shallow depth infiltrates downward owing to gravity, saturated and capillary zones are formed near and just above the slip surface. Therefore, the rate of decrease in the volumetric water content is expected to be relatively slow with depth. In other words, assuming that the capillary zone of sandy soil forming the upper layer of the slip surface is low in height, the slip surface may exist at a depth where the rate of decrease is zero. This can be obtained by connecting the rate of decrease of the volumetric water content at each depth to a straight line. On the other hand, even for “without slip surface,” the decrease rate of volumetric water content due to gravity drainage is expected to be slower at deeper depths than at shallow depths. However, the difference is smaller compared with the “with slip surface” case, and it is possible that the difference between the two becomes clear over time.

VERIFICATION OF THE VALIDITY OF THE PREDICTION METHOD USING NUMERICAL ANALYSIS

To verify the validity of the hypothesis shown in Fig.1, a one-dimensional analytical model simulating the slip surface was designed and evaluated using the saturated-unsaturated seepage flow program–HYDRUS-2D. Water flow is calculated using the Richards equation [11] and a finite element method. The van Genuchten model [12] is used to express the soil–water characteristic curve, and the Mualem model [13] is used to estimate the unsaturated hydraulic conductivity.

Analytical Method

Figure 2 shows the analytical model. In this study, a boundary layer assumed to be a slip surface was set at a depth of 120 cm, and the hydraulic conductivity of the upper and lower layers was changed to show whether there is a slip surface or not. Concretely, the analytical model for two cases listed in Table 1 was prepared. For the lower layer, four patterns of 1, 1/10, 1/100, and 1/1000 times of permeability of the upper

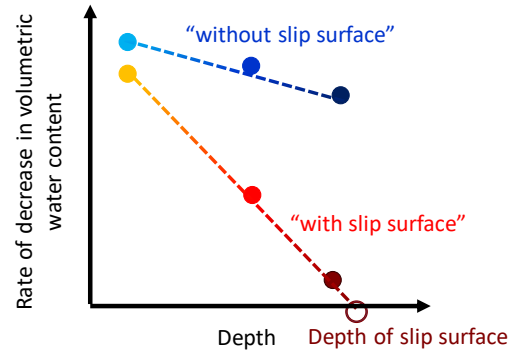


Fig.1 Conceptual diagram of the rate of decrease in the volumetric water content at each depth after rainfall “with and without slip surface”

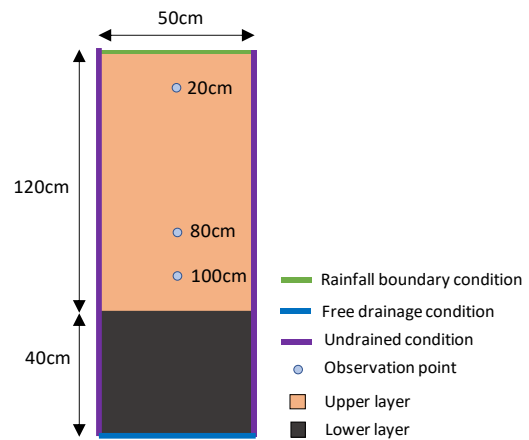


Fig.2 One-dimensional analytical model

Table 1 Parameters in each case

	Case1		Case2	
	Upper	Lower	Upper	Lower
k_s	0.57	(1) 0.57×10^0	0.074	(1) 0.074×10^0
		(2) 0.57×10^{-1}		(2) 0.074×10^{-1}
		(3) 0.57×10^{-2}		(3) 0.074×10^{-2}
		(4) 0.57×10^{-3}		(4) 0.074×10^{-3}
θ_r	0.153	0.034	0.065	0.034
θ_s	0.430	0.460	0.410	0.460
α	0.085	0.016	0.075	0.016
n	1.60	1.37	1.89	1.37

layer were set. The lower layer with lower permeability is classified as “with slip surface.” The hydraulic conductivity of the upper layer was set by estimating the upper and lower limits of the hydraulic conductivity of decomposed granite soil. The other water characteristic parameters were set based on the references. The observational depths were set to 20, 80, and 100 cm, according to the position where the sensor was installed on the actual slope. The rainfall intensity was 30 mm/h, and it stopped when the infiltration surface reached the boundary layer. When the volumetric water content at each observational

depth started decreasing, the rate of decrease in the volumetric water content at each elapsed time was calculated by changing the time intervals in the order of 12, 32, and 60 min. The calculated results were used to evaluate the depth of the slip surface that was estimated based on the conceptual diagram in Fig.1. Hereinafter, it is referred to as the estimated slip surface depth.

Results and discussion

Figure 3 shows the change in the rate of decrease in the volumetric water content over time in cases 1-(1) and 1-(4). If the decreased rate shows a negative value owing to the formation of a saturated zone in the boundary layer, it is plotted as zero for convenience. Based on these figures, it can be confirmed that the depth of the slip surface changes with time and is not uniquely determined, as shown in Fig.1. In case 1-(1), the estimated depth of the slip surface after 60 min roughly agreed with the boundary layer of 120 cm, but it deepened (arrows in the figure) with time. On the other hand, in case 1-(4), the estimated depth of the slip surface after 60 min roughly agreed with the boundary layer of 120 cm, but the depth slightly rose (arrows in the figure) with time.

Figure 4 shows the change in the rate of decrease in the volumetric water content over time in cases 2-(1) and 2-(4). As in Fig.3, if the rate of decrease shows a negative value, it is plotted as zero for convenience. In case 2-(1), the estimated slip surface depth changes to a deeper side with time, whereas in case 2-(4), it changes to a shallower one. This tendency is similar to cases 1-(1) and (4) in Fig.3. To clarify these relationships, Figures 5 and 6 show the changes in the estimated slip surface depth with time in cases 1-(1) to (4) and cases 2-(1) to (4), respectively.

Based on Fig.5, it was confirmed that the estimated depth of the slip surface was almost the same, regardless of the hydraulic conductivity of the lower layer till 60 min of the elapsed time and that the depth tended to change with time. In addition, the estimated depth of the slip surface varies at 120–360 min. In cases 1-(1) and (2), the depth of the slip surface tended to increase with time. On the other hand, as in case 1-(3), when the hydraulic conductivity decreases, the slope of the graph becomes gentler, and the estimated slip surface depth tends to approach the boundary layer of 120 cm. When the hydraulic conductivity is further reduced, as in case 1-(4), compared with the boundary layer, the estimated depth of the slip surface tends to be shallower with time. This is because a saturated zone is formed by the infiltration surface reaching the boundary layer, and the decrease rate at a depth of 100 cm changed to a negative value owing to the influence of the capillary zone. Based on the results in Fig.6, the estimated depth of slip surface tended to increase

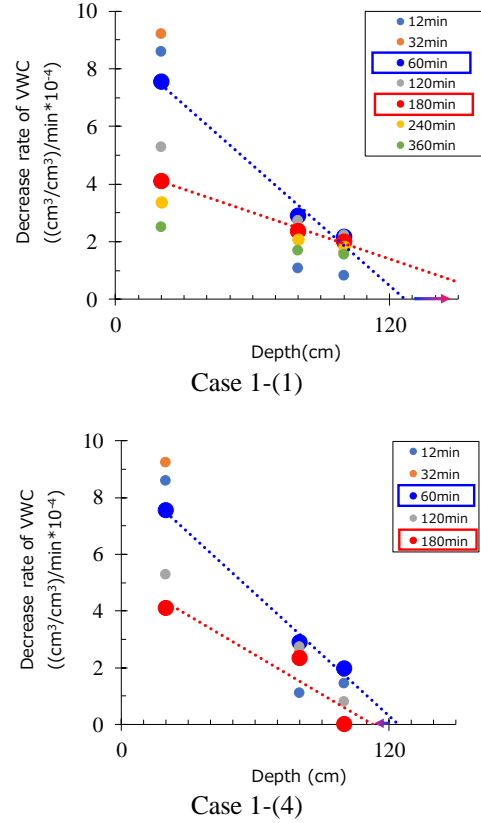


Fig.3 Change in the decrease rate of volumetric water content over time in Case 1

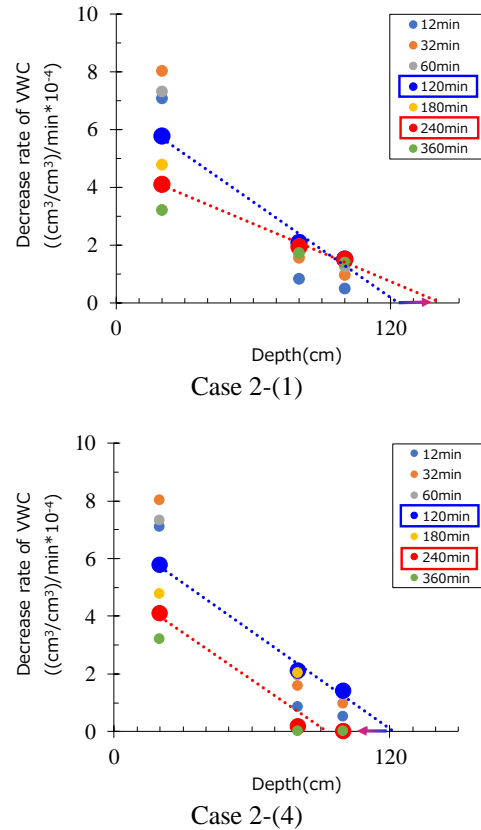


Fig.4 Change in the decrease rate of volumetric water content over time in Case 2

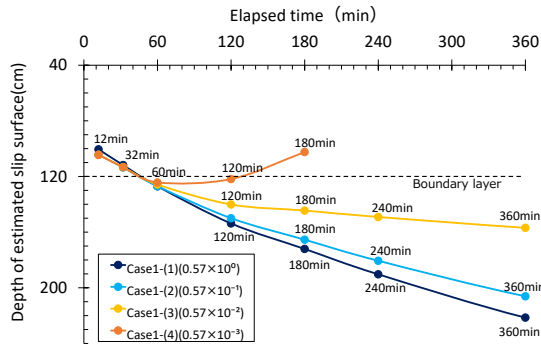


Fig.5 Changes in the estimated slip surface depth with time in Case 1

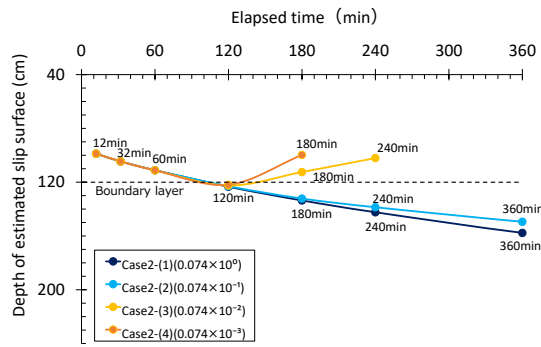


Fig.6 Changes in the estimated slip surface depth with time in Case 2

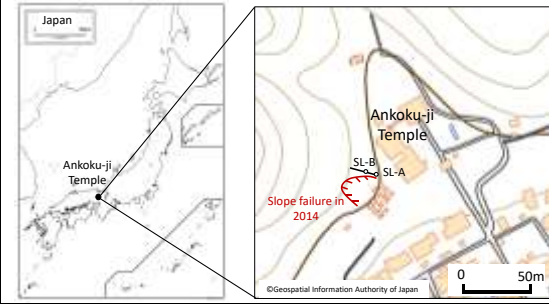
with time in cases 2-(1) and (2) with high hydraulic conductivity (Fig.5). On the contrary, in cases 2-(3) and (4) where the hydraulic conductivities are low, graphs with a convex downward line are seen, and the depths at the lowest point of the graphs are almost coincident with the boundary layer of 120 cm.

Considering the above results, it is possible to distinguish “with slip surface” and “without slip surface” by analyzing the time change of the estimated slip surface depth. The slip surface depth is the depth at which the slope of the graph approaches zero with the elapsed time or the depth at the lowest point of the downward convex graph.

ON-SITE VERIFICATION

Here, the validity of the slip surface depth estimation method proposed in previous chapter is verified based on the field measurements. The outline information of the study site is listed in Table 2. The study site is located at a mountain slope behind the Ankoku-ji temple in Ayabe City, Kyoto Prefecture. In 2014, rainfall-induced slope failures occurred in this site. Therefore, the slopes with the weathered soil are monitored to analyze their health. Soil moisture sensors and water level gauges were installed at the toe of the slope (SL-A) and the middle part of the slope (SL-B) to analyze rainwater infiltration behaviors. Based on the previous studies, three soil moisture sensors were installed along the depth of the

Table 2 Outline of the study site

Ankokuji temple, Ayabe, Kyoto Pref.	
	
Soil Classification (JGS)	SC _s G
Slope type	Natural slope
Slope angle	40°
Depth of soil moisture sensors	20cm, 80cm & 100cm
Depth of water sensor	110cm
Measurement period	2019/10/24-27

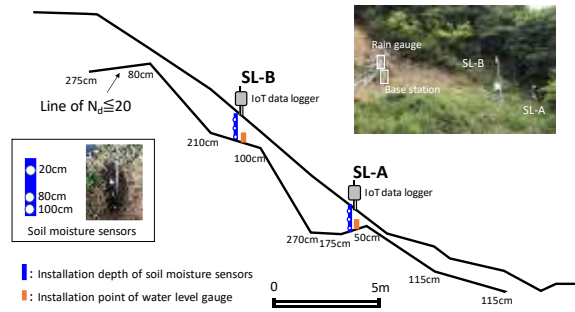


Fig.7 Installation information of each sensor in the study site

Table 3 Physical properties

Dry density ρ_d (g/cm ³)	1.46
Wet density ρ_t (g/cm ³)	1.87
Density of soil particle ρ_s (g/cm ³)	2.911
Natural water content w (%)	27.7
Gravel (%)	16.8
Sand (%)	43.3
Silt (%)	17.6
Clay (%)	22.3
Maximum particle size (mm)	19

slope. The installation depth of the soil moisture sensors and water level gauge was determined based on the values of N_d at each location. Here, $N_d \leq 20$ is set as the boundary layer. The installation information of each sensor is shown in Fig.7. Moreover, a rain gauge for observing rainfall was installed in the study site. The data recorded in the IoT (Internet of things) data logger can be monitored in real time on the Web via the base station. The physical properties are listed in Table 3.

Figures 8 and 9 show time-series variation in rainfall, volumetric water content, and water level in SL-A and SL-B. The measurement interval of rainfall and water content is 10 min, and the measurement

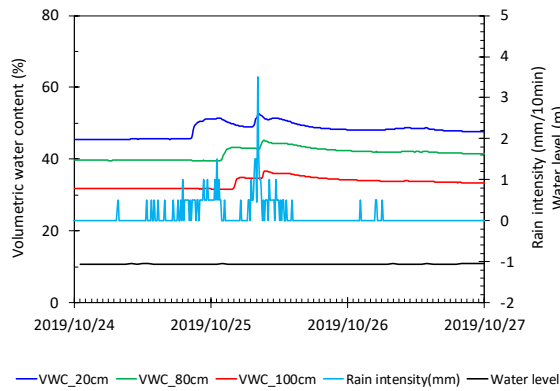


Fig. 8 Time series variation in rainfall, volumetric water content, and water level in SL-A.

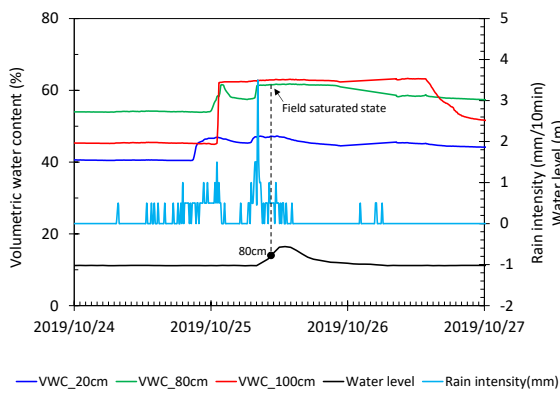


Fig. 9 Time series variation in rainfall, volumetric water content, and water level in SL-B.

interval of water level is 60 min. As the volumetric water content is calculated using the calibration formula of the manufacturer, only the relative change is emphasized. As shown in Fig.8, it can be estimated that the water permeability in the soil is high because the volumetric water content at each depth repeatedly increases and decreases in response to rainfall. Therefore, there was no tendency for the water level to increase in the boundary layer during the observation period. On the other hand, in Fig.9, although the volumetric water content increases orderly from the shallow part due to rainfall, the volumetric water content at depths of 80 and 100 cm is relatively larger than that at 20 cm. The timing when the volumetric water content at a depth of 80 cm showed a peak value roughly corresponds with the timing when the water level gauge was at 80 cm, indicating that the depth of 80 cm is in the field-saturated state.

Based on the analytical method described in pervious chapter, the rate of decrease in volumetric water content was calculated by changing the time interval from the time when the volumetric water content began to decrease at each observation depth after rainfall. Figures 10 and 11 show the changes in the rate of decrease in the volumetric water content

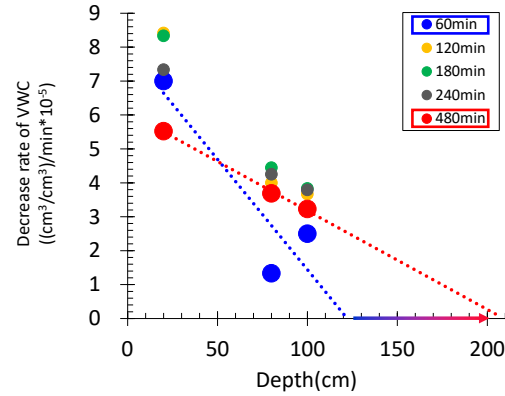


Fig. 10 Change over time in the decrease rate of volumetric water content in SL-A

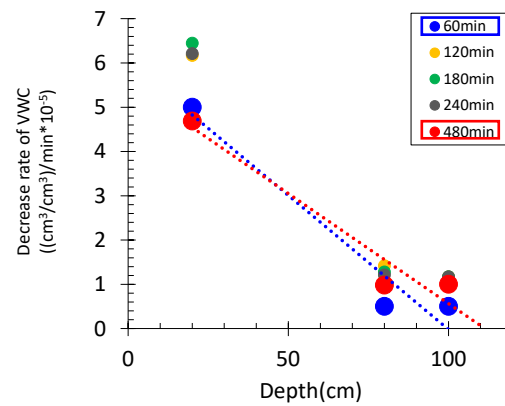


Fig. 11 Change over time in the decrease rate of volumetric water content in SL-B

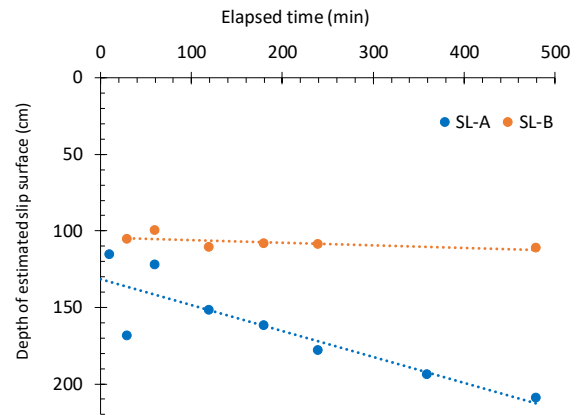


Fig.12 Changes in the estimated slip surface depth with time in case 2.

over time in SL-A and SL-B. Figure 10 shows that the estimated depth of the slip surface in SL-A becomes deeper with time, and the estimated depth also becomes deep. On the other hand, Figure 11 shows that the estimated depth of the slip surface at SL-B varies slightly regardless of time, and the estimated depth remains at 100–110 cm. To clarify these relationships, Figures 12 shows the changes in the estimated slip surface depth with time in SL-A and SL-B, respectively. The estimated depth of slip the

surface in SL-A becomes deeper with time. This tendency is similar to case 1-(1) and (2) in Fig.5 and case 2-(2) and (2) in Fig.6, implying that there is no slip surface in the shallow layer where slope failure is a matter of concern. On the other hand, the estimated depth of the slip surface in SL-B is constant at 100–110 cm regardless of the elapsed time. It suggests that the slip surface may exist at the depth of ~110 cm, and this tendency is (roughly) similar to case 1-(3) in Fig.5.

CONCLUSIONS

The purpose of this research proposes a method to install a sensor at an appropriate position for monitoring slope soundness against heavy rainfall. In this study, a method to predict the existence and depth of slip surfaces based on the rate of decrease of the volumetric water content in the soil after rainfall was analytically examined. And its applicability is verified in the actual slopes. The research findings are as follows.

From the numerical analysis, it is confirmed to distinguish “with slip surface” and “without slip surface” by analyzing the time change of the estimated slip surface depth. The slip surface depth is the depth at which the slope of the changes in the estimated slip surface depth with time approaches zero with the elapsed time. The validity of the slip surface depth estimation method proposed in numerical analysis is verified based on the field measurements. As a result, it was confirmed that the depth of the slip surface estimated from the observation data by using the water level gauge and the soil moisture sensors agreed with the depth of the slip surface estimated by the proposed method. From these results, it is suggested that the slip surface can be predicted by applying the prediction method obtained from the analysis to the measurement result of the actual slope.

ACKNOWLEDGMENTS

This research was partly supported by Garant-in-Aid of Scientific Research (17K00615 and 19K04599). We express our gratitude.

REFERENCES

- [1] Saito M., Prediction of Slope Failure due to the Third Creep. Landslides. Journal of the Japan Landslide Society, Vol. 4, No. 3, 1988, pp. 1-8. (in Japanese)
- [2] Fukuzono T., A Method to Predict the Time of Slope Failure Caused by Rainfall Using the Inverse Number of Velocity of Surface displacement. Landslides. Journal of the Japan Landslide Society, Vol. 22, No. 2, 1985, pp. 8-13. (in Japanese)
- [3] Uchimur T., Towhata I., Wang L., Nishie S., Yamaguchi H., Seko I., and Qiao J., Precaution and Early Warning of Surface Failure of Slopes Using Tilt Sensors. Soils and Foundations, Vol. 55, No. 5, 2015, pp. 1086-1099.
- [4] Ishizawa T., Sakai N., Moroboshi T., and Fukuzono T., Effectiveness of Underground Displacement Measurement Using Inclinator for Prediction of Slope Failure. Landslides. Journal of the Japan Landslide Society, Vol. 50, No. 6, 2013, pp. 256-267. (in Japanese)
- [5] Morikawa H., Inokuchi T., Hattanji T., Sassa K., Ochiai H., and Wang G., Failure Processes in a Full-Scale Landslide Experiment Using a Rainfall Simulator. Landslides, Vol. 1, No. 4, 2004, pp. 277-288.
- [6] Sasahara K. and Ishizawa T., Time Prediction of an Onset of Shallow Landslides Based on the Monitoring of the Groundwater Level and the Surface Displacement at Different Locations on a Sandy Model Slope. Japanese Geotechnical Journal, Vol. 11, No. 1, 2016, pp. 69-83.
- [7] Koizumi K., Sakuradani K., Oda K., Komatsu M., and Ito S., Relationship Between Initial Quasi-Saturated Volumetric Water Content and Rainfall-Induced Slope Deformation Based on a Model Slope Experiment. Journal of GeoEngineering, Vol. 13, No. 4, 2018, pp. 179-187.
- [8] Chae B. G. and Kim M. I., Suggestion of a Method for Landslide Early Warning Using the Change in the Volumetric Water Content Gradient due to Rainfall Infiltration. Environmental Earth Sciences, Vol. 66, 2012, pp. 1973-1986.
- [9] Tohari A., Nishigaki M., and Komatsu M., Laboratory Rainfall-Induced Slope Failure with Moisture Content Measurement. Journal of Geotechnical and Geoenvironmental Engineering, Vol. 133, No. 5, 2007, pp. 575-578.
- [10] Koizumi K., Oda K., Komatsu M., Ito S., and Tsutumi H., Slope Structural Health Monitoring Method Against Rainfall-Induced Shallow Landslide. IOP Conference Series: Materials Science and Engineering, Vol. 615:012046, 2019, pp. 1-8.
- [11] Richards L. A., Capillary Conduction of Liquids Through Porous Mediums. Physics, Vol. 1, 1931, pp. 318-333.
- [12] van Genuchten, M., A Closed-Form Equation for Predicting the Hydraulic Conductivity of Unsaturated Soils. Soil Science Society of America Journal, Vol. 44, No. 5, 1980, pp. 892-898.
- [13] Mualem, Y., A New Model for Predicting the Hydraulic Conductivity of Unsaturated Porous Media. Water Resources Research, Vol. 12, No. 3, pp. 513-522.

FUNDAMENTAL STUDY ON INSTALLATION POSITION OF SENSORS FOR ON-SITE MONITORING FOCUSING ON SLOPE FAILURE

Haruki Iwamoto¹, Keigo Koizumi², Mitsuru Komatsu³ and Hiroshi Tsutsumi⁴

^{1,2} Graduate School of Engineering, Osaka University, Japan;

³ Graduate School of Environmental and Life Science, Okayama University, Japan;

⁴ West Nippon Expressway Co. Ltd., Japan

ABSTRACT

Rainfall-induced slope failure occurs frequently owing to the effect of recent extreme weather. Our research is aimed at the direct evaluation of slope stability by using a real-time monitoring system on the slope. However, several problems remain to be solved to allow for the practical use of this monitoring method, for example, determining how many sensors should be installed or where they should be installed on the slope. To address these questions, in this study, we determine the position that is more effective for the installation of a sensor for slope monitoring based on laboratory experiments. In addition, we propose a method for estimating an appropriate position. The results show that the proposed method for estimating the point at which the water level rises agrees well with the critical point of slope failure obtained through the laboratory-based model slope experiments. However, this result is only feasible under a constant rainfall condition, and its verification with respect to the effects on actual slopes remains to be solved in the future.

Keywords: Volumetric Water Content, Shallow Landslide, Rain Intensity, Sensor Location, Shear Deformation

INTRODUCTION

In recent years, natural disasters caused by heavy rainfall, especially those causing traffic blockage and human casualties have been frequent in Japan, where 70% of the land is made up of mountains. Currently, highways management company use only a rainfall information as a traffic-control standard in the event of abnormal rainfall. Although this method is simple and convenient, it does not consider the mechanism of slope failure. Our research group conducted field observations and model slope experiments and found that when rainwater infiltrates slopes during heavy rainfall, the volumetric water content of the surface ground temporarily reaches an equilibrium state ("quasi-saturated state") and displacement occurs after the volumetric water content in equilibrium ("initial quasi-saturated volumetric water content (IQS)") is exceeded. In other words, the prediction of the slope deformation caused by rainfall is possible by monitoring whether the volumetric water content reaches the IQS or not. Based on these findings, the authors considered that determining whether the traffic control is executed is possible by using IQS. However, the current works on slope monitoring have not yet considered a method determining the location of sensor installation position; such a method is currently being determined empirically. Therefore, in this study, the authors attempted to determine the appropriate sensor location based on model slope experiments to accurately detect slope hazards during slope monitoring.

LITERATURE REVIEW

This section provides an overview of literature on surface failure. Yagi, Yatabe, and Yamamoto [1] conducted rainfall model experiments to elucidate the mechanism of slope failure during heavy rainfall, and they found that excess pore water pressure at the bottom of the toe of the slope is one of the causes of slope failure. Kohgo, Saito, Niide, and Hori [2] conducted a rainfall model experiment and reported that negative pressure is released from the toe of slope, which is then is saturated, and the saturation progresses gradually to the top of the slope, leading to failure. Sako, Suda, Fukugawa, and Kitamura [3] conducted infiltration and failure tests using decomposed granite soil and found that after rainwater infiltration, groundwater started accumulating at the bottom of the soil layer, and failure occurred at the toe of the slope owing to the increased seepage force associated with pore water runoff from the toe of slope. Koizumi, Sakuradani, Oda, Ito, Fukuda, Feng, and Takemoto [4] conducted model slope experiments for surface failure under constant rainfall intensity and clarified the relationship between volumetric water content and displacement, as shown in Fig. 1. The figure also shows that (1) the volumetric water content initially increases with rainwater infiltration, and then (2) reaches a quasi-saturated state, resulting in an equilibrium state of volumetric water content. The quasi-saturated state is that in which the inflow and outflow volumes are equal in an unsaturated state

during the infiltration process, and the volumetric water content at this time is defined as the IQS. With further watering, (3) unsaturated capillaries are formed with the increase in the groundwater level, and the volumetric water content increases again from IQS. Eventually, (4) the groundwater level rises to the sensor position and reaches a saturated state. Displacement occurs after re-elevation from the IQS, i.e., after the formation of the groundwater level. Therefore, it is assumed that the displacement occurs after the volumetric water content reaches IQS. As shown in Fig. 2, the location of the seepage face and groundwater level can be estimated by measuring the volumetric water content at multiple depths in the vertical direction. For example, at time T_C , the volumetric water contents in the deeper levels (points D_U and D_L) rose again and reached saturation, while the volumetric water content at the shallow point (S) remains in equilibrium; then, the position of the groundwater level can be estimated to be between points S and D_U .

Thus, the mechanism of slope failure is largely related to the water content in the soil, especially the groundwater level. Therefore, monitoring the soil water behavior before and after the formation of the groundwater level is important, i.e., the water behavior from rainwater seepage to groundwater level rise must be monitored to predict the slope failure.

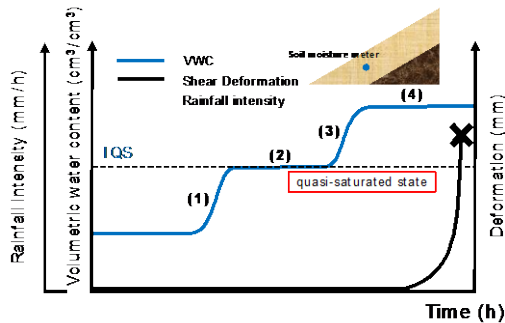


Fig. 1 Relationship between volumetric water content and displacement

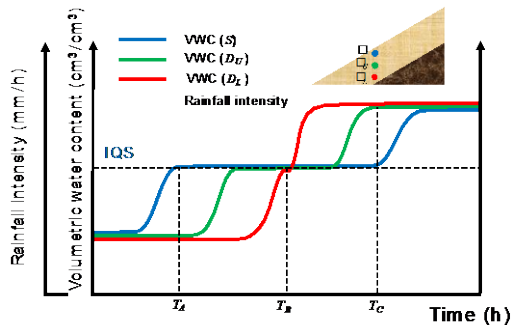


Fig. 2 Estimation of water state in the soil according to the volumetric water content

PREDICTION AND VERIFICATION OF POINTS OF WATER-LEVEL OCCURRENCE

This section explains the mechanism of slope failure. Rainwater infiltrates into the vertical direction in the slope, and the water that reaches the slip surface is concentrated at the toe of the slope as seepage flow, creating a water level. Then, slope failure occurs owing to the decrease in effective stress caused by the increases in soil mass weight and pore pressure. Therefore, if the point of occurrence of water level can be estimated and the rainwater seepage and deformation behaviors can be measured near this point, the slope danger can be detected more quickly.

The current method for determining sensor locations involves a handy dynamic cone-penetration test to determine the N_d values at each depth along the slope, and then connecting the points with $N_d = 20$, as shown in Fig. 3, to estimate the boundary between the topsoil and bedrock layers, and select locations where rainwater is likely to concentrate. However, as the N_d value obtained by the handy dynamic cone-penetration test is an index of the ground hardness and not of soil permeability.

Therefore, a new method is proposed for estimating the point of water-level occurrence. Figure 4 shows a conceptual diagram depicting the behavior of the volumetric water content in the case of continuous rainfall of certain intensity measured using soil-moisture meters installed at the same depths at points A, B, and C, as shown in Fig. 3. As each meter was installed at the same depth, the volumetric water content would theoretically begin to increase at about the same time, resulting in a quasi-saturated state. Subsequently, as the water level rises from the toe of the slope, the volumetric water content is expected to increase again in the order of A, B, and C. Let t be the time when the quasi-saturated state continues, then $t_A < t_B < t_C$. If a soil-moisture meter is installed at point P , the quasi-saturated state of this point is expected to be almost zero, because the water level is formed shortly after the rainwater reaches the soil-moisture meter. Therefore, Fig. 5 shows the horizontal distance from the point of water-

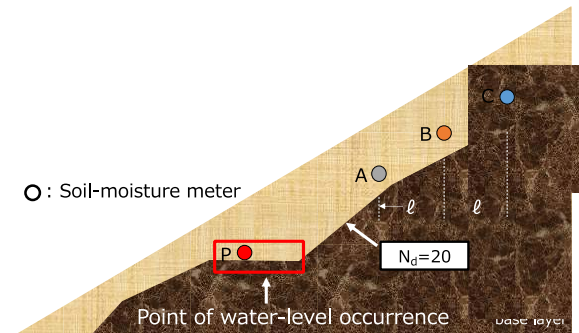


Fig. 3 Conceptual diagram of the location of installation of soil-moisture meters

level occurrence plotted on the horizontal axis, and times t_A , t_B , and t_C in Fig. 4 are plotted on the vertical axis. Water-level occurrence point P can be estimated by finding the intersection of the line connecting these plots and the horizontal axis.

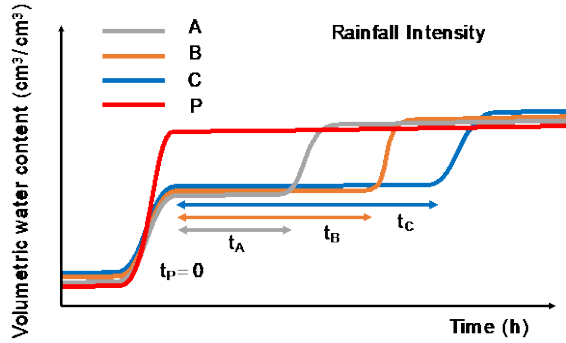


Fig. 4 Conceptual diagram of the change in volumetric water content over time

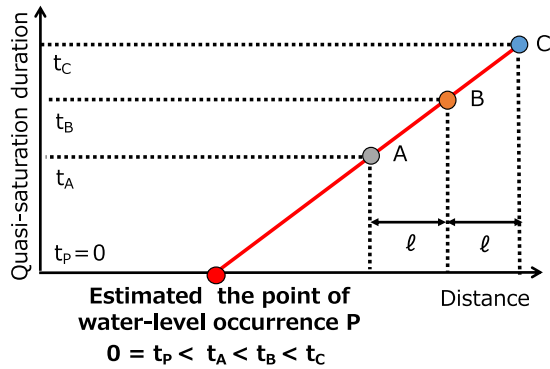


Fig. 5 Conceptual diagram of quasi-saturation duration time t

VALIDATION OF THE ESTIMATION METHOD THROUGH SATURATED AND UNSATURATED SEEPAGE-FLOW ANALYSIS

Summary of the Analysis

The saturated-unsaturated seepageflow analysis was performed using the software, HYDRUS-2D, which is a general-purpose program for predicting two-dimensional soil moisture and salinity transport [5]. In this software, the water flow is based on the Richards equation and the solute transfer is based on the transfer–dispersion equation. Both are computed using the finite element method.

Figure 6 shows the analysis model used in this study, and Table. 1 lists the soil parameters. As shown in Fig. 6, the red dots indicate the observation points for the volumetric water content (31-cm deep), and the rainfall intensity was set to 96 mm/h.

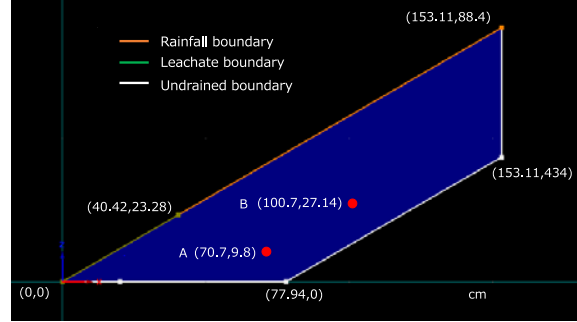


Fig. 6 Analysis model

Table 1 SWCC parameters

Sample	Granite Soil
Residual Volumetric Water Content (θ_r)	0
Saturation Volumetric Water Content (θ_s)	0.377
Hydraulic Conductivity (k_s)	0.726 cm/min
Parameter Related to Air Ingress Value (α)	0.0821/cm
Dimensionless Parameter (n)	3.33
Dimensionless Parameter (l)	0.5

Analysis Results

The change in volumetric water content over time is plotted in Fig. 7. The volumetric water content at observation points A and B at the same depth increased simultaneously owing to water infiltration from the ground surface because of rainfall. Subsequently, the rate of change in the volumetric water content decreased and reached quasi-saturated state. Then, the volumetric water content increased again in the order of A and B due to the water level was formed.

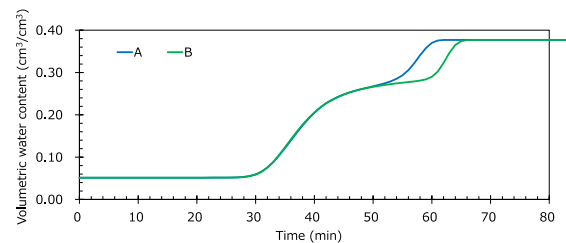


Fig. 7 Analysis-based change in volumetric water content over time

Estimation of the Point of Water-Level Occurrence

The quasi-saturated duration was calculated from the data of volumetric water content at each observation point, and the point of water-level occurrence was estimated. The time when the change

in volumetric water content was below $0.005 \text{ (cm}^3/\text{cm}^3\text{)}/\text{min}$ was defined as the quasi-saturation start time. Furthermore, the time when the change increased above $0.005 \text{ (cm}^3/\text{cm}^3\text{)}/\text{min}$, the volumetric water content was judged to start rising again. The quasi-saturated duration time, t , is calculated by subtracting the start time of the re-rising of the volumetric water content from the start time of quasi-saturated at each observation point. Fig. 8 plots the horizontal distance from the point of water-level occurrence to the quasi-saturated duration time; the result shows an approximate straight line. If the intersection of the approximation line and the horizontal axis is defined as the point of water-level occurrence, the error is 8 cm from the actual point of water-level occurrence, implying that the point of water-level occurrence could be estimated with high accuracy.

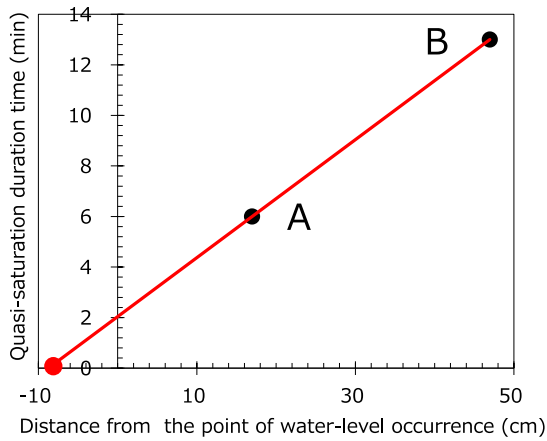


Fig. 8 Estimation of point of water-level occurrence

VERIFICATION THROUGH MODEL EXPERIMENTS

Summary and Method of Model Slope Experiments

Figure 9 provides an overview of the model slope, and the physical properties of the samples are shown in Table 2. In this experiment, a model slope of 1500 mm (length) \times 300 mm (width) \times 890 mm (height) was constructed with a topsoil thickness of 450 mm and slope of 30° . The experimental conditions are shown in Table 3. The base of the topsoil layer was assumed to be a sliding surface, on which clay was applied for the undrained condition. To confirm water-seepage behavior in the depth and slope directions, soil-moisture meters were installed at seven locations, as shown in Fig. 9, and the volumetric water content was measured at 1-min

intervals. An image-sensing technology [3] was used to measure the ground-surface displacement. In addition, a camera was set up at a position facing the slope model, and displacement measurement targets were set up at three locations, as shown in Fig. 9. The ground surface was opened to receive water that was sprinkled to simulate rainfall and drainage conditions. The watering intensity was set at 96 mm/h. To mitigate the effect of collapse settlement on the displacement measurements as much as possible, the experiment was started after the surface layer was slightly wet.

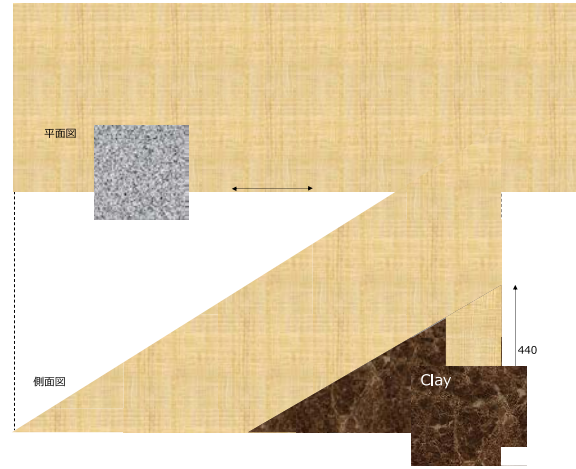


Fig. 9 Overview of the model slope

Table 2 Physical properties of the sample

Sample	Granite Soil
Initial Water Content (w)	5.0%
Soil Particle Density (ρ_s)	2.607 g/cm^3
Setting Dry Density (ρ_d)	1.629 g/cm^3
Maximum Dry Density (ρ_{dmax})	1.766 g/cm^3
Hydraulic Conductivity (k_s)	$1.21 \times 10^{-2} \text{ cm/s}$
Void Ratio (e)	0.6

Table 3 Experimental conditions

Boundary Condition	Top Surface	Drainage
	Back Side	Undrained
	Side Surface	Undrained
	Bottom Surface	Undrained
Slope Gradient		30°
Water Sprinkling Strength		96 mm/h

Experimental Results

The change in ground-surface displacement over time is plotted in Fig. 10. Considering the time of

failure, surface displacement initiated at all points about 27 min after the start of the experiment. At about 41 min, a small failure was observed near the toe of the slope, after which small failures occurred continuously from the toe to the top of the slope. Failure at point A occurred at around 48 min, and those at points B and C occurred at around 52 min.

The change in volumetric water content over time is plotted in Figs. 11(a), (b), and (c). Regarding the behavior of volumetric water content at line B, the volumetric water content increased in order from B1 to B2 to B3 owing to water infiltration from the ground surface and reached quasi-saturated state. Subsequently, the volumetric water content increased again in the order of B3 to B2 to B1. The behavior of line C is similar to that of line B. The results agree with those of previous studies showing that displacement occurs after the volumetric water content exceeds IQS.

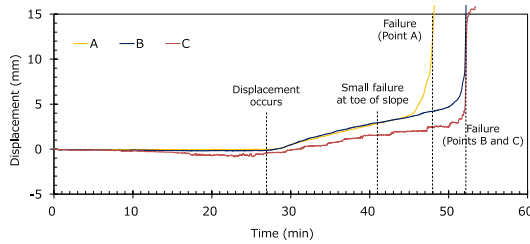
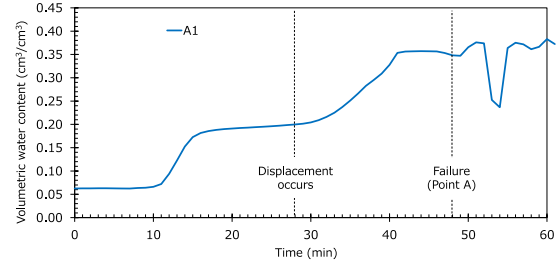


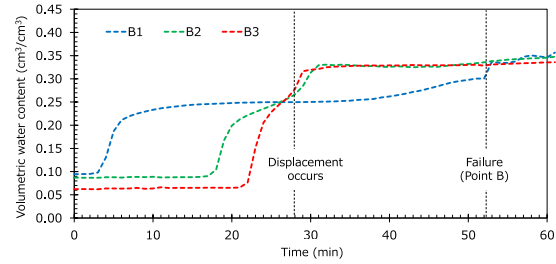
Fig. 10 Change of ground-surface displacement over time

Estimation of the Point of Water-Level Occurrence

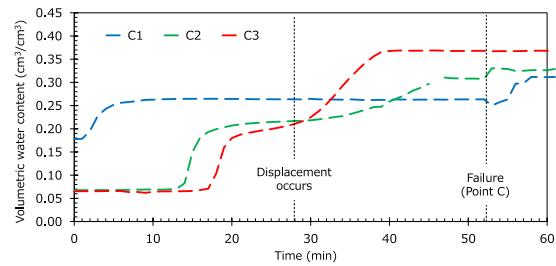
The quasi-saturated duration is calculated using the data of volumetric water content at each measurement point, and the point of water-level occurrence is estimated. The time when the change in volumetric water content was below $0.01 \text{ (cm}^3/\text{cm}^3\text{)}/\text{min}$ was defined as the quasi-saturation start time, and the time when the change increased above $0.01 \text{ (cm}^3/\text{cm}^3\text{)}/\text{min}$ was defined as the time when the volumetric water content started to rise again. However, if the change did not exceed $0.01 \text{ (cm}^3/\text{cm}^3\text{)}/\text{min}$ again, the time at which the change reached its maximum was considered to be the quasi-saturation end time. The quasi-saturated duration is calculated by subtracting the start time of the re-rising of volumetric water content from the start time of quasi-saturation at each observation point. The horizontal distance from the point of water-level occurrence is plotted against the quasi-saturated



(a) Line A



(b) Line B



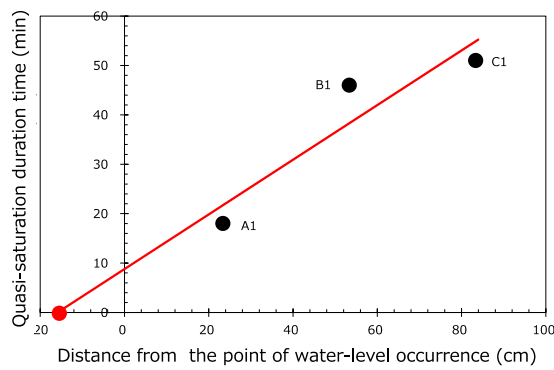
(c) Line C

Fig. 11 Change in volumetric water content over time according to the line of measure

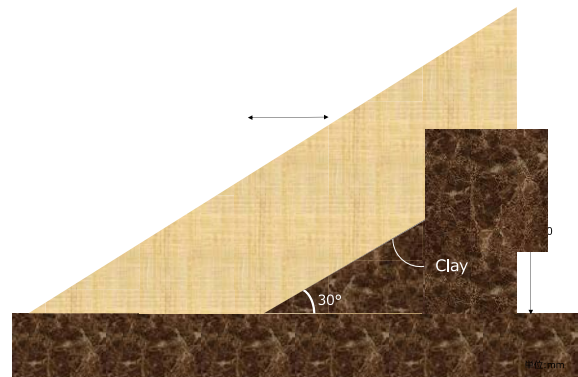
duration, and the approximate straight lines are shown in Fig. 12 (10-cm depth) and Fig. 13 (31-cm depth) for each measurement depth. If the intersection of the approximation line and the horizontal axis is defined as the point of water-level occurrence, at a measurement depth of 10 cm (A1, B1, C1), the error was 16 cm from the actual point of water-level occurrence, while it was 10 cm at the measurement depth of 31 cm (B2, C2); therefore, the actual point of water-level occurrence could be estimated with reasonable accuracy.

CONCLUSION

The authors investigated a method for predicting slope failure by focusing on soil water during rainfall. In this study, the appropriate locations for installations of sensors for slope monitoring were examined based on model slope experiments to detect slope hazards more accurately. A method for

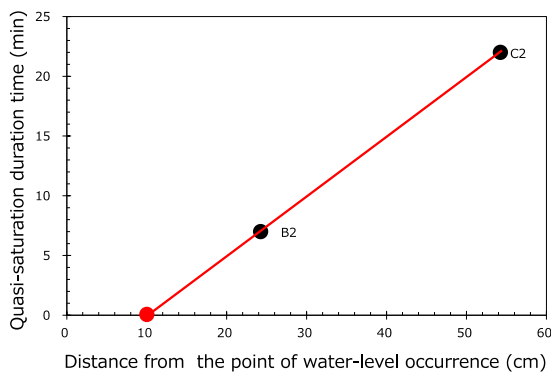


(a) Estimation of the point of water-level occurrence

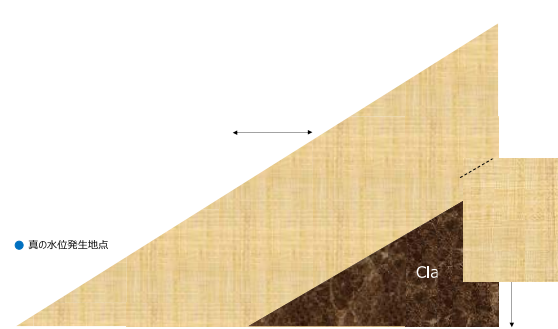


(b) Estimated location of the water-level occurrence

Fig. 12 Estimated point of water-level occurrence from the measured depth of 10 cm



(a) Estimation of the point of water-level occurrence



(b) Estimated location of the water-level occurrence

Fig.13 Estimated point of water-level occurrence from the measured depth of 31 cm

estimating the point of water-level occurrence was presented based on the relationship between the distance between the sensors and the quasi-saturated duration time calculated using the analysis of saturated-unsaturated seepage flow. The validity of the proposed method was verified through model slope experiments. The results suggest that slope hazards can be reasonably detected by installing sensors at the estimated point of water-level occurrence. The proposed method will be applied to actual slope monitoring in the future.

REFERENCES

- [1] Yagi N., Yatabe R., and Yamamoto K., Slope failure due to seepage of rainwater. *Journal of JSCE*, Vol. 1983, Issue 330, 1983, pp. 107-114.
- [2] Kohgo Y., Saito H., Niide T., and Hori T., Slope safety following rainfall with model slopes, *Japan National Conference on Geotechnical Engineering*, E-14, Issue 991, 2013, pp. 1981-1982.
- [3] Sako K., Suda T., Fukugawa R., and Kitamura R., Soil tank tests on seepage and failure behavior of masa slope due to rainfall, *Proceedings of the 4th Symposium on Sediment-Related Disasters*, 2008, pp. 21-26.
- [4] Koizumi K., Sakuradani K., Oda K., Ito S., Fukuda Y., Feng M.Q., and Takemoto M., Fundamental research on advancement of regulation standard for expressway management against rainfall-induced surface failure, *Journal of JSCE Ser. C (Geo-engineering)*, Vol. 73, Issue 1, 2017, pp. 93-105.
- [5] Simunek, J., van Genuchten M.T., and Senja, M., The HYDRUS Software Package for Simulating the Two- and Three-Dimensional Movement of water, Heat, and Multiple Solutes in Variably-Saturated Media, March 2006.

A METHOD FOR REAL-TIME EVALUATION OF THE PROPERTIES OF COMPACTED SOIL FROM ACCELERATION RESPONSE OF COMPACTION ROLLER

Hiroyuki Nagai¹, Yoshiaki Kikuchi², Sou Ihara², Shohei Noda², Taichi Hyodo³ and Fumio Tatsuoka^{2,4}

¹Hazama Ando Corp.; ²Tokyo University of Science; ³Toyama Prefectural University; ⁴Tokyo University

ABSTRACT

In recent years, a number of soil structures were damaged by frequently occurring severe earthquakes and heavy rainfalls. In relation the above, the Ministry of Land, Infrastructure, Transport and Tourism Japan is advocating the “i-Construction” promoting the development of new technologies that can improve construction efficiency and can extend the life time of infrastructures including soil structures. It was recently shown that the soil compaction and the properties of compacted soil are controlled by the dry density ρ_d and the degree of saturation S_r , which can be evaluated typically by RI tests as a fast method. Yet, this method is time-consuming and can be performed only at a limited number of places. To improve the efficiency of soil compaction control, real-time and continuous compaction control ensuring high quality of compacted soil is required. We studied a method to evaluate the values of ρ_d and S_r based on the ground stiffness estimated from the acceleration response of vibratory compaction roller in real time and continuously (called the *CCV* method) together with proper control of field compaction energy level. By analyzing a large amount of data from on-site compaction tests, an empirical equation expressing the *CCV* value, as a soil stiffness index, as a function of ρ_d and S_r irrespective of the number of pass was developed. The ρ_d and S_r values for a given *CCV* value can be estimated based on this equation either when the water content ratio can be reasonably assumed or when the compaction energy level is controlled to be equal to a given specified value.

Keywords: CCV, Embankment, Compaction, Dry density, Degree of saturation

INTRODUCTION

In recent years, natural disasters, such as large earthquakes and heavy rainfall, have occurred frequently. In addition, the damage caused by such disasters has increased rapidly, e.g., the collapse of embankments, such as roads and railways, and the construction of residential land [1]. Therefore, construction methods and quality control methods that can realize high-quality embankments are required.

The Ministry of Land, Infrastructure, Transport and Tourism has proposed i-Construction for promoting the research and development of new technologies for improving work efficiency and safety and prolonging service life [2]. Therefore, a real-time soil compaction control method over the area of concerned earthwork is required to improve the construction efficiency and the quality of compacted soil.

In conventional soil compaction control, sand replacement tests or *RI* tests are performed after compaction at a limited number of places over the concerned area to obtain the dry density ρ_d and the water content ratio w of soil. This method is, however, time-consuming.

It is known that the on-site *CBR* is a function of the dry density ρ_d and the degree of saturation S_r irrespective of compaction energy level (Tatsuoka,

2015). In this study, an empirical equation expressing the response acceleration value (i.e., *CCV* value) of vibratory compaction roller as a function of ρ_d and S_r was derived by analyzing data from full-scale field compaction tests. It is shown the *CCV* value is representative of the stiffness of compacted soil in the field. This empirical equation is used to draw the contour lines of *CCV* values the ρ_d and w plane and the contour lines were compared with the compaction curve obtained by the standard compaction tests (*1E_c*). It is shown that the dry density during a given compaction process is accurately evaluated based on the empirical function for *CCV* when the water content ratio is known.

MATERIALS AND METHODS

Embankment Material

Gravel sand mixed with fine particles with a maximum particle size of $D_{\max} = 75.0$ mm was used to perform a rolling compaction test. A picture of the embankment material is shown in Fig 1, and its physical properties are shown in Table 1. Fig. 2 shows the grain size distribution curve of the field fill material used in the field full-scale compaction test (Fig. 5) and those of the samples that were

prepared by removing particles larger than a particle diameter either $D = 37.5$ mm or $D = 9.5$ mm.



Fig. 1 Picture of embankment material

Table 1 Properties of field fill material

Parameter	Value
Soil particle density (g/cm^3)	2.778
Maximum grain size (mm)	75.0
Fine fraction content (%)	10.1
Uniformity coefficient	334
Coefficient of curvature	16.2
Classification	Gravel sand mixed with fine particles
Symbol	G-FS
Liquid limit w_L (%)	29.6
Plastic limit w_P (%)	19.7
Plasticity index I_P	9.9
Compaction test ($D_{\max} = 37.5$ mm)	JIS A 1210
Maximum dry density (Standard proctor) $\rho_{d\max}(\text{g}/\text{cm}^3)$	1.897
Optimum water content ratio (Standard proctor) w_{opt} (%)	14.8
Optimum degree of saturation S_{ropt} (%)	88.5

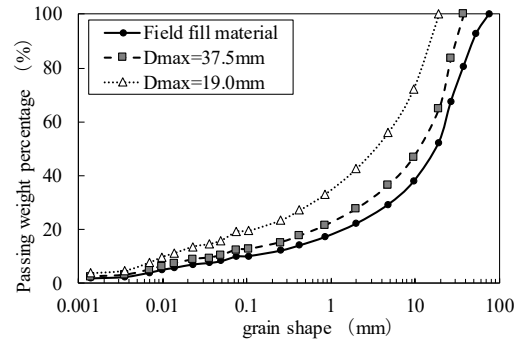


Fig. 2 Grain size distribution curve

Laboratory Test

A laboratory compaction test (JIS A 1210) was carried out by employing the B-c method (Standard Proctor: $1E_c$) using the sample with $D_{\max} = 37.5$ mm (Fig. 5). The compaction curve for other D_{\max} values shown in Figs. 6 and 7 were obtained by the Walker-Holtz method (Walker and Holtz, 1951).

To evaluate the internal friction angle of compacted soil, a series of drainage triaxial compression tests (JGS 0524-2009) were conducted (hereinafter referred to as the CD test) on specimens with dimensions of $\Phi 5$ cm \times $H 10$ cm produced by using the material with $D_{\max} = 9.5$ mm. The compacted states of the specimens are shown in Fig. 6. The CD test was performed after by saturating the prepared specimens.

Field Test

Fig. 3 shows the full-scale compaction test yard and the zones in which quality tests were performed. The compaction test yard was 20 m long, 6 m wide, and 60 cm thick. The yard consisted of two layers with a thickness of 30 cm each. The first layer was a preliminary layer, which was constructed by applying rolling compaction 8 times using an 11 ton

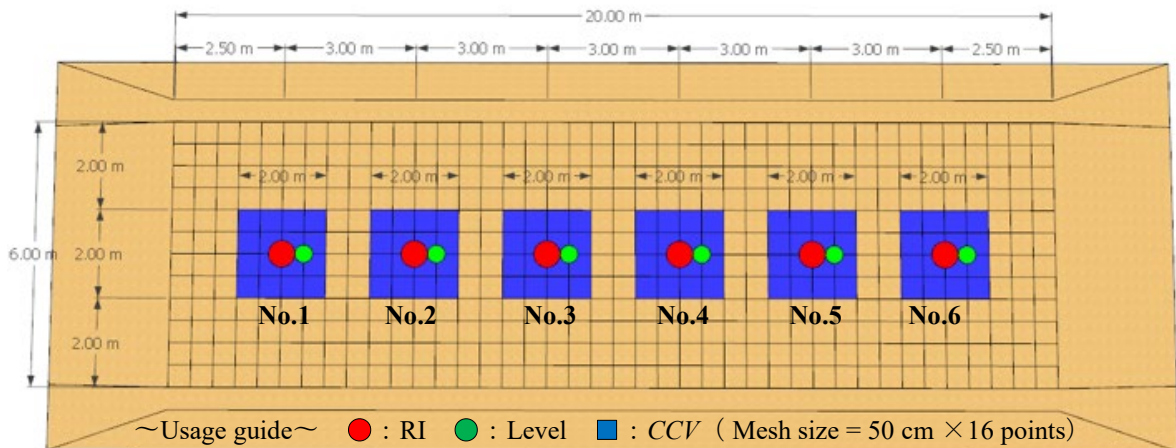


Fig.3 Full-scale compaction test yard and quality test area

vibratory compaction roller to the embankment material with an average water content ratio of $w_n = 11\%$. The second layer was the test layer, which was constructed by applying rolling compaction 16 times to the fill material with an average water content ratio of $w_n = 11\%$. While constructing the second layer, *CCV* measurement was performed on the entire area of the yard from the response acceleration records of the vibrating roller. After compaction passes $N = 2, 4, 6, 8$, and 16, at measurement points 1 to 6 shown in Fig. 3, the settlement was measured and the dry density of the top 20 cm was evaluated by the *RI* method.

In *CCV* measurement method, an acceleration sensor is attached to the vibration axis of the front wheel of the vibratory compaction roller as shown in Fig 4, and the soil stiffness is evaluated from the response acceleration of the vibratory compaction roller during compaction [3]. The index referred to as the *CCV* value is used to evaluate soil stiffness in real time over the area of earthwork. The *CCV* value can be calculated by attaching an acceleration sensor to the iron wheel (front wheel) of the vibration roller and analyzing the acceleration waveform of the iron wheel vibration obtained during construction. The empirical equation for the *CCV* value is given by Eq. (1) [3].

$$CCV = (S_1 + S_3 + S_4 + S_5 + S_6) / (S_1 + S_2) \times 100 \quad (1)$$

where S_2, S_1, S_3, S_4, S_5 , and S_6 are the amplitude spectra at $f_0, 0.5f_0, 1.5f_0, 2f_0, 2.5f_0$, and $3f_0$, respectively, and f_0 is the fundamental frequency of the vibrating roller. The *CCV* value can be measured at 0.2 s intervals. The construction area is arbitrarily divided into meshes, and the *CCV* values acquired when the vibratory compaction roller passes through the meshes are averaged. A GNSS antenna was installed on the vibratory compaction roller to obtain the position information during construction. Thus, the locations of the *CCV* measurement points could be accurately determined. In this study, the rolling compaction yard was divided into 50 cm meshes and *CCV* values were obtained for each mesh, as shown in Fig. 3.

The *CCV* values obtained using 2 m meshes (blue hatching in Fig. 3) were used in the analysis



Fig. 4 Picture of acceleration sensor

shown below. These meshes included the *RI* test and level measurement zones.

TEST RESULTS

Laboratory Test

Fig. 5 shows the results of the laboratory compaction test performed using the sample with $D_{max} = 37.5$ mm.

As shown in Fig.6 at the compacted states Nos.1-3 of the specimens tested in the CD tests, the ρ_d value was $(D_c)_{IEc} = 95\%$ of $[(\rho_d)_{max}]_{IEc}$, while the water content ratio was different.

When the degree of compaction, D_c (i.e., ρ_d), increases under the condition that saturation S_r is constant, the internal friction angle tends to always increase [5]. For an allowable lower bound of an angle of ϕ equal to 30° , it was examined whether the ϕ values exceed this lower bound when $(D_c)_{IEc} \geq 95\%$ for the water content ratio at Nos. 1 - 3. Table 2 shows the conditions for the CD test and the measured internal friction angle, ϕ . $\phi \geq 30^\circ$ for all S_r when $(D_c)_{IEc} \geq 95\%$ can be confirmed. It was considered that $\phi \geq 30^\circ$ can be ensured for any S_r if $(D_c)_{IEc} \geq 95\%$ with the field fill material with $D_{max} = 75.0$ mm [6].

In Fig. 7, the acceptable zone for compacted states of the field fill material with $D_{max} = 75.0$ mm is indicated in relation to its compaction curve ($1E_c$) inferred by the Walker-Holtz method from the compaction curve ($1E_c$) evaluated by the laboratory compaction test ($1E_c$) on the material with $D_{max} = 37.5$ mm (shown Fig. 3). The allowable lower bound of ρ_d corresponding to $(D_c)_{IEc} = 95\%$ for $D_{max} = 75.0$ mm is indicated.

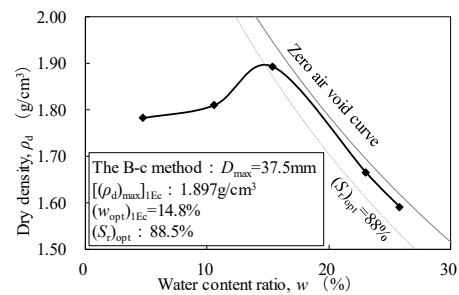


Fig. 5 Compaction test

Table 2 Results of drainage triaxial compression tests

No.	Dry density ρ_d (g/cm ³)	Water content w (%)	Degree of saturation S_r (%)	Internal friction angle Φ_d (°)
1	1.573	15.7	58	32.3
2	1.568	21.0	72	36.6
3	1.554	27.6	95	34.6

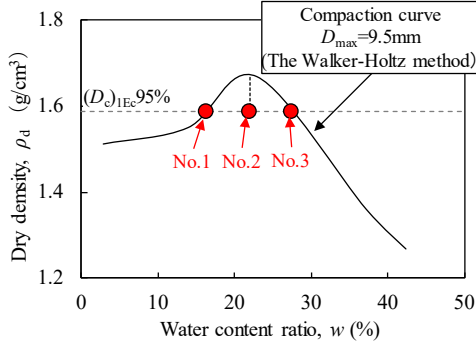


Fig. 6 Compacted states of specimens for triaxial compression tests

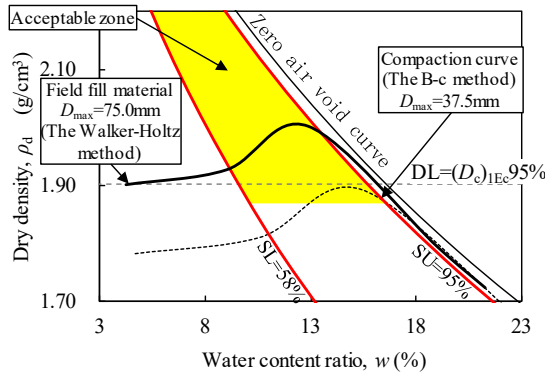


Fig. 7 Acceptable zone in compaction control

Field Test

Relationship between the number of compaction passes and wet density ρ_t , w , ρ_d , S_r , and CCV value

Figs. 8 to 12 show all the data measured at the six points shown in Fig. 3. Figs. 8 to 11 show the relationship between ρ_t , w , ρ_d , and S_r and the number of compaction passes N obtained by the field compaction tests, where the values of ρ_t and w were those measured by the *RI* tests, while the values ρ_d and S_r are those calculated from these measured values.

As shown in Figs. 8 and 9, the values ρ_t and w noticeably differ depending on the measurement point. In particular, the value of w measured at point No.1 was lowest and the one at point No.2 was highest, different by 3–4% from each other. This fact means that, to accurately evaluate the dry density from a given *CCV* value, we cannot rely on a given fixed average water content ratio for the area but the local water content ratio at the place where this *CCV* value is obtained should be evaluated. In addition, the values at the same measurement point slightly fluctuate as the number of compaction passes increases. This fact should

also be taken into account when evaluating local water content ratio.

The values of ρ_d and S_r strongly also depend on the measurement point, as shown in Figs. 10 and 11. Yet it may be seen that the values of ρ_d and S_r tend to increase significantly until the number of compaction passes N becomes 2. Then, as N increases from 6 to 16, the values of ρ_d and S_r either increase gradually or tend to converge.

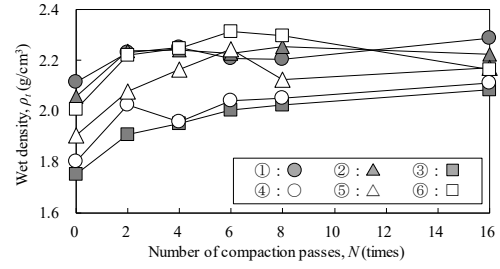


Fig. 8 Relationship between wet density ρ_t and number of compaction passes N

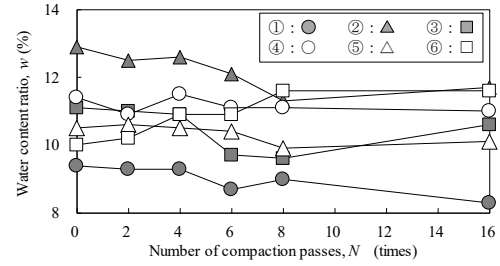


Fig. 9 Relationship between water content ratio w and number of compaction passes N

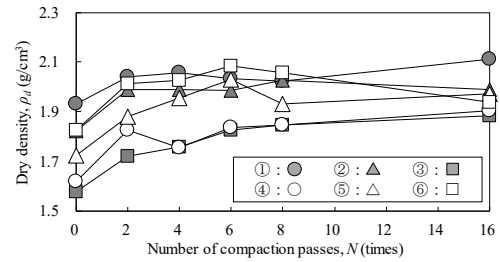


Fig. 10 Relationship between dry density ρ_d and number of compaction passes N

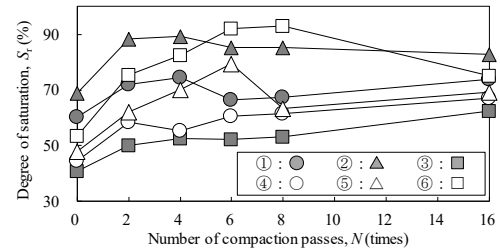


Fig. 11 Relationship between degree of saturation S_r and number of compaction passes N

Fig. 12 shows the relationship between the CCV value and the number of compaction passes N . Similar to ρ_t , w , D_c , and S_r , the CCV value strongly depends on the measurement point. At each measurement point, the CCV value increases until N becomes 8, reaching a maximum at $N = 8$, and then starts noticeably decreasing as N increases from 8 to 16, unlike the values of ρ_d and S_r . This trend may be due to that, as N increases from 8 to 16, the CCV value increases with an increase in ρ_d , while it decreases with an increase in S_r , while the effects of the latter factor are generally stronger than those of the former factor.

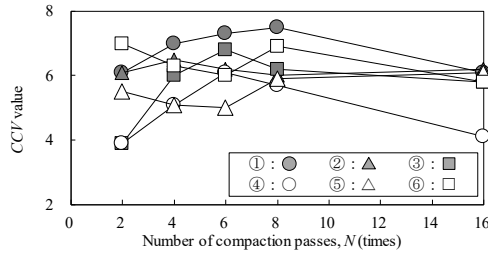


Fig.12 Relationship between CCV value and number of compaction passes N

Empirical equation for estimating ρ_d and S_r using CCV value

In the following, we propose an empirical equation expressing the CCV values as a function of S_r and ρ_d , in the same way as the field CBR data analyzed by Tatsuoka et al. [7-9]. The field CBR data are shown in Fig. 13a, which were obtained from a long-term research by full-scale compaction tests conducted at the Institute of Construction Mechanization (1965–1990) using many different compaction machines on the same type of sandy loam soil prepared at different water content ratio. The proposed empirical equation for CBR is expressed by Eqs. (2) and (3):

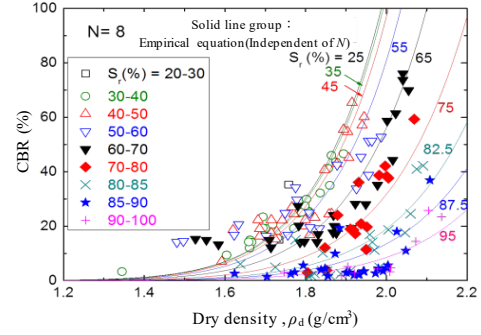
$$CBR = f_{CBR}(S_r) \cdot (\rho_d / \rho_w - b)^c \quad (2)$$

$$f_{CBR}(S_r) = A_2 + (A_1 - A_2) / [1 + \exp\{(S_r - x_0)/dx\}] \quad (3)$$

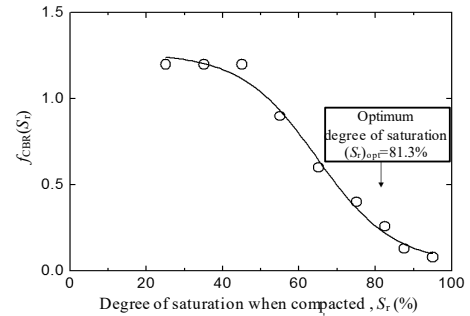
The constants in Eqs. (2) and (3) were found as $b = 0.4$, $c = 9.5$, $A_1 = 1.26$, $A_2 = 0.042$, $x_0 = 64.8$, and $dx = 9.97$. The unit of S_r in Eqs. (2) and (3) was %, and all the other constants were dimensionless quantities.

The relationships between CBR and ρ_d for different S_r values were fitted by Eq. (2): firstly by finding relevant values of parameters b and c by which Eq. (2) can fit the whole data; and then by finding the value of $f_{CBR}(S_r)$ by which Eq. (2) can fit the relation for the respective values S_r . In Fig. 13(b), the values of $f_{CBR}(S_r)$ obtained as above are plotted

against S_r . It may be seen from Fig. 13(a) that Eq. (2) captures very well the following trends of behaviour of the data: 1) for a fixed value of S_r , the CBR value consistently increases with an increase in ρ_d in the same way irrespective of the S_r value; and 2) for a fixed value of ρ_d , the CBR value consistently decreases with an increase in S_r in the same way irrespective of the ρ_d value.



(a) Relationship with saturation S_r at the end of compaction as a parameter



(b) S_r function $f_{CBR}(S_r)$

Fig.13 Relationship between on-site CBR and dry density obtained in the full-scale compaction test conducted at the Institute of Construction Mechanization [7,9]

In this study, we analyzed the data obtained from the field full-scale compaction test and examined whether empirical equations for CCV values in the same form as Eqs. (2) and (3) are relevant. Here, the empirical relationship between ρ_d , S_r , and CCV is given by Eqs. (4) and (5).

$$CCV = f_{ccv}(S_r) \times (\rho_d / \rho_w - b)^c \quad (4)$$

$$f_{ccv}(S_r) = \frac{D}{1 + \exp(ES_r)} \quad (5)$$

Fig.14 shows all the measured CCV values for different values of S_r are plotted against the ρ_d value. The data are classified based an interval of S_r of 5% (i.e., $50\% \leq S_r < 55\%$, $55\% \leq S_r < 60\%$, $60\% \leq S_r < 65\%$, $65\% \leq S_r < 70\%$, $70\% \leq S_r < 75\%$, $75\% \leq S_r < 80\%$, $80\% \leq S_r < 85\%$, $85\% \leq S_r < 90\%$, and $90\% \leq S_r < 95\%$). The solid curves

shown in Fig. 14 represent the CCV - ρ_d relation for the respective ranges of S_r obtained by Eq. (4) with $b = 0.4$ and $c = 9.5$ and the value of $f_{CCV}(S_r)$ obtained by Eq. (5). Eq. (5) was defined so that Eq. (4) fits the whole data. That is, in Fig. 15, the value of $f_{CCV}(S_r)$ obtained as $CCV / (\rho_d / \rho_w - b)^c$ of each data is plotted against S_r . A rather unique relation is obtained in a form very similar to the one for the field CBR seen in Fig. 13(b). The average relation represented by a broken curve was defined as Eq. (5) with $D = 2.0$ and $E = 0.04$.

It may be seen from Fig. 14 that the fitted Eq. (4) is generally consistent with the data points. It is to be noted that, although the fitting is relatively poor with the data for $S_r = 65-70\%$ (■ in the figure) and $70-75\%$ (□ in the figure), the fitting is rather acceptable for $S_r = 75-95\%$, which covers the optimum degree of saturation $(S_r)_{opt} = 88.5\%$. $(S_r)_{opt}$ is the value of S_r where the maximum dry density $(\rho_d)_{max}$ is obtained in a laboratory compaction test. As $(S_r)_{opt}$ is rather insensitive to variations of soil type and compaction energy level (CEL) in a given project, $(S_r)_{opt}$ could be defined as the target S_r value irrespective of inevitable variations of soil type and CEL to optimize the soil compaction efforts (i.e., to obtain $(\rho_d)_{max}$) for given soil type and CEL.

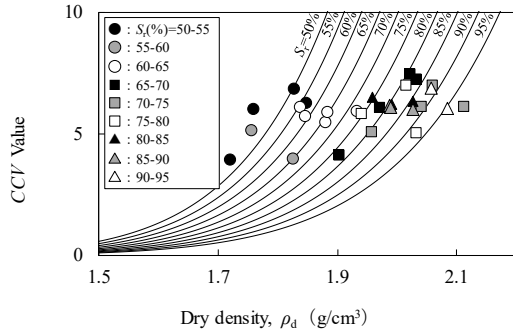


Fig.14 Relationship between CCV and ρ_d

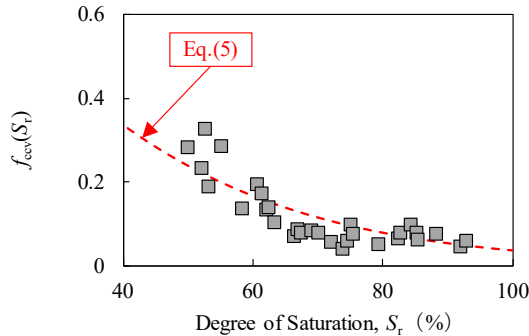


Fig.15 Relationship between $f_{CCV}(S_r)$ and S_r

COMPACTION MANAGEMENT METHOD USING EMPIRICAL EQUATION

The CCV value is expressed as a function of ρ_d and S_r by Eqs. (4) and (5): i.e., by Eq. (6). Eq. (7) is obtained from Eq. (6) by using w instead of S_r .

$$CCV = \left(\frac{2.0}{1 + \exp(0.045S_r)} \right) \times (\rho_d / \rho_w - 0.4)^{9.5} \quad (6)$$

$$CCV = \left(\frac{2.0}{1 + \exp\left(0.04 \frac{\rho_d \rho_{sw}}{\rho_s - \rho_d}\right)} \right) \times (\rho_d / \rho_w - 0.4)^{9.5} \quad (7)$$

If the target ρ_d is determined and w and ρ_s are known, the target CCV value can be determined from Eq. (7). Moreover, if ρ_s and w are known, ρ_d can be calculated when the CCV value is measured during construction. Therefore, real-time compaction management over the area of compaction, which is the purpose of this work, can be realized by utilizing Eq. (7).

In the following, the validity of Eqs. (6) and (7) in the estimation of ρ_d is examined. Fig.16 shows the plots of the measured and estimated values of ρ_d and the measured value of w in relation of the compaction curve of the field fill material with $D_{max} = 75$ mm. The estimated values of ρ_d were obtained by substituting the respective measured sets of CCV value and w into Eq. (7). The measured and estimated values of ρ_d are generally in good agreement, although the estimation is rather inaccurate for the data for $S_r = 65-75\%$ with the estimated values being lower than the measured values.

Fig.17 shows the relationship between the measured and estimated values of ρ_d . Shown in this figure are the lines for $Y = X$, $Y = X - 0.1$ and $Y = X + 0.1$ together with the approximate curve obtained using the least squares method, for which the correlation coefficient (R^2) between the measured and estimated values is 0.7023. The line $Y = X$ indicates that the measured and estimated values are equal to each other. Nearly all the data are close to the line $Y = X$, and all the data points are located between the lines for $Y = X + 0.1$ and $Y = X - 0.1$. Furthermore, a relatively high value of $R^2 = 0.7023$ confirms that the estimation accuracy is rather high. Based on this, we can conclude that the accuracy of estimating ρ_d using Eqs. (6) and (7) is generally good.

Next, the compaction management method referring to the contour lines of the CCV value calculated from the estimation equation is examined. Fig.18 shows a vertical line where $w = 9\%$ and the contour lines for CCV values of 1, 5, 10, 11.2, and 30 obtained from Eq. (6), together with the compaction curve for the field fill material ($D_{max} = 75$ mm). Along each contour line of the CCV values, as ρ_d increases, the w value increases when $S_r < S_{ropt}$, reaches the maximum value slightly before $S_r = S_{ropt}$ is attained, and decreases in the range of $S_r > S_{ropt}$.

ρ_d is estimated by taking into account this trend of behaviour, as explained below.

The average w value of each clod of fill material unloaded from a dump truck was obtained by performing RI measurement, and this w value was defined as the representative value of the area where the clod was spread. It is assumed that the water content ratio over the concerned area of compaction is constant at $w = 9\%$, which is equal to the average value of respective clods. In the compaction process, ρ_d changes along the contour line of $w = 9\%$. Point A is the point where the contour lines of CCV value = 11.2 contacts the $w = 9\%$ line. This implies that the maximum CCV value at $w = 9\%$ is 11.2.

Based on this, if the maximum CCV value can be obtained in advance by measuring the w of the fill material and using an empirical equation. If CCV values higher than this maximum value, it is likely that the actual local water content ratio is lower than the assumed value (equal to 9 % in this case), which requires the careful measurements of local water content ratio and proper adjustments of water content ratio in the subsequent compaction work.

Next, the case when the measured CCV value below the maximum value is obtained is analyzed. That is, as shown in Fig.18, the contour lines of CCV value = 10 and $w = 9\%$ intersect at two points B and C . This implies that there are two possible solutions for ρ_d . We must judge whether ρ_d is in the range of $S_r \leq S_{ropt}$ (initial stage of compaction) or $S_r > S_{ropt}$ (late stage of compaction). On the other hand, the CCV value changes during the compaction process as shown in Fig. 12. That is, the CCV value tends to increase in the early stage of compaction and decrease in the late stage of compaction. According to this trend, if the current compaction stage can be determined by examining the trend of change in immediately preceding CCV values and total compaction time until the present time, it is possible to accurately evaluate ρ_d .

Thus, when estimating ρ_d based on the CCV value and w using the empirical equation, it is important to consider not only the CCV value but also the history of number of compaction pass.

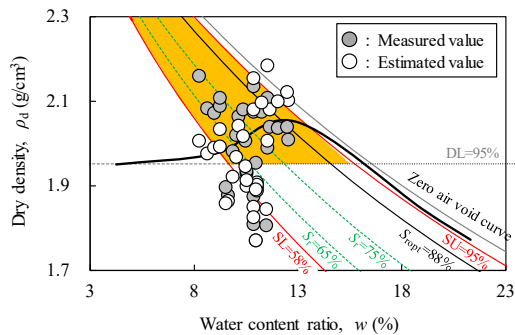


Fig.16 Results of compaction test on ρ_d - w plot

This allows for real-time and compaction management over the concerned area of compaction. It is expected that a high-quality embankment structure can be realized by employing a rational construction method, such as the one proposed in this paper.

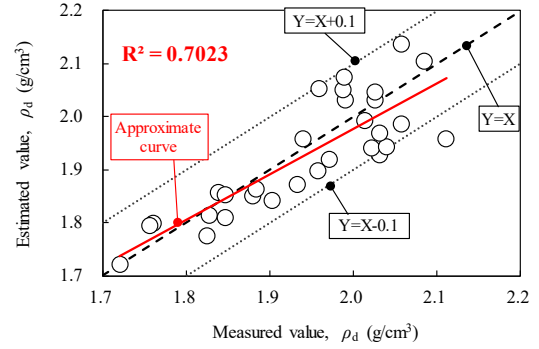


Fig.17 Comparison of measured and estimated values of ρ_d

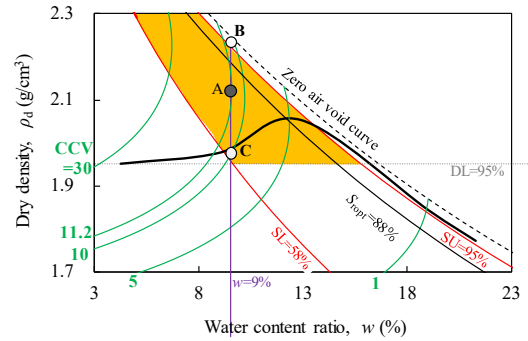


Fig.18 Compaction control method using contour lines of CCV values

CONCLUSION

A field full-scale compaction test was carried out to develop a method for estimating ρ_d and S_r based on CCV values to realize high-quality embankment construction. The main findings of this study are as follows:

- (1) The results of the rolling compaction test show that the local values of w , ρ_d , S_r , and CCV differ considerably depending on the measurement point. Moreover, the local value of w at each measurement point slightly fluctuates as the number of compaction passes N increases. These facts indicate that it is imperative to accurately evaluate instantaneous local water content ratio at places where CCV values are evaluated.
- (2) ρ_d and S_r increase significantly when $N = 2$, gradually increase as N increases from 2 to 6, and tend to converge as N increases from 6 to 16. The CCV values increase as N increases

from 2 to 8, reach a maximum when $N = 8$, and decrease as N increases from 8 to 16. This fact indicates that CCV is not a unique function of ρ_d , but the effects of S_r are also important.

- (3) The CCV value can be expressed by Eq. (6), in which ρ_d and S_r are independent variables and the number of passes and compaction energy are not considered as variables. The accuracy of estimating ρ_d using the empirical equation increases with the accuracy of S_r and $f_{CCV}(S_r)$.
- (4) If the target ρ_d is determined and w and ρ_s are known, the target CCV value can be determined from Eq. (7). Moreover, if ρ_s and w are known, ρ_d can be calculated when the CCV value is measured during construction. Therefore, real-time compaction management over the concerned area of compaction, which is the purpose of this work, can be realized.
- (5) When the w of the fill material is assumed to be constant, the CCV value reaches the maximum immediately before S_r becomes equal to $S_{r\text{opt}}$. At the time of construction, the required high compaction state can be achieved by confirming that the CCV value has reached its maximum after a predetermined number of compaction passes.
- (6) When the CCV value is below the maximum value, ρ_d can be accurately evaluated by considering the CCV value along with the number of compaction passes. Real-time compaction management over the concerned area can be realized by combining the procedures (5) and (6).

The results of this study show that the compaction management using the empirical equation for the CCV value based on ρ_d and S_r is effective. This method can be applied to evaluate and improve the real time quality control of embankments. In the future, the authors will investigate a method for the real-time measurement of w and a method of evaluating the quality of embankments with a higher accuracy.

REFERENCES

- [1] Watanabe K. Watanabe H., Burst Factors and Restoration Method of Construction of the Fujinuma Dam, Water land and environmental engineering, 2015, pp.866-867.
- [2] Kondo K., Issues for the spread of ICT earthworks, Construction Management Technology, 2017, pp.13-18.
- [3] East Nippon Expressway Company Limited, Central Nippon Expressway Company Limited, West Nippon Expressway Company Limited., Quality control of embankments using the roller acceleration response method, Civil Engineering and Construction Management Procedures, 2017, pp.127-166.
- [4] Walker F.C. and Holtz W.G., Control of Embankment Material by Laboratory Testing. Trans ASCE, Vol. 77, No. 108, 1951, pp.1-25,
- [5] Ihara S. Okada M. Magara K. Noda S. Nagai H. Sandanbata I. Kikuchi Y, and Tatsuoka F., Experimental analysis of the effect of gravel content on compaction and strength properties of sand gravel, GEOKANTO, 2019.
- [6] Uemoto Y. Shibuya S. Hashimoto Y. and Kawajiri S., Influence of grain size distribution characteristics on compaction and deformation-strength characteristics of gravelly fill material, Japanese Geotechnical Journal, Vol.6, No.2, 2011, pp181-190.
- [7] Tatsuoka,F, Importance of the Control of the Degree of Saturation in Soil Compaction, Engineering for dams No.354, 2016, pp.3-16.
- [8] Tatsuoka F., Compaction Characteristics and Physical Properties of Compacted Soil Controlled by the Degree of Saturation. in Proc. of 15th Pan-American Conf. on SMGE and 6th Int. Conf. on Deformation Characteristics of Geomaterials, Buenos Aires, 2015, pp.40-76.
- [9] Tatsuoka et al., Geotechnical engineering technical notes, Embankment compaction, No,1~20, The foundation engineering, 2013 ~2015.

MECHANICAL STRENGTH OF PEAT SOIL TREATED BY FIBER INCORPORATED MICROBIAL CEMENTATION

Meiqi Chen¹, Sivakumar Gowthaman², Kazunori Nakashima² and Satoru Kawasaki²

¹Graduate School of Engineering, Hokkaido University, Japan; ²Faculty of Engineering, Hokkaido University, Japan

ABSTRACT

Peat soil is an accumulation of partially decayed vegetation, formed under the condition of nearly permanent water saturation, which makes the high moisture and compressibility as two main features of peat. In recent years, lack of construction lands diverts the attention of researchers to make use of marginal grounds, like peatland, after some improvements. The past decade has witnessed a growing interest towards microbial induced carbonate precipitation (MICP) due to its reliability, wide application and potential contribution to sustainable and green development. There are two primary aims of this study: (i) investigating the feasibility and effectiveness of MICP in peat soil combined with bamboo fiber reinforcement, and (ii) ascertaining the mechanism of bamboo fiber incorporated MICP. Bamboo fiber possesses some unparalleled advantages owing to its fast growth and ability to survive in diverse climates. This study differs from previous researches in the use of native bacteria isolated from the peat soil, while most of them were conducted using exogenous bacteria which might pose a threat regarding adaption and microbial pollution. Different concentration of cementation resources (1-3 mol/L) and proportion of fibers (0-50%) were studied, and each case was well designed. Treated samples were subjected to fall cone test at certain time intervals to estimate the undrained shear strength. The results revealed that the samples with higher fiber content gained higher strength than others did, whereas high initial cementation resources in soil could contribute to the decline of strength. Microscale observations were also performed on treated samples to clarify the mechanism of MICP incorporated with fiber.

Keywords: Microbial induced carbonate precipitation (MICP), Peat soil, Bamboo fiber, Fall cone test, Native bacteria

INTRODUCTION

Peat is a type of soft soil with high content of fibrous organic matters, which is produced by the incomplete decomposition and disintegration of sedges, trees, mosses, and other vegetation growing in wetland and marshes in the anoxic condition [1]. Consequently, it is often referred as problematic soil due to its low shear strength, high compressibility and high water content [2].

Methods to improve peat soils are typically soil replacement, reinforcement to enhance strength and stiffness, stone columns, piles, chemical admixtures etc. [3], [4]. Chemical stabilization like grouting and mixing using cement and lime, which is one of the most preferred methods to improve the soil for the economical reason [3], [4]. In recent years, although known as the most useful artificial material for construction, cement has suffered criticisms related to its contribution to greenhouse gas emission. According to the UNEP annual report of 2010, to produce 1 ton of cement, 1 ton of CO₂ will be released into the environment, which means annually about 7-8% of overall CO₂ emissions are coming from cement industries [5], [6]. There is an increasing concern that some of these traditional methods are being

disadvantaged for the harmful environmental effects.

In recent years, a considerable body of literature is springing up around the theme of MICP (microbial induced carbonate precipitation). The MICP is a relatively innovative technique developed via biological processes, in which the production of calcium carbonate bio-cement relies on the performance of microbial urease [3], [7]. Up to now, several studies have confirmed the effectiveness of MICP on the application of removing contaminants from the air and water, preventing liquefaction, reducing compressibility and permeability, improving soil bearing capacity and so on [3], [4], [8]. The application of this technique could to some extent reduce the dependence on cement products whereby it can be an alternative of green development to traditional methods. In this research, another sustainable material is the bamboo. As one type of most common plant fiber material, it has some unparalleled merits due to its fast growth, survivability under diverse climates and excellent engineering properties [9].

This study set out to investigate the usefulness of bamboo fiber combined with MICP in soil improvement: to assess the feasibility and efficiency of MICP on bamboo fiber reinforced peat soil and to

reveal the mechanism in the solidification process. For these purposes, ureolytic bacteria isolated from local peat soil were examined before being utilized in solidification tests; different proportion of bamboo fibers were mixed into the peat to clarify the effect on moisture and strength change; the concentration of cementation material was investigated as one of the significant factors governing the effectiveness of MICP. Finally, fiber incorporated microbial cementation experiments were conducted.

MATERIALS AND METHODS

Characteristics of Soil

The distribution of peat lands in Hokkaido, Japan can be observed in Fig. 1. Peat soil used in this research was obtained from Iwamizawa city (43°18'17.9"N 141°40'23.9"E), Hokkaido (Fig. 1), from the depth of 3 m underground. Collected peat samples were then preserved in the sterile containers under the temperature of 4 °C and then subjected to some laboratory examinations. The intrinsic characteristics of peat soil were obtained in the laboratory, shown in Table 1. According to the American Society for Testing and Materials (ASTM) standard [10], the peat soil can generally be categorized as one of the followings: (i) fibrous, (fiber content $\geq 67\%$), (ii) hemic or semi-fibrous and or (iii) sapric or amorphous (fiber content $< 33\%$). Based on the analysis, the Iwamizawa peat soil was found to be falling under semi-fibrous category.

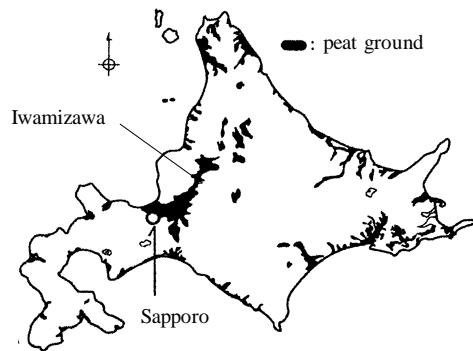


Fig. 1 Distribution of peat ground in Hokkaido [1]

Table 1 Basic characteristics of Iwamizawa peat

Parameters	Values
Water content	711 - 824 %
Density	1.821 g/cm ³
Ignition loss	65.815 %
pH	4.6 - 4.8
k	10^{-4} - 10^{-5} cm/s

Note: Samples were examined from the lower layer to upper layer; k is coefficient of permeability.

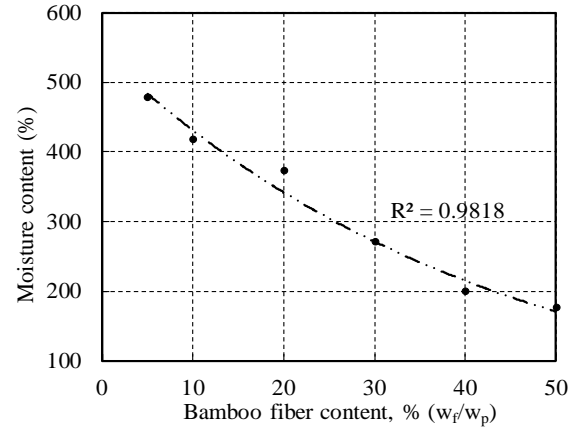


Fig. 2 Variation of moisture absorption with bamboo fiber content

Characteristics of Fiber

The bamboo fiber utilized in this study was made of bamboos with natural moisture content about 26%, with a uniform grain size from 150 to 200 μm . Prior to utilizing the bamboo fiber for solidification test on peat soil, the water absorbing capacity of bamboo fiber was investigated. Totally six cases with bamboo fiber to peat soil ratio at 5%, 10%, 20%, 30%, 40% and 50% were prepared, weighed and dried in the oven at 105°C for more than 48 hours until the mass variation was found to be negligible [11]. The results are shown in Fig. 2, depicting a significant decrease in the water content of peat with increasing fiber content. It is worth noting that the water content could be reduced by half with 20% of fiber addition.

Isolation and Characterization of Bacteria

Isolation of native bacteria

Isolation was conducted by a sequence of dilution (10^1 - 10^3) of peat soil and then being plated on the NH_4 -YE agar medium [12], [13]. After 72 hours of culture at 30°C, colonies were inoculated into new plates using a platinum loop to obtain a purified single colony from groups of distinctive bacteria. Following the purification process, the bacteria were cultured for 24 hours as the preparation of the urease activity test.

Identification of ureolytic bacteria

During the process of urea hydrolysis, the pH of solution increases over time. Urease activity test using cresol-red could realize the identification by a simply qualitative observation on the color change from yellow to purple, indicating an increase in pH from 7.2 to 8.8. Detailed experimental process could be found in the following previous works [12], [13].

The bacteria were added into the testing solution, shaken sufficiently, then incubated at 45°C for 2 hours. Species changed the color into purple was identified as urease activity positive.

16S rRNA sequencing and analysis

According to the Japanese laws as to the microorganism utilization, it is a must to examine the bio-safety level of bacteria, in case the unknown bacteria would be harmful to human body. Finally, the isolates were characterized by sequencing their 16S rDNA and comparing with the database of Apollon DB-BA 9.0, Gen Bank, DDBJ (DNA bank of Japan) and EMBL (European Molecular Biology Laboratory).

Urease activity and growth curve measurement

Quantitative measurement of bacterial population and urease activity were realized by colorimetry, which is used to test the concentration of a solution by measuring its absorbance of a specific wavelength of light. In case of the determination of bacterial population, the optical density was scanned at the wavelength of 600 nm (OD_{600}). This parameter was set as 630 when measuring the urease activity of bacteria by spectrophotometric determination of ammonia as Indophenol [12], [14].

Treatment and Evaluation

Solidification test

Injection method and mixing method are currently two of the most popular methods for investigating the efficiency of solidification using MICP. In this study, the unique characteristics of peat soil made the choice of mixing method for its reliability and validity. First, $NaCO_3$ was used to adjust the pH condition of peat soil, followed by mixing of cementation resources: $CaCl_2$ (Ca^{2+}), urea (CO_3^{2-}) and ureolytic bacteria (urease). In each 150 g of peat soil, only 15 mL of

bacteria ($OD_{600}=11$, 2-day cultured) were used. Different proportion (10%-50%) of bamboo fibers were added to keep the water content of peat soil at a relatively low level. Sufficient mixing was always followed by adding process. Cases set in this experiment were depicted in the Table 2. Molded samples were then put into an incubator with constant temperature of 30°C for curing. Examinations were carried out after 48 hours and on day 7.

Fall cone test

Fall cone test was conducted according to the JGS 0142-2009 [15]. One advantage of this method is that it could be applied on soft clay materials [16]. And for peat, it avoids the problem of the organic matter. The test is based on an approximate relation between the undrained shear strength (τ_f) and the depth of penetration (h), as presented in Eq. 1. K is the fall cone factor which depends mainly on the cone angle, and Q is the cone weight.

$$\tau_f = KQ/h^2 \quad (1)$$

Table 2 Different cases in this experiment

Case	Cementation resources/ V_s	Proportion of fiber (W_f/W_p)
Only MICP	A-1	1 mol/L
	A-2	2 mol/L
	A-3	3 mol/L
Only fiber	B-1	20%
	B-2	30%
	B-3	40%
	B-4	50%
MICP incorporated with fiber	C-1	20%
	C-2	30%
	C-3	40%
	C-4	50%

Note: V_s is sample volume; W_f is weight of fiber; W_p is weight of peat soil.

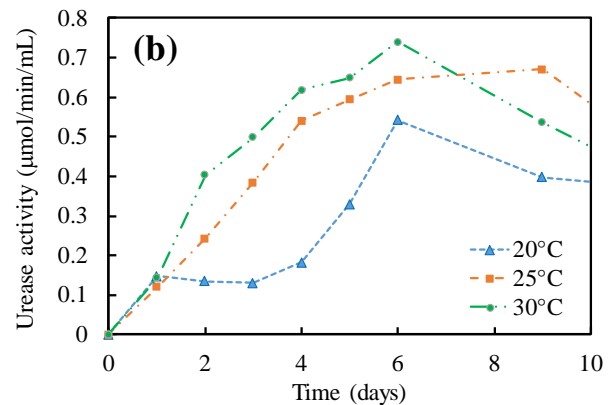
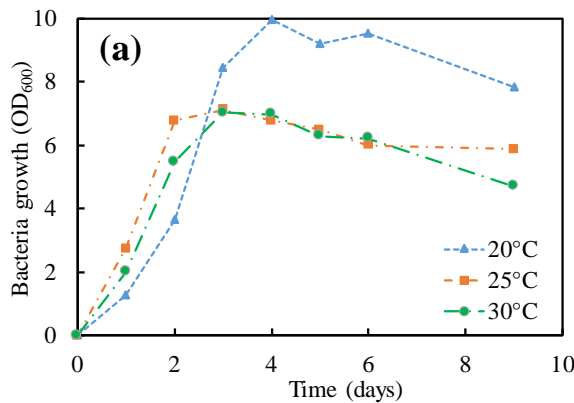


Fig. 3 Performance of PS-1 under different temperatures: (a) growth curve and (b) urease activity

RESULTS

Bacteria Performance

In total, 14 isolated species were tested, of which three species were finally identified as ureolytic bacteria. Two of them were sent to DNA Data Bank and characterized as *Staphylococcus edaphicus* (PS-1) and *Oceanobacillus profundus* (PS-5). After the preliminary analysis, PS-1 was chosen for further experiments as per its higher relative performance, and its performance under different temperature were confirmed by a series of tests. Figure 3 reveals that, for the first few days, there has been a gradual rise in the population of bacteria (showed as OD₆₀₀), irrespective of the incubation temperature. However, this number reached a peak at the temperature of 20°C after four days. As per the urease activity tests, the bacteria, on the other hand, showed the highest preference at high temperature. The activity under 30°C peaked around 0.75 U/mL after 6 days of culturing.

Strength Characteristics

MICP on peat soil (without fiber)

To study the effect of initial concentration of resources, the peat soil was treated preliminary by MICP. As shown in bar chart (Fig. 4), the improvement of peat soil made by MICP seems to be insignificant here, and the development of undrained shear strength declined steadily along with the increase of concentration of cementation material added. Based on the observations, therefore, 1 mol/L was chosen to be appropriate for further experiments.

Fiber incorporated MICP on peat soil

Figure 5(a) presents the experimental data on the strength of fiber reinforced peat soil. The improvement of peat soil with as small as 10% fiber addition was negligible. However, as the fiber content increased to 50%, the shear strength grew by more than 40 times after 7 days of curing under the constant temperature of 30°C. What stands out in Fig. 5(b), which describes the efficiency of MICP incorporated with fiber, is the dramatic growth of undrained shear strength in samples with 50% of fiber, reached 43 kPa, improved by more than 80 times of the untreated, twice of that of fiber reinforced. It also can be clearly seen in this figure that no significant increase in cases with lower fiber content.

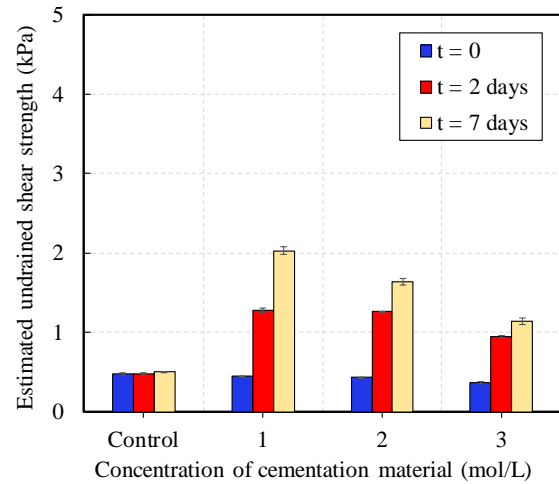


Fig. 4 Effect of different initial concentration of cementation resources

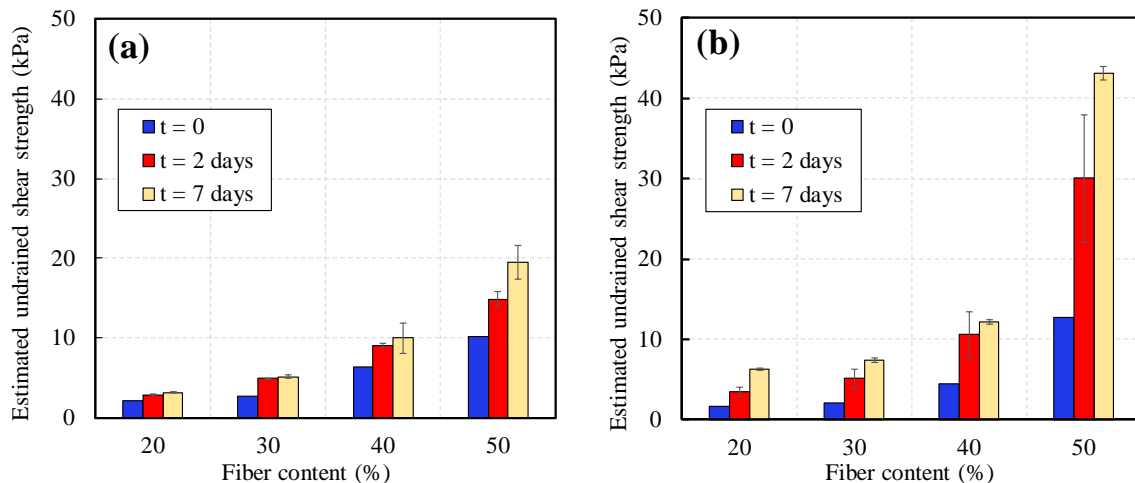


Fig. 5 Fiber incorporated MICP with different concentrations of cementation material:

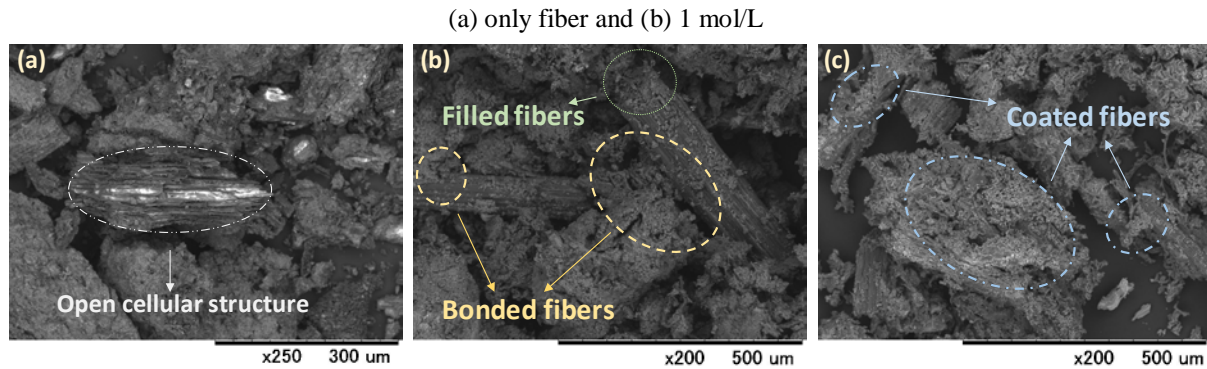


Fig. 6 SEM images of peat soil: (a) untreated; (b-c) MICP- treated

SEM Observation

The results obtained from the SEM (scanning electron microscope) analysis of untreated and treated peat soil are compared in Fig. 6. Fig. 6(a) shows the microstructure of the untreated peat soil. As indicated, fibers were found to be at various sizes and shapes; open cellular structure could also be seen in fibers of untreated soil, suggesting a high degree of decay. When the MICP treatment was applied, the fibers were bonded together by the precipitated calcium carbonate (as depicted in Fig. 6(b)). Certain amount of calcium carbonate was also found to be randomly precipitated on the surface of fibers, which might contribute to the increase in surface roughness. Moreover, the precipitated calcium carbonate tended to crystalline within the open pore structure of the decayed fibers, and a clear microstructure of enhanced fiber material is presented in Fig. 6(c). Overall, the microscopy analysis has provided important insights to understand the mechanism how the strength improvement is achieved in peat soil.

DISCUSSION

Previous studies [17], [18], [19] evaluated the effectiveness of chemical stabilization on peat, of which the results showed that the strength was significantly improved when the considerable amount of pozzolanic materials were mixed *in-situ* or *ex-situ*. Therefore, traditional methods such as Portland cement are firmly being demanded, although some adverse environmental effects are often reported. MICP is a recent call, which is believed to have the potential for stabilizing a wide range of soils. Among the studies performed to this date, only very little were focused on improving peat material, and the improvements were found to be relatively poor [20], which is essentially due to the high moisture content, weak skeleton of peat and intrinsic chemical conditions.

In this study, it has been found that the initial

concentration of resources mixed significantly governs the effectiveness of MICP. The results showed that the increasing the initial concentration of resources decrease the strength gaining of peat soil. A possible explanation of this might be that high concentration of MICP chemicals (particularly urea) might affect the urease enzyme. During the experimentation, the softening of peat soil was experienced with the increase in resource concentrations. Basically, peat soil is rich in colloids which are charged nano~micro particles, responsible for most of the chemical responses of peat soil. High concentration of resources would induce the fierce chemical reaction within a short time, leading to the increase in ion-exchange and possibly softening the peat. However, when the moisture is controlled by the fibers, a significant enhancement is achieved in MICP treatment (as compared in Fig. 5).

The query that was not addressed in this study was how this method could alter the consolidation responses of peat soil, which is an important parameter to evaluate. Another limitation may be the limited supply of resources, and multiple mixing phased might further improve the mechanical responses of peat soil. Despite of the possessed limitations, the study suggests the potential value of bamboo fiber in engineering field. Further investigations are necessary to firmly establish the technique with a deeper understanding of the approach.

CONCLUSIONS

The fall cone test, micro-scale observation and a series of examinations were conducted for MICP incorporated with different bamboo fiber ratios, in order to clarify the feasibility and effectiveness of fiber incorporated MICP on peat soil and to ascertain its mechanism. Conclusions could be drawn as below:

- (i) The addition of bamboo fiber could greatly reduce the water content of peat soil, resulting in an improvement in strength.

- (ii) With the increase of initial concentration of cementation material, the strength gain decreased.
- (iii) The undrained shear strength of peat soil was improved by more than 80 times using MICP incorporated with 50% of bamboo fiber, twice as values obtained from cases of fiber only.
- (iv) MICP filled the cellular structure, coated and bonded separate fibers together, increasing the roughness of the fiber surface to make them a whole.

ACKNOWLEDGMENTS

Authors express the gratitude to Civil Engineering Research Institute for Cold Region (Sapporo, Japan) for their fullest supports and technical assistance. This work was partly supported by JSPS KAKENHI Grant Number 19H02229.

REFERENCES

- [1] Huat B. B. K., Organic and Peat Soil Engineering. 1st edn. University Putra Malaysia Press, Serdang, Malaysia, 2004, pp. 1-15.
- [2] Kazemian S., Huat B. B. K., Prasad A., Barghchi M., A state of art review of peat: Geotechnical engineering perspective, Int. J. Phys. Sci., Vol. 6, 2011, pp. 1974-1981.
- [3] DeJong J. T., Mortensen B. M., Martinez B. C., Nelson D. C., Bio-mediated soil improvement, Ecol. Eng., Vol. 36, 2010, pp. 197-210.
- [4] Whiffin V. S., van Paassen L. A., Harkes M. P., Microbial carbonate precipitation as a soil improvement technique. Geomicrobiol. J., Vol. 24, 2007, pp. 417-423.
- [5] UNEP Annual Report 2010: United Nations Environment Programme; ISBN 9789280731491, 2011.
- [6] Islam M. T., Chittoori B. C. S., Burbank M., Evaluating the Applicability of Biostimulated Calcium Carbonate Precipitation to Stabilize Clayey Soils, J. Mater. Civ. Eng., Vol. 32, 2020, pp. 1-11.
- [7] Portugal C. R. M. e., Fonyo C., Machado C. C., Meganck R., Jarvis T., Microbiologically Induced Calcite Precipitation biocementation, green alternative for roads – is this the breakthrough? A critical review, J. Clean. Prod., Vol. 262, 2020, 121372.
- [8] Ivanov V., Chu J., Applications of microorganisms to geotechnical engineering for bioclogging and biocementation of soil in situ. Rev. Environ. Sci. Biotechnol., Vol. 7, 2008, pp. 139-153.
- [9] Gowthaman S., Nakashima K., Kawasaki S., A state-of-the-art review on soil reinforcement technology using natural plant fiber materials: Past findings, present trends and future directions, Materials (Basel), Vol. 11, 2018, 553.
- [10] ASTM D1997-13: Standard test method for laboratory determination of the fiber content of peat samples by dry mass, ASTM International 2013.
- [11] ASTM D2216-19: Standard Test Methods for Laboratory Determination of Water (Moisture) Content of Soil and Rock by Mass.
- [12] Gowthaman S., Iki T., Nakashima K., Ebina K., Kawasaki S., Feasibility study for slope soil stabilization by microbial induced carbonate precipitation (MICP) using indigenous bacteria isolated from cold subarctic region, SN Appl. Sci., Vol. 1, 2019, 1480.
- [13] Gowthaman S., Mitsuyama S., Nakashima K., Komatsu M., Kawasaki S., Biogeotechnical approach for slope soil stabilization using locally isolated bacteria and inexpensive low-grade chemicals: A feasibility study on Hokkaido expressway soil, Japan, Soils Found., Vol. 59, Issue 2, 2019, pp. 484-499.
- [14] Bolleter W. T., Bushman C. J., Tidwell P.W., Spectrophotometric Determination of Ammonia as Indophenol, Anal. Chem., Vol. 33, Issue 4, 1961, pp. 592-594.
- [15] JGS, 2009. Testing Methods and Their Interpretation for Geotechnical Materials (in Japanese).
- [16] Tanaka H., Hirabayashi H., Matsuoka T., Kaneko H., Use of fall cone test as measurement of shear strength for soft clay materials, Soils Found., Vol. 52, Issue 4, 2012, pp. 590-599.
- [17] Kalantari B., Huat B. B. K., Load-bearing Capacity Improvement for Peat Soil. European Journal of Scientific Research, Vol. 32, Issue 2, 2009, pp. 252-259.
- [18] Erdem O. Tastan, Tuncer B. Edil, F. ASCE, Craig H. Benson, F. ASCE; and Ahmet H. Aydilek, M. ASCE, Stabilization of Organic Soils with Fly Ash, J. Geotech. Geoenviron. Eng., Vol. 137, Issue 9, 2011, pp. 819-833.
- [19] Hayashi H., Nishimoto S., Strength Characteristic of Stabilized Peat using Different Types of Binders. International Conference on Deep Mixing Best Practice and Recent Advances, Sweden, CD-R, Vol. 1, 2005, pp. 55-62.
- [20] Canakci H., Sidik W., Kilic I. H., Bacterail Calcium Carbonate Precipitation in Peat. Arab J Sci Eng., Vol. 40, 2015, pp. 2251-2260.

HYDRAULIC CONDUCTIVITY CHARACTERISTICS OF A FINE- GRAINED SOIL POTENTIAL FOR LANDFILL LINER APPLICATION

Jonathan M. Tiongson¹ and Mary Ann Q. Adajar²

¹ Faculty, Mindanao State University-Iligan Institute of Technology, Philippines;

² Faculty, De La Salle University, Manila, Philippines

ABSTRACT

Sanitary landfills (SLFs) are usually employed as final waste disposal facility to protect public health and the environment. As a result of rapid population growth and urbanization, there is currently a great demand to construct SLFs in the Philippines. The hydraulic conductivity characteristics of remolded samples of a locally abundant fine-grained soil compacted at different compaction energy level is investigated to determine the suitability of the soil as landfill liner material. The hydraulic conductivity of lining system is one very salient feature of the SLF to prevent contamination of nearby soil and water sources. The physical properties of the soil are determined through a series of laboratory tests which includes the grain-size distribution, specific gravity, Atterberg limits, soil classification, Cation Exchange Capacity (CEC), X-ray powder diffraction (XRD) and scanning electron microscopy-energy dispersive X-ray spectroscopy (SEM-EDS). The falling head laboratory test was conducted to determine the saturated coefficient of hydraulic conductivity. A numerical model was formulated that can predict hydraulic conductivity as a function of the void ratio. The resulting coefficient of hydraulic conductivity ranges from 1.98×10^{-6} to 1.0×10^{-7} cm/sec meet the Philippine standard requirement. The soil being classified as clay loam can readily be used as top lining material. However, additional study on unconfined compressive strength and volumetric shrinkage among other parameters is recommended prior to use of the fine-grained soil as bottom lining material as soil amendment maybe necessary.

Keywords: Hydraulic conductivity, Permeability, Landfill Liner, Sanitary Landfill

INTRODUCTION

Sanitary landfills (SLFs) are usually employed as final waste disposal facility to protect public health and the environment. As a result of rapid population growth and urbanization, there is currently a great demand to construct SLFs in the Philippines on top of the statutory requirement set forth by Republic Act (RA) 9003 otherwise known as the "Ecological Solid Waste Management Act of 2000". This law requires all local government units (LGUs) to transition from open dumpsite to controlled dumpsite, and eventually to a sanitary landfill (SLF) not later than February 2006. However, as February 2020, only 108 sanitary landfills or 6 percent of the total required number of 1700 landfills nationwide as reported in the Philippine Environmental Management Bureau website. The construction for more SLFs gives rise to the need for sustainable materials especially for the lining system. The lining system in SLF is one of the most important features of the facility to provide containment against environmental degradation that may cause adverse effect to public health. Compacted clayey layer, geomembrane, geosynthetic clay layer or a composite of these may constitute the barrier component of the liner which should have a low

hydraulic conductivity and the ability to attenuate pollutants migrating through.

In this study, the saturated hydraulic conductivity of a locally abundant fine-grained soil is explored as part of a much bigger study on the possible use of that soil as compacted soil lining material for a municipal SLF. The use of compacted soil lining with or without admixture of clay is common due its relatively low cost, accessibility, durability, high resistance to heat, and other factors among other liner materials [1]. Some marginalized materials are also studied as potential landfill liners such as residual soil [2], dredged marine soils [3], compost [4], fly ash used as soil treatment in combination with bentonite [5] among others. Published literature on the use of compacted soil in the Philippines as landfill liner is limited.

Compacted soil liner consists of a mineral layer which satisfies hydraulic conductivity and thickness requirements along with other technical requirements such as cation exchange capacity (CEC) which varies for different countries. The hydraulic conductivity is the principal factor that affects hydraulic barrier performance. Typical hydraulic conductivity value must be less than or equal to 1×10^{-7} cm/sec for soil liners and covers to contain hazardous waste, industrial waste and

municipal solid waste. Other considerations in choosing the soil liner material include but not limited to shear strength, swelling and volumetric shrinkage. Most soils that possess the properties shown in Table 1 will meet these requirements [6].

Table 1 Specifications for Soil Liner Materials [6]

Soil Property	Range of Values
Percentage of Fines (%)	$\geq 39-50$
Plasticity Index (%)	$\geq 7-10$
Percentage Gravel (%)	$\leq 20-50$
Maximum Particle Size (mm)	25-50 mm

Hydraulic conductivity or permeability of soil is the capacity of soil to allow water to pass through it. Soils are permeable due to the existence of interconnected voids through which water flow from points of high energy to points of low energy. Permeability of soils are affected by particle size, void ratio, properties of pore fluid, shape of particles, structure of soil mass, degree of saturation, absorbed water, entrapped air and organic impurities in water, temperature, and stratification of soil. Reduction in void ratio will result to decrease in permeability. For the same soil sample, only the void ratio will be the most significant factor. In compacted soils, the compaction variables also greatly influence the hydraulic conductivity.

In this paper, the saturated hydraulic characteristics of a local fine-grained soil as potential landfill liner material compacted at three different compaction energy level were investigated. The values obtained from the test is compared to the requirements of RA 9003 and its implementing rules and regulations (IRR) as shown in Table 2. Relations to estimate the saturated hydraulic conductivity in terms of the corresponding void ratio at the different compactive efforts were developed and validated with the previous related studies.

Table 2. RA 9003 and its IRR Hydraulic Conductivity and Soil Thickness Requirements

Landfill Category	Capacity (tons/day)	Min. Requirement for k (cm/sec) and thickness (cm)
I	≤ 15	1×10^{-5} & 60
II	$> 15 \leq 75$	1×10^{-6} & 75
III	$> 75 \leq 200$	1×10^{-7} & 75 or 60*
IV	> 200	1×10^{-7} & 60*

Note: *Build together with synthetic liner of 1.5 mm thick

The findings will be used for initial assessment and design purposes of the local fine-grained soil for

possible utilization as soil liner without discounting the need of an actual conduct of field hydraulic conductivity test as well as other requirements set forth by the aforementioned law and its IRR. The information can be utilized as a part of the basis for soil modification whenever needed prior to utilization as a construction material.

MATERIALS AND METHODS

Source of the Fine-Grained Soil Sample

The soil sample used was excavated from a proposed sanitary landfill site in the municipality of Kauswagan, Lanao del Norte, Philippines. The sample was taken at a depth of least 2 meters to exclude organic matters. The soil looks to be reddish-brown. The soil consistency is sticky, plastic when moist and firm when dry. Figure 1 shows the soil sample used in the study.



Fig. 1 Moist Soil Sample

Preliminary Experimental Program

The preliminary laboratory tests in the study is summarized in Table 3.

Table 3 Preliminary Experimental Program

Test	Test Standard
Grain Size Analysis	
-Mechanical Method	ASTM D6913
-Hydrometer Method	ASTM D7928
Specific Gravity Test	ASTM D854
Liquid Limit Test	ASTM D4318
Plastic Limit Test	ASTM D4318
Shrinkage Limit Test	ASTM D427
Min. Index Density Test	ASTM D4254
Max. Index Density Test	ASTM D4253
XRD	
SEM-EDX	
Compaction Test	
-Reduced Proctor	Daniel & Benson [7]
-Standard Proctor	ASTM D698
-Modified Proctor	ASTM D1557

CEC

US EPA 9081*

Note: *United States Environmental Protection Agency

The physical properties were determined through a series of laboratory tests which are the grain-size distribution including both the mechanical and hydrometer analysis, specific gravity, Atterberg limits covering the plastic limit, liquid limit and shrinkage limit and soil classification as per Unified Soil Classification System (USCS). Cation Exchange Capacity (CEC) conducted through the Sodium Acetate Distillation-Titration Method employed to determine exchangeable ions. X-ray powder diffraction (XRD) was performed on soil sample to obtain a mineralogical analysis of the sample. The analysis used manually ground oven-dried soil sample of fine powder passing sieve No. 200. The sample was scanned from 3° to 70° at a scanning rate of 1 degree per minute. Scanning electron microscopy was done to provide a broad character of the soil microfabric. Soil samples oven-dried at 105°C of grains passing sieve No. 200 were used to remove moisture, coarse and organic material are used for this as well as in Energy dispersive X-ray spectroscopy (EDX) analysis which was used to determine the elemental composition of the surface of the soil specimen. The laboratory compaction test was carried out using Modified Proctor Test, Standard Proctor Test and Reduced Proctor Test [7] to represent varying compaction energy of equipment in the field. Three runs of test for each compactive efforts.

RESULTS

Grain Size Distribution

The grain size distribution (GSD) is graphically depicted in Fig. 2 with mechanical and hydrometer test combined. The mechanical sieve analysis yielded a small 2% of fine sand and majority 98% of silt and clay. The GSD curve exhibits a poorly graded soil. Considering the percentage of soil grains passing No. 200 sieve more than 50%, the soil is said to be fine-grained and is expected to respond poorly to compaction.

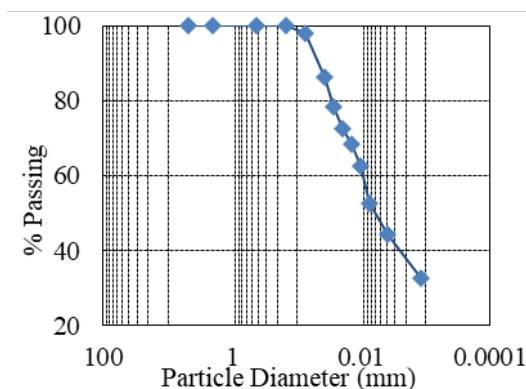


Fig. 2 Grain Size Distribution Curve

Soil Constants

The various laboratory tests resulted to the values for soil physical properties as shown in Table 4. The resulting experimental specific gravity value falls within the range of 2.6 to 2.9 typical for clayey and silty soils. The value of the Plasticity Index (PI) falls within the range of 20-40 which is for the highly plastic soils. The values for liquid limit and plasticity index are subsequently used as inputs for soil classification in addition to the percentage fines discussed in the previous subsection.

Table 4. Soil Constants [8]

Soil Property	Value
Specific Gravity, G_s	2.66
Liquid Limit, LL,	88.49
Plastic Limit, PL	55.68
Plasticity Index, PI	32.81
Shrinkage Limit, SL	29.69
Min. Void Ratio, e_{\min}	1.07
Max. Void Ratio, e_{\max}	1.55
Min. Dry Unit weight, $\gamma_{d\min}$, kN/m^3	10.24
Max. Dry Unit weight, $\gamma_{d\max}$, kN/m^3	12.59

Soil Classification

In accordance with the Unified Soil Classification System (USCS), the soil sample is classified as elastic silt with designation MH. The values of the soil properties being percent finer passing No. 200 $> 50\%$, liquid limit $> 50\%$, plasticity index plots below the "A" line and percentage passing of sand or gravel < 15 to 29%. However, the said soil is classified as clay loam according to the United States Department of Agriculture and are good landfill cover or top lining material [9].

XRD Result

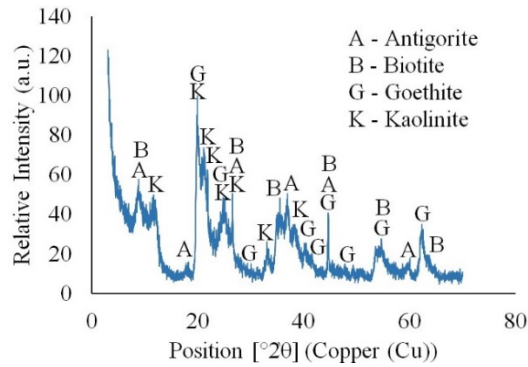


Fig. 3 X-ray Diffractogram of the Soil Sample

The resulting XRD pattern shows sharp peaks as depicted in Fig. 3. The result suggests that the soil sample comprises mainly of the crystal phases of kaolinite, biotite, antigorite, and goethite.

SEM-EDX

A micrograph for the soil sample at 100, 000x magnification factor is exhibited by Fig. 4. The image shows sub-angular and sub-rounded shapes like those of granular soils. It also reveals large intergranular voids. Also visible are flakey, spheroidal, tubular morphological attributes and inter granular voids usually associated to clay minerals. A flakey configuration in the soils is common in fine-grained varieties such as clay and silt enabling those types of soil to have large surface areas for moisture adsorption. The image gives an impression that the soil contains many components such as mica, clay species (silicates) occurring in platy, sheet, flake structure in the family of phyllosilicates and few organic materials.

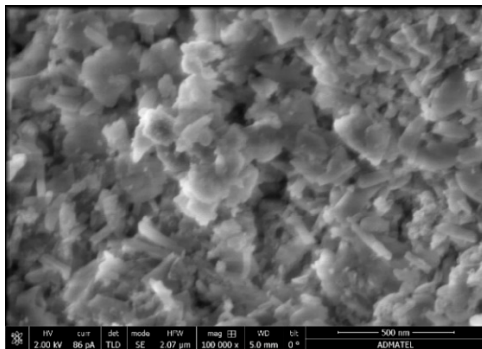


Fig. 4 SEM Micrograph at 100, 000x magnification of the Soil Sample

The elemental analysis yields that oxygen, aluminum, and silicon comprised most of the soil sample with traces of iron, carbon, titanium and calcium which are among the most abundant elements in the Earth's crust. These are the elements which compose the family of phyllosilicates. The

weight percentage distribution is as shown in Table 5.

Table 5. EDX Elemental Distribution

Element Name	Symbol	Weight Percentage
Oxygen	O	52.4
Aluminum	Al	16.6
Silicon	Si	16.6
Iron	Fe	6.9
Carbon	C	6.7
Titanium	Ti	0.7
Calcium	Ca	0.1

Compaction Tests

A set of the typical compaction curves for the soil sample compacted with the three compactive efforts is shown in Fig. 5. It is observable that the maximum dry unit weight increases with the increase in compactive effort while the optimum water content decreases with the increase in compactive effort. All the curves are well below the zero-air voids curve.

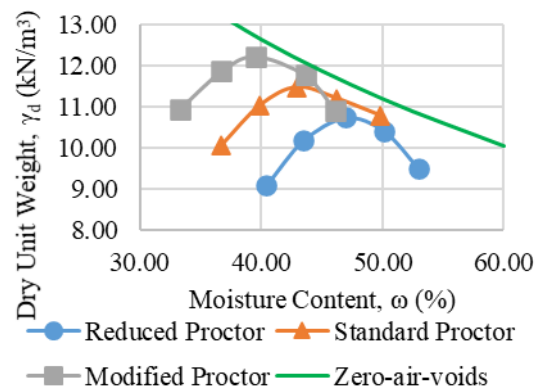


Fig. 5 Typical Compaction Curve

Cation Exchange Capacity

The resulting laboratory test for CEC yield a value 7.76 cmol/kg which falls within typical value for kaolinite of 5-15 cmol/kg.

Hydraulic Conductivity

The permeability test was carried out on remolded samples with compaction energies corresponding to the three compactive efforts in a rigid wall permeameter with a cross-sectional area of 5.73 square centimeter and height of soil specimen of 7.60 centimeters using distilled water as permeant. Further, the permeability test was performed under a falling head condition under a hydraulic gradient of around 20.

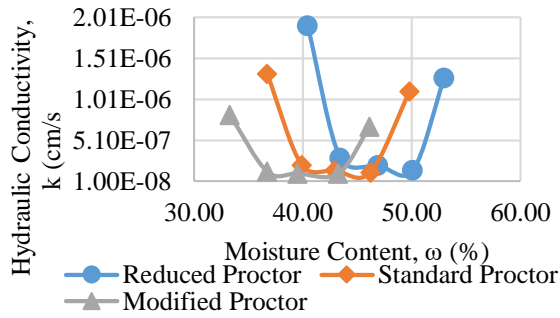


Fig. 6 Hydraulic Conductivity versus Moisture Content

The hydraulic conductivity coefficient was calculated using Darcy's law. The saturated hydraulic conductivity result ranges for the three compactive efforts from 1.98×10^{-6} to 1.0×10^{-7} cm/sec which can be said to be of low hydraulic conductivity. This range falls within the typical values for elastic silt [9]. The values meet the Philippine requirement depending on the targeted category of the SLF. Figure 6 shows a typical plot of the hydraulic conductivity, k versus the moisture content, ω at the three compaction efforts. It can be observed that the values of the hydraulic conductivity decrease as the compactive effort is increased. It is notable that the values of k is lowest to the left of the optimum moisture content. This agrees to the earlier finding of a similar study that soils that are more plastic and have a great quantity of fines yield lower hydraulic conductivity when compacted wet of the optimum [10].

Predictive Models

Predicting the hydraulic conductivity, k of soils accurately and dependably is among the lingering problem for geotechnical engineering as laboratory studies have shown that hydraulic conductivity is influenced by a lot of parameters as discussed in the introduction section. One equation widely used is the Kozeny-Carman relation wherein k is a function as a function of the void ratio of soils, shape constant, specific surface area of particles, particle density of soil, unit weight and viscosity of the fluid permeant. However, the model is not appropriate for clayey soils as it assumes no electrochemical reactions between the solid particles and permeant. Research studies have been made on possible relationships between hydraulic conductivity and void ratio, e of fine-grained soils. One relationship established is that a linear relation between the logarithm of the hydraulic conductivity and the void ratio for clays [11]-[12]. In this study, a linear regression analysis on the void ratio and logarithm of the hydraulic conductivity per compactive effort to develop a predictive model. The output of the test is presented

in a semi-log plot, the hydraulic conductivity in a logarithmic scale and the void ratio in arithmetic scale as ordinate abscissa, respectively.

The equation can take form:

$$k = cf_e \quad (1)$$

where:

c = material constant

k = hydraulic conductivity in cm/sec

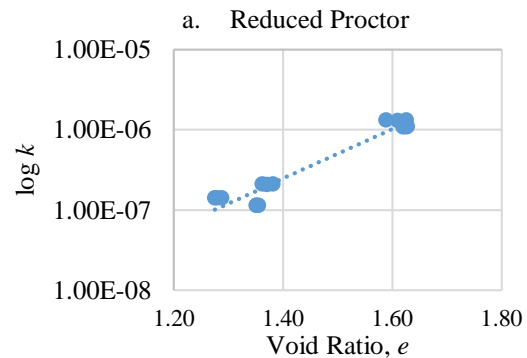
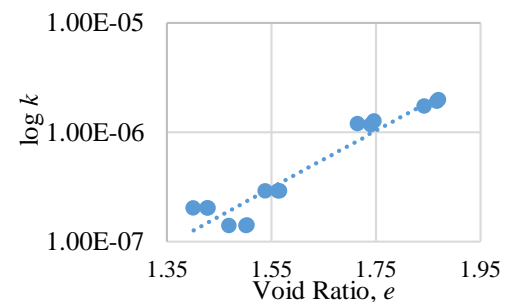
f_e = function describing the effect of void ratio

The regression analysis yielded the quantities in Table 6 together with the coefficient of determination R^2 . A high correlation coefficient, i.e. close to ± 1.0 suggests a strong linear relationship exist between the variables. This underpins the strength of the linearity of the regression equation.

Table 6 Coefficients for the Regression Model

Compactive Effort	c	f_e	R^2
Reduced Proctor	3.0×10^{-11}	$\exp^{6.00e}$	0.92
Standard Proctor	1.0×10^{-11}	$\exp^{7.10e}$	0.93
Modified Proctor	3.0×10^{-12}	$\exp^{8.81e}$	0.92

The high values of the coefficient of determination R^2 indicates that the model fits the data well. The values are comparable to similar studies [13]-[14]. Figure 7 depicts the plots of the $\log k$ versus the void ratio at the three compactive efforts.



b. Standard Proctor

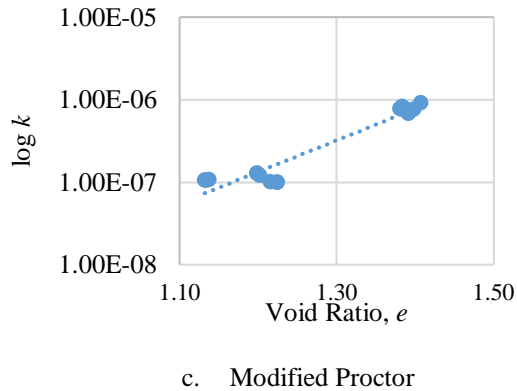


Fig. 7 Plot of the $\log k$ versus e for the Three Compactive Efforts

The models can be useful to soil similarly situated and the strength lies on the simplicity with only void ratio as the parameter. Those can be helpful to specify field compaction.

CONCLUSIONS

Based on this study, the following conclusions can be drawn:

The fined-grained soil as elastic silt based on USCS or clay loam based on USDA. The soil being classified as clay loam can readily be used as top lining material or cover. The soil is said to be of high plasticity. The soil sample composition consists mainly of the crystal phases of kaolinite, biotite, antigorite, and goethite from the XRD analysis and consistent from the SEM-EDX results.

The resulting coefficient of hydraulic conductivity ranges from 1.98×10^{-6} to 1.0×10^{-7} cm/sec meet the Philippine standard requirement depending on the SLF Category. The Strong correlation was developed between the logarithm of the hydraulic conductivity and the void ratio at the three compactive efforts.

Further study is warranted on field hydraulic conductivity test, unconfined compressive strength and volumetric shrinkage to provide baseline information for design and quality assurance purposes. Those are additional information necessary for soil modification as maybe desired for the utilization of the soil as marginalized bottom SLF lining material.

REFERENCES

[1] Wang M. C. and Huang C.C., Soil Compaction and Permeability Prediction Models, J. Environ. Engrg., ASCE Vol. 110, Issue 6, 1984, pp.1063–1083.
 [2] Yong L. L., Emmanuel E., Purwani R. and Anggraini V., Geotechnical Assessment of

Malaysian Residual Soils for Utilization as Clay Liners in Engineered Landfills, International Journal of GEOMATE, Vol.16, Issue 58, June 2019, pp.20 – 25.
 [3] Anuar N. M., Chan C. and Johan S.F.S.M., An Innovative Sanitary Landfill System with Dredged Marine Soils (DMS) as Liner Material: Geo-Environmental Studies, International Journal of GEOMATE, Vol.14, Issue 41, Jan. 2018, pp.181-185.
 [4] Hermawansyah Y., Hadinata F., Dewi R. and Hanafiah, Study of Compost Use as an Alternative Daily Cover in Sukawinatan Landfill Palembang, International Journal of GEOMATE, Vol. 15, Issue 51, Nov. 2018, pp. 47-52.
 [5] Nguyen L.C., Chu H. L. and Ho L.S., Soil Treatment by Bentonite and Fly Ash for Liners of Waste Landfill: A Case Study in Vietnam, International Journal of GEOMATE, Vol. 17, Issue 63, Nov. 2019, pp. 315-322.
 [6] Daniel D.E., Geotechnical Practice for Waste Disposal, Chapman and Hall, London, 1993, p. 140.
 [7] Daniel D. and Benson C., Water Content-Density Criteria for Compacted Soil Liners, J. Geotech. Engrg., ASCE, Vol. 116, Issue 12, 1990, pp. 1811-1830.
 [8] Tiongson, J.M. and Adajar, M.A.Q., Compaction Characteristics of a Fine-Grained Soil Potential for Landfill Liner Application, International Journal of GEOMATE, Vol. 19, Issue 71, July 2020, pp. 211-218.
 [9] The Unified Soil Classification System, Waterways Exp. Sta Tech. Mem., 1953, pp. 3-357 (including Appendix A, 1953, and Appendix B, 1957), US Army Corps of Engineers, Vicksburg, Miss.
 [10] Benson, C.H. and Trast, J., Hydraulic Conductivity of Thirteen Compacted Clays, J. Geotech Geoenviron. Eng., Vol. 43, Issue 6, 1995, pp. 669-681.
 [11] Taylor, D. W., Fundamentals of Soil Mechanics, John Wiley and Sons, Inc., N.Y., 1948, pp. 97-123.
 [12] Lambe, T. W. and Whitman, R.V., Soil Mechanics, John Wile and Sons, Inc., N.Y., 1969, pp. 281-294.
 [13] Adajar, MA.Q. and Zarco, MA.H., An Empirical Model for Predicting Hydraulic Conductivity of Mine Tailings, International Journal of GEOMATE, Vol. 7. No.2, 2014, pp. 1054-1061
 [14] Tiongson J.M. and Adajar M.A.Q., Viability of Kauswagan Soil as Sanitary Landfill Liner, Conference Proceedings of DLSU Research Congress, June 2018, Volume 6, Series 2, p.3.

GEOTECHNICAL CHARACTERIZATION OF ALLUVIAL SOIL AS AN ALTERNATIVE ROADWAY CONSTRUCTION MATERIAL

Emerzon S. Torres¹ and Mary Ann Q. Adajar¹

¹Department of Civil Engineering, Gokongwei College of Engineering, De La Salle University, Philippines

ABSTRACT

The rapid infrastructure development in the Philippines over the past years poses problem on construction cost due to the limited supply of suitable road foundation materials within economic haul distances. An economic and sustainable solution is to use locally available but suitable materials. This study utilized the naturally-occurring alluvial soil along the Angat Riverbanks as a potential road foundation material. Geotechnical characterization of the alluvial soil was performed including direct shear and California bearing ratio (CBR) tests. The findings of the index properties showed that the alluvial soil is 92% sand, non-plastic, and was classified as poorly-graded sand. A CBR of 41% makes the river sand a suitable subbase course material. However, the sample failed on the gradation requirement for subbase application due to lacking of coarse aggregates. From the direct shear tests, the soil showed brittle failure that yields peak shear stress and dilative volume change behavior. The critical state friction angles for dry and saturated conditions are 37.52° and 36.61° , respectively. Morphological analyses were also performed to further evaluate the material composition of the alluvial soil. The sedimentological analysis found that the sample is both texturally and compositionally immature. Sediments are angular to subrounded and moderately sorted. Correspondingly, the SEM-EDX revealed flocculation with flakey particles and small inter granular voids that justifies the shear strength of the sand. It is recommended to blend coarse aggregates with the alluvial soil to meet the gradation requirements and possibly increase its bearing strength for base course applications.

Keywords: Alluvial soil, Road foundation, CBR, Direct shear strength, Morphology

INTRODUCTION

The "Build, Build, Build" program of the Department of Public Works and Highways (DPWH) of the Philippines promises a significant construction development in the Philippines. In the recent Philippine Infrastructure Report of 2017, strong growth in the construction and infrastructure industry was predicted to occur over the next five years. The report shows that the real growth will reach 12.5% between 2017 and 2021, while the average annual growth will reach 11.2% for the construction sector [1]. The Philippine Development Plan launched in 2017, aims to change the Philippine income trend as an upper-middle-income country by 2022 [1]. This trend resulted in the urge to developing infrastructure and therefore boost the construction industry in the country [2].

It follows that there is a greater need for construction materials such as embankment and road foundation aggregates. However, there are three emerging challenges on sourcing of aggregate materials for road construction: (1) geographical distribution of natural deposits of high-quality aggregates needed for road construction is uneven in nature and not found in some areas, (2) in areas where high-quality aggregates exist, gravel mines and rock quarries are being either lost to another land uses or

restricted from mining due to public perception and conservation efforts, and (3) higher quality standards may further reduce the amount of usable aggregates mined from specific sources [3].

Searching for alternative construction materials is considered a sustainable way of development if secondary material is free from hazardous components and does not have any adverse long-term effects [4]. Road construction costs can be very high because of the limited opportunity of locating suitable road base material within economic haul distances [5]. It is preferable and economical to use and to stabilize, if necessary, locally available but abundant materials than to import conventional aggregates.

One thing that is abundant in the Philippines is its alluvial deposits of soils. The alluvium occupies approximately 15 percent of the land surface of the archipelago [6]. The alluvium is the soil transported by water and settled along riverbanks. It is usually most extensively developed in the lower part of the course of a river, forming floodplains and deltas, but may be deposited at any point where the river overflows its banks.

Alluvial soil was already researched for its suitability as an alternative road foundation aggregate in various countries [7] [8]. However, alluvial soils in the Philippines are yet to be explored. Due to its archipelagic characteristics, Philippine lands is

composed of approximately 15% alluvium. The country experiences the rise of rivers and streams during the rainy season, which results in the formation of floodplains and thick alluvial deposits.

The province of Bulacan alone, the house of the 153-km Angat River with a catchment area of 1,085 km², is composed mainly of alluvial orders of soil. Alluvial soils along the rivers are considered part of the lowland soils, and these soils represent the heavy use of land resources being easily accessible to the general populace.

Alluvial soils are mainly used for agricultural purposes. However, problems arise when some of the soils possess high permeability that crops cannot grow. This is attributed to the sandy soil types, such as Quingua and Obando soil series, present along the Angat River [9]. With a thickness of 2 to 4 meters and covers more than 810 hectares, this fine sandy soil is a potential source of road embankment materials [9].

The main objective of this study was to characterize and assess the potential of the naturally occurring alluvial soils when used as a road subgrade, subbase course, and embankment materials. The DPWH Standards was the major reference on the classification of the alluvial soil on its suitability [10]. Table 1 shows the parameters and requirements based on the DPWH specifications for subgrade, subbase course, and for select granular backfill of mechanically stabilized earth.

Table 1 DPWH Standards for road foundation [10]

Parameter	Requirement	
Subgrade course		
Gradation	All particles are finer than 75mm	not more than 15 mass percent will pass the 0.075 mm sieve
Atterberg limits	PI not more than 6	LL not more than 30
Unit weight	greater than 7.85 KN/m ³	
Subbase course		
Gradation	All particles are finer than 50mm	not more than 12 mass percent will pass the 0.075 mm sieve
Soaked CBR	not less than 30% at MDD condition	
Dust ratio	Less than or equal to 2/3	
Atterberg limits	PI not more than 12	LL not more than 35
Select granular backfill		
Gradation	all particles must be smaller than 100mm	
	particles finer than 0.0425mm must be 0 – 60 percent by mass	
	at most 15% of the particles are finer than 0.075mm	

Friction angle	not less than 34%
----------------	-------------------

MATERIALS AND METHODS

Source of Alluvial Soil

The alluvial soils were gathered from a vacant land in Brgy. Laog in the municipality of Angat, Bulacan. The soils are located along the riverbanks. Disturbed samples were used since the roadway construction materials are actually blending of different materials with specific gradation. The oven-dried and moist-tamped soil is shown in Fig. 1.

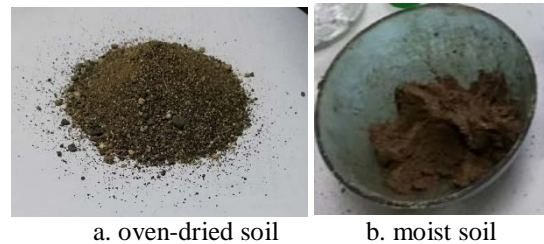


Fig. 1 Soil sample used in this study

Experimental program

The laboratory tests performed on the samples are enumerated in Table 1. These procedures were based from either ASTM or AASHTO standards to establish a reference in evaluating the index properties and strength of the alluvial soil. Morphology includes the SEM-EDX analyses, texture, and mineral identification. These material analyses supported the results of laboratory tests and explained the soil behavior that is important for long-term applications.

CBR tests in accordance with AASHTO T193 were performed for the alluvial soil compacted at the maximum dry density and under soaked conditions to simulate the worst possible scenario in the field. Moreover, specimens were soaked for 96 hours (4 days). However, a shorter immersion period of not less than 24 hours was applied, as suggested by the AASHTO standards, if the shorter period did not affect the test results.

Direct shear tests in accordance with ASTM D 3080 were performed for the alluvial soil to complete its geotechnical characterization. This study considered fully saturated conditions to simulate the worst-case scenario and dry condition to see the strength of the alluvial soil at the most possible condition. The samples were subjected to varying vertical stresses: 13.63 KPa, 27.75KPa, and 83.25 KPa. The first vertical stress would capture the low-stress condition while the second and third vertical stress will simulate the 1.5m and 4.5m overburden pressure in the field. The relative compaction will be 60%, 80%, and 90% to represent the medium dense,

dense, and very dense conditions, respectively. Moist tamping was done to achieve the desired density of the reconstituted sample. For the saturated condition, the specimen was soaked in distilled water before transferring to the direct shear apparatus tank filled with water. Unconsolidated undrained condition was performed because of the non-plastic and cohesionless property of the soil sample. The test ran at 1.25 mm/min rate of shearing.

Table 2 Experimental program for alluvial soil

Test	Test Standard
Grain Size Analysis	ASTM D6913
Specific Gravity Test	ASTM D854
Atterberg Limits Test	ASTM D4318
Compaction test	ASTM D698
Max. Index Density Test	ASTM D4253
Min. Index Density Test	ASTM D4254
CBR Test	AASHTO T193
Direct Shear Test	ASTM D3080
SEM-EDX	-
Sedimentology	-

RESULTS

Particle Size Distribution

Figure 2 shows a typical particle size distribution curve. Generally, a soil is referred to as well graded if the uniformity coefficient (C_u) is larger than about 4–6 and coefficient of curvature (C_c) is between 1 and 3 [11]. The alluvial has a C_u of 5.11 and C_c of 1.2. It has an effective grain size (D_{10}) is 0.29. Based on its D_{10} , the soil falls on a medium size sand [12]. The alluvial soil comprises of 92% sand, 6% gravel, and 1% silt. Based on the gradation requirements of DPWH, the soil is not suitable for subbase course application due to its insufficient amount of coarse particles.

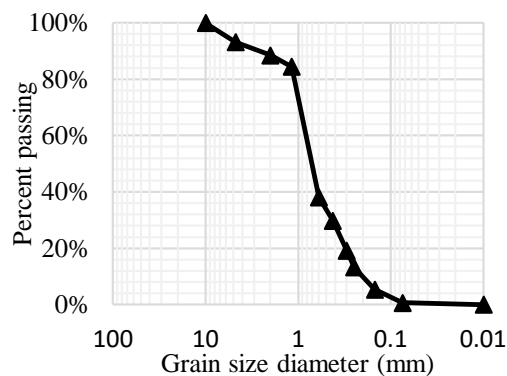


Fig. 2 Particle size distribution curve

Soil Constants

The material constants is presented in Table 4. The specific gravity of 2.60 is common to sandy soils [13]. The zero plasticity that is common to sand – silt particles complies with the low plasticity requirement for the road foundation materials. The modified effort was employed during compaction to concur with the DPWH standards for subbase/base course materials. The alluvial soil reached a maximum dry density of 19.66 KN/m³ at an optimum moisture content of 10.65%. It absorbs water and produces a wide range bell-shaped curve that falls on well-graded to fine sands [12].

Table 3 Soil Constants

Soil Property	Value
Specific Gravity, G_s	2.60
Liquid Limit, LL %	Non-plastic
Plastic Limit, PL %	Non-plastic
Min. Void Ratio, e_{\min}	0.48
Max. Void Ratio, e_{\max}	0.91
Max. Dry Unit Weight, $\gamma_{d\max}$ kN/m ³	19.66
Optimum Moisture Content, ω_{opt} %	10.65

Soil Classification

According to the Unified Soil Classification System (USCS), the alluvial soil is a poorly-graded sand. On the other hand, the AASHTO classified it under A-1-b with group index of zero. Considered granular material, the alluvial soil had a rating of excellent to good subgrade material according to the AASHTO classification system.

Soil Strength

California Bearing Ratio

Stipulated by the DPWH (2013) standard specifications, the bearing strength is defined by the CBR value obtained from AASHTO T93 provisions. The alluvial soil obtained CBR values at 2.54mm and 5.08mm penetrations of 30.77% and 41.03%, respectively. These values correspond to the typical CBR of poorly graded sand classified by the USCS and of A-1-b soils identified by AASHTO [14]. Based on these CBR values, the alluvial soil had a bearing strength suitable for subbase course application as per the DPWH specifications.

Direct Shear Strength

In regards with the direct shear test, for both dry and saturated conditions, it was observed that as the normal load increases the value of the critical state shear stress or the shear stress at failure increases. The shear strength or the critical state shear stress is the shear strength at which the volume change ceases.

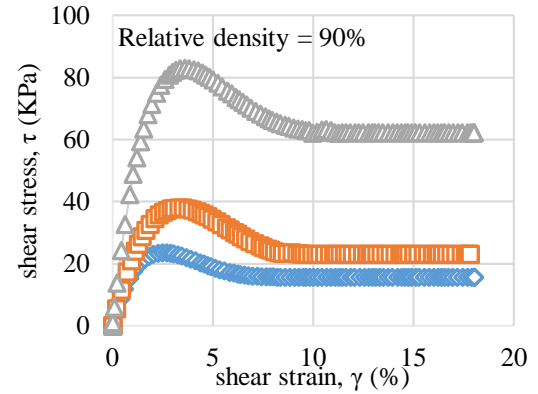
For the dry condition, stress-strain curves follow a similar pattern. As the shear strain starts to manifest, the dry soil behaves elastically (linear curve) until yielding occurs. At this point, the linear region starts to form a curvature as it approach a peak as shown in Fig. 3a. This phenomenon is called strain-hardening. Furthermore, after the soil reach a peak shear stress, a strain-softening phenomenon happened before it approach the critical state. This is attributed to the particle crushing and reorientation [13]. It can also be observed from the volumetric strain-shear strain plots in Fig. 3b that during strain hardening the soil changes its volumetric behavior from compression to expansion. Moreover, the dry samples exhibit dilation continuously until the graphs asymptotically approach a critical region where volume change stops. This is known as the critical state.

It is noticeable that the 13.63 kPa normal load soil sample experiences the greater volumetric expansion. Thus, it is concluded that the increasing normal load directly affects the volumetric expansion of the soils.

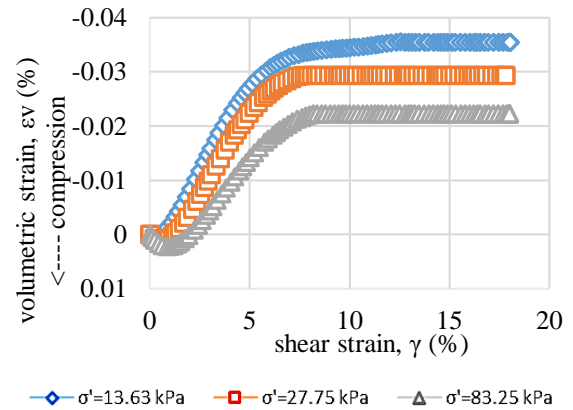
Figure 4 displays the stress-strain and volume change relationships of the saturated alluvial soil subjected to direct shear test. Slight variations from the results of the dry condition can be observed. First, the reduction of shear strength is very obvious since at saturated condition soil loses strength because of the presence of water as shown in Table 4. Second, the stress-strain curves for the 60% relative-density soils show no peak stress under the highest normal load (83.25KPa). In addition, dilation were not observed in this test sample. The reason for this is that a higher normal load can suppress the peak stress and the dilatancy [13].

From Table 4, critical shear strength at different initial relative densities are almost the same for a particular effective normal stress. Secondly, the effective normal stress varies directly with the critical shear strength. Moreover, the densest soil specimens (Relative density = 90%) experience the largest volumetric expansion. Negative values of volumetric strain denotes soil expansion. The idea is that dense soil has the greater chance to expand than to compress upon shearing [13].

From the direct shear test, the critical state friction angle for dry condition is 37.52° while the saturated alluvial possess a 36.61° angle of internal friction. These values fittingly fall on the typical range of friction angle for sand of 27° to 37° [13]. From the DPWH standards, the soil sample used in this study is a suitable select granular backfill material.



a. Shear stress – shear strain curve



b. Volumetric strain – shear strain curve

Fig. 3 Stress-strain and volume change behavior of alluvial soil for very dense dry conditions.

Table 4 Critical state values

Alluvial soil	Normal effective stress, KPa	Dr = 90%	Dr = 80%	Dr = 60%
Critical state shear strength (kPa)				
Dry condition	13.63	15.58	15.58	15.63
	27.75	23.11	24.44	24.05
	83.25	62.16	59.58	64.97
Saturated condition	13.63	13.61	12.28	11.55
	27.75	22.45	21.44	23.05
	83.25	60.96	57.69	64.02
Critical state volumetric strain (mm/mm)				
Dry condition	13.63	-0.035	-0.026	-0.018
	27.75	-0.029	-0.024	-0.017
	83.25	-0.022	-0.021	-0.012
Saturated condition	13.63	-0.013	-0.014	-0.009
	27.75	-0.009	-0.008	-0.002
	83.25	-0.001	0.002	0.009

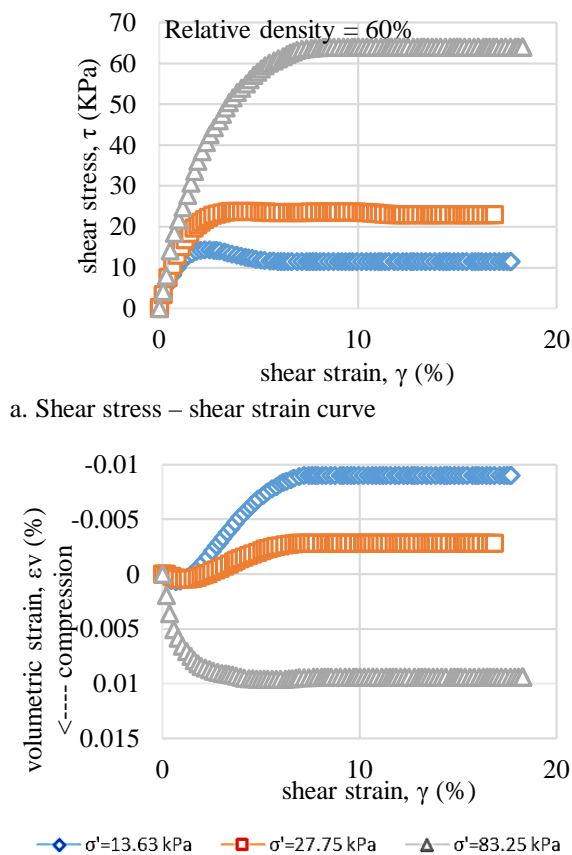


Fig. 4 Stress-strain and volume change behavior of alluvial soil for medium dense saturated conditions.

Morphology

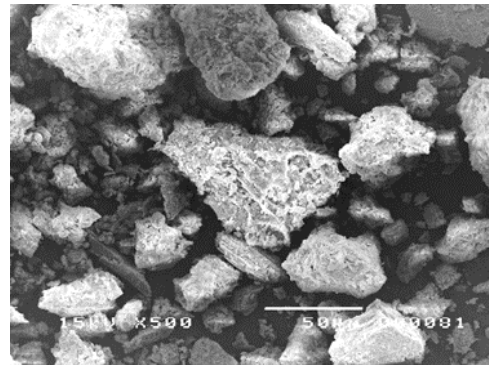
SEM – EDX

Figure 6 depicts the micrographs of the alluvial soil sample. The soil contains many components such as blocks of minerals, clay, clay accessory minerals, and organic materials. There are highly varied shapes and size ranges as shown in Fig. 6a. Soil exhibits small inter granular voids. It has flocculation with flakey particles usually associated with clay as well as plagioclase laths and an indication of early stages of weathering as shown in Fig. 6b. Lastly, Fig. 6c revealed inter granular voids with flakes and that is common to clay minerals in sedimentary soils [12].

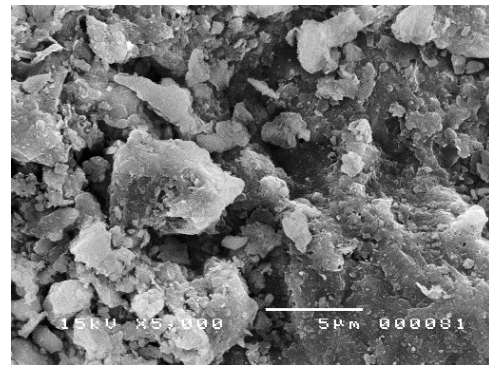
Sedimentology

The analysis revealed a texturally and compositionally immature sedimentary soil. Texture and composition are two components to describe maturity. Texture provides a description of how rounded and sorted the sample is. Composition describes how much the soil composition is changing towards more stable minerals and components. An immature soil has the greater chance to breakdown

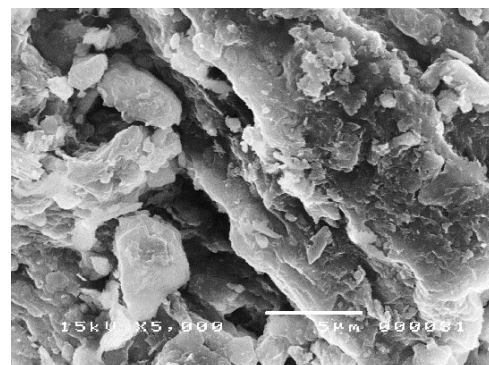
and undergo weathering. The grain-size curve as shown in Fig. 2 validates the immaturity of the alluvial soil grains [12].



a. 500x magnification



b. 5,000x magnification (larger than 0.075mm)



c. 5,000x magnification (finer than 0.075mm)

Fig. 6 SEM micrographs of the soil sample

About the composition, the altered fragments are composed mainly of silicified, quartz, and chloritized fragments. Lithic fragments are basaltic in composition with varying textures. The sample have sparsely distributed broken chips of plagioclase with quartz, augite, epidote and hornblende. The result of EDX shows a soil that is made up mainly of oxygen,

carbon, silicon, aluminum, iron, and magnesium with small amounts of calcium and titanium. All of these elements corresponds with the mineralogical analysis.

CONCLUSION

Based on this study, the following conclusions can be drawn:

The alluvial soil sample is a poorly graded sand with textural and compositional immature grains of quartz, basalt, chloritized, and altered fragments. It has no plasticity and the alluvial soil reached a maximum dry density of 19.66 KN/m³ at an optimum moisture content of 10.65%.

The bearing strength based on the CBR value at 5.08mm penetration of 41.03% revealed that the alluvial soil is a suitable subbase course aggregate based on the DPWH Standards. However, the soil failed on the gradation requirement for subbase course because the amount of coarser particles is insufficient.

For the direct shear strength, from the slope of the failure lines critical state friction angle for dry condition is 37.52° while the saturated alluvial possess a 36.61° angle of internal friction. Both brittle and ductile failure were observed from the test data which allows the stress-strain behavior to experience peak and dilatancy for the volume change behavior. It is a suitable select granular backfill material.

Further work on this research is recommended to focus on the blending of alluvial soil with coarser aggregates to comply with the gradation requirements and to possibly promote its application to base course.

ACKNOWLEDGMENTS

The authors would like to acknowledge the support of DOST-ERDT for providing financial assistance for this research, the laboratory testing assistance of DPWH-BRS, and the help of Mr. Michael Torres for the material acquisition. Also, the study would not be possible without the help of the DLSU Civil Engineering Faculty.

REFERENCES

- [1] Philippines Infrastructure Report Q3 2017, <https://www.giiresearch.com/report/bmi177867-infrastructure.html>.
- [2] Philippines: Building Competitive, Sustainable and Inclusive Cities, 2017, <http://www.worldbank.org/en/news/press-release/2017/05/29/philippines-building-competitive-sustainable-and-inclusive-cities>
- [3] Xia, Y., & Tutemluer, E., Best value granular material for road foundations, Minnesota Department of Transportation, 2012, <http://www.dot.state.mn.us/research/TS/2012/201201.pdf>.
- [4] Gautamm, P. K., Kalla, P., Jethoo, A. S., Agrawal, R., & Singh H., Sustainable use of waste in flexible pavement: A review, *Construction and Building Materials*, 180, 2018, pp. 239-253.
- [5] Frempong, E. M., & Tsidzi, K. E. N., Blending of marginally suitable tropical sub-base materials for use in base course construction, *Construction and Building Materials*, 13, 1999, pp. 129-141.
- [6] Wernstedt, F. L., *The Philippine island world*, University of California Press, 1983.
- [7] Dano, C., Hicher, P. Y., & Tailliez, S., Engineering properties of grouted sands, *Journal of Geotechnical and Geoenvironmental Engineering*, 130(3), 2004, pp. 328-338.
- [8] Patell, Rashmi S., & Desai, M. D., CBR predicted by index properties for alluvial soils of South Gujarat, *Indian Geotechnical Conference - 2010, GEOTrendz*, 2010.
- [9] Japan International Cooperation Agency, Feasibility study report on the improvement of the operation and maintenance of national irrigation systems (AMRIS) Volume II, National Irrigation Administration, Philippines, 1984.
- [10] Department of Public Works and Highways, Standard specification for Highways, Bridges and Airports, 2013.
- [11] Das, B.M., *Advanced Soil Mechanics* (5th ed.), CRC Press, 2019.
- [12] Terzaghi, K., Peck, R., & Gholamreza, M., *Soil Mechanics in Engineering Practice*, Wiley, 1996.
- [13] Budhu, M., *Soil Mechanics and Foundations* 3rd Ed., Wiley, 2011.
- [14] Liu, T. K., A review of engineering soil classification systems, *Highway Research Board Record* 156, 1967, pp. 1-22

RESISTANCE FORCE AND GROUND BEHAVIOR IN THRUST PROTECTION FOR BURIED PIPES USING GEOGRID GABION

Hiroyuki Araki¹ and Daiki Hirakawa²

Faculty of Engineering and Design, Kagawa University, Japan;

²Faculty of Science and Engineering, Chuo University, Japan

ABSTRACT

The bend section of a buried water supply pipeline transfers a thrust force to the ground. Thus, a concrete block is typically installed at the bend for protection. However, the concrete block may become unstable when the ground around the concrete block liquefies during an earthquake. In a previous study, we proposed the use of a geogrid gabion composed of a geogrid basket and gravel as a thrust-protection method. In this method, the geogrid gabion is placed on the ground in the direction of the thrust force. It is desirable for a geogrid gabion to be installed close to the pipe. However, the pipe and gabion must be separated for the effective compaction of soil around the pipe during construction. In this study, the effects of the horizontal distance on the thrust force protection performance of the geogrid gabion were evaluated by applying a horizontal force on a buried pipe model in a saturated ground model. The results revealed that the resistance force acting on the pipe increased regardless of the horizontal distance; the resistance force acting on the pipe was highest when the pipe moved close to the geogrid gabion. Based on the relationship between the resistance and the ground behavior, the resistance force was modeled as the sum of the passive earth pressure acting on the pipe and the resistance increment due to the passive earth pressure acting on the geogrid gabion.

Keywords: Buried pipe, Thrust force, Gabion, Resistance force, Strain distribution

INTRODUCTION

A thrust force is generated in the outward direction of the bend section of buried pipes, e.g., water supply pipelines. The pipe is normally designed to resist the passive earth pressure and circumferential surface friction acting on the bend section. If the thrust force is estimated to exceed the resistance due to the passive earth pressure and surface friction, a concrete block is typically installed in the bend section, as shown in Fig. 1a. The concrete block is installed to increase the resistance by expanding the passive earth pressure-receiving area and increasing the friction at the bottom due to its heavyweight. However, a concrete block is expected to have the following disadvantages: generating a high inertial force at the bend due to the heavyweight of the concrete block during an earthquake, and significantly decreasing the resistance to thrust force or the stabilization when the ground around the pipe is liquefied. For example, it has been reported that the bend section detached when the surrounding ground liquefied [1].

If the proximity section of the bend is straight with sufficient length, a certain section of a pipe, including the bend, maybe welded instead of installing a concrete block. In this method, the passive earth

pressure acting on the entire welded section is larger than that acting only on the bend, and a larger resistance to the thrust force is estimated. However, some cases of pipe detachment at the boundary between welded and non-welded sections during earthquakes have been reported, and the inaccuracy of the calculation of the passive earth pressure acting on the welded section has been pointed out [2].

Therefore, a new thrust-protection method is required. Kawabata et al. [3][4] proposed the use of a geogrid as a thrust-protection method. In this method, the geogrid is connected to the pipe on the inside of the bend to act as a lateral anchor. Several model experiments revealed that the lateral displacement of a pipe protected with the geogrid is lower than that of a pipe protected with a concrete block.

In [5], we proposed a new thrust-protection method involving the use of a geogrid gabion installed in the passive area of the buried pipe as a pressure-receiving structure (Fig. 1b). It is assumed that the passive earth pressure acting on the geogrid gabion and the surface friction of the geogrid acted as the resistance force against the thrust force. The basket is made of a polymer geogrid to obtain long-term stability against environmental events. Gravel with high permeability is used as the filling material of the basket, which is expected to retain effective

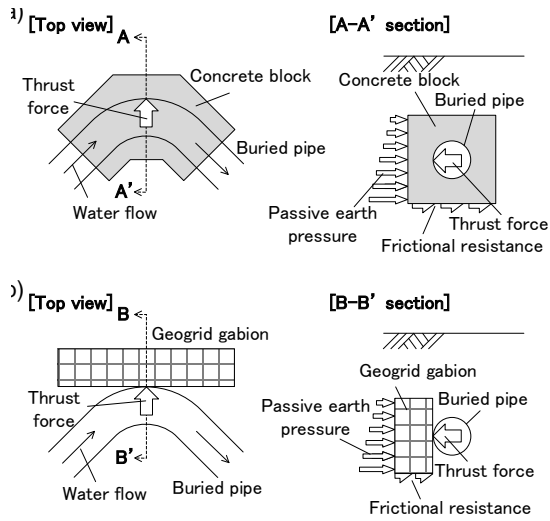


Fig. 1 Schematics of the a) concrete-block and b) proposed thrust-protection method [5][6].

stress by dispersing excess pore water pressure during an earthquake. The geogrid gabion is also expected to resist deformations due to the thrust force because the gravel is confined by the geogrid basket. In [5][6], we found that the displacement of the pipe protected with a geogrid gabion was reduced and that the bottom part of the geogrid gabion should be buried deeper than the pipe owing to its high stability; the large width of the geogrid gabion prevented its rotation in the ground.

The geogrid gabion should be installed close to a pipe but at a sufficient distance to allow the effective compaction of the soil around the pipe during construction. Therefore, the effects of the initial distance between a pipe and a geogrid gabion should be clarified. Moreover, the resistance force acting on a pipe protected with a geogrid gabion has hardly been discussed in the previous study. In this study, the resistance force acting on a pipe and ground behavior are discussed to further clarify the effects of thrust protection by conducting model experiments reproducing the horizontal distance between a pipe and a geogrid gabion.

OUTLINE OF THE LATERAL LOAD TEST

Test Conditions

Lateral load tests were conducted to evaluate the resistance of a pipe and the behavior of the ground when a thrust force is applied laterally to the pipe. Although the ground is assumed to be three-dimensionally deformed when the thrust force is

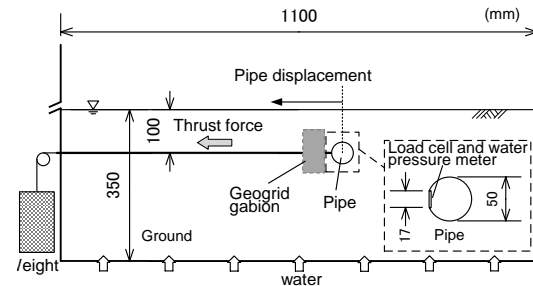


Fig. 2 Schematic of the lateral load test set-up.

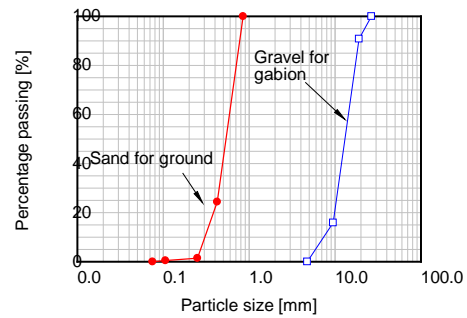


Fig. 3 Particle size distribution.

applied from the bend, it is difficult to evaluate the deformation of the ground owing to the complexity of the boundary conditions. For simplification, we modeled the model as a plane strain problem, with the cross-section B-B', as shown in Fig. 1b [5][6]. Figure 2 shows a schematic of the lateral load test set-up. The pipe model was loaded laterally inside the ground model constructed in a testing box. To evaluate the effects of the initial horizontal distance between a geogrid gabion and a pipe, several tests with different distances were conducted.

The ground model was constructed with Mikawa silica sand No. 5 (soil particle density, $\rho_s = 2.675 \text{ g/cm}^3$) with the particle size distribution shown in Fig. 3. The maximum dry density and the optimum water content of the silica sand were 1.525 g/cm^3 and 14.7% , respectively. The ground model was constructed by wet tamping using silica sand with a water content of 13% to achieve a compaction layer thickness of 50 mm and a dry density of 1.374 g/cm^3 .

The pipe model was designed as a straight cylinder with a diameter of 50 mm and a length of 390 mm . The pipe model had a smooth surface and was buried in the ground model at a depth of 100 mm from the ground surface. A simulated thrust force was applied laterally to the pipe model through a stainless-steel loading shaft, and the displacement of the loading shaft was measured as the pipe displacement d_p . A pore water pressure meter and a load cell with a

17 mm width pressure plate were installed on the side of the pipe model, as shown in Fig. 2. Under the loading of the simulated thrust force, the lateral earth stress σ_p and pore water pressure u_p acting on the pipe model were measured using a load cell and water pressure meter, respectively. The effective value of the lateral earth stress acting on the pipe model σ'_p is defined as $(\sigma_p - u_p)$.

The geogrid gabion model consisted of gravel ($\rho_s = 2.807 \text{ g/cm}^3$) and a polypropylene net, as shown in Fig. 4. The geogrid gabion had a height of 100 mm and a width of 50 mm. The particle size distribution of the gravel is shown in Fig. 3. The dry density of the whole gabion was set to approximately 1.4 g/cm^3 . The depth of the geogrid gabion model center from the ground surface was set to be the same as that of the pipe model. To prevent the migration of silica sand into the geogrid gabions, a non-woven fabric was laid on the upper surface. The non-woven fabric was not laid on the side and bottom sections to simplify the condition between the geogrid gabion and silica sand in the model test.

Test Cases and Procedure

Table 1 shows the parameters of the test cases considered. To reproduce the initial horizontal distance between the geogrid gabion model and the pipe model D_h , three cases with D_h values of 15, 50, and 100 mm were considered, as shown in Fig. 5. The smallest value of D_h was set to 15 mm to ensure good compaction around the pipe (case G3). Considering a pipe diameter D of 50 mm, the D_h values of 15, 50, and 100 mm represented as $0.3D$, $1.0D$, and $2.0D$, respectively.

If the geogrid gabion is not installed, it is presumed that the passive area of the ground in contact with the pipe mainly resists the thrust force. The boundary of the passive area is assumed to be located between Line A and Line B, as shown in Fig. 5, and varies according to the internal friction angle of the ground. In case G6, most of the geogrid gabion was placed outside the ground passive area in contact with the pipe. In this study, a total of four cases were analyzed, including the above three cases, and case N2 without a geogrid gabion.

In the lateral load test, a simulated thrust force F was applied to the pipe model after the ground model was saturated with water. The simulated thrust force was loaded until the changes in the pipe displacement converged. The same procedure was repeated with a stepwise increase in the value of F .

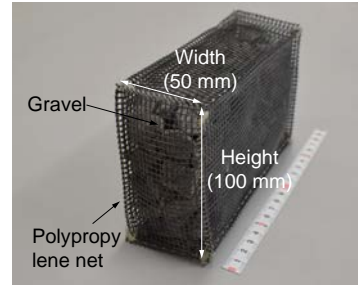


Fig. 4 Photograph of geogrid gabion model.

Table 1 Experimental cases considered.

	Initial horizontal distance, D_h	Thrust force, F [N]
Case N2	—	149
Case G3	0.3D	149–254
Case G4	1.0D	149–277
Case G6	2.0D	149–301

D: pipe diameter of 50 mm.

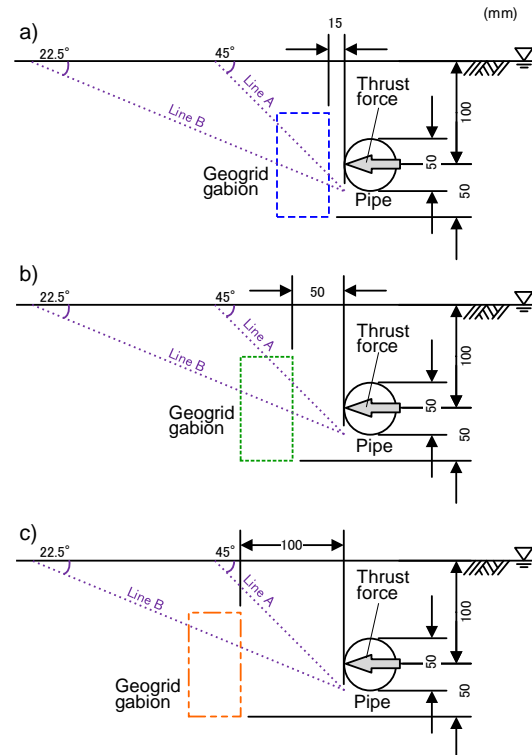


Fig. 5 Schematic of the geogrid gabion layout; a) case G3, b) case G4, and c) case G6.

The values of σ_p , u_p , and d_p were measured under the loading of the simulated thrust force. The experiment was finished when the value of σ'_p began to decrease. For Case 6, the experiment was finished when the pipe displacement converged under a load F of 301 N because the pipe displacement reached the limit of the loading device.

Aluminum markers with a diameter of 7 mm were embedded in the side of the ground model beforehand, and the displacement of the markers following the deformation of the ground was observed by analyzing the images taken from the side of the testing box. The maximum shear strain γ_{\max} in the ground model was calculated for each four-node rectangular element using four markers.

TEST RESULTS AND DISCUSSION

Pipe Displacement and Resistance

Fig. 6 shows the relationships between F and d_p just before unloading in each step. It can be seen that, in case N2, the pipe displacement with a loading of 149 N increases to nearly 30 mm. In the other cases with the geogrid gabion under 149 N loading, the pipe displacements are lower than those in case N2. Under loading of 200 N or less, the d_p value in case G3 is small compared to those in cases G4 and G6, which indicates that the pipe displacement is highly restrained when the initial distance between the pipe and the geogrid gabion is small. It should be noted that the d_p value in case G3 significantly increases under loading of 254 N.

Figure 7 shows the relationships between σ'_p and d_p during loading. Assuming that the surface friction of the pipe model is small owing to the smooth surface of the pipe, most of the resistance to the thrust force is due to the passive earth pressure. In this study, the value of σ'_p is used as a representative indicator of the resistance acting on the pipe model, although σ'_p was measured in a small area on the side of the pipe model.

From Fig. 7, it can be seen that in case N2 without a geogrid gabion, the σ'_p value reaches its peak at approximately 8 kPa and then gradually decreases. In contrast, in the cases with a geogrid gabion, the peak values of σ'_p are larger than that in case N2, and the slopes of the σ'_p and d_p relationships decrease as D_h increases. It should be noted that the relationship between σ'_p and d_p in case G6 might have trended upward continuously if a thrust force larger than 301 N had been applied.

Figure 8 shows the relationships between the peak σ'_p and d_p at the peak values of σ'_p . The peak values of σ'_p in cases G3, G4, and G6 are at least twice that in case N2. It is clear that the resistance acting on the pipe model is increased when the geogrid gabion is installed.

Figure 9 shows the relationship between d_p at the peak values of σ'_p and D_h . The d_p value at the peak

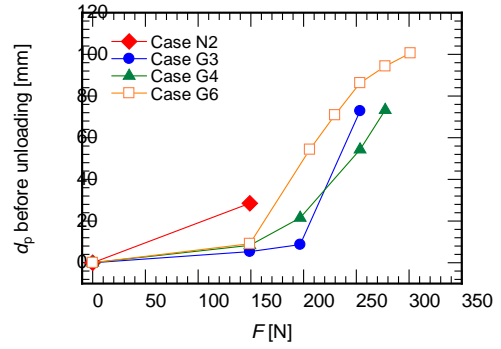


Fig. 6 Relationships between F and d_p just before unloading in each step.

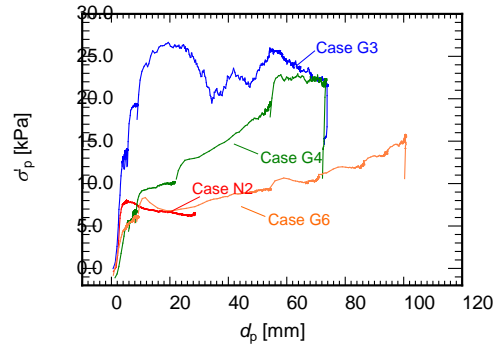


Fig. 7 Relationships between σ'_p and d_p .

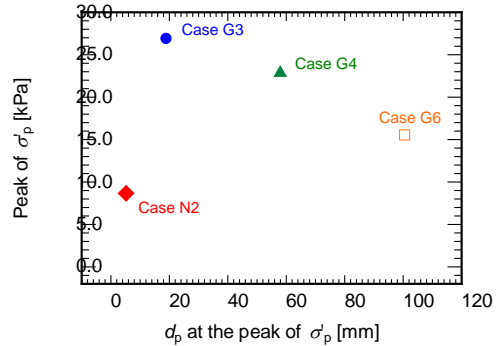


Fig. 8 Relationships between the peak values of σ'_p and d_p at the peak values of σ'_p .

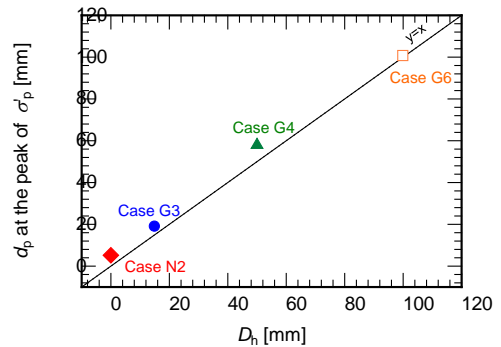


Fig. 9 Relationships between d_p at the peak values of σ'_p and D_h .

values of σ'_p linearly increases with D_h . This indicates that the resistance acting on the pipe is highest when the pipe model approaches the geogrid gabion.

Ground Deformation

Fig. 10 shows the distributions of γ_{\max} in the ground when the pipe displacement is approximately 20 mm. The thrust force was applied in the left direction in all cases.

In case N2, the band of high shear strain is distributed from the left side of the pipe model to the ground surface, which indicates that the boundary of the passive area in the ground (Fig. 10a). The band of high shear strain on the right side of the pipe model is the active area of the ground.

In case G3, the geogrid gabion moves by approximately 15 mm horizontally, and the share strain increases from the bottom of the geogrid gabion to the ground surface (Fig. 10b). This indicates that the geogrid gabion resists the thrust force received from the pipe, and the passive area in the ground is larger than that in case N2. This geogrid gabion is located across the boundary of the passive area of the pipe model (Fig. 5a), and the thrust force is probably transmitted to the geogrid gabion smoothly.

In case G3, the effective value of the lateral earth stress acting on the pipe reaches its peak value when the pipe displacement is 19 mm (Fig. 8), which was observed under a loading F of 254 N (Fig. 6). When the pipe displacement is 19 mm, a band of a high shear strain of approximately 30% formed in the passive area in contact with the geogrid gabion (Fig. 10b), and the stress state in the band is assumed to be in the residual state. The thrust force of 254 N seems to exceed the resistance force, and therefore, the pipe displacement significantly increases from 9 to 73 mm upon a loading F of 254 N.

In contrast, a high strain band appears in between the pipe and geogrid gabion in case G6 (Fig. 10d). Most of the geogrid gabion is located outside the passive area in contact with the pipe model; subsequently, the thrust force is assumed to be hardly transmitted to the geogrid gabion. Hence, the resistance to the thrust force is mainly due to the passive earth pressure acting on the pipe model. This is also supported by the fact that the relationship between σ'_p and d_p in case G6 is similar to that in case N2 at d_p below approximately 20 mm (Fig. 7).

In case G4, although a high share strain band appears between the pipe and geogrid gabion, the shear strain slightly increases in the passive area in contact with the geogrid gabion (Fig. 10c). Therefore,

the thrust force is assumed to be hardly transmitted to the geogrid gabion through the passive area of the pipe. The σ'_p value in case G4 is larger than that in

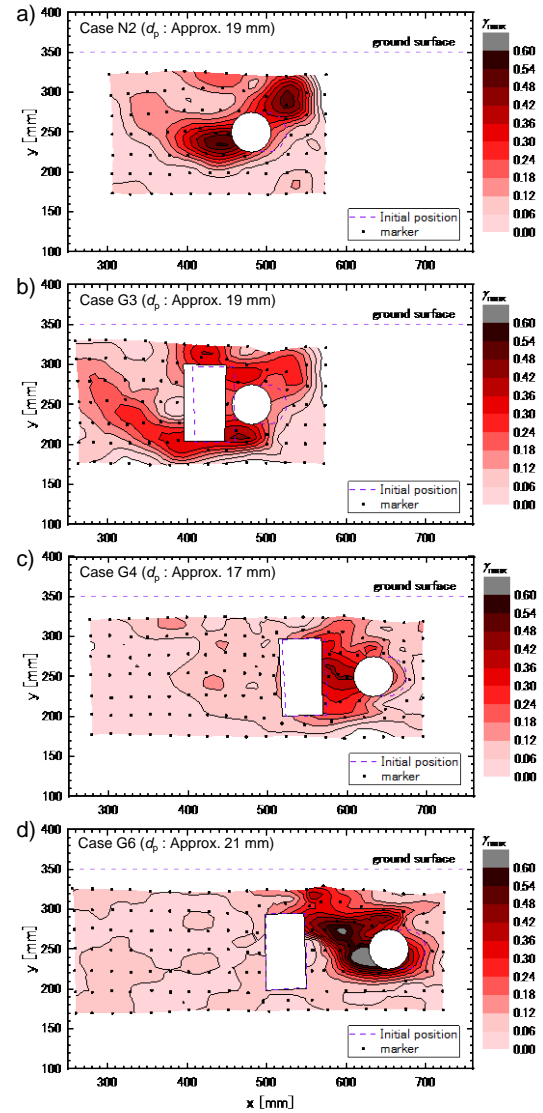


Fig. 10 Distribution of maximum shear strain at a d_p of approximately 20 mm; a) case N2, b) case G3, c) case G4, and d) case G6.

case N2 and G6 when the pipe displacement is approximately 20 mm, as shown in Fig. 7, probably because the passive earth pressure acting on the geogrid gabion also acts as a resistance.

Resistance by Geogrid Gabion

Figure 11 shows a schematic of the resistance force in the thrust-protection using a geogrid gabion based on the experimental results. The resistance force to thrust force is modeled as the sum of the

passive earth pressure acting on the pipe and the resistance increment provided by the geogrid gabion.

When the value of D_h is as small as $0.3D$, the

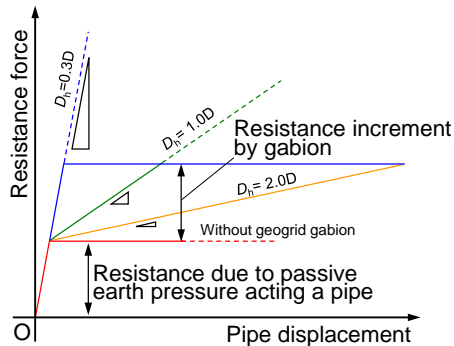


Fig. 11 Schematics of the resistance force by using geogrid gabion.

thrust force from a pipe is transferred quickly to a geogrid gabion. Therefore, the resistance force increases even when the pipe displacement is small.

In contrast, when D_h is greater than $1.0D$, the resistance is due to the passive earth pressure mainly acting on the pipe. As the pipe approaches the geogrid gabion, the thrust force is transmitted to the geogrid gabion; subsequently, the resistance due to the passive earth pressure acting on the geogrid gabion increases gradually.

The increase in resistance is assumed to depend on the size of the pressure-receiving area of the geogrid gabion. Under these experimental conditions, the resistance with the geogrid gabions is estimated to be at least two times greater than that without the geogrid gabions, regardless of the value of D_h .

CONCLUSIONS

The use of a geogrid gabion as a thrust-protection method for buried pipes was tested on a model with different initial distances between the geogrid gabion and the pipe. The conclusions are summarized as follows:

- 1) The resistance force of the pipe was higher when the geogrid gabion was installed, regardless of the initial horizontal distance between the geogrid and the pipe.
- 2) In cases where the initial horizontal distance was more than $1.0D$, the resistance force acting on the pipe gradually increased as the pipe displacement increased and was highest when the pipe approached the geogrid gabion.

- 3) When the initial distance was as small as $0.3D$, the resistance force rapidly increased even when the pipe displacement was small.
- 4) As the pipe approached the geogrid gabion, the thrust force was transmitted to the geogrid gabion; subsequently, the resistance due to the passive earth pressure acting on the geogrid gabion was gradually provided to the pipe.
- 5) The resistance force was modeled as the sum of the passive earth pressure acting on the pipe and the resistance increment provided by the geogrid gabion.

ACKNOWLEDGMENTS

The authors would like to thank Mr. Nichiri Kusunose and Mr. Kotaro Ngamori for their help with the experiments. This study was supported by JSPS KAKENHI Grant Number 19K15090.

REFERENCES

- [1] Mohri Y., Yasunaka M. and Tani S., Damage to Buried Pipeline Due to Liquefaction Induced Performance at the Ground by the Hokkaido Nansei-Oki Earthquake in 1993, Proceedings of First International Conference on Earthquake Geotechnical Engineering, IS-Tokyo, 1995, pp. 31–36.
- [2] Mohri Y., Ono S., Suzuki K.: Seismic damage to large-diameter pipelines, The Foundation Engineering & Equipment, Vol.48, No.1, pp. 40–43, 2020. (in Japanese)
- [3] Kawabata T., Sawada Y., Uchida K., Hirai T. and Saito K., Model Tests on Thrust Protecting Method for Buried Bend with Geogrid, Geosynthetics Engineering Journal, Japan Chapter of International Geosynthetics Society, Vol. 19, 2004, pp. 59–64. (in Japanese)
- [4] Kawabata T., Sawada Y., Mohri Y. and Ling I., Dynamic Behavior of Buried Bend with Thrust Restraint in Liquefying Ground, Journal of Japanese Society of Civil Engineering, Vol.67, No. 3, 2011, pp. 399–406. (in Japanese)
- [5] Araki H. and Hirakawa D., Model Tests on Thrust Protecting Method for Buried Pipe by Using Geogrid Gabion, Journal of Japanese Society of Civil Engineering, Vol. 74, No. 1, 2018, pp. 106–117. (in Japanese)
- [6] Araki H. and Hirakawa D., Effects of thrust protecting method for buried pipe using geogrid gabion of different sizes, International Journal of GEOMATE, Vol. 16, No. 158, 2019, pp. 62–68.

A STUDY ON SOIL RESISTIVITY MEASUREMENT USING READILY INSTALLABLE ELECTRODES MOUNTED ON DRIVING-PIPES

Hidetake Matsui¹, Tadafumi Fujiwara¹, Hiroyasu Ishii¹ and Yoh Takahata¹

¹ Taisei Corporation, Japan

ABSTRACT

Soil resistivity measurement is one of the survey methods widely used for subsurface investigation. The method has recently been studied as a useful tool to verify the range and quality of soil improvement. Although it has been suggested that electrodes should be placed as close to target areas and as many in surrounding sections as possible, it requires time and cost to drill boreholes to arrange many electrodes in the ground. This would be a main reason why resistivity measurement has not been widely used in practice for soil improvement. Recently, however, we have developed readily installable electrodes mounted on a driving pipe (called the measurement pipe here), which could apparently lower the installation cost. This paper outlines the measurement pipes and shows some preliminary test results to verify the driving performance of the measurement pipes and the applicability of the equipped electrodes for measurement of soil resistivity as well as ground resistance. The paper also presents the field test results obtained from a jet grouting site. These results show that the measurement pipe could be driven 9m in an hour into the ground where SPT-N value was less than 5, and that the electrodes on the measurement pipe could be applied for measurement of soil resistivity and ground electrical resistance. It is implied that soil resistivity change caused by soil improvement could be detected by the measurement of ground resistance.

Keywords: Soil resistivity, Ground resistance, Driving-pipe, Soil improvement, Jet grouting

INTRODUCTION

Soil improvement methods, which can improve soil properties such as strength and water cut-off performance, have been widely used as an essential technique especially in the construction of structures located on soft sediments. In the quality check of soil improvement works, it is necessary to confirm that the soil has been improved to the required property, and that the entire targeted area has been improved as planned. However, the improved soils cannot be observed directly, and are sampled only partially from a limited number of boreholes or tested with a limited number of specimens.

Soil resistivity measurement is one of the survey methods widely used for subsurface investigation. It has recently been studied as a useful tool to verify the range and quality of improved soils [1]. Focusing on an electrical resistivity difference between groundwater and chemical grout, Komine et al. proposed a method to visualize chemically grouted area with electrical resistivity tomography [2]-[4]. On the other hand, Fujii et al. investigated a relationship between the coefficient variation of the resistivity of improved soil and the rotation number of mixing blade, and suggested that the efficiency of deep mixing method could be evaluated by measuring soil resistivity [5].

It has been suggested that the accuracy of resistivity measurements could be improved by placing electrodes as close to a measurement target as possible [4], and it is clear that the more electrodes are placed, the higher the measurement accuracy.

However, in the conventional electrodes placing, it requires time and cost to drill boreholes to arrange many electrodes in the ground. This would be a main reason why resistivity measurement has not been widely used in practice for soil improvement to date.

Recently, we have developed readily installable electrodes mounted on a driving pipe (hereinafter, called “the measurement pipe”), which could apparently lower the installation cost [6], [7]. This paper outlines the measurement pipes and shows some preliminary test results to verify the driving performance of the measurement pipes and the applicability of the equipped electrodes for the measurement of soil resistivity and ground resistance. The paper also presents the field test results obtained from a jet grouting site.

DEVELOPMENT OF MEASUREMENT PIPE

Outlines

We have originally developed a steel driving-pipe for rapid arrangement of air/chemicals injection wells used for soil remediation [8]. Depending on how stiff the soil is, the installation of the steel driving-pipe may take from only several tens of seconds to several minutes per meter. Newly developed measurement pipes are based on this technique. Electrode parts of the steel pipe are exposed but the other surface is covered with polyvinyl chloride plastic for electrical insulation, while securing enough strength and rigidity for driving into ground. Although soil

resistivity has generally been discussed in the soil improvement evaluation, we also focus on the ground electrical resistance. It is because ground resistance implies the resistance between electrodes in ground and the point of zero potential, and it could be obtained more easily than obtaining soil resistivity. Since ground resistance depends on soil resistivity around an electrode, changes in soil resistivity caused by soil improvement might also be detected by measuring ground resistance.

Details of developed measurement pipes

To verify driving performance of measurement pipes and the applicability of the equipped electrodes for soil resistivity and ground resistance measurements, four different measurement pipes were developed and manufactured (see Fig. 1). Pipes No.1 and 2 have single electrode at the tip of the pipe and the whole pipe surface is insulated by polyvinyl chloride plastic. The difference in these two pipes is the shape of the electrode: pipe No.1 has a conical electrode while No.2 has the same conical electrode with a 50 mm high ring extension. In both pipes, the electric current flows through the internal steel pipe to electrode. Pipes No.3 and 4 have conical electrode at the tip and several 20 mm high ring electrodes on the side. The three electrodes on pipe No.3 are individually connected to electric cables and these three cables are led to ground surface through the inside of the pipe. Therefore, electric current can be applied to these three electrodes at the same time. Pipe No.4 has a conical electrode at the tip of pipe and nine ring electrodes on the side, but these ten electrodes are not connected to electric cables in advance. To apply electric current to these electrodes, an electric cable with a brush tip is inserted into the internal steel pipe after the driving installation and connected to a single selected electrode. Since electric current flows through this movable cable, multiple electrodes on pipe No.4 cannot be applied an electrical current at the same time.

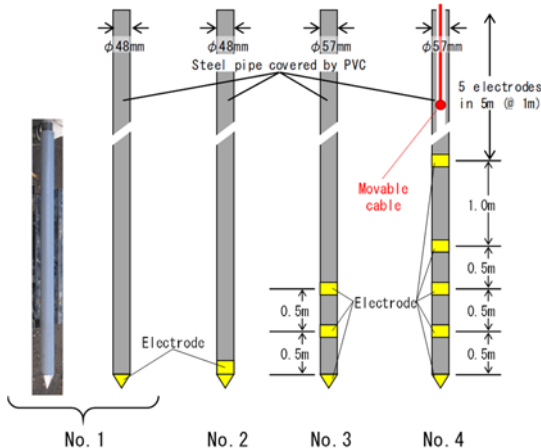


Fig. 1 Schematic of developed measurement pipes.

PRELIMINARY TEST TO VERIFY DEVELOPED PIPES

To verify the driving performance of the pipes and the applicability of the equipped electrodes, the measurement pipes mentioned above were driven into ground and used for soil resistivity and ground resistance measurements.

Ground conditions of the test field

Figure 2 shows soil profiles of the test field: Top layer from the ground surface to a depth of 3.9 m consists of backfilled sand and clay (SPT-N value < 5); the second layer to a depth of 8.2 m consists of silt and sandy silt (SPT-N value < 5); the third layer to a depth of 11.0 m consists of fine sand (SPT-N value < 10); and groundwater level is about 2.9 m below ground surface. Figure 2 also shows soil resistivities measured in laboratory by using borehole samples from several depths.

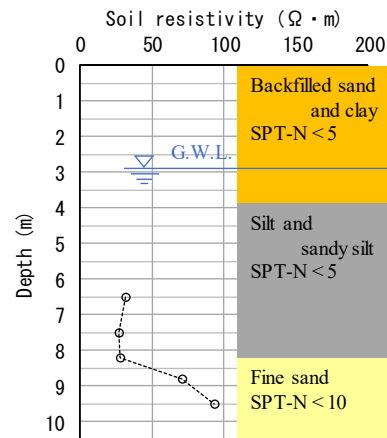


Fig. 2 Soil profiles of the test field.

Test conditions

Figure 3 shows the arrangement of the measurement pipes and auxiliary electrodes. The measurement pipes were arranged at 2 m interval and driven to a depth of about 9 m from the ground surface to verify the driving performance by a self-propelled boring machine (ECO-3V, YBM Co., Ltd. Japan).

Table 1 shows 6 measurement cases. In four cases from A-1 to A-4, ground resistance was measured by the three-pole method using each measurement pipe with two auxiliary electrodes. In case B-1, soil resistivity was measured by the Pole-Pole array method using selected two of the three electrodes on pipe No.3 with two auxiliary electrodes. In case B-2, soil resistivity was measured by the Wenner array with only the tip electrodes of the four pipes No.1 to 4. Here, apparent soil resistivity was calculated with the results obtained from cases B-1 and B-2, assuming that the target ground was uniform.

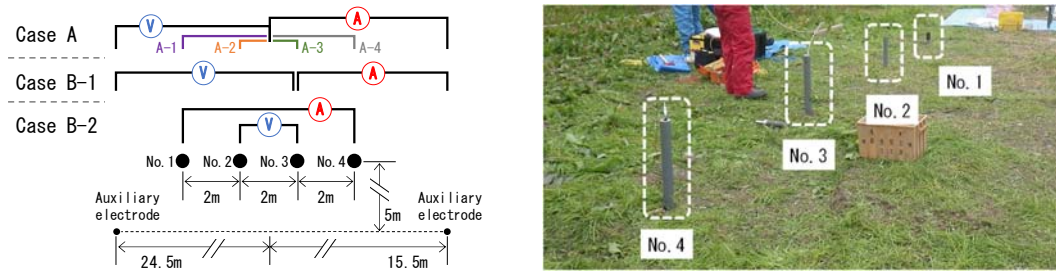


Fig. 3 Arrangement of measurement pipes and auxiliary electrodes with circuit in the preliminary test.

Table 1 Measurement cases in the preliminary test

Case	Pipe	Measured value	Remarks
A-1	No.1	Ground resistance	Using a tip electrode on No.1 and 2 pipe, every 1 m from a depth of 1 m to a depth of 9 m.
A-2	No.2	Ground resistance	
A-3	No.3	Ground resistance	
A-4	No.4	Ground resistance	
B-1	No.3	Soil resistivity	Using selected two of the three electrodes on No.3 pipe, every 1 m from a depth of 5 m to a depth of 9 m (3 times at every 1 m).
B-2	No.1-4	Soil resistivity	Using tip electrodes of four driven pipes (only 1 measurement at a depth of 9 m).

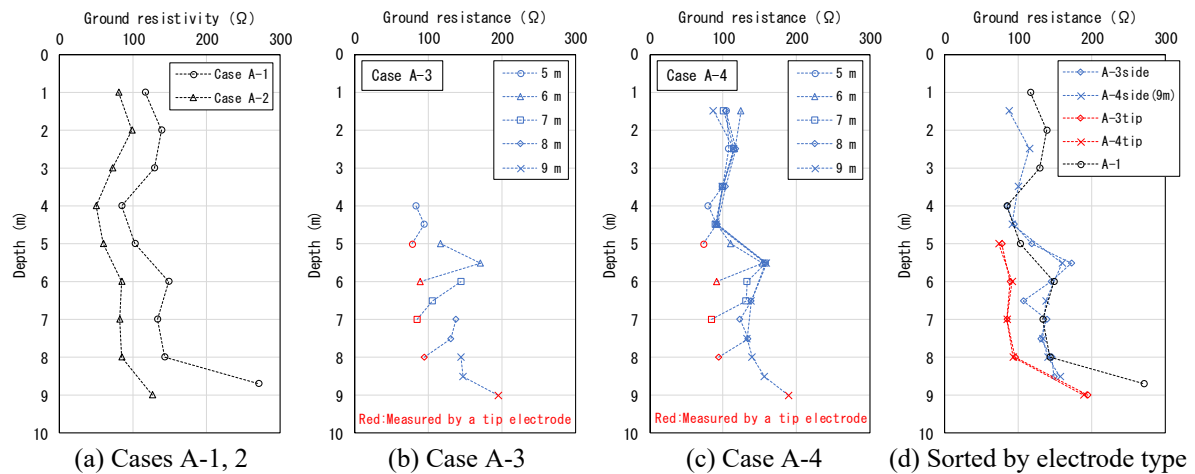


Fig. 4 Measurement results of ground resistance (Cases A-1 to A-4).

Test results

Driving performance of measurement pipe

Since the measurement pipes are divided into pieces of 1 m long except the tip part, it was necessary to alternate the pipe driving and pipe connecting processes. In the test, it took approximately 30 seconds to drive a pipe 1 m into ground when the SPT-N value was less than 5, regardless of the type of pipe. On the other hand, time required to connect pipes varied according to the type of pipe. In pipes No.1, 2 and 4, pipe connecting process was necessary to connect screw parts only, which took less than 2 minutes. On the contrary, it took more than 3 minutes

in pipe No.3 because it was required that electric cables had also to be connected in the process; all in all, it took less than an hour to drive pipes 9m into ground. It was confirmed through the test that the electrodes could be arranged in the ground in a short period of time when the developed measurement pipes were used, compared to the conventional electrode arrangement method in boreholes.

Applicability of equipped electrodes for soil resistivity and ground resistance measurements

Figure 4 shows the measurement results of ground resistance. It may be seen that ground resistances measured in cases A-1 and A-2 did not coincide with

each other, but their distribution trends were similar at depths (see Fig. 4 (a)). It seems that the measured resistivity was lower in case A-2 than in case A-1, since the electrode used in case A-2 had a larger surface area than that in case A-1. In cases A-3 and A-4, it was observed that the measured ground resistance was lower at a tip electrode than that at the ring electrode on the side (see Fig. 4 (b), (c)). It is also likely that this was caused by the difference in electrode size at the pipe tip and on the side. On the other hand, the results measured by the same type of electrode showed almost the same value at each depth (see Fig. 4 (d)). However, the results of A-1 did not coincide the values measured on side of A-3 and A-4 although those electrode size and shape were almost same. This implied that the electricity supply method in cases A-1 and A-2 using internal steel pipe might have increased the measured values compared to that in cases A-3 and A-4.

Figure 5 shows the measurement results of soil resistivity. Soil resistivity at a depth of 8.9 m measured in case B-2 was 46.8 $\Omega\cdot\text{m}$ and it was close to the measured value in case B-1 at 8.75m (43.7 $\Omega\cdot\text{m}$). Although it was a limited comparison, the soil resistivities obtained from in-situ and laboratory testing could be seen almost same level from a depth of 6.5m to a depth of 7.5 m.

Through the test, it was confirmed that the developed measurement pipes could be applied for the measurement of ground resistance and soil resistivity.

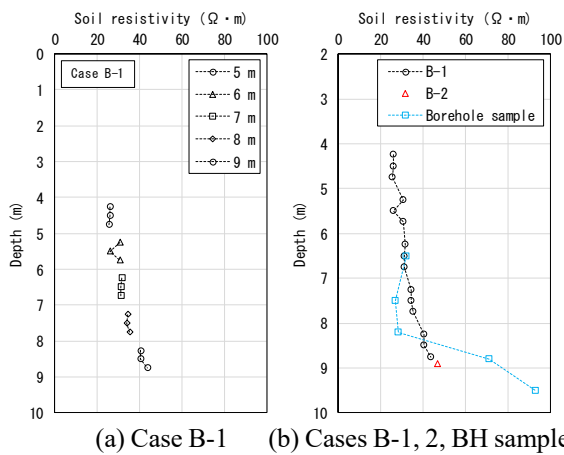


Fig. 5 Measurement results of soil resistivity (cases B-1, B-2 and borehole sample).

TRIAL MEASUREMENT OF GROUND RESISTANCE BEFORE AND AFTER JET GROUTING

Based on the results of the preliminary test discussed above, a trial measurement of ground resistance was conducted before and after a cement jet grouting in an actual construction site. The pipes No. 1 and 2 (shown in Fig.1) were used, focusing on

ground resistance as an easy index that might help evaluate the changes in soil resistivity around electrodes.

Measurement conditions

Figure 6 shows the arrangement of measurement pipes, auxiliary electrodes and soil-cement columns created by jet grouting. Measurement apparatuses were arranged a few hours before jet grouting. Column in design has a diameter of 3.5 m and a height of 4 m, that was created at depths between 2 m and 6 m. Two measurement pipes were arranged horizontally 1.75 m away from the injection point (radius of the column in design). The distance between the two pipes was 2m and the tip electrode was placed at a depth of 4 m, which was the mid height of the column.

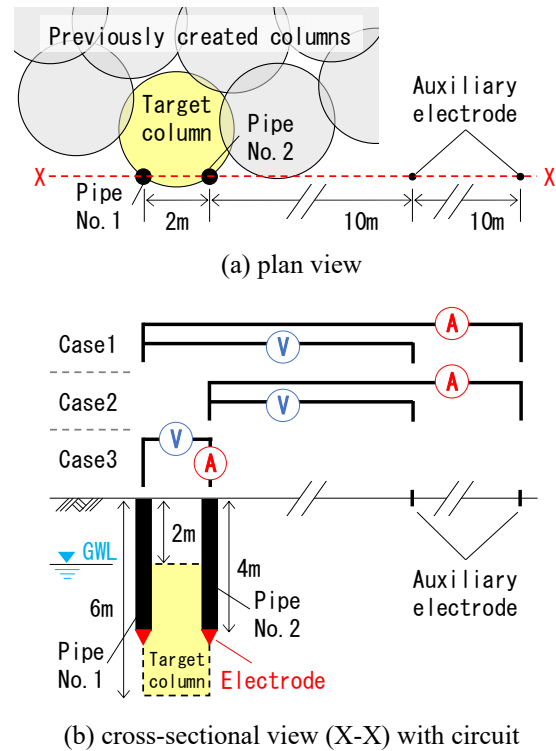


Fig. 6 Measurement pipes and electrodes arrangement with circuit diagram of each case.

Table 2 shows measurement cases. In cases 1 and 2, ground resistance around the electrodes was measured at pipes No.1 and 2 individually, while in case 3, total ground resistance around the two electrodes was measured using both pipes No.1 and 2. In order to confirm the changes in ground resistance caused by jet grouting each measurement was repeated three times, before jet grouting, just after jet grouting, and one day after jet grouting. In addition, the resistivity of the soil discharged from jet grouting work was also measured to confirm the actual resistivity of improved area.

Table 2 Measurement cases

Case	Pipe	Measured value
1	No.1	Ground resistance
2	No.2	Ground resistance
3	No.1,2	Sum of ground resistances

Results of trial measurement

Table 3 shows measurement results of ground resistance in the site and the resistivity of discharged soil. In case 1, three values of measured ground resistance were almost same, and the effect of jet grouting was not observed. On the other hand, in cases 2 and 3, lower ground resistance was observed after, compared to before the jet grouting. Since the resistivity of the discharged soil shown in Table 3 was obviously lower than the general range of natural soil resistivity, it seemed that decreases in the ground resistance in cases 2 and 3 were caused by jet grouting. In case 1, the ground resistance measured before the jet grouting was close to that measured just after the jet grouting in case 2. Therefore, measurement before jet grouting in case 1 might have been affected by surrounding columns created previously.

Through the trial measurement, it seemed that the changes in ground resistivity caused by jet grouting could be evaluated easily and readily using the developed measurement pipes. How to visualize the improved area and evaluate the improved soil quality will be investigated in the next stage, using the developed measurement pipes.

Table 3 Measured ground resistance in the site and discharged soil resistivity

Case	Ground resistance (Ω)		
	Before	Just after	Day after
1	22.4	22.0	21.6
2	55.8	25.4	24.6
3	183.0	48.0	47.0
Resistivity (Ω -m)			
Discharged soil	1.23	1.49	

CONCLUDING REMARKS

To provide a rapid electrode arrangement method for soil resistivity and ground resistance measurement, the driving pipes were developed. Their effectiveness was then examined through the preliminary test and the trial measurement in the field.

The results obtained in the study show that the measurement pipe could be driven 9 m in an hour into the ground where the SPT-N value was less than 5, and that the electrode of measurement pipe could be applied for soil resistivity and ground resistance measurements. It was implied that the changes in soil resistivity caused by soil improvement could be

detected by the measurement of ground resistance.

On the other hand, the followings are the remaining issues which would be typical factors to decide the proposed method limitation:

- As an issue relating to driving performance, maximum driving lengths must be identified based on ground conditions such as SPT-N value and soil properties.

- As an issue relating to the soil resistivity measurements, acceptable original ground resistivity ranges must be clarified to secure evaluable difference in soil resistivity of soil improved part.

Also, the optimization of electrodes arrangement must be pursued to minimize installation costs. To solve these issues, additional laboratory and field testing are under planning by authors.

Through these efforts, we will make the proposed method fit to practical use in near future. Furthermore, we hope it will contribute to realization of “real-time” management system of quality assurance for soil improvement works, which is the authors image as a next-generation system.

REFERENCES

- [1] Lin C.-P., Lin C. H., Wu P. L., Wang H. R. and Liu H. C., Geophysics-assisted control and evaluation of ground improvement, Proceedings of the 16th Asian Regional Conference on Soil Mechanics and Geotechnical Engineering, Invited Lecture III, 2019.
- [2] Komine H., Evaluation method of void filling of chemical grouting by electrical resistivity (in Japanese), Journal of Japan Society of Civil Engineers, No.463/III-22, 1993, pp. 153-162.
- [3] Komine H., Applicability of evaluation of improved region by resistivity tomography in chemical grouting (in Japanese), Journal of Japan Society of Civil Engineers, No.561/III-38, 1997, pp. 89-98.
- [4] Komine H. and Goto K., Verification of evaluation for chemical grouted region using resistivity tomography by field test (in Japanese), Journal of Japan Society of Civil Engineers, No.603/III-44, 1998, pp. 129-138.
- [5] Fujii H., Kawamura M., Tamura M., Watanabe K. and Mizoguchi E., Quality evaluation method for soil-cement column by deep mixing method (in Japanese), Journal of the Society of Materials Science, Vol.53, No.1, 2004, pp. 9-12.
- [6] Fujiwara T., Matsui H. and Takahata Y., Field test of ground resistivity measurement using driving type electrode pipe (in Japanese), Proceedings of the Japan National Conference on Geotechnical Engineering, 2020 (submitted).
- [7] Fujiwara T., Matsui H., Ishii H. and Aoki T., Soil resistance measurement of improved soil columns using driving type pipe with electrodes (in

- Japanese), Proceedings of the 75th Japan Society of Civil Engineers Annual Meeting, 2020 (submitted).
- [8] Takahata Y., Matsui H., Ishii H. and Horikoshi K., Development of driving-type injection pipe for soil remediation and improvement (in Japanese), Report of Taisei Technology Center, No.45, 2012, pp. 52-1-52-6.

THE CONTRIBUTION OF PILES TO THE AVOIDANCE OF THE RAINFALL-INDUCED SLOPE FAILURE

Yujia Wang¹, John V. Smith¹ and Majid Nazem¹

¹RMIT University, Australia

ABSTRACT

Rainfall is the major cause of the slope failure in South Gippsland, Victoria, Australia. These slope failures typically impact the rural road infrastructure in the form of requiring regular maintenance and continuous cost. This issue thus is fixed by an integrated slope-stabilisation method that combines the gabion-faced geogrid-reinforced retaining-wall and the pile. This integrated reinforcement system has been investigated with a three-dimensional non-linear finite element approach. An elastic-perfectly plastic model with Mohr-Coulomb criterion is used to describe the behaviour of the soil and the gabion basket. The piles are shown to make a significant contribution to the retaining system. The factor of safety was increased by approximately 30% and the horizontal displacement at the retaining wall crest was reduced by 75%. Comparison between the model of the field pile configuration (diameter 0.4 m and spacing 1.4 m) and models of a range of pile diameters and spacings showed that the field pile configuration is efficient with respect to the volume of concrete piles required.

Keywords: Slope stabilisation; Pile retaining structure; Geogrid-reinforced retaining-wall; Gabion basket; Finite element.

INTRODUCTION

The failure of slopes traversed by the rural roads of South Gippsland, Victoria, Australia frequently requires stabilization by construction of retaining walls [1]. The technique applied is geogrid-reinforced retaining walls (GR-RW) as has been widely used for local public sector retaining wall projects [2]. Roadside stabilisation with GR-RW has benefits including cost-effectiveness, ability to tolerate settlements, aesthetic appeal of the stone filled gabions and good performance [3].

Piles are also used as a method of slope stabilisation, and the effect of piled retaining wall in resisting lateral soil movement of a slope has been investigated by many researchers [4]-[5]. In this study, the method used is the finite element method (FEM) which can provide coupled solutions in which the pile response and slope stability are considered simultaneously.

The present research investigates the contribution of piles in increasing the stability of a slope when integrating the pile retaining structure into the conventional gabion-faced geogrid-reinforced retaining wall (GF-GR-RW). This study compares the representative indicators of the stability of the slope, the critical slip surface, the horizontal displacement, and the FoS. The results demonstrate the significant contribution of integrating the pile into GF-GR-RW.

STUDY AREA

Site Location

The study area is in South Gippsland, Victoria,

Australia. The stability of the slopes in South Gippsland has a major impact on the road infrastructure that is maintained by the local government authority. An example of the slope reinforcement system, which integrates piles into the GF-GR-RW, used in this area to stabilise the slope is shown in Fig. 1.



Fig. 1. GF-GR-RW with piles used in South Gippsland

Slope Configuration

The field conditions replicated in the model include a GF-GR-RW installed to stabilise a road cutting. Piles were installed at the toe of the retaining wall (prior to its construction) with a diameter of 0.4 m and a centre-to-centre spacing of 1.4 m (a gap of 1 m between piles). For comparison, other configurations were also modelled. These configurations included GF-GR-RW without piles (Fig. 2(a)) and piles which are not embedded into a

weathered rock layer (Fig. 2(b)). For clarity, the simpler cases will be presented prior to the more complicated case (Fig. 2(c)).

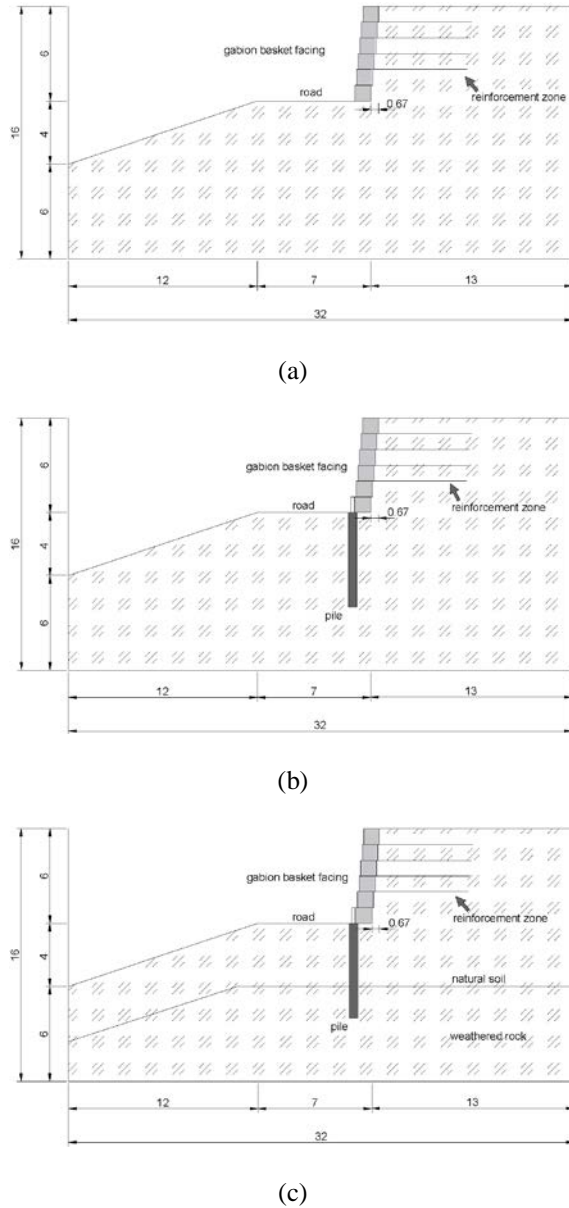


Fig. 2 Slope configurations: (a) GR-RW (b) GR-RW with piles (c) GR-RW with piles embedded in the stable layer (dimension in meters)

The dimensions of the gabion baskets are 1 m cubes filled with quarried rock. The facing of the retaining wall is composed of six layers of gabion basket which are stacked with a stepped pattern to form a gradient of 9V:1H. In the model, the length of the pile is 6m, and the embedded length of the pile in the weathered rock layer is 2m. The diameter (D), centre-to-centre spacing (S), and the presence or absence of a weathered rock layer are varied for the purpose of making the comparison between different cases as summarised in Table 1. C0 represents the

case that is only stabilised by GR-RW without the piles, (C1-C4) represent the cases that have the piles but no weathered rock layer with the increase of the S/D ratio, and (C5-C8) represent the cases that have the piles and the pile is embedded in the weathered rock layer with the increase of the S/D ratio.

Table 1 Pile configurations

	Centre-to-centre spacing (m)	Diameter (m)	S/D	Embedded length in stable layer (m)
C0	-	-	-	-
C1	1.4	1	1.4	-
C2	1.4	0.4	3.5	-
C3	4	1	4	-
C4	4	0.4	10	-
C5	1.4	1	1.4	2
C6	1.4	0.4	3.5	2
C7	4	1	4	2
C8	4	0.4	10	2

NUMERICAL MODELLING

Material Properties

The slope model is composed of two types of material, a natural soil underlined by a stable layer of weathered rock. The material properties of slope and reinforcement are summarised in Table 2. The strength of the soil and the weathered rock is determined based on the previous study [1]. The strength of the pile and the steel is C30 and S500, respectively. The geogrid is the typical polyester (PET) geogrid (GGW) and the strength is determined by the standard. For the gabion basket, the strength properties are determined based on the compression test and the direct shear test of the gabion basket group.

Table 2 Material properties

Material	γ (kN/m ³)	ϕ' (°)	c' (kPa)
natural soil	20	20	10
weathered rock	23	35	200
pile	23	-	-
gabion basket	17	45	560
steel	79	-	-
geogrid	2	-	-

Mesh Configurations

Regarding the mesh of the three-dimensional model, the solid element including the pile, steel, the gabion basket, and the slope is discretised by eight-

node brick elements (C3D8) without reduced integration, and the geosynthetic is discretised by four-node membrane elements (M3D4). A structured mesh technique was used for the solid elements and membrane elements. Fig. 3 shows the finite element mesh of the reinforcement system and the finite element mesh of the slope, consisting of 160,952 nodes and 130,926 elements, adopted in the calculation. The computation time for the analysis of each case is about 1h, and the computations are performed on the platform of National Computational Infrastructure (NCI) using 32 core 2.6 GHz High-Performance Computing (HPC) with 31 GB random access memory. The mesh sensitivity and convergence criteria were also investigated by comparing simulation results due to the use of different shape or number of elements to make sure that the current shape and size of the mesh used for this modelling is fine enough so that the results of simulations are not sensitive to mesh density.

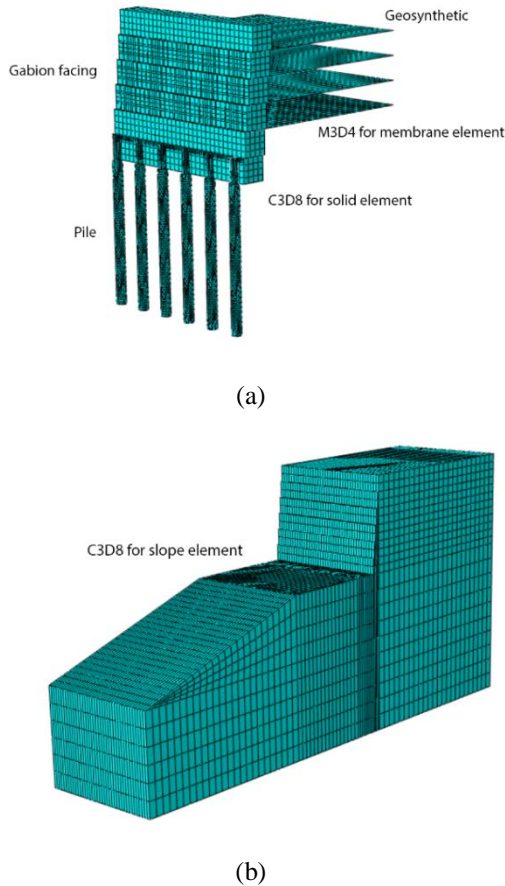


Fig. 3 Meshed model: (a) Meshed reinforcement; (b) Meshed slope

SHEAR STRENGTH REDUCTION FINITE ELEMENT METHOD (SSR-FEM)

The reduced shear strength parameters c_r and φ_r are given by:

$$c_r = \frac{c'}{\text{SRF}} \quad (1)$$

$$\varphi_r = \arctan\left(\frac{\tan\varphi'}{\text{SRF}}\right) \quad (2)$$

where SRF is the strength reduction factor. The FoS is equal to the value of SRF.

In strength reduction calculation, the factored shear strength parameters c_r and φ_r replace the corresponding values of c' and φ' by

$$c_r = \frac{c'}{f(t)} \quad (5)$$

$$\varphi_r = \arctan\left[\frac{\tan\varphi'}{f(t)}\right] \quad (6)$$

where $f(t)$ = field variable [$f(t) = (a - b)t + b$]; t = time increment for every calculation step in *Abaqus* ($0 \leq t \leq 1$); a and b = adjustable factors ($a > b$). The value of a and b can be determined by the user based on the estimated range of the FoS. It can also be found that the field variable is increasing with the increment of the step time, which means during the calculation, the value of c' and φ' would be reduced progressively until the failure happens. The non-convergence of the solution is the indication of the slope failure, when it occurs, the value of FoS would be obtained which is equal to the value of the field variable of the final incremental step. Once the value of the FoS is obtained, the graphical output of the index 'U1' of *Abaqus* will be used to indicate the value of the horizontal displacement within the model [6], including the pile head deflection. From the horizontal plane of the model, the soil arching effect between piles will be indicated by the relative horizontal displacement between the moving and the stationary soil masses. From the vertical plane of the model, the significant effect of piles in reducing the horizontal soil displacement will be presented. In addition, the reduction in the size of the critical slip surface of the slope will also be represented by 'U1' because of the reduction in the horizontal soil displacement. The accuracy and effectiveness of the Strength Reduction Finite Element Method (SR-FEM) conducted within *Abaqus* have been validated by [7]-[8], and it represents an effective tool to conduct this parametric study.

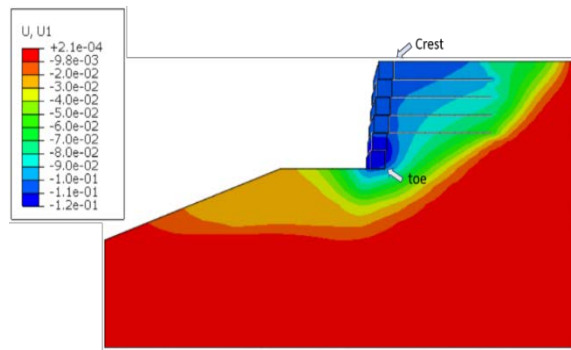
ANALYSIS OF RESULTS

Lateral Soil Movement

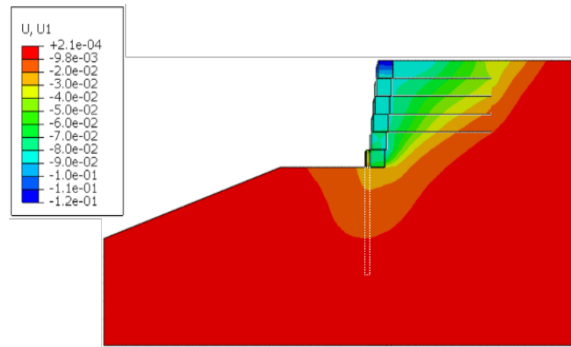
To better understand the effect of the piles within this system in reducing the lateral movement of soil in the slope, a comparison of three cases is represented by the vertical plane of the model. These three cases are: (1) no piles (C0); (2) with piles (C2) and (3) with the piles embedded in the weathered rock

layer (C6). The pile diameter and spacing in these cases is the field site condition.

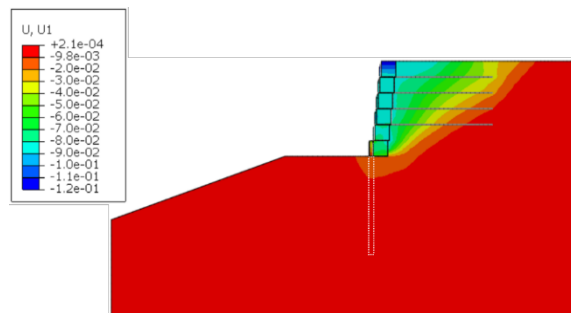
The lateral soil movement of the slope that is only stabilised by the GR-RW (C0) is much larger than the other two cases. The length of the failure surface of the slope that without the piles (C0) extends almost to the toe of the lower slope and with a large depth which is defined as a deep-seated failure, the volume of the unstable soil mass is also much larger than the other two cases (Fig. 4(a)). With the piles present at the toe of the slope but not embedded in the stable layer (C2), the depth of the lateral movement up to the position of the piles is almost the same as observed for no piles, but the magnitudes of displacement are greatly reduced (Fig. 4(b)). With piles embedded in a stable layer (C6), the depth and the length of lateral movement has been reduced significantly (Fig. 4(c)).



(a)



(b)

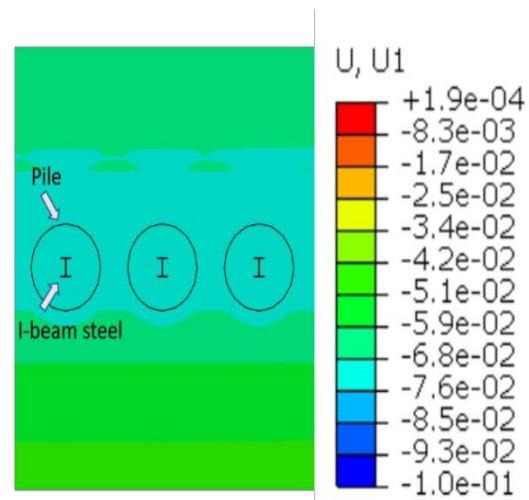


(c)

Fig. 4 Horizontal displacement: (a) Without piles (C0) (b) With piles (C2) (c) With piles embedded in a stable layer (C6) (cross section is located along the centre line of the model; U, U1 represents the horizontal soil movement in metre)

Comparison of four cases in the horizontal plane of the model illustrates the pile configurations considered. In particular, the stress elevations between piles is noted as the result of the soil arching effect. These four cases are selected as follows: (1) $S/D=1.4$ (C1); (2) $S/D=3.5$ (C2); (3) $S/D=4$ (C3); (4) $S/D=10$ (C4). These four cases are all without the embedment of piles into a weathered rock layer.

The different S/D ratio represents the different magnitude of the soil arching effect (Fig. 5). When the S/D ratio of the piles is equal to 1.4 (C1), the pile deflection is the same as the horizontal displacement of the surrounding soil (Fig. 5(a)), which is a clear manifestation of the strong arching effect. Compared with the S/D ratio which is equal to 10 (C4), the soil at the interval of the piles displaces much larger than the pile head deflects (Fig. 5(d)), which represents that the soil at the interval of the piles is hardly confined by the soil arching effect and flows between the piles. This phenomenon indicates that the soil arching effect within this reinforcement system is gradually diminishing with the increase of the S/D ratio. The distribution of the horizontal displacement contours of the soil and the pile presents a similar pattern when the S/D ratio of the piles is equal to 3.5 (C3) and 4 (C4). The contour of the horizontal soil displacement under these two conditions can be considered as effective soil arching (Fig. 5(b) (c)), which could provide support to the soil mass and confine the flow of the soil between the piles effectively.



(a)

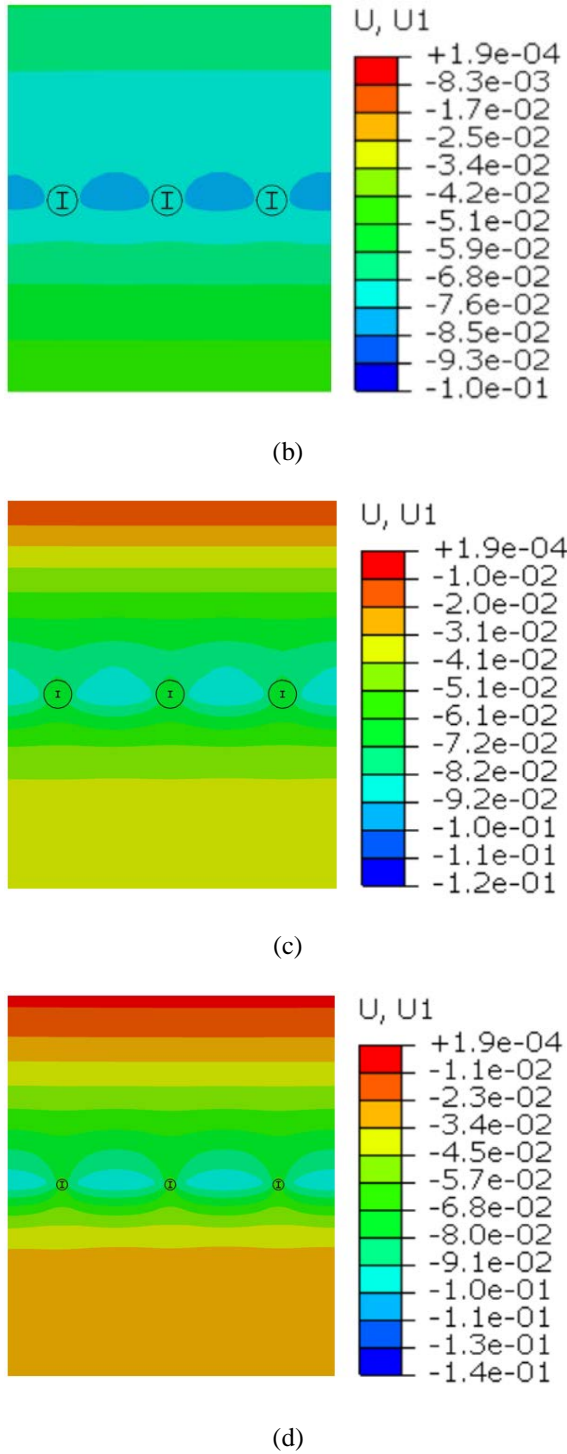


Fig. 5 Lateral movement of soil in the horizontal plane: (a) $S/D=1.4$ (C1) (b) $S/D=3.5$ (C2) (c) $S/D=4$ (C3) (d) $S/D=10$ (C4) (the cross-section is located along the surface 0.5m lower than road; two intervals between three piles are selected; the movement of the soil is from top to bottom in the picture; U, U1 represents the lateral soil movement in meter)

To investigate the contribution of the piles in reducing the horizontal displacement of the slope, all 9 cases with varied pile configurations were studied.

The following result, expressing the horizontal displacement at toe and crest of the slope, with respect to the variation of the pile configurations is obtained and shown in Fig. 6.

For the case of no piles (C0), the lateral movements at toe and crest are much greater than all the other cases with the piles (C1-C8). In the case of no stable layer and with the largest S/D ratio (C4), the horizontal displacements at toe and crest are smaller than C0. Such a reduction in the horizontal displacement is estimated at 17% of the crest to 29% of the toe of the slope. The existence of the piles reduces the lateral soil movement significantly, i.e., the effect of including piles in reducing the horizontal displacement of the slope has been demonstrated.

Regarding the lateral movement at the toe of the slope, the value of the horizontal displacement is reduced significantly if the pile is embedded in the weathered rock layer. Such a reduction is estimated as 22% for the corresponding case when S/D ratio is equal to 10 (C4&C8), for another corresponding case when S/D ratio equals to 1.4 (C1&C5), such a reduction is estimated as 31%. The reduction in lateral soil movement is increasing with the decrease of the ratio of S/D from 10 to 1.4. The advantages of the embedding piles into weathered rock layer in reducing the horizontal displacement of the slope can also be demonstrated.

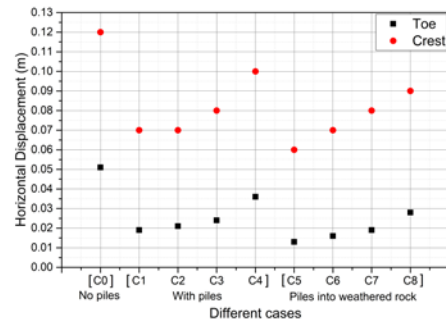


Fig. 6 Horizontal displacement at toe and crest for different cases (Table 1)

Factor of Safety

To study the contribution of the existence of the piles in influencing the FoS of the slope, the value of FoS of all cases (C0-C8) is calculated and shown in Fig. 7.

The FoS of the case without piles (C0) is 1.26, while the lowest value of the FoS for the case that has the piles is 1.43 (C4&C8). Such increment in the FoS is estimated as 13%. The soil arching effect with a large S/D ratio which equals to 10 (C4&C8) is relatively weak, but the FoS is still increasing compared with the case of without piles (C0), thus, the contribution from the piles in increasing the FoS

of the retaining structure can be demonstrated.

For cases without the weathered rock layer (C1-C4), the FoS increases from 1.43 to 1.48 with the decrease of the S/D ratio, whereas for the cases that have a weathered rock layer (C5-C8), the FoS increases significantly from 1.44 to 1.85 with the decrease of the S/D ratio. The increase in the FoS is approximately 28%.

In addition, based on the pile configuration (Table 1), each value of the S/D ratio corresponds to two different cases, and these two cases are defined as corresponding cases, the difference between two cases that have the same S/D ratio is whether or not the pile is embedded in a weathered rock layer. When the S/D ratio equals to 1.4 (C1&C5), the contribution of the weathered rock layer in the increment of FoS is estimated as 28%, it is 14% for the S/D ratio of 3.5 (C2&C6), 8% for the S/D ratio equals to 4 (C3&C7), and no increment in the FoS for the S/D ratio equals to 10 (C4&C8) because of the relatively weak soil arching effect. It can also be found that the effectiveness of the weathered rock layer in increasing the FoS of the slope will be influenced significantly by the S/D ratio of the piles.

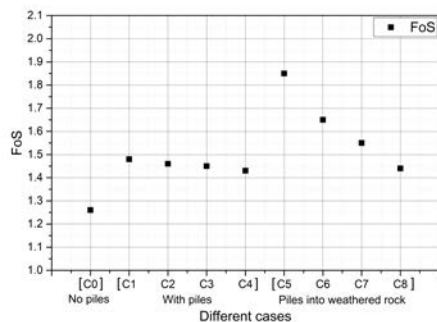


Fig. 7 FoS for different cases (Table 1)

CONCLUSIONS

In South Gippsland, a specific reinforcement system has been applied by integrating soil reinforcement with geogrid, gabion facings and piling. The effectiveness of this reinforcement system has been demonstrated by investigating the lateral soil movement and the FoS of the slope using three-dimensional finite element analysis. For the slope stabilised using only gabions and geogrid, the size of the slip surface is relatively large, and the slope failure mode is deep-seated. However, for the slope stabilised with the addition of piles, a smaller critical slip surface developed through the toe of the reinforced slope. This reduction in the size of the critical slip surface leads to an improvement in the stability of the slope.

The reinforcement method including geogrid and

gabion facings and piling at the retaining wall toe has been found to reduce the horizontal displacement at the retaining wall crest by 75% from 51 mm to 13 mm and increase the FoS of the slope by 31% from 1.26 to 1.65. Comparison with models of a range of pile diameters and spacings found the field configuration used (diameter 0.4 m and spacing 1.4 m) is efficient with respect to the volume of piles required.

The focus of this study is the assessment of the contribution of the embedded pile. The rainfall is the major cause of the slope instability, therefore, the infiltration and the surface runoff of the rainfall deserve a deep investigation for the future study.

ACKNOWLEDGEMENT

The authors would like to thank the staff from the South Gippsland Shire Council for the assistance of the site visiting. Facilities of the National Computational Infrastructure (NCI) were used for the processing of the numerical model.

REFERENCES

- [1] Smith J. Rapid and progressive deterioration of local road assets caused by slope instability in regional Victoria, Australia. In: Proceedings of 1st International Conference on Infrastructure Failures and Consequences (ICIFC2014). 2014.
- [2] Gu M, Collin JG, Han J, Zhang Z, Tanyu BF, Leshchinsky D, et al. Numerical analysis of instrumented mechanically stabilized gabion walls with large vertical reinforcement spacing. *Geotextiles and Geomembranes*. 2017;45(4):294-306.
- [3] Yoo C, Kim S-B. Performance of a two-tier geosynthetic reinforced segmental retaining wall under a surcharge load: Full-scale load test and 3D finite element analysis. *Geotextiles and Geomembranes*. 2008;26(6):460-72.
- [4] Bathurst RJ, Vlachopoulos N, Walters DL, Burgess PG, Allen TM. The influence of facing stiffness on the performance of two geosynthetic reinforced soil retaining walls. *Canadian Geotechnical Journal*. 2006;43(12):1225-37.
- [5] Hatami K, Bathurst RJ. Development and verification of a numerical model for the analysis of geosynthetic-reinforced soil segmental walls under working stress conditions. *Canadian Geotechnical Journal*. 2005;42(4):1066-85.
- [6] Abaqus. ABAQUS user's manual. Version 6.14.
- [7] Griffiths D, Lane P. Slope stability analysis by finite elements. *Geotechnique*. 1999;49(3):387-403.
- [8] Dawson E, Roth W, Drescher A. Slope stability analysis by strength reduction. *Geotechnique*. 1999;49(6):835-40.

SIMULATING EARTHQUAKE-INDUCED SLOPE FAILURES USING A SOLID-FLUID COUPLING MODEL BASED ON THE SMOOTHED PARTICLE HYDRODYNAMICS FRAMEWORK

Yusuke Ono¹

¹Faculty of Engineering, Tottori University, Japan

ABSTRACT

Various numerical analysis methods have been developed to simulate earthquake-induced slope failures. Simulations of earthquake-induced slope failures require capabilities to reproduce some factors, including the trigger level of an input ground motion and a travel distance of debris. For reproducing a trigger level of an input motion, the finite element method based on solid mechanics has been used. For reproducing a travel distance of debris, simulation methods based on the fluid dynamics have been applied. This study presents a new approach to simulate an earthquake-induced slope failure, coupling the solid mechanics and the fluid dynamics, based on the framework of the smoothed particle hydrodynamics (SPH). The presented approach allows us to simulate an earthquake-induced slope failure from its triggering stage to its accumulation stage. The presented approach demonstrated its capabilities to reproduce the trigger level of ground motion and a travel distance of debris through several simulation cases. The paper concluded that the presented approach could be a promising method to simulate earthquake-induced slope failures.

Keywords: Earthquake-induced slope failure, Smoothed particle hydrodynamics, Earthquake response, Run-out

INTRODUCTION

Once a strong earthquake strikes a mountainous area, slope failures, landslides, and rockfalls are likely to occur [1]. The 1994 Northridge earthquake (Mw 6.7) triggered more than 11,000 slope failures that killed 61 people [2]. The 2004 Chuetsu earthquake (Mw 6.6) induced about 9200 slope failures, and 68 people lost their lives [3]. More than 200,000 slope failures were caused by the 2008 Wenchuan earthquake (Mw 7.9) and resulted in 87,633 casualties [4].

Numerical simulation techniques have been developed to reproduce an earthquake-induced slope failure. The sliding block model is used to examine the occurrence possibility of slope failure for a certain level of earthquake excitation [5]. The finite element (FE) analysis can be used to investigate slope stability more precisely than the analysis using the sliding block model [6]. Typically, a slope is modeled by an elastic or an elastoplastic solid material in the FE analysis. However, the FE analysis has difficulties in simulating a flow-like slope failure.

For simulating a flow-like slope failure, the smoothed particle hydrodynamics (SPH) method has been applied recently. The SPH method was initially invented in the field of astrophysics [7]. Afterward, the application of the SPH method has extended to fluid dynamics and solid dynamics. A slope failure occurred in the municipal solid waste was simulated by the SPH with a Bingham fluid model [8]. The SPH

with a Bingham fluid model was also applied to earthquake-induced landslides [9]–[11]. These studies report that the SPH with a Bingham fluid model can reproduce surface profile of post-failure and run-out distance.

The aim of this paper is to develop a coupling model of solid and fluid dynamics into the SPH framework for simulating an earthquake-induced slope failure or landslide. The developed model is expected to simulate an entire process of an earthquake-induced slope failure: response to an earthquake ground motion, occurrence of flow sliding, and accumulation of debris.

SIMULATION MODEL

First, the framework of the SPH method is introduced. Second, the SPH discretization of equations of motion is given for a solid body and a fluid, respectively. Third, a new coupling model of solid-fluid dynamics is proposed.

SPH framework

The SPH framework consists of two fundamental approximation techniques: kernel approximation, and particle approximation. The kernel approximation is based on the following identical equation:

$$f(x) = \int_D f(x') \delta(x - x') dx' \quad (1)$$

where $f(x)$ is a function of the position vector x ; $\delta(x)$ is the Dirac delta function; D is the problem domain. The kernel approximation in the SPH is defined by replacing $\delta(x)$ by a smoothing kernel function $W(x)$:

$$f(x) \approx \int_D f(x') W(x - x', h) dx' \quad (2)$$

where h is called the smoothing length that prescribes the width of the function. A smoothing kernel function $W(x)$ must be a differentiable even function and must satisfy with the following conditions:

$$\int_D W(x, h) dx = 1 \quad (3)$$

$$\lim_{h \rightarrow \infty} W(x, h) = \delta(x) \quad (4)$$

The particle approximation is introduced by the discretized form of Eq. (2) as follows:

$$f(x_i) \approx \sum_{j=1}^N m_j \frac{f(x_j)}{\rho_j} W(x_i - x_j, h) \quad (5)$$

where m_j denotes the mass of particle j .

Equation of motion

The equation of motion of a solid body or a fluid is given by,

$$\frac{dv^\alpha}{dt} = \frac{1}{\rho} \frac{\partial \sigma^{\alpha\beta}}{\partial x^\beta} + b^\alpha \quad (6)$$

where α and β denote the coordinate directions; x^α is the position vector; v^α is the velocity vector; t is time; ρ is density; $\sigma^{\alpha\beta}$ is the stress tensor; b^α is the body force. The SPH form of the equation of motion is given by,

$$\frac{dv_i^\alpha}{dt} = \sum_{j=1}^N m_j \left[\frac{\sigma_i^{\alpha\beta}}{\rho_i^2} + \frac{\sigma_j^{\alpha\beta}}{\rho_j^2} \right] \frac{\partial W_{ij}}{\partial x_j^\beta} + b_j \quad (7)$$

Solid-fluid coupling model

In the present study, we propose that the stress tensor for a particle is computed by coupling solid and fluid states as follows:

$$\sigma^{\alpha\beta} = \beta(t)(\sigma^{\alpha\beta})^s + \{1 - \beta(t)\}(\sigma^{\alpha\beta})^f \quad (8)$$

where the superscript s and f denote solid and fluid state, respectively; $\beta(t)$ is a weight function for coupling the stresses of solid and fluid states and is defined by

$$\beta(t) = \exp\{-\gamma(t_f - t)\} \quad (9)$$

where γ is a coupling control parameter; t_f is the time when the stress tensor reaches the failure surface first time. For solid-state of a particle, the stress tensor is calculated by the elastic constitutive model,

$$(\sigma^{\alpha\beta}) = -p\delta^{\alpha\beta} + 2G\epsilon^{\alpha\beta} \quad (10)$$

where p is the isotropic pressure; $\delta^{\alpha\beta}$ is the Kronecker delta; G is the shear modulus; $\epsilon^{\alpha\beta}$ is the strain tensor. The isotropic pressure (p) is calculated by

$$p = K\epsilon^{\alpha\beta} \quad (11)$$

where K is the elastic bulk modulus.

On the other hand, the Bingham fluid model is applied to calculate the stress tensor of fluid-state. The stress tensor of fluid-state $(\sigma^{\alpha\beta})^f$ is written by

$$(\sigma^{\alpha\beta})^f = -p\delta^{\alpha\beta} + \tau^{\alpha\beta} \quad (12)$$

where $\tau^{\alpha\beta}$ is the shear stress tensor and is given by,

$$\tau^{\alpha\beta} = \eta\epsilon^{\dot{\alpha}\beta} + \tau_y \quad (13)$$

where η is the viscosity coefficient; $\epsilon^{\dot{\alpha}\beta}$ is the strain rate tensor; τ_y is the yield shear stress. To compute the isotropic pressure p of fluid, Eq. (11) is also applied.

The Mohr-Coulomb failure criterion is applied for both solid and fluid states of a particle. Furthermore, the strength reduction factor (S_R) is introduced. The relations between the internal friction angle of solid-state (ϕ_s) and that of fluid state (ϕ_f) is defined by

$$\phi_f = S_R \phi_s \quad (14)$$

The same (S_R) is used for the cohesion:

$$c_f = S_R c_s \quad (15)$$

where c_s is the cohesion of solid-state of a particle; c_f is the cohesion of fluid-state.

Boundary condition

The dynamic boundary condition is applied to model the rigid box in the simulation. The positions of the boundary particles are fixed, while the same procedure as for the other particles computes the stress tensors of the boundary particles.

Rayleigh damping

For stabilizing a simulation and absorbing the vibration of a model, Rayleigh damping is applied in this study. Rayleigh damping is commonly used in earthquake engineering. The application of Rayleigh damping to the SPH framework is appeared in the reference [13].

Time integration

The Verlet time integration scheme is used to update the velocities and the positions of the particles, and the fixed time increment of 1.0×10^{-4} s is applied.

NUMERICAL EXAMPLE

A slope model is considered as an example to demonstrate the performance of the developed coupling model. The properties of the example slope model and other parameters required to execute the simulation is presented in this chapter.

Slope model

The geometry of the example slope model is shown in Fig. 1. The slope angle of the model is 60° . The material properties for solid and fluid states of the slope are listed in Tables 1 and 2.

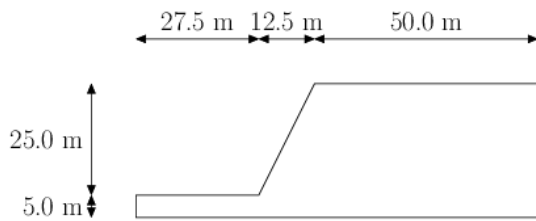


Fig. 1 The geometry of the slope model.

Table 1 Material properties for solid-state

Property	Value (Unit)
Density (ρ^s)	1.964×10^3 (kg/m ³)
Young's modulus (E)	1.675×10^6 (kPa)
Poisson's ratio (ν)	0.346
Cohesion (c^s)	150.0 (kPa)

Internal friction angle (ϕ^s)	20.0 ($^\circ$)
--------------------------------------	-------------------

Table 2 Material properties for fluid-state

Property	Value (Unit)
Density (ρ^f)	1.964×10^3 (kg/m ³)
Viscosity coefficient (η)	2.00 (Pa·s)
Cohesion (c^f)	$150.0 S_R$ (kPa)
Internal friction angle (ϕ^f)	$20.0 S_R$ ($^\circ$)

Note: S_R denotes strength reduction factor

Input ground motion

The sinusoidal wave of the amplitude with 6.0 m/s/s is used as the horizontal ground motion (Fig. 2). For the vertical direction, the gravity load is applied. From $t=0$ to 3 (s), no horizontal excitation is applied to stabilize the slope model to the gravity. The horizontal excitation starts at $t=3$ (s), and its amplitude increases gradually. From $t=9$ (s), the amplitude decreases and becomes zero at $t=10$ (s).

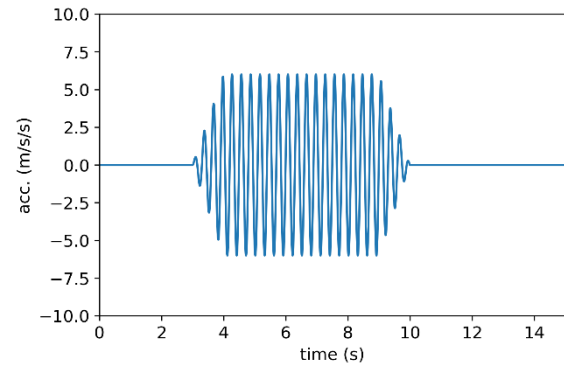


Fig. 2 The time history of the input acceleration.

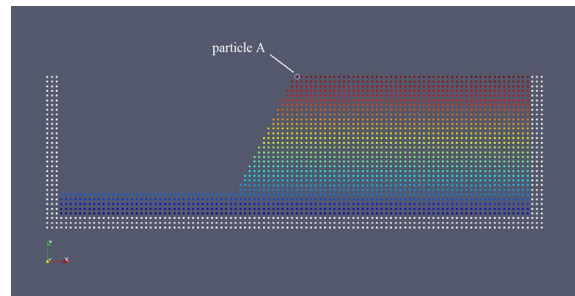


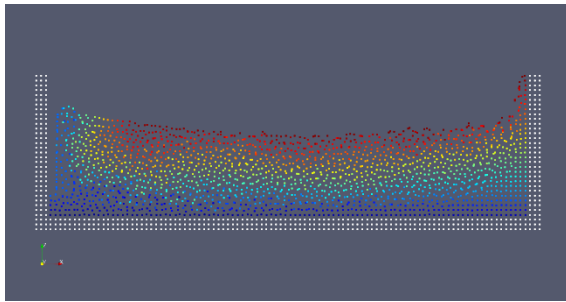
Fig. 3 The initial arrangement of particles.

Results

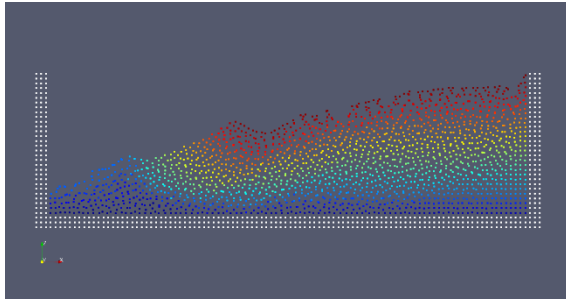
Figure 3 shows the initial configuration of the particles. The particles are placed homogeneously with 1.0 m intervals. The cubic spline type kernel function is used, and its smoothing length of the kernel function is 2.3 m. In total, 2,404 particles are used, including the boundary particles. The colors of

the particles show their vertical positions, except the boundary particles colored in white.

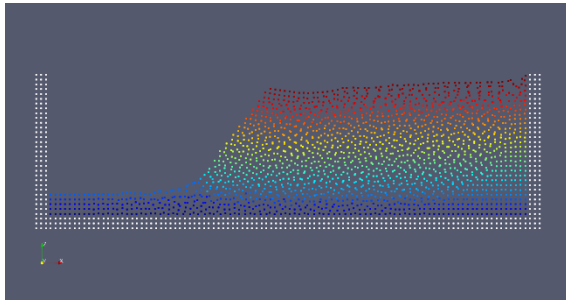
Figure 4 compares the profiles of the slope model after the horizontal excitation at $t=15$ (s) for various strength reduction factors: (a) $S_R=0.10$; (b) $S_R=0.25$; (c) $S_R=0.50$. The colors indicate the initial height of the particles, except the boundary particles that are colored in white. The same color-coding is commonly used in Fig. 6. The coupling parameter (γ) is 100.0. From these results, the effect of the strength reduction factor is revealed. The smaller value of S_R facilitates the deformation of the slope. For the case of $S_R=0.10$, the slope model is fluidized and deforms significantly. For the case of $S_R=0.5$, the slope model is not fluidized, although it deforms slightly.



(a) $S_R=0.10$, $\gamma=100.0$



(b) $S_R=0.25$, $\gamma=100.0$



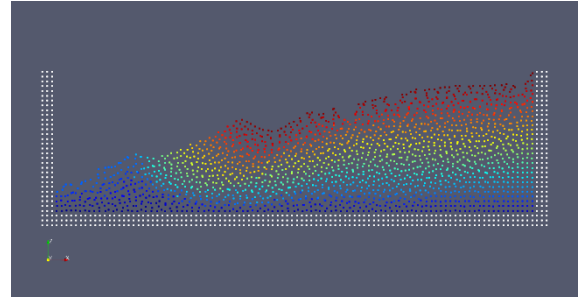
(c) $S_R=0.50$, $\gamma=100.0$

Fig. 4 Slope profiles after the horizontal excitation for $S_R=0.10$, 0.25, and 0.50.

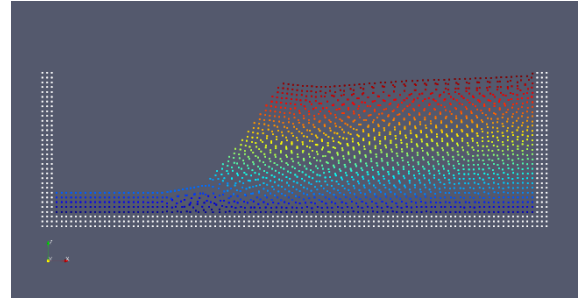
On the other hand, Fig. 5 compares the results for (a) $\gamma=100.0$ and (b) $\gamma=1.0$. The strength reduction factor (S_R) is the same and is 0.25. The result suggests that the larger value of the coupling parameter γ makes the slope model stable. For the

larger value of the coupling parameter $\gamma=100.0$, the slope model collapses, while it deforms slightly for the smaller value of $\gamma = 1.0$.

Figure 6 compares the vertical motion of particle A, which is indicated in Fig. 2, for $S_R=0.10$, 0.25, and 0.50. The effective time range of the horizontal ground motion is indicated in the figure. The moment when particle A starts moving is the same for all cases. For $S_R=0.10$, the slope model fluidizes, and particle A starts moving earlier than for the other cases. For $S_R=0.50$, the slope model fluidizes gradually, and the particle moves slowly. For $S_R=0.50$, the behavior of the slope model is intermediate of the other two cases.



(a) $S_R=0.25$, $\gamma=100.0$



(b) $S_R=0.25$, $\gamma=1.0$

Fig. 5 Slope profiles after the horizontal excitation at $t=15$ (s) for $\gamma=100.0$ and 1.0.

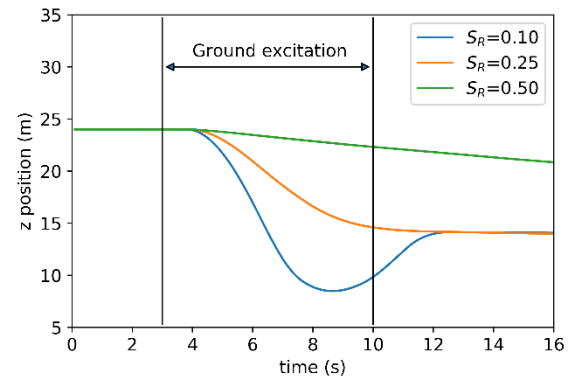


Fig. 6 The vertical motions of particle A for $\gamma=100.0$, $S_R=0.10$, 0.25, and 0.50.

The vertical motions of particle A for $S_R=0.25$, $\gamma=100.0$ and 1.0 are compared in Fig. 7. The coupling

parameter (γ) has the effect of delaying fluidization. For the case of $\gamma=1.0$, the slope model deforms gradually after the horizontal excitation ends. For $\gamma=100.0$, the deformation of the slope model begins and finishes during the horizontal excitation.

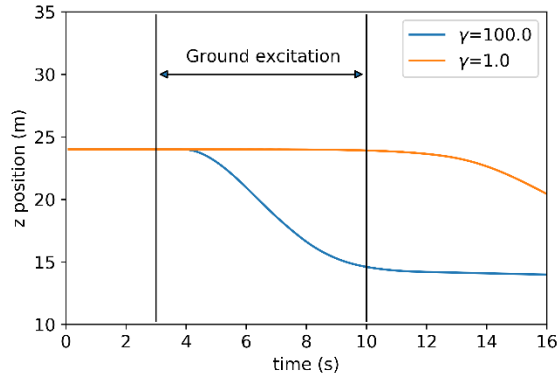


Fig. 7 The vertical motions of particle A for $S_R=0.35$, $\gamma=100.0$ and 1.0 .

DISCUSSION AND CONCLUSIONS

In the application of the SPH method to earthquake-induced slope failures and landslides [8]–[11], fluid models such as Bingham fluid are commonly used to reproduce the fluidization and deposition process. In these studies, the occurrence process of a slope failure has been ignored. On the other hand, previous studies [12]–[15] attempted to simulate all processes of a slope failure or a landslide: occurrence, fluidization, and deposition. However, their studies are based on solid mechanics and have not adequately reproduced fluidization and decomposition processes.

In this study, we have developed a model coupling solid and fluid models. The developed model allows us to simulate the whole process of an earthquake-induced slope failure or landslide: the occurrence of failure, fluidization, and sedimentation. As a further study, an appropriate method for setting the simulation parameters corresponding to the material properties must be developed.

ACKNOWLEDGMENTS

This work was supported by JSPS KAKENHI Grant Number 18H01523.

REFERENCES

- [1] Keefer D. K., Landslides caused by earthquakes, Geological Society of America Bulletin, Vol. 95, pp.406–421, 1984.
- [2] Harp E.L. and Jibson R.W., Landslides triggered by the 1994 Northridge, California, earthquake, Bull. Seismol. Soc. Am., Vol. 86. pp. S319–S332,

- 1996.
- [3] Sekiguchi H. and Sato H., Feature and distribution of landslides induced by the Mid Niigata Prefecture earthquake in 2004, Japan, Landslides, Vol. 43, pp.142–154, 2006.
- [4] Dai F. C., Xu C., Yao X., Xu L., Tu X. B., and Gong Q. M., Spatial distribution of landslides triggered by the 2008 Ms 8.0 Wenchuan earthquake, China, J. of Asian Earth Sci., Vol. 40, pp.883–895, 2011.
- [5] Jibson, R. W., Predicting earthquake-induced landslide displacements using Newmark's sliding block analysis, Transportation Research Record, Vol. 1411, pp.9–17, 1993.
- [6] Toki K., Miura F., and Oguni, Y., Dynamic slope stability analysis with a non-linear finite element method, Earthquake Engineering & Structural Dynamics, Vol. 13, Issue 2, pp. 151–171, 1985.
- [7] Gingold R. A. and Mohaghan J.J., Smoothed particle hydrodynamics: Theory and application to non-spherical stars, Monthly Notices of the Royal Astronomical, Vol. 181, pp.375–389, 1977.
- [8] Huang Y., Dai Z. L., Zhang W. J., and Huang M.S., SPH-based numerical simulations of flow slides in municipal solid waste landfills, Waste Management and Research, Vol. 31, Issue 3, pp.256–264, 2013.
- [9] Huang Y., Dai Z., Zhang W., and Chen Z., Visual simulation of landslide fluidized movement based on smoothed particle hydrodynamics, Natural Hazards, Vol. 59, Issue 3, pp.1225–1238, 2011.
- [10] Dai Z., Huang H., Cheng H., and Xu Q., 3D numerical modeling using smoothed particle hydrodynamics of flow-like landslide propagation triggered by the 2008 Wenchuan earthquake, Engineering Geology, Vol. 180, pp. 21–33, 2014.
- [11] Dai Z., Wang F., Huang Y., Song K., and Iio A., SPH-based numerical modeling for the post-failure behavior of the landslides triggered by the 2016 Kumamoto earthquake, Geoenvironmental Disasters, Vol. 3, 2016.
- [12] Ono Y., Nishida S., and Kiyono J., SPH Simulation for Seismic Behavior of Earth Structures, Proc. of 14th World Conference on Earthquake Engineering, Paper No.14-0145, 2008.
- [13] Ono Y., SPH Simulation of Earthquake-induced Slope Failure, Proc. of 15th World Conference on Earthquake Engineering, Paper No.22185, 2012.
- [14] Bui H.H. and Fukagawa R., An improved SPH method for saturated soils and its application to investigate the mechanisms of embankment failure: Case of hydrostatic pore-water pressure, International Journal for Numerical and Analytical Methods in Geomechanics, Vol.37, pp.31–50, 2013..
- [15] Chen W. and Qiu T., Simulation of earthquake-induced slope deformation using SPH method, International Journal for Numerical and Analytical Methods in Geomechanics, Vol.38, Issue 3, pp.297–330, 2014.

EVALUATION ON THE PERFORMANCE OF MICP TREATED SLOPE SOIL UNDER ACID RAIN ENVIRONMENT

Sivakumar Gowthaman¹, Arash Mohsenzadeh², Kazunori Nakashima¹, Hiromi Nakamura³ and Satoru Kawasaki¹

¹Faculty of Engineering, Hokkaido University, Japan; ²Department of Civil and Environmental Engineering, Amirkabir University of Technology, Iran; ³Hokkaido Office, East Nippon Expressway Company Limited, Japan

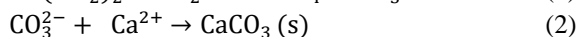
ABSTRACT

Microbial induced carbonate precipitation (MICP), through the field of bio-mediated geotechnical engineering, has gained significant momentum in research industry during recent past, which has promoted the strategy nearly to field application stage. The aim of this study is to evaluate the durability of MICP specimens under the exposure of acidic environment. The representative soils from an erosion prone slope were treated to different cementation levels on the basis of MICP. The acidic environment was enabled under different pH conditions (ranging 3.0-6.0) through two different mechanisms: (i) infiltration and (ii) immersion, both of which represent acid rainfall and water-logged environments, respectively. The influence of infiltration rate was studied under two potential rainfall intensities, and in each case, specimens were infiltrated by acid rain volume equals fifteen-year rainfall volume. The results indicate that decrease in environment pH increased the corrosion of CaCO_3 , resulting considerable loss in both mass and unconfined compressive strength (UCS). However, the increased cementation level showed high durability of specimens. The results also revealed that the contact time of acid rain significantly governed the rate of corrosion, i.e. specimens subjected to lower infiltration rate showed higher loss of mass and UCS compared to that of higher rate. Moreover, the immersed specimens showed relatively a similar response of those subjected to low infiltration. Overall, this study addressed one of the prime environmental hurdles which might possibly be experienced in the field, advancing the understanding on performance of slope near-surfaces conserved by MICP.

Keywords: Microbial induced carbonate precipitation (MICP), slope near-surface stabilization, durability, acid rain, cementation level

INTRODUCTION

Microbial induced carbonate precipitation (MICP), is relatively a novel and environmental-friendly soil stabilization technique and has gained significant momentum in recent years. The MICP treatment relies on urea hydrolysis; the urease produced by supplied or enriched bacteria catalyzes the urea hydrolysis, resulting the production of ammonium and carbonate ions (Eq. 1). The produced carbonate ions then react to precipitate calcium carbonate in the presence of calcium resources (Eq. 2) [1], [2]. This precipitated calcium carbonate functions as bio-cement, bonding the adjacent soil particles preferentially at particle-particle contacts and enhancing the aggregate stability and strength characteristics.



Stabilization of slope near-surface against aggregate instability is one of the serious concerns in the field of Geotechnical Engineering. The widely used traditional methods are primarily cement-based and/or bitumen-based, and they would appear to be ill-advised from a sustainability perspective. In recent years, MICP is often one of the scientists' and/or

engineers' proposal as a new sustainable alternative [3], [4]. The researches have already been initiated and demonstrated the viability of the technique in various standpoints, promoting the strategy nearly to field application stage. Accordingly, Salifu et al. [5] showed that the MICP could improve the stability of slope aggregates under repeated tidal currents, concluding that relatively a shallow treatment would be sufficient for coastal protection. The use of native bacteria was another appeal from the sustainable perspective, and that was proposed and demonstrated for stabilizing expressway slope soils [6], [7]. In another work, Gowthaman et al. [8] addressed the effect of particle size distribution on MICP responses, suggesting that presence of silt in small quantity tends to filter more bacteria at near-surface zone and results stable slope surfaces.

Despite of the considerable works, the studies addressing the longevity of MICP treatment under climatic factors are limited. Regarding the rainfall-induced impairments, treating the slope by 1 mol/L cementation resources was found to have better durability responses against erosion [9]. Considering the effects from seasonal frosts (subarctic regions), Gowthaman et al. [10] found that higher the precipitated content of calcium carbonate the stronger the inter-particle connections, leading to high aggregate stability and durability against freeze-thaw

actions. Provided alkaline conditions persist, the longevity of MICP treated soils can be expected to be stable for more than fifty years [11]. On the other hand, CaCO_3 material is chemically susceptible to acidic environment; therefore, longevity and durability of MICP treatment under the exposure of acid rainfall is often a question to be explored, and that remains as a hurdle for applications to the fields experiencing acid rainfalls. Therefore, the objective of this paper is to evaluate the durability of MICP treated soils under the exposure of acid rainfall environment.

MATERIALS AND METHODS

Soil and preparation

An erosion-prone expressway slope located in Onuma (Hokkaido, Japan) was selected for the current study. The slope soil can be classified as poorly graded (SP) fine sand according to the Unified Soil Classification System (USCS). Results from X-Ray fluorescence (XRF) analysis revealed that the silica is the dominant soil mineral, and the organic content was found to be negligible. Table 1 summarizes the fundamental geotechnical properties of slope soil.

Table 1 Fundamental characteristics of slope soil

Property	pH	D ₅₀	C _u	C _c	G _s
Values	6.997	0.23	2.5	0.8	2.71

Note: D₅₀ is the mean particle diameter (i.e., grain diameter at 50%); C_u is the coefficient of uniformity; C_c is the coefficient of curvature; G_s is the specific gravity.

The soil columns (30 mm in diameter; 50 mm in height) were prepared by tamping in three layers to the average density of around $1.6 \pm 0.1 \text{ g/cm}^3$, followed by the MICP treatment.

Bacteria and MICP treatment

Lysinibacillus xylanilyticus were the bacteria used herein to induce urea hydrolysis. The above ureolytic bacteria were isolated from the same slope soil; the detail on isolation process and characterization can be found in previous works [6], [8]. For the cultivation of bacteria, ammonium-yeast extract media ($\text{NH}_4\text{-YE}$, ATCC 1376) was used, which consisted of 20 g/L of yeast extract, 15.7 g/L of tris buffer and 10 g/L of ammonium sulfate. The media was inoculated with the bacteria pre-culture and subjected to shaking incubation at 25°C and 160 rpm. After 48-72 hours of growth, the bacteria culture was used for the MICP treatment (the optical density OD₆₀₀ was around 4.0).

During the MICP treatment, a two-phase surface percolation method [12] was incorporated: initial supply of bacteria culture, followed by multiple

supplies of cementation solution. Between the two phases, a period of 2-3 hours was allowed for bacteria cells to be attached with the soil particles [13]. All the solutions were supplied at the top of the columns at relatively a constant flow rate of 4 mL/min. Concentration of cementation solution used for the treatment was 1 mol/L, and which was similar to many previous works [14], [15]. The cementation media consisted of 110.9 g/L calcium chloride, 60 g/L urea and 6 g/L of nutrient broth.

In this study, three different levels of cementation (i.e., % of CaCO_3) were considered (C-1, C-2 and C-3). Different durations of MICP treatments were performed to achieve different levels of cementation. For C-1, around 7 number of cementation injections were performed. Around 10 number of injections were performed for C-2, and 14 injections for C-3. In another terms, the C-1, C-2 and C-3 levels can be demarcated as precipitated CaCO_3 content ranging between 12-14%, 16-18% and 21-23%, respectively. Measurement of CaCO_3 content was determined using the acid reaction method [8].

Acid rain (AR) simulation test

Accelerated test was applied in acid rain (AR) simulation. In real situations, AR could potentially be in contact with MICP treated slope near-surface at two possible conditions: (i) during infiltration and/ or (ii) submerged, and both conditions were investigated in this study. In order to reproduce the process of AR interaction, an infiltration setup was arranged as shown in Fig. 1. Effects of various parameters such as level of cementation (C-1, C-2 and C-3), pH of AR solution (3.0, 4.5 and 6.0) and intensity of AR (20 and 100 mm/h) were evaluated. The intensity of AR was controlled herein by the rate of delivery of the AR solution at specimen top as shown in Fig. 1.

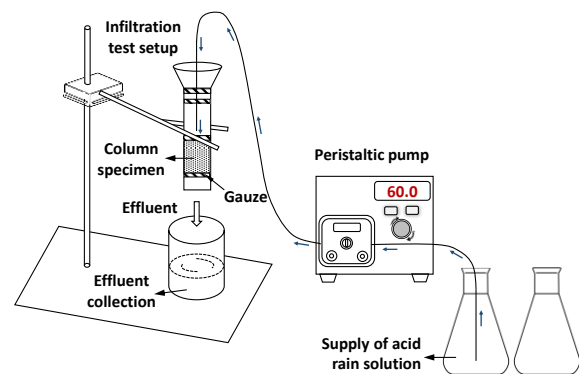


Fig. 1 Experimental set up of the AR infiltration

AR solution was prepared by dropping a certain volume of 1 mol/L nitric acid (HNO_3) and sulfuric acid (H_2SO_4) to deionized distilled water, and the pH levels were adjusted to 3.0, 4.5 and 6.0. The infiltration quantity of AR (Q_{inf}) was estimated based on the average annual precipitation in study location (Onuma, Hokkaido), as per the given equation (Eq. 3). Similar to the previous works, it was assumed that one-third of the total precipitation infiltrates in to the slope and two-third would be surface-runoff [16], [17].

$$Q_{inf} = \frac{1}{3} P_{avg} A \quad (3)$$

where, the P_{avg} stands for the annual average precipitation of study location (1210 mm), and A is the cross-sectional area of the specimen (7.06 cm^2). Accordingly, specimens were infiltrated by AR solution equivalent to the precipitation of 15 years. The AR solution was delivered to the specimens at

two rates, and the rates were chosen on the basis of typical high and low rain fall intensities (around 20 and 100 mm/h, respectively).

For the submerged condition, specimens were soaked completely into corrosion-resisting cylindrical molds containing AR solution. As the pH values of the AR solutions were changing due to the consumption of protons (H^+) by the reaction with CaCO_3 , the solution was replaced every 24 hours by newly prepared AR (to the total volume equivalent to the precipitation of 15 years). At the same time, the concentration of leached calcium ions was measured in the reacted solution. In addition, with the different immersion times, the weight loss was measured. Finally, all the treated specimens were oven-dried for 48 hours, followed by the estimation of the UCS. The UCS of the treated specimens were estimated by needle penetration tests in accordance with JGS 3431-2012 [18].

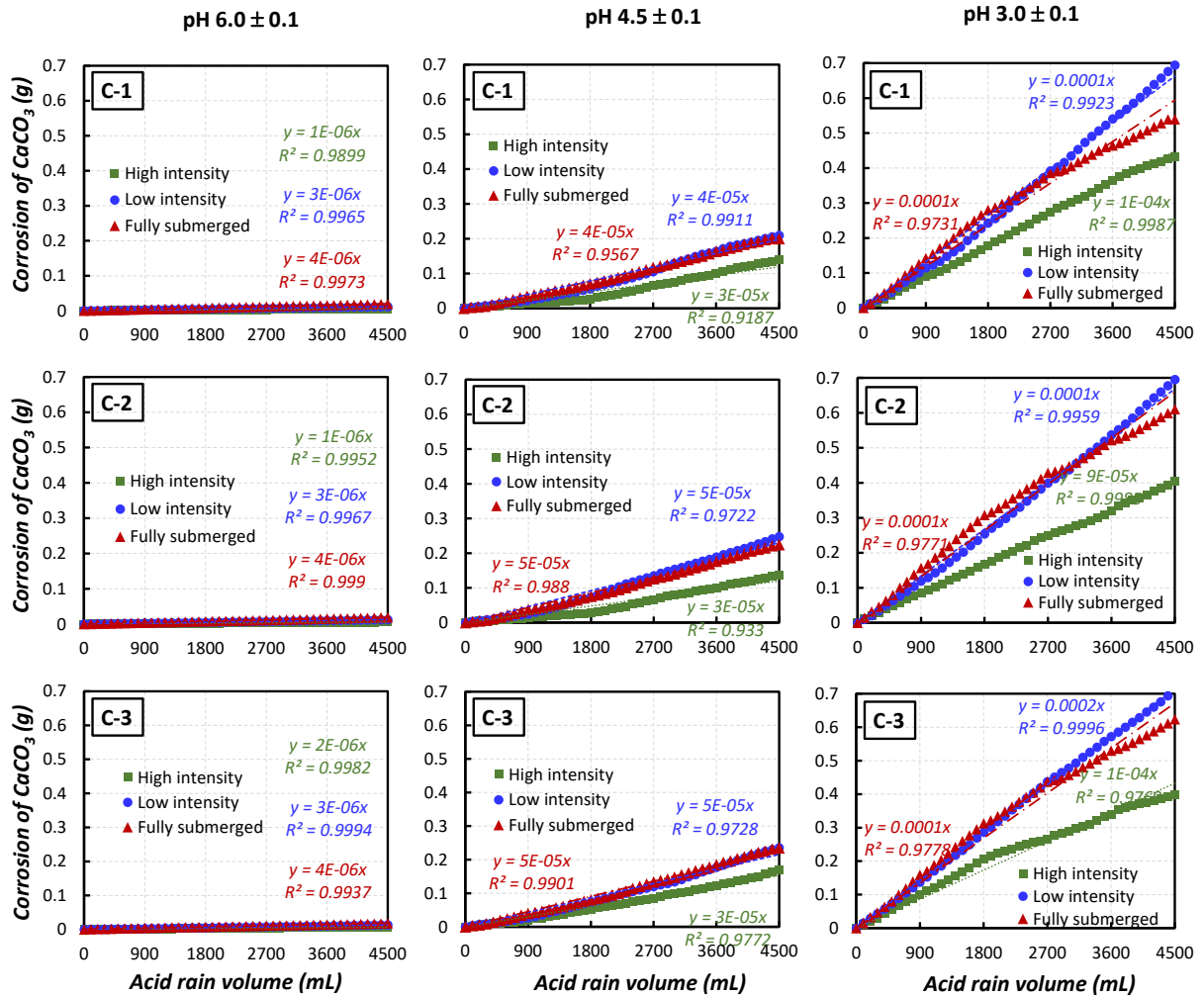


Fig. 2 The corrosion of calcium carbonate during the AR simulation test

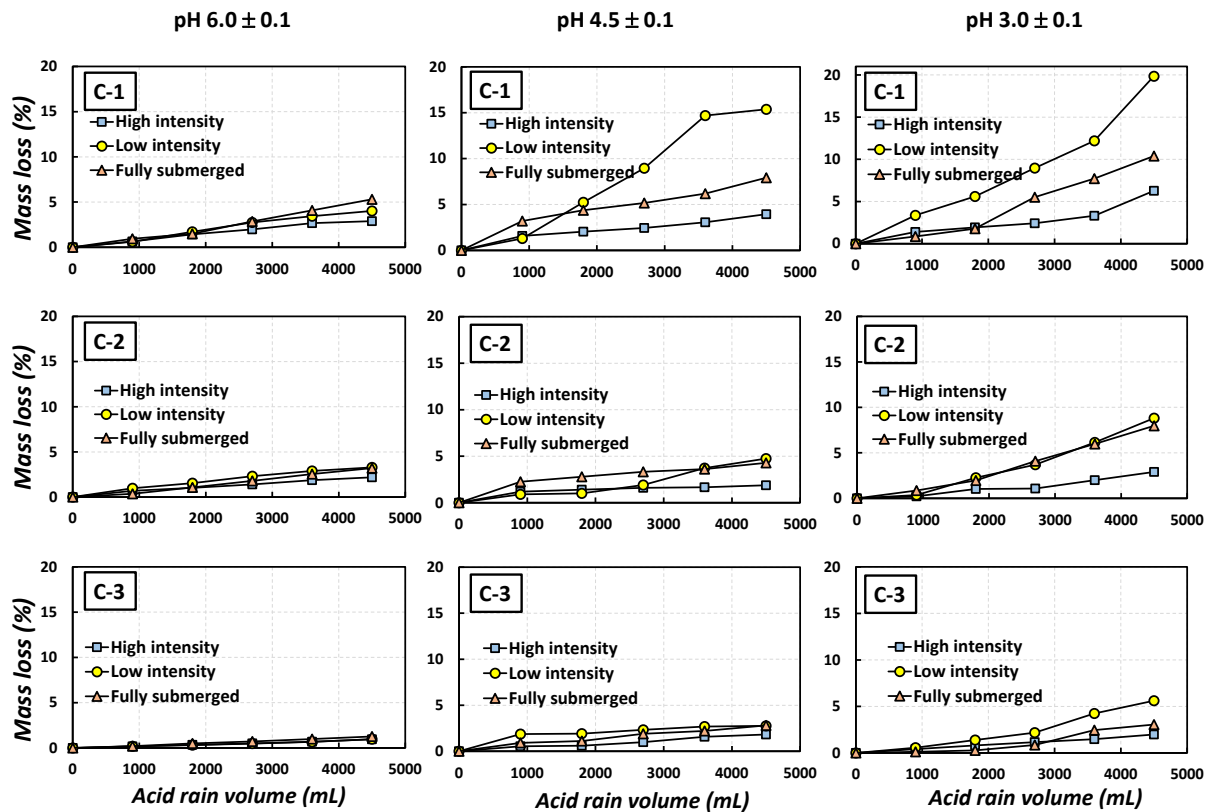


Fig. 3 Mass loss of the specimens subjected to AR

RESULTS

Corrosion of CaCO_3

The chemical reaction between AR and calcium carbonate could result in the dissolution of CaCO_3 that precipitated in MICP specimens. During the test, leached calcium ions was continuously measured from the effluent of the specimens. From the Ca^{2+} concentrations, the corroded calcium carbonate was theoretically estimated in each case, and the results are plotted and compared in Fig. 2. From the plots, it can be clearly observed that regardless of specimen cementation level, the corrosion of CaCO_3 was highly reliant on the pH condition of AR solution. Minor corrosion rates of calcium carbonate were observed to the specimens exposed to AR of pH 6.0, and the corrosion rate showed an increasing tendency with the decrease in pH condition. For instance, when the pH of AR decreased from 6.0 to 4.5, the corrosion rate increased by around 10 times, and that rate further increased at pH of 3.0.

The corrosion rate of calcium carbonate was also considerably influenced by the intensity of AR (Fig. 2). The low intensity of AR (20 mm/h) resulted higher corrosion rate compared to that under high intensity (100 mm/h). For example, by the end of the test (at pH 3.0), the specimens showed the corrosion of around 0.7 g CaCO_3 under low intensity of AR, which

was around 1.75 times higher than the corrosion experienced under high intensity of AR. This could be attributed to the contact time of AR within MICP specimens. During the high intensity of AR, certain hydraulic pressure was developed on the surface (due to ponding), which tended to infiltrate the AR at high rates. The less contact time of AR with soil MICP matrix resulted the less reaction with CaCO_3 . On the other hand, the low intensity facilitated relatively slow infiltration, allowing sufficient time to the reaction with CaCO_3 during the percolation.

Mass Loss

Fig. 3 shows the mass loss of MICP samples as a function of delivered volume of acid rain at different pH conditions. As shown, the mass loss rate of MICP treated specimens increased with increasing delivered volume, and that increases with the increase in pH of the AR. The tendency of mass loss rate (Fig. 2) is in a good agreement with the corrosion rate of calcium carbonate (Fig. 3). However, the cementation level highly governed the rate of mass loss. For example, by the end of the test (at pH 3.0), all the specimens (C-1, C-2 and C-3, i.e. irrespective of the level of cementation) showed the same corrosion of calcium carbonate. The soil losses, on the other hand, were up to around 20%, 9% and 5% for C-1, C-2 and C-3 specimens, respectively, suggesting that high

cementation level attributes to high durability of MICP treatment against AR induced erosion.

From the physical observation, it could be seen that the specimens treated to high cementation level (C-3) showed lower physical impairments than those of low cementation levels (C-1). The specimens subjected to low intensity of AR delivery showed higher surficial damage compared to that of high intensity of AR. As the AR was delivered to the specimens from the top, the proton concentration of AR was high and effective at the supply point, resulted high dissolution of CaCO_3 at surface. When the solution reached specimen depths, the certain quantity of protons has already been reacted and neutralized, which leads to the less reaction at bottom specimens. At the same time, the specimens tested under submerged conditions showed clear damage structure on cylindrical surfaces as well, as the entire surface of the specimens was directly exposed to AR solution when submerged. The specimens treated by AR of pH 3.0 showed higher observable damages compared to those subjected to AR of pH 4.0. It also should be noted that specimens subjected to AR of pH 6.0 did not show any observable changes.

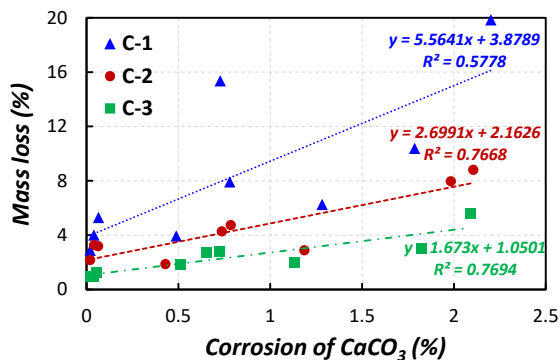


Fig. 4 Relationships between corroded CaCO_3 and mass loss at different cementation levels

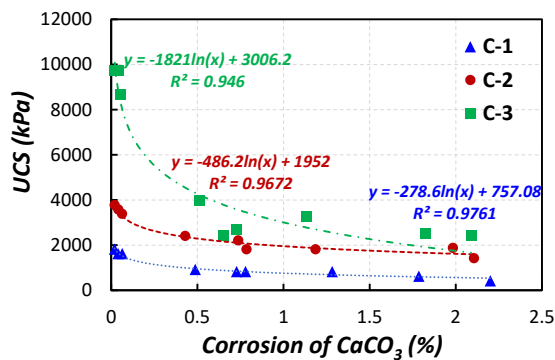


Fig. 5 Variation of UCS with corrosion of CaCO_3 content at different cementation levels

DISCUSSION

The corrosion of calcium carbonate bio-cement is the degradation mode of MICP under the exposure of AR environment. Under the high intensity AR delivery, the corrosion of calcium carbonate was low. In contrast, when the AR is delivered by low rate of infiltration or fully submerged conditions, the rate of corrosion was high, which is due to the sufficient reaction time given. Regardless of the conditions tested, the ultimate factor that determines the responses of the specimens exposed to AR, is the corroded quantity of calcium carbonate. Fig. 4 presents the compilation of mass loss data versus corresponding corrosion of calcium carbonate. The results suggest that the mass loss, with the corrosion of CaCO_3 , can be fairly evaluated by linear relationships.

Fig. 5 presents the compilation of test data, i.e., UCS plotted against the corrosion of calcium carbonate. The results indicate that the UCS of the specimens exponentially decrease with the increase in corrosion of CaCO_3 for all the levels of cementation. The exponential tendency in decrease can be explained by the decay of matrix support. During the MICP treatment, the cementation begins at particle contact, increasing the strength gradually (progression of contact cementation); with the increasing treatment, the crystals starts to grow within the pore spaces, sometimes bridging the particles [2], [6], leading to rapid increase in strength at latter stage. The exponential progression of UCS in MICP soils was evidenced in many previous studies [6], [19]. The results presented herein (Fig. 5) demonstrate that the UCS follows relatively the similar path for the decrease during corrosion.

The results (Figs. 4 and 5) prove that the treatment durability essentially depends on high cementation levels. At high cementation level (e.g. C-3), particle contact points are cemented stiffly by higher quantity of calcium carbonate compared that in lower levels (e.g. C-1). For the same supply of AR, the corrosion of calcium carbonate might be same, irrespective of the level of cementation; however, the connections points could more quickly be debonded/ weakened in low cementation levels, showing high susceptibility to AR. On the other hand, for debonding/ weakening the particle contacts in high cementation levels, more calcium carbonates are required to be corroded, suggesting high longevity in performance.

CONCLUSIONS

Hypothetically, it was believed that the MICP treated soils are susceptible to acid rain conditions. However, this study has demonstrated that the durability and longevity can be considerably

enhanced by the levels of cementation. The tests suggest that the corrosion rate of calcium carbonate depends on the pH of acid rain and intensity. However, the loss of soil particles and strength loss due to corrosion of CaCO_3 is highly governed by the level of cementation. In another words, for the same quantity of corrosion, the higher the cementation level the lower the loss of mass and UCS, enhancing the longevity of the treatment.

REFERENCES

- [1] Danjo T., and Kawasaki S., Microbially Induced Sand Cementation Method Using *Pararhodobacter* sp. Strain SO1, Inspired by Beachrock Formation Mechanism, *Mater. Trans.*, Vol 57, 2016, pp. 428-437.
- [2] DeJong J.T., Mortensen B.M., Martinez B.C., and Nelson D.C., Bio-mediated soil improvement, *Ecol. Eng.*, Vol 36, 2010 pp. 197-210.
- [3] Stabnikov V., Ivanov V., and Chu J., Construction Biotechnology: a new area of biotechnological research and applications, *World J. Microbiol. Biotechnol.*, Vol 31, 2015, pp. 1303-1314.
- [4] Naveed M., Duan, J., Uddin, S., Suleman, M., Hui, Y., and Li, H., Application of microbially induced calcium carbonate precipitation with urea hydrolysis to improve the mechanical properties of soil, *Ecol. Eng.*, Vol 153, 2020.
- [5] Salifu E., MacLachlan E., Iyer K.R., Knapp C.W., and Tarantino A., Application of microbially induced calcite precipitation in erosion mitigation and stabilisation of sandy soil foreshore slopes: A preliminary investigation, *Eng. Geol.*, Vol. 201, 2016, pp. 96-105.
- [6] Gowthaman S., Mitsuyama S., Nakashima K., Komatsu M., and Kawasaki S., Biogeotechnical approach for slope soil stabilization using locally isolated bacteria and inexpensive low-grade chemicals: A feasibility study on Hokkaido expressway soil, Japan, *Soils Found.*, Vol. 59, Issue 2, 2019, pp. 484-499.
- [7] Gowthaman S., Mitsuyama S., Nakashima K., Komatsu M., and Kawasaki S., Microbial Induced Slope Surface Stabilization using Industrial-Grade Chemicals: A Preliminary Laboratory Study, *Int. J. GEOMATE*, Vol 17, Issue 60, 2019, pp. 110-116.
- [8] Gowthaman S., Iki T., Nakashima K., Ebina K., and Kawasaki S., Feasibility study for slope soil stabilization by microbial induced carbonate precipitation (MICP) using indigenous bacteria isolated from cold subarctic region, *SN Appl. Sci.*, Vol. 1, 2019, 1480.
- [9] Jiang N.J., Tang C.S., Yin L.Y., Xie Y.H., and Shi B., Applicability of Microbial Calcification Method for Sandy-Slope Surface Erosion Control, *J. Mater. Civ. Eng.*, Vol. 31, 2019.
- [10] Gowthaman S., Nakashima K., and Kawasaki S., Freeze-Thaw Durability and Shear Responses of Cemented Slope Soil Treated by Microbial Induced Carbonate Precipitation, *Soils Found.*, 2020 (in press).
- [11] Dejong J.T., Soga K., Kavazanjian E., and et al., Biogeochemical processes and geotechnical applications: Progress, opportunities and challenges, *Geotechnique*, Vol. 63, 2013, pp. 287-301.
- [12] Cheng L., and Cord-Ruwisch R., Upscaling Effects of Soil Improvement by Microbially Induced Calcite Precipitation by Surface Percolation, *Geomicrobiol. J.*, Vol. 31, 2014, pp. 396-406.
- [13] Martinez B.C., DeJong J.T., Ginn T.R., Montoya B.M., Barkouki T.H., Hunt C., Tanyu B., and Major D., Experimental Optimization of Microbial-Induced Carbonate Precipitation for Soil Improvement, *J. Geotech. Geoenvironmental Eng.*, Vol 139, 2013, pp. 587-598.
- [14] Omeregie A.I., Palombo E.A., Ong D.E.L., Nissom P.M., Biocementation of sand by *Sporosarcina pasteurii* strain and technical-grade cementation reagents through surface percolation treatment method, *Constr. Build. Mater.*, Vol. 228, 2019, 116828.
- [15] Cheng L., Shahin M.A., and Mujah D., Influence of Key Environmental Conditions on Microbially Induced Cementation for Soil Stabilization, *J. Geotech. Geoenvironmental Eng.*, Vol. 143, 2016, 04016083.
- [16] Bakhshipour Z., Asadi A., Huat B.B.K., Sridharan A., and Kawasaki S., Effect of acid rain on geotechnical properties of residual soils, *Soils Found.* Vol. 56, 2016, pp. 1008-1020.
- [17] Kamon M., and Ying C., Effect of acid rain on physico-chemical and engineering properties of soils, *Soils Found.*, Vol. 37, 1997, 23-32.
- [18] JGS 3431-2012, Japanese Stand. Explan. Geotech. Geoenvironmental Investig. Methods, No. 1, JGS Publication (in Japanese), Tokyo, 2012, pp. 426-432.
- [19] van Paassen L.A., Ghose R., van der Linden, T.J.M., van der Star, W.R.L., and van Loosdrecht, M.C.M., Quantifying Biomediated Ground Improvement by Ureolysis: Large-Scale Biogrout Experiment, *J. Geotech. Geoenvironmental Eng.*, Vol. 136, 2010, 1721-1728.

ESTIMATION OF SUBSURFACE STRUCTURE AND GROUND MOTION CHARACTERISTICS IN THE DAMAGED AREAS DUE TO THE 2016 CENTRAL TOTTORI PREFECTURE EARTHQUAKE, JAPAN

Isamu Nishimura¹, Tatsuya Noguchi¹ and Takao Kagawa¹
¹ Engineering, Tottori University, Japan

ABSTRACT

On October 21, 2016, an earthquake with M_{JMA} 6.6 occurred in the central part of Tottori Prefecture, Japan. Observed JMA seismic intensity were 6 lower at Kurayoshi city, Yurihama and Hokuei towns. Housing damages due to the earthquake were concentrated in limited areas. In this study, we carried out microtremor observations around damaged areas, and estimated subsurface structures and ground motion characteristics with previously conducted studies. We consider that the relationship between ground motion characteristics and damage, and found that the damage occurred at the parts where the layer thicknesses change steeply. We suspect that the damages concern to two- or three- dimensional effects of subsurface structures.

Keywords: Microtremor observation, Seismic observation, Subsurface structure, the 2016 central Tottori prefecture Earthquake

INTRODUCTION

An earthquake with M_{JMA} 6.6 occurred in the central part of Tottori Prefecture, Japan on October 21, 2016. Recorded JMA seismic intensity were 6 lower at Kurayoshi city, Yurihama and Hokuei towns (Fig.1) [1]. Housing damages were concentrated in limited areas at the flatland in Hokuei town, and at the edge of mountain in Yurihama town [2], [3]. We consider the damages might be caused by site amplification due to subsurface structures.

The mainshock and aftershocks had been observed at NIED's K-NET and KiK-net, and observation sites of local governments in Tottori Prefecture and temporary sites of Tottori University. From the analysis of those strong motion records, variation of site amplifications due to differences in subsurface structure were suggested. Also, nonlinear soil response due to the strong ground motions were suspected at Ryuto (TGAR) and Hisadome (YRAR) observation sites in Yurihama town, and Hashita (HJA) site in Hokuei town [3].

In order to evaluate strong motions, nonlinear soil responses, and the relationship between ground motion and damage, it is necessary to understand detailed subsurface structure and ground motion characteristics. In this study, we carried out microtremor observations around the strong motion observation sites and damaged areas, and estimated subsurface structures and ground motion characteristics. Additionally, deeper ground structure was estimated from aftershock records.

OBSERVATION

Housing damages and previous study of the target area

Housing damages due to the mainshock of the 2016 earthquake was concentrated in the limited areas at the flatland in Hokuei town, and at the mountainside in Yurihama town. In the damaged areas are shown in Fig. 1, roof tile damage was recognized based on blue sheet coverage from the satellite image [4], and confirmed by site visits and interviews. In this study, an area with 50m radius from the damaged houses was considered as the housing damage area.

According to the previous study [3], [5], predominant period of microtremor in Yurihama town is about 0.5-2.0 seconds, and about 0.8-1.5 seconds in Hokuei town. It is considered that the periods are correspond to thickness of soft layer with S-wave velocities less than 400 m/s.

Summary of observation

Single-point observations were carried out at 294 sites in Yurihama town and 162 sites in Hokuei town, mainly in residential areas and strong motion observation sites. In areas where roof tile damages are concentrated, we made observations at 50 m intervals. The equipment used was JU410, a three-component accelerometer with 24bits recorder. The specifications with wave amplification factor 100, sampling frequency 100 Hz or 200 Hz, and recording

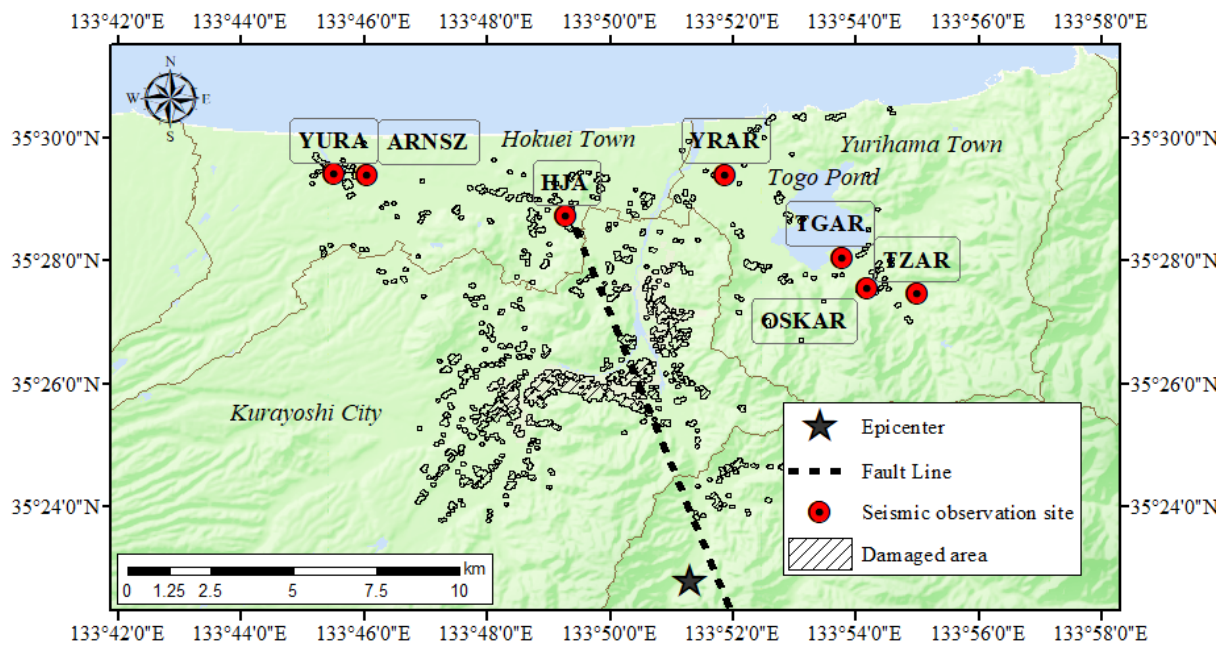


Fig 1. Epicenter and fault line [1], damaged area and seismic observation sites

time about 10-15 minutes wave used.

Array observations were conducted at 7 sites: 4 strong motion observation sites (YRAR, TGOAR, HJA, YURA) and 3 temporary aftershock observation sites (OSK, TZAR, ARNSZ) (Fig.2). Four JU410s synchronized by GPS clocks were used for the measurement. One seismometer was placed at the center of a circle and other three were placed around circumference to form an equilateral triangle. Sampling frequency was used 200 Hz, amplification factor was the same as for single-point observation, and recording time was about 15 minutes. The array radius was set within the range of 0.6 to 30 m, depending on the observation site, to evaluate S-wave velocity structures of Quaternary sediments.

Aftershock observations were placed at Oshikadani and Takatsuji (OSK, TZAR) where roof tiles damages were dominant. Oshikadani site had been maintained from July 24, 2017 to July 2, 2018, and Takatsuji site has been working from October 20, 2015 to present. The observation equipment used was a sensor integrated recorder CV-374A, and the sampling frequency was 100 Hz. The seismometers were installed indoors on a solid foundation, such as at the entrance of a building where external power can be secured.

ANALYSIS

Microtremor records

From a single-point observation record, Fourier spectra were calculated, and smoothed using a Log window with a coefficient of 20 [6]. Average spectra were calculated from at least 10 stable 20.48 second

sections. From the Fourier spectra, horizontal to vertical spectral ratios (H/V) were calculated, and predominant periods were visually estimated. Many H/Vs were unimodal with a single distinct peak. In some areas such as mountainside where multiple peaks were observed, the predominant period was estimated in consideration of continuity with adjacent unimodal sites. Fig. 2 shows the entire predominant period distribution in the central Tottori Prefecture.

In analysis of array observation, reanalyses including the past research data [3], [5] were performed in order to unify the velocity structure of the lowermost surface. The analysis procedure was as follows. Using the open analysing tool [7], phase velocity dispersion curves of array observation record were estimated based on the CCA method [8]. At least five sections were selected by automatic extraction using RMS values of microtremor recordings with 10.24 seconds segments. Next, power spectra in those sections were smoothed with 0.3 Hz bandwidth Parzen window, and averaged. Finally phase velocity dispersion curves were determined. Phase velocity dispersion curves obtained at each radius were integrated each observation site considering their continuity.

Using the phase velocity dispersion curves and microtremor H/Vs obtained from single-point microtremor recording at the center of the array, subsurface structure models were estimated from forward modeling based on the fundamental mode of Rayleigh waves. S-wave velocities were determined with reference to previous studies [3], [5] and borehole data around the site [9]. Then modeling was performed by changing the layer thickness. Densities were set referring previous researches, and P-wave

velocities were set from S-wave velocities [10]. Table 1 shows the resulting subsurface structure model.

Aftershock records

In analysing aftershock records, the previous research data [3], [5] were involved with nearly employed data to make analyses by same standard. The analysis procedure of aftershock records was as follows. Time windows of 10.24 seconds with cosine tapers of 5% of both ends were applied from S-wave arrival. Analysis record length was prolonged to 20.48 seconds with adding zero data. Fourier spectrum was calculated and smoothed with 0.2 Hz bandwidth Parzen window. From the Fourier spectrum of each component, the spectral ratio of horizontal to vertical (strong ground motion H/V) was evaluated. In this study, about 10 aftershocks were analysed and then averaged to obtain H/V at each site.

Subsurface structure models, were at first estimated by forward modeling, with modifying the model by comparing the observed and theoretical H/V based on the diffuse wave field theory [11] of strong ground motion H/V. As an initial model, shallow structures were estimated based on the array observation models described above, and deep structures were assumed from previous research [5], [12]. Based on the model, final structure model was estimated from inversion analysis by a hybrid heuristic search method [13] with genetic algorithm (GA) and simulated annealing (SA). Damping constant h is assumed to be 0.03 for S-wave velocities of 100 m/s or less, 0.02 for 100-400 m/s, and 0.01 for 400 m/s or more. The inversion code was created by Yasui et al. [14].

Other inversion parameters were as follows. For GA, number of trials was 10, number of samples was

30, number of generations was 300, crossover probability was 0.7, mutation probability was 0.01, and dynamic mutation and elite selection were considered. For SA, temperature drop function was equation (1), with coefficients $a=0.5$, $c=1.0$, initial temperature $T_0=100$, and number of temperature updates was 10.

$$T = T_0 \exp(-ck^a) \quad (1)$$

S-wave velocity and layer thickness of the first layer and the bottom layer were fixed, and value of the other layers were searched within a range of $\pm 25\%$ from the initial value. The search targets were S-wave and P-wave velocities and layer thicknesses. Densities were set from an empirical formula [15] from S-wave velocity. Fig. 3 shows the resulting S-wave velocity column diagrams from shallow to deep layers.

DISCUSSIONS

Predominant period of microtremor H/V

Predominant periods in Fig.2 are 0.8-1.6 seconds around YRAR and 0.4-0.8 seconds around TGAR, OSKAR and TZAR. Predominant periods around ARNSZ and YURA are 1.0-1.6 seconds, and HJA at northern Kurayoshi Plain are 0.4-1.0 seconds. Many microtremor H/Vs with a single peak were observed at northern Kurayoshi Plain and around Togo Pond, and many H/Vs with multiple peaks were observed at Nishizono and Yurashuku regions (Fig.4). It probably

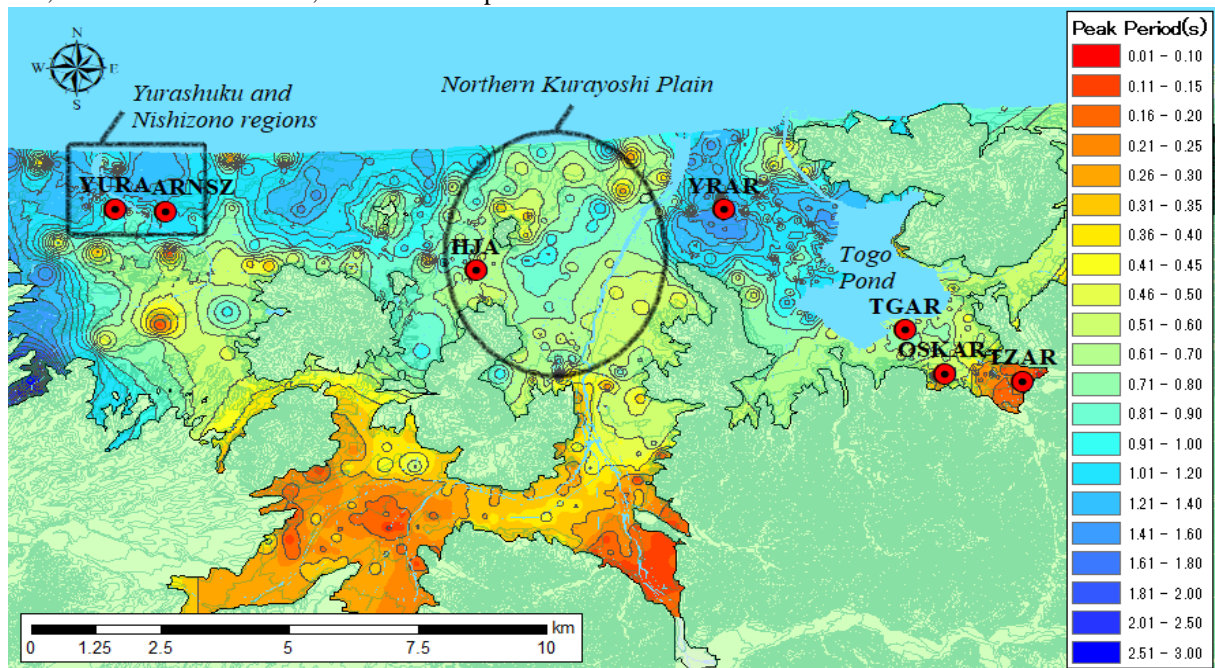


Fig 2. Predominant period distribution map in the central Tottori Prefecture

Table 1. Subsurface structures based on array observation

Yurihama Town

Site	Thickness (m)	$\rho(t/m^3)$	Vp(m/s)	Vs(m/s)
YRAR (Hisadome)	33	1.6	1430	140
	75	1.8	1730	400
	100	2.1	2070	700
	∞	2.2	2620	1200
TGAR (Ryuto)	9	1.6	1390	90
	8	1.7	1510	200
	50	1.8	1730	400
	100	2.1	2070	700
OSKAR (Oshikadani)	8	1.6	1400	100
	3	1.7	1510	200
	30	1.8	1730	400
	100	2.1	2070	700
TZAR (Taka tsuji)	4	1.6	1390	100
	4	1.7	1510	200
	100	2.1	2070	700
	∞	2.2	2620	1200

Hokuei Town

Site	Thickness (m)	$\rho(t/m^3)$	Vp(m/s)	Vs(m/s)
HJA (Hashita)	9	1.6	1380	80
	5	1.7	1460	150
	10	1.8	1510	200
	12	1.9	1730	400
ARNSZ (Nishizono)	∞	2.2	2620	1200
	10	1.7	1430	130
	10	1.7	1510	200
	70	1.8	1730	400
YURA (Yurashuku)	60	2.1	2070	700
	∞	2.2	2620	1200
	11	1.7	1490	180
	65	1.8	1730	400
	80	2.1	2070	700
	∞	2.2	2620	1200

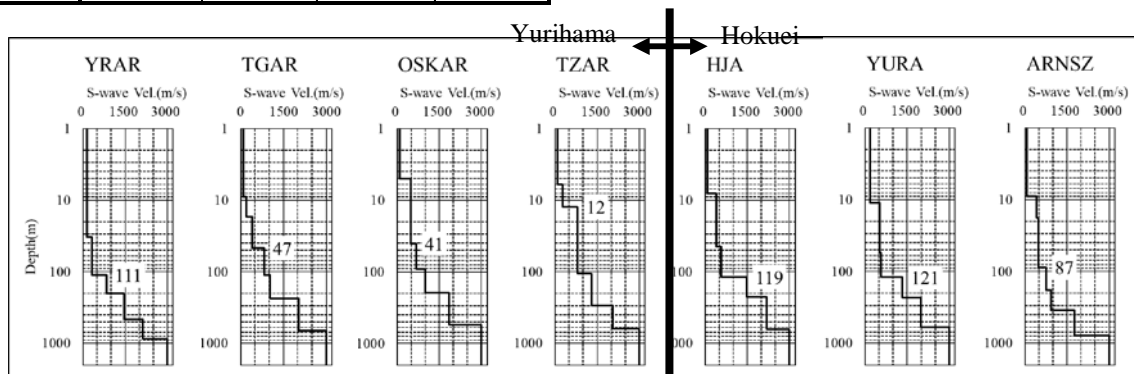


Fig 3. S-wave velocity structure column diagrams

reflects the difference of velocity structures in surface layers.

Estimation of subsurface structure

From the borehole data around observation sites [9], S-wave velocities of 100 m/s or less in Table 1 are considered to be clay or silt layers, and S-wave velocity of 200 m/s is considered to be sand layer. Table 1 shows that the thickness of soft layer with S-wave velocity of 80-200 m/s is 6-33m at each site and it tends to be thicker to coastal plain and thinner to inland. It was found that there were silt layers with S-wave velocities of 80-140 m/s in the surface layer at Hisadome (YRAR), Ryuto (TGAR) and Hashita

(HJA). It is suggested that the silt dominant layers caused nonlinear response reported in the areas.

Deeper subsurface structures were estimated from aftershock observation records. The numbers in Fig. 3 indicate the depth from surface layer to engineering seismic base layer. From the subsurface structure model, the basement depth tends to be deeper to the coastal plain. This is consistent with the tendency for the predominant periods become longer to the plain. It is found that the thicknesses to deeper subsurface structure with S-wave velocity more than 700 m/s were different between Yurihama town and Hokuei town.

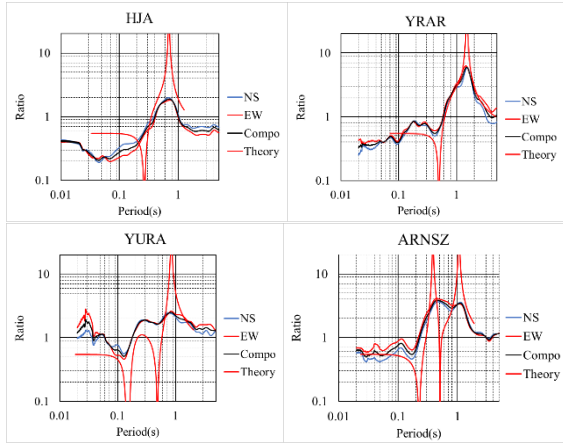


Fig 4. Microtremor H/V at center of array observation sites

Consideration on housing damage

Amplification at each site was evaluated using AVS30 and ARV that are simple indicators of ground amplification [16]. ARV was calculated by Equation (2). AVS30 is the average S-wave velocity down to 30m underground. Table 2 shows AVS30 and ARV at each site. ARV at YRAR and HJA where housing damages were not dominant are around 2.5, and OSKAR and ARNSZ where damages are widespread are around 2.0. Unfortunately, clear relationship is not found between housing damage and ARV.

$$\log ARV = 1.83 - 0.66 \log AVS30 \quad (2)$$

Table 2. AVS30 and ARV at array sites

Yurihama	YRAR	TGAR	OSKAR	TZAR
AVS30	140	174	220	328
ARV	2.59	2.25	1.98	1.48

Hokuei	HJA	ARNSZ	YURA
AVS30	142	197	276
ARV	2.56	2.07	1.65

In areas where housing damage is concentrated at Nishizono and Yurashuku regions, surface layer thicknesses were estimated and their special changes were examined. S-wave velocities and predominant periods (Tp) were used to estimate the layer thicknesses (H) from equation (3). In both areas, short predominant period Tp1 and long predominant period Tp2 are estimated, and the layer thicknesses were estimated by the peaks from the equation (3).

$$H_i = \frac{V_s \cdot T_{pi}}{4} \quad (3)$$

Fig. 5 shows that the layer thicknesses from Tp1 are deeper from south to northwest and the layer

thicknesses from Tp2 are deep in limited area. Comparing damaged area and the layer thicknesses, they overlap along the boundary where the layer thickness of Tp2 change. This suggests effects of 2-D or 3-D shapes of engineering seismic base on housing damage.

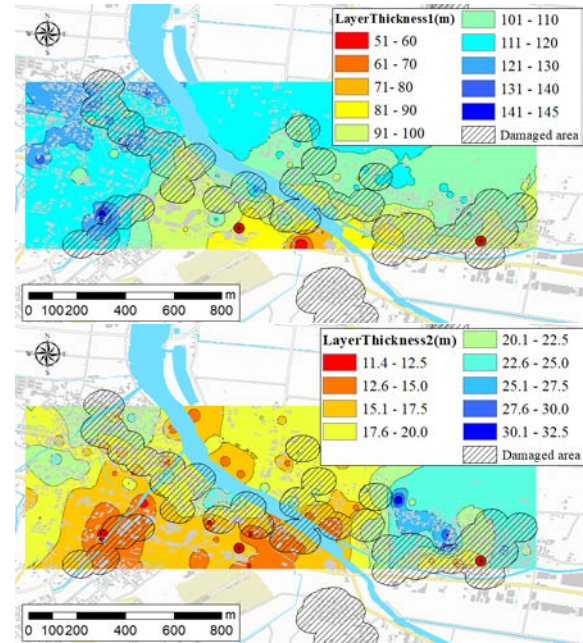


Fig 5. Layer thickness at Nishizono and Yurashuku regions (upper map: Tp1, lower map: Tp2)

CONCLUSIONS

In this study, we carried out microtremor and earthquake observations around damaged area due to the 2016 Central Tottori Prefecture earthquake. We estimated subsurface structure and evaluated ground motion characteristics to consider the relationship between those and damages. As a result, the followings were found.

H/Vs obtained from the single-point observation of microtremor tend to have a longer predominant period in coastal plain than inland area.

Phase velocity dispersion curves were obtained from microtremor array observation data, and the S-wave velocity structure was estimated from them. In Hisadome, Ryuto and Hashita where nonlinear responses were observed, low velocity silt layers were found in surface layer, and it is highly suspected that the layers were related to the nonlinear responses in the area.

Deeper subsurface structures were estimated from aftershock observation records. As a result, it was found that the thicknesses to deeper subsurface structure with S-wave velocity more than 700 m/s were different between Yurihama town and Hokuei town.

Comparing ground amplification indexes estimated from our models with housing damage, the relevance was found to be weak. From layer thicknesses estimated from predominant periods and surface S-wave velocities, it was found that the damage occurred at the part where the layer thickness changed steeply. Therefore, it is suspected that the damage caused by irregular subsurface structures with 2-D or 3-D effects. We need to continue our study about the effects.

ACKNOWLEDGMENTS

For inversion analysis, we used the code by Dr. Yuzuru Yasui. Mr. Ichihashi, a member of volunteer fire department in the local government, and Mr. Yamamoto, a technical staff member of the Faculty of Engineering, Tottori University, cooperated in setting up observation sites at Oshikadani and Takatsuji, collecting data, and reporting the local damages. We appreciate to everybody who supported our research.

REFERENCES

- [1] Japan Meteorological Agency: Evaluation of the earthquake on October 21, 2016 in central Tottori Prefecture, <https://www.static.jishin.go.jp/resource/monthly/2016/20161021_tottori.pdf>, [Viewed on June 11, 2020].
- [2] Kagawa, T. (2017): 2016 Central Tottori Earthquake (M6.6), *Earthquake Journal*, No.63, pp.14-22. (in Japanese)
- [3] Kagawa, T., Noguchi, T., Yoshida, S. and Yamamoto, S. (2017): Effect of the surface geology on strong ground motions due to the 2016 Central Tottori Earthquake, *Japan, Earth, Planets and Space*, 69:106 DOI 10.1186/s40623-017-0689-0.
- [4] Honda, Y., Mochizuki, K., Shimomura, H. and Monma, N. (2017): Automatic extraction of blue sheet-covered housing from satellite images of 2016 Central Tottori Earthquake, *Japan Society for Disaster Information Studies, Proceedings of the 19th conference*, pp.244-245. (in Japanese)
- [5] Noguchi, T., Nishikawa, H., Yoshida, S. and Kagawa, T. (2019): Estimation of subsurface structure and characteristics of ground vibration based on microtremor and seismic observation in the central Tottori Prefecture, Japan, *Journal of Japan Association for Earthquake Engineering*, Vol. 19, Issue 6, pp 258-271. (in Japanese with English abstract)
- [6] Konno, K., Ohmachi, T. (1995): A smoothing function suitable for estimation of amplification factor of the surface ground from microtremor and its application, *Transactions of the Japan Society of Civil Engineers*, No525/I-33, pp247-259. (in Japanese with English abstract)
- [7] Cho, I., Tada, T. and Shinozaki Y. (2009): Possibility of microtremor array opened up by general theory :Release of analysis tool BIDO, *Seismological Society of Japan Fall Meeting in 2009*. (in Japanese)
- [8] Cho, I., Tada T. and Shinozaki Y. (2006): Centerless circular array method: Inferring phase velocities of Rayleigh waves in broad wavelength ranges using microtremor records, *J. Geophys. Res.*, 111, B09315.
- [9] National Research Institute for Earth Science and Disaster Resilience: GeoStation, <<https://www.geo.stn.bosai.go.jp/>>, [Viewed on October 9, 2019].
- [10] Kitsunezaki, C., Goto, N., Kobayashi, Y., Ikawa, T., Horike, M., Saito, T., Kurota, T., Yamane, K., Okuzumi, K. (1990): Estimation of P- and S-wave velocities in deep soil deposits for evaluating ground vibrations in earthquake, *Natural disaster science*, 9-3, 1-17. (in Japanese with English abstract)
- [11] Kawase, H., Sanchez-Seama, F.J. and Matsushima, S. (2011): The optimal use of horizontal-to-vertical spectral ratios of earthquake motions for plane waves, *Bull. Seism. Soc. Am.* Vol.101, No.5, pp.2001-2014.
- [12] Noguchi, T., Nishikawa, H., Yoshida, S. and Kagawa, T. (2016): Subsurface structure and evaluation of site effects at strong ground motion observation sites in Tottori Prefecture, *JSCE Journal of Earthquake Engineering*, Vol.72, Issue 35, pp.646-658. (in Japanese with English abstract)
- [13] Yamanaka, H. (2007): Inversion of surface-wave phase velocity using hybrid heuristic search method, *Geophysical Exploration*, Vol. 60, Issue 3, pp-265-275. (in Japanese with English abstract)
- [14] Yasui, Y., Nishikawa, H., Maeda, T., Cho, I., Kojima, K., Koketsu, K. and Miyajima, M. (2014): Applicability of an inversion of earthquake H/V spectral ratios for soil structures – a case study using records in Fukui Prefecture, *JSCE Journal of Earthquake Engineering*, Vol.70, Issue 4, pp.628-643. (in Japanese with English abstract)
- [15] Ota, T., Emori, K. and Kasai, Y. (2001): Building foundation earthquake resistance / vibration / control, *Kyoritsu Shuppan*, pp-339.
- [16] Midorikawa, S., Matsuoka, M. and Sakugawa, K. (1994): Site Effect of Strong- Motion Records Observed during the 1987-Chiba-kentohoki, *Japan Earthq. Eng. Sympo*, Vol.3, pp.85-90.

EVALUATION OF SCENIC HEALING AT VIEWPOINTS IN PARKS CONSIDERING DIFFERENCES IN MIGRATION BEHAVIOR

Kazuki Ito¹, Kazunari Tanaka¹

¹ Civil Engineering department, Osaka Institute of Technology, Japan

ABSTRACT

This paper contributes to a set of prescriptive principles for planners and others to use in planning and regulating the design and management of green landscape formation. The research background is that it originates in the mineralization of the city by optimizing the efficiency of the city based on the national land creation plan of the Ministry of Land, Infrastructure, Transport and Tourism. The research method was a quantitative analysis based on the results of the questionnaire surveys. As a result, the quantitative standard based on the healing point in the green landscape formation became clear. This suggests that the harmony of the landscape ratio between natural and artificial landscape formation may reduce the stress inherent in humans.

Keywords: Landscape, Healing, Migratory Behavior, Urban Design

INTRODUCTION

The Ministry of Land, Infrastructure, Transport and Tourism is promoting compact cities and location optimization plans as upstream policies for land creation in response to the current urban structure where population decline is occurring.

Amid the trend of shrinking cities, a variety of structures and people will be concentrated in the central city area in the future. Let's not forget that it is beneficial to cities to be centralized, streamlined and optimized. Optimization and efficiency are important for the development and conservation of the city, but they are always detrimental to the material properties and functions of the city. It is necessary to create an attractive city, not just city planning. In addition, in the revision of the Urban Green Space Law (2018), it is feared that the attractiveness of park stocks will decline as a qualitative issue toward the creation of green towns. I think this suggests that the park, which is a public space, is a place for people to relax and to be a tool to solve the weakening of communication with families and society.

The "attractive" city in this study is meant to be a city that provides healing. Healing has various effects such as psychological relief, euphoria, and productivity improvement. Healing is said to come from landscape experiences. From the "Worker Health Condition Survey" conducted by the Ministry of Health, Labor and Welfare every five years, the impact of stress is increasing year by year, and it is consistent with both men and women by age group. In city planning consideration, it is necessary to approach it from the perspective of solving or mitigating social problems.

In order to promote optimization and efficiency

for a city and to build an attractive city (in terms of healing), we must pay attention to the migratory behavior in urban green spaces. Focusing on migratory behavior based on the idea that elucidating the factors that cause behavior, and exploring the law of behavior contributes to the development of this research, in other words, focusing on basic human behavior in behavior analysis. This leads us to the goals of grasping the change in psychological potential associated with the transition of the visual landscape during the migratory behavior of a green space, clarifying quantitatively and qualitatively the extraction of the healing factors and the structure, and demonstrating how to evaluate healing in terms of a place.

Most of the past studies on healing attempt to systematically grasp the psychological and verbal healing of the subject's landscape from the scenic landscape (no distinction between real space and virtual space). [1] [2] [3] Comparison of the conventional method *landscape evaluation method* and the proposed new method here to further improve the accuracy of identifying the aspect of the landscape such as the unique structures and colors, the impression, and factors affecting the impression etc. [4] [5] [6] In general, with landscapes such as scenic landscapes and sequence landscapes, we identify the incentives and values, and the occurrence of experience that can be obtained from them. These studies capture landscapes with an emphasis on versatility, not just healing. [7] [8] This study attempts to clarify the relationship between the target public space that does not depend on the landscape and the surrounding environment from a psychological aspect through a questionnaire survey. [9] Unlike the previous research, the emphasis here is on recognizing landscape recognition as a place, that

landscape analysis is being attempted as a viewpoint field, and that discussions on semantic recognition seem to have a limit. [10]

Although research on healing and impressions of streetscapes has been performed from numerous past studies, it is hard to say that there are much sufficient discussions on “healing”. Although there are past studies that analyze healing from one angle of the landscape, no previous studies have grasped healing as a place. This study attempts to quantitatively analyze healing as a place by grasping the routes in the target landscape from different migratory behaviors.

RESEARCH METHODS

The analysis method used a descriptive and quantitative analysis based on a questionnaire survey using materials obtained by field observation. The location of this research from Nakanoshima Park in Chuo Ward, Osaka City, Osaka Prefecture - Japan.

Outline of Target Area

It was the first designated scenic park in Osaka, established in 1884. The surrounding area is lined with historic buildings such as the Central Public Hall and Nakanoshima Library, and is easily accessible by public transportation from the Keihan and Midosuji Lines, and in recent years has attracted attention as a tourist destination. The main pedestrian flow routes are limited due to the structure of the park, and there are many park users who walk around according to these routes. The landscape of healing is captured by focusing on the limited flow routes.



Fig. 1 Geographical location of Nakanoshima Park

Analysis Techniques

The analysis techniques used in this study include:

- Questionnaire survey
- Landscape analysis
- Correlation analysis

First, we will cover the details of the questionnaire survey. The starting point is the starting point of the target park route. Shooting points are set at 10m intervals from each starting point, and shooting is

performed from the viewpoint height of 1.6m along the route. Patterns were shot in two ways, clockwise and counterclockwise. A questionnaire survey on the two patterns of sequence landscape will be conducted based on the photographs taken.

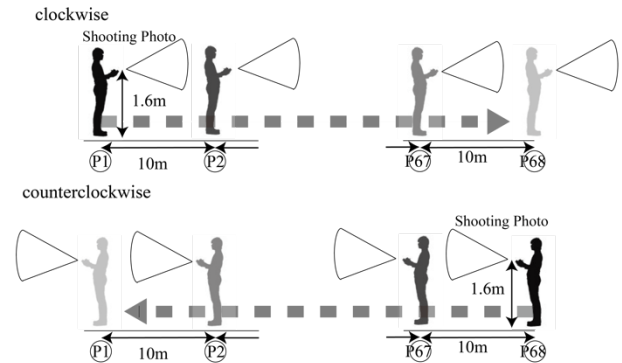


Fig. 2 How to collect local materials

Second, the details of the landscape analysis are described. The landscape analysis will be conducted on 8 points that feel healing and 3 points that do not feel healing, for a total of 11 points. The landscape constituent elements of each landscape image are extracted mainly using Photoshop. The landscape components are roughly divided into “natural resources”, “artificial resources”, and others. In addition, natural resources will be subdivided into 5 items such as *trees*, *sky*, *rivers*, *roses*, and *others*; and artificial resources will be subdivided into 4 items such as *roads*, *humans*, *structures inside and outside the premises*, and *others*. In selecting these items, Hayashi et al. (3) referred to the selection of the elements that make up the urban streetscape.

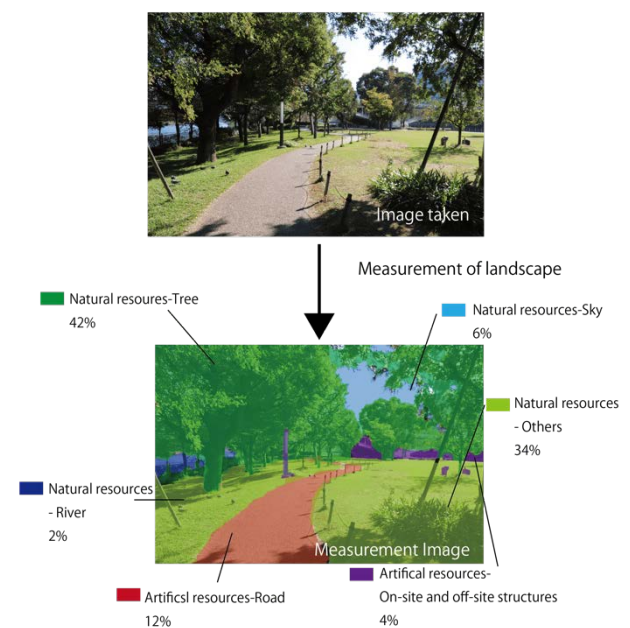


Fig. 3 Example of simple extraction of landscape

elements

Finally, we'll discuss the details of correlation analysis. Correlation analysis is performed using the healing assessment value and the ratio of landscape components, which were analyzed using Microsoft Excel.

RESULTS AND DISCUSSION

Results and discussion of the questionnaire survey

The questionnaire survey was conducted on a total of 20 students, mainly belonging to the same university. Since it is between *clockwise* and *counterclockwise*, the points are labeled as clockwise and counterclockwise. Eight points (points 24, 25, 26, 27, 28, 63, 64, 65) are considered the points of view that are particularly easy to see the landscape and healing effects. Point 28 has the highest score of 45 points. A total of 54 points were evaluated as positive. On the other hand, there are 3 spots (20,34,49) where no healing was felt. Overall, point 34 is significantly lower than other points, at -47 points. A total of 14 points were evaluated as negative. For Nakanoshima Park (which was surveyed this time) it is considered from the results that there are a mixture of local healing points and non-healing points. Moreover, the results suggest that the landscape distribution of natural resources and artificial resources has a greater relationship than the observed data.

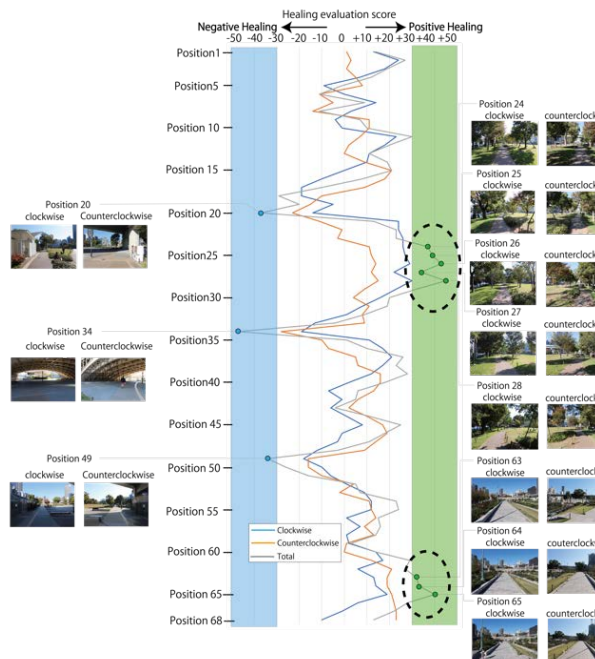


Fig. 4 Changes in questionnaire results at each observation position

Results and discussion of the landscape analysis

As mentioned before, the ratio of the landscape from each observation point was calculated for each landscape element. Figures 5 and 6 show the landscape-only components that are expected to be affected by the unique landscape from the survey results. An example of a place where you can easily feel healing is a landscape that contains many natural resources such as trees, sky, low-rise trees and lawns. In addition, the scenery with a good view is divided into two patterns at the observation points. These are, 1) a landscape that is rich in greenery (natural resource) and 2) a landscape where natural resources and artificial resources exist at the same ratio. On the other hand, the place where it is hard to feel healing is a landscape with a very high proportion of roads and structures inside and outside the site. Regarding the relationship between healing and landscape, the above-mentioned questionnaire survey hypothesized the importance of natural resources and artificial resources, but landscape analysis suggested the existence of landscape components that can be judged to be effective.

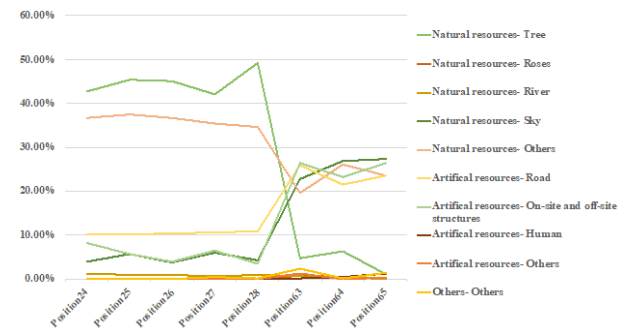


Fig. 5 Percentage of landscape components at points where healing is felt

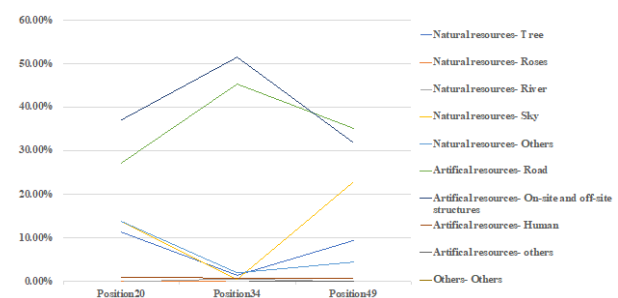


Fig. 6 Percentage of landscape components at points where healing is not really felt

Result discussion of the correlation analysis

The correlation with the healing evaluation from the correlation coefficient is shown in Tab. 1 and Fig.8-15. Following multicollinearity, the level with a significance probability of 0.01% or less will be adopted. From the results, differences were observed

from the analysis for natural resources-trees and other structures, artificial resources-roads, and structures inside and outside the site. A statistically significant difference was observed for all items except for “natural resources-trees” which had a slight positive correlation. For “natural resources-others”, positive correlations were found, and highly accurate analysis results were obtained. “Man-made resources-Roads” showed a negative correlation, and a certain degree of accuracy was also found. It can be seen that the “artificial resources-structures inside and outside the site” also had a negative correlation as with roads, and the accuracy of results also holds a certain high level.

Considering the correlation analysis, from the results, it can be seen that there is a positive effect on healing when trees exceed 40% of the landscape composition. At points 20, 34, 49 where the proportion of trees is low, the healing score is very low regardless of whether the rotation is clockwise or counterclockwise. However, although the percentage of trees was low at points 63 to 65, the average healing score was higher than that at points 24 to 28 in the counterclockwise direction. From this, the arrangement of trees in the landscape is considered. The composition of the landscape differs depending on whether the trees are in the near view or distant view from the viewpoint. In other words, although the tree itself has a positive function in healing, it is speculated that its arrangement is important.

Next, we will look at “natural resources-other items”. Similar effects can be seen in the effects of other items in the clockwise and counterclockwise directions. Natural resources-Other items mainly include lawns and bushes in the landscape. From the results, if the composition ratio is 25% or more, it has a positive effect on healing. Focusing on points 20, 65 in the clockwise direction and point 63 in the counterclockwise direction, the outliers are those with a large error from the regression line. Clockwise point 20 makes up 20% of natural resources-others, and there is a good possibility that a positive evaluation will be obtained. However, healing results is very low. It is considered that this is related to the public toilet, which is a man-made structure in the near view of point 20. Public toilets belong to the category of “structures inside and outside the premises”, and it is considered that the higher the proportion of structures, the more negatively impacted the healing is. Therefore, it is considered that the reason why point 20 is calculated as an outlier with a large error is the public toilet in the landscape. Clockwise point 65 has a similar natural resource-other landscape ratio to location 20, but receives a positive healing rating. We think that this is related to the roses and children in the foreground. The proportion of roses at point 65 is 0.68%, which is higher than other points. The percentage of people are high, at 1.61%. From the results, the higher the percentage of people, the lower the healing evaluation, but it is considered that adult

males at point 20 and female girls at point 65 are affected by gender and age group. It is assumed that these factors are the cause of error. Counterclockwise 63 has a high positive healing rating despite a low ratio of natural resources-other. This indicates that the landscape before point 63 is relevant. Since the bridge and the east side of the park can be seen from the landscape, and the details can be clearly seen at point 63, the visibility of the landscape affects the healing evaluation regardless of the increase / decrease in other ratios of natural resources.

Next, we will look at “population resources-roads”. From the results, it is considered that the higher the proportion of road area in the landscape, the more negative the effect on healing. At the points 20,34,49 where healing is not felt, the ratio exceeds about 30%. On the other hand, all healing points are less than 30%. I think this will be an index in the composition of the landscape that is considered healing.

Finally, we will consider the “population resources-structures inside and outside the site”. Mainly these on-site and off-site structures include streetlights, benches, signs, etc. inside the park, and buildings outside the park. Healing is divided into positive and negative, with the ratio of structures inside and outside the site comprising about 30%. In the clockwise direction, points 24 to 28 form the highest scoring group; and in the counterclockwise direction, points 63 to 65 form the highest scoring group. From this, it is not necessary that the proportion of the structures inside and outside the site in the landscape is low, and it can be inferred that there are conditions such as the traits and the number of things that make up the structure themselves. From the above, we were able to understand the landscape components related to healing evaluation and their criteria.

Table.1 Correlation coefficient of each landscape component

		p* < .05 p** < .01 p*** < .001	
Division	Landscape components	Correlation coefficient	
		clockwise	counterclockwise
Natural resources	Trees	0.729***	0.336
	Roses	0.014	0.417
	River	0.447*	0.309
	Sky	-0.250	0.288
	Others	0.909***	0.778***
Artificial resources	Road	0.816***	0.786***
	On-site and off-site structures	0.885***	0.733***
	Human	-0.433	-0.395
	Others	0.076	0.255
Others	Others	0.314	0.434

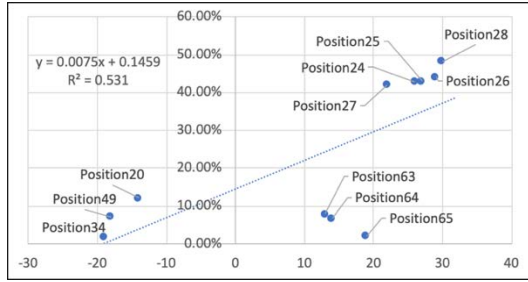


Fig.8 Correlation of Clockwise-Natural resources-Tree

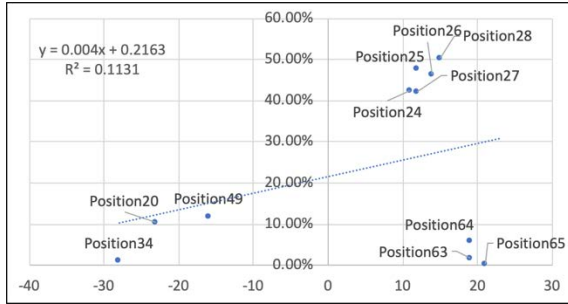


Fig.9 Correlation of Counterclockwise-Natural resources-Tree

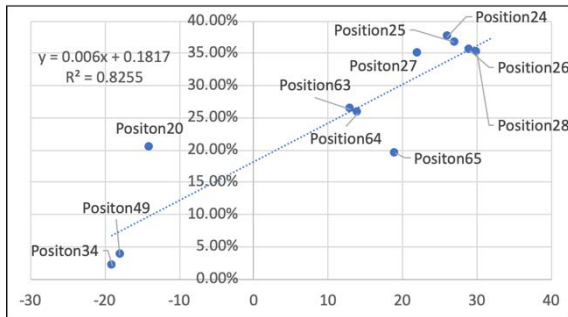


Fig.10 Correlation of Clockwise-Artificial resources-Others

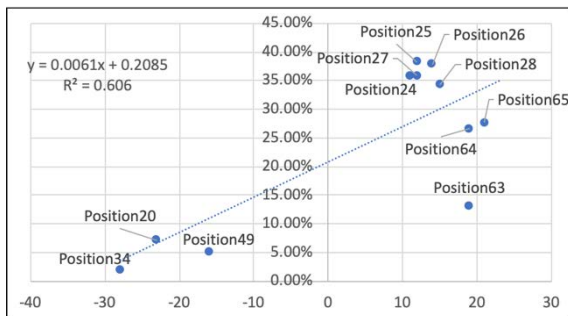


Fig.11 Correlation of Counterclockwise-Artificial resources-Others

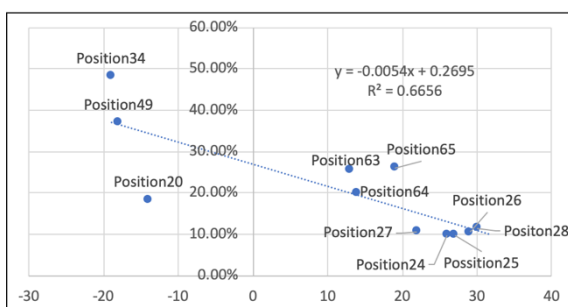


Fig.12 Correlation of Clockwise-Artificial resources-Road

CONCLUSIONS

In this study, we conducted a survey analysis over three phases regarding healing evaluation considering the difference in migratory behavior, and clarified the criteria of landscape constituent elements that provide healing as a place. The results are summarized below.

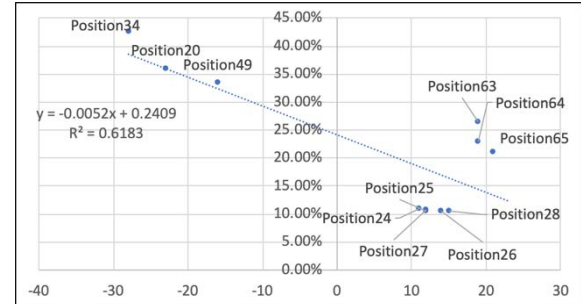


Fig.13 Correlation of Counterclockwise-Artificial resources-Road

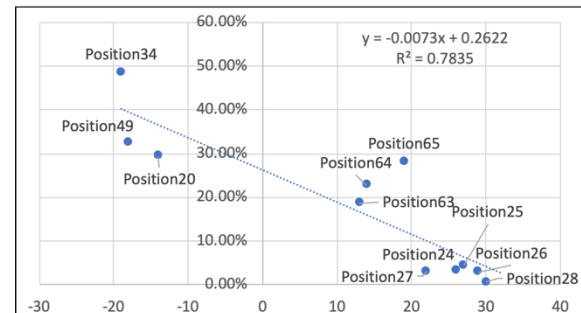


Fig.14 Correlation of Clockwise-Artificial resources-On-site and off-site structures



Fig.15 Correlation of Clockwise-Artificial resources-On-site and off-site structures

Tab.2 Impact criteria for components

Landscape components	Positive influences	Negative influences
Natural resources-Trees	$X \geq 40\%$	$40\% \geq X$
Natural resources-Others	$X \geq 25\%$	$25\% \geq X$

Artificial resources- Road	$30\% \geq X$	$X \geq 30\%$
Artificial resources- On-site and off-site structures	$30\% \geq X$	$X \geq 30\%$

ACKNOWLEDGMENTS

This paper was supported by the Osaka Institute of Technology and its affiliated professor Kazunari Tanaka's equipment. We would like to express our gratitude.

REFERENCES

- [1] Kazuko KOGA, Yutaka IWASAKI, Exploring Emotional Experiences of the Healing Effects of Greenery: A Text Mining Analysis, Environmental Information Science Academic Research Paper Presentation 32 (2018) pp.269-274
- [2] Hikaru Nagata , Effects of Healing in Urban Environment-Impact of Landscape-, Laboratory of urban planning and management, Tokyo City University
- [3] Fusayo Asano, Yoshihide Takaesu, Noriko Yamamoto, Survey on Images of “Healing Landscape”, Japanese Society of People-Plant Relationships journal 5(2) pp.25-30,2006
- [4] Yuichi SAKAI, Yoshio FUJII, An Analytical Method of Streetscape Evaluation, J.JILA 65(5) pp.833-836, 2002
- [5] Taro Kagawa, Ayako Taniguti, Satoshi Fuji, Quantitative evaluation of landscape improvement measures using simple evaluation model for streetscape, Journal of the City Planning Institute of Japan, No.6 pp.31-41, 2009
- [6] Saya Mori, Tomohide Okada, A study on the characteristics of landscape that promotes the migratory behavior of the narrow streets in the city block, Conference for Architecture and Infrastructure Environment journal, No.13, pp.556-564, 2017
- [7] Masahiro Hayashi, Hiroshi Nakahara, Revaluation of the Urban Landscape Using the Time Axis -Characterization of Sequential Landscape for the Improvement of Value in the Metropolitan Suburbs, BULLETIN OF JSSD, Vol.64, No.1, pp.59-68, 2017
- [8] Kazuki Nakamura, Masatsu Kii, Evaluation of the quality of walking space by pedestrian attributes based on perceptual factors, Conference for Architecture and Infrastructure Environment journal, No.11, pp.205-211, 2015
- [9] Nozomi Kimura, Mihoko Matsuyuki, Fumihiko Nakamura, Shino Miura, Ryo Ariyoshi, A study on the Effects of Public Spaces on Area Image Perceptions and Pedestrian Walking Behavior in City Centers -A Case Study of Monami Ikebukuro Park-, Journal of the City Planning Institute of Japan , Vol.53 No.3 , 2018
- [10] Hiroyasu Shirayanagi, Katsuya Hirano, Limits of field semantic recognition, Journal of the City Planning Institute of Japan, No.6 pp.160-165,201

ANALYSIS OF EMBANKMENT STRESSES PRODUCED DURING CONSTRUCTION AND IN-SERVICE PHASES CONSIDERING EMBANKMENT GEOMETRIES

Shin-ichi KANAZAWA¹ and Haruna IGARASHI²

¹National Institute of Technology, Fukushima College, Japan; ²OYO Corporation

ABSTRACT

Soil compaction tests are carried out to improve embankment construction engineering characteristics, such as stability and deformation. For construction, enclosed embankment structures perform total strengthening and a measure of drainage functions. This provides stability, improves deformation properties, and prevents the degradation or rot of objects placed in the embankment fill. Nevertheless, chances are that inadequate compaction will cause material, such as rocks or stones, to fall from the slope surface, as well as erosion. Therefore, the standards for embankment slope steepness set forth the use of a 1:1.8 ratio, permissible on an as-needed basis to allow for mechanical rolling for compaction. When constructing steep embankment slopes, it is necessary to conduct embankment stability checks and fully consider the provision of slope protection to prevent erosion. However, differences in stress conditions attributable to varying slope steepness have not been elucidated. In this study analyzes embankment construction in terms of different construction seasons and slope change, using the unsaturated soil-water-air coupled FEM analysis program. In this way, more accurate qualitative evaluation could be achieved.

Keywords: Embankment Geometries, Unsaturated soil, Compaction, Finite element analysis

INTRODUCTION

In recent years, torrential rain and other extreme weather events have caused frequent disasters across the world. It is urgently necessary to establish an analysis technique to continuously evaluate and examine the quality of embankment structures during construction and in-service phases. In this regard, it is important to determine the initial stress. Normally, embankment structures are made up of compacted earth in order to improve stability and deformation properties. However, existing reports present many cases of collapsed embankment structures that fail due to torrential rains.

Currently, to evaluate embankment stability against heavy rains, Embankment relies heavily on four factors: treatment of foundation ground, quality of embankment materials, degree of compaction, and handling of water. Specifically, the guidelines place importance on drainage. In addition, engineers rely on rules of thumb in carrying out embankment work, maintenance, and management. Considering these conditions, it is highly probable that, in the future, importance will be placed on embankment maintenance and management against torrential rains.

Another set of important factors includes embankment drainage measures and when the embankment is subjected to the effects of rainfall. Drainage measures taken against rainfall during embankment construction differ from those taken during the in-service phase. Rainfall affects the

embankment intermittently after the commencement of construction and during the in-service phase. Accordingly, rainfall during construction may change stress conditions inside the embankment. However, embankments are constructed in no specific season and are subject to various levels of rainfall during construction. Generally, embankments are not constructed in the rainy season; although, occasionally, this happens for unavoidable reasons. In such cases, attention is paid to weather, and drainage measures are implemented. Moreover, embankments are subject to climate conditions, such as repeated drying and wetting cycles. Therefore, the effects of stress behavior occurring during transitions between unsaturated and saturated conditions are not negligible. Hence, to estimate the initial stress conditions taking place after embankment construction, it is important to consider the effects of dry and wet climate conditions. This leads to the need for analysis techniques that consider climatic conditions, such as rainfall and evaporation.

Moreover, differences in the steepness of embankment slopes are an important factor. Standards are in place that specify embankment slope steepness for different embankment materials and heights. In general, low embankments are regarded as not at risk for a major collapse if their slope steepness is 1:1.5 and their construction is sound. This does not apply to those embankment materials that are problematic, specifically in terms of quality. However, at the slope steepness of 1:1.5, the slope

face is unlikely to receive adequate compaction. Chances are that inadequate compaction will cause material, such as rocks or stones, to fall from the slope surface, as well as erosion. Therefore, the standards for embankment slope steepness set forth the use of a 1:1.8 ratio, permissible on an as-needed basis to allow for mechanical rolling for compaction. When constructing steep embankment slopes, it is necessary to conduct embankment stability checks and fully consider the provision of slope protection to prevent erosion. However, differences in stress conditions attributable to varying slope steepness have not been elucidated.

To meet this challenge, this study analyzes embankment construction in terms of different construction seasons and slope change, using the unsaturated soil-water-air coupled FEM analysis program (DACSAR-MP)[1].

RESEARCH METHOD

Soil/Water/Air Coupled Finite Analysis Code

The finite element analysis code used in this study formulates the unsaturated soil constitutive model proposed by Ohno et al [2]. This model is framed as the soil/water/air coupled problem using the three-phase mixture theory. Equation (1) shows the effective stress. Equation (2) shows the base stress tensor and suction stress. Equation (3) shows suction.

$$\boldsymbol{\sigma}' = \boldsymbol{\sigma}^{\text{net}} + p_s \mathbf{1} \quad (1)$$

$$\boldsymbol{\sigma}^{\text{net}} = \boldsymbol{\sigma} - p_a \mathbf{1}, \quad p_s = S_e s \quad (2)$$

$$s = p_a - p_w, \quad S_e = \frac{S_r - S_{rc}}{1 - S_{rc}} \quad (3)$$

Here, $\boldsymbol{\sigma}'$ is the effective stress tensor; $\boldsymbol{\sigma}^{\text{net}}$ is the base stress tensor; $\mathbf{1}$ is the second order unit tensor; $\boldsymbol{\sigma}$ is the total stress tensor; s is the suction; p_s is the suction stress; p_a is the pore air pressure; p_w is the pore water pressure; S_r is the degree of saturation; S_e is the effective degree of saturation; and S_{rc} is the degree of saturation at $s \rightarrow \infty$. Equations (4), (5), (6) and (7) provide the yield function.

$$f(\boldsymbol{\sigma}', \zeta, \varepsilon_v^p) = MD \ln \frac{p'}{\zeta p_{sat}} + \frac{MD}{n_E} \left(\frac{q}{Mp'} \right)^{n_E} - \varepsilon_v^p = 0 \quad (4)$$

$$\zeta = \exp \left[(1 - S_e)^{n_s} \ln a \right], MD = \frac{\lambda - \kappa}{1 + e_0} \quad (5)$$

$$p' = \frac{1}{3} \boldsymbol{\sigma}' : \mathbf{1}, q = \sqrt{\frac{3}{2} \mathbf{s} : \mathbf{s}} \quad (6)$$

$$\mathbf{s} = \boldsymbol{\sigma}' - p' \mathbf{1} = \mathbf{A} : \boldsymbol{\sigma}', \mathbf{A} = \mathbf{I} - \frac{1}{3} \mathbf{1} \otimes \mathbf{1} \quad (7)$$

Here, n_E is the shape parameter; ε_v^p is the plastic volume strain; M is the q/p' in the limit state; D is the dilatancy coefficient; p_{sat} is the yield stress at saturation; a and n_s are the parameters representing the increase in yield stress due to unsaturation; λ is the compression index; and κ is the expansion index. Equation (8) shows pore water velocity. Equation (9) shows air velocity. Pore water and air flow follow Darcy's law.

$$\tilde{v}_w = -\mathbf{k}_w \cdot \text{grad} h \quad (8)$$

$$\tilde{v}_a = -\mathbf{k}_a \cdot \text{grad} h_a, h_a = \frac{p_a}{\gamma_w} \quad (9)$$

Here, \tilde{v}_w is the pore water velocity; \tilde{v}_a is the air velocity; \mathbf{k}_w is the hydraulic conductivity; \mathbf{k}_a is the coefficient of air permeability; h is the total head; γ_w is the unit weight of water; and h_a is the pneumatic head. Equations (10)-(11) show hydraulic conductivity and the coefficient of air permeability by way of Mualem's [3] formula and the Van Genuchten [4] formula.

$$\mathbf{k}_w = k_{rw} \mathbf{k}_{wsat} = S_e^{1/2} \left[1 - \left(1 - S_e^{1/m} \right)^m \right]^2 \mathbf{k}_{wsat} \quad (10)$$

$$\mathbf{k}_a = k_{ra} \mathbf{k}_{ares} = (1 - S_e)^{1/2} \left(1 - S_e^{1/m} \right)^{2m} \mathbf{k}_{ares} \quad (11)$$

Here, k_{rw} is the ratio of hydraulic conductivity; k_{ra} is the ratio of coefficient of air permeability; m is the Mualem constant; \mathbf{k}_{wsat} is the hydraulic conductivity at saturation; \mathbf{k}_{ares} is the coefficient of air permeability in dry conditions. Equations (12)-(13) show the continuous formula of pore water and air using three-phase mixture theory.

$$n \dot{S}_r - S_r \dot{\varepsilon}_v + \text{div} \tilde{v}_w = 0 \quad (12)$$

$$(1 - S_r) \dot{\varepsilon}_v + n \dot{S}_r - n(1 - S_r) \frac{\dot{p}_a}{p_a + p_0} - \text{div} \tilde{v}_a = 0 \quad (13)$$

Here, n is porosity; $\dot{\varepsilon}_v$ is volumetric strain; and

p_0 is atmospheric pressure. The elasto-plastic constitutive model obtained from Equation (4) and the equilibrium equation [Equations (12) - (13)] are formulated as the soil/water/air coupled problem.

ANALYSIS CONDITIONS

Analysis Conditions

Table 1 and Fig. 1 show analysis material parameters used for both foundation ground and embankment and moisture characteristic curves. The value was obtained by experiment. Figure 3 shows the embankment used for analysis and its analysis regions. Regarding the size of the analysis region, the foundation ground was set to 15 m long and 45 m wide and the embankment was set to 3 m and 15 m long at the top and bottom, respectively, and 6 m high. The foundation ground was set as saturated between the ground level and 3 m above ground level. Slopes were set to three levels: 1:1, 1:1.5, and 1:2. The construction period was set to one month. After being laid down, each individual 30 cm layer was subjected to loading and unloading pressures of 500 kPa to represent compaction. For displacement boundaries, the lower end of the foundation ground was fixed in the vertical and horizontal directions. These conditions were used to conduct a plane strain analysis (Ignore depth). The water level boundaries of the foundation ground were set to be drained at the top and bottom boundaries and undrained at the right and left boundaries. Regarding drainage measures, a drainage layer (3 m long and 0.6 m high) was provided at the toe of the slope, and the entire slope face was covered with vegetation mats as a root element (to consider only evaporation effects). The water permeability coefficient of the drainage layer was set to 500 times that of the embankment, with the air permeability coefficient being 100 times the water permeability coefficient. Other conditions specified in the *Embankment Earthwork Guidelines* [5] were also fulfilled. Figure 2 shows rainfall conditions [6] used for the analysis. Amounts of rainfall observed in 2016 in Utsunomiya, Tochigi Prefecture were used as rainfall conditions to simulate the average amount of rainfall in Japan (approx. 1,750 mm). The analysis selected spring, summer, fall, and winter seasons, as shown in the figure. For the analysis, the embankment construction process was assigned a seasonally averaged daily amount of rainfall. Evaporation rates were also matched with rainfall seasons.

Subsequent to an analysis of initial stresses inside embankment, observations of differences with

Table.1 Material Parameter

λ	κ	M	m	S_{r0}	k_a
0.18	0.037	1.33	0.8	0.15	1.00
n	n_E	a	v	G_s	k_w
1.0	1.3	10.0	0.33	2.7	0.01

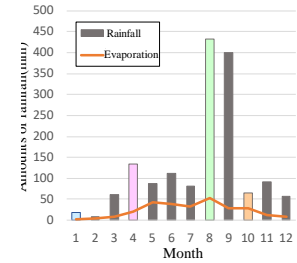
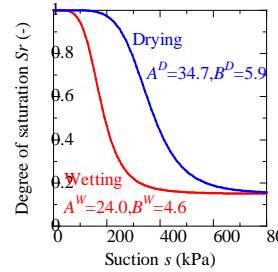


Fig.1 Moisture characteristic curve Fig.2 Rainfall condition

embankment construction season¹, and an analysis of stresses in embankments in service for 10 years, this

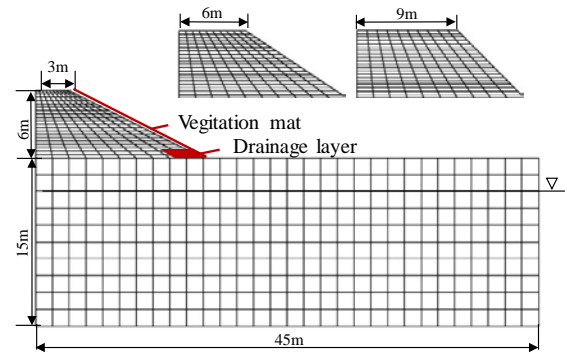


Fig. 3 Analysis mesh

study evaluated embankment failure, assigning embankment treatments of 10 mm to 50 mm per hour rainfall. These were applied as torrential rainfall for 1 h and continuous rainfall for 5 h.

3.2 Stress Change inside Embankments in Service for 10 Years, Noting Contributions of Differences in Slope Face Angle

Figure 4 summarizes analysis results for embankments in service for 10 years in terms of mean effective principal stress, void ratio, deviatoric stress, suction, shear strain, and critical state determination ratio.

First, the foundation ground will be examined. The values of mean effective principal stress are high with respect to all angles (I). The values represented in the void ratio distributions are small for all seasons (II). These results are interpreted as fully demonstrating compaction effects according to the relationships between void ratio and effective stress.

Next, the mean effective principal stress values

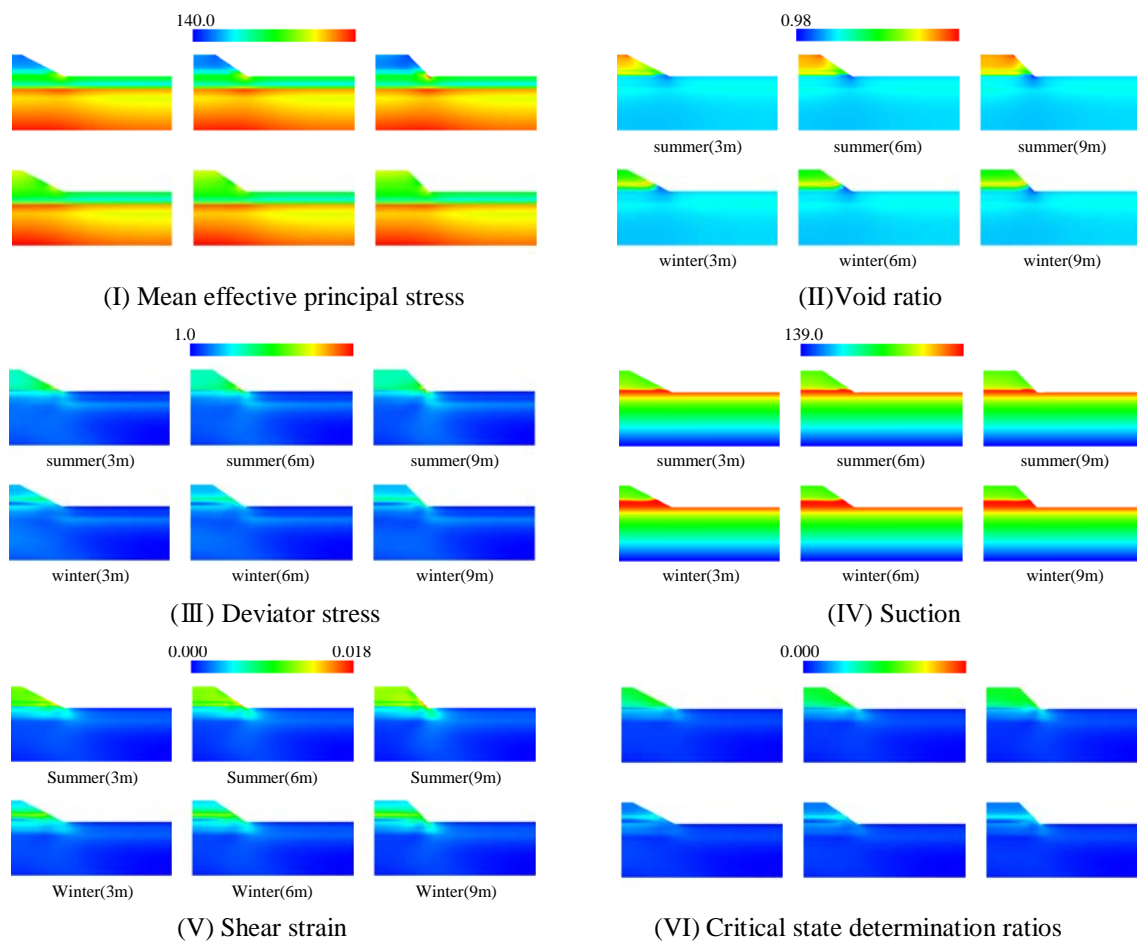


Fig. 4 Summarizes analysis results

inside embankment will be compared, noting seasonal differences. According to I, values are high in winter when the amount of rainfall is small. In contrast, values are low in summer when the amount of rainfall is large. Meanwhile, according to II, the void ratio values are lower in winter than in summer. In summer, values are high in the slope area. Probable causes of these results are volumetric expansion due to rainfall and the loss of suction in summer, as represented by the suction distribution (IV). Moreover, strength and deformation properties improve with increasing suction (decreasing degree of saturation). Consequently, the internal strength of the embankment is likely to be high in the low rainfall seasons. Shear strain values are low in winter as revealed by shear strain distributions (V), while in summer, a slight sign of rotational slip is present. The maximum shear strain value is approximately 1.8%, at which a failure can occur if torrential rain or other extreme weather conditions occur.

A comparison considering angle differences reveals that according to I, mean effective principal stress values at the toe of the slope are larger for cases

of embankment having a 9 m long top than with embankment having a 3 m long top. Additionally, according to II, void ratio values at the toe of the slope are small. This is interpreted to mean that at higher slope angles, compressive forces are applied more intensively to the toe of the slope. Meanwhile, shear strain values (V) at the toe of the slope are higher for embankment with a 9 m long top than for embankment with a 3 m long top. The critical state determination ratios (VI) indicate no risk of failure under the current conditions. However, at steeper slope angles, the risk of failure is likely high, notably at the toe of the slope.

Figure 5 presents matrices showing results that represent the relationship between the amount and duration of rainfall (in Summer). The analysis assumed that risk of failure was present at levels of 3% or higher shear strain and 1.00 or higher critical state determination ratios. Cases with no concern about failure are indicated with a circle (Blue) and those with a concern about failure are indicated with a cross (Yellow). Generally, concern about failure was present with increasing amount and duration of rainfall. The matrices reveal no difference between varying slope steepness.

To understand rainwater infiltration conditions at

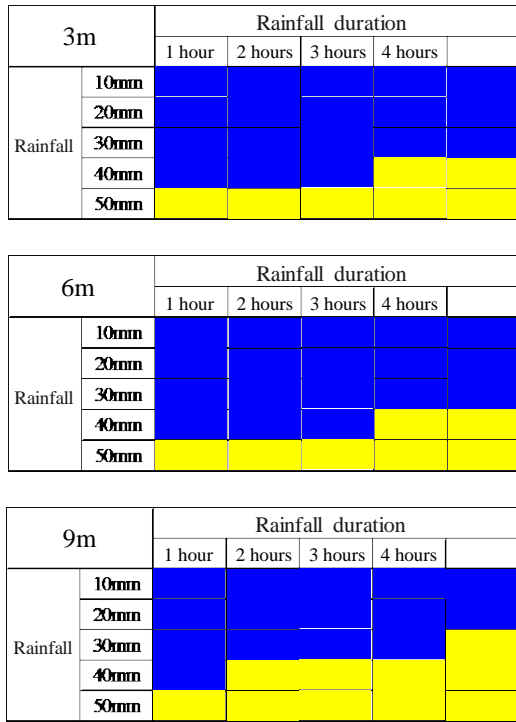


Fig. 5 Matrices showing results

average rainfall intensity, Fig. 6 shows stress distributions rendered thorough an analysis of continued rainfall at 30 mm/h. Top contour diagrams represent stress conditions inside the embankment immediately following 5 h of 30 mm/h rainfall. Bottom graphs show the relationships between the analysis period and individual stresses, revealing changes over time in each stress. The colors of the curves correspond to the colors of embankment elements shown in the middle.

The mean effective principal stress values (I) are low at the top and slope face, which were areas with assigned rainfall. The values at the toe of the slope increase with increasing slope steepness. The graphs also reveal that the mean effective principal stress values at the toe of the slope are higher with increasing steepness of embankment, and that as rainfall continues, values inside the embankment increase while values at the slope face decrease.

The degree of saturation values (II) at the toe of the slope are low. Therefore, the drainage layer is satisfactorily functional. The values are high at the top and slope face, which were assigned rainfall, with no sign of rainwater infiltration into the embankment interior. This ascertains that moisture infiltrates the embankment along the surface layer. This is interpreted to mean that because of the rapid rate of rainfall assigned, the moisture had little time to enter the inner part of the embankment and thus flowed through the surface layer. Specifically, the analysis

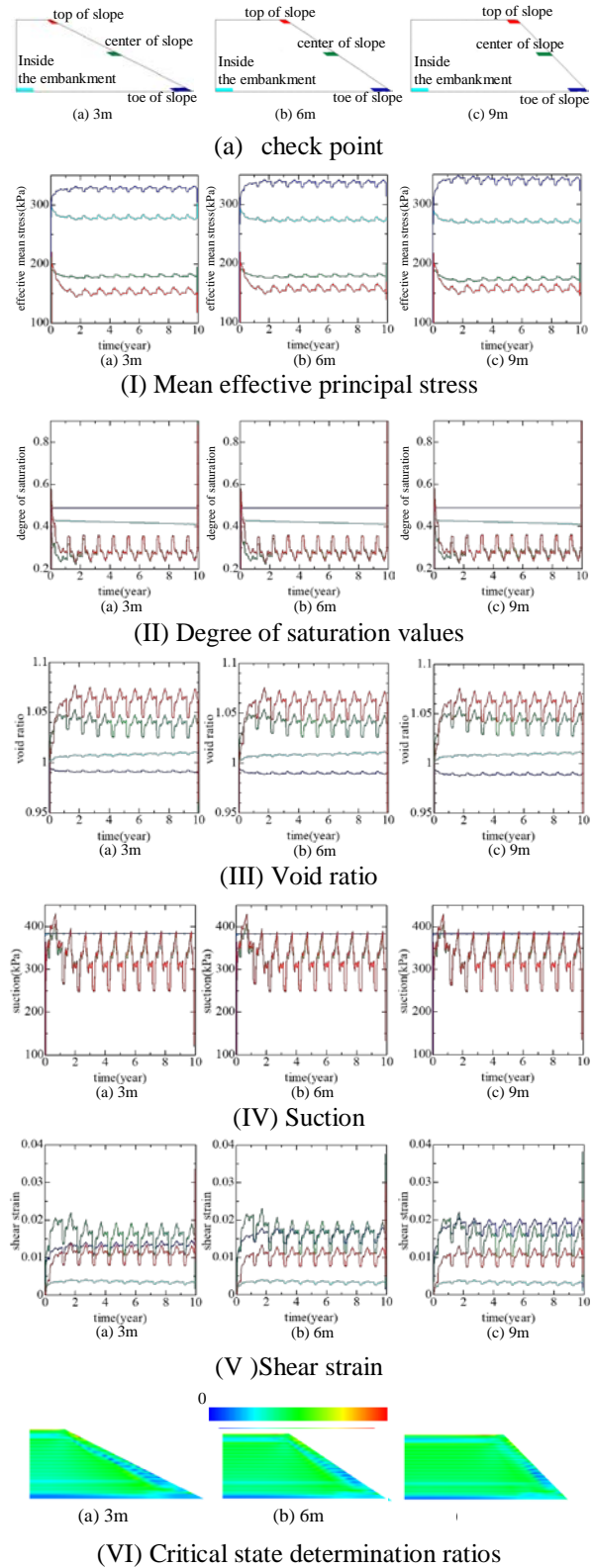


Fig. 6 Summarizes analysis results

techniques used in this study accounted for ground infiltration capacity. The computation took ground infiltration capacity into account so as not to allow rainfall to cause a positive pore pressure at the ground level. Therefore, the surface layer water flow was

rendered, and this simulation suggested, as a result, the formation of a surface layer slip. Moreover, the degree-of-saturation values inside the embankment and at the toe of the slope are virtually constant against the passage of time, as shown by the graphs. The values at the toe of slope are high due to rainfall after embankment construction.

Void ratio values (III) at the toe of the slope are low, with smaller values occurring more intensively at the toe of the slope with increasing slope steepness. The graphs also reveal that the void ratio values are higher, although slightly, at the center of the slope face, while the values are of lower intensity at the toe of the slope with increasing slope steepness. The values decrease substantially along the slope face due to rainfall.

Suction values (IV) are low at the top and slope face of the embankment, which are areas assigned rainfall. Because strength and deformation properties increase with increasing suction, it is highly probable that the strength of the slope is low. Moreover, the graphs reveal virtually constant suction values inside the embankment and at the toe of the slope where the drainage layer is present. Suction values at the slope face are largely affected by the amount of rainfall and substantially decrease due to rainfall.

Shear strain values (V) are high at the top and slope face of the embankment, which are areas assigned rainfall. The values at the toe of the slope are higher with increasing slope steepness. The graphs also show that shear strain values at the slope face increase due to rainfall and that the values at the toe of slope are higher with increasing slope steepness. This suggests the presence of vulnerable regions at the top and along the slope face, the emergence of vulnerable regions at the toe of the slope with increasing slope steepness, and resultant higher risks of embankment failure.

The critical state determination ratios (VI) prove no risk of failure under the current conditions. Nonetheless, at higher slope steepness, failure risks are thought to be high at the toe of the slope.

These findings indicate the occurrence of vulnerable regions at the top and along the slope, the emergence of vulnerable regions at the toe of the slope with increasing slope steepness, and higher risks of embankment failure as a result of torrential rains on an embankment in service for 10 years. Meanwhile, neither shear strain nor critical state determination ratios exceeded the set limits. Therefore, under the current conditions, there is no concern about failure.

CONCLUSION

Using the unsaturated soil-water-air coupled FEM analysis program (DACSAR-MP, dissolved-air model), this study provided an analytical representation of stress changes in embankment caused by rainfall during construction and internal mechanical behaviors of embankment assigned torrential rains during the in-service phase.

Although matrices and contour diagrams showed little differences in stress conditions between varying slope steepness, graphs drawn to describe changes in individual stress conditions against the passage of time made differences in stress conditions visually clear between varying levels of slope steepness.

Future challenges include simulating the embankment construction phase using the properties of soil materials from actual ground. In this way, more accurate qualitative evaluation could be achieved. The conclusions in this study were reached using limited conditions, with the analysis results obtained under ideal conditions. It is necessary to conduct analyses simulating actual torrential rains in the future, using analysis conditions better representing the natural environment.

REFERENCES

- [1] Kanazawa, S., Toyoshima, K., Kawai, K., Tachibana, S. and Iizuka, A.: Analysis of mechanical behavior of compacted soil with F.E. method, *Journal of JSCE*, No.68 (2), pp.291-298, 2012.
- [2] Ohno, S., Kawai, K. and Tachibana, S.: Elastoplastic constitutive model for unsaturated soil applied effective degree of saturation as a parameter expressing stiffness, *Journal of JSCE*, Vol.63/No.4, pp.1132-1141, 2007.
- [3] Mualem, Y.: A new model for predicting the hydraulic conductivity of unsaturated porous media, *Water Re-sources Research*, Vol.12, No.3, pp.514-522, 1976.
- [4] Van Genuchten: A closed-form equation for predicting hydraulic of unsaturated soils, *Soil Science Society American Journal*, Vol.44, pp.892-898, 1980.
- [5] Japan Road Association,: Roadway Workers - Fill Construction Guidelines, 2010.
- [6] Japan Meteorological Agency: <http://www.jma.go.jp/jma/index.html>.

DEVELOPMENT OF THE GROUND INJECTION METHOD USING GEO-POLYMER MATERIAL

*Satoshi Tashiro¹, Naoaki Suemasa¹, Takamitsu Sasaki² and Koichi Nagao³

¹ Tokyo City University, Japan ;² Kyokado Engineering co. Ltd, Japan ;³ Sato kogyo co. Ltd, Japan

ABSTRACT

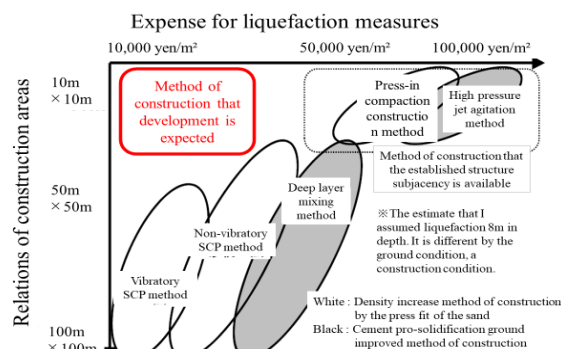
Severe liquefaction damage has frequently occurred due to earthquakes in the soft grounds in Japan. At present, although various liquefaction countermeasure methods have been proposed and applied, it has been required to develop a new countermeasure method applicable for narrow spaces such as residential areas at an inexpensive cost. In this study, we focused on a fine particles grouting method and adopted fine geo-polymer as a grouting material. The fine particles grouting method is a kind of soil stabilization technique in which fine particles are injected into sand layers to fill the voids of sand so that the soil is solidified and reinforced. Geo-polymer (GP) is well known as a construction material used for ancient Roman buildings and Egyptian pyramids, and its high strength has been maintained even after more than 2000 years have passed. In order to make this method more effective, we consider the following three factors are necessary; firstly to choose an optimum "combination" of materials containing GP, secondly to develop "micronization" to pulverize the materials to be very fine enough to be injected into ground, and finally to establish a "permeation" method to deliver the fine particles into the voids of sand in ground. In this report, the first factor, the "combination" was focused on and several patterns of combinations of fine particles were selected and their solidification and compressive strength were investigated.

Keywords: Liquefaction, The fine particles grouting method, Geo-polymer, combination

INTRODUCTION

Severe liquefaction damage has frequently occurred due to earthquakes in soft grounds in Japan. Figure 1 shows the relationship between construction area and the expense for liquefaction measures [1]. At present, although various liquefaction countermeasure methods have been proposed and applied, there is hardly any suitable countermeasure methods applicable for small spaces such as residential areas at an affordable cost, as shown in the red frame in Fig. 1.

Fig.1 Relations of construction areas and expense for liquefaction measures



In this study, we focused on a fine particles grouting method and adopted fine geo-polymer as a grouting material. This method uses a soil stabilization technique in which fine particles are injected into sand layers to fill the voids of sand so that the soil

is solidified and reinforced. Geo-polymer (GP) is well known as a construction material used for ancient Roman buildings and the Egyptian pyramids, and its high durability has been maintained even after more than 2000 years have passed. In order to make this method using GP more effective, a research process was made as shown in Fig. 2. It indicates the following three factors are necessary; firstly to choose an optimum "combination" of materials containing GP, secondly to develop "micronization" to pulverize the materials to be very fine enough to be injected into ground, and finally to establish a "permeation" method to deliver the fine particles into the voids of sand in ground. In this report, the first factor, the "combination" was focused on and several patterns of combinations of fine particles were selected and their solidification and compressive strength were investigated.

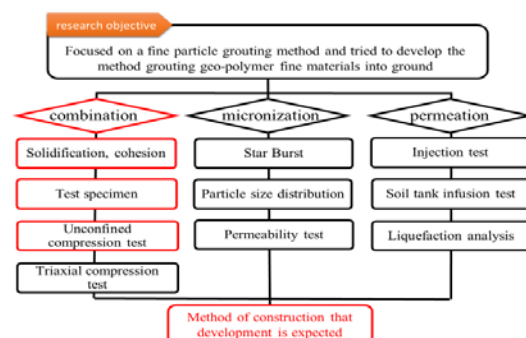


Fig. 2 Research process

SOLIDIFICATION PRINCIPLE OF GROUTING MATERIALS

At first, an understanding of a solidification principle of GP is important to use the material properly. GP [2] is made by mixing water with alkaline silica solution (active material in a solidification process), and an active filler (amorphous substance particles containing a component active in an alkaline region) instead of cement. Alkaline silica solution is substituted with sodium silicate, and an active filler is substituted with industrial by-products such as fly ash (FA) or blast furnace slag fine particles (BS). Fig. 3 shows the solidification images of cement and GP. As for cement, the water added to cement is absorbed and reacted with a alkaline component to become hydrate crystal, as cement particles solidify to become an aggregate, in which a large number of thorns on the surface of cement particles are connected with each other as shown in Fig. 3 (a). As for GP, on the other hand, when metal ions eluted from an active filler are contacted with alkaline silica solution (silicate), crosslinked polymer is generated during crosslinking a silicic acid compound, so that the particles of active filler are compacted with mineral indeterminate form gel as shown in Fig. 3(b).

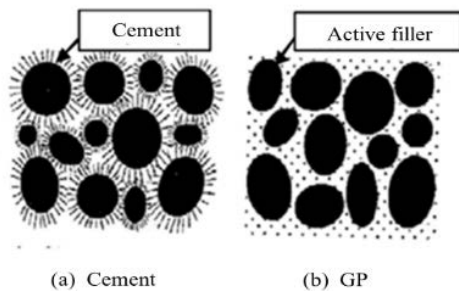


Fig. 3 Solidification images of cement and GP

Fig. 4 shows a solidification principle of GP. According to Ikeda [3], the alkaline silica solution forming GP consists of active silica and alkaline sources, and the fillers are classified in two kinds of an activity filler and the inert filler. The active silica contains silica such as water glass, and the alkaline source, such as sodium and calcium hydroxide, contains a component which react with the active silica. By mixing these materials, silicate is generated while alkaline silica solution is generated. It is said that the fillers are selected in terms of mineral characteristics and activity, and, in particular, FA and BS have high activity and affect silicate crosslinking, whereas the inert filler such as quartz sand does not react to silicate by itself but plays a role in aggregating and reinforcing the strength of GP. Since GP does not use cement, there are advantages that the expense can be reduced, a quantity of carbon dioxide emission can be

suppressed in a process of manufacturing and its durability can be maintained longer than conventional concrete. In addition, as a result of having examined fine particles grouting materials of a non-cement system, Uemura et al. [4] confirmed that they are effective enough for liquefaction countermeasures. From these perspectives, GP is expected as a new promising grouting material.

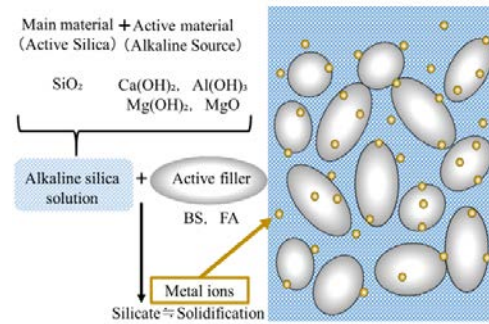


Fig. 4 Solidification principle of GP

COMBINATION EXAMINATION USING PLURAL FINE PARTICLES

Experiment summary

In this study, the followings were performed by using fine particles mixtures: confirmation of solidification of chemical solutions, pH measurement, and unconfined compression tests. The fine particles were put in a beaker in a room where the temperature was set at 25 ± 3 °C and the states of solidification and the pH were measured in 1, 3, and 7 days after the mixing. The solidification was measured by observing the states and confirming the resistance when penetrating a 3mm-diameter metal bar. In addition, four cases among all the combinations in Table 1, which showed enough solidification, were selected for unconfined compression tests. The test specimens were formed at a relative density $Dr=60\%$ with the mixture of grouting materials and the quartz sand No. 6, and then wet-cured at a normal temperature. Then unconfined compression tests were carried out on the improved test specimens after 3, 7, and 28 days of curing. The method of preparing the test specimen is shown in Fig. 5. In order to facilitate unmolding of the specimen, grease was applied on the plastic mold inside and OHP sheet was spread in the bottom of the test specimen beforehand. In a process of preparing the specimen, the sand and the grout materials were injected in the mold to keep having flooding parts and the density was adjusted by tapping the side of the mold with a wooden hammer. After injection was completed, a porous

plate was installed in the upper end of the test specimen to level the upper part, and the relative density was confirmed at $Dr=60\pm3\%$.

The combination conditions for this experiment (Table 1) were arranged, in which a weight ratio of water to particles was 0.1, and the grout materials used for the experiment were as follows: second crushed SiO_2 as main material, active silica, magnesium hydroxide ($Mg(OH)_2$), calcium hydroxide ($Ca(OH)_2$), aluminium hydroxide ($Al(OH)_3$) and magnesium oxide (MgO) as alkaline sources to activate, and FA and BS which contain amorphous silica as active filler. Fig. 6 shows the grain size accumulation curves of the grout materials used in the experiment. All the materials were absolutely dried and powdered.

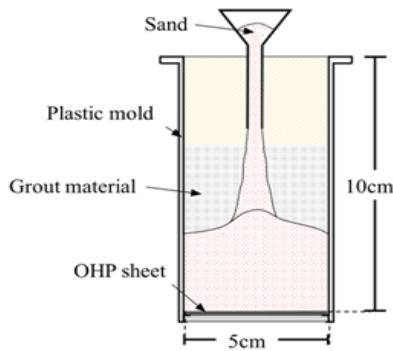


Fig. 5 Method of preparing test specimen

Table 1. Combination conditions

Case	pH(Day)				Solidification(Day)				Combination(g)				P/W
	0	1	3	7	0	1	3	7	SiO_2	$Mg(OH)_2$			
A1	9.0	9.1	8.7	8.6	×	×	×	○	8.999	1.010			0.1
A2	9.2	9.1	9.0	8.8	×	×	×	△	4.490	1.010	4.490		0.1
A3	9.2	9.3	9.1	8.8	×	×	×	×	4.490	1.010	4.490		0.1
A4	9.2	9.3	9.1	8.8	×	×	×	△	2.990	1.010	2.990	2.990	0.1
B1	12.2	10.3	10.0	9.9	△	○	○	○	8.999	1.010			0.1
B2	12.5	10.1	9.8	9.4	×	○	○	○	4.490	1.010	4.490		0.1
B3	12.3	11.7	11.3	10.8	×	○	○	○	4.490	1.010	4.490		0.1
B4	12.5	12.3	11.1	10.9	×	○	○	○	2.990	1.010	2.990	2.990	0.1
C1	8.3	6.3	6.9	7.9	×	○	○	○	8.999	1.010			0.1
C2	7.7	7.2	6.9	7.9	×	○	○	○	4.490	1.010	4.490		0.1
C3	7.7	7.2	6.9	7.2	×	×	○	○	4.490	1.010	4.490		0.1
C4	8.3	8.2	8.2	8.1	×	×	○	○	2.990	1.010	2.990	2.990	0.1
D1	10.5	12.4	10.1	9.9	×	△	○	○		8.999	1.010		0.1
D2	10.5	12.4	12.2	11.5	×	△	○	○		8.999	1.010		0.1
D3	10.4	12.2	11.9	11.2	×	△	○	○		8.999	0.505	0.505	0.1
D4	10.5	12.2	11.9	9.8	×	○	○	○		1.010	8.999		0.1
D5	10.5	12.2	11.7	-	×	○	○	○		1.010	8.999		0.1
D6	10.5	11.9	10.9	-	×	○	○	○		1.010	4.500	4.500	0.1

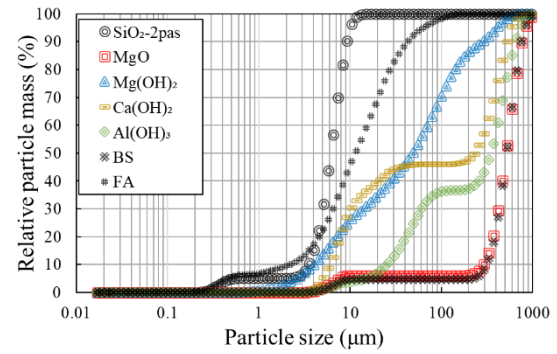


Fig. 6 Grain size accumulation curve of grout materials

Laboratory findings and consideration

The solidification and the pH obtained from the tests are shown in Table 1 and the changes in pH of each case in Fig. 7. In Table 1, the marks represent as follows. ○: solidified, ×: unsolidified, and △: the state between ○ and × (satisfying the conditions that the surface of chemical solution inclined when a beaker inclined, and a hole made by inserting a metal bar to a mixed specimen did not close). Due to the demolding failures at D5 and D6, their pHs were unmeasurable. Comparisons were made from Table 1 and Fig. 7, focusing on active materials. First, in the cases with $Mg(OH)_2$, the pHs were approximately 9 and the changes over time were likely to be small, and less solidifications were confirmed. Next, in $Ca(OH)_2$, the initial pHs were approximately 12 and decreased with solidification. In $Al(OH)_3$, the pHs were approximately 8 and there were two patterns that the pHs decreased in the early days of curing (C3, C4) and remained unchanged over time (C1, C2). Finally, in MgO , the initial pHs, approximately 10, remained unchanged in the early days of curing with FA, however, the pHs increased to approximately 12 with BS, and then decreased with solidification in both cases.

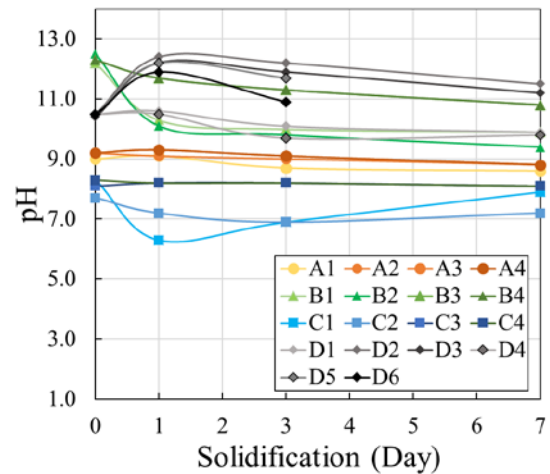


Fig. 7 Changes in pH of each case

Among all the cases, Fig. 8 shows the fully solidified four cases, B2, B3, C2, and D5. There was a tendency that the alkaline component neutralized during solidification so that the pH significantly decreased.

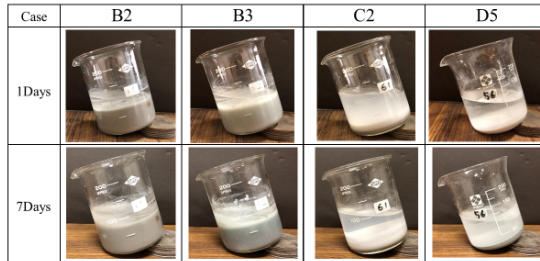


Fig. 8 Cases of full solidification

Unconfined compression tests were carried out on the above cases. The states of the test specimens after the tests are shown in Fig. 9 and the results of applying maximum compressive stresses on the specimens in 3, 7 and 28 days of curing are shown in Fig. 10.

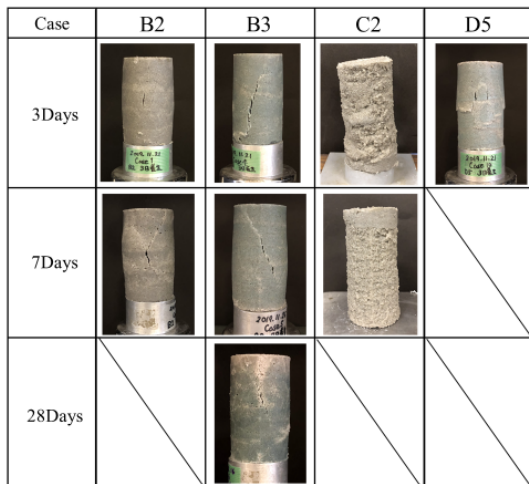


Fig. 9 States of test specimens after unconfined compression tests

In Fig. 9, all the improved test specimens became independent in 3-day curing, which indicates all the combinations of chemical solutions were solidified because only quartz sand No. 6 is not capable to be independent. Among them, split failure was confirmed in B2 and D5, while shear failure was confirmed in B3. In 7-day curing, although C2 and D5 were temporarily independent, but unable to maintain enough durability for unconfined compression tests so that the maximum compressive stresses were set at 0 kN/m² as seen in Fig. 10. On the other hand, the changes in color of specimens were confirmed in some cases where unconfined compression tests were carried out. For example, compared 7-day to 1-day curing in B3 in Fig 9, the color changed to be blue. From this, there is a possibility that color changes by a reaction of chemical solution.

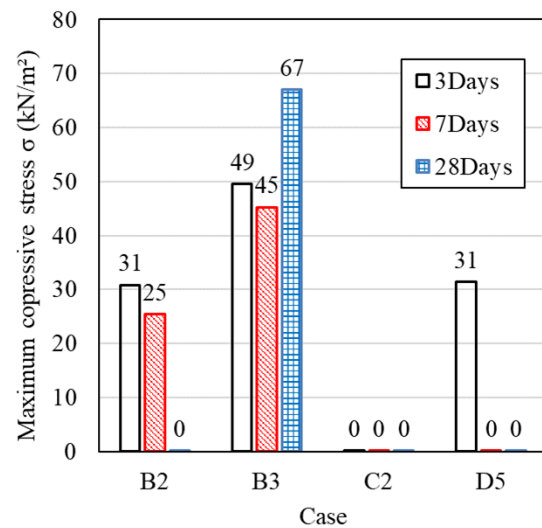


Fig. 10 Maximum compressive stress

Comparison was made focusing on amorphous silicas in the cases where SiO₂ was used as a main material. In the combination of Al(OH)₃, C2, since the pH was neutral and the change with the elapse of time was smaller than those of Ca(OH)₂ and MgO, the durability tended to easily deteriorate. Next, in the cases where Ca(OH)₂ was used as active material, the pH had a tendency to decrease close to be neutral in the early days and the strength was reinforced more with BS (B3) than FA (B2). As known from Table 2, FA contains much SiO₂ whereas BS contains much CaO. It is thought that the durability changed depending on the difference in characteristics and activity of mineral. On the other hand, when MgO was used as active material and BS was added, the pH changed not to be neutral but to be alkaline in the early days, so that the chemical solution was temporarily solidified but did not lead to strength increase.

Table 2. Chemical components (FA, BS)

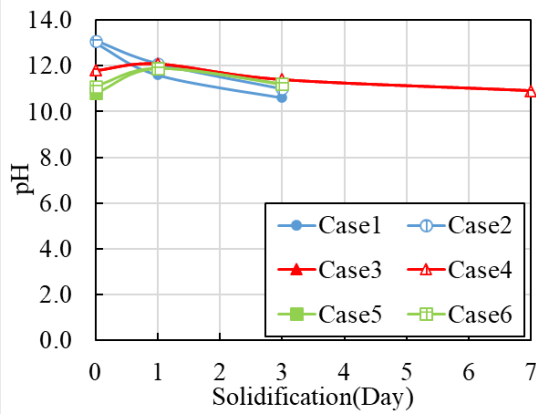
	SiO ₂	Al ₂ O ₃	CaO	MgO	T-Fe	Fe ₂ O ₃
FA	40.1%-74.4%	15.7%-35.2%	0.3%-10.1%	0.2%-7.4%	-	1.4%-17.5%
BS	33.8%	13.4%	41.7%	7.4%	0.4%	-

The strength of all the test specimens decreased from 3-day to 7-day curing, however, the strength of B3 in 28-day curing exceeded that of 3-day. We consider the reason of the decrease after 3-day curing was caused by errors resulting from the mixing method to manufacture specimens.

COMBINATION EXAMINATION USING TWO KINDS OF BLAST FURNACE SLAG

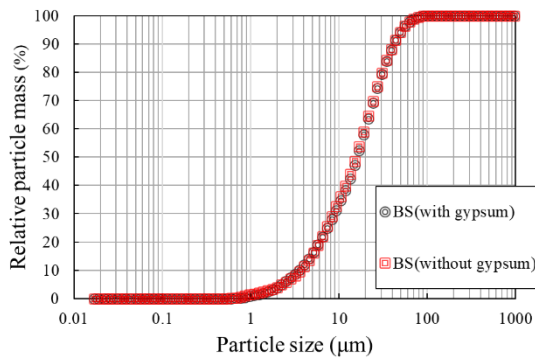
Experiment summary

From the findings from Chapter 3 that the



strength was reinforced in the cases of Ca (OH)₂+BS and MgO+BS combinations, the following materials were used in this chapter. SiO₂: as main material, BS with gypsum and without gypsum: active fillers, and Ca (OH)₂ and MgO: active materials. The examination items were solidification of chemical solution, pH measurement, and unconfined compression test. Table 3 shows solidification and the pHs. The

Case	pH(Day)				solidification(Day)				combination(g)			P/W
	0	1	3	7	0	1	3	7	SiO ₂	Ca(OH) ₂	BS(with gypsum)	
1	13.0	11.6	10.6	-	×	○	○	○	4.50	1.00	4.50	0.1
2	13.1	12.1	11.0	-	×	○	○	○	4.50	1.00	4.50	0.1
3	11.8	12.1	11.4	10.9	×	○	○	○	1.00	4.50	4.50	0.1
4	11.8	12.1	11.4	10.9	×	○	○	○	1.00	4.50	4.50	0.1
5	10.8	11.9	11.2	-	×	△	○	○	4.50	1.00	4.50	0.1
6	11.1	11.9	11.2	-	×	△	○	○	4.50	1.00	4.50	0.1



specimens were made using the selected 4 kinds of combinations which showed sufficient solidification in Chapter 3 and then cured under the same conditions. Unconfined compression tests were carried out on these specimens. Grain size accumulation curves of grout materials are shown in Fig. 11. SiO₂ and MgO used in this experiment were same as those in Chapter 3 and BS with gypsum and without gypsum were absolutely dried and powered conditions.

Table 3. Solidification and pH

Fig. 11 Grain size accumulation curves of grout materials

Laboratory findings and consideration

The changes in pH in these cases are shown in Fig.12. There was no significant difference in the pHs between the cases of BS with gypsum and that without gypsum, and a similar tendency was seen in Fig. 7. In addition, due to failures at demolding, the pHs were unmeasurable in Case 1, 2, 5, and 6 in 7-day curing.

Fig. 12 Changes in pH of each case

Since solidification was confirmed in all combinations except for Case 5 and 6, where the states were △ in 1-day curing, unconfined compression tests were carried out only on Case 1, 2, 3, and 4. Fig. 13 and Fig. 15 show the stress-strain curves of 28-day cured specimens and the results of unconfined compressive strength of 3, 7, and 28-day cured specimens in each case, respectively. Regarding the behavior before failure for 28-day cured specimens, the compressive stresses gently increased with strain in Case1 and 2, whereas sharply increased in Case 3. In contrast, the post-peak compressive stresses gently decreased in Case 1 and 2, whereas suddenly decreased in Case 3. From these, it was confirmed that Case3 was high in initial rigidity, but low in ductility.

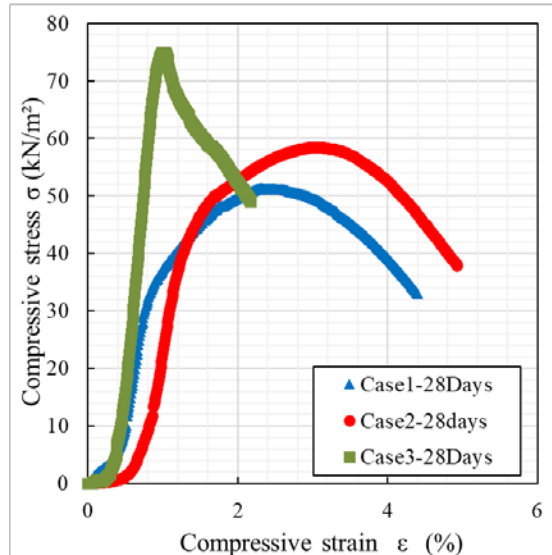


Fig. 13 Stress-strain relations of 28-day curing

The state of each test specimen is shown in Fig. 14. The color changed into light blue in Case 1 and 2 in 1-day curing, but no color variation was observed in Case 3 and 4. In 7-day of curing, the color changed into light blue in Case1, 2 and 3, but dark blue in Case 4. Thus, it is thought that the color changed according as the chemical solutions reacted with

each other and solidified. In Case 4, however, although the color changed, the test specimen collapsed. As a result, similar to D5 (MgO+BS combination) in Chapter 3, the change of color was related to solidification of the chemical solutions but it did not necessarily lead to strength increase.

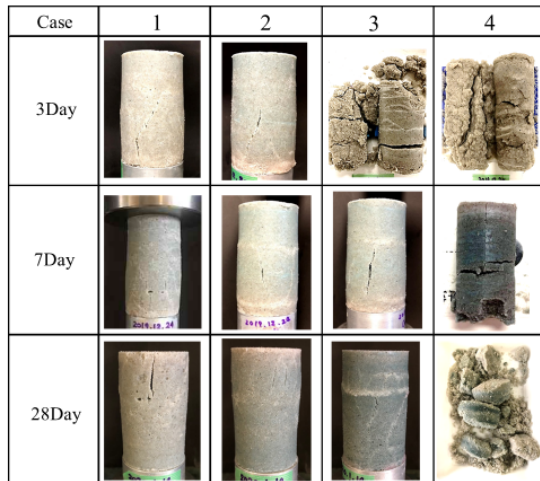


Fig. 14 State of each test specimen

Since the maximum compressive stress of Case 3 (with gypsum) was bigger than that of Case 2 (without gypsum) in 28-day of curing as seen from Fig. 15, it was revealed that the effect of gypsum was low in the case of $\text{SiO}_2 + \text{Ca}(\text{OH})_2 + \text{BS}$, but the strength increased in the case of $\text{MgO} + \text{BS}$. Gypsum ($\text{CaSO}_4 \cdot 2\text{H}_2\text{O}$) [7], which is composed of sulfate and calcium, solidifies when mixed with water. It appears that solidification was promoted in the process that the contained calcium was consumed and the pH changed from alkaline to neutral.

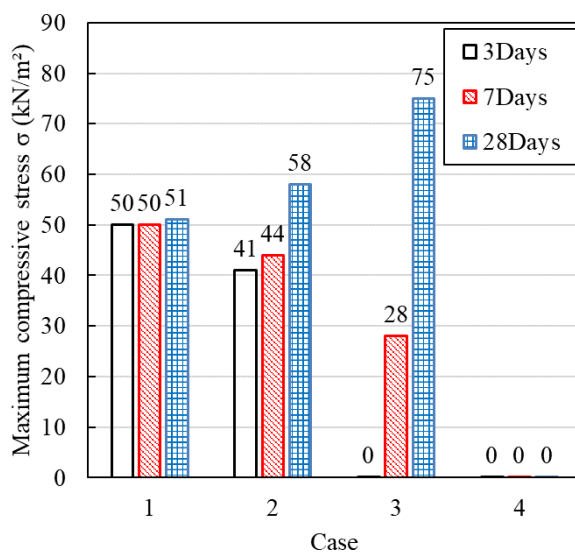


Fig. 15 Maximum compressive stress

CONCLUSION

Based on Chapter 3, according as pH changed, the solidification strength was reinforced more in the case of BS than that of FA in the early days of curing. In addition, when compared the cases of BS with and without gypsum, there was a possibility that gypsum could promote solidifying from the findings in Chapter 4. As seen from B3 of Chapter 3 and Case 1 of Chapter 4, the combinations that showed great decrease in pH in the early period of curing, had a tendency of high strength due to active alkali consumption. With the goal of obtaining high strength and long-term durability of the fine particles grouting materials, the effects on a solidification mechanism will be examined in relation to combinations of fine particles, changes in pH, and crystal structures.

ACKNOWLEDGEMENT

Have Taiheiyo Cement Corp. Sano, Ishimoto provide high-purity silica to Suzuki Kogyo Chikaishi in Cal technical center ($\text{Ca}(\text{OH})_2$) to JFE Steel Corporation Oka in BS on performing this study, thank you very much for your help. I write it down here and express gratitude.

REFERENCES

- [1] Study on earthquake-resistant measures Committee of the creation residential land: Guide - to protect a single-family house from study on earthquake-resistant measures committee's report - liquefaction of the creation residential land, Japanese Geotechnical Society Kanto Branch, p209, 2014
- [2] Koji Harada: Study on durability of geo-polymer mortar, concrete engineering annual memoirs, Vol.33, No.1, pp1937-1942, 2011
- [3] Ko Ikeda: Become normal temperature solidification and the materials of the mineral particles with the geo-polymer binder, resources and material, the Mining and Materials Processing Institute of Japan, Vol.114, p.497-500, 1998
- [4] Kentaro Uemura: Study on ground improvement technology by the penetration infusion of mixed fine particles infusion materials, Tokyo City University doctoral dissertation, pp.59-80, 2018
- [5] Association of Japanese fly ash: Science, physical property, www.japan-flyash.com of the fly ash
- [6] JFE Steel Corporation: Steel slag product general catalog
- [7] Fuji gypsum: Material, www.fujisekkou.com called the gypsum

EVALUATION OF EARTHQUAKE-INDUCED SLOPE FAILURE HAZARD USING THE ANALYTIC HIERARCHY PROCESS METHOD

Masanori Kohno¹ and Yusuke Ono¹

¹Faculty of Engineering, Tottori University, Japan

ABSTRACT

Landslides or slope failures are often caused by an earthquake. The 2018 Hokkaido Eastern Iwate Earthquake and the 2016 Kumamoto Earthquake in Japan caused many slope failures widely and densely. This study suggested an earthquake-induced slope failure hazard mapping method using the analytic hierarchy process (AHP) and a geographic information system (GIS) for two specific districts: Atsuma district in Hokkaido and Minamiaso district in Kumamoto. The earthquake-induced slope failure hazard assessment system used here is based on the landslide distribution (NIED catalog, Japan) including tens of thousands of places in Atsuma and Minamiaso districts. We considered relationships between landslide distribution and factors of landslide hazard (elevation, slope angle, slope type, catchment degree, geology and vegetation). These relations were introduced to pairwise comparisons of factors in the AHP method. The AHP method was applied to evaluate slope failure hazard rank. An earthquake-induced slope failure hazard map was created based on the slope failure hazard rank of I-V. Two earthquake-induced slope failure distributions are almost consistent with the slope failure hazard rank. These results provide a practical method useful for evaluating earthquake-induced slope failure hazards.

Keywords: Earthquake-induced slope failure, AHP method, GIS, Landslide distribution

INTRODUCTION

Alteration by volcanic hydrothermal systems and the formation of crushing and weathering zones over geologic time have occurred widely throughout the Pacific region. As a result of these geologic processes, fragile geological features and steep topography can be found on the surface of the Earth. Landslides or slope failures are often caused by an earthquake. The 2018 Hokkaido Eastern Iwate Earthquake and the 2016 Kumamoto Earthquake in Japan caused many slope failures widely and densely (Fig. 1, Plots of slope failure distributions are based on GSI [1] and NIED [2]). The prediction of the risk of slope failure and establishment of appropriate measures is extremely important. However, the implementation of preventive measures in all locations that are at risk of slope failure is financially challenging. This necessitates the identification of slopes with a high risk of collapse and the implementation of investigative countermeasures based on the level of priority. Previous studies have tried the slope failure hazard mapping based on various techniques. More recently, many researchers and engineers studied the landslide hazard assessment using geographic information system (GIS) [3]–[9]. Furthermore, some researchers reported that method of evaluation of slope failure hazard using the analytic hierarchy process (AHP) method [6], [9]–[18]. This method can be eliminated subjective/empirical judgment of researchers/engineers. However, as the methods that use the AHP model are limited to evaluation within the

landslide topography, the method used in this study mainly considers re-active type landslides. This method was developed by several skilled engineers, who have conducted landslide surveys over many years. However, it largely depends on the subjective and empirical judgments of the evaluators, and it requires time and a high level of skill because the evaluation factors are subdivided.

This study suggested an earthquake-induced slope failure hazard mapping method using the AHP method and a GIS for two specific areas: Atsuma district in Hokkaido and Minamiaso district in Kumamoto. The Atsuma and Minamiaso districts are within the inner Kamuikotan metamorphic belt and Ryoke belt [19], respectively. Hence, the AHP and GIS analytical range in this study are these geological belt districts (Fig. 1).

METHODOLOGY

The AHP is a decision-making method developed by Saaty [20] and is also an analytical method that determines the importance weight of evaluation factors based on paired comparison. First, the relationship between the landslide topography area and the evaluation factors/elements area (i.e., the area ratio of the two) was statistically clarified based on the landslide distribution map [21] (Fig. 1) of Kamuikotan metamorphic belt and Ryoke belt. As shown in Fig. 2, this study is used raster data of landslide body. In this study, there are six evaluation factors related to the level of risk of landslide based on the AHP as follows: elevation, slope angle, slope

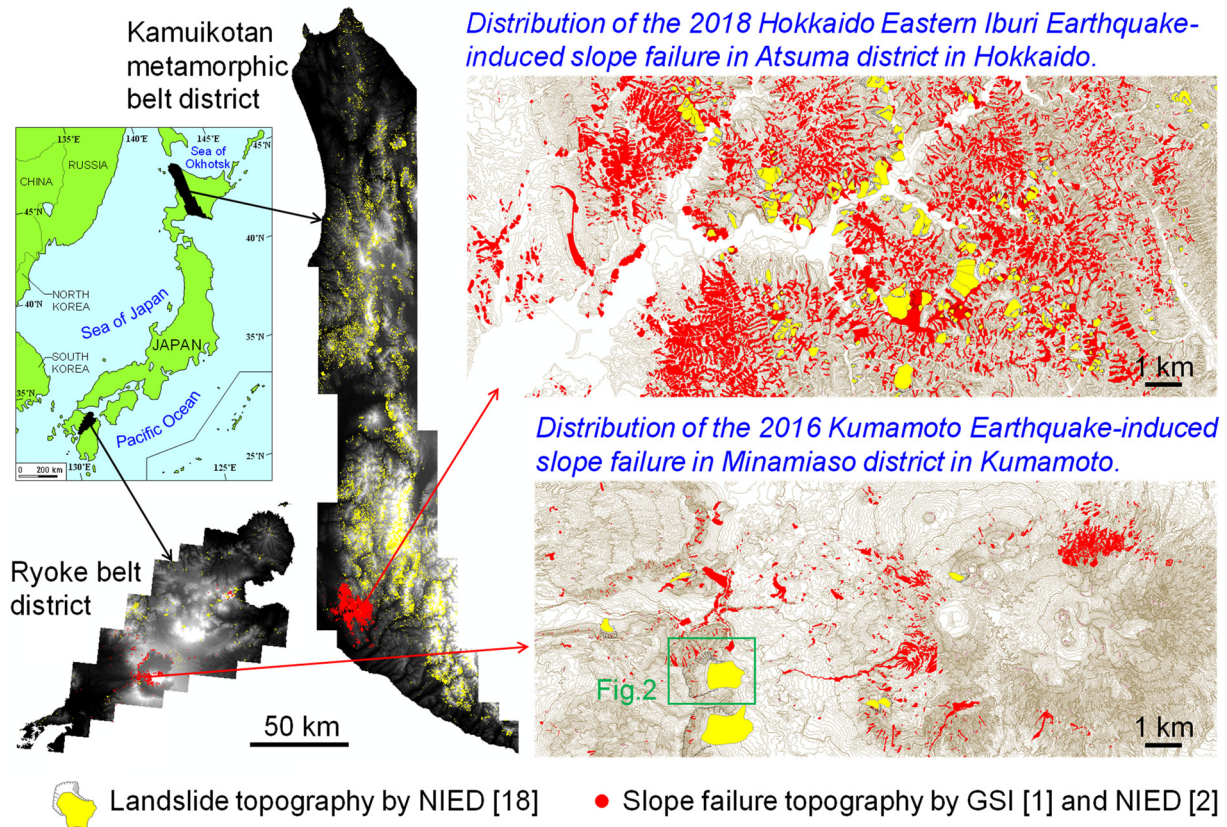


Fig. 1 Location of the study area (Kamuiikotan metamorphic belt and Ryoke belt districts), and distribution map of the landslides in Atsuma and Minamiaso districts.

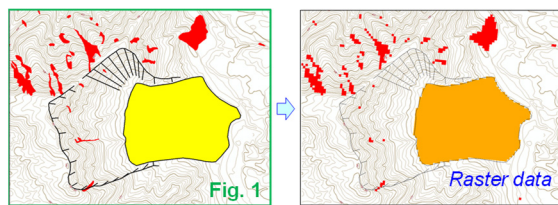


Fig. 2 Conversion of landslides topography to raster data (20 m × 20 m cell).

type, catchment degree, geology, and vegetation. The topographic, geological and vegetation data used in this study are Digital Elevation Model (DEM10B) by GSI [22], Seamless Digital Geological Map of Japan (1:200,000) by Geological Survey of Japan [23] and The Natural Environmental Information GIS by Biodiversity Center of Japan [24]. The slope type can be divided into 9 specific types (Fig. 3), based on Suzuki [25]. In the calculation of catchment degree, Terrain Analysis Using Digital Elevation Models [26] is incorporated into GIS.

A hierarchical system for landslide risk assessment was constructed based on these set of evaluation factors. From this hierarchical structure, the importance weight of each element is first calcu-

	Ridge slope (r)	Straight slope (s)	Valley slope (v)
Convex slope (X)	(Xr)	(Xs)	(Xv)
Rectilinear slope (R)	(Rr)	(Rs)	(Rv)
Concave slope (V)	(Vr)	(Vs)	(Vv)

Fig. 3 Basic classification of slope type (Based on Suzuki [25]).

lated, and then the importance weight between the higher evaluation factors is calculated. Saaty [20] gave a nine points scale. Equal importance is 1; moderate importance is 3; strong importance is 5;

very strong importance is 7; and absolute importance is 9. 2, 4, 6 and 8 are assigned for compromises between the above. That is the subjective and empirical judgment of the engineer is indispensable when using the AHP standard nine points scale. Therefore, in this study, the importance weights were calculated by introducing the statistical survey results of the relationship between the landslide topography distribution and the factors in the paired comparison. Landslide hazard mapping is conducted by ranking the landslide risk for each evaluation factor based on the estimated importance weight of each hierarchy and totaling the landslide risk scores applicable to each evaluation factor on each slope using GIS. Finally, evaluation factors with maximum impact are identified and their suitability is examined by comparing the composed landslide hazard map with the slope failure distribution due to earthquake.

EARTHQUAKE-INDUCED SLOPE FAILURE HAZARD MAPPING

Pairwise comparisons of factors in the hierarchy level 1 and 2

As an example, relationship between landslide distribution and factor (slope type), and the pairwise comparisons of factor (slope type) in the hierarchy level 2 are shown in Figs. 4 and 5. Slope failures are densely distributed in convex-ridge, concave-ridge, convex-valley and concave-valley slope type area. According to these results, it is thought that slope failure linked to earthquake is closely related to slope type. The weight of hierarchy level 1 (Fig. 6) is calculated based on Kohno et al [18]. The landslide hazard score p is calculated using the AHP hierarchy weight, and is given by Eq. (1) [18]:

$$p = \frac{W_1 W_2}{W_{2MAX}} \times 100 \quad (1)$$

where W_1 is the weight of hierarchy level 1, W_2 is The weight of hierarchy level 2, W_{2MAX} is the highest weight of hierarchy level 2. Landslide hazard mapping is performed on the basis of the hazard rank classified from I to V, with the totaled landslide risk score corresponding to each evaluation factor (overlaid using GIS; Fig. 7) for a certain slope (raster data: 20 m × 20 m cell), set as the total landslide risk score P . If the total score P is large, the risk of landslide is high, and if the score is small, the risk is low.

Landslide hazard mapping based on 6 factors

One example of landslide hazard map in Kamuikotan metamorphic belt and Ryoke belt distri-

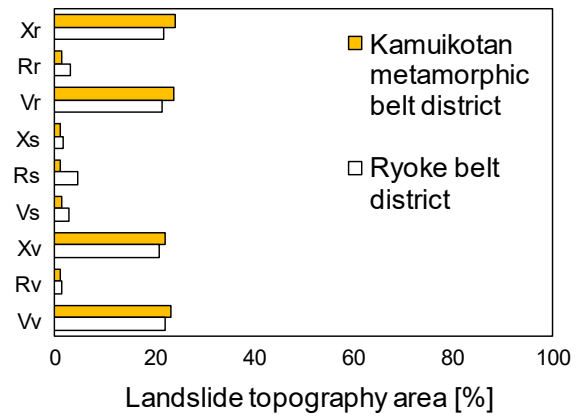


Fig. 4 One example of relationship between landslide distribution and evaluation factors (e.g. slope type). Abbreviations in this figure correspond to Fig. 3.

Level 2	Xr	Rr	Vr	Xs	Rs	Vs	Xv	Rv	Vv	weight
Xr	1	17.00	1.02	23.91	22.14	16.59	1.09	20.36	1.04	24.29
Rr	0.06	1	0.06	1.41	1.30	0.98	0.06	1.20	0.06	1.43
Vr	0.98	16.69	1	23.47	21.74	16.28	1.07	19.98	1.02	23.85
Xs	0.04	0.71	0.04	1	0.93	0.69	0.05	0.85	0.04	1.02
Rs	0.05	0.77	0.05	1.08	1	0.75	0.05	0.92	0.05	1.10
Vs	0.06	1.02	0.06	1.44	1.34	1	0.07	1.23	0.06	1.46
Xv	0.92	15.59	0.93	21.94	20.32	15.22	1	18.68	0.95	22.29
Rv	0.05	0.83	0.05	1.17	1.09	0.81	0.05	1	0.05	1.19
Vv	0.96	16.35	0.98	23.00	21.30	15.95	1.05	19.58	1	23.37

Fig. 5 One example of pairwise comparisons of evaluation factors (e.g. slope type) in the hierarchy level 2. Abbreviations in this figure correspond to Fig. 3.

Hierarchy level 1		A	B	C	D	E	F	weight
A	Elevation	1	0.67	0.60	1.80	0.71	0.83	13.64
B	Slope angle	1.50	1	0.89	2.70	1.07	1.25	20.43
C	Slope type	1.68	1.12	1	3.02	1.20	1.39	22.87
D	Catchment degree	0.55	0.37	0.33	1	0.40	0.46	7.57
E	Geology	1.40	0.93	0.83	2.52	1	1.16	19.09
F	Vegetation	1.20	0.80	0.72	2.17	0.86	1	16.40

Fig. 6 One example of pairwise comparisons of evaluation factors in the hierarchy level 1.

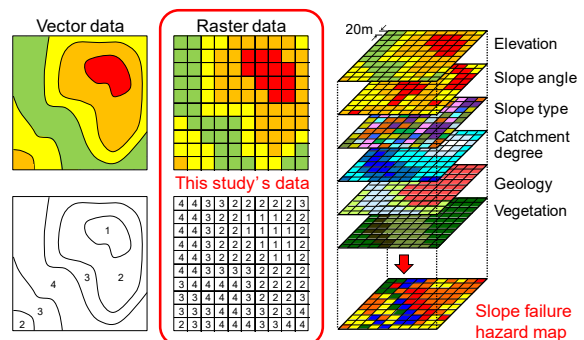


Fig. 7 GIS model's raster data overlaying.

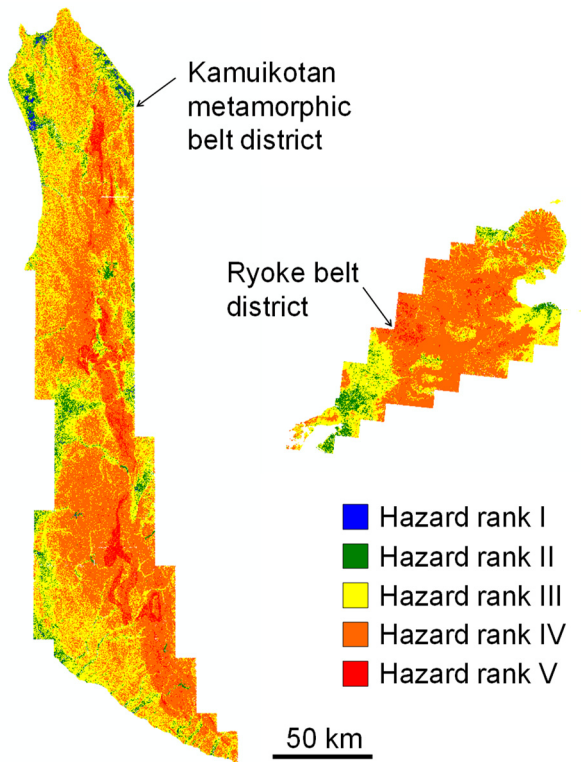


Fig. 8 One example of landslide hazard map in Kamukotan metamorphic belt and Ryoke belt districts.

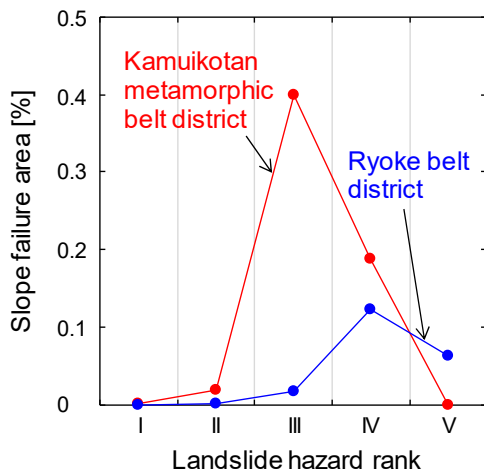


Fig. 9 Relationship between landslide hazard rank and slope failure distributions in the landslide hazard map of Fig. 8.

cts, and relationship between landslide hazard rank and slope failure area based on these maps are shown in Figs. 8 and 9.

The composed landslide hazard map clearly shows that landslides did not necessarily occur in areas with high landslide risk. Therefore, the landslide hazard map created using this method does

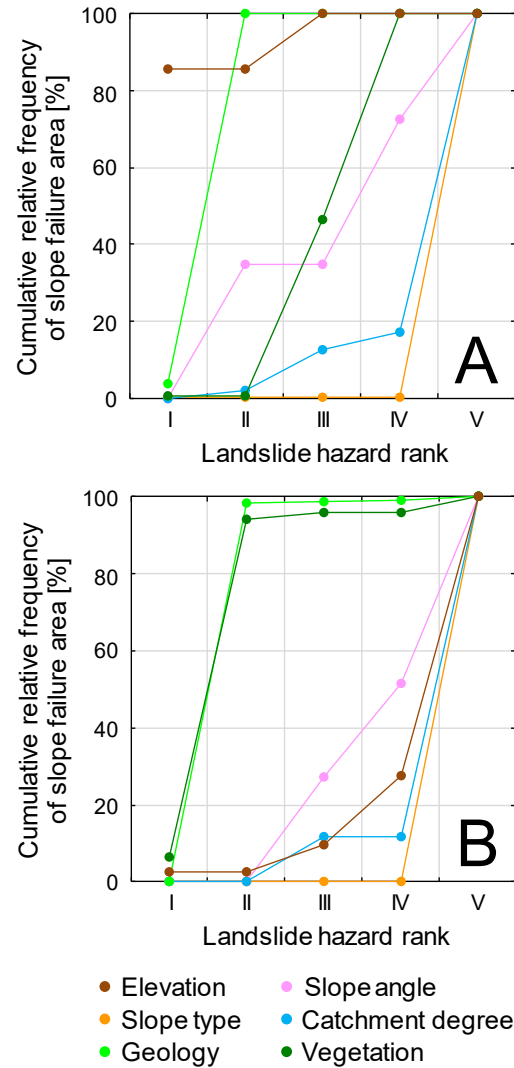


Fig. 10 Relationship between landslide hazard rank and cumulative relative frequency. Each weight of the hierarchy level is 99.9%. A: Kamukotan metamorphic belt district, B: Ryoke belt district.

not necessarily represent the slope failure distribution caused by earthquakes.

Landslide hazard mapping based on topographical factors

Thus, we investigated the factors among the evaluation factors that had maximum effect on slope failure. This method calculates the landslide risk score by positioning the importance of evaluation factors in hierarchy level 1 as 99.9 and the importance of other evaluation factors as 0.2 and performs landslide hazard mapping accordingly. As a result, relationship between landslide hazard rank and cumulative relative frequency is shown in Fig. 10. Slope angle, slope type, and catchment degree

were found to exert maximum effect on slope failure distribution due to earthquake in both districts. Therefore, we performed landslide hazard mapping by employing only slope angle, slope type, and catchment degree as evaluation factors and investigated the relationship between the composed hazard map and slope failure distribution. Relationship between landslide hazard rank and slope failure distributions in the landslide hazard map based on slope angle, slope type and catchment degree is shown in Fig. 11. With the increasing landslide hazard rank, the slope failure area shows the trend of increase. There was significant correspondence between all case hazard ranks and slope failure distribution.

CONCLUSION

This study suggested an earthquake-induced slope failure hazard mapping method using the AHP and a GIS for two specific districts: Kamuikotan metamorphic belt and Ryoke belt district.

In this study, the importance weights were calculated by introducing the statistical survey results of the relationship between the landslide topography distribution and the factors in the paired comparison in AHP. The AHP method was applied to evaluate slope failure hazard rank. An earthquake-induced slope failure hazard map was created based on the slope failure hazard rank of I-V. As a result, slope angle, slope type, and catchment degree were found to exert maximum effect on slope failure distribution due to earthquake in both districts: Atsuma district in Hokkaido and Minamiaso district in Kumamoto. There was significant correspondence between all case hazard ranks and two earthquake-induced slope failure distributions.

This study is used to identify the factors that are related to landslides, establish a relation between the factors and landslides, to predict the landslide hazard in the future based on such a relationship. Our methods provide a practical method useful for evaluating earthquake-induced slope failure hazards. Aiming at further development of evaluation of landslide hazard in the future, we will apply our method to various districts.

ACKNOWLEDGMENTS

This work was partly supported by research grant (Principal Investigator: Masanori Kohno) of Japan Society of Erosion Control Engineering, research grant (Principal Investigator: Masanori Kohno) of Chugoku Construction Public utility Association, and Grants-in-Aid for Scientific Research “KAKENHI” (Grant Number 18H01523, Principal Investigator: Yusuke Ono) of Japanese Society for the Promotion of Sciences (JSPS). These supports are gratefully acknowledged.

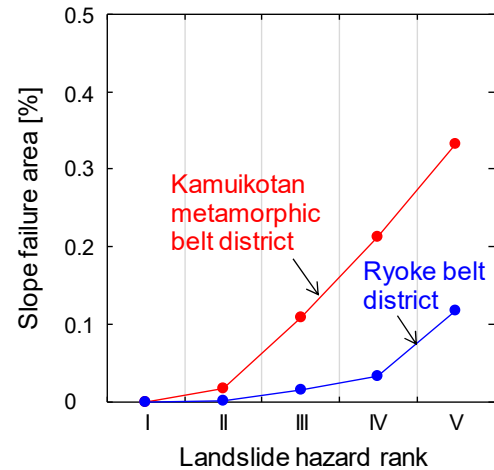


Fig. 11 Relationship between landslide hazard rank and slope failure distributions in the landslide hazard map based on slope angle, slope type and catchment degree in the Kamuikotan metamorphic belt and Ryoke belt districts.

REFERENCES

- [1] Geospatial Information Authority of Japan (GSI), Landslide distribution map by the 2018 Hokkaido Eastern Iburu Earthquake, 2018, <https://www.gsi.go.jp/BOUSAI/H30-hokkaido-iburi-east-earthquake-index.html> (in Japanese), Accessed April 2020.
- [2] National Research Institute for Earth Science and Disaster Resilience (NIED), Landslide distribution map by the 2016 Kumamoto Earthquake, 2016, <https://www.bosai.go.jp/mizu/dosha.html> (in Japanese), Accessed April 2020.
- [3] Nagata H., Sakaguchi T. and Kojima S., Analysis of topographic and geologic factors in unstable slope distribution using GIS, *Journal of the Japan Society of Engineering Geology*, Vol. 46, Issue 6, 2006, pp.320-330 (in Japanese).
- [4] Zhou G., Yokota N., Cheng G. and Kitazono Y., An advanced slope failure hazard mapping method by combining GIS and Hayashi's quantification methods theory, *Journal of the Japan Society of Engineering Geology*, Vol. 49, Issue 1, 2008, pp.2-12 (in Japanese).
- [5] Wang L., Sawada K. and Moriguchi S., Landslide susceptibility mapping by using logistic regression model with neighborhood analysis: A case study in Mizunami city, *International Journal of GEOMATE*, Vol. 1, Issue 2, 2011, pp.99-104.
- [6] Phukon P., Chetia D. and Das P., Landslide susceptibility assessment in the Guwahati City, Assam using Analytic Hierarchy Process

- (AHP) and Geographic Information System (GIS), *International Journal of Computer Applications in Engineering Sciences*, Vol. 2, Issue 1, 2012, pp.1-6.
- [7] Hamasaki E., Higaki D. and Hayashi K., Buffer movement analysis and blunder probability analysis for GIS-based landslide susceptibility mapping -A case study of the 2008 Iwate-Miyagi Nairiku Earthquake, Japan-, *Landslides – Journal of the Japan Landslide Society*, Vol. 52, Issue 2, 2015, pp.51-59 (in Japanese).
- [8] Priyono K.D., Jumadi, Saputra A. and Fikriyah V.N., Risk analysis of landslide impacts on settlements in Karanganyar, Central Java, Indonesia, *International Journal of GEOMATE*, Vol. 19, Issue 73, 2020, pp.100-107.
- [9] Tsuda H., Proposal for a new method on slope failures survey by AHP, *Landslides – Journal of the Japan Landslide Society*, Vol. 36, Issue 1, 1999, pp.4-11 (in Japanese).
- [10] Miyagi T., Prasad G.B., Tanavud C., Potichan A. and Hamasaki E., *Landslide risk evaluation and mapping -Manual of aerial photo interpretation for landslide topography and risk management-*, Report of the National Research Institute for Earth Science and Disaster Prevention, No.66, 2004, pp.1-137.
- [11] Yagi H., Higaki D. and JLS Research Committee for Detection of Landslide Hazardous Sites in Tertiary Distributed Area, *Methodological study on landslide hazard assessment by interpretation of aerial photographs combined with AHP in the middle course area of Agano River, Central Japan, Landslides – Journal of the Japan Landslide Society*, Vol. 45, Issue 5, 2009, pp.358-366 (in Japanese).
- [12] Pourghasemi H.R., Pradhan B. and Gokceoglu C., Application of fuzzy logic and analytical hierarchy process (AHP) to landslide susceptibility mapping at Haraz watershed, Iran, *Natural Hazards*, Vol. 63, Issue 2, 2012, pp.965-996.
- [13] Hasekioğullari G.D. and Ercanoglu M., A new approach to use AHP in landslide susceptibility mapping: a case study at Yenice (Karabuk, NW Turkey), *Natural Hazards*, Vol. 63, Issue 2, 2012, pp.1157-1179.
- [14] Kayastha P., Dhital M.R. and Smedt F.D., Application of the analytical hierarchy process (AHP) for landslide susceptibility mapping: A case study from the Tinau watershed, west Nepal, *Computers & Geosciences*, Vol. 52, 2013, pp.398-408.
- [15] Kohno M. and Maeda H., Experiment on landslide hazard mapping, based on AHP method, in consideration of point load strength of hydrothermally altered rock: -Example in the Ohekisawa-Shikerebenbetsugawa landslide area, Japan-, *Landslides – Journal of the Japan Landslide Society*, Vol. 50, Issue 3, 2013, pp.121-129 (in Japanese).
- [16] Kil S.-H., Lee D.K., Kim J.-H., Li M.-H. and Newman G., Utilizing the analytic hierarchy process to establish weighted values for evaluation the stability of slope revegetation based on hydroseding applications in South Korea, *Sustainability*, Vol. 8, Issue 1, 2016, 58.
- [17] Zhang J. He P., Xiao J. and Xu F., Risk assessment model of expansive soil slope stability based on Fuzzy-AHP method and its engineering application, *Geomatics, Natural Hazards and Risk*, Vol. 9, Issue 1, 2018, pp. 389-402.
- [18] Kohno M., Noguchi T. and Nishimura T., *Landslide hazard mapping in the Chugoku Region using AHP method and GIS, Japan-, Landslides – Journal of the Japan Landslide Society*, Vol. 57, Issue 1, 2020, pp.3-11 (in Japanese).
- [19] Isozaki Y., Maruyama S., Aoki K., Nakama T., Miyashita A. and Otoh S., Geotectonic subdivision of the Japanese Islands revisited: Categorization and definition of elements and boundaries of Pacific-type (Miyashiro-type) Orogen, *Journal of Geography*, Vol. 119, Issue 6, 2010, pp.999-1053 (in Japanese).
- [20] Satty T.L., *The Analytic Hierarchy Process*, McGraw-Hill Int. Book Co., New York, 1980, pp.1-287.
- [21] National Research Institute for Earth Science and Disaster Resilience (NIED), Digital archive for Landslide Distribution Maps, http://dil-opac.bosai.go.jp/publication/nied_tech_note/landslidemap/gis.html (in Japanese), Accessed April 2020.
- [22] Geospatial Information Authority of Japan (GSI), Digital Elevation Model (DEM10B), <https://fgd.gsi.go.jp/download/menu.php> (in Japanese), Accessed April 2020.
- [23] Geological Survey of Japan, National Institute of Advanced Industrial Science and Technology (AIST), Seamless Digital Geological Map of Japan (1:200,000), <https://gbank.gsj.jp/seamless/> (Basic version, data update date: 29 May, 2015) (in Japanese), Accessed April 2020.
- [24] Biodiversity Center of Japan, The Natural Environmental Information GIS, https://www.biodic.go.jp/trialSystem/top_en.html (in Japanese), Accessed April 2020.
- [25] Suzuki T., *Introduction to Map Reading for Civil Engineers Volume 1 -Geomorphological Basis for Map Reading-*, Kokon Shoin, Publishers, Tokyo, 1997, pp.1-200.
- [26] Tarboton, D., *Terrain Analysis Using Digital Elevation Models*, <http://hydrology.usu.edu/taudem/taudem5/>, Accessed April 2020.

ESTIMATION OF SUBSURFACE STRUCTURE BASED ON MICROTREMOR AND SEISMIC OBSERVATION IN THE DAMAGED AREA DUE TO 2018 HOKKAIDO EASTERN IBURI EARTHQUAKE, HOKKAIDO, JAPAN

Tatsuya Noguchi¹, Isamu Nishimura¹, Yusuke Ono¹ and Masanori Kohno¹

¹Faculty of Engineering, Tottori University, Japan

ABSTRACT

To investigate a cause of serious damages of the 2018 Hokkaido Eastern Iburi Earthquake, we observed microtremors and aftershocks at a landslide area and around strong ground motion observation stations. Subsurface velocity structures were determined by using a heuristic approach based on forward calculation by using phase velocities and H/V spectra. As a result, S-wave velocity structures were estimated, and predominant frequency of H/V spectra were obtained. The predominant frequencies of H/V spectra of the microtremor and seismic are 0.8Hz to 5Hz. The S-wave velocity of the uppermost layer is 75 to 130 m/s, and its thickness is around 10 m. Especially, it is suggested that the uppermost layer of volcanic ash had caused a landslide in the Atsuma Town sites. The predominant frequency corresponds to the thickness of alluvial layers with S-wave velocities of 75 to 300 m/s. It was also found that the predominant direction of the horizontal earthquake ground motion of the landslide was affected by the topography of the mountain.

Keywords: microtremor, S-wave velocity, the 2018 Hokkaido Eastern Iburi Earthquake, landslide

INTRODUCTION

The 2018 Hokkaido Eastern Iburi Earthquake occurred in the eastern Hokkaido Iburi district, and seismic intensity 6+ was recorded at several locations such as Atsuma, Abira, and Mukawa Town [1]. According to the seismic intensity distribution map estimated by the Japan Meteorological Agency, a seismic intensity area of 6+ or 7 was estimated over a wide area in the eastern region of Hokkaido Iburi [2]. This earthquake caused widespread landslides around Atsuma Town near the epicenter. In addition, buildings were locally damaged in Mukawa Town and Abira Town [3]. To study the causes of these damages, it is necessary to investigate the subsurface structure and strong ground motion characteristics. Therefore, in this study, we conducted microtremor observations at the site of landslide, the site of building damage, and the site where seismic intensity of 6+ or more was observed. In addition, temporary aftershock observations were also conducted at the site of landslide.

OBSERVATION

Microtremor observation

In this study, the following 5 points were targeted. These are the landslide site in Atsuma Town(ATM), the building damage site in Mukawa Town (MKW1), JMA observation point 'Shikanuma' where seismic intensity 7 was recorded (SKN), and K-NET observation point site HKD126 (MKW2), HKD127

(OIW) where seismic intensity 6+ was recorded. The location of the observation sites is shown in Fig. 1.

Microtremor array observation was conducted at all sites. A three-component acceleration type seismometer (JU410) was used for the observation. JU410 is a device that can record microtremors with a period of 0.05 to 10 seconds. In the array observation, four seismometers were used, one on the center of the circle and three on the circumference at equal intervals. Each device was synchronized with the GPS clock. The sampling frequency for measurement was 200 Hz, and the observation time was 15 minutes. The array radii were 1 m for ATM, MKW1, MKW2 and OIW, and 1 and 4 m for SKN. At the landslide site, one seismometer was installed

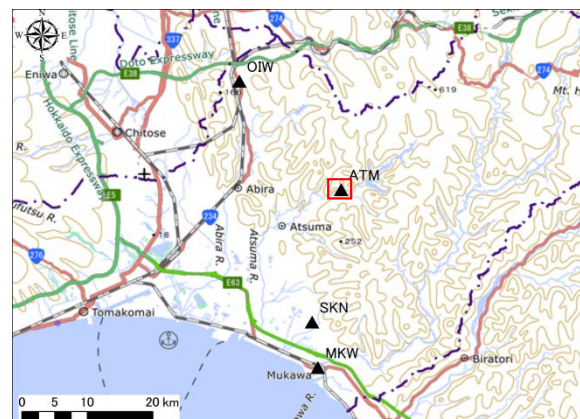


Fig.1 Location of the observation sites (Red line area is display area of Fig.5)

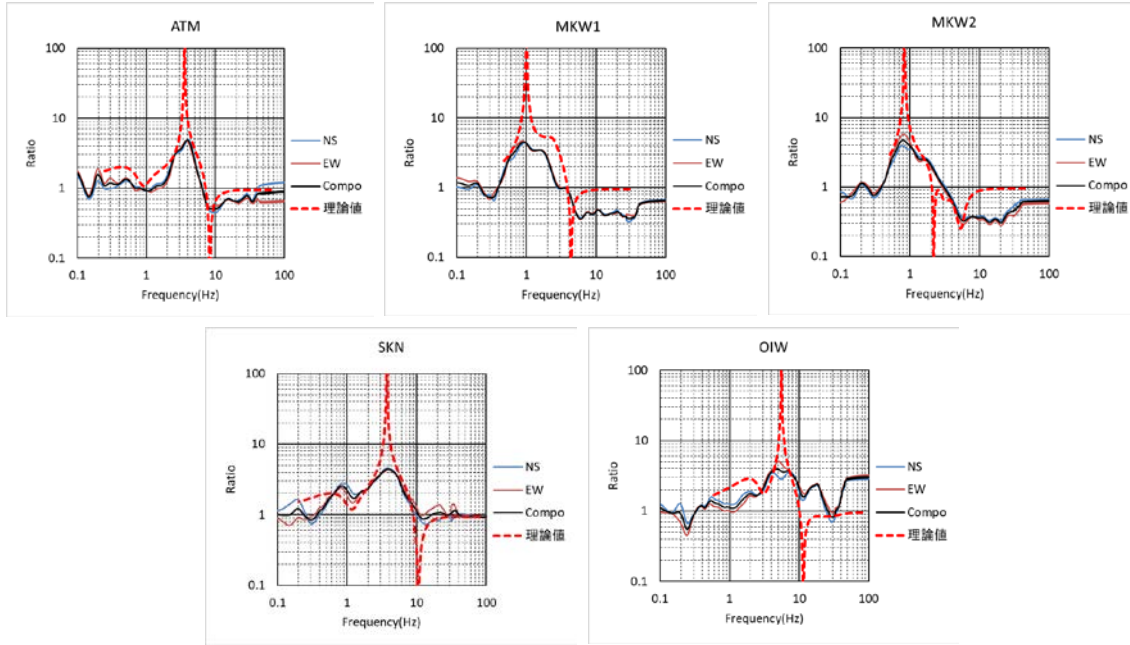


Fig.2 H/V spectra of microtremors (NS: North-South, EW: East-West, Comp: Composition, red dashed lines are the theoretical value of the Rayleigh wave by subsurface structure model)

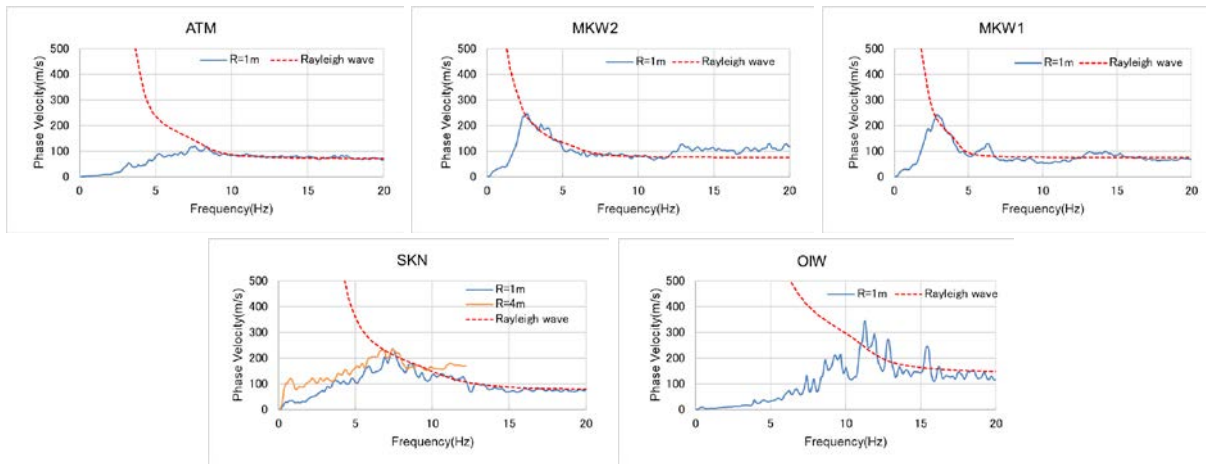


Fig.3 Dispersion curves of phase velocity (Solid lines are curves obtained for each radius. Red dashed lines are the theoretical value of the Rayleigh wave by subsurface structure model)

Table 1 Specifications of observed earthquake

Date and time	Latitude	Longitude	Depth	Magnitude
11/08/2018 0:54:32.2	42°33.7' N	141°56.2' E	24km	Mj 3.2
11/08/2018 11:15:13.4	42°13.7' N	141°23.5' E	104km	Mj 3.7
11/08/2018 11:34:24.8	42°47.1' N	142°0.5' E	37km	Mj 2.7

at the mountainside (ATM_T) and one at the foot (ATM_B) of the mountain. At this place, the sampling frequency for measurement was 100 Hz, and the observation time was 10 minutes. The ATM_B was installed at almost the same position as the array observation point (ATM), and the ATM_T was installed near the seismograph used in the seismic observation described later.

Temporary seismic observation

Temporary seismic observation was carried out from November 7th to November 8th, 2018 at the landslide site of Atsuma Town. For the seismic observation, we used a system in which a three-component velocity seismometer (KVS300) was connected to the data recorder (HKS9700) by a cable.

Table 2 Subsurface structure models

ATM				MKW1				MKW2			
Thickness (m)	ρ (t/m ³)	Vp(m/s)	Vs(m/s)	Thickness (m)	ρ (t/m ³)	Vp(m/s)	Vs(m/s)	Thickness (m)	ρ (t/m ³)	Vp(m/s)	Vs(m/s)
4	1.5	1370	75	9	1.2	1380	80	6	1.2	1380	80
3	1.6	1460	150	35	1.7	1570	250	15	1.5	1460	150
3	1.7	1620	300	80	1.9	1900	550	40	1.7	1570	250
60	1.9	1900	550	∞	2.2	2620	1200	40	1.9	1900	550
250	2.1	2070	700					∞	2.2	2620	1200
∞	2.2	2620	1200								

OIW				SKN			
Thickness (m)	ρ (t/m ³)	Vp(m/s)	Vs(m/s)	Thickness (m)	ρ (t/m ³)	Vp(m/s)	Vs(m/s)
2	1.5	1430	130	3	1.5	1380	80
5	1.6	1470	160	4	1.6	1460	150
30	1.9	1900	550	6	1.7	1620	300
60	2.1	2070	700	30	1.9	1900	550
∞	2.2	2620	1200	200	2.1	2070	700
				∞	2.2	2620	1200

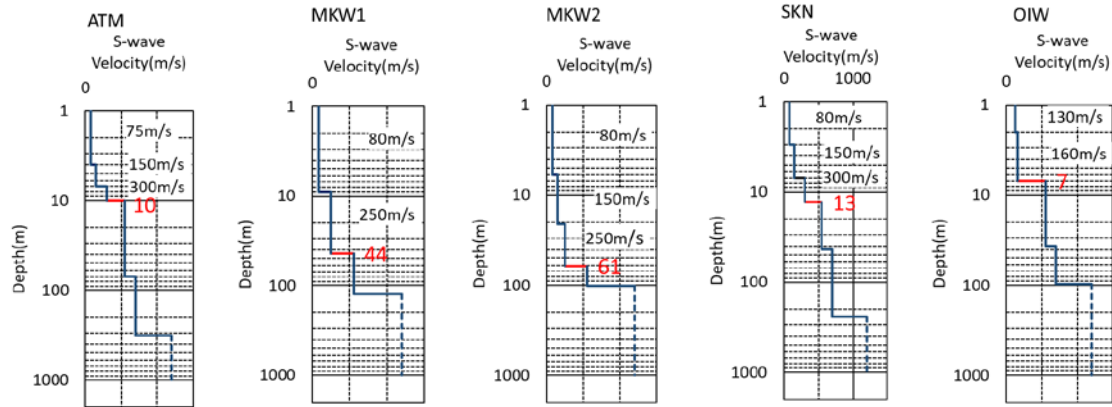


Fig.4 S-wave velocity structures (Black numbers are S-wave velocity value. Red numbers are depth to layer of $V_s=550$ ms)

The seismograph was buried near the ATM_T where the mountainside and no landslide occurred. The observation specifications are continuous recording at a sampling frequency of 200 Hz, time calibration with GPS clock, and battery drive. Three earthquakes could be recorded during the temporary observation during the observation period. The specifications of the observed earthquakes are shown in Table 1. The observation points are shown in described later Fig.5.

ANALYSIS

Microtremor observation data

For the analysis of the 3-component single-site observation data, portions of 20.48s without artificial noise were selected from the array observation records. A horizontal-to-vertical spectral ratio (H/V spectrum) was calculated by using the averaged each component Fourier spectra of the selected data. Horizontal components were composed. Spectra were smoothed by a log-window [4] with coefficient of 20. H/V spectra of each sites are shown in Fig.2.

For array observation data, the phase velocity

dispersion curves were estimated based on the CCA method [5]. The setting conditions for the analysis are as follows. At least 5 sections were selected by automatic extraction using the RMS value of the microtremor record of each seismograph with a segment length of 10.24 seconds. The power spectrum of these sections was smoothed by a Parzen window with a bandwidth of 0.3 Hz and then averaged. Using the power spectrum of each seismograph, the phase velocity dispersion curve was obtained based on the CCA method [5]. Dispersion curves of phase velocity are shown in Fig.3.

The velocity structures were determined on forward calculation based on borehole data of PS-logging and geological situation. We determined the subsurface structures to satisfy the H/V spectra and the dispersion curves of phase velocity by using fundamental mode of Rayleigh wave in the frequency range of 2 - 40Hz. The parameters of the subsurface structure models are number of layers, density, P-wave velocity; Vp, S-wave velocity; Vs and layers thickness. The physical property values of the subsurface structure models are shown in Table 2. The S-wave velocity structures are shown in Fig.4.

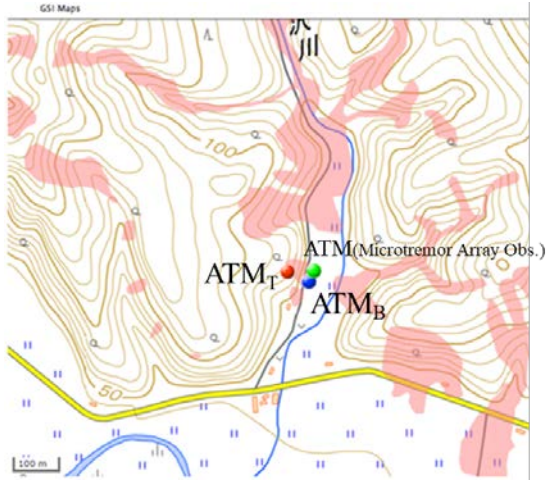


Fig.5 Location of observation and topographic map at landslide site (Orange area is landslide area)

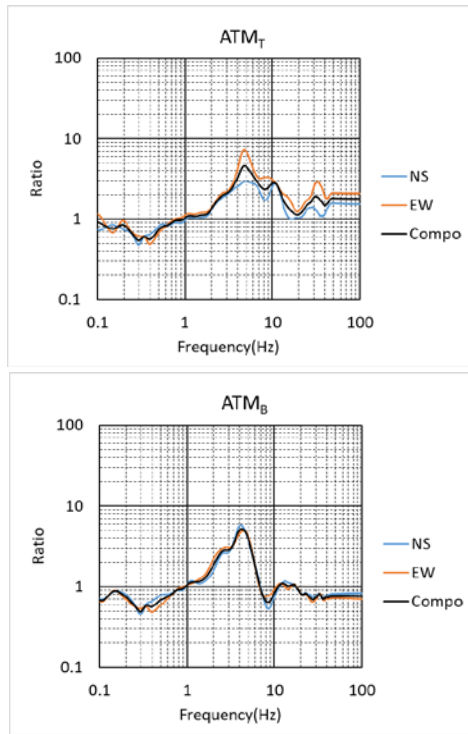


Fig.6 H/V spectra of microtremor in ATM site

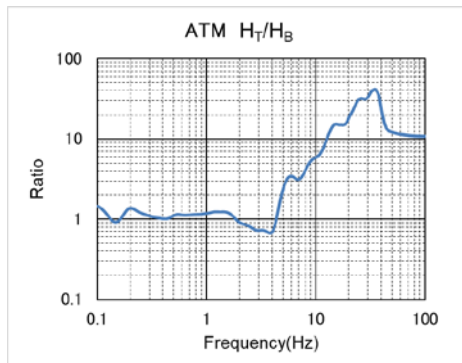


Fig.7 Horizontal spectral ratio H_T/H_B in ATM site

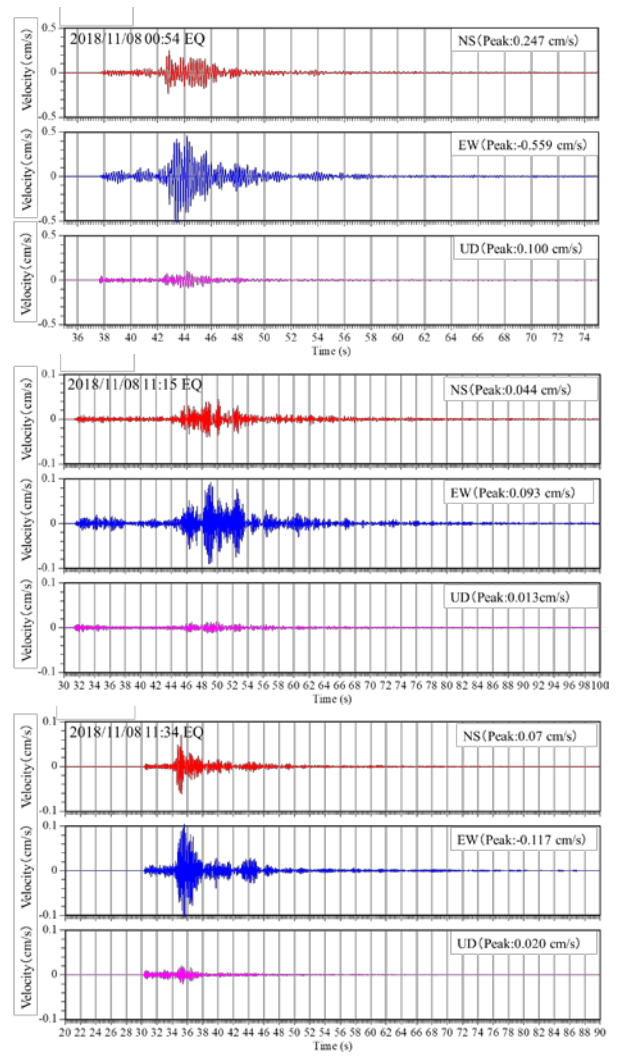


Fig.8 Velocity waveforms

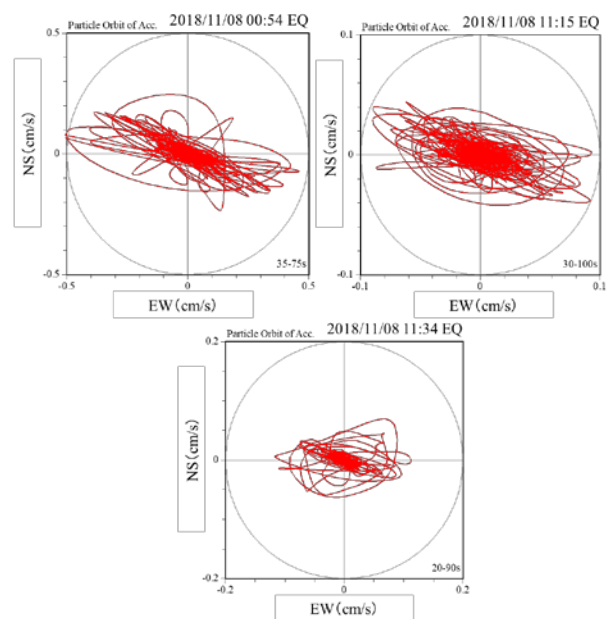


Fig.9 Particle motions of horizontal components

Seismic observation data

The data processing is as follows. 10.24 seconds of the S wave part of each component was cut out from the seismic record, and after applying a cosine taper with a half cycle of 0.5 seconds to both ends, zero data was added to 20.48 seconds. The Fourier spectrum of each component was calculated by smoothing with a Parzen window with a bandwidth of 0.2 Hz. The H/V spectrum was calculated from the Fourier spectra of these three components.

RESULTS

Microtremor H/V spectra

As a feature of the H/V spectra, there is clear peak at all points (Fig.2). The predominant frequencies of the H/V spectra are ATM: 3.96Hz, MKW1: 0.78Hz, MKW2: 0.93Hz, SKN: 3.86Hz, and OIW: 4.79Hz. The detailed situation of the H/V shape is as follows. There is a small peak at 1.14 Hz in SKN, and a small peak near 1.5Hz in MKW1, and there is a phenomenon that the shape near the peak is different in OIW.

S-wave velocity structures

The S wave velocity structure at each point is as follows (Table 2, Fig.4). The layer thickness of the soft soil layer ($V_s=80$ to 300m/s) is described. The layer thickness of the low-velocity layer is $V_s=80\text{m/s}$, 3-9m (OIW is none). The thickness of $V_s=150\text{m/s}$, 300m/s under the first layer is max 60m in Mukawa-town (MKW1, MKW2), and the thickness of the other sites is 7-10m. The geological condition of this area is that the ash layers of Tarumae volcanoes are widely distributed [6]. Therefore, it is considered that the first layer of the landslide site (ATM) corresponds to the volcanic ash layer of Tarumae Volcano, and that the first layer of the ground model corresponds to the collapsed layer. Layers with S-wave velocities less than 300m/s at other points correspond to alluvium or volcanic ash layers. As for the soil type of the alluvium, the layers of clay, gravel, and silt are alternated in Mukawa town, according to the PS logging information of K-NET (HKD126). In addition, it was reported that a non-linear ground response occurred at the earthquake observation point (HKD126) in Mukawa Town [7], which may be related to building damage. In the future, it is necessary to study the non-linear ground response based on the ground structure model obtained in this study and to clear the factors causing the damage.

The deep structure is as follows. The maximum layer thickness of the $V_s=550\text{m/s}$ and $V_s=700\text{m/s}$ layers is 80m and 250m, respectively. The $V_s=550\text{m/s}$ layer is considered to correspond to diluvial or volcanic sediments, and the $V_s=700\text{m/s}$

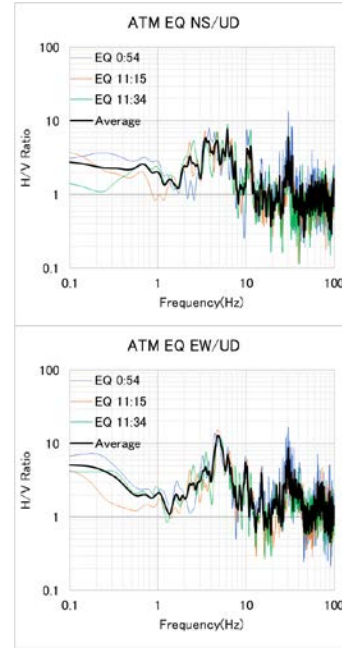


Fig.10 H/V spectra of earthquakes at ATM

and 1200m/s layers to tuff or Neogene sedimentary rocks. The estimation accuracy is lower than that of the shallow structure model because the dispersion curves of phase velocity were not obtained sufficiently in the frequency range required for analysis. However, the $V_s=550\text{m/s}$ and 700m/s layer thicknesses are reasonable results because they are almost consistent with the previous estimation results [7] of microtremor observation at HKD126.

Microtremors at landslide site

Location of observation and topographic map at landslide site is shown in Fig.5. Fig.5 is a map in which the area where the landslide occurred (orange area) is overlaid on the topographic map, and also shows the tremor observation points in this study. H/V spectra of the mountainside (ATM_T) and foot (ATM_B) of mountain are shown in Fig.6. The NS component of the horizontal motion is the blue line, the EW component is the orange line, and the composited value is the black line in Fig. 6. A clear peak can be confirmed around 5Hz at both points. There is a peak near 10Hz, which is higher than ATM_B in the high frequency band of 4Hz or more at ATM_T . Also, although the EW component is larger than the NS component in ATM_T , there is no difference in each component in ATM_B (Fig.6). The result of calculating the spectral ratio of the horizontal component H_T/H_B (combined values in NS and EW directions) to the spectrum between both points is shown in Fig.7. The H_T/H_B gradually increases in the frequency band from 4Hz to 30Hz (Fig.7).

Seismic ground motions at landslide site

The velocity waveforms of the three seismic records observed are shown in Fig.8. The particle motions of the velocity record of the horizontal component with the NS direction as the vertical axis and the EW direction as the horizontal axis are shown in Fig.9. The H/V spectra are shown in Fig.10 (The black line shows the average of the three earthquake values). The amplitude of the EW component is larger than that of the NS component for all earthquakes (Fig.8). From the particle motions of horizontal component, the EW direction is predominant, and the axis of the predominant direction is slightly rotated clockwise (Fig.9). Furthermore, from the topographic map (Fig.5) near the observation point, the direction of the slope is almost the same as the predominant direction of the particle motion. The characteristic of H/V is that the EW component is larger than the NS component near the peak of 5Hz (Fig.10). It is possible that such seismic motion characteristics contributed to the landslide. In the future, it is necessary to study the factors that cause these phenomena in more detail and clear the mechanism of landslide caused by this earthquake.

CONCLUSIONS

- 1) In Mukawa Town, the predominant frequency of microtremor H/V was 0.8 - 0.9Hz, and it was found that the soft soil layers with $V_s=80 - 300\text{m/s}$ was thickly deposited in the ground structure. It is considered that this layer amplified the ground motion, and the possibility of nonlinear response was also suggested.
 - 2) The predominant frequency of microtremor H/V at other seismic stations was 4 Hz at Shikanuma, the JMA site of Atsuma Town, and 5 Hz at K-NET site HKD127, Abira Town. From the ground structure model, it was found that there were soft soil layers at those points and the layer thickness was thinner than that of K-NET site HKD126 in Mukawa Town.
 - 3) At the landslide site in Atsuma Town, the predominant frequency of microtremor H/V is 5Hz, and the subsurface structure has a volcanic ash layer with $V_s=75 - 80\text{m/s}$. It is possible that this layer collapsed on the slope near this point.
 - 4) As for the characteristics of microtremors and seismic motions at the landslide site, it was found that the amplitude of the EW component seismic motion is larger at the mountainside than at the foot of mountain. In addition, it was found that the characteristics of the H/V spectra were that the spectral ratio was larger in the frequency band higher than 4Hz and that the EW component was larger near the peak of 5Hz in the seismic ground motion.
- In the future, we plan to evaluate the earthquake

motion based on the information obtained from the observation. Furthermore, based on the results, we plan to examine the factors causing the strong ground motion and the factors causing the landslide caused by the earthquake.

ACKNOWLEDGMENTS

We used seismic intensity information from the Japan Meteorological Agency, and the borehole information on K-NET and KiK-net of the National Research Institute for Earth Science and Disaster Prevention. We used the basic map information of the Geospatial Information Authority of Japan as the base map for the location of the observation points.

REFERENCES

- [1] JMA website “Seismic intensity database”, (<https://www.data.jma.go.jp/svd/eqdb/data/shindo/Event.php?ID=9901267>), (in Japanese).
- [2] JMA website “Estimated seismic intensity distribution map, 03:08 on September 06, 2018 Iburi district Middle East M6.7”, (https://www.data.jma.go.jp/svd/eeew/data/suikai/201809060308_146/201809060308_146_1.html), (in Japanese).
- [3] Cabinet Office Japan website “Disaster management in Japan”, (http://www.bousai.go.jp/updates/h30jishin_hokkaido/pdf/310128_jishin_hokkaido.pdf), (in Japanese).
- [4] Konno K. and Ohmachi T., A smoothing function suitable for estimation of amplification factor of the surface ground from microtremor and its application, *Journal of JSCE*, No.524/1-33, 1995, pp.247-259 (in Japanese with English abstract).
- [5] Cho I., Tada T., and Shinozaki Y., Centerless circular array method: Inferring phase velocities of Rayleigh waves in broad wavelength ranges using microtremor records, *Journal of Geophysical Research*, 2006, Vol.111, B09315.
- [6] Hirose W., Kawakami G. Kase Y., Ishimaru S., Koshimizu K., Koyasu H. and Takahashi R., Preliminary report of slope movements at Atsuma Town and its surrounding areas caused by the 2018 Hokkaido Eastern Iburi Earthquake, Report of the geological survey of Hokkaido, Vol.90, 2018, pp.33-44 (in Japanese).
- [7] Takai N., Shigefuji M., Horita J., Nomoto S., Maeda T., Ichiyonagi M., Takahashi H., Yamanaka H., Chimoto K., Tsuno S., Korenaga M. and Yamada N.: Cause of destructive strong ground motion within 1–2 s in Mukawa town during the 2018 Mw 6.6 Hokkaido eastern Iburi earthquake, *Earth, Planets and Space*, Vol. 71, 2019, 10.1186/s40623-019-1044-4.

STUDY ON COLLAPSE MECHANISM OF RIVER LEVEE DUE TO EXTERNAL WATER LEVEL FLUCTUATION

Hayato Suzuki¹, Shin-ichi Kanazawa², Yudai Tonoki¹

¹ Social Environmental Systems Engineering Course, National Institute of Technology, Fukushima College,
Advanced Course Program, Japan

² Civil and Environmental Engineering, National Institute of Technology, Fukushima College, Japan

ABSTRACT

In recent years, extreme weather events related to global climate change have caused enormous damage in Japan. Catastrophically, riverbanks have been repeatedly destroyed by heavy rain in various parts of Japan. Among them, the damage caused by Typhoon No. 19 in 2019 was the most serious. Fundamentally, a river embankment is a very important disaster prevention structure to protect riverside residents from damage, such as that caused by flooding. For this reason, we must ensure sufficient safety. However, design methods based on the current guidelines are not based in well-established technical knowledge. In order to prevent collapse, it is urgently necessary to elucidate the collapse mechanism of riverbanks. Therefore, in this study, we investigated the collapse mechanism of the river embankment through model experiments, and we analyzed the factors contributing to collapse. We aimed to understand the difference in permeation surface formation due to the difference in the speed of water level rise and layer thickness. In addition, a soil moisture meter was used to check the change in saturation inside the model. The experiments were performed with a total of 4 treatments at layer thicknesses of 20 mm and 40 mm and rates of water level rise of 3.5 cm / min and 7.0 cm / min.

Keyword: River Embankment , External water level fluctuation , Model experiment , Unsaturated soil

RESEARCH BACKGROUND AND PURPOSE

In recent years, global climate change has caused enormous damage in Japan. As one of the worst outcomes, riverbanks have been repeatedly destroyed by heavy rains in various parts of Japan. The Kinugawa embankment collapse during heavy rain in the Kanto and Tohoku regions in September 2015 and Typhoon No. 19, which caused damage to all parts of Japan, in October 2019 describe just some examples. In recent years, severe damage has also been caused by local heavy rainfall. Fourteen people died in heavy rains in the Kanto and Tohoku regions and many houses floated away due to river dike collapse (totally destroyed: 81 buildings, half destroyed: 7045 buildings, floor flooding: 2495 buildings, underfloor flooding: 13159 buildings. [1] In typhoon 19, 66 died, 13 went missing and 398 were seriously injured. In addition, the embankment collapsed into 71 rivers, including first-class rivers such as the Chikuma River and Abukuma River. Housing and welfare facilities were also severely damaged, (totally destroyed: 85 buildings, half destroyed: 324 buildings, floor flooding: 24266 buildings, underfloor flooding: 21474 buildings) , resulting in a major disaster. [2] In Japan, such disastrous events have occurred one after another in recent years. A river embankment is an extremely important disaster prevention structure to protect the lives of riverside residents from floods and other disasters.

Therefore, it is necessary to secure sufficient safety. External factors related to inundation of riverbanks include overflow, scouring, and seepage. These three factors are caused by rainfall. To date, when we glimpse the current situation, where regulations on design and maintenance of river levees have not been clarified, the role of these structures as disaster prevention for floods caused by recent local heavy rainfall have become extremely important. However, design methods based on the current guidelines are not based on well-established technical knowledge. Moreover, because collapse mechanisms are not fully understood, it is urgently necessary to clarify the collapse mechanisms of river embankment.

Therefore, in this study, we conducted an experiment that focus on the piping phenomenon, for which the cause is more complicated. This was attempted because we thought it necessary to review the system of embankment design, which required knowing the structure and content of river embankment. Therefore, we prepared various treatments to confirm what kind of influences are exerted in each collapse mode. To achieve this purpose, we conducted an infiltration experiment using a model embankment. A soil moisture meter (EC-5) was installed inside the model to measure saturation. A model embankment was prepared by setting the rate of water level rise at 1.4 cm / min and 7.0 cm / min and the layer thickness at 20 mm and 40 mm.

From this, the difference in the collapse form and the transition of saturation were examined. A video of the formation of the infiltration surface was also recorded.



Fig.1 Chikuma River at Typhoon No. 19

THE PROCESS OF RIVER EMBANKMENT COLLAPSE

According to the current guidelines, dikes made of soil can easily cause floods and overtopped levees. This occurs even if the flood level is below the planned water level, as the levee may be damaged due to infiltration and erosion, may lead to bank damage.

The process of bank breakage due to each cause is shown below.

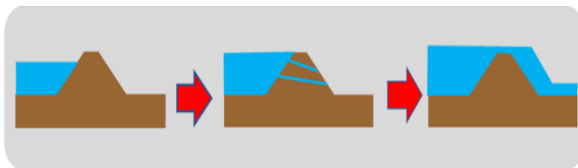


Fig. 2 Levee overtopping process



Fig. 3 Osmotic collapse process

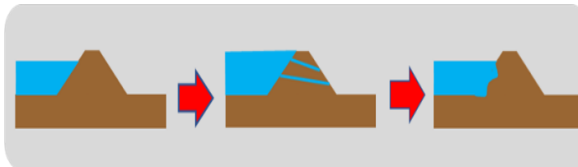


Fig.4 Washbori process

Levee damage due to erosion and overflow is caused by the movement of soil particles that make up the dam body. This occurs by eroding the dam surface or the dam skirt by the scavenging force of running water or overflow water during flooding. It is speculated that weakening of the surface of the bank due to the infiltration of rainfall is closely related. On the other hand, levee damage due to infiltration increases pore water pressure due to the

infiltration of river water or rainfall at the time of flood into the levee body and the foundation ground. This reduces the apparent strength of the levee body. Rainfall not only weakens the surface layer of the dam or levee, but it also increases the saturation within the soil of the embankment. This internal water flow can move soil particles leading to internal erosion or piping, a major cause of embankment weakening.

In addition, when a large earthquake occurs, the levee is largely submerged and deformed due to the liquefaction of the foundation ground. In such cases, river water constantly flows into the inside of the levee in the zero meter area. It is also assumed that a disaster will occur in these instances. [3]

PHYSICAL PROPERTIES OF SOIL

Prior to the model experiment, the properties of silica sand Nos. 6, 7, and 8 mixed sand (mixing ratio 5: 2: 5) used for the embankment were set to the following physical properties, according to the guidelines of the Geotechnical Society. A description of each test procedure to obtain the physical properties is omitted, and the test results are described below.

- ① Compaction test
Optimum water content : 8.2%
Optimum dry density : 1.570g/cm³
- ② Soil particle test
 $\rho_s=2.61\text{g/cm}^3$
- ③ Relative density test
Relative density : 15.03%(Therefore loose sand)
- ④ Particle size test
Effective particle size : 2.10
Uniformity coefficient : 10.36
Curvature coefficient : 2.05
Fine grain content rate : 12.7%

From the results of these tests, it was found that the model sample was classified as "sand containing SF fine particles" using triangular coordinates.

It was found that this sample had a poor composition and was prone to penetration and disintegration. In this experiment, the infiltration phenomenon and the collapse form of the river embankment are examined. As the samples exhibiting the above-described measured physical properties can remarkably demonstrate test results, they are therefore considered suitable for this test.

EXPERIMENT OUTLINE

As shown in Fig. 5, a 0.1m foundation ground and embankment were prepared in a 1.4m × 0.7m × 0.3m acrylic soil layer. Silica sand Nos. 3 and 5 were used at the foundation ground of 0.08 m and

0.02 m, respectively. In addition, silica sand Nos. 6, 7, and 8 were mixed at 5: 2: 5 for the embankment.

The dimensions of the embankment were 200 mm in height, 1: 2 slope and 100 mm width at the top.

When preparing the embankment, a soil moisture meter (EC-5) was inserted at each point 1 to 8, as shown in Fig. 5, to measure the degree of saturation. In this case, each number from 1 to 8 is each CH number. In the experimental procedure, the flow rate is set from the right side of the soil layer to raise the water level. Regarding the water level rise, the rate of rise in water level was increased by 1.4 cm / min or by 7.0 cm / min by referencing the rainfall data of the Chikuma River during Typhoon No. 19 in October 2019. If the water level rises directly into the foundation ground, it may be eroded by water pressure, so a space was provided between the foundation ground and the water inlet. It can be said that the provision of this space improved the reproducibility of the experiment by approaching the phenomenon of an actual river embankment. Moreover, two treatments were used for the layer thickness of the embankment, 20 mm and 40 mm.

Combining each rate of water level rise with each layer thickness, the experiment was conducted with a total of four treatments, or cases. Each case was set as shown in Table 1 below. The vertical is the layer thickness, and the horizontal is the speed of water level rise. In addition, the change in saturation at each measurement point until the embankment collapse was recorded with data collection software, and the appearance of the infiltration surface was recorded by video.

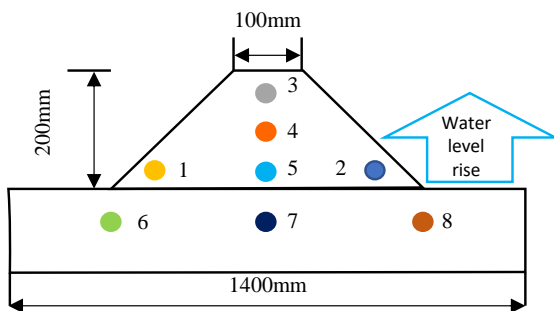


Fig. 5 Manufacturing embankment map

Table 1 Case settings

	Water level rising speed 1.4cm/min	Water level rising speed 7.0cm/min
Layer thickness 20 mm	Case1	Case2
Layer thickness 40 mm	Case3	Case4

Rate Of Water Level Rise

The speed of water level rise was calculated by referring to the rainfall data of the Chikuma River during Typhoon No. 19, which occurred in October 2019, with reference to the fast and slow rates of rise.

We set 7.0 cm / min for the fast case and 1.4 cm / min for the slow case, converted them to L / min, and set the flow rate to achieve these fast and slow water level rises. In order to maintain a constant rate of water level rise from the start of water level rise to overflow, the space for increasing the transition on the side of the embankment was divided into three equal parts, and the flow rate in each section was calculated using the volume. The experiment was conducted by adjusting the flow rate for each.

Saturation Measurement Method

A soil moisture meter "EC-5", a data logger and data collection software were used to measure the degree of saturation inside the embankment. EC-5 outputs soil moisture as a voltage from the permittivity of soil. A calibration formula for converting the output voltage value into soil moisture was prepared in advance, but the embankment material used in the experiment was recalibrated to improve the accuracy. Since each EC-5 had individual differences, we calibrated each of the eight EC-5 used.

EXPERIMENTAL PROCEDURE

If the layer thickness was 20 mm, it was divided 10 times, and if the layer thickness was 40 mm, it was divided 5 times. Using this process, the embankment was prepared.

The moisture content was set to 6.2% in order to focus on the formation of the infiltrated surface and the morphology of fracture. This is because $\pm 2\%$ of the optimum water content is allowed according to actual construction guidelines. In addition, the reason why -2% was used is that 6.2% was considered to be capable of producing an embankment with a smaller dry density and a weaker state than the compaction test.

The experimental procedure was as follows.

① Fabrication of foundation ground

The required amount of silica sand No. 3 was placed in the soil layer and tamped to a height of 80 mm. The necessary amount of silica sand No. 5 was added and tamped to a height of 20 mm.

② Making the model embankment

The soil amount calculated for each layer to a specified density (dry density: 1.545) was mixed with water to a water content ratio of 6.2% and compacted until it reached a height of 20 mm or 40 mm (after tamping). After completion of compaction,

the model was cured for 1 day and excess soil was removed.

The slope surface was made smooth.

③ Recording

A video camera was used to take a picture of the formation of the infiltrated surface and the state of the bank breakage inside the dam. The EC-5 were used to record the saturation monitoring inside the dam.

④ Water level rise

The water level was provided at the set discharge, with reference to the rainfall data of the Chikuma River.

EXPERIMENTAL RESULT

Results shown in Fig. 5 confirm that in case 1 the infiltration surface was formed up to the inner side of the embankment as the water level increased, and over time the infiltration surface was formed from the slope on the inner side of the embankment to the upper part of the embankment. Results also confirmed that the degree of saturation increased at each point, corresponding to the timing of the infiltrated surface formation. It is highly probable that a landslide created at the bottom of the sediment was caused by lateral infiltration pressure and buoyancy from below due to the inundation from the ground and the lower part of the dam body. The dike weakened and collapsed. Next, results shown in Fig. 6 confirm that in case 2, the infiltrated surface was formed in the shape of an arc from the outside of the embankment, and the inundation was caused by overflow before the infiltration reached the inside of the embankment. However, the water content increased at the point where no infiltrated surface was formed (CH1, 6). From this, it can be inferred that water channels were formed. In case 2, unlike case 1, the saturation value remained low as a whole.

Therefore, the infiltration phenomenon likely has little effect on the collapse form because the permeated flow rate is small. Next, the experimental results for a layer thickness of 40 mm are discussed.

As shown in Fig.7 for case 3, when the layer thickness is 20 mm, water permeates the entire embankment area and enters from the foundation ground and the lower part of the dam body. Due to the buoyancy from below, the toe of the embankment became weak and the embankment broke at this point. In case 4, as shown by Fig. 8, the levee was breached by overflow before water penetrated the entire embankment. The saturation change and the process of infiltrated surface formation are shown below. As described above, since there was no difference in the morphology due to a change in layer thickness, we consider the difference in morphology to be caused by the rate of water level rise. Figures 6 and 8 show the saturation transitions for cases 1 and 3. After the water level

rose, saturation reached 100% in the order of the area outside the embankment (2, 8) → the lower part of the embankment (5, 7) → the central part of the embankment (4) and the area near the embankment (1, 6) → the upper part of the embankment (3).

About 18 minutes after the water level started rising, the saturation level of the entire levee reached 100%.

In addition, the transitions of saturation in case 2 are shown in Figs. 7 and 9. After the water level rose, the saturation level increased from the outer levee to the outer basin (2,8) to the lower part of the levee body (5,7), and about 8 minutes after the water level rose, the levee broke due to overflow. At this point, the saturation level of the levee (1 and 6) and the upper part of the levee (4 and 3) increased. From this, it was confirmed that when the water level rises quickly, the levee breaks due to overflow before the water penetrates the entire levee body. It was also confirmed that when the water level rises slowly, it penetrates into the entire levee body and the bottom of the dike inside the levee becomes weak and breaks. These results demonstrate that water penetration rate in cases 2 and 4 was faster than in cases 1 and 3.

Fig.6-9 shows the saturated boundary formed in the in the infiltration. Also, Fig.14-17 shows the final collapse morphology in each case.

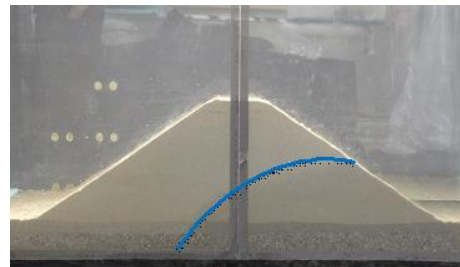


Fig.6 case1 (Layer thickness 20 mm: 1.4 cm / min)

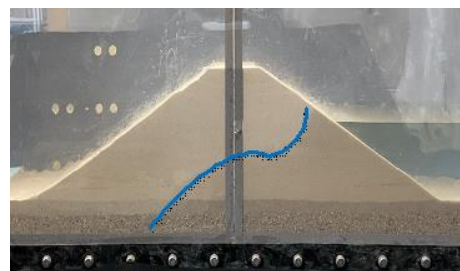


Fig.7 case2 (Layer thickness 20 mm: 7.0 cm / min)

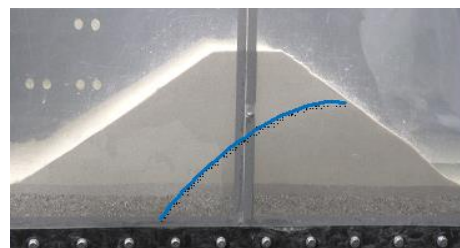


Fig.8 case3 (Layer thickness 40 mm: 1.4 cm / min)

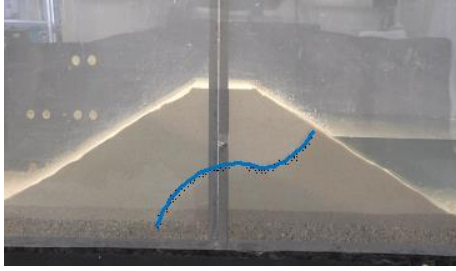


Fig.9 case4 (Layer thickness 40 mm: 7.0 cm / min)

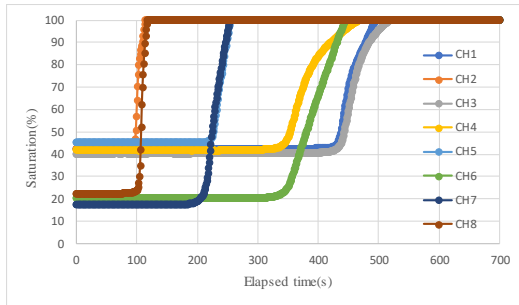


Fig.10 Transition of saturation (case1)

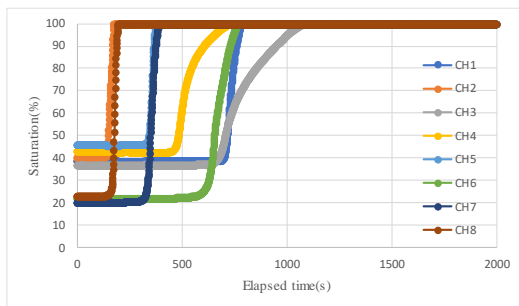


Fig.11 Transition of saturation (case2)

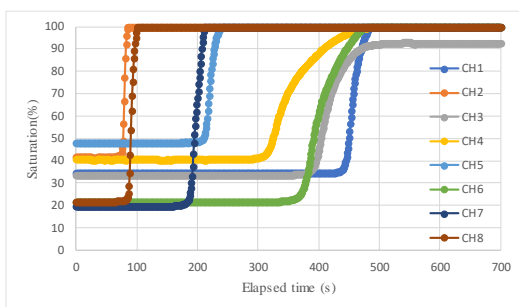


Fig.12 Transition of saturation (case3)

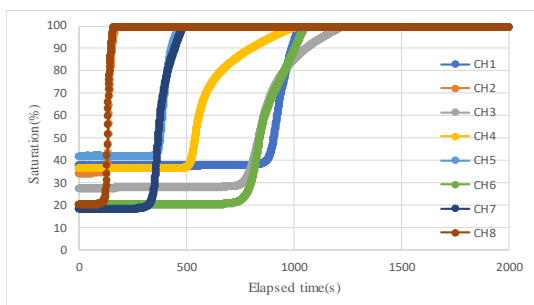


Fig.13 Transition of saturation (case4)



Fig.14 case1 Collapse form



Fig.15 case2 Collapse form



Fig.16 case3 Collapse form



Fig.17 case4 Collapse form

CONCLUSION

The experimental results confirmed that layer thickness did not influence the collapse form, which largely depended on the degree of water level rise in the tank. In case 1 and case 3, the infiltrated surface was formed from the area outside the embankment to the area near the embankment, but in CH1, 3, 6 the saturation level started to rise at almost the same time. Figures 6 and 8 confirm that CH1 and CH6 reached the saturation level of 100% a little faster. The reason for this is likely that the infiltrated surface was formed earlier from the foundation ground / lower part of the levee body, and buoyancy was generated inside the levee, causing saturation. This suggests that collapse was caused by osmotic pressure from the lateral direction and the buoyancy force from the downward direction on the bottom of the dike in the embankment, which is likely a weak area. The structure inside the levee should be reviewed with a slow water level rise. Also, case 2 and case 4 confirm that the infiltrated surface was formed vertically from the outer side of the embankment and about half of the embankment was infiltrated and destroyed by overflow. In this case, the structure inside the levee body was not very relevant, and there was no evidence of collapse on the outside of the levee surface. Therefore, the height of the levee body itself or reinforcement of the inside levee can prevent disasters. Since the change due to the layer thickness was small, the results of the rate of water level rise are summarized as follows.

(1) Case1 and case3

The infiltrated surface was found to form up to the inside of the embankment and then infiltrated into the crown as the water level rose.

It was found that the infiltrated surface penetrated into the entire levee body and gradually collapsed in the vicinity of the underground levee.

(2) Case2 and case4

The infiltrated surface was found to form vertically and then penetrated into the embankment side in this way.

It was found that before the water penetrated the entire bank, the levee collapsed due to overflow.

Mr. Tsuneoka and Mr. Furumoto, Ms. Obata, Mr. Wakasa [4] stated that the entire embankment will reach a nearly fully saturated state when the infiltration surface rises without any measures.

This also confirms the validity of this experiment. In addition, Mr. Sekine and Mr. Sato, Mr. Kan [5] stated that the movement of debris leads to the

destruction of the formation of the terrain on the step, resulting in the promotion of collapse.

It is necessary to confirm not only the layer thickness and the rate of water level rise, but also the soil mix, the type of silica sand used, and the compaction strength to confirm changes in the collapse mode of the embankment in various states.

It is also important to note that there is no fundamental difference in the degree of basic bonding between soil particles and the effect of adhesive force within the bank. Understanding these needs, this experiment provides useful information and knowledge for considering the failure mechanism of actual embankment.

In addition, Mr. Fukuhara and Mr. Mori, Mr. Hattori [6] have conducted experiments using plants collected from actual embankments, and the erosion resistance of the high-stem herbaceous plants that grow on the river embankment is mainly due to the resistance of leaves and stems in the upper part of the vegetation. This resistance is exhibited when the flow velocity is reduced. In the future, it may be possible to obtain more useful experimental results by adding not only silica sand but also plants.

REFERENCES

- [1] Fire Department "About the damage situation related to heavy rain by 2015 typhoon No. 18" (December 16, 2016)
- [2] Weathernews
<https://jp.weathernews.com/news/29409/>
- [3] National Technical Center: Guide for structural examination of river embankments (revised version), 2012 ,pp.8-9.
- [4] Nobuyuki Tsuneoka, Kazushi Furumoto, Toshiko Obata, Satoshi Wakasa : "Large-scale model test for measures to strengthen the infiltration of riverbanks" ; 37th Geotechnical Research Conference (2002)
- [5] Masato Sekine , Kosuke Sato, Toshiki Kan : "Study on the effect of gravel and clay contained on the failure process of simulated river embankment" ; JSCE ProceedingsB1 (Water engineering) Vol.74,No.5,2018,I_1099-I_1104.
- [6] Naoki Fukuhara , Hiroto Mori, Atsushi Hattori : "Experimental Study on Erosion Resistance of High Stem Grass and Plants Using Large Specimens Collected from River Embankment" ; JSCE ProceedingsB1 (Water engineering) Vol.70,No.4,2014,I_1351-I_1356.

STRESS ANALYSIS OF RIVER EMBANKMENT CONSIDERING EXTERNAL WATER LEVEL FLUCTUATION

Tsubasa Ichijo¹, Shin-ichi Kanazawa²

¹ Social Environmental Systems Engineering Course, National Institute of Technology, Fukushima College,
Advanced Course Program, Japan;

²Civil and Environmental Engineering, National Institute of Technology, Fukushima College, Japan

ABSTRACT

In recent years, local downpours frequently occur in various parts of Japan, and embankments are destroyed by these downpours. Many embankments are historical products of flood control that have been reinforced as they age by raising their height. However, the structure of the river embankment was developed based on information from disasters that actually occurred, and analysis of the destruction of the structure was not considered in design. Furthermore, until now, mechanisms of levee collapse have been discussed, but they have not been fully elucidated. Therefore, in this study, embankment analysis considering difference of layer thickness was performed by using the unsaturated soil / water / air coupled element finite method analysis program (DACSAR-MP). Stress behavior in the embankment during the rise of the river water level due to rainfall was analytically expressed, and the effect of the stress was considered to analytically investigate the collapse mechanism of the river embankment. From this work, it was analytically confirmed that embankment failure mode differed depending on differences in the speed of water level rise.

Keywords: River embankment, Unsaturated soil, Penetration, Collapse

INTRODUCTION

Due to global climate change, there have been frequent reports of local torrential rains in various parts of Japan in recent years, with associated river dike collapse. Among these, the breach of the embankment of the Chikuma River caused by Typhoon No.19 in October 2019 stands out. An embankment is an extremely important disaster prevention structure that protects the lives of riverside residents from floods, and it is necessary to ensure the safety of these structures.

Regarding water infiltration resistance, erosion resistance and seismic resistance ratings required for river levees, the existing rules for satisfying the earth levee principle and cross-sectional shape have been revised, and the magnitude of the external force applied to the levees before the earth structure is constructed has been stipulated. As a general rule, the design of levees for each river should be optimized considering topography, weather, and river shape. However, the mechanism of destabilization and deformation of levees due to floods or earthquakes has not yet been fully elucidated [1], and the current guidelines do not necessarily represent well-established technical knowledge.

On the other hand, the difficulty of elucidating the mechanisms of river levee infiltration and stability problems is because these problems deal with unsaturated soil, intermediate soil, compacted soil and unsteady phenomena. Overflow, erosion, seepage,

and earthquakes are the causes of riverbank breakage due to changes in the outside water level. Of these, all except for earthquakes are caused by rainfall, and the risk of riverbank breakage is increasing due to the recent local heavy rainfall. Currently, as an evaluation method for embankment structures, arc slip analysis is performed using the infiltration analysis results, such as rainfall, in the embankment design method. Nonetheless, deformation analysis is not performed, and infiltration analysis and stability analysis are performed individually. However, the infiltration problem and the deformation problem are coupled, and it is hard to say that the current embankment evaluation method is sufficient.

It is thought that local torrential rain will increase in the future, and it can be said that the risk of bank breakage will increase alongside this. Since the damage caused by river embankment is enormous, it is urgent to take measures against embankment failure, and for that purpose, it is important to elucidate the destruction mechanism of the river embankment.

In this study, using the unsaturated soil / water / air coupled element finite method analysis program (DACSAR-MP) [2], we focused on embankment reinforcement and conducted the embankment analysis considering differences in layer thickness. The purpose of this study is to analytically elucidate river levee collapse mechanisms by analytically expressing the stress behavior in the levee body

during river water level rise due to and considering the effect of rainfall.

RESEARCH METHOD

Soil/Water/Air Coupled Finite Analysis Code

The finite element analysis code (DACSAR-MP) [2] used in this study formulates the unsaturated soil constitutive model proposed by Ohno et al [3]. This model is framed as the soil/water/air coupled problem using the three-phase mixture theory. Equation (1) shows the effective stress. Equation (2) shows the base stress tensor and suction stress. Equation (3) shows suction.

$$\boldsymbol{\sigma}' = \boldsymbol{\sigma}^{\text{net}} + p_s \mathbf{1} \quad (1)$$

$$\boldsymbol{\sigma}^{\text{net}} = \boldsymbol{\sigma} - p_a \mathbf{1}, \quad p_s = S_e s \quad (2)$$

$$s = p_a - p_w, S_e = \frac{S_r - S_{rc}}{1 - S_{rc}} \quad (3)$$

Here, $\boldsymbol{\sigma}'$ is the effective stress tensor; $\boldsymbol{\sigma}^{\text{net}}$ is the base stress tensor; $\mathbf{1}$ is the second order unit tensor; $\boldsymbol{\sigma}$ is the total stress tensor; s is the suction; p_s is the suction stress; p_a is the pore air pressure; p_w is the pore water pressure; S_r is the degree of saturation; S_e is the effective degree of saturation; and S_{rc} is the degree of saturation at $s \rightarrow \infty$. Equations (4), (5), (6) and (7) provide the yield function.

$$f(\boldsymbol{\sigma}', \zeta, \varepsilon_v^p) = MD \ln \frac{p'}{\zeta p_{sat}} + \frac{MD}{n_E} \left(\frac{q}{Mp'} \right)^{n_E} - \varepsilon_v^p = 0 \quad (4)$$

$$\zeta = \exp \left[(1 - S_e)^{n_s} \ln a \right], MD = \frac{\lambda - \kappa}{1 + e_0} \quad (5)$$

$$p' = \frac{1}{3} \boldsymbol{\sigma}' : \mathbf{1}, q = \sqrt{\frac{3}{2}} \mathbf{s} : \mathbf{s} \quad (6)$$

$$\mathbf{s} = \boldsymbol{\sigma}' - p' \mathbf{1} = \mathbf{A} : \boldsymbol{\sigma}', \mathbf{A} = \mathbf{I} - \frac{1}{3} \mathbf{1} \otimes \mathbf{1} \quad (7)$$

Here, n_E is the shape parameter; ε_v^p is the plastic volume strain; M is the q/p' in the limit state; D is the dilatancy coefficient; p_{sat}' is the yield stress at saturation; a and n_s are the parameters representing the increase in yield stress due to unsaturation; λ is the compression index; and κ is the expansion index. Equation (8) shows pore water velocity. Equation (9) shows air velocity. Pore water and air flow follow

Darcy's law.

$$\tilde{v}_w = -\mathbf{k}_w \cdot \text{grad} h \quad (8)$$

$$\tilde{v}_a = -\mathbf{k}_a \cdot \text{grad} h_a, h_a = \frac{p_a}{\gamma_w} \quad (9)$$

Here, \tilde{v}_w is the pore water velocity; \tilde{v}_a is the air velocity; \mathbf{k}_w is the hydraulic conductivity; \mathbf{k}_a is the coefficient of air permeability; h is the total head; γ_w is the unit weight of water; and h_a is the pneumatic head. Equations (10)-(11) show hydraulic conductivity and the coefficient of air permeability by way of Mualem's [4] formula and the Van Genuchten [5] formula.

$$\mathbf{k}_w = k_{rw} \mathbf{k}_{wsat} = S_e^{1/2} \left[1 - \left(1 - S_e^{1/m} \right)^m \right]^2 \mathbf{k}_{wsat} \quad (10)$$

$$\mathbf{k}_a = k_{ra} \mathbf{k}_{ares} = (1 - S_e)^{1/2} \left(1 - S_e^{1/m} \right)^{2m} \mathbf{k}_{ares} \quad (11)$$

Here, k_{rw} is the ratio of hydraulic conductivity; k_{ra} is the ratio of coefficient of air permeability; m is the Mualem constant; \mathbf{k}_{wsat} is the hydraulic conductivity at saturation; \mathbf{k}_{ares} is the coefficient of air permeability in dry conditions. Equations (12)-(13) show the continuous formula of pore water and air using three-phase mixture theory.

$$n \dot{S}_r - S_r \dot{\varepsilon}_v + \text{div} \tilde{v}_w = 0 \quad (12)$$

$$(1 - S_r) \dot{\varepsilon}_v + n \dot{S}_r - n(1 - S_r) \frac{\dot{p}_a}{p_a + p_0} - \text{div} \tilde{v}_a = 0 \quad (13)$$

Here, n is porosity; $\dot{\varepsilon}_v$ is volumetric strain; and p_0 is atmospheric pressure. The elasto-plastic constitutive model obtained from Equation (4) and the equilibrium equation [Equations (12) - (13)] are formulated as the soil/water/air coupled problem.

Moisture Characteristic Curve Used In The Analysis

For a soil-water characteristic curve model, a model capable of hysteresis expression, as proposed by Kawai et al. [6], is used. In addition, to determine the logistic curve in the case of DRY and WET, derived from arbitrary suction and the degree of saturation, the logistic curve equation of Sugii and Uno [7] was used. This makes it possible to grasp the moisture conditions of sloped ground where complex water balance occurs. Figure 1 exhibits the soil-water

characteristic curve used in this study.

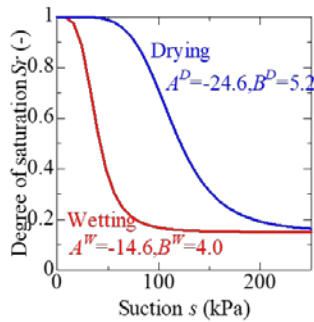


Fig. 1 Soil water characteristic curve

INTERIOR CHANGES IN THE DIKE WITH EMBANKMENT COMPLETION

Analysis Conditions

Figure 2 shows the analytical model. The foundation ground was 3m long and 45m long, and the dam body was 5m long, 5m at the top, and 25m at the bottom, with a slope of 1: 2 [8]. The mesh of the model is 1m each for the foundation ground, 10 cm for the levee body, and it was divided into 25 parts horizontally. The right side of the analytical model was assumed to be the river side, and the drainage layer was 0.6m in length and 6m in width from the left end of the embankment.

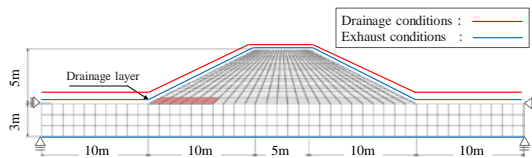


Fig. 2 Finite element mesh diagram

The material used in the analysis was silt mixed with sand for the foundation ground and sand mixed with silt for the dam body. Table 1 shows the material constants, and Fig. 3 shows the moisture characteristic curve. Table 1.1 is the material constant used for the foundation ground, and Table 1.2 is the material constant used for the dam body. Figure 3.1 shows the moisture characteristic curve used for the foundation ground, and Fig. 3.2 shows the moisture characteristic curve used for the dam body. The material constants shown in Table 1 are λ : swelling index, k : compression index, M : critical stress ratio, m : shape parameter of unsaturated hydraulic conductivity, n : magnification parameter of

consolidation yield stress in unsaturated state, nE : Fitting parameter of EC model, e_0 : Initial void ratio, ν : Poisson's ratio, k_x : Horizontal hydraulic conductivity, k_y : vertical hydraulic conductivity, S_{r0} : critical saturation, and G_s : soil particle specific gravity. The initial saturation of the material used for embankment was set to 60%, and the initial suction was determined from Fig.3.2. The drainage layer has a permeability coefficient and an air permeability coefficient set to 500 times that of the embankment. The material constants other than the permeability coefficient and the permeability coefficient of the drainage layer are the same as those of the bank body. The displacement boundary was fixed vertically at the bottom of the foundation ground and horizontally at the top of the foundation ground. For the hydraulic boundary, the lower and upper ends of the foundation ground and the upper part of the dam body were drained. As for the air boundary, the upper end of the foundation ground and the upper end of the dam were exhausted.

Table 1.1 Foundation ground material parameters

λ	k	M	m	n	nE
0.18	0.037	1.33	0.8	1	1.3
e_0	ν	$kx(m/day)$	$ky(m/day)$	S_{r0}	G_s
1.2	0.33	0.1	0.1	0.15	2.7

Table 1.2 Levee material parameters

λ	k	M	m	n	nE
0.18	0.013	1.33	0.8	1	1.3
e_0	ν	$kx(m/day)$	$ky(m/day)$	S_{r0}	G_s
1	0.33	8.7	8.7	0.15	2.7

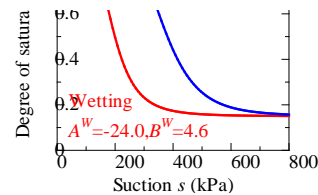


Fig. 3.1 Soil-water characteristic curve (Foundation ground)

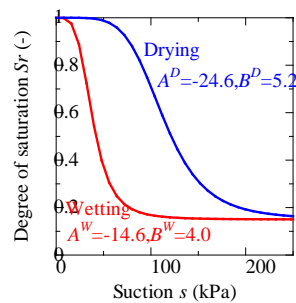


Fig. 3.2 Soil-water characteristic curve (Levee)

3.2.1 Analysis method

In the embankment analysis, layers were spread one-by-one. An evenly distributed load was applied, and compaction was repeated until the height of the embankment reached 5m. Layers of 0.3m and 0.6m were prepared. The rolling strength was 300kPa. In the analysis, elements were generated to create a heap, and loading and unloading was repeated with an evenly distributed load to simulate compaction. This schematic diagram is shown in Fig. 4.

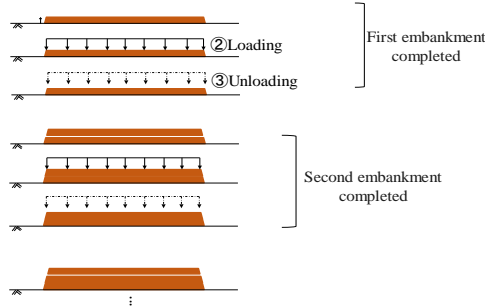


Fig.4 Embankment analysis schematic

3.2.2 Analysis result

Fig. 5 shows a visualization of each stress at the completion of the embankment (layer thickness: left 0.3 m, right 0.6m). From the top, the effective mean stress p' , void ratio e , deviatoric stress q , shear strain ε_s , suction s , and degree of saturation S_r are shown. First, the effective mean stress p' exhibits a higher value in the foundation ground than in the embankment due to the effect of compaction during embankment construction. In addition, the gap ratio e is higher toward the upper part of the levee body, and the layer thickness of 0.6m is particularly remarkable in this respect. Next, the shear strain ε_s shows a higher value near the boundary between the foundation and the levee than in the levee. Therefore, it is possible that there was already weakening when the embankment was completed, although not enough to cause failure. In addition, as the position where the drainage layer is located contains more water than the surrounding area, the void ratio e is low. Comparing layer thickness, the value of 0.6m shows smaller mean effective principal stress, and the gap ratio e is larger in the upper part of the dam body. At 0.6m, layer boundaries occur at the mean effective stress p' , the void ratio e , and the deviatoric stress q . Therefore, it is considered that the levee body compacted with a layer thickness of 0.6m has a discontinuity at the layer boundary, in contrast to the lack of this discontinuity with 0.3m layer thickness, resulting from insufficient compaction.

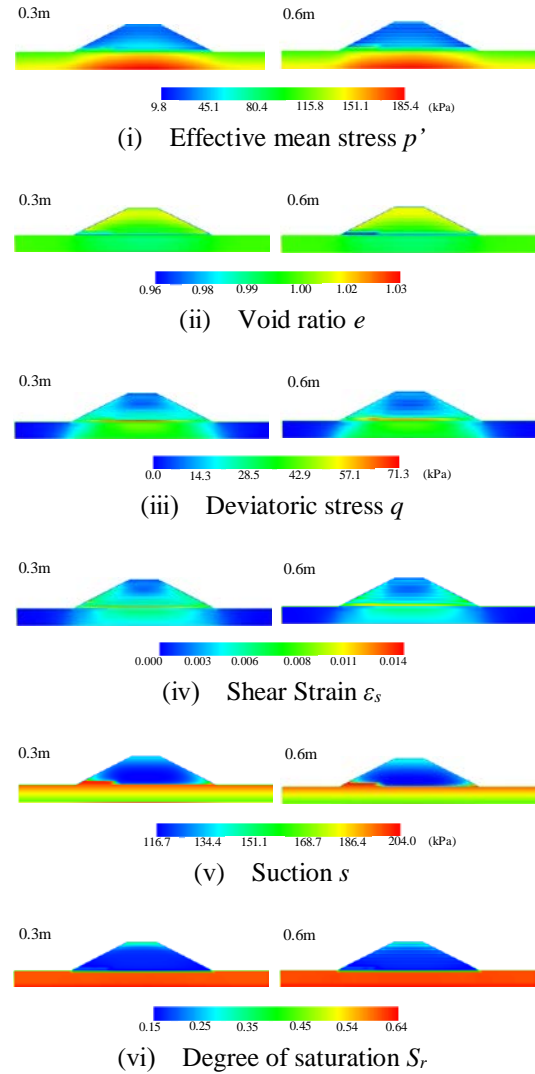


Fig. 5 Summarizes analysis results

CHANGES IN THE LEVEE DUE TO RISING WATER LEVELS

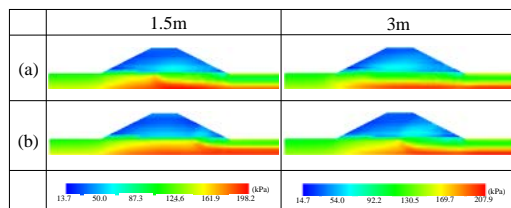
Water level fluctuation analysis was carried out using the analytical model used for embankment analysis. The right side of the embankment was used to raise the water level. This is expressed by applying water pressure to the levee body and the foundation ground after raising the head of water on the right slope of the embankment where water infiltrates, along with the foundation ground. The water head and water pressure applications were repeated until the crown reached 3m. In addition, the rate of water level rise was set to 1.4cm/min and 14cm/min [9]. (Rise rate: (A)1.4cm/min, (B)14cm/min)

Next, we paid attention to the difference in the speed of water level rise. Figure 6 shows the analysis results for each stress. Each figure shows the average effective principal stress p' , axial differential stress q ,

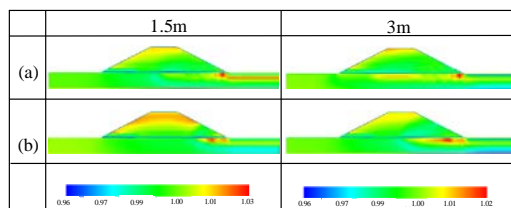
shear strain ε_s , void ratio e , suction s , and degree of saturation S_r from the top. From the left of the figure, the water level of each stress is extracted at 1.5m and 3m.

First, from results of the effective mean stress p' , strength is considered to decrease as the water level rises, and the value inside the levee decreases from the infiltration surface. In addition, the void ratio e also decreases inside the levee from the infiltration surface as the water level rises, and volume compression is considered to occur. Second, from the degree of saturation S_r , it can be seen that values for the foundation ground and the lower part of the levee become lower as the water level rises. At a slower velocity of (A) 1.4cm/min this value is higher than at a faster velocity of (B) 14cm/min. Finally, the shear strain ε_s indicates that the value at the tail end of the embankment is higher, suggesting that the tail end becomes a weak part of the embankment as the water level rises. For each stress, the change in velocity in (A) was more remarkable than that in (B). This is probably because at the slower the rising speed, the infiltration time of the river water was longer. In particular, the degree of saturation S_r was significantly different with different rising speeds, and a large difference in the formation of the infiltration surface was confirmed. The velocity (A) formed a smooth infiltration surface, and the velocity (B) formed a vertical infiltration surface. It is considered that (A) first infiltrated from the foundation ground and then infiltrated upward from the ground to the bank body.

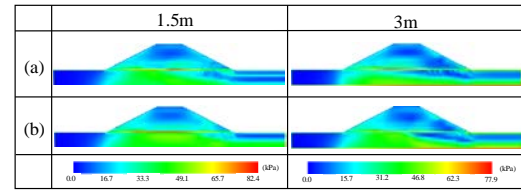
At this time, the levee body can be considered as subject to buoyancy due to leftward infiltration from the levee exterior and upward infiltration from the foundation ground, suggesting the possibility of piping. In contrast to (A), (B) is considered to have caused infiltration only from the lower left side of the embankment to form a vertical infiltration surface, suggesting that water overflow may occur.



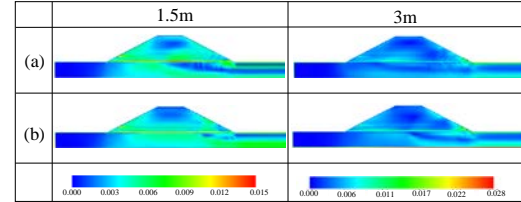
(i) Effective mean stress p'



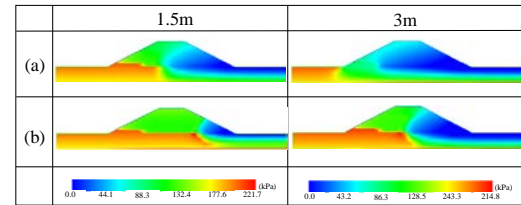
(ii) Void ratio e



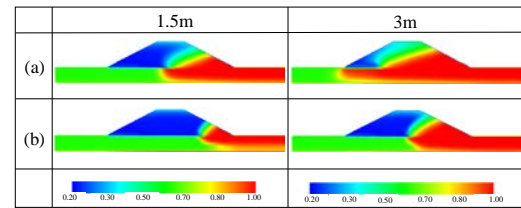
(iii) Deviatoric stress q



(iv) Shear Strain ε_s



(v) Suction s



(vi) Degree of saturation S_r

Fig. 6 Summarizes analysis results

Furthermore, in order to study the detailed behavior of saturation S_r in the levee, changes in the water level rise of the elements in the levee are visualized graphically. The position of each element is shown in Fig. 7, and the behavior in the ascending process is shown in Fig. 8 (Fig. 8.1: 1.4cm/min, Fig. 8.2: 14cm/min). The graph shows the time (unit:day) horizontally and the saturation S_r vertically. From Fig. 8.1, it can be confirmed that not only the elements 126, 160, 885 and 1385, but also the element 113 and the elements 101 and 187, are changing from the unsaturated state to the saturated state. From this, water is considered to have penetrated to the inner side of the bank, forming water channels, and this result also suggests that piping may occur. Because all the elements located on the foundation ground are saturated and element 101 is saturated earlier than element 187 on the ground side of the embankment, it can be confirmed that water permeates from the foundation ground earlier than from the embankment exterior. Figure 8.2, shows that the time required for saturation of each element remains almost unchanged, and that the levee body is saturated at a stretch in a

short time compared to the speed of 1.4cm/min. From this, it is possible to confirm the vertical infiltration in the levee body, and it is unlikely that water channels form. Therefore, it is considered that the slower the rising speed is, the higher the possibility of water channel formation.

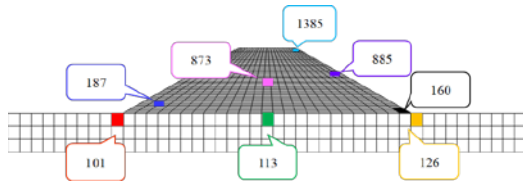


Fig.7 Position of each element

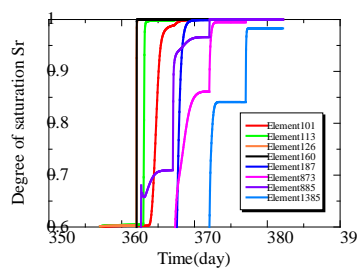


Fig.8.1 Transition of saturation of each element

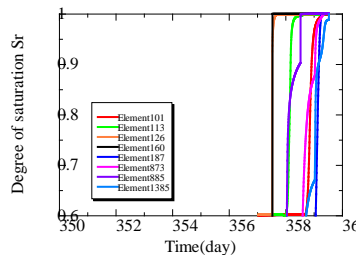


Fig.8.2 Transition of saturation of each element

CONCLUSION

Based on the results obtained from the embankment analysis and the water level rise analysis, the following conclusions are developed.

- (1) When the layer thickness is large, the average effective principal stress p' and the void ratio e are small at the completion of the embankment, resulting in a discontinuity at the layer boundary.
- (2) When the water level rises, the osmotic pressure of the outer water level is dominant, and therefore, the dominance of collapse due to the change in layer thickness was not observed. Therefore, it was confirmed that the difference in height of padding did not significantly affect the infiltration, and destruction was caused mainly by infiltration due to the rise of the water level.
- (3) As the water level rises, the strength inside the levee decreases, the volume is compressed, and the inside of the levee is saturated, thus collapse

is considered to occur within the levee. In addition, collapse progresses into the levee body as the water level rises.

- (4) When the rate of water level rise is slow there is a high possibility of collapse due to the long infiltration time of river water. If the ascending speed is high, it is likely that the river will overtop the levee before collapse occurs.
- (5) A gentle infiltration surface formed when the speed of water level rise was slow, and a vertical infiltration surface was formed when the water velocity was high. In particular, when the speed is slow, the dam body may be subjected to upward penetration from the foundation ground in addition to leftward penetration from the outside of the embankment. This results in buoyancy and the formation of water channels in the foundation ground to cause piping.

REFERENCES

- [1] Japan Institute of Country-ology and Engineering: River embankment guide (Revised edition), 2012, pp.1.
- [2] Kanazawa, S., Toyoshima, K., Kawai, K., Tachibana, S. and Iizuka, A.: Analysis of mechanical behavior of compacted soil with F.E. method, journal of JSCE, No.68 (2), 2012, pp.291-298.
- [3] Ohno, S., Kawai, K. and Tachibana, S.: Elastoplastic constitutive model for unsaturated soil applied effective degree of saturation as a parameter expressing stiffness, Journal of JSCE, Vol.63/No.4,2007,pp.1132-1141.
- [4] Mualem, Y.: A new model for predicting the hydraulic conductivity of unsaturated porous media, Water Re-sources Research, Vol.12, No.3, 1976 ,pp.514-522.
- [5] Van Genuchten: A closed-form equation for predicting hydraulic of unsaturated soils, Soil Science Society American Journal, Vol.44, 1980,pp.892-898.
- [6] Kawai, K., Wang, W. and Iizuka, A.: The expression of hysteresis appearing on water characteristic curves and the change of stresses in unsaturated soils, Journal of applied mechanics, Vol.5, pp.777-784, 2002. Kimura S., Journal Paper Title, J. of Computer Science, Vol. 1, Issue 2, 1987, pp. 23-49.
- [7] Sugii T. and Uno T.: Modeling the New Moisture Characteristic Curve, Journal of JSCE, 1995 ,pp.130-131.
- [8] Japan Road Association,: Roadway Workers - Fill Construction Guidelines, 2010,pp.163.
- [9] Ministry of Land,Infrastructure,Tranceport and Tourism Hokuriku Regional Development Bureau:Chikuma River Embankment Survey Committee materials, 2019, pp.8.

ANALYTICAL STUDY ON QUALITY EVALUATION OF EMBANKMENT STRUCTURE WITH A VIEW TO LONGER LIFE

Emika Nakamura¹, Shin-ichi Kanazawa²

¹ Social Environmental Systems Engineering Course, National Institute of Technology, Fukushima
College, Advanced Course Program, Japan

² Civil and Environmental Engineering, National Institute of Technology, Fukushima College, Japan

ABSTRACT

In recent years, the demand for quality evaluation of earth structures has been increasing, coupled with a strong demand for cost reduction in construction projects. In order to respond to such social trends, it is urgently necessary to carefully examine the design conditions and construction processes for earth structures. At present, mechanical construction capability and the number of experienced site technicians are improving, and it is necessary to study the construction conditions that will lead to the quality of the embankment from a long-term perspective. Additionally, in the future, simplification of work such as high-speed construction using AI or unmanned operation will be required. Therefore, in this study, we evaluate the change in stress during long-term service by performing the analysis after changing the rolling strength and the spreading thickness construction conditions of the embankment. Understanding the effects of these techniques will contribute to shortening the construction period with a view to extending the life of the embankment.

Keywords: Embankment, Longer life, Cost reduction, Finite element method

INTRODUCTION

Soil structures are compacted to improve stability and deformation characteristics. However, many cases of dikes collapse due to local torrential rains and typhoon torrential rains have been reported, and the collapse mechanism has not been completely clarified.

The stability of the embankment against heavy rainfall is considered to depend strongly on four factors: the treatment of the foundation ground, the quality of the embankment material, the degree of compaction, and the treatment of water. Among these, the cause of embankment collapse in many cases is the treatment of water.

Although embankment structures are initially properly drained according to land and environmental conditions, embankments frequently collapse. One causal factor is that the construction and maintenance of the embankment depends on engineer experience. Soil consists of three phases: a solid phase, liquid phase and gas phase, and the embankment and underlying ground below the water table are often in an unsaturated state containing air or dissolved air. It is considered that gas is dissolved and released into the liquid phase as the pore air pressure changes due to rainfall infiltration, resulting in volume compression. As a result, it is possible that current construction guidelines do not have sufficient drainage measures and embankment maintenance requirements to withstand recent heavy rainfall. In addition, drainage measures for the embankment and the time at which it is affected by rainfall are important factors. It is thought that the influence of

rainfall during construction weakens the inside of the embankment, but timing of construction cannot be fixed, and the amount of rainfall received during construction varies. In addition, construction is generally not carried out in the rainy season, but in some cases this is unavoidable. To counter these adverse weather conditions, drainage measures are taken while paying attention to the weather, but the effects of rainfall during construction and the effect of the initial stress state at the completion of embankment have not been clarified. At normal sites, the embankment is exposed to climatic conditions, such as repeated dry and wet conditions, and the effects of the behavior of unsaturated soil cannot be ignored. Therefore, in order to obtain a precise initial stress state, it is necessary to consider the influence of the dry and wet mechanical conditions. It is also necessary to propose a method for estimating the initial stress state in consideration of the dry and wet mechanical conditions, such as rainfall and evaporation.

In addition, mechanical construction capability on site and the experience of engineers are improving, and it is necessary to study the construction conditions that will lead to high quality embankment from a long-term perspective. Additionally, in the future, simplification of work, such as high-speed construction using AI and unmanned operation will be required.

In this study, embankment analysis considering compaction and rainfall / evaporation history is performed using soil / water / air coupled finite analysis code. Differences in compaction strength of

the embankment, layer thickness of construction, and the amount of rainfall are analyzed, and stress change during the long-term service process are evaluated. This analysis contributes to shortening the construction period with a view to extending the life of the embankment. In addition, by grasping the mechanical behavior inside the embankment through this analysis, this study also aims to enable understanding the design needed for required performance of the embankment in the future.

RESEARCH METHOD

Soil/Water/Air Coupled Finite Analysis Code

The finite element analysis code (DACSAR-MP) [1] used in this study formulates the unsaturated soil constitutive model proposed by Ohno et al [2]. This model is framed as the soil/water/air coupled problem using the three-phase mixture theory. Equation (1) shows the effective stress. Equation (2) shows the base stress tensor and suction stress. Equation (3) shows suction.

$$\boldsymbol{\sigma}' = \boldsymbol{\sigma}^{\text{net}} + p_s \mathbf{1} \quad (1)$$

$$\boldsymbol{\sigma}^{\text{net}} = \boldsymbol{\sigma} - p_a \mathbf{1}, p_s = S_e s \quad (2)$$

$$s = p_a - p_w, S_e = \frac{S_r - S_{rc}}{1 - S_{rc}} \quad (3)$$

Here, $\boldsymbol{\sigma}'$ is the effective stress tensor; $\boldsymbol{\sigma}^{\text{net}}$ is the base stress tensor; $\mathbf{1}$ is the second order unit tensor; $\boldsymbol{\sigma}$ is the total stress tensor; s is the suction; p_s is the suction stress; p_a is the pore air pressure; p_w is the pore water pressure; S_r is the degree of saturation; S_e is the effective degree of saturation; and S_{rc} is the degree of saturation at $s \rightarrow \infty$. Equations (4), (5), (6) and (7) provide the yield function.

$$f(\boldsymbol{\sigma}', \zeta, \varepsilon_v^p) = MD \ln \frac{p'}{\zeta p_{sat}} + \frac{MD}{n_E} \left(\frac{q}{Mp'} \right)^{n_E} - \varepsilon_v^p = 0 \quad (4)$$

$$\zeta = \exp \left[(1 - S_e)^{n_s} \ln a \right], MD = \frac{\lambda - \kappa}{1 + e_0} \quad (5)$$

$$p' = \frac{1}{3} \boldsymbol{\sigma}' : \mathbf{1}, q = \sqrt{\frac{3}{2} \mathbf{s} : \mathbf{s}} \quad (6)$$

$$\mathbf{s} = \boldsymbol{\sigma}' - p' \mathbf{1} = \mathbf{A} : \boldsymbol{\sigma}', \mathbf{A} = \mathbf{I} - \frac{1}{3} \mathbf{1} \otimes \mathbf{1} \quad (7)$$

Here, n_E is the shape parameter; ε_v^p is the plastic volume strain; M is the q/p' in the limit state; D is

the dilatancy coefficient; p'_{sat} is the yield stress at saturation; a and n_s are the parameters representing the increase in yield stress due to unsaturation; λ is the compression index; and κ is the expansion index. Equation (8) shows pore water velocity. Equation (9) shows air velocity. Pore water and air flow follow Darcy's law.

$$\tilde{v}_w = -\mathbf{k}_w \cdot \text{grad} h \quad (8)$$

$$\tilde{v}_a = -\mathbf{k}_a \cdot \text{grad} h_a, h_a = \frac{p_a}{\gamma_w} \quad (9)$$

Here, \tilde{v}_w is the pore water velocity; \tilde{v}_a is the air velocity; \mathbf{k}_w is the hydraulic conductivity; \mathbf{k}_a is the coefficient of air permeability; h is the total head; γ_w is the unit weight of water; and h_a is the pneumatic head. Equations (10)-(11) show hydraulic conductivity and the coefficient of air permeability by way of Mualem's [3] formula and the Van Genuchten [4] formula.

$$\mathbf{k}_w = k_{rw} \mathbf{k}_{wsat} = S_e^{1/2} \left[1 - \left(1 - S_e^{1/m} \right)^m \right]^2 \mathbf{k}_{wsat} \quad (10)$$

$$\mathbf{k}_a = k_{ra} \mathbf{k}_{ares} = (1 - S_e)^{1/2} \left(1 - S_e^{1/m} \right)^{2m} \mathbf{k}_{ares} \quad (11)$$

Here, k_{rw} is the ratio of hydraulic conductivity; k_{ra} is the ratio of coefficient of air permeability; m is the Mualem constant; \mathbf{k}_{wsat} is the hydraulic conductivity at saturation; \mathbf{k}_{ares} is the coefficient of air permeability in dry conditions. Equations (12)-(13) show the continuous formula of pore water and air using three-phase mixture theory.

$$n \dot{S}_r - S_r \dot{\varepsilon}_v + \text{div} \tilde{v}_w = 0 \quad (12)$$

$$(1 - S_r) \dot{\varepsilon}_v + n \dot{S}_r - n(1 - S_r) \frac{\dot{p}_a}{p_a + p_0} - \text{div} \tilde{v}_a = 0 \quad (13)$$

Here, n is porosity; $\dot{\varepsilon}_v$ is volumetric strain; and p_0 is atmospheric pressure. The elasto-plastic constitutive model obtained from Equation (4) and the equilibrium equation [Equations (12) - (13)] are formulated as the soil/water/air coupled problem.

STRESS ANALYSIS DURING THE SERVICE PROCESS

Analysis Condition

In this study, embankment analysis of embankment structure considering rainfall and evaporation was performed using unsaturated soil / water / air coupled finite element method analysis program (DACSAR-MP). Table 1 shows the material parameters used in the analysis, and Fig. 1 shows the moisture characteristic curve, where λ : the swelling index, κ : the compression index, $M = (p'/q)$: the stress ratio, n_E : the fitting parameter of the EC model, a : parameter for determining the magnification of consolidation yield stress due to desaturation, m : unsaturated hydraulic conductivity parameters, S_{r0} : saturation of adsorbed water, k_a : air permeability coefficient, ν : Poisson's ratio, G_s : soil particle specific gravity, and k_w : saturated hydraulic conductivity.

The analysis area is assumed to be foundation ground measuring 15 m in length x 45 m in width, with embankment 3 m wide at the top, 15 m wide at the bottom and 6 m high. The foundation ground has a saturation level of 50% up to 3 m from the ground surface, and a 90% saturation level deeper than 3 m from the ground surface. The displacement boundary was fixed vertically and horizontally at the lower end of the foundation ground, and the hydraulic boundary was drained at the top and bottom and undrained at the left and right.

Table 1 material parameters

λ	κ	M	m	S_{r0}	k_a (m/day)
0.18	0.037	1.33	0.8	0.15	1.0
n	n_E	a	ν	G_s	k_w (m/day)
1.0	1.3	10.0	0.33	2.7	0.01

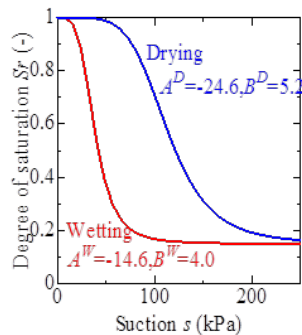


Fig.1 Soil water characteristic curve

Stress analysis conditions in the service process due to differences in construction conditions

In this study, layer thickness and compaction strength are considered as construction conditions.

Compaction was expressed by loading and unloading each layer under the load conditions of 300, 600, and 900 kPa, after construction at 0.3 and 0.6 m layer thicknesses during a construction period of one month. Figure 2 shows the analysis area at a layer thickness of 0.3 m, and Figure 3 shows the analysis area at 0.6 m.

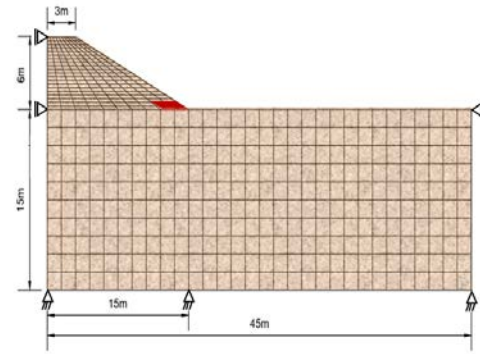


Fig.2 Analysis area with a thickness of 0.3m

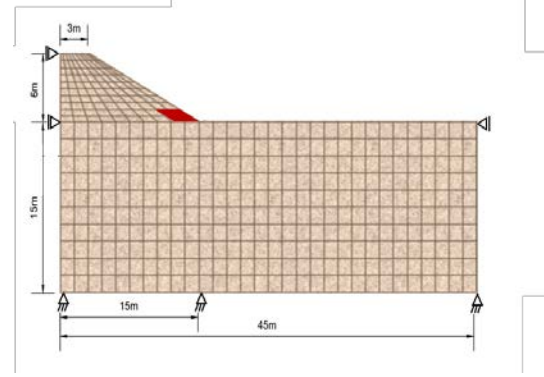


Fig.3 Analysis area with a thickness of 0.6m

Stress analysis conditions in the service process due to differences in climatic condition

In this study, rainfall during construction is considered a climatic condition.

Because the amount of precipitation changes from month to month, the amount of precipitation the embankment receives during the civil engineering work will differ depending on the month in which the construction is implemented. Therefore, by changing the construction time, the stress change due to differences in rainfall during construction will be investigated and compared. The rainfall history used in this study is shown in Fig. 4. For the rainfall applied during construction, the annual rainfall history of Fukuoka City in Fukuoka Prefecture in 2010 was used to simulate average rainfall in Japan. For stress analysis during embankment service due to

the differences in construction conditions, total rainfall of 1729 mm was corrected to one month, and rainfall of 144.1 mm was applied. For stress analysis in service due to different climatic conditions, we prepared 3 cases with characteristic rainfall, as shown in Fig. 4.

These three cases provide the lowest rainfall in January, the highest rainfall July, and an average rainfall in April; i.e. 50.5mm in January, 199.5mm in April, and 453.5mm in July. These rainfall conditions were applied throughout construction, and then the embankment analysis was performed.

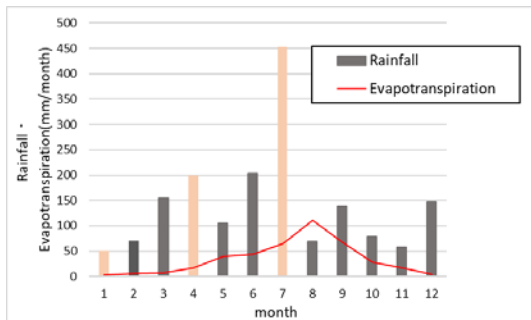


Fig.4 Fukuoka Prefecture monthly rainfall and evaporation history (2010)[5]

Analysis Result

Stress analysis results in the service process due to differences in construction conditions

Figures 5 to 10 show the initial stress distributions under load conditions of 300, 600, and 900 kPa, divided into layer thicknesses of 0.3 and 0.6 m, respectively.

From the average effective principal stress distribution in Fig. 5, no significant difference due to the difference in rolling compaction strength (300, 600, 900 kPa) can be confirmed. The same is true when looking at the comparison based on layer thickness (0.3m, 0.6m). One notable difference is that the layer boundary at the layer thickness of 0.6 m is clearer than the distribution of layer boundaries at the layer thickness of 0.3 m.

In all stress distributions, the average effective principal stress in the foundation ground is large, and the void ratio distribution is small, as shown in Fig. 7. This suggests that the embankment fully reflects the compaction effect from the e - $\log P'$ relationship. In the degree of saturation distribution shown in Fig.6, a discontinuity at the layer boundary of the embankment is apparent. From these visualizations, embankment with a layer thickness of 0.6 m has a larger discontinuous surface than with a layer thickness of 0.3 m, which tends to affect the compaction performance. Thus, although a change in the stress distribution due to the difference in layer thickness could be confirmed, there was no significant difference due to the compressive strength.

Next, from the void ratio distribution in Fig. 7, it can

be seen that there is a tendency for expansion due to the large void ratio value in the surface layer of the embankment, which indicates loose compaction of this region. It also seems that there is a change in the surface layer of the embankment at layer thicknesses of 0.3m and 0.6m. However, as the difference in value is about 0.001, it can be said that there is no significant difference due to layer thickness. Also, no significant difference due to compressive strength can be confirmed.

Finally, from the shear strain distribution shown in Fig. 8, it can be confirmed that the morphology of surface slip has already appeared; although, the fracture risk is low because of the low shear distribution value. This is because this value at the surface layer is small, even when looking at the axial stress distribution in Fig. 9, suggesting that the embankment surface layer is likely to become weak during embankment. Therefore, caution is advised in these cases, as the surface layer may be damaged if it is affected by heavy rain after construction.

From the above, it can be said that there was almost no change in the initial stress due to the difference in rolling strength (300, 600, 900 kPa), and there was no significant change due to the layer thickness (each initial stress value) (0.3, 0.6 m). However, at a layer thickness of 0.6 m, large discontinuities occur at the layer boundaries, suggesting that different layer thicknesses affect compaction performance. In summarizing the results of the initial stress analysis due to the difference in the construction conditions, it can be said that the differences in the layer thickness and load conditions, which are the construction conditions, have little effect on each initial stress.

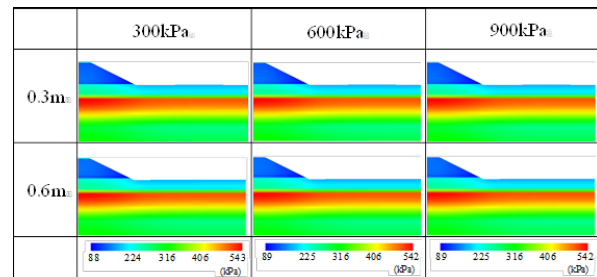


Fig.5 Effective mean stress p'

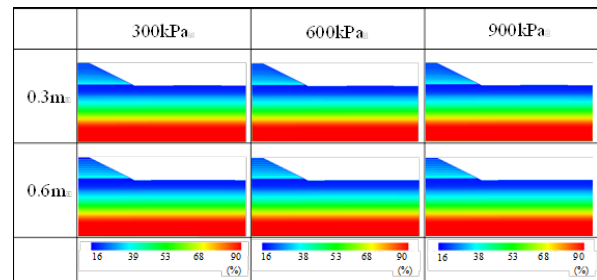
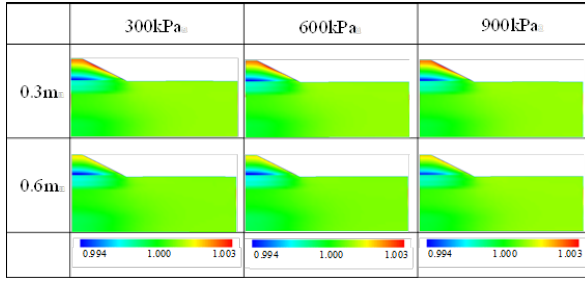
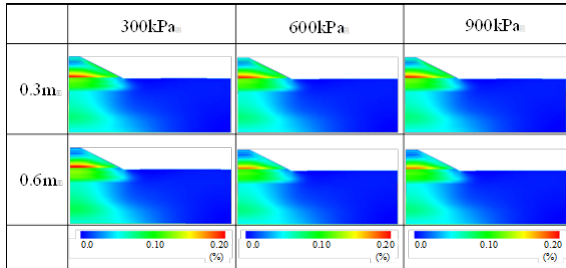
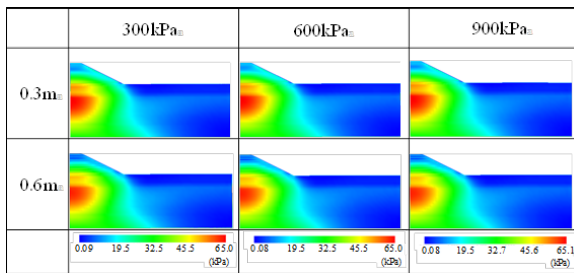
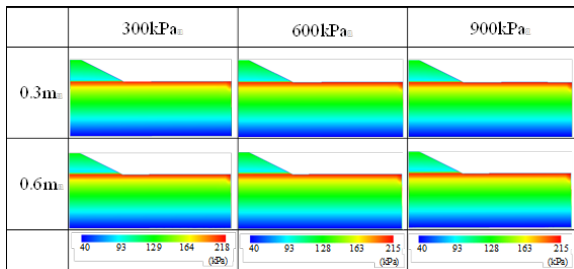


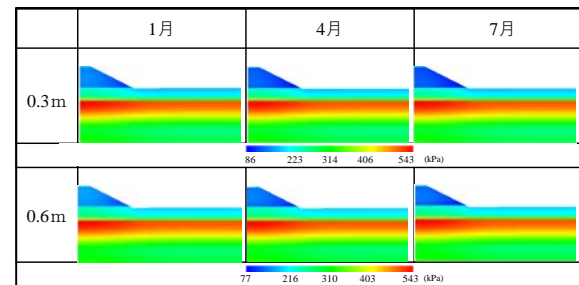
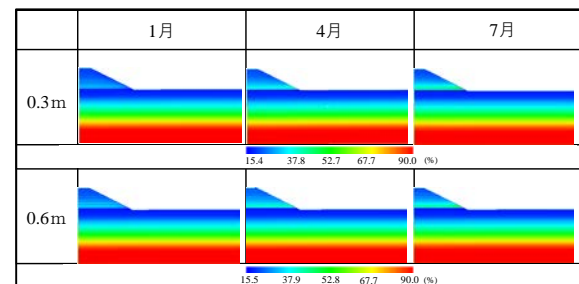
Fig.6 Degree of saturation S_r


 Fig.7 Void ratio e

 Fig.8 Shear Strain ε_s

 Fig.9 Deviatoric stress q

 Fig.10 Suction s

Stress analysis results in the service process due to differences in climatic conditions

This section describes the results of embankment analysis at applied rainfall of 50.5 mm in January, 199.5 mm in April, and 453.5 mm in July. However, when comparing the initial stress distributions with different rolling strengths for each construction time by layer thickness, no stress change due to different loading conditions could be confirmed at any construction time. In examining this, it was determined that carrying out the stress analysis only for the embankment with a compaction strength of 300 kPa would yield valid results. Therefore, Figures 11 to 16 show the outline of each stress distribution of each layer thickness when the construction time was changed, using the analysis results at the

compressive strength of 300 kPa. Precipitation increases in the order of January, April, and July. From Fig. 11, it can be confirmed that the effective stress in the embankment decreases as the amount of rainfall applied during construction increases. In addition, the distribution of the void ratio, as shown in Fig. 13, increases at the embankment surface layer in the order of January, April, and July. From these tendencies, it can be said that the embankment surface layer is loosely compacted. Furthermore, the value of the void ratio in the lower part of the embankment becomes smaller as the amount of rainfall increases, which suggests that the self-weighting effect of rainfall causes the interior of the embankment to become dense. A similar tendency can be confirmed from the shear strain distribution in Fig.14. Also, although the shear strain in the surface layer of the embankment is large and the surface slip takes form, the risk of fracture is low at this point because the value is small. From the axial stress distribution shown in Fig. 15, it can be confirmed that the embankment surface layer during construction is weak. No significant difference in stress distribution due to layer thickness could be confirmed. As described above, changes in initial stress distribution due to differences in construction time, that is, differences due to rainfall during construction, were confirmed. In other words, it was found that levees constructed during periods of low rainfall were stronger than levees constructed during periods of high rainfall. The higher the rainfall, the higher the risk of damaging the weaker embankment surface.


 Fig.11 Effective mean stress p'

 Fig.12 Degree of saturation S_r

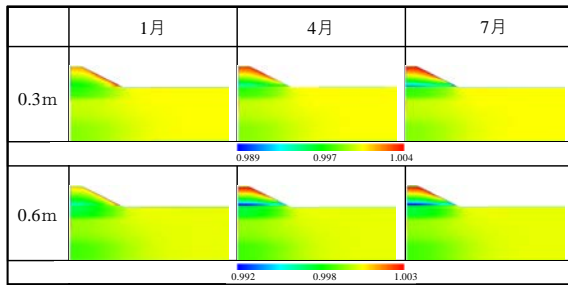


Fig.13 Void ratio e

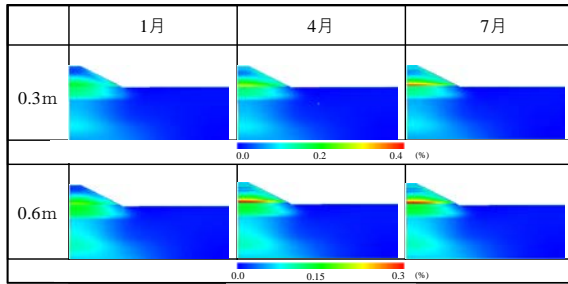


Fig.14 Shear Strain ε_s

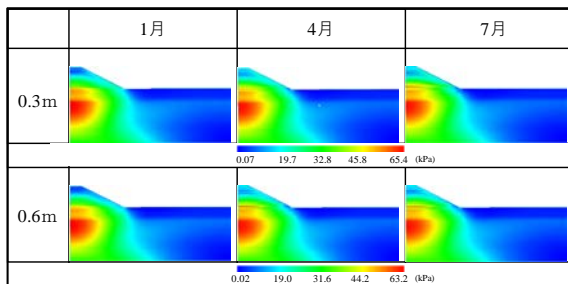


Fig.15 Deviatoric stress q

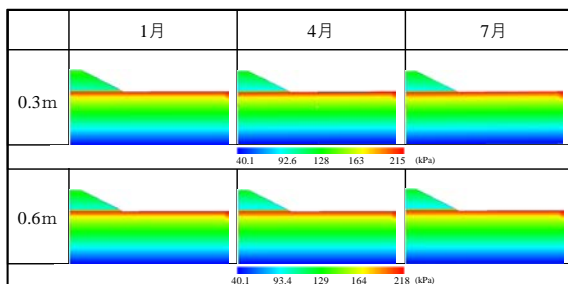


Fig.16 Suction s

CONCLUSION AND FUTURE OUTLOOK

From the results of this study, it was possible to confirm the effects of differences on the stress inside the embankment in construction conditions, which depended on the compaction strength and the layer thickness of the embankment, as well as climatic conditions, which depended on season of construction. The stress analysis results during embankment service due to the difference in construction condition confirmed no change in the load conditions compared in this study but a difference in the size of the discontinuous surface that

formed. As a result, there is almost no difference in compressive strength (300, 600, 900 kPa) and layer thickness (0.3m, 0.6m) due to differences in construction conditions over a long period of time. Therefore, at the present time, no problems are anticipated with carrying out the embankment construction a compressive strength of 300 kPa, which can reduce costs, and a layer thickness of 0.6 m, which can shorten the construction period.

The stress analysis results during embankment service due to the difference in climatic conditions confirmed that dikes constructed during the low rainfall season are stronger than dikes constructed during the high rainfall season. In other words, it is advisable to build levees during periods of low rainfall. However, it is necessary to continue studying heavy rainfall after construction and changes in stress distribution after several years. In summary, climatic conditions are more likely to change embankment stress conditions than construction conditions. However, these results are only trends at this stage. In the future, we would like to study additional construction conditions and climatic conditions and consider various process scenarios. The changes in stresses during long-term use of levees can also be assessed by analytically examining how these differences change the internal stresses of levees after decades. From the viewpoint of extending the life of these structures, it is also possible to conduct feedback analysis after the embankment is constructed and to monitor vulnerable points.

REFERENCES

- [1] Shinichi Kanazawa, Shinya Tachibana, Atsushi Izuka: Analytical study on drainage capacity of embankment structure, JSCE Proceedings A2 (Applied mechanics), Vol.71, pp.429-436, 2015.
- [2] Ohno, S., Kawai, K. and Tachibana, S.: Elastoplastic constitutive model for unsaturated soil applied effective degree of saturation as a parameter expressing stiffness, Journal of JSCE, Vol.63/No.4, pp.1132-1141, 2007.
- [3] Mualem, Y.: A new model for predicting the hydraulic conductivity of unsaturated porous media, Water Resources Research, Vol.12, No.3, pp.514-522, 1976.
- [4] Van Genuchten: A closed-form equation for predicting hydraulic of unsaturated soils, Soil Science Society American Journal, Vol.44, pp.892-898, 1980.
- [5] Japan Meteorological Agency: Japan Meteorological Agency: <http://www.jma.go.jp/jma/index.html>.

NUMERICAL INVESTIGATION ON PILE BEHAVIOR DUE TO THE RISING GROUNDWATER EFFECT

Harutus Phoban¹, Uma Seeboonruang¹ and Prateep Lueprasert¹

¹Faculty of Engineering, King Mongkut's Institute of Technology Ladkrabang, Thailand

ABSTRACT

Since the late 1990s, the changing of groundwater level in the aquifer beneath Bangkok has been realized because the enforcement of groundwater laws and improvement of water supply have been adopted. Then, the groundwater with piezometric drawdown has rising to almost hydrostatic equilibrium. In the principle of soil mechanics, when the porewater pressure in soil mass increases, the effective stress decreases. This can affect to underground structures. Under the soft ground condition such as Bangkok, Thailand, pile foundations are commonly constructed to support structures. With decreased effective stresses, the loss of ultimate load carrying capacity of existing piles can be occurred and the structures can be damaged. This research investigates the effects of the groundwater rising on pile foundation in Bangkok subsoil. Advanced numerical model with the fully coupled flow deformation analysis, both groundwater flow and soil deformation behaviors with time dependent conditions are modelled, is conducted by using PLAXIS 2D code. The results found that the calculation type of fully coupled flow deformation can express the pile-soil movement behavior. The pile-soil heave and the pile load capacity be significantly reduced during the groundwater rising event. Despite the reduction of pile load capacity with groundwater changed not enough to failure (Factor of safety <1.0), the pile stability should be concerned and the optimum groundwater level must be controlled.

Keywords: Groundwater rising, Pile capacity, Numerical modeling, Bangkok subsoil, Fully coupled flow deformation analysis

INTRODUCTION

In the past, Bangkok has been mainly taken the water resource from deep well pumping from aquifers underneath the city. Specifically, the groundwater pressure was declined to 31 m below ground surface (m bgs) in 1997 in central city area (Rommaninart Park) [1]. After that, the groundwater level was slightly increased, the Thailand Department of Groundwater Resources prompted the policy.

Groundwater levels are rising in many urban areas because of reduced pumping from the underlying aquifers for industrial processes. That is a problem common to many cities founded and effected on underground structures (i.e., metro tunnels, deep foundations, etc.). Recent many researches, an increasing trend in groundwater level due to the deindustrialization process was observed in urban aquifers all around the world: Aswan (Egypt), London (England), Paris (France), Naples (Italy), Milan (Italy), Tokyo (Japan) and Bangkok (Thailand). The groundwater pressure rising in the urban areas was the result of a decreasing in groundwater pumping, which was not appropriately managed. That thus caused damages to underground structures and infrastructures.

Pile foundations are commonly installed to carry loads from building into the soil by skin friction and end bearing. The increasing of porewater pressure leads to decreasing of the effective stresses, a loss in

ultimate load carrying capacity of existing piles are occurred. Recently research investigated the impact of the groundwater rising in Bangkok, for example, [2], [3] to study effects of groundwater drawdown and rebound from deep well pumping in Bangkok on piled foundation of buildings. They reported that for a short pile of length in the order of 30 m, the bearing capacity may be reduced by 40% in the future when the groundwater level is allowed to rebound close to the ground surface for the pile installed during the period of maximum ground drawdown in 1997. However, they considered only analytical method on pile capacity. In this research, the numerical model was carried out to investigate the pile behavior due to the rising groundwater event. A Fully coupled flow-deformation analysis is conducted to analyse the simultaneously development of deformations and pore pressures in saturated and partially saturated soils as a result of time-dependent changes of the hydraulic boundary conditions [4], [5]. The pile-soil movement, load distribution along the pile, and the reduction of pile capacity were observed.

GEOLOGY AND HYDROGEOLOGY OF THE STUDY AREA

The data obtained from central plain area of Thailand are used for this study. During the past 50 years, the study area, has been rapidly developed with

urbanization, especially Bangkok, the capital of Thailand. The geology and hydrogeology beneath the study area are significantly changed. Thus, the geological and hydrological change of this area have been studied by many researchers. However, there are well-documented reports in few literatures [1], [6].

The geology conditions of study area were covered by the marine and alluvial deposits. At the shallow depth of the entire area, the subsoils were almost uniform with consisting of soft clay, stiff clay and sand. At the greater depth, the stiff to hard clay and dense sand layers were found. The first dense sand layer with thickness ranging about 5-10 m is generally located below stiff clay layer (the depth of about 20-25 m from the ground surface). The hard clay layer was found underneath first dense sand layer. Second dense sand layer locating at depth about 45-60 m from ground surface is below the hard clay layer.

Bangkok aquifer system is identified as 8 aquifers by JICA [6] with continuous relatively impermeable aquitards (clay layers). Each layer with a thickness of 30-70 m, from ground surface consisting of the Bangkok (BK), Phra Pradeang (PD), Nakorn Luang (NL), Nonthaburi (NB), Sam Khok (SK), Phayathai (PT), Thonburi (TB) and Pak Nam (PN) aquifers, respectively. Groundwater is mainly pumped from the PD, NL and NB aquifers at the depths about 100 m to 200 m.

In the past decade, the groundwater demand for utility and industrial systems was very high as shown in Fig. 1. [1], [7]. With serious controlling the amount of water pumping and utilizing the tap water supply, the groundwater pumping decreased while the trend of piezometer rise up to the hydrostatic after 1997. This current research focuses on PD aquifer (about 100 m bgs) due to the rising trend of piezometer may impact to the pile.

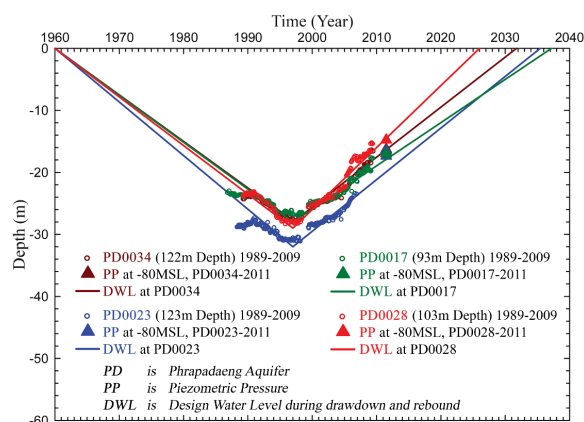


Fig. 1 Piezometric levels changed with time in Bangkok [1]

NUMERICAL MODELING OF PILE FOUNDATION ANALYSIS

Reference case

The geological condition and static pile load test pile data of Silom-Sathon located in the inner-city zone of Bangkok are used to model in this research. Construction of this building was completed in 1999, having 20 floors. The pile foundation of this building was installed during the period of maximum groundwater drawdown (1997-1999). The bored pile diameter of 1m with pile tip of -55 m bgs was constructed by using wet process.

The change of groundwater levels with time at Phrapadaeng aquifer for modelling was acquired from observation data at the monitoring groundwater station PD0023 (Fig. 1), where was located at Metropolitan Electricity Authority Substation Thung Maha Mek (about 1 kilometers from the building reference). The rate of groundwater rising was approximated of +0.75 m/year from years 1997 (GWL -30 m bgs) to 2037 (GWL -0 m bgs)

Modelling and Boundary Condition

Soil model and Parameters

Finite element (FE) method using software PLAXIS 2D was used to investigate the mechanical behavior of single piles foundation under axial load and groundwater level rising load on Bangkok soft clay. The Linear-Elastic Perfectly-Plastic Mohr-Coulomb model and hardening soil with small strain stiffness (HSS) model which can simulate stiffness dependent on stress, strain and paths was applied. Parameters were adopted and modified from [1], [8]-[10], who studied and calibrated the model parameters for Bangkok soils. All parameters are summarized in Table 1.

The numerical result of pile load test was compared with monitoring data in field test as shown in Fig. 2. The failure load of 1600 ton was evaluated by Mazurkiewicz (1972)'s method. The working load of 640 ton are applied on the pile head for this study that was considered with factor of safety (F.S) of 2.5.

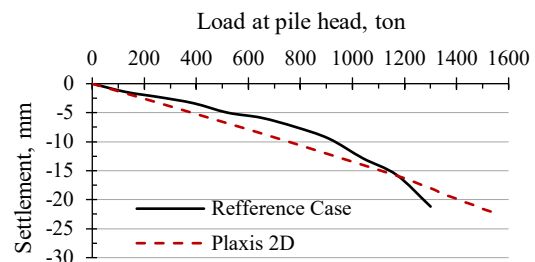


Fig. 2 Measured load settlement curve compared with field test and numerical analysis

Table 1. Model parameters used in analyses

Parameters	Unit	Weathered clay	Soft clay	Medium stiff clay	Stiff to very stiff clay	1 st Sand	2 nd sand	Hard clay	Pile
<i>Model</i>	-	MC	HS Small	HS Small	HS Small	MC	MC	HS Small	Linear elastic
<i>Material type</i>	-	Undrained	Drained	Drained	Drained	Drained	Drained	Drained	Non-porous
γ_{sat}	kN/m ³	17	16.5	18	20	20	20	20	24(Unsat)
E_{50}^{ref}	kN/m ²	E'=6000	800	1650	8500	E'=85800	E'=85800	30000	E=2.70E7
E_{oed}^{ref}	kN/m ²	-	850	1650	9000	-	-	30000	-
E_{ur}^{ref}	kN/m ²	-	8000	5400	30000	-	-	120000	-
<i>power (m)</i>	-	-	1.00	1.00	1.00	-	-	1.00	-
C'_{ref}	kN/m ²	Su=40	1.00	10.00	25.00	0.1	0.1	40.00	-
ϕ'	degree	0	23	25	26	36	37	24	-
ψ	degree	0	0	0	0	5	5	0	-
$\gamma_{0.7}$	-	-	0.05000	0.00100	0.00100	-	-	0.00150	-
G_0^{ref}	kN/m ²	-	10000	16000	50000	-	-	124000	-
ν'_{ur}	-	0.30	0.20	0.20	0.20	0.30	0.30	0.20	$\nu(nu) = 0.15$
P_{ref}	kN/m ²	-	100	100	100	-	-	100	-
K_0^{nc}	-	-	0.74	0.65	0.50	0.5	0.5	0.50	-
R_f	-	-	0.90	0.90	0.90	-	-	0.90	-
R_{inter}	-	-	0.75	0.75	0.75	0.75	0.75	0.75	1
<i>OCR</i>	-	-	1.2	2	2	-	-	1.1	-
k_x	m/day	8.640E-7	8.640E-5	8.640E-4	8.640E-4	1.600	0.800	8.640E-5	-
k_y	m/day	8.640E-7	8.640E-5	8.640E-4	8.640E-4	1.600	0.800	8.640E-5	-

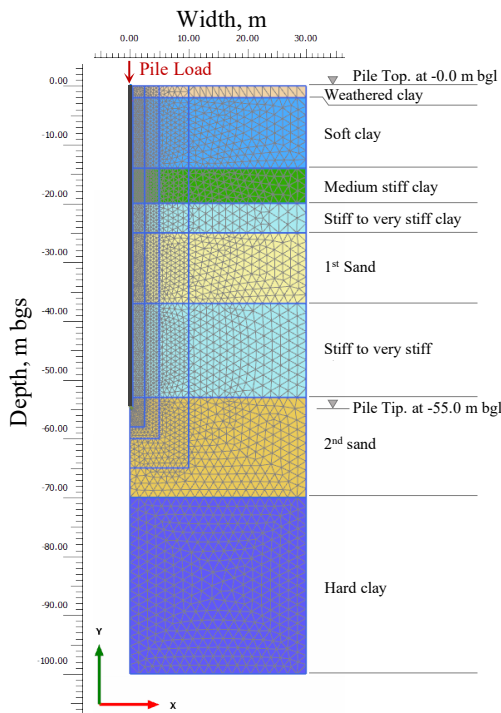


Fig. 3 Geometry of the problem and 2D Finite element mesh used in this analysis

Geometry Model and Boundary Condition

The 2D FE mesh indicating the single bored pile, soil profile and element discretization is depicted in in Fig. 3. The bored pile with diameter of 1.0 m and depth of 55.0 m bgs is considered. For the displacement boundary conditions, all vertical sides were restrained against lateral movement but permitted for vertical movements. The bottom of the mesh was fixed (no movement all directions). For the ground water condition, groundwater flow on bottom

mesh is set to be no flow condition (no vertical flow) while the horizontal flow is set in all vertical side of mesh. The groundwater head was controlled by flow functions, the groundwater level change with time dependent was defined in this step. The size of model is 80 m for width and 100 m depth. The size of model is greatly larger than the required distance of six times the pile diameter at the side and the pile base.

The analysis steps

This analysis focus on the pile-soil movement, load distribution along the pile, and the reduction of pile capacity during groundwater level rising event. The soil without piled in initial stage, the groundwater starts from the ground surface (Hydrostatic pressure) was controlled by flow function to decrease of -0.75 m/year in 40 years. Then, the pile foundation of this building was installed during the period of maximum ground drawdown (1997). The load at top of pile was maintained to constant by working load for a period of 40 years that had been rising of groundwater rate of +0.75 m/year.

In the first step, stress in soils was initialized according to K0,NC. After that, bored pile was constructed, Rinter between pile and soils were active. This model was assumed that the soil displacement has not occur during the bored pile was installing. For pile loading, Surface load is applied on cross section area of pile by 8120 kN/m² or 640 ton (working load). In groundwater rising step, the groundwater level changing with time dependent was defined. The calculation type to Fully coupled flow deformation analysis is condition in this step. The time interval are 14,600 days (Approximate 40 years from 1997 to 2037). The groundwater rising was defined rate +0.75 m/year. The groundwater head with time of this model was presented in Fig. 4, that

related to piezometric levels changed with time in Bangkok at PD0023 in Fig. 1. The summaries of stage modeling and pile-soil movements during the groundwater changing were demonstrated in Fig. 4, the ground surface movements depend on groundwater head changing, the similarly behavior was presented in full field test by Armishaw and Cox [11], and the pile foundation show less heave than the surrounding soil surface during the groundwater rising event as a results of centrifuge tested by Morrison [12], [13].

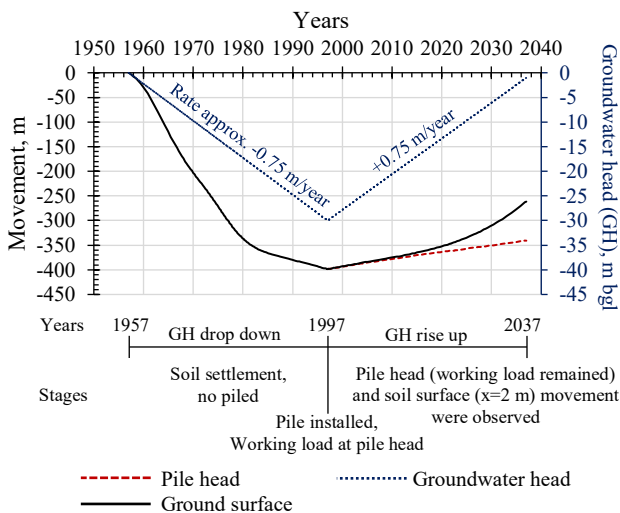


Fig. 4 Pile-soil movements with groundwater changing in the model.

RESULTS AND DISCUSSIONS

Pile-soil movement

The pile-soil movements before and after the groundwater rising event was showed in Fig.5, the pile foundation and the soil heave. The large soil heave was found near the soil surface. However, the pile foundation show less heave than the surrounding soil above neutral point (level of zero pile soil displacement), that represents decreasing of friction force between soil and pile because the effective stress was reduced by the rising groundwater. The behaviors were seen to effect pile settlement relative to the ground surface during the rising of groundwater.

Stress distribution in pile

Fig. 6 shows vertical stress distribution along the depth under the friction pile. Which represent stress profile at each year. The neutral point demonstrating the depth of soil causing pile settlement relative to the surface of pile. According to groundwater level raising, the soil surround pile surface was forced by

uplift, cause the pile was heave. The load distribution was transferred form compression zone to tension zone. For after rising groundwater event, the end bearing was expressed at the end of pile.

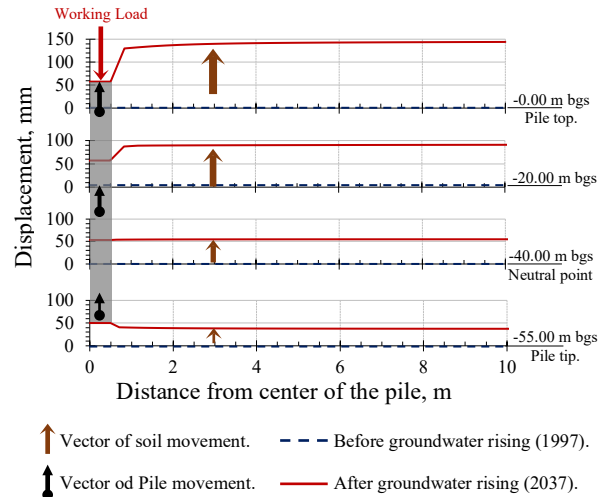


Fig. 5 Soil displacement at varies depth after groundwater rising event

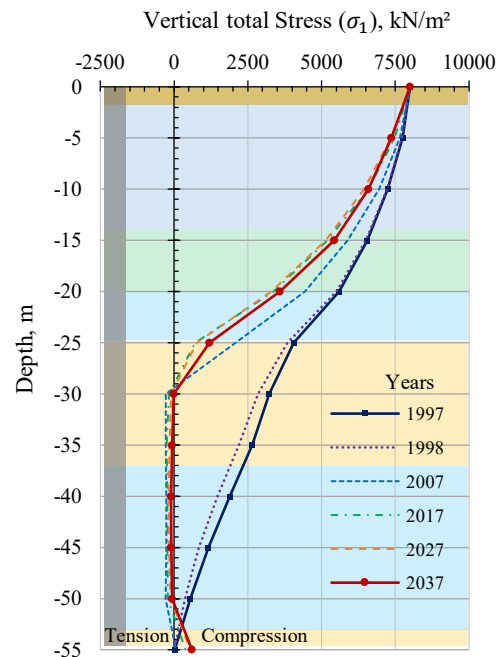


Fig. 6 Stress distribution along the pile during groundwater level rising event

Pile capacity

The reduction of pile capacity was represented in Fig.7. The magnitude of pile settlement was decided at -20 mm, comparable to that of the pile capacity reduce by 20%, that relative to the loss of the ultimate load for the increased pore water pressure. Despite to the pile will not reach up to fail, but the some of pile

that have less of factor of safety (F.S.) must reconsider to the stability of the pile.

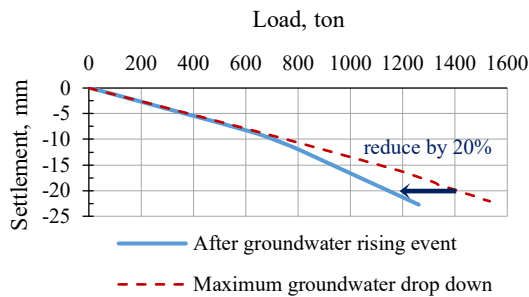


Fig. 7 Reduction of pile capacity.

CONCLUSIONS

The fully coupled flow deformation analysis, both groundwater flow and soil deformation behaviors with time-dependent conditions in Plaxis program can express the pile-soil movement behavior, that correspond the previous study in a full field test and centrifuged test by Armishaw and Cox [11] and Morrison [12], [13] respectively. The results of the numerical modelling found that:

- The pile foundation show less heave than the surrounding soil surface during the groundwater rising event.
- The load distribution along the pile was transferred from compression zone to tension zone at lower part near neutral point of the pile.
- The pile load capacity be significantly reduced by the increase in groundwater head.

Despite the reduction of pile load capacity with groundwater changed not enough to failure (Factor of safety <1.0), the pile stability should be concerned and the optimum groundwater level must be controlled.

ACKNOWLEDGMENTS

The authors would like to extend deep gratitude to the Research and Researchers for Industry (Grant No. PHD58I0003) and King Mongkut's Institute of Technology Ladkrabang Research Fund (Grant No. KREF046012) for the financial sponsorship (PLAXIS Software).

REFERENCES

[1] DGR., Groundwater and Land Subsidence investigation project, Department of Groundwater Resources, 2013.
 [2] K. Intachai, Analytical Assessment on Pile Capacity in View of Effects of Groundwater Drawdown and Rebound Associated with Deep

Well Pumping in Bangkok, Master thesis, AIT, 2016.
 [3] Department of Groundwater Resources and Seven associated consultants Co., Ltd., The effect to underground structure cause by the groundwater rising in Bangkok aquifer around Bangkok Metropolitan Region, Final report, 2011.
 [4] Galavi, Vahid & Brinkgreve, R. & Bonnier, Paul & Gonzalez, Nubia. Fully coupled hydro-mechanical analysis of unsaturated soils, Computational Geomechanics I (ComGeo I), At Juan-les-Pins, France, 2009, pp.486-495
 [5] Galavi, Vahid, Groundwater flow, fully coupled flow deformation and undrained analyses in PLAXIS 2D and 3D, Internal report, Plaxis BV 2010, research department, 2009.
 [6] JICA, DMR, and PWD, The study on management of groundwater and land subsidence in the Bangkok Metropolitan area and its vicinity, Interim report, 3, Kokusai Kogyo Co. Ltd, Tokyo, Japan, 1995.
 [7] N. Tussanee, Situation of groundwater in Bangkok metropolitan area, Available at: <http://www.gwcr.org>, Accessed June 10, 2015.
 [8] Thayanan B. et al., Settlement prediction of large diameter bored pile in Bangkok soils. Sixth International Conference on Geotechnique, Construction Materials and Environment, 2016.
 [9] Surarak, C., Likitlersuang, S., Wanatowski, D., Balasubramaniam, A., Oh, E., Guan, H., Stiffness and strength parameters for hardening soil model of soft and stiff Bangkok Clays, Soils and Foundations 52 (4), 2012, pp.682–697.
 [10] Likitlersuang, S., Teachavorasinskun, S., Surarak, C., Oh, E. and Balasubramaniam, A., Small Strain Stiffness and Stiffness Degradation Curve of Bangkok Clays. Soils and Foundations, 53(4), 2013, pp.498–509.
 [11] Armishaw J. W. and Cox D. W., The effects of changes in pore water pressures on the carrying capacities and settlements of driven piles end bearing in sand and gravel stratum, Proc. Conf. on Recent developments in the design and construction of piles. I.C.E., London, 1979, pp.227-236.
 [12] Morrison P. R. J. and Taylor R. N. Foundations in a rising groundwater environment, Proc. Int. Conf. on Groundwater Problems in Urban Areas, ICE, London, 1994a, pp.342-354.
 [13] Morrison P. R. J. and Taylor R. N. Modelling of foundations in a rising groundwater environment, Proc. Int. Conf. Soil Mechanics and Foundation Engineering. New Delhi, 1994b, Vol. 2 pp.655-658.

COUPLED ANALYSIS CONSIDERING DENSITY CHANGE OF UNSATURATED SOIL

Daiki Yamashita¹ and Shin-ichi Kanazawa²

¹ Social Environmental Systems Engineering, National Institute of Technology Fukushima College, Japan;

² Civil and Environmental Engineering, National Institute of Technology Fukushima College, Japan

ABSTRACT

In recent years, with the increase in sudden heavy rainfall, such as typhoons and guerrilla heavy rain, there are many reports of the collapse of soil structures on a global scale. People are suffering from the danger of soil structure disasters almost every year. This is partly due to the analysis of the factors leading to the collapse of soil structures and the fact that the mechanisms are not fully understood. In this study, the ground behavior of embankment and river embankment considering rainfall and rising water level were examined using the air-dissolved unsaturated soil / water / air coupled finite analysis code. In the current analysis code for unsaturated soil, " $\dot{\rho} \mathbf{g} = 0$ " is used in the incremental balancing equation. Therefore, it is not possible to consider the influence of a state change due to external factors, that is, the change of the unsaturated density. The purpose of this study is to propose an incremental balancing equation applied to unsaturated soil and reflect it in the conventional analysis code. In this way, this study attempts to construct an analysis code that considers density change due to external factors in unsaturated soil.

Keywords : Numerical analysis, Density change, Unsaturated soil, Finite element method

INTRODUCTION

In recent years, due to the effects of global warming, sudden heavy rains such as typhoons and guerrilla heavy rains are increasing. Along with this, there are many reports of collapse of and damage to soil structures on a global scale. Even in Japan, due to the effects of Typhoon No. 19 in 2019, about 140 river dikes broke and suffered enormous damage nationwide [1]. At that time, many river dikes under the jurisdiction of the country, such as the YOSHIDA River (Miyagi), the ABUKUMA River (Fukushima), and the CHIKUMA River (Nagano), broke. This was partly due to the analysis of the factors leading to the collapse of soil structures and the fact that the mechanisms are not fully understood. Therefore, it is urgently necessary to understand the behavior of the foundation ground of soil structures over a long period of time. In geotechnical engineering, there are many studies looking at the optimal design of an embankment structure that focus on predicting the structure's long-term performance by using numerical analysis. In this laboratory, we have clarified the ground behavior of embankment and river embankment considering rainfall and rising water level using the air-dissolved unsaturated soil / water / air coupled finite analysis code "DACSAR-MP"[2]. However, in the current analysis code for unsaturated soil, the term of the density change over time in the incremental balancing equation is " $\dot{\sigma} + \dot{\rho} \mathbf{g} = 0$ " is " $\dot{\rho} \mathbf{g} = 0$ ". For this reason, the

current analysis cannot consider state change due to external factors, that is, the influence of the density change of the unsaturated state. This is because the time change of the density " $\dot{\rho}$ " is not formulated. Therefore, the purpose of this research is to propose an analysis code considering the time change of the density by newly proposing the time change of the density and reflecting it in the DACSAR-MP program. In addition, we compare the analysis results with the conventional analysis code (without density change) and the newly constructed analysis code (with density change) to verify the usefulness of the change.

DENSITY CHANGE OVER TIME

Necessity

In conventional finite element analysis, it is not possible to consider the effect of state change due to external factors, that is, the effect of unsaturated density change. Taking the collapse of a river embankment as an example, overflow, erosion, seepage, and earthquakes are all causes of river embankment failure due to fluctuations in external water level. Of these, three, excluding earthquakes, are due to rainfall. Therefore, using the existing analysis code, we have tried to understand the behavior of soil structures by performing analysis with rainfall and water level rise for the river embankment. However, the existing analysis code cannot consider the effect of unsaturated density

change. In other words, it is impossible to obtain more accurate analysis results because the density does not change with time, and it is not possible to consider the inflow and outflow of water into the ground. Therefore, it is necessary to propose the equilibrium formula of unsaturated soil for more precise analysis.

Proposal of a Term for Density Change with Time

First, Equation (1) shows the relationship of relative densities in each phase.

$$\bar{\rho}_\alpha = \frac{M_\alpha}{V} = \frac{V_\alpha}{V} \rho_\alpha (\alpha = s, f, a) \quad (1)$$

Here, the relative volume of each layer is expressed as follows from the relationship between the void ratio, porosity, and saturation and the three-phase diagram of soil. Equations (2), (3), and (4) are the relative volumes of the soil, liquid, and gas phases in this order.

$$\frac{V_s}{V} = \frac{1}{1+e} = \frac{n}{e} = \frac{n(1-n)}{n} = 1-n \quad (2)$$

$$S_r = \frac{V_w}{V_v} = \frac{V_w}{V} \Rightarrow \frac{V_w}{V} = S_r \frac{V_v}{V} = S_r \frac{V - V_s}{V} = n S_r \quad (3)$$

$$\frac{V_a}{V} = \frac{V - V_s - V_w}{V} = n(1 - S_r) \quad (4)$$

From this, the relative density of each phase is as follows. Equations (5), (6), and (7) are the relative densities of the soil, liquid, and vapor phases in this order.

$$\bar{\rho}_s = (1-n)\rho_s \quad (5)$$

$$\bar{\rho}_w = n S_r \rho_w \quad (6)$$

$$\bar{\rho}_a = n(1-S_r)\rho_a \quad (7)$$

Therefore, Equation (8) shows the overall density relationship.

$$\rho = \bar{\rho}_s + \bar{\rho}_w + \bar{\rho}_a \quad (8)$$

Next, let us consider the time variation of the density of each phase. Equations (9), (10), and (11) are the changes over time in the density of the soil, liquid, and gas phases.

$$\dot{\bar{\rho}}_s = ((1-n)\rho_s) = -\dot{n}\rho_s \quad (9)$$

$$\dot{\bar{\rho}}_w = (n S_r \rho_w) = \dot{n} S_r \rho_w + n \dot{S}_r \rho_w \quad (10)$$

$$\dot{\bar{\rho}}_a = (n(1-S_r)\rho_a) = \dot{n}(1-S_r)\rho_a - n \dot{S}_r \rho_a \quad (11)$$

Finally, the time variation of the overall density is expressed by Equation (12), so $\dot{\rho}$ is proposed as in Equation (13).

$$\dot{\rho} = \dot{\bar{\rho}}_s + \dot{\bar{\rho}}_w + \dot{\bar{\rho}}_a \quad (12)$$

$$\dot{\rho} = -\dot{n}\rho_s + \dot{n} S_r \rho_w + n \dot{S}_r \rho_w + \dot{n}(1-S_r)\rho_a - n \dot{S}_r \rho_a \quad (13)$$

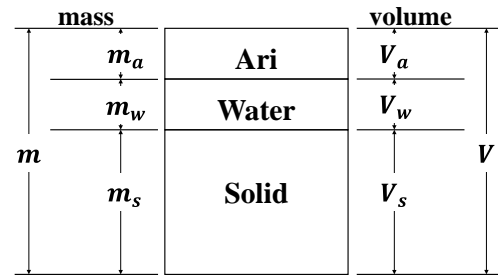


Fig. 1 Three-phase diagram of soil

Density Change Reflected in the Analysis Code

For the effective stress equation considering the term of density change with time, which was proposed in the previous section, weak formulation was performed. After that, spatial discretization was performed using the finite element method. Furthermore, time discretization was performed by the Euler method. This formula, reflected in the program of the analysis code "DACSAR-MP" (see the next chapter), is used in this laboratory, and a new analysis code was created in consideration of the effect of temporal density changes.

SOIL / WATER / AIR COUPLED FINITE ANALYSIS CODE

The finite element analysis code "DACSAR-MP" [2] used in this study formulates the unsaturated soil constitutive model proposed by Ohno et al [3]. This model is framed as the soil/water/air coupled problem using the three-phase mixture theory. Equation (14) shows the effective stress. Equation (15) shows the base stress tensor and suction stress. Equation (16) shows suction.

$$\sigma' = \sigma^{\text{net}} + p_s \mathbf{1} \quad (14)$$

$$\sigma^{\text{net}} = \sigma - p_a \mathbf{1}, \quad p_s = S_e s \quad (15)$$

$$s = p_a - p_w, S_e = \frac{S_r - S_{rc}}{1 - S_{rc}} \quad (16)$$

Here, σ' is the effective stress tensor; σ^{net} is the base stress tensor; $\mathbf{1}$ is the second order unit tensor; σ is the total stress tensor; s is the suction; p_s is the suction stress; p_a is the pore air pressure; p_w is the pore water pressure; S_r is the degree of saturation; S_e is the effective degree of saturation; and S_{rc} is the degree of saturation at $s \rightarrow \infty$. Equations (17), (18), (19) and (20) provide the yield function.

$$f(\sigma', \zeta, \varepsilon_v^p) = MD \ln \frac{p'}{\zeta p_{sat}} + \frac{MD}{n_E} \left(\frac{q}{Mp'} \right)^{n_E} - \varepsilon_v^p = 0 \quad (17)$$

$$\zeta = \exp \left[(1 - S_e)^{n_s} \ln a \right], MD = \frac{\lambda - \kappa}{1 + e_0} \quad (18)$$

$$p' = \frac{1}{3} \sigma' : \mathbf{1}, q = \sqrt{\frac{3}{2}} \mathbf{s} : \mathbf{s} \quad (19)$$

$$\mathbf{s} = \sigma' - p' \mathbf{1} = \mathbf{A} : \sigma', \mathbf{A} = \mathbf{I} - \frac{1}{3} \mathbf{1} \otimes \mathbf{1} \quad (20)$$

Here, n_E is the shape parameter; ε_v^p is the plastic volume strain; M is the q/p' in the limit state; D is the dilatancy coefficient; p_{sat} is the yield stress at saturation; a and n_s are the parameters representing the increase in yield stress due to unsaturation; λ is the compression index; and κ is the expansion index. Equation (21) shows pore water velocity. Equation (22) shows air velocity. Pore water and air flow follow Darcy's law.

$$\tilde{v}_w = -\mathbf{k}_w \cdot \text{grad} h \quad (21)$$

$$\tilde{v}_a = -\mathbf{k}_a \cdot \text{grad} h_a, h_a = \frac{p_a}{\gamma_w} \quad (22)$$

Here, \tilde{v}_w is the pore water velocity; \tilde{v}_a is the air velocity; \mathbf{k}_w is the hydraulic conductivity; \mathbf{k}_a is the coefficient of air permeability; h is the total head; γ_w is the unit weight of water; and h_a is the pneumatic head. Equations (23)-(24) show hydraulic conductivity and the coefficient of air permeability by way of Mualem's [4] formula and the Van Genuchten [5] formula.

$$\mathbf{k}_w = k_{rw} \mathbf{k}_{wsat} = S_e^{1/2} \left[1 - \left(1 - S_e^{1/m} \right)^m \right]^2 \mathbf{k}_{wsat} \quad (23)$$

$$\mathbf{k}_a = k_{ra} \mathbf{k}_{ares} = (1 - S_e)^{1/2} \left(1 - S_e^{1/m} \right)^{2m} \mathbf{k}_{ares} \quad (24)$$

Here, k_{rw} is the ratio of hydraulic conductivity; k_{ra} is the ratio of coefficient of air permeability; m is the Mualem constant; \mathbf{k}_{wsat} is the hydraulic conductivity at saturation; \mathbf{k}_{ares} is the coefficient of air permeability in dry conditions. Equations (25)-(26) show the continuous formula of pore water and air using three-phase mixture theory.

$$n \dot{S}_r - S_r \dot{\varepsilon}_v + \text{div} \tilde{v}_w = 0 \quad (25)$$

$$(1 - S_r) \dot{\varepsilon}_v + n \dot{S}_r - n(1 - S_r) \frac{\dot{p}_a}{p_a + p_0} - \text{div} \tilde{v}_a = 0 \quad (26)$$

Here, n is porosity; $\dot{\varepsilon}_v$ is volumetric strain; and p_0 is atmospheric pressure. The elasto-plastic constitutive model obtained from Equation (17) and the equilibrium equation [Equations (25) - (26)] are formulated as the soil/water/air coupled problem.

COMPARATIVE ANALYSIS

In this study, we examined the validity of the newly proposed analysis code that includes the effect of temporal density changes. Analyses were performed using the conventional analysis code that does not consider the influence of temporal density change (hereinafter, old analysis code) and the analysis code proposed here that considers the influence of temporal density change (hereinafter, new analysis code). The two analysis codes were used under the same analytical conditions, and a comparative study was conducted.

Analysis Condition

The new and old analysis codes for the soil / water / air coupled finite code "DACSAR-MP" [2] were used under the same conditions.

Moisture characteristic curve used by analysis

For a soil-water characteristic curve model, a model capable of hysteresis expression, as proposed by Kawai et al. [6], is used. In addition, to determine the logistic curve in the case of DRY and WET, derived from arbitrary suction and the degree of saturation, the logistic curve equation of Sugii and Uno [7] was used. This makes it possible to grasp the

moisture conditions of sloped ground where a complex water balance occurs. Figure 2 shows the soil-water characteristic curve used in this study.

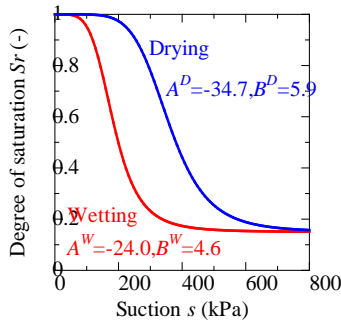


Fig.2 Soil water characteristic curve

Material parameters

Table 1 shows the material parameters used in this study. Material parameters were determined considering the results of previous studies by Honda et al [8]. Here, λ is the compression index; κ is the swelling index; M is the marginal state parameters; m is the unsaturated permeability coefficient of Mualem; n is the E_c model parameters; n_E is the magnification ratio of yield surface; e_0 is the initial gap ratio; ν is the Poisson's ratio; and S_{r0} is the critical degree of saturation.

Table 1 Material parameters

λ	κ	M	m	n
0.180	0.037	1.33	0.80	1.0
n_E	e_0	ν	S_{r0}	G_s
1.3	1.2	0.33	0.15	2.7
k_x [m/day]		k_y [m/day]	ρ_a [t/m ³]	
0.10		0.10	0.0012	

In this analysis, the sand-mixed silt used for general soil structures is assumed.

Permeability coefficient [k (m/s)]				
10^{-11}	10^{-9}	10^{-7}	10^{-5}	10^{-3}
Practically impermeable	Very low	Low	Medium	High
Cohesive soil	sand-mixed silt		Sand and gravel	Gravel

Fig. 3 Permeability coefficient

Analysis model

Figure 4 shows the analytical model used for the comparative analysis. The numbers in the figure indicate element numbers. The displacement boundaries are as follows.

Upper side : Free
Bottom : x, y axis fixed
Right side : x-axis fixed

Left side : x-axis fixed

Here, the water head boundary is given an undrained condition. The air boundary is a non-exhaust condition.

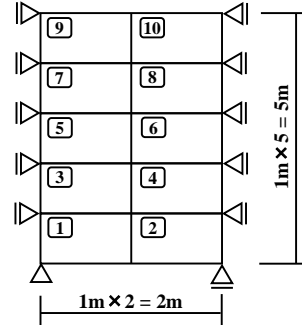


Fig. 4 Analysis model

Flow condition

As the flow rate condition in this analysis, 1.0×10^{-3} m/day rainfall was applied to the upper surface of the model for 900 days (90000 steps). At this time, the daily average rainfall of 5.0×10^{-3} m/day was calculated from the annual average rainfall of 1529 mm/year in Tokyo [9], and the rainfall was set so that it did not differ much from the actual rainfall. The initial saturation was $S_r = 60\%$.

Analysis Result

In this study, we compare the analysis results of the new and old analysis codes regarding saturation, volume strain and total stress. In addition, for the new analysis code, we verified the reaction force at the bottom of the model.

Saturation (S_r)

Figure 5 shows the degree of saturation values and the differences in the analysis using the new and old analysis codes at typical STEP numbers. (The difference is the result of the new analysis code minus the result of the old analysis code.)

From Figure. 5, we can confirm the difference in the degree of saturation in the analysis using the new and old analysis codes. Here, both results show a similar degree of saturation increase as the number of STEPs increase. Furthermore, the evaluation is performed by focusing on the number of steps. First, from the time immediately after the analysis to the early stage of analysis, the results from the old analysis code show a slightly higher degree of saturation, but the difference is only 0.0095% at the time of STEP10000. In other words, from the time immediately after the analysis to the beginning, there is almost no effect due to the consideration of $\dot{\rho}$ in the incremental balance equation. However, as the

number of STEPs increases, the difference in degree of saturation increases rapidly. Figure 6 shows the difference in degree of saturation between the new and old analysis codes. As shown here, the difference in saturation exhibits an exponential relationship. For this reason, the difference in degree of saturation in this analysis becomes noticeable at around STEP 40000. Furthermore, it is clear that at STEP80000, the difference becomes a remarkable discrepancy of about 2.1%.

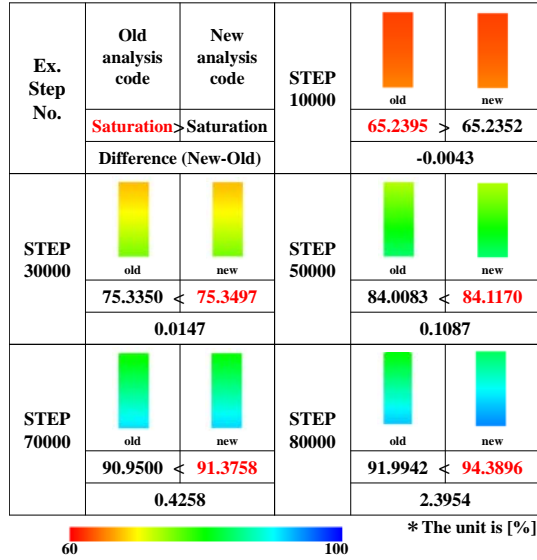


Fig. 5 Change in degree of saturation

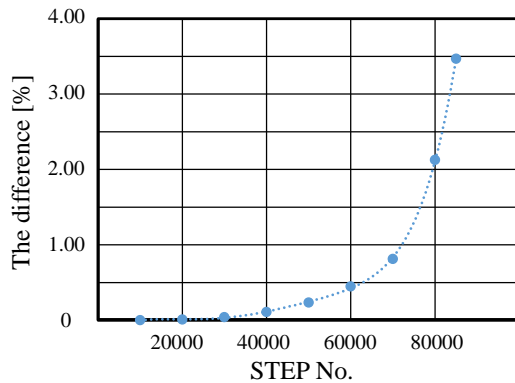


Fig. 6 Difference in saturation between new and old analysis codes

Total stress

The changes over time of total stress in the analysis using the new and old analysis codes are shown below. Figure 7 shows the upper model, and Fig. 8 shows the lower model. As seen in Figs. 7 and 8, the total stress value in the new analysis code exceeds the total stress value in the old analysis code in both the upper and lower parts of the model. This is the effect of the consideration of $\dot{\rho}$ on the

incremental balance formula. It is considered that the newly proposed $\dot{\rho}$ term affects the distribution of total stress immediately after the analysis. This suggests that the density term has a large effect on the total stress.

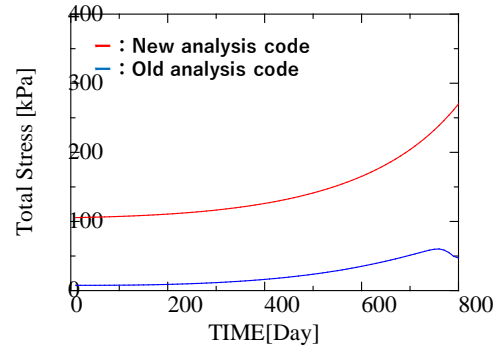


Fig.7 Total stress at the top of the model

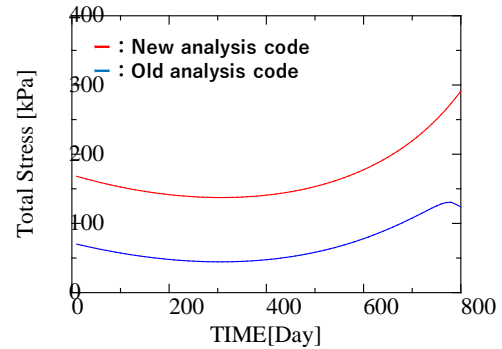


Fig.8 Total stress at the bottom of the model

Reaction force verification

In this study, we also verified the reaction force to confirm the consistency of the new analysis code considering the time variation of density. Figure 9 is a model that measures the reaction force. The model is a 1m x 1m element with nine nodes. The displacement boundaries are as follows.

Upper side : Free

Bottom : x, y axis fixed

Right side : x-axis fixed

Left side : x-axis fixed

In addition, the water head boundary is an undrained condition and the air boundary is a non-exhaust condition. As the flow rate condition, 10 days (1000 steps) of 1.0×10^{-2} m/day rainfall was applied to the top of the model. Table 2 summarizes the results. Table 2 shows the reaction force values at the main STEPs at the contact points at the bottom of the model, "No. 1, No. 2, No. 3," and their totals. As a result, the reaction force at the bottom of the model increases as the number of steps increases. This

confirms that the new analysis code is properly processing the flow rate condition, and the analytical consistency is therefore recognized.

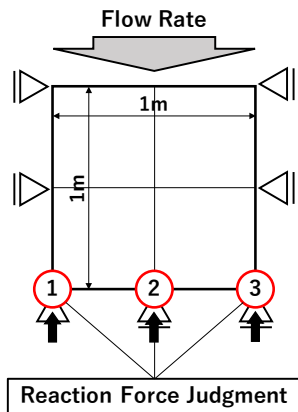


Fig.9 Reaction force verification model

Table 2 Total stress value

	No.1	No.2	No.3	Total
250	1.128	3.963	0.657	5.749
500	1.364	4.719	1.020	7.102
750	1.638	5.562	1.452	8.652
1000	1.933	6.377	1.923	10.232

* Positive Upward

$\times 10^{-2}$ [kN]

CONCLUSIONS

First, the reaction force verification confirmed the consistency of the new analysis code. The analysis results using the new analysis code also confirmed that saturation and total stress tended to increase compared to the old analysis code. This demonstrated that the influence of the temporal change of density in the incremental balance equation cannot be ignored in the numerical analysis of unsaturated soil. It became particularly clear that the difference in the degree of saturation increases with the increase in the number of STEPs, suggesting that the difference becomes large in long-term analysis. Furthermore, in this study, analysis was performed considering the average flow rate in Japan. However, the change in the degree of saturation becomes more remarkable when the analysis considers a flow rate that corresponds to the sudden heavy rain which has frequently occurred in recent years. In other words,

this strongly suggests that the effect of the change in density over time cannot be ignored. Moreover, many of the numerical analyses in geotechnical engineering aim at long-term prediction. Therefore, in long-term analysis, such as embankment analysis, a large difference between the results of the old analysis code and the new analysis code are expected. In the future, we will perform more detailed analysis, in addition to changing external factors, to confirm embankment behavior more precisely.

REFERENCES

- [1] Cabinet Office: About the damage situation to affect typhoon 19th in the first year of Reiwa, 2020, pp24-25.
- [2] Kanazawa, S., Toyoshima, K., Kawai, K., Tachibana, S. and Iizuka, A.: Analysis of mechanical behavior of compacted soil with F.E. method, journal of JSCE, No.68 (2), 2012, pp.291-298.
- [3] Ohno, S., Kawai, K. and Tachibana, S.: Elastoplastic constitutive model for unsaturated soil applied effective degree of saturation as a parameter expressing stiffness, Journal of JSCE, Vol.63/No.4, 2007, pp.1132-1141.
- [4] Mualem, Y.: A new model for predicting the hydraulic conductivity of unsaturated porous media, Water Re-sources Research, Vol.12, No.3, 1976, pp.514-522.
- [5] VanGenuchten: A closed-form equation for predicting hydraulic of unsaturated soils, Soil Science Society American Journal, Vol.44, 1980, pp.892-898.
- [6] Kawai, K., Wang, W. and Iizuka, A.: The expression of hysteresis appearing on water characteristic curves and the change of stresses in unsaturated soils, Journal of applied mechanics, Vol.5, 2002, pp.777-784. Kimura S., Journal Paper Title, J. of Computer Science, Vol. 1, Issue 2, 1987, pp. 23-49.
- [7] Sugii T. and Uno T.: Modeling the New Moisture Characteristic Curve, Journal of JSCE, 1995, pp.130-131.
- [8] Honda M., Iizuka A., Ohno S. Kawai K. and Wang W.: A study of the evaluation method for deformation characteristic of compacted soil, Journal of JSCE, Vol.40, No.2, 2000, pp.99-110.
- [9] Ministry of Internal Affairs and Communications Statistics Bureau: Japanese statistics 2019, 2019, p6.

MUTUAL RELATIONSHIP BETWEEN SUFFUSION AND SHEAR BEHAVIOR IN TRIAXIAL COMPRESSION APPARATUS

Taichi Ishimaru¹, Motoyuki Suzuki¹ and Tomoki Wakamatsu¹

¹Graduate School of Science and Technology for Innovation, Yamaguchi University, Japan

ABSTRACT

Aged embankment structures, affected by long-term seepage, are safety hazards. Internal erosion occurs when soil particles move inside open spaces and eventually flow out of embankment structures together with water. Among the types of internal erosion, the phenomenon whereby only the fine particles flow out, while the skeleton of the coarse soil particles remains, is called “suffusion”. It has been pointed out that changes in the skeletal structure cause changes in the strength of embankments. However, the behavior of suffusion and the factors that it affects are still unclear. The authors previously investigated the influences of suffusion on soil strength. In the present study, a modified triaxial compression testing system was established in order to simulate the suffusion inside specimens. A series of tests was conducted under conditions of different void ratios and filter pore opening sizes. Before and after the water was supplied to the specimens, drained triaxial compression was imposed on them. The amount of discharged soil and the turbidity of the drained water were examined after the tests. As a result, in many cases, both the peak and the residual strength decreased regardless of changes in the void ratio by suffusion. Moreover, no difference in the rate of internal erosion due to shearing was observed.

Keywords: Suffusion, Internal erosion, Embankment structure, Seepage

INTRODUCTION

Aged embankment structures affected by seepage are safety hazards. The phenomenon by which soil particles move inside open spaces of the ground and eventually flow out of embankment structures together with water is called internal erosion. It is one of the main causes of embankment structure failures. There are four types of internal erosion. This paper focuses on one of them, “suffusion”. Suffusion is the phenomenon whereby only the fine particles flow out, while the skeleton of the coarse soil particles remains, as shown in Fig. 1. It has been pointed out that changes in the skeletal structure cause changes in the strength of the embankment [1], [2], [3]. However, suffusion behavior and the many factors that it affects are still unclear. In this study, a modified triaxial compression testing system was established in order to simulate the suffusion inside a specimen. In the apparatus, only fine particles can be discharged from the specimen through the sieve by seepage. A series of tests was conducted under conditions of different void ratios and filter pore opening sizes. Two approaches were taken in this study. First, to investigate the changes in the drained shear behavior of the soils affected by suffusion, drained triaxial compression was imposed on the specimen after water was supplied to it. Second, to investigate the influence of shearing on the suffusion behavior, the amount of discharged soil and the turbidity of the drained water were examined before and after shearing. Measuring the turbidity helped to capture the small suffusion behavior.

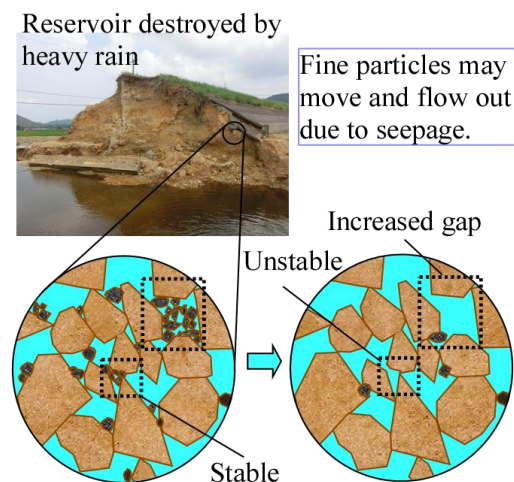


Fig. 1 Image of suffusion

TEST MATERIAL

The soil samples used in this study contained decomposed granite soil collected in Ube, Yamaguchi, Japan and called “Ube Masado”. There are many reservoir embankments made of decomposed granite soil in the chugoku region of Japan. The fines content F_c of Ube Masado is 5.2%. Figure 2 shows the physical properties and the particle size distribution of Ube Masado. The stability of the internal erosion of these soil samples was evaluated using the index proposed by [5], and it was found that internal erosion is likely to occur.

TEST METHOD

Test Apparatus

Figure 3 shows a schematic diagram of the modified triaxial compression apparatus used in this study with photos of the modified parts. It was produced by referring to the experimental apparatus designed by [6]. The soil specimens were approximately 50 mm in diameter and 100 mm in height. At the bottom, where each specimen was located, an acrylic plate, with 21 holes each having a diameter of 5 mm, and mesh with a diameter of either 250 μm or 425 μm , were installed. One or the other of the meshes was selected for each experiment. These parts allowed only fine particles, smaller than the size of the sieve, to flow out of the specimen under the application of water flow. In addition, soil particles were easily discharged by providing a funnel-shaped depression in the bottom of the specimen and changing the size of the tube located between the pedestal and the lower tank from one with an inner diameter of 2 mm to one with an inner diameter of 4.5 mm. The upper and lower tanks were connected to the upper and lower parts of the specimen, respectively, and the difference between the water level of the upper and lower tanks gave the specimen a downward seepage flow. The drainage, consisting of discharged water and soil particles, collected in the lower tank.

Test Procedure

Preparation of Specimens

All the soil specimens were prepared by the moist tamping method and had the same initial water content ($w = 10\%$). The specimens here were made with various void ratios, e , in the range of 0.45 to 0.65. After placing each specimen on the pedestal, the saturation process was conducted in the same way as that in general triaxial compression tests. After the B value was 0.95 or greater, all the specimens were isotopically consolidated to the mean effective stress of 30 kPa. Up to this point, the procedure is the same for all the specimens. Three tests, called “NE: No Erosion”, “EBS: Erosion Before Shearing”, and “EAS: Erosion After Shearing”, respectively, were performed after this process. The procedure for the three tests will be described in the following.

Pattern 1: NE (No Erosion)

These tests were performed to investigate the drained shear behavior of the soil affected by no erosion. After the consolidation process, a drained shear test was performed with an axial strain rate of 0.5 %/min until the axial strain reached 15%.

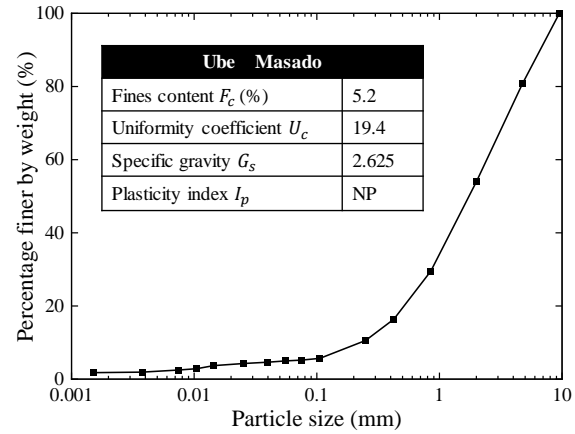


Fig. 2 Physical properties and particle size distribution curves

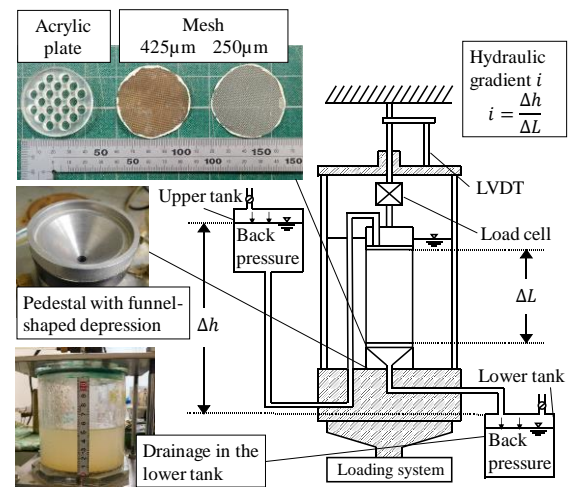


Fig. 3 Schematic diagram of apparatus used in this study

Pattern 2: EBS (Erosion Before Shearing)

These tests were performed to investigate the changes in the drained shear behavior of the soil affected by erosion in comparison to the results of NE. After the consolidation process, the difference between the water levels in the upper and lower tanks was adjusted to approximately 500 mm, and initial hydraulic gradient i was 5. The hydraulic gradient was defined as

$$i = \frac{\Delta h}{\Delta L} \quad (1)$$

where Δh is the water head difference (difference between the water levels in the upper and lower tanks) and ΔL is the height of the specimen.

It should be noted that the hydraulic gradient in this study (a value of 5) was too high compared to the critical hydraulic gradient. However, suffusion did not occur in the case of the lower value, and the tube

was clogged with discharged soil particles in the case of the higher value. Therefore, this value of hydraulic gradient was adopted in the present study.

After the consolidation process, the permeation process was performed until the lower tank was full (about 785 ml). In this process, the seepage direction was downward and suffusion occurred. The change in axial displacement was measured by an LVDT displacement sensor. Next, a drained shear test was performed at an axial strain rate of 0.5 %/min until the axial strain reached 15%.

Pattern 3: EAS (Erosion After Shearing)

These tests were performed to investigate the influence of shearing on the suffusion behavior. After the consolidation process, a drained shear test was performed at an axial strain rate of 0.5%/min until the axial strain reached 15% by the same method as NE. The permeation process was then performed with the same hydraulic gradient as EBS, while maintaining the axial strain of 15%.

After EBS and EAS Tests

After the EBS and EAS tests, the amount of drainage and the turbidity of the drainage were measured. Then, the mass of the discharged soil particles was measured after they had been oven dried.

TEST RESULTS

Status of discharged soil particles

Table 2 shows the test conditions in this study. Each parameter is explained in a note located below the table. Erosion rate R_e was defined by [1] as

$$R_e = \frac{m_{ds}}{m_{s0}} \times 100 (\%) \quad (2)$$

where m_{ds} is the dry mass of the discharged soil particles and m_{s0} is the initial dry mass of each specimen.

Figure 4 shows the relationship between e_{bs} and R_e . R_e is generally low, namely, 0.7% or less. When using the mesh 250 μ m in diameter, R_e is higher as the specimen becomes denser. On the other hand, when using the mesh 420 μ m in diameter, R_e is relatively higher as the specimen becomes looser. It was found in this study that suffusion is likely to occur with the combination of the 420- μ m diameter mesh and a loose specimen. There was no difference in R_e between EBS and EAS.

Figure 5 shows the relationship between the concentration and the turbidity of the drainage. Concentration SS is defined as

Table 2 Test conditions in this study

Test-ID	e_0	e_{ac}	e_{as}	e_{bs}	R_e (%)
NE-1	0.487	0.469	-	-	-
NE-2	0.467	0.453	-	-	-
NE-3	0.571	0.550	-	-	-
NE-4	0.607	0.587	-	-	-
NE-5	0.581	0.564	-	-	-
EBS-250-1	0.488	0.476	0.476	-	0.39
EBS-250-2	0.528	0.506	0.483	-	0.37
EBS-250-3	0.596	0.575	0.557	-	0.11
EBS-420-1	0.478	0.465	0.463	-	0.20
EBS-420-2	0.480	0.461	0.438	-	0.33
EBS-420-3	0.565	0.549	0.560	-	0.68
EBS-420-4	0.614	0.594	0.600	-	0.44
EAS-250-1	0.466	0.450	-	0.512	0.33
EAS-250-2	0.545	0.526	-	0.565	0.31
EAS-420-1	0.588	0.564	-	0.446	0.07
EAS-420-2	0.549	0.519	-	0.511	0.24

Note:

Test-ID: {Experimental code - (Sieve size of mesh) - Number}

e_0 : Initial void ratio, e_{ac} : Void ratio after consolidation, e_{as} : Void ratio after shearing, e_{bs} : Void ratio before shearing, R_e : Erosion rate.

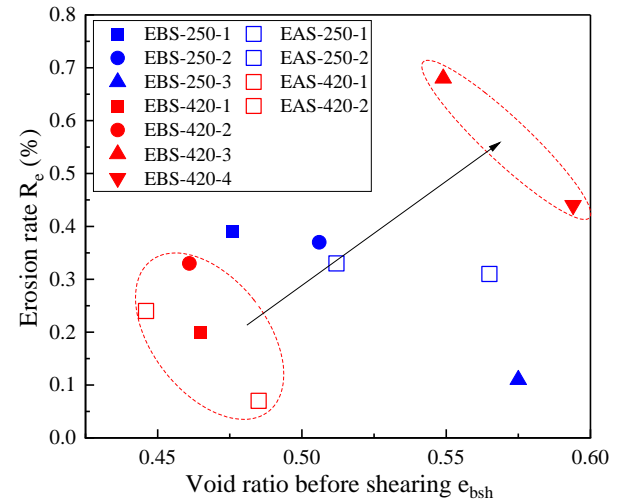


Fig. 4 Relationship between e_{bs} and R_e

$$SS = \frac{m_{ds}}{V_{dw}} \quad (3)$$

where m_{ds} is the dry mass of the discharged soil particles and V_{dw} is the volume of discharged water.

The relationship between the concentration and the turbidity of the calibration suspensions is also shown in Fig. 5. Four calibration samples were taken from the Ube Masado using four sieves, with mesh sizes of 75 μ m, 106 μ m, 250 μ m, and 420 μ m, and named C75, C106, C250, and C420, respectively. 80 types of suspensions were made, and their turbidity was measured. The 80 types of suspensions differed in calibration samples (4 types: C75, C106, C250, and

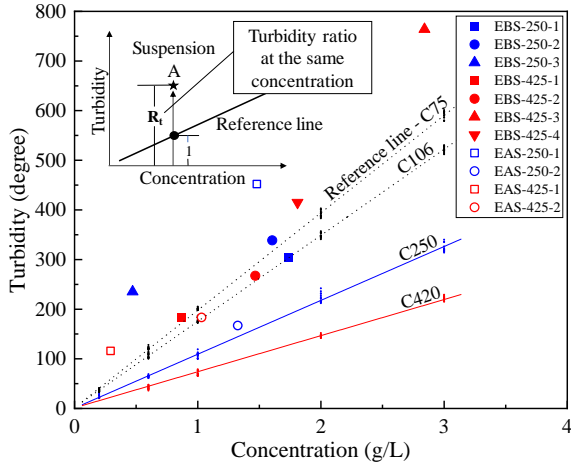
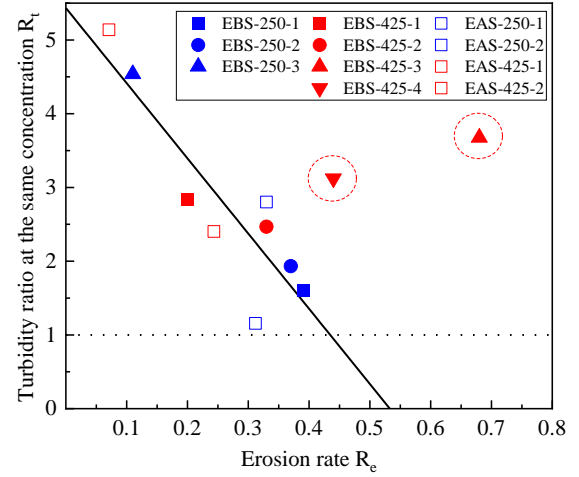
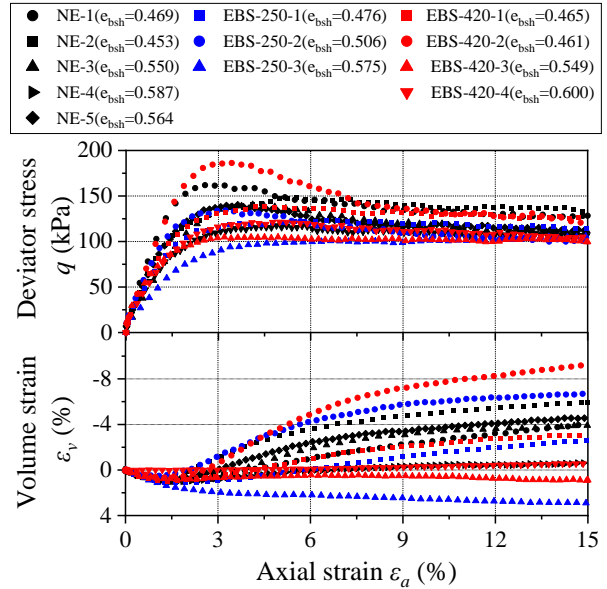
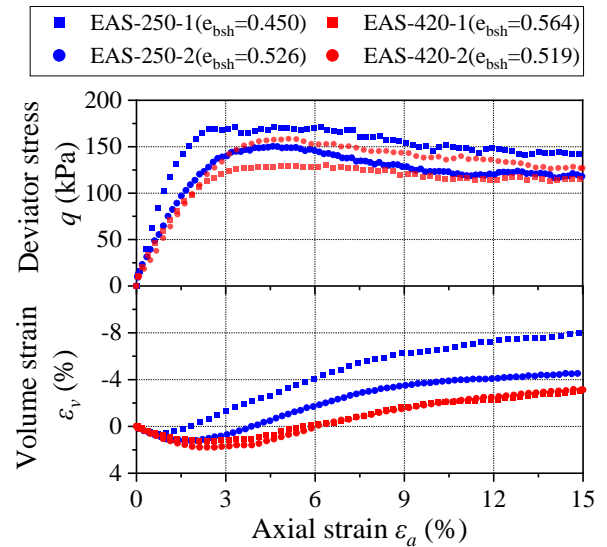


Fig. 5 Relationship between concentration and turbidity of suspensions

C420), SS (5 types: 0.2, 0.6, 1.0, 2.0, and 3.0 g/L), and volume of suspensions (4 types: 0.05, 0.25, 0.50, and 2.5 L). According to Fig. 5, the concentration and turbidity of the calibration samples showed a linear relationship when the type of calibration samples was the same. Further, the slope of the best fitting line became smaller as the size of the soil particles contained in the suspensions was larger. These results are thought to reflect the turbidimeter's characteristics whereby the surface area of the soil particles in the unit volume increases as the particle size of the suspended substance decreases and the amount of turbidity increases [7]. There was no effect on the turbidity measurement due to the differences in the volumes of the suspensions. Here, each best fitting line is called the "reference line". The turbidities of the experimental drainage were plotted above reference lines of C420 and C250. In addition, a lot of data were plotted above the reference line of C75. It is supposed that many soil particles with a particle size of 75 μm or less were discharged from the specimen, although meshes with a sieve size of 250 μm or 420 μm were used in the test. Furthermore, as shown schematically in Fig. 5, when the relationship between the concentration and the turbidity of suspension A is plotted, the ratio of the turbidity of suspension A and the turbidity on the reference line in the same concentration of suspension A is called "Turbidity ratio at the same concentration R_t ". It means that the larger the value of R_t , the larger the distribution of soil particles with a smaller particle size than the calibration samples used in the reference line.

Figure 6 shows the relationship between R_e and R_t . In calculating R_t , the reference line of C250 was used with the 250- μm diameter mesh, and the reference line of C420 was used with the 420- μm diameter mesh. The lower the R_e , the larger the R_t . The fact that only the small soil particles flowed out is thought to have contributed to the low erosion rate. The R_t of EBS-420-3 and EBS-420-4 for R_e were


 Fig. 6 The relationship between R_e and R_t

 Fig. 7 Relationship between $\epsilon_a \sim q \sim \epsilon_v$ in cases of NE and EBS

 Fig. 8 Relationship between $\epsilon_a \sim q \sim \epsilon_v$ in case of EAS

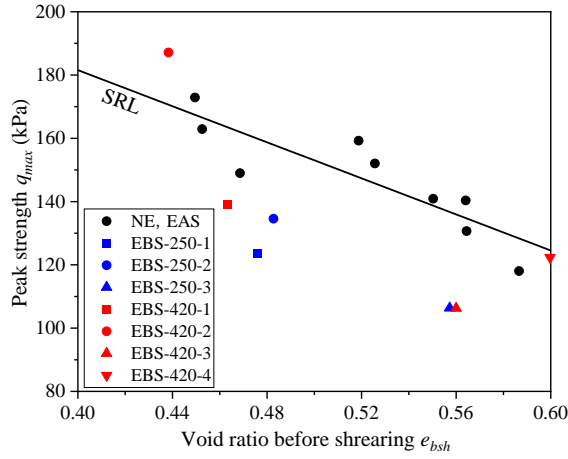
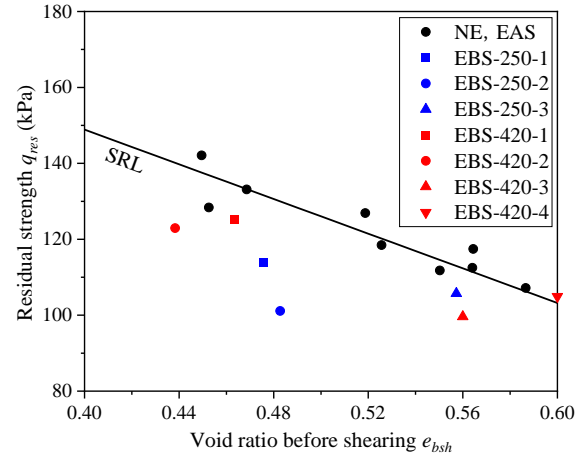
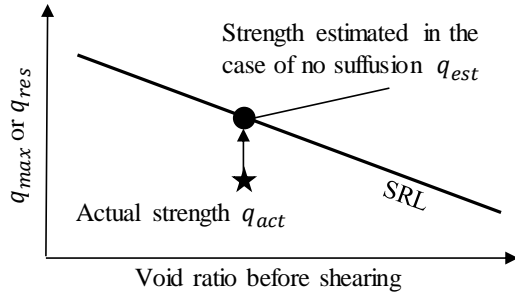
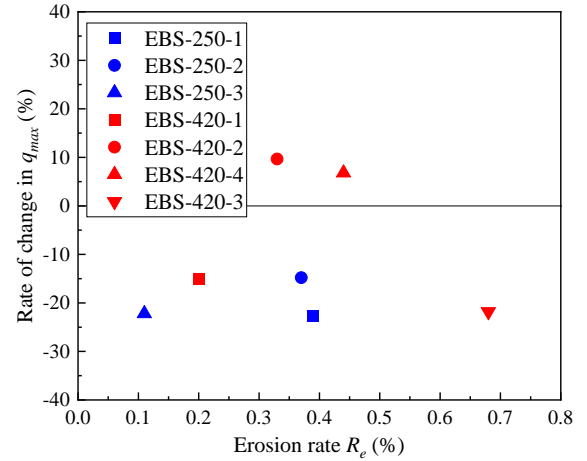
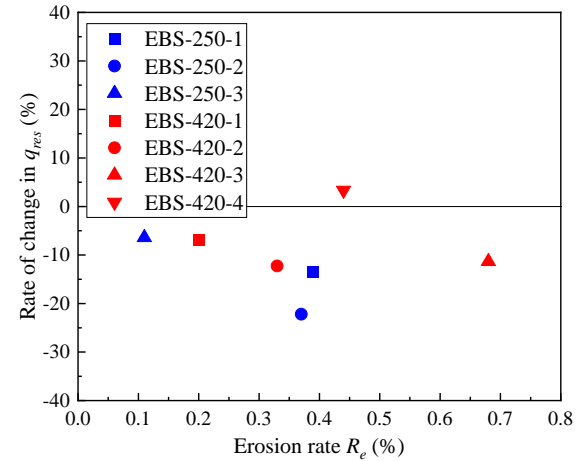

 Fig. 9 Relationship between e_{bs} and R_e

 Fig. 10 Relationship between e_{bs} and R_e


Fig. 11 Relationship between concentration and turbidity of suspensions

higher than the other data. As shown in Fig. 4, these cases for the combination of the 420- μ m mesh and the loose specimen, R_e , were also high. It is thought that sudden clogging is less likely to occur here than in the other test cases and that the soil particles with a small particle size flowed out smoothly from many parts of the specimen.

Relationship between e_{bsh} and q_{max} , q_{res}

Figure 7 shows the relationship among axial strain ε_a , deviator stress q , and volume strain ε_v in the cases of NE and EBS. Figure 8 shows the relationship among $\varepsilon_a \sim q \sim \varepsilon_v$ in the case of EAS. In these tests, it is difficult to perfectly match the void ratio before shearing e_{bsh} ($e_{bsh}=e_{ac}$: in the cases of NE and EAS and $e_{bsh}=e_{bs}$: in the case of EBS), and it is not possible to simply compare the difference in shear behavior due to suffusion. This is because there are three factors involved in the change in the gap ratio of the specimen: (1) the change in volume due to consolidation, (2) the change in volume due to seepage, and (3) the change in the drying density of the specimen due to the loss of soil particles. Therefore, direct focus was placed on the relationship between e_{bsh} and peak strength q_{max} or residual strength q_{res} , and the effect of suffusion on strength


 Fig. 12 Relationship between R_e and R_t

 Fig. 13 Relationship between R_e and R_t

was examined. Here, q_{res} was the deviator stress at the time the axial strain was 15%.

Figure 9 shows the relationship between e_{bsh} and q_{max} , and Fig. 10 shows the relationship between e_{bsh} and q_{res} . The solid lines shown in Figs. 9 and 10 are the best fitting lines to the data of the cases of NE and EAS. These data were not affected by

seepage. Through these solid lines, the reasonable results whereby q_{max} and q_{res} decrease with increasing e_{bsh} can be understood. These solid lines are called “Strength Reference Lines (SRLs)”. The data for EBS are plotted at positions outside the SRL. It was found that q_{max} and q_{res} are different among NE, EAS, and EBS, even if e_{bsh} is the same. [1] and [2] have pointed out that there is a factor that changes the strength besides the change in the void ratio. The results of these tests support the point.

Here, the ratio of the change in q_{max} , influenced by suffusion, was calculated as

$$\frac{q_{act} - q_{est}}{q_{est}} \times 100 \quad (3)$$

where q_{act} is the strength measured in the EBS and q_{est} is the strength estimated in the case of no suffusion. A schematic diagram is shown in Fig. 11 to explain these parameters. The ratio of the change in q_{res} was also calculated in a similar way. Figure 12 shows the relationship between R_e and the ratio of the change in q_{max} , and Fig. 13 shows the relationship between R_e and the ratio of the change in q_{res} . The ratio of the change for each strength was a negative value for many cases, so it is thought that each strength decreased regardless of the change in void ratio. On the other hand, each strength increased by suffusion in some cases. In the case of EBS-420-2, the peak strength increased and the residual strength decreased. Noticeable strain softening was observed. For both peak strength and residual strength, there was no relationship between R_e and the ratio of the change in each strength. Since R_e is less than 0.7%, it is considered that not only the discharged soil particles, but also the moving soil particles in the specimen, affected the strength greatly.

CONCLUSIONS

In this study, two approaches were taken for the triaxial compression apparatus. First, to investigate the changes in the drained shear behavior of the soil affected by suffusion, drained triaxial compression was imposed on specimens after water had been supplied to them. Second, to investigate the influence of shearing on the suffusion behavior, the amount of discharged soil and the turbidity of the drained water were examined before and after shearing. The main results of this paper are summarized as follows:

1. It was found in this study that the combination of a 420- μ m diameter mesh and a loose specimen is likely to cause suffusion.
2. The higher the erosion rate, the smaller the turbidity ratio at the same concentration. When the situation makes erosion difficult, only the soil particles with a small particle size can pass through the gaps, and the soil particles with a large particle size stay in the specimen.
3. No difference was observed between before and after shearing for either the erosion rate or the turbidity ratio at the same concentration.
4. Even though the void ratio before shearing was the same, the peak strength and the residual strength differed depending on the condition of suffusion or no suffusion.
5. No relationship was observed between the erosion rate and the rate of change for each strength. Since the erosion rate was less than 0.7%, it is thought that not only the discharged soil particles, but also the moving soil particles in the specimen, affected the strength greatly.

REFERENCES

- [1] Sato, M. and Kuwano, R., Laboratory testing for evaluation of the influence of a small degree of internal erosion on deformation and stiffness, *Soils and Foundations*, Vol. 58, Issue 3, 2018, pp.547-562.
- [2] Ke, L. and Takahashi, A., Experimental investigations on suffusion characteristics and its mechanical consequences on saturated cohesionless soil, *Soils and Foundations*, Vol. 54, Issue 4, 2014, pp.713-730.
- [3] Ouyang, M., Takahashi, A., Influence of initial fine content on fabric of soils subjected to internal erosion, *Canadian Geotechnical Journal*, Vol. 53, 2016, pp.299-313.
- [4] Kenney, T. C., and Lau, D., Internal stability of granular filters, *Canadian Geotechnical Journal*, Vol. 22, 1985, pp. 215–225.
- [5] Ke, L. and Takahashi, A., Triaxial erosion test for evaluation of mechanical consequences of internal erosion, *Geotechnical Testing Journal*, Vol. 37, Issue 2, 2014, pp.347-364.
- [6] Yokoyama, K., The influence of particle size on turbidity output and the instructions for using turbidity sensor in the field, *Journal of JSCE*, Vol. 698, 2002, pp.93-98 (in Japanese).

INVESTIGATION OF TIME-SERIES EXTENSOMETER DATA IN A CONCRETE LINED MINE SHAFT

Jordan Tyler Kalyvas¹, John Victor Smith¹ and Gang Ren¹

¹RMIT University, Australia

ABSTRACT

Data from extensometers installed in a concrete lining of a mine shaft is analysed to interpret the pattern of deformation. The shaft is an important mine infrastructure which is at risk of damage. Five years of monitoring data are reviewed for this study. Analytical and numerical methods are applied to resolving the geometric components of the deformation. The deformation pattern is interpreted in terms of the in situ stress conditions and mining activities at the location. The lining is shown to undergo elliptical and translational deformation components. The deformation is interpreted in terms of stress fields. The local mining history and the presence of two significant faults influence the deformation pattern observed in the mine shaft. The deformation recorded by the extensometers is inferred to represent a sequence of slow stress waves passing through the shaft pillar during mine excavation.

Keywords: Mine shaft, extensometers, concrete lining, deformation

INTRODUCTION

A copper mine shaft is outfitted with six extensometers embedded in the shaft lining rock mass interface. The mine shaft is located in Mt Isa in the north of Queensland, Australia [1]. The shaft has shown signs of degradation and cracking dating back to 1980 [2]. Selected data from six extensometers, which have been collecting data wirelessly since May, 2015. A period from July to September 2017 is analysed in this study.

Mining in the location will be briefly reviewed to provide context for the instrument observations. The mining occurring closest to the shaft is toward the northwest from the shaft and approximately 200 m below the level of the extensometers use to collect data for this study (Fig. 1).

Mining via this shaft during 2017 included approximately 340,000 t of stoping in the first half of 2017 concluding on 25th July 2017. During that time 120,000 t was excavated from a stope approximately 60 m from the shaft. Mining of areas accessed from this shaft did not recommence until 21st November 2017. During that time mining occurred in locations accessed by other shafts. Therefore events 1-5 occurred near the conclusion of a phase on mining close to the shaft. Whereas events 6 to 8 occurred during a time of no local mining activity.

The time of day at which mine blasting occurs is limited for safety reasons. Excavation blasting at the mine is tightly restricted to a 45 minute window centred on 8am and 8pm such that blasting does not occur at other times. Only event 6 occurred at a time that corresponds with the blasting time. The following two events (7 and 8) appear to have occurred at approximately 24 hour intervals after

event 6, however, these events commenced a number of hours before the blasting time at the mine. Therefore there is no indication that the events are directly related to blasting at the mine.

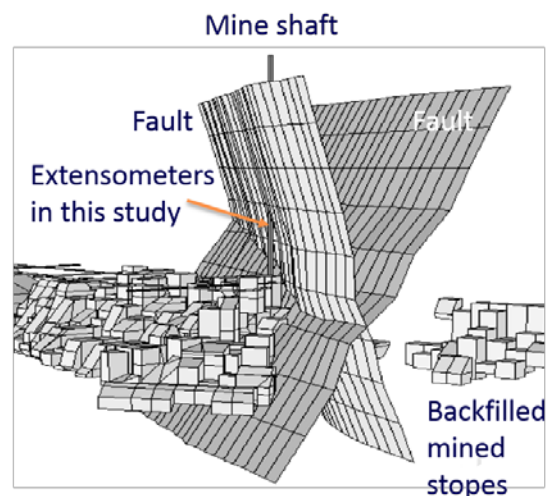


Fig. 1 Layout of the mine shaft, faults and mined stopes, after [3].

This paper investigates the detailed deformation of the recorded displacements to determine if the events also include other systematic components such as elliptical or translational deformation. The direction of the deformation components is studied to identify internal consistency and to compare with regional geological structure and stress conditions. The variation of deformation magnitude over time is investigated to infer time-dependent rheological behaviour of the rock mass in the mine.

DATA COLLECTION

Displacement data from the extensometers has been wirelessly collected in real time since installation. The six extensometers lie in the horizontal plane around the shaft and are anchored in the rock mass (Fig. 2)..

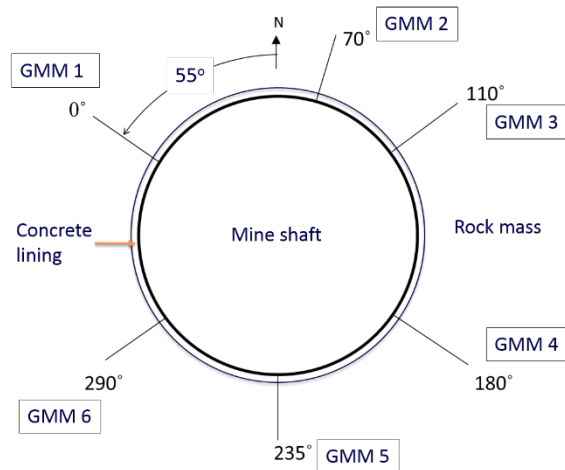


Fig. 2 Horizontal layout of the mine shaft and extensometers (Ground movement monitors, GMMs).

An example of readings from extensometer ring 2 at a depth of 577 m is shown in Fig. 3. Ring 2 is in the approximate location where two steeply dipping faults intersect the shaft (Fig. 1). The time interval between records (spacing on x-axis) varies as the system does not take a reading if all extensometers show displacement below a threshold.

The data shown in Fig. 3 were collected from July to September of 2017. Within this data set, a number of ‘events’ appear to be recorded by similar movements of each extensometer (GMM1-6). Eight of the apparent events have been selected for detailed analysis (labelled 1-8 in Fig. 3). The events in July are lower in magnitude, less distinct in shape and less regular in timing compared to the events in September. The three events in September are of the highest magnitude and show distinct rises and falls of the displacement during the events. of the peak displacements and durations are shown in Table 1. During this time period, and in the preceding 12 months, other events of sufficient magnitude to be analysed were not observed.

Table 1 Summary of events recorded in extensometers in shaft ling

Event	Max displ. mm	Time of max. D/M/Y Hr:Min	Duration Hours
1	2.33	23/07/2017 17:36	N/A
2	1.57	26/07/2017 18:23	2.55
3	2.40	28/07/2017 18:39	0.50
4	4.20	1/08/2017 14:26	0.92
5	1.10	3/08/2017 23:52	N/A
6	5.50	20/09/2017 8:10	8.42
7	6.40	21/09/2017 5:26	8.09
8	9.97	22/09/2017 6:36	4.82

DATA ANALYSIS

Episodes of contraction are shown as incremental changes in GMM readings over time. The deformation observed by the extensometers is calculated as an incremental radial contraction over a given period of time. An example of this data is shown in Fig. 3.

Within each event, the sequence of readings with the highest magnitude have been selected for detailed analysis in order to maintain a higher signal to noise ratio. The raw data has been processed by comparing each data point during an event to a baseline value that the extensometer showed before and after the observed event. The difference between the values during each event and a baseline was obtained. These values are the radial displacements recorded by each extensometer.

Radial displacements were fitted to least squares models which are derived from three superimposed components. Circular (uniform radial), elliptical (deviatoric) and translational. The sum of residuals squared in reference to the recorded incremental radial displacement was calculated. This is a familiar approach when using monitoring data to find changes of shape within tunnels [4].

The displacement episodes show a variety of peak shapes (Fig. 3). Radial displacements are fitted to least squares models which are derived from three superimposed components. Circular (uniform radial), elliptical (deviatoric) and translational. Parameters in one example are calculated for each component in each model. Results show a significant reduction in the sum of the residuals squared as components are

added to the least squares model. Indicating each component added increases the quality of fit for the model. Further residual analysis shows that the addition of each component improves the residual plot distribution. The observation that each extensometer records a displacement of similar magnitude suggests that a significant component of the deformation is a uniform radial contraction of the lining

DISCUSSION

The eight events analysed in this study were selected as they represented a period with clear signals with all six extensometers functioning. One of the key aspects of the observations to explain is the duration of the events. The duration of the events ranges from a few minutes (single reading) to over 8 hours. Vibration from blasting or pressure waves from the initial changes of stress in the rock mass around excavated slopes would be expected to propagate at a far higher velocity than the events observed. Previous research has identified the main situations where creep should be taken into account are the deformation of pillars and progressive closure of caverns in soft rock mines and the slow ‘diffusion’ of stress between faults that may trigger earthquakes [5]. The time-dependence of deformations associated with faults has been investigated in the temporal and spatial relationships of Californian earthquakes and the associated stress changes [6]; limitations on spatial interaction of faults globally [7] and numerical simulation of viscous contributions to the relationship between displacement and stress distribution in fault system [8].

The rock mass at Mount Isa is unlikely to be as low in strength as the coal and salt deposits referenced by [5]. Mining activities in the vicinity of the shaft culminated and concluded around the time of the first five events analysed in this study. Mining activities did not occur in the vicinity of the shaft for the remaining two months during which the remaining three events occurred. It is possible that adjustment of stress following mining in the vicinity of the shaft is responsible for the events observed in the instrumental data. The presence of two significant fault zones near the location of the instruments could also provide the local low rock mass strength to explain the inferred creep movement. Deformation observed in the monitoring data is seen to rise to a peak deformation which returns over time to its original position. This deformation pattern is inferred to represent a stress wave which has moved through the rock mass and been recorded by the extensometers in the mine shaft. The time-scale of the stress waves appears to vary from rapid events leaving only a single record in the continuously monitored instruments to slower waves leaving multiple instrument records over many hours. The

systematic pattern of rising and falling of the displacements and the consistent orientation of the elliptical component of the displacements supports the interpretation of these records as transient stress pulses or waves moving through the rock mass.

The mechanical interpretation would be that of a spring and dashpot in series [9]. Where shaft lining and surrounding rock-mass act as a spring and the faults act as a viscoelastic system of spring and dashpot in series. Initially strain is accommodated entirely in the spring. The stress in the spring subsequently decays as time-dependent displacement occurs on the dashpot. In the situation being investigated, elastic strain is caused by the initial partial closure of stopes excavated by mining. The stress associated with the strain is dissipated by creep deformation in the weak rock of the fault zones and/or the backfilled stopes (Fig. 1).

The inferred relationships are as follows. The mine shaft is fitted with a rosette of extensometers. Excavation of stopes causes deformation of the rock mass. The deformation can be considered in terms of elastic and creep behaviours. Faults and excavated stopes can dissipate the elastic strain by creep. This all occurs within the remote/in situ stress conditions. The shape of the highest magnitude events comprises a steep increase in magnitude followed by a less steep (slower) reduction in magnitude. This shape is inferred to be consistent with a more rapid loading of the rock mass followed by a slower dissipation of the stress.

The translational component of deformation is inferred to represent the effects of deformation out of the horizontal plane. It is possible that the translation represents a bending or buckling deformation of the shaft. At present no attempt at explaining the relationship between the N-S compression and the NE translation is made. However, it is anticipated that this will provide an interesting relationship to look for in numerical simulations.

CONCLUSIONS

Extensometers installed in the mine shaft lining record compression of the lining occurring sporadically. Such compression has been investigated in eight separate events over a five-month period. The duration of the events is variable but most lasted between 1 record to over 8 hours. The events are inferred to represent time-dependent (creep) deformation in the rock mass. The creep rate may be controlled by the rate at which nearby fault zones or backfilled stopes dissipate stress by ductile creep. The initiation of the sequence of events in this study is inferred to have commenced due to prior excavation of stopes in the mine and the consequent readjustment of stress. The displacement of the extensometers is approximated by a uniform circular contraction. Model accuracy was increased by

applying an elliptical deformation (ovalisation) and further increased by also applying a translational component. The elliptical component of the deformation indicates north-south compression. The

translational component is inferred to represent longitudinal elastic bending of the shaft.

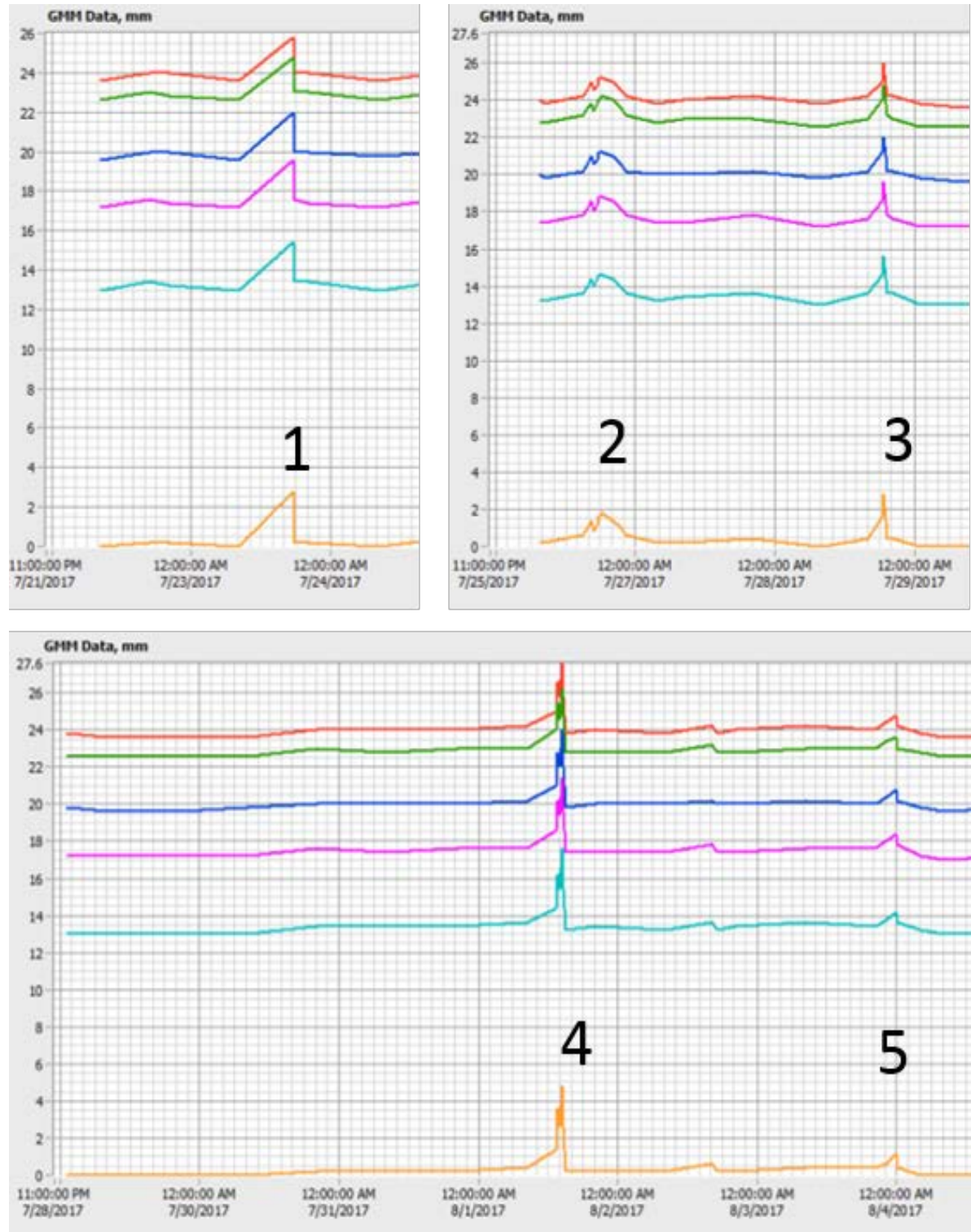


Fig. 3 Displacements of extensometers recorded in a mine shaft. Vertical axis in millimetres and horizontal axis labelled by days.

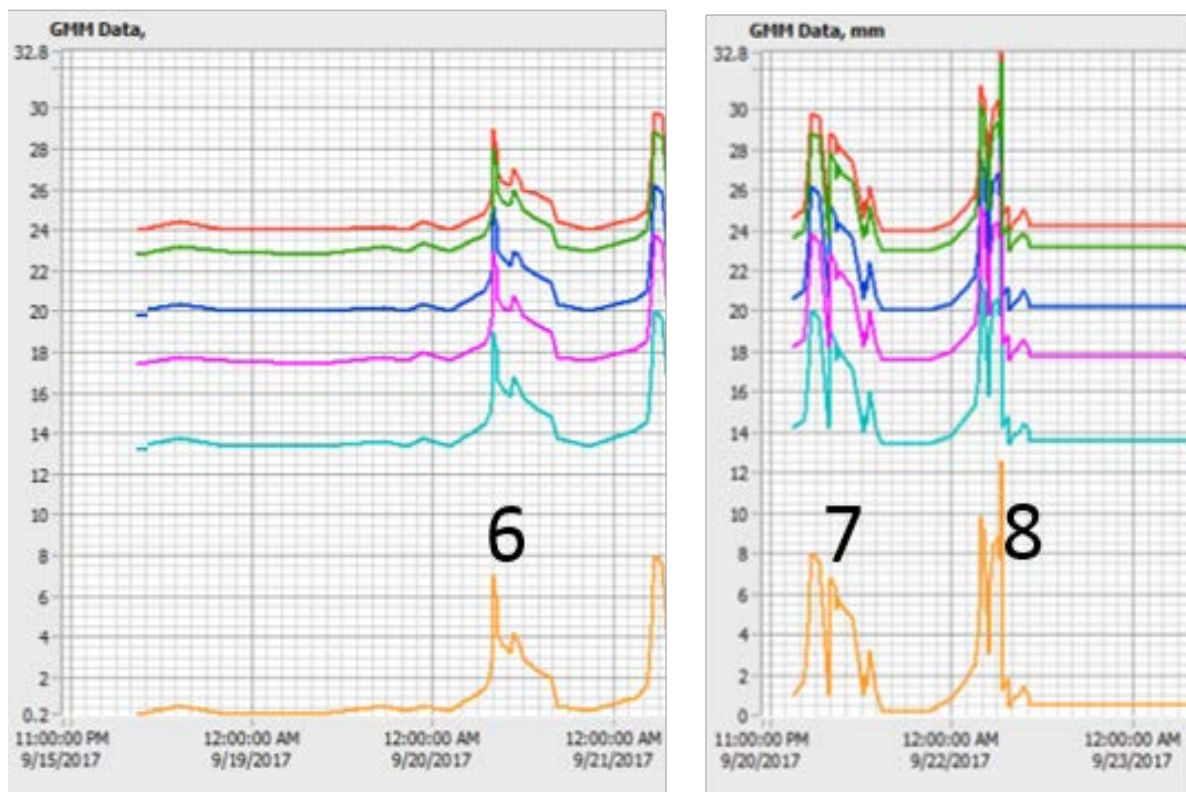


Fig. 3 (continued) Displacements of extensometers recorded in a mine shaft. Vertical axis in millimetres and horizontal axis labelled by days

ACKNOWLEDGMENTS

Mine Design Technologies Australia are acknowledged for provided the extensometer data used in this study.

REFERENCES

- [1] Bruneau G., Tyler D.B., Hadjigeorgiou J., and Potvin Y., Influence Of Faulting On A Mine Shaft—A Case Study: Part I—Background And Instrumentation. *International Journal of Rock Mechanics and Mining Sciences*. Vol. 40, Issue 1, 2003a, pp. 95-111.
- [2] Potgieter, G.S., November. Work Conducted In Preparation For Partial Extraction Of X41 Shaft Pillar At Mount Isa Mines. In *Proceedings of the International Seminar on Design Methods in Underground Mining*. Australian Centre for Geomechanics. 2015., pp.273-290.
- [3] Bruneau, G., Hudyma, M.R., Hadjigeorgiou, J., and Potvin, Y., Influence of faulting on a mine shaft—a case study: part II—Numerical modelling. *International Journal of Rock Mechanics and Mining Sciences*, Vol. 40, Issue 1, 2003b. pp.113-125.
- [4] Xie, X., and Lu, X., Development Of A 3D Modeling Algorithm For Tunnel Deformation Monitoring Based On Terrestrial Laser Scanning. *Underground Space*, Vol. 2, Issue 1, 2017, pp.16-29.
- [5] Jaeger, J.C., Cook, N.G., and Zimmerman, R., 2009. *Fundamentals of rock mechanics*. John Wiley & Sons.
- [6] Ziv, A. and Rubin, A.M., Static Stress Transfer And Earthquake Triggering: No Lower Threshold In Sight?. *Journal of Geophysical Research: Solid Earth*, Vol. 105, Issue B6, 2000, pp.13631-13642.
- [7] Huc, M. and Main, I.G., Anomalous Stress Diffusion In Earthquake Triggering: Correlation Length, Time Dependence, And Directionality. *Journal of Geophysical Research: Solid Earth*, Vol. 108, Issue B7, 2003, pp.2324-2336.
- [8] Sone, H. and Uchide, T., Spatiotemporal Evolution Of A Fault Shear Stress Patch Due To Viscoelastic Interseismic Fault Zone Rheology. *Tectonophysics*, Vol. 684, 2016, pp.63-75.
- [9] Bland, D.R., 1960. *The theory of linear viscoelasticity*. Pergamon, Oxford and New York.

LIMIT ANALYSIS OF THE FUNDAO TAILINGS DAM SLOPE FAILURE IN BRAZIL 2015

Juan Hernandez Espinoza¹, John V. Smith² and Majid Nazem²

¹ GHD Perth, Australia; ²RMIT University, Australia

ABSTRACT

The investigation intends to ascertain the failure mechanisms that lead to the collapse of one of the biggest mining structures in South America, the Fundao Tailing dam. The results obtained during the before mentioned investigation suggested that the dam was stable under drain and undrained conditions. The most recent investigation published in 2016 an valuation of the Fundao Tailing Dam Failure using limit analysis approach, implemented the Limit Equilibrium approach to study the dam's stability. The software Optum G2 was used to generate a virtual representation of the studied sections and to evaluate the stability conditions. Detailed event reports were used to construct the layering of weak slimes and stronger sand tailings. The analysis carried out during this investigation using the Limit Analysis method and introducing the notion of continues layers of slimes with specific strength parameters, indicated that the dam would have failed under these two conditions.

Keywords: Tailings, Limit analysis, Slope failure, Dam stability

INTRODUCTION

The storage of mining waste is a problem in which geotechnical engineering has a wide field of application. Current mining processes of extraction generates a massive volume of waste as fine-grained rock silt called tailings. Tailings consist of a mixture of a fine ground rock with water in variable proportions, additives are also added during the mineral extraction process.

In the traditional mining industries, the tails leave the extraction plant with a high liquid ratio: solid, with a consistency of a viscous sludge. In the form of paste the tailing can be pumped, so that its transportation can be done through spigots and pipelines and eventually poured in along the dam embankment to generate the uniform growth of the dam [1]. Once the slurry materials are poured inside the dam the settlement and consolidation of the tailings begin. The thickest fraction is deposited near of the discharge points while the fine fraction flows by gravity towards the centre of the tank and finally settle there [2].

In upstream raising method, dikes are raised step by step mainly on the tailing beach. Due to these continue increases of heights, water pressure develops within the tailing when low hydraulic conductivity is present. The increase of water pressure within tailing may result in the decrease of shear strengths which may result in the failure of the dam. Dams constructed in upstream are several times more likely to fail as less material to retain the tailing is used [3].

The latest disasters occurred in Brazil drawn the attention of specialist on the field due to the fact that most of tailings have been associated to the upstream

design method. The disaster that occurred on November 2015 at the Fundao dam resulted in the discharge of a torrent of mud that buried buildings and people. It has been reported that around 43 millions of cubic meters of iron were released killing 19 people [4].

The report released by the Fundao tailing dam review panel "Immediate Causes of the Failure of the Fundao Dam" concluded that a chain of events and conditions contribute the failure of the dam. It has been argued that the main failure mechanism that led to the flow slide of the dam was the liquefaction of the saturated tailings. The panel indicated that seismic activities were recorded in the area the same day of the incident and therefore assumed the phenomena was accountable for initiating the dam's flow slide [4].

The Fundao tailing dam review panel have reported that eyewitness descriptions and videos ascertain several things. The failure begun in the Fundao dam left abutment, the dam flow slide occurred due to the liquefaction of the tailings and that the transformation from solid too little occurred suddenly.

This study investigates the conditions and failure mechanisms that could have led to the structural instability of the Fundao tailing dams. A study of the failure mechanism through the implementation of limit analysis method is implemented to demonstrate how saturated sands and interbedded slimes contributed to the failure. Results obtained by limit analysis methods will be discussed and compared to the results obtained from the Fundao review panel.

BACKGROUND

In November of 2015, the iron ore mine in the

South East of Germano, close to the city of Mariana, Brazil, suffered a fissure at the Fundao tailings dam. The failure released 43 millions of cubic meters of waste into the environment. Nineteen people died, including five residents of the village and 14 employees of the Samarco mining company that operated the mine. The mud travelled 650 kilometres and ended up in the Atlantic Ocean 17 days later [4].

According to Garcia et al. [5] there is evidence that the 7000 km² of toxic plume reached important biodiversity conservation areas in the Atlantic Ocean, including Abrolhos National Park, one of the most emblematic protected areas in Brazil, and three other marine protected areas, Costa das Algas, Santa Cruz, and Comboios in Espirito Santo state, threatening endemic and rare species of marine fauna. Models of river discharge dispersion predict long-term consequences near the city of Rio de Janeiro and the consequences of the dam burst in the Atlantic Ocean are still not fully assessed [6].

The limit equilibrium method (LE) has been commonly used during the last decades to study the geotechnical stability of tailing dams, this numerical analysis method was implemented by the Fundao tailing dam review panel. The principal advantages this method offers is that complex soil profiles can be modelled in a variety of loading conditions and can also provide quick results [7].

Despite the fact the limit equilibrium analysis has been refined during the last years using vertical slices and global analysis methods it has been agreed that it has some disadvantages when compared to the Limit analysis (LA) approach [8, 9]. According to [10], Limit equilibrium frequently assumes that collapse will follow a particular assumed geometry, which are effective for simple geotechnical problems, yet may encounter difficulties when considering complex problems. Conversely, the limit analysis approach has demonstrated that it can provide agreeable results without assuming a determine slip surface or the statics of slopes, is suitable to analyse various geotechnical conditions with complex geometries, loadings and boundary conditions and it accounts for nonlinear materials [7].

LIMIT EQUILIBRIUM

The number of methods used, which give different results and sometimes contradictory are a sample of the uncertainty that characterizes the analysis of stability. The most popular limit equilibrium methods used by geotechnical engineers are the proposed by Bishop and Janbu which in their theoretical conception the equilibrium of the forces and momentum are not balanced. The factor of safety obtained through these methods generally differs significantly from the results obtained when using procedures that satisfy balance, such as the Spencer's and Morgenstern-Price method [11].

Although a direct comparison between the various methods is not always possible, the factors of safety obtained with the Bishop's method differ approximately by 5% with respect to more precise solutions, while the simplified method of Janbu generally underestimates the factor of safety up to 30%, although in some cases overestimate them to values of 5% [11]. All the before mentioned methods are based on static equilibrium forces of interslice forces, moments or overall moment. Figure 1 presented below exemplifies how the sliding masses are divided into vertical segments.

LIMIT ANALYSIS

This method is based on the concepts of lower-limit and upper-limit, the same concepts have been used in the calculation of the safety factor for the analysis of slopes by some researchers [8]. LA does not employ assumptions for statics; however, the selection of failure mechanism is required. In these methods, the failure mechanism must be imposed under the conception of a rigid body. Some of the failure mechanisms that have been employed are rotational plane, translational plane and logarithmic spiral [12].

Upper bound theorem

According to [13], if a set of external loads acts on a failure mechanism and the work done by the work done by the external loads in an increment of displacement equals the work done by the internal stresses, the external loads obtained are not lower than the true collapse loads.

Lower bound theorem

The lower limit theorem is based on a statically permissible field of stresses in which the work done by the surface loads in the contour, where the speed is prescribed, must be greater than or equal to the work done by surface loads in any field of statically permissible efforts [13].

TAILING DAM CONSTRUCTION METHODS

The construction of dams and dikes to collect mining-metallurgical waste is an innovation of the 20th century. Before the arrival of treated minerals, the extraction processes were carried out with much thicker particles and the waste was not systematically collected. Waste from ore recovery operations was generally discharged on a surface near the mine or bodies of water. There are still some farms with discharges to rivers or the sea, but in most cases, barren dikes have become an essential part of mining operations. Currently, the most common way to store

waste from the mining process is through construction of a dam in which the tails are deposited by the hydraulic filling procedure. Solids minerals are mixed with a certain amount of water and/or chemicals so that they acquire the consistency of a mud that is pumped by pipes to the points of discharge [14]. It is usual that for economic reasons the dam is built in stages, by successive rises. There are three fundamental methods of construction of waste dams according to the method of regrowth of the retention dam which we will describe below:

Lateral Extrusion

The lateral extrusion can be defined as the lateral deformation of the materials when is being squeezed due to the continuous loads by which materials are subjected as the dam increases in height. The expert panel report [4] contended that the materials that are immediately above are forced to conform to this movement, experiencing a reduction in the horizontal stress that confined them. Experts have also indicated that lateral extrusion as static liquefaction trigger mechanism is not new or without precedent [15].

VALIDATION

The following section presents a detailed description of the procedures carried out to determine the stability conditions of the Fundao tailing Dam. The main objective of each validation process is to make sure all the necessary steps are taken towards fulfilling deliverables and proposed milestones. The step-by-step plan implemented to develop a feasible model that represents the conditions of the dam at the time of failure are presented following:

Formulation of the problem: The problem formulation consisted on clearly establish what are the problems that are intended to be addressed, the global objectives to be achieved and what resources are required to achieve them in the expected time. These aspects have been stated in the chapter 1 of this investigation.

Collection of the relevant data: All the data required to build the model have been previously collected by the Fundao Review Panel and is provided in the “Report on the Immediate Causes of the Failure of the Fundao Dam” [4]. The elements of the investigation used for the development of the model are described below.

Reconstruction of the dam geometry

The dam’s geometry was re-constructed by following the data provided in appendix B of the before mentioned report and the monthly topography surveys presented in the same appendix. This

appendix describes all the outputs that resulted from the analysis using the geographic information system (GIS). The GSI is a computer program that allowed to store, capture check and display all the data related to the progressive elevations of the Fundao’s dam surface.

Reconstruction of the tailings stratigraphy

The section B6 of the appendix B of the Fundao investigation describes the procedures carried out to establish the raising history of slimes. Moreover, this section discloses the spatial distribution of slimes as well as the slimes production history. This information is considered to be essential for the analysis of the model since the stability analysis is strongly affected by this aspect. In appendix A of this report the slimes depositional history is presented.

ANALYSIS

The purpose of the following analysis is to determine whether the interbedded slimes layering had an impact on the stability of the Fundao Dam or not. During the validation of the model, the slimes were considered to be continuous and a homogeneous mass as per the assumptions made by the review panel. However, investigations on the historical tailing’s discharges show that the deposition of the slimes was not consistent and was constantly interrupted by the release of loose sands. The slimes distribution table shows that 47 layers of slimes were deposited in this section, the thickness of these layers varied from 0.5m to 13.5 (Fig. 1). Studies developed by [16], point out that the stability of the slopes can be strongly influenced by the presence of interbedded layers of clays. The authors concluded that the stability of the slopes containing interbedded slimes using the Limit analysis approach depicted a deeper slip surface and an unfavourable factor of safety than when they ran the same analysis using the Limit Equilibrium method.

The flow-slide that occurred at the Fundao dam could not be demonstrated through the analysis Limit Equilibrium approach. The intention of the following analysis is to incorporate the existence of the slimes deposited in discontinued layers and to prove that this condition could have influenced the structural integrity of the dam. In addition, the properties of the slimes obtained during the laboratory test were considered for this analysis. It is expected that due to the nature of these two materials slimes and sand would have affected the stability of the Fundao Dam differently from a material with combine strengths parameters. The specific strength parameters of the slimes were collected from the Appendix I of the

Fundao Investigation. The adjusted strength parameters used during the analysis are shown in Table 1. The configuration of the model followed the same guidelines used for the validation of the models.

Table 1 Slimes strength parameters

Material	Unit weight (kN/m ³)	Effective friction angle (degrees)	Effective cohesion (kPa)
Compacted Sand Tailings	22	35	5
Loose Sand Tailings	22	33	-

Slimes	22	12.4	-
Weathered Phyllite	22	32	40

The analysis of the section 01 with the continuous layers of slimes shows a significant dropped in the factor of safety, however, the mechanism of failure is similar to the obtained by the review panel. A factor of safety of 1.03 under drained conditions indicates that the stresses are at the allowable limit, yet the factor obtained is dangerously close to be less than 1 which suggest the failure could have occurred even at this state (Table 2, Fig. 2).

Table 2 Comparison table Limit analyses vs Limit equilibrium.

Analysis Type	Slimes Distribution	Analysis mode	Slimes Strength Assumption (degrees)	Factor of Safety
Limit Equilibrium	Continuous Slimes	Undrained	28	1.87
Limit Analysis	Interbedded Slimes	Undrained	12	0.79

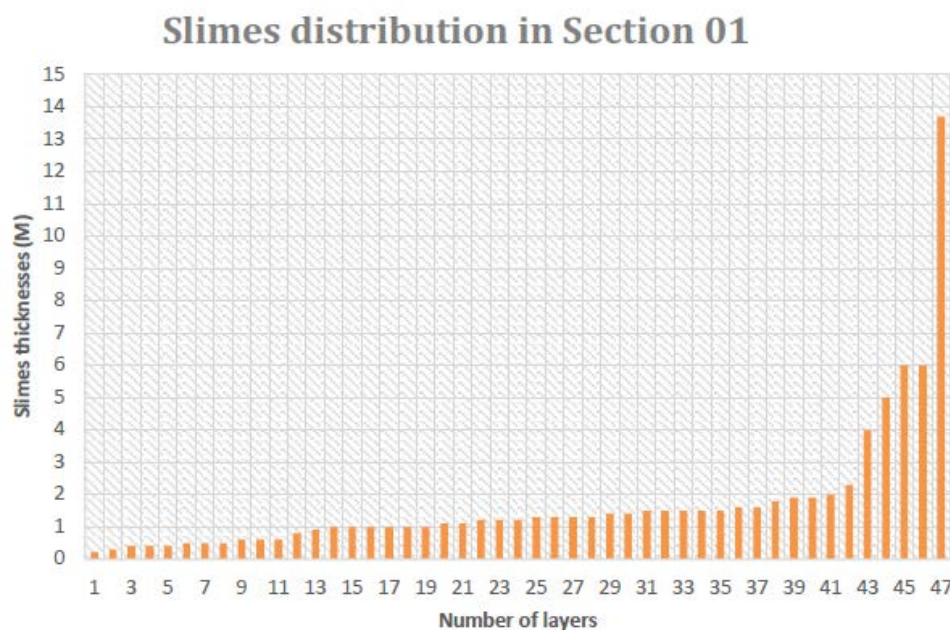


Fig. 1 Section 01: number and thickness of slimes layers detected in tailings during post-failure investigation [4].

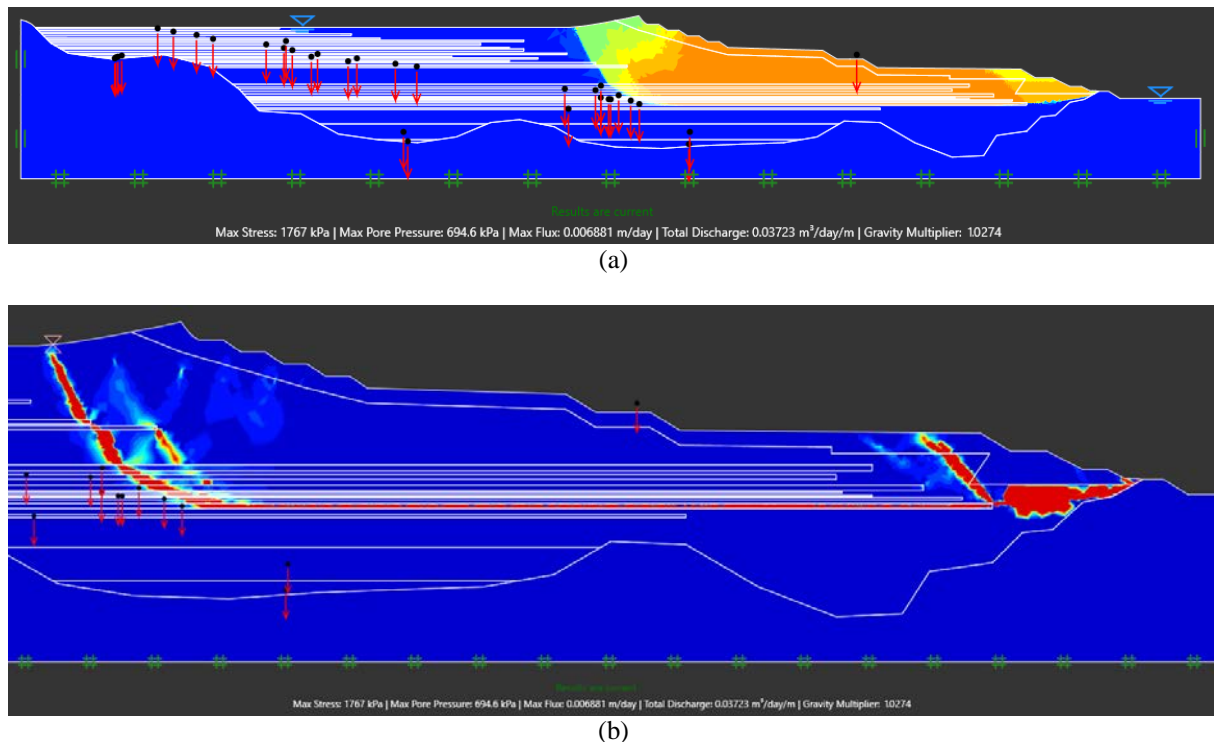


Fig. 2 Section 01 (a) Long term analysis – Displacement. (b) Long term analysis – Shear dissipation

CONCLUSIONS

The results obtained using the Limit analysis approach using the lower and upper bound theorems are presented in terms of safety factors. The values obtained during the validation of the sections A and B agrees well with the values obtained by the review panel. The formulation of the problem is rather simple and it can be concluded that the upper and lower bound approach provides more accurate and effective results.

ACKNOWLEDGMENTS

This study was conducted as part of a Master of Engineering qualification.

REFERENCES

- [1] Ormann L., Zardari M.A., Mattsson H., Bjelkevik A. and Knutsson S., Numerical Analysis of Strengthening By Rockfill Embankments On An Upstream Tailings Dam. Canadian Geotechnical Journal, Vol. 50, Issue 4, 2013, pp.391-399.
- [2] Blight G.E., Formation of Tailings Dam Beaches. In International Conference On Soil Mechanics and Geotechnical Engineering. XV ICSMGE, Istanbul, 2001, pp.1893-1897.
- [3] Grimalt J.O., Ferrer M., Macpherson E., The Mine Tailing Accident in Aznalcollar. Science of the Total Environment. Vol. 242, Issue 1, 1999 pp.3-11.
- [4] Morgenstern NR, Vick SG, Viotti CB, Watts BD. Fundão tailings dam review panel report on the immediate causes of the failure of the Fundão dam. Cleary Gottlieb Steen & Hamilton LLP, New York. 2016.
- [5] Garcia L.C., Ribeiro D.B., de Oliveira Roque F., Ochoa-Quintero J.M. and Laurance, W.F., Brazil's Worst Mining Disaster: Corporations Must Be Compelled To Pay The Actual Environmental Costs. Ecological Applications, Vol. 27, Issue 1, 2017, pp.5-9.
- [6] Palu MC, and Julien PY. Modeling the Sediment Load of the Doce River after the Fundão Tailings Dam Collapse, Brazil. Journal of Hydraulic Engineering. 2019 May 1; Vol. 145, Issue 5, 2019, pp.0501900201-0501900214.
- [7] Duncan J.M., State of The Art: Limit Equilibrium and Finite-Element Analysis of Slopes. Journal of Geotechnical Engineering, Vol. 122, Issue 7, 1996, pp.577-596.
- [8] Cheng Y.M. and Zhu L.J., Unified Formulation for Two Dimensional Slope Stability Analysis and Limitations In Factor Of Safety Determination. Soils and Foundations, Vol. 44, Issue 6, 2004, pp.121-127.
- [9] Khabbaz H., Fatahi B., and Nucifora C., Finite Element Methods Against Limit Equilibrium Approaches for Slope Stability Analysis. In

- Australia New Zealand Conference on Geomechanics 2012. Geomechanical Society and New Zealand Geotechnical Society.
- [10] Leshchinsky B., Comparison of Limit Equilibrium and Limit Analysis for Complex Slopes. In Geo-Congress 2013: Stability and Performance of Slopes and Embankments III San Diego, California, United States, pp.1280-1289.
- [11] Fredlund D. G. and Krahn J., Comparison of Slope Stability Methods of Analysis. Canadian Geotechnical Journal, Vol. 14, Issue 3, 1977, pp.429-39.
- [12] Michalowski R.L., Slope Stability Analysis: A Kinematical Approach. Geotechnique, Vol. 45, Issue 2, 1995, pp.283-293.
- [13] Yu H.S., Salgado R., Sloan S.W. and Kim J.M., Limit Analysis Versus Limit Equilibrium for Slope Stability. Journal of Geotechnical and Geoenvironmental Engineering, Vol. 124, Issue 1, 1998, pp.1-11.
- [14] ANCOLD, Guidelines On Tailings Dams – Planning, Design, Construction, Operation and Closure – Revision 1. Australian National Committee On Large Dams Incorporated, 2012.
- [15] Martin T.E. and McRoberts, E.C., Some Considerations in The Stability Analysis of Upstream Tailings Dams. In Proceedings of the Sixth International Conference on Tailings and Mine Waste, Vol. 99, pp. 287-302. Rotterdam, Netherlands: AA Balkema, 1999.
- [16] Sazzad M.M., Mazumder S. and Moni M.M., Seismic Stability Analysis of Homogeneous and Layered Soil Slopes by LEM. International Journal of Computer Applications, Vol. 975, 2015, p.8887.

EXPERIMENT REGARDING MONTMORILLONITE CONTENT AND STRENGTH PROPERTIES IN BENTONITE UNDER THE INFLUENCE OF HEAT

Rie Suzuki¹, Shin-ichi Kanazawa², Masaki Yanai¹ and Yoshino Osamu³

¹Social Environmental Systems Engineering Course, National Institute of Technology, Fukushima College,
Advanced Course Program, Japan

²Civil and Environmental Engineering, National Institute of Technology, Fukushima College, Japan

³Nishimatsu Construction CO., LTD

ABSTRACT

At present, underground geological disposal at depths greater than 300 m is considered a viable disposal option for high-level radioactive waste generated from the reprocessing of spent fuel used in nuclear power plants. In geological disposal, bentonite is employed as the primary component of buffer material to fill gaps between waste and geologic rock. However, specification details have yet to be completely determined. It is anticipated that the buffer material will be exposed to high temperature due to the heat generated by the vitrified solid. This study aims to understand the mechanical properties of bentonite buffer material by employing uniaxial compression tests with temperatures between 30°C to 90°C applied to bentonite specimens having received a temperature history treatment of 200°C applied over six months. Results show that the maximum compressive strength of the sample given the temperature history is lower than that of the sample without the temperature history. Furthermore, the montmorillonite content of the sample given a temperature history of 200°C also decreased. The reason for the decrease in strength seems to be that the compaction energy during fabrication decreased due to the decrease in the montmorillonite content. This is because the specimens were fabricated so that the dry density was constant. It seems that the maximum compressive stress decreased with increasing temperature regardless of temperature history. The reason for this seems to be microcracks, which appear to decrease rigidity and, therefore, compressive strength.

Keywords: Bentonite, Silica sand, Uniaxial compressive strength, Montmorillonite content

INTRODUCTION

The spent nuclear fuel generated by nuclear power generation produces high-level radioactive waste when it is reprocessed. As a disposal method, geological disposal to a depth of 300m or below is often employed¹⁾. Geological disposal is a disposal method that isolates and confines radioactive materials from the human environment for an extremely long period of time. It is a multi-barrier system that combines an artificial barrier made of vitrified solid, carbon steel over pack, and bentonite cushioning material with a natural barrier made of stable rock, deep underground. The cushioning material filled between the waste and the bedrock has water-impermeable properties, self-sealing properties, various sorption delay properties, thermal conductivity, chemical buffering properties, over pack supporting properties, and stress buffering properties, among others. These properties are expected to be maintained for long periods of time. Naturally occurring clay is drawing attention as a material that can relatively satisfactorily satisfy these functions. Among these natural clay materials, compressed bentonite has the following

characteristics.

- (1) Ability to control water movement due to low water permeability.
- (2) A mechanism for expanding with the infiltration of water to fill voids in the compressed bentonite and cracks in the adjacent rock mass.
- (3) Cation exchange capacity to adsorb cation nuclides.

Therefore, bentonite is considered to be the most effective cushioning material. Bentonite is a clay whose main component is the smectite. Smectite is a generic name for montmorillonite, beidellite, nontronite, saponite, hectorite, saucornite, and stevensite clay minerals. Among them, montmorillonite is a representative clay mineral. The smectite contained in bentonite, which has been verified as a cushioning material in Japan, is also montmorillonite. The crystals of clay minerals are composed of overlapping silicic acid tetrahedral sheets and alumina octahedral sheets. Bentonite has remarkable swelling and water-absorbing properties, very low water permeability, and high cation exchange capacity. However, details about the mechanical properties of bentonite cushioning

materials considering the temperature history due to nuclide decay heat have not been fully grasped. Therefore, in this study, uniaxial compression tests were performed on specimens containing bentonite and silica sand (either with an applied temperature history or without an applied temperature history), and the results were compared. From this, the strength characteristics of bentonite cushioning material with temperature are better understood.

EXPERIMENTAL OUTLINE

In this study, changes in the strength characteristics are clarified by applying change in temperature to bentonite-silica sand mixed samples that have been given a temperature history. In the experiment, a cylindrical specimen with a diameter of 35 mm and a height of 80 mm was prepared. The temperature history was applied to powdered bentonite. In an actual disposal facility, bentonite compacted at high pressure is considered the best material from the viewpoint of improving the performance and workability of the cushioning material. Therefore, a method of applying temperature history by placing the compacted bentonite specimen into the drying furnace is considered valid. However, in the above method, a temperature gradient is likely generated inside the test piece, creating a nonuniform temperature history condition. Therefore, in this study, we adopted the method of applying temperature history to powdered bentonite. Heat was applied by placing the specimen in a water tank whose temperature was kept constant. After a certain period of time, a uniaxial compression test was performed with the specimen kept in the water tank. The montmorillonite content was measured by performing a methylene blue adsorption measurement test on the sample after destruction.

EXPERIMENT METHOD

Specimen Preparation

- (1) Bentonite and silica sand No. 8 were mixed at a ratio of 7: 3.
- (2) The sample was placed in a stainless steel vat and placed in a temperature-controlled oven for 6 months to provide a temperature history. The temperature history was applied to the bentonite sample while the vat was opened, and the drying furnace was kept at atmospheric pressure. In this study, the temperature measured in the drying furnace was the heating temperature of bentonite.
- (3) The sample was taken out and the water content was adjusted using a hand mixer and a

sprayer. The water content was measured by the microwave oven method (500w, 15 minutes).

- (4) The mass at which the dry density was 1.6 Mg/m^3 was determined and weighed with an electronic balance.
- (5) The measured sample was divided into 5 parts, put into a mold, and compacted with a tamping rod.
- (6) The top of the mold was covered and compressed with a hydraulic jack for 10 minutes. The molding pressure was set to 40 MPa.
- (7) After 10 minutes, the height of the specimen and the diameter of the upper and lower specimen were measured with a caliper. The mass was weighed with an electronic balance.

Temperature Measurement Test Inside The Specimen

In order to determine the time needed to apply the temperature to the test piece, the internal temperature was measured while applying the temperature. A sample without temperature history was compacted to make a specimen, and paulownia was used to make a hole. After that, a thermocouple was inserted inside the specimen, and the rate of temperature increase was measured while the temperature was applied.

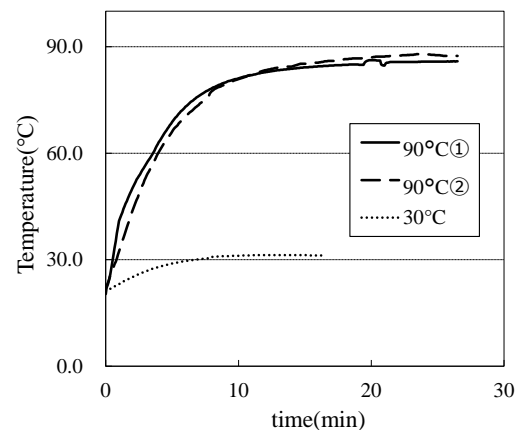


Fig. 1 Relationship between temperature inside the specimen and time

Figure 1 shows the relationship between internal temperature and time when the specimen was placed in a water tank maintained at various temperature. When the specimen was placed in a water tank maintained at 30 °C, it can be seen that 10 minutes after the temperature was applied, the internal temperature reached 30°C and achieved an equilibrium state. When the specimen was placed in

a water tank maintained at 90 °C, it can be seen that the internal temperature reached about 90°C 20 minutes after the temperature was applied and achieved an equilibrium state. Therefore, temperature is considered to be adequately applied inside the specimen by these set heating times. Based on these results, the heating time was set to 15 minutes at 30°C, 20 minutes at 60°C, and 25 minutes at 90°C.

Uniaxial Compression Test

Figure 2 shows a schematic diagram of the Uniaxial compression tester. Table 1 shows the test condition, and table 2 shows the sample condition.



Fig. 2 Uniaxial compression tester

Table 1 Test condition

silica sand No.	No.8
silica sand ratios (%)	30
saturation (%)	30
dry density (Mg/m ³)	1.6

Table 2 Sample condition

Silica sand No. 8 particle density (Mg/m ³)	2.702
Kunigel V1 particle density (Mg/m ³)	2.606
Silica sand No. 8 particle size (mm)	0.08~0.2
Kunigel V1 particle size (mm)	~0.05

- (1) A compression auxiliary device and a rubber sleeve were attached to the specimen. Heat resistant rubber was attached to the top and bottom to prevent water from entering. The specimen was placed in a water tank and heated

with warm water.

- (2) The heating time was set to 30°C for 15 minutes, 60°C for 20 minutes, and 90°C for 25 minutes.
- (3) After applying heat, the uniaxial compression test was performed with the specimen kept in the water tank. At this time, the loading speed was set to 0.4 mm/min. The reason for this is that the bentonite-silica sand mixed specimen used in this test exhibits a very brittle fracture morphology, and this speed allowed for minute deformation up to the fracture to be observed in detail.
- (4) The water content of the destroyed specimen was measured.
- (5) The maximum compressive stress, the strain at the maximum compressive stress, and the elastic modulus were obtained based on the results.

Methylene Blue Adsorption Test [2]

- (1) 1.000 g of methylene blue powder was weighed in a crucible and dried in a drying oven for 10 to 26 hours.
- (2) The material was removed from the drying oven, let stand to cool in a desiccator for about 1 minute, and then weighed with an electronic balance.
- (3) The amount of methylene blue needed was calculated according to the following formula, and the original reagent bottle was used to weigh the medicine packing paper. The dried methylene blue was discarded.

Methylene blue amount (g)

$$= \left(\frac{0.855}{\text{weight after drying (g)}} \right) \times 3.74 \times \frac{1}{2} \quad (1)$$

- (4) Methylene blue was transferred to a beaker, ion-exchange water was added, and the mixture was stirred with a glass rod to dissolve methylene blue.
- (5) The solution was transferred to a 500 ml brown volumetric flask, and ion-exchanged water was added to a volume of 500 ml.
- (6) The solution was allowed to stand overnight with occasional shaking to ensure complete dissolution.
- (7) 17 g of sodium diphosphate + hydrate was weighted and dissolved it in 500 ml of ion-exchanged water.
- (8) 50 ml of 2% sodium pyrophosphate solution was placed in a 200 ml conical beaker, and the sample (bentonite) was placed in the solution.
- (9) The beaker was covered, stirred gently with a

magnetic stirrer, and then boiled gently with the rotor in place.

- (10) After allowing to cool, the solution was stirred and gently boiled again.
- (11) After allowing the solution to cool to room temperature, 60% of the saturated adsorption amount of methylene blue solution was added and stirred for 30 seconds.
- (12) The solution was sampled with continuous stirring and by dropping it onto the filter paper.
- (13) Titration was performed by adding 1 ml of methylene blue solution.
- (14) Steps (12) and (13) were repeated until a pale blue halo was confirmed.
- (15) Titration was performed, and when a pale blue halo was confirmed, the mixture was stirred for 2 minutes and then dropped onto the filter paper. Negative ion-bearing montmorillonite adsorbs positive ion-bearing methylene blue. The halo appears as a blue smear around spots of unabsorbed methylene blue.
- (16) Step (15) was repeated until the halo width became 1.5 to 2.0 mm. The halo width was measured three times with a caliper and the average value was used.
- (17) The montmorillonite content (methylene blue adsorption amount) was calculated from the amount of methylene blue added when the halo width was about 1.5 to 2.0 mm. The calculation formula is shown below.

Adsorption amount of methylene blue
(mmol / 100g)

$$= \text{Methylene blue solution consumption (ml)} \times 2 \quad (2)$$

- (18) The amount of methylene blue adsorbed on 100% montmorillonite Kunigel V1 is 140 mmol / 100g. The montmorillonite content was determined by this ratio. After this, the bentonite-silica sand mixed sample was converted to the value of 100% bentonite. The calculation formula is shown below.

$$\text{Adsorption amount of methylene blue} = \frac{0.50 \times (\text{montmorillonite content})}{0.35} \quad (3)$$

0.50 : Mass of sample used for test (g)
0.35 : Mass of bentonite during the test (g)

TEST RESULTS AND DISCUSSION

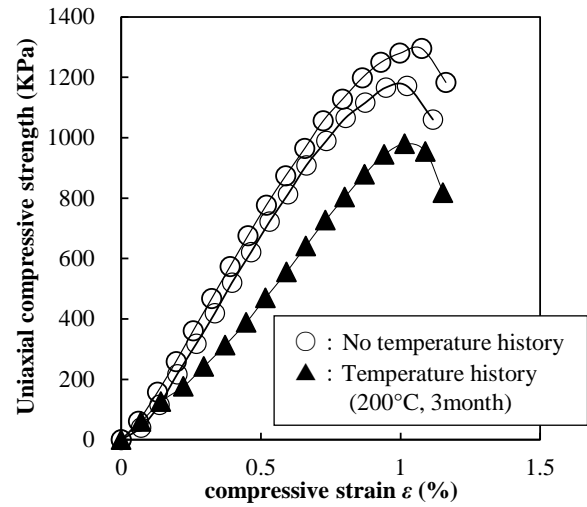


Fig. 3 Maximum compressive stress-compressive strain result

Table 3 compressive strain and elastic modulus

compressive strain (temperature history) ε_f (%)	1.05
Elastic coefficient (temperature history) E_{50} (MN/m ²)	149.3
compressive strain (temperature history) ε_f (%)	0.97
Elastic coefficient (temperature history) E_{50} (MN/m ²)	138.9
compressive strain (no temperature history) ε_f (%)	1.02
Elastic coefficient (no temperature history) E_{50} (MN/m ²)	94.9

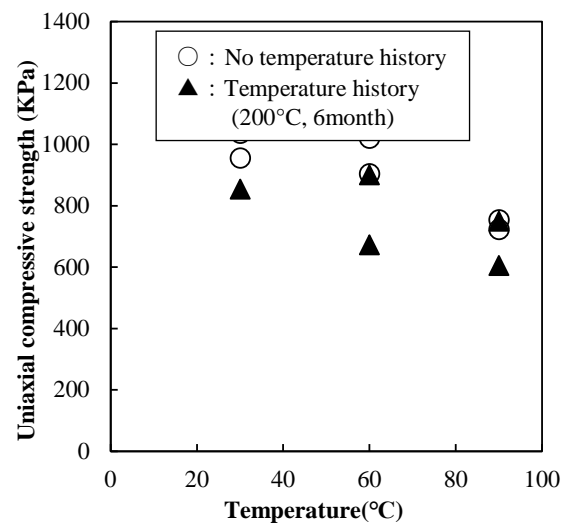


Fig. 4 Relationship between maximum compressive

strength and temperature

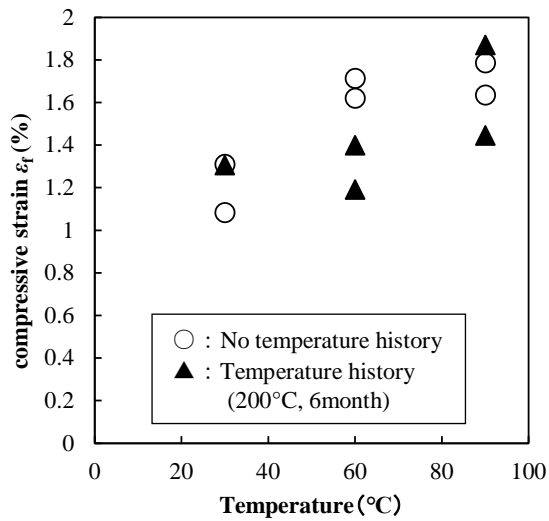


Fig. 5 Relationship between compressive strain and temperature

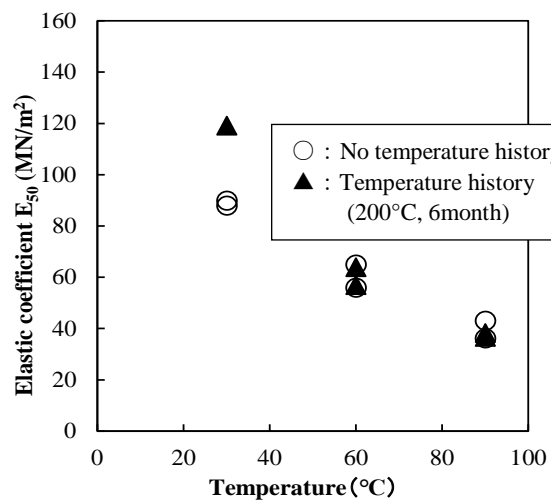


Fig. 6 Relationship between elastic modulus and temperature

Table 4 Results of methylene blue adsorption test (No temperature history, no temperature change)

MB solution consumption (ml)	28	29.5
MB adsorption amount (mmol/100g)	56	59
Montmorillonite content (%)	57.1	60.2

Table 5 Results of methylene blue adsorption test (Temperature history 3 months, No temperature change)

MB solution consumption (ml)	25
MB adsorption amount (mmol/100g)	50

Montmorillonite content (%)	51.0
-----------------------------	------

Table 6 Results of methylene blue adsorption test (Temperature history 6 months, Temperature change 30 degrees)

MB solution consumption (ml)	25
MB adsorption amount (mmol/100g)	50
Montmorillonite content (%)	51.0

Table 7 Results of methylene blue adsorption test (Temperature history 6 months, Temperature change 90 degrees)

MB solution consumption (ml)	25
MB adsorption amount (mmol/100g)	50
Montmorillonite content (%)	51.0

Figure 3 shows the changes in the stress-strain curve of the specimen with and without temperature history. The maximum compressive stresses of the samples without temperature history were 1180kN/m² and 1300kN/m². For the samples with temperature history maximum compressive stresses were 980kN/m². It can be seen that the maximum compressive strength of the samples with temperature history is reduced by 200-320kN/m² compared to the samples without temperature history. Table 4-7 shows that the montmorillonite content of the sample given a temperature of 200°C decreased by 6.1 to 9.2%. In general, it is said that the swelling property decreases as the montmorillonite content decreases [1]. Takegahara et al. [3] stated that the higher the content of montmorillonite, the higher the swelling property, so the energy required to fabricate specimens with the same density increases and the strength increases. On the other hand, in this study, as the specimens were manufactured so that the dry density was constant, it is considered that the compaction energy at the time of preparation decreased and the strength decreased due to the decrease in the montmorillonite content.

Figure 4 shows the results of a uniaxial compression test with varying temperatures. It can be seen that the maximum compressive stress decreases with increasing temperature regardless of the presence or absence of temperature history. A possible cause of the decrease in compressive strength due to temperature rise is the effect of cracks caused by thermal expansion of the specimen. Bentonite is generally considered to have very low air permeability. Microcracks may be generated on the surface or inside the material due to the thermal

expansion of internal interstitial air and the evaporation of interstitial water caused by the influence of heat. It is considered that the compressive strength decreased due to the decrease in rigidity caused by the inclusion of microcracks. As this effect increases with rising temperature, compressive strength is considered to decrease with increasing temperature.

CONCLUSION

In this paper, the mechanical behavior of bentonite cushioning material was investigated in consideration of the existence of temperature history and the method of applying temperature in the geological disposal facility. From this, the following conclusions were obtained.

- (1) When a temperature history of 200°C for 6 months was provided, the maximum compressive stress and elastic modulus of the specimen decreased, and the montmorillonite content also decreased. It is considered that the decrease in montmorillonite content decreased the compaction energy specimen production. With this, the strength also decreased.
- (2) The maximum compressive stress decrease as the temperature of the specimen rises, regardless of the presence or absence of temperature history. The reason for this is considered to be the decrease in rigidity and the decrease in compressive strength due to the effect of cracks caused by thermal expansion of the specimen. As this effect increases with rising temperature, the compressive strength is considered to decrease with increasing temperature.

In actual disposal facilities, the use of bentonite compacted at high pressures is considered from the viewpoint of improving the performance and workability of the cushioning material. The compacted bentonite has a high dry density and is considered to be affected by the decay heat of high-level radioactive waste [1]. Furthermore, it is said that the temperature inside the cushioning material is in the range of 65 to 165 °C due to the decay heat. However, in this test, using powdered bentonite compacted after given a temperature history of

200 °C, the characteristics of the cushioning material in the actual disposal facility were not reproduced. Therefore, in order to reproduce the cushioning material in an actual disposal facility, it is necessary to apply heat at high temperature and perform a uniaxial compression test after manufacturing the specimen. This time, the temperatures applied after the specimens were set to 30 °C, 60 °C, and 90 °C. In the future, we would like to improve the water tank heater and perform a uniaxial compression tests at higher temperatures.

A swelling test is also planned in parallel with the uniaxial compression test. Future work would investigate the swelling characteristics of bentonite cushioning materials under various conditions, with and without temperature history, and clarify the relationship between strength characteristics and swelling characteristics. We would also like to investigate the mechanical properties of bentonite. Furthermore, we would like to build a database using a methylene blue adsorption amount measurement test results and improve the accuracy of the data.

REFERENCES

- [1] Japan Nuclear Cycle Development Institute(JAEA): Technical reliability of geological disposal of high-level radioactive waste in Japan-The second report of geological disposal research and development-General report, JNC TN1400 99-020, IV-3
- [2] Yu H., Tetsuichi T., (National Institute of Advanced Industrial Science and Technology, Research Institute for Geo-Resources and Environment, Mineral Resources Research Group) : Method of the methylene blue adsorption test for bentonite at AIST , Geological Survey of Japan Research Materials, no.555(2012)
- [3] Tatsuhiko T., Ryouichi M., (Radioactive Waste Management Funding and Research Center) : Mechanical test and mechanical stability study of bentonite / sand mixture , 58th Annual Scientific Lecture Meeting of JSCE (September 2003)

A VALIDATION OF SHALLOW SLOPE FAILURE MONITORING METHOD BASED ON THE FIELD SOIL MOISTURE OBSERVATIONS

Mitsuru Komatsu¹ and Keigo Koizumi²

¹Graduate School of Environmental and Life Science, Okayama University, Japan;

²Graduate School of Engineering, Osaka University, Japan

ABSTRACT

In recent years, attempts have been made to utilize the soil moisture data observed in the field to monitor the slope stability and issue an alert if necessary. The method examined in this study is based on the initial quasi-saturated volumetric water content at which the soil water content temporarily equilibrates with rainfall infiltration, and the field saturated water content reached when the groundwater table rises. In order to issue an alert, it is necessary to determine thresholds for these parameters. In previous studies, the method has been applied only to relatively homogeneous embankment slopes and natural slopes of decomposed granite soil. The applicability to other soil types is unknown. In this study, focusing on the natural slopes composed of cohesive soils originating from sandstone and mudstone, the thresholds were obtained from laboratory and field experiments. Evaluation of the field data using the obtained thresholds indicated that when using the experimental values, accuracy of unsaturated hydraulic conductivity is essential. It was also suggested that, soil moisture needs to be measured at various depths based on the heterogeneity of the site to capture the profile with a reasonable spatial resolution.

Keywords: Shallow landslide, Volumetric moisture content, Unsaturated hydraulic conductivity, Quasi saturated, Field saturated

INTRODUCTION

Rainfall-induced shallow landslides have become more frequent owing to recent occurrences of extreme weather in Japan. In July 2018, heavy rainfall events led to serious damages to the geo-structures and natural slopes in Okayama, Japan [1]. Fig.1 shows the cumulative precipitation measured at the Okayama weather station in July 2018. The two peaks in the rainfall intensity exceed 20 mm/h during the precipitation (total 385.5mm) over 48 h were the main cause of the damages to natural slopes and geo-structures.

In recent years, attempts have been made to utilize the soil moisture data observed in the field to monitor the slope stability and issue an alert if necessary [2]–[3]. The method examined in this study is based on the initial quasi-saturated volumetric water content (θ_{QS}) at which the soil water content temporarily equilibrates with the rainfall infiltration, and the field saturated water content (θ_{FS}) reached when the groundwater table is formed. In order to issue an alert, it is necessary to determine thresholds for these parameters. In previous studies, the method has been applied only to relatively homogeneous embankment slopes and natural slopes of decomposed granite soil. The applicability of the method to other soil types is unknown. In this paper, focusing on the natural slopes composed of cohesive soils originating from sandstone and mudstone, the thresholds were

obtained from laboratory and field experiments.

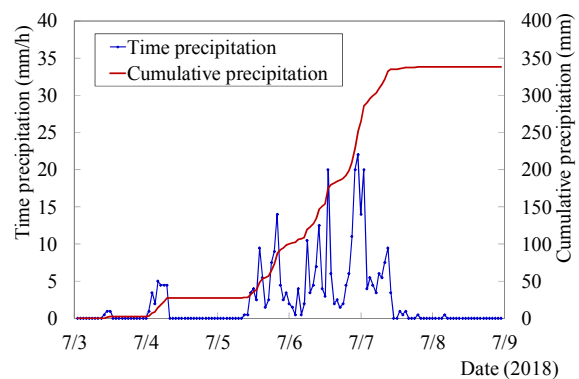


Fig. 1 Precipitation in July 2018 Okayama.

METHOD

Field Locations

Field locations are shown in Fig. 2. Within the natural slopes on the east side of “Handayama” site located in Okayama-city, two locations where a shallow landslide took place by a heavy rain in July, 2018 were studied [4]. These natural slopes composed of cohesive soils originating from sandstone and mudstone. The scale of the slope failure and monitoring point are shown in Fig. 3. The angle of the slope is less than 30 degrees and is

relatively small, but presents a bench shape. The investigation and observation were carried out in an unstable lump.

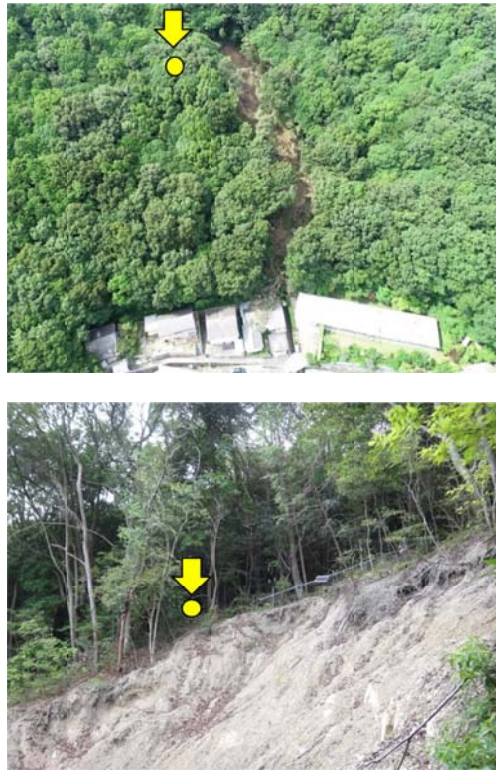


Fig. 2 Field location of monitoring point.

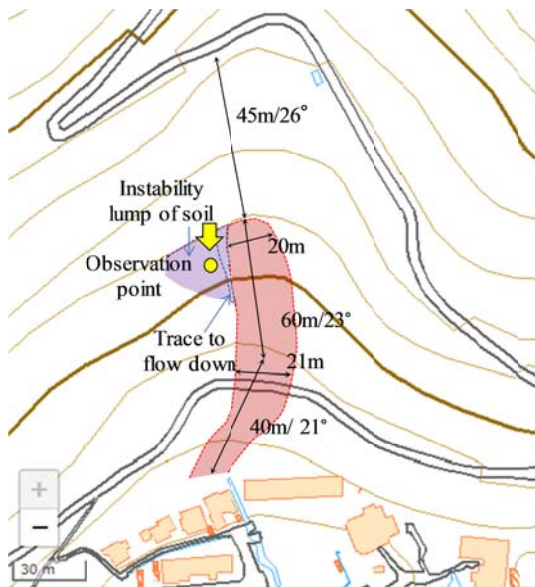


Fig. 3 Scale of slope failure and monitoring point.

Evaluation method of early warning information of rainfall-induced slope failure

A flow chart to determine whether or not the slope monitoring is required using soil water

content is shown in Fig. 4. The depth of the base layer (approximately 60cm) was confirmed from a simple dynamic cone penetration test result as shown in Fig.5. It was decided to install soil moisture sensors at three depths (20cm, 40cm, 60cm). Then, the model of the unsaturated hydraulic conductivity was identified after carrying out the basic property characterizations, saturated hydraulic test, pressurized hydraulic test and water retention test for the soil sample.

The soil moisture sensor was calibrated using the soil sample with varied water content based on the soil water retention test results, and this calibration was used for the field injection test and to interpret the field-monitored data. Furthermore, the field data was evaluated after carrying out field injection test, and the IQS curve (relationships between water content and rain fall intensity) was developed.

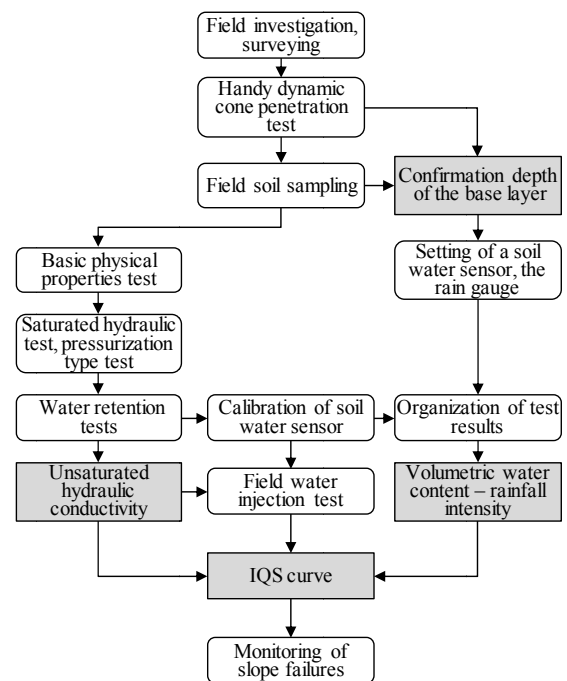


Fig. 4 Flow of an estimate of IQS and the evaluation method.

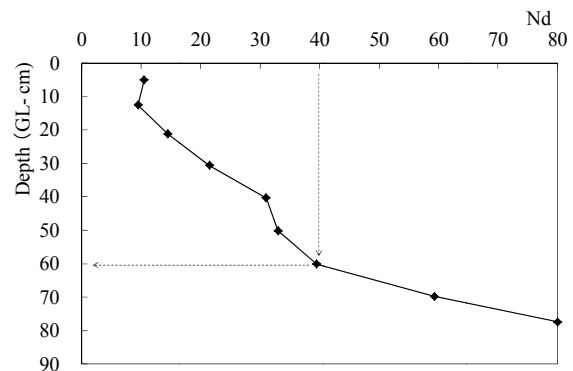


Fig. 5 Test results of simple dynamic cone penetration.

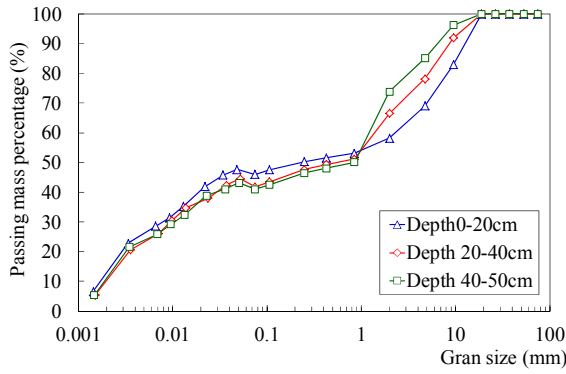


Fig. 6 Grain size distribution of the field soils.

Fig. 6 illustrates the cumulative grain size curve of the samples. The disturbed sample from each depth (0-20cm, 20-40cm, 40-50cm) was collected although the molding was difficult with the presence of gravels when collection of the block sampling was tried in the test field. It was assumed that each sample would represent the depth of the soil water sensor (20cm, 40cm, 60cm), despite the difference in the collection depths of the samples.

RESULTS AND DISCUSSION

Estimation of the IQS curve

The van Genuchten–Mualem (VG) model [7] fitted to the water characteristic curve data obtained by the water retention test (the soil column method; diameter 50mm, height 100cm, the cyclometer method; WP4C, METER Environment Inc.) is shown in Fig. 7. Then, the unsaturated hydraulic conductivity curve estimated based on the saturated hydraulic test and water retention test are compared with the pressurized hydraulic test results. These data has difference to become the tendency to suddenly decrease near saturation, a fitting data of estimated unsaturated hydraulic conductivity curve again is shown in Fig. 8.

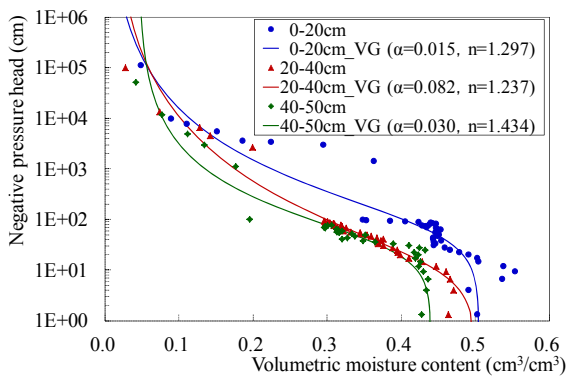


Fig. 7 Results of water retention tests and fitted VG-model curves [7]

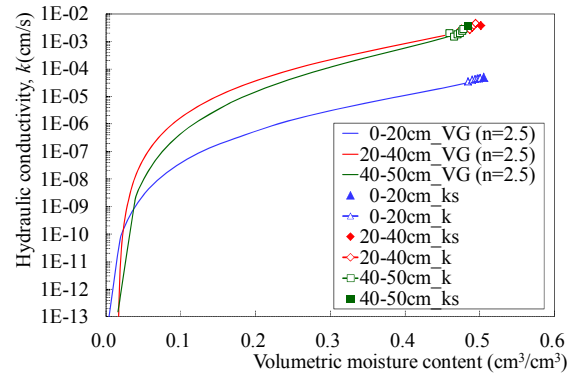


Fig. 8 Unsaturated hydraulic conductivity from saturated hydraulic test and pressurized test, and the fitted VG-model.

Furthermore, the field injection test [6] shown in Fig. 9 was carried out to measure a volumetric water content and hydraulic conductivity under the field saturated condition. The soil moisture sensor was emplaced at the bottom of the borehole and water was injected under a constant head. The result that with correction of saturated hydraulic conductivity is shown in Fig. 10, because a difference of up to two orders of magnitude was seen when comparing the field test result with the estimated unsaturated hydraulic conductivity curve.



Fig. 9 Field water injection test.

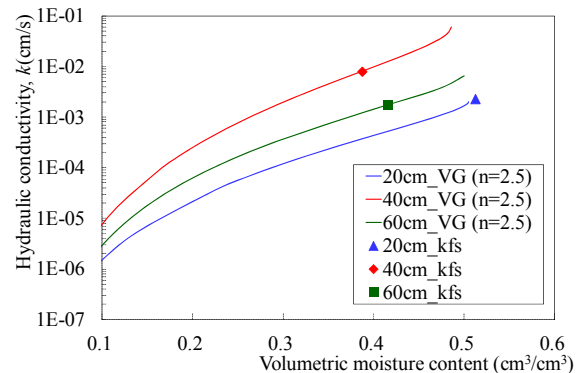


Fig. 10 Adjustment by the spot injection test result

Verification of the IQS curve

Field water spray test shown in Fig.11 was conducted to inspect the validity of the estimated IQS curve. A stainless steel ring with a fixture with a diameter of 10cm is inserted to a depth of 5cm from the ground surface, and water is sprayed with the same intervals in the ring.

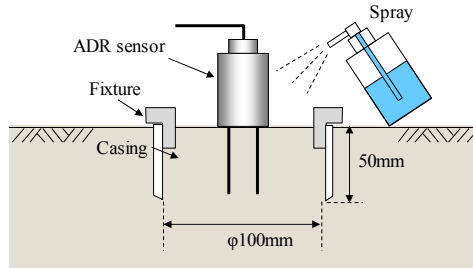


Fig. 11 Field water spray test

The resulted IQS curve arranged for the rainfall intensity and the relations of the volume water content based on Fig.10 is shown in Fig. 12 and Table 1. The results show that the IQS curves generally agree well (errors: 7-12%) with the field water spray test results within an exception of one of the volumetric water content values for 20cm (error: 28%).

Evaluation of field monitoring data

The measurement result of approximately five months is shown in Fig.13. Although a couple of

precipitation events with more than 10mm/h were observed during this time period, there were a few changes observed in the inclination angle.

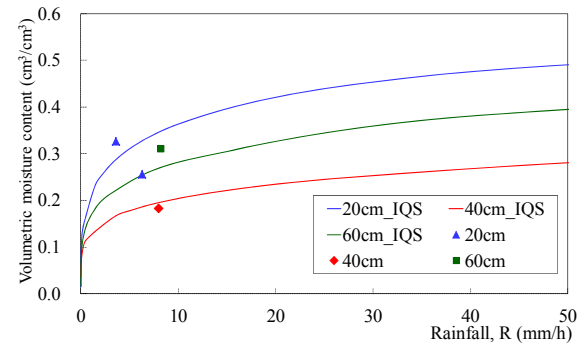
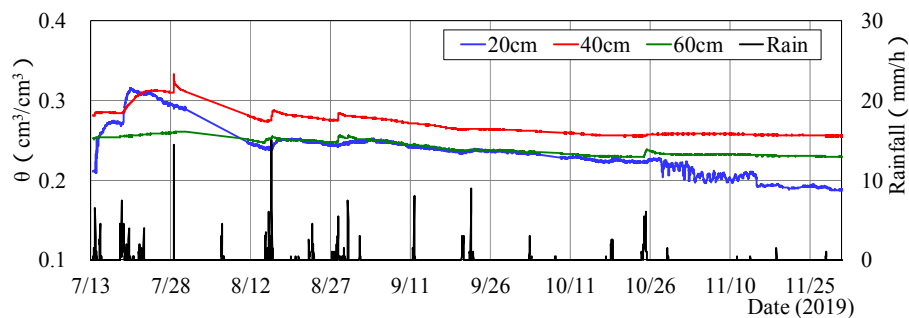


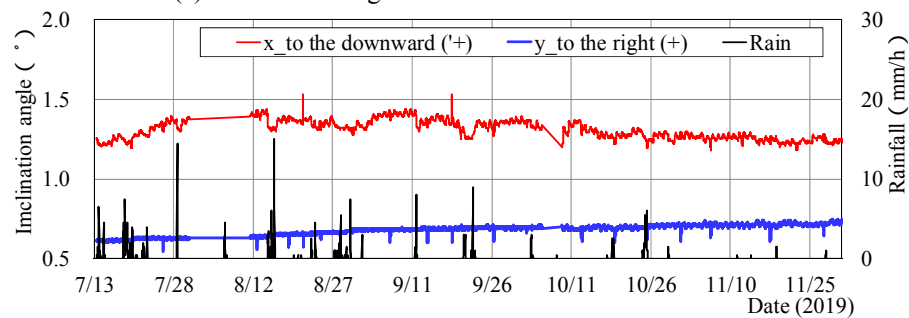
Fig. 12 Comparison between IQS curves and field water spray test results

Table 1 Comparison of the volumetric moisture content between IQS curves and field water spray test results

Depth (cm)	R (mm/h)	IQS		(-IQS)/IQS(%)
20	6.3	0.256	0.328	28
	3.6	0.327	0.287	-12
40	8.0	0.183	0.195	7
50	8.2	0.310	0.348	12



(a) Transient changes in the volumetric water content



(b) Transient changes in the inclination angle

Fig. 11 Results of field monitoring

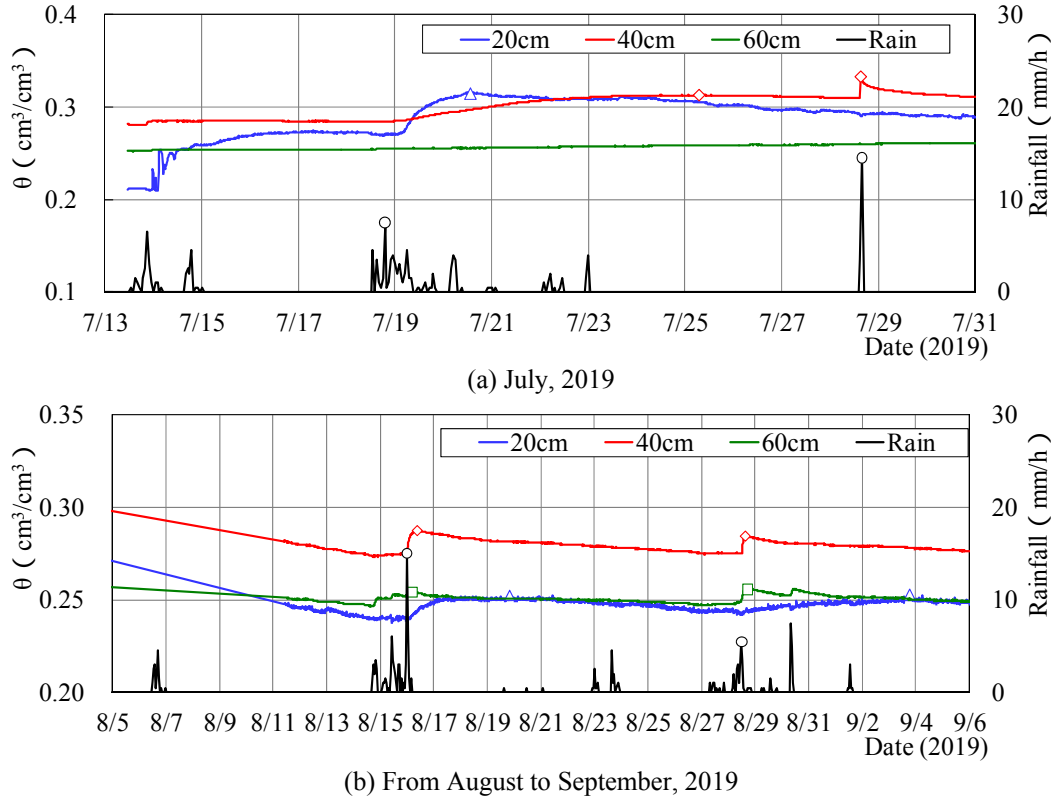


Fig. 14 Extraction of the value of IQS

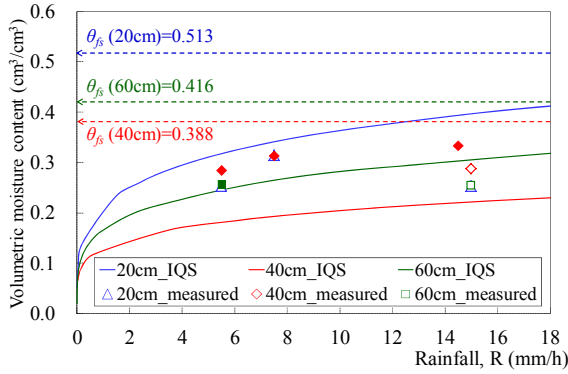


Fig. 15 Evaluation by the figure IQS curve

For four times of large precipitation events of this period observed from July to September, it was evaluated using the greatest rain intensity and the peak value after the rise of the volumetric water content as shown in Fig.14.

The cause for the extremely slow responses observed at the depth of 20cm is unknown. It could e.g., be; setting condition of the sensor at 20cm, existence of a low permeable layer around 20cm, the water bypass influence that increases water content at deeper locations.

The results are plotted together with the IQS curves in Fig.15. This graph shows that permeability

is lower 60cm than 40cm, and 20cm is lower than 60cm as shown in Fig. 10.

Three values turned out higher than the IQS curves (and in a figure) at depth 40cm and 60cm, and the rest is lower than the IQS curves.

The IQS is a dimensionless parameter defined as the volumetric water content divided by the IQS corresponding to the rainfall intensity:

$$IQS = \frac{\theta}{\theta_{IQS}}, \quad FS = \frac{\theta}{\theta_{fs}} \quad (1)$$

where IQS and FS is the index of θ_{iqs} and θ_{fs} , respectively. θ is the measured value of volumetric water content. When $IQS = 1.0$, the volumetric water content reaches the quasi-saturated state. In addition, when $IQS > 1$, a water layer forms at the bottom of the surface layer and the volumetric water content starts increasing and reaches the saturated volumetric water content from deep to shallow. $FS = 1$ show in a ground water, $FS > 1$ shows that ground water table increase.

The measured volumetric water content are divided by IQS and FS and plotted as a function of the rainfall intensity in Fig.14 and Fig.15, respectively.

From these results, the IQS index is less than 1 except for those at 40cm IQS index; in this period was judged to be at low risk of the slope failure.

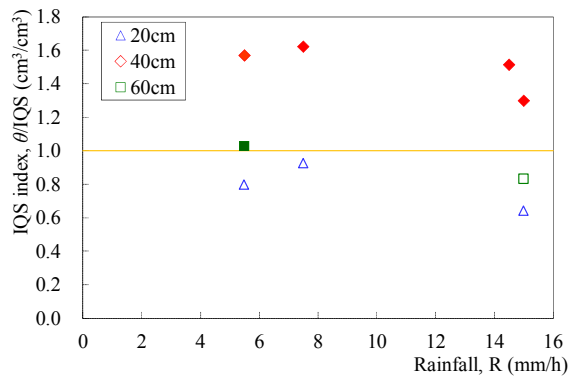


Fig. 14 Evaluation by the IQS index.

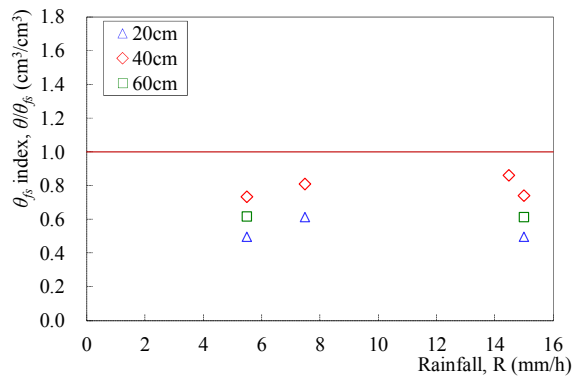


Fig. 15 Evaluation by the FS index.

CONCLUSIONS

In this paper, focusing on the natural slopes composed of cohesive soils originating from sandstone and mudstone, the thresholds were determined from laboratory and field experiments. Evaluation of the field monitoring data using the obtained the soil moisture-based indice, IQS and FS indicated that when using the experimental values, accuracy of unsaturated hydraulic conductivity is essential. It was also suggested that, soil moisture profile needs to be measured at various depths based on the heterogeneity of the site.

ACKNOWLEDGMENTS

The authors acknowledge R.Yamamoto for technical assistance with the field work and experiments. This study was partially supported by Grant-in-Aid for Scientific Research (17K00615 and 19K04599).

REFERENCES

- [1] Nishimura S., Takeshita Y., Nishiyama S., Suzuki S., Shibata T., Shuku T., Komatsu M., Kim B. : Disaster report of 2018 July Heavy Rain for geo-structures and slopes in Okayama, Soils and Foundations, Vol.60, Issue 1, 2020, pp.300-314.
- [2] Tohari, A., Nishigaki M., Komatsu M., Laboratory Rainfall-Induced Slope Failure with Moisture Content Measurement, Journal of Geotechnical and Geoenvironmental Engineering, ASCE, Vol.133, No.5, 2007, pp.575-587.
- [3] Koizumi k, Sakuradani K, Oda K, Ito S, Fukuda Y, Feng Q M and Takemoto M Fundamental research on advancement of regulation standard for expressway management against rainfall-induced surface failure J. Jpn. Soc. Civil Eng., Ser.C (Geosphere Engineering) Vol.73, No.1, 2017, pp.93–105
- [4] Koizumi K, Sakuradani K, Oda K, Komatsu M and Ito S., Relationship between initial quasisaturated volumetric water content and rainfall-induced slope deformation based on a model slope experiment J. GeoEng. Vol.13, No.4, 2018 , pp.179–87.
- [5] Koizumi K., Oda K., Komatsu M., Ito S. and Tsutsumi H., Slope structural health monitoring method against rainfall-induced shallow landslide, 7th International Conference on Euro Asia Civil Engineering Forum, IOP Conf. Series: Materials Science and Engineering 615, 2019.
- [6] Komatsu M., Kita, H., Koizumi K., A Basic Study on Measuring Field Saturated and Effective Porosity Using an Injection to Borehole, Ground Engineering, Vol.35, No.1, 2017, pp.225-232 (in Japanese)
- [7] Van Genuchten, M.Th.: A closed-form equation for predicting the hydraulic conductivity of unsaturated soils, Soil Science Society of America Journal, vol. 44, No.5, 1980, pp.892–898.

A STUDY ON MIGRATION OF KAOLIN CLAY SUSPENSION IN THE PORES USED FOR REDUCING SAND LAYER PERMEABILITY

Keisuke Takahashi¹, Mitsuru Komatsu¹, Toru Iwata¹, and Kouji Takimoto²

¹Graduate School of Environmental and Life Science, Okayama University, Japan;

²Sanyou Clay Industry Co., Ltd., Okayama, Japan

ABSTRACT

When constructing tunnels in the urban areas, NATM method is adopted in some cases due to restrictions on the construction conditions. A highly permeable sand layer is often encountered, which hinders the safe operation in the construction work. In such a case, an additional cost is needed for a proper engineering countermeasure, which could also lead to an excessive burden on the environment. The countermeasures against groundwater inflows are roughly based either on draining the water to lower the groundwater pressure or grouting to reduce the permeability of the ground. Cement, water glass and urethane are often used as grout materials, which raise issues of possible impact to the environment as well as their cost. Kaolinite is a natural clay material that has a small impact on the environment. In this study, for specimens of glass beads with various particle sizes, we investigated the behavior of the injected clay suspension, as well as the migration/clogging behavior in the pores via a set one-dimensional horizontal column experiments with varied hydraulic gradient. The results showed that the particle size ratio of the clay to the glass beads can be well explained by the conventional clogging index, and that the migration speed in the pores is dominated by the viscosity of the clay suspension. The findings are helpful in selecting the clay suspension with an appropriate particle size for an efficient reduction of the permeability of the water conducting layer.

Keywords: Kaolin clay suspension, Viscosity, Hydraulic conductivity reduction, Hydraulic gradient, Critical velocity

INTRODUCTION

When constructing tunnels in urban areas, NATM (New Austrian Tunneling Method) is adopted in some cases due to restrictions on the construction conditions [1]. However, like the Hakata station square cave-in accident which occurred on November 8, 2016, there is great concern to influence the surface of the ground with the progress of the construction in the shallow subsurface [2]. A highly permeable sand layer is often encountered, which hinders the construction work [3]. In such a case, additional cost arises for a proper engineering countermeasure, which could also lead to an excessive burden on the environment. The countermeasures against groundwater inflows are generally based either on draining the water to lower the groundwater pressure or grouting to reduce the permeability of the ground. Cement, water glass and urethane are often used as the grout materials. Because these are not of natural origin, however, their impact to the environment is unknown, and their cost is high. A non-pressurized grouting of clay with non-hardening and non-swelling characteristics was applied to the construction of underground oil storage caverns [4]. Because of clay weakness and instability (non-solidification) as a grouting material, the injection was conducted without a grouting pump but by

pouring diluted clayey water into the rock. It thus took a long time for the permeability of the extensive rock mass to get reduced.

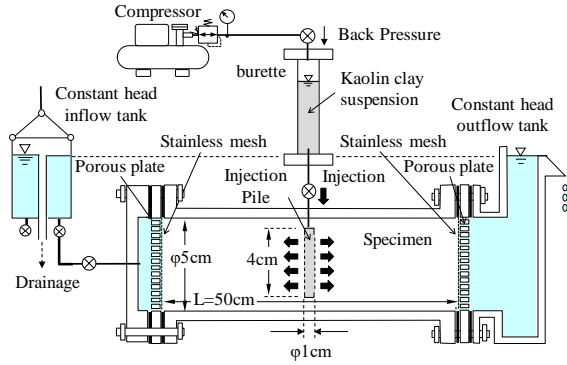
Kaolinite is a natural clay material (Kaolin clay, hereinafter referred to as clay) that has a small impact on the environment. There are some studies to reduce permeability by injecting kaolin clay suspension into the sand layer. It has been suggested that there are certain clay types and mixing ratios for effectively reducing the permeability [5], and investigated the behavior of the injected clay suspension, as well as the migration behavior in the pores via a set one-dimensional horizontal column experiments with varied hydraulic gradient [6]. In this study, same column tests was conducted in the laboratory experiment for specimens of glass beads with various particle sizes.

MATERIAL AND METHODS

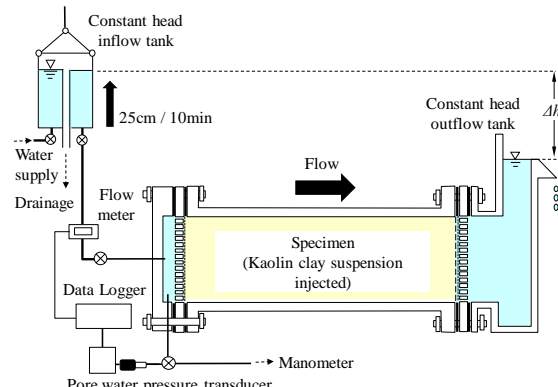
Test setup and procedures

The schematic diagram and photograph of the experimental apparatus are shown in Fig. 1. This experiment consisted of two steps, (a) injection of the clay suspension, (b) one-dimensional flow test with a stepwise controlled hydraulic head. The soil specimen was wet-packed into the acrylic column

with a diameter of 5 cm and a length 50 cm. A stainless steel mesh and a porous plate were placed at both ends. The bulk density of specimen was increased by manually tapping the column wall. A perforated injection pipe with opening rate 45%, 1 cm in diameter and 4 cm in length, covered by stainless steel mesh was installed at the central location of the test specimen.



(a) Injection of clay suspension.



(b) One-dimensional flow test with stepwise controlled hydraulic head.

Fig. 1 Schematic diagram of the experimental apparatus.

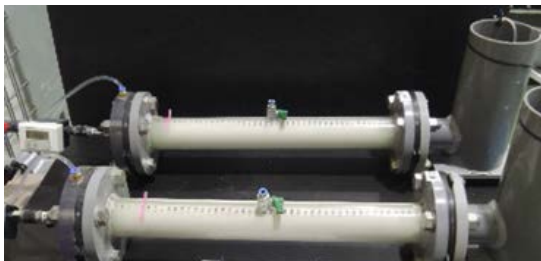


Photo. 1 Photograph of the specimens with injected clay suspension.

Photo. 1 shows the specimens with injected clay suspension. After the injection, the water head

applied on the upstream side was increased stepwise (25cm/10min), and the water flow rate was measured by a using a flow meter installed at the inflow side of the test specimen. The hydraulic head on the upstream side was measured by a manometer and pressure transducer at the head in the cap of the inflow.

Materials

Kaolin clay and its suspension

Fig. 2 illustrates the grain size distributions curve of the clays used in this experiment. Three types of clays (c3, c5, and c7) with various mean particle diameters (M.P.D.s) were prepared. The soil grain density (ρ_s), grain size, uniformity coefficient, and curvature coefficient of each clay are listed in Table 1.

Fig. 3 illustrates the viscosity of the clay suspensions for various clay–water weight (c/w) ratios. Then rotational viscometer was carried out for each suspension. The grain size of c5-type clay is approximately the same as that of c3, and that of c7 is the largest. In addition, c3 and c5 resemble the viscosity coefficient, but c7 shows that the viscosity does not increase even if the c/w ratio increases.

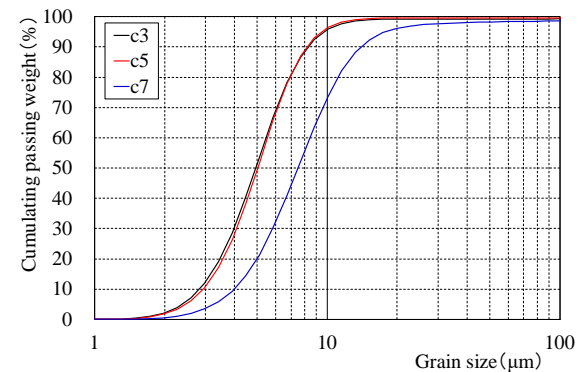


Fig. 2 Grain size distribution curve of three types of clay used in this experiment.

Table 1 Selected physical properties of the Kaolin clays.

Physical properties	Kaolin clay		
	c3	c5	c7
Clay grain density, ρ_s (g/cm ³)	2.748	2.736	2.713
85% grain size, D_{85} (μm)	7.49	7.48	12.36
50% grain size, D_{50} (μm)	6.14	6.33	10.95
15% grain size, D_{15} (μm)	3.16	3.27	4.53
Uniformity coefficient, U_c	1.02	1.02	1.02
Curvature coefficient U_c'	1.94	1.90	2.12
M.P.D.s (μm)	4.93	5.03	7.48

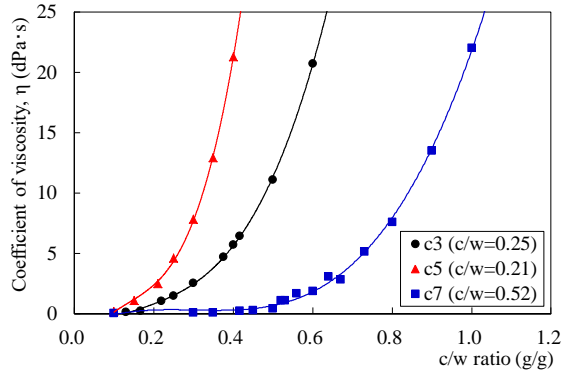


Fig. 3 Viscosity of the clay suspensions.

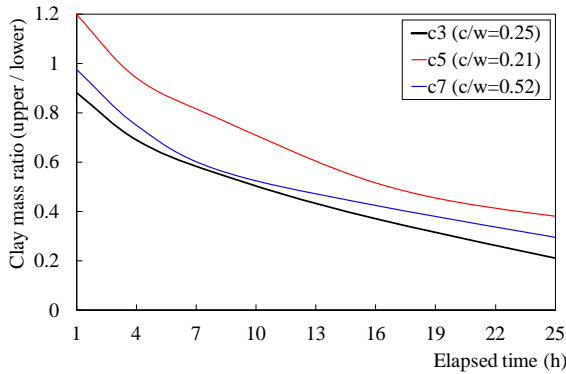


Fig. 4 Time efficiency of sedimentation of clay suspension. (clay mass ratio of upper part/lower part)

Fig. 4 illustrates the time efficiency of sedimentation of clay suspension. The upper suspension of the test specimen and suspension of the lower part were pulled out using a cylinder-shaped container every time, and the clay was weighed after drying in an oven, respectively. It was assumed a ratio of clay mass that floated in the each part (upper clay mass / lower clay mass). It showed that sedimentation rate of c5 was the slowest, and the sedimentation speed of each kind of clay slowed down roughly after eight hours.

Specimen (Grass beads)

Fig. 5 illustrates the grain size distribution curve of the grass beads used as specimen in this experiment. Five types (#20, #40, #50, #60, #80) with various mean grain diameters were used. The glass beads grain density (ρ_s), grain size, uniformity coefficient, and curvature coefficient of each grass beads are listed in Table 2.

Flow condition before the clay injection

Based on the observation in the actual tunnel construction [3], the largest hydraulic gradient and velocity acting beyond the excavation face were

calculated by using the numerical seepage analysis. As a result, the water level of the inflow/outflow difference condition before the injection of clay suspension was set so that the hydraulic gradient is $i = 3.0$.

Experiment condition setting

Table 3 and Table 4 list the experimental cases and the physical properties of clay suspensions. From the previous research [5], the relationships between the clay-water weight (c/w) ratio and the maximum to reduce for hydraulic conductivity of river sand showed that the most suitable combination (optimal) c/w ratio of c3, c5 and c7 are 0.25, 0.21, and 0.52, respectively. In addition, a case of c7 which c/w of 0.30 is added for nearly same level of the density as c3 and c5.

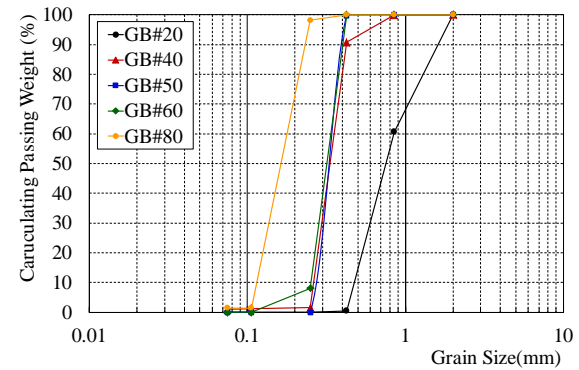


Fig.5 Grain size distribution curve of the river sand and grass beads.

Table 2 Selected physical properties of the grass beads.

Physical properties	Grass beads				
	#20	#40	#50	#60	#80
ρ_s (g/cm ³)	2.561	←	←	←	←
D_{50} (μm)	550	160	150	140	76
D_{15} (μm)	500	98	98	95	66
U_c	1.27	2.17	1.17	1.20	1.21

Table 3 Experimental cases and physical properties of clay suspensions.

Case	Clay suspension		
	Clay-water weight ratio c/w ratio (g/g)	Density ρ_c (g/cm ³)	Coefficient of viscosity η (dPa·s)
c3 (0.25)	0.21	1.148	1.46
c5 (0.21)	0.25	1.188	2.51
c7 (0.52)	0.52	1.385	1.10
c7 (0.30)	0.30	1.149	0.10

Table 4 Experimental cases and physical properties of grass beads.

Case	Grass beads	
	Dry density ρ_d (g/cm ³)	Porosity n (%)
#20	1.604	37.4
#40	1.583	35.7
#50	1.569	38.7
#60	1.576	38.5
#80	1.558	39.1

RESULTS AND DISCUSSIONS

Clay injection tests

According to the filter law, the filters need to satisfy the condition without entry of the soil that when $D_{15}/d_{85} < 6$, where D_{15} means 15% by mass of the filter particles are finer than that size and 85% of the particles are finer than d_{85} particle size of the base material [7]. Therefore, when $D_{15}/d_{85} > 6$, finer particles pass through the filter materials. Here in, d_{85} is the particle size of the clay, D_{15} is the particle size of the grass beads. $D_{15}/d_{85} < 6$ implies that the clay suspension cannot be injected into the pores of the grass beads if there is no effect of viscosity of suspension.

Table 5 lists the experimental results of the injection tests. Clay c7 was not able to inject into GB#80. The value of filter law was calculated 5.33, less than 6 of the index. It was suggested that the migration of this clay suspension could be well predicted by the filter law.

Table 5 Results of the injection tests.

case	GB#20	GB#40	GB#50	GB#60	GB#80
c3 (0.25)	Y [66.67]	— [12.67]	— [12.67]	— [12.33]	Y [8.53]
c5 (0.21)	Y [66.67]	Y [12.67]	— [12.67]	— [12.33]	Y [8.53]
c7 (0.52)	Y [41.67]	— [7.92]	— [7.92]	— [7.71]	N [5.33]
c7 (0.30)	Y [41.67]	Y [7.92]	Y [7.92]	Y [7.71]	N [5.33]

Note: “Y” means the possible to inject, “N” means the not possible to inject. [] is the calculated D_{15}/d_{85} .

Fig. 6 illustrates the injected volume for the c7(0.30) suspension cases. The viscosity of this case was 0.10, close to water. The injection was terminated when the clay suspension has been visually confirmed at the both end boundaries of the

test specimen. Therefore, the clay suspension may not fully fill the pores near the both ends. In GB#20 and GB#40, the same amount was injected while slightly less for GB#50. D_{15}/d_{85} of GB#40 and GB#50 are same, 7.92, but 85% particle size of GB#50 is larger than GB#40. There is a less volume of injection for GB#60, it resulted likely from the clogging during the injection. Therefore, the feasibility of the injection well followed the filter law, but the quantitative evaluation regarding the volume of injection requires an additional procedure/index.

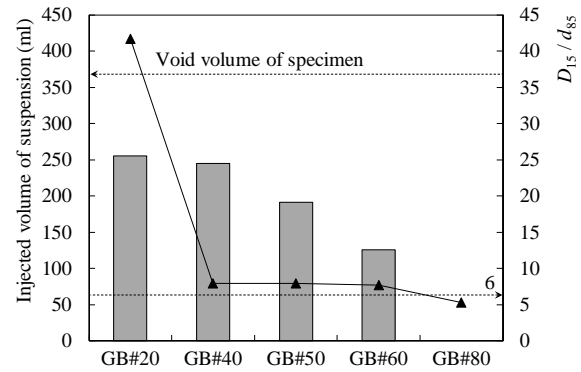


Fig.6 Injected volume of clay suspension, c7(0.30).

Permeability tests

Hydraulic behavior under the changing hydraulic gradient

Fig. 7 and Fig. 8 illustrate the total head and the flow rate in the permeability test cases for GB#20 and c3(0.25), c5(0.21), c7(0.52), respectively. The total head for c3 shows the tendency that is slightly lower than that of the constant head tank in $h=50\text{m}\sim 75\text{cm}$ and became more significant after $h=100\text{cm}$. The flow rate increases immediately following the change in the head and quickly stabilizes afterwards, it showed large change at the setting head $h=100\text{cm}$. Case c7 showed a tendency similar to c3 up to $h=50\text{cm}$, but the total head decreased much below from at the setting head from $h=75\text{cm}$, and the flow rate greatly increased progressively from $h=25\text{cm}$ of the initial stage. c5 followed that a difference occurred at the setting head was $h=125\text{cm}$, and it followed that the flow rate greatly increased setting at the setting head from $h=100\text{cm}$.

Fig. 9 and Fig. 10 illustrate hydraulic conductivity and hydraulic gradient calculated based on Fig. 7 and Fig. 8, respectively. For c3, it is estimated that a large amount of clay flowed out by migration of the clay through the void because the hydraulic conductivity rose at a hydraulic gradient

$i=1.0$. Case c5 showed the smallest hydraulic conductivity after the injection, the variation of hydraulic conductivity became large in hydraulic gradient $i=1.5$, hydraulic conductivity finally same as other two kinds level. In case c7, it was assumed that the migration of the clay in the void began and flowed out when the hydraulic gradient reached $i=0.25$, and c7, and as for the subsequent hydraulic gradient, it was found that a residual clay effect of this phenomenon.

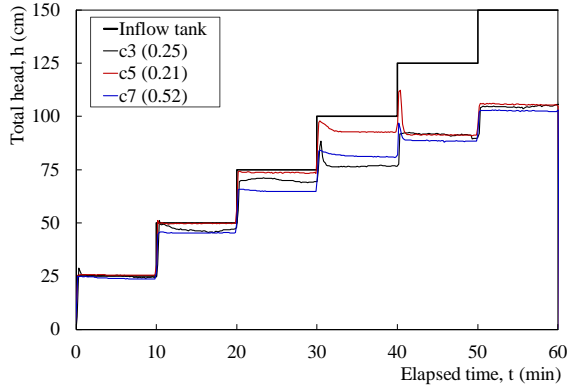


Fig.7 Total head with time of test case GB#20.

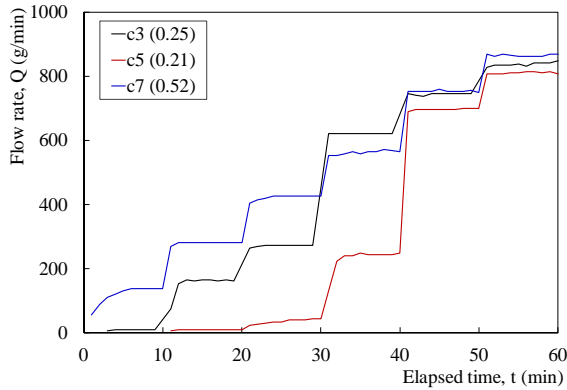


Fig.8 Flow with time of test case GB#20.

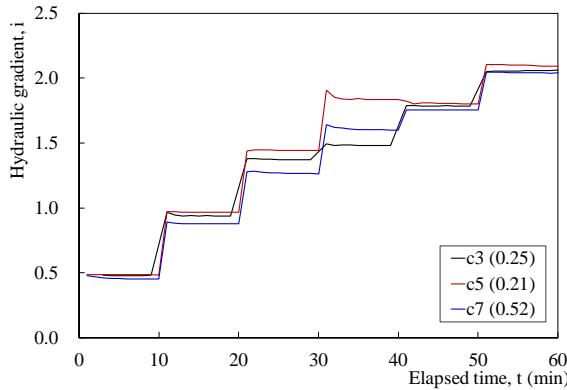


Fig.9 Hydraulic gradient with time of test case GB#20.

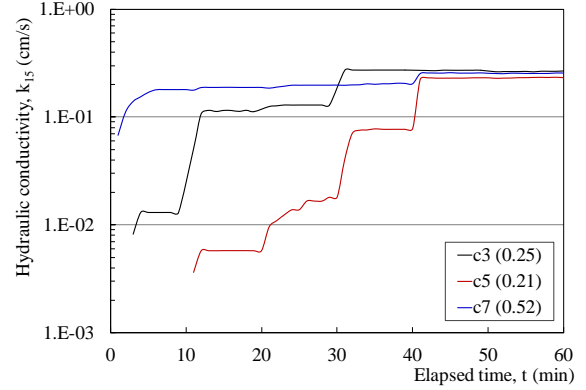


Fig.10 Hydraulic conductivity with time of test case GB#20.

In these results, the hydraulic conductivity after the clay injection varied according to the type of the clay, and it also became clear that the permeability change with the increase of the hydraulic gradient was different.

Residual and runoff clay

The injected, residual and runoff masses of each clay are shown in Fig. 11. Clay c7 was injected most in terms of the density of clay suspension. The fraction of the residual clay (residual mass / injection mass) was 12.5, 17 and 15.5% for c3, c5 and c7, respectively, showing the highest value for c5.

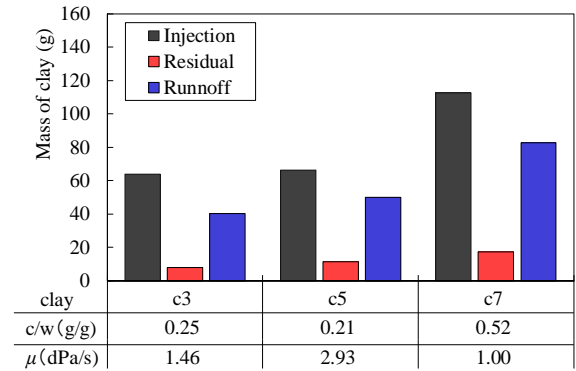


Fig.11 Mass of clay of test case GB#20.

Multi Particulate Critical Velocity

Multi particulate critical velocity under the one-dimensional horizontal flow is shown in Eq. (1) [8].

$$V_{cm} = n^{1/m} \frac{6\mu}{\rho_w d} \left\{ \sqrt{\frac{\rho_w(\rho_s - \rho_w) g d^3}{54 \mu^2} + 1} - 1 \right\} \quad (1)$$

where, V_{cm} : multi particulate critical velocity (cm/s),
 n : porosity, m : constant decided with the Reynolds

number, μ : coefficient of viscosity of the water ($\text{g/cm} \cdot \text{s}$), ρ_w : density of the water (g/cm^3), d : particle diameter (cm), ρ_s : soil particle density (g/cm^3), g : gravitational acceleration (cm/s^2).

The multi particulate critical velocity (V_{cm}) calculated for each of the permeability tests under varied hydraulic gradients are shown in Fig. 12.

It is understood that V_{cm} is drastically smaller than the pore velocity observed in the experiments. In other words, it shows that the particles start to migrate, and the clay runoff occurs under the large velocity rather than the calculated V_{cm} . Furthermore, it was assumed that a factor that affects the V_{cm} existed because the clay particles remained in the pores of the glass beads in the experiments. Therefore, the coefficient of viscosity of Eq.(1) is not considered the viscosity of the suspension.

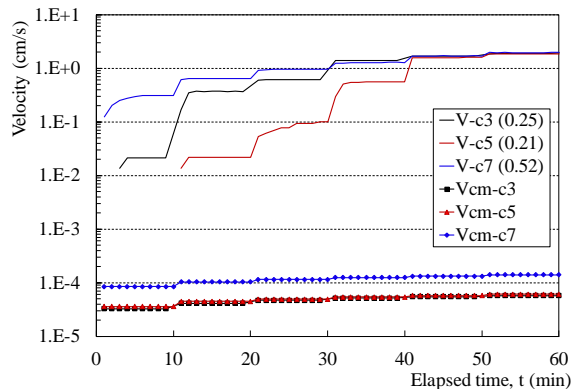


Fig.12 Measured pore velocity (V) and the multi particulate critical velocity (V_{cm}).

CONCLUSIONS

In this study, for specimens of glass beads with various particle sizes, we investigated the behavior of the injected clay suspension, as well as the migration behavior in the pores via a set one-dimensional horizontal column experiments with a diameter of 5 cm and a length of 50 cm under the varied hydraulic gradient.

The results showed that the ratio of the particle sizes of the clay to the glass beads can be well explained by the conventional clogging index, and that the migration speed in the pores is dominated by the viscosity of the clay suspension.

ACKNOWLEDGMENTS

The authors acknowledge T. Kojima for technical assistance with the experiments. This study

was partially supported by Grant-in-Aid for FUSO Innovative Technology Fund (2019).

REFERENCES

- [1] Matsushita Y., Shibata T., Kinoshita K., Hashimoto T. and Imanishi H., Deformation Behavior and Stability of the Tunnel Crown Rock Shallow NATM In Urban Site, Proceedings of Tunnel Engineering, JSCE, Vol.1, 1991, pp.29-34. (in Japanese with English abstract)
- [2] Mitani Y., Cave-in Accident and its Restoration on New Nanakuma-line of Fukuoka City Subway, Geotechnical Engineering Magazine, Vol.67, No.6, 2019, pp.4-7. (in Japanese)
- [3] Takahashi K., Mitsumasa T., Yoshimoto H., Oogane T. and Komatsu M., Adoption Example of the Tunnel Auxiliary Construction Method for Soft Unconsolidated Ground in Urban Area Using the Mountain Tunneling Method, NATM, Ground Engineering, Chugoku Branch of Japanese Geotechnical Society, Vol.35, No 1, 2018, pp.53-160. (in Japanese)
- [4] Miyanaga Y., Makita T., Ebara M. and Hatano T., A Non-Pressurized Grouting Method using Clay for Controlling Groundwater - A Theory of Clay Grouting and the Construction Record of Kuji Underground Oil Storage Plant Journal of the Japan Society of Engineering Geology, Vol.35, No.4, 1994, pp.23-35 (in Japanese with English abstract)
- [5] Komatsu M., Takahashi K. and Takimoto K., Pressurized clay injection method using kaolinite for controlling groundwater of a saturated sand layer, 7th International Conference on Euro Asia Civil Engineering Forum, IOP Conf. Series: Materials Science and Engineering, 615, 012047, 2019, pp.1-8.
- [6] Takahashi K., Komatsu M. and Takimoto K., Evaluation of Kaolin Clay-injected Ground Permeability Based on Changes in Hydraulic Gradient, Ground Engineering, Chugoku Branch of Japanese Geotechnical Society, Vol.37, No.1, 2019, pp.145-150. (in Japanese)
- [7] Bertram G. E., An Experimental Investigation of Protective Filters. Harvard Soil Mechanics Series, No.7, 1940, 26p.
- [8] Sugii T., Teranishi K. and Zju H., Evaluation of Erosion Resistance Performance of River Levee Using Multi Particulate Critical Velocity, Advances in river engineering, Vol.24, 2018, pp.619-624. (in Japanese with English abstract)

A REVIEW ON THE UNDERSTANDING OF THE PROPERTIES OF GRANULATED BENTONITE MIXTURES IN THE RADIOACTIVE WASTE DISPOSAL CONCEPTS

Mazhar Nazir¹, Ken Kawamoto² and Toshihiro Sakaki³

¹ Ph. D Student, Department of Civil and Environmental Engineering, Saitama University, Saitama, Japan.

² Professor, Department of Civil and Environmental Engineering, Saitama University, Saitama, Japan.

³ Former Professor, Department of Civil and Earth Resources Engineering, Kyoto University, Kyoto, Japan.

ABSTRACT

Since long, bentonite has been examined as a potential sealing material in the Engineered Barrier Systems (EBS) for the geological disposal of radioactive waste due to its favorable physical and chemical properties. The research evolution has led to the adaption of Granulated Bentonite Mixtures (GBM) as a candidate buffer/backfill material owing to the high compaction properties, operational advantage and closure of gaps between the seal and host rock. A thorough understanding of the behavior of GBM is essential to design and construct an efficient repository. This paper summarizes a review of former experimental studies conducted on the GBM over the past two decades. The contents include Thermal, hydraulic and mechanical (THM) characteristics, gas transport and microstructure. The work comprises preparation of a summary table listing material properties, sample scale, methodology, test conditions and graphical representation of results. Based on the review, prospects for further investigations/studies on the GBM's THM and gas transport properties from the microstructural perspective have also been recommended for better understanding of the behavior of GBM.

Keywords: Engineered barrier systems (EBS), radioactive waste disposal, granulated bentonite mixtures (GBM), experimental studies

INTRODUCTION

Various repository design concepts have been evolved and studied over the last four decades [1]. These include encapsulation of nuclear waste in a metallic canister surrounded by a backfilling/buffer material emplaced in deep geological formations in vertical holes or horizontal tunnels [1,2]. Owing to its favorable physical and chemical properties, bentonite has been studied as a backfilling/buffer material in the nuclear waste disposal concepts [3]. These properties include low permeability and high retention capacities [4,5], high swelling capacity [3,5], thermal characteristics [3] and micro-porous structure [5]. Many design concepts use pre-compacted blocks of bentonite as barrier and backfilling materials [4]. Alternatively, Granulated Bentonite Mixtures (GBM) consisting of granules (highly compressed pellets) and powders of bentonite have also been considered [6]; and adopted by National Cooperative for the Disposal of Radioactive Waste (NAGRA) in the prototype Full-scale Emplacement (FE) experiment [7] and Engineered Barrier (EB) experiment [8,9] at the Mont Terri rock laboratory in Switzerland. The objective of using GBM is to achieve good compaction properties and operational advantages including easy transportation and in-situ placement/backfilling. Additionally, the GBM is considered to provide a high capability to adapt to the irregular rock wall conditions [10].

In a typical repository environment, the GBM barrier will be subjected to radiogenic heat of the

waste canister and other complex hydro-mechanical processes resulted from the infiltration of groundwater or hydration from the surrounding rock as well as the generation of various gases as a result of metal corrosion or by the degradation of organic wastes. Therefore, an assessment of complex Thermo Hydro-Mechanical (THM) and thermo-hydro-geochemical processes is essential to achieve a safe repository design and ensuring the long-run safety.

The emplaced buffer GBM should be capable; to maintain its low water permeability and develop a sufficiently high swelling pressure to maintain a good contact between the host rock and waste, and to ensure rapid dissipation of radiogenic heat as well as hold enough permeability to allow the transport of gases without cracking and rupturing of the buffer/barrier [3]. Various studies have been conducted to understand the behavior of GBM. This paper summarizes a review of the former experimental studies performed in the last couple of decades to understand the thermal, hydraulic, mechanical and geochemical behavior of the GBM.

THERMAL PROPERTIES

The thermal properties of various GBMs have been obtained in the laboratory by thermal probe analyzers and the results are presented in Fig.1. Table 1 provides a summary of the relevant details on the materials, and experimental methodology. The results indicate that, for a fixed water content, thermal

conductivity increases with increasing dry density [11,12]. Tang [11] noted high thermal conductivity values at higher water contents. In the FE experiment, Müller [7] observed a slight increase in the thermal conductivity values measured for a period of almost one year after the start of heating indicating slow wetting of the GBM due to water inflow at a very low rate (Fig. 2).

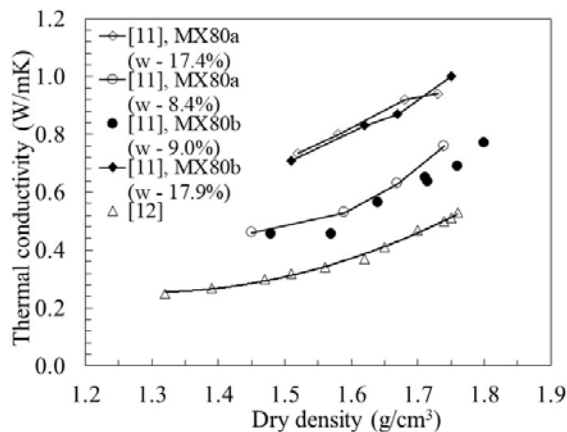


Fig. 1 Effect of dry density and moisture content on thermal conductivity [11,12]

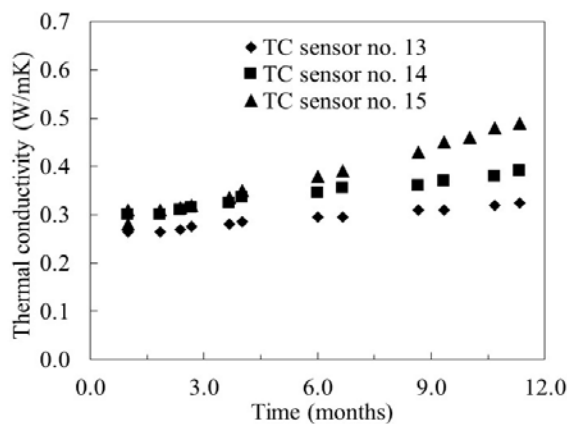


Fig. 2 Transient changes in in-situ GBM thermal conductivity [7].

HYDRAULIC PROPERTIES

Hydraulic conductivity of the GBM in saturated conditions was determined in laboratory permeability tests. The materials, methodology and the experimental conditions adopted are summarized in Table 1. The results show that hydraulic conductivity decreases with increase in dry density (Fig. 3) [8,9,13]. Villar [14] investigated the effect of temperature on the saturated hydraulic conductivity by a thermostatically controlled oedometer cell under

constant volume conditions. The results indicated that the hydraulic conductivity decreased with increasing temperature (Fig. 4). Masuda [13] reported the work on the effect of salinity content of groundwater on hydraulic conductivity of granulated bentonite. Salinity content had a strong influence on the hydraulic conductivity. The saline water resulted in higher hydraulic conductivity values as compared to the fresh water.

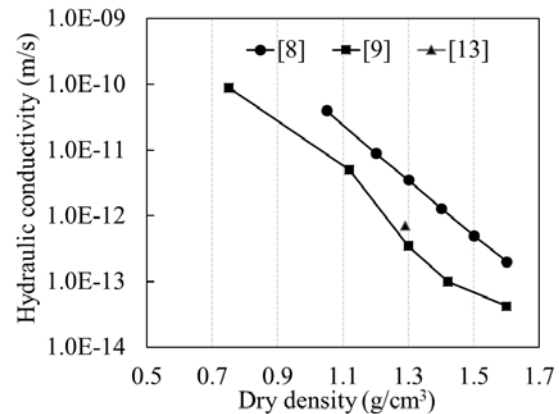


Fig. 3 Effect of dry density on hydraulic conductivity [8,9,13]

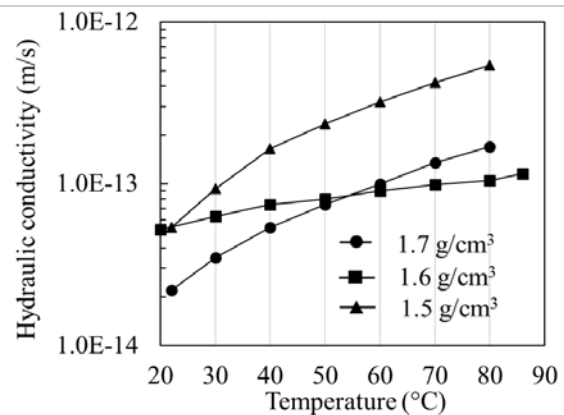


Fig. 4 Effect of temperature on hydraulic conductivity [14]

MECHANICAL PROPERTIES

The swelling characteristic of the GBMs has been tested in the laboratory using oedometers/rigid cells under constant volume conditions. Table 1 summarizes the experimental conditions adopted for the swell pressure testing. The results show that lower density samples developed low swell pressure values and the swelling pressure increases with increasing dry density (Fig. 5) [2,8,9,14–20]. The temperature controlled swelling characteristics have been observed in a thermostatically controlled oedometer

cell and results depicted that the swelling pressure decreases with increase in temperature (Fig. 6) [14].

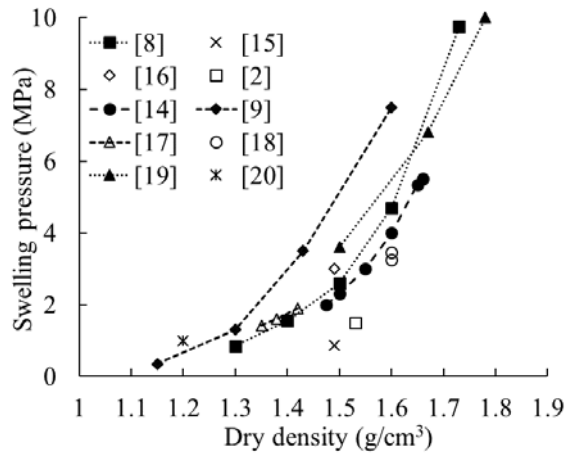


Fig. 5 Variation of swelling pressure as a function of dry density [2,8,9,14–20], y-axis swelling pressure

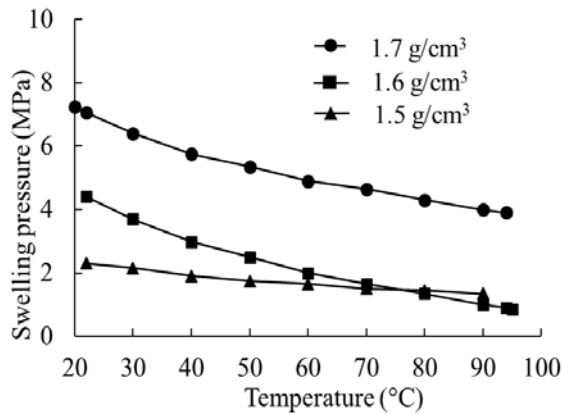


Fig. 6 Effect of temperature on swelling pressure in samples prepared at different dry densities [14], y-axis swelling pressure

GAS TRANSPORT

Table 1 summarizes the methodology adopted to measure the gas permeability. The results indicate that gas permeability; increases with increasing porosity (Fig. 7) [21] and decreases with increase in dry density (Fig. 8) [22]. Liu [23] conducted gas permeability experiments on the in-situ GBM samples retrieved from the EB experiment. The results indicated extremely low permeability (in the order of 10^{-21} m²) and they suggested the bentonite barrier hardly a medium for gas transport.

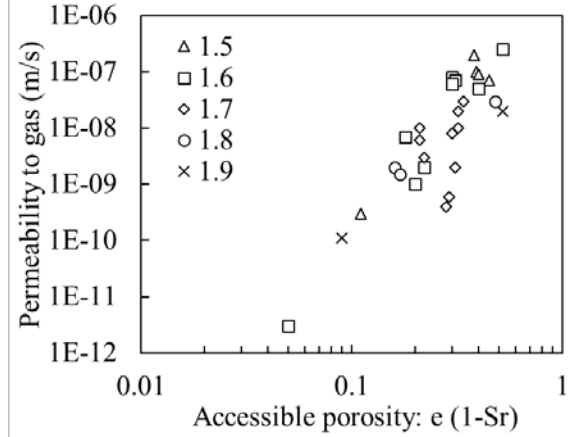


Fig. 7 Gas permeability as function of porosity in specimens compacted at different dry densities with water contents [21]

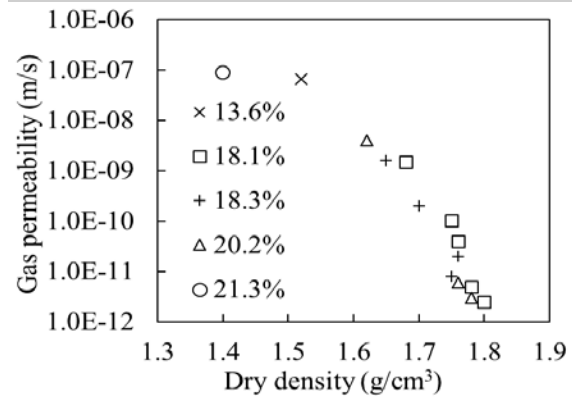


Fig. 8 Average gas permeability as function of dry density for different water contents [22]

MICROSTRUCTURE

Microstructural changes occur in the bentonite as a result of compression at the time of emplacement and swelling during the hydration process afterwards. Hence, investigations at microstructural level are crucial for better understanding of the behavior of the bentonite at higher structural levels [24]. Microstructural features have been investigated by several methods including Mercury Intrusion Porosimetry (MIP), Scanning Electron Microscopy (SEM) and Microfocus X-ray Computed Tomography (MFXCT). Lloret [24] studied the effect of compaction (dry density 1.4 g/cm³ to 1.68 g/cm³) on Pore Size Distribution (PSD) characteristic of FEBEX granular bentonite by MIP. A bi-modal PSD was observed, with a dominant value of 20 nm representing pores inside the clay aggregates and larger pores ranges from 20 μ m (at 1.68 g/cm³) to 30 μ m (at 1.4 g/cm³) corresponding to the inter-granular

Table 1 Summary of the materials and methodology adopted for the determination of thermal, hydraulic, mechanical and gas transport properties

Properties	Bentonite/Material Type	Gradation (mm)	Sample size (mm)	Apparatus/Methodology	Controlling Parameter(s)	Ref.
Thermal	MX-80	< 2	50 x 70	Heating wire probe thermal analyzer	Dry density, water content	[11]
	Wyoming USA (similar to MX80)	0.1-6.3	60 x 150	KD2 Pro thermal analyzer TR-1 probe	Dry density	[12]
	GBM in FE experiment	0.1-9.5	full-scale	Field measurements by thermal sensors	Time	[7]
Hydraulic	Spanish GBM	0.01-10	n/a	Constant gradient permeability tests, steady state conditions	Dry density	[8]
	MX-80	< 10	35 x 10	Small sample holders, 20°C, 17 days hydration time	Dry density	[9]
	Pellets mixture	0.075 – 19	n/a	Laboratory experiments	Dry density	[13]
	FEBEX GBM	< 5	50 x 12	Oedometer cell equipped with a silicone oil thermostatic bath, constant volume conditions	Temperature	[14]
Mechanical	MX-80 Pellet /Powder (80/20)			Samples prepared at DD of 1.49 g/cm ³ in constant volume cell of 70 mm dia.		[15]
	Pellet (7x7mm), Powder (<2mm)			oedometer, 440 days hydration time		
	MX-80, Pellet /Powder (80/20), Pellet 7x7mm,		60 x 120	Constant volume conditions cell, monitored for 160 days, sample prepared at dry density of 1.49 g/cm ³		[16]
	MX-80	0.16-10	70 x 483.9	Heated Column experiment, sample prepared at dry density of 1.47 g/cm ³ , monitored for 3 years		[2]
	FEBEX GBM	< 5	50 x 12	Oedometer cell, constant volume conditions, 30°C	Dry density, temperature	[14]
	MX-80	< 10	35 x 10	Small samples holders, 20°C, 17 days hydration time	Dry density	[9]
	FEBEX GBM, EB experiment	0.075-9.5	full-scale	In-situ swelling pressure measured by sensors, in-situ temperature and relative humidity (17 °C, 48%)	Dry density	[17]
	Spanish GBM	0.01-10	n/a	Wetting at constant volume	Dry density	[8]
	FoCA, pellets and powder material			Oedometer tests, samples of 50, 100 and 120 height samples prepared at dry density of 1.6 g/cm ³ , Monitored for 100 days to more than 1-year evolution of swelling pressure with time		[18]
	MX-80	0.065-4	75x15	Constant volume swelling tests in rigid cells		[19]
	MX-80 shot-clay, sand (60%) and gravel (30%) fractions		75.3 x 18.8	In-situ core samples recovered from the shot-clay experiment at the Grimsel URL, constant volume swelling tests in laboratory, maximum swell pressure observed 10 days after the flooding		[20]
Gas Transport	FEBEX grains	< 5	n/a	Nitrogen gas used as fluid, injected at low pressure,	Effect of porosity	[21]
	FEBEX	< 5	38 x 78	A triaxial cell, Nitrogen gas as fluid.	Dry density	[22]
	GBM in EB experiment	In-situ specimens retrieved from EB experiment at Mont Terri Rock Laboratory Switzerland, argon gas used as fluid, steady state method, triaxial cell, Confining pressure 1MPa, gas pressure 0.6 MPa				[23]

pores. The results indicated that the pore structure of the inter-granular pores was mainly controlled by the compaction density. The SEM observations also complimented the PSD data. SEM photomicrographs were used to study the size of intergranular pores as function of compaction intensity in the samples compacted at dry density 1.40 g/cm^3 and 1.65 g/cm^3 ; larger intergranular pore sizes identified in the low-density sample [24]. Structural changes including homogenization processes and fractures were investigated by MFXCT during the hydration of pellet and powder mixtures [16,25].

CONCLUSIONS: FUTURE AREAS OF STUDY

Many research programs are in progress since 1970s to evolve a safe and sustainable repository concept for the disposal of high-level radioactive waste, yet, no final repository has been constructed [26]. Despite the large amount of studies on the bentonite materials used as a buffer/backfill in the repository, some knowledge gaps remain. In-situ experiments with a large focus on GBM are also in progress to understand the coupled effects of complex thermo-hydro-mechanical and chemical processes, e.g. FE and HEE experiments and EB experiment (dismantled) at the Mont Terri rock laboratory and in Switzerland.

Several factors influence the heat and mass transport processes through the porous medium. The thermal characteristics of the porous medium are governed by the various factors including composition, grain and pore size structure, dry density [27], porosity [27,28] and moisture content [28]. The gas diffusion and advection are the prevailing mechanisms for transport of gases through the soil [26,29]. Selin [36] pointed out the diffusion to be a dominant transport mechanism for the gas transport through bentonite barriers unless the applied pressure becomes greater than the swelling pressure and back pressure (total stress). The gas transport through the porous media is controlled by various factors including dry density, particle size, and macro-porosity [29]. The review has shown that the above listed factors coupled with the microstructural features need further study in future for better understanding of the behavior of GBM as the buffer and the mass transport processes through the GBM and bentonite-based granular materials.

ACKNOWLEDGMENTS

This work was supported by JSPS KAKENHI Grant Number 17H03301.

REFERENCES

- [1] Dixon D., Sandén T., Jonsson E., and Hansen J., Backfilling of deposition tunnels: Use of bentonite pellets, SKB P-11-44, ISSN 1651-4416, February 2011.
- [2] Villar M. V., Martín P. L., Romero F. J., Iglesias R. J., and Gutiérrez-Rodrigo V., Saturation of barrier materials under thermal gradient, *Geomechanics for Energy and the Environment*, Vol. 8, 2016, 38–51.
- [3] Arthur R., Sasamoto H. and Yui M., Potential complications in the development of a thermodynamic database for hyperalkaline, argillaceous systems, *Proceedings of the International Workshop on Bentonite-Cement Interaction in Repository Environments*, Nuclear Waste Management Organization of Japan (NUMO), October 2004, NUMO-TR-04-05.
- [4] Imbert C., and Villar M. V., Hydro-mechanical response of a bentonite pellets/powder mixture upon infiltration, *Applied Clay Science*, Vol. 32, Issue 3–4, 2006, pp.197–209.
- [5] Wersin P., Johnson L. H., and McKinley I. G., Performance of the bentonite barrier at temperatures beyond 100°C : A critical review, *Physics and Chemistry of the Earth*, Vol. 32, Issue 8–14, 2007, pp.780–788.
- [6] Volckaert G., Bernier F., Alonso E., Gens A., Samper J., Villar M. V., Martín P.L., Cuevas J., Campos R., Thomas H.R., Imbert C., and Zingarelli V., Thermal-hydraulic-mechanical and geochemical behavior of the clay barrier in radioactive waste repositories (model development and validation), *Nuclear Science and Technology*. EUR 16744. Commission of the European Communities, Luxembourg, 1996, pp. 722.
- [7] Müller H. R., Garitte B., Vogt T., Köhler S., Sakaki T., Weber H., Spillmann T., Hertrich M., Becker J., Giroud N., Cloet V., Diomidis N., and Vietor T., Implementation of the full-scale emplacement (FE) experiment at the Mont Terri rock laboratory, *Swiss Journal of Geosciences*, Vol. 110, Issue 1, 2017, pp. 287-306.
- [8] Mayor J-C., García-Siñeriz J-L., Alonso E., Alheid H-J., and Blümling, P., Engineered barrier emplacement experiment in Opalinus Clay for the disposal of radioactive waste in underground repositories, *Technical Report*, ENRESA: Empresa Nacional de Residuos Radiactivos, February, 2005, 1–101.
- [9] Karnland Q., Nilsson U., Weber H. and Wersin

- P., Sealing ability of Wyoming bentonite pellets foreseen as buffer material - Laboratory results, *Physics and Chemistry of the Earth*, Vol. 33, Issue SUPPL.1, 2008, pp.472–475.
- [10] Alonso E.E., Romero E. and Hoffmann C., Hydromechanical behavior of compacted granular expansive mixtures, experimental and constitutive study, *Géotechnique*, Vol. 61, Issue 4, 2011, pp.329–344.
- [11] Tang A. M. and Cui Y. J., Effects of Mineralogy on Thermo-Hydro-Mechanical Parameters of MX80 Bentonite, *Journal of Rock Mechanics and Geotechnical Engineering* Vol. 2, Issue 1, 2010, pp.91–96.
- [12] Sakaki T., Lüthi F. B., Vogt T., Uyama M., and Niunoya S., Heated fiber-optic cables for distributed dry density measurements of granulated bentonite mixtures : Feasibility experiments, *Geomechanics for Energy and the Environment*, Vol. 17, 2019, pp.57–65.
- [13] Masuda R., Asano H., Toguri S., Mori T., Shimura T., Matsuda T., Uyama M., and Noda M., Buffer Construction Technique Using Granular Bentonite, *Journal of Nuclear Science and Technology*, Vol. 44, Issue 3, 2007, pp.448–455.
- [14] Villar M. V., and Gomez-Espina R., Report on Thermo-Hydro-Mechanical Laboratory Tests Performed by CIEMAT on Febex Bentonite, 2004-2008, *Informes Técnicos Ciemat*, 1178, 2009, pp. 67.
- [15] Molinero-Guerra A., Cui Y-J., He Y., Delage P., Mokni N., Tang A. M., Aïmedieu P., Bornert M. and Bernier F., Characterization of water retention, compressibility and swelling properties of a pellet/powder bentonite mixture. *Engineering Geology*, Vol. 248, 2019, pp.14–21.
- [16] Molinero-Guerra A., Aïmedieu P., Bornert M., Cui Y-J., Tang A. M., Sun Z., Mokni N., Delage P., and Bernier, F., Analysis of the structural changes of a pellet/powder bentonite mixture upon wetting by X-ray computed microtomography, *Applied Clay Science*, Vol. 165, Issue August, 2018, pp.164–169.
- [17] García-Siñeriz J. L., Villar M. V., Rey M., and Palacios B., Engineered barrier of bentonite pellets and compacted blocks: State after reaching saturation. *Engineering Geology*, Vol. 192, 2015, pp.33–45.
- [18] Maugis P., and Imbert C., Confined wetting of FoCa clay powder/pellet mixtures: Experimentation and numerical modeling, *Physics and Chemistry of the Earth*, Vol. 32, Issue 8–14, 2007, pp.795–808.
- [19] Seiphoori A., Thermo-hydro-mechanical characterisation and modelling of Wyoming granular bentonite, Technical Report 15-05, EPFL, Lausanne, Report prepared on behalf of NAGRA, 2015.
- [20] Ferrari A., Seiphoori A., Rüedi J., and Laloui, L., Shot-clay MX-80 bentonite: an assessment of the hydro-mechanical behavior, *Engineering Geology*, Vol. 173, 2014, pp.10-18.
- [21] Villar M. V., Thermo-hydro-mechanical characterisation of a bentonite from Cabo de Gata. A study applied to the use of bentonite as sealing material in high level radioactive waste repositories, ENRESA, 01/2002, Madrid, pp. 258.
- [22] Villar M. V., Gutiérrez-Rodrigo V., Martín P. L., Romero F. J., and Barcala, J. M., Gas Transport in Bentonite, Technical Report, *Informes Técnicos Ciemat*, December, 2013.
- [23] Liu J-f., Wu Y., Cai C-Z., Ni H-y, Cao X-l, Pu H., Song S-b., Pu S-y., and Skoczylas F., Investigation into water retention and gas permeability of Opalinus clay. *Environmental Earth Sciences*, Vol. 77, Issue 5, 2018.
- [24] Lloret A., and Villar M. V., Advances on the Knowledge of the Thermo-Hydro-Mechanical Behaviour of Heavily Compacted FEBEX Bentonite, *Physics and Chemistry of the Earth*, Vol. 32, Issue 8–14, 2007, pp. 701–715.
- [25] Van Geet M., Volckaert G., and Roels S., The Use of Microfocus X-Ray Computed Tomography in Characterising the Hydration of a Clay Pellet/Powder Mixture.” *Applied Clay Science*, Vol. 29, Issue 2, 2005, pp.73–87.
- [26] Sellin P., and Leupin O. X., The use of clay as an engineered barrier in radioactive-waste management- A review, *Clays and Clay Minerals*, Vol. 61, Issue 6, 2014, pp.477–498.
- [27] Engelhardt I., Finsterle S., Thermal-hydraulic experiments with bentonite/crushed rock mixtures and estimation of effective parameters by inverse modeling, *Applied Clay Science*, Vol. 23, 2003, pp.111–120.
- [28] Côté J., and Konard J.M., Thermal conductivity of base-course materials, *Can. Geotech. J.*, Vol. 42, 2005, pp.61–78.
- [29] Hamamoto S., Moldrup P., Kawamoto K., and Komatsu T., Effect of Particle Size and Soil Compaction on Gas Transport Parameters in Variably Saturated, Sandy Soils. *Vadose Zone Journal*, Vol. 8, Issue 4, 2009, pp. 986–995.

THE NEW ADVANCED PROTOTYPE OF AIRBORNE VISUAL CONTROL OF A GROUND ROBOT

Oleg Kupervasser^{1,2*}, Hennadii Kutomanov¹, Vitalii Sarychev², and Roman Yavich¹

¹Department of Mathematics, Ariel University, Israel; ²Transist Video Llc, Skolkovo, Russia

*Corresponding Author

ABSTRACT

Unmanned autonomous robots will be widely used very soon for land use, treatment, and monitoring. The paper addresses the problem of visual navigation of ground robots using a camera positioned at a certain elevation above the confined area. The main idea is that robot's "eyes" is not located on the robot but are independent autonomous system. As a result, the "eyes" can go up and observe the robot from above. This patented technology of airborne vision-based control of ground robots is already described previously in "International Journal of GEOMATE" and Geomate2019 conference paper (Ehrenfeld et al., 2020). There was described in detail the small toy prototype with very simple algorithms and very shortly the next more complex prototype. In the current paper we present detailed algorithms for navigation and control of this complex prototype. The system consists of the USB camera on the tower (4 meters) connected to the computer which controls the big ground robot by sending Wi-Fi commands. For navigation (recognition of the ground robot, finding its position and orientation) we use deep learning (artificial neural network). It was demonstrated that this robot can pass two main tests: travelling along some predefined path and random walk inside of some predefined boundary.

Keywords: Vision-based navigation, Visual Navigation, Ground Robots, Tethered Platform, Airborne Control, Prototype, Vision-Based Navigation, Artificial neural network, Deep learning convolution network, Autopilot, Time delay, Stability of differential equations

INTRODUCTION

Unmanned autonomous robots will be widely used very soon for land use, treatment, and monitoring [1-3]. The most popular outdoor robots are currently robot-lawnmowers used for bounded operation area. However, the different very interesting applications for such robots can be found. Let us give yet several examples:

- 1) It is a remote-controlled slope mower [4]. Currently, remote control of a human operator is used for such mowers. However completely autonomous robots can be made using technology proposed in this paper.
- 2) Robotic Fruit Harvester - the FFRobot [5]
- 3) Robots for fire protection [6]
- 4) Autonomous wheelchair for disabled people [7]

The paper addresses the problem of visual navigation (vision-based navigation) of ground robots using a camera positioned at a certain elevation above the confined area. Vision-based navigation of robots is like human navigation by the help of eyes vision. However, it is not necessary to build eyes into the robot. It is possible to put eyes on a top position and from the top position the robot can see itself and its motion. It means airborne terrestrial robot control [3,8-12]. One of the

developments is to take into account delays in the control system.

The described above system may be used for coordination, navigation and control of ground robots (automated transport, automated agricultural machines, municipal and aerodrome vehicles, garden lawnmowers and so on).

The key innovation of the study is the system of navigation and intercoordination. The system includes one or more robots, located on the controlled area; one or more robot tracing devices on the suspended tethered platforms; natural or artificial markings; charger; and central module for robot coordination and orientation detection. The information is transferred to the central module from all the tracing devices. The system central module is equipped with the calculation module located or on the suspended platform, or on the ground, or on the charger or on the robot. The calculation module is possible to calculate coordinates and orientation of robots and to form the control commands, based on the information received from all the above described devices. This visual system can also be used for preventing collision of ground robot with children or animals. Also, we can use this visual system for security purposes.

The technical result is the development of the robot efficient coordination using the devices located on the towers, the aerial apparatuses tracing

the robots on the controlled area, supervising their environment including natural and artificial markings. One of the developments is to take into account delays in the control system.

The system (the proof of concept) was defined as following (Fig. 1):

- 1) The tower (4 meters).
- 2) The USB camera on the tower connected to computer.
- 3) The computer which controls the big ground

robot by sending Wi-Fi commands, supplied by software for finding its position and orientation using deep learning (artificial neural network) from USB camera images.

- 4) The ground robot.

It was demonstrated that this robot can pass two main tests: travelling along some predefined path and random walk inside of some predefined boundary. A reader can find these tests here [13,14].

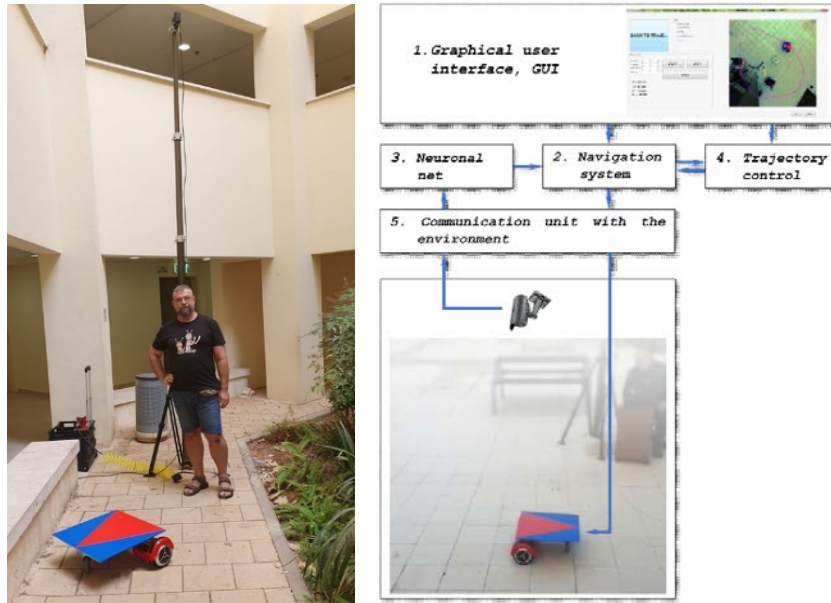


Fig. 1. Airborne terrestrial robot control.

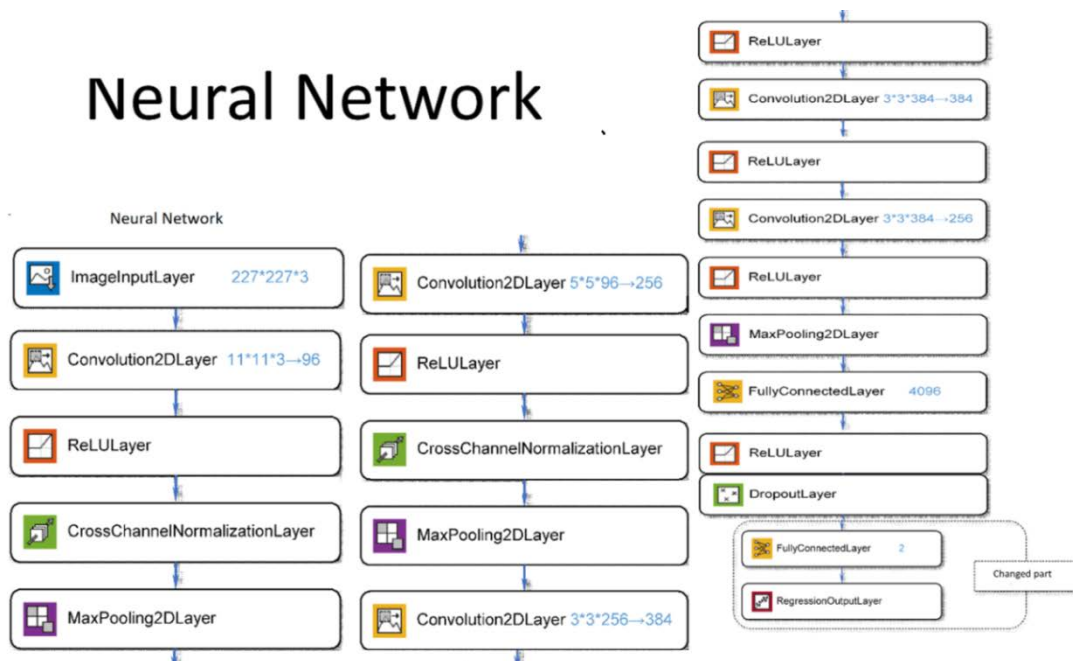


Fig. 2. Transformed AlexNet in Matlab.

CONTROL AND NAVIGATION SYSTEM

Most visual recognition methods use set of correspondent characteristic points [15] to locate the ground robot with respect to an observation camera. In this case, various SIFT functions are usually used to highlight the correspondent characteristic points [15]. These methods require a large database of functions, efficient search methods and a lot of time for calculations.

Using a deep learning convolution neural network can significantly reduce data processing time and increase accuracy.

Despite the massive enthusiasm for neural networks and their active implementation in computer applications, their use to determine the coordinates of objects relative to cameras is not investigated practically.

However, there are a series of interesting works by A. Kendall, M. Grimes and R. Cipolla (University of Cambridge) [16, 17], who used a convolutional neural network to determine camera coordinates, and are pioneers of the use of deep learning methods in navigation. In their works, they determined the coordinates and angles of rotation of the camera using images of Cambridge Landmarks building, made by pedestrian smartphone's camera.

Unlike the authors of [16,17], who used images of buildings from ground level and using cameras mounted on ground robots, we need to find the position of a ground robot relative to a camera in an upper position. The neural network was based on the popular AlexNet network with minor changes in the structure and training mode. AlexNet [18] is the name of a convolutional neural network (CNN), designed by Alex Krizhevsky and published with Ilya Sutskever and Krizhevsky's doctoral advisor Geoffrey Hinton. AlexNet competed in the ImageNet Large Scale Visual Recognition Challenge on September 30, 2012, significantly outperforming other networks. In the original AlexNet, there are only 8 levels (5 convolutional and 3 fully connected). For our tasks, we removed the last two fully connected layers, and replaced them with one fully connected layer with 4 outputs (x, y coordinates and trigonometric functions $\sin()$ and $\cos()$ for the rotation angle α) or 7 outputs (x, y, $\sin(\alpha)$, $\cos(\alpha)$, coordinate, angle and total errors) and one regression layer. That is, we used the pre-trained AlexNet network to solve the regression problem: determining two coordinates and course angle of the robot (Fig. 2).

We used two-step network training method.

At the first stage, we set the task of teaching the network to determine the coordinates and course angle of the robot in ideal visibility conditions.

For this, we used the part of the sample in which the robot is fully open and clearly visible. Number of such images in the sample was 9293.

We built a network containing 4 outputs - the two coordinates of the robot in the image, as well as the sine and cosine of its rotation course angle. We did not use the direct value of the angle when training the network, since the angle values have a gap at -180: 180, which leads to big errors at angles close to these values.

The sine and cosine Sin_{NN} and Cos_{NN} calculated by the network were used to calculate the angle of rotation of the robot through a weighted average, where the weights of each of the calculated angles is directly proportional to the rate of function change. For example, for $Sin_{NN} > 0$ and $Cos_{NN} > 0$ we get:

$$\alpha \approx \frac{\arcsin(Sin_{NN}) * |Cos_{NN}| + \arccos(Cos_{NN}) * |Sin_{NN}|}{|Cos_{NN}| + |Sin_{NN}|} \quad (1)$$

Training was carried out using the solver “adam”, training took place in 200 epochs with 500 batch size. This network made it possible to determine the coordinates of the robot with an accuracy of 2.4 pixels in an image of 227 X 227 pixels size and an angle with an accuracy of 4 degrees.

Further, this network was tested on a full sample of 12,000 images, and for each image three values were determined:

- coordinate error

$$err_{coord} = \sqrt{(x_{real} - x_{net})^2 + (y_{real} - y_{net})^2} \quad (2)$$

- angle error

$$err_{angle} = 1000 \cdot \sqrt{(\sin \alpha_{real} - \sin \alpha_{net})^2 + (\cos \alpha_{real} - \cos \alpha_{net})^2} \quad (3)$$

- total error

$$err_{full} = err_{coord} + err_{angle} \quad (4)$$

Finally, the err_{full} is total error value for images, in which the robot is fully visible, is ranged from 0 to 150, for images where the robot is partially visible - from 150 to 1500, and for images where the robot was not visible - from 500 to 4500 (Fig. 3).

At the second stage a network was built, where, in addition to the coordinates and trigonometric functions of the angle, the network was trained to

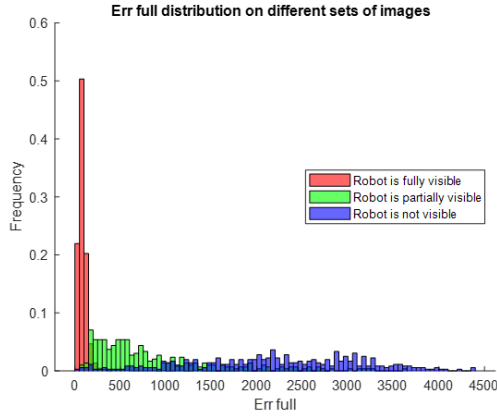


Fig. 3 The total error distribution for different visibilities of the robot.



Fig. 4. The different images of the robot from the dataset

predict err_{full} , err_{coord} , err_{angle} . Thus, by teaching the network to predict the possible error value, we got a tool that allows us not only to determine the coordinates, but also to verify the accuracy of their determination. If the robot turned out to be completely or partially covered by environmental objects, we saw this from the increase in the predicted errors.

This approach allowed us to avoid working with two networks, the first of which would be classifying, and determining the presence of the robot in the image, and the second would be finding its coordinates and angle. The classification problem has been replaced by the regression task of error prediction.

Training was carried out using full sample of 10,000 images and the solver “adam”, training took place in 200 epochs with 500 batch size. Thanks to modeling in Unity, the dataset was generated programmatically. At each step, the position and angle of rotation of the robot, as well as the location of the elements of the working platform, were randomly selected. Lighting simulated sunlight falling from various angles and directions. As a background, 50 different textures were used to achieve independence of determining the coordinates of the robot from background elements (Fig. 4). 12,000 rgb images of size 3036 X 3036 containing robots were generated. Among the images were also shots where the robot was partially or completely covered by environmental objects or the tower of the camera. A file was also prepared with information about the coordinates of the robot and the rotation angle. Then, based on these images,

a set of images reduced to 227 X 227 pixels was prepared.

AUTOMATIC CONTROL

Let us define the following variables and parameters used in equations of motion for the ground robot (see Fig. 5):

1) For variables describing motion:

x и y – coordinates of ground robot; α – angle of rotation of the robot on the plane; v – translation velocity of the robot; ω – angle velocity of the robot

2) Ground robot parameters:

R – wheel radius; l – distance between wheels

3) Controlling signals:

ω_R и ω_L – angle velocities of rotation of the right and left wheels

It is shown in [19] that forward movement and rotation are described by the system of equations:

$$\dot{x} = v \cos \alpha; \dot{y} = v \sin \alpha; \dot{\alpha} = \omega; \quad (5)$$

$$v = \frac{R(\omega_R + \omega_L)}{2}; \omega = \frac{2R(\omega_R - \omega_L)}{l} \quad (6)$$

Since the system is nonlinear, it's too hard to use those equations to analyze stability. We need to linearize those equations on the premise that the parameters $x(t)$, $y(t)$, $\alpha(t)$, $v(t)$, $\omega(t)$ corresponding with steady flight get small increments $\delta x(t)$, $\delta y(t)$, $\delta \alpha(t)$, $\delta v(t-\tau)$, $\delta \omega(t-\tau)$ caused by perturbations action on a path.

We estimate robot trajectory by polygonal chain path. This path consists of linear motion along line segments with constant translational velocity and zero angular velocity (Rotation), and rotations in vertices with constant angular velocity and zero translational velocity (Linear motion).

For the case when stationary parameters cannot provide stability of the desirable stationary trajectory themselves, we need to use autopilots (Fig. 6). An autopilot states the controlling parameters $\delta v(t-\tau)$, $\delta \omega(t-\tau)$ to be functions of the output controlled parameters (), which are deviations from the desirable stationary trajectory $\delta x(t)$; $\delta y(t)$; $\delta \alpha(t)$. The values of the output parameters can be obtained by autopilot from navigation measurements, for example, from vision-based navigation, inertial navigation, satellite navigation and so on. On the basis these navigation measurements, the autopilot forms controlling signals to decrease undesirable deviation. Unfortunately, there always exists some in getting information about the output-controlled parameters to autopilot for any navigation measurements. So, we have a problem, because of the lack of some necessary information for controlling. In the paper [20] we demonstrate that we are possible even for such conditions with the time delay to get controlling signal providing a stable path.

Final solution from [20] are following:

For rotation, the stationary solution is

$$\alpha(t)=\omega t+\varphi; v(t)=0; \varphi=0 \quad (7)$$

where control parameters are following:

$$\delta v(t-\tau) = -2 a_r \cos(\omega(t-\tau))\delta x(t-\tau) - 2 a_r \sin(\omega(t-\tau))\delta y(t-\tau)$$

$$\text{where } \omega \neq 0, a_r > |\omega|; \quad (8)$$

$$\delta \omega(t-\tau) = b_\alpha \delta \alpha(t-\tau) \text{ where } b_\alpha < 0. \quad (9)$$

For linear motion, the stationary solution is

$$\alpha(t)=\alpha; v(t)=v \quad (10)$$

where control parameters are following:

$$\delta v(t-\tau) = -a_l \cos(\alpha)\delta x(t-\tau) - a_l \sin(\alpha)\delta y(t-\tau)$$

$$\text{where } a_l > 0; \quad (11)$$

$$\delta \omega(t-\tau) = a \sin(\alpha) \delta x(t-\tau) - a \cos(\alpha) \delta y(t-\tau) - 2b \delta \alpha(t-\tau)$$

$$\text{where } av > 0; b > \sqrt{av}. \quad (12)$$

The delay time is following:

$$\tau \leq \min\left(\frac{1}{2e|b|}, \frac{1}{e|a_l|}, \frac{1}{e|b_\alpha|}, \frac{1}{2e|a_r|}\right) \quad (13)$$



Fig. 5 Ground robot

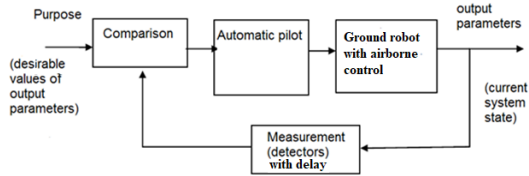


Fig. 6 Automatic control

EXPERIMENTAL RESULTS

We developed software using designed algorithms. It was demonstrated in real experiments that it is possible to carry out two options to drive the ground robot: random movement in user predefined boundaries and user predefined route ([13,14] and Fig. 7).

CONCLUSIONS

It was demonstrated that it is possible to carry

out two options to drive the ground robot:

- A random movement in user predefined boundaries
- A user predefined route

As a result, we proved that it is possible to maintain stable movement of a ground robot even when time delay exists in transfer information about output control parameters from navigation measurement devices to autopilot.

We can find control parameters for the particular case of visual airborne navigation of ground robot and estimated max possible delay of the system.

We also demonstrate that the neural network is an effective tool for determining the coordinates of an object: fast, high-precision, insensitive to interference, changes in the environment and lighting.

The quality of determining coordinates allows you to build a high-quality control system for a ground robot.

Obviously, the proposed methods can also be used to solve other problems where it is necessary to determine the coordinates of the observed object.

The future work includes the following:

- 1) Creation a system for developing possible trajectories
- 2) Creation a system for inter-coordination of several robots.
- 3) Recognition of the environment of robots: ground markers, obstacle, moving objects
- 4) Recognition of robot operation results: how much grass is mowed, which part of the operation area is treated.

However, the developed robot is only prototype. The main future work is creation of working robot for mass-production. The working robot can be:

- 1) It is a remote-controlled slope mower [4].
- 2) Robotic Fruit Harvester - the FFRobot [5]
- 3) Robots for fire protection [6]
- 4) Autonomous wheelchair for disabled people [7]



Fig 7. Two experimental tests - random movement in user predefined boundaries and user predefined route.

REFERENCES

- [1] Kupervasser O., Sarychev V., Rubinstein A. and Yavich R., Robust positioning of drones for land use monitoring in strong terrain relief using vision-based navigation, *International Journal of GEOMATE*, Vol.14, Issue 45, 2018, pp. 10-15
- [2] Djaja K., Putera R., Rohman R. A. F., Sondang I., Nanditho G. and Suyanti E., The Integration of Geography Information System (GIS) and Global Navigation Satellite System-Real Time Kinematic (GNSS-RTK) for Land use Monitoring, *International Journal of GEOMATE*, Vol.13, Issue 36, 2017, pp. 31-34
- [3] Ehrenfeld I., Kupervasser O., Kutomanov H., Sarychev V. and Yavich R., Algorithms Developed for Two Porotypes of Airborne Vision-Based Control of Ground Robots, *International Journal of GEOMATE*, 2020, Vol.19, Issue 72, 2020, pp. 217 - 224
- [4] <https://www.greenclimberna.com/>
- [5] <https://www.insightssuccess.com/ffrobotics-creating-a-new-age-for-fruit-harvesting/>
- [6] <https://www.robotpompier.com/en/>
- [7] Pires G., Honório N., Lopes C., Nunes U., Almeida A.T., Autonomous wheelchair for disabled people, *Proceedings of the IEEE International Symposium on Industrial Electronics, 1997 (ISIE97)*, pp. 797-801
- [8] Ehrenfeld I., Kogan M., Kupervasser O., Sarychev V., Volinsky I., Yavich R., Zangbi B., Visual navigation for airborne control of ground robots from tethered platform: creation of the first prototype, in *Proceeding of the IEEE International Conference on New Trends in Engineering and Technology, GRTIET, Tirupathi, Chennai, Tamil Nadu, India, Sept, 2018*, p. 96
<http://grt.edu.in/news/international-conference-on-new-trends-in-engineering-and-technology-icntet-2018/>
- [9] Kupervasser O. Yu., Kupervasser Yu. I., Rubinstein A. A., Russian Utility model: Apparatus for Coordinating Automated Devices, Patent № 131276, Russia, Nov 12, 2012
- [10] Kupervasser O.Yu., Kupervasser Yu.I., Rubinstein A.A., German Utility model: Vorrichtung für Koordinierung automatisierter Vorrichtungen. Patent Nr. 21 2013 000 225, Germany, Jul 10, 2015
- [11] Kupervasser O. Yu., Franch Utility model application: Coordination System for Ground Movable Automated Devices. Utility model, publication number 3037157, France, Jun 4, 2016,
<http://bases-brevets.inpi.fr/en/document-en/FR3037157.html?s=1482862654519&p=5&cHash=1f6f99c78cfb2124b5accb92be338388>
- [12] Kupervasser O. Yu., Russian Invention: Method for coordination of ground moving automated devices with the help of single central control system, Patent № 2691788, Russia, July 05, 2015
- [13] <https://www.youtube.com/watch?v=ekxAM9Uytzc>
- [14] <https://www.youtube.com/watch?v=KYuXCAzTiPE>
- [15] Lowe D. G., Distinctive Image Features from Scale-Invariant Keypoints, *International Journal of Computer Vision*, Vol.60, 2004, pp. 91–110
- [16] Kendall A., Grimes M., Cipolla R., PoseNet: A Convolutional Network for Real-Time 6-DOF Camera Relocalization, *arXiv:1505.07427 [cs.CV]*
- [17] Kendall A., Cipolla R., Geometric Loss Functions for Camera Pose Regression with Deep Learning, *arXiv:1704.00390 [cs.CV]*
- [18] Krizhevsky A., Sutskever I., Hinton G. E., ImageNet classification with deep convolutional neural networks, *Communications of the ACM*, Vol.60, Issue 6, 2017, pp. 84–90.
- [19] Prof. Raul G. Longoria, Turning Kinematically, Spring 2015
<https://docplayer.net/31417021-Turning-kinematically.html>
- [20] Domoshnitsky A., Kupervasser O., Kutomanov H., Yavich R., A method for stabilization of ground robot path controlled by airborne autopilot with time delay, accepted to Springer Preceedings

INVESTIGATION OF OPEN-PIT MINE DRAINAGE FEATURES

Cristhiana Perdigão¹, Ashley Dyson², Mohammadjavad Yaghoubi³ and Thomas Baumgartl⁴
^{1,2,3,4} School of Engineering, Information Technology and Physical Sciences, Federation University,
Australia

ABSTRACT

As control measures of ground and surface water, horizontal bores have played a very long term and essential role in maintaining the stability of mine batters. In coal open-cut mines, joints or geological discontinuities in coal seams can control the groundwater flows. The water pressure, caused by the flow and hydrostatic pressures inside the joints can contribute to batter failure due a greater active force than the shear strength of the slip surface. In this research, the drainage performance of horizontal bores is assessed to investigate and compare the profiles of various bores. A recently developed camera for bore investigation is employed in this project to visually inspect the horizontal drains. This study has taken place in an operational brown coal mine located in Gippsland, region of Victoria, Australia. Joints and water flow variation along the bores, observed through the camera inspection, are discussed. Results to date showed that the camera is an effective tool to inspect the boreholes and allow the interpretation of the visual observations.

Keywords: Horizontal bore, Bore outflow, Visual inspection, Drainage

INTRODUCTION

Horizontal bores are essential infrastructures for maintaining the stability of open-pit mines. The installation of horizontal drains helps to decrease the water table elevation and reduce pore pressures within soil or rock units. Reduction of the water pressures results in the increase of the shear strength of soil, and accordingly, improvement of slope stability [1]. Using horizontal bores for lowering the groundwater levels are generally recognized as the most economical method available [2]. They are usually used where the groundwater cannot be reached by other conventional drainage methods such as trench drains. Although the implementation of horizontal drains is a common practice for slope stability, there seems to be limited information available on the assessment of their performance over time and requirements for maintenance.

The primary objective of this paper is to describe a methodology that has been conducted to assess the drainage performance of horizontal bores and to investigate their features. Profiles of various bores are compared with the aim to correlate their features (e.g. intersecting joints and joint density) with their performance. This study has been conducted at Yallourn Mine, an operational brown coal mine in the Latrobe Valley, located in Victoria, Australia. The Latrobe Valley coal seams are broken up by sets of widely spaced continuous joints, which provide planes for movement to occur and allow direct access for water to depth. The dominant joint set within the coal seams is generally sub-vertical and continuous through the full thickness of the coal. These joints can connect to any surface water body or readily accessible water source. Water flow through the

joints can potentially impact the slope stability by increasing the likelihood of block sliding and/or increasing the potential for adverse pore pressures within the coal units [3].

METHODOLOGY

The bores for this research were selected according to their characteristics presented in Table 1 (age, depth and location). Results presented in this paper are from the bores presented in Figure 1.

Table 1 Selected bore's characteristics

Bore Code	Total Depth (m)	Installation Year
N6853	300	2013
N5224	200	1999
N6852	400	2013



Figure 1: Locations of the studied bores at Yallourn

Water Flow

This part of the study addresses the linkage of rainfall and response time of the magnitude of water flow on the performance of individual boreholes. Water flow and temperature analysis provide a better understanding about whether or not a borehole is draining groundwater or simply withdrawing short term recharge water from surface water. Each water flow meter (Figure 2) contains a data logger that records the number of tips (events) and water temperature. The temperature profile may be useful as it indicates whether the water being drained by the borehole is originating from the groundwater or from the surface as the groundwater tends to have higher temperatures than the surface recharge water due to coal low thermal conductivity.



Figure 2: Flow meter connected to a selected bore

Horizontal Borehole Camera

There are a variety of options to investigate the conditions of drilled horizontal boreholes. Due to the length of bores, which can vary from 150m to 500m, and the high-moisture environment they are installed in, conventional instrumentation such as boreholes televiws or fibre optic cables would be impractical or ineffective for the exploration of bores. As such, a

camera unit has been developed by researchers at the Geotechnical and Hydrological Engineering Research Group (GHERG) for this project, presented in Figure 3. The unit includes a submersible camera which can be inserted into the drain bores using a drilling rig to collect visual internal information of the boreholes including presence and characteristics of joints such as location, infill material, flow condition, evidence of shear and blockage. This unit can capture and record real-time images along the length of the drain up to 400 m.

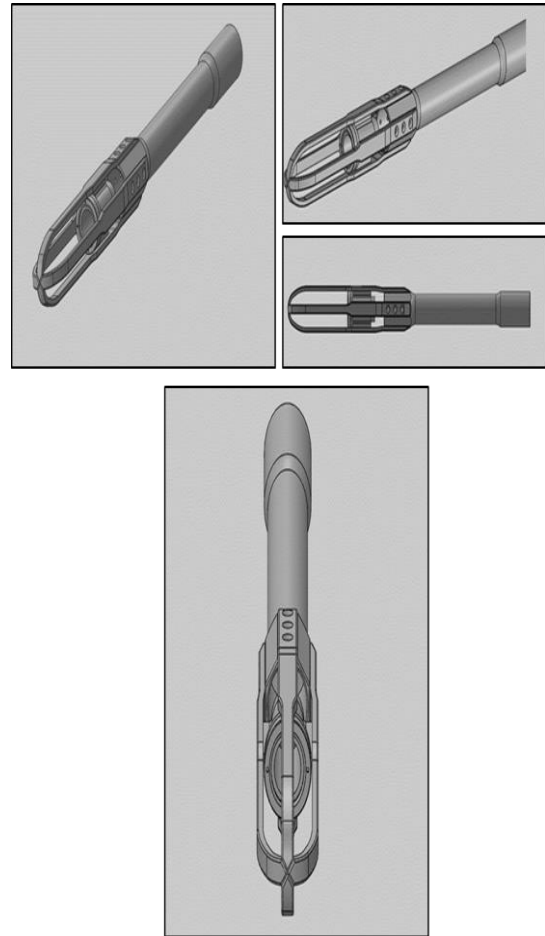


Figure 3: Horizontal Borehole Camera.

RESULTS AND DISCUSSION

Water Flow

The effects of rainfall on the moisture conditions within residual soil slopes through pore-water pressure measurements using tensiometers and piezometers were discussed in [4], [5]. These studies observed a 1-2 day delay response in water pressure, with respect to the start of the rainfall event. Figure 4 presents data collected in regards to the outflow for three different bores during the same period of time and therefore, under the same precipitation rate conditions.

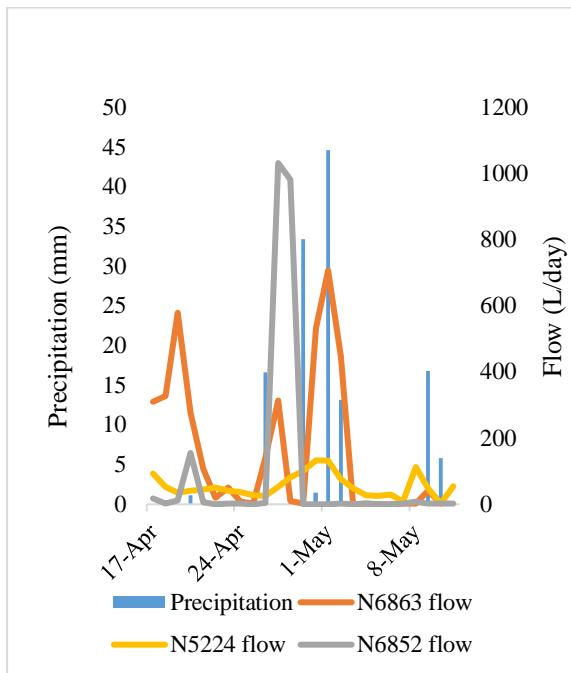


Fig 4: Precipitation rate and the outflow rate of selected bores

Different flow responses to rain might be related to local joints characteristics, for instance how tightly the joints are, how they are connected and their orientation.

The data collected for this research revealed that different sets of boreholes behave differently in terms of flow and response to rain events. The response is governed by mine activity and local geology, particularly, joint networks.

Observations in the field have shown there is no relationship between the age and discharge rate of bores, as some of the recently drilled drains are dry, but some drilled in 1984 are discharging well. The reason behind this is unknown. One assumption is that internal stress releases within the coal may cause some disconnections due to transverse coal block movements along horizontal drains, thereby reducing drainage capacity of the drain bores. A second assumption is that sediment accumulation in the bores restricts flows or even causes blockages. A further cause may be the changes in the catchment for this bore and groundwater replenishment from the surface.

Physical parameters of water are included in the investigation to reveal potential relationships of the duration of flow through the coal matrix and temperature changes and can be used to detect the travel time of water. Figure 5 shows the outflow temperature for the selected bores and how for N5224 and N6853 it varies with the air temperature. While N6852 outflow water temperature is mostly constant regardless of the variation of air temperature over the days and rain events during a certain period. Bore N6852 is an example of one of the selected bores that are draining groundwater (Figure 6).

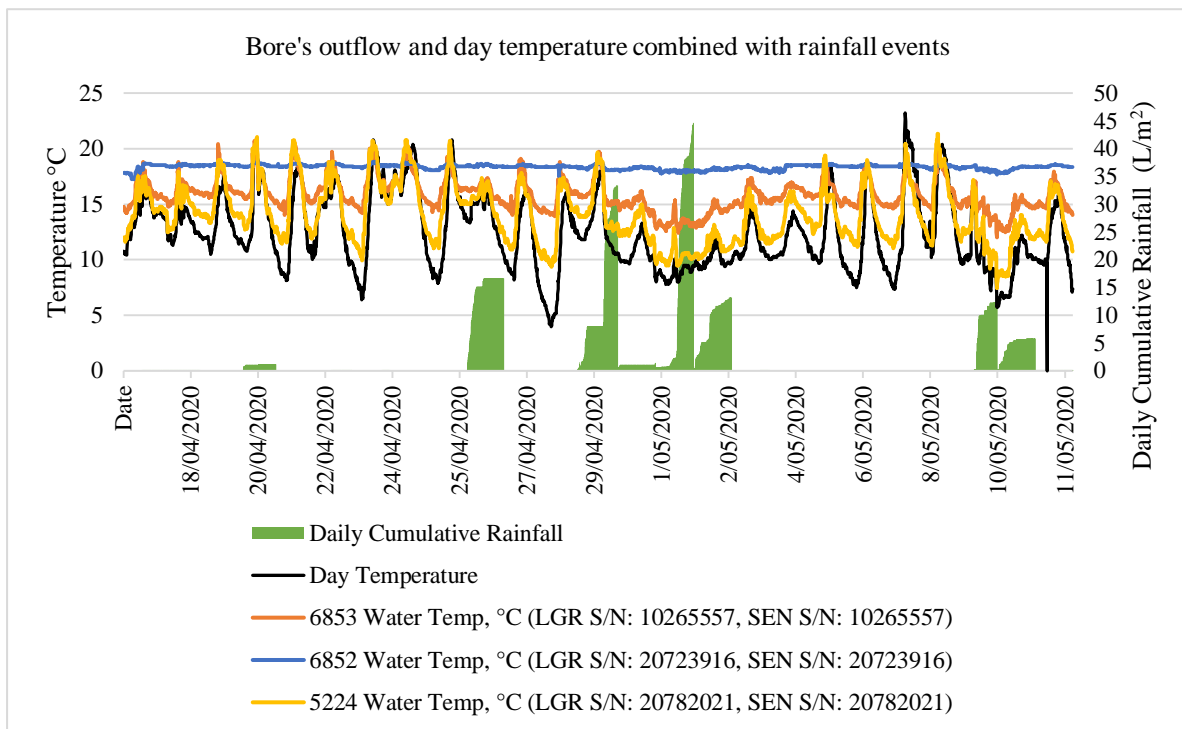


Figure 5: Bore's outflow temperature variation along with precipitation events and day temperature

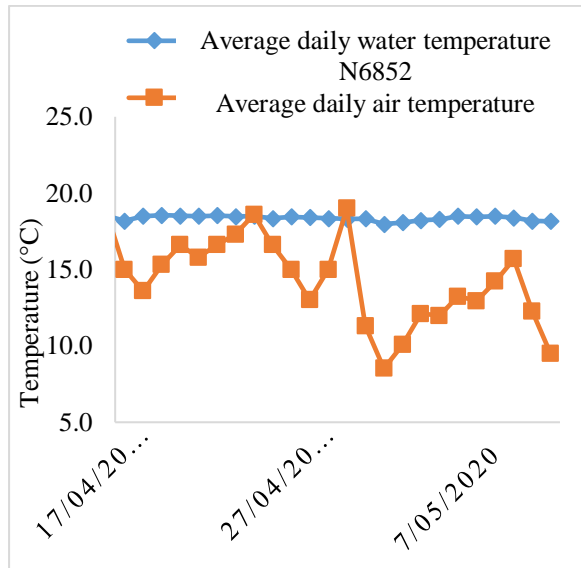


Figure 6: Outflow average temperature of N6852

Camera Inspection

Various features inside deep horizontal bores such as joints as well as variations in water flow, material properties and geometry were observed during the visual inspection. These features are discussed below.

Joints and Variations in Water Flow

As expected, joints could be observed inside the bores (Figure 7) as they are the most numerous and obvious structural features in the brown coals in this specific region [6]. Flow of water through a joint into the borehole can be observed in the top left photo.

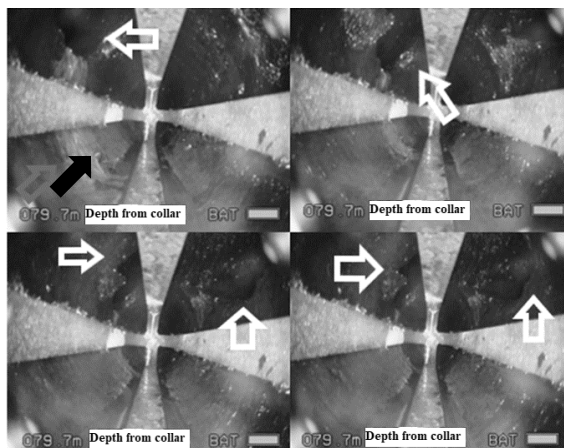


Figure 7: Joint observed through the camera inspection inside the bore pointed by white arrows.

Joints in the brown coal batters are typically sub-vertical, comprise two sub-orthogonal sets and penetrate the full depth of the coal seam [7]. The horizontal bores are drilled in a way to ensure intersections within vertical joints are created to

facilitate drainage of rainfall-runoff that has entered the joints in the coal and to drain groundwater in coal. It has been evidenced through camera inspection, that in some occurrences, a bore intersecting a joint may function as an alternative pathway for waterflow and divert flow using the bore as a connecting medium through a different joint and associated bore (Figure 8).

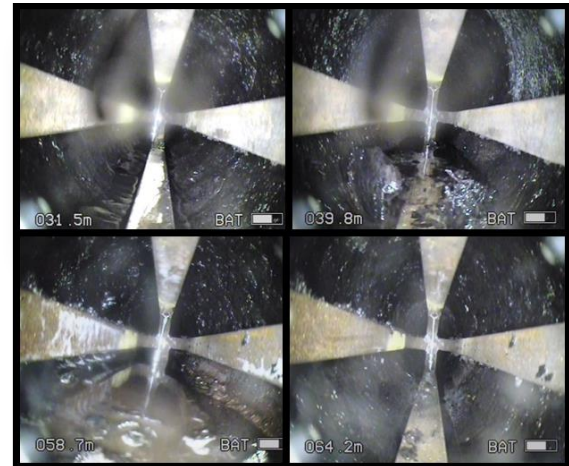


Figure 8: Variation of water flow along the bore

CONCLUSIONS

Flow data collected for this study has revealed that different sets of boreholes behave differently in terms of flow and response to rain events and groundwater recharge.

Outflow temperature has shown to be a good indicator of whether the water being drained by the borehole is coming from the groundwater or the surface as collected data has shown that for bores draining surface water, the outflow temperature varies according to the air temperature. In contrast, for bores draining groundwater, the outflow temperature is mostly constant as observed on bore N5224.

Features inside the deep horizontal bores such as joints as well as variations in water flow were observed with a camera specifically designed for this purpose. Results to date showed that the camera is an effective tool to inspect the boreholes. Future camera inspections, flow and temperature monitoring will lead to further knowledge about the possible causes of the reduction in the efficiency of horizontal boreholes.

ACKNOWLEDGMENTS

Financial support for this research has been provided by Energy Australia and the Geotechnical and Hydrological Engineering Research Group from Federation University, Australia.

REFERENCES

- [1] Pohl, G., Carrol, R., Reeves, D., Parashar, R., Muhunthan, B., Thiyagarajah, S., Willoughby, K. (2013). Design Guidelines for Horizontal Drains used for Slope Stanilization. Washington State Department of Transportation.
- [2] Rahardjo, H., Satyanaga, A., & Leong, E. (2011). Unsaturated soil mechanics for slope stabilization. *Unsaturated Soils: Theory and Practice*, 103-117.
- [3] Department of Economic Development, Jobs, Transport and Resources. (2015). Guideline for Managing Ground Control Risks in Victorian Brown Coal Mines.
- [4] Ng, C., Zhan, L., Bao, C., Fredlund, D., & Gong, B. W. (2003). Performance of an Unsaturated Expansive Soil. (pp. 53(2): 143-157). *Géotechnique*.
- [5] Ng, C., Springman, S. M., & Alonso, E. (2008). Monitoring the Performance of Unsaturated Soil Slopes. (pp. 26(6):799-816). *Geotechnical and Geological Engineering* Kimura S., Journal Paper Title, J. of Computer Science, Vol. 1, Issue 2, 1987, pp. 23-49.
- [6] Barton, C. (1981). Regional stress and structure in relation to brown coal open cuts of The Latrobe Valley, Victoria. *Journal of the Geological Society of Australia*, 28, 333-339
- [7] Shaghaghi, T., Tolooiyan, A., & Mackay, R. (2018, April 10 to 13th). Numerical investigation of potential pore water pressure changes in jointed brown coal due to waste material placement against a brown coal open-cut batter. Sevilla, Spain: XIV Congreso Internacional de energia y Recursos Minerales.

A COMPREHENSIVE LEACHATE STUDY OF FIRED-CLAY BRICKS INCORPORATING CIGARETTE BUTTS

Halenur Kurmus and Abbas Mohajerani

School of Engineering, RMIT University, Australia

ABSTRACT

The use of cigarette butts (CBs) in the construction industry has received considerable interest in recent years to develop environmentally friendly materials. This present paper reports the leaching behavior of Ni, Cu, As, Hg, Cd, Pb, Se, Cr, Ag, Zn, and Ba for both green and fired clay bricks incorporating CBs according to the Australian bottle leaching procedure (ABLP). The leaching of heavy metals was compared for both green (before firing) and fired clay bricks (after firing) to study the influence of firing on the leaching ability of bricks. To assess the suitability of fired clay bricks incorporating CBs, the leachate concentrations were compared to the concentration limits for heavy metals set by the EPA solid industrial waste hazard categorization thresholds. To investigate how the pH affects the leaching behavior of the metals studied for various environmental situations, three pH values, 2.9, 5.0, and 9.2, were used. The findings revealed that the leaching of heavy metals from the fired clay bricks was substantially lower than that of the concentration limits and green bricks. Therefore, bricks modified with CBs can be categorized as non-hazardous waste. The paper also presents the mechanical and physical properties of fired clay bricks incorporated with CBs.

Keywords: Cigarette Butts; Leachate Analysis; Recycling; Fired Clay Bricks; Waste Management

INTRODUCTION

Cigarette butts (CBs) are one of the most common litter items found on beaches and represent 25-50% of the litter collected from streets and roads [2]. It is estimated, worldwide every year, 6 trillion cigarettes are smoked, and roughly 4.5 trillion are discarded in the environment [3]. CBs contain carcinogenic and toxic substances, therefore, when littered can potentially pollute groundwater, soil, and waterways and harm the biota and aquatic life [4].

Littered CBs can remain in the environment for up to 18 months due to the poor biodegradability of cellulose acetate filters while leaching heavy metals and toxic chemicals [5]. Cellulose acetate filters are designed to partially preserve particulate smoke components. The major toxic agents include nicotine, polycyclic aromatic hydrocarbons (PAHs), compounds specific to Solanaceae, nicotiana alkaloids, and catechols [6, 7].

Various studies have been conducted to investigate the transfer of toxic metals in tobacco to the filter of a cigarette [8-10]. The common and harmful heavy metals found in CBs include Se, As, Cd, Cu, Ba, Pb, Zn, Hg, Cr, Ag, and Ni.

Landfilling and incineration are the common methods applied for the disposal of collected CBs. However, neither method is environmentally friendly or economical. Therefore, the method of recycling has gained growing interest. Mohajerani et al. [11] carried out comprehensive studies on recycling CBs in fired clay bricks [12-16]. In addition Mohajerani et al. [17] investigated extensively the use of CBs in asphalt concrete [18, 19]. Other recycling methods

include recycling CBs in the production of cellulose pulp [20], as a corrosion inhibitor [21, 22], as sound-absorbing material [23, 24] and as a biofilm carrier [25, 26]. However, placing CBs in fired clay bricks pose an environmental risk of toxic leaching during the use and disposal of the construction material. Therefore, it is crucial to perform a leachate analysis of heavy metals to classify and quantify those harmful constituents.

Therefore the objective of this study was to perform a leachate analysis on green (before firing) and fired bricks (after firing) incorporating 0%, 0.5%, 1%, 1.5%, and 2% CBs by wt based on the Australian leaching procedure (ABLP) [27]. The Inductively Coupled Plasma Mass Spectroscopy (ICP-MS) was utilized to analyze the samples for heavy metals. To examine the effect of different environmental conditions on the leaching capability of bricks incorporated with CBs and the metals studied, pH values 2.9, 5.0, and 9.2 were selected. The leachate concentrations of metals Se, As, Cd, Cu, Ba, Pb, Zn, Hg, Cr, Ag, and Ni were examined for both green (before firing) and fired bricks (after firing) and compared to analyze the effect of firing on the leaching capability of heavy metals. Moreover, the leachate results were compared to the solid industrial waste hazard categorization published by the EPA Victoria Industrial Waste Resource Guidelines [1] to determine the suitability of the fired clay bricks incorporating CBs.

MATERIALS AND METHODS

Characterization of Raw Materials

Clay material was supplied by PHG Bricks in Victoria. The particle size distribution (PSD) of the soil was determined using sieve analysis. According to the Unified soil classifications, the soil can be classified as sandy, silty clay (MC) [28]. The CBs were supplied by Buttout Australia Pty Ltd. The as-received CBs were firstly subjected to the pretreatment of drying in the oven at 105° for 24 h.

The chemical composition of the raw materials was determined by X-ray fluorescence (XRF). It can be seen in Fig. 1 that the main constituents of the brick soil were silicon dioxide and aluminum oxide. X-ray diffraction (XRD) was used to evaluate the crystalline phase. As can be seen in Fig. 2, quartz was the main phase of the raw material.

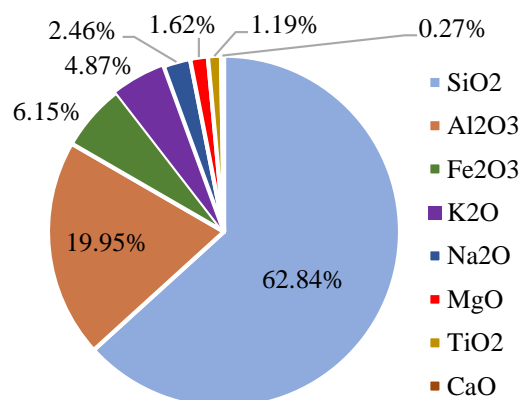


Fig. 1 Clay material chemical composition

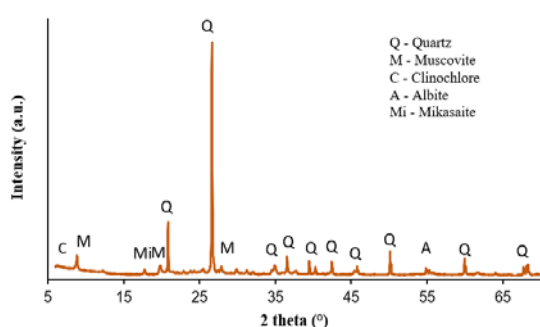


Fig. 2 XRD patterns of clay material

Preparation of Brick Samples

Selected mixtures containing 0.5%, 1%, 1.5% and 2% CBs by wt were prepared. The raw mixtures were mixed and homogenized by using a Hobart mechanical mixer for 25 min with a 15.5% water content. Cylindrical specimens were prepared using a compactor with a compaction pressure of 240 kPa and dried at 105° for 24 h. The green bricks were fired at 1050° for 3h. The firing step was carried out in an electrical furnace. The following technological properties of the fired clay bricks incorporating CBs

have been determined in accordance with the Australian Standards [29]: water absorption [30], initial rate of absorption (IRA) [31], shrinkage, compressive strength [32], efflorescence [33] and density [34].

Leachate Analysis

The ABLP was used to evaluate the leaching of heavy metals from the prepared brick samples. Heavy metals Chromium (Cr), Copper (Cu), Silver (Ag), Barium (Ba), Mercury (Hg), Selenium (Se), Nickel (Ni), Cadmium (Cd), Arsenic (As), Lead (Pb), and Zinc (Zn) were analyzed for green and fired clay bricks incorporating CBs. In following the ABLP, the brick samples were initially crushed and sieved using a 2.4 mm sieve. To simulate various environmental conditions and determine the correlation between the leachate and the pH solution, pH values 2.9, 5.0, and 9.2 were selected and prepared. The leachate samples were prepared based on a 1:20 ratio in screw-capped bottles. The samples were then placed in an agitator for 18 hr to be mixed and then filtered through a 0.45 microfilter. The filtered samples were analyzed using an ICP-MS for heavy metals.

RESULTS AND DISCUSSION

Properties of Brick Samples

Shrinkage is a critical concern. Samples with a higher content of CB waste, 2%, resulted in a significant decrease in both height and diametric shrinkage of 1.96% and 3.1%, respectively. This compared to controlled bricks with a height and diametric shrinkage rate of 3.07% and 4.64%, respectively.

The addition of CBs reduced the bulk density of the clay brick, and the values varied depending on the quantity of waste incorporated. Bulk density decreased from 2114.33 kg/m³ to 1971.8 kg/m³ with the addition of 1.5% CBs by wt. The addition of CBs has an effect on water absorption. Bricks incorporating 1% and 2% CBs by wt showed a water absorption rate of 12.1% and 13.1% compared to 9% for controlled clay bricks.

The results demonstrate that the controlled bricks have a higher strength capacity compared to the bricks incorporating CBs. The highest compressive strength was 48.64 MPa for bricks with 0% CBs and decreased to 28.34 MPa with the inclusion of 1.5% CBs by wt. The decrease in strength is associated with the loss of organic content in the CBs, which resulted in the formation of macropores and lowered the strength of the CB amended bricks.

Leachate Analysis of Fired Clay Bricks

Table 1 summarizes the results for heavy metals

for fired clay bricks incorporating 0%, 0.5%, 1%, 1.5% and 2% CBs using the ABLP method for pH 2.9, 5.0 and 9.2. As shown in Table 11, the metal concentrations of the leachate are trivial when compared to the regulatory threshold limits set by the Industrial Waste Resource Guidelines [1]. The results confirm that fired clay bricks incorporating 0%, 0.5%, 1%, 1.5%, and 2% CBs by wt. are categorized as non-hazardous waste for distinct pH values as they are less than the regulatory limits for heavy metals.

The results show that differences in pH over a wide range of precipitation affect the leaching behavior of metals in the fired clay bricks.

Generally, the increase in CB content in the brick resulted in a decrease in metal contamination for Zn, Ba, Cr, and Ni. Bricks incorporating CBs were more prone to leaching heavy metals in areas with highly acidic rain compared to the natural range of precipitation.

As shown in Fig. 3, a direct relationship between the pH and the metal concentration leachate was found for Zn, Cu, Ba and Ni. A decrease in pH from 9.2 to 2.9 resulted in an increase in the metal concentration leached for bricks incorporating 1% and 2% CBs by wt. Therefore we can confirm metals Zn, Cu, Ba, and Ni are more likely to leachate in areas with highly acidic rain compared to the natural scope of precipitation.

Table 1 Leachate results for heavy metals in crushed brick samples using the ICP-MS.

Heavy Metals	EPA Victoria solid waste thresholds ^a	Concentration Level (mg/L)														
		Percentages of CBs by mass														
		0%			0.5%			1%			1.5%			2%		
		pH	pH	pH	pH	pH	pH	pH	pH	pH	pH	pH	pH	pH	pH	pH
		2.9	5.0	9.2	2.9	5.0	9.2	2.9	5.0	9.2	2.9	5.0	9.2	2.9	5.0	9.2
Cr	2.5	0.004	0.014	0.009	0.005	0.015	0.007	0.028	0.013	0.056	0.007	0.012	0.009	0.011	0.016	0.016
Ni	1.0	0.007	0.044	0.004	0.010	0.043	0.003	0.056	0.041	0.025	0.008	0.039	0.003	0.203	0.043	0.010
Cu	100	1.559	0.523	0.035	1.536	0.557	0.043	1.134	0.543	0.053	1.496	0.480	0.042	0.860	0.499	0.035
Zn	150	1.792	0.628	0.104	1.909	0.645	0.140	2.291	0.406	0.267	1.867	0.335	0.045	2.251	0.543	0.222
As	0.35	0.005	0.010	0.003	0.011	0.011	0.005	0.004	0.014	0.006	0.044	0.038	0.015	0.005	0.015	0.001
Se	0.5	-	0.002	-	0.002	0.002	-	0.013	0.002	0.003	0.003	0.003	0.002	0.015	0.003	-
Ag	5.0	-	0.001	-	-	0.009	-	-	-	-	-	-	-	-	0.001	-
Cd	0.1	0.001	0.001	-	-	0.001	-	-	0.001	-	-	-	-	-	0.001	-
Ba	35.0	1.450	1.648	1.447	1.473	1.770	1.100	3.708	1.481	2.279	1.530	1.044	1.312	2.747	2.098	1.032
Hg	0.05	-	-	-	-	-	-	-	-	-	-	-	-	-	-	-
Pb	0.5	0.012	0.010	0.001	0.005	0.008	0.001	0.050	0.006	0.006	0.003	0.007	0.001	0.011	0.010	0.002

^a Industrial Waste Resource Guidelines [1]

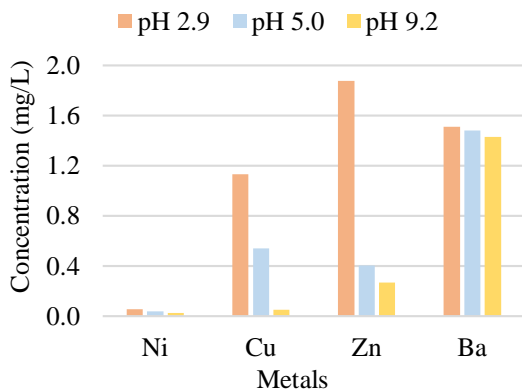


Fig. 3 Relationship observed between pH value and metal concentrations leached from 1% CB bricks.

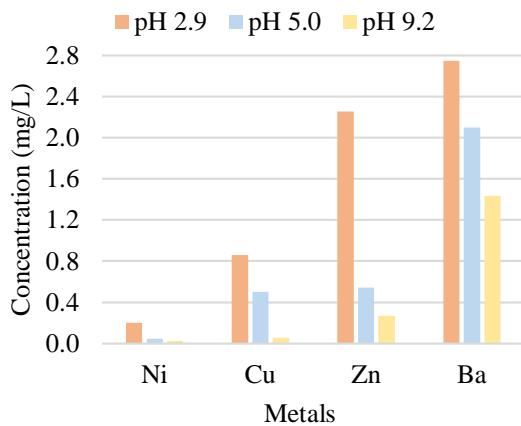


Fig. 4 Relationship observed between pH value and metal concentrations leached from 2% CB bricks.

Green Bricks and Fired Bricks Comparative Analysis

To investigate the disparities between the metal concentration leachate before and after firing of 0%, 0.5%, 1%, 1.5%, and 2% CB brick samples, pH 9.2 was selected (Figs. 7 – 8). It was found after the firing process of bricks, the leachate concentrations were notably lower. This is generally due to the sintering process which confined the metals within the brick structure during the high temperatures.

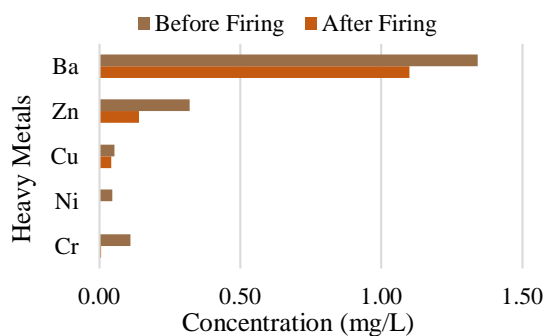


Fig. 5 Heavy metal concentration of 0.5% CB

content bricks before and after firing.

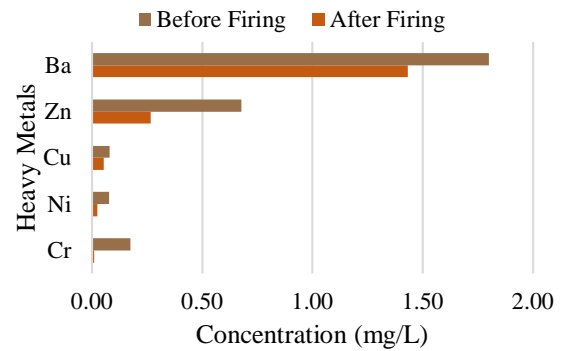


Fig. 6 Heavy metal concentration of 1% CB content bricks before and after firing.

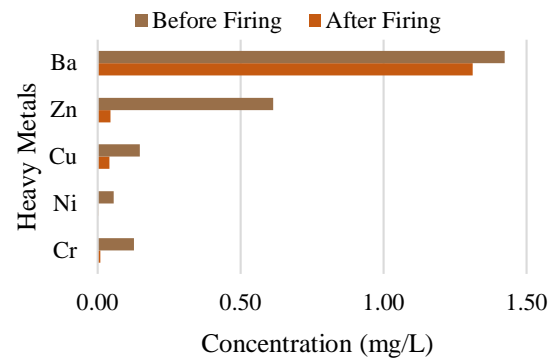


Fig. 7 Heavy metal concentration of 1.5% CB content bricks before and after firing.

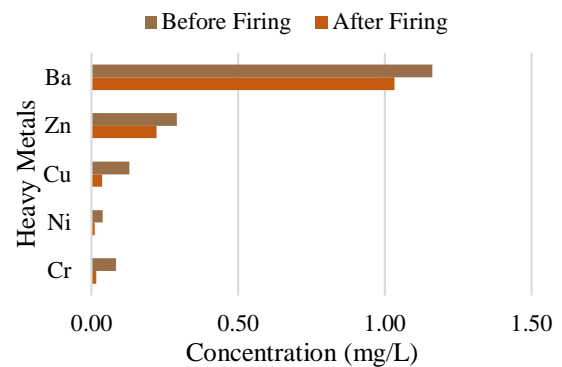


Fig. 8 Heavy metal concentration of 2% CB content bricks before and after firing.

In addition the leaching percentage drop was determined for 0.5%, 1%, 1.5%, and 2% CB brick samples. It was found Ni and Cr achieved a 95% and 93% drop in leachate concentration for bricks incorporating 1.5% CB content. While bricks incorporating 0.5% and 1% CBs by wt. achieved a leaching drop of 56% and 61% for Zn. In general, over 50% of all tested heavy metals were immobilized after firing for 0.5%, 1%, 1.5%, and 2% CB bricks compared to green bricks. Incorporating

CBs in fired clay bricks resulted in a decrease in the metal contamination of the toxic waste, which can be an environmental advantage compared to the littering of CBs.

CONCLUSION

In conclusion, the incorporation of CBs in fired clay bricks offers a sustainable and environmentally friendly solution to a growing pollution issue. Concerns regarding the possible leachate of heavy metals from bricks recycled with CBs during the use and disposal of the construction material are clarified with encouraging results.

The compressive strength of CB brick samples was greatly dependent on the percentage of organic content in the brick mixtures. However, they were considerably above the minimum compressive strength requirement of 17.2 MPa. The addition of CBs delivered less dense and porous bricks, with improved thermal insulation properties. The water absorption and IRA results were within the acceptable range, and the CB brick manufactured samples indicated they were capable of withstanding adequate weather conditions.

The leachate results for fired clay bricks incorporating 0%, 0.5%, 1%, 1.5%, and 2% CBs by mass were found to be below the regulatory limits set by the EPA Victoria solid industrial waste guidelines. Therefore, bricks modified with CBs can be categorized as non-hazardous waste. The leaching of Cr and Ni was almost completely hindered after the firing process of clay bricks incorporating 0.5% and 1.5% CBs by mass. In addition, more than 50% of all the tested heavy metals were immobilized after firing for 0.5%, 1%, 1.5%, and 2% CBs by mass bricks. Hence the addition of CBs in fired clay bricks may be a feasible option to hinder the heavy metals present in CBs.

REFERENCES

- [1] Industrial Waste Resource Guidelines. Solid Industrial Waste Hazard Categorization and Management, E.P.A. Victoria, 2009. Viewed April 12, 2018, <file:///C:/Users/s3432918/Downloads/IWRG631.pdf>.
- [2] Heaton, C.G., Michael Cummings, K., O'Connor, R.J., and Novotny, T.E. Butt really? The environmental impact of cigarettes, *Tobacco Control*. 2011, 20(1).
- [3] Kurmus, H. and Mohajerani, A. The toxicity and valorization options of cigarette butts, *Waste Management*. 2020, 104, 104-118.
- [4] Dobaradaran, S., Schmidt, T.C., Lorenzo-Parodi, N., Jochmann, M.A., Nabipour, I., Raeisi, A., Stojanović, N., and Mahmoodi, M. Cigarette butts: An overlooked source of PAHs in the environment?, *Environmental pollution*. 2019, 249, 932-939.
- [5] Novotny, T.E., Lum, K., Smith, E., Wang, V., and Barnes, R. Cigarettes butts and the case for an environmental policy on hazardous cigarette waste, *International journal of environmental research and public health*. 2009, 6(5), 1691-1705.
- [6] Lee, W. and Lee, C.C. Developmental toxicity of cigarette butts—An underdeveloped issue, *Ecotoxicology and environmental safety*. 2015, 113, 362-368.
- [7] Micevska, T., Warne, M.S.J., Pablo, F., and Patra, R. Variation in, and causes of, toxicity of cigarette butts to a cladoceran and microtox, *Archives of Environmental Contamination and Toxicology*. 2006, 50(2), 205-212.
- [8] Kazi, T., Jalbani, N., Arain, M., Jamali, M., Afridi, H., Sarfraz, R., and Shah, A. Toxic metals distribution in different components of Pakistani and imported cigarettes by electrothermal atomic absorption spectrometer, *Journal of hazardous materials*. 2009, 163(1), 302-307.
- [9] Ifelebuegu, A., Lale, E., Mbanaso, F., and Theophilus, S. Facile Fabrication of Recyclable, Superhydrophobic, and Oleophilic Sorbent from Waste Cigarette Filters for the Sequestration of Oil Pollutants from an Aqueous Environment, *Processes*. 2018, 6(9), 140.
- [10] Behera, S.N., Xian, H., and Balasubramanian, R. Human health risk associated with exposure to toxic elements in mainstream and sidestream cigarette smoke, *Science of the total Environment*. 2014, 472, 947-956.
- [11] Mohajerani, A., Kadir, A.A., and Larobina, L. A practical proposal for solving the world's cigarette butt problem: Recycling in fired clay bricks, *Waste management*. 2016, 52, 228-244.
- [12] Kadir, A.A. and Mohajerani, A. Recycling cigarette butts in lightweight fired clay bricks, *Proceedings of the Institution of Civil Engineers-Construction Materials*. 2011, 164(5), 219-229.
- [13] Kadir, A.A. and Mohajerani, A. Possible utilization of cigarette butts in light-weight fired clay bricks, *International Journal of Civil and Environmental Engineering*. 2008, 2(9), 137-141.
- [14] Kurmus, H. and Mohajerani, A. A continuation study on recycling cigarette butts in fired clay bricks, paper presented to WEC2019: World Engineers Convention 2019, 2019.
- [15] Kurmus, H. and Mohajerani, A. Recycling of Cigarette Butts in Fired Clay Bricks: A New Laboratory Investigation, *Materials*. 2020, 13(3), 790.
- [16] Abdul Kadir, A. and Mohajerani, A. Physico-mechanical properties and leachate analysis of

- clay fired bricks incorporated with cigarette butts, 2008.
- [17] Mohajerani, A., Tanriverdi, Y., Nguyen, B.T., Wong, K.K., Dissanayake, H.N., Johnson, L., Whitfield, D., Thomson, G., Alqattan, E., and Rezaei, A. Physico-mechanical properties of asphalt concrete incorporated with encapsulated cigarette butts, *Construction and Building Materials*. 2017, 153, 69-80.
 - [18] Rahman, M.T., Mohajerani, A., and Giustozzi, F. Possible Recycling of Cigarette Butts as Fiber Modifier in Bitumen for Asphalt Concrete, *Materials*. 2020, 13(3), 734.
 - [19] Rahman, M.T., Mohajerani, A., and Giustozzi, F. Published. Recycling cigarette butts in bitumen for flexible pavements, in WEC2019: World Engineers Convention 2019, 2019, Engineers Australia. p. 701.
 - [20] Teixeira, M.B.d.H., Duarte, M.A.B., Garcez, L.R., Rubim, J.C., Gatti, T.H., and Suarez, P.A.Z. Process development for cigarette butts recycling into cellulose pulp, *Waste Management*. 2017, 60, 140-150.
 - [21] Zhao, J., Zhang, N., Qu, C., Wu, X., Zhang, J., and Zhang, X. Cigarette butts and their application in corrosion inhibition for N80 steel at 90 °C in a hydrochloric acid solution, *Industrial & Engineering Chemistry Research*. 2010a, 49(8), 3986-3991.
 - [22] Zhao, J., Zhang, N., Qu, C., Zhang, J., and Zhang, X. Comparison of the Corrosion Inhibitive Effect of Anaerobic and Aerobic Cigarette Butts Water Extracts on N80 Steel at 90° C in Hydrochloric Acid Solution, *Industrial & Engineering Chemistry Research*. 2010b, 49(24), 12452-12460.
 - [23] Escobar, V.G. and Maderuelo-Sanz, R. Acoustical performance of samples prepared with cigarette butts, *Applied Acoustics*. 2017, 125, 166-172.
 - [24] Maderuelo-Sanz, R., Escobar, V.G., and Meneses-Rodríguez, J.M. Potential use of cigarette filters as sound porous absorber, *Applied Acoustics*. 2018, 129, 86-91.
 - [25] Sabzali, A., Nikaeen, M., and Bina, B. Performance evaluation of cigarette filter rods as a biofilm carrier in an anaerobic moving bed biofilm reactor, *Environmental technology*. 2012, 33(15), 1803-1810.
 - [26] Sabzali, A., Nikaeen, M., and Bina, B. Evaluation of cigarette filters rods as a biofilm carrier in integrated fixed film activated sludge process, *World Academy of Science, Engineering and Technology*. 2011, 5, 82-87.
 - [27] Standards Australia 2019. Wastes, sediments and contaminated soils. Part 3: Preparation of Leachates-Bottle Leaching Procedure (AS4439.3). SAI Global Limited.
 - [28] Standards Australia 2009. Methods for Testing Soils for Engineering Purposes. Soil Classification tests - Determination of the particle size distribution of a soil - Standard method of analysis by sieving (AS1289.3.6.1). SAI Global Limited.
 - [29] Standards Australia 2003. Masonary Units and Segmental Pavers and Flags - Methods of Test - Sampling for Test (AS1289.5.5.1). SAI Global Limited.
 - [30] Standards Australia 2003. Masonry units and segmental pavers and flags - Methods of test - Determining water absorption properties (AS/NZS 4456.14), SAI Global Limited.
 - [31] Standards Australia 2003. Masonry units and segmental pavers and flags - Methods of test - Determining initial rate of absorption (AS/NZS 4456.17), SAI Global Limited.
 - [32] Standards Australia 2003. Masonry units and segmental pavers and flags - Methods of test - Determining compressive strength of masonry units (AS/NZS 4456.4), SAI Global Limited.
 - [33] Standards Australia 2003. Masonry units and segmental pavers and flags. Methods of test - Determining potential to effloresce (AS4456.6). SAI Global Limited.
 - [34] Standards Australia 2003. Masonry units and segmental pavers and flags - Methods of test - Determining moisture content, dry density and ambient density (AS/NZS 4456.4), SAI Global Limited.

EFFECT OF FINES CONTENT ON LIQUEFACTION CHARACTERISTICS

Wen LIU¹, Shoji KAMAO² and Kei YOKOYAMA¹

¹Graduate Student, Department of Civil Engineering, Nihon University, JAPAN

²Associate Professor, Department of Civil Engineering, Nihon University, JAPAN

ABSTRACT

The 1995 Hanshin Earthquake confirmed that soil containing fine fraction would be liquefied. In many cases, the effect of fine fraction on liquefaction strength has not been clarified yet. In particular, it is not so many researches that have used samples containing a large amount of fine fraction, although the fine fraction presents the predomination in its field. Therefore, the purpose is to clarify the effect of fine fraction on the liquefaction strength of sand clay within the parameters of the skeleton void ratio. The fine fraction content of the specimens has a distinct span from small to large. The coarse-grained soil used Toyoura sand which was mixed with 0~40% Kaolin clay in a dry state. The specimens (D=50mm H=100mm) are made by using the dry tamping method. These specimens were used to do the undrained cyclic triaxial test. The results of the tests show that when the skeleton void ratio does not exceed the maximum void ratio of sand, the fine fraction does not affect liquefaction strength regardless of its type. And the liquefaction strength of the specimen has a certain relationship with the skeleton void ratio. When the skeleton void ratio exceeds the maximum void ratio of sand, the fine fraction is in the remarkable position. And the liquefaction strength has a good correlation with the fine fraction void ratio.

Key words: liquefaction strength, fines content, undrained cyclic test, sand clay

INTRODUCTION

The main grounds where seismic liquefaction events occur are generally recognized as loosely deposited, saturated sand grounds. However, liquefaction of fine fraction has been confirmed by the 1995 Hanshin Earthquake^[1] and the 2011 Great East Japan Earthquake, which caused severe liquefaction of reclaimed land in the Tokyo Bay area from Shinkiba to Urayasu. And the researches have been carried out to clarify the liquefaction mechanism of fine fraction and its effects on liquefaction strength. As a result of these studies, it was found that (1) The liquefaction strength decreases with the increase of fine fraction content, and there is a fine fraction content with the lowest liquefaction strength^[2]. (2) There is a good correlation between the skeleton void ratio and the liquefaction strength, where a part of the fine grain content is considered as a void^{[3],[4]}. However, there is no unified view on the effect of fine fraction of liquefaction strength, due to different methods of density control and specimen preparation among researchers. In particular, few studies have been conducted on samples that contain a large amount of fine fraction up to the region where fine fraction are dominant. And the effect of fine fraction on liquefaction strength in the region where fine fraction are dominant has not been clarified.

The purpose of this study is to clarify the effect of fines content on liquefaction characteristics by performing undrained cyclic triaxial tests on specimens with the same method from small to large fines content. In this study, the skeleton void ratio e_s ^[5] is defined as the void ratio of all the fine grains in the sand as pore space. The skeleton void ratio e_f is defined as the porosity of clay only, assuming that the silt content is part of the skeletal structure. The void ratio e_{ff} is the void ratio that ignores the volume of the coarse grains and focuses only on the fine grains. It is an indicator of the degree of grain blockage.

EXPERIMENT OVERVIEW

In this study, undrained cyclic triaxial tests were carried out to determine the liquefaction strength of each sample. An overview of the experiment is given below

Sample

For the all samples, Toyoura sand was used as the coarse-grained material and Kaolin clay was used as the fine fraction material. And the mixing ratio (percentage of dry mass of fine fraction material to total dry mass) was varied by 5% in the range of 0~40%. In order to examine the effect of the difference in the properties of the fine fraction,

Fujinomori clay was also used. And the sample of Fujinomori clay with a mixing ratio of 5~15% was used. Each soil mixture shall be referred to as K5 or F10, depending on the initials of the names of the fine fractions and the proportion of the mixture. Each mixed soil was prepared by mixing each sample in an air-dried state until it became homogeneous in a container. The main physical properties and particle size distributions of each sample are shown in Table 1 and Fig. 1.

As shown in Table 1, Kaolin clay and Fujinomori clay are both low plasticity clays, but as shown in the clay content, Fujinomori clay contains more silt than Kaolin clay.

Table 1 Physical properties of the sample

Sample	Soil particle density	Plasticity index	Fine particle fraction content	Clay fraction content	Mean diameter
	ρ_s (g/cm ³)	I_p	FC (%)	CC (%)	D_{50} (mm)
Toyouura	2.640	NP	0	0	0.161
Kaolin	2.714	13.7	100	64	0.003
Fujinomori	2.535	20.4	92	37	0.009

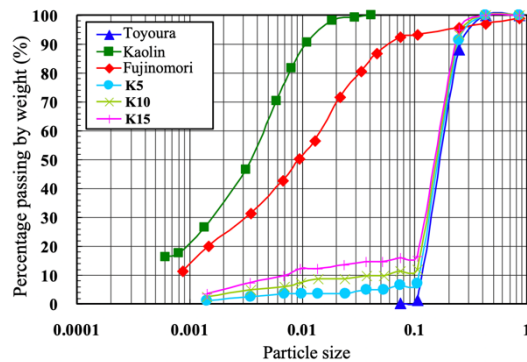


Fig. 1 Particle size distribution curves the sample

Experimental Method

The specimen is a cylindrical sample of 5 cm in diameter and 10 cm in height. The specimens were divided into ten equal parts and then divided into ten layers, each layer of which was solidified with a rammer. After the specimens were prepared at a predetermined density, the specimens were first allowed to stand on their own at a constraint pressure of 20 kPa, and then saturated by applying 200 kPa of back pressure with de-aired water, which is about three times the volume of the specimens. Subsequently, consolidation was performed with effective constraint pressure $\sigma'_c=100$ kPa. The consolidation time was set as shown in Table 2 for each sample, taking into account that the consolidation could be completed sufficiently. After the consolidation was completed, the B-value was measured to confirm the saturation, and the back pressure was further applied to make

the B-value more than 0.95. After confirming that the B-value was more than 0.95, the material was repeatedly loaded with a sinusoidal wave of 0.1 Hz frequency at the prescribed cyclic stress ratio $R(=\sigma_d/2\sigma'_c)$. The test conditions for each sample are shown in Table 2.

Table 2 Test conditions for cyclic triaxial tests

Sample	Density () indicates D_r (%)	Initial void ratio e_0	Consolidation time t (hour)	Cyclic stress ratio $R(=\sigma_d/2\sigma'_c)$
Toyouura	Loose (40)	0.828	0.5	0.12, 0.13, 0.15
	Medium (60)	0.757	0.5	0.16, 0.17, 0.18
	Dense (80)	0.687	0.5	0.21, 0.22, 0.24
K5	Loose	0.828	1	0.09, 0.10, 0.14
	Medium	0.757	1	0.12, 0.14, 0.16
	Dense	0.687	1	0.15, 0.17, 0.18
K10	Loose	0.828	5	0.08, 0.10, 0.12
	Medium	0.757	5	0.08, 0.10, 0.12
	Dense	0.687	5	0.10, 0.11, 0.12
K15	Loose	0.828	12	0.08, 0.10, 0.12
	Medium	0.757	12	0.08, 0.10
K20	Medium	0.757	24	0.07, 0.08, 0.09
K25	Medium	0.757	24	0.08, 0.09
K30	Medium	0.757	24	0.10, 0.12, 0.15
K35	Loose	0.828	24	0.08, 0.09
	Medium	0.757	24	0.09, 0.11, 0.13
K40	Loose	0.828	24	0.09, 0.13
	Medium	0.757	24	0.11, 0.13, 0.15
F5	Medium	0.757	4	0.10, 0.11, 0.12
F10	Medium	0.757	12	0.10, 0.11, 0.12
F15	Medium	0.757	20	0.10, 0.11, 0.12

*The Confining pressure of Consolidation is 100 kPa

*The load repeats with a sinusoidal wave of 0.1 Hz frequency at the specified cyclic stress ratio

Density Management Method

In liquefaction studies, the relative density D_r is often used as a parameter to express the density of specimens, and the density is also controlled by the relative density D_r in studies with samples containing fine fraction. However, the applicable scope of the "Minimum and Maximum Density Test of Sand (JIS A 1224)" for calculating the relative density is defined as the sand that remains more than 95% in a 75 μ m sieve. And it is difficult and inappropriate to control the density by using the relative density for a sample containing many fine fraction such as the one used in this study.

Therefore, the minimum and maximum densities of Toyoura sand ($\rho_{dmin}=1.341$ g/cm³ and $\rho_{dmax}=1.633$ g/cm³) were used for liquefaction tests by using only Toyoura sand in this study. In order to consider the effect of density change, the relative density D_r was adjusted to be 40%(Loose), 60%(Medium), and 80%(Density). And the void ratio e_0 was adjusted to 0.828(Loose), 0.757(Medium), and 0.684(Density) to be the same value as the void ratio e_0 when the density was adjusted by using Toyoura sand only, then the effect of density change was considered.

EXPERIMENT RESULTS

Liquefaction Strength Curve

Figure 2(a)~(c) shows the liquefaction test results for each sample. It shows the relationship between the cyclic stress ratio R and the number of cycles N required to reach both amplitude axial strains $DA=5\%$. Fig. 2(a) shows the cyclic strength curves for the liquefaction test by using Toyoura sand only and for the cyclic triaxial test using Fujinomori mixed soil with a constant density and varying only the fines content. As the density of Toyoura sand increases, the cyclic stress ratio at a certain number of loading cycles increases, and the curve moves upward, indicating that the resistance to liquefaction becomes stronger. In addition, Dense shows a tendency for the curves that are commonly found in dense sands to rise.

Besides, the cyclic strength curve of Fujinomori mixed soil moved to the bottom as the fines content increased, indicating that the soil's resistance to liquefaction became weaker. Fig. 2(b) shows the cyclic strength curves for K5 to K15 with varying densities; as for K5, the curve moves upward with increasing density, as in the case of Toyoura sand, but it becomes weaker as the content of K10, K15 and Kaolin clay increases. For the same densities, the cyclic strength curve is located at the bottom of the curve as the fines content increases. Fig. 2(c) shows the cyclic strength curves for the cyclic triaxial tests using from K20 to K40.

It was found that the curve was located upward for samples with higher fines content, and the resistance to liquefaction was higher.

Relationship Between Fine Particle Fraction Content And Liquefaction Strength

In this study, the cyclic shear stress R was used as "liquefaction strength R_{20} " to indicate the resistance to liquefaction when both amplitudes of strain $DA=5\%$ were reached at 20 times of cyclic loading (shown as dashed line in Fig.2). Fig. 3 shows the relationship between the liquefaction strength R_{20} and the fines content FC calculated from the cyclic strength curve for each sample. The fines content FC in the figure is equal to the ratio of fines content in the Kaolin mixed soil, but is slightly smaller than the ratio of fines content in the Fujinomori mixed soil. The reason is that a small amount of sand is contained in the Fujinomori clay. The figure shows that the liquefaction strength of the Kaolin mixed soil, Medium, decreases with the increase in the fines content, and then increases after the lowest liquefaction strength R_{20} , is found at $FC=20\%$. In the range of $FC=0\sim15\%$, the liquefaction strength R_{20} increased with rising

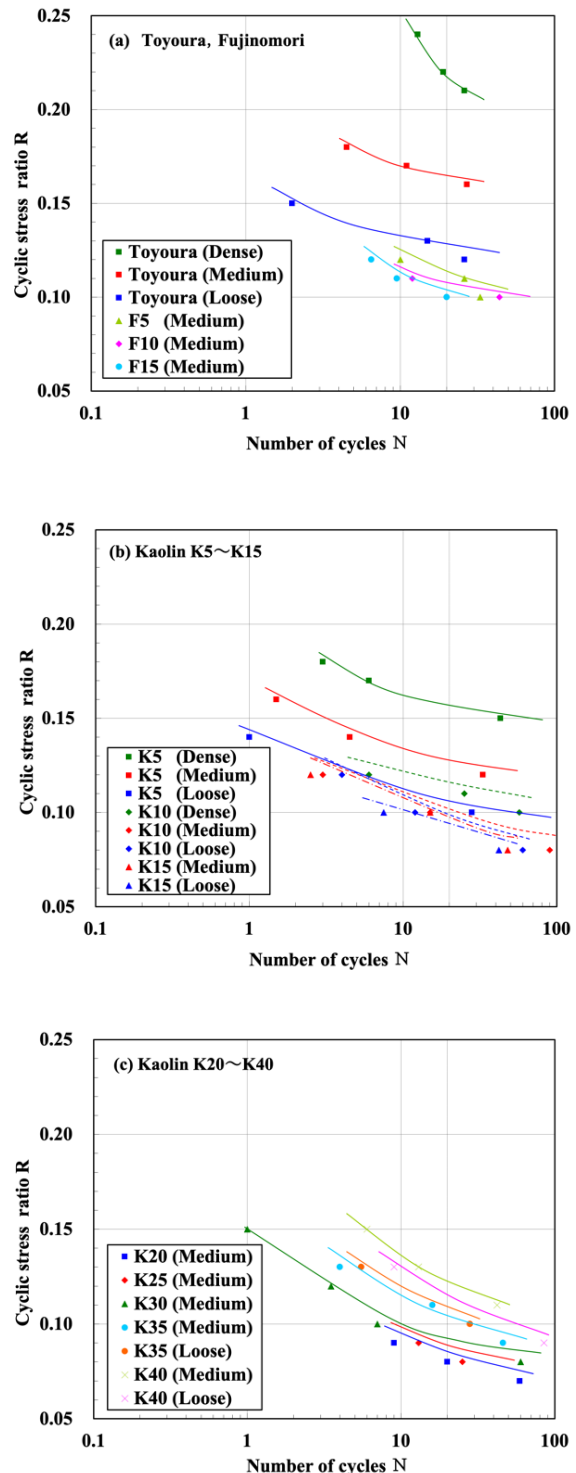


Fig. 2 Cyclic strength for each sample

density in all the samples, but the growth in liquefaction strength R_{20} became smaller with increasing fines content, and the liquefaction strength R_{20} in K15 was almost the same for Loose and Medium. The liquefaction strength of R_{20} decreased due to an increase in the fraction of fine

fraction in the soil, although it was slightly different from that of Kaolin mixed soil.

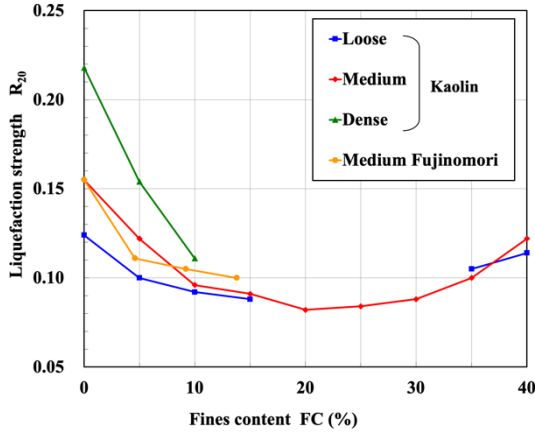


Fig. 3 Effect of fines content on liquefaction strength R_{20}

Relationship Between Various Void Ratios and Fine Particle Content

When investigating the strength of a soil with a grain size intermediate between sand and clay, such as the sample used in this study, it is very important to pay attention to the skeletal structure of the soil.

Therefore, in this study, with the void ratio e , the effect of fine fraction on liquefaction properties was considered using "Skeleton void ratio e_s , e_f "^[4] and "Fine fraction void ratio e_{ff} "^[6]. The skeletal void ratio e_s is the void ratio when all fine fractions are considered as pores, while the skeletal void ratio e_f is the void ratio when only clay is considered as a void, it was assumed that the silt content contributes to the skeletal structure. The fine fraction void ratio e_{ff} is a void ratio that ignores the volume of coarse-grains and focuses only on the fine fraction, which is an indicator of how well the fine fraction is plugged. The void ratios can be obtained by the following Eq. (1)~(3) using the symbols shown in Fig. 4.

$$\text{Skeleton void ratio } e_s = \frac{V_{v(sand)}}{V_{s(sand)}} \quad (1)$$

$$\text{Skeleton void ratio } e_f = \frac{V_{v(sand)} - V_{s(silt)}}{V_{s(sand)} + V_{s(silt)}} \quad (2)$$

$$\text{Fine fraction void ratio } e_{ff} = \frac{V_v}{V_{s(clay)} + V_{s(silt)}} \quad (3)$$

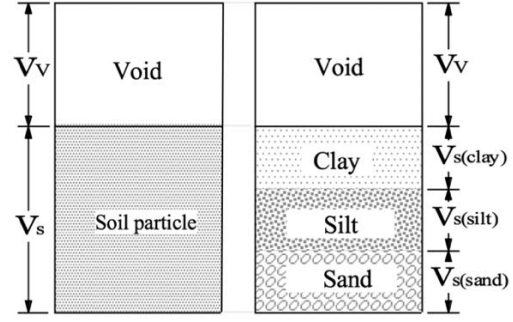


Fig. 4 Schematic of mixed samples

The changes in void ratio e , skeleton void ratio e_s and e_f , and fine fraction void ratio e_{ff} with increasing fine fraction content in Medium of Kaolin mixed soils are shown in Fig. 5. The void ratios in the figure are values immediately before the cyclic loading process, and are calculated from the initial void ratio e_0 of the specimen, the axial displacement until the consolidation process, and the consolidated drainage amount. From the figure, the void ratio e is smaller than the initial void ratio e_0 (dashed line in the figure) in the range of $FC=0\sim 25\%$. It decreased with the increase in fine fraction content. This may be due to the fact that the fine fraction content in the specimens made in the dry state shrinks due to the pore water and the volume compression increases with the increase of the fine fraction content.

Like the void ratio e , the void ratio of fine fraction, e_{ff} , also tends to decrease with the increase in the content of fine fraction same as the void ratio e . The void ratio decreases sharply in the region with lower content of fine fraction, and then gradually decreases, ascending to the void ratio of Kaolin clay when it is compacted at 100kPa (single dotted line in the figure).

On the other hand, the void ratio of both skeletons is increasing due to the growth of fine fraction content. The void ratio of both skeletons tends to increase rapidly from around $FC=25\%$, suggesting a structural change. The skeletal void ratio e_s exceeds the maximum void ratio of Toyoura sand only (the two-dotted line in the figure) at around $FC=15\%$. From this, it is considered that before $FC=15\%$, sand particles form a skeleton, and fine fraction have a skeleton structure that enters the gap formed by sand particles. while after $FC=15\%$, it is thought that fine fraction form a skeleton between sand particles or that sand particles are floating in the fine fraction.

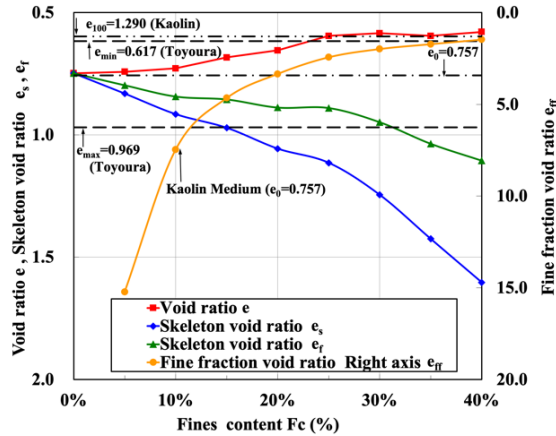


Fig. 5 Relationship between fines content and various void ratios

Relationship Between Various Void Ratios And Liquefaction Strength

The relationship between the void ratio e and the liquefaction strength R_{20} is shown in Fig. 6. In the figure, it can be seen that the volume compression tends to increase with a looser initial void ratio. And that liquefaction strength, R_{20} , decreases and then increases with an augmentation in the fine fraction content. However, there is no direct relationship between the void ratio e and the liquefaction strength R_{20} , since the liquefaction strength varies greatly depending on the sample even at the same void ratio.

Figures 3 and 5 show that the relationship between the void ratio and the liquefaction strength R_{20} decreases in the range of $FC=0\sim20\%$, even though the density rises with increasing void ratio e . This suggests that the decrease in liquefaction strength R_{20} in the range of $FC=0\sim20\%$ is due to the increase in the skeleton void ratio, and the skeleton void ratio may have a strong influence on the liquefaction strength. The relationship between the skeleton void ratio e_s and e_f and the liquefaction strength R_{20} of each sample with $FC = 0\sim20\%$ is shown in Fig. 7. The liquefaction strength of both skeleton void ratio decreased with the increase in the skeleton void ratio. However, the liquefaction strength R_{20} varies in the small void ratio e_r , whereas the liquefaction strength e_s lies on the same curve in all the void ratios, regardless of whether the soil is mixed with Kaolin or Fujinomiri, and it can be said that the void ratio e_s and the liquefaction strength R_{20} are categorically related. It is found that in the range of $FC=0\sim15\%$, the skeletal structure of the soil is formed by sand, and the fine fraction content has no effect on the liquefaction strength, the liquefaction strength R_{20} is determined by the skeleton void ratio e_s .

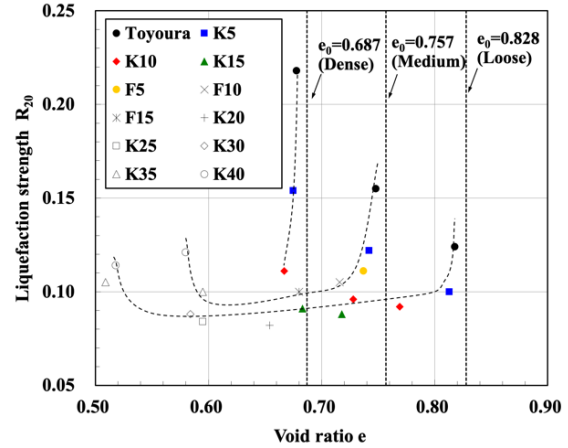


Fig. 6 Relationship between void ratio e and liquefaction strength R_{20}

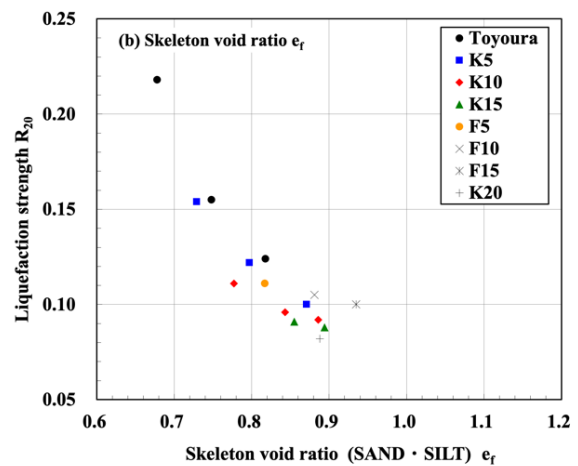
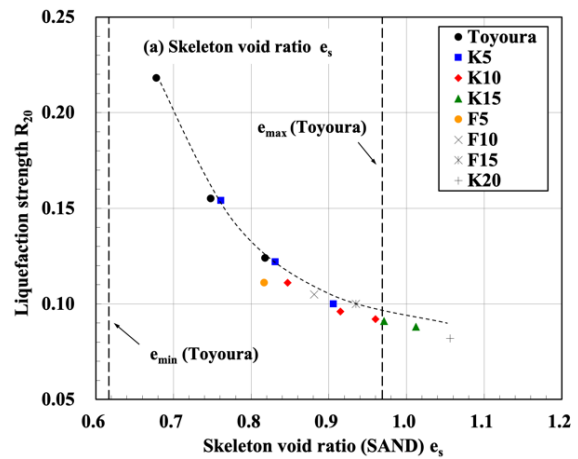


Fig. 7 Relationship between Skeleton void ratio e_s , e_f and Liquefaction Strength R_{20}

Furthermore, from Figs 3 and 5, the skeletal gap ratio e_s increases rapidly at $FC=25\%$ and since the liquefaction strength R_{20} has also begun to increase, in the skeletal structure of soil, fine fraction cannot fit in the gaps of sand, it is considered that the sand is in a state of floating in the fine fraction and has a skeletal structure with properties similar to those of cohesive soil.

Therefore, it is presumed that the liquefaction strength depends on the state of the fine fraction. It is considered to be closely related to the fine fraction void ratio e_{ff} . The relationship between the fine fraction void ratio e_{ff} and the liquefaction strength R_{20} is shown in Fig. 8. The liquefaction strength R_{20} of K100 (Kaolin clay only) in the figure is taken from the study by Kuwano [2]. It is the same as the one in the previous article. In Fig. 8, the liquefaction strength R_{20} is almost the same regardless of the fine fraction content and density, at $FC=30\%$ the liquefaction strength R_{20} increases rapidly. From this, it can be said that $FC=30-40\%$ sand particles floats in the fine fraction, and the liquefaction strength R_{20} has a good correlation with the fine fraction void ratio e_{ff} . In the case of $FC=15-30\%$, the skeleton void ratio e_s exceeds the maximum void ratio e_{max} of Toyoura sand, but there was no increase in the liquefaction strength observed after $FC=30\%$. In the range, it is possible to judge it as an intermediate region between the region where sand particles forms the skeleton and the region where fine fraction is predominant.

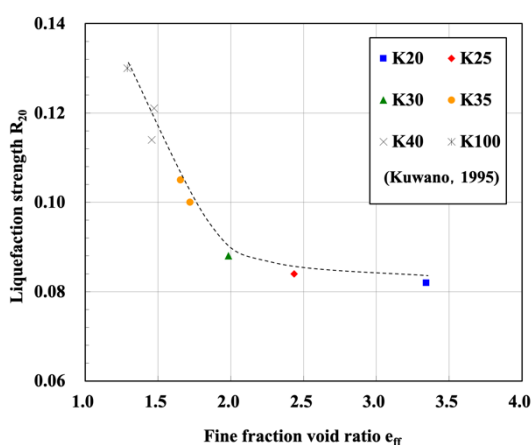


Fig. 8 Relationship between Fine fraction void ratio e_{ff} and liquefaction strength R_{20}

CONCLUSION

In this study, the effect of fine fraction content on liquefaction characteristics was investigated by undrained cyclic triaxial test by using a mixture of samples with a constant void ratio e and varying FC in the range of 0~40%. As a result, the following findings were obtained.

- (1) In the region with a skeletal void ratio e_s that does not exceed the maximum void ratio of sand only ($e_s < e_{max}$), the fine fraction makes no difference to the liquefaction strength. And the liquefaction strength R_{20} is categorically related to the "Skeleton void ratio e_s ", notwithstanding the type of fine fraction.
- (2) With a skeleton void ratio e_s above the maximum void ratio for sand only ($e_s > e_{max}$), the liquefaction strength R_{20} has a good correlation with the "Fine fraction void ratio e_{ff} " in the region where the fine fraction is predominant.
- (3) An intermediate region exists between these two regions, and the liquefaction strength R_{20} is approximately equal to the liquefaction strength R_{20} when the skeleton void ratio e_s is total up to the maximum void ratio of sand only.

REFERENCES

- [1] Kazama M., Kagatani T., Yanagisawa E., Peculiarities of liquefaction resistance of masado, Journal of JSCE No.645/III-50 pp153-160, 2000. (In Japanese only)
- [2] Kuwano J., Iimura H., Nakazawa H., Sugihara K., Liquefaction strength of sand containing kaolin clay, 50th JSCE Annual meeting, pp.506-507, 1995. (In Japanese only)
- [3] Ishikawa S., Masayuki H., Ikuko S., Rolando O., Nakata Y., Norimasa Y., Cyclic shear properties of non-plastic low plastic fine fraction mixed soil, 42nd JGS Annual meeting, pp.158-159, 2007. (In Japanese only)
- [4] Nabeshima Y., Nagasaw T., Tamotsu M., Evaluation of liquefaction strength of sands containing fines based on clay fraction, 38th JGS Annual meeting, pp.239-240, 2003. (In Japanese only)
- [5] Thevanayagam S., Shenthan T., Mohan S., Liang J., Undrained fragility of clean sands, silty sands, and sandy silts, Journal of geotechnical and geoenvironmental engineering 128 (10), pp.849-859, 2002.
- [6] Sato M., Oda M., Kazama H., Ozeki K., Fundamental study on the effect of fines on liquefaction strength of reclaimed ground, Journal of JSCE No.561/III-38, pp.271-282, 1997. (In Japanese only)

STUDY ON ROTATION ANGLE ESTIMATION METHOD OF UPLIFT FOUNDATION CONSIDERING PLASTICITY REGION

Yasuhide Mochida¹ and Makoto Minemoto²

¹ Prof. Ritsumeikan University, Japan

² Graduate School of Science and Engineering, Ritsumeikan University, Japan

ABSTRACT

Seismic stability calculation on the direct foundation of continuation is designed always and by the seismic intensity method (level 1 ground motion), and it is not necessary to check horizontal load bearing capacity method (level 2 ground motion). On the other hand, it is thought that a reasonable design method for a direct foundation during a large-scale earthquake can be established by appropriately evaluating the non-linear behavior caused by the floating of the end of the direct foundation. Therefore, a method for estimating the rotation angle of a floating foundation considering nonlinear behavior during a large-scale earthquake was proposed. At this time, as the evaluation at the time of plasticization, a uniform contact pressure was generated by a linear function. However, finite element method (FEM) analysis and previous experiments have confirmed that a high contact pressure is generated directly at the compression end of the foundation. In this study, we improve the idea that the slope of the contact pressure is uniform, and propose an evaluation formula that considers that a high contact pressure occurs at the compression end side. By improving the evaluation formula, the state of the contact pressure can be made closer to the actual condition of foundation, and it is possible to realize an evaluation closer to an experiment.

Keywords: Four or five keywords (First characters of each keyword are in uppercase letters), Italic

INTRODUCTION

It's said to be the one which doesn't need always to come about stable calculation at the time of an earthquake in present spread foundation, design by seismic intensity method (level 1 earthquake motion) and verify a ultimate lateral strength way (level 2 earthquake motion) at the time of an earthquake. This is because an energy absorption could expect a basic edge by going up because there was a margin to the load bearing capacity of the foundation because spread foundation was generally supported in the good ground, and I could think excessive damage didn't occur to foundation. On the other hand, it's able to establish a rational design way in the time of a large-scale earthquake of the spread foundation to estimate nonlinear behavior by an edge's of such spread foundation going up uplift appropriately. A rotation angle estimation method of the uplift foundation which considered nonlinear behavior in the time of a large-scale earthquake is proposed by the past study.

But the situation that the high ground pressure which isn't uniform in a compression edge by an FEM and the past experiment occurs isn't considered. The valuation plan which considered expensive contact pressure distribution in the compression edge using FEM and past formula are proposed by this research.

PAST NONLINEAR BEHAVIOR VALUE IN LARGE-SCALE EARTHQUAKE

The moment footing base subgrade reaction shows by the past nonlinear rotation angle estimation method is expressed with that and a resisting moment. Distribution of subgrade reaction with a change in a resisting moment is considered as follows. The moment which acts on a basic base first, the subgrade reaction state will be the trapezoid distribution at the small stage. Because the tension doesn't act on it between the basis and the foundation when the moment which acts after that exceeds uplift foundation limit moment M_0 the ground reaction state will be the triangle distribution, and leap RI occurs to a basis. A relation between a resisting moment and the footing rotation angle is expressed in the form of the formula (1) here. All over the formula (1) in the formula (2) reaches and is the formula (3), and basic uplift limit moment M_0 and uplift limit rotation angle a_0 are shown from an indicated relation.

$$a = \frac{M}{I \cdot K_v} \quad (1) \quad M_0 = \frac{BN}{6} \quad (2)$$

$$a_0 = \frac{2N}{B^2 DK_v} \quad (3)$$

M : Resisting moment a : Footing rotation angle

I : Moment of inertia of area M_0 : Uplift limit moment

a_0 : Uplift limit rotation N : Vertical force which acts on a basic base

K_v : Vertical coefficient of subgrade reaction B :

Basic width of the horizontal load direction of application

D : Basic width which crosses at right angles in horizontal load direction of application

A basic rotation is considered only at the part I do subgrade reaction work of in uplift starting later. The formula (4) reaches and is the formula (5), and rotation angle which answers to a resisting moment and that at this time is shown.

$$M = N \left(\frac{B}{2} - \frac{x}{3} \right) \quad (4) \quad a$$

$$= \frac{2N}{x^2 DK_v} \quad (5)$$

The subgrade reaction action width which is x: horizontal load direction of application here.

The one which normalized by uplift limit moment M_0 and uplift limit rotation angle a_0 is indicated in the formula (6) to show a relation between a resisting moment and the rotation angle irrespective of the basic size to an action of the load beyond uplift ascent limit moment M_0 .

$$\frac{M}{M_0} = 3 - 2 \sqrt{\frac{a_0}{a}} \quad (6)$$

Further, M/M_0 shows the weight location of the subgrade reaction distribution, and a relation with the weight location of the triangle shows that it's the uplift critical state in $M/M_0 = 1$.

At this time, contact pressure distribution is asked as the distribution of the primary winding-shaped in conformity with the trapezoid distribution and the triangle distribution, etc. Calculation formula of the maximum ground contact pressure is indicated by trapezoid distribution formula (7) and triangle distribution formula (8).

$$\sigma_{max} = \frac{2N(\sum_{i=1}^n a_i + y)}{\sum_{i=1}^{n-1} a_i b_i (2 \sum_{k=1}^n a_k - a_i + 2y)} \quad (7)$$

$$\sigma_{max} = \frac{2N(\sum_{i=1}^n a_i - y)}{\sum_{i=1}^{n-1} a_i b_i (2 \sum_{k=1}^n a_k - a_i - 2y) + (a_n - y)^2 b_n} \quad (8)$$

a_i : Basic width of the eccentricity direction where B is divided into the optional width

b_i : Optional basic width of the crossing at right angles which corresponds to a_i direction

y : The distance of the point that the ground pressure will be 0 from a compression opposite edge

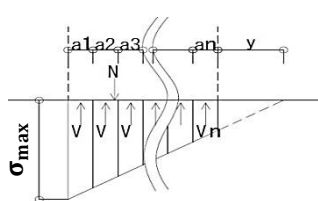


Fig.1 Trapezoid ground pressure distribution

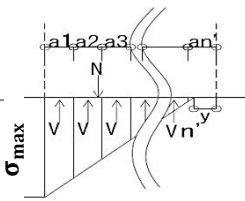


Fig.2 Triangle ground pressure distribution

NONLINEAR BEHAVIOR EVALUATION WHICH CONSIDERED THE PLASTIC LEVEL OF THE FOUNDATION

When a/a_0 approaches ∞ by an estimation method of the past nonlinear rotation angle, M/M_0 will be the curved line which approaches 3. This means that the action location of the resultant approaches an edge of a footing, but plasticity occurs to the ground in a basic edge at the real ground, and I approach the load of the ultimate bearing power state finally. The state that ground reaction in a basic edge reached limit bearing unit capacity of foundation for the first time is set as the surrender critical state (Fig.3 $M = M_1$) so also to consider plasticity of this foundation by this research, and we assume that the ground reaction distribution after that will be the trapezoid distribution again, and after that, it is closer in the ultimate bearing capacity state (Fig.3 $M = M_2$).

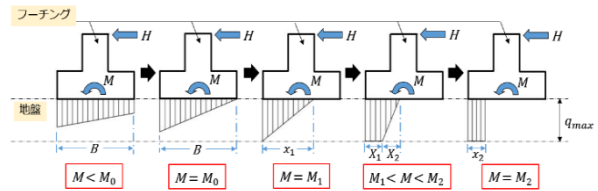


Fig.3 Change in the vertical subgrade reaction distribution which considered a plastic area

The formula (9) reaches and it's the formula (10) respectively from vertical balance, and the surrender critical state and the subgrade reaction action width which can be put in the ultimate bearing power state can show here.

$$x_1 = \frac{2N}{Dq_{max}} \quad (9)$$

$$\frac{N}{Dq_{max}} \quad (10)$$

$$x_2 =$$

The formula (11) reaches and is the formula (12), and the surrender critical state and the resisting moment which can be put in the ultimate bearing power state are shown.

$$M_1 = N \left(\frac{B}{2} - \frac{2N}{3Dq_{max}} \right) \quad (11)$$

$$M_2 = N \left(\frac{B}{2} - \frac{N}{2Dq_{max}} \right) \quad (12)$$

When we assume that the subgrade reaction distribution will be the trapezoid distribution after surrender critical state arrival again, the relation which is indicated by the formula (13) in ground reaction action width X_1 , X_2 at this time and subgrade reaction action width x_2 which can be put in the ultimate bearing capacity state stands up.

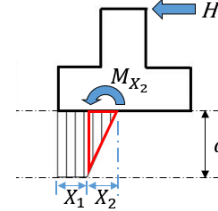
$$2x_2 = 2X_1 + X_2 \quad (13)$$

When an indicated relation is used for the formula (13), the resisting moment which can be put behind foundation plasticity is expressed in the formula

(14).

$$M = N \left(\frac{B}{2} - \frac{12x_2^2 + X_2^2}{24x_2} \right) \quad (14)$$

The formula (15) reaches, and the moment which thinks a basic revolution occurs only by subgrade reaction in X_2 part and exerts a geometrical moment of inertia and a revolution at this time is the formula (16), and the rotation angle of the basis is expressed in the formula (17).



$$I_{X_2} = \frac{X_2^3 D}{12} \quad (15)$$

$$\alpha_2 = \frac{X_2^2 D q_{max}}{12} \quad (16)$$

$$a = \frac{q_{max}}{K_{vi} X_2} \quad (17)$$

Fig.4 Ground reaction force from M_1 to M_2

Relation of the $M/M_0 \sim a/a_0$ which can be put behind foundation plasticity is expressed in the formula (18) finally here.

$$\frac{M}{M_0} = \frac{M_2}{M_0} - \frac{B^3 D^3 q_{max}^3}{16 N^3 \left(\frac{a}{a_0} \right)^2} \quad (18)$$

ESTIMATION OF THE NONLINEAR ROTATION ANGLE WHICH CONSIDERED A PLASTIC AREA

We assumed that the rotation angle of the spread foundation which can be put behind foundation plasticity applies a regulation of energy to a relation of $M/M_0 \sim a/a_0$ and presumes. This way of thinking is the way of thinking with which transformation of elastoplastic body proceeds until the occasion which thought a spring was linear and the transformable energy when a spring has the nature of the elastoplasticity, become equivalent (Vertical line area = Slanted line area). It's to apply a regulation of energy to a relation of the uplift curved line which prescribed the M_L which shows a basic linear reply in alignment_large and considered the upper limit value of these linear reply and degree of subgrade reaction through the starting point and the point which is the uplift limit by this research, and I find the rotation angle. When it's possible to express this relation in the formula (19), and this is put in order, it's possible to get a quadratic equation of the form as shown in the formula (20). It's possible to get the rotation angle of the spread

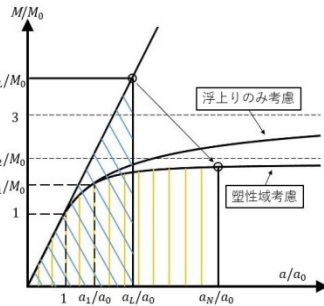


Fig.5 Estimation of the nonlinear rotation angle using a regulation of energy

foundation which can be put behind foundation plasticity by solving the ceremony derived from the formula (20) using the formula of the solution (21).

$$\int_1^{\frac{a_N}{a_0}} \left\{ \frac{a}{a_0} \right\} dt \frac{a}{a_0} = \int_1^{\frac{a_1}{a_0}} \left\{ 3 - 2 \sqrt{\frac{a_0}{a}} \right\} dt \frac{a}{a_0} + \int_{\frac{a_1}{a_0}}^{\frac{a_N}{a_0}} \left\{ \frac{M_2}{M_0} - \frac{B^3 D^3 q_{max}^3}{16 N^3 (a/a_0)^2} \right\} dt \frac{a}{a_0} \quad (19)$$

$$\alpha \left(\frac{a}{a_0} \right)^2 + \beta \left(\frac{a}{a_0} \right) + \gamma = 0 \quad (20)$$

$$a = \frac{-\beta + \sqrt{\beta^2 - 4\alpha\gamma}}{2\alpha} a_0 \quad (21)$$

FEM ANALYSIS OUTLINE

To find the ground pressure you can't estimate by a valuation plan of existence, to make the FEM analysis model which can express basic rising according to real ground, reproduction of level load testing is tried. Experiment was the one which added the horizontal force until considerable rising installed model foundation on the artificial ground, and formed, and subgrade reaction and the rotation angle were recorded. A flow of experimental reproduction by an FEM is indicated on figure 6. The plate bearing test put into effect targeted for the experimental artificial ground first is reproduced by a vertical loading analysis.

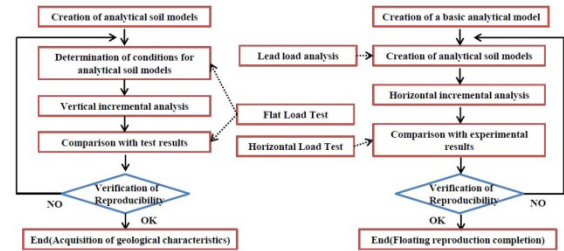


Fig.6 FEM Experimental Reproduction flow

VERTICAL LOADING ANALYSIS BY FEM

FEM analysis model is built so that a load sinking relation like flat plate loading test result may be indicated.

(1) Analysis model outline

An analysis model of a vertical load analysis is indicated on figure 7. The loading plate is made strength. The physical properties value of the ground model in an early stage is indicated in table 1. The physical properties value of the foundation is consulting an experiment and uses a correction R-O model for nonlinear characteristics. The system of the correction R-O model is shown as follows.

$$\frac{G}{G_0} = \frac{G}{1 + \alpha |\gamma G|^\beta} \quad (22)$$

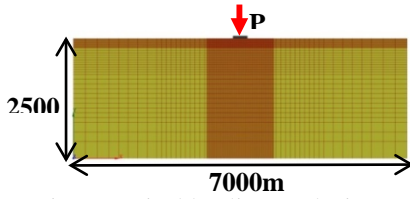


Fig.7 Vertical loading analysis

$$\alpha = \left(\frac{2}{\gamma_{0.5} G_0} \right)^\beta \quad (23) \quad \beta = \frac{2\pi h_{\max}}{2 - \pi h_{\max}} \quad (24)$$

At this point, G : modulus of rigidity, G_0 early

item	symbol	unit	physical property
unit weight	γ	kN/m ³	16.17
modulus of elasticity	E_0	MN/m ²	20.05
modulus of elasticity of shear	G_0	MN/m ²	7.71
Poisson's ratio	ν	-	0.3
adhesive power	c	kN/m ²	20
Internal friction angle	Φ	deg	28.8
Reference strain	$\gamma_{0.5}$	-	0.001
Maximum attenuation constant	h_{\max}	-	0.21

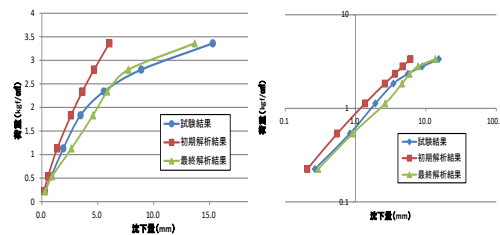
stage modulus of rigidity, γ : The shearing strain, $\gamma_{0.5}$: standard distortion (The shearing strain when G/G_0 will be 0.5), h_{\max} : biggest damping constant. Among these it's G_0 , $\gamma_{0.5}$, h_{\max} to have to establish it, and G_0 presumes from the early stage gradient of the flat plate loading test. $\gamma_{0.5}$, h_{\max} uses mean in a sandy soil. The boundary condition fixes a base of ground model and makes the side a vertical roller. A loading plate and a boundary in the ground include the nonlinear connection element even a lateral loading analysis uses. The input load of the vertical loading analysis is indicated in inside front. Incremental analysis is performed using 7 loads recorded by a test.

(2) Analysis result

The settlement of the ground just below the load

Table.2 Lead straight load analysis of input

Step No.	1	2	3	4	5	6	7
ΔP (kN)	1.98	2.75	5.23	6.21	4.43	4.11	4.92
P(kN)	1.98	4.73	9.96	16.17	20.6	24.71	29.63



(a) arithmetic scale (b) logarithmic scale

Fig.8 Flat Plate Load Test Results and

plate at each loading was determined and compared with the test results. Figure 3 shows a comparison

between the test results and the analytical results. Since it was not possible to obtain the same subsidence curve with the properties shown in Table 1 as in the flat-plate loading test, it was repeated by adjusting the values of $\gamma_{0.5}$ and h_{\max} were adjusted. Finally, the highest value of $\gamma_{0.5} = 0.00021$ and $h_{\max} = 0.208$ was obtained for the test results. Close load-settlement relationships are shown.

HORIZONTAL LOADING ANALYSIS BY FEM

The foundation weight of 2.7t with a clear rotation angle is analyzed as Case 1, and the foundation weight of 3.4t with a recorded ground reaction force distribution is analyzed as Case 2. t as Case 1 and 3.4t as Case 2, where the ground reaction force distribution is recorded. Repeatability is checked by comparing the rotation angle and neutral axis position.

(1) Outline of the analysis model

The analytical model for horizontal loading

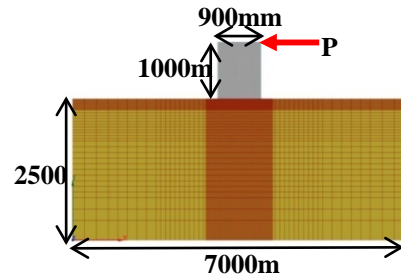
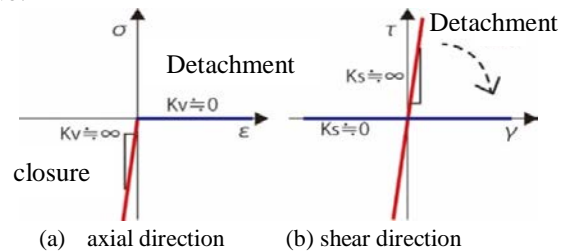


Fig.9 Horizontal loading model

analysis is shown in Figure 4. The model foundation is assumed to be rigid, and the physical properties of the ground are $\gamma_{0.5}$, h_{\max} is obtained from the vertical loading analysis, and The boundary conditions are the same as in the vertical loading analysis, and the values in Table 1 are used in other cases. The boundary conditions are the same as in the vertical loading analysis, and Figure 5 shows the characteristics of nonlinear connecting elements at the boundary between the model foundation and the ground. The loadings in Case 1 and Case 2 are assumed to be horizontal loads. Table 3 shows the input loads for the horizontal loading analysis, where the loads in Case 1 and Case 2 are assumed to be the horizontal loads for the incremental analysis. do.



(a) axial direction (b) shear direction

Fig.10 nonlinear connection element characteristics

(2) Analysis results

Table.3 Comparison of experimental and analytical results

	P(kN)	Comparison	experiment	FEM(initial)	FEM(after adjustment)
Case1	3.97	Rotation angle(°)	0.10	0.23	0.11
	9.65		1.00	2.69	1.04
Case2	3.72	neutral axis "y"(mm)	-65	-111	-96
	5.00		46	14	27
	9.34		440	280	220
	10.70		523	350	360
	11.77		667	400	410

Table 3 shows a comparison of the experimental and analytical results. The distribution of ground reaction forces in the experiment is rough, recorded for each of the six pressure receiving plates, so a linear approximation was used to determine the approximate neutral axis position was determined. Neutral axis and rotation angle were not close to the experimental values in the ground properties obtained by vertical loading analysis.

The adjusted values in Table 4 are the nonlinear properties of the subgrade model modified so that the rotation angle matches the experimental values, and $G_0 = 12 \text{ MN/m}^2$, $\gamma_{0.5} = 0.00021$, $h_{\max} = 0.208$. As a result of the investigation of the neutral axis by changing the physical properties of the ground, the neutral axis position of the FEM was lower than that of the experimental value. A tendency to decrease in size was observed. Based on the above, we give priority to reproduction by comparison of the rotation angle. Figure 7 shows the relationship between the experimental and FEM results.

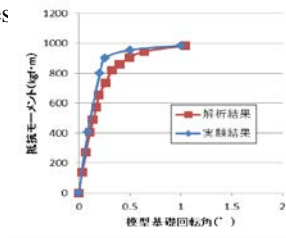


Fig.11
Case1.M-0

We were able to create an analytical model that shows a rotation angle close to the experimental values, and we can say that the FEM was able to replicate the lifting of the foundation.

COMPARISON OF EXPERIMENTAL AND FEM ANALYSIS AND SIMPLE CALCULATION METHODS

The ground pressure calculation method is a method to calculate the neutral axis by dividing the basement into arbitrary number of n compartments and solving the linear and cubic equations shown below.

$$\alpha y^3 + \beta y^2 + \gamma y + c = 0 \quad (25)$$

$$\alpha y^3 + \beta y^2 + \gamma y + c = 0 \quad (26)$$

where y: the distance from the opposite edge of the compressed edge to the neutral axis, α, β, γ, c : from a_n, b_n and d coefficients (shown in Table 4), n: the number of foundation divisions, a_n, b_n : the width of the nth division of the foundation and Depth, d: the distance from the compression edge to the location of eccentric load action. The solution to equation (25) is a trapezoidal distribution with the neutral axis outside the base, and the solution to equation (26) is a triangle with the neutral axis in the base Represents the ground pressure distribution. Ground pressure is obtained using formulas (7) and (8).

The calculation was carried out by dividing the bottom of the model foundation into 6 compartments of $150 \times 900 \text{ mm}$ ($n=6$). Table 5 shows the calculation results of the neutral axis and maximum ground pressure at each load, the trapezoidal distribution at 3.7kN, and the maximum ground pressure at 3.7kN. The distribution of ground pressure was triangular except for the following two points. Overall, the neutral axis of the ground pressure distribution was closer to the experimental data than the FEM results, but the ground pressure tended to be smaller than the experimental value, and the ground pressure was lower than the experimental value. The simple method was used to calculate the ground pressure distribution. In the experiments and FEM, the ground pressure tended to increase at the foundation end, and the simplified calculation method showed that the ground pressure distribution was higher than the ground pressure distribution at the foundation end. The neutral axis position is assumed to be

Table.4 General formula for each coefficient in the basic division number n

α	β	γ	c
h_n	$-n \left(\sum_{i=1}^n a_i \right)$	$\sum_{i=1}^n a_i h \left(\sum_{j=1}^n a_j h - a_i h \right)$	$-\left[\sum_{i=1}^n a_i h \left(\sum_{j=1}^n a_j h - a_i h \right) \right] - h \left[\sum_{i=1}^n a_i h \left(\sum_{j=1}^n a_j h - a_i h \right) \right]$

linear, so the neutral axis position is considered to be small.

CONSIDERATION OF GROUND PRESSURE CORRECTION VALUE

Table.5 Simplified calculation results

Load case(kN)	neutral axis "y"(mm)	Maximum ground pressure(kN/m²)
3.72	-154.62	71.75
5.00	0.18	82.29
9.34	390.93	145.45
10.70	513.93	191.52
11.77	609.72	255.08

Calculate the correction value of the maximum ground pressure to express the increase in the ground pressure at the edge using the simple calculation method. The correction factor is determined by comparing the ground contact

pressure distribution and the experimental ground reaction force distribution. Figure 12 shows the relationship between the ground pressure distribution and the corrected ground pressure distribution based on the results of the FEM analysis. Since the ground pressure distribution tended to increase from the position of $a_{cp} = 1/6 B$, Figure 12 shows that the Assume that the change in ground pressure increases at the position of a_{cp} , as shown in the figure. Assuming that the correction factor for the maximum ground contact pressure σ_{max} at the compression side is p and the correction factor for the ground contact pressure σ_{cp} at the change point a_{cp} is q , and the corrected ground contact pressure distribution is balanced with the vertical load N , the following equation is obtained.

$$a_{cp}\sigma_{max}p + (B - y_e)\sigma_{cp}q = \frac{2N}{b_1} \quad (27)$$

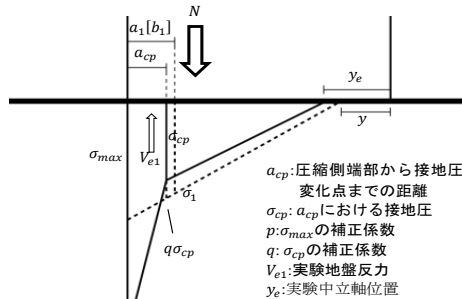


Fig.12 Concept of pressure di

$$a_{cp}\sigma_{max}p + \left\{a_1 + \frac{B-y}{B-y}\right\} \sigma_{cp}q = \frac{2V_{e1}}{b_1} \quad (28)$$

Here, except for p and q , we use the simplified calculation method and experimental results. Using equations (27) and (28), the correction factor for Case2P=3.72kN and P=5.00kN is calculated and The p and q values of the two were close, $p \approx 1.30$ and $q \approx 0.97$. Verification of p and q values Therefore, the maximum corrected ground pressure at P=9.34 kN and the corrected neutral axis were found to be The ground pressure was 189 kN/m² and the corrected neutral axis was 440 mm, and the neutral axis agreed with the experimental values. Since the maximum ground contact pressure exceeded the limit bearing capacity at 70 kN, the maximum ground contact pressure after correction was also calculated in accordance with the actual condition. In addition, it can be said that the effect of ground stiffness and nonlinearity on the maximum ground contact pressure is small, as shown in Figure 11. The ground pressure increase at the edge of the ground due to the ground pressure correction value

$p \approx 1.30$ and $q \approx 0.97$, regardless of the physical properties of the ground It is possible to obtain the ground pressure distribution that takes into account

EXPERIMENTAL DISCUSSION AND EVALUATION

With regard to the rotation angle, the calculated value based on the estimation method obtained in (19)-(21) and the rotation angle of the foundation obtained by the experiment We compared the calculated values by the inferred method with the experimental values. Before geotechnical soil stabilization, there is no significant difference between the experimental and calculated values of the existing estimation methods. After geotechnical plasticization, the difference between the experimental and the predicted values is large as the resistance moment increases. However, by applying the estimation method that takes into account the critical bearing capacity of the ground, it was found that after the ground was plastised, there was a tendency to become In addition, relatively high accuracy was recorded in (27) and (28).

The equations (27) and (28) for the maximum ground pressure distribution are more accurate than the existing equations.

CONCLUSIONS

In the present study, the critical bearing capacity of the ground is taken into account to ensure the high accuracy of raising foundations even after ground plasticity. The nonlinear rotation angle and maximum ground pressure can be estimated. However, in this study, the dynamic inertia forces are calculated by replacing them with static loads, so the behavior of the earthquake Therefore, we believe there is room for improvement in the proposed estimation method. Therefore, we believe that there is room for improvement in the proposed estimation method.

REFERENCES

- [1] Nishimura,A and Haya,H : Study on Design Method of Direct Foundation Considering Plasticity Range, Report of Railway Research Institute, 1992
- [2] Ueda,K: Simple Calculation Method for Ground Pressure Distribution Based on the Interaction between a Rigid Foundation Base and the Ground , 2014.9
- [3] Committee on Design Examples of Highway Bridges: Design Calculation Examples of Road Bridges, 2000.11
- [4] Furuyamada,K and Miyamoto,Y and Miura,K: Surface soils evaluated from in-situ sampling data at multiple sites. Nonlinear Characteristics of the Geotechnical Engineering, The 38th Annual Conference of the Geotechnical Engineering Society of Japan, 2003.7.

THE EFFECT OF CEMENT ADDITIVE TO IMPROVE STRENGTH OF GRATI SOFT SOIL

Yulvi Zaika¹, Harimurti², Adista Fahara³, Nisa Safira⁴, Wahid Darmawan⁵
^{1,2,3,4,5}Engineering Faculty, University of Brawijaya, Indonesia

ABSTRACT

Soft soils identified as soil with high compression and low strength in high water content. The various methods are carried out to decrease the compressibility and increase the carrying capacity. The use of Portland Cement (PC) as a soft soil stabilization material has been known for a long time. Although in terms of cost is higher than lime or waste material such as fly ash, but the content of the compound in cement is complete and the quality is more assured, thus cement is still very reliable. This research aims to investigate the improvement in the strength of soft soils after mix additives cement and changes in physical properties. Laboratory experiments will be carried out such as physical properties test, compaction, and CBR tests to determine semen content of 5%, 8%, 12%, and 15%. Furthermore, triaxial and consolidation tests will also be conducted to investigate several aspects related to strength such as curing time and the percentage of improved soil on site. Based on the results of the triaxial test, there was an improvement in the shear strength of the soil with an increase in the friction angle in the soil but a decrease in cohesion. The shear strength and stiffness is directly proportional to the percentage of PC in the soil.

Keyword: cement, remedial, soft soil, strength

INTRODUCTION

Kedaung Wetan Village is a village that is part of the Grati sub-district, Pasuruan, East Java, Indonesia. Grati is one of the districts that is passed by the Gempol Pasuruan Toll Road (Fig.1) which is part of the Trans Java Toll Road on the toll road that connects Grati and Tongas which has a length of 13.5 km.



Fig. 1. Location of soil sample

SPT data shows that soils up to 12 m deep are very soft soils and 12 m to 16 m are categorized as soft soils, where previously they were paddy fields. The soil require to be improved to sustain the pavement structure and vehicles.

Soft soil problems are found in various places in the world, and the improvement technology is also developing very fast. There are some alternatives methodology such as accelerate consolidation by

using PVD, remediation of soil to increase the strength. The PVD which is very much discussed by several experts [1-4]. PVD usage is discussed in the case of road structures with high embankment. Numerical analysis using finite element program to determine the behaviour of soft soils after PVD is installed by assume as a channel that have permeability coefficients.

The method which is widely used to improve the bearing capacity of soils and reduce compressibility by using additive material. The additives that have been highly recommended are PC and lime. Some researchers conducted experiments to mix the lime for different soft soils such as in Malaysia [5] and Egipt [6-7]. From this study it is known that curing time [8] is can significantly increase soil strength. The use PC to improve the stability of soft soils has also been widely investigated by researcher [7-10] which can be done on the improvement of shallow or deep soils by using the deep soil mixing (DSM) method[11].

The purpose of this study is to investigate physical and especially mechanical properties of cement improved soft soil

EXPERIMENTAL INVESTIGATION

Soil Sample

Soil sample is hight-plasticity silt soils with low shear strength, which classified as soft soils. The properties of soil can be shown in Table 1[12]

Table 1. Physical characteristic of soil sample

Parameter	Unit	Value
Liquid Limit	%	56,12
Plastic Limit	%	43,36
Shrinkage Limit	%	11,86
Saturated Density	kN/m ³	17,21
Coefficient of Permeability	cm/dt	0.00037
Maximum Dry Density	kN/m ³	12,46
Optimum Water Content	%	31
Coefficient Consolidation	cm ² /dt	0,001
Coefficient Compression		0.445

Based on [12], the compressive strength of natural soil are depended on moisture content of soil in such as Eq. (1)

$$q_u = -6.6 \omega + 382.9 \quad (\text{kPa}) \quad (1)$$

where ω is the water content in percent. The soil will be in soft condition ($25 < q_u < 10 \text{ kPa}$) at $54.2 < \omega < 56.5\%$ water content and in very soft condition ($q_u < 10 \text{ kPa}$) at water content more than $56.5.2\%$.

Methodology Testing

Laboratory experiments conducted to investigate changes in the natural soil mixed with PC of physical and mechanical properties. The key to success in getting the maximum strength is to determine the percentage of additives that are most representative by considering various aspects that influence them. The compaction test was carried out to find out the optimum water content of each percentage of additive replacement that is 5%, 8%, 10%, 12% and 15%. Every dosage of remedial soil will be investigated by plasticity, unconfine compressive, CBR and triaxial test. CBR experiments will be carried out under submerged and unsubmerged conditions to investigate whether the remedial soil is retained to the water. The triaxial and unconfined compression tests were run to obtain the shear strength parameter. The experiments were also carried out after the samples were treated for 4, 7, 14 and 28 days.

RESULT AND DISCUSSION

Pozzolanic effect on soil plasticity

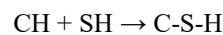
Three stages occur when the soil is mixed with cement, namely: absorption of water by calcium in cement which occurs quickly and gives the effect of heat and reduction of soil water content. The second stage is the replacement of ions where negatively charged soil will attract Ca in the cement quickly causing an increase in the cohesiveness of the soil grains. The third stage is the pozzolanic reaction

where silica and alumina in the soil will react with calcium silicate hydrate. This formation occurs continuously in a long time and causes the soil to become hard.

Pozzolan reaction is a chemical reaction that occurs in PC after the addition of pozzolan. Pozzolan reaction changes the conversion of silica-rich precursors without cementing properties, to calcium silicate, with good cementing properties. In chemical terms, a pozzolanic reaction occurs between calcium hydroxide, also known as portlandite ($\text{Ca}(\text{OH})_2$), and silicate acid (written as H_4SiO_4 or as $\text{Si}(\text{OH})_4$) as Eq.2 :



or



Product $\text{CaH}_2\text{SiO}_4 \cdot 2 \text{H}_2\text{O}$ is calcium silicate hydrate, also abbreviated C-S-H in the chemical notation of cement,

Pozzolan reaction is a long-term reaction, which involves dissolved silicic acid, water and CaO or $\text{Ca}(\text{OH})_2$ or other pozzolan to form a strong cementation matrix. This process is often irreversible. A high amount of free calcium ions and high pH 12 and above is required to start and maintain a pozzolanic reaction. This is because at a pH of around 12, the solubility of silicon and alumina ions is high enough to support the pozzolanic reaction.

Table 2. Soil Plasticity

Soil Composition	Liquid Limit (%)	Plastic Limit (%)	Plasticity Index (%)
Natural Soil	56,12	43,36	12,75
5%	53,58	41,69	11,89
8%	51,56	41,55	10,05
10%	51,05	41,41	9,63
12%	50,05	41,24	8,8
15 %	46,18	41	5,18

The presence of water in soil pores has an effect on the technical properties of fine-grained soils which are defined within the boundary that distinguishes the properties of the soil, namely the liquid limit as the lower limit of viscous flow, the plastic limit as the lower plastic limit and the shrinkage limit as the lower limit of changes in me. The addition of PC in soft soils reduce the liquid limit, plastic limit and also the plasticity index as shown in Table 2. as a result of the decline in soil plastic properties causes changes in soil type from

dominant clay(A-7-5) to soil dominated by silt (A5) based on AASHTO classification.

Pozzolanic effect for strength of soil

Remedial of clay soil with (PC) is a chemical process that can change the structure of the soil by forming larger aggregate grains that will have a very beneficial effect. Chemical events occur between soil and (PC), when both are mixed by adding an amount of water.

CBR test results in Fig. 2 show the increase in the un-soaked and soaked CBR with increasing PC content with the difference of curves insignificant.

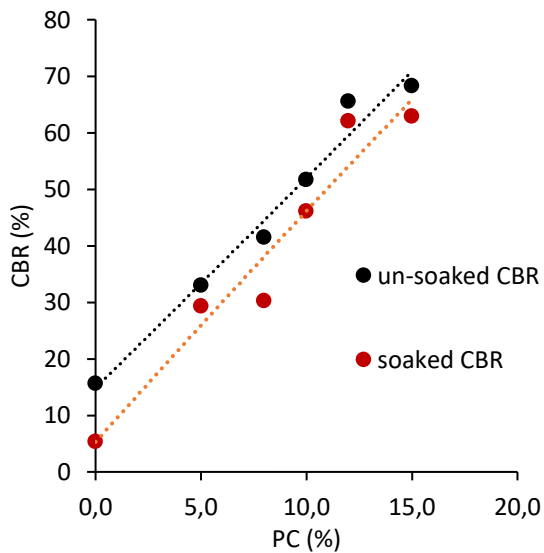


Fig.2. Percentage of PC versus CBR

The value of the friction angle in moving up with the presence of a PC like Fig. 3, but the cohesiveness reduce after reach some value insignificant as show in Fig.4.

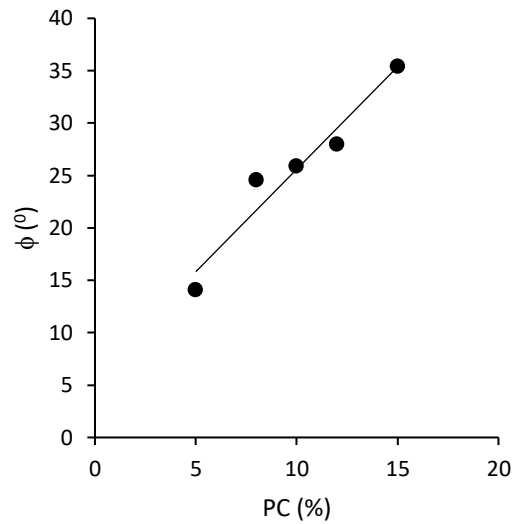


Fig. 3. Influence PC to friction angle

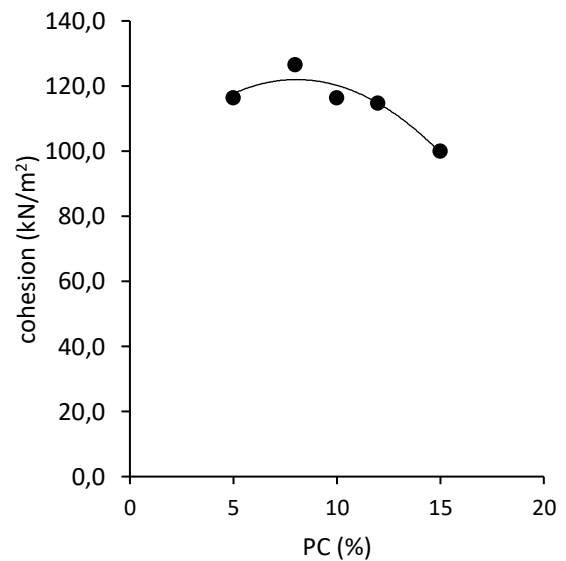


Fig. 4. Influence PC to cohesion

Besides the strength, changes in soil stiffness due to the addition of PC need to be known by presenting the axial stress and strain relationships from unconfined experiments like the Fig. 5.

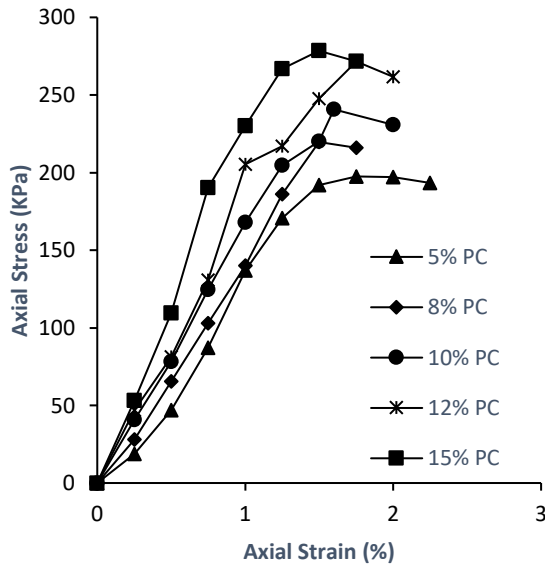


Fig. 5. Axial stress and strain of variation PC improved soil

It was noted that the failure strain changed irregularly but the compressive stress and secant modulus increased with the addition of OPC content in the soil mixture as shown Table 3.

Table 3. Mechanical Properties of stabilized soft soil

PC %	Failure Strain %	Compressive Strength kPa	Secant Modulus Mpa
5	1,75	197,5	5,64
8	1,5	219,7	7,32
10	1,6	240,7	7,52
12	1,75	271,6	7,76
15	1,5	278,5	9,28

Based on [13-14] there is a relationship between the ratio of water and PC content with compressive strength (q_u) and secant modulus (E_s), which is the higher the PC content, the optimum water content of the mixture will be decreased. This relationship is presented in the power function in the form of Eq.(3) and (4):

$$q_u = \frac{A}{(w/c)^B} \quad (3)$$

$$E_s = \frac{M}{(w/c)^N} \quad (4)$$

Where A, B, C and D are empirical constants.

Result of the unconfined compressive test the relation between q_u and w/c presented in the Fig.6 and E_s and w/c in Fig. 7, which formulation in Eq. 5 and 6 as follows:

$$q_u = \frac{312,5}{(w_c/c)^{0,285}} ; R^2 = 0,949 \quad (5)$$

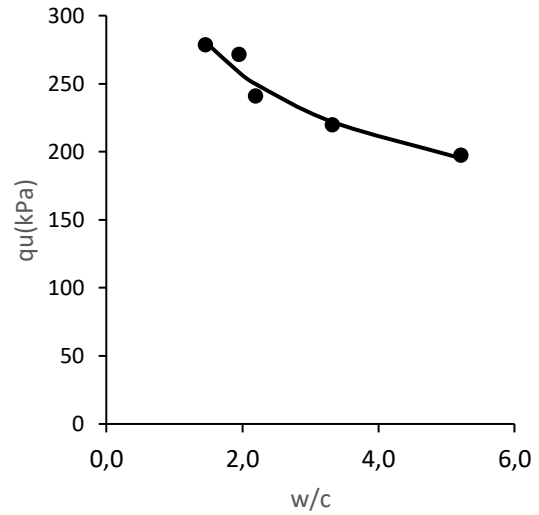


Fig. 6 Fitted curve of strength development PC stabilized soil.

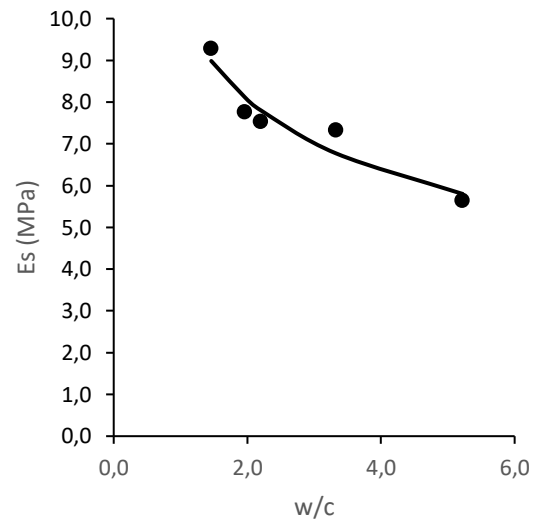


Fig. 7. Fitted curve of secant modulus development PC stabilized soil

$$E_s = \frac{10,231}{(w_c/c)^{0,343}} ; R^2 = 0,911 \quad (7)$$

Shear strength parameter prediction

The hypotheses [15] of w/c as prime parameter to achieve phenomenological model for predicting the mechanical properties of specimen stabilized PC. From this research it is proposed formulation to predict the friction angle and cohesion based on w/c parameter.

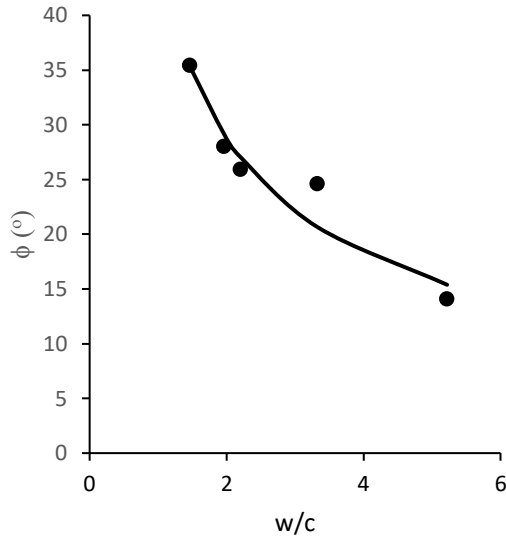


Fig. 8 Fitted curve of friction development PC improved soil

Figure 8 and Eq. 8 estimated friction of w/c.

$$\phi = \frac{45,33}{(w/c)^{0,654}} ; R^2 = 0,909 \quad (8)$$

If the cohesion is related to the w / c parameter, the regression analysis that is different from the friction angle must be performed. The formulation represented the best curve fit is in the Fig.9 and Eq.9.

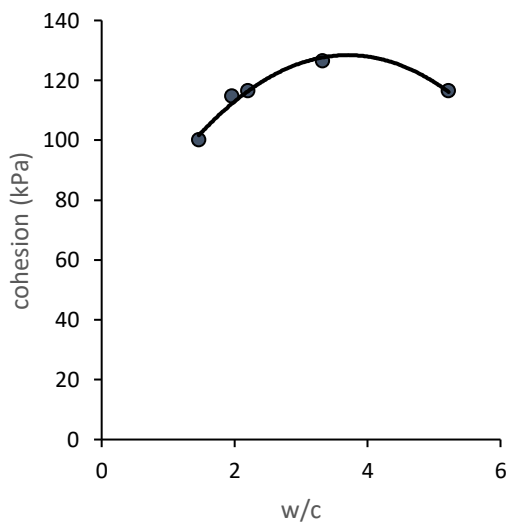


Fig. 9 Fitted curve of cohesion development in PC stabilized soil

Formulations that can be used to predict cohesion of the w / c parameter are expressed in the equation.

$$c = -5,3 \left(\frac{w}{c} \right)^2 + 39,4 \frac{w}{c} + 55,3 ; R^2 = 0,97 \quad (9)$$

Influence of curing time for improved strength

The results of data analysis determined that the optimum of cement content in the soil mixture is 10%. The strength will be developed in 4, 7, 14 and 28 days.

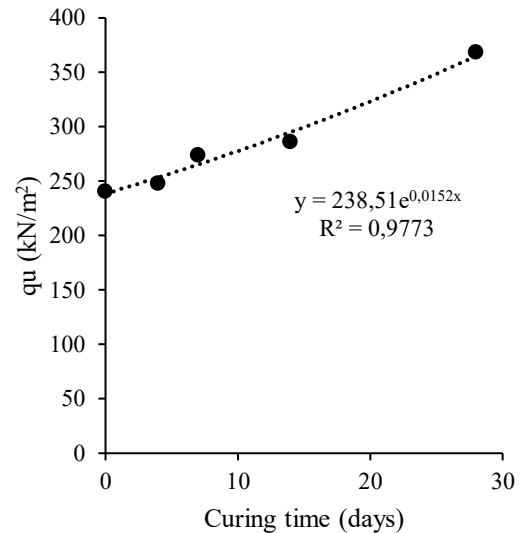


Fig. 10 Effect curing time to the compressive strength

It is took the time for pozolanic processes to reach very significant high strength. An increase in the strength of soft soil after mixed with a PC at a percentage of 10% and immediately compacted optimally, an increase of up to 387%. If treatment is carried out 4, 7 and 14 days, then the increase in around 400% more and if the curing time takes 28 days, the compressive strength reaches 646%.

To find out whether the effect of water on the improved soil the soaked CBR test will be conducted. Fig11 shows the deviation of value of unsoaked and soaked CBR without treatment around 6%. If curing is carried out more than 24 days, the improved soil becomes more stable.

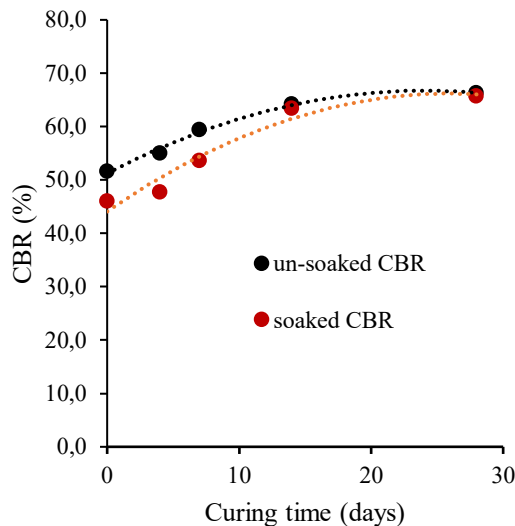


Fig 11. Curing time to develop the strength

CONCLUSION

The water content of soft soils will affect the strength of soils in this case is a type of clayey silt soil. The use of additives such as PCs improved the physical and mechanical properties. Changes in physical properties can be found by the reduction in plastic.

Based on the unconfined compressive test results the parameters q_u and E_s can be formulated by the ratio of water and PC content (w/c). The addition of PC dosage will reduce w/c but increase q_u and E_s . The same phenomenon also applied to the friction angle that it can be defined in a mathematical equation.

The cohesion define as polynomial second order equation to define in w/c factor.

When the curing time applied the improved soil will rise the strength l and also more stable because the water intrusion from the environment.

References

1. Sakleshpur, V.; Pezzi, M.; and Salgado, R. (2018). Ground Engineering Using Prefabricated Vertical Drain: A review, *Geotechnical Engineering Journal of the SEAGS & AGSSEA*, 49(1), 45-64.
2. Tedjakusuma, B. (2012). Application of Prefabricated Vertical Drain in Soil Improvement, *Civil Engineering Dimension*, 14(1), 51-56.
3. Rajesh, B.G.; Chukka, S. K.; and Dey, A. (2018). Finite element modeling of embankment resting on soft ground stabilized with prefabricated vertical drains, *Geotechnical Engineering*, 49 (4) 63-72.
4. Chai, J.C; Shen, S.L.; Miura, N.; and Bergado, D.T. (2001). Simple method of modeling PVD-improved Subsoil, *Journal of geotechnical and geoenvironmental engineering*, 127(11), 965-972.
5. Zukri A.: Pekan Soft Clay Treated with Hydrated Lime as a Method of Soil Stabilizer, Malaysian Technical Universities Conference on Engineering & Technology, Prosedia Engineering 53, 37-41, Elsevier, (2013).
6. Sakr, M., A, Shahin, M., A, and Metwally, Y., M.: Utilization of Lime for Stabilizing Soft Clay Soil of High Organic Content, *Geotechnical, and Geological Engineering*, Springer Science+Business Media B.V. (2009).
7. Mansour, M., A., Samieh, A., M., and Matter, H., E.: Engineering Properties of Cement/lime-stabilized Egyptian Soft Clay, *International Symposium on Geohazards and Geomechanics*, IOP Conf. Series: Earth and Environmental Science 26 (2015) 012041.
8. Harichane K, Ghrici M, Kenai S, Effect of curing time on shear strength of cohesive soils stabilized with combination of lime and natural pozzolana, *Geotechnical Engineering*, *International Journal of Civil Engineering*, Vol. 9, No. 2, June 2011
9. Cong M, Longzho C and Bing C, Analysis of strength development of soft clay stabilized with cement-based stabilizer, *Construction and Building Materials*, 71(2014) 354-362, Elsevier.
10. Pandey A, Soil Stabilization using cement, *International Journal Civil Engineering Technology (IJECIET)*, Volume 8, Issue 6, June 2017.
11. Frikha, W, Zargayoun, H., Boussetta, S., and Bouassida, M.: Experimental Study of Tunis Soft Soil Improved by Deep Mixing Column, *Geotechnical, and Geological Engineering*, Springer International Publishing Switzerland, (2017)
12. Zaika Y and Rachmansyah A, Geotechnical behaviour of soft soil in East Java, Indonesia, *IOP Conference Series: Materials Science and Engineering*, 615 (2019) 012043, IOP Publishing doi:10.1088/1757-899X/615/1/012043.
13. Horpibulsuk S, Rachan R Sluddeepong A and Chinkulkijniwat A, Streng development in cement admixed Bangkok Clay; Laboratory and Field Investigation
14. Miura M, Horpibulsuk S and Nagaraj T S, Engineering behavior of cement stabilized clay at high water content, *Soils and Foundations* Vol.41, No.5, 33- 45, 2001
15. Cong M, Longzhu C and Bing C, Analysis of strength development in soft clay stabilized with cement based stabilizer, *Construction and Building Materials*, 2014, Elsevier, 71, 354-362.

LABORATORY MODEL TEST ON CONTACT EROSION BETWEEN SAND AND SILTY CLAY LAYERS

Pradeep Pokhrel¹, Jiro Kuwano¹

¹Department of Civil and Environmental Engineering, Saitama University, Japan

ABSTRACT

Internal erosion is one of the major causes of the failure of hydraulic structures, road pavement and the natural deposits ground as well. Except suffusion and piping, contact erosion is also a type of internal erosion that can mostly occur at the foundation of embankment dams and dikes, in the road pavement and the alluvial fan deposition valley. This phenomenon occurs when the seepage flow exists at the interface of fine and coarse soil layer where fine particles are detached and transported through the voids of coarse soil layer. During 2013-2017 numerous sinkholes have been observed in Armala area of Pokhara valley in central Nepal. The locations of the sinkholes were observed mostly at paddy fields in the alluvial fan deposit. Sinkhole affected area was investigated twice in a year of 2015, 2016 and 2017. Based on the subsurface ground condition and the location of hidden cavity, it is assumed that an internal contact erosion was occurred, and this phenomenon leads to the formation of subsurface hidden cavity and collapse sinkholes in the Armala area. Mechanics of contact erosion was studied in the laboratory by performing a series of small-scale parallel flow contact erosion test. Physical model of the experiment was prepared with the soil having the similar grain size and physical properties to the onsite granulometry. A cavity was observed at the interface when the DL clay is overlying the coarse sand. In addition, the amount of discharged soil decreases with the increase of overburden pressure.

Keywords: Sinkhole, Bore-hole, Contact erosion, Flow velocity, Piping

INTRODUCTION

Internal erosion is one of the major causes of the failure of hydraulic structures, road pavement and the collapsed sinkholes in the natural deposits ground as well. Except suffusion and piping, contact erosion is also a type of internal erosion that can mostly occur at the foundation of embankment dams and dikes, in the road pavement and the alluvial fan deposition valley. This phenomenon occurs when the seepage flow exists at the interface of fine and coarse soil layer where fine particles are detached and transported through the voids of coarse soil layer. Various research has been conducted on contact erosion in the context of dikes [1], embankment dams [2], [3], [4] and road pavement [5]. Previous authors [1], [2], [3] [4] conducted a parallel flow contact erosion test simulating the internal contact erosion that most frequently encountered in the hydraulic structures. A perpendicular flow contact erosion test was performed to simulate the internal contact erosion below the pavement layers due to the fluctuation of water table [5]. For the significant occurrence of parallel flow internal contact erosion, two conditions should be fulfilled [1], [2], [3], [4]. First one is the geometrical condition where the size of the voids of coarse soil should be large enough than the grain size of the fine soil. So that all the fine particles can pass through the voids of coarse soil. Second, the hydraulic condition where the seepage velocity is high enough to scour and transport the fine particles

through the void of coarse soil. In the past, the research mainly focuses on the mechanics of contact erosion and the threshold flow velocity for the initiation of contact erosion. This study focuses on the internal contact erosion to understand the phenomenon that leads to sinkhole formation using the soil material having the similar physical and geometrical properties of the onsite soil. The maximum grain size of the coarse soil used in this study is significantly finer than the coarse soils used by the previous researcher. The effect of overburden pressure on the erosion rate was studied.

Background of The Research

During November 2013 to 2017, numerous (more than 200) sinkholes have been observed in Armala area of Pokhara valley in central Nepal. The locations of the sinkholes were observed mostly at paddy fields in the alluvial fan deposit. An example of sinkhole in the Armala area is shown in the Fig. 1. The subsurface materials deposited in the sinkhole affected area are unconsolidated silty clay, sand, and gravel. Sinkhole affected area was investigated twice in a year of 2015, 2016 and 2017 and the results obtained from the investigation were reported in [6], [7], [8]. During the investigation, a bore hole logging with standard penetration test (SPT) was conducted at one point near the observed sinkhole. A thick white silty clay layer was found at a depth of 4 m to the 20 m from the ground level [7], [8]. In addition, a hidden cavity

of 2.5 m height was discovered at a depth of 7.5 m to 10 m from the ground level.



Fig. 1 A sinkhole in the Armala area.

To study the soil strata parallel to sinkhole cavity discovered from bore hole survey, some scarp located on the right bank of the nearby river (Kali Khola) also observed. It was identified from these scarp that a 0.05 m thick sand seams layer lies in between the silty clay layers at a depth of 9 m from the ground surface which is the same level as the sinkhole cavity discovered from the borehole investigation. Figure 2 shows the outcrops just after the shaping (left), ground water discharged after 5 minutes (center) and eroded silty clay in the form of slurry after 11 minutes (right). The orientation of the soil strata at the outcrops is illustrated in a schematic diagram in Fig. 3. At the outcrops, groundwater discharged at the interface of sand and silty clay layers was observed after the 5 minutes of shaping. Possibly, it is due to the presence of high permeable sand layer in between the silty clay layers. The discharge of groundwater was taking place at both the upper and lower interface of a sand layer which is attached with the silty clay layers. In addition, more amount of discharged water was observed at the upper interface of a sand layer i.e. silty clay layer overlaying a sand layer at the outcrops. However, internal erosion was observed at both the side of a sand layer and therefore, the presence of sand layer could be one of the factors to trigger may internal contact erosion on the site. Internal erosion

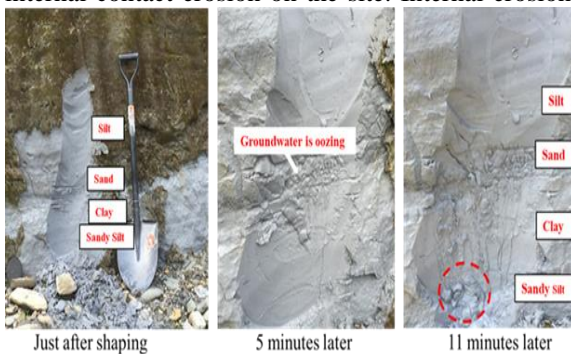


Fig. 2 Groundwater oozing from sand layer.

not takes place at that location if there was only the presence of silty clay in the subsurface of Armala.

The main source of groundwater flow in the sinkhole affected area is seepage flowing from the hill side to the main stream. According to the local residents, excavation of aggregates from the riverbed of the main stream was started from 1990's for the commercial purpose. Due to the excavation of aggregate, the riverbed of the main stream was lowered with time. It increased the hydraulic gradient in the ground and the subsurface water velocity. The required hydraulic condition for the internal erosion is fulfilled and therefore, contact erosion causing cavities was accelerated. The path of seepage flow from the source to the exit shows that the groundwater flows parallel to the interface of soil layers. All these evidences show that, the presence of a sand seam within silty clay layers could be one of the factors to trigger parallel flow internal contact erosion and hidden cavity formation in the Armala area. Therefore, a series of small scale parallel flow contact erosion test was conducted in the laboratory to observe the contact erosion and its phenomenon to lead the cavity formation. Physical model of the experiment was prepared with the soil having the similar grain size and physical properties to the onsite granulometry. The maximum grain size of the coarse sand used in this study is 2.3 mm which is significantly finer than the coarse soils used by the previous authors [1], [2], [3], [4].

EXPERIMENTAL SETUP

The schematic diagram of parallel flow contact erosion test apparatus is shown in Fig. 4. It consists of two water tanks, inlet and outlet connected to a U-shape acrylic box containing a fine and coarse soil combination. The overall inner dimension of the U-shape acrylic box is 30 cm long, 12 cm wide and 15 cm high. Base plate, Porous plate, DL clay layer, sand layer, porous plate and piston is placed simultaneously from bottom to the top. In each test, 10 cm thick DL clay layer is placed on the top of 1 cm thick sand layer in the case of fine soil overlying the coarse soil and reverse configuration with the



Fig. 3 Illustration of soil strata at the outcrops.

same thickness of soil was made in the case of coarse soil overlaying the fine soil. An acrylic plate of 1 cm × 12 cm opening was placed between the soil chamber and inlet-outlet box so that the openings of the soil specimen box coincide with the cross section of the coarse sand layer. Steel mesh of sieve No. 150 was placed at the opening of the plate. So that only DL clay can pass through the mesh. When the valve is open, water is flowing through the coarse sand layer and parallel to the fine soil surface. A bellofram cylinder is connected to the piston through a load cell to apply the given overburden pressure to the soil sample to reproduce the overburden pressure on the site.

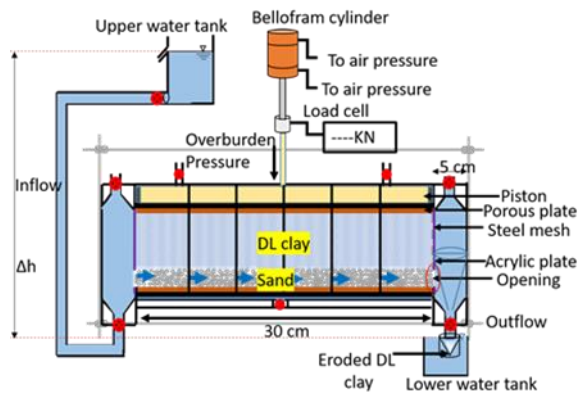


Fig.4 Schematic diagram of parallel flow contact erosion test apparatus.

A series of experiment was performed with the stepwise increase in water head difference at the time interval of 30 minutes at constant overburden pressure. With the increase of water head difference, the flow velocity increases as well. Flow velocity, V (cm/s) is calculated by using the formula $V = Q/A_c$ where Q (cm^3/s) is the discharged water measured which depends on coarse sand permeability and A_c (cm^2) is the cross section area of the coarse sand which is same as the cross section of the opening. Turbidity of the discharged water was measured in every 5 minutes of each interval to find the concentration of DL clay in the discharged water.

TESTED SOILS

The white silty clay located in the hidden cavity is a non-plastic silty clay composed of 79% silt, 16% clay and 5% sand. Grain size distribution of this white silty clay was analyzed by conducting hydrometer test and sieve analysis method. The D_{10} , D_{30} and D_{60} grain size of this silty clay soil are 0.0014 mm, 0.005 mm, 0.023 mm respectively. Test material used in this study comprised of DL clay, which is the commercial name of the soil and silica sand No.3 and silica sand No.5. DL clay is a non-plastic silt composed of 90% silt and 10% clay which shows the similar properties

and grain size of silty clay found in the Armala area. In this study, DL clay was considered as fine soil whereas silica sand No. 3 and silica sand No. 5 were considered as coarse material. Figure 5 shows the gradation curve of the tested soils. The median grain size of silica sand No. 3, silica sand No. 5 and DL clay are 1.6 mm, 0.6 mm, and 0.028 mm, respectively. The maximum grain size of the coarse sand is 2.3 mm which is significantly finer than the coarse soils used by the previous researchers for the contact erosion test. The geometrical and physical properties of the tested soils are given in Table 1.

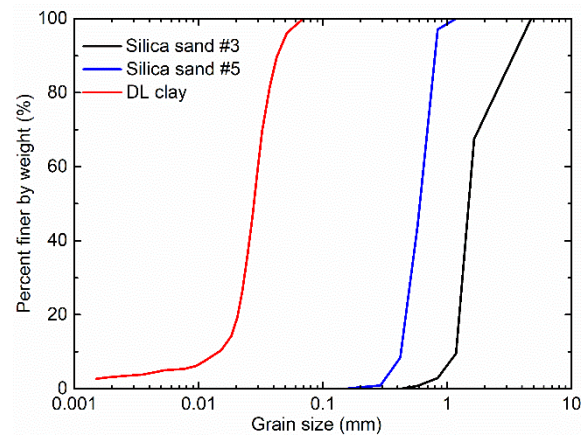


Fig.5 Particle size distribution of tested soils.

Table 1 Geometrical and physical properties of soils.

Properties	Unit	DL clay	Silica Sand#3	Silica sand#5
ρ_s	g/cm ³	2.654	2.56	2.56
ρ_{dmax}	g/cm ³	1.538	1.462	1.543
ρ_d	g/cm ³	1.384	1.388	1.383
D_{15}	mm	-	1.3	0.45
D_{50}	mm	0.0280	1.6	0.6
D_{85}	mm	0.0395	-	-
C_u	-	1.935	1.417	1.553
C_c	-	1.168	0.961	0.927
K_s	m/s	6×10^{-7}	5×10^{-4}	1×10^{-4}

Where, ρ_s – density of the particle, ρ_{dmax} – maximum dry density, ρ_d – dry density, D_{15} – 15 % percentile of soil grain size, D_{50} – median grain size of soil, D_{85} – 85 % percentile of soil grain size, C_u – coefficient of uniformity, C_c – coefficient of curvature, K_s – coefficient of permeability

In 1984, Sherard proposed D_{15}/d_{85} ratio as a filtering criterion, where D_{15} (mm) is the 15% percentile of the coarse soil grain size and d_{85} (mm) is the 85% percentile of the fine soil grain size. Based on the experiments, they found that filtering criteria are $D_{15}/d_{85} \leq 4$ and $D_{15}/d_{85} \leq 9$ depending on the fine soil [9], [10]. The tested soils, in this study does

not validate this criterion. It means, the void size of the sand used in the test have large enough to pass the totally or partially the grain of DL clay.

Fine soil was prepared at optimum water content and compacted five successive layers of 2 cm thick on the soil chamber to achieve the 90% of the maximum density by static compaction method. The corresponding dry density of fine soil at 90% degree of compaction is 1.384 g/cm^3 . Coarse sand was placed manually at the relative density of 50% and its corresponding dry density of silica sand No. 3 and silica sand No. 5 are 1.388 g/cm^3 and 1.383 g/cm^3 respectively. The permeability of the fine soil $6.68 \times 10^{-7} \text{ m/s}$ is significantly smaller than the permeability of coarse soil $1.26 \times 10^{-4} \text{ m/s}$. So that water will flow only thorough the coarse soil layer.

EXPERIMENTAL PROGRAM

In this study, six parallel flow contact erosion tests were performed, considering the configuration of fine and coarse soil combination, types of coarse material and the applied overburden pressures. Two types of soil configuration, coarse sand overlaying the DL clay and DL clay overlaying the coarse sand, were used in the tests. The collapse sinkholes that discovered in the Armala area were usually shallow depth of range 1 to 5.5 m. To reproduce the same depth of cavity and sinkhole discovered at the site, 40 kPa and 70 kPa overburden pressure were applied in the tests. Test conditions are summarized in Table 2.

Table 2 Test conditions

Test No.	Soil configuration	Overburden pressure (kPa)
1	*SS #3 / DL clay	40
2	SS #3 / DL clay	70
3	DL clay / SS #3	40
4	DL clay / SS #3	70
5	DL clay / SS #5	40
6	DL clay / SS #5	70

*SS-Silica sand

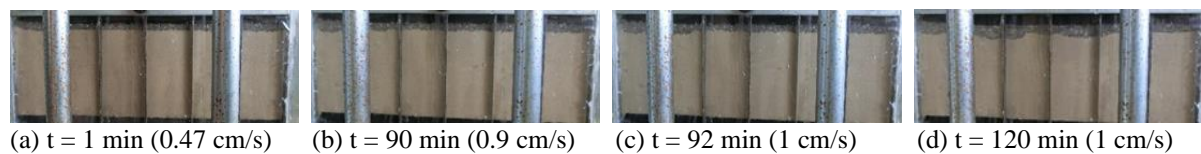


Fig. 6 Propagation of erosion with time (Coarse sand overlaying the DL clay).

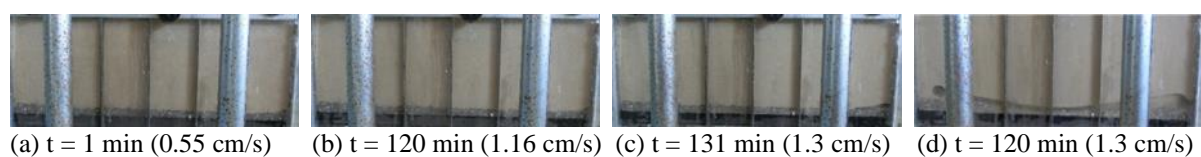


Fig. 7 Propagation of erosion with time (DL clay overlaying the coarse sand).

EXPERIMENTAL RESULTS

Observation of Erosion at the Interface

When the valve is open, water flows through the coarse sand at the interface of DL clay and sand layers. All the experiments were started with a small flow velocity. At low flow velocity, no erosion at the interface was observed. Also, the measured turbidity value of the discharged water corresponding to the small flow velocity was small. It means, the shear force generated by the water flow is smaller than the stress exerted by the fine particles at the interface. So that, the fine soils are in stable state and shows non-erosion behavior at low flow velocity. With the increase of flow velocity, continuous erosion was observed at the interface.

In the case of coarse sand overlaying the DL clay, collapse of the coarse sand grain was observed even in small erosion rate. Probably, it is due to the non-cohesive behavior of coarse sand. At the time of continuous erosion, both the fine and coarse soils particles at the interface are in unstable state. Fine particles at the interface were detached and transported through the voids of coarse material due to flow. At the same time, the rate of erosion tended to increase but the unstable coarse particles are not able to transform the overburden stress. Indeed, the unstable coarse particles were collapsed due to the effect of gravity and clogging effect was observed. So, the amount of eroded soil may have been affected by this clogging effect. The observation result shows that, the contact erosion phenomenon in this configuration leads the surface settlement if the coarse material is a non-cohesive soil. The propagation of erosion with time is shown in Fig. 6.

In the case of DL clay overlaying the coarse sand, a cavity was observed at the interface. The propagation of erosion with time when DL clay overlaying the silica sand is shown in Fig. 7. The arch of the cavity formed by the erosion was seems to be stable due to the cohesion of DL clay. During the continuous erosion, the fine soil at the interface was

flowed out with water where a piping phenomenon was observed. The density of the DL clay decreases at the interface with continuous erosion and resulting the concentration of flow at one location. With the passage of time, the flow concentrated at the unstable part and the cavity propagate in the horizontal and vertical direction. The observation result shows that, the contact erosion phenomenon in this configuration leads the formation of subsurface cavity and finally collapse sinkhole.

Concentration of DL Clay in the Discharged Water and Critical Flow Velocity

Concentration of the soil particles in the discharged water is the key factor to analyze the behavior of erosion with time. The flow velocity corresponding to the non-zero turbidity considered as threshold velocity to initiate the contact erosion of fine soil [2], [3], [4]. Turbidity of the discharge water was measured in every 5 minutes of each interval of 30 minutes. The relationship between the turbidity and the concentration of DL clay was obtained from the several measurements of turbidity by sampling from predetermined quantities of soil particles. The eroded fine particles may sediment in the discharge pipe which can affect the turbidity measurement and the erosion rate. The tendency of flow velocity and the eroded mass in the discharged water was also measured through sampling to cross check the validity of turbidity measurement. In this method, discharge sample was collected in every 5 minutes of each interval for 5 seconds. The weight of all the samples are measured and placed in an electric oven for dried. The result of flow velocity, eroded mass measured through sampling and turbidity with time at different overburden pressure are shown in Fig. 8 and Fig. 9.

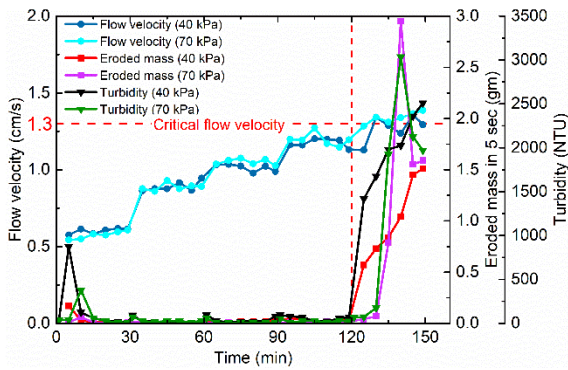


Fig. 8 Measurement of flow velocity, turbidity, and eroded mass with time. (DL clay / silica sand #3).

The concentration of the DL clay in the discharged soil was zero at low flow velocity. The concentration increases significantly with the increase of flow velocity from certain threshold value.

This threshold flow velocity is called the critical flow velocity. The turbidity value and the sampling eroded mass shows that continuous erosion initiated after 120 minutes that correspond to the flow velocity of 1.3 cm/s for the coarse silica sand No. 3 and 0.91 cm/s for the silica sand No.5. The critical flow velocity depends on the grain size of coarse soil and its value decreases with the decrease in grain size of coarse material [1]. The fluctuation pattern of measured eroded mass and the turbidity of the discharged water are similar.

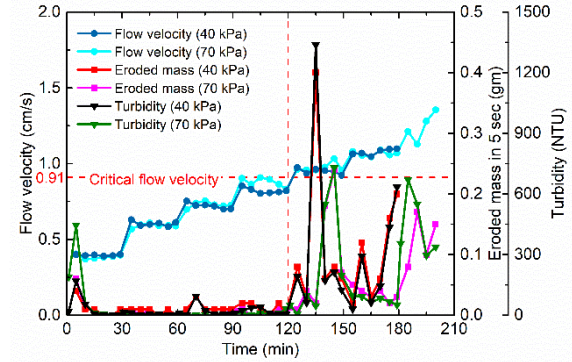


Fig. 9 Measurement of flow velocity, turbidity, and eroded mass with time. (DL clay / silica sand #5).

The critical flow velocity obtained from experimental results was slightly smaller than the critical flow velocity proposed by Guidoux in 2010 refer to “Eq. (1)” [2]. Probably, it is due to the effect of coarse soil grain size and the properties of DL clay. The coarse soil grain size used in this study has significantly smaller than the material used by previous researcher.

$$u_{cr} = 0.7\eta_F \sqrt{\left(\frac{\rho_s - \rho_w}{\rho_w}\right)gd_H \left(1 + \frac{\beta}{d_H^2}\right)} \quad (1)$$

Where, u_{cr} (m/s) - critical flow velocity, η_F - porosity of coarse soil, ρ_s (kg/m³) - density of fine soil grains, ρ_w (kg/m³) - density of water, g (m/s²) - gravity acceleration, d_H (m) - effective diameter of fine soil, β (m²) - adhesive properties of particles.

Effect of Overburden Pressure on Erosion Rate

Amount of discharge water in each interval was collected in a container to measure the eroded mass. The effect of overburden pressure on the amount of erosion or erosion rate was clearly seen from the graph of cumulative eroded mass in Fig. 10. It is seen that the amount of erosion is less in the case of 70 kPa compared to the 40 kPa overburden pressure in all cases of experiments. In real, coarse soil layer is compressed with the increase of overburden pressure. The contact surface between fine soil and coarse soil increases with compression. It means, the total

volume of voids in the coarse soil layer decreases. It results in the less amount of the fine particles transported through the voids. The permeability of the coarse soil also decreases with the compression. Therefore, overburden pressure has an inverse effect on the erosion rate.

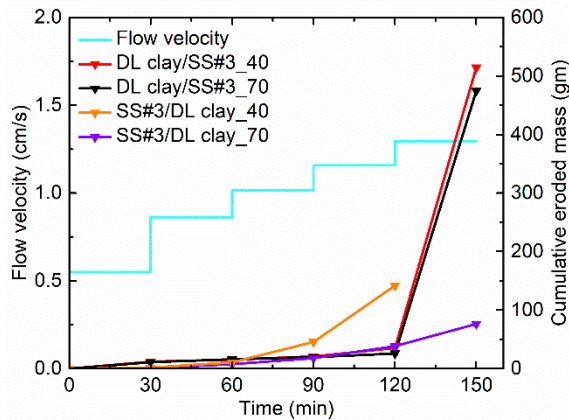


Fig. 10 Cumulative eroded mass with flow velocity.

Possible Mechanism of Internal Erosion in Armala

In fact, contact erosion was initiated at the interface of silty clay and sand seam in the Armala area. When the groundwater flowing through the sand seam, not only the sand but the surficial part of the white silty clay at the interface gets saturated. The saturated part of the silty clay loses their stability and is detached and transported through the coarse sand seam. Experimental results show that, the contact erosion is highly accelerated with piping formation when the fine soil overlying the coarse sand. Similar phenomenon was anticipated in the Armala area. Large amount of subsurface fine materials was eroded, and subsurface cavities were formed. With time, the subsurface cavities increase width and height and finally collapse as a sinkhole.

CONCLUSIONS

A series of contact erosion tests was conducted and the mechanism of internal erosion in Armala area was studied. Following conclusions were drawn from the study.

- 1) At low flow velocity, fine and coarse soil particles at the interface are in stable state and thus contact erosion is insignificant. Erosion is significant when the flow velocity is greater than certain threshold velocity called as critical flow velocity.
- 2) A cavity was observed at the interface when the DL clay layered above the coarse sand layer. Contact erosion following piping phenomenon was observed in this configuration which leads the large amount of erosion rate.

- 3) The surface area prone to erosion and total volume of voids decreases with increase of overburden pressure. Thus, overburden pressure has an inverse effect on the erosion rate.

REFERENCES

- [1] Bezuijen, A., Klein Breteler, M., and Bakker, K.J. Design criteria for placed block revetments and granular filters, in Proceedings of 2nd International Conference on Coastal and Port Engineering in Developing Countries, Beijing, China, 1987, pp. 1-15.
- [2] Guidoux, C., Faure, Y.-H., Beguin, R., and Ho, C.-C., Contact erosion at the interface between granular filter and various base-soils with tangential flow, J. Geotech. Geoenviron. Eng., Vol. 136, No. 5, 2010, pp. 741-750.
- [3] Beguin, R., Faure, Y.-H., Guidoux, C., and Philippe, P., Hydraulic Erosion along the Interface of Different Soil Layers, in Proceedings of 5th International Conference on Scour and Erosion, San Francisco, USA, 2010, pp. 387-396.
- [4] Philippe, P., Beguin, R., and Faure, Y. H. Contact erosion, In Erosion in Geomechanics Applied to Dams and Levees, Wiley/ISTE, 2013, pp. 101-192.
- [5] Jegatheesan P., Sothilingam P., Arulrajah A., Disfani M. M., and Rajeev P., Laboratory Model Test on Contact Erosion of Dispersive Soil Beneath Pavement Layers, Geotechnical Testing Journal, Vol. 38, No. 6, 2015, pp. 1-9.
- [6] Pokhrel, R. M., Kiyota, T., Kuwano R., Chiaro, G., Katagiri, T., and Arai, I., Preliminary Field Assessment of sinkhole damage in Pokhara, Nepal, International Journal of Geoengineering Case histories, Vol. 3, No. 2, 2015, pp. 113-125.
- [7] Kuwano, R., Kiyota, T., Pokhrel, R. M., Katagiri, T., Ikeda, T., Yagiura, Y., Yoshikawa, and T., Kuwano, J., Investigation into the multiple recent sinkholes in Pokhara, Nepal, in Proceedings of 8th International Conference on Scour and Erosion, UK, 2016, pp. 1117-1122.
- [8] Yagiura, Y., Takemasa, M., Yoshikawa, T., Kiyota, T., Katagiri, T., Ikeda, T., and Pokhrel, R. M., Follow-up survey of sinkhole damage in Pokhara, Nepal – Riverbed Lowering and Subsequent Groundwater Lowering Causing Numerous Sinkholes in Pokhara, Nepal Since 2013-, in Proceedings of 7th Japan-Taiwan Workshop on Geotechnical Hazard from Large Earthquake and Heavy Rainfall, Taiwan, 2017.
- [9] Sherard, J. L., Dunnigan, L. P., and Talbot, J. R., Basic properties of sand and gravel filters, J. Geotech. Eng., Vol. 110, No. 6, 1984a, pp. 684-700.
- [10] Sherard, J. L., Dunnigan, L. P., and Talbot, J. R., Filters for silt and clays, J. Geotech. Eng., Vol. 110, No. 6, 1984b, pp. 701-718.

UNIAXIAL COMPRESSION TEST OF BENTONITE UNDER VARIOUS CONDITIONS

Masaki Yanai¹, Shinichi Kanazawa¹, Rie Suzuki¹ and Osamu Yoshino²

¹National Institute of Technology, Fukushima College, Japan; ²Nishimatsu Construction CO.,LTD

ABSTRACT

At present, underground geological disposal at depths greater than 300 m are considered a viable disposal option for high-level radioactive waste generated from the reprocessing of spent fuel used in nuclear power plants. In geological disposal, bentonite is employed as the primary component of buffer material filling gaps between waste and geologic rock. Bentonite has remarkable water absorption swelling capability and low permeability characteristics. Bentonite buffers are generally mixed with silica sand to improve workability and reduce costs. However, specification details have yet to be completely determined. It is anticipated that the buffer material will be exposed to high temperature due to the heat generated by the vitrified solid. In this study, uniaxial compression tests were carried out on specimens made of a mixture of bentonite and silica sand. The purpose of this study is to clarify the mechanical properties of bentonite silica sand mixed specimens by comparing the results of this study with those of the previous study [1~5]. In addition to using the temperature change by water tank curing, as carried out in the previous study, the uniaxial compression test was also carried out while continuously applying temperature to the specimen.

Keywords: Bentonite, Geological disposal, temperature, Uniaxial compression test

1. INTRODUCTION



At present, the use of bentonite as a buffer material for geological disposal is being examined. Bentonite fills gaps due to its water intake swelling properties and low permeability, thus preventing the leakage of groundwater contaminated with high levels of radiation. In Japan, various tests, such as swelling pressure tests and uniaxial compression tests, have helped to characterize swelling performance and mechanical properties of bentonite [6]. During the disposal period, the bentonite buffer is exposed to various conditions. It is feared that backfill materials and buffer materials may permeate and saturate from the surrounding bedrock due to heat generation from the vitrified material and infiltration and saturation of groundwater during the disposal period. In this study, in order to understand the mechanical properties of bentonite buffer materials, the uniaxial compression test was carried out with varying degrees of saturation and specimen temperatures. In addition to tests using temperature change by the water tank curing, tests with continuously applied temperature were also carried out.

2. TEST METHOD

The initial conditions were set at a dry density of 1.6 Mg/m³ and a saturation of 30% and 90%. Temperatures of 30 °C, 50 °C, 70 °C and 90 °C were applied to bentonite (Kunigel V1) with No. 5 silica sand ratios of 30%. The test with 90% saturation was carried out at 30 °C, 60 °C and 90 °C. Table 1

summarizes the physical and chemical properties of Kunigel V1 and silica sand.

Table 1 Physical and chemical properties of Kunigel V1 and silica sand

Kunigel V1	
Silica sand No.5	
soil particle density(Mg/m ³)	2.61
Montmorillonite content(%)	51
Silica sand No. 5 particle density(Mg/m ³)	2.62
Silica sand No. 5 particle size(mm)	0.3~0.8

2.1 Sample Preparation Method

A mixed sample of bentonite and silica sand was prepared at a ratio of 7:3 for Kunigel V1 and silica sand particle size no. 5. The properties of each sample are shown in Tables 2, 3, and 4. Equation (1) was used for the effective clay density[7] of JAEA.

$$\rho_e = \frac{\rho_d(100 - R_s)}{(100 - \frac{\rho_d R_s}{\rho_s})} \quad (1)$$

(1) where, ρ_e : effective clay density, ρ_d : dry density, ρ_s : soil particle density of silica sand, R_s : silica sand mixing ratio

Table 2 Properties of each sample at the 7:3 mixing ratio

silica sand No.	No.5
Mixed soil particle density(Mg/m ³)	2.610
Void ratio	0.631
Effective clay density(Mg/m ³)	1.371

2.2 Methylene Blue Adsorption Test

The montmorillonite content of bentonite in Table 1 was measured with reference to the Methylene blue adsorption measurement method [8] of AIST.

The methylene blue adsorption test is a test to estimate surface area and cation adsorption capacity using the adsorption of methylene blue by montmorillonite, which is a main component of bentonite. In this test method, methylene blue is added to a solution in which bentonite is dispersed, and a drop of the solution is dropped on filter paper to make a dark blue spot of 1 cm in diameter. Fig.1 shows the adsorption amount of methylene blue. When the amount of added methylene blue is large, blue bleeding, called a halo, appears around the spot. The halo is considered to be the methylene blue that the bentonite could not adsorb. In this study, the appearance of a halo is judged to be the maximum adsorption of methylene blue on bentonite.

The calculation of the amount of adsorbed methylene blue is given by the following equation:

Adsorbed amount of methylene blue (MB) per 100 g of sample [mmol] = concentration of MB solution [mmol/l] × amount of MB solution added [ml] × (1/1000) × (100 [g]/Weight of the sample [g])

As a result of the test, the montmorillonite content of the Kunigel V1 used in this study was 51%.

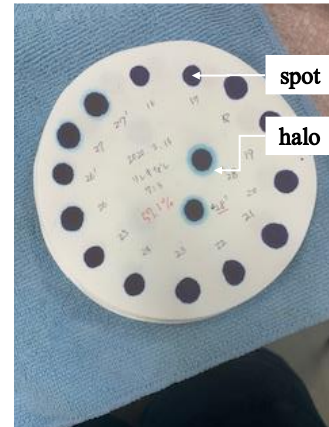
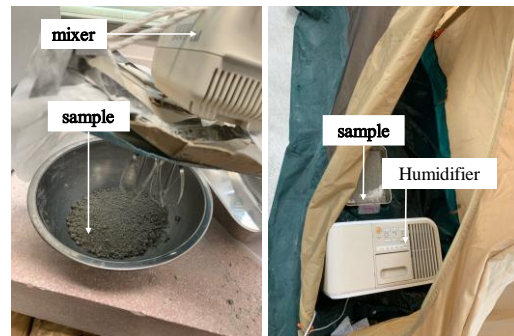


Fig. 1 Methylene blue adsorption test

2.3 Water Content Adjustment

The water content of the mixed samples was adjusted to a saturation of 30% and 90%. The procedure is shown below.

- (1) The sample was mixed using a spray and mixer as shown in Fig. 2 (1).
- (2) For the water content adjustment at high saturation, the water content of the sample was adjusted using a humidifier and a tent to shorten the time, as shown in Fig. 2 (2).
- (3) The water content was measured using a microwave oven (500 W, 15 min) to shorten the time.



- (1) Mixer and sample (30%)
- (2) Humidifier and sample

Fig. 2 Water content adjustment

2.4 Specimen Molding

The sample was divided into five layers, each placed in the mold and compacted. Afterwards, static compaction (40 MPa, 10 min) was applied with a hydraulic jack to produce the test specimen.

Equations (2) and (3) were used for the mass of the specimen, assuming that the volume of the specimen was constant.

$$e = \frac{\rho_s}{\rho_d} - 1 \quad (2)$$

$$S_r = \frac{w\rho_s}{e\rho_w} \quad (3)$$

(2) where, e : void ratio, ρ_s : soil particle density, ρ_d : dry density : (3) and where, S_r : degree of saturation, w : water content, ρ_s : soil particle density e : void ratio, ρ_w : water density (1.00Mg/m^3).

2.5 Temperature Change

(1) Temperature change by water tank curing

In order to avoid water contact with the specimen, the temperature change was applied to the specimen by attaching an impervious sheet to the specimen and curing for 24 hours in the water tank (at 30°C , 50°C , 70°C , 90°C), during which time the temperature was kept constant. After curing, the impervious sheet was removed from the specimen; the volume was measured again; the compression auxiliary equipment was installed; and the uniaxial compression test was carried out. Figure 4 shows the temperature curing of the specimen in the water tank.

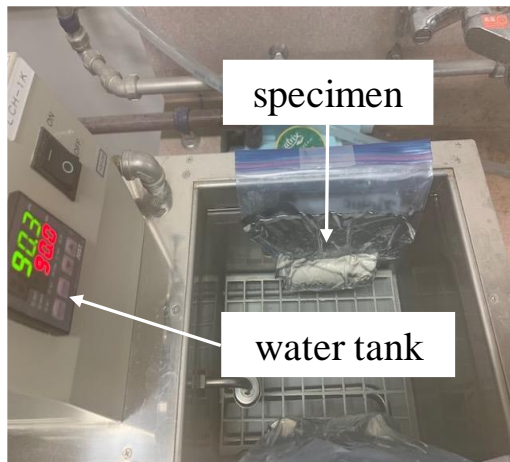


Fig. 3 Temperature change by water tank curing

(2) Uniaxial compression test in a temperature environment

A rubber sleeve was attached to the specimen to prevent water from coming into contact with the prepared specimen. Next, a water tank container capable of keeping the temperature constant was installed in the main body of the uniaxial compression tester, and the test piece with the compression assist device was installed in the water tank container for 25

minutes to reach the set temperature (30°C , 50°C , 70°C , 90°C). After this, the uniaxial compression test was carried out under continuous heating. It was confirmed that the curing time allows the specimen to reach the set temperature in advance.

Figure 4 shows the uniaxial compression test with continuous temperature.



Fig. 4 Uniaxial compression test in a temperature environment

2.6 Uniaxial Compression Test

The compression test was carried out at a fixed loading speed of 0.4 (mm/min) . An electric screw jack system of 10 kN capacity was employed as a testing machine. The test method was carried out referring to the uniaxial compression test method of the JIS standard.[8]

3. TEST RESULTS AND DISCUSSION

Figure 5 shows the results of the uniaxial compression test in which the temperature was changed by curing in a water tank, and Fig. 6 shows the results of the uniaxial compression test in a temperature environment. Figure 7 shows the distribution of water content by curing in a water tank, and Fig. 8 shows the distribution of water content in a test conducted under a temperature environment.

3.1 Results of Tests in Which the Method of Applying the Temperature Change was Varied

Figures 5 and 6 confirm that the maximum compressive strength decreased linearly in the water tank curing in the uniaxial compression test in which the temperature was changed. In the uniaxial compression test under the temperature environment, it was confirmed that the compressive strength tended to decrease rapidly with the rise in temperature from

a certain threshold. With the rise of the temperature, the factors causing the reduced compressive strength appear to be multiple. The first factor is the expansion of specimen volume. It is possible that pore water and air expanded by heat were difficult to discharge due to the low permeability and air permeability of bentonite. According to Charles's law, as the volume of gas is proportional to temperature, the expansion of air is about 1.07 times at 50°C, about 1.13 times at 70°C, and about 1.20 times at 90°C, compared to a temperature of 30°C. The volume expansion of water is about 1.01 times at 50°C, about 1.02 times at 70°C, and about 1.03 times at 90°C, based on the density of water at 30°C. Therefore, it is considered that the occurrence of minute cracks due to the expansion of water and air reduce strength characteristics. In addition, the effects of cracks generated by the drying shrinkage of the specimen surface is also considered. Figure 7 shows the distribution of water content before and after the test in the water tank. In addition, Fig. 8 shows the distribution of water content in the test conducted under the thermal environment. In both cases, it was confirmed that the water content after the test tended to decrease with increasing temperature. It is considered possible that the higher the temperature applied to the specimen, the higher the evaporation from the surface or the inside of the specimen and the lower the strength characteristics due to the cracking caused by drying shrinkage. At this time, cracking in the inside of the specimen could not be confirmed, but cracks by drying shrinkage were confirmed in the test after curing on the surface.

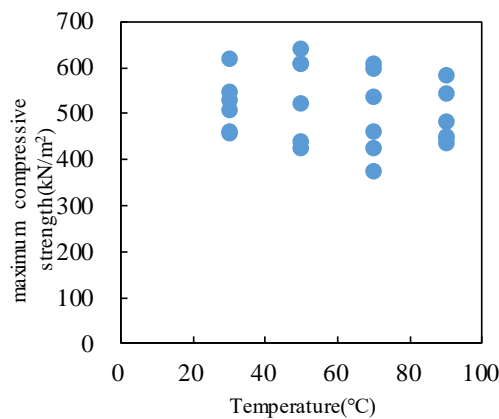


Fig. 5 Uniaxial compression test by water tank curing

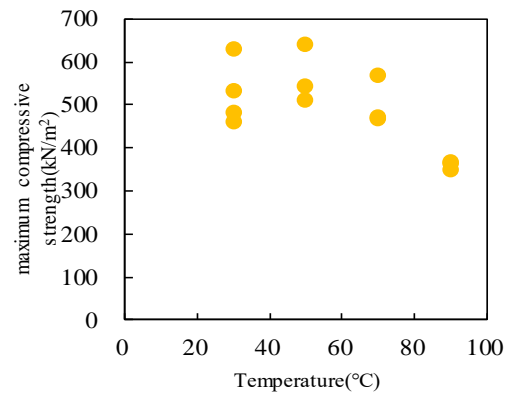


Fig. 6 Uniaxial compression test in a temperature environment

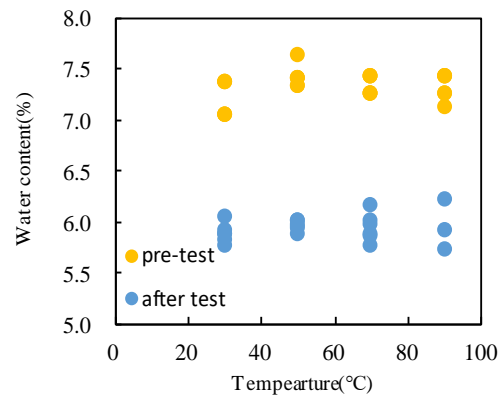


Fig. 7 Distribution of water content in water tank curing test

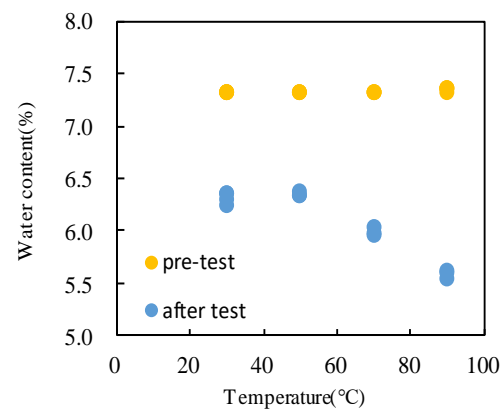


Fig. 8 Distribution of moisture content in the test in a thermal environment

3.2 Results of Uniaxial Compression Tests at High Saturation

Figure 9 shows the results of uniaxial compression tests with varying temperature and saturation. Figure 10 shows the stress-strain curve at 30°C, and 90% saturation, and Figure 11 shows the stress-strain curve at 90°C and 90% saturation. Figure 12 shows the distribution of water content.

Figure 9 shows that the results of the uniaxial compression test under a saturation degree of 90% could not confirm increasing strength with a rise in temperature. However, the stress-strain curves in Figs. 10 and 11 demonstrate different fracture patterns. Ductile fracture with large plastic deformation until fracture is observed in Fig. 10, and brittle fracture with rapid fracture is observed in Fig. 11. The change in water content is likely related to the cause of such fractures. The water content distribution in Fig. 12 confirms that the water content before and after the test did not change under the condition of 30°C, but the water content tended to decrease rapidly under the condition of 90°C. The test environment of 90°C is considered to have become a factor in decreasing the water content, and the fracture form exhibited brittle fracture with the lowering of the water content.

In addition, according to the uniaxial compression test conducted by Nishimura under high-temperature action, uniaxial compression strength was reported not to change with temperature rise.

These results suggest that the uniaxial compressive strength of bentonite specimens at high saturation did not change with increasing temperature.

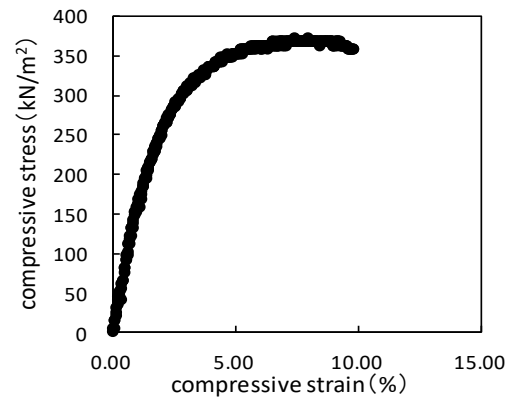


Fig. 10 Stress-strain curve (30°C)

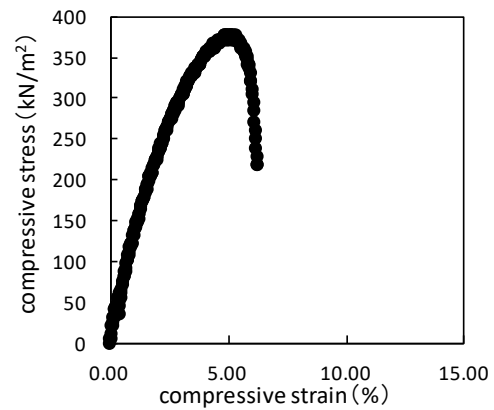


Fig. 11 Stress-strain curve (90°C)

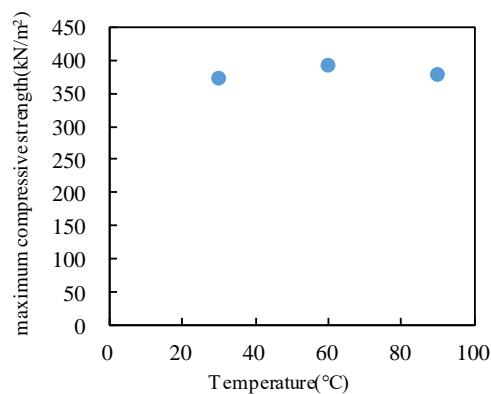


Fig. 9 Uniaxial compression tests varying temperature and saturation

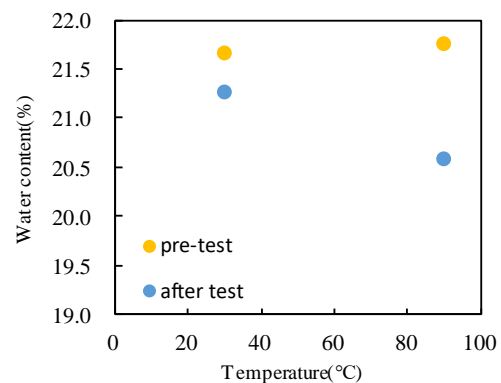


Fig. 12 Distribution of water content

4. CONCLUSION

In this study, the uniaxial compression test of bentonite mixed with silica sand was carried out considering temperature and degree of saturation. The findings from this study are as follows:

- (1) The maximum compressive strength of bentonite-silica sand mixed specimens decreased linearly with increasing temperature.
- (2) Since the water content of the specimen decreased after the test, cracks likely occurred on the surface and interior of the specimen, leading to the decrease in strength.
- (3) In the uniaxial compression test at high saturation, the effect of the strength by temperature could not be confirmed, but the difference in the fracture form was apparent.

In future studies, the uniaxial compression test in which the degree of saturation is varied will be continuously carried out, and the data will be collected cumulatively.

REFERENCES

- [1] Ichikawa N., Kanazawa S., Hayashi H., and Ishiyama K., Study on the mechanical behavior of bentonite buffer considering temperature and saturation changes in geological disposal facilities., *Journal of JGS (CD-ROM)* ., 2017.
- [2] Muto N., Kanazawa S., Hayashi H., Ishiyama K., and Iizuka A., Dynamic Characteristics of Bentonite Buffer Material Considering Temperature, Density and Saturation in Stratum Disposal Facility, *Environmental Ground Engineering Symposium.*, *Journal of JGS*, Vol.12, 2017, pp567-570.,
- [3] Muto N., Kanazawa S., Hayashi H., Hoshi T., and Koji Ishiyama., Experimental study on mechanical properties of bentonite buffer considering various conditions., *Journal of JSCE(CD-ROM)*., 2018.
- [4] Yanai M., Kanazawa S., Ichikawa N., Muto N., Kobayashi S., and Ishiyama K., Uniaxial compression test of bentonite buffer material with varying silica sand content and temperature., *Journal of JSCE.*, (CD-ROM), VII-133, 2019.
- [5] Yanai M., Kanazawa S., Ichikawa N., Muto N., Kobayashi S., and Ishiyama K., Experimental study on mechanical properties of bentonite mixed with silica sand considering temperature change., *Environmental Ground Engineering Symposium, Journal of JGS.*, Vol.14., 2019., pp467-470.
- [6] Japan Nuclear Cycle Development Institute (1999): Technical confidence on the disposal facilities for high level radioactive wastes 2nd Report.
- [7] Horiuchi Y., Takagi T., Method of the methylene blue adsorption test for bentonite at AIST., *Research Materials of the Geological Survey of Japan.*, No.555(2012).
- [8] JIS A 1216:2009, Method for uniaxial compression test.
- [9] Japan Nuclear Cycle Development Institute (1999): Engineering technology for geological disposal
- [10] Nishimura T., Effect of saltwater and high temperature on the engineering properties of compacted bentonite., *Journal of JSCE.*, CS7-013., 2018., pp.25-26.

STUDY ON SOIL-BENTONITE VERTICAL CUTOFF WALLS WITH EARTHQUAKE-PROOF PERFORMANCE

Koji Watanabe¹, Shinya Matsushita², Daisuke Ueno³ and Masaaki Hasegawa³

¹Department of Civil Engineering, Aichi Institute of Technology, Japan; ²Matsushita M&C Lab Co. Ltd., Japan; ³SeikoTone Co. Ltd., Japan

ABSTRACT

Vertical cutoff walls using low permeable materials are often constructed at contaminated sites to contain the contaminants and to prevent their migration in the aquifer. The purpose of this study is to develop the soil-bentonite vertical cutoff walls with earthquake-proof performance. The soil-bentonite vertical cutoff wall which is developed in this study is a rather flexible material compared with other typical barrier materials such as soil-cement mixing material. In this study, laboratory-scale fundamental tests and in-situ full scale test were performed to evaluate the hydraulic performance and the quality of cutoff wall. The following findings were obtained from this study. Firstly, the hydraulic conductivity showed the high value and decreased with the confining pressure from the triaxial hydraulic conductivity tests. The hydraulic conductivity values of soil-bentonite cutoff wall have the excellent correlation with the confining pressures due to overburden pressures. Secondly, according to the in-situ full scale test, it is confirmed from the results of CPT that the soil-bentonite vertical cutoff wall which is developed in this study can be constructed the constant quality along to the depth direction by using TRD (Trench cutting Re-mixing Deep wall) method. In addition, it is examined that the soil-bentonite vertical cutoff wall has the high hydraulic conductivity from hydraulic conductivity test for the core sampling specimen of in-situ full scale test.

Keywords: Vertical cutoff wall, Earthquake-proof performance, Hydraulic conductivity, CPT test

INTRODUCTION

Vertical cutoff walls using low permeable materials are often constructed at contaminated sites to contain the contaminants and to prevent their migration in the aquifer. It is also needed to the leakage control of river embankment and regulating pond. Figure 1 summarizes the concept of applicability on vertical cutoff walls. The usual countermeasure for the migration and the leakage control is to construct the soil-cement cutoff wall. However, it is pointed out that the soil-cement cutoff wall is damaged when the earthquake happens. Moreover, the barrier performance of cutoff wall decreases as the crack of cutoff wall occurs.

The purpose of this study is to develop the soil-bentonite vertical cutoff walls with earthquake-proof performance. The soil-bentonite vertical cutoff wall which is developed in this study is a rather flexible material compared with other typical barrier materials such as soil-cement mixing material. There are some previous researches to examine the performance of soil-bentonite cutoff walls [1]–[3]. These researches are subjected to construct the vertical cutoff walls by mixing powdered bentonite and in-situ soil. The results of previous researches are reported as follows;

1. It is possible to construct the low permeable cutoff walls as bentonite and in-situ soil are mixed.
2. The damage of cutoff walls does not occur when

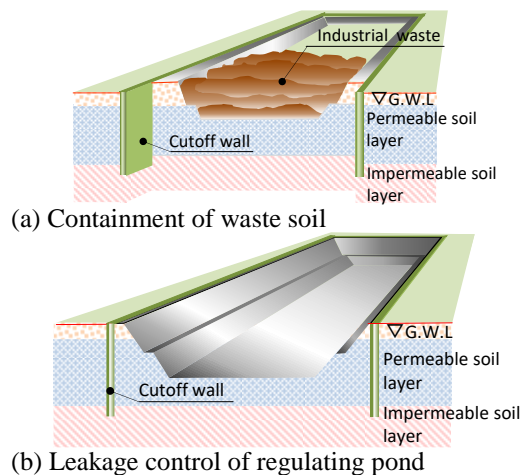


Fig. 1 Concept of vertical cutoff walls.

the large deformation happens in the ground.

3. Corrosion and degradation does not occur because it is stable that the major component of bentonite is inorganic substance such as montmorillonite

4. Sludge amount due to the construction of cutoff walls decreases as bentonite and in-situ soil are mixed in the construction process.

In this study, the construction of vertical cutoff walls is supposed by mixing of heavily concentrated specialty bentonite slurry and in-situ soil. The laboratory-scale fundamental tests and in-situ full scale test were performed to evaluate the

hydraulic performance and the quality of cutoff wall.

CONSTRUCTION METHOD OF SOIL-BENTONITE CUTOFF WALLS

The vertical cutoff wall with earthquake-proof performance is constructed by TRD (Trench cutting Re-mixing Deep wall) method as shown in Fig. 2. Figure 3 also indicates the construction machinery which is applied the construction of vertical cutoff wall. The construction process is described as follows;

1. The agitated auger which is chainsaw type shape connects the base machinery and this auger inserts into in-situ ground.
2. The specialty bentonite slurry injects into the in-situ ground and the chainsaw type auger agitates in-situ ground as the chainsaw type auger moves to horizontal direction.

It may be suggested that the homogeneous cutoff wall is constructed by using TRD method.

LABORATORY-SCALE TESTS

The laboratory-scale tests are carried out to confirm the fundamental performance of cutoff wall in this chapter. The fundamental study which is described in this chapter is used the artificial cutoff wall material to clarify the performance.

Making Process of Cutoff Wall Material

The compounding condition of artificial cutoff wall material is proposed in Table 1. The constitutional materials are sand (Silica sand No. 5), Kaolin clay (only Case 2), Ca-bentonite, water and ion-exchange material. The making process of cutoff wall is described as follows;

1. The predetermined sand and water are mixed homogeneously by the rotary-type mixer. (i.e. model ground material) Here, the predetermined Kaolin clay is added in the Case 2.
2. The predetermined Ca-bentonite and water are mixed homogeneously. (i.e. injection liquid)
3. The predetermined ion-exchange material and water are mixed homogeneously. (i.e. injection activating agent)
4. The injection liquid and injection activating agent are added to the model ground material.

Physical Properties

The physical properties of vertical cutoff wall material are shown in Table 2. The plastic index of material for Case 2 is smaller than that for Case 1. Figure 4 indicates the grain size distribution of vertical cutoff wall material. According to Fig. 4, the fine content of Case 2 dominates that of Case 1.

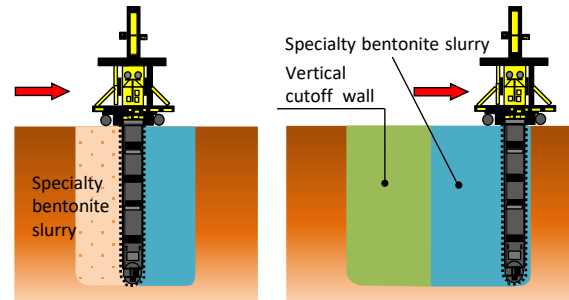


Fig. 2 Concept of vertical cutoff walls.



Fig. 3 Construction machinery for TRD method.

Table 1 Compounding condition.

	Soil type	Sand (g)	Kaolin clay (g)	Water (g)	Ca-bentonite (g)	Ion-exchange material (g)
Case 1	Sandy soil	1713	-	480.4	122.6	4.4
Case 2	Composite soil	1486.6	165.2	541.6	122.6	4.4

Table 2 Physical properties of vertical cutoff wall.

Case 1		Case 2	
Liquid limit w_L (%)	47.1	Liquid limit w_L (%)	38.8
Plastic limit w_p (%)	16.0	Plastic limit w_p (%)	10.6
Plastic index I_p	31.1	Plastic index I_p	28.2

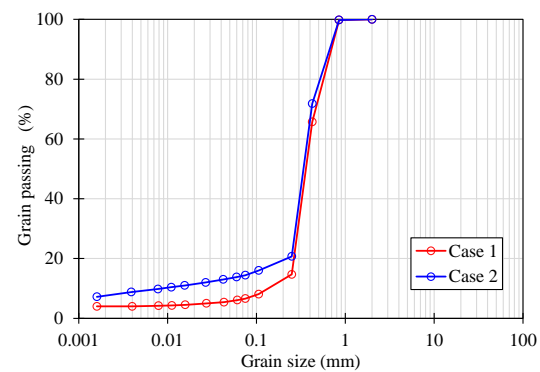


Fig. 4 Grain size distribution.

Water Absorption Expansive Pressure Test

The water absorption expansive pressure test for the vertical cutoff wall material is carried out to evaluate the confining pressure for the triaxial compression test and the triaxial hydraulic conductivity test. The confining pressure which is acted in the triaxial compression test and the triaxial hydraulic conductivity test is considered based on

the expansive pressure obtained from this test. The time history curves of expansive pressure are suggested in Fig. 5. From Fig. 5, the expansive pressure does not occur in both Case 1 and Case 2. Therefore, it is said that the target confining pressure is acted in the triaxial compression test and the triaxial hydraulic conductivity test.

Triaxial Compression Test

The triaxial compression tests are carried out to obtain the strength and deformation characteristics of the vertical cutoff wall material. The condition of triaxial compression tests are CU bar (Consolidated Undrained) and strain rate 0.1%/min. Three kinds of confining pressure such as $\sigma_r' = 50, 100$ and 200 kPa are adopted in the triaxial compression tests.

The results of triaxial compression tests are shown in Fig. 6 and Fig. 7 including the relationships between deviator stress and axial strain and the relationships between pore water pressure and axial strain. According to Fig. 6 and Fig. 7, the maximum deviator stress increases as the confining pressure increases. The trend indicates that the deviator stress reaches the maximum value in the Case 1. However, it is said that the deviator stress increases because the deviator stress does not reaches the maximum value in Case 2. The pore

water pressure shows the negative pressure in the Case 1 and the positive pressure in the Case 2 respectively. The strength parameters are evaluated from the results of triaxial compression tests as described as follows;

Case 1: $c = 124.1$ (10.9) kN/m^2 , $\phi = 33.1$ (37.1) deg.

Case 2: $c = 3.7$ (1.4) kN/m^2 , $\phi = 24.5$ (32.6) deg.

Where, c : cohesion, ϕ : internal friction angle.

Here, the strength parameters are shown by total stress and effective stress. The values shown in parentheses are obtained from effective stress.

Triaxial Hydraulic Conductivity Test

The triaxial hydraulic conductivity tests are

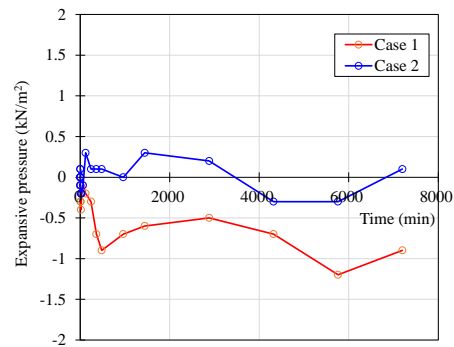


Fig. 5 Time history curves of expansive pressure.

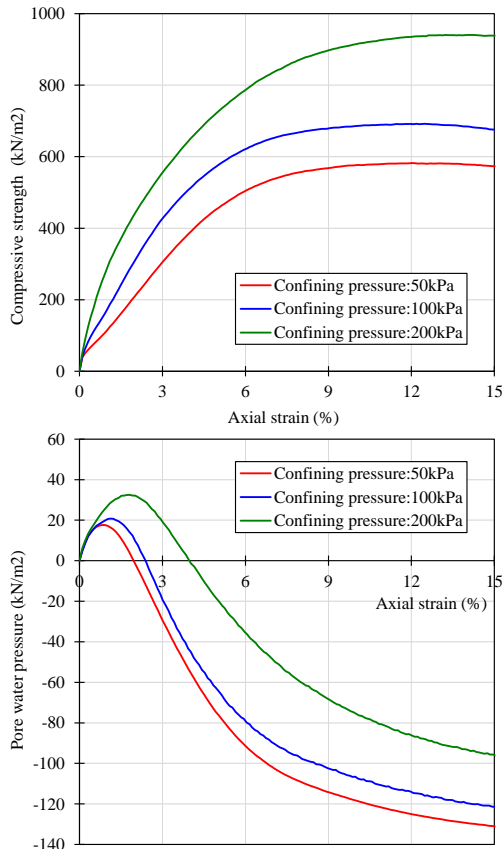


Fig. 6 Results of triaxial compression test for Case 1.

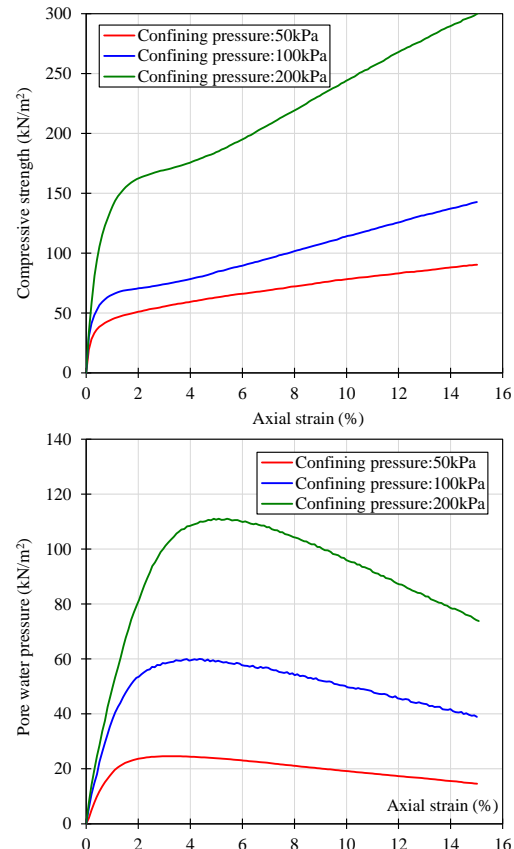


Fig. 7 Results of triaxial compression test for Case 2.

carried out to estimate the effect of confining pressure on the hydraulic conductivity for the vertical cutoff wall material. The triaxial apparatus is used to prevent the water leakage from the side surface of the specimen. The results of hydraulic conductivity obtained from the triaxial hydraulic conductivity tests are suggested in Fig. 8. According to Fig. 8, the trend indicates that the hydraulic conductivity decreases as the confining pressure increases. It is observed that the obtained experimental values are fitted as the function of confining pressure. The hydraulic conductivity values of soil-bentonite cutoff wall have the excellent correlation with the confining pressures due to overburden pressures.

IN-SITU FULL SCALE TEST

The vertical cutoff wall in this in-situ full scale test is constructed by using TRD method. The details of construction method and process are described in the chapter of CONSTRUCTION METHOD OF SOIL-BENTONITE CUTOFF WALL. The in-situ full scale test is carried out to evaluate the quality of constructed cutoff wall and the applicability of RI-CPT (Radio Isotope-Cone Penetration Test) for the quality management after construction.

Condition of In-situ Full Scale Test

The condition of in-situ full scale test is shown in Fig. 9. The constructed cutoff wall is also inserted in Fig. 9. The ground consists of buried soil, loam, tuffaceous clay and fine sand. The dimensions of each tested cutoff wall are 8000mm in length, 550mm in width and 20m in depth. The compounding condition of injection slurry is changed at the middle section of cutoff wall in the planer direction. Thus, the quality of cutoff wall is confirmed two different conditions on the one cutoff wall. Table 3 shows the compounding conditions of injection slurry.

RI-CPT is carried out to examine the quality of cutoff wall and the applicability of quality management. RI-CPT can be measured wet density of ground and three components (tip resistance, shaft resistance and pore water pressure). In this in-situ full scale test, the measurement of RI-CPT along the depth direction is carried out at the middle section of cutoff wall. Moreover, the core sample along the depth direction is obtained from the wall of No. 1 to examine the performance of cutoff wall.

Results of RI-CPT and Laboratory Test

Figure 10 indicates the results of RI-CPT obtained from the in-situ full scale test. The values

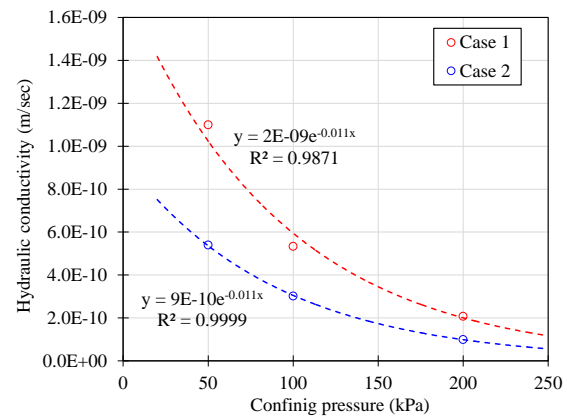


Fig. 8 Relationships between hydraulic conductivity and confining pressure.

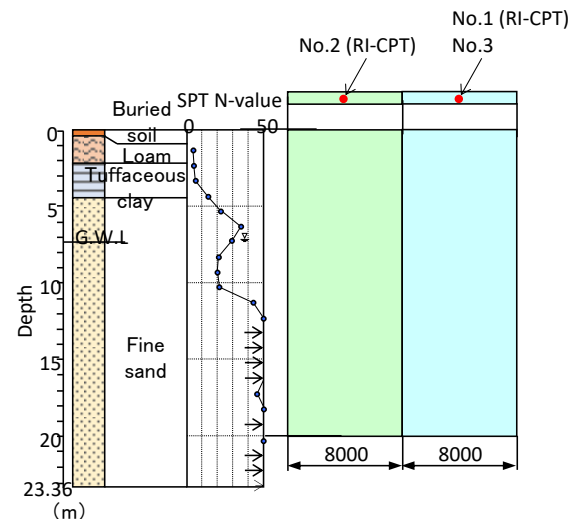
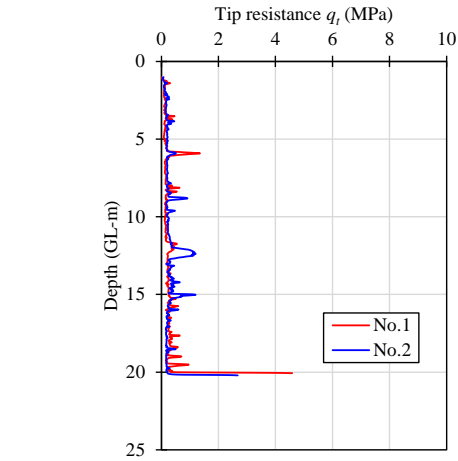


Fig. 9 Condition of in-situ full scale test.

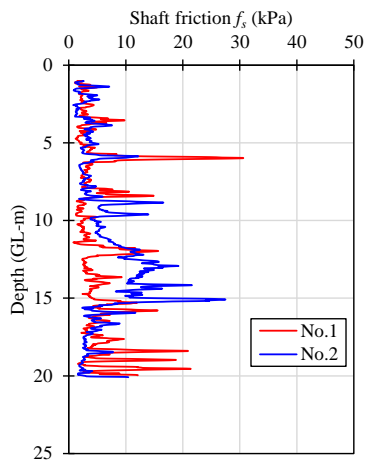
Table 3 Compounding condition.

	Ca-Bentonite concentration (%)	Injection ratio (%)		Dispersing agent (%)
		Ca-Bentonite	Ion-exchange material	
No.1	50	30	5	0.33
No.2	45	30	5	0.33

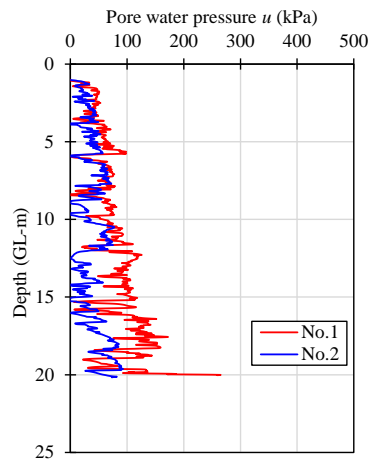
which are shown in Fig. 10 (a)~(c) increase in the depth direction as the effective stress increases. It is confirmed that the values of tip resistance and shaft friction at the depth of GL-6.0 shows the large values in the Case 1. It is also observed that the tip resistance and the shaft friction increase rapidly at the depth of GL- 4.0, 6.0, 9.0, 12.0 and 15.0m in the Case 2. This fact implies that there is the thin soil layer which includes the sand component at the relevant depth as mentioned the above sentence. The inclined angle distribution as shown in Fig. 10 (d) indicates the large value at the deeper depth. However, it is seen that the vertical accuracy of RI-



(a) Tip resistance

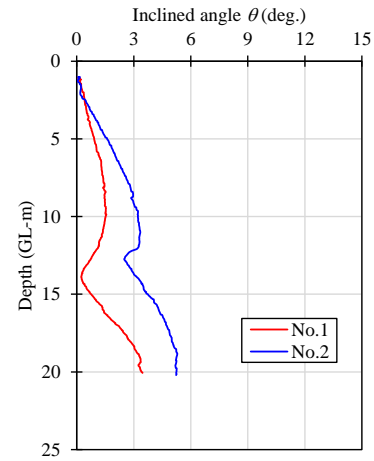


(b) Shaft resistance

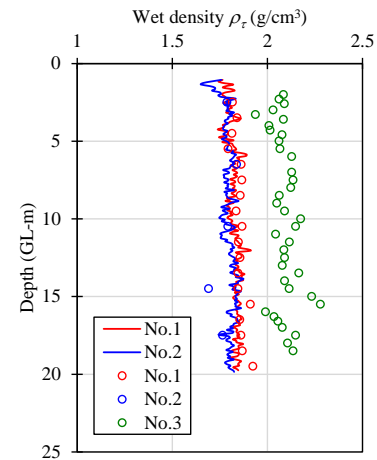


(c) Pore water pressure

CPT is kept along the depth direction because the values of inclined angle is small. Figure 10 (e) plots the wet density distribution obtained from the RI-CPT and the laboratory test of core sample. Here, the solid lines and the circular plots indicate the value of RI-CPT and the value of laboratory test respectively. It is observed that the wet density is the almost constant value along the depth direction.



(d) Inclined angle



(e) Wet density

Fig. 10 Results of RI-CPT

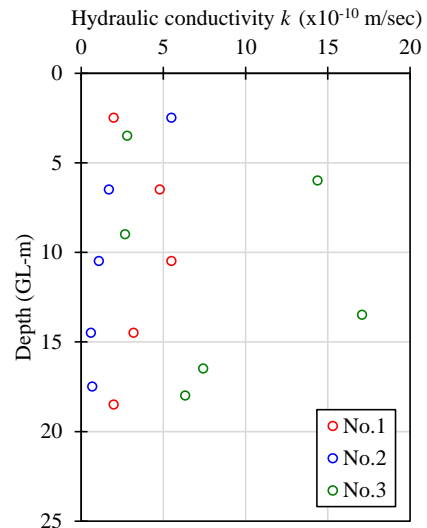


Fig. 11 Results of hydraulic conductivity tests

Compared to the results of RI-CPT and that of laboratory test, the wet density from the RI-CPT agrees almost with that of laboratory test. Thus, it may be concluded that the quality of cutoff wall which is constructed by TRD method indicates the constant quality in the depth direction.

Figure 11 suggests the hydraulic conductivity distribution for the core sampling specimen obtained from the test cutoff wall. The triaxial hydraulic conductivity test is carried out the specimen No. 1 and No. 2. On the other hand, the one dimensional hydraulic conductivity test which is injected the pressured water is carried out the specimen No. 3. In Fig. 11, the obtained hydraulic conductivity values show the ranges of $6.1 \times 10^{-11} \sim 1.7 \times 10^{-9}$ (m/s). Therefore, it is said that the constructed test cutoff wall is impermeable and that has the high barrier performance.

The results of unconfined compression test for the core sampling specimen is plotted in Fig. 12. The values of unconfined compression test indicate the ranges of $12 \sim 28 \text{ kN/m}^2$. This fact implies that the cutoff wall is constructed the constant quality in the depth direction.

CONCLUSIONS

The purpose of this study is to develop the soil-bentonite vertical cutoff walls with earthquake-proof performance. The soil-bentonite vertical cutoff wall which is developed in this study is a rather flexible material compared with other typical barrier materials such as soil-cement mixing material. In this study, laboratory-scale fundamental tests and in-situ full scale test were performed to evaluate the hydraulic performance and the quality of cutoff wall. The following findings were obtained from this study.

1) The hydraulic conductivity showed the high value and decreased with the confining pressure from the triaxial hydraulic conductivity tests. The hydraulic conductivity values of soil-bentonite cutoff wall have the excellent correlation with the confining pressures due to overburden pressures.

2) According to the in-situ full scale test, it is confirmed from the results of CPT that the soil-bentonite vertical cutoff wall which was developed in this study was constructed the constant quality

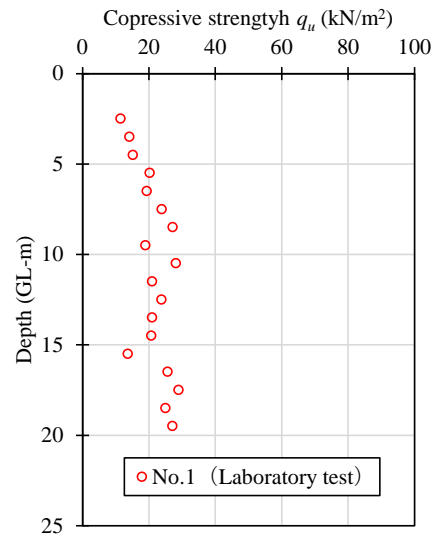


Fig. 12 Results of unconfined compression test

along to the depth direction as TRD (Trench cutting Re-mixing Deep wall) method was used. In addition, it is examined that the soil-bentonite vertical cutoff wall has the high hydraulic conductivity from hydraulic conductivity test for the core sampling specimen of in-situ full scale test.

REFERENCES

- [1] Evans J. C., Shackelford C. D., Yeo S. S. and Henning J., Membrane Behavior of Soil-bentonite Slurry-trench Cutoff Walls. *Soils and Foundations*, Vol. 17, No. 4, 2008, pp. 316-322.
- [2] Yeo S.S., Shackelford C. D. and Evans J. C., Hydraulic Conductivity and Compressibility of Soil-bentonite Back-fill Amended with Activated Carbon, *Journal of Geotechnical and Geoenvironmental Engineering*, ASCE, Vol. 135, No. 5, 2009, pp. 664-672.
- [3] Takai A., Inui T., Katsumi T., Kamon M. and Araki S., Factors Affected The Hydraulic Barrier Performance of Soil-bentonite Mixture Cut-off Wall, *Journal of Japan Society of Civil Engineers, Ser. C (Geosphere Engineering)*, Vol. 68, No. 1, 2012, pp. 1-14.

FUNDAMENTAL STUDY ON TRENCH STABILITY OF DIAPHRAGM WALL

Yuki Sasaki¹, Koji Watanabe¹, Makoto Arakawa² and Tadahisa Yamamoto²

¹ Department of Civil Engineering, Aichi Institute of Technology, Japan; ² Obayashi Corporation, Japan

ABSTRACT

The diaphragm wall construction method is used as the retaining wall in the large excavation and the adjacent construction because the diaphragm wall has the high stability in the excavation. It is important to be stable the trench of diaphragm wall in the construction process from the excavation to the concreting. There are some previous studies on the trench stability of diaphragm wall. However, it is needed to evaluate the trench stability on the complicated conditions such as the adjacent construction. The purpose of this study is to evaluate the trench stability of the diaphragm wall on the simple construction condition. The centrifuge model tests and the numerical analysis were carried out to evaluate the trench stability of the diaphragm wall. In the centrifuge model tests, the model ground was prepared the medium dense sandy ground (Relative density $D_r=40$ and 60%). All the tests were conducted under 50G. It is examined that the failure mode of trench is influenced by the model ground conditions. The FEM numerical analysis was carried out to simulate the failure mode based on the centrifuge model tests. The SSR (Shear Strength Reduction) method was used to the numerical analysis. According to the numerical analysis, it is concluded that it is possible to simulate the failure mode which was obtained from the centrifuge model tests.

Keywords: Diaphragm Wall, Trench Stability, Centrifuge Model Test, FEM, Shear Strength Reduction Method

INTRODUCTION

The diaphragm wall method is used as a retaining wall in the large excavation and the adjacent construction because the diaphragm wall has the high stability during the excavation. Figure 1 indicates a series of construction process for the diaphragm construction method. The diaphragm wall method is also shown in Photo 1. It is important to be stable the trench of diaphragm wall in the construction process from the excavation to concreting. There are some previous studies on the trench stability of the diaphragm wall. The diaphragm wall is generally stable that the fluid pressure such as the slurry in the trench supports the earth pressure of ground around the trench summarized in JGS (1988) [1]. The previous evaluation methods of stability on the trench proposed by Sato et al. (1975), Kanatani et al. (1984) and Higuchi et al. (1994) based on the above described concept [2]–[4]. The global safety factor of trench stability is calculated by the limit equilibrium method assuming the slip surface. However, there is the difference of calculated global safety factor because the assumed slip surface on the trench according to the trench evaluation method differs. The different evaluation method is used in the practical engineering because the shape of slip surface on the trench of diaphragm wall is unclear. The centrifuge model test is adopted as experimental approach to solve the problems as mentioned the above sentence. The purpose of centrifuge model

test is to simulate the equivalent stress and strain field for the actual ground under the centrifugal acceleration field. Katagiri et al.(2000) carried out the centrifuge model tests to confirm the trench stability of diaphragm wall [5]. They suggested that the stability condition of slurry trenches was dependent on the length of trench, and the lateral confining force around the sliding block decreased at the yield condition. Ishii et al. (2001) carried out the three dimensional elasto-plastic FEM simulations including the shear strength reduction method to examine the trench stability of diaphragm wall based on the centrifuge model tests [6]. It may be concluded that the global safety factor which was obtained from FEM simulation could be evaluated accurately. However, this study is subjected to the partially stability problem such as only the excavation process.

The purpose of this study is to develop the evaluation method for the trench stability by the experimental approach and the numerical approach. The centrifuge model tests were carried out to examine the failure mechanism. Moreover, the shear strength reduction FEM (here after, SSR-FEM) was performed to simulate the experimental results and to confirm the applicability of SSR-FEM for the trench stability of diaphragm wall.

CENTRIFUGE MODEL TEST

The centrifuge model test which can be simulated the equivalent stress and strain field for

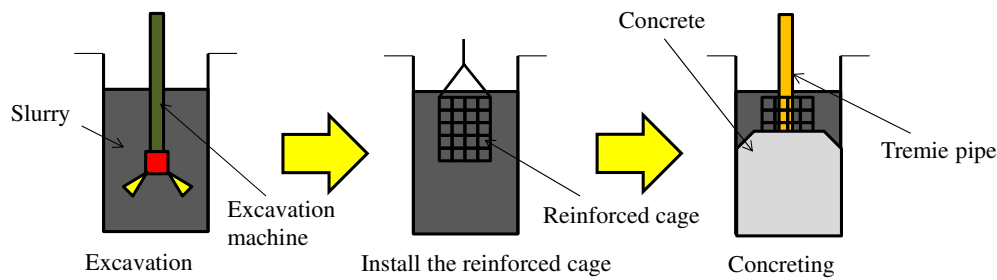


Fig. 1 Construction process for the diaphragm construction method



(a) Excavation process



(b) Concreting process

Photo 1 Diaphragm wall method

the actual behavior by considering the similarity laws is the experimental approach to apply this study.

The beam type centrifuge apparatus was used to this study. The beam type centrifuge apparatus consists of the whirling arm, the driving device, the measuring device installed in the arm and the system to record the video.

Method of Centrifuge Model Test

The test name of centrifuge model test such as Case 1 and Case 2 show the test case of relative density $D_r=40\%$ and $D_r=60\%$ respectively. The purpose of centrifuge model test is to grasp the effect of model ground conditions on the trench stability for the model diaphragm wall. The centrifuge model tests were carried out by using two kinds of model ground conditions such as the relative density $D_r=40$ and 60% to focus the failure mechanism of model trench.

The schematic view of centrifuge model is proposed in Figure 2. The shape of model trench has the three-dimensional shape with a width 48mm, a length 80mm, and a height 500mm. It is possible to observe the deformation behavior when the ground deformation occurs in the experiment because the front of soil container which is installed model trench is made by the acrylic window.

The centrifuge model tests were conducted under 50G of centrifuge acceleration field. The model stable liquid in the model trench decreases when the

target centrifuge acceleration of 50G reaches. The mud membrane to stable the model trench is simulated by plastic package which has a thickness of 0.1mm. The model stable liquid which is poured in the model trench is used the salty water (Specific gravity, 1.05). Here, the specific gravity of stable liquid used in the experiment is equivalent to that of actual stable liquid such as bentonite slurry. Silica sand No.7 was used in the centrifuge model test. Figure 3 shows the grain distribution curve of Silica sand No. 7, and the physical properties of that are shown in Table 1. The model ground was prepared by air-pluviation method using Silica sand No. 7 to achieve a relative density of $D_r=40\%$ and $D_r=60\%$ when the model trench equipped with the spacer between the plastic package and the model ground was installed in the soil container. The thin soil layer made by color Silica sand No. 7 was installed at every 50mm intervals of depth direction in the model ground to observe the failure mode. Moreover, the target in front of the soil container such as the acrylic window to conduct the image analysis for the observation of ground deformation was installed around the model trench. After preparing the model ground, it is poured the model stable liquid into the model trench approximately 20mm above the ground surface. Then, the model ground is saturated by pouring the water from the bottom of soil container. The spacer between the model trench and the model ground is pulled out when the model ground is saturated. Here, the stable

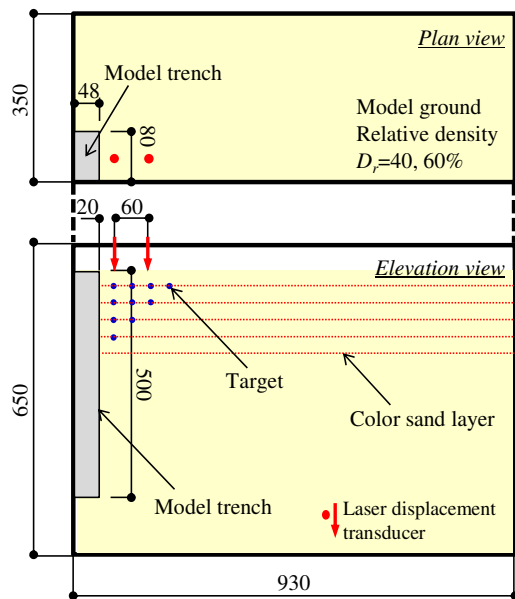


Fig. 2 Schematic view of centrifuge model

Table 1 Physical properties

Soil particle density ρ_s (g/cm^3)	2.654
Mean diameter D_{50} (mm)	0.185
Maximum void ratio e_{\max}	1.193
Minimum void ratio e_{\min}	0.698

liquid can be drained by controlling the solenoid apparatus. The pore water pressure transducer was used to measure the stable liquid level in the model trench. The laser displacement transducer was used to measure the settlement of ground surface.

Results of Centrifuge Model Test

In this chapter, the results of centrifuge model tests are described in the prototype scale.

Figure 4 indicates the relationships between settlement and stable liquid level in model trench. Here, the result as shown in Figure 4 (a) is Case 1 such as the case of relative density $D_r=40\%$, and that as shown in Figure 4 (b) is Case 2 such as the case of relative density $D_r=60\%$. The measurement locations at the ground surface are 1.0m and 4.0m from the model trench respectively. According to Figure 4, the settlement on the ground surface increases as the stable liquid level in the model trench decreases. Especially, Figure 4 (a) has a pronounced tendency to decrease, and the settlement on the ground surface begin to increase since immediately after the drawdown of model stable liquid, the settlement of ground surface eventually showed a large increase of approximately 2m.

Compared with Case 1 and Case 2, it is seen that

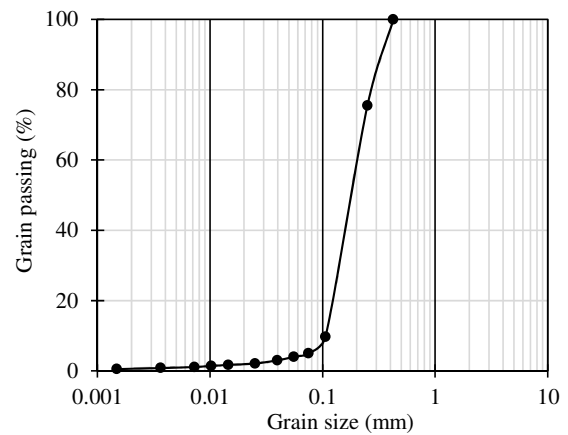
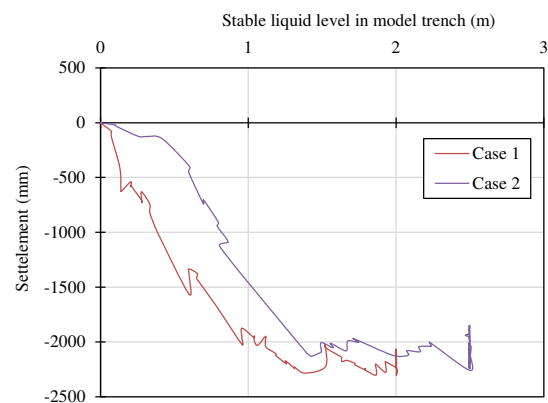
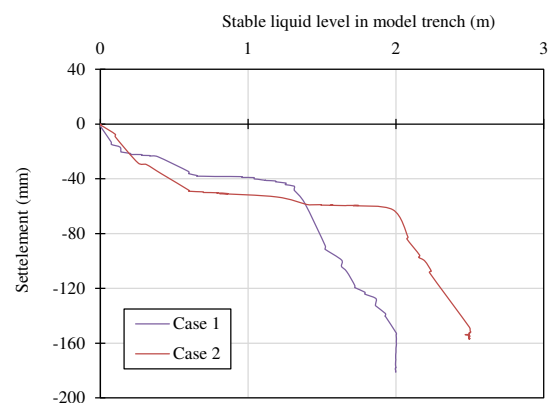


Fig. 3 Grain size distribution curve



(a) 1m from model trench



(b) 4m from model trench

Fig. 4 Relationships between settlement and stable liquid level in model trench

the settlement of Case 1 occurs when the stable liquid level in the model trench is small. This result implies that the relative density of Case 1 is small. The settlement and the stable liquid level in the model trench are almost alike up to 1.3m decrease as proposed in Figure 4(b). After that the settlement of Case 1 shows a large increase.

The target to obtain the deformation of model

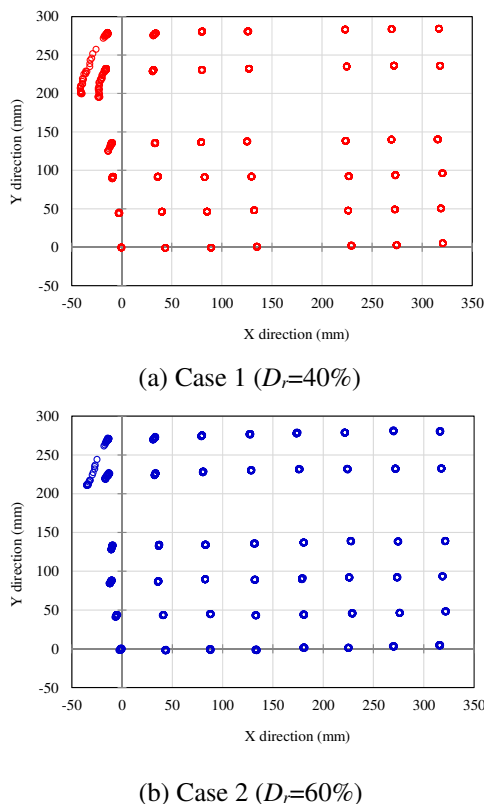


Fig. 5 Results of image analysis (Case1 and 2)

ground was installed along the acrylic window, and the image analysis was carried out by tracking the target movement sequentially. Figure 5 shows the results of image analysis. According to Figure 5, it is pointed out that the settlement at the location of 50mm in the X-direction from the model trench shows the large displacement in both Case 1 and Case 2. Compared with Case 1 and Case 2, Case 1 shows a large displacement near the model trench. It is said that the ground deformation of model ground near the model trench become noticeable in Case 1 because the relative density is small and model ground is loose. In this experiment, the failure of model ground was observed at near the ground surface because the self-weight of model ground above the water level acts to the model ground as the surcharge pressure due to the change of the ground water level.

FEM NUMERICAL ANALYSIS

The SSR-FEM which is the elasto-plastic FEM simulations including the shear strength reduction method can be evaluated the global safety factor which is defined by limit equilibrium methods without assuming slip surface. In addition, there are some advantages to deal with the complicated conditions and to be considered the confining pressure which acts to a sliding earth mass naturally

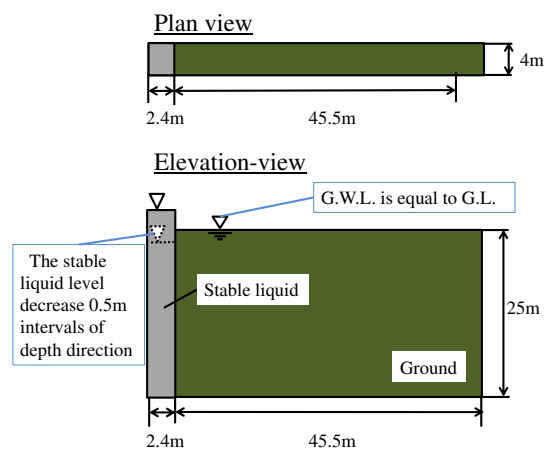


Fig. 6 The schematic view of the numerical analysis

Table 2 Scales on analysis model

Scales	Ground model	Trench model	Guide wall
x (width)	45.5	2.4	0.5
y (depth)	4	4	4
z (height)	25	25	2.5

Unit: (m)

because the elasto-plastic FEM simulations take up deformation problems in SSR-FEM.

Method of FEM Numerical Analysis

The purpose of this analysis is to simulate the results of centrifuge model tests as described the previous chapter. The SSR-FEM simulation of Case 2 was carried out by using Midas GTS-NX. The model trench is one fourth of the trench in the prototype scale by considering symmetry on the trench. The failure criterion of soil is defined by Mohr Coulomb's equation. The iteration process is based on the modified Newton Raphson method. The upper value of iterations is set in 500. The convergence criterion is given by the ratio divided displacement increment by the total displacement, 10^{-5} is set in this study. It is judged the FEM is diverged when the criterion is not achieved less than 10^{-5} within 500 iterations. Figure 6 indicates the schematic view of numerical analysis model, $\Delta H=+1.0m$ is set as the initial state. Here, $\Delta H=+1.0m$ means the stable liquid level is 1.0m higher than the groundwater level (i.e. the ground surface). The stable liquid level decrease 0.5m intervals of depth direction at every analytical step from the initial state. The deformation behavior was also confirmed by calculating the global safety factor at every analytical step. Table 2 shows the scales on the analytical model which are classified

as model ground, model trench and model guide wall in the prototype scale. Here, the guide wall to prevent the failure of model trench is used to the actual construction site. The X, Y and Z in Table 2 is width, depth and height respectively. Figure 7 indicates the mesh division and the model trench located at left side in the finite element mesh. The mesh division in X direction was finely at the model ground near the model trench, but the other directions are equally divided. The analytical parameter of ground and stable liquid are shown in Table 3. The material parameters of cohesion c' , internal friction angle ϕ' and elastic modulus E_{50} is determined based on the triaxial compression tests. The cohesion c' obtained from the triaxial compression tests is 2.90kN/m². However, cohesion c' used in numerical analysis is set as 0kN/m² because the results of centrifuge model test are considered. The elastic modulus regarding the ground sand have characteristics which depend on confining pressure. However, the elastic modulus in this analysis is adopted as the constant value such as the smallest value in the triaxial test. The Poisson's

ratio is obtained from the result on K_0 consolidation test. The density of model ground is calculated by using void ratio e and specific gravity G_s . In the boundary condition, the displacement on the bottom surface, back surface and right side surface is confined in the all direction (X, Y and Z). The displacement in front of mesh is confined in the only the X direction. The pressure difference between the stable liquid and the groundwater act to the left side.

Results of FEM Numerical Analysis

The results of numerical analysis are described in the prototype scale in this chapter.

Figure 8 (a) and (b) show the contour of X-direction displacement when the difference of water level ΔH is +0.0m and -1.0m. Both Figure 8 (a) and (b) show the deformation immediately after the failure. According to the contour of X-direction

Table 3 Analytical parameter of ground and stable liquid

Properties	Ground	Stable liquid
Density, ρ (g/cm ³)	1.90	1.05
Elastic modulus, E' (kPa)	8837	
Poisson's ratio, ν	0.277	
Cohesion, c' (kPa)	0	
Internal friction angle, ϕ' (deg)	38.8	
Dilatancy angle, ψ' (deg)	38.8	

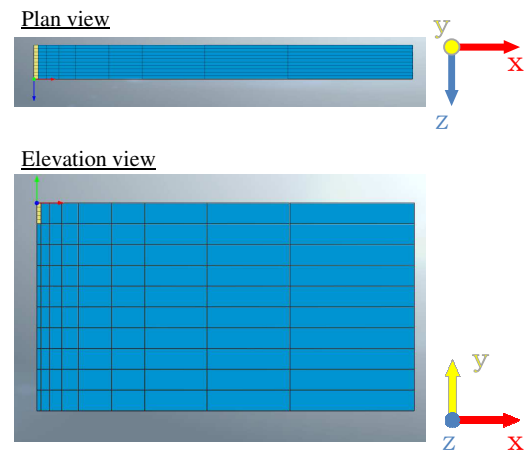


Fig. 7 Finite element mesh used for simulation

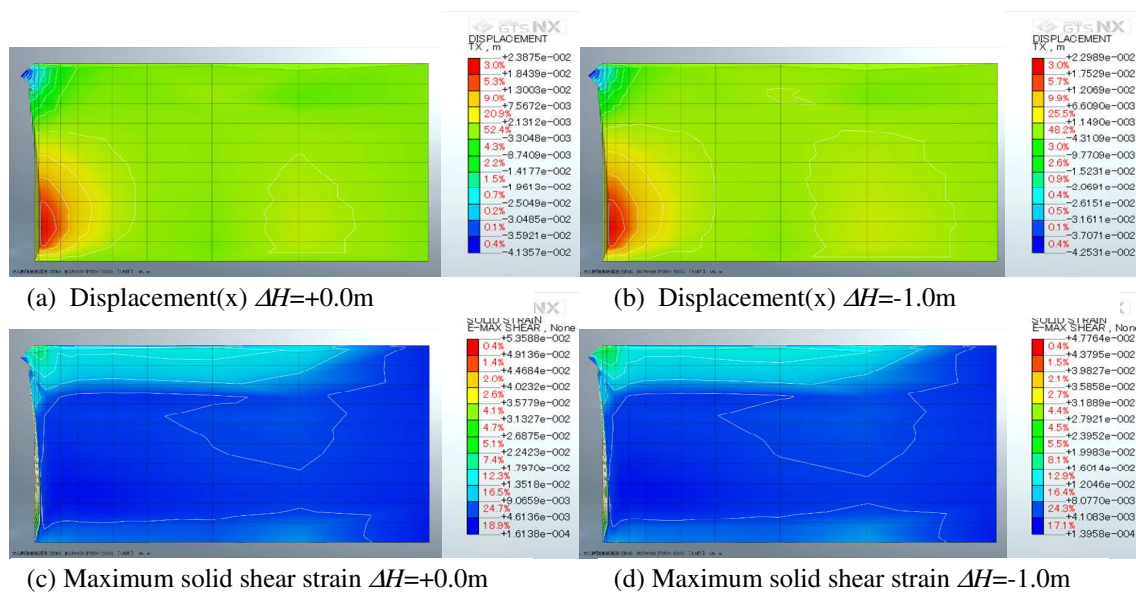


Fig. 8 Displacement (X) and maximum solid shear strain

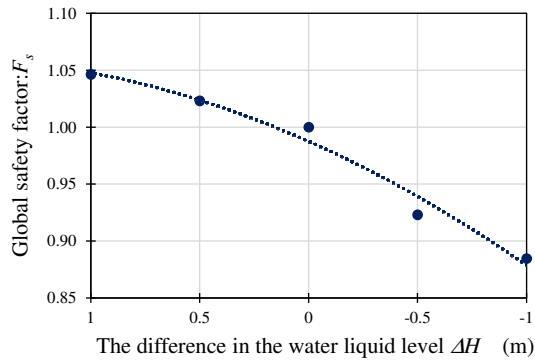


Fig. 9 Relationships between global safety factor F_s and the difference in the water level ΔH

displacement, the deformation toward to the trench was confirmed at the shallow location on the ground near the trench. In addition, the deformation toward to the ground was also examined at the deeper zones of the ground near the trench. Figure 8 (c) and (d) show the contour of maximum shear strain analyzed when the difference of water level ΔH is +0.0m and -1.0m. According to Figure 8 (c) and (d), it is seen that the noticeable deformation occurs at the shallow location near the ground surface. The purpose of the SSR-FEM is simulated the ground on relative density $D_r=60\%$. It corresponds to Figure 5 (b) of the results on image analysis. According to Figure 5 (b), the similar behavior was obtained at the shallow location near the ground surface. Therefore, it is suggested that the deformation behavior for the centrifuged model test can be simulated by SSR-FEM as described in this chapter.

The relationships between global safety factor and the difference of the water level ΔH are shown in Figure 9. Here, the difference in the water level ΔH means the difference between the water level and the groundwater level. From the results of Figure 9, the global safety factor decrease as the stable liquid decrease. These relationships can be expressed the secondarily approximated equation. The global safety factor is equal to approximately 1.0 when the difference in the water level ΔH is +0.0m. After that, the global safety factor has a pronounced tendency to decrease. In the centrifuge model test, it was confirmed the ground failure at the state among approximately $\Delta H=-0.5$ m. Therefore, it was guessed that the global safety factor can also be simulated.

CONCLUSIONS

The purpose of this study is to confirm the trench stability of diaphragm wall by the centrifuge model

test and the numerical analysis. The following findings were obtained from this study.

- 1) The centrifuge model tests were carried out to examine the difference of model condition. Compared with Case 1 and Case 2, Case 1 such as $D_r=40\%$ shows a large displacement. It is concluded that the ground deformation of model ground near the model trench become noticeable in Case 1 because the relative density is small and model ground is loose.
- 2) It is seen that the noticeable deformation occur at the shallow location near the ground surface in both the centrifuge model tests and the numerical analysis. It is suggested that the deformation behavior for the centrifuge model test can be simulated by the numerical analysis of SSR-FEM.
- 3) The global safety factor is equal to approximately 1.0 when the difference in the water level ΔH is +0.0m. After that, the global safety factor has a pronounced tendency to decrease. It was guessed that the global safety factor can be also simulated by the numerical analysis of SSR-FEM.

REFERENCES

- [1] Japanese Geotechnical Society (1988). *Diaphragm Wall Construction Method*, Japanese Geotechnical Society (in Japanese).
- [2] Sato, H. & Akino, N. (1975). "Stability Analysis for Slurry Trench", *Proceedings of 10th Annual Conference of Japanese Geotechnical Society*, 1023-1026 (in Japanese).
- [3] Kanatani, Y. & Akino, N. (1984). "Full-sized Test on Stability of Vertical Sides for Slurry Trench Excavation", *Soils and Foundations*, Vol. 24, No. 4, 171-182 (in Japanese).
- [4] Higuchi, Y., Touda, J., Nakura, K. & Kawasaki, K. (1994). "A New Stability Analysis Method for Slurry Trenches Constructed in Sandy Ground", *Tsuchi-to-Kiso*, Vol. 24, No. 3, 7-12 (in Japanese).
- [5] Katagiri, M., Ishii, T., Saitoh, K., Masuda, T., Aizawa, F. & Ugai, K. (2000). "Observation and Evaluation on Failure Mechanism of Slurry Trenches in Sandy Ground", *Journal of Japanese Society for Civil Engineering*, No. 666, III -53, 127-143 (in Japanese).
- [6] Ishii, T., Saitoh, K., Kuwabara, K. & Ugai, K. (2001). "Stability Analysis by 3-D Elasto-Plastic Finite Element Method for Slurry Trenches Constructed in Sandy Ground", *Journal of Japanese Society for Civil Engineering*, No. 673, III -54, 1-14 (in Japanese).

A PRACTICAL APPROACH TO DETERMINE THE TEMPERATURE CORRECTION FOR EC-5 MOISTURE SENSORS EMBEDDED IN VERTOSOL

Rajitha Shehan Udukumburage¹, Chaminda Gallage² and Les Dawes³

^{1,2,3} Science & Engineering Faculty, Queensland University of Technology, Australia

ABSTRACT

The expansive soils are predominant in arid and semi-arid regions, and they are highly moisture sensitive. The investigation of the climate-ground interaction of expansive soils is extremely important to understand the hydro-mechanical responses of such soils. During the past decade, the low cost and simple methods to reliably monitor the soil volumetric water content have been popular among the geotechnical practitioners. As a result, EC-5 moisture sensors have been widely used in agricultural and scientific projects due to the minimized salinity and textural effects on the final volumetric water content readings. The changes in soil volumetric water content profile can be effectively monitored using soil-specifically calibrated EC-5 sensors. However, due to the temperature sensitivity of EC-5 sensors, a suitable correction factor is essential to determine the actual volumetric water content of the expansive soil. In this study, the authors present a simple and practical approach to calibrate EC-5 sensors incorporating the temperature effect. This simple calibration approach enhances the accuracy of the EC-5 moisture profiling and eventually leads to safe decision making of geotechnical practitioners.

Keywords: Unsaturated soil, Soil moisture, Temperature correction, EC-5 moisture sensors

INTRODUCTION

The unsaturated soil behaviour and the soil properties are significantly dependent on the soil moisture conditions [1-4]. Therefore, it is imperative to identify accurate methods and instrument to investigate the moisture variations in soil profiles [1-7]. These investigations include laboratory-based element tests, model tests and field-based investigations. The moisture sensitivity of expansive clays are considerably greater compared to non-reactive soils and hence, much attention has been given to these soils lately [3-11].

Expansive soils are widely distributed in arid and semi-arid regions in the world [8-9]. The surface soils in Queensland, Australia alone consists of more than 40% of these reactive soils. The swell-shrink characteristics of expansive soils when subjected to alternate wet-dry cycles have caused severe repercussions for the light-weight structures founded on these clays [10-11]. Therefore, the geotechnical practitioners and researchers have identified the importance of the climate-ground interaction in expansive soils and investigated their behaviour under field and laboratory conditions during the past 2 decades [8-14]. Based on the current research, the variations in soil moisture causes changes in soil suction which eventually results in surface and sub-soil movements in expansive soil strata [8-10], [15-16]. Therefore, it is utmost important to determine the changes in soil moisture profile to investigate the expansive soil behaviour under different climatic conditions [8,9,15].

The monitoring of the soil water content in expansive soils has been conducted based on both destructive and non-destructive methods; however, the non-destructive methods are widely accepted due to minimum disturbance to long-term in-situ monitoring [17-19]. The radioactive non-destructive methods such as gamma-ray attenuation and neutron scattering have been mostly avoided due to possible health hazards. As a result, the non-destructive methods based on the dielectric constant of the media have been trending during the past decade to monitor the volumetric water content profile in expansive clays [20-23]. EC-5 moisture sensors can be identified for its wide application in research as non-destructive, dielectric sensors based on capacitance principle. The simplicity, cost and the ability to take point measurements due to small size have been beneficial for geotechnical practitioners when compared to the other commercially available options [24-28].

According to Decagon, EC-5 sensors use 70 MHz frequency which minimizes the textural and salinity effects [8,9,15,16]. The volumetric water content measurement of EC-5 sensors depend on the surrounding soil volume of the probes. The change in volumetric water content in expansive clays occurs due to the volume changes in both the surrounding soil and water [8,9,29,30]. Therefore, additional considerations for embedment and calibration of EC-5 sensors are required. Generally, these sensors capable of measuring the volumetric water contents of saturated soils up to 60%; however, is highly dependent on the soil [10,11,15,18,20,22].

EC-5 sensors are mostly soil-specifically calibrated for volumetric water content without incorporating the temperature effect due to the complexities involved in expansive soils [31-34]. This study presents a simple and practical approach to determine the temperature correction function for a given expansive clay. These findings may be useful for geotechnical practitioners and researchers to soil specifically calibrate EC-5 sensors maintaining high accuracy and thereby obtain a reliable moisture profile for their project-related decisions.

TEST MATERIAL

Natural expansive grey clay collected from Sherwood, Queensland, in Australia was used in this study. These grey Vertisol soils are widespread in the south-east Queensland region and representative of subsoil conditions in Brisbane. Infiltration in these soils is moderate-to-low and known for swell-shrink responses due to climate changes [35]. For laboratory model and element tests, 250 kg (dry soil mass) of expansive grey Vertisol was extracted and carefully transported to Queensland University of Technology (QUT) with in-kind support from 'The SoilTesters'.

The basic soil classification of the test material was conducted according to Australian Standards (AS 1289.3. 6.3, 2003; AS 1289.3.5.1, 2006; AS 1289.3.4.1, 2008; AS 1289.3.1.1, 2009a; AS 1289.3.2.1, 2009b; AS 1289.3. 6.1, 2009c). The grain size distribution of the test material was obtained from the combination of sieve and hydrometer analyses. It contains 77.3% fines (particles finer than 75 microns) and 50.2% of clay (particles finer than 2 microns). Other basic properties of the clay, including liquid limit (LL), plasticity index (PI), linear shrinkage (LS), and the specific gravity were determined in accordance with Australian Standard test methods, and they were 67%, 37.2 %, 13.4%, and 2.68, respectively [29-34]. The soil was classified as CH (Clay of High Plasticity) according to the Unified Soil Classification System (USCS). The compaction properties ($MDD = 1.75\text{g/cm}^3$, $OMC = 18\%$) were determined from the modified proctor compaction test. X-ray diffraction (XRD) analysis carried out on the test material identified smectite minerals, which predominantly contribute to the expansive nature of the soil.

METHODOLOGY

EC-5 sensors are ideal to measure soil moisture content in localized areas due to the small sensor length (50 mm) and its small area of influence. These sensors need to be properly calibrated for the temperature variations to obtain a precise representation of the sensor output due to the

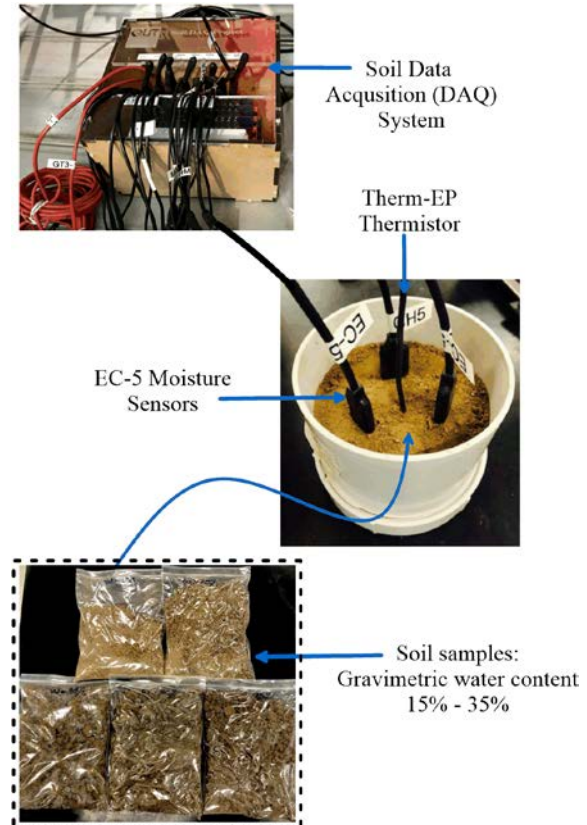


Fig. 1 – EC5 moisture sensor calibration and data acquisition

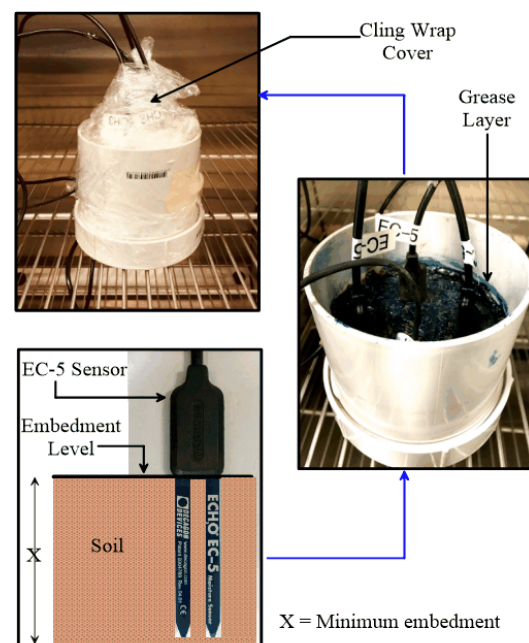


Fig. 2 – EC5 moisture sensor embedment in expansive soil

moisture variations within the range of 0-60% vwc. The independency to salinity and soil texture accompanied with low cost build-up makes EC-5s

preferable to use in research subsequent to rigorous soil specific calibration, resulting in 1-2% accuracy.

In this study, soil samples of five different known gravimetric moisture contents (i.e. 15%, 20%, 25%, 30% & 35%) were static compacted to achieve dry density of 1.2g/cm³. The entire sensor body of EC-5 sensors were embedded on the compacted soil as shown in fig. 1. The minimum sample height for the sensor calibration was maintained more than that of sensor body (i.e. 50 mm) to ensure the entire area is contacted by the soil to obtain a precise correlation between volumetric water content (%) and the sensor output voltage as shown in fig. 2.

Since EC-5 moisture measurements are very sensitive to temperature, temperature correction factors were developed by measuring soil moisture at different temperatures. Calibrated temperature sensor (Therm-EP) was embedded to acquire the temperature variation throughout the measuring duration. Soil moisture was maintained constant during the experimentation by applying a thick grease layer on the topsoil surface. Final gravimetric moisture content of the soil was measured by oven drying the test sample to make sure the moisture is successfully maintained. Likewise, the same procedure was adopted for all the moisture contents to derive a correlation between the volumetric water content (%), temperature (°C) and the sensor voltage output (V).

RESULTS & DISCUSSION

The results of this study investigate the volumetric water content variations of grey Vertosol at different temperature conditions. Figure 3 illustrates the variation of EC-5 moisture sensor responses under

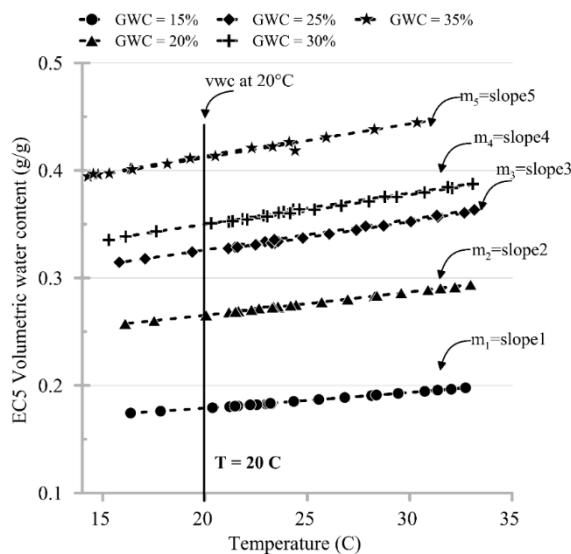


Fig. 3 – EC5 moisture sensor responses with temperature variations

controlled temperature variation inside the environmental chamber. Relative humidity inside the chamber was maintained at a reasonable value of 60% during the investigation. The experimental results indicated a significant variation of dielectric responses of EC-5 moisture sensors (vwc) when the temperature varies from 15°C to 33°C during heating and cooling cycles.

The volumetric water content of grey Vertosol at a given soil temperature can be derived with respect to 20 °C. Equations 1 and 2 demonstrate the representative calibration equation for EC-5 moisture sensor.

$$\theta_T = \theta_{20} - \varepsilon_T(m, \Delta T) \quad \text{Eq. 1}$$

$$\theta_T = (1.383 \times A_{EC5} - 1.0868) - [m \times (T - 20)] \quad \text{Eq. 2}$$

Where;

θ_T = Volumetric water content at T° C temperature

θ_{20} = Volumetric water content at 20° C temperature

$\varepsilon_T(m, \Delta T)$ = Temperature correction factor

m = Change in volumetric water content for unit change in temperature corresponds to volumetric water content of sample at 20° C

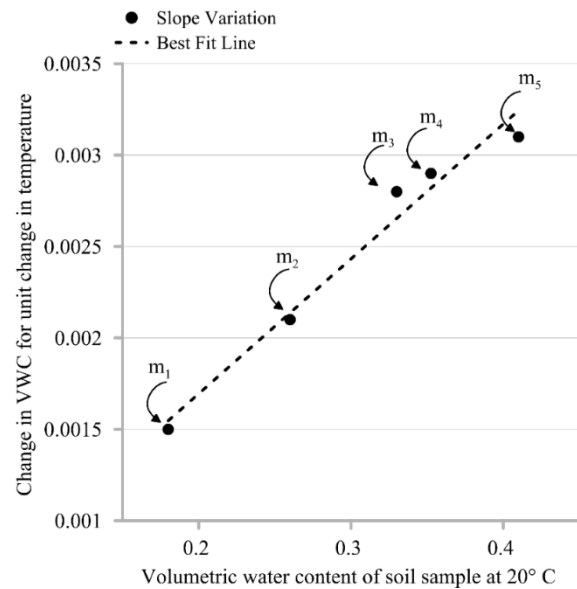


Fig. 4 – Sample slope variation with respect to the volumetric water content at reference temperature

The temperature calibration was conducted with respect to $T = 20^\circ \text{C}$ and ‘m’ value for Eq. 3 can be determined from Fig. 4 provided that volumetric water content of the soil at 20°C is known. Equation 3 presents the statistical relationship obtained between the ‘volumetric water content of soil at 20°C ’ and ‘change in vwc for unit change in temperature’ that can be used to derive Eq. 4; temperature calibrated volumetric water content of EC5.

$$m = 0.0074 \times \theta_{20} + 0.0002 \quad \text{Eq. 3}$$

$$\theta_T = (1.383 \times A_{\text{EC5}} - 1.0868) - \{0.0074 \times \theta_{20} + 0.0002\} \times (T - 20)$$

$$\theta_T = (1.383 \times A_{\text{EC5}} - 1.0868) - \{0.0074 \times (1.383 \times A_{\text{EC5}} - 1.0868) + 0.0002\} \times (T - 20) \quad \text{Eq.4}$$

Where;

A_{EC5} = Sensor voltage output from Soil DAQ

CONCLUSIONS

The climate-ground interaction of expansive clays is imperative to monitor to understand the soil responses due to climate variations. The volumetric water content of expansive soils has been identified as one of the critical parameters to investigate the stress state variables (i.e. soil suction and displacement) in such soils. The use of EC-5 moisture sensors to monitor the changes in volumetric water content profile has been trended due to low cost and simplicity of the sensors. However, the use of these sensors for expansive soil investigations requires the incorporation of temperature calibration. The complexities involved in the current calibration methods have restricted the use of these low-cost sensors.

This study introduced a practical and simple approach to accurately calibrate EC-5 sensors by incorporating the temperature effect. The method has been successfully validated for grey Vertosol and can be used to soil specifically calibrate any EC-5 sensor embedded in expansive clays. This approach enhances the applicability of low-cost EC-5 moisture sensors to accurately monitor the volumetric water content profile in expansive soils. Consequently, the quality of the data acquired can be maintained at a reliable state for the decision making of the end-user (i.e. geotechnical practitioners). As a result, the quality of the geotechnical application and eventually, the safety of human lives may be improved.

ACKNOWLEDGMENTS

Authors gratefully acknowledge the technical staff at Queensland University of Technology (QUT) for providing the on-campus & off-campus (Banyo Pilot Plant) laboratory facilities to conduct the test series. Further, the gratitude should be extended to Steve Hackworth from THE SOILTESTERS for providing the in-kind support for the project. The first author acknowledges the scholarship for doctoral degree received from QUT, Australia.

REFERENCES

- [1] Abeykoon A, Gallage C.P, Dareeju B.S, Trofimovs J. 2018. Real-time monitoring and wireless data transmission to predict rain-induced landslides in critical slopes, *Australian Geomechanics Journal*, 53 (3), p61-76.
- [2] Gallage C, Kodikara J.K., Uchimura T. 2013. Laboratory measurement of hydraulic conductivity functions of two unsaturated sandy soils during drying and wetting processes, *Soils and Foundations*, 53 (3), p417-430.
- [3] Garcia E.F., Gallage C., Uchimura T. 2007. Function of permeable geosynthetics in unsaturated embankments subjected to rainfall infiltration, *Geosynthetics International*, 14 (2), pp. 89-99.
- [4] Gallage C., Tehrani N., Williams D. 2017. Instrumented large soil-column to investigate climate-induced ground deformation in expansive soil, *Proceedings of the 19th International Conference on Soil Mechanics and Geotechnical Engineering*, p1147-1150.
- [5] Gallage C., Jayakody Arachchige S., Uchimura T. 2012. Effects of slope inclination on the rain-induced instability of embankment slopes, *Proceedings of the Second International Conference on Geotechnique, Construction Materials and Environment*, p196-201.
- [6] Shannon B., Gallage C., Kodikara J.K. 2010. Experimental modelling of coupled water flow and associated movements in swelling soils, *Proceedings from the 3rd International Conference on Problematic Soils*, p295-302.
- [7] Gallage C., Garcia E., Peiris A., Uchimura T., Ochiai, H. 2005. Use of soil-water characteristics curve in determination of stability of embankments during drying and wetting processes, in *Advanced experimental unsaturated soil mechanics: Proceedings of the International Symposium on Advanced Experimental Unsaturated Soil Mechanics 2005*, Italy, Trento, pp. 351-358.
- [8] Udukumburage R.S., 2019. Laboratory based parametric study on the swell responses in

- expansive vertosols. *International Journal of GEOMATE* 17(64): 185–191.
- [9] Udukumburage R.S., Gallage C. and Dawes L., 2018. Loaded swell tests to estimate the heave of the expansive soil in instrumented soil column. In *Proceedings of the 8th International Conference on Geotechnique, Construction Materials and Environment*, GEOMATE (Huat B, Shiau J, Hossain Z and Anggraini V (eds)). The GEOMATE International Society, Kuala Lumpur, Malaysia, pp. 390–395.
- [10] Udukumburage, R.S., 2020. Investigation of climatic-induced ground responses in expansive soils (Doctoral dissertation, Queensland University of Technology).
- [11] Udukumburage, R.S., Gallage, C., and Dawes, L., 2020. An instrumented large soil column to investigate climatic ground interaction, *International Journal of Physical Modelling in Geotechnics*, 1-17.
- [12] Gallage C and Uchimura T., 2010. Effects of dry density and grain size distribution on soil-water characteristic curves of sandy soils. *Soils and Foundations* 50(1): 161–172.
- [13] Gallage C, Kodikara JK, Chan D and Davis P., 2008. A comparison of the results of the numerical analysis and the physical behaviour of a pipe buried in reactive clay. In *Proceedings of the 12th International Conference of the International Association for Computer Methods and Advances in Geomechanics*, Goa, India (Jadhav M (ed.)), pp. 1276–1284.
- [14] Chan D, Rajeev P, Kodikara JK, Gallage CP, [2016] Field performance of in-service cast iron gas reticulation pipe buried in reactive clay, *Journal of Pipeline Systems Engineering and Practice*, 7 (2), p1-15
- [15] Udukumburage, R.S., Gallage, C., and Dawes, L., 2019. Investigation of the effect of initial water content and surcharge on volume change behaviour of compacted grey Vertosol, In *13th Australia New Zealand Conference on Geomechanics*, Sydney, Australia, pp. 1029-1033.
- [16] Udukumburage R.S., Gallage C. and Dawes L., 2019. Oedometer based estimation of vertical shrinkage of expansive soil in a large instrumented soil column. *Heliyon* 5(9): e02380.
- [17] Sakaki, T., Limsuwat, A., Smits, K.M. and Illangasekare, T.H., 2008. Empirical two - point α - mixing model for calibrating the ECH2O EC - 5 soil moisture sensor in sands. *Water resources research*, 44(4).
- [18] Cobos, D.R. and Chambers, C., 2010. Calibrating ECH2O soil moisture sensors. Application note, pp.1-5.
- [19] Rosenbaum, U., Huisman, J.A., Weuthen, A., Vereecken, H. and Bogaen, H.R., 2010. Sensor-to-sensor variability of the ECH 2 O EC-5, TE, and 5TE sensors in dielectric liquids. *Vadose Zone Journal*, 9(1), pp.181-186.
- [20] Kodikara J, Rajeev P, Chan D and Gallage C., 2014. Soil moisture monitoring at the field scale using neutron probe. *Canadian Geotechnical Journal* 51(3): 332–345.
- [21] Kizito, F., Campbell, C.S., Campbell, G.S., Cobos, D.R., Teare, B.L., Carter, B. and Hopmans, J.W., 2008. Frequency, electrical conductivity and temperature analysis of a low-cost capacitance soil moisture sensor. *Journal of Hydrology*, 352(3-4), pp.367-378.
- [22] Bogaen, H.R., Huisman, J.A., Oberdörster, C. and Vereecken, H., 2007. Evaluation of a low-cost soil water content sensor for wireless network applications. *Journal of Hydrology*, 344(1-2), pp.32-42.
- [23] Kodešová, R., Kodeš, V. and Mraz, A., 2011. Comparison of two sensors ECH2O EC-5 and SM200 for measuring soil water content. *Soil and Water Research*, 6(2), pp.102-110.
- [24] Gallage C, Chan D and Kodikara J., 2012. Response of a plastic pipe buried in expansive clay. *Proceedings of the Institution of Civil Engineers – Geotechnical Engineering* 165(1): 45–57.
- [25] Gallage C, Tehrani K and Williams D., 2017a. Instrumented large soil-column to investigate climate-induced ground deformation in expansive soil. *Proceedings of the 19th International Conference on Soil Mechanics and Geotechnical Engineering*, Seoul, Korea (Kim D (ed.)). ISSMGE, London, UK, pp. 1147–1150.
- [26] Gallage C, Udukumburage R, Uchimura T and Abeykoon T., 2017b. Comparison of direct and indirect measured soil-water characteristic curves for a silty sand. *International Journal of GEOMATE* 13(39): 9–16.
- [27] Gallage C, Uchimura T, 2016. Direct shear testing on unsaturated silty soils to investigate the effects of drying and wetting on shear strength parameters at low suction, *Journal of Geotechnical and Geoenvironmental Engineering*, 142 (3), p1-9
- [28] Chan D, Rajeev P, Gallage C and Kodikara J., 2010. Regional field measurement of soil moisture content with neutron probe. In *Proceedings of the Seventeenth Southeast Asian Geotechnical Conference* (Li J and Lin M (eds)). Taiwan Geotechnical Society, Taipei, Taiwan, pp. 92–95.
- [29] Chan D, Gallage C, Rajeev P and Kodikara J., 2015a. Field performance of in-service cast iron water reticulation pipe buried in reactive clay. *Canadian Geotechnical Journal* 52(11): 1861–1873.
- [30] Chan D, Rajeev P, Kodikara J and Gallage C., 2015b. Field performance of in-service cast iron gas reticulation pipe buried in reactive clay. *Journal of Pipeline Systems Engineering and*

- Practice 7(2): 04015025.
- [31] Parsons, L.R. and Bandaranayake, W.M., 2009. Performance of a new capacitance soil moisture probe in a sandy soil. *Soil Science Society of America Journal*, 73(4), pp.1378-1385.
- [32] Limsuwat, A., Sakaki, T. and Illangasekare, T.H., 2009. Experimental quantification of bulk sampling volume of ECH2O soil moisture sensors. *Proceedings of the 29th Annual American Geophysical Union Hydrology Days*, 25, p.27.
- [33] Chung, W.Y., Villaverde, J.F. and Tan, J., 2013. Wireless Sensor Network Based Soil Moisture Monitoring System Design. In *FedCSIS Position Papers* (pp. 79-82).
- [34] Francesca, V., Osvaldo, F., Stefano, P. and Paola, R.P., 2010. Soil moisture measurements: Comparison of instrumentation performances. *Journal of irrigation and drainage engineering*, 136(2), pp.81-89.
- [35] Isbell, R., 2016. *The Australian soil classification*: CSIRO publishing.

EXISTENCE OF SILT SEAM LAYER TRIGGERING FLOW LIQUEFACTION ON THE PALU M_w 7.5 EARTHQUAKE 2018

Dandung Sri Harninto¹ and Widjoyo A. Prakoso²
^{1,2} Civil Engineering and Environmental, Indonesia University, Indonesia

ABSTRACT

Palu M_w 7.5 earthquake on 28 September 2018 caused extra ordinary geotechnical event in the world. Not only building damage, tsunami caused by submarine landslide, but also the most dramatically event was huge scale of flow liquefaction. In the area studied, flow movement was more than 100 meters. Another location, the flow was more than 1,000 meters. This must be extra ordinary phenomena of liquefaction, which never happen at other sites in the world so far. Geological formation of Palu city has been formed from young alluvial fan which have sourced from mountain at east-west of the city. The formation is dominated by loose non-cohesive material, and fully saturated due to very shallow ground water table. Sedimentation has been occurred layer by layer for long time process, then it formed layers with variety of density and hydraulic properties. Moreover, during these processes there were chance of weathering, and this could form series of layer with low permeability called silt seam. In order to find out presence of silt seam layer inside deposit we have conducted trenching observations. There were three pits of trenching, with depth 5-meters and 30-meters length in one location of flow liquefaction called Lolu Village. Appreciation for non-commercial map application which can help make superimpose before-after earthquake map with quite good precision. By the superimpose this trenching successfully dug cross between flow and non-flow liquefaction area and cut one sand boil structure. So that we could differ layers of soil between these areas correctly by finding existence of silt seam interlayer. By using void redistribution/water film theory from Kokusho [24], this report will explore possibility facts as triggering huge magnitude of flow liquefaction.

Keywords: Palu Earthquake 2018, Liquefaction, Trenching, Silt Seam

INTRODUCTION

M_w 7.5 earthquake struck Palu and Donggala City, Central Sulawesi, Indonesia on 28 September 2018, as consequence of releasing energy of Palu-Kore fault where aligned west side of Palu City. This event created several catastrophic disasters, and caused large number of casualties, destroyed housings, buildings, and many infrastructures such roads, power lines, bridges, and water channels, etc. Tsunami, ground shaking, landslide arrived almost at the same time and the most extreme liquefaction disaster ever on earth caused by earthquake.

Indonesia Meteorology, Climatology and Geophysical Agency [4] reported that epicenter of the mainshock was about 72 km north of the city with depth 10 km. Series of significant foreshocks ($M_w > 4.4$) occurred four hours before and main shock arrived with magnitude M_w 7.5, and it was followed also by series of aftershocks ($M_w > 5.7$) for the period of 48 minutes since main shock. Epicenters of significant foreshocks-mainshock-aftershocks were documented sweep over area Palu City (fig. 1).

BMKG and JICA (Japan International Corporation Agency) [1] have released time history data of ground acceleration of mainshock from one survival seismograph station near Palu City (Balara Station) as fig. 2. Unfortunately, for other shocks writer have no access to get them. If we studied series

of earthquake magnitude data in table fig. 3 from BMKG, other ground accelerations record should be significantly contributed for generating extreme disaster, especially liquefaction. BMKG web site (link: <http://shakemap.bmkg.go.id>) shown spread out earthquake magnitude data (as table at fig. 3). Recognition from level of catastrophic occurred [2], USGS reported a much larger peak ground motion acceleration and reached magnitude of 0.7g and this value might be possible (fig. 2).

Before the Palu 2018 earthquake -for example devastating liquefaction in Niigata, Japan (1964) and Alaska, USA (1964)-, lateral spreading had magnitude of teen meters or even less and prompted some differential settlement which generated tilting of buildings or houses. However, Palu earthquake generated not only common liquefaction occurred, but also hundred meters either lateral spreading or soil mass flow which brought all objects moving downslope with very gentle grade (2-3 %). Liquefaction itself so far has never made fatalities, but the liquefaction spawned thousand fatalities, buried, and revolved them under deposit of sand which changed from solid transformed to mud (liquid) for some period.

Palu City, Indonesia is located at complex tectonic formation where collision of three plates comprising

Eurasian, Indo-Australia, and Philippines Sea. Besides. There were at least three features of Palu city associated to liquefaction disaster:

1. Palu city is just located across Palu-Kora fault, aligned from north to south of the city. This fault has slip rate around 58 mm/year [13]. This tectonic landscape will make Palu city become very susceptible to high earthquake event..
2. Palu low land mostly consist of young alluvium formed by sediment transport from east and west side of mountains [2]. In general, deposit mostly originate from boulder, gravel, and sand with loose consistency. Natural water stream called Palu river divide the city at centre with slope of valley around 1-6 %.
3. The valley area is located at middle of mountains; annual rain intensity is extremely low at most 500-mili meter annually. Conversely, ground water table was very shallow and there were some water springs blown up ground surface and possibility artesian spring. There was unlined water irrigation canal system at eastern part of the city which has been operating since 80', many experts alleged that this canal had contributed significantly saturated sand deposit at east side of Palu [1], [5], [12].

LIQUEFACTION

Liquefaction is a phenomenon where saturated soil deposit reduces stiffness and strength due to the generation of high excess pore pressures during earthquake shaking. In certain condition the excess could be the same with total overburden pressure ($r_u=1$), and then effective pressure practiced zero, it means solid soil deposit for the time being behaves as liquid. Evidence of liquefaction in the event had been onsite, we found number of sand boils footprint (fig. 5). Sand boil structure is formed by sand ejecta from sand deposit of underlayer as releasing excess pore water pressure which brought some fraction of sand.

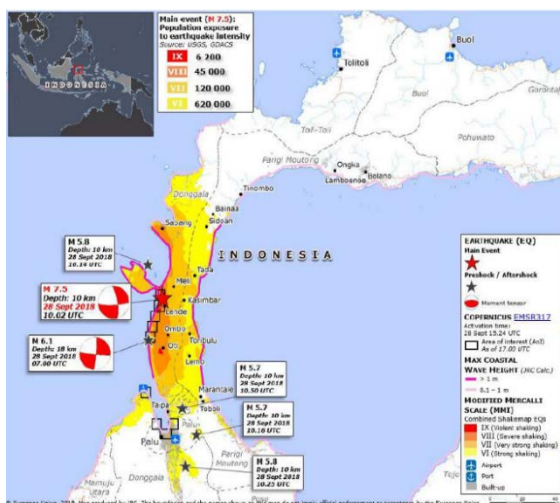


Fig. 1 Epicenter of the earthquake [2]

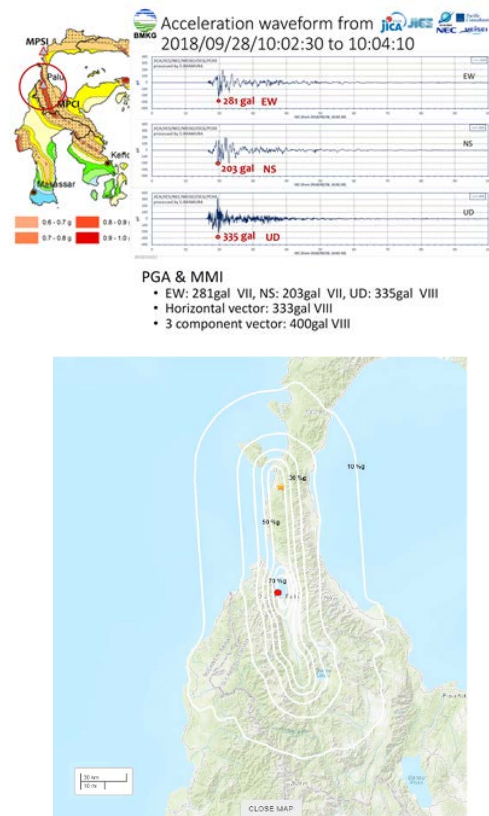


Fig. 2 Time history of ground acceleration BMKG&JICA (2018) [1] & USGS PGA data [2]

28-09-2018 18:42:49 WIB	-1.20	119.84	4.8	10 Km	Minahassa Peninsula, Sulawesi	ShakeMap	Station List
28-09-2018 18:39:13 WIB	-0.51	119.75	4.7	10 Km	Minahassa Peninsula, Sulawesi	ShakeMap	Station List
28-09-2018 18:36:28 WIB	-0.42	119.76	4.4	10 Km	Minahassa Peninsula, Sulawesi	ShakeMap	Station List
28-09-2018 17:50:28 WIB	-0.76	120.04	5.9	10 Km	Minahassa Peninsula, Sulawesi	ShakeMap	Station List
28-09-2018 17:47:45 WIB	-0.46	119.91	5.0	10 Km	Minahassa Peninsula, Sulawesi	ShakeMap	Station List
28-09-2018 17:34:53 WIB	0.04	119.76	4.7	10 Km	Minahassa Peninsula, Sulawesi	ShakeMap	Station List
28-09-2018 17:25:05 WIB	-0.98	119.99	5.7	14 Km	Minahassa Peninsula, Sulawesi	ShakeMap	Station List
28-09-2018 17:16:51 WIB	-0.8	120.01	5.8	10 Km	Minahassa Peninsula, Sulawesi	ShakeMap	Station List
28-09-2018 17:14:25 WIB	0.09	119.94	6.1	10 Km	Minahassa Peninsula, Sulawesi	ShakeMap	Station List
28-09-2018 17:14:21 WIB	0.1	119.83	6.3	17 Km	Sulawesi, Indonesia	ShakeMap	Station List
28-09-2018 17:02:45 WIB	-0.2	119.89	7.4	11 Km	Sulawesi, Indonesia	ShakeMap	Station List
28-09-2018 17:02:44 WIB	-0.18	119.85	7.7	10 Km	Minahassa Peninsula, Sulawesi	ShakeMap	Station List
28-09-2018 17:02:43 WIB	-0.22	119.85	7.4	10 Km	Minahassa Peninsula, Sulawesi	ShakeMap	Station List
28-09-2018 15:25:01 WIB	-0.38	119.96	5.1	10 Km	Minahassa Peninsula, Sulawesi	ShakeMap	Station List
28-09-2018 14:28:37 WIB	-0.35	119.87	4.9	10 Km	Minahassa Peninsula, Sulawesi	ShakeMap	Station List
28-09-2018 14:17:14 WIB	-0.09	119.86	4.6	10 Km	Minahassa Peninsula, Sulawesi	ShakeMap	Station List
28-09-2018 14:11:17 WIB	-0.35	119.96	4.4	10 Km	Minahassa Peninsula, Sulawesi	ShakeMap	Station List
28-09-2018 14:00:00 WIB	-0.35	119.82	5.9	10 Km	Minahassa Peninsula, Sulawesi	ShakeMap	Station List

Fig. 3 Magnitude of foreshock, mainshock and aftershock of Palu earthquake 2018 [4]

As Bradley [12] reported that mostly downhill area of unlined canal occurred lateral spreading (figure 4) with variation of magnitude. The crown of slide was generally along irrigation canal, however, at uphill of canals were still good, no evidence either liquefaction or lateral spreading at all. However, in several areas such as at Petobo, Lolu Village and Jono Oge (Sidera) where occurred in hundred-meter of spreading and it engendered huge number of casualties especially at Petobo area (fig. 4).

Basic mechanism could be the same for all locations -even though the thesis is being still debatable-. It started with fluidization of certain area of sand deposit which initiated by liquefaction, with gentle slope of land commenced a long-distance lateral spreading caused by gravitational force. At the upper part of the area started to retrogressive collapse which caused by lost their counterweight at toe,

underwent high excess pore water pressure created water sprang out (seepage) huge volume of water on surface and perhaps followed by land subsidence as consequently of sand deposit contraction process. Water mixed with fine sand-silt formed mud flow and sparked more destructive process. Finally, all eroded and debris material with very high-water content glided to downstream or stacked create deposition fill. The hypothetic mechanism has not firmed yet, many researchers are still working to discover accurate one.

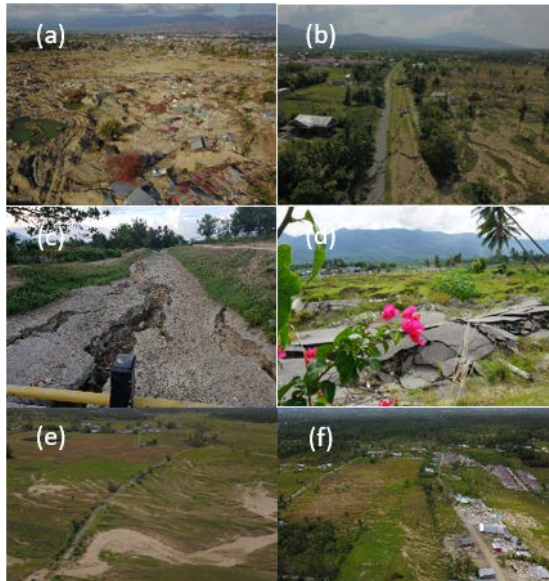


Fig. 4 Disaster footprints: (a) Balaroa, (b) Petobo, (c) Petobo Irrigation Canal, (d) South Sibalaya, (e) Jono Oge, (f) Lolu Village

The above mechanism proposed by writer was similar with Manson [2]. This suggestion is without any contribution of breakage of confined aquifer. Since JICA [9] suggested that there was contributed of confined aquifer breakage which maintenance excess pore water pressure kept high, this was argued by Ishihara [11] as well. This hypothesis must be quite difficult to be proven, even though that will be possibility happened. However, all the above mention



Fig. 5 One of sand boil at Lolu Village site

Hall [5] and Bradley [12] that construction and operation an unlined agriculture canal (fig. 4 & fig.6) had played a large role in the slope failure. Yearly water seepage from the canal increased height of water table accordingly saturated the underlaying loose soil layer and caused of it making them liquefaction prone.

To know magnitude of lateral displacement, we also have measured magnitude of lateral spreading use Google Earth Pro. At time being, we have been only focusing at Lolu Village site with some reason which will be discussed later. We use figure published by Bradley [12], to help describe magnitude of lateral spreading. The longest distance was 155-meters (yellow arrow line), and relative long distance occurred at northern part of area. At southern part, displacement distance was average 70-meters. At eastern part or upper hill, lateral displacement was average 25-meters. Outside landslide area, many objects were measured as well where lateral movement with magnitude less than 10-meters.

TRENCHING OBSERVATIONS

There must be distinct onsite sand deposit characteristic to make as discussed above could

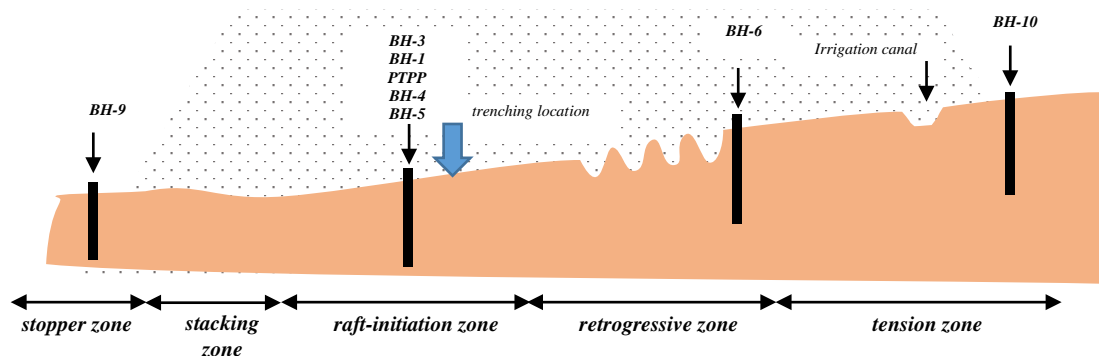


Fig. 6 Alienation of flow and affected area

researchers have agreed including Watkinson and

happen. Understanding of this mechanism is

important since the flow liquefaction areas were most deadly compare to outside area. It should be valuable for mitigation hazards purposes for next communal settlement planning. Lolu Village was exceptional site and thought as main mechanism of purely liquefaction without any involvement from other force such as water inundating from breakage of main water canal. Except Balaroa, other big lateral spreading including Petobo, Jono Oge and South Sibalaya, all of them involved huge volume of water from breakage canal since top-crown of landslides were also started at breakage of canal. Understanding at Lalo Village will be useful to recognize mechanism for other areas, because magnitude moving objects at ground surface were triggered purely by liquefaction.

We have divided Lolu Village liquefaction area into two area; called “flow area” and “affected area”. Flow area is inside blue line (fig. 5) where lateral spreading generated more than 10-meters till maximum 153 meter and affected area is outside where less than 10-meter. As discussed above about basic mechanism argued by writer at long direction (east to west), the area has been alienated into several zones (fig. 6): tension, retrogressive, raft-initiation, stacking and stopper zone.

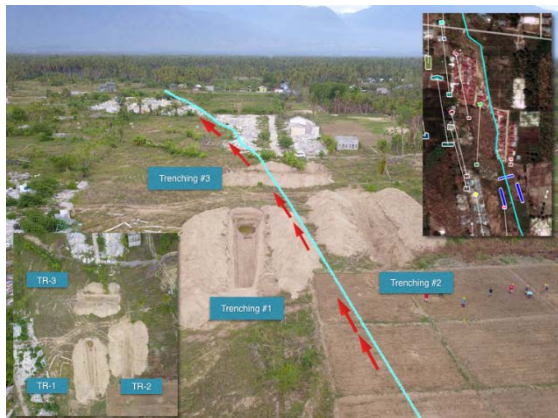


Fig. 7 Orientation of trenching at Lolu Village slide area

In order to understand basic mechanism between two kind of area, we have conducted trenching observation to recognize layering of soil at two areas. Trenching were excavated of three pits at raft-initiation zone (fig. 6). First was at flow area alongside with movement direction called trenching #1. Second was at affected area called trenching #2 and third was perpendicular with slide movement, cross flow and affected area called trenching #3. These trenching were excavated in April 2019 or six months aftermath. Dimension of trenching pit were approximately 5-meters wide, 5-meters depth and 30 meters long. Orientation of trenching plotted over area can be seen at fig. 7.

Log clustering of trenching wall have been done soon after preparing clear surface. After trenching excavation with heavy equipment (excavator), wall

surface was carefully cleaned to have clearer surface with smaller equipment such as brush, hoe, trowel, and geology hammer. Kind of deposit based on grain composition are defined to ease clustering with either eye or hand feeling. We created grid line 50x50 cm over the wall surface with synthetics rope, these grids will help to draw cluster according to grain composition. We have defined into seven fractions: sand-gravel-boulder (SGB), sand-gravel (SG), coarse-sand (SC), fine-sand (FS), sandy-silt (SS), clay-silt-plastics (CSP), and top-soil (TS). Perhaps these clustering were not precisely caused defined only by eye or hand-feeling. Even though, this method needs extra work and extra care to draw cluster correctly, if we only define from photo taken, stratigraphy created by excavator bucket will confuse to differ one cluster with another cluster.

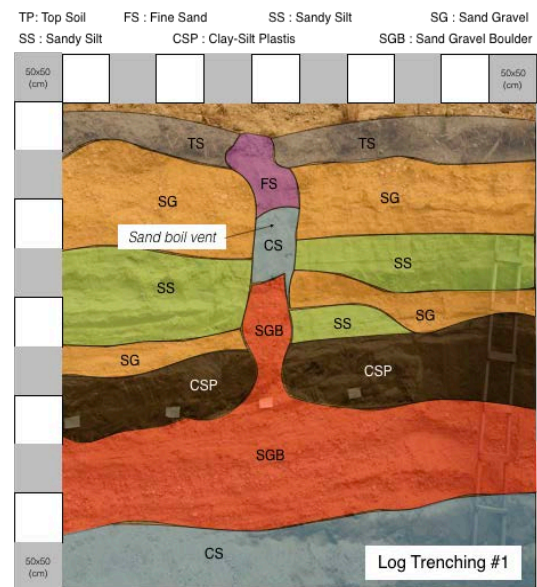


Fig. 8 Interpreted trench log trenching#1 south wall

We fortunately disclosed cross section of sand boil footprint which had reservoir of deposit started at sand-gravel-boulder (GB layer), please refer to fig. 8. At first one meter, composition of sand boil at throat was still the same with reservoir resource. And then next 0.5-0.75 bigger grain fraction had left underneath only finer sand was able to be flowed up,

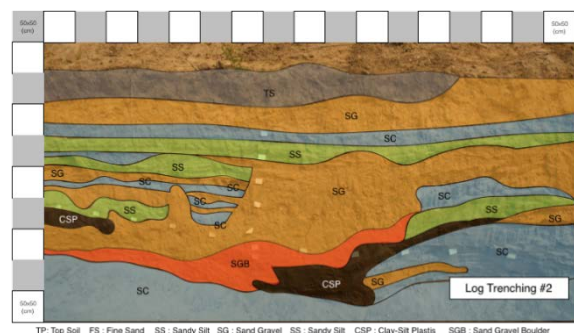


Fig. 9 Interpreted trench log trenching#2 south wall

1-meter rest was fully of fine sand at vent and created crater at surface.

This log fig. 9 is at affected area, we did not find a continue clay silt plastic layer. Layering of deposit was observed not too regular if it compares to flow area. Clay-silt-plastics fraction was also presence, however not too significant, and formed in-regular formation. Mostly the deposit consists of sand gravel and some interbedded sandy silt. Possibility this deposit experienced random movement instead of block (raft) movement. Unfortunately, we did not discover any sand boil at this section, even this area also had number of sands boil. But if we look at layering deposit form of sand gravel (SG) which punched the above layer indicated there was high excess pore water pressure which try to push up to surface.

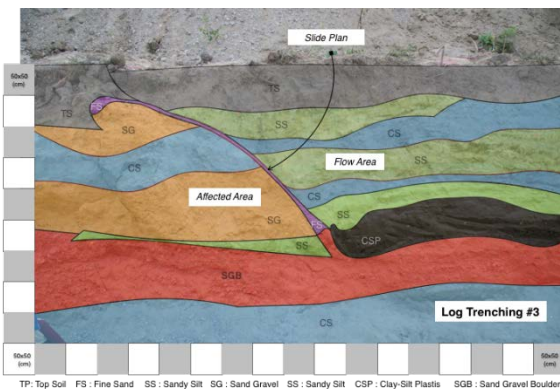


Fig. 10 Interpreted trench log trenching #3 east wall

At cross section between flow area and affected area, at slide surface there was a thin fine sand path started from reservoir of sand-gravel-boulder continue till surface (fig. 10). The footprint of this phenomena can be seen from photo taken (fig. 11), along the boundary there were huge quantity of fine sand which blown up and spread over this boundary line. During releasing excess pore water pressure, this zone supposed to be conduit “long sand boil”.

From our trenching work, we have concluded that at elevation -3-meters from ground surface on we have found clay silt plastic layer which have permeability much lower than both above and under their layer with thickness 0.3 up to 0.5-meters on both area of trenching at the same level. We predict that thickness of significant movable layer was about 3.0-meter at this trenching point, it is also just confirmed by fact result at trenching #1. However, if we look magnitude of lateral deformation at southern part of flow area with longer distance and then the thickness of movable layer could be much thicker.

DISCUSSION

Kokusho [24] has proposed useful theory to explain such kind of phenomena. Series of laboratory and onsite research work done by him contribute

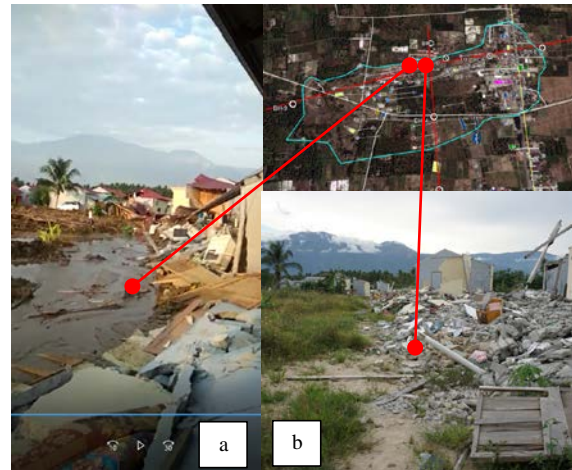


Fig. 11 Long continue sand boil at boundary line affected area and flow area (a) one day aftermath (b) four months aftermath

significantly to understand this mechanism. Void redistribution which generated during and after shaking will become basic theory to develop other factors. Trenching observation has been conducted as advise from him to knowing what real mechanism inside sand deposit.

Simple mechanism for the stable water film generation schematically indicated in fig. 12. The series of test results clearly indicates that a water film is readily formed just after the onset of liquefaction beneath a sandwiched sublayer with smaller permeability and stays there much longer than the re-sedimentation time of the liquefied sand particles. This indicates that the liquefied sand is actually in the drained condition locally, allowing the void

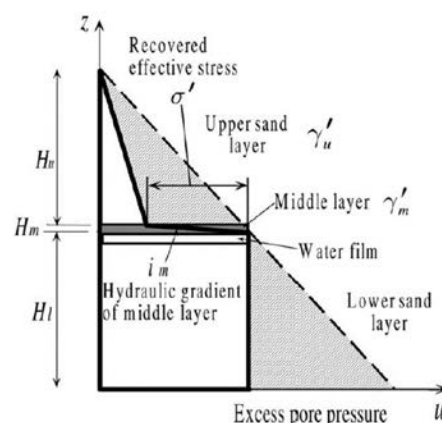


Fig. 12 Water film/void redistribution generation mechanism [24]

redistribution to occur. Soil layering structures providing this mechanism seems to be abundant in the field, introducing multiple water films at different depths [24].

From three pit trenching observations which have explored already, we argue that void redistribution/water film had been engendered during or especially just after earthquake shaking. This argument has been proven by presence of seam silt or clay silt plastics at elevation -3 meters from ground surface. We cannot explore more deeper layer because either stability of trenching consideration or we had reached ground water level.

We realized that trenching has successfully explored only small and shallow part of either huge movement part or right mechanism, it still could be cannot catch up whole mechanism yet. However, from trenching data taken can be concluded an important point: that seam silt was exist at least single layer at elevation app. 3-meters and this is become one of boundary the releasing excess pore water pressure trap. During earthquake and aftermath, there were possibility that underneath this layer generated thick water film which have zero shear strength, this layer was being one of slide surface of the deposit. If there were series of silt seam, and all of them were creating series of water film layer at the same time, and then it can be understood that long distance gliding of mass soil could be happen.

If we learned from sand fraction inside conduit of sand boil, we have speculated there was a big excess water pressure bult up under silt seam layer. Because not only fine fraction which forcing up but also gravel also flown up from reservoir of sand-gravel-boulder (SGB) underneath. Deeper elevation of liquefied layer should have higher excess pore water pressure and stayed inside the deposit for long time caused many “obstacles” from silt seam for releasing pressure and created water film for long time as well. This condition had maintained deposit in liquid phase for relative long period and gave enough time to glide or flow long distance of displacement to downhill.

CONCLUSION

Liquefaction disaster caused by Palu Earthquake 2018 have been still generating questions for many researchers in the world. Geology and geotechnical mechanism have been developing to know what exactly occur inside the sand deposit. Writer have tried also contributing to enrich knowledge by conduct trenching observations and other series of series to explore possibility scenario. This report has concluded some important as follow thought:

1. Presence of silt-clay-plastics layer have played important contribution to product long distance of lateral spreading, and by trenching observation this thesis has been proven at location we conduct the test.
2. From interpretation log, there are some cluster of sand-silt, this content called non-plastic fine grain. Existence of such kind of deposit as proposed by Kokusho [24] cause soil deposit underwent

contraction during shear loading. Contraction inside saturated sand deposit will generate excess pore water pressure. High excess pore water pressure will maintain soil in liquid phase.

3. Trenching observations has provided new term of liquefaction. Sand boil so far only have point of crater, however now we recognize long continue sand boil plane where fine sand blown up along the boundary line of sliding.
4. Many “obstacles” from silt seam for releasing excess pore pressure. This condition had maintained deposit in liquid phase for relative long period and gave enough time to glide or flow long distance of displacement to downhill till deposit came back to solid state and stopped.
5. Because limitation depth of trenching with consideration of safety and elevation of ground water level, the exact presence of silt seam is only limitation in range of 5 meters depth. For other depth we need other method, CPT will be reliable test to know in detail presence of silt seam at other depths.

Writer advice that further research should be conducted to understanding more accurate regarding the mechanism. As fact found at this trenching, writer recommend other method to get un-disturb sample. If possible, a continue sample so that we will know exactly presence of silt-seam at other depths let say till 20- or 30-meters depth. Because with long magnitude of lateral movement must involve very thick liquefied layer of deposit.

ACKNOWLEDGMENT

We have many parties to thank for giving encouragement of this report: our team in University Indonesia especially Prof. Widjono A. Prakoso, Past immediate Chairman of Indonesia Society for Geotechnical Engineering (HATTI) Prof. Masyhur Irsyam and team, and GEER (Geotechnical Extreme Events Reconnaissance), USA team including H. Ben Banson, Aron P. Gallant, Jack Montgomery, Joe Wartman, and Daniel Hutabarat for worth moment along with all them for site reconnaissance joint survey in Palu. We would like also to thank for many valuable discussion and lecture from Kenji Ishihara, Susumu Yasuda, Takeji Kokusho, Ikou Towhata and Hisashi Furuichi (JICA) during they visited on site in Palu and series of lecture in Jakarta, Indonesia.

REFERENCE

- [1] Andhika Sahadewa, Masyhur Irsyam, Rahma Hanifa, Andi Kartawiria, Agus Himawan, Requel Mikhail, Dandung Sri Harninto, Agus Muntohar, Didiek Djarwadi, Widjono Prakoso, D.H. Natawijaya, Hamzah Latief, M. Asrurifak, L. Faizal, A. Sabarudin, Sigit Pramono, M. Daryono, Ramli Nazir (2019), Geotechnical

- Overview of the 2018 Indonesia Palu Earthquake”, Handout of VII International Conference on Earthquake Geotechnical Engineering, Rome, Italy, 17-20 June 2019.
- [2] Aaron P. Gallant, Jack Montgomery, H. Benjamin Mason, Daniel Hutabarat, A. Nicole Reed, Joseph Wartman, Masyhur Irsyam, Pintor T. Simatupang, Idrus M. Alatas, Widjojo A. Prakoso, Didiek Djarwadi, Rahma Hanifa, Paulus Rahardjo, Lutfi Faizal, Dandung S. Harninto, Aksan Kawanda, Agus Himawan, Widodo Yasin (2019), “The Sibalaya flowslide initiated by the 28 September 2018 MW 7.5 Palu-Donggala, Indonesia earthquake”, Landslides DOI 10.1007/s10346-020-01254-1.
 - [3] H. Benjamin Mason, Aaron P. Gallant, Daniel Hutabarat, Jack Montgomery, A. Nicole Reed, Joseph Wartman, Masyhur Irsyam, Widjojo Prakoso, Didiek Djarwadi, Dandung S. Harninto, Idrus Alatas, Paulus Rahardjo, Pintor Simatupang, Aksan Kawanda, Rahma Hanifa (2019), Geotechnical Reconnaissance: The 28 September 2018 M7.5 Palu-Donggala, Indonesia Earthquake Version 1.0. Geotechnical Extreme Events Reconnaissance Report.
 - [4] Indonesia Meteorology, Climatology and Geophysical Agency, 2018 <http://shakemap.bmkg.go.id>
 - [5] Ian M. Watkinson and Robert Hall , Impact of Communal Irrigation of the 2018 Palu Earthquake-triggered Landslid. Nature Geoscience, 2019, Article 10.1038/s41561-019-0448-x.
 - [6] Ikuo Towhata, Geotechnical Earthquake Engineering. 2008, Springer.
 - [7] Ikuo Towhata, Shogo Maruyama, Kin-ichi Kasuda, Junichi Koseki, Kazue Wakamatsu, Hiroyoshi Kiku, Takashi Kiyota, Susumu Yasuda, Yuichi Taguchi, Shogo Aoyama, Toshihiko Hayashida, Liquefaction in the Kanto region during the 2011 off the pacific coast of Tohoku earthquake. Soil and Foundations, 2014, 54(4):859-873.
 - [8] I.M. Idriss, R.W. Boulanger, Semi-empirical procedures for evaluating liquefactionpotential during earthquakes. Soil Dynamics and Earthquake Engineering, 2006, 26 : 115-130.
 - [9] JICA Study Team, Brief Explanation of “Nalodo” Assessment & Mitigation”, Handout National Workshop on Joint Research. Assesment Mitigation of Liquefaction Hazards on 9th October 2019, Indonesia University.
 - [10] Kenji Ishihara (1993), Liquefaction and Flow Failure During Earthquake, Geotechnique 43, 1993, No.3, 351-415.
 - [11] Kenji Ishihara, Site Characterization of Behavior of Sandy Soils, Handout National Workshop on Joint Research, Assessment Mitigation of Liquefaction Hazards, 2019, Indonesia University.
 - [12] Kyle Bradley, Rishav Mallick, Harisma Andikagumi, Judith Hubbard, Ella Meilinda, Adam Switzer, Nairong Du, Gilles Brocard, Dedy Alfian, Benazir Benazir, Guangcai Feng, San-Ho Yun, Jędrzej Majewski, Shengji Wei and Emma M. Hill, Earthquake-triggered 2018 Palu Valley Landslides Enabled by Wet Rice Cultivation, Nature Geoscience, 2019, Article 10.1038/s41561-019-0444-1.
 - [13] Mudrik Rahmawan Daryono, Paleoseismologi Tropis Indonesia (Dengan Studi Kasus Di Sesar Sumatra, Sesar Palukoro-Matano, dan Sesar Lembang), Disertasi Doktor Program Studi Sain Kebumian, 2016, Institut Teknologi Bandung.
 - [14] Mitsuo Okmura, Kohei Ono, Utari S. Minaka, Tadahiro Inoue, Ryuji Inaba, Rytaro Tanaka, Adi Maulana, Ardy, Arsyad, Sabri, Purwanto, Sukirman Nurdin , Liquefaction-induced Large Scale Flowslide in Sibalaya –Investigation to Underlying Mechanism-, Handout of International Seminar on Developing Mitigation Technique for Liquefaction Disasters : Case Study from Palu Earhquake 7.4 M_w Sulawesi Tengah, 2019, Hasanuddin University.
 - [15] Pepen Supendi, Andri Dian Nugraha, Sri Widiyantoro, Chalid Idham Abdullah, Nanang T. Puspito, Kadek Hendrawan Palgunadi, D. Daryono and Samsul Hadi Wiyono, Hypocenter Relocation Of The Aftershocks Of The Mw 7.5 Palu Earthquake (September 28, 2018) And Swarm Earthquakes Of Mamasa, Sulawesi, Indonesia, Using The BMKG Network Data, Geoscience Letter 6:18, 2019, Article 10.1186/s40562-0148-9.
 - [16] P.K. Robertson, and C.E. (Fear) Wride, Evaluation Cyclic Liquefaction Potential Using The Cone Penetration Test, Canadian Geotechnical Journal, 1998, Vol. 35, 442-459.
 - [17] Ross W. Boulanger and Stephen P. Truman, Void Redistribution in Sand Under Post-Earthquake Loading, Canadian Geotechnical Journal, 1996, Vol. 33, 829-834.
 - [18] R.W. Boulanger, D.M. Moug, S.K. Munter, A.B. Price and J.T. DeJong, Evaluating Liquefaction and Lateral Spreading in Interbedded Sand, Silt and Slay Deposit Using the Cone Penetrometer. Geotechnical and Geophysical Characterisation, Australian Geomechanics Society, 2016, Sydney, Australia, 81-97.
 - [19] Susumu Yasuda, Prediction of Liquefaction and Countermeasure Against Liquefaction, Handout National Workshop on Joint Research, Assesment Mitigation of Liquefaction Hazards on 9th October 2019, Indonesia University.
 - [20] Takaji Kokusho, Innovative Earthquake Soil Dynamics. Taylor & Francis Gorup, 2017.
 - [21] Takaji Kokusho, M.ASCE, Fumiko Ito, Yohta

- Nagao, and A. Russel Green, M. ASCE, Influence of Non/Low-Plastic Fines and Associated Aging Effect on Liquefaction Resistance, *Journal of Geotechnical and Geoenvironmental Engineering ASCE*, 2012, 138 (6), 747-756.
- [22] Takeji Kokusho, Water Film in Liquefied Sand and Its Effect on Lateral Spread”, *Journal of Geotechnical and Geo-environmental Engineering*, 1999, 125 (10), 817-826.
- [23] Takeji Kokusho and Tetsuro Kojima, Mechanism for Postliquefaction Water Film Generation in Layered Sand, *Journal of Geotechnical and Geoenvironmental Engineering*, 2002, 128 (2), 129-137.
- [24] Takaji Kokusho, Current State of Research on Flow Failure Considering Void Redistribution in Liquefied Deposits. *Soil Dynamic and Earthquake Engineering* 23, 2003, 585-603.
- [25] Takeji Kokusho, Mechanism for Water Film Generation and Lateral Flow in Liquefied Sand Layer, *Soil and Foundations Vol. 40*, 2000, No. 5, 99-111.
- [26] Takej Kokusho and Katsuhisa Fuji, Water Films Involved in Post-Liquefaction Flow Failure in Niigata City During the 1964 Niigata Earthquake. *Pro. International Conferences on Recent Advances in Geotechnical Earthquake Engineering and Soil Dynamics*, 2001, 25.
- [27] Yamaguchi, T. Mori, M. Kazama, N. Yoshida, Liquefaction in Tohoku district during the 2011 off the Pacific Coast of Tohoku Earthquake. *Soils and Foundations*, 2012, 52 (5) : 811-8129.

EXPERIMENTAL RESEARCH ON THE INFLUENCE OF DISTANCE BETWEEN CFG PILES ON THE FOUNDATION TREATMENT RESULT IN VIETNAM

Doanh Phu Bui¹, Tung Hoang¹, Phuong Viet Nguyen¹, Duc Viet Ngo¹ and Cuong Phu Cao¹

¹Faculty of Road and Bridge, National University of Civil Engineering, Hanoi, Vietnam

ABSTRACT

According to government statistics, there are currently about 19 thermal power plants under operation, emitting about 20 million tons of fly ash annually which is classified as hazardous waste, an urgent environmental problem. In the context of lack of construction materials, this research aiming at promoting consumption of the fly ash through application of CFG (cement - fly ash - gravel) pile - a type of pile using a mixture of cement, fly ash, aggregate to handle the foundation for construction works that may help consume part of the fly ash. This paper introduces the results of an experimental research on the influence of distance between CFG piles on soft soil treatment. The optimal fly ash component is about 25% of binder content, and the reasonable distance between the piles is from 4d to 6d (d- diameter of the pile). This can be an effective solution for soft soil treatment since it is reasonable both in terms of price and construction time. It is also easy for quality control in Vietnam.

Keywords: CFG (cement fly ash gravel); composite foundation, experimental research, distance effect

INTRODUCTION

As a developing country, Vietnam has been facing the shortage of electricity and there will more and more new thermal power plants in order to satisfy the related increasing demands. These thermal power plants have been emitting a large number of hazardous waste, ash (comprising 75% of fly ash), which causes environmental pollution. This is considered one of the consequences of the development, causing a headache for Vietnamese authorities [1]. In this circumstance, the researches on applying fly ash as a construction material have been conducted since 80s of this century. However, the objective of those studies was mainly for generating high-quality fly ash mixture as an adhesive for concrete. Recently, studies in Vietnam have focused on the consumption of fly ash, such as putting into roadbed [2], geopolymer concrete [3], and pervious concrete [4]. In this trend, the application of a large amount of fly ash to produce low-cost, low-strength concrete mixture for foundation treatment is very necessary.

The CFG (Cement Flying-ash Gravel) pile is a type of pile using mixture of cement, fly ash, aggregate of stone (gravel) to form a low-strength concrete pile for foundation treatment in basic construction works. Through pile length, distance between piles and pile cap cushion layer as well as the right mixture ratio of pile materials, the pile can satisfy the required load capacity of treated foundation, achieving high load capability, small variation and simple construction. The low-cost CFG piles have been applying in mass construction works in some countries in the world. However,

there is no theoretical study and experiments in Vietnam on CFG pile application on foundation treatment in construction works. So with advantages in foundation treatment in construction works and large amount of fly ash consumption for thermo electricity plants, CFG piles application is perfectly efficient and suitable for works in cost saving and simple construction, quality assurance and easy in quality control while fly ash pollution is mitigated, solving the waste issue for thermal power plants.

Hence, the research on CFG application in foundation treatment in basic construction works plays pivotal role with high practical and feasible meaning in order to improve quality as well as to reduce cost of basic construction works in Vietnam.

CFG PILES IN SOFT SOIL FOUNDATION TREATMENT

CFG Development

CFG pile application is classified as an embankment measure on pile system according to the list of embankment treatment methods on soft soil. CFG piles together with soil between piles and pile cap cushion layer form a combination foundation to ensure stability for embankment foundation on soft soil.

In 1985, Foundation Institute of China Academy of Building Research studied CFG pile application based on foundation with ballast pile added in cement and fly ash to generate high-strength piles. CFG piles were made by specialized machine and mixture of CFG pile materials were poured in place into pre-drilled empty tube and finally the piles were

formed in the ground. With advantages of high load capability, small variation, simple construction and low cost, this method has been popularly applied for construction of houses, car roads, railways and yards in China and some other countries in the world. Researches in China on theoretical models, calculation theory, technical requirements on materials and construction technology have been conducted.

Structure, Specifications and Working Principle of CFG piles

CFG piles with diameter from 350mm to 600mm. By changing cement content and ratio in the CFG pile mixture, pile strength varies from C10 to C25, forming the intermediate piles between two forms of hard and soft piles [5], [6]. CFG piles works with soil in between through its cap cushion arrangement, which form the combined foundation so that the foundation can utilize load capability of soil between piles and also transport the embankment load down to good geological layer to increase stability and reducing settlement risk for the embankment, bringing in high technical and economic efficiency. Furthermore, the pile mixture takes good use of fly ash from thermal power plant without reinforcement steel frame to save material cost, extending higher economic efficiency.

CFG pile method is calculated and designed based on working principle of the combined foundation. The main factors covering ingredients and ratio of pile materials, pile length, distance between piles, size of pile cap, structure and thickness of pile cap cushion and construction technique need carefully calculating, designing, experimenting, analyzing to satisfy requirements of foundation strength treatment.

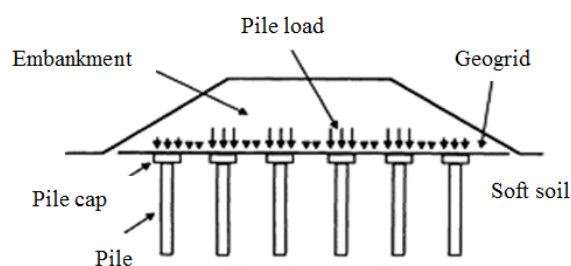


Fig. 1 Stress of embankment on the combined foundation.

Distance between piles must be defined through load capability of the combined foundation, physical characteristics of geological layers and construction techniques. The experimental studies on centrifugal acceleration model show that the distance between piles should be equal to 3-6 times of pile diameter [7]. In order to reduce cost, distance between piles should be set as largest as possible, however, there is no experiment study on the distance between piles which is equal to 6 times of pile diameter.

Length of pile is designed to touch the geological layer with good load capability to transport down the load from embankment. In other cases, pile length can be calculated according to the friction load. Because pile strength is larger than embankment strength so the stress on piles is also higher than the one on soil between piles (Figure 1).

The pile cap is usually designed with concrete in order to distribute more load from embankment on pile, sizing down pile diameter, increasing distance between piles and saving more materials. Size of pile cap affecting the load distribution capability of cap cushion layer is designed to be around 10% ~ 30% working area of piles [7].

The cushion layer on pile cap is designed to adjust stress of piles and soil between piles, reducing stress at pile cap, reinforcing load capability of foundation. Design of cushion layer is an important technique in treatment for the CFG combined foundation, which is pivotal task to ensure the load capability of piles and foundation. Structure of cushion layer comprises medium size sandstone, coarse-grained sand, selected sand, ballast aggregate or pebble gravel with size of sand stone no larger than 30mm. A geotextile layer can be spread on pile cap to form a cushion to distribute load on piles. The cushion layer should be 150÷500mm thick, compression strength is not greater than 0.9. The thickness of this cushion layer increases in par with the rise of pile diameter and distance between piles [8].

Based on theoretical study and in laboratory experiment on design CFG pile for foundation treatment with distance between piles which is equal to 6 times of pile diameter, authors have done experiment on site to verify the working ability of combined foundation and piles, of which, distance between piles is set to be equal $4d$ and $6d$ of piles (d is pile diameter) for embankment foundation model with height of 4m.

EXPERIMENT IN ROOM DEFINES RATIO OF FLY ASH IN COMBINED CFG MIXTURE

Aggregate Design for CFG Mixtures

Authors has conducted experiments in laboratory with three different fly ash types from Pha Lai thermal power plant, Nghi Son thermal power plant, and Ninh Binh introgenous fertilizer plant to mix aggregate to find proper ratio of fly ash/adhesives in CFG mixtures.

Within experiment scope, authors selected the ratio water/cement =0.65 to study. The designed aggregate is 7 and ratio of fly ash replacing adhesive content from 0%~35%. Through absolute volume calculation method, calculation for aggregate for 1m^3 CFG mixtures as follow:

Table 1 Calculation result of aggregate concrete using fly-ash additives for 1m³

F/C (%)	Cement (Kg)	Fly Ash (Kg)	Sand (Kg)	Stone (Kg)	Water (Liter)
0	280	0	802.67	989.33	194.67
10	252	28	799	982.67	194.67
15	238	42	796	980	194.67
20	224	56	793.33	977.33	194.67
25	210	70	790.67	974.33	194.67
30	196	84	788.67	972.67	194.67
35	182	98	786	970.67	194.67

Experiment Result

Experimental sample number is prepared in accordance with standard “TCVN 3118:1993 Concrete – Compression strength” [9].

Number of samples: 6 cube samples: 10 x 10 x 10 (cm) to define compression strength R_n ; Combined samples 7x6x3=126.

Aggregate Design Result

The selected compression strength value is the average values from 6 samples. R_n values at 3 days; 7 days, 14 days and 28 days. Experimental results show that the CFG mixtures using fly ash from Nghi Son plant and other fly ash with replacing ratio of 35% the adhesive objects still satisfy compression strength value $R_n > 10\text{MPa}$, which are suitable to be used in CFG pile construction.

Table 2. Compression Strength R_n values at 28 days of fly ash from Nghi Son plant.

F/C	R_i at 28 th day (MPa)						R_{ntb6}
	R_{n1}	R_{n2}	R_{n3}	R_{n4}	R_{n5}	R_{n6}	
0%	15.5	15.7	15.8	15.6	15.9	15.7	15.7
10%	14.6	14.8	14.7	14.8	14.9	14.7	14.7
15%	13.2	13	13.1	13.2	13	13.2	13.1
20%	11.7	11.6	11.5	11.6	12	12	11.7
25%	10.9	10.8	10.6	10.7	10.8	10.9	10.8
30%	10.6	10.7	10.8	10.6	10.7	10.5	10.7
35%	10.6	10.7	10.5	10.8	10.5	10.6	10.6

Hence, from selected materials (PC40 But Son cement, Red River black sand, fly ash from Pha Lai, Nghi Son thermal power plants, and Ninh Binh introgenous fertilizer plant; gravel and water), authors aim to figure out optimal aggregate ratio, ensuring cost effectiveness in manufacturing CFG pile production for foundation treatment in construction works.

EXPERIMENT ON SITE CFG PILE CONSTRUCTION

Experimental Site and Geological conditions

Experimental site is at the Experiment Site within the National University of Civil Engineering at Ha Nam province.

Using approved geological parameters [10], in accordance with the geological survey report LKBS02, surveyed depth at 15m with geological layers: Soil covering layer: Pond and field mud, brown gray and dark gray (1). 0.5m thickness; Mixed clay layer with organic soil, gray-brown and soft clay (2) 3.9m thickness; Mixed clay layer with fine sand bed brown gray, dark gray, soft clay (3) 7.3m thickness; Mixed sand layer, brown gray, dark gray and soft clay (3) thickness covering the rest of surveyed height. Use of data of physical properties of soil layers follows its appendix. Depth of underground water: 0.00m.

Density of embankment material: 1.8 T/m³ (compacted black sand embankment with K85).

Technical Scale of Experiment

Section 1: Design with different load capacity, each 20m section with pile arrangement as shown in the photo, pile diameter 0.5m, length 12m, pile cap diameter 1.1m with distance between piles 3m, average embankment height 4m.

Section 2: Design with larger load capability of section 1 with length of 15m for the works to be used as container warehouse, foundation for low-rise buildings (5 storeys and below), pile diameter 0.5m and length 12.0m, pile cap diameter 1.1m with distance between piles of 2m and average embankment height 4m.

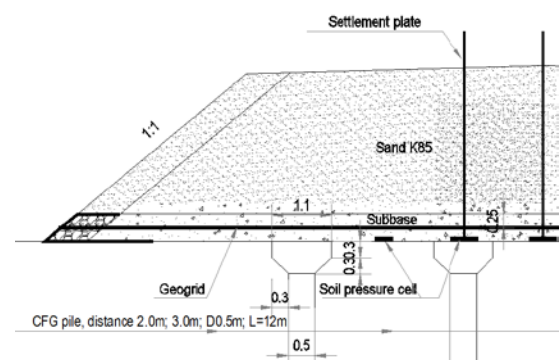


Fig. 2 1/2 Section 1 experiment embankment cross-section

Construction Technique

Construction Materials

CFG pile material: gravel 1x2, from Ha Nam quarry, Red River black sand, Nghi Son thermo electricity plant fly ash and But Son PC40 cement;

Pile cap cushion material: Aggregate gravel type 2 from Ha Nam quarry; Geotextile with tensile strength 50kN/m. Embankment material: Red River black sand $\gamma = 1.8 \text{ T/m}^3$. Other materials: Gene tubes; Settlement plate.

CFG Pile Aggregate Construction

The design parameters of CFG piles are results of survey with fly ash/adhesive ratio (Fly-ash/cement) with replacing fly ash content ratio of 25%, Water/cement ratio is 0.65

Table 3. Selected aggregate for CFG pile construction

F/C (%)	Cement (Kg)	Fly ash (Kg)	Sand (Kg)	Stone (Kg)	Water (Liter)
25	210	70	790.67	974.33	194.67

CFG Pile Construction Technique



Fig. 3 CFG pile construction process



Fig. 4 Pile site after construction

Based on the geological survey results, authors decided to select the mini drilling stuffing technique to conduct construction and form piles according to the design.

Installation of measuring equipment

Authors arranged 6 soil pressure cells with 2.0MPa cell at pile cap, 0.2 MPa at soil between pipe cap. Cell position as show as diagram below.

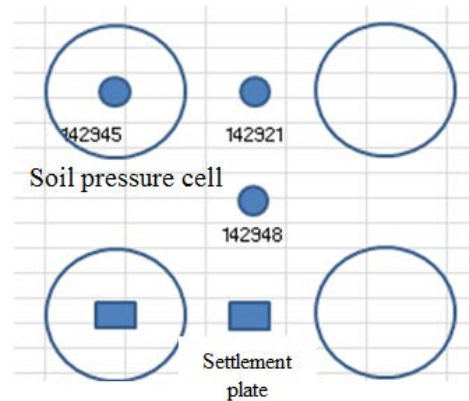


Fig. 5 Soil Pressure Cell diagram at 2m pile distance

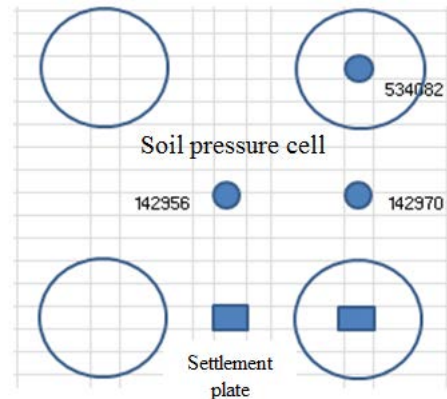


Fig. 6 Soil Pressure Cell diagram at 3m pile distance

ANALYSIS OF EXPERIMENT RESULT

Settlement Monitoring Result by Settlement Plate

Settlement monitoring result is shown in the below tables:

Table 4. Settlement monitoring results at 2m pile distance position

Plate	Settlement Value by Day (cm)					
	Day 1	Day 3	Day 5	Day 10	Day 30	Day 60
#1	1.7	2.3	2.3	2.3	2.4	2.4
#2	5.2	6.3	6.4	6.5	6.5	6.5

Findings:

Foundation is completely stable, settlement measurement results show the settlement value at soil between piles is higher than the one on pipe. Settlement measurement results at 3m pile distance is higher than the ones at the 2m pile distance.

Settlement values of soil between piles are small at beginning and gradually increasing. After the 3rd

days, the values become stable, reaching maximum at 9.2cm.

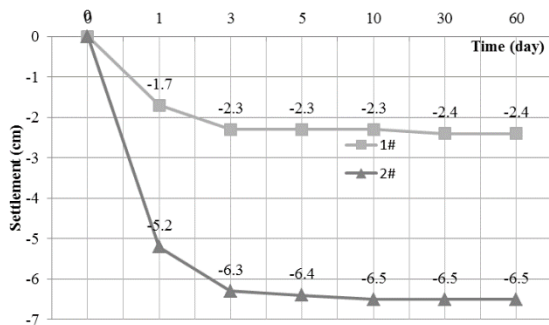


Fig. 7 Settlement measurement results at 2m pile distance position

Table 5. Settlement measurement results at 3m pile distance position

Plate	Settlement Value by Day (cm)					
	Day 1	Day 3	Day 5	Day 10	Day 30	Day 60
#3	2.2	3.2	3.2	3.3	3.4	3.5
#4	6.2	8.8	8.9	9.0	9.1	9.2

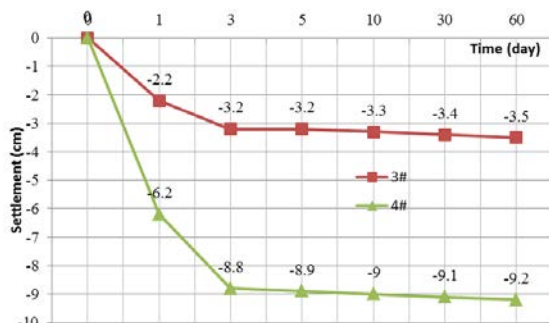


Fig. 8 Settlement measurement results at 3m pile distance position

Pressure Measurement Results at Pile Cap and Soil between Piles

Pressure measurement results at pile cap and soil between piles as show in table 6:

Table 6. Pressure measurement results at pile cap and soil between piles at 2m distance

Cell	Pressure value (MPa)				
	CP	CP	CP	Day 1	Day 3
142945	0.028	0.042	0.077	0.108	0.119
142921	0.022	0.033	0.061	0.054	0.058
142948	0.015	0.019	0.03	0.027	0.029

Cell	Pressure value (MPa)				
	Day 5	Day 10	Day 30	Day 60	/
142945	0.13	0.141	0.143	0.144	/
142921	0.053	0.05	0.048	0.049	/
142948	0.028	0.027	0.026	0.026	/

Cons.Process (CP)

Pressure measurement values on soil and soil between piles show that the value didn't vary clearly at the beginning of construction process until the embankment reached height of 4m where the values vary significantly and pressure of load gradually shift to piles through pile cap cushion layer. The maximum value at pile cap is 0.143MPa, minimum value at soil between 4 piles is 0.026MPa. Foundation works on principle of combination and on vertical then pressure also varies and gradually stable.

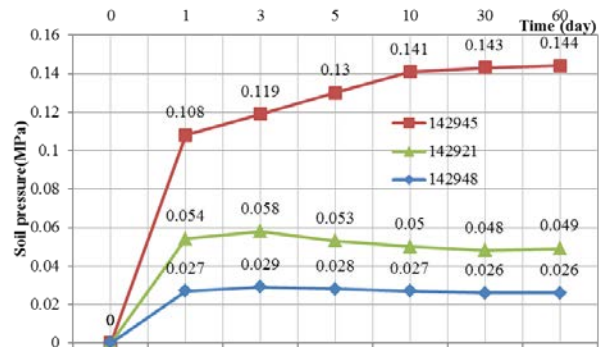


Fig. 9 Soil pressure results at 2m pile distance position

Table 7. Pressure measurement results at pile cap and soil between piles at 3m distance

Cell	Pressure value (MPa)				
	CP	CP	CP	Day 1	Day 3
534082	0.016	0.039	0.069	0.097	0.107
142970	0.024	0.049	0.066	0.067	0.068
142956	0.017	0.036	0.071	0.074	0.077
Cell	Pressure value (MPa)				
	Day 5	Day 10	Day 30	Day 60	/
534082	0.119	0.131	0.136	0.137	/
142970	0.066	0.064	0.062	0.064	/
142956	0.075	0.072	0.07	0.07	/

Cons.Process (CP)

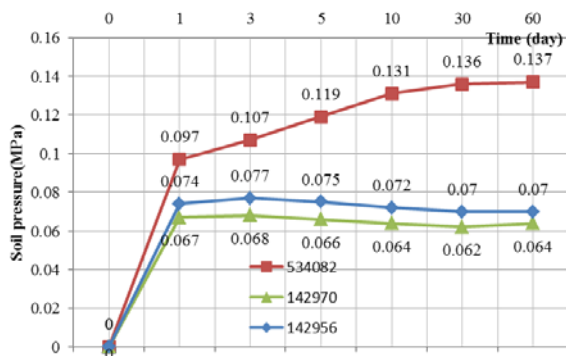


Fig. 10 Soil pressure results at 3m pile distance position

CONCLUSION AND SUGGESTIONS

Conclusion

Through experiment in room and on site the soft foundation treatment by CFG pile with different distance between piles, the following findings have been gained:

1) Authors designed CFG mixtures using fly ash from 3 different sources, experiment results show the fly ash ratio in the mixture between 20%~35% then adhesive can assure quality for CFG to contribute to the consumption of fly ash emissions from thermal power plants.

2) CFG pile is the low-strength concrete C10~C15 with the designed pile distance of 2.0m~3.0m equal to 4d~6d, combining with the pile cap covering 12%~27% pile working area then the method can handle soft foundation with high stability at small settlement value.

3) Soft foundation treatment method with CFG pile brings economic-technical efficiency and easy control in quality as well as help contribute to consumption large amount of fly ash and this method should continue researching and evaluating in the coming time.

Recommendations

The following recommendations are raised during experiments:

Foundation treatment with CFG pile for construction works can be popularly deployed in Mekong Delta region where thermal power plants with a high amount of fly ash emission exist. The treatment method should be piloted in the region before application.

With the advantages of low cost and easy quality control comparing with normal ballast piles, it is suggested that standards for design and construction of foundation treatment with CFG pile should be developed to serve as a basis for mass infrastructure construction in Vietnam.

REFERENCES

- [1] Prime Minister of the Socialist Republic of Vietnam (2017), Decision No. 452/QĐ-TTg approving the scheme to promote treatment and use of ash, slag, plaster of thermal power plants, chemical plants, fertilizers as raw materials for construction materials production and in construction works.
- [2] Hoang T., Nguyen V.P., and Thai H.N, Use of coal ash of thermal power plant for highway embankment construction, in CIGOS 2019, Springer, Singapore, pp.433-439. DOI: https://doi.org/10.1007/978-981-15-0802-8_67
- [3] Pham T.T., Nguyen T.T., Nguyen N.L., Nguyen V.P., A neural network approach for predicting hardened property of geopolymer concrete. International Journal of GEOMATE, 2020, Vol.19, Issue 74, pp.193–201. DOI: <https://doi.org/10.21660/2020.74.72565>
- [4] Nguyen T.T., Phan Q.M., Pham T.T., Nguyen V.P., Experimental study on mechanical and hydraulic properties of porous geopolymer concrete. International Journal of GEOMATE, 2020, Vol.19, Issue 74, pp.66–74. DOI: <https://doi.org/10.21660/2020.74.41280>.
- [5] Ministry of Construction of the People's Republic of China (2002), Code for Design of Building Foundations GB 50007-2002.
- [6] Ministry of Housing and Urban-Rural Development of China (2012), Technical code for ground treatment of buildings - JGJ 79-2012.
- [7] Doanh, BUI Phu, Qiang LUO, Liang ZHANG, and Xing SU, Analysis on pile spacing effect of composite foundation with high strength piles by centrifugal model test. Journal of the China Railway Society, Vol.31, Issue 6, 2009, pp.69-75.
- [8] P. D. Bui, Q. Luo, L. Zhang, Y. Yang, Geotechnical centrifuge experiment and force analysis of reinforced cushion with pile cap net structure embankment. Proceedings of the 4th Asian Regional Conference on Geosynthetics. China (Shanghai), 2008, 185-190. ISBN: 978-3-540-69312-3.
- [9] Vietnam Standard TCVN 3118:1993. Heavyweight concrete - Method for determination of compressive strength.
- [10] Approved Design drawings of Experimental in National University of Civil Engineering. Ha Nam Province, 2017.

DESIGNING GABION STRUCTURES UNDER MULTI CRITERIA OBJECTIVES WITH GOAL PROGRAMMING

Vuttichai Chatpattananan¹, Tanadol Kongsomboon², and Vatanavongs Ratanavaraha³

^{1,2}Department of Civil Engineering, King Mongkut's Institute of Technology Ladkrabang

³Suranaree University of Technology, Nakhon Ratchasima, Thailand

ABSTRACT

Gabion structure is a set of stacked prefabricated cages filled with rocks. These gabion cages are made of prefabricated steel wire, polypropylene or polyethylene or nylon. Rearranging these gabion cages mainly follows the suppliers' guidelines or governmental design drawings. Designing this gabion structure, at a minimal, must satisfy many design criteria in passing external stability in sliding, overturning or eccentricity, and bearing capacity. Good gabion design should also balance the toe bearing stress and heel bearing stress. By nature of this multi criteria objectives in designing this gabion structure, this paper proposes a goal programming. Mixed integer optimization model is also combined with goal programming to set optimization models in designing gabion structures. A 3-meter gabion retaining wall is used to compare the design of using the proposed optimization approach with the design provided by an available online supplier guideline. The finding of this paper shows that using goal programming techniques that is multicriteria in nature gives better optimum results in designing gabion structure than using only optimization technique with only one objective.

Keywords: Gabion, Goal programming, Multi criteria decision making, Retaining wall

INTRODUCTION

Gabion

Gabions are cages made of hexagonal mesh fabric or steel wire mesh. These cages or boxes are widely used in construction works as a retaining structure, an erosion protection, coastal protection, pipe protection, and other usages such as Araki & Hirakawa, 2019 [1]. As a gravity retaining structure, this gabion retaining structure uses its self-weight to resist the lateral earth pressure behind it and also support vertical surcharge resting on top of the gabion structure.

The gabion cages typically are 2 meters long, 1 meter wide, and 1 meter high as shown in Fig 1. ASTM A975 [2] provides gabion sizes with 1 meter in width, varying lengths of 2, 3, 4 meters, and varying heights of 1, 0.5, 0.3 meters. BS8002 [3] also gives gabion shapes in 0.5 meter box in lengths of 2 m to 6 m, 1 m to 2 m widths and 0.3 m, 0.5 m and 1 m in depths.

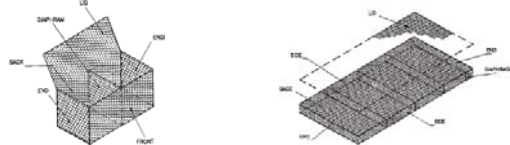


Fig. 1 Gabion (left) and Revet Mattress (Right), ASTM A975-97 [2]

Gabion Structures

Arranging different sizes of gabions can facilitate the design of gabion wall. The gabion wall can be shaped in front slope, rear slope, or trapezoidal shape as shown in Fig.2. Flexibility in gabion shapes and sizes leave a room to utilized optimization techniques in setting gabion wall.

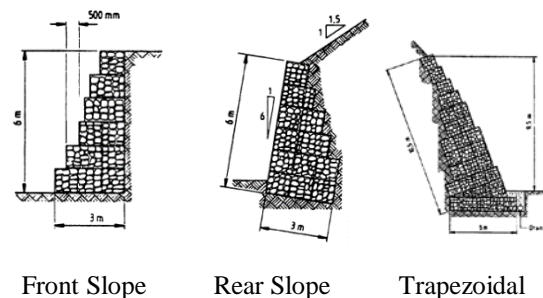


Fig. 2. Gabion Wall Shapes, BS8002 [3]

Designing Gabion Structures

Designing gabion structure as a gravity wall as shown in Fig. 2 needs to meet external stability in sliding, bearing, and overturning. There is no need in internal stability checking except using gabion as a facing unit and combined with other reinforcements. The reinforcement can be geogrid or even anchors as shown in Fig. 3. Global stability checking is also omitted since the global stability depends on the actual site location and the global stability can be checked either using limit equilibrium method (LEM)

or finite different method (FEM) by using softwares.

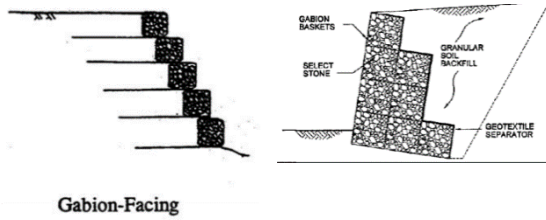


Fig. 3 Gabion Facing with Geogrid Reinforcement (left), FHWA-NHI-10024 [4] Compared with Traditional Gabion Gravity Wall (right) [FHWA-SA-96-038 [5]

Optimization Techniques used in Designing Gabion Structures

Hence, designing a gabion structure is a constrained optimization problem by nature since the design needs to be the most economical as possible while needs to satisfy all stability constraints.

Also designing gabion structure faces many multicriteria by nature as aforementioned. Of course, the first objective is the design the most economically. Another objective, for example, is to equalize the vertical stress at toe and the vertical stress at heel of the gabion structure as recommended by Environmesh 2007 [6].

Some papers apply optimization techniques in designing retaining walls such as Saribas 1996 [7] that uses nonlinear optimization model in designing reinforced concrete-cantilever retaining walls. Basudhar 2008 [8] applies nonlinear cost optimization model in designing mechanically stabilized earth (MSE) walls by using Sequential Unconstrained Minimization Technique (SUMT) instead of directly solving nonlinear optimization model which may not give the exact solution. However, there is no paper directly using optimization technique in designing gabion wall.

This paper proposes mixed integer nonlinear programming combined with goal programming approach to solve gabion design problem which is a multicriteria problem in nature.

DESIGN EXAMPLE

Environmesh, 2007 [6] gives a design example of 3.1 gabion wall with a total cross section of 3.87 m² as shown in Fig. 4.

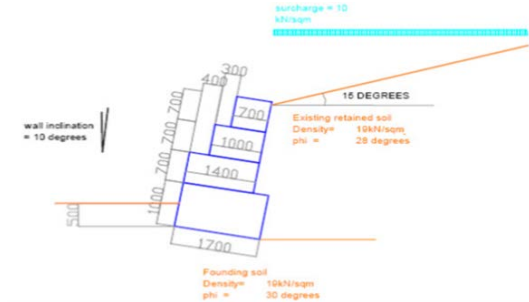


Fig. 4. Dimension of Gabion Structure from Environmesh Designed Example [Enviromesh, 2007])

Design Parameters

From Environmesh [6] example, the design parameters are as follows.

Geometry

Slope Wall height, $H = 3.1$ m where $y_1 = 1.0$ meter, $y_2 = y_3 = y_4 = 0.7$ meter and $b_w = 1.7$ meter, $b_2 = 1.4$ meter, $b_3 = 1.0$ meter, $b_4 = 0.7$ meter. Slope angle of the retained soil, ϵ , is 15 degree. Wall inclination, α , is 10 degree.

Materials

Soil friction angle, ϕ , is 28 degree.

Soil density, $\gamma = 19$ kN/m³.

Gabion density, $\gamma_g = 16$ kN/m³.

Foundation soil density, $\gamma_f = 19$ kN/m³.

Foundation soil internal friction angle, ϕ_f , is 30 degree.

Bearing capacity parameters,

$$N_q = e^{\pi \tan \phi} \tan^2(45 + \phi/2) = 18.4 \quad (1.1)$$

$$N_c = \cot \phi (N_q - 1) = 30.1 \quad (1.2)$$

$$N_\gamma = (N_q - 1) \tan 1.4 \phi = 15 \quad (1.3)$$

Loading

Surcharge, $P_0 = 10$ kN/m².

Earth Pressure

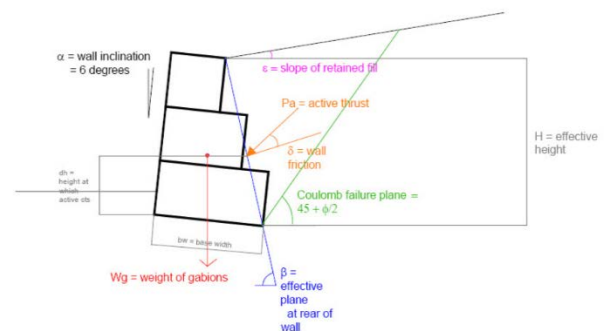


Fig. 5. Coulomb Active Earth Pressure Environmesh, 2007[6]

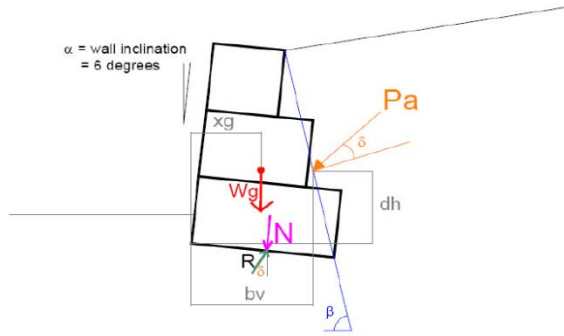


Fig. 6. d_h and b_v , Environmesh, 2007 [6]

Inclination angle to vertical plane, β , is 94.46 degree.

Retained Wall friction reduction by geotextile, δ , is 28 degree where $\delta = \phi$ if no geo-textile or 0.9ϕ with geotextile.

Active earth pressure coefficient (Bowles [9]), $K_a = 0.364$ from

$$K_a = \frac{\sin^2(\beta + \phi)}{\sin^2\beta \sin(\beta - \delta) \left[1 + \frac{\sin(\phi + \delta) \sin(\phi - \epsilon)}{\sin(\beta - \delta) \sin(\beta + \epsilon)} \right]} \quad (2.1)$$

The triangular pressure acting on the wall, $P_a = 43.4$ kN

$$P_a = 0.5 K_a \gamma H^2 + P_0 K_a H. \quad (2.2)$$

Horizontal component $P_h = 39.8$ kN, as shown in Fig. 5.

$$P_h = P_a \cos(90 - \beta + \delta) \quad (2.3)$$

Vertical component $P_v = 17.3$ kN from

$$P_v = P_a \sin(90 - \beta + \delta). \quad (2.4)$$

Variables

Vertical distance to P_a , $d_h = 0.852$ meter. From

$$d_h = H/3(H + 3P_0/\gamma)/(H + 2P_0/\gamma) - b_w \sin\alpha \quad (3.1)$$

as shown in figure 4. This is from moment

$$\text{equivalent, } ((1/2)\gamma_s H + P_0)d_{h'} = (1/2)\gamma_s H(H/3) + P_0(H/2).$$

Horizontal distance from toe to P_a , $b_v = 1.741$ meter as shown in Fig. 4.

$$b_v = b_w \cos\alpha - d_h/\tan\beta \quad (3.2)$$

Horizontal distance to W_g as shown in Fig. 6.

$$X_g = x_g \cos\alpha + y_g \sin\alpha \quad (3.3)$$

Resisting moment,

$$M_r = P_v b_v + W_g X_g. \quad (3.4)$$

Overturning moment,

$$M_o = P_h d_h. \quad (3.5)$$

Safety factor against overturning,

$$FS_o = M_r/M_o. \quad (3.6)$$

Normal Force on plane of sliding

$$N = W_g + P_v. \quad (3.7)$$

Tangential Forces,

$$T = P_h. \quad (3.8)$$

Sliding resistance

$$F_r = (N \cos\alpha + T \sin\alpha) \tan\phi. \quad (3.9)$$

Driving force,

$$F_d = T \cos\alpha - N \sin\alpha. \quad (3.10)$$

Safety factor against sliding,

$$FS_s = F_d/F_r. \quad (3.11)$$

Reaction eccentricity,

$$e = \frac{b_w}{2} - \frac{M_r - M_o}{N}. \quad (3.12)$$

e is a free variable which is unrestricted in sign.

Note that negative eccentricity causes reverse overturning to the back side (earth filled) of the wall.

Vertical stress at toe,

$$\sigma_t = \frac{N}{b_w} \left(1 + \frac{6e}{b_w} \right) \quad (3.13)$$

where vertical stress at heel,

$$\sigma_h = \frac{N}{b_w} \left(1 - \frac{6e}{b_w} \right). \quad (3.14)$$

Allowable soil bearing stress,

$$q_a = P_0 N_q + 0.5 \gamma_s b_w N_\gamma. \quad (3.15)$$

Safety factor against bearing,

$$F_b = \sigma_t/q_a. \quad (3.16)$$

Design Output

In fact, Environmesh [6] provides two approaches in designing gabion systems. One is called “gabion 27 system”. Another is called “gabion 39 system”. For this 3-meter height gabion structure example. The 27 system has 4 layers and the 39 system has 3 layers. In fact, the gabion 27 system with 4 layers is already illustrated in the calculation previously. The output for these two systems is compared and later shown in table 1.

OPTIMIZATION MODELS

Optimization techniques are applied here. Three model are proposed. The first model is a mixed integer nonlinear programming (MINP) model. The other two are goal programming models. One is preemptive goal programming model and another is weighted goal programming model. The design parameters for the three models are as follows:

Design Parameters

Geometry Constants and Soil Parameters

Environmesh [6] design example is borrowed here. The example is a 3.1 meter gabion structure. The following constants are used here.

Slope angle of the retained soil, ϵ , is 15 degree.

Inclination angle to vertical plane, β , is 94.46 degree.

Soil cohesion, c is 0 kPa.

Soil friction angle, ϕ , is 28 degree.

Soil density, $\gamma = 19$ kN/m³.

Retained Wall friction reduction by geotextile, δ , is 28 degree.

Wall inclination, α , is 10 degree.

Surcharge, $P_0 = 10 \text{ kN/m}^2$.

Instead of using original Environmesh example with 4 layers gabion as mentioned before, this model uses 6 gabion layers with $y_1 = y_2 = y_3 = y_4 = y_5 = y_6 = 0.5 \text{ meter}$

Calculated Constants

Active earth pressure coefficient, $K_a = 0.364$.

The triangular pressure acting on the wall, $P_a = 43.4 \text{ kN}$.

Horizontal component $P_h = 39.8 \text{ kN}$.

Vertical component $P_v = 17.3 \text{ kN}$.

Bearing capacity parameters, $N_q = 18.4$, $N_c = 30.1$, $N_\gamma = 15$.

Vertical centroid

$$yy_1 = y_1/2 = 0.25, \quad (4.1)$$

$$yy_2 = y_1 + y_2/2 = 0.75 \quad (4.2)$$

$$yy_3 = y_1 + y_2 + y_3/2 = 1.25 \quad (4.3)$$

$$yy_4 = y_1 + y_2 + y_3 + y_4/2 = 1.75 \quad (4.4)$$

$$yy_5 = y_1 + y_2 + y_3 + y_4 + y_5/2 = 2.25 \quad (4.5)$$

$$yy_6 = y_1 + y_2 + y_3 + y_4 + y_5 + y_6/2 = 2.75 \quad (4.6)$$

Mixed Integer Nonlinear Programing

Mixed integer nonlinear programming (MINP) model minimizes the minimum gabion weight while satisfying the external stability constraints in sliding, overturning, and bearing stability. This is done by adjusting the decision variables

Objective Function

$$\text{Min } W_g \quad (\text{O 1: MIP})$$

Decision Variables

The decision variables are as follows:

b_w : gabion width (m) at the base layer

b_i : gabion width (m) at layer i , $i = 2, 3, 4, 5, 6$

x_{Fi} : offset (m) of gabion at the front at layer i , $i = 2, 3, 4, 5, 6$

x_{Bi} : offset (m) of gabion at the back at layer i , $i = 2, 3, 4, 5, 6$

i_w : positive integer variable of gabion wall width at the base.

i_i : positive integer variable of gabion wall width at layer i , $i = 2, 3, 4, 5, 6$

Constraints

Width Constraint Group

$$b_2 = b_w - x_{2F} - x_{2B} \quad (\text{C 1.1: layer 2})$$

$$b_3 = b_2 - x_{3F} - x_{3B} \quad (\text{C 1.2: layer 3})$$

$$b_4 = b_3 - x_{4F} - x_{4B} \quad (\text{C 1.3: layer 4})$$

$$b_5 = b_4 - x_{5F} - x_{5B} \quad (\text{C 1.4: layer 5})$$

$$b_6 = b_5 - x_{6F} - x_{6B} \quad (\text{C 1.5: layer 6})$$

Integer Width Group

$$b_w = 0.5 i_w \quad (\text{C 2.1: base width})$$

$$b_2 = 0.5 i_2 \quad (\text{C 2.2: layer 2 width})$$

$$b_3 = 0.5 i_3 \quad (\text{C 2.3: layer 3 width})$$

$$b_4 = 0.5 i_4 \quad (\text{C 2.4: layer 4 width})$$

$$b_5 = 0.5 i_5 \quad (\text{C 2.5: layer5 width})$$

$$b_6 = 0.5 i_6 \quad (\text{C 2.6: layer6 width})$$

Non-negativity Integer Width Group

$$b_w \geq 1, b_2 \geq 1, b_3 \geq 1, b_4 \geq 1, b_5 \geq 1, b_6 \geq 1 \quad (\text{C 3.1 - 3.6: integer width})$$

Weight Constraint

$$W_g = \gamma_g (y_1 b_w + y_2 b_2 + y_3 b_3 + y_4 b_4 + y_5 b_5 + y_6 b_6) \quad (\text{C 4: gabion weight})$$

Horizontal Centroid Constraint Group

$$xx_1 = b_w/2 \quad (\text{C 5.1: base layer})$$

$$xx_2 = x_{2F} + b_2/2 \quad (\text{C 5.2: layer 2})$$

$$xx_3 = x_{2F} + x_{3F} + b_3/2 \quad (\text{C 5.3: layer 3})$$

$$xx_4 = x_{2F} + x_{3F} + x_{4F} + b_4/2 \quad (\text{C 5.4: layer 4})$$

$$xx_5 = x_{2F} + x_{3F} + x_{4F} + x_{5F} + b_5/2 \quad (\text{C 5.5: layer 5})$$

$$xx_6 = x_{2F} + x_{3F} + x_{4F} + x_{5F} + x_{6F} + b_6/2 \quad (\text{C 5.6: layer 6})$$

Horizontal Moment Group

$$xxm_1 = y_1 b_w xx_1 \quad (\text{C 6.1: base layer})$$

$$xxm_2 = y_2 b_2 xx_2 \quad (\text{C 6.2: layer 2})$$

$$xxm_3 = y_3 b_3 xx_3 \quad (\text{C 6.3: layer 3})$$

$$xxm_4 = y_4 b_4 xx_4 \quad (\text{C 6.4: layer 4})$$

$$xxm_5 = y_5 b_5 xx_5 \quad (\text{C 6.5: layer 5})$$

$$xxm_6 = y_6 b_6 xx_6 \quad (\text{C 6.6: layer 6})$$

Vertical Moment Group

$$yy m_1 = y_1 b_w yy_1 \quad (\text{C 7.1: base layer})$$

$$yy m_2 = y_2 b_2 yy_2 \quad (\text{C 7.2: layer 2})$$

$$yy_m3 = y_3 b_3 yy_3 \quad (C)$$

7.3: layer 3)

$$yy_m4 = y_4 b_4 yy_4 \quad (C)$$

7.4: layer 4)

$$yy_m5 = y_5 b_5 yy_5 \quad (C)$$

7.5: layer 5)

$$yy_m6 = y_6 b_6 yy_6 \quad (C)$$

7.6: layer 6)

Center of Gravity

$$x_g = \frac{y_1 b_1 x x_1 + y_2 b_2 x x_2 + y_3 b_3 x x_3 + y_4 b_4 x x_4}{y_1 b_w + y_2 b_2 + y_3 b_3 + y_4 b_4} \quad (C8.1: \text{horizontal centroid})$$

$$y_g = \frac{y_1 b_1 y y_1 + y_2 b_2 y y_2 + y_3 b_3 y y_3 + y_4 b_4 y y_4}{y_1 b_w + y_2 b_2 + y_3 b_3 + y_4 b_4} \quad (C8.2: \text{vertical centroid})$$

$$xx_g = x_g \cos \varepsilon + y_g \sin \varepsilon \quad (C 8.3: \text{centroid})$$

Sliding Stability

$$N = W_g + P_v \quad (C 9.1: \text{reaction})$$

$$\frac{(N \cos \alpha + P_h \sin \alpha) \tan \phi}{P_h \cos \alpha - N \sin \alpha} \geq 1.5 \quad (C 9.2: \text{sliding factor of safety})$$

Overturning Stability

$$d_h = H/3(H + 3P_0/\gamma_s)/(H + 2P_0/\gamma_s) - b_w \sin \alpha \quad (C 10.1: d_h)$$

$$b_v = b_w \cos \alpha - d_h / \tan \beta \quad (C 10.2: b_v)$$

$$M_r = P_v b_v + W_g x x_g \quad (C 10.3: \text{resisting moment})$$

$$M_o = P_h d_h \quad (C 10.4: \text{overturning moment})$$

$$M_r / M_o \geq 2 \quad (C 10.5: \text{moment factor of safety})$$

Eccentricity

$$e = \frac{b_w}{2} - \frac{M_r - M_o}{N} \quad (C 11.1: \text{eccentricity})$$

$$|e| \leq b_w / 6 \quad (C 11.2: \text{eccentricity limit})$$

By replacing e which is a free variable with e^+ and e^- which are positive variables by using the

relationship $e = e^+ - e^-$.

This constraint is converted to $e^+ - e^- \leq b_w / 6$

Where

e^+ : positive eccentricity. In this case, the wall will lean toward facing.

e^- : negative eccentricity. In this case, the wall will lean toward the retained soil.

Bearing

$$\sigma_t = \frac{N}{b_w} \left(1 + \frac{6e}{b_w} \right) \quad (C 12.1: \text{vertical bearing at toe})$$

$$q_a = P_0 N_q + 0.5 \gamma_s b_w N_\gamma \quad (C 12.2: \text{soil bearing capacity})$$

$$\sigma_t / q_a \geq 2.5 \quad (C 12.3: \text{bearing factor of safety})$$

Width/Height Ratio

Suggested by Ortigo and Sayao, 2004 [10] that the base width should occupy about 0.4H to 0.6H. Hence, b/H lower bound for all 6 layers is set at 0.4 in constraint 12.1 to 12.6 while the b/H upper bound is set at 0.6 in constraint 13.

$$b_w / H \geq 0.4, \quad \frac{b_2}{H} \geq 0.4, \quad b_3 / H \geq 0.4, \quad b_4 / H \geq 0.4, \quad b_5 / H \geq 0.4, \quad b_6 / H \geq 0.4$$

(C 12.1 – 12.6: minimum width)

$$b_w / H \leq 0.6 \quad (C 13: \text{maximum width})$$

MINP solution

By mainly adjusting the decision variables in gabion layer widths $b_w, i_w, b_i, i_i, i = 2, 3, 4, 5, 6$, the solution of this mixed integer nonlinear programming model 1 gives the minimum weight $W_g^* = 52$ kN/m. The eccentricity $e = 0.242$ meter as shown in table 1.

Preemptive Goal Programming

Preemptive goal programming is used in this model by sequential assign the two goals as shown below.

Goal 1: minimum gabion weight, W_g

Goal 2: minimum eccentricity, e

The first preemptive goal is done by assigning the first objective function as:

$$\text{Min } W_g \quad (O 2.1: \text{preemptive goal 1})$$

The set of constraints is the same as in model 1.

The solution of the first preemptive goal of model 3 gives the minimum weight $W_g^* = 48$ kN/m where the eccentricity $e = 0.233$ meter as shown in table 1.

From this optimum solution in goal 1, the second preemptive goal is assigned with this second objective function. This second goal is trying to equalize the vertical stress at the toe to be the same as the vertical stress at the heel. In other words, this objective function is trying to minimize the eccentricity to be zero. Since the vertical stress at toe is $\sigma_t = \frac{N}{b_w} \left(1 + \frac{6e}{b_w} \right)$ and the vertical stress at heel is $\sigma_h = \frac{N}{b_w} \left(1 - \frac{6e}{b_w} \right)$, Equalizing $\sigma_t = \sigma_h$ implies that $e = 0$. This is done by adjusting the decision variables of the offsets x_{Fi} and x_{Bi} , $i = 2, 3, 4, 5, 6$ of the gabion layers. The second objective function is as follows.

$$\text{Min } e^+ - e^- \quad (O 2.2: \text{preemptive goal 1})$$

Except one constraint is added to satisfy the first goal, the other constraints are the same as in model 1. The added constraint is as follows:

$$W_g = 48 \quad (\text{C 14: satisfying the first goal})$$

The solution of the second goal of model 3, which is the optimum solution of this model, gives the minimum eccentricity $e^* = 0.002$ meter which is less than the eccentricity in the previous first preemptive goal model at $e = 0.233$ meter. Of course, the minimum weight $W_g^* = 48$ kN/m which is the same as the previous first preemptive goal model since this minimum weight is enforced as a constraint in the second preemptive goal model. The detail of the solution is shown in table 1.

Weighted Goal Programming

Weighted goal programming is used in this model by assigning a set of weights to handle 2 objectives as follow.

Goal 1: minimum gabion weight, W_g

Goal 2: minimum eccentricity, e

The weights assigned to the five goals are 2 to goal 1 and 1 to goal 2. The reason behind assigning such weights is largely based on the importance of each goal, Taylor, 2006 [11].

Hence the objective function is:

$$\text{Min } 2W_g + e^+ + e^- \quad (\text{O 3: weighted goal})$$

The set of constraint is the same as in model 1:

The solution of the first preemptive goal of model 3 gives the minimum weight $W_g^* = 48$ kN/m where the eccentricity $e = 0.233$ meter as shown in table 1.

COMPARISON OF THE MODELS

The comparison of the all the designs are shown below. Note that although the MINP model, which tries to minimize that gabion weight, yields a lesser gabion weight than the original Environmesh 27 system and 39 system, the MINP gives a larger value of eccentricity than the original Environmesh 27 system and 39 system. The result from using MINP model does not follow the good suggestion in the design that tries to equalize vertical stress at the toe with the vertical stress at the heel by setting the eccentricity to be close to zero.

The preemptive goal programming model which tries to combine the two goals in achieving the

minimum weight and forcing eccentricity to be close to zero gives a better design result. This gives a lower gabion weight, as seen in column G-2 in table 1, also gains a lesser eccentricity at 0.002 m which is close to zero.

The weighted goal programming model, which subjectively assigns the objective weights of 2 and 1 to the first goal in minimum weight and the second goal in forcing eccentricity to be zero, also gain the same result as in using preemptive goal.

Table 1 Comparison of the Designs

Model	27	39	MINP	G-1	G-2	G-3
H, m	3.1	3	3	3	3	3
W_g, kN	61.92	72	52	48	48	48
e, m	0.086	0.172	0.242	0.233	0.002	0.25
FSO	2.72	2.87	2.00	2.00	2.45	2.45
FSS	1.87	1.83	1.60	1.52	1.52	1.52
FSB	7.14	6.18	4.48	4.89	9.37	9.37

Note:

Column description

27 – Environmesh 27 system design

39 – Environmesh 39 system design

MINP – Mixed integer nonlinear programming design

G-1 – Preemptive goal programming, 1st goal: min W_g

G-2 – preemptive goal programming, 2nd goal: min e

G-3 – Weighted goal programming

Row description

H – Wall height in m

W_g – Gabion Weight in kN/m

e – Eccentricity in m

FSO – Overturning Factor of Safety

FSS – Sliding Factor of Safety

FSB – Bearing Factor of Safety

The calculation details including the widths and offsets of all the models are shown in table 2.

Table 2 Calculation Details of the Designs

Model	27	36	MINP	G-1	G-2	G-3
H, m	3.1	3	3	3	3	3
α	10	6	10	10	10	10
b_w, m	1.7	2.0	1.5	1.5	1.5	1.5
b_2, m	1.4	1.5	1.5	1.5	1	1
b_3, m	1.0	1.0	1	1	1	1
b_4, m	0.7	-	1	1	1	1
b_5, m	-	-	1	0.5	1	1
b_6, m	-	-	0.5	0.5	1	0.5
x_{2F}, m	0	0	-	-	0.5	0.5
x_{2B}, m	0.3	0.5	-	-	-	0
x_{3F}, m	0.4	0	0.066	0.145	-	0.006
x_{3B}, m	0	0.5	0.434	0.355	-	0.494
x_{4F}, m	0.3	-	-	-	-	-
x_{4B}, m	0	-	-	-	-	-
x_{5F}, m	-	-	-	0.048	-	-
x_{5B}, m	-	-	-	0.452	-	-
x_{6F}, m	-	-	0.007	-	0.5	0.5
x_{6B}, m	-	-	0.493	-	-	-
W_g, kN	61.92	72	52	48	48	48
e, m	0.086	0.172	0.242	0.233	0.002	0.25
M_s	96.4	101.9	70.3	67.0	82.0	82.0
M_o	35.5	35.5	35.2	33.5	33.5	33.5
FSO	2.72	2.87	2.00	2.00	2.45	2.45
F_r, kN	49.4	53.3	43.4	40.7	40.7	40.7
F_d, kN	26.4	29.1	27.0	26.7	26.7	26.7
FSS	1.87	1.83	1.60	1.52	1.52	1.52

Q_w , kN	437.1	481.7	407.3	407.3	407.3	407.3
σ_v , kN	61.2	78.0	90.9	83.3	43.5	43.5
FSB	7.14	6.18	4.48	4.89	9.37	9.37

Note: table 2 uses the same column description and row description as those in table 1.

CONCLUSIONS

Although optimization techniques such as mixed integer nonlinear programming (MINP) is a good tool in helping the design in choosing the good combination of many decision variables. This MINP has a limit in achieving only one objective. In this case, goal programming is a good alternative in achieving more than one objectives.

Also, many nonlinear programming problems does not guarantee the optimum exact solution but will give only the approximated solution that sometimes may not be a good solution. This can be seen in table 1 that although MINP can give a lesser weight than the original Environmesh 27 system and 39 system but MINP model gives a larger eccentricity than the 27 system and 39 system. In table 1, preemptive goal programming gains a lesser weight and a lesser eccentricity than the MINP model.

Note that the weighted goal model gives the same result as the preemptive goal model although the weights for the two goals are subjectively assigned as 2 and 1. Hence, there is a room for a further work to investigate the effects of the weights assign to the design output.

Also, this goal programming approach can be used in other geotechnical, especially other retaining wall structures, that needs to achieve many objectives and design criteria at the same time.

REFERENCES

- [1] Araki H, Hirakawa D., 2019, Effects of Thrust Protecting Method for Buried Pipe Using Geogrid Gabion of Different Sizes. *International Journal of GEOMATE*, June 2019, Vol.16, Issue 58, pp.62 – 68.
- [2] ASTM A975-97, 'Double-Twisted Hexagonal Mesh Gabions and Revet Mattresses (Metallic-Coated Steel Wire or Metallic-Coated Steel Wire with Poly (Vinyl Chloride) (PVC) Coating)', American Standard Testing Association, 2003.
- [3] BS8002, 'Code of Practice for Earth Retaining Structures', British Standards Institution, 2015.
- [4] FHWA-NHI-10024, Federal Highway Administration, 2001. Mechanically Stabilized Earth Walls and Reinforced Soil Slopes Design and Construction Guidelines.
- [5] FHWA-SA-96-038, Federal Highway Administration, 1996. Geotechnical Engineering Circular No. 2. Earth Retaining Systems.
- [6] Enviromesh, 2007. Designing with Gabions Volume 1. A Reference Guide for the Designing of Mass Gravity Gabion Walls.
- [7] Saribas A., Erbatur F., Optimization and Sensitivity of Retaining Structures, *Journal of Geotechnical Engineering*, 1996, pp. 649-656.
- [8] Basudhar, P. K., Vashistha, A., Deb, K. and Dey, A. (2008): Cost optimization of reinforced earth walls, *Geotechnical and Geological Engineering*, Vol.26, No.1, February 2008, pp. 1 - 12.
- [9] Bowles J. E. 2001, *Foundation Analysis and Design*, McGraw-Hill.
- [10] Ortigao A. R., Sayao A. S., 2004. *Handbook of Slope Stabilisation*, Springer.
- [11] Taylor B. W., 2006. *Introduction to Management Science*, Ninth Edition, Prentice Hall.

INTRODUCTION OF ARTIFICIAL INTELLIGENCE SYSTEM FOR SUPPORTING SOIL CLASSIFICATION

Shinya Inazumi¹, Kazuhiko Kojima²,
Hiroyuki Hashida³ and Ken-ichi Shishido⁴

¹Shibaura Institute of Technology, Japan; ²Otowa Co. Ltd., Japan;
³Sumice Kenzai Co. Ltd., Japan; ⁴Tomec Corporation, Japan

ABSTRACT

From the perspective of soil engineering, soil is uncertain and heterogeneous. Therefore, if an attempt is made to determine the soil classification of a soil without a precise test, for example, an engineer's individual judgement is often involved in making the determination based on his/her own experiences. In relation to acquiring vast and varied knowledge which is easily influenced by individual experiences, the purpose of this research is to gather the know-how of engineers and to create a certain index for use in making on-site judgments that are likely to be more inclusive of various data than those of individual engineers. In order to expand the application of artificial intelligence (AI) in the field, the possibility of image recognition by artificial intelligence is shown through the use of machine learning. This paper discusses the potential of image recognition by artificial intelligence, using a machine learning technique called deep learning, for the purpose of expanding the cases which employ artificial intelligence. In this research, it is shown that artificial intelligence, along with deep learning, can be applied to soil classification determination by performing simple deep learning with a model using a neural network.

Keywords: Soil classification, Machine learning, Neural network, Deep learning, Image recognition

INTRODUCTION

As an example of previous studies in geotechnical engineering and related fields, Ito [1], [2] prepared 150 sample photographs for three types of soil, namely, organic soil, gravel-mixed sand, and silt-mixed sand. As a result, it was shown that the rate of accuracy obtained by the model (the predictive value of the model against the real phenomenon) improved as the number of learning sessions was increased to 30, 100, 300, and 1000 times. On the other hand, when the 150 sample photographs were converted to grayscale, the black organic soil became almost black and the features of the images were lost. This led to the problem of the black organic soil images being erroneously recognized as silt-blended sand with few features. In addition, in the research by Kiso-Jiban Consultants Co., Ltd. [3], an AI program using deep learning was developed for three types of rock images, namely, granite, andesite, and mudstone, taken with a digital camera instead of a high-precision camera, such as a single-lens reflex camera. As a result, the rate of accuracy of the AI program was 88% for a total of 100 rock images consisting of 60 granite, 20 andesite, and 20 mudstone pieces. Furthermore, it was shown that the accuracy of this AI program determination exceeded that of geologists and soil engineers.

In this study, it is verified that the model misrecognition caused by the loss of image features reported in Ito's study [1], [2] occurs even when another soil type is set as the discrimination target. In

addition, although a digital camera was used in the research by Kiso-Jiban Consultants Co. Ltd. [3], we will examine here whether a smartphone with different features from a digital camera can be applied to an AI program.

CONDUCT MODEL LEARNING

The purpose of this research is to create the basis for a model to be used to make judgements on soil classification that can be utilized on a site-by-site basis. For this reason, the soils to be classified were divided into three types: clay ($D_{50} = 0.008$ mm), sand ($D_{50} = 0.7$ mm), and gravel ($D_{50} = 4$ mm) with the water content adjusted to 0 for simplicity. Clay, sand, and gravel, whose particle sizes were adjusted by conducting a sieving test, were put in a transparent plastic cup as shown in Figs. 1, 2, and 3, considering this practice as a difference from the previous studies [1], [2], [3]. The images were taken with a smartphone (iPhone 7) camera. Comparing the performances of the smartphone camera and the digital camera (FUJIFILM X-T4) released at the time of the experiment, the iPhone 7 has 12 million pixels and the digital camera has 26 million pixels. In addition, the size of the image sensor related to image noise (the larger the image, the more faithful the image to the subject) is 4.8×3.6 mm for the iPhone 7 and 23.5×15.6 mm for the digital camera. It is seen that the photographs were shot indoors. As for the clay, 200 photographs were taken both with and without lighting (400 in total). As for the sand, 200



Fig. 1 Image of clay taken

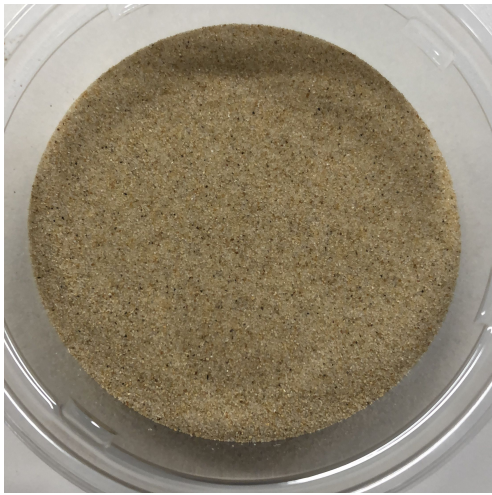


Fig. 2 Image of sand taken



Fig. 3 Image of gravel taken

photographs were also taken with and without lighting (400 in total). As for the gravel, 100

Table 1 Types and numbers of images taken

	Clay	Sand	Gravel	(Total)
With lights	200	200	100	500
Without lights	200	200	100	500
(Total)	400	400	200	1000

Table 2 Parameters used

Learning coefficient	1e-06
Batch size	20
Number of learning	70
Image size during learning (px)	56×56

photographs were taken with and without lighting (200 in total). In order to see the influence of the difference in the amount of data on the learning results, only the gravel had a different amount of data. In order to secure the data variation, adjustments such as switching the presence or absence of lighting during shooting and adding vibration or rotation to the cup to change the appearance of the surface were added. Vibration was applied so that the arrangement of the particles on the sample surface would be completely different, and rotation was performed in 90-degree units. These processes were combined to prevent the data from becoming uniform. This is because, even if a large number of identical images are copied and prepared, the effect of the learning model will be weak.

Table 1 presents a list of prepared images. These 1000 images were used as the learning data, and a total of 60 images of each randomly selected 20 images were used as model accuracy verification data.

In this research, the soil images were learned as a model using deep learning by the convolutional neural network and by the steepest descent method. At that time, each parameter was set as shown in Table 2.

LEARNING RESULTS

Figure 4 shows the transition of accuracy with respect to the number of learning sessions. The transition of the error is shown in Fig. 5. From these figures, it can be seen that the accuracy improves and the error decreases as the number of learning sessions increases. The error referred to here is the one defined by Eq. (4). Finally, an accuracy of about 86% was recorded for the image data for learning and about 77% for the data for verification. Here, the accuracy is the rate at which the images of clay, sand, and gravel used for learning can be accurately identified. In other words, out of a total of 1000 learning data images, about 86% (about 860) of the images were correctly classified.

In order to confirm whether the model can

correctly recognize the training data, Table 3 shows the judgment results for each soil type among the training data. The table shows how the model determined each soil type. For example, as a result of inputting 400 learning images showing clay as a true value into the model, 313 of the images were determined to be clay. At the same time, 87 of the images had the true value of clay, but the model misidentified them as sand. From the table, it can be seen that all the sand was correctly recognized and only about half of the gravel was correctly recognized. In particular, the gravel and clay were often mistaken for sand.

In addition, learning and classification were performed in this study by targeting only three types of soil. However, considering further development, not only the adjustment of parameters but the expansion of corresponding soil is the first issue. As shown in Figs. 6 and 7, clay and sand, which look very similar to human eyes, can be discriminated by the model. Therefore, like the fine sand in Fig. 8, there

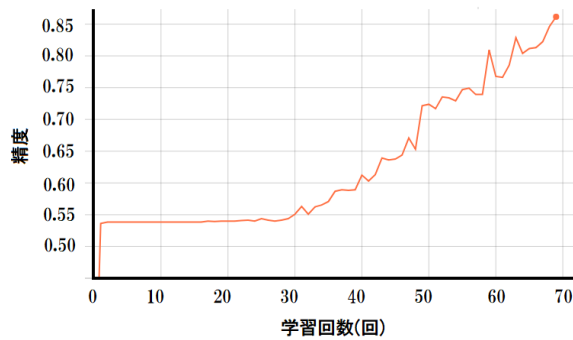


Fig. 4 Transition of accuracy with learning coefficient $1e-6$

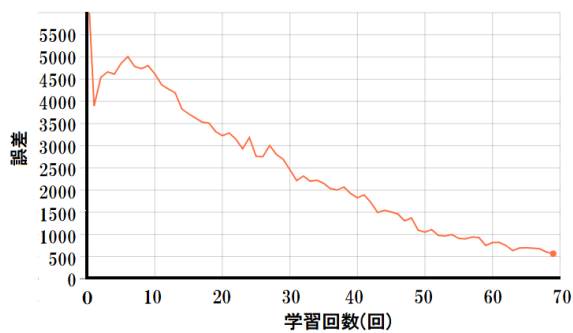


Fig. 5 Transition of error in learning coefficient $1e-6$

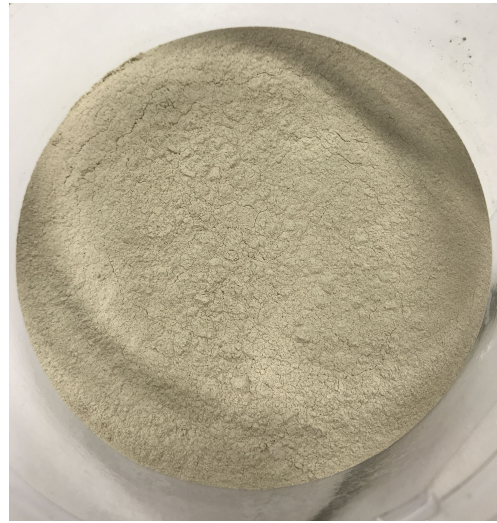


Fig. 6 Clay that has been identified correctly



Fig. 7 Sand that has been identified correctly

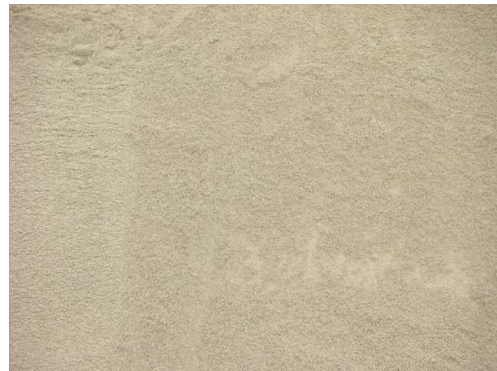


Fig. 8 Example image of fine sand

Table 3 Judgment results for each soil type

True value	Clay			Sand			Gravel		
	Clay	Sand	Gravel	Clay	Sand	Gravel	Clay	Sand	Gravel
Judgment result	313	87	0	0	400	0	10	83	107

are various soil types. It is possible to obtain a generalization performance for various types of soils by preparing several types, securing a sufficient amount of data for learning, and conducting the learning sessions with a sufficiently large number of pixels. It is thought that this will soon be possible.

CONCLUSIONS

In this study, deep learning was performed with a model using a neural network. For three types of soil, namely, clay, sand, and gravel, an AI model was created that was conscious of the practical simplicity of the images used. It was shown that this AI model can be applied to make judgments on soil classification. As a result, a high recall rate of 1 was obtained for sand. This means that all the sand images could be identified as sand. On the other hand, a high matching rate was obtained for clay and gravel. This means that images of clay and gravel can be carefully discriminated without much mixing of different types of images. Regarding the parameters, if the number

of pixels in the image during the learning sessions is too small, the features of the images cannot be detected sufficiently and the accuracy decreases. If the number of pixels is increased, the features can be detected and the accuracy increases.

REFERENCES

- [1] Ito, M (2017): Possibility of automated soil quality judgment by machine learning, Proceedings of ZENCHIREN Technology Forum 2017 Asahikawa, (<http://www.takuhokuchika.co.jp/machinelearning/resume.pdf>).
- [2] Utsuki, S., Nakaya, M. and Tsuruta, R. (2018): Construction of a geological information management system using AI, CIM and image processing technology, Journal of Japan Society of Engineering Geology, Vol. 58, No. 6 pp. 408-415.
- [3] Kiso-Jiban Consultants Co.,Ltd. (2019): <https://www.kisojiban.com>.

UNSATURATED SHEAR STRENGTH OF EXPANSIVE SOILS FROM NATURAL SLOPES IN QUEENSLAND

Tharindu Abeykoon¹, Chaminda Gallage² and Jessica Trofimovs³

^{1,2,3}Science and Engineering Faculty, Queensland University of Technology, Australia

ABSTRACT

Expansive soils exhibit significant changes in the swell and shrink behaviour upon variations of moisture content. Majority of soils in Queensland are expansive; consequently, failures in natural slopes with expansive characteristics are commonly reported under climate-induced soil moisture variations. In order to understand the failure mechanism of such soil slopes, it is vital to analyse slope stability under unsaturated conditions. The current study employed undisturbed soil samples from natural slopes in Queensland, and determined the basic soil properties, including the soil-water characteristic curve (SWCC), and unsaturated shear strength to facilitate the analysis of rainfall-induced slope failure mechanism. A series of conventional direct shear tests were conducted for different moisture contents under various vertical stresses. The test results were analysed to obtain the variation of the apparent cohesion and the effective friction angle of the soil with moisture content and suction. The study presents an empirical equation to predict the cohesive component in the shear strength of unsaturated expansive soils as an exponential function of suction. The formulation originated from multiple linear regression analysis for data sets obtained from shear tests using undisturbed soils with varying moisture contents. The empirical equations can realistically predict the reduction in soil cohesion due to wetting ($R^2 = 0.8791$). The study provides an alternative to the quantitative estimation of unsaturated shear strength of expansive soils.

Keywords: Unsaturated soil, unsaturated shear strength, Expansive soil, slope stability, Direct shear test

INTRODUCTION

The understanding of soil interface shear strength is vital in designing and analysing the stability of geotechnical structures [1-6]. The cohesive strength of unsaturated soils plays an important role in the stability of both natural and artificial soil slopes, [7, 8] in which the reduction of the soil cohesion due to wetting can cause shear deformation of the slopes at a previously unsaturated shallow layer. Therefore, determination of the critical condition for sliding requires a slope stability analysis, including an effect for the loss of cohesion.

As shear strength tests on unsaturated soils are costly and time-consuming, simple and indirect methods, have been developed to obtain the shear strength of unsaturated soils for engineering purpose. Numerous researchers suggested that the shear strength of unsaturated soils could be predicted using different equations [9]. Based on the soil-water characteristic curve (SWCC), various theoretical and empirical models were proposed for prediction of unsaturated shear strength. However, minimum compelling attempts were made on the analysis of the characteristics of unsaturated shear strength, and the relationship between the shear strength parameters and suction of unsaturated expansive soils.

This paper presents the results of a series of direct shear tests on unsaturated soils from natural slopes in Maleny, Queensland, Australia. Direct shear testing of unsaturated soils is desirable since less time is

required to reach the failure of the soil specimen compared to the triaxial test. The time to failure in the direct shear test is significantly reduced because the specimen is relatively thin. However, a lengthy testing period is expected for unsaturated soils due to the low coefficient of permeability of the soil. In this paper, an empirical equation is suggested for the prediction of unsaturated shear strength as a function of suction.

The equation was obtained from a multiple linear regression analysis of the results of direct shear tests using undisturbed expansive soils with varying moisture contents. Even though the equation lacks a theoretical validity from a physical standpoint, but has practical advantages, especially for geotechnical engineering purposes.

STUDY AREA

The study area is located in Lake Baroon catchment, Maleny, Queensland, Australia (26.72 °S 152.87 °E). Mapleton - Maleny plateau, which has been documented as a highly susceptible area for rainfall-induced slope failures since the mid - 1950s. (e.g. [10]). Slope failures and mass movements of sediment into the waterways within the Lake Baroon catchment are recognised as a significant risk to water quality and the water storage capacity of Lake Baroon, which is used to supply water to South East Queensland. Approximately 170 mass movement landforms have been identified within the Lake

Baroon catchment, and the study area is one such high-risk slope. This landslide site hosted a voluminous, single-failure rotational landslide in 2008 following heavy rainfall.

TEST MATERIAL

The test series herein employed soils from the Lake Baroon catchment. Undisturbed samples from seven locations of the study area were collected at various depths ranging from the surface down to 4 m. Initially, a trench was created to the desired depth with an excavator and then 500 mm long sampling tubes (diameter 75 mm) were inserted into the soil by connecting a specially modified adaptor to the excavator's arm as in Fig. 1.



Fig. 1 Insertion of soil sampling tube by the modified adaptor to the excavator's arm

Table 1 summarises the results of the laboratory tests conducted to determine the index properties of the soil according to Australian standards.

Table 1 Index soil properties

Classification Test	Results
Grain size Distribution	% finer than 75 μm > 79% Clay % = 41.0 %
Atterberg Limits	LL = 67.2 % PI = 28.2 %
Linear Shrinkage	LS = 13.4 %
Specific Gravity	$G_s = 2.67$
X-ray diffraction (XRD)	Presence of Smectite minerals (> 30 %)

Note: LL = Liquid limit; PI = Plastic index; LS = Linear shrinkage

TEST PROCEDURE

Undisturbed soil samples were collected from Lake Baroon catchment. Soil sampling tubes were employed in collecting undisturbed samples from seven locations at various depths. In-situ density and the moisture content of soil were determined for each

sampling location. The soil samples were used to determine SWCC, swelling characteristics and unsaturated shear strength.

A dewpoint potentiometer (Fig. 2) was employed in determining SWCC, which is the graphical relationship between soil suction and water content (gravimetric or volumetric) or degree of saturation. The dew point potentiometer measures water potential from 0 to -300 MPa with an accuracy of ± 0.1 MPa from 0 to -10 MPa and ± 1 % from -10 to -300 MPa. The high total suctions measured from WP4C Dewpoint potentiometer were assumed to consist of negligible osmotic suction effect and hence, used as matric suctions. These samples were initially prepared for known water contents and placed in enclosed containers to prevent any moisture loss prior to testing. Further, to obtain the SWCC, a best fitting relationship was established using the logarithmic model proposed by Fredlund and Xing [11] as presented Eq. (1) and (2).

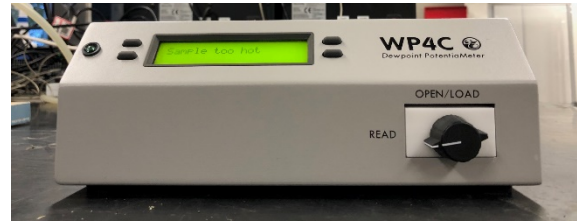


Fig. 2 WP4C Dewpoint potentiometer for suction measurement

$$\theta(\psi, a, n, m) = \frac{C(\psi) \theta_s}{\{\ln [2.718 + \left(\frac{\psi}{a}\right)^n]\}^m} \quad (1)$$

$$C(\psi) = \frac{-\ln(1 + \frac{\psi}{\psi_r})}{\ln(1 + 10^6/\psi_r)} + 1 \quad (2)$$

where a is equal to the air-entry suction; n is the tangent to the curve at the inflexion point (in the transition zone); m is related to the residual water content; $C(\psi)$ is a correction function; ψ_r is the suction corresponding to a given water content, and θ_s is the saturated volumetric water content.

A series of oedometer based one-dimensional consolidation tests (Fig. 3) were conducted as prescribed in AS 1289.6.6.1-1998 for soil samples for various initial water contents and dry densities under different surcharges to determine the rate of shearing for each direct shear test [12]. At the completion of the primary consolidation, the time to reach 50% consolidation (t_{50}) and following empirical equations were used to determine the shearing rate (Eq. (3) and (4)). Taylor's square root of time fitting method was used to determine t_{50} during the study. The selected surcharge values for this study were 50, 100, 150, 200 and 250 kPa. Samples were tested for different initial

volumetric water contents from 25% to 43% to replicate in-situ water contents. The samples were cured for four days prior to the oedometer tests. The soil samples prepared for known initial gravimetric moisture contents were then statically compacted to achieve the target density to replicate in-situ density. Subsequently, a representative sample was cut into a consolidation ring, followed by the placement of filter papers and porous disks, at the top and the bottom of the sample. The samples were then subjected to the aforementioned surcharges.



Fig. 3 Conventional oedometer apparatus used for the shear rate determination

$$t_f = 50t_{50} \quad (3)$$

$$R = d_p/t_f \quad (4)$$

where t_f is the time to failure in minutes, d_p the shear displacement at which peak strength is likely to be reached, in millimetres and R is the required shearing rate.

To obtain cohesion (c) and friction angle (ϕ') for the same in-situ water content of soil as in oedometer tests, five direct shear tests on five identical soil samples (the same density and water content) were conducted with variation in the normal stresses 50, 100, 150, 200 and 250 kPa as prescribed in AS 1289.6.2.2 - 1998. The maximum failure shear stresses were then plotted with the corresponding normal stress to obtain c and ϕ' for the given water content. The shearing rate determined from the oedometer tests were adopted for the direct shear tests. The same procedure was repeated for five different water contents to replicate in-situ water contents.

The direct shear apparatus (Fig. 4) accommodated samples with a diameter of 63.5 mm and a height of 25 mm. The soil samples prepared for the predetermined initial moisture contents were statically compacted to achieve the target density. Subsequently, a representative sample was cut into a shear ring, as shown in Fig. 4, followed by the placement of filter papers and porous disks, at the top and the bottom of the sample.

After determining c and ϕ' for different water

contents, using the SWCC, which was measured for the same density, the suction corresponding to the volumetric water content was obtained and ultimately the variation of c with the suction was adopted to determine ϕ^b .

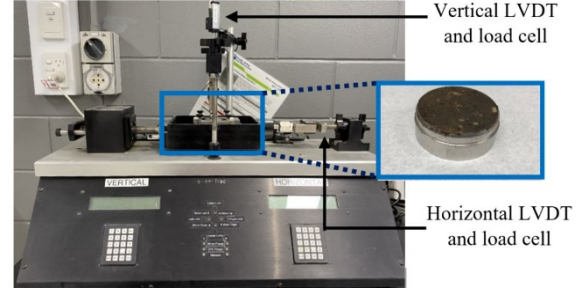


Fig. 4 Direct shear apparatus and the soil sample compacted into the cutting ring for direct shear test

RESULTS AND DISCUSSION

The SWCC

The total suction (ψ) was measured based on the relative humidity concept, and the SWCC equation proposed by Fredlund and Xing [11] was used in this study. However, due to the negligible osmotic suction, the total suctions were assumed as the matric suctions. Figure 5 depicts the SWCC for the test material.

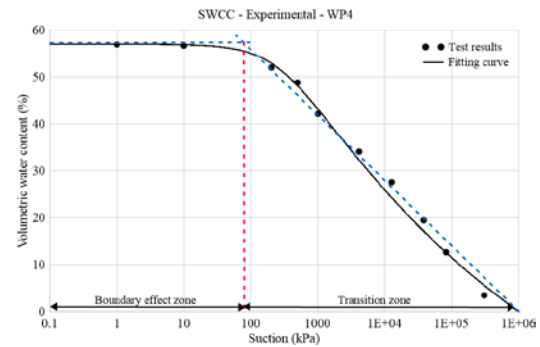


Fig. 5 The SWCC for the test material

The air-entry suction is about 85 kPa, and the residual degree of saturation 8.2%. The SWCC is clearly step-phased with the boundary effect zone and the transition zone well defined while the residual zone is not well defined. In the boundary effect zone, the soil is almost saturated, and the water content is nearly independent of suction, while the shear strength develops linearly with suction. In the transition zone, the water content decreases drastically as the suction increases, and the shear strength varies nonlinearly with suction. In the residual zone, the water content has a residual value. For sandy and silty soils, the shear strength is independent of suction; by contrast for clayey soils, it

increases slightly with the suction increase [9].

Shearing rate

The t_{50} determined using Taylor's square root of time fitting method was adopted in calculating the shearing rate. Initially, compression vs square-root-of-time plot was produced as depicted in Fig. 6. Figure 6 presents the compression vs square-root-of-time plot for the volumetric water content of 34.6% under normal stresses 50, 100, 150, 200 and 250 kPa. The construction as prescribed in AS 1289.6.6.1-1998 was then employed in determining shearing rates. Table 2 summarises the shearing rates determined for the volumetric water content of 34.6%, and a similar procedure was followed in determining shearing rates for soil specimens with other moisture contents.

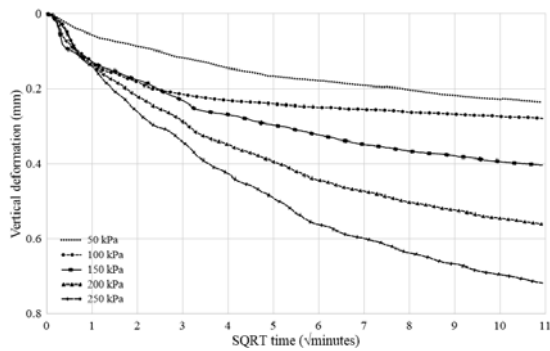


Fig. 6 The compression versus square-root-of-time plot for the volumetric water content of 34.6%

Table 2 Shearing rates determined for the volumetric water content of 34.6%,

Normal stress (kPa)	t_{50} (min)	Shear rate (mm/min)
50	7.247	0.055
100	6.317	0.063
150	5.898	0.069
200	4.628	0.086
250	6.450	0.062

Direct shear tests

Direct shear tests were conducted for all the five moisture contents under the same normal stresses 50, 100, 150, 200 and 250 kPa. Figure 7 presents the variation of shear stress with horizontal displacement for the soil specimens with the volumetric water content of 34.6%. Figure 7 depicts that the peak shear stresses were increased with the normal stress and curves are clearly step-phased. In the beginning, the shear stress increases very rapidly with the increase of shear displacement. Then, after a certain stress value, the slope of the curve declines. It also suggests that when the normal stresses increase from 50 to 250

kPa, the stress-strain relationship of the specimen changes from strain-softening to strain-hardening.

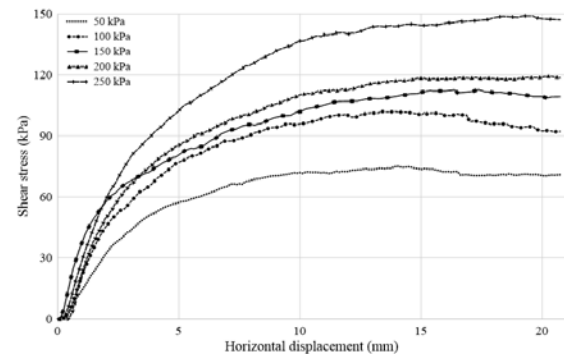


Fig. 7 Variation of shear stress with horizontal displacement under different normal stresses for the volumetric water content of 34.6%

Shear strength

The shear strength of the soils decreased with the increase in moisture content. Average volumetric water contents ranged from 0.25 to 0.43 for the test material (44.0 - 75.4% saturation). Figure 8 shows the results with a simple linear regression for each of the volumetric water content. Table 3 lists the values of the y-intercept and the inclination of the regression lines (i.e. cohesive strength and angle of shearing resistance in terms of simple linear regression), along with the corresponding suction values as per the Fredlund and Xing [11] fitting curve presented in Fig. 5.

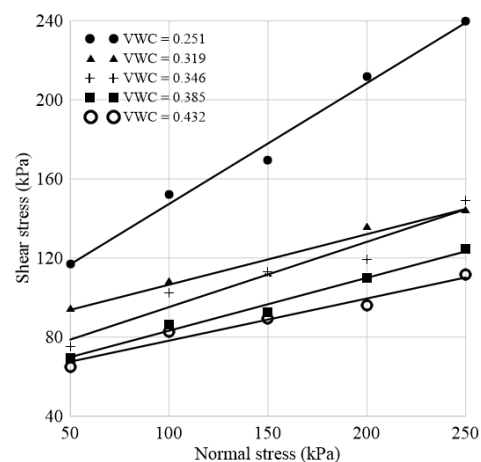


Fig. 8 Results of the direct shear tests (The solid lines indicate the simple linear-regression lines for each specimen group)

Table 3 Shear strength parameters obtained by simple linear regression with suction

Volumetric water content (m ³ /m ³)	Cohesion (kPa)	Friction angle (Degree)	Suction (kPa)
0.251	86.28	31.42	11258.7
0.319	81.01	14.32	4364.8
0.346	65.25	18.24	3043.5
0.385	56.52	14.97	1827.7
0.432	56.93	12.02	991.8

The inclinations of the regression lines are largest in the driest conditions and drastically decreases for the wetter samples, converging at 12–18° (Fig. 8; Table 3). In other words, the angle of shearing resistance of the moist soils seems to be constant, independent of volumetric water content, except in the driest condition.

The y-intercepts of the regression lines decreased with increasing moisture content and approached a minimum value at the more saturated condition (Table 3). Figure 9 shows the relationships between the corresponding suction values for the average volumetric water content in each group and the y-intercept of the regression lines. The values of the y-intercept tend to increase linearly on the semi-log scale (i.e. the cohesive strength of the soils exponentially increase with an increase in suction).

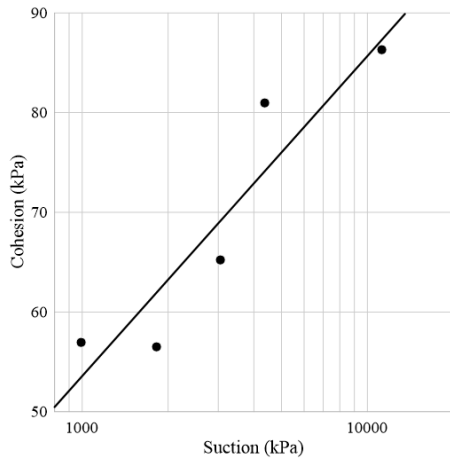


Fig. 9 Relationship between the corresponding suction values for the average volumetric water content and cohesive strength

Formulation of shear strength as a function of suction

On the basis of the shear strength reduction characteristics (Figs. 8 and 9), it was assumed that: (1) the angle of shearing resistance takes a constant value; (2) an exponential function is valid to express the relationship between apparent cohesion and suction.

From this, the regression function can be postulated as follows:

$$\tau = \sigma' \tan \phi' + C e^{\mu \psi} \quad (5)$$

where τ is shear strength, σ' is net normal stress, ψ is suction, ϕ' is the effective angle of shearing resistance, C is a hypothetical minimum value of cohesion (when $\psi = 0$), and μ is a coefficient related to the susceptibility of strength increment ($\mu > 0$).

To determine the values of unknowns (i.e. ϕ' , C and μ), Eq. 5 should be linearised as in below Eq. 6:

$$\ln [\tau - \sigma' \tan \phi'] = \mu \psi + \ln C \quad (6)$$

Using the linearised Eq. 6, multiple regression analyses were conducted by considering arbitrary ϕ' . For arbitrary ϕ' values, simple linear regression analyses were conducted for data sets of $\ln [\tau - \sigma' \tan \phi']$, and ψ to determine the ϕ' with the highest coefficient of determination, as shown in Fig. 10.

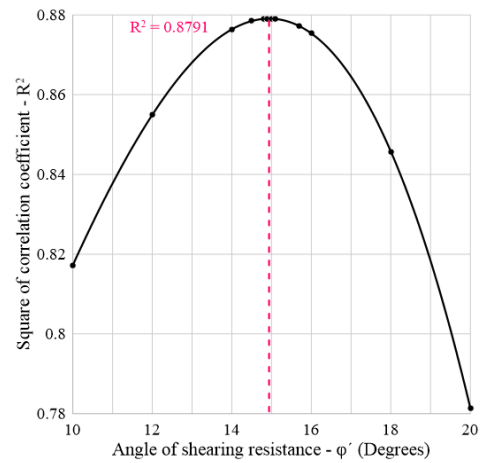


Fig. 10 Variation in square of correlation coefficient of Eq. 6 with respect to the varied value of ϕ'

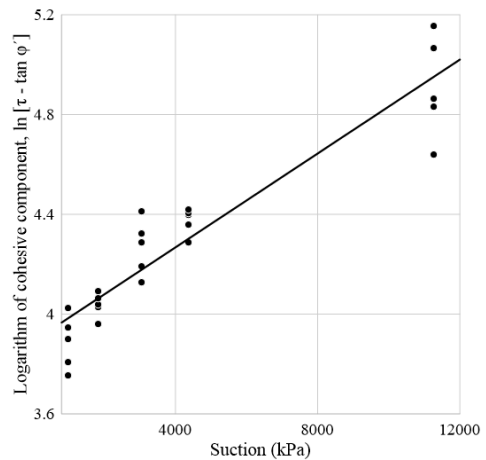


Fig. 11 The relationships between the logarithm of cohesive shear strength and suction

The shear strength of test material was well represented by the below regression function $\tau = \sigma' \tan 14.9^\circ + 56.61e^{3.89\psi}$ as depicted in Fig. 11 ($R^2 = 0.8791$). The regression variables in the equations include the liquefaction characteristics of the soils, effects of lubrication and susceptibility to changes in pore-water pressure during the shear deformation. For this reason, the values should be considered purely as empirical parameters for the soils, each of which has inherent geotechnical behaviours.

CONCLUSIONS

The cohesive strength of an unsaturated expansive soil was formulated as an exponential function of suction. In the formulation, shear strength τ was expressed as $\tau = \sigma' \tan \phi' + Ce^{\mu\psi}$; where σ' is net normal stress, ϕ' is the effective angle of shearing resistance, C is minimum cohesion, μ is a susceptibility coefficient, and ψ is suction of soil. An advantage of this formulation is that all the parameters required are available without any extensive soil testing. The variables can be obtained by a basic shear test and a subsequent regression analysis. It is considered that this empirical method provides a convenient alternative for engineering practice.

ACKNOWLEDGMENTS

Authors gratefully acknowledge the technical staff at Queensland University of Technology (QUT) for providing the laboratory facilities to conduct the test series. Further, gratitude should be extended to Steve Hackworth from THE SOILTESTERS for providing the in-kind support for the project. The first author acknowledges the scholarship for the doctoral degree received from QUT, Australia.

REFERENCES

- [1] C. Gallage and T. Uchimura, "Direct Shear Testing on Unsaturated Silty Soils to Investigate the Effects of Drying and Wetting on Shear Strength Parameters at Low Suction," *Journal of Geotechnical and Geoenvironmental Engineering*, vol. 142, 2016.
- [2] M. P. Amarasinghe, L. I. N. De Silva, and C. Gallage, "The effect of lateral confinement on the settlement characteristics of shallow foundations on sand," *International Journal*, vol. 15, pp. 258-265, 2018.
- [3] S. Jayakody, C. Gallage, and J. Ramanujam, "Effects of reclaimed asphalt materials on geotechnical characteristics of recycled concrete aggregates as a pavement material," *Road Materials and Pavement Design*, vol. 20, pp. 754-772, 2019.
- [4] C. Gallage, S. Jayakody, and T. Uchimura, "Effects of slope inclination on the rain-induced instability of embankment slopes," in *Proceedings of the Second International Conference on Geotechnique, Construction Materials and Environment*, 2012, pp. 196-201.
- [5] C. Gallage, J. Kodikara, and T. Uchimura, "Laboratory measurement of hydraulic conductivity functions of two unsaturated sandy soils during drying and wetting processes," *Soils and Foundations*, vol. 53, pp. 417-430, 2013.
- [6] C. Gallage, R. Udukumburage, T. Uchimura, and T. Abeykoon, "Comparison of direct and indirect measured soil-water characteristic curves for a silty sand," *International Journal of GEOMATE*, vol. 13, pp. 9-16, 2017.
- [7] T. Abeykoon, C. Gallage, and J. Trofimovs, "Optimisation of sensor locations for reliable and economical early warning of rainfall-induced landslides," in *Ninth International Conference on Geotechnique, Construction Materials and Environment (GEOMATE 2019)*, Japan, 2019, pp. 69-74.
- [8] T. Abeykoon, C. Gallage, B. Dareeju, and J. Trofimovs, "Real-time monitoring and wireless data transmission to predict rain-induced landslides in critical slopes," *Australian Geomechanics Journal*, vol. 53, pp. 61-76, 2018.
- [9] S. Vanapalli, D. Fredlund, D. Pufahl, and A. Clifton, "Model for the prediction of shear strength with respect to soil suction," *Canadian Geotechnical Journal*, vol. 33, pp. 379-392, 1996.
- [10] W. F. Willmott, *Slope Stability and Its Constraints on Closer Settlement on the Mapleton-Maleny Plateau, Southeast Queensland: Geological Survey of Queensland*, 1983.
- [11] D. G. Fredlund and A. Xing, "Equations for the soil-water characteristic curve," *Canadian geotechnical journal*, vol. 31, pp. 521-532, 1994.
- [12] R. S. Udukumburage, C. Gallage, and L. Dawes, "Oedometer based estimation of vertical shrinkage of expansive soil in a large instrumented soil column," *Heliyon*, vol. 5, p. e02380, 2019.

A LABORATORY METHOD FOR ACCURATE CALIBRATION OF STRAIN-GAUGE TYPE SOIL PRESSURE TRANSDUCERS

Chamara Prasad Gunasekara Jayalath¹ and Chaminda Gallage¹

¹ School of Civil and Environmental Engineering, Queensland University of Technology, Australia

ABSTRACT

Strain-gauge type soil pressure transducers are widely used in health monitoring and laboratory and field investigation on the performance of geo-structures to accurately measure the soil pressure. Even though these pressure plates are sold with the factory-measured calibration factors, these sensors should be re-calibrated in the laboratory before using them because the calibration can be affected by the data-logging system and the length of the cable used. Therefore, in this study, a laboratory calibration procedure for strain-gauge type soil pressure plates was proposed. The soil pressure transducer was embedded in a uniform-fine- sand medium in a specially designed pressure cell, and the pneumatic pressure was applied into the system as gradual increments. After that, the calibration chart of the pressure gauge was developed based on the sensor outputs for different pressures applied. Then the calibrated soil pressure transducer was used in the laboratory pavement model test to measure soil pressure at the base-subgrade interface under a surface loading area. The measured soil pressure values were compared with the estimated vertical stresses from elastic theories to validate the pressure measurements and the calibration process of the soil pressure transducer. The test results revealed that there is a satisfactory agreement between the pressure measured by the soil pressure transducer and theoretical estimations. Thus, the calibration process of the soil pressure transducer and its outputs are proven to be accurate.

Keywords: Vertical stress in soil, Geotechnical Instrumentation, Pavement subgrade, Soil pressure transducers

INTRODUCTION

The accurate measurement of soil or earth pressure is essential in health monitoring and, laboratory and field investigation on the performance of geo-structures [1]-[9]. Vibrating wire and strain-gauge type pressure plates are widely used to measure soil pressures. Strain-gauge type soil pressure plates are commonly used in laboratory model tests due to its high accuracy, less sensitivity to temperature, and availability in different sizes. Even though these pressure plates are sold with the factory-measured calibration factors, it is vital to re-calibrate these transducers in the laboratory before using them [10] as the calibration can be affected by several factors, for instance, the data-logging system and the length of the cable used. Therefore, as a common practice, several laboratory methods are used to calibrate soil pressure sensors.

The most common calibration methods of soil pressure cells are dead weight calibration (DWC), fluid/pneumatic calibration and soil calibration. In the DWC method, the calibration is performed by placing known dead weights directly on the sensing area of the pressure cell in increments. Majority of the researchers prefer to calibrate pressure sensors by DWC method as it is less time consuming, economical and easy to perform without much-advanced equipment and technical experience [11]. Generally, fluid/pneumatic calibration is highly

recommended compared to the DWC method as the former method provides more accurate results [12]. In this method, the calibration is performed in a calibration chamber by applying hydrostatic or air pressure in increments. However, this method demands advanced laboratory facilities and technical knowledge, which are not available in most laboratories. As an alternative, the soil-calibration method can be used in the laboratory to calibrate soil pressure cells. Therefore, in this study, a laboratory calibration procedure for strain-gauge type soil pressure plates using sand is proposed. Then the calibrated soil pressure transducer was used in a laboratory pavement model test to measure soil pressure at subgrade-base interface under a circular-area loading applied on the top surface. The measured soil pressures were compared with the estimated vertical stresses from elastic theories to validate the pressure measurements and the calibration process of the soil pressure transducer.

Soil Pressure Transducer

A soil pressure transducer (See Fig.1) with 1MPa capacity was used in this experimental study. The outside diameter and the thickness of the pressure plate are 200mm and 25.5mm, respectively. The percentage of rated output (%RO) of the pressure gauge has been specified as 1%, and the diameter of the sensing area is 166mm. It is designed with a dual-

diaphragm structure that can minimise the displacement of a sensing area, and thereby can keep the stress distribution undisturbed under pressure. This type of soil pressure gauges is widely used to measure the pressure in soil and to monitor the behaviour of embankments.

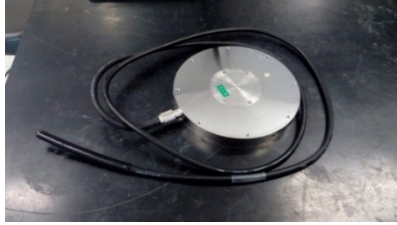


Fig.1 Soil pressure transducer

METHODOLOGY

A specially designed pressure cell [13, 14] (See Fig.2 (a)) made of acrylic was used to calibrate the soil pressure transducers. The internal diameter and the height of the cell are 360mm and 400mm respectively. Uniform-fine sand was used in this calibration. The particle size distribution and properties of the sand are given in Fig.3 and Table 1, respectively. The sand was filled up to 250mm, and the sand surface was properly levelled. After that, the soil pressure transducer was placed on top of the sand layer. The level of the top surface of the sensor was checked with a spirit level (bubble level), as shown in Fig.2 (b). Then the sand was filled to have a 50mm thick sand layer above the top of the sensor. The sand surface was levelled, and the inner wall of the cell was cleaned to remove all the attached sand and dust. Oil was applied on the inner wall of the cell to minimise the friction between the wall and the piston. After that, the piston was placed inside the cell and valves were connected to supply the pneumatic pressure into the setup.



(a)



(b)

Fig.2 calibration of soil pressure transducers; (a) The pressure cell; (b) Embedding the soil pressure

transducer in the cell

Pressure above 750kPa (i.e. 785kPa) was applied into the setup for 24 hours to allow the particle rearrangement of the sand under high pressures applied. From the initial trials conducted before this experiment, it was found that the required pressure to overcome the friction between the piston and the wall of the cell is negligible. Since the sand thickness above the top surface of the sensor is thin (i.e. 50mm), and the friction is negligible, it is reasonable to assume that the pressure applied on the sensor is equal to the applied pressure into the setup. The pressure into the system was increased approximately up to 750kPa in 50kPa increments. The pressure gauge was connected to a data logger, and the sensor readings were recorded in parts per million (ppm) for each pressure increment. Based on the sensor outputs for different applied pressures, the calibration chart of the pressure gauge was developed.

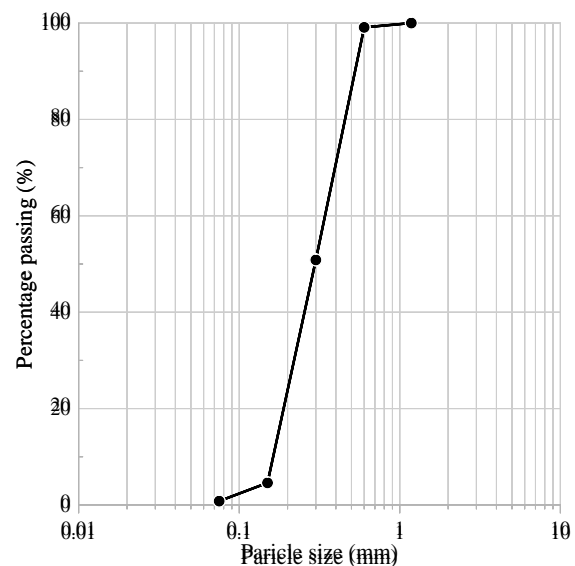


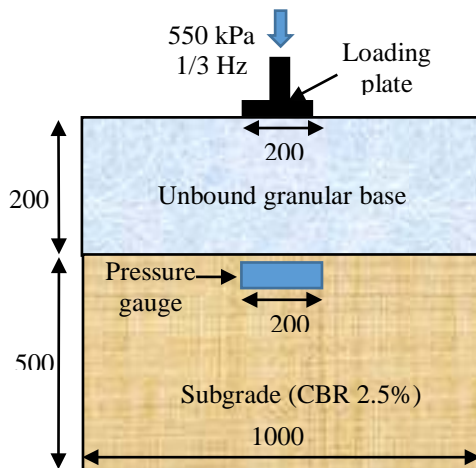
Fig.3 Particle size distribution of sand used in the calibration of soil pressure transducers

Table 1 Properties of sand used in the calibration of soil pressure transducers

Property	Value
D_{10} (mm)	0.165
D_{30} (mm)	0.220
D_{60} (mm)	0.340
Coefficient of curvature (Cc)	2.06
Coefficient of uniformity (Cu)	0.86

This soil pressure transducer was used to measure the pressure applied at the base-subgrade interface of unbound-granular pavement-models during a cyclic

loading test series. The schematic diagram of the experimental setup of the cyclic-loading pavement test is shown in Fig.4. A granular pavement with 200mm unbound-granular base and 500mm thick subgrade with 2.5% unsoaked-CBR was selected in the present study to verify the pressure measurements given by the pressure gauge. The pressure gauge was embedded in the subgrade close to the base-subgrade interface and below the centre of the loading area as shown in Fig.5. In this experiment, the maximum load of 17.31kN was applied through a 25mm thick and 200mm diameter steel plate to create a tyre-contact pressure of 550kPa with a frequency of 0.33Hz. More details of the conducted test can be found in [15] and [16]. The pressure sensor was connected to the data logger, and the readings were recorded for every five seconds. After that, the captured sensor outputs were converted to pressure readings using the developed calibration equation.



Note: Not to scale

All dimensions are in millimetres

Fig.4 The schematic diagram of the experimental setup of the cyclic-loading pavement test



Fig.5 Installation of the soil pressure transducer

The measured soil pressure values were compared with the calculated values from two elastic-theories methods, namely the Boussinesq method [17] and Fox L. method [18], to validate the measured values and the calibration process of the soil pressure gauge. Even though the Boussinesq equation for vertical stresses under uniformly loaded circular area has been derived for homogeneous, elastic, and isotropic mediums, it was used for this two-layer system for a rough estimation of vertical stresses at the base-subgrade interface. The pressure applied at the base-subgrade interface was also computed based on the chart for the vertical stresses on the interface stresses developed by the Fox L. method.

RESULTS AND DISCUSSION

The applied vertical pressure values were plotted against the corresponding sensor readings to develop the calibration chart of the soil pressure transducer, as shown in Fig.6. The equation for the regression line of the plotted points was adopted as the calibration equation of the sensor. The obtained calibration equation perfectly fits the data as the coefficient of determination is equal to one ($R^2=1$). Later, this calibration equation was utilised to determine the vertical stresses applied at the base-subgrade interface of the laboratory-scale unbound-granular-pavement model.

Fig.7 illustrates the variation of the vertical stress at the base-subgrade interface of the laboratory-scale unbound-granular-pavement model. Three curves were produced depending on the technique (e.g. pressure gauge, Boussinesq method and Fox L. method) used to measure/estimate vertical stresses during the test. All three curves were plotted approximately up to 120,000 cycles where the cycling loading test was stopped. Results show that the estimated vertical stresses from the Boussinesq method are always higher than the Fox L. method. Soon after the commencement of the loading, the vertical stress applied at the base-subgrade interface was measured as 170kPa whereas the estimated stresses were 169kPa and 144kPa respectively from the Boussinesq equation and Fox L. method. The measured vertical stresses follow the similar shape and magnitudes of the vertical stress development that has been computed by the Boussinesq method in the initial stage of the test, approximately up to 27,000 cycles where the measured vertical stress lies at 260kPa. Then, the measured vertical stresses by the soil pressure transducer fluctuate in between the vertical stress values that have been estimated by the two elastic-theory methods up to 100,000 cycles. Afterwards, the measured vertical stresses follow the similar shape and magnitudes of the vertical stress variation that has been estimated by the Fox L.

method until the end of the test where the measured vertical stress was 313kPa.

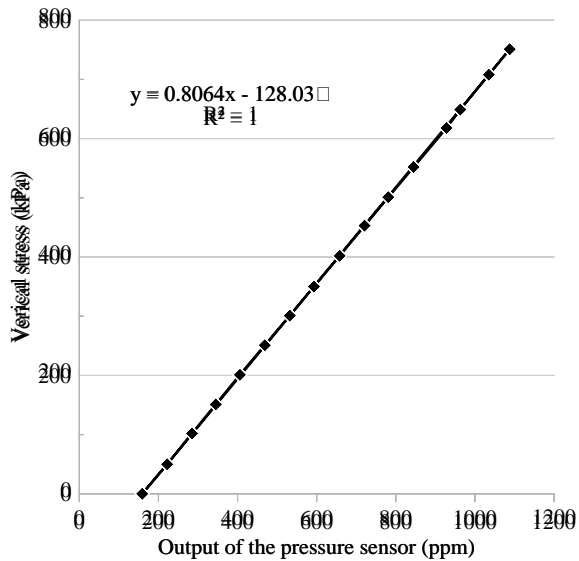


Fig.6 Calibration chart of the soil pressure transducer

As mentioned in the methodology section, the Boussinesq equation has been developed to estimate vertical stresses of homogeneous, elastic and isotropic mediums but the tested pavement section has two layers (i.e. subgrade layer and granular base layer) which have completely different material properties. Each layer alone can be considered as homogeneous and elastic; however, both subgrade and granular materials are cross-anisotropic. The referred chart from the Fox L. method for the vertical stresses on the interface has been developed for two-layer pavement systems considering the influence of the ratio of the elastic modulus of the top and the bottom layers (E_1/E_2). As the subgrade CBR value is 2.5%, the elastic modulus of the subgrade has been estimated to be 25MPa based on the approximation that elastic modulus of pavement material is ten times its CBR value as has been specified in Austroads Guide to Pavement Technology Part 2: Pavement Structural Design [19]. Based on the mechanistic-pavement design principals, the average elastic modulus of the granular base, which was limited by the weak subgrade was estimated as 51MPa. Therefore, the E_1/E_2 of the pavement section is approximately two (i.e. $E_1/E_2 = 2$). However, in the Boussinesq case, E_1/E_2 ratio must be assumed as one (i.e. $E_1/E_2 = 1$) even when it is used for a two-layer system. These assumptions may result in slight differences between the actual pressure measurements and estimated vertical stresses from these theoretical methods. Overall, it is evident that a reasonable agreement between the pressures measured by the sensor and the theoretical

estimations is apparent. Thus, the calibration process of the soil pressure transducer and its outputs are proven to be accurate. Therefore, the proposed calibration method can be used to calibrate soil pressure cells in the laboratory accurately.

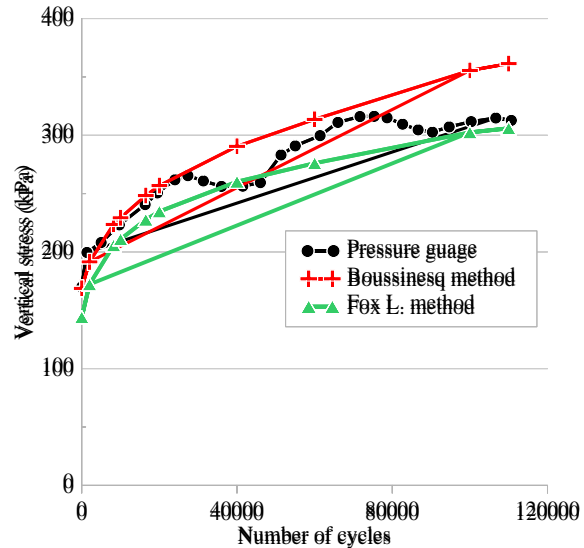


Fig.7 Development of the vertical stress at the base-subgrade interface

CONCLUSIONS

Based on the test results of the calibration of the pressure transducer, and the comparison of measured pressures with theoretical estimations, the following conclusions can be drawn:

- The developed calibration equation perfectly fits the data as the coefficient of determination is equal to one ($R^2=1$); therefore, it can be assumed as accurate.
- A satisfactory agreement between the sensor measurements and theoretical estimations is evident. Thus, the calibration process of the soil pressure transducer and its outputs are proven to be accurate.
- The presented calibration method can be effectively used as a laboratory calibration methodology to calibrate soil pressure cells accurately.

ACKNOWLEDGMENTS

The authors acknowledge the continued support of the Department of Transport and Main Roads (TMR) and Australian Road Research Board (ARRB) by providing the required funding for the instruments including data logger and pressure sensors for this research study and supplying the required testing materials. Thanks are also extended to the technical staff of Banyo Pilot Plant Precinct of Queensland University of Technology (QUT) for their great support and assistance during the pavement model test. Further, the first author would like to thank his colleagues and friends who helped in preparing the

pavement model, and for QUT for providing him with a scholarship to pursue his postgraduate studies.

REFERENCES

- [1] Gallage C., Kodikara J.K., Chan D., Response of a plastic pipe buried in expansive clay, *Proceedings of the Institution of Civil Engineers: Geotechnical Engineering*, 165 (1), 2012, pp.45-57
- [2] Chan D., Gallage C.P., Rajeev P., Kodikara J.K., Field performance of in-service cast iron water reticulation pipe buried in reactive clay, *Canadian Geotechnical Journal*, 52 (11), 2015, pp.1861-1873
- [3] Chan D., Rajeev P., Kodikara J.K., Gallage C.P., Field performance of in-service cast iron gas reticulation pipe buried in reactive clay, *Journal of Pipeline Systems Engineering and Practice*, 7 (2), 2016, pp.1-15
- [4] Chan D., Gallage C., Gould S., Kodikara J.K., Bouazza A., Cull J., Field instrumentation of water reticulation pipe buried in reactive soil, In *Ozwater'09: Australia's National Water Conference and Exhibition*, Melbourne, Victoria, Australia, 2009, pp.9-16
- [5] Gallage C.P., Kodikara J.K., Chan D., Davis P., A comparison of the results of the numerical analysis and the physical behaviour of a pipe buried in reactive clay, in *Proceedings of the 12th International Conference of the Association for Computer Methods and Advances in Geomechanics (IACMAG)*, 2008, pp.1-9.
- [6] Kodikara J., Davis P., Gallage C., Chan D., Gould S. and Zaho X.L., Behaviour of a polyethylene pipe buried in reactive soil. *Proceedings of the 7th National ASTT Conference*, Sydney, Australia, 2008 (CD ROM publication).
- [7] Gallage C., Chan D., Gould S., Kodikara J.K., Behaviour of an in-service cast iron water reticulation pipe buried in expansive soil, In *Ozwater'09: Australia's National Water Conference and Exhibition*, 16-18 March 2009, Melbourne, Victoria, Australia, 2009, pp.1-8
- [8] Gallage C.P., Chan D., Kodikara, J.K., Ng P.C., Discussion: Response of a plastic pipe buried in expansive clay, *Proceedings of the Institution of Civil Engineers: Geotechnical Engineering*, 166 (3), 2013, pp.328- 330.
- [9] Gallage C., Gould S., Chan D., Kodikara J., Field measurement of the behaviour of an in-service water reticulation pipe buried in reactive soil (Altona North, Victoria), Monash University, Australia, Research report RR10. 2008.
- [10] Chen Q., Abu-Farsakh M., and Tao M., Laboratory evaluation of geogrid base reinforcement and corresponding instrumentation program. *Geotechnical testing journal*, 32(6), 2009, pp.516-525.
- [11] Gade V. K., and Dasaka, S., Calibration of Earth Pressure Sensors. *Indian Geotechnical Journal*, 2017, pp.1-11.
- [12] Ramírez A., Nielsen J. and Ayuga, F., On the use of plate-type normal pressure cells in silos: Part 2: Validation for pressure measurements. *Computers and electronics in agriculture*, 71(1), 2010, pp.64-70.
- [13] Gallage C.P., Mostofa M., Vosolo DA, Rajapakse J.P., A new laboratory model of a slaking chamber to predict the stability of on-site coal mine spoils, *International Journal of GEOMATE*, 10 (22), 2016, pp.2065-2070
- [14] Gallage C.P., Mostofa M., Vosolo D.A., Rajapakse J.P., Laboratory investigation on the effects of overburden pressure, water, and time on slaking induced material property degradation of coal mine spoil, *Geotechnique, Construction Materials and Environment*, 2015, pp.395-400
- [15] Jayalath. C.P.G, Gallage C., Dhanasekar M., Dareeju B., Ramanujam J., and Lee J. Pavement model tests to investigate the effects of geogrid as subgrade reinforcement. In Liu, H, Mills, P, Ruxton, N, & Mazengarb, C (Eds.) *Proceedings of the 12th Australian and New Zealand Young Geotechnical Professionals Conference*. Australian Geomechanics Society, Australia, 2018, pp.1-8.
- [16] Wimalasena K. and Jayalath C.P.G., Effect of geogrid reinforcement in weak subgrades. *International Journal*, 18(65), 2020, pp.140-146.
- [17] Boussinesq J., *Application des Potentials à L'Etude de L'Equilibre et du Mouvement des Solides Elastiques*, Gauthier-Villars, Paris, 1883.
- [18] Fox L., Computation of traffic stresses in a simple road structure. *Proc. 2nd ICSMFE*, 1948, 1, 1948, pp.236-246
- [19] *Austroroads Guide to Pavement Technology Part 2: Pavement Structural Design*. Austroroads Inc.: Sydney, Australia, 2012.

NUMERICAL SIMULATION OF INHIBITORY EFFECT OF SUBSIDENCE FOR THE LEANING PAGODA BY GROUND IMPROVEMENT

Yuko Ishida¹, Hajime Ito² and Ryoichi Fukagawa³

¹ Civil Engineering and Environment Course, Osaka Prefecture University College of Technology, Japan;

² JIP Techno Science Corporation., Japan;

³ Department of Science and Engineering, Ritsumeikan University, Japan

ABSTRACT

The Wat Krasai pagoda in Ayutthaya, Thailand, leans mainly toward the north. The main cause of deformation of the pagoda is soft clay sediments and one of the other causes is the deterioration of bricks and mortar which compose the pagoda. In 2013, the surface of the lower part of the pagoda was covered with new bricks to suppress weathering as the restoration work. Additionally, the original bases were reconstructed by new bricks piled around the pagoda up to a height of approximately 2.3 m above the ground. We conducted field surveys twice a year from 2014 and confirmed that the ground surface deformed during the rainy season and cracks and irregularities generated in the reconstructed structures. In 2019, we found a gap was created between the restored base and the pagoda at the southside. As a result of the measuring of inclination and these surveys, we thought that the pagoda has been continuously sinking toward the north and it has possible of subsidence in the future. Therefore, a countermeasure to stop the inclination of the pagoda is needed. In this study, ground improvement is assumed as a countermeasure work for an unequal settlement and the numerical simulation was conducted to grasp the effect of ground improvement. The results indicate that the weight of new bricks due to restoration work in 2013 promote subsidence and inclination of the pagoda. In addition, ground improvement is effective for settlement, decreased the amount of subsidence with increasing the thickness of ground improvement.

Keywords: Consolidation analysis, Differential settlement, Soil improvement, World heritage, Inclined Pagoda

INTRODUCTION

Ayutthaya in Thailand is located approximately 90 km north of Bangkok and was the capital of the Ayutthaya dynasty, which lasted 417 years from 1350. The “Historic City of Ayutthaya” was recognized as a World Heritage site in 1991 owing to the following criteria: “The historic city of Ayutthaya is an excellent testimony for the development of true Thai national art.” The Ayutthaya ruins are characterized by tall pagodas and monumental proportions of Buddhist monasteries [1]. Some historical buildings made of bricks, such as pagodas and walls of temples, have tilted or collapsed, as shown in Fig. 1. This study focused on the conservation of the leaning pagoda at Wat Krasai from the viewpoint of cultural property protection. The objective of this study is to stop the tilting of the pagoda and enable the inheritance of historical assets in a good condition for the future. We observed the condition of the pagoda and surrounding assets twice a year from 2014, started monitoring groundwater fluctuation 2016 onward, and measured the angle of the pagoda from 2018. These results indicated that the pagoda was still sinking and leaning. Therefore, a countermeasure to stop the inclination of the pagoda is needed. In this paper, the simulation results are reported for cases wherein the ground

improvement is conducted as a countermeasure for unequal settlement.

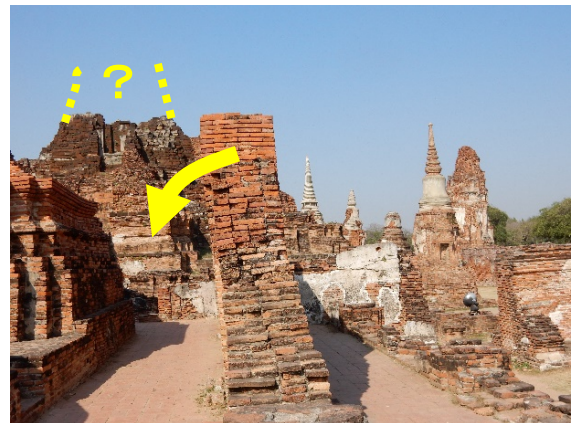


Fig. 1 Brickwork at Wat Mahathat
(Photograph taken on March 1, 2016)

HISTORY OF WAT KRASAI

According to the signboard at the Wat Krasai site, there is no evidence of its historical information or period of construction. However, it can be surmised

that Wat Krasai was built at least prior to 1767 owing to its use as a Burmese army base during the second Burmese–Siamese War. Additionally, Wat Krasai has been mentioned in the Late Ayutthaya Period as the burial site of Phra Si Sin, who was charged with treason to King Na Rai the Great, who ruled between 1656 and 1688. Assuming that Wat Krasai was erected in the days of King Nar Rai, it can be inferred that it has been approximately 360 years since it was constructed.

When the Wat Krasai temple was built, it was surrounded by walls. The principal pagoda, Chedi, was bell-shaped, built on an octagonal foundation, which was a popular Chedi style in the early Ayutthaya period. The principal pagoda was surrounded by four auxiliary Chedis. In front of the principal pagoda, a building is presumed to be a Ubosot. However, we cannot confirm the existence of the walls, four auxiliary Chedis, and the Ubosot as of 2010, based on the data from Google Earth [2]. In 2013, extensive restoration work was conducted at Wat Krasai. Before restoration, the surface bricks of the principal pagoda had deteriorated and the octagonal foundation had collapsed or was buried underground, as shown in Fig. 2. As part of the restoration, a lower part of the deteriorated surface of the principal pagoda was covered with new bricks, and a new octagonal foundation and square base were reconstructed, as shown in Fig. 3. Additionally, the walls surrounding the precinct and the foundation of the auxiliary Chedis were reconstructed. A ground survey was conducted ahead of the restoration in the southeast and northwest regions of the pagoda. The ground investigation confirmed that the thickness of the second layer, which is composed of soft cohesive soil, was thicker in the northwestern part than in the southeastern part. One of the possible causes for the pagoda leaning toward the north is the second clay layer. Many bricks were used during this restoration work, wherein a new weight was loaded onto the ground.



Fig. 2 Photograph of principal pagoda before restoration



Fig. 3 Principal pagoda after restoration (Photograph taken on February 22, 2014)

PROBLEMS OF BRICKWORK BUILDINGS IN AYUTTHAYA

Bricks are mainly made of clay or mud and shaped into a rectangular parallelepiped and then sun-dried or fired in a kiln. Thereafter, owing to fluctuations in temperature and repeated humidity, they degrade and return to the soil. Such deterioration of bricks is a common problem in historical brick buildings around the world. Several studies on historical brick structures have focused on the deterioration of bricks. Nishiura et al. confirmed the progression of brick deterioration in Egyptian remains during their conservation study [3].

Because some stucco remained on the surface of the historical brick buildings in Ayutthaya, it is possible that the entire surface was protected by a stucco at the beginning of construction. However, when the plaster on the surface wore away due to deterioration over time, it exposed a means for water penetration that melts the clay mortar and weakens the structure, possibly leading to an eventual collapse. Therefore, ICOMOS Thailand points out that the deterioration of bricks and mortar due to water is one of the risks of Thai monuments [4]. Ishizaki et al. carried out moisture measurements, precipitation salt surveys, and meteorological observations on historical brick buildings in Ayutthaya and determined the relation between brick deterioration and moisture migration in brick materials [5]. In addition, Ishizaki et al. conducted a moisture migration analysis before and after the surface layer waterproof strengthening treatment of the Sukhothai Brick Buddha. The results of the analysis showed that the water content of the sediment decreased due to the

waterproof treatment, consistent with the measurement results [6]. Yoshida et al. created an analytical model for heat and moisture transfer in the Sukhothai Brick Buddha. Additionally, they showed that the possible cause of discoloration was the movement of the components of the stucco and bricks to the surface associated with the internal moisture, leading to evaporation [7].

We have been observing the restored pagoda, reconstructed wall, and basements of Chedis at Wat Krasai twice a year from 2014. Deterioration of the brick block of pagoda restored in 2013 was identified in 2017, as shown in Fig. 4. The restored bricks are piled up according to the inclination of the original bricks; therefore, water gathers through joints on the north side. In fact, bricks on the northwest side, having a larger inclination, are significantly deteriorated. When the brick deteriorates and collapses, the voids of the brick block are compressed and the volume decreases. The pagoda has a distortion. We infer that partly breaking bricks by deterioration can possibly affect the deformation of the pagoda.

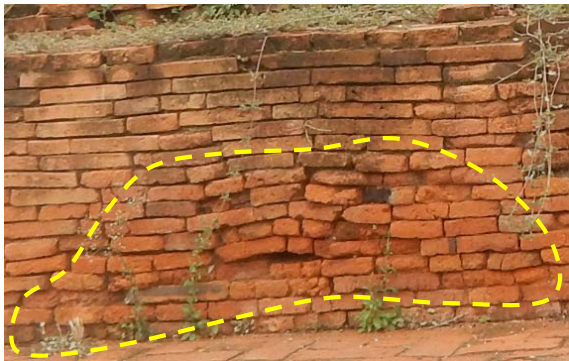


Fig. 4 Deterioration of bricks of the Wat Krasai pagoda (Photograph taken on May 17, 2017)

Historical brick buildings have other issues owing to soft ground. Kuchitsu indicated that the structural problem of brick buildings due to uneven settlement was greater than that owing to the weathering of salts and biodeterioration by moss and lichens [8]. In a study that nondestructively investigated the deterioration of stone materials at Angkor ruins, Uchida indicated that the uneven settlement of the ground and the deformation of the platform had a significant influence on the structure [9].

The deformation of the reconstructed wall owing to the softening of the ground during the monsoons of 2017 was confirmed at Wat Krasai, as shown in Fig. 5. Several cracks were recognized at the reconstructed base of the Chedi and the pagoda. In addition, we observed a gap between the main body of the pagoda and the adjoining reconstructed square base in 2019, as shown in Fig. 6. An increasing this gap width was confirmed in February 2020. Resulting

from these surveys and measurements, we speculate that the main body of the pagoda has been sinking toward the north separately from the reconstructed base surrounding the main body. We thought that one of the causes of subsidence of the pagoda is adding the weight of new bricks by the restoration, and one of the other causes is without countermeasures against the soft clay layer such as ground improvement.



Fig. 5 Deformation of brick wall at Wat Krasai (Photograph taken on May 17, 2017)



Fig. 6 The gap between the main body and reconstructed basement of the pagoda (Photograph taken on August 20, 2019)

INHIBITION OF INCLINE OF STUPA BY GROUND IMPROVEMENT

Ground improvement is a common countermeasure method against the soft ground. There are many problems that should be solved in the actual construction if this method is chosen for

countermeasure work of Wat Krasai. However, we only examine the effect of ground improvement by numerical simulation in this paper.

Analysis models for the numerical simulation

Bricks of the Wat Krasai pagoda are covered with weak binding by soft mortar, and it is assumed that individual blocks move flexibly. In addition, sand was filled inside the reconstructed square brick base of the pagoda. Therefore, the pagoda behaves differently from a completely rigid body. However, the pagoda was treated as a structural body in the analysis.

A nonlinear finite element analysis was performed with the plane strain condition using PLAXIS, which is a finite element program software. It is assumed that it took two years to build the Wat Krasai pagoda based on inquiries with the archeologists of the Ayutthaya historical park. After construction to restoration in 2013, it was set to 360 years. In 2013, restoration bricks were added to the pre-restoration model of the pagoda. Additionally, the end of analysis was set to after 100 years, from 2013.

The composition formula of the sandy soil was used as a linear elastic model, and that of the clay soil was used as an elasto-plastic model as per the Sekiguchi–Ohta model. This is widely prevalent in Japan because it considers the occurrence of plastic strain accompanying the anisotropy of naturally deposited clay. A procedure to determine the input parameters of the Sekiguchi–Ohta model was previously developed by Iizuka et al. [10].

Parameters and analysis cases

Wat Krasai pagoda is hollow, with an approximate height of 26.9 m. The cross-section of analysis is shown in Fig. 7. The soil layers comprised five layers. The thicknesses of the layers and each parameter are shown in Table 1 and 2. The parameters of the brick are listed in Table 3.

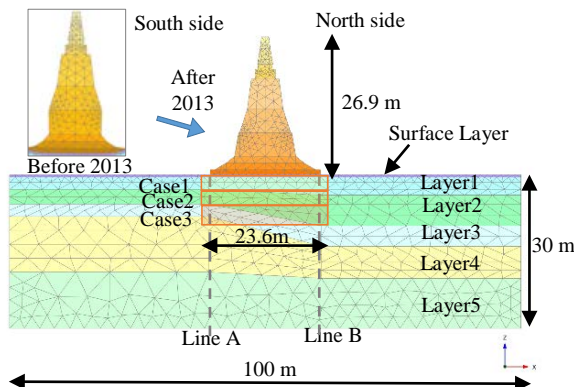


Fig. 7 Cross-section of the Analysis

Table. 1 Thickness of soil layers and parameters

Thickness	Surface	1st Layer	2nd Layer
Line A (m)	0.5	2.350	2.890
Line B (m)	0.5	3.48	6
Thickness	3rd Layer	4th Layer	5th Layer
Line A (m)	2.42	10.840	11.000
Line B (m)	3.99	6.26	9.77

Table. 2 Soil parameters of each layers

Layer	Surface	1st Layer	2nd Layer
Constitution rule of soil	Mohr-Coulomb	Elasto-plastic (Sekiguchi-Ohta)	Elasto-plastic (Sekiguchi-Ohta)
M	-	1.035	1.009
Λ	-	0.5915	0.5764
D	-	0.0726	0.0726
ν'	0.2	0.358	0.362
K_0	-	0.559	0.568
e_0	-	1.223	1.324
E [kN/m ²]	8540	-	-
γ_{unsat} [kN/m ³]	19.2	19.2	17.1
γ_{sat} [kN/m ³]	19.2	19.2	17.1
k [m/day]	2.40E-06	2.40E-06	3.60E-06
Layer	3rd Layer	4th Layer	5th Layer
Constitution rule of soil	Linear elastic	Elasto-plastic (Sekiguchi-Ohta)	Linear elastic
M	-	1.128	-
Λ	-	0.6444	-
D	-	0.0611	-
ν'	0.3	0.344	0.3
K_0	-	0.525	-
e_0	-	0.940	-
E [kN/m ²]	15050	-	28560
γ_{unsat} [kN/m ³]	19.0	19.2	19.0
γ_{sat} [kN/m ³]	20.0	19.2	20.0
k [m/day]	2.00E-04	3.60E-06	1.20E-03

Table. 3 Material properties of bricks

Material model	Lineare elasticity
Density	1.546 g/cm ³
Young's modulus	5.0×10^5 g/cm ²
Poisson ratio	0.07
Unitweight	15.15 kN/m ³
Density	1.546 g/cm ³

The area of ground improvement is set to the reconstructed square basement, 1.0 m on the outside. The depth of ground improvements are set for each case as follows:

- Case.1: No ground improvement
- Case.2: GL-3.0 m
- Case.3: GL-6.0 m
- Case.4: GL-10.0 m

RESULTS AND DISCUSSION

The temporal change in the inclination of the pagoda in Case 1 is shown in Fig. 8. The inclination

was calculated from the south and north points, as indicated in Fig. 9. The result indicates that a rapid incline occurred during the construction of the pagoda. It is assumed that consolidation was promoted at the second soft clay layer at an early stage. After rapid inclination, only a slight tilt occurred. Furthermore, because the additional weight was loaded to the ground by the restoration work in 2013, the inclination was promoted. This is consistent with the situation in which a gap occurs between the main body of the pagoda and the reconstructed square basement. The inclination of the pagoda will gradually increase in the future. The measured inclination of the pagoda was approximately 2° to 11° [11]; therefore, the result may be underrepresented.

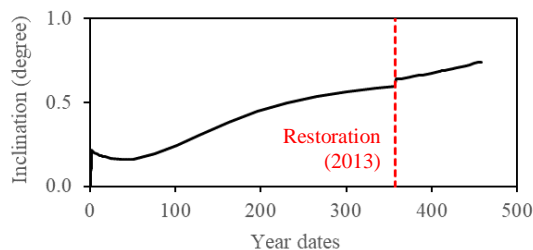


Fig. 8 Temporal change of inclination (Case 1)

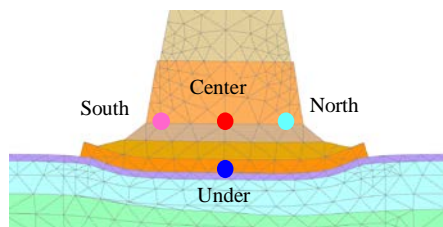


Fig. 9 Output reference points

The temporal change in the settlement of the pagoda 300 years after construction in all cases is shown in Fig. 10. The settlement of the pagoda also tends to gradually increase in the future. However, the results indicate that ground improvement prevents subsidence. In addition, the effect of prevention for subsidence increases with the thickness of the ground improvement.

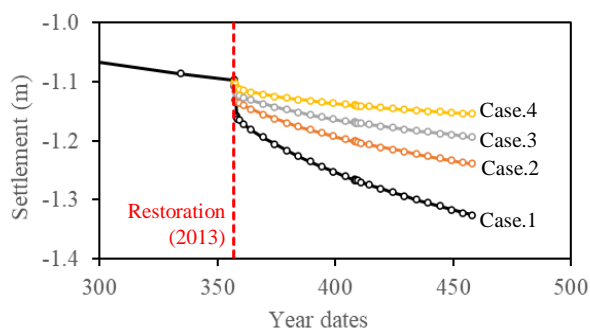


Fig. 10 Temporal change of settlement (all cases)

CONCLUSIONS

In this study, several changing conditions of the pagoda and surrounding ground were described based on observation. It is thought that the main body of the pagoda has been sinking toward the north separately from the reconstructed base surrounding the main body, and necessary of countermeasure for subsidence of the pagoda is also described.

In addition, the simulation was carried out, wherein cases were considered for ground improvement as a countermeasure work for an unequal settlement. The results indicate the following:

1. The settlement and inclination of the pagoda tend to increase in the future.

2. The possibility that the settlement and inclination of the pagoda are promoted by the restoration work, which uses many bricks is confirmed. This is consistent with the situation wherein the gap occurs between the main body of pagoda and the reconstructed square basement.

3. The amount of inclination of the pagoda from the analysis results has possibility was underestimated, because it is not equal to the actual situation.

4. The effect of preventing settlement of ground improvement was confirmed by comparing with and without ground improvement. Additionally, the effect of prevention for subsidence increases with the thickness of ground improvement.

For the better conservation of Wat Krasai pagoda, we should notice not only the behavior of the inclination of the pagoda but also structural deterioration such as crack, gap, deformation, brick deterioration. Moreover, a restoration work of historical brickwork buildings that need to adding many bricks should consider influence by its new weight and deterioration by the condition of gathering water.

ACKNOWLEDGMENTS

We would like to sincerely thank the Third Regional Office of Fine Arts and the Ayutthaya Historical Park for their cooperation and information. Additionally, we are grateful to Dr. Weerakaset Suanpaga and Mr. Chalermchai Trakulphudphong of Kasetsart University for helping with the Wat Krasai investigations. This research was partially funded by the Muching Fund of the Institute of Disaster Mitigation for Urban Cultural Heritage, Ritsumeikan University.

REFERENCES

- [1] UNESCO., Historic City of Ayutthaya, <https://whc.unesco.org/en/list/576/>, 2019.5.25 Access.
- [2] Yuko I. Ayaka O. Weerakaset S. Chalemnchai T. Chaweewan D. Masamitsu F. and Ryoichi F., Estimation of initial void ratio of consolidated clay based on one-dimensional consolidation theory, *International Journal of GEOMATE*, Vol. 14, Issue 46, 2018, pp.51-56.
- [3] Tadateru N. Hiroyuki K. Sakuji Y., Preservation and utilization of ruins -From the preservation process of the Egyptian adobe remains -, Conference proceedings, in Proc. 21th conference on Japan society for science studies on cultural properties, 2004, pp.42-43. (in Japanese)
- [4] ICOMOS Thailand., Heritage at Risk, Thailand, https://www.icomos.org/risk/world_report/2000/thail_2000.htm, 2019.5.25 Access.
- [5] Takeshi I. Nobuaki K. Tadateru N. Jirka S., Analysis of Water Regime in Historical Brick Buildings in Ayutthaya, Thailand, *Science for conservation*, No.38, 1999, pp.154-163. (in Japanese)
- [6] Takeshi I. Tadateru N. Jiri S. Martinus G., Numerical Analysis of the Water Regime of Buddha Monuments in Skhothai, Thailand, *Science for conservation*, No.39, 2000, pp.43-50. (in Japanese)
- [7] Yuri Y. Shunichi H. Daisuke O., Degradation of a Big Buddha in Skhothai ruins, *J. Environ. Eng., AIJ*, Vol. 78, No.689, 2013, pp. 561-567.
- [8] Nobuaki K., Survey Report on the Stones and Their Weathering at Historic Monuments in Thailand, *Science for conservation*, No.37, 1998, pp.59-68. (in Japanese)
- [9] Etsu U., Stone materials and their non-destructive examination in the Angkor monuments, *BUTSURI-TANSA*, Vol.60, No.3, 2007, pp.223-234.
- [10] Atsushi I. Hideki O., A determination procedure of input parameters in elasto-viscoplastic finite element analysis, *Soils nad Foundations*, Vol.27, No.3, 1987, pp.71-87.
- [11] Yuko I. Ayaka O. Weerakaset S. Chalemnchai T. Chaweewan D. Masamitsu F. Ryoichi F., Estimation of initial void ratio of consolidated clay based on one-dimensional consolidation theory, *International Journal of GEOMATE*, Vol.14, Issue 46, 2018, pp.51-56.

APPLICATION OF ABAQUS PROGRAM TO INVESTIGATE THE EFFECT OF VARIATION IN SUBGRADE LAYER PROPERTIES ON THE DAMAGE OF FLEXIBLE PAVEMENT STRUCTURE

Saad Farhan Ibrahim AlAbdullah¹, Maryam Hussain Hassan², Suha Aldahwi³

^{1,3} Faculty of Engineering, Isra University, Amman, Jordan;
² Faculty of Engineering, Al.Mustansiriyah University, Iraq

ABSTRACT

The major purpose of the pavement structure is to reduce stresses in the subgrades so that there is little or no deformation in the subgrade. Therefore, the more the subgrade is resistant to deformation, the thinner the pavement will be, thus reduction in the construction cost of the road. Good quality subgrade soils are preferable for durable roads but they are not always available for highway construction. Finite Element techniques can be effectively applied to simulate different pavement problems that could not be modeled using the simpler multi-layer elastic theory. Thus, finite element *Abaqus* 6.14-1 program is used in this study. The laboratory tests are carried out on both the natural and stabilized soil samples that used as subgrade layer to determine the properties of subgrade that will be used as inputs for the finite element *Abaqus* program. The natural samples tested with three percentages of moisture contents (11.5%, 13.5%, and 15.5%). Different types of stabilizers are used in this study in form of mixture of two types of stabilizers. So, mixture of lime-kaolin (3%, 4%), mixture of silica fume-Poly Vinyl Alcohol (2%, 2%), mixture of Rice Husk Ash-Poly Vinyl Alcohol (3%, 2%), and 2% of silica fume are used as stabilizers. The pavement application by Abaqus program indicating that, the characteristics of subgrade layer have a big influence on the vertical deformation of whole pavement. The combination of (3% of Rice Husk Ash and 2% of Poly Vinyl Alcohol) as a stabilizer to the subgrade layer reduces the deformation about (9.5 %). While the addition of (3% of Lime and 4% of Kaolin) led to regard the deformation about (7.8%).

Key word: Subgrade, Strength, Deformation, Finite element method, Shear strength, Elastic modulus.

INTRODUCTION

Finite Element Method is the dominate discretization technique in the structural mechanics. The basic concept in the physical interpretation of finite element method is the subdivision of the mathematical model for disjoint components of simple geometry called finite element. (Kim, 2007) studied the non-linear modulus and deformation behavior of the fine grained soil that used as a subgrade layer and the unbounded aggregate for the base/subbase layers with respect to repeated wheel loads by using Abaqus program. Abaqus is a commercial finite element modeling program. This program is suite of engineering analysis software packages used around the world for the simulation of the physical response of structures and soil bodies for loads, impact, contact, temperature and the other environmental conditions (*Abaqus Theory Manual*, 2009). (Shafabaksh et al., 2013) used the Abaqus software to investigate the dynamic response of pavement in term of elastic behavior. The results of this work indicating that, there is a reduction in the longitudinal strain in the asphalt layer. Also the comparison between the strains computed at the field and those of model is a suitable accommodation. (Yassenn et al., 2015) suggested the using of linear elastic modeling to determine the expected fatigue and rutting damage in flexible pavements due to the traffic loads.

METHODOLOGY

Three dimensional finite element method is the best approach to analyze more accurately critical pavement response through the minimizing or eliminating the assumptions of the two dimensional analysis. The analysis in (3D) method is more complicated as compared with the axisymmetric because of the extra coupling that will occur in additional direction.

The responding of each element is expressed in terms of a finite number of degrees of freedom that characterized as the value of unknown function at a set of nodal points. For typical finite element analysis by any software, it's very important to provide the following information:

- ❖ The geometry of the structure.
- ❖ Elements connecting.
- ❖ Materials properties.
- ❖ The boundary conditions or the restraints.
- ❖ Load or the details of forcing function.
- ❖ The options of analysis process.

The solution process in finite element method can be summarized in the following steps:

- ❖ Dividing the structure into pieces (the meshing step).
- ❖ Connecting the elements at the nodes form on approximate system of equations for the whole structure.

- ❖ Solving the equations that involve the unknown quantities at the nodes.
- ❖ Calculating the desired quantities such as stresses, strains at the selected element.

Materials and Tests

The soil used in this research is brought from AL- Sader city at the east of Baghdad. The sample is taken from (2-4m) depth below the existing ground surface. The soil transferred in plastic bags to soil mechanics laboratory of the highway and transportation engineering department. Tests are carried out on the soil samples to determine the physical and chemical properties. The tests included particle size distribution, soil classification and description, specific gravity, Atterbirg limits.

Tables (1) and (2) represent the physical properties and chemical composition of the soil sample used in this study.

Table (1): Physical Properties of Soil Samples.

Index Property	Value
Liquid Limit (L.L.)	
Plastic Limit (P.L.)	
Plasticity Index (P.I.)	
Specific gravity (G_s)	2.65
% Gravel	0
% Sand	20
% Silt	24
% Clay	56
AASHTO Classification	A-7-6
Unified Soil Classification System (U.S.C.S.)	CL

Table (2): Chemical Properties of Soil Samples.

Index Property	Value
Total Soluble Salts (T.S.S.)	10.8
Organic Matter Content	2.4%
Total Sulphate Content	1.45%
PH Value	7.9
Gypseous Content	3.57

Figure (1) shows the grain size distribution of the soil sample.

Table (4): Chemical Properties of Hydrated Lime

Composition	Percent by Weight
CaO	71
Al ₂ O ₃	0.5
SiO ₂	4
Fe ₂ O ₃	0.4
MgO	2.5
SO ₃	0.3
Active CaO	52

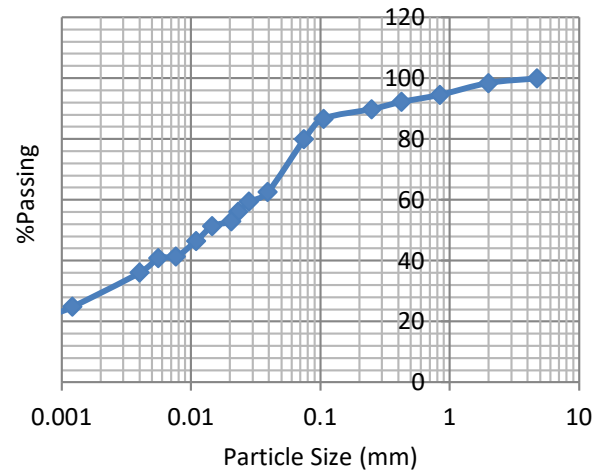


Figure (1): Grain Size Distribution of Soil Sample.

Lime-Kaolin Mixture

Both of these materials are brought from the local market. In this study hydrated lime $Ca(OH)_2$ is used. In this work 3% of lime and 4% of kaolin are mixed and added to the natural soil. The additives and soil are mixed until obtaining homogeneous mixture in color. Physical and chemical properties for both lime and kaolin are shown in tables (3), (4), (5) and (6).

Table (3): Physical Properties of Hydrated Lime

Properties	Lime
Form	Fine dry white powder
Color	White
Specific Gravity	2.3
PH (25 ⁰ C)	12.93
Finess (m ² /Kg)	657

Table (5): Physical Properties Kaolin

Property	Index
Specific Gravity	2.58
Liquid Limit (L.L.)	57
Plastic Limit (P.L.)	27
Plasticity Index (P.I.)	30
Soil Symbols (USCS)	CH

Table (6): Chemical Composition of Kaolin.

Composition	Percent by Weight
SiO ₂	51.6
Al ₂ O ₃	33
CaO	1.5
Fe ₂ O ₃	1.4
MgO	0.6
L.O.I.***	12.1

Silica-Fume

Silica-fume is brought from the local market. It's a highly effective material because of the high silica content and the extreme fineness. This stabilizer is available in two colors weight and dark grey. In this study **2%** of silica-fume is used as a percent of the dry weight of the natural soil. Physical and Chemical properties of this stabilizer are shown in tables (7) and (8) respectively.

Table (7): Physical Properties of Silica-Fume According to (ASTM C1240-03).

Physical Property	S.F.
%Retaining on 45-µm (No. 325) sieve, Max.	7
Specific Surface, Min., m ² /g	21
Specific gravity	2.231

Table (8): Chemical Properties of Silica-Fume According to (ASTM C1240-03).

Oxide Composition	S.F.
SiO ₂ , Min. percent	90
Moisture Content, Max. percent	0.68
Loss of Ignition, Max. percent	2.86

Mixture of Rice Husk Ash (RHA) and Poly Velyin Alcohol (PVA)

RHA is obtained from the mailing of rice ash which is brought from Al-Meshkhab in Al-Najaf city. The rice ashes are burn at (**600 C**) for **2** hours. In controlled temperature then the by-product is mailed to obtain the **RHA** in powder form. Plate (3.1) shows the rice husk and rice husk ash. **PVA** is a white to yellow powder that obtained from the local market. In this research (**3% of RHA**) is mixed with

(**2% of PVA**) the added to the natural soil to study the effective of this additive on the soil. Tables (9) and (10) show the physical and chemical properties of **RHA**.

Table (9): Physical Properties of RHA.

Property	Value
Grain Size Distribution (% Finer than)	4.75 mm
	2.0 mm
	0.595 mm
	0.425mm
	0.149 mm
	0.075 mm
Specific Gravity	2.03

Table (10): Chemical Composition of RHA (after Oyetola and Abdullah, 2006).

Composition	Percent by Weight
SiO ₂	86
Al ₂ O ₃	2.6
Fe ₂ O ₃	1.8
CaO	3.6
MgO	0.27

Silica-Fume and Poly Vinyl Alcohol (PVA)

In this study a mix of (**2% Silica-Fume**) and (**2% PVA**) is used. Before the using of this mixture, the three additives are mixed together and then added to the natural soil.

MATERIALS PROPERTIES

For understanding and investigating the distribution of stresses, strains and displacement in the pavement layers with the variation in subgrade layer properties, **3D** models are created by finite element **Abaqus** program. The simulation of subgrade layer in this case included the using of drucker prager to produce the elasto-plastic behavior. The angles of friction (ϕ) and cohesion stress (C) were determined through the direct shear test while the values of

modulus of elasticity (E) are obtained from the results of *U.C.S.*

Layer	Density (Kg/cm ³)	E (Mpa)	ϕ	Poisson's ratio (ν) *
Asphalt Surface	2310	1200	-	0.35
Subbase	2200	110	-	0.35
Lime and Kaolin S.F.	1640	18.9	38.7	0.4
Stabilized Subgrade (RHA and PVA)	1692	10.5	42.1	0.4
(S.F. and PVA)	1680	21.5	46.6	0.4
	1660	12.9	40.3	0.4

*Poisson's ratio from Huang (2004).

SIMULATION OF MOVING LOAD

The application of layered theory for the design of flexible pavement included the assumption of circular contact area for each tire. This assumption is not correct but the error is very small. So, for simplification the analysis of flexible pavement, a single circular with same contact area as the duals is used to simulate a set of dual tires instead of using two circular areas. The contact pressure on the pavement is equal to the tire pressure. The contact area can be in the form of square and two half circles (Huang, 2004). According to (Yoder and Witczack, 1975), the wheel load that applied on the pavement ranging from (80 KN to 90 KN). In this study the load of one tire is considered equal to (96 Kg) and it distributed uniformly over the total contact area. The pressure used in this research equal to (550 Mpa). The simulation of moving load on the pavement structure included division the pavement into (12) Steps to simulate the path of tire on the asphalt surface layer, each step consist of number of cycles

through the using of *time-amplitude tabular*. Step by step loading is used to simulate the motion of wheel in a determined speed. The loading place must be moved in a gradual form in order to have a complete wheel turn. Figure (2) represents the steps of loading used in finite element *Abaqus* program. The simulation of repeated load by using time-amplitude tabular is shown in figure (3).

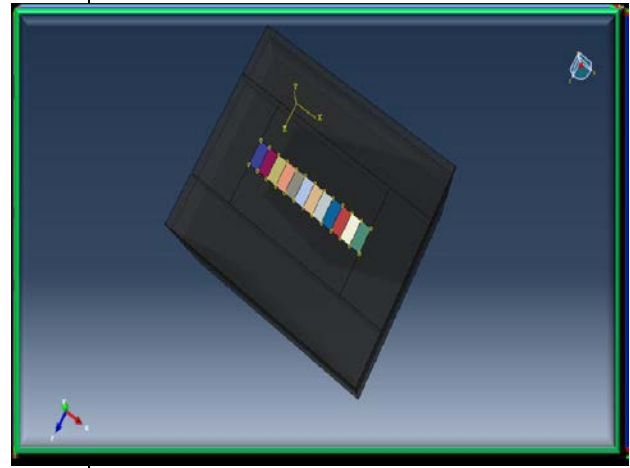


Figure (2): Steps Used to Simulate Moving Load in Finite Element Abaqus Program.

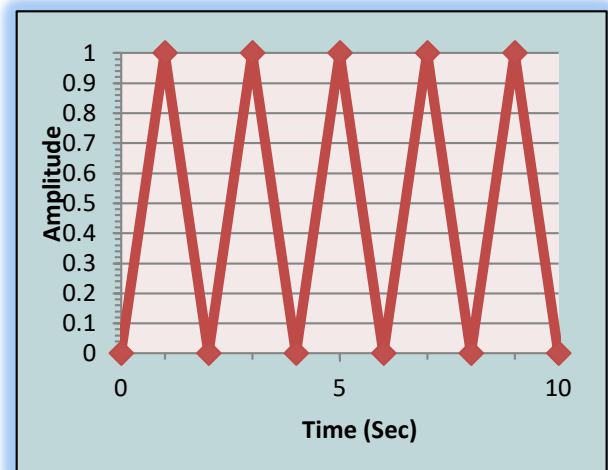


Figure (3): Simulation of Moving Load by Using Time-Amplitude Tabular.

BOUNDARY CONDITIONS

The boundary conditions of the model have important effect in the prediction of response of the model. Steel box is assumed to be used, so the bottom of subgrade and the sides of each layer is assumed to be fixed. In other word, there is no horizontal or vertical movement in this case. The

nodes along the edges of pavement are assumed free to move vertically but forced in the horizontal direction. Figure (4) represents the boundary conditions of the model.

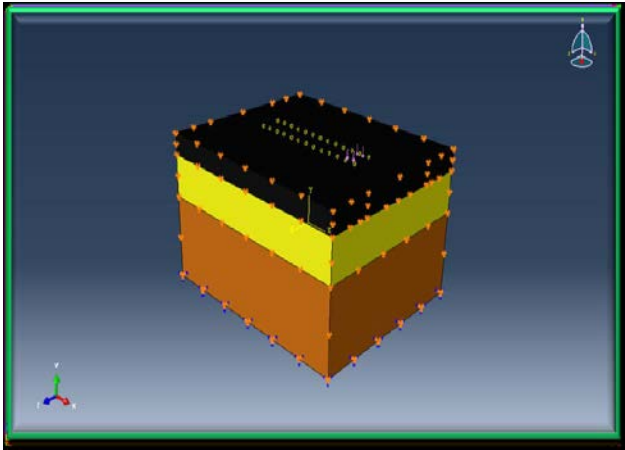


Figure (4): Boundary Conditions of the Model Simulated by Finite Element Abaqus Program.

FINITE ELEMENT TYPE

All the parts of the model that created by finite element *Abaqus 6.14-1* are modeled using (8) nodes continuum three dimensional brick element (*C3D8R*) with reduced order numerical integration available in Abaqus program. This element has the ability to represent large deformation, geometric and material nonlinearities. Solid element (*C3D8R*) has three degrees of freedom at each node, translations in the nodal *X*, *Y* and *Z* directions. The layers of pavement are simulated with the same shape to reserve the continuity of the nodes between the sequential layers.

MESHING SIZE

The mesh of model is considered in way to provide best and more accurate results. So, (8) nodes linear brick reduced integration elements (*C3D8R*) meshing is used to improve convergence rate. (*C3D8R*) elements are of quadratic type. Quadratic elements have better results than the linear interpolation element (*Hadi and Bodhinayake, 2013*). Fine mesh size is used around the loading area, along the wheel path and at the interface between layers where the gradients of stresses and strains are higher. Figure (5) shows the mesh size for all layers of the model.

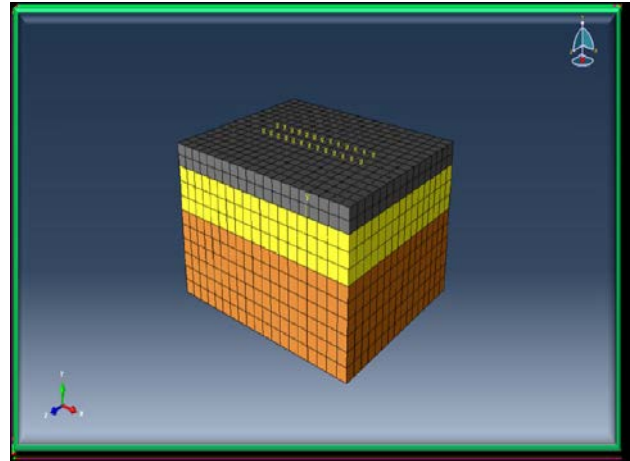


Figure (5): Meshing of all Parts of the Model.

INTERACTION MODELING TECHNIQUES

To contact the parts of model together by using *Abaqus* program, it's very important to define the surfaces of interaction between two layers. There is several formulation of contact in *Abaqus* program. Each formulation is depending on the choice of contact discretization, tracking approach and assignment of (*master*) and (*slave*) roles for the contact surfaces. The interaction technique permits merging two regions together. In this study, (*Surface to Surface*) contact with small sliding is used for all the contact interactions in the model which assumed a comparatively small sliding but could submit to an arbitrary rotation of the bodies. The formulation of interaction between the layers of model is shown in figure (6).

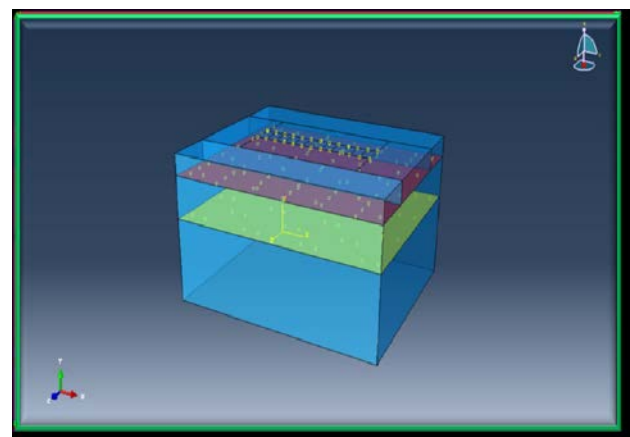


Figure (6): Formulation of Interaction between the Layers of the Model.

RESULTS AND DISCUSSIONS

To study the influence of variation in subgrade layer properties on the permanent deformation of the flexible pavement structure, seven models are built by using finite element *Abaqus* program. In this research, the comparison between these models based primarily on the permanent deformation. Figures (7) through (13) show the vertical permanent deformation for the natural and stabilized models.

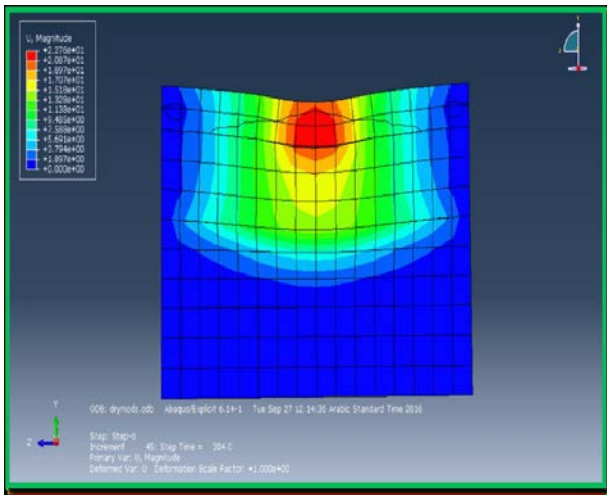


Figure (7): Vertical Deformation for Natural Model
Compacted at Dry Side

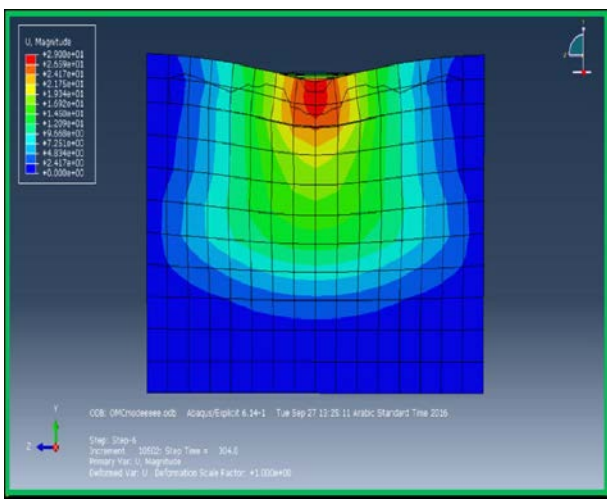


Figure (8): Vertical Deformation for Natural Model
Compacted at O.M.C.

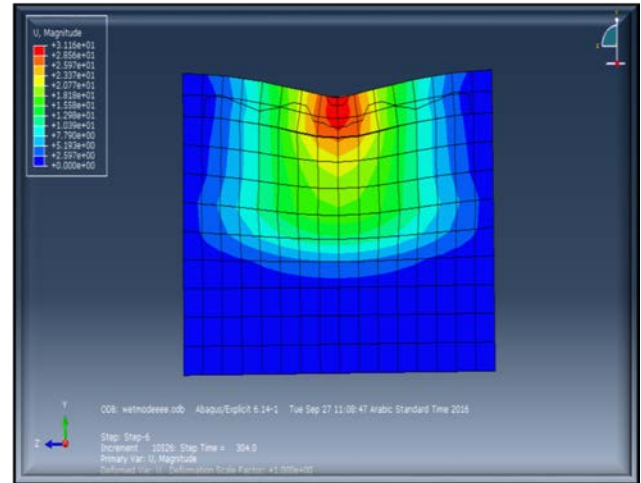


Figure (9): Vertical Deformation for Natural Model
Compacted at Wet Side.

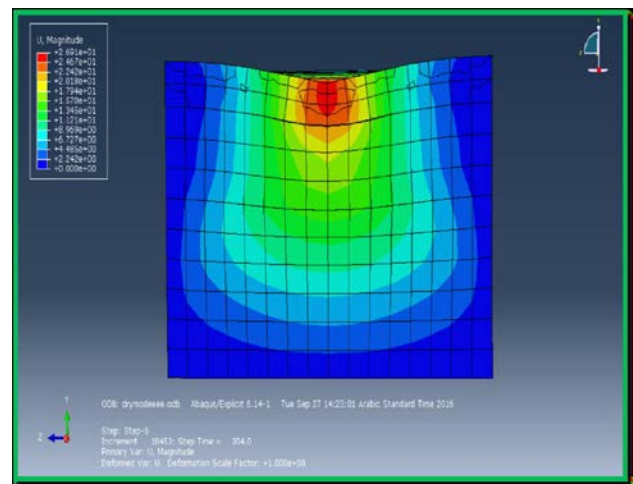


Figure (10): Vertical Deformation for Stabilized Model
with (3% of Lime and 4% of Kaolin).

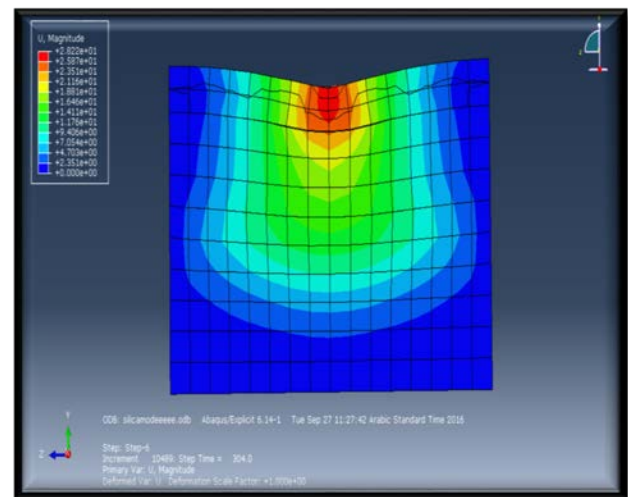


Figure (11): Vertical Deformation for Stabilized Model
with (2% of Silica Fume).

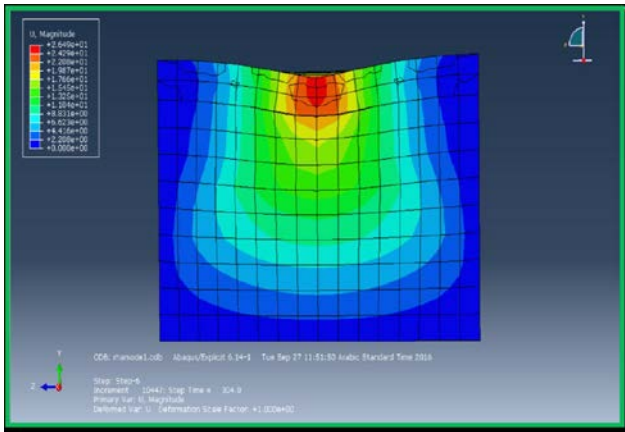


Figure (12): Vertical Deformation for Stabilized Model with (3% of RHA and 2% of PVA).

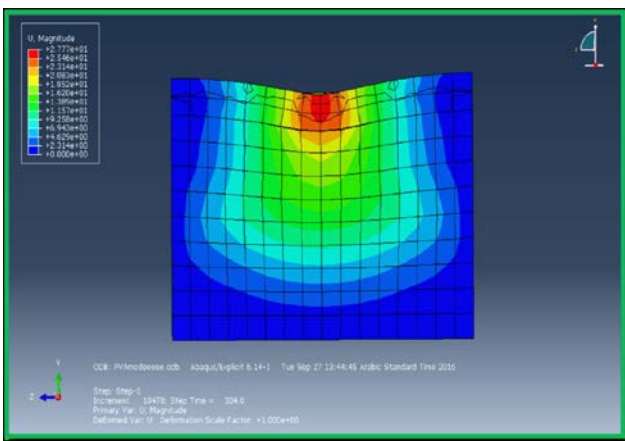


Figure (13): Vertical Deformation for Stabilized Model with (2% of Silica Fume and 2% of PVA).

For the models with untreated subgrade layer it's noted that, the vertical deformation reduced about (5.3%) due to the increasing of moisture from (11.5%) to (13.5%). The increasing in moisture to (15.5%) results in increasing the surface deformation about (7.8%).

The using of (3% of RHA and 2% of PVA) as stabilizers for the subgrade layer led to improving the deformation to (9.5%) as compared with untreated model. The other stabilizers improved the deformation with different percentages. Figures (14) and (15) illustrated the values of vertical deformation for the natural and stabilized models respectively.

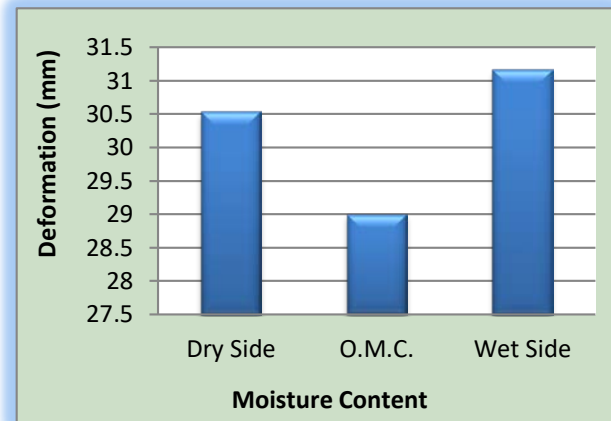


Figure (14): Vertical Deformation for Elasto-Plastic Models with Natural Subgrade Compacted at Different Moisture Contents.

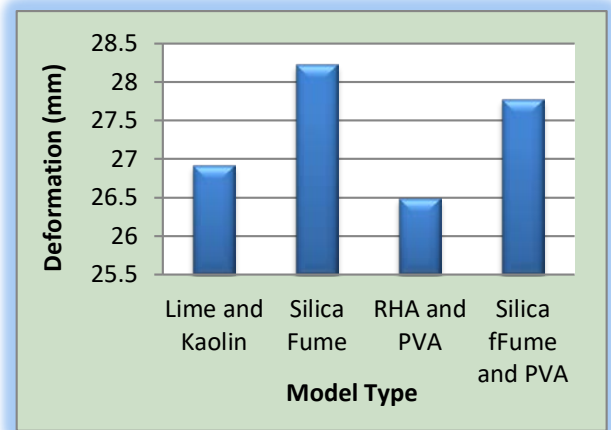


Figure (15): Vertical Deformation for Elasto-Plastic Models with Stabilized Subgrade Compacted at Optimum Moisture Contents.

The percentage of improvement in vertical deformation due to using stabilized subgrade layer with different stabilizers is shown in figure (16) below.

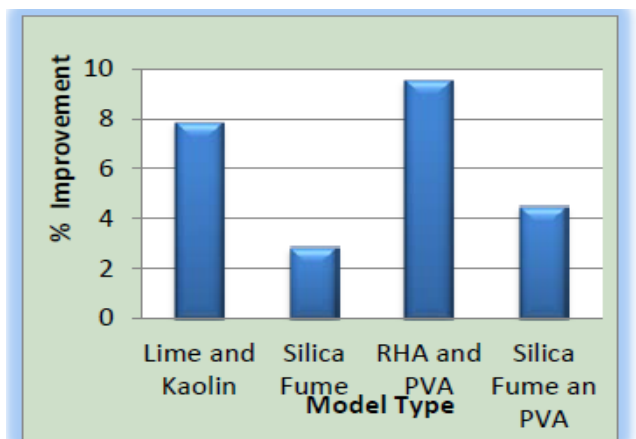


Figure (16): Percentages of Improvement in Vertical Deformation Due to Using Stabilized Subgrade Layers.

CONCLUSIONS

The untreated subgrade layer that compacted at the wet side resulting in high vertical deformation due to the applied traffic loading as compared to the subgrade layers compacted at dry or *O.M.C.*

All types of stabilizers used in this research improved the deformation but the addition of combination of (*RHA and PVA*) gives a less deformation as compared to the other types of stabilizers.

REFERENCES

- [1] Abaqus Theory Manual, (2009): Hibbitt, Karlsson and Sorenson, Inc, INC.
- [2] Kim, M., (2007): "*Three-Dimensional Finite Element Analysis of Flexible Pavements Considering Nonlinear Pavement Foundation Behavior*", Ph.D. Thesis, College of Engineering, Department of Civil Engineering, University of Illinois, Urbana-Champaign.
- [3] Shafabakhsh, G.A., Taleb, M., Motamedi, M., and Badroodi, S.K., (2013): "*Validation of Load Movement on Flexible Pavement Using Pennsylvania Field Test*", Technical Journal of Engineering and Applied Sciences. 3(22): pp. 3125-3130.
- [4] Yassenn, O.M., Hafez, M.A., Endut, I.R., Ishak, S.Z., and Yasseen, H.M., (2015): "*Finite Element Modeling of Flexible Pavement*", Journal of Multidisciplinary Engineering Science and Technology (JMEST), Vol. 2, Issue. 1, pp.115-120.

DEVELOPMENT OF A COMBINATION OF A ROTARY PENETRATION TYPE SAMPLER

*Katsuya Iwai¹, Naoaki Suemasa¹ and Tsuyoshi Tanaka¹

¹Faculty of Engineering, Tokyo City University, Japan

ABSTRACT: The Swedish Weight Sounding (SWS) test is a ground survey method often used in residential areas. However, it is difficult to determine soil properties and understand soil quality accurately only by the SWS results. If it becomes possible to collect undisturbed samples by inexpensive and simple sampling, it could be applied to a wide range of construction designs such as pile foundation works. The purpose of this study is to establish an inexpensive, simple and accurate ground survey method by a combination of a rotary penetration type sampler (Screw Driving Sampler), and an improved SWS tests, the Screw Driving Sounding test (SDS test). In this report, after carrying out the SDS test and sampling by a SD Sampler (SD sampling) in actual ground, the laboratory test results were compared with the boring test results obtained from neighboring ground. As results of an unconfined compression test, since an unconfined compressive strength was large but a deformation coefficient was small, it was revealed that the sample was disturbed at some parts. However, when comparing the result of SD sampling with that of boring test, contamination was not observed in the physical test on the sample obtained by SD sampling. As a result, it was confirmed not only that sedimentation status of the ground could be estimated through the SDS test but also more detailed soil properties could be investigated with SD sampling.

Keywords: Sampling, sampler, sounding, boring test, unconfined compression test

1. INTRODUCTION

The Swedish Weight Sounding (SWS) test, which is more inexpensive and simpler than the boring test, is commonly used for ground survey in residential areas. However, the SWS test can determine only soil hardness but not soil properties. If it becomes possible to collect samples by an inexpensive and simplified sampling method, it could be feasible to assess liquefaction potential by grain size analysis on the collected samples. In addition, if a collected sample is undisturbed, it could be applied to a wide range of construction designs such as pile foundation works. The purpose of this study is to establish an inexpensive, simple and accurate ground survey method by a combination of a rotary penetration sampler (Screw Driving sampler), and an improved SWS test, the Screw Driving Sounding test (SDS test). In this report, after carrying out the SDS test and sampling by a SD sampler (SD sampling) in the actual ground, the laboratory test results were compared with the boring test results obtained from neighboring ground.

2. SD SAMPLER

Figure 1 and Table 1 show a photo and a summary of SD samplers, respectively and Fig. 2 shows a SD sampling procedure. The SD sampler is composed of a piston, blades and double tube structure including an outer tube and a sampling

tube to reduce frictional resistance between the sampling tube and a wall of borehole during sampling. The penetration of the sampling tube is based on a ball screw mechanism. The test procedure was as follows; first the sampler was penetrated through a borehole pre-excavated by a sounding test to a selected position with no rotation, and then the rods were rotated and lifted off for collecting a sample. There are three types of samplers with different diameters, including a large sampler to collect an undisturbed sample used for an unconfined compression test and a small and a medium sampler for physical tests.



Fig. 1 SD samplers

Table 1. Summary of SD samplers

	outer diameter (mm)	inner diameter (mm)	maximum sample length(mm)	use	
S	32	18	350	physical test	(soil)
M	36	25	350		(clay)
L	44	36	350	mechanics test	

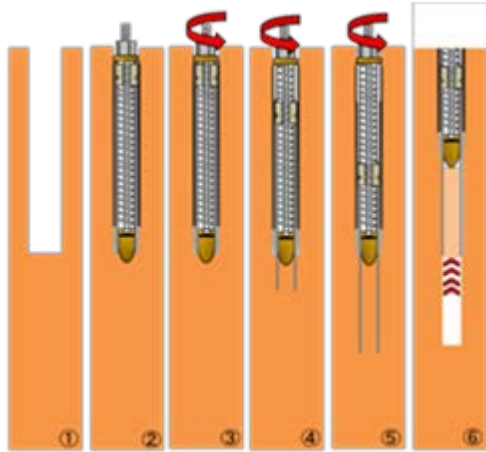


Fig. 2 SD sampling procedure

3. SDS TEST

Fig. 3, Fig. 4 and Fig. 5 show a photo of the SDS test machine, a test procedure and a summary of torque and load applied on the rod, respectively. The SDS test results were studied based on the plastic analogy model obtained from the constitutive law of soil stress and strain. The rotary penetration was regarded as deformation behavior caused by a combined load of a vertical load and torque. During the test, a vertical load was added with 125N at each rotating in seven stages from 250N to 1000N, and after 25cm penetration, the rods were lifted off by 2cm and the torque was gauged to reduce peripheral frictional resistance (Fig. 4). There were 9 measurement items: penetrate depth, load, average torque, maximum/minimum torque, settlement speed, half rotation amount and settlement amount. In addition, to reduce peripheral frictional resistance, a vertical component W_f and a horizontal component applied on the rods T_f were subtracted from practically gauged load W_a and torque T_a (Figure 3), respectively.



Fig. 3 SDS test machine

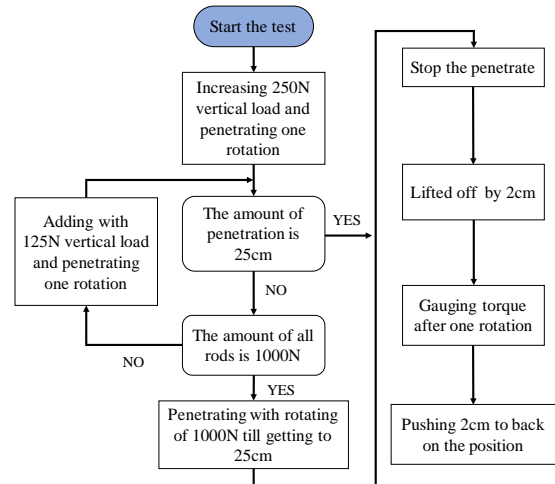


Fig. 4 Test procedure

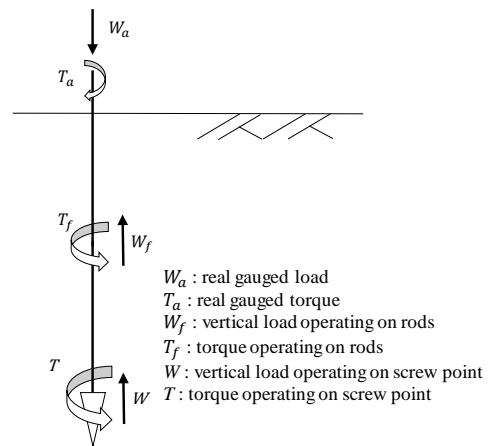


Fig. 5 Summary of torque and load on rods

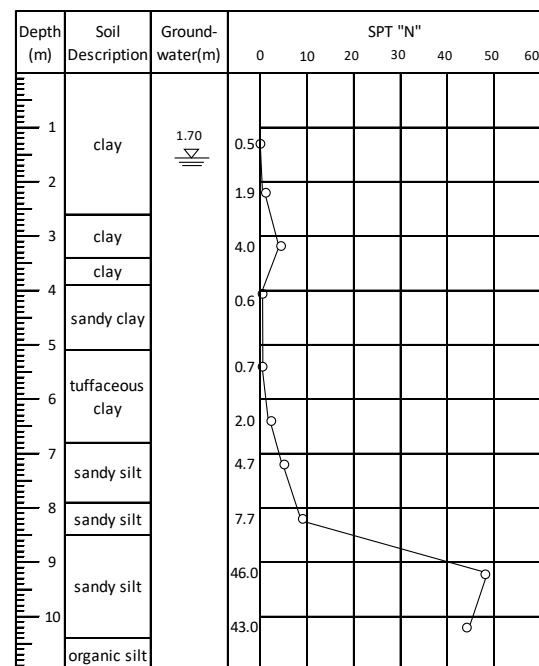


Fig. 6 Results of SPT and soil profile

4. SD SAMPLING IN ACTUAL GROUND

Fig. 6 shows the SPT test results and a soil profile. While the boring test was carried out except for the part from the ground surface to approximately 2.5m depth, SD sampling was carried out at the same time, where samples were collected with a SD sampler from designated eight points between 3.00m to 8.00m depth on the clay ground. A series of tests were carried out on the collected samples including unconfined compression tests, water content tests and liquid/plastic limit tests.

4-1. SAMPLING RESULTS

Fig. 7 shows the water content test results of collected samples by thin-walled sampling in the boring test (TW sampling) and SD sampling (w_n), and Fig. 8 shows the liquid/plastic limit test results of TW and SD samplings (w_l , w_p), respectively. First, focusing on the water content test results of both samples, the values were close at 4m, 6m and 7m depths. Moreover, the values from the liquid/plastic limit tests on both samples were close as well. From the results that both samples at each depth were likely to be equivalent in the physical properties, it was revealed that contamination was not caused during SD sampling.

Fig. 9 shows the unconfined compression test results of TW and SD samplings (q_u). Compared the unconfined compressive strengths of both samples at 4m depth, the values were very close. At deeper depths, on the other hand, the unconfined compressive strengths of SD sampling were basically same but relatively larger than those of TW sampling. Then, the deformation modulus was focused on to confirm sample disturbance. Fig. 10 shows the deformation modulus (E_{50}). At 4m depth, the both deformation moduli were close, but at deeper depths, the deformation moduli of SD sampling were smaller than those of TW sampling.

From the results of the unconfined compression tests, we considered that the unconfined compressive strengths were affected by the positional relationship between the sampling and the structure. Since the deformation moduli were small, it appeared that disturbance occurred in the samples of SD sampling at depths deeper than 4m.

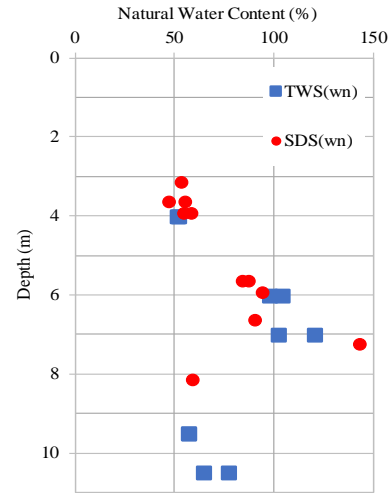


Fig. 7 Water content test results

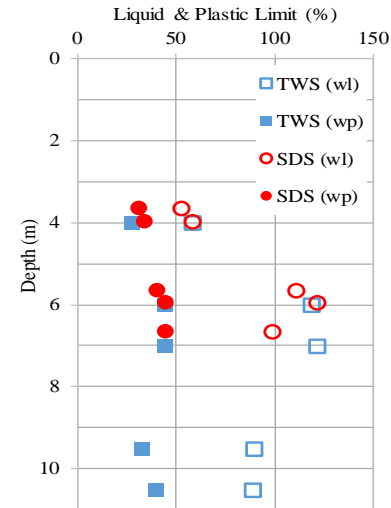


Fig. 8 Liquid/plastic limit test results

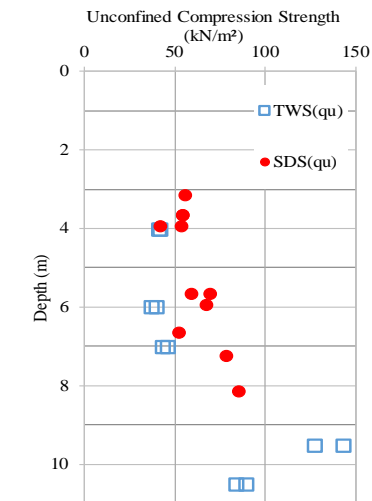


Fig.9 Unconfined compression test results

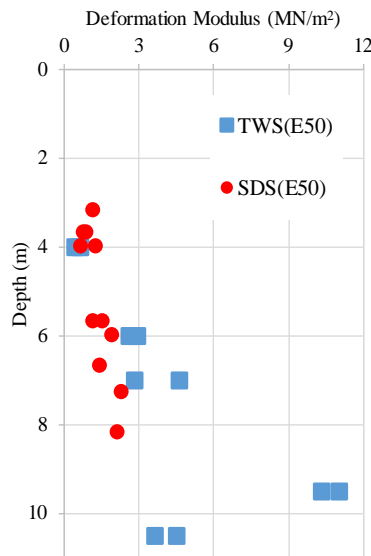


Fig. 10 Deformation modulus

5. SDS TEST AND SD SAMPLING

To understand accumulation conditions of the ground, the SDS test and SD sampling were carried out. After the SDS test was conducted in the ground approximately 20m away from the boring test position and up to 10.25m depth, the depth for SD sampling was determined from the response of measured torque. Then, samples were collected by a medium sampler and applied to water content tests and liquid/plastic limit tests to investigate their physical property.

5-1. SDS TEST RESULTS

Fig. 11 shows $E_{0.25}$ obtained from the SDS test and N-value from the boring test, where $E_{0.25}$ represents an energy amount when penetrating 25cm and calculated from torque, the number of rotation, load and depth. As seen in Fig 11, the behavior of $E_{0.25}$ tended to be similar to that of N-value. Therefore, there is a possibility that $E_{0.25}$ could be an alternative of N-value.

Compared torque from the SDS test with N-value as shown in Fig 12, similar tendencies were seen in both behaviors, same as $E_{0.25}$. In addition, focusing on only torque behavior, it was assumed that the stratum of 0-2m depth was a reclaimed ground because the torques fluctuated significantly. Focusing on 2-4m and 4-6m depths, the torques increased according as depth increased and a sudden decrease was observed when passing 4m and 6m parts, respectively. While, N-value decreased at depths deeper than 6m as well. From the results, there is a possibility that these two parts were assumed to be stratum boundaries. Furthermore, since the test ground was 11.0m TP

above sea level, the ground at depths deeper than 6m used to be under sea level centuries ago so that the stratum was assumed to be marine clay.

According to the torque results, the ground of 2-10.25m was clarified into three stratums: 2~4m, 4~6m and 6-10.25m depths.

SD sampling was carried out at additional four points with different torque values between 3m and 6m depths to understand stratum boundaries at 4m and 6m depth, respectively.

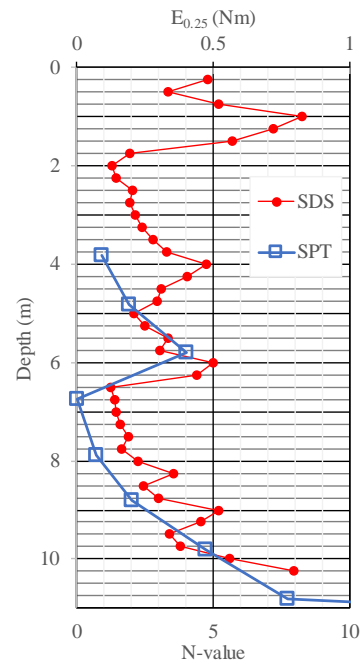


Fig. 11 $E_{0.25}$ and N-value

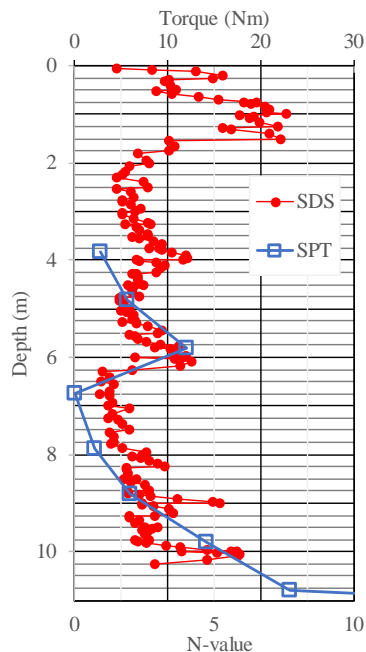


Fig. 12 Torque and N-value

5-2. SD SAMPLING RESULTS

Fig. 13 shows the water content test results (w_n) and Fig. 14 shows the liquid/plastic limit test results (w_l , w_p). There was a tendency that the water contents increased as depth increased, however, a wider difference was seen between 4m and 5m depth, compared with the difference between 3m and 4m and that between 5m and 6m. Similarly, the liquid limit and the plastic limit increased as depth increased. It resulted from increasing of sand in the stratum at depths shallower than 6m by recession of the sea or deposit of sediment.

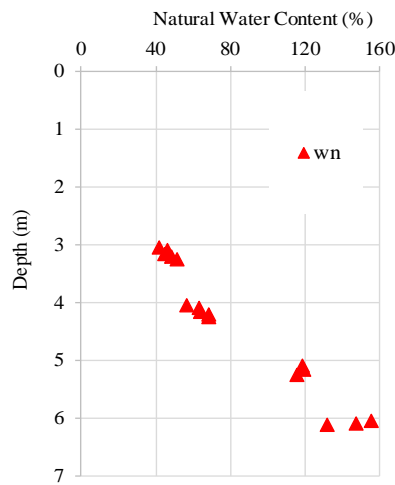


Fig. 13 Water content test results

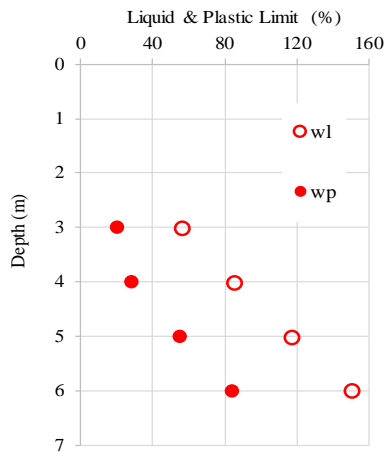


Fig. 14 Liquid/plastic limit test results

Fig. 15 shows a plasticity chart and Fig. 16 shows a liquidity index calculated from liquid/plastic limit test. Differences were seen in the physical properties between 3m and 4m depth with clay and 5m and 6m depth with silt (Fig. 15). The liquidity indexes of 5m and 6m depth were close to one, while those of 3m and 4m depth were lower than one. In particular, the liquidity index of 4m

depth with a large torque was the lowest of the four samples (Fig. 16). As one of the reasons, the test site was adjacent to a structure so that the ground may have been affected by it and accordingly the intensity became high around 4m depth.

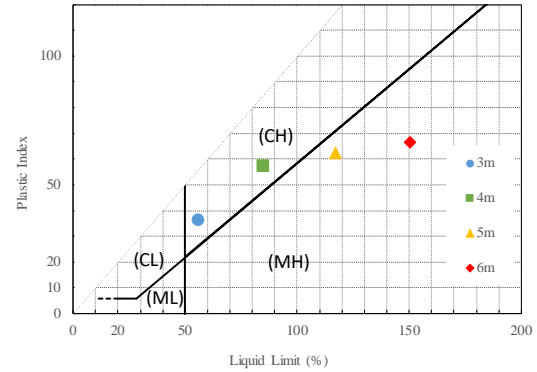


Fig. 15 Plasticity chart

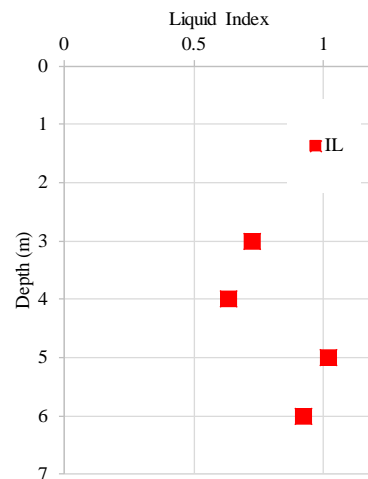


Fig. 16 Liquidity index

6. CONCLUSION

It was confirmed from the physical test results that SD sampling was capable to collect samples from a target depth without disturbing a borehole. The unconfined compression test results also revealed that little disturbance was observed in the samples collected by a SD sampler on the whole, although the quality was not as high as that of thin-walled sampling.

In addition, there was a possibility for E0.25 obtained from the SDS test results to be an alternative to N-value, by evaluating an accumulation state from a torque response. Properties of soil stratum and accumulation states were investigated in more detail by SD sampling based on the SDS test results.

In conclusion, a better understanding was obtained on usability of SD sampling in combination with the SDS test in this study. In order to improve sampling accuracy, more SD samplings will be carried out on various types of grounds as well as a consolidation test and an unconfined compression test with measuring suction.

7. REFERENCES

- [1] General Incorporated Foundation Better Living, "Utilization technology of ground survey results by SDS test", 2013.
- [2] Tanaka, Tsuyoshi and Naoaki Suemasa, Kazuya Itoh, Naoko Ishida, Shinichi Yamato, "Development of the new soil sampler", Proceedings of the japan national conference on geotechnical engineering, 2016
- [3] Tsuji, Kouhei and Minoru Yamashita, Naoaki Suemasa, Tsuyoshi Tanaka, Yasuo Sugano, Shinichi Yamato, "An application of new sounding method (SDS) which measures torque to the river embankment survey", Proceedings of the japan national conference on geotechnical engineering, 2016

BASE-ROCK ELEVATION MEASUREMENT USING SINGLE AND ARRAY MICROTREMOR INVESTIGATION

Windu Partono¹, Sukanta¹, Frida Kistiani¹, Undayani Cita Sari¹ and Kukuh Cahya Adi Putra¹

¹Civil Engineering Department, Engineering Faculty, Diponegoro University, Semarang 50275, Indonesia

ABSTRACT

Site-specific ground motion analysis is a method for developing surface ground motion and surface spectral acceleration. The analysis is performed by conducting propagation analysis from base-rock to surface elevation. The important information needs for site-specific ground motion analysis is the position of base-rock or bedrock below the surface level. This paper presents the investigation results of base-rock elevation at the Diponegoro University Semarang, Indonesia. The background reasons why the base-rock investigation of this university area shall be performed because this area is located closed to three seismic sources (Semarang, Lasem and Demak shallow crustal faults). The base-rock elevation prediction at the study area was performed using a combination of microtremor test and soil boring investigations. The base-rock elevation prediction developed using microtremor test was verified using soil profile developed from soil boring investigation. Based on soil boring and microtremor investigations, the base-rock elevation at the university area is predicted at 30 m to 60 m below the surface level.

Keywords: Base-rock, Ground Motion, Propagation Analysis, Microtremor, Shallow Crustal Fault

INTRODUCTION

Site-specific ground motion analysis is a method for developing surface ground motion, usually in terms of displacement, acceleration and velocity time histories. Surface response spectral acceleration and amplification factor can also be calculated or obtained using this method. The analysis is conducted as a complementary analysis for buildings and other structures resistance design and evaluation against seismic forces. Surface spectral acceleration for buildings design in Indonesia usually performs using amplification or site factor and multiplying this site factor with spectral acceleration at base-rock elevation. ASCE/SEI 7-16 [1] introduce the requirement of site-specific ground motion analysis for buildings located at soft soil (site class SE) and medium soil (site class SD) having a specific minimum Risk Targeted Maximum Considered Earthquake (MCE_R) S_S and S_1 spectral acceleration. ASCE/SEI 7-16 states that all structures located on site class SD and SE having an MCE_R - S_1 minimum or equal to 0.2 g shall be evaluated using site-specific ground motion analysis. One of the important information for performing site-specific ground motion analysis is obtaining the base-rock elevation. The base-rock elevation can be obtained or predicted using typical invasive soil boring investigation and non-invasive microtremor test, either using single or array microtremor investigation.

This paper explains the base-rock investigation research at Diponegoro University area. The study area is located at the southern part of Semarang, the capital city of Central Java Province, Indonesia. Base

on the New Indonesian Seismic Hazard Map 2017 [2], the university area is located closed to three different seismic sources, Semarang, Lasem and Demak crustal fault traces. The base-rock investigation at this area is part of seismic microzonation research for the university area. Seismic vulnerability analysis due to a specific scenario earthquake motion study is still on going. The study is performed because most of the buildings within the university area were designed and constructed following the old version of Indonesian seismic code. The base-rock prediction level was conducted using a combination of single and array microtremor test and soil boring investigations. Figure 1 shows the position of the university area against three closed seismic sources. All seismic sources are located less than 10 kilometers to the University area.

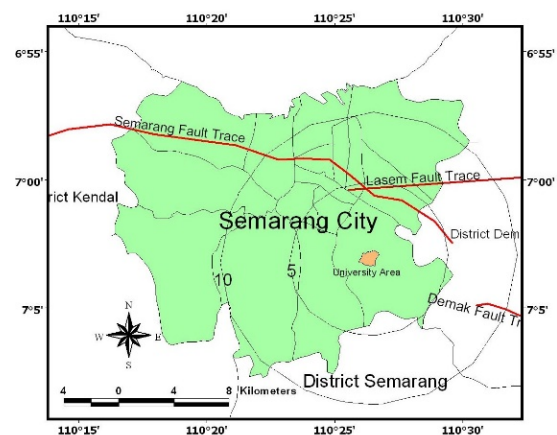


Fig. 1 Seismic sources positions and the

corresponding distance to the university area

Based on the New Indonesian Seismic Code 2019 (SNI 1726:2019) [3], the MCE_R-S_S and MCE_R-S_1 spectral response acceleration of the study area are in between 0.87-0.891g and 0.373-0.38g respectively. Figure 2 shows the 2019 MCE_R-S_S map. Figure 3 shows the 2019 MCE_R-S_1 map. Based on those two spectral MCE_R acceleration, a site-specific ground motion will be analyzed at the university area as a complementary analysis using surface response spectral acceleration.

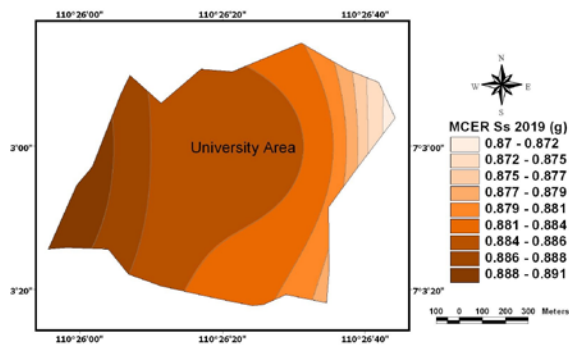


Fig. 2 MCE_R-S_S 2019 map of the university area

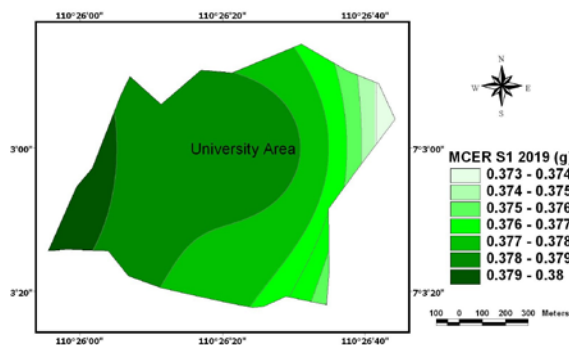


Fig. 3 MCE_R-S_1 2019 map of the university area

METHODOLOGY

Base-rock elevation prediction at the university area is performed as part of the same research conducted at the whole area of the city. This research is part of the seismic microzonation research of Semarang City and already started from 2015 and still on-going [4]. The base-rock investigation for the whole city area is started by conducting 241 single station seismometer investigation and following the same method proposed by [5, 6]. The purpose of this investigation is to obtain the dominant frequency of soil sediment at the microtremor equipment position. Figure 4 shows the position of 241 single station microtremor investigations. The dominant frequency for each microtremor position is calculated using Horizontal to Vertical Spectrum Ratio (HVSr) formula developed by [7, 8]. Figure 5 shows two

examples of HVSr curve developed at the study area. The dominant frequency (F_0) obtained from HVSr curve used for base-rock prediction [9, 10, and 13]. The base-rock prediction elevation is calculated following the empirical formulae developed by [14, 15]. Equation 1 shows the formula used for predicting base-rock elevation [14, 15]. The variable “Z” at Eq. 1 represents the thickness of the soil sediment above the base-rock elevation. Table 1 shows the “m” and “n” constant values used for sediment thickness calculation. The Z values obtained at all single microtremor positions surrounding the study area are used for developing the base-rock elevation map of the study area.

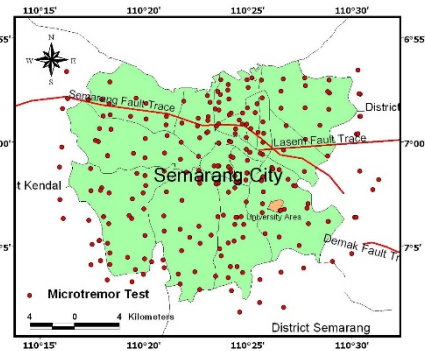


Fig. 4 Single station seismometer investigation at Semarang

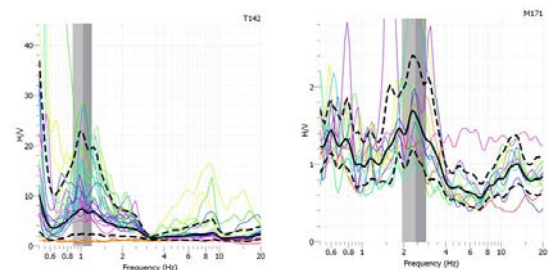


Fig. 5 Two example HVSr analysis results at two point within the university area

$$Z = mFo^n \quad (1)$$

Table 1 m and n values used for sediment thickness calculation

References	m	n
[14]	96	-1.388
[15]	108	-1.551

Following the single station seismometer investigation, array microtremor investigations was performed at the university area. The purpose of this investigation is to find the predicted soil profile in terms of shear wave velocity (V_s) profile at the study

area. Based on the Vs data or Vs profile, the base-rock elevation can be predicted following the standard criteria describes by [1, 3]. SNI 1726:2019 [3] and ASCE/SEI 7-16 [1] states that the minimum Vs = 750 m/sec (rock) and minimum Vs=1500 m/sec (hard rock) can be used for adjusting rock properties. The basic concepts of array seismometer analysis almost equal with single station seismometer analysis. All data developed using single seismometer is analyzed as an array data.

Eight boring investigations are conducted at the study area. The purpose of this investigation is to find the soft rock or hard rock elevation at the boring position. All boring investigation at the study area were conducted until maximum 30 m depth. Figure 6 shows the array microtremor and soil boring investigation positions.

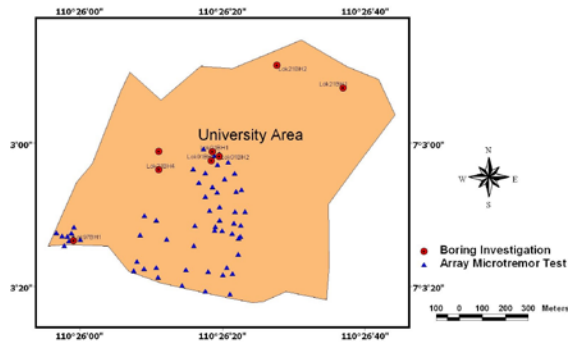


Fig. 6 Array microtremor and soil boring investigations at the study area

RESULTS AND DISCUSSION

Single station microtremor investigation conducted at the university area produce a dominant frequency (Fo) map. This map was performed by conducting spatial analysis. Figure 7 shows the spatial analysis results of dominant frequency map at the study area. All dominant frequencies (Fo) data obtained from single station seismometer test at the study area are used for base-rock elevation prediction. Figure 8 shows the base-rock elevation prediction results conducted at the study area. It can be seen in this figure the base-rock elevation at the study area are divided into two different elevation 0-30 m (area 1, red area) and 30-60 m (area 2, green area). Due to the restriction of soil boring investigations, the base-rock elevation is divided into two different depths. All boring investigations are executed until maximum 30 m depth. Three boring investigations are located at area 1, however another five boring investigations are located at area 2.

Based on the information related with base-rock elevation, array microtremor analysis was then performed at the study area. Figure 9 shows three different cross section positions for developing array microtremor analysis and developing vs profile.

Figure 10 until Figure 12 show the three different results of soil profile in terms of shear wave velocity (Vs) profile. Based on Fig. 10 base-rock elevation is located minimum 40 m depth below the surface level.

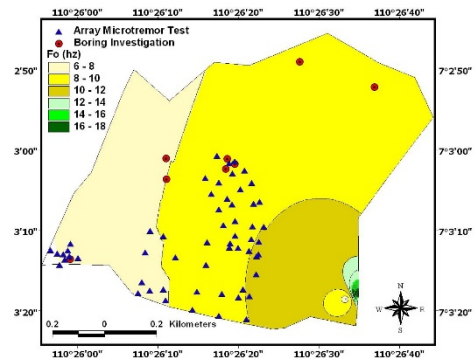


Fig. 7 Dominant frequency (Fo) map of the study area

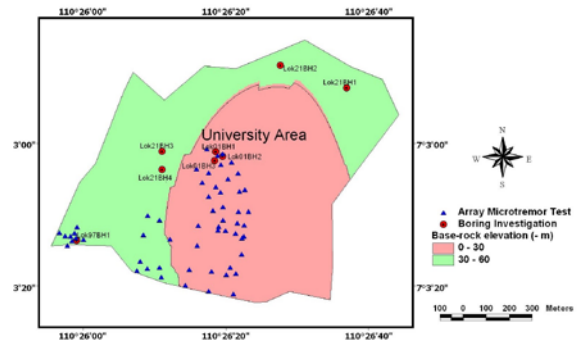


Fig. 8 Base-rock elevation map of the study area

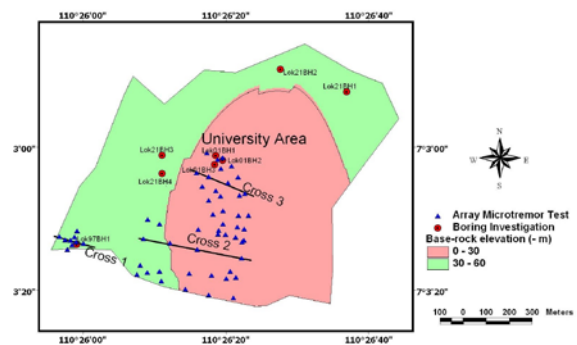


Fig. 9 Cross section positions

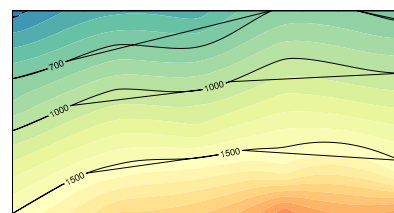


Fig. 10 Vs profile at cross section no 1 developed

from 5 seismometer position

Based on three different cross section positions, the base-rock elevation can be proved using boring investigation results at cross section no 3. From the Vs profile the base-rock or hard-rock layer having shear wave velocity minimum 1500 m/s can be found at 30 m or maybe less than 30 m below the surface level. The Vs profile developed at cross section no 3 will make base-rock level easy to predict. Based on figure 10 or cross section no 1 the base-rock elevation can be predicted at 50 m below the surface level. However, it is difficult to predict the elevation of base-rock based on cross section no 2.

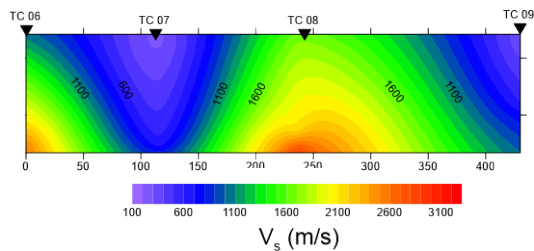


Fig. 11 Vs profile at cross section no 2 developed from 4 seismometer position

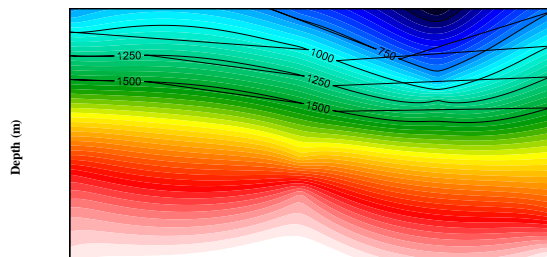


Fig. 12 Vs profile at cross section no 3 developed from 4 seismometer position

To verify the base-rock elevation, 8 boring investigation are performed at the study area. Figure 13 shows two different boring investigation results collected from boring no Bh1 (Fig. 13 (a)) and Bh2 (Fig. 13 (b)), two example boring-log data collected from area 1 and area 2 respectively. A good correlation between soil boring investigation and array microtremor investigations results was measured in this research especially at the university area. As it can be seen in Fig. 13 (a) the base-rock elevation is easily to predict by conducting the minimum shear wave velocity of 1500 m/sec. The base-rock elevation was observed at approximately 30 m below the surface level (cross section no 3). Sand-stone sample was observed at the boring no Lok01Bh1 at 25 to 30 m below the surface level.

Base-rock elevation were observed at three boring locations at area 1. However, no rock sample obtained at five boring positions at area 2. Fig 13(b) shows an example of boring-log record at area 2 (cross section no 1 and 2). Figure 14 shows the correlation of N-SPT (Standard Penetration Test) result and Vs profile developed at boring no BH1. Figure 15 shows the correlation of N-SPT data and Vs profiles at boring no Bh2.

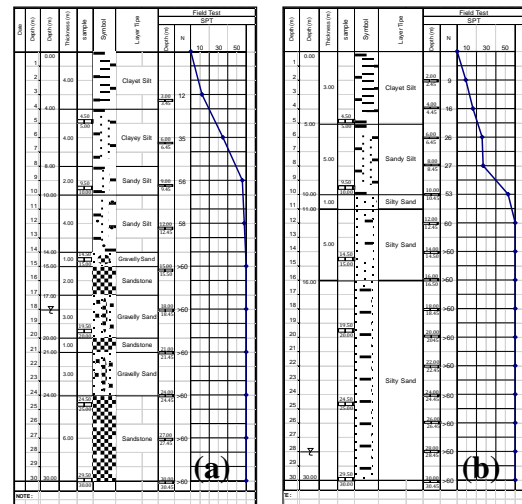


Fig. 13 Two sample boring log results area 1 Bh1 (a) and area 2 Bh2 (b)

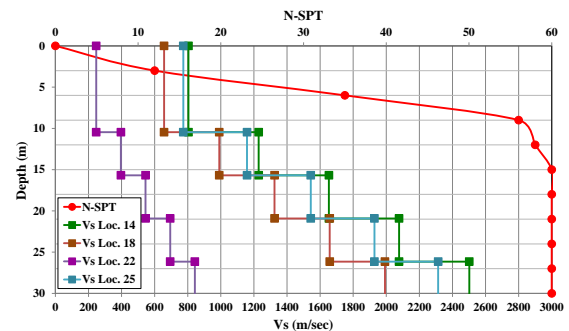


Fig. 14 N-SPT and Vs correlation at cross section no 3

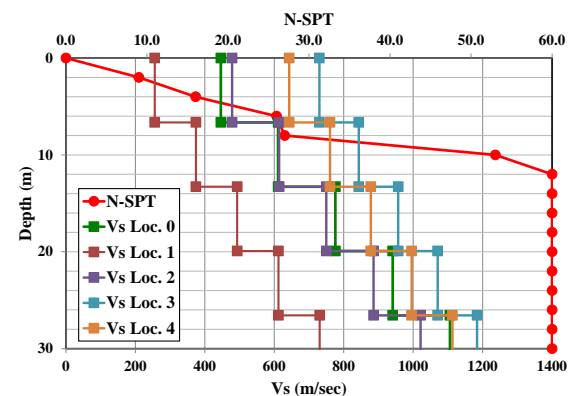


Fig. 15 N-SPT and Vs correlation at cross section no 3

no1

Figure 14 shows the correlation of Vs profile developed from array microtremor with 4 geophones and soil boring investigation result. The analysis was conducted at cross section no 3 position. Based on the Vs profiles, the maximum Vs value obtained at 30 m below the surface level is 2502 m/sec and the minimum Vs value at this level is 843 m/sec and the average Vs value is 1913 m/sec. The average Vs value from 25 m to 30 m is greater than 1500 m/sec. Following [1] and [3] the hard rock samples will be obtained at minimum 26 m below the surface level. Based on the boring-log result conducted at this array position as can be seen at Fig. 13(a) the sand stone sample was obtained from 26 to 30 m below the surface level. The N-SPT profile was also obtained from the same boring position. However, it is difficult to evaluate the hard rock position based on the N-SPT data. Due to the capability of N-SPT spoon sampler apparatus, for all N-SPT greater than 60, the boring master will stop the blowing proses and write the N-SPT record ">60" into the boring-log. Sand stone samples are also observed at other two boring investigation positions. A good output performance of base-rock investigation was observed at area 1.

Figure 15 shows the same Vs and N-SPT correlation conducted at array 1 position. Five geophones for ambient vibrations measurement were installed at this position. In average no Vs value at 30 m below the surface level reach 1500 m/sec. The average Vs value collected from five geophones is less than 1500 m/sec. Based on the average Vs data, it is difficult to obtain the base-rock samples at this array investigation position. Base on the boring-log report, no soft rock or hard rock samples obtained from the soil boring investigation. As it can be seen at Fig. 13 (b), the N-SPT values obtained from 12 m to 30 m below the surface level are greater than 60.

Based on the microtremor and soil boring investigations conducted at the University area, base-rock elevation can be predicted using single and array microtremor investigations. Base-rock elevation can be predicted when the Vs data observed by microtremor equipment reach minimum 1500 m/sec.

CONCLUSIONS

Development of base-rock elevation is one of the most important data or information needs for seismic hazard analysis and site-specific ground motion analysis. Base-rock elevation can easily be predicted using single and array microtremor or seismometer investigation. Following the microtremor investigation, in terms of base-rock elevation, the study area is divided into two different sub-area, the first area having a maximum of 30 m and the second area is predicted having a maximum of 60 m base-rock elevation.

Based on eight boring investigations results for verifying the base-rock elevation, the sand stone (hard rock) samples were observed at three boring positions having a maximum of 30 m depth (first area). However, no hard rock samples observed at other five boring positions (second area).

Single and array microtremor investigations can be used as a complement method in predicting base-rock measurements. Boring investigations shall be conducted to verify the microtremor investigation results. A minimum of 1500 m/sec of shear wave velocity values should be applied for base-rock elevation measurements. However, if the vs value obtained on site less than 1500 m/sec, the predicting base-rock elevation is difficult to perform. For verifying base-rock elevation located at minimum 100 m depth, the soil boring investigation will spend a lot of money and time.

ACKNOWLEDGMENT

This research was financially supported by the Ministry of Education and Culture, The Republic of Indonesia through Research Grant 2019 and 2020.

REFERENCES

- [1] ASCE/SEI 7-16: Minimum Design Loads and Associated Criteria for Buildings and Other Structures. American Society of Civil Engineers, 2017.
- [2] National Center for Earthquake Studies: Indonesian Seismic Sources and Seismic Hazard Maps 2017, Centre for Research and Development of Housing and Resettlement, Ministry of Public Works and Human Settlements, ISBN 978-602-5489-01-3, 2017, pp. 1-377.
- [3] SNI 1726:2019, Seismic Resistance Design Code for Buildings and Other Structures, Jakarta, 2019, pp. 1-238.
- [4] Partono W., Prabandiyani S.P.R., Irsyam M. and Maarif S.: Seismic Microzonation of Semarang Indonesia based on Site Response Analysis using 30 m Soil Deposit Model. Jurnal Teknologi, Vol. 78:8-5, 2016, pp. 31-38.
- [5] Claudet S.B., Baise S., Bonilla L.F., Thierry C.B., Pasten C., Campos J., Volant P. and Verdugo R., Site effect evaluation in the Basin of Santiago de Chile using ambient noise measurements, Geophys. J. Int., 176, 2009, pp. 925-937.
- [6] Johansson J.A.T., Mahecha E.A.L., Acosta A.T.T. and Arellano J.P.M.: H/V Microtremor Measurements in Pisco, Peru after the 2007 August 15 Earthquake, The 14th World Conference on Earthquake Engineering, Beijing, China, (2008).
- [7] Nogoshi, M. and Igarashi, T.: On the amplitude characteristics of microtremor, Part 2, J. Seism. Soc. Japan, 24, 1971, pp. 26-40.

- [8] Nakamura Y.: A Method for Dynamic Characteristic Estimation of Subsurface Using Microtremor on The Ground Surface, Quarterly Report of Railway Technical Research Institute, vol. 30, 1989, pp. 25-33.
- [9] Sun-Woo M., Palanidoss S., Yunhoa Z., Ganapathiraman V. and Taeseu K.: Bedrock depth evaluation using microtremor measurement in Singapore: empirical guidelines at weathered granite formation in Singapore, *Journal of Applied Geophysics*, 171, 2019, 103866, pp. 1-9.
- [10] John W. L., Gregory V S., Eric A. W. and James S. C.: Estimation of Bedrock Depth Using the Horizontal-to-Vertical (H/V) Ambient-Noise Seismic Method, *Symposium on the Application of Geophysics to Engineering and Environmental Problems*, September 2008,
- [11] Sunaryo, Harti Umbu Mala, and Anom Prasetyo, Earthquake Microzonation Study on Batubesi Dam Nuha, East Luwu, South Sulawesi, Indonesia, *International Journal of Geomate*, Vol 15, Issue 48, 2018, pp. 148 – 154.
- [12] Yamanaka M., Hachimura T. and Hasegawa S., Distribution of Landfill by Geophysical Exploration Methods at Illegal Industrial Wastes Disposal Site, *International Journal of Geomate*, Vol 9 (17), 2015, pp. 1342-1347.
- [13] Koesuma S., Ridwan M., Nugraha A. D., Widiyantoro S. and Fukuda Y.: Preliminary Estimation of Engineering Bedrock Depths from Microtremor Array Measurements in Solo, Central Java, Indonesia, *Journal of Mathematical and Fundamental Sciences*, Vol 49, No 3, 2017
- [14] Chun H. K., Chun-Te C., Che-Min L., Kuo-Liang W., Jyun-Yan H., Shun-Chiang C., S-wave velocity structure and site effect parameters derived from microtremor arrays in the Western Plain of Taiwan, *Journal of Asian Earth Sciences*, Vol. 128, 2016, pp. 27-41.
- [15] Ibs-von Seht, M. and Wohlenberg, J.: Microtremors measurements used to map thickness of soft soil sediments, *Bulletin of the Seismological Society of America*, v.89, 1999, pp.250-259.
- [16] Parolai, S., Bormann, P., and Milkert, C.: New relationships between Vs, thickness of sediments, and resonance frequency calculated by the H/V ratio seismic noise for Cologne Area (Germany), *Bulletin of the Seismological Society of America*, v.92, 2002, pp. 2521-2527.

OUTFLOW CHARACTERISTICS OF FINE PARTICLES IN TWO KINDS OF WATER-PASSING EXPERIMENTS USING A COLUMN

Tomoki Wakamatsu¹, Motoyuki Suzuki¹ and Taichi Ishimaru¹

¹Graduate School of Sciences and Technology for Innovation, Yamaguchi University, Japan

ABSTRACT

In embankment structures affected by seepage flow over a long period, such as river levees and reservoir dams, soil particles flow into the voids and flow out of the embankments. The phenomenon whereby fine soil particles move to the interior of embankments is called “internal erosion”. This progressive phenomenon in which only the fine soil particles flow out, while the skeleton of the coarse soil particles remains, is called “suffusion”. Suffusion causes a reduction in the strength of the embankment materials. Embankments affected by suffusion may collapse due to heavy rain and earthquake events. However, the mechanism of suffusion remains unclarified. In this study, two kinds of water-passing experiments were performed with our developed cylindrical column apparatus in order to examine the progression and the continuity of suffusion, and the flow rate, turbidity of the drainage water and mass of the discharged soil were continuously measured. Some experiments have been performed in previous studies to reproduce suffusion artificially, but it was difficult to continuously collect and analyze the discharged soil. This is because the amount of discharged soil was low and the particle size was small in the cases of specimens of a general size. Thus, an attempt was made here to conduct a particle size analysis using a turbidimeter in order to overcome these problems. As a result, the changes in the discharged soil particle size could be traced, and it could be clarified that the soil particles with a small particle size were transported to the lower part of the specimen and that a portion of the particles flowed out.

Keywords: Suffusion, Internal erosion, Embankment structure, Seepage

INTRODUCTION

In embankment structures affected by water storage, such as riverbanks and reservoirs, sometimes muddy water leaks from the ground surface. When the leak is turbid, there is a risk of collapse, which is one of the important items to check during inspections. As shown in Fig. 1, it is possible for the fine particles to flow out of an embankment while the skeleton of coarse soil particles remains. This phenomenon is called “suffusion” and it may reduce the strength of the embankment materials used as the ground material. Recent studies have revealed that suffusion also causes a decrease in the ground-bearing capacity [1], [2]. In other words, if suffusion continues, the stability of the embankment structure will be lost over time. However, the process and mechanism of suffusion, as well as its effect on an embankment’s stability, are unclear.

In this study, two types of downward water-passing experiments, involving the discharge of fine particles, were carried out with a cylindrical column to examine the progress and continuity of suffusion. In previous research, the discharged soil particles were so few that a continuous analysis was difficult. In this research, an attempt was made to analyze the particle size of the discharged soil by measuring the turbidity of the wastewater as one method to solve the problems. Thus, the progress of suffusion was considered from the viewpoint of particle size.

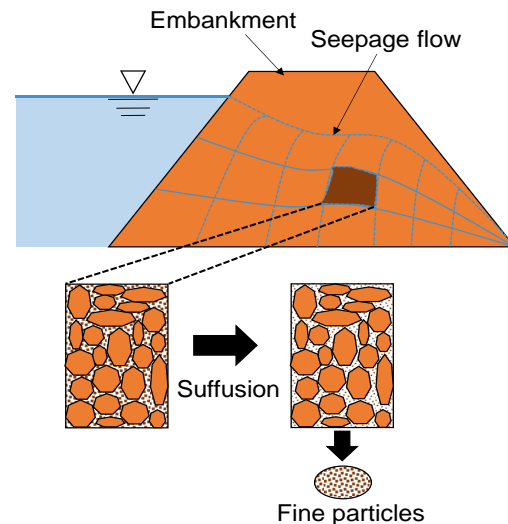


Fig. 1 Image of suffusion

PARTICLE SIZE ANALYSIS USING A TURBIDIMETER

It is difficult to continuously collect and analyze discharged soil particles. This is because, in an experiment, they are too small and too few in number to reproduce suffusion. In this study, a particle size analysis of the soil particles discharged in each experiment was performed using a turbidimeter. The

particle size of the discharged soil was estimated by comparing the turbidity of the pre-prepared calibration suspensions with the turbidity of the drainage in the experiment.

Turbidimeter information and features

The turbidimeter used in this study is turbidimeter TR-55 manufactured by Kasahara Chemical Co. The principle of turbidity measurement is the transmitted and scattered light measurement method. The transmitted light and scattered light of parallel light from an LED light source are measured at the same time, and the turbidity is converted from the ratio. The feature of this method is that the scattering intensity increases as the total surface area of suspended substances in a unit volume increases. Thus, the turbidity value increases as the particle size of the suspended substances decreases [3]. This feature of turbidity was applied to the experiments.

Procedure for turbidity measurement

10 ml of sample water was collected from the agitated drainage and transferred to a measurement cell using a pipette. After the bubbles on the wall of the measurement cell were removed by shaking, the cell was set in the turbidimeter. After waiting about 10 seconds for the sample water to be stable, the turbidity was measured. The measured water was not returned to the used suspension; the same measurement was performed four times using other measurement cells. At the start and end of each experiment, the turbidity of the purified water (used as a control) and the tap water was measured in the same way; the turbidity remained below 0.02 degrees and 2 degrees, respectively. The turbidity of the water was negligible.

Drawing reference lines

First, four calibration samples were prepared. The samples were taken from Ube Masado soil using four sieves, with mesh sizes of 75 μm , 106 μm , 250 μm , and 420 μm , and named C75, C106, C250, and C420, respectively. Then, 80 different suspensions were made, and their turbidity was measured. The 80 suspensions differed in calibration samples (four types: C75, C106, C250, and C420), SS (five types: 0.2, 0.6, 1.0, 2.0, and 3.0 g/L), and volume (four types: 0.05, 0.25, 0.50, and 2.5 L). Figure 2 shows the relationship between the turbidity of the suspensions and concentration SS. Concentration SS is defined here as

$$SS = \frac{m_{ds}}{V_{dw}} \quad (1)$$

where m_{ds} is the dry mass of the suspended soil

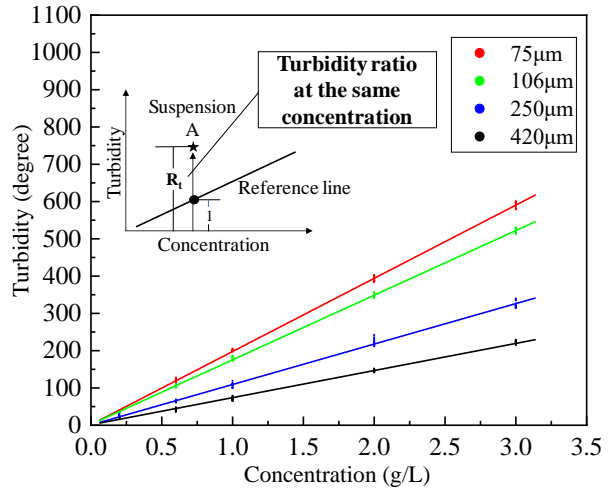


Fig. 2 Relationship between concentration and turbidity of suspensions

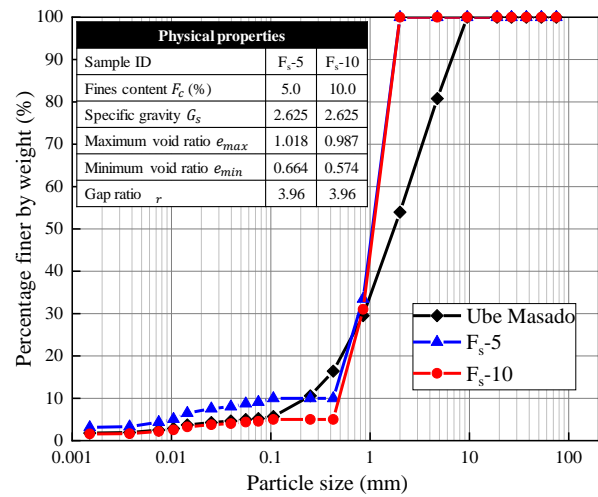


Fig. 3 Physical properties and particle size distribution curves

particles and V_{dw} is the volume of water.

According to Fig. 2, the concentration and turbidity of the calibration samples showed a linear relationship when the types of samples were the same. Furthermore, the slope of the best fitting line became smaller as the size of the soil particles contained in the suspensions became larger. There was no effect on the turbidity measurement due to the differences in the volume of the suspensions. Here, each best fitting line is called the “reference line”. The schematic diagram in Fig. 2 shows the ratio of the turbidity of suspension A to the turbidity on the reference line of the same concentration when the relationship between the concentration of this certain suspension A and the turbidity is plotted. This ratio was defined as the “Turbidity ratio at the same concentration R_t ” and used in the experiment as a parameter for the outflowing soil particles. The larger the turbidity ratio at the same concentration, the larger the distribution of smaller particle sizes than the calibration samples.

EXPERIMENTAL MATERIAL

The soil samples used in this study contained decomposed granite soil, called “Ube Masado”, because this type of soil is often used in reservoir embankments. The “Ube Masado” was collected in Yamaguchi, Japan. Figure 3 shows the particle size distribution and the physical properties of the soil. The Ube Masado was divided into four groups of more than 2 mm, 420 μm ~2 mm, 106 μm ~420 μm , and less than 106 μm by sieving, and then mixed to have the soil particle distribution shown in Fig. 3. The two types of prepared soils were named “f_s-5” (Fine sand: 5%) and “f_s-10” (Fine sand: 10%). In this study, the soil particles with a particle size of 420 μm or more are called “coarse particles”, while those with a particle size of 106 μm or less are called “fine particles”. Here, the percent of fine particles is the “fines content”. The particle size distribution in Fig. 3 implies that the coarse particles form a skeleton, while the fine particles are present in the voids.

The stability of the internal erosion of this sample was evaluated with the index proposed by Chang and Zhang [4]. The many stability indexes related to internal erosion were rearranged. Soil with an absent portion of the particle size distribution, such as with these samples, is called a “gap-graded soil”. It is said that the internal stability of gap-graded soils with fines contents less than 10% may be dominated by the gap ratio (G_r). The G_r is defined as the ratio of the maximum particle size, d_{max} , to the minimum particle size, d_{min} , of the severely under-represented portion on the particle size distribution curve:

$$r = \frac{d_{max}}{d_{min}} \quad (2)$$

When the condition of $F_c \leq 10\%$ is satisfied, “ $G_r < 3$ ” is determined to be internally stable and “ $G_r > 3$ ” is determined to be internally unstable. All samples used in this study satisfied $F_c \leq 10\%$ and the gap ratio was 3.96 ($d_{min} = 106 \mu\text{m}$ and $d_{max} = 420 \mu\text{m}$). Therefore, it can be said that the particle size distribution is internally stable and that internal erosion is likely to occur.

EXPERIMENTAL METHOD

Experimental Apparatus

Fig. 4 presents a schematic diagram of the experimental apparatus used in this study. It was produced by referring to the experimental apparatus designed by [5]. At the bottom, where each specimen was located, an acrylic plate, with 108 holes each having a diameter of 5 mm, and mesh with a diameter of 420 μm , were installed. These parts allowed only fine particles, smaller than the size of the sieve, to

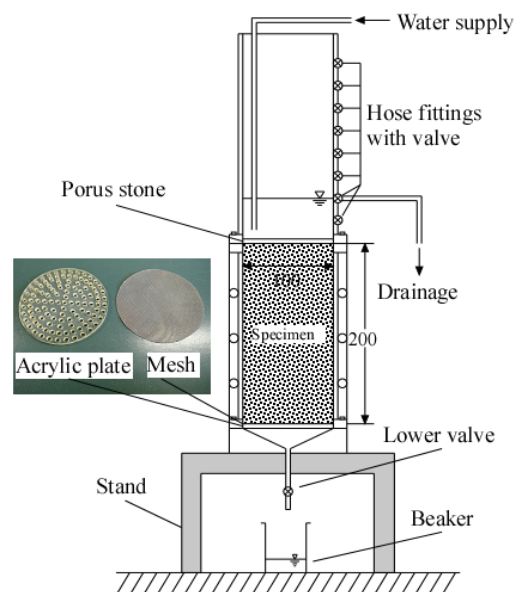


Fig. 4 Schematic diagram of apparatus used in this study

flow out of the specimen under the application of water flow. In addition, soil particles were easily discharged by providing a funnel-shaped depression in the bottom of the specimen.

Experimental Procedure

Two kinds of water-passing experiments were conducted here. One was performed while maintaining a constant water level; this experiment and its process are called the “constant water-passing experiment” and the “constant water-passing process”, respectively. The other was performed under the conditions of repeated supplying and draining; this experiment and its process are called the “repeating water-passing experiment” and the “repeating water-passing process”, respectively.

Constant water-passing experiment

Specimens were prepared by tamping every four layers of soil samples in order to adjust the water content to 10%. The target gap ratio was 0.85 or 0.80. Before the experiments, water seeped into the specimen until it permeated the surface. At this time, in order to prevent soil particles from flowing out, water was flushed from the surface of the porous stone side by turning the specimen upside down. After placing the specimen upside down and installing it in the apparatus, water was poured onto the top of the specimen. The water surface position was adjusted such that the hydraulic gradient was 1.125. At the start of the test, the specimen saturation was about 70%.

When the valve at the bottom is open, water permeation starts. After each beaker had filled to

about 100 ml, following the start of water permeation, the beakers were collected and numbered from 1~14. During the experiment, the sampling time for each beaker was measured. After each experiment, the amount of drainage and the turbidity of the drainage were measured. Then, the mass of the discharged soil particles was measured after being oven dried.

Repeating water-passing experiment

The repeating of the water-passing experiment was continued using the same specimen as for the cases of fs-5_0.85 (2), (3), (4) and (5) in the constant water-passing experiment. The repeating of the water-passing process is shown in Fig. 5. When the experiment was completed, the water supply onto the top of the specimen was stopped. Simultaneously, the water was drained from the bottom of it. In Pattern 1, the lower valve was closed 5 minutes after stopping the water supply. In Pattern 3, the lower valve was closed 24 hours after stopping it. After that, the specimen was divided into six layers. On the other hand, in Pattern 2, 500 ml of water was supplied onto the upper surface of the specimen 5 minutes after stopping the water supply. In Pattern 4, 500 ml of water was supplied onto the upper surface of the specimen 24 hours after stopping it. In both patterns, this process was repeated nine times. Finally, the lower valve was closed 5 minutes after the last supply of water in Pattern 2 and 24 hours after it in Pattern 4. After the lower valve was closed, the specimen broke apart in 5 minutes in Pattern 2 and in 24 hours in Pattern 4. The specimen was divided into six layers in the height direction, and the water content for each layer was measured (Fig. 6). Each layer was washed with water on a 106 μm sieve, and the residue was oven dried. The mass of the residue was measured to calculate the fines content. Furthermore, the soil particles of the passing portion were collected together with water, and R_t was calculated by measuring the turbidity of the suspensions.

EXPERIMENTAL RESULTS

Results of constant water-passing experiments

Amount of discharged soil particles

Fig. 7 shows the relationship between the average flow rate and the total amount of discharged soil particles. Experimental IDs mean {sample ID_Initial void ratio_(Number)}. Even if the experimental conditions are the same, the average flow rates will be different. Initial saturations were around 70%, and it is possible that water preferentially flows through the parts with high saturation. It is thought that the differences in the flow rates were affected during the initial saturation. In both f_s -5 and f_s -10, the higher the average flow rate, the higher the total amount of

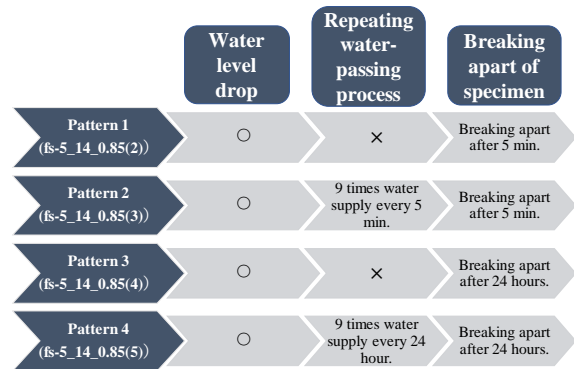


Fig. 5 Flowchart of repeating water-passing experiment

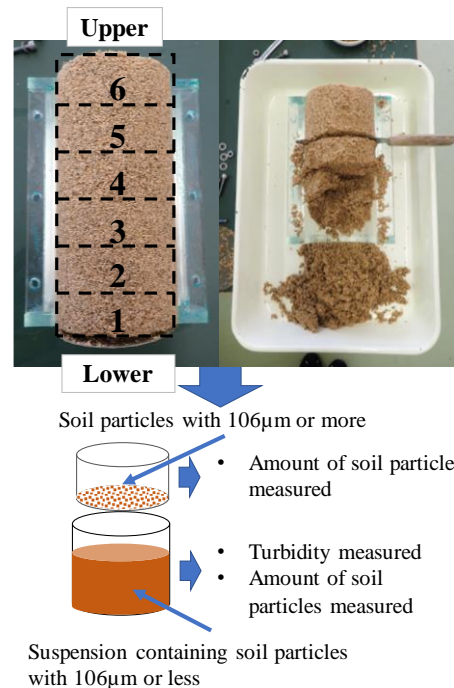


Fig. 6 Breaking apart of specimen after the experiments

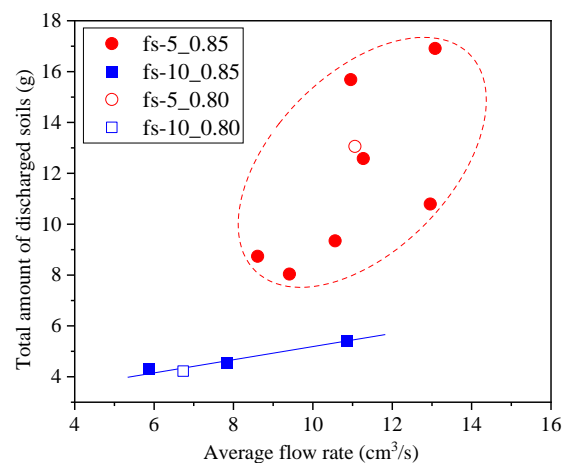


Fig. 7 Relationship between average flow rate and total amount of discharged soil particles

discharged soil particles. In addition, the total amount of discharged soil particles in the case of fs-5 was greater than that in the case of fs-10. Fig. 8 shows the discharge of soil particles for each beaker in the constant water-passing experiments. In all cases, the amount of discharged soil gradually decreased when the water flow increased. In the five cases of fs-5_0.85, the amount of discharged soil particles became the maximum at the time of beaker No. 2. It is thought this is because the water which had collected in the depression of the lower plate flows out first. When the water flow exceeded 600 ml (beaker No. 3), the amount of discharged soil particles per 100 ml decreased to 0.2 g or less.

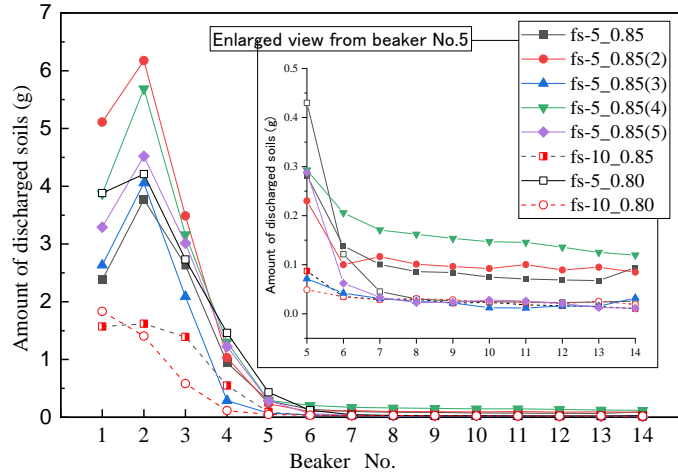


Fig. 8 Amount of discharged soil particles for each beaker (constant water-passing experiments)

Turbidity ratio at the same concentration

Fig. 9 shows the R_t for each beaker. C106 was selected as the reference line. The original particle size distribution of the fines in the specimen is the same as that for C106. If the fine particles are discharged from the specimens with the same as original particle size, R_t should be about 1. The R_t of beaker 1 is about 1.7 to 2.5 in all cases. It is supposed that many particles with a particle size of 106 μm or less were discharged from the specimens. Here, for the brief explanation given below, the relatively small particles among the fine particles are expressed as “clay”. In all cases, there is a tendency for R_t to increase to beaker No. 4-6 (water flow is about 400 ml to 600 ml) and then to decrease. It is thought that 400 to 600 ml of the clay is preferentially discharged from the specimens, and thereafter, less clay is discharged.

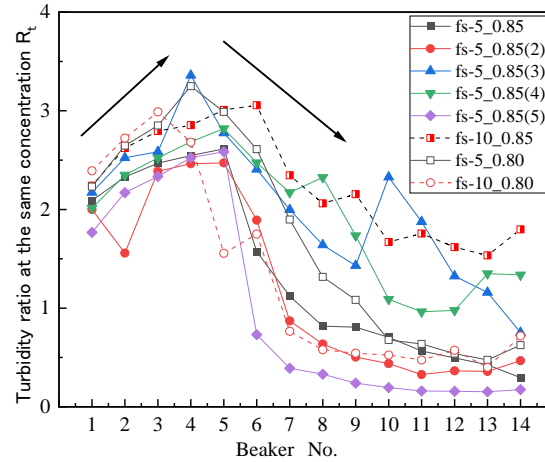


Fig. 9 R_t for each beaker (constant water-passing experiments)

Repeating Water-Passing Experiments

Amount of discharged soils

Fig. 10 shows the discharge of soil particles from each beaker in the repeating water-passing experiment. Although the discharge of soil particles almost stopped during the constant water-passing process, soil particles began to be discharged again during the repeating water-passing process in the case of Patterns 2 and 4.

Turbidity ratio at the same concentration

Fig. 11 shows the R_t for each beaker in the repeating water-passing experiments. In Patterns 2 and 4, R_t increased rapidly to about 2.5 after the first supply of water. Even after the first supply of water, R_t remained at 2 or more. These values for R_t were similar to the peak value for R_t during the constant water-passing process. In the experiments, the water flowed under unsaturated conditions, so that, in the

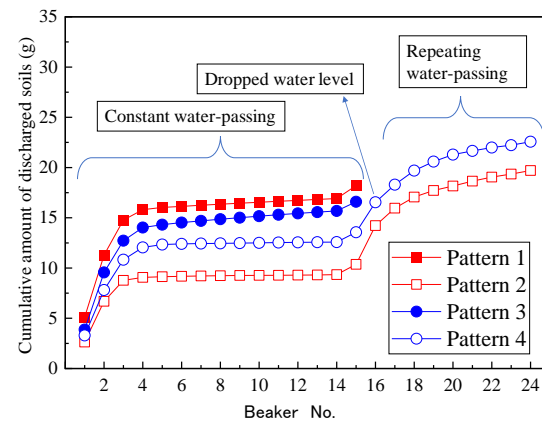


Fig. 10 Cumulative amount of discharged soil particles for each beaker (repeating water-passing experiments)

constant water-passing process, it is thought that the water first flowed through the part where the initial saturation had been higher. It is supposed that the route where the water flow changed with each passage of water during the repeating water-passing process caused the erosion of the part that was not

subjected to an outstanding flow or the movement of soil particles. Furthermore, the fact that R_t increased during the repeating water-passing process is thought to have contributed to the fact that erosion occurred in new areas where clay had remained.

Breaking apart of specimen after the experiments

Fig. 12 shows vertical distributions of the fines content and the rate of change in R_t when the R_t of the uppermost layer was 1, for the specimen divided after the experiment. The fines contents of Patterns 1 and 3 were below the initial fines contents of the all layers. On the other hand, the fines contents of Patterns 2 and 4 were larger from the uppermost layer to the lowermost layer. It is thought that the fine particles moved from the upper layer to the lower layer, and that clogging occurred around the lower part. The rates of R_t in Patterns 2 and 4 became larger from the uppermost layer to the lowermost layer. It is believed that the clay predominantly moved from the upper layer to the lower layer.

CONCLUSIONS

In this study, two types of water-passing experiments were conducted to examine the progress and continuity of suffusion. The main results of this paper are summarized as follows:

1. In the water-passing experiments under constant water level conditions, more clay was discharged from the fine particles in the specimen, and the clay was discharged first.
2. In the water-passing experiments under constant water level conditions, the discharge of soil particles almost stopped when the water flow was about 400 ml to 600 ml. After that, the discharge of soil particles restarted when the water flow condition was repeated. The soil particles flowing out of the newly eroded part contained a large amount of clay that had not flowed out during the constant water level flow process.
3. Due to repeating the water-passing process, the clay content in the upper part of the specimen moved to the lower part. In addition, since fine particles in the lower part of the specimen were higher than those at the initial stage, it was possible that retention had occurred near the mesh.

REFERENCES

- [1] Sato, M. and Kuwano, R., Laboratory testing for evaluation of the influence of a small degree of internal erosion on deformation and stiffness,

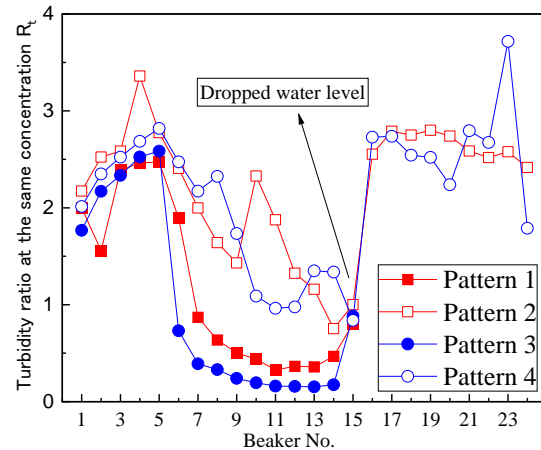


Fig. 11 R_t for each beaker (repeating water-passing experiments)

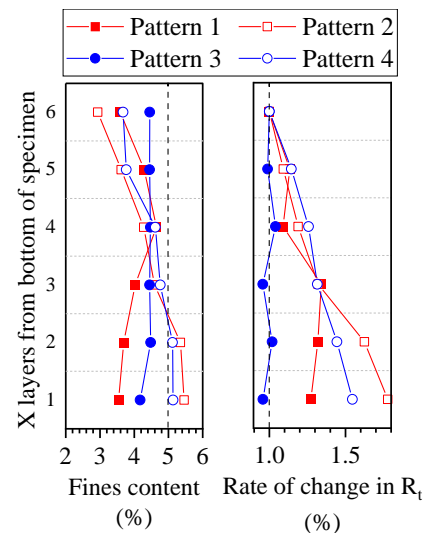


Fig. 12 Fines content and rate of change in R_t for each layer

Soils and Foundations, Vol. 58, Issue 3, 2018, pp. 547-562.

- [2] Ke, L. and Takahashi, A., Experimental investigations on suffusion characteristics and its mechanical consequences on saturated cohesionless soil, Soils and Foundations, Vol. 54, Issue 4, 2014, pp. 713-730.
- [3] Yokoyama, K., The influence of particle size on turbidity output and the instructions for using turbidity sensor in the field, Journal of JSCE, Vol. 698, 2002, pp. 93-98 (in Japanese).
- [4] Chang, D. S. and Zhang, L. M.: Extended internal stability criteria for soils under seepage, Soils and Foundations, Vol. 53, Issue 4, 2013, pp. 569-583.
- [5] Ke, L. and Takahashi, A., Triaxial erosion test for evaluation of mechanical consequences of internal erosion, Geotechnical Testing Journal Vol. 37, Issue 2, 2014, pp. 347-364.

APPLICATION OF COMPUTER VISION TECHNIQUE IN RAPID SOIL CLASSIFICATION

Aw, Y.J.E.¹, Koh, J.W.¹, Chew, S.H.¹, Tan, S.E.D.², Cheng, L.M.², Yim, H.M.A.², Ang, L.J.L.² and Chua, K.E.²

¹Faculty of Engineering, National University of Singapore, Singapore; ²Building & Infrastructure Group, Housing & Development Board, Singapore

ABSTRACT

Singapore's Staging Grounds (SGs) receive hundreds of truckloads of excavated soil from construction sites daily and barge it to land reclamation sites as infill material. The excavated soil needs to be classified into two broad types (i.e. "Good Earth" and "Soft Clay"), according to particle size distribution (PSD) and water content (w), for appropriate use and treatment before and after infilling. However, conventional laboratory tests for PSD and w pose time and manpower constraints at SGs. Thus, computer vision technique is adopted for non-destructive, non-intrusive and instantaneous classification of excavated soils upon delivery to SGs. A 4-stage procedure of rapid soil classification with computer vision was established: (1) "soil image acquisition", (2) "image processing", (3) "image analysis", and (4) "decision making". A study was conducted with 40 soil images and samples collected from SGs. Five parameters of Grey Level Co-occurrence Matrix (GLCM) were obtained for each image. PSD and w of each sample were determined from conventional laboratory tests. 32 soil samples formed the training set to establish an Artificial Neural Network (ANN) model using the back-propagation network, correlating GLCM parameters with PSD and w results. The remaining 8 samples were used as the test set. This trained ANN model is found to be able to differentiate the soil images in less than a minute, and thus able to classify soils into "Good Earth" or "Soft Clay" with accuracy as high as 82.5%. This computer vision method will enable the SGs to achieve much higher productivity with good accuracy in terms of classifying soil received.

Keywords: Computer vision technique, Soil classification, Rapid and non-destructive method, ANN, Training and testing sets

INTRODUCTION

Singapore's staging grounds (SGs) serve the dual purpose of receiving excavated soil from the construction industry and supplying land reclamation projects with a useful construction resource (Fig. 1). Trucks transport unwanted excavated soil from construction sites to staging grounds located along the coast of Singapore. This excavated soil is loaded into barges and is then transported to various land reclamation sites for use as an infill material. It is important to ascertain the quality and type of the soil received at the staging grounds so that appropriate land reclamation and soil treatment methods can be used. With hundreds of trucks passing through the staging grounds daily, staging ground operators have begun looking into ways to optimize operations and improve the quality of checks on site.

Definition of Classification Classes

Despite originating from different geological formations in various parts of Singapore, excavated soils received at SGs can be broadly classified into two groups – "Good Earth" and "Soft Clay" – based primarily on PSD and water content.



Fig. 1 Transported by trucks to staging ground (left), then loaded onto barges for transportation offshore (right)

According to the staging grounds' classification criteria, "Good Earth" soils must contain at least 65% by weight of coarse particles ($> 63\mu\text{m}$) and have a water content of less than 40%. Soils classified as "Good Earth" generally have a higher percentage of coarse particles and relatively low water content, making it a suitable material for constructing revetment bunds. It also contains some percentage of fine particles that makes it ideal for compaction – a standard and less costly ground improvement technique – as the topmost layer of reclaimed land above sea level.

On the other hand, "Soft Clay" soils have a higher percentage of fine particles, or a high water content, or both. These soils tend to have slow gain in shear strength and large settlement over time, and hence

require more costly ground improvement techniques, such as vacuum consolidation, in order to be effectively used as the bulk of infill material below sea level.

Current Classification Methods

The Housing & Development Board (HDB) manages Singapore's two largest staging grounds with the highest daily throughput. Their current practice is to generally classify excavated soil by construction site, using information from the borehole logs. At the SGs, the weigh-bridge operator does a quick inspection of the soil type in each truck via a CCTV (closed-circuit television) camera – a “Good Earth” soil may then be “reclassified” to “Soft Clay” if the soil visibly has high water content i.e. is in a slurry state.

However, the current practice fails to consider Singapore's highly varying geology. Large volumes of “Good Earth” may be misclassified as “Soft Clay”, such that coarser excavated soil that could have been used for revetment bunds would be sub-optimally used as infill material. Unnecessary costs may also be incurred from using more expensive ground improvement techniques for misclassified “Soft Clay” soil.

This presents an opportunity for introducing an additional layer of quality control at the SGs. Performing this classification at the receiving point (i.e. at SGs) avoids the over-generalization apparent in the current practice. This enhanced ability to carry out on-site classification of the excavated soils received will translate into cost-savings in terms of maximal recovery of “Good Earth” material and reduction in ground improvement costs.

The introduction of new methods in the field will need to take into account the operational considerations of the SGs. Any improvements to the operations cannot compromise quality and efficiency of the existing staging ground system that has been optimized to cope with the high daily throughput of trucks. Such requirements render traditional soil investigation methods unsuitable. Testing methods to determine in-situ water content and soil index properties typically takes 2 to 3 days and require samples of the soil to be tested in highly controlled conditions. Rapid, non-destructive methods using highly specialized spectrometers are costly to implement for the classification of large volumes daily. Therefore, this paper will focus on the feasibility study of using computer vision in soil classification on-site.

Computer Vision

Computer vision, also known as machine vision, is the science that develops the theoretical and algorithmic basis by which useful information about

an object or scene can be automatically extracted and analyzed from an observed image, image set, or image sequence [3]. Designed to replace human effort in the performance of a given process, a typical process in a computer vision involves: (1) image acquisition; (2) image processing; (3) image analysis; and (4) decision-making. Some examples are listed in Table 1.

Table 1 Examples of computer vision applications and their abilities

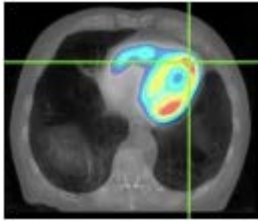
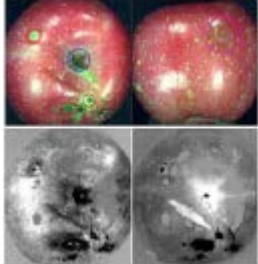

Example	Ability
	Medical Images - Isolation and visual emphasis of a specific region of interest
	Food Images - Detection of surface properties (e.g. irregularities) for non-destructive inspection and testing
	Satellite Images - Image segregation based on image properties (e.g. color, image texture)

Image Color

The most commonly used format is the byte image (each pixel brightness value stored as 8-bit integer) of value between 0 and 255. This is similar to the widely-used Red-Green-Blue (RGB) color model which was used in many research.

A study by Chung et al. [4] demonstrated that image color, particularly RGB, can be used to develop a soil texture classification algorithm. However, in this study, preliminary trials using RGB as input values showed that classification accuracy was relatively low (48%). It may be highly probable that it is not possible to establish clear color groups with distinct soil properties, as the excavated soil used in this study are not homogeneous in color, especially in residual soils that contain a mixture of colors but have virtually indistinguishable soil properties. Hence, an alternative scheme is needed for this study.

Image Texture

In soil investigation, soil texture refers to how the soil feels to human touch (e.g. sandy, clayey, granular, fine etc.). However, image texture in computer vision, in terms such as fineness, coarseness, smoothness, and graininess are determined by the spatial arrangement of pixel brightness values. For irregular textures – such as that of excavated soils – it is most ideal to use statistical analysis methods.

One of the most popular methods are co-occurrence features obtained from a grey level co-occurrence matrix (GLCM) [3]. Connors and Harlow [5] found that GLCM is best in discriminating terrain types from aerial photographs. Given that it possesses the highest accuracy among statistical methods and has been extensively used in other fields, GLCM is adopted for this study.

In the GLCM method, 14 Haralick textural features can be obtained [3], and are listed in Table 2.

Table 2 Grouping of 14 Haralick texture features

Contrast Group	*Contrast (CON)
	*Inverse Difference Moment (IDM)
	Dissimilarity
Orderliness Group	*Angular Second Moment (ASM)
	Energy
	*Entropy (ENT)
	Maximum Probability
Descriptive Statistics of the GLCM	GLCM Mean
	GLCM Variance / Standard
	Deviation
	*Correlation (COR)

* The five most commonly used textural features considered in this study.

Scaling of Water Content, w , by Liquid Limit

When classifying samples into water content (w) of “more than 40%” or “less than 40%” based on HDB’s classification criteria, it was found that very few samples fall into the latter group. It is not appropriate to consider w alone as w value at the time of inspection may not represent the true nature of soils. Under non-raining weather conditions, most soils would have been exposed to the atmosphere at stockpile pits and subjected to drying. Moreover, the appearance and behavior of soil fundamentally depends on w relative to the Atterberg Limits (Plastic Limit (PL) and Liquid Limit (LL)). Hence, w/LL was selected to be used in place of w .

METHODOLOGY

Sampling of Data

Conventional soil index properties tests (in

accordance to BS 1377:1990) were conducted on the 40 samples retrieved from one of HDB’s staging grounds. The soil images were captured by Nikon D5300 digital single-lens reflex cameras mounted on the roof of one of the weigh-bridge stations. The cameras were set with aperture $f/22.0$ and ISO 100; largest image size of 6000 x 4000 pixels were chosen and images were stored in .jpeg format.



Fig. 2 Full-sized image (left) with a ROI of 1000 x 1000 pixels cropped for analysis (right)

ImageJ, an open-source Java image processing program developed by an international group of contributors from various institutions [6], was used in this study. Due to constraints of truck sizes, a region-of-interest (ROI) of 1000 x 1000 pixels was cropped from each image from any selected location (Fig. 2). 3D Color Inspector plugin was run on each ROI of the 40 samples (i.e. images), and the images were then converted to 8-bit greyscale using a weighted average of the R, G, and B values. The GLCM Texture plugin was used to calculate the five commonly used GLCM Haralick textural features (ASM, CON, COR, ENT, IDM).

ANN Structure, Parameters and Training

The ANN models used were developed using NeuralWorks Professional II/Plus, a software by NeuralWare, Carnegie, USA [7]. All models were experimented using back-propagation networks (BPN) in supervised mode. Generalized delta rule (epoch = 1) was adopted during learning and the sigmoid function was specified as the transfer function. Learning coefficient values and momentum were set to recommended values by the developer NeuralWare [8].

40 samples collected were split (80-20 rule) into a “seen” data-set of 32 samples for training, and an “unseen” data-set of 8 samples to test the trained network. Input parameters using three possible image color (i.e. channel values of Red, Green and Blue) fared poorly in preliminary trials and were hence disregarded. Input parameters using five main image texture feature values (i.e. ASM, CON, COR, ENT, IDM) were employed instead. Individually, CON and COR achieves a higher classification accuracy and hence a combination of CON and COR will be trialed along with the use of all five parameters.

In determining the number of outputs, two general

grouping methods were explored. The first was a “2-group” method that consists of two soil groups as output: “Good Earth” and “Soft Clay”. The second was a “3-group” method that consists of three soil groups as output: “Good Earth”, “Soft Clay-A” and “Soft Clay-B”. The latter subdivided the “Soft Clay” soils further based on the Percentage of Fines.

RESULTS AND DISCUSSION

Soil Index Properties Tests

For the 40 samples tested, amongst those samples that were classified as “Good Earth” by the current practice, the Percentage of Fines ranged from 20.5% to 72.0% (averaged 50.1%), with w ranging from 9.3% to 40.5% (averaged 20.6%). Those samples that were classified as “Soft Clay” by the current practice had the Percentage of Fines ranged from 16.0% to 77.0% (averaged 44.7%), with w ranging from 11.4% to 40.6% (averaged 24.3%) excluding an outlier of 83.5%. No distinguishable differences on the percentage of fines between the two soil types classified according to the current practice were observed.

HDB specifies that soils that contain more than 35% of fine particles would be considered “Soft Clay”. This threshold not only concurs with the standards in the British Soil Classification System [9], but can also be supported by a study on the effects of fines content on some engineering properties of soil [10]. This study shows that the California Bearing Ratio (CBR) – an indicator of the mechanical strength – of the soils tested decreased with increasing fines content. It is of interest to note that the CBR decreases rapidly when the percentage of fines reaches 35-40%, and stabilizes afterwards.

ANN Classification Model

Two rounds of ANN experiments were conducted. In the first round, the effectiveness of using ANN models to predict different soil properties was tested. Five Haralick textural features (ASM, CON, COR, IDM, ENT) were used according to (1) Percentage of Fines and (2) w/LL . Five hidden layer nodes are used as recommended [6]. The results are summarized in Table 3.

In general, higher classification accuracy was observed for classification according to Percentage of Fines. The results also indicate that using these five parameters to classify soils into 2 groups yield higher accuracy than classifying into 3 groups, regardless of the number of hidden layers used in ANN model. It was also noted that, in the classification according to w/LL , better accuracy was obtained with 1 hidden layer and classification into 2 soil groups. Using w/LL , classification into 3 soil groups or using 2 hidden layers yielded very poor accuracy.

Table 3 Classification accuracy of the first round

Textural Features	5: ASM, CON, COR, IDM, ENT			
	Soil Property	Percentage of Fines		w/LL
Hidden layers		1	2	1 2
2-group		87.5%	87.5%	87.5% 37.5%
3-group		75.0%	75.0%	37.5% 37.5%

The second round of experiments was to refine the ANN model by reducing input parameters to only two Haralick textural features (i.e. CON and COR), and predicting according to only Percentage of Fines. The results are summarized below in Table 4.

Table 4 Classification accuracy of the second round

Textural Features	2: CON, COR			
	Soil Property	Percentage of Fines		w/LL
Hidden layers		1	2	1 2
2-group		100%	87.5%	- -
3-group		50.0%	50.0%	- -

Similar to the first round, classification according to Percentage of Fines and into 2 groups yielded higher accuracy than classifying into 3 groups.

Comparing the results of first round and second round, it was observed that for classification into 2 groups, classification accuracy increased when only one hidden layer was used (from 87.5% to 100%), but remains the same (i.e. 87.5%) when moved from round 1 to round 2. On the other hand, for the 3-group classification, classification accuracy decreased from 75% to 50%, for either 1 or 2 hidden layers, from round 1 to round 2. Since better classification accuracy was achieved, the final model will make use of only two textural features (i.e. CON and COR) as inputs for ANN model, run with one hidden layer and classifying into 2 groups, based on Percentage of Fines.

In this ANN, the use of two Haralick textural features gave better prediction results than the use of five Haralick textural features, possibly because some textural parameters within a given group are strongly correlated (according to study by Hall-Beyer [11]). For examples, CON and IDM both belong in the *Contrast Group*, containing the term $|i - j|$. The same can be said for ASM and ENT, which both belong to the *Orderliness Group* and have $p(i,j)$ in their equations. Hence, for classification problems, Hall-Beyer suggested using at most one parameter

from each group. Results from this study seems to confirm the findings by Hall-Beyer, i.e. the texture features of CON and COR combination performs better than using all five texture features.

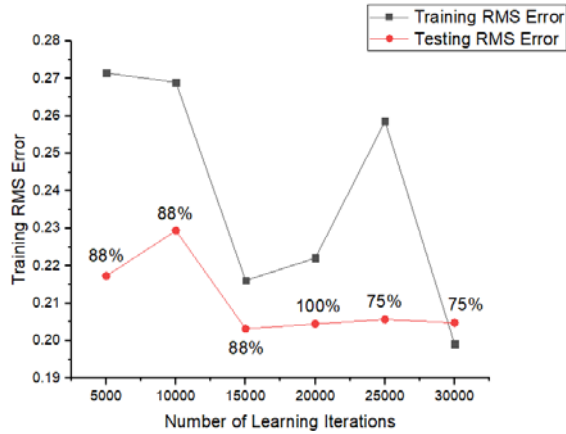


Fig. 3 RMS error vs. number of learning iterations (classification accuracy in brackets)

With this ANN configuration, the effect of learning iterations was studied and results shown in Fig. 3. From Fig. 3, it can be seen that the model achieved the highest classification accuracy at and 15,000 to 20,000 iterations for training set. The sharp increase in training root-mean-squared (RMS) error after 20,000 iterations and subsequent large fluctuations may be attributed to over-training of the network. For testing set, iterations of more than 15,000 learning cycle will neither improve nor worsen the RMS error.

The complete data-set of 40 samples were presented to the ANN model (as shown in Fig. 4), and the comparison between the predictions from ANN and the actual results drawn from PSD and w in physical tests are shown in Table 5.

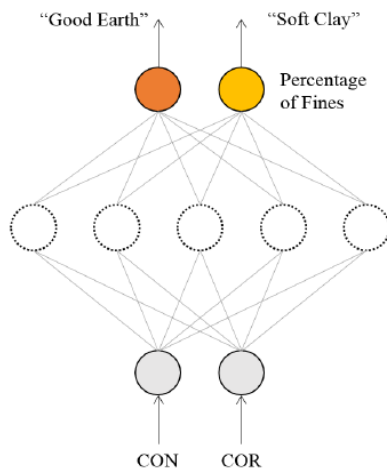


Fig. 4 Final ANN selected for this research

The overall classification accuracy of the final model is 82.5% (33 out of 40 samples). Furthermore, it seemed to be able to predict better in terms of “Soft Clay”, achieving $25/29 = 86.2\%$ accuracy. For “Good Earth” material, the prediction accuracy using this set of ANN Model is only $8/11 = 61.58\%$. It is noted that the 32 training samples were presented as random, independent and unseen inputs to the trained ANN model.

Table 5 Confusion matrix for ANN classification with the selected ANN model

		ANN prediction results	
		“Good Earth”	“Soft Clay”
Actual results from PSD and w	“Good Earth”	8 \checkmark <i>True Negative</i>	3 <i>False Positive</i>
	“Soft Clay”	4 <i>False Negative</i>	25 \checkmark <i>True Positive</i>

\checkmark indicates the number of samples with the same result “correctly predicted” by both the ANN as compared to the actual results from laboratory tests.

In the case of SGs, a false “Good Earth” is arguably worse than a false “Soft Clay” as the former could lead to a weaker material unknowingly being used as revetment bunds, whereas the latter could result in higher costs for more expensive ground improvement techniques for clayey soils. Therefore, a true “Soft Clay” can be referred to as the *True Positive*, while a false “Good Earth” can be treated as the *False Negative*. Precision (Eq. 1) and recall (Eq. 2) are calculated as follows:

$$\text{Precision} = \frac{\text{True Positive}}{\text{True Positive} + \text{False Positive}} \quad (1)$$

$$\text{Recall} = \frac{\text{True Positive}}{\text{True Positive} + \text{False Negative}} \quad (2)$$

Using the result from all 40 samples, the precision is calculated to be $25/28 = 0.89$ while the recall is calculated to be $25/29 = 0.86$. With both values, the F1 score is calculated as 0.87 using Eq. 3:

$$F1 = 2 \times \frac{\text{Precision} \times \text{Recall}}{\text{Precision} + \text{Recall}} \quad (3)$$

CONCLUSIONS

The final ANN model (with 1 hidden layer) is able to achieve a relatively high overall accuracy of 82.5% in classifying soils into two groups (“Good Earth” and “Soft Clay”) according to Percentage of Fines, using two textural features of CON and COR as input parameters. It has also achieved a decent recall value of 0.86. In cases where a high cost is associated with *False Negative* (false “Good Earth”), recall may be a model metric to be used in comparing

models. The model is also able to “correctly” classify some soils samples that were previously misclassified based solely on borehole log data and visual inspection.

This study concluded that using GLCM pixel values produces better results than using pure RGB values in terms of ANN modelling. Furthermore, results from this study seems to confirm the findings by Hall-Beyer [11], i.e. the texture features of CON and COR combination performs better than using all five texture features.

However, several limitations include the low number of samples available during the period of study as well as only a single type of illuminance. Further studies will include the direct extension of current work by collecting more samples for training and testing, and the introduction of different illumination conditions to confirm the possibility of errors due to variation in illuminance. Parallel repositioning of the camera and light source with the soil surface will also be considered in future studies. Further parametric studies can be performed on the ANN model to identify the most suitable initial values when the soil database is expanded.

The concept of relating image texture properties to soil properties using artificial neural networks was found to be feasible and useful in developing a rapid classification method that is more accurate than existing methods. Moreover, it is automatable and able to complete the entire classification process on-site within a minute. This method would in turn allow for maximal recovery, recycling, and appropriate use and treatment of excavated materials for land reclamation. The use of computer vision meant that this quality control measure is rapid, non-intrusive, and automatable; it affords rapid classification without imposing additional human labor and cycle time for the staging grounds.

ACKNOWLEDGMENTS

The research was made possible with the support of the Housing & Development Board (HDB),

Singapore, through the project fund granted to the National University of Singapore (NUS) for the HDB-NUS Joint Study Agreement on the Reuse of Excavated Material for Land Reclamation Works.

REFERENCES

- [1] R. M. Haralick and L. G. Shapiro, *Computer and Robot Vision*, 1st ed., Boston: Addison-Wesley Longman Publishing Co., Inc. , 1992.
- [2] S.-O. Chung, K.-H. Cho, J.-W. Cho, K.-Y. Jung and T. Yamakawa, "Soil texture classification algorithm using RGB characteristics of soil images," *Faculty of Agriculture, Kyushu University*, vol. 57, no. 2, pp. 393-397, 2012.
- [3] R. W. Connors and C. A. Harlow, "A theoretical comparison of texture algorithms," *IEEE Transactions on Pattern Analysis and Machine Intelligence*, Vols. PAMI-2, no. 3, pp. 204-222, 1980.
- [4] ImageJ, "Contributors," 2019. [Online]. Available: <https://imagej.net/Contributors>.
- [5] NeuralWare, *NeuralWorks Professional II/PLUS*, 2013.
- [6] NeuralWare, "NeuralWorks Professional II/PLUS: Getting Started (A Tutorial for Microsoft Windows Computers)," NeuralWare, Carnegie, 2001.
- [7] British Standards Institution, *British soil classification system for engineering purposes*, 1981.
- [8] A. L. Ayodele, F. F. A and M. O. Ogendengbe, "Effect of fines content on some engineering properties of lateritic soil in Ile-Ife," *Journal of Engineering Research* , vol. 9, no. 32, 2009.
- [9] M. Hall-Beyer, "The GLCM Tutorial," 2007. [Online]. Available: <http://www.fp.ucalgary.ca/mhallbey/>. [Accessed 3 March 2016].

UTILISATION OF RECYCLED MATERIALS IN STABILISATION OF EXPANSIVE SOILS: A REVIEW

Jiasheng Zhu¹, Mohammad Saberian¹, Haiyun Luo¹, Junkai Gong¹, Manlin Liu¹, Gang Ren¹ and Jie Li¹

¹ School of Engineering, RMIT University, Melbourne, Victoria, Australia

ABSTRACT

The large and continuous consumption of natural aggregates is firmly against economic and environmental sustainability due to the high exploiting costs and transportation costs. On the other hand, due to the growing amount of waste materials and the running out of landfills, the disposal of waste materials has become another global issue. In recent years, the construction industry in the world has entered a stage of rapid development. The occupation of natural resources by concrete as the largest human-made material and the negative impact on the environment has also triggered discussions on sustainable development. The amount of waste concrete demolished in the world every year, waste concrete generated by new construction and waste concrete discharged by concrete factories and prefabricated component plants, is huge. In addition, the generation of byproducts and commercial and industrial waste materials is a global concern. Therefore, industries and researchers have recently focused on the applications of recycled waste materials in construction and civil engineering. This paper provides a review on the utilisation of recycled materials for the improvement of expansive soils for geotechnical applications.

Keywords: Expansive soils; Construction and demolition materials; Commercial and industrial waste; Soil improvement; Sustainability.

INTRODUCTION

Expansive soil refers to the clay soil that exhibits considerable volume changes when the suction or moisture content of the soil changes. Specifically, the volume change is manifested by expansion under humidity and shrinkage under drought [1]. The failure of lightly loaded structures due to the movement of the expansive soil has been reported around the world. The problem is particularly acute in Australia, where about 20% of the land is covered by expansive soil. Most of Australia's capital cities and regional centres have issues related to expansive soil [2], [3].

High concentrations of expansive soils have been identified in Victoria, particularly in the northern and western regions of Melbourne [2]. The swelling clay soil is the clay with the latter type of expansibility. The swelling of clay can be classified into two different types, one is the elastic rebound of the compressed soil because of the decreasing in compressive force, and another one is the expansion or contraction of soil caused by water content change. The most important element to reveal the swelling characteristics of soil is clay minerals [4].

The major minerals of clay in the reactive soil are montmorillonite, kaolinite, as well as illite [5]. Montmorillonite has the maximum amount of expansive potential [4]. The distinctive characteristic of expansive clay is its low strength and cohesion when the soil is wet. Nevertheless, when the soil is short of water, it becomes very stiff. One of the

biggest issues with swelling clay is consolidation settlement under long-term load, and another issue is the considerable volume change of expansive soil depending on the moisture content, which is related to climatic conditions. Expansive soil would shrink dramatically under dry conditions, and expands significantly with the increase of humidity [5], [6]. The basic mechanism of swelling for clay soil is primarily relative to the amount and type of pore spaces and their interaction with water. As a result, the swelling may occur within the early five to eight years after the completion of the construction, which causes the deformation and cracking of the structure and reduces the bearing capacity and service life of the structure [7].

Nowadays, one of the major global environmental problems is the disposal of waste materials, including construction and demolition (C&D) wastes and commercial and industrial waste materials. C&D wastes comprise primarily of solid waste (such as asphalt, concrete, bricks, and plasterboard), metals (such as aluminium and steel), organics (such as timber), glass and other materials [8]. The worldwide generation of solid waste has recently exceeded 17 billion tonnes per annum and is projected to hit 27 trillion tonnes by 2050 [9]. For instance, around 9 million tonnes of C&D wastes are produced in Australia annually that comprise 30.5% of overall wastes generated in Australia [10].

In helping to alleviate this problem, it should be considered necessary to recycle and reuse C&D wastes. Fortunately, solid recycled waste materials

can be used in a wide variety of civil and construction projects such as road pavement, foundations, and backfilling of underground service pipelines [11]. Using waste materials in road pavement and other construction projects can remarkably reduce the consumption of natural materials in quarries, reduce the disposal of landfills, and reduce greenhouse gas emissions. Thus, recycling and reusing waste materials in civil engineering applications, rather than using natural resources, would significantly reduce the carbon footprint of the projects, meanwhile improving the defects of expansive soil [12].

This study aims to review the implications of different recycled waste materials for the improvement of unsuitable expansive clays and explore the influences of the waste materials on the geotechnical properties and mechanical behavior of expansive soils.

ADOPTION OF RECYCLED CONCRETE AGGREGATES FOR STABILISATION OF EXPANSIVE SOIL

With the rapid urban development and population growth, recently, the production and disposal of C&D waste have become another environmental issue worldwide [13]. Consequentially, both the natural resource consumption and landfilling spaces are facing considerable challenges. As a substitution of natural aggregates, recycled concrete aggregates (RCA) has been studied and used as a choice for the reuse of C&D wastes in road infrastructure.

Early studies show that the reuse of C&D waste in civil projects could be applied against the high cost of natural aggregates and significantly reduce the CO₂ emission by 65% [14]. It was observed that the addition of RCA could improve the mechanical properties of expansive soil. The shear capacity of the clay incorporating RCA was significantly improved [15]. According to the studies of [16], the inclusion of RCA to clay resulted in increasing the unconfined compressive strength and shear strength properties, as shown in Table 1. It was observed that the clay soil improved by 15% RCA was strong enough to be adopted in pavement applications. [17] reported that the inclusion of RCA to clay leads to decreasing the energy absorption capacity and swelling of the clay.

However, in order to minimise the negative effects due to the nature of RCA, further studies and tests are to be conducted including the appropriate percentage of RCA content, aggregate size, and performance with multiple materials.

Table 1 Effects of RCA on the strength properties of clay [16].

RCA (%)	Cohesion (kPa)	Friction angle (degree)	UCS (kPa)
0	21.4	27.5	171
5	23.4	29.2	205
10	24.7	34.4	258
15	34.6	36.9	275

USING WASTE GLASS FOR STABILISATION OF EXPANSIVE SOIL

The manufacturing of glass and the landfilling of waste glass has been considered as the main environmental issues in recent years. Over 300,000 tonnes of recovered glass were stocked in Victoria [18]. The two main products of glass reprocessing are cullet and glass fines. Cullet is a higher-grade product that used to produce new glass. However, the proportion of cullet used in glass manufacturing is limited because of the introduction of impurities. Glass fines are a lower grade product, mainly used for civil construction, road construction, concrete aggregate, building, and road aggregate [19]. The waste glass is generally accepted as recycled material for civil construction because the silica content of the glass is high, and the use of glass does not hurt the environment and human health [20].

[21]-[23] pointed out that the properties of clay soil obtained an improvement after the addition of glass powder or fibre. This improvement was embodied in the increasing of California Bearing Ratio values, shear strength, and internal friction angle as well as the reduction in optimum water content and plasticity of the stabilised soil. [24] studied the effects of different proportions (2%, 4%, 6% and 8%) of the broken glass on the properties of expansive soil. The laboratory results showed that the mixing of 4% crushed glass with expansive soil could effectively improve the geotechnical properties of the soil. With the increase of the amount of crushed glass, the liquid limit and specific gravity of the composite specimen decreased, and the plastic limit increased, due to the addition of broken glass which is a granular material [24].

It was also observed that the bearing capacity and shear strength improved by adding crushed glass in the soil [24]. [25] investigated the feasibility of stabilising clay soil by the addition of crushed glass waste. The result showed that when the content of glass increased, the values of optimum moisture content and cohesion of soil decreased, and maximum dry density, California bearing ratio, and friction angle increased.

[26] pointed out that with the addition of soda-lime glass dust, with a size of less than 300 µm, both

maximum dry density and plastic limit of clayey soil increased, and both values of the compressive strength and swell index reduced. [27] evaluated the effects of waste soda-lime glass powder, with the size of less than 75 μm , on the geotechnical properties of expansive clay. It was concluded that soda-lime glass powder could improve the geotechnical properties of reactive clay soil as the swelling of the soil decreased significantly when the percentage of glass powder increased. Experimental results illustrated that soda-lime glass powder had positive effects on the optimum moisture content, maximum dry density, and Plasticity Index of the expansive clay. Also, California bearing ratio and unconfined compressive strength increased with the addition of glass powder [27] (Fig. 1).

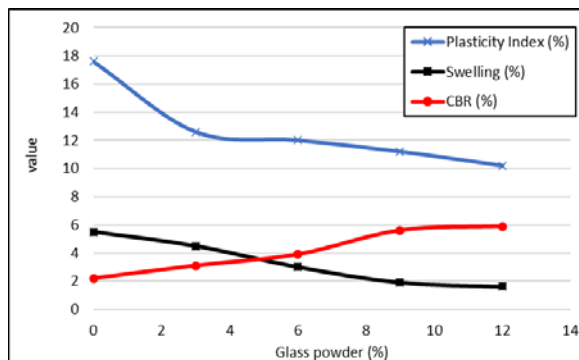


Fig. 1 Effects of soda-lime glass powder on the geotechnical properties of clay [27].

USING STEEL SLAG TO STABILISE EXPANSIVE SOILS

Steel slag is an accessory product of the manufacture steel due to the reaction between the impurities (CO_2 , SiO_2 , P, Mn etc.) and lime [28]. A large amount of steel slag from boulder form to dust form is generated accompanied by the enormous need of steel annually around the world. Meanwhile, a large proportion of the steel slag is still treated by landfills or dumpsites, which causes hazardous impacts to the environment due to its metallic ingredients [29], [30]. Nowadays, steel slag has been used to enhance the mechanical performance of expansive soils [31]. Generally, the major factor of the stabilisation function is achieved by the cation exchanges between the steel slag and expansive soil.

It was shown that a comprehensive improvement in the strength is achieved by adding steel slag into expansive soil. Specifically, when adding 8% of steel slag into the soil, it significantly increased the California bearing ratio of the clay by 40% [32]. It is also found that both liquid limit and plasticity index of expansive soil dropped dramatically by 33% and 75%, respectively with the addition of 30% steel slag, which indicates that steel slag is acceptable as a stabiliser or modifier of expansive soil [33]. Most significantly, an improvement of 50% in unconfined

compressive strength was obtained with the inclusion of 50% steel slag in the clay soil sample. However, due to the presents of free periclase and lime, it is found that steel slag has an issue of volume expansion in subgrade applications under humidity, and the physical shape of steel slag will also lead to a high void space which threatens the long-term stabilisation of soil [33].

USING FLY ASH FOR THE STABILISATION OF EXPANSIVE SOIL

Fly ash is a byproduct of coal-burning, which is collected by electrostatic precipitators in thermal power plants [4]. The essential components of fly ash are silicon dioxide (SiO_2), calcium oxide (CaO), and aluminium oxide (Al_2O_3), and its particles are spherical in size, which make it easy to mix with soil [34].

[35] reported the pH values of fly ash range from 1.2 to 12.5, and most of the fly ashes tend to be alkaline. Fly ash can be divided into three categories: acidic ash, mildly alkaline ash with pH 8–9, strongly alkaline ash with pH 11–13 [36]. The three most common types of fly ash are Class C, Class F, and Class N fly ashes. Class F fly ash can be produced by burning bituminous coal and anthracite [37]. Class C fly ash is produced by burning sub-bituminous coal and burning lignite [37]. Class F fly ash is less pozzolanic than Class C fly ash due to a lower CaO content. [37] pointed out that Class C fly does not need additional additives for the pozzolanic reaction because it is self-cementitious; however, Class F fly ash needs cement or lime for pozzolanic reaction due to it has a low content of calcium oxide [37].

[38] Studied the effectiveness of using fly ash as a stabiliser in expansive soil. The results showed that the plastic limit and maximum dry unit weight of the soil increased from 31% to 44% and from 13.91 kN/m^3 to 14.3 kN/m^3 , respectively when the fly ash content increased from 5% to 20%. The swell potential and swelling pressure decreased with the addition of fly ash to the clay [38] (Fig 2). [39] studied the effect of Class C fly ash on engineering properties of expansive soil. It was pointed out that adding fly ash to the soil led to reducing the swell potential of highly plastic clays. Also, it was shown that adding fly ash helped to reduce the amount of clay size particle, plasticity index, and the swell potential.

[40] evaluated the compaction and unconfined compressive strength of stabilised black cotton soil by using fine and coarse fly ash mixtures. The research found out that adding both sizes of fly ash could improve the strength of the soil. Also, the peak

strength of the fine ash mixture was 25% higher than the coarse fly ash mixtures. [41] studied the behavior of expansive soils stabilised with fly ash and fly ash-lime blends. The results showed that when by increasing the amount of fly ash and lime-fly ash contents, the optimum water content and the maximum dry unit weight decreased, and swell potential and shrinkage of the soil reduced. Furthermore, it was concluded that the inclusion of 9–12% fly ash to the soil is the optimum content for stabilisation of the expansive soil. Addition of fly ash to expansive soil not only effectively reduced the hydraulic conductivity, swell pressure, plasticity index and swell potential, but also increased the shear strength, permeability and dry unit weight [34].

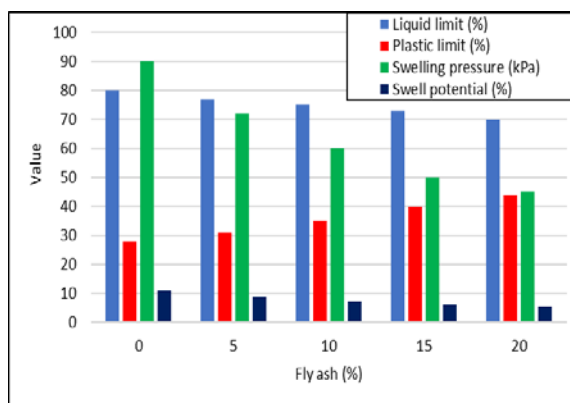


Fig. 2 Effects of fly ash on the geotechnical properties of expansive clay [38].

INCLUSION OF RUBBER TO EXPANSIVE SOIL

In Australia, the production of the waste tire is more than 500,000 tons annually, and the treatment and recycling of scrap tires have caused considerable environmental issues since most of the scrap tires are treated by landfilling and are barely degraded in a short time [42]. Meanwhile, accompanying with the continuous consumption of natural material, the crumb rubber has been used for road construction as a substitution of natural materials for pollution reduction and cost reduction [43], [44].

Specifically, investigations on crumb rubber revealed that it could provide low shrinkage but better impact resistance, water resistance, acid resistance, and freezing & thawing resistance, which explains that the crumb rubber is functional as a stabiliser for expansive soils.

It was observed that the inclusion of rubber to expansive clay leads to increasing the UCS and reduction in the swell-shrinkage capacity [45] (Fig 3). [46] reported that the addition of rubber to clay improved the ductility of the soil but decreased the CBR. Also, [47] concluded that rubber could provide higher frictional resistance and better mechanical interlocking to the clay. To conclude,

crumb rubber can provide suitable mechanical and geotechnical properties to clay soils. Nonetheless, most studies only focus on the performance of one or few specific percentages of crumb rubber, but in order to make the best use of rubber, the specific best rubber content and size are needed to be further explored in practical as the specification when using rubber-based applications.

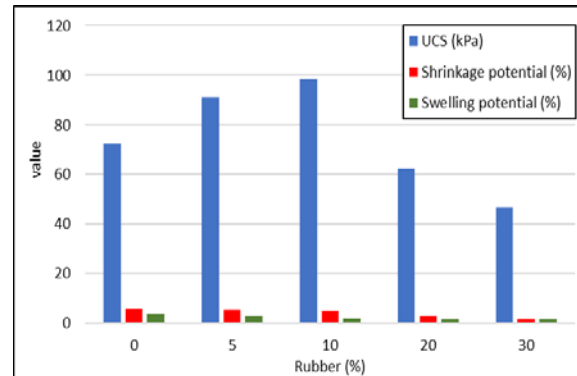


Fig. 3 Effects of rubber on the geotechnical properties of reactive clay [45].

CONCLUSIONS

The current paper aimed to provide a review on the possible applications of waste materials, including construction and demolition wastes and commercial and industrial wastes and their effectiveness for the stabilisation of unsuitable expansive clay soils. In this paper, the effects of RCA, glass, steel slag, fly ash, and rubber on the mechanical properties of expansive clay soils were reviewed. It can be concluded that the adoption of waste materials can provide promising results not only for the stabilisation of clay soils, but also in terms of the reduction of the negative environmental impacts of the waste materials. Therefore, by the inclusion of waste materials in expansive clay soils, the geotechnical properties can be improved, the negative environmental impacts related to the generation of waste materials would be reduced, and the environmental footprints of construction projects would be minimised.

REFERENCES

- [1] Li J. and Cameron D., A Case Study of a Courtyard House Damaged by Expansive Soils. *Journal of Performance of Constructed Facilities*. Journal of Performance of Constructed Facilities, ASCE, Vol. 16, Issue 6, 2002, pp. 169-175.
- [2] Li J., Cameron D.A. and Ren G., Case Study and Back Analysis of a Residential Building Damaged by Expansive Soils. *Computers and Geotechnics*, Vol 56, 2014, pp. 89-99.

- [3] Li J., Zou J., Bayetto P. and Barker N., Shrink-Swell Index Database for Melbourne. Australian Geomechanics Journal, Vol. 51, Issue 3, 2016, pp. 61-76.
- [4] Bhuvaneshwari S., Robinson R.G. and Gandhi S.R., Stabilization of Expansive Soils Using Fly Ash. Fly Ash India, Vol. 8, 2005, pp. VIII 5.1-VIII 5.10.
- [5] Xu Y., Jamhiri B. and Memon S. A., On the Recent Trends in Expansive Soil Stabilization Using Calcium-Based Stabilizer Materials (CSMs): A Comprehensive Review. Advances in Materials Science and Engineering, Vol. 2020, 2020, pp. 1-23.
- [6] Jahandari S., Saberian M., Tao T., Faridfazel Mojtahedi F., Li J., Ghasemi M., Rezvani S. and Li W., Effects of Saturation Degrees, Freezing-Thawing, and Curing on Geotechnical Properties of Lime and Lime-Cement Concretes. Cold Regions Science and Technology, Vol. 160, 2019, pp. 242-251.
- [7] Jahandari S., Toufigh M., Li J. and Saberian M., Laboratory Study of the Effect of Degrees of Saturation on Lime Concrete Resistance due to the Groundwater Level Increment. Geotechnical and Geological Engineering, Vol. 36, 2018, pp. 413-424.
- [8] Kabirifar K., Mojtahedi M., Wang C. and Tam V.W.Y., Construction and Demolition Waste Management Contributing Factors Coupled with Reduce, Reuse, and Recycle Strategies for Effective Waste Management: A review. Journal of Cleaner Production, Vol. 263, 2020, pp. 121265.
- [9] Tang Z., Li W., Tam V.W.Y. and Xue C., Advanced Progress in Recycling Municipal and Construction Solid Wastes for Manufacturing Sustainable Construction Materials. Resources, Conservation & Recycling: X, Vol. 6, 2020, pp. 100036.
- [10] Saberian M. and Li, J., Investigation of the Mechanical Properties and Carbonation of Construction and Demolition Materials Together with Rubber. Journal of Cleaner Production, Vol. 202, 2018, 553-560.
- [11] Saberian M., Li J., Nguyen B.T. and Setunge S., Estimating the Resilient Modulus of Crushed Recycled Pavement Materials Containing Crumb Rubber Using the Clegg Impact Value. Resources, Conservation and Recycling, Vol. 141, 2019, pp. 301-307.
- [12] Saberian M., Shi L., Sidiq A., Li J., Setunge S. and Li C.-Q., Recycled Concrete Aggregate Mixed with Crumb Rubber Under Elevated Temperature. Construction and Building Materials, Vol. 222, 2019, pp. 119-129.
- [13] Saberian M., Li J., Nguyen B. and Wang G., Permanent Deformation Behaviour of Pavement Base and Subbase Containing Recycled Concrete Aggregate, Coarse and Fine Crumb Rubber. Construction and Building Materials, Vol. 178, 2018, pp. 51-58.
- [14] Saberian M. and Li J., Long-Term Permanent Deformation Behaviour of Recycled Concrete Aggregate with Addition of Crumb Rubber in Base and Sub-Base Applications. Soil Dynamics and Earthquake Engineering, Vol. 2019, 121, 436-441.
- [15] Sivakumar V., Mckinley J.D. and Ferguson D., Reuse of Construction Waste: Performance Under Repeated Loading. Proceedings of the Institution of Civil Engineers-Geotechnical Engineering, Vol. 157, Issue 2, 2004, pp. 91-96.
- [16] Kianimehr M., Shourijeh P.T., Binesh S.M., Mohammadinia A. and Arulrajah A., Utilization of Recycled Concrete Aggregates for Light-Stabilization of Clay Soils. Construction and Building Materials, Vol. 227, 2019, pp. 116792.
- [17] Cabalar A.F., Zardikawi O.a.A. and Abdulnafoo M.D., Utilisation of Construction and Demolition Materials with Clay for Road Pavement Subgrade. Road Materials and Pavement Design, Vol. 20, Issue 3, 2019, pp. 702-714.
- [18] Saberian M., Li J. and Setunge S., Evaluation of Permanent Deformation of a New Pavement Base and Subbase Containing Unbound Granular Materials, Crumb Rubber and Crushed Glass. Journal of Cleaner Production, Vol. 230, 2019, pp. 38-45.
- [19] Sustainability Victoria, A Business Case for Councils to Use Local Recycled Products in Pavement Construction, Recycled products in Pavement Construction. Sustainability Victoria, pp.1-8.
- [20] Saberian Boroujeni M., Li J. and Cameron D., Effect of Crushed Glass on Behavior of Crushed Recycled Pavement Materials Together with Crumb Rubber for Making a Clean Green Base and Subbase. Journal of Materials in Civil Engineering, Vol. 31, Issue 7, 2019, pp. 1-7.
- [21] Nirmala R. and Shanmugapriya M., Feasibility Study on Enhancing the Properties of Subgrade Material using Waste Glass. International Journal of Chemical Sciences. Vol. 15, Issue 1, 2017, pp. 106.
- [22] Mishra U., Enhancement in Subgrade soil Strength Using Glass Powder as Discrete Fiber: A Review. International Research Journal of Engineering and Technology (IRJET), Vol. 4, Issue 4, 2017, pp. 2395-0056.
- [23] Marcus A., Sakeer F., Tp S., George S.J. and George S., A Comparative Study on the Effects of Different Waste Materials on Weak Soil for Better Pavement Subgrade. International Research Journal of Engineering and Technology (IRJET), Vol. 4, 2017, pp. 2129-2132.
- [24] Al-Neami, M. A., Alsoudany, K., Dawod, A., & Ehsan, E. Q., Remediation of Cohesive Soils

- Using Waste Glass. In International Conference of Technology and Science, Catholic Academic-Freiburg–Germany, 2015, pp. 125-137.
- [25] Fauzi A., Djahuri Z. and Fauzi U.J., Soil Engineering Properties Improvement by Utilization of cut Waste Plastic and Crushed Waste Glass as Additive. *International Journal of Engineering and Technology*, Vol. 8, Issue 1, 2016, pp. 15.
- [26] Nuruzzaman M. and Hossain M., Effect of Soda Lime Glass Dust on the Properties of Clayey Soil. *Global Journal of Researches in Engineering*, Vol. 14, 2014, pp. 19-14.
- [27] Canakci H., Aram A.L. and Celik F., Stabilization of Clay with Waste Soda Lime Glass Powder. *Procedia engineering*, Vol. 161, 2016, pp. 600-605.
- [28] Barišić I., Netinger Grubeša I. and Hackenberger Kutuzović B., Multidisciplinary Approach to the Environmental Impact of Steel Slag Reused in Road Construction. *Road Materials and Pavement Design*, Vol. 18, Issue 4, 2017, pp. 897-912.
- [29] Shalabi, F., Asi, I., & Qasrawi, H., Use of Steel Slag to Improve the Engineering Properties of Base-Coarse Material. In *Proceedings of the International Engineering Conference on Hot Arid Regions*, 2010, pp. 16-20.
- [30] Qasrawi H., The Use of Steel Slag Aggregate to Enhance the Mechanical Properties of Recycled Aggregate Concrete and Retain the Environment. *Construction and Building Materials*, Vol. 54, 2014, pp. 298-304.
- [31] Gu X., Yu B., Dong Q. and Deng Y., Application of Secondary Steel Slag in Subgrade: Performance Evaluation and Enhancement. *Journal of Cleaner Production*, Vol. 181, 2018, pp. 102-108.
- [32] Akinwumi I., Soil Modification by the Application of Steel Slag. *Periodica Polytechnica Civil Engineering*, Vol. 58, Issue 4, 2014, pp. 371-377.
- [33] Zumrawi M.M.E. and Babikir A.a.-a.A., Laboratory Study of Steel Slag Used for Stabilizing Expansive Soil. *Asian Engineering Review*, Vol. 4, Issue 1, 2017, pp. 1-6.
- [34] Taher, Z., Effectiveness of Polymer for Mitigation of Expansive Soils, *Doctoral Dissertation*, Colorado State University, 2017, pp. 7-44.
- [35] Kolbe, J. L., Lee, L. S., Jafvert, C. T. and Murarka, I. P., Use of Alkaline Coal Ash for Reclamation of a Former Strip Mine. In *World of Coal Ash (WOCA) Conference*, USA, pp. 1-15.
- [36] Yao Z.T., Ji X.S., Sarker P.K., Tang J.H., Ge L.Q., Xia M.S. and Xi Y.Q., A Comprehensive Review on the Applications of Coal Fly Ash. *Earth-Science Reviews*, Vol. 141, 2015, pp. 105-121.
- [37] ASTM C618-19, Standard Specification for Coal Fly Ash and Raw or Calcined Natural Pozzolan For Use In Concrete, *Astm.org*. Available at: <<https://www.astm.org/Standards/C618.htm>>.
- [38] Phani Kumar B.R. and Sharma R.S., Effect of Fly Ash on Engineering Properties of Expansive Soils. *Journal of Geotechnical and Geoenvironmental Engineering*, Vol. 130, Issue 7, 2004, pp. 764-767.
- [39] Nalbantoğlu Z., Effectiveness of Class C Fly Ash as an Expansive Soil Stabilizer. *Construction and Building Materials*, Vol. 18, Issue 6, 2004, pp. 377-381.
- [40] Takhelmayum G., Savitha A.L. and Krishna G., Laboratory Study on Soil Stabilization Using Fly Ash Mixtures. *International Journal of Engineering Science and Innovative Technology (IJESIT)*, Vol. 2, Issue 1, 2013, pp. 477-482.
- [41] Zha F., Liu S., Du Y. and Cui K., Behavior of Expansive Soils Stabilized with Fly Ash. *Natural hazards*, Vol. 47, Issue 3, 2008, pp. 509-523.
- [42] Saberian M., Li J., Boroujeni M., Law D. and Li C.-Q., Application of Demolition Wastes Mixed with Crushed Glass and Crumb Rubber in Pavement Base/Subbase. *Resources, Conservation and Recycling*, Vol. 156, 2020, pp. 104722.
- [43] Saberian M., Li J., Nguyen B.T. and Boroujeni M., Experimental and Analytical Study of Dynamic Properties of UGM Materials Containing Waste Rubber. *Soil Dynamics and Earthquake Engineering*, Vol. 130, 2020, pp. 105978.
- [44] Siddique R. and Naik T.R., Properties of Concrete Containing Scrap-Tire Rubber—an Overview. *Waste Manage (Oxford)*, Vol. 24, Issue 6, 2004, pp. 563-569.
- [45] Soltani A., Deng A., Taheri A. and O'Kelly B.C., Engineering Reactive Clay Systems by Ground Rubber Replacement and Polyacrylamide Treatment. *Polymers*, Vol. 11, Issue 10, 2019, pp. 1675.
- [46] Yadav J.S. and Tiwari S.K., Evaluation of the Strength Characteristics of Cement-Stabilized Clay–Crumb Rubber Mixtures for its Sustainable Use in Geotechnical Applications. *Environment, development and sustainability*, Vol. 20, Issue 5, 2018, pp. 1961-1985.
- [47] Soltani A., Deng A., Taheri A., Mirzababaei M. and Nikraz H., Interfacial Shear Strength of Rubber-Reinforced Clays: A Dimensional Analysis Perspective. *Geosynthetics International*, Vol. 26, Issue 2, 2019, pp. 164-183.

OPTIMUM UTILIZATION OF RICE HUSK ASH WASTE FOR GROUND IMPROVEMENT

Najmun Nahar^{1,2}, Zakaria Hossain¹ and Noma Tamaki³

¹Graduate School of Bioresources, Mie University, Japan, ²Life and Earth Science, Jagannath University, Bangladesh, ³Make Integrated Technology Company, Osaka, Japan

ABSTRACT

The disposal of the abundance of rice husk ash in rice-producing countries is creating problems in environmental contamination and health hazard. The usage of rice husk ash waste mixed with cement in the soil is considered as one of the possible ground improvement techniques that are environmentally viable. The soil sample of this study is classified as A-2-4 or SW-SM. In this study, five mix types of rice husk ash waste and cement in the soil are investigated for its effect on maximum dry density (MDD), optimum moisture content (OMC), bearing capacity, and permeability through the Standard proctor compaction test, California Bearing Ratio (CBR) test, and constant head permeability test. The test results illustrate that the soil with rice husk ash and cement improves the engineering properties of the soil. It is concluded that the soil-rice husk ash-cement combination can be used for ground improvement.

Keywords: Soil texture; Optimum moisture content; California bearing ratio; Permeability coefficient; Ground improvement

INTRODUCTION

Rice husk is an agricultural by-product of rice and produced from paddy during the milling process [1], which is plentifully available in many rice-producing countries [2]. Rice Husk Ash (RHA) is formed when rice husk is burnt under controlled temperature [3]. Every year about 20 million tons of RHA are produced throughout the world [4]. Due to lack of its utilization, the massive amount of RHA is discarded at open places, riversides, and abandoned areas, which causes environmental pollution [5] and also poses a health hazard due to local air pollution. However, RHA is a pozzolanic material, and it contains around 85–90% amorphous silica, which is reactive as a pozzolan to replace part of Portland cement [6-7]. It can potentially use as a construction material for various geotechnical applications such as industrial, commercial, housing projects, and infrastructure construction for dams, tunnels, ports, roadways, etc.

On the other hand, the production of cement, a key binding component of concrete, is costly, consumes high energy, depletes natural resources, and emits enormous amounts of greenhouse gases [8] that also causes environmental degradation, severe pollution [9-11], and even health hazards. So, if most of the RHA were to be used in ground improvement, it would not only get rid of dumping RHA but would also have decreased the CO₂ emissions to the atmosphere by bringing down the cement production. As a pozzolanic material, usage of rice husk ash in cement/concrete that brings about some advantages, like improving strength, enhancing durability, or decreasing carbon dioxide emissions, etc. [12]. RHA

is not a new material for soil improvement. The application of RHA in soil has shown dramatic success in many types of soils around the world. Moreover, the researches on the utilization of RHA and OPC at a nominal dosage in soil samples were very limited. Therefore, the present study attempts to assess the role of RHA as ground improvement and to investigate the optimum percentage combination of soil-cement-RHA.

MATERIALS AND LABORATORY TEST

Materials Used

In this study, testing specimen were comprised of soil, RHA, and cement. The soil sample was collected from the Handa area, Tsu City, Mie Prefecture, Japan.

Table 1 Physical properties of soil

Parameters	Values
Specific gravity (ρ_s)	2.74 g/cm ³
Maximum dry density ($\gamma_{dry\ max}$)	1.696 g/cm ³
Optimum Water Content (W_{opt})	17.50%
Sand (75 μ m - 2 mm)	89%
Silt (5 - 75 μ m)	9%
Clay < 5 μ m	2%
Liquid limit, LL	37.52%
Plastic limit, PL	28.97%
Plasticity Index, PI	8.55%
AASHTO classification	A-2-4
ASTM D-2487 classification	SW-SM

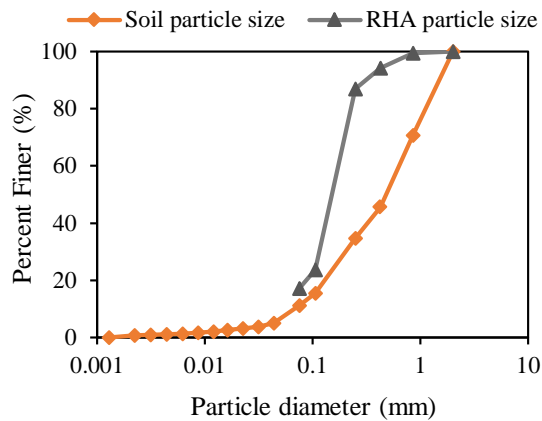


Fig. 1 Particle size distribution curve of soil and RHA

Table 2 Physical and chemical properties of RHA

Properties	Parameters	Values
<i>Physical properties</i>	Average Particle Size	0.1 to 0.3 μm
	Loss of Ignition	85%
	Specific Gravity	0.12 g/cm ³
	Burning Temperature	600°C
	Burning Time	24 hours
<i>Chemical properties</i>	Silica (SiO ₂)	91.10%
	Carbon dioxide (CO ₂)	4.35%
	Potassium Oxide (K ₂ O)	2.40%
	Calcium Oxide (CaO)	0.57%
	Phosphorous Penta Oxide (P ₂ O ₅)	0.52%
	Sulphur Tri Oxide (SO ₃)	0.38%
	Chlorine (Cl)	0.18%
	Magnesium Oxide (MgO)	0.16%
	Manganese Oxide (MnO)	0.14%
	Iron Oxide (Fe ₂ O ₃)	0.05%
	Alumina (Al ₂ O ₃)	0.03%
	Others	0.12%

The physical properties of soil were determined through a series of laboratory tests and presented in Table 1. From the graph of particle size distribution by sieve and hydrometer analysis of soil, the coefficient of gradation (C_u) and the coefficient of curvature (C_c) values are correspondingly 9.275 and 0.906, and from the Atterberg limit test, the plasticity index (PI) is 8.55%. According to the Unified Classification of Sandy soils by ASTM D-2487, the particular soil is well-graded sand with silt, and the symbol is SW-SM as the coefficient of gradation (C_u) of soil particles are greater than or equal to 6, and the coefficient of curvature (C_c) value is between 1 and 3

($C_u \geq 6$ and $1 \leq C_c \leq 3$) besides with plasticity index is greater than 7 ($PI > 7$). According to the American Association of State Highway and Transportation Officials (AASHTO) soil classification system, the particular soil is Silty gravel and sand (A-2-4), where percent passing no. 200 sieve $\leq 35\%$, $LL \leq 40$ and $PI \leq 10$ (Fig.1 and Table 1). Readymade RHA was collected from Make Integrated Technology (MIT) company, Osaka, Japan. The basic properties of RHA are given in Table 2, and the particle size distribution of RHA is shown with soil particle size in Fig.1. Ordinary Portland cement (Type I) was used in this study, which is very available in local markets and commonly used for construction purposes. The chemical properties of this type of cement can be found in other research [13]. The ordinary tap water in the laboratory was used in all of the specimens.

Mix Designs of Specimen

For the chemical stabilization of soil, it is essential to fix the proper mix design of specimens [14]. Some relevant studies have been conducted using different ratios of RHA with cement in soil. Soil with RHA 5%, 10%, 15%, 20% of and 6%, 8%, 10% of cement were used for clayey soil stabilization [15]; RHA 4%, 8%, 12% and only 2% cement of soil weight were considered for showing the effects of RHA on geotechnical properties of soil from paddy field [16]; some experiments were conducted with taking 0%, 5%, 10%, 15%, 20%, 25%, 30% of RHA and 0%, 2%, 4%, 6%, 8%, 10%, 12%, 14% cement in residual soil [17]. In this study, 5%, 10%, 15% of RHA addition with 2%, 4%, 6% cement of weight of SW-SM type soil were used as the mixing design of the samples, which is presented with index in Table 3.

Table 3 Investigated mixtures with indices

Mix design	Index
Soil (Control)	Control
Soil + 2% Cement + 5% RHA	S+2C+5R
Soil + 2% Cement + 10% RHA	S+2C+10R
Soil + 2% Cement + 15% RHA	S+2C+15R
Soil + 4% Cement + 5% RHA	S+4C+5R
Soil + 6% Cement + 5% RHA	S+6C+5R

Specimen Preparation

Soil-RHA-cement mixtures were mixed homogeneously in a big tray, and water was gentle to the dry mix. In the case of the California bearing ratio test and permeability test, the amount of water was mixed for each specimen below 2-3% from the optimum moisture content (OMC), which was calculated from the compaction test. Three specimens

were prepared and tested for each mix type. The specimens were designed for those tests considering the curing period for the same day (0 day) and seven days (7 days). In the case of the same day, specimens were tested after 30 minutes passed from the specimen preparation time. For seven days curing period, after setting the specimen into the mold, it was wrapped with a plastic bag for maintaining the moisture content of the specimens. The specimen was taken out from the plastic after seven days of curing, and then the tests were performed.

Laboratory Test

Compaction test

According to Japanese Industrial Standards (JIS-A-1210), the Standard Proctor compaction test was conducted to determine the optimum moisture content (OMC). Maximum dry density (MDD) of soil control and other mix types. The applied apparatus for performing the test was a 10 cm diameter cylindrical compaction mold equipped with a base and a collar, rammer mass of 2.5 kg, and a falling height of 30 cm (Fig. 2). In the compaction mold, the soil was compacted in three layers with 25 blows for each layer.

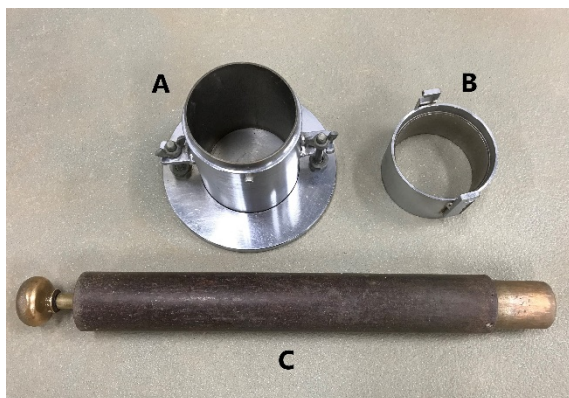


Fig.2 Standard Proctor compaction apparatus- A) Base with mold; B) Collar; and C) Rammer

In the compaction mold, the RHA mixed soil was compacted in three layers with 25 blows for each layer. For each mix type, Soil-RHA was manually mixed homogeneously in dry condition. Subsequently, different moisture contents were added homogeneously by manual mixing like the previous step for getting the expected moisture content.

California bearing ratio test

All California bearing ratio tests were carried out based on Japanese Industrial Standards (JIS-A-1211).



Fig. 3 CBR test apparatus- A) Automated rammer, and B) CBR machine

The CBR test specimens were prepared in steel molds with an internal diameter of 15 cm and a height of 17.5 cm. For each mix type, Soil-RHA-cement was mixed homogeneously, where water was used below 2-3% from the OMC of the soil weight. The specimens were compacted in the three layers under 67 blows for a per layer using an automatic rammer (Fig.3). The automatic rammer had a diameter of 5.0 cm, a mass of 4.5 kg, and a falling height of 45.0 cm. The CBR values obtained by CBR testing calculated from the following Eq. (1).

$$CBR \text{ Value (\%)} = \frac{\text{Load Strength}}{\text{Standard Load Strength}} \times 100 \quad (1)$$

Permeability Test

The permeability tests were conducted by the constant head permeability test method based on JIS 1218. The specimen for permeability tests were prepared in the steel mold, which is 10.0 cm in diameter and 6.2 cm in height. The specimens were compacted manually by using 2.5 kg rammer with a falling height of 30.0 cm. The permeability coefficients were calculated using the Eq. (2) where Q is the flow rate (cm^3); L is the height (cm); h is the Pressure (cm); A is the cross-sectional area (cm^2); t is the Time (s).

$$K (\text{permeability coefficient}) = QL / (hAt) \quad (2)$$

RESULT AND DISCUSSIONS

Compaction Characteristics

The variations of MDD and OMC with RHA and cement addition with soil are presented in Figs. 4 and 5. The figures illustrate that with increasing the amount of RHA and cement, OMC increases, but MDD decreases significantly. After mixing the RHA and cement with soil, the quantity of fines increases in the soil that needs more water for hydration, and

this trend also found in some researches [15-19]. The declining direction of dry soil density specifies that the low compaction energy requires achieving the MDD of a particular specimen that reduces the compaction cost [20, 21].

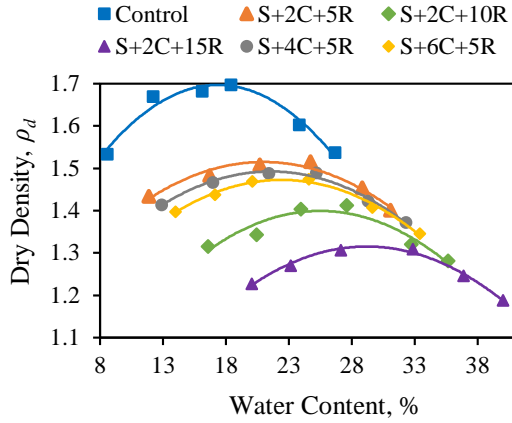


Fig. 4 Compaction curves of Control and soil-RHA-cement combination types

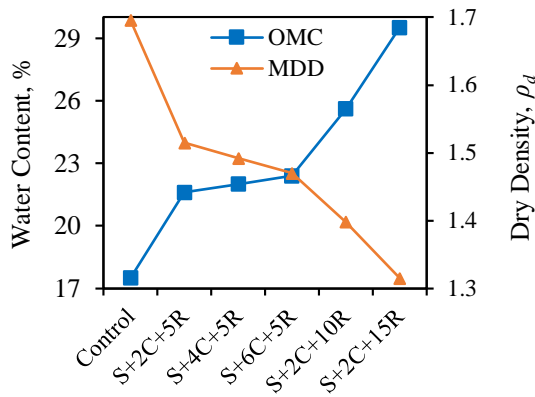


Fig. 5 Variation of OMC and MDD of Control and soil-RHA-cement combination types

3.1 Results of CBR tests

From Figs. 6 and 7, it can be noticed that all the load-penetration curves of the CBR control specimen and five different specimens of RHA and cement mixed soils follow a typical trend considering the curing period 0 and 7 days of CBR tests. Fig. 8 displays that the calculated CBR values for the penetration depth of 2.5 mm of the specimens are increased after seven days' exception of Control. The CBR value of the control specimen was obtained as 41.5%. The CBR value was decreased with increasing the amount of RHA, particularly for the specimens comprised of RHA 5%, 10%, 15%, and cement 2% in the soil considering both cases without and with the curing periods.

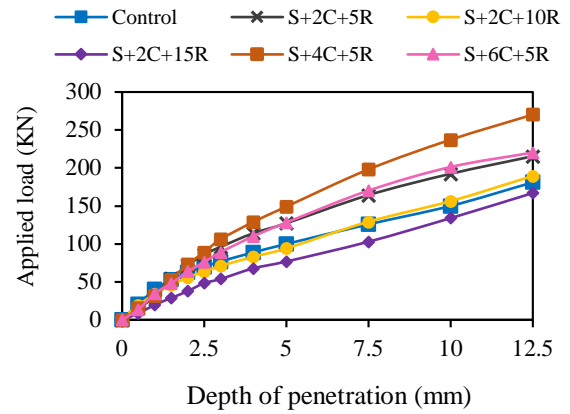


Fig. 6 Load penetration curve of Control and soil-RHA-cement combination types for 0 day

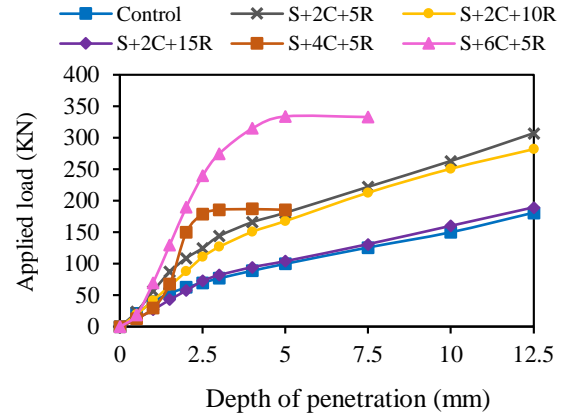


Fig. 7 Load penetration curve of Control and soil-RHA-cement combination types for 7 days

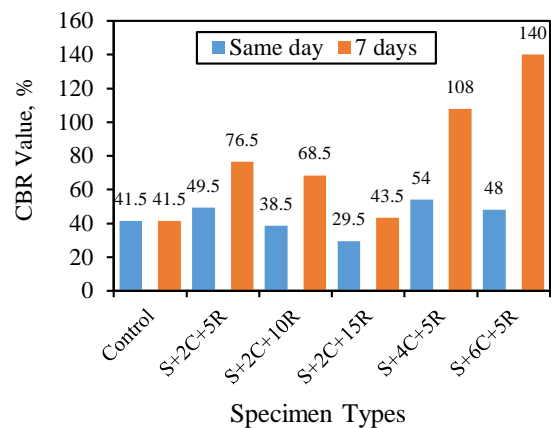


Fig. 8 Comparison among CBR values of Control and soil-RHA-cement types for 0 and 7 days

On the contrary, with increasing the amount of cement at 2%, 4%, 6%, with 5% RHA, the CBR values increased. The specimen of S+6C+5R reaches

the highest CBR value (140%) after seven days curing, and this value increases 92% from 0 days to 7 days in this research (Fig. 8).

Results of the permeability test

Figure 9 represents the test results on the permeability coefficient of soil-RHA-cement combination types for 0 and 7 days of the curing period. The permeability coefficient of all specimens increases with increasing the age of the specimens' exception of Control. The S+2C+15R specimen had the highest permeability coefficient for the same day test, and the S+2C+5R combination was achieved with the highest permeability co-efficient, and S+6C+5R was showed the second-highest permeability after seven days curing. The permeability coefficient increases with increasing the amount of cement content in the soil that is similar to other studies [14].

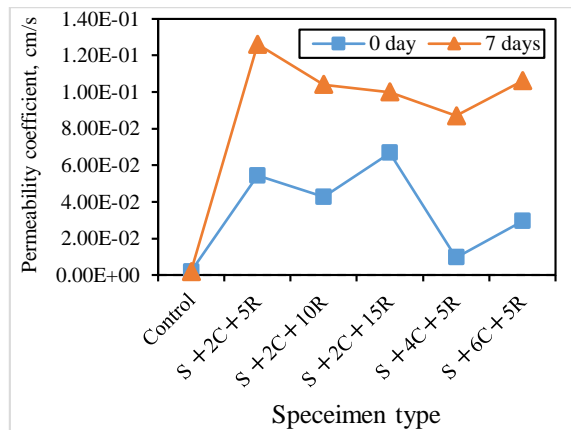


Fig. 9 Variation of permeability coefficient of Control and soil-RHA-cement types for 0 and 7 days

CONCLUSIONS

The following conclusions can be drawn based on the results obtained from the experiment on soil-RHA-Cement in the paper:

- The OMC increases with increasing the amount of RHA and cement in the soil, but MDD decreases.
- Considering the age of the specimen, the CBR values of all specimens increase after seven days. The maximum CBR value was found for S+6C+5R combination after curing, and this value increases 92% from 0 days to 7 days.
- The permeability coefficient also increases with time for all specimens. S+2C+15R specimen had the highest permeability coefficient for the same day test, and S+2C+5R was showed the highest permeability co-efficient after seven days

curing and the S+6C+5R combination exhibited the second highest permeability.

- RHA can potentially improve the soil with cement and can replace the amount of cement that reduces the construction cost, particularly for rice-producing developing countries.

ACKNOWLEDGMENT

We would also like to thank Ms. Toshichita Maime for her assistance during the research at Mie University.

REFERENCES

- [1] Singh, B., Rice husk ash. In Waste and Supplementary Cementitious Materials in Concrete, 2018, pp. 417-460
- [2] Chandrasekhar, S. A. T. H. Y., Satyanarayana, K. G., Pramada, P. N., Raghavan, P., and Gupta, T. N., Review processing, properties and applications of reactive silica from rice husk—an overview, *Journal of materials science*, Vol. 38, Issue 15, 2003, pp. 3159-3168.
- [3] Babaso, P. N., and Sharanagouda, H., Rice husk and its applications: review, *International journal of current microbiology and applied sciences*, Vol. 6, Issue 10, 2017, pp. 1144-1156.
- [4] Soltani, N., Bahrami, A., Pech-Canul, M. I., and González, L. A., Review on the physicochemical treatments of rice husk for production of advanced materials, *Chemical engineering journal*, Vol. 264, 2015, pp. 899-935.
- [5] Pode, R., Potential applications of rice husk ash waste from rice husk biomass power plant, *Renewable and Sustainable Energy Reviews*, Vol. 53, 2016, pp. 1468-1485.
- [6] Chopra, D., and Siddique, R., Strength, permeability and microstructure of self-compacting concrete containing rice husk ash, *Biosystems engineering*, Vol. 130, 2015, pp. 72-80.
- [7] Ramakrishnan, S., Velraj Kumar, G., and Ranjith, S., Behavior of cement-rice husk ash concrete for pavement, *International Journal of Emerging Trends in Engineering and Development*, Vol.1, 2014, Issue 4.
- [8] Khan, R., Jabbar, A., Ahmad, I., Khan, W., Khan, A. N., and Mirza, J., Reduction in environmental problems using rice-husk ash in concrete, *Construction and Building Materials*, Vol. 30, 2012, pp. 360-365.
- [9] Malhotra, V. M., Role of supplementary cementing materials in reducing greenhouse gas emissions, In *Infrastructure regeneration and rehabilitation improving the quality of life through better construction: a vision for the next millennium*, 1999, pp. 27-42.

- [10] Sabir, B. B., Wild, S., and Bai, J., Metakaolin and calcined clays as pozzolans for concrete: a review, *Cement and concrete composites*, Vol. 23, Issue 6, 2001, pp. 441-454.
- [11] Worrell, E., Price, L., Martin, N., Hendriks, C., and Meida, L. O., Carbon dioxide emissions from the global cement industry, *Annual review of energy and the environment*, Vol. 26, Issue 1, 2001, pp. 303-329.
- [12] Siddique, R., and Khan, M. I., *Supplementary cementing materials*, 2011, Springer Science & Business Media.
- [13] Hossain, M. Z., and Sakai, T., The effectiveness of nominal dosage of ordinary cement on strength and permeability of clayey soil, *Journal of the Japanese Society of Soil Physics*, Vol. 110, 2008, pp. 25-35.
- [14] Nasiri, M., Lotfalian, M., Modarres, A., and Wu, W., Optimum Utilization of Rice Husk Ash for Stabilization of Sub-Base Materials in Construction and Repair Project of Forest Roads, *Croatian Journal of Forest Engineering: Journal for Theory and Application of Forestry Engineering*, Vol. 37, Issue 2, 2016, pp. 333-343.
- [15] Kaur, I. and Jha, J. N., Effects of Rice Husk Ash - Cement Mixtures on Stabilization of Clayey Soils, *IJCA Proceedings on International Conference on Advancements in Engineering and Technology* Vol. 8, 2016, pp.30-33.
- [16] Ahmad, J., Rosli, M. I. F., and Rahman, A. S. A., The Effect of Rice Husk Ash (RHA) Mixtures on Geotechnical Properties of Soil, In *Regional Conference on Science, Technology and Social Sciences*, 2018, pp. 345-352
- [17] Basha, E. A., Hashim, R., Mahmud, H. B., and Muntohar, A. S., Stabilization of residual soil with rice husk ash and cement, *Construction and building materials*, Vol. 19, Issue 6, 2005, pp. 448-453.
- [18] Eberemu, A. O., and Sada, H., Compressibility characteristics of compacted black cotton soil treated with rice husk ash, *Nigerian Journal of Technology*, Vol. 32, Issue 3, 2013, pp. 507-521.
- [19] Alhassan, M., Permeability of lateritic soil treated with lime and rice husk ash, *Assumption University Journal of Thailand*, Vol. 12, Issue 2, 2008, 115-120.
- [20] Muntohar, A. S., and Hantoro, G., Influence of rice husk ash and lime on engineering properties of a clayey subgrade, *Electronic Journal of Geotechnical Engineering*, Vol. 5, 2000, pp. 1-9.
- [21] Eisazadeh, A., Bhurtel, A. and Phai, H., May. Compaction characteristics of Bangkok clay stabilized using rice husk ash, bottom ash, and lime. In *IOP Conference Series: Materials Science and Engineering*, Vol. 527, 2019, Issue 1, pp. 012039.

Construction Material

FIELD EXPERIMENTS TO INVESTIGATE PULL-OUT MECHANISM OF FLIP-TYPE GROUND ANCHORS INSTALLED IN CLAY SOIL

Shota Yoshida¹, Tatsunori Matsumoto², Mimu Yoshida³

^{1,2}Graduate School of Science and Technology, Kanazawa University, Japan; ³Daisho Co., Ltd., Japan

ABSTRACT

The pull-out mechanism of plate, strip, or circular anchors other than flip anchors in sandy and clayey ground conditions has been mostly studied in laboratory experiments; however, there are few field studies on this subject. For the widespread practical application of flip anchors, this study aims to provide results of field pull-out experiments of actual flip anchors driven into clayey and sandy soils. A test site was selected comprising a top sand layer with a clay layer underneath. Vane shear tests were conducted in the clay layer to measure the undrained shear strength, c_u . Moreover, a total of 27 flip anchors were driven into the position of 2 m pitch grid using a percussion driving device and pulled out using a hydraulic jack. All anchors were driven into the clay layer at two different depths. The anchors in the sand layer had a greater pull-out force than the corresponding anchors in the clay. The pressure acting on the anchor increased with decreasing projected area of the anchor. In the clay layer, the pressure was the same regardless of the project area of the anchor plate. The maximum pull-out forces measured ~~on~~ in the clay layer were estimated using the interpretation method of the T-bar penetration test.

Keywords: Flip-type ground anchor, Field experiment, Pull-out experiment, Clay soil

INTRODUCTION

Flip-Type Earth Anchors

Flip-type earth (ground) anchors (hereinafter, “flip anchor”) are effective for reinforcing slopes such as soil nailing and ground anchors against slope failures owing to heavy rains and for supporting tower structures against strong winds. Because they can be installed underwater, they are used as an anchor base for floating objects such as solar panels and floating piers.

Figure 1 shows the flip anchors. Fig. 2 shows an installation process of the anchors. The flip anchors are driven into the ground as percussion anchors with the anchor head closed (Fig. 2a). After driving into a designated depth, the anchor head rotates to open by pulling it with a jack (Fig. 2b) such that soil pressure sufficiently acts on it. Because the grouting and curing periods of grout are not required, flip anchors are suitable for small-scale reinforcement or restoration works in emergency situations. Although the installation of flip anchors is simple and fast, the mechanism of their pull-out resistance has not been completely understood to date.

Objectives of this Research

The behaviors of square, rectangular, or circular anchors in sandy ground conditions have been previously studied. Ground failure patterns and certain methods for designing the pull-out capacity have been proposed [2–10]. For clayey soil conditions, several studies have proposed empirical approaches to estimate the uplift capacity of various plate anchors [11–18]. However, there is no similar research on flip anchors. Moreover, field experiments have not been conducted to estimate the pull-out capacity of actual flip anchors.

To widely use flip anchors in practical applications, this study aims to provide the results of field pull-out experiments of various sizes of actual flip anchors driven into clayey and sandy soils. Moreover, based on experimental results, a design method for the pull-out capacity of flip anchors in clay is discussed.

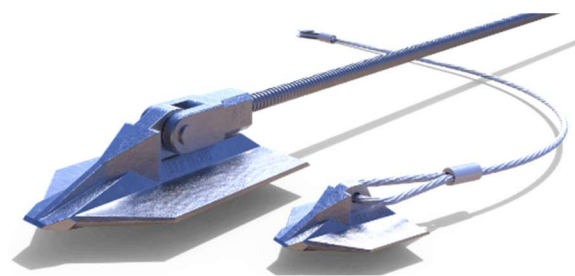


Fig. 1 Flip type earth anchor [1].

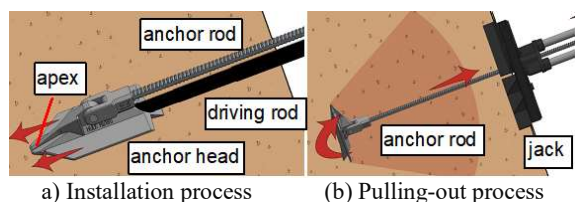


Fig. 2 Installation process of a flip type earth anchor [1].

OUTLINE OF FIELD EXPERIMENT

Property of the Ground

The test site was located at Shiga Prefecture, Japan. Figure 3 shows a total of 27 flip anchors, which were set at a position of 2 m pitch grids comprising three rows: A, B, and C. Moreover, nine anchors were installed in each row.

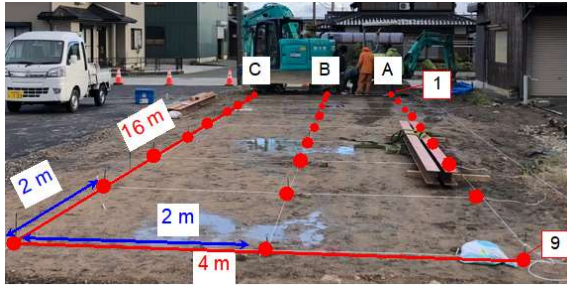


Fig. 3 Ground used for the pull-out experiments.

The ground comprised a top sand layer overlying a soft clay layer. Portable dynamic cone penetration tests (DCPTs) were conducted at ten locations (Fig. 4). The DCPT device comprised a cone with a diameter of 25 mm, a drop hammer mass of 5 kg, and a hammer drop height of 500 mm. The converted SPT N -values were empirically estimated from DCPT results. The N -value converted to a depth of 2 m within the top sand layer was around 5, and increased to around 15 near a depth of 3 m.

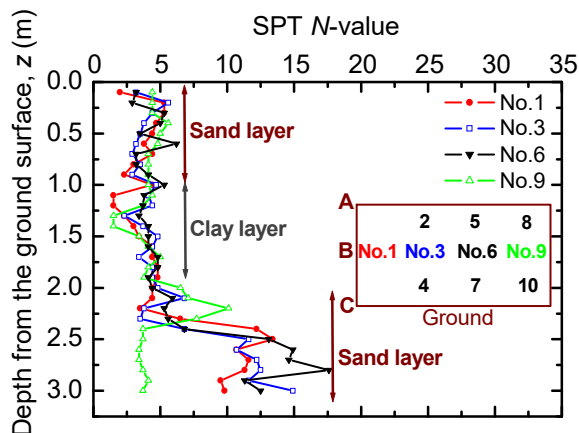


Fig. 4 Converted SPT N -values of the ground.

Furthermore, the test ground was excavated at two locations in the test site for direct soil observation. The top sand layer was 1-m deep, followed by the clay layer to a depth of 1.8 m. Moreover, flip anchors were driven in the top sand layer or clay layer.

As shown in Fig. 5, the clay layer comprised two types of clay. The blue colored clay contained a small amount of sand particles and the black colored clay was pure sticky clay.

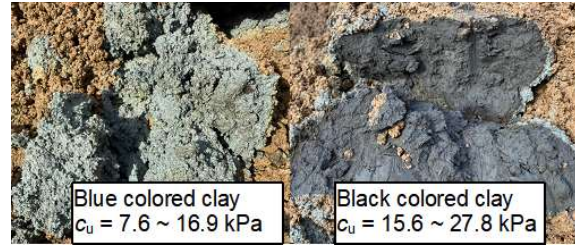


Fig. 5 Types of clay in the ground.

The former was located on the top portion of the clay layer. Vane shear tests were conducted in the clay layer to measure the undrained shear strength c_u . The black colored clay had a relatively larger c_u than the blue colored clay.

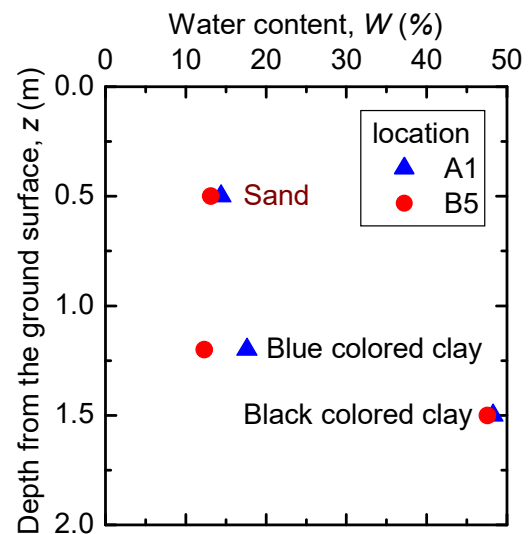


Fig. 6 Water content W of the ground.

Figure 6 shows the water content W of the ground. The water content of the black clay was nearly three times that of blue colored clay. No significant difference was observed in the water content at each location.

Flip Anchors Used in the Experiments

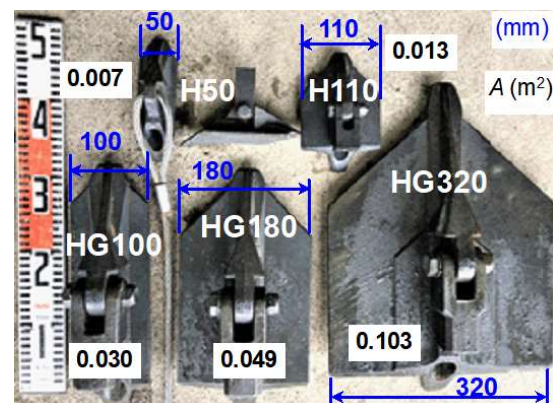


Fig. 7 Flip anchors used in the experiments.

As demonstrated in Fig. 7, five types of flip anchors were used in the experiments. The smaller and larger ones are the H and HG series. The number after H and HG denotes the width of the anchors.

Experimental Cases and Procedure

As listed in Table 1, a total of 26 cases of pull-out experiments were conducted. Depth z denotes the depth of the apex of the closed anchor plate.

Table 1 Experimental cases

Case	Anchor	Depth, z (m)	Soil	Max. force, F_{\max} (kN)
A1	HG320	1.8	Clay	*37.3
A2	HG320	1.2	Sand	35.8
A3	HG180	1.2	Sand	51.1
A4	HG100	1.2	Sand	45.9
A5	HG320	1.8	Clay	*16.2
A6	H110	1.0	Sand	26.0
A7	H50	1.0	Sand	14.0
A9	HG320	1.8	Clay	*13.1
B1	HG100	1.8	Clay	-
B2	HG100	1.8	Clay	*7.9
B3	H50x2	1.0	Sand	16.2
B4	H110	1.0	Sand	20.5
B5	HG100	1.8	Clay	*12.5
B6	H110	1.8	Clay	*6.1
B7	H110	1.8	Clay	*8.5
B8	H50	1.8	Clay	*4.5
B9	HG100	1.8	Clay	*8.8
C1	HG180	1.8	Clay	*17.1
C2	HG320	1.2	Sand	66.1
C3	HG180	1.2	Sand	64.3
C4	HG100	1.2	Sand	62.7
C5	HG180	1.8	Clay	*17.7
C6	H110	1.0	Sand	37.6
C8	H50	1.0	Sand	22.3
C9	HG180	1.8	Clay	*12.5
BC2.5	H50	1.0	Sand	10.7

Note: * F_{\max} between the depths of 1.8 and 1.3 m.

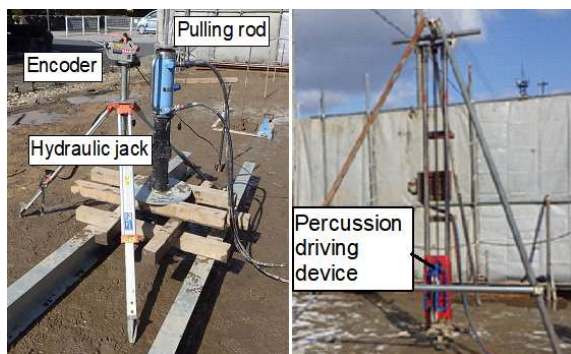


Fig. 8 Percussion driving device and hydraulic jack.

Figure 8 shows that the anchors were driven using a percussion device and pulled out using a hydraulic jack. The pull-out force F and upward displacement w were measured while pulling out the anchors.

RESULTS OF THE EXPERIMENTS

Pull-Out Force vs Upward Displacement

Figures 9–13 compare the relation between the pull-out force F and upward displacement w of anchors planted in the sand and clay layers.

Figure 4 shows the sand and clay layers, which were separated at a depth of 1 m. In the early stages of pull-out loading, the behaviors of all anchors showed similar trends. For all anchors except the HG320 anchor in the sand layer, the pull-out resistance is mobilized very quickly with a small upward displacement w and then levels off.

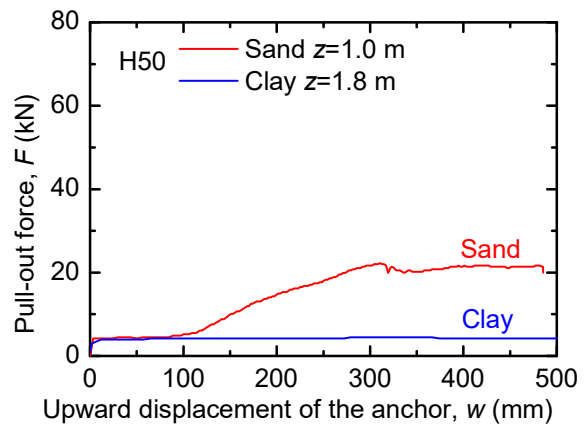


Fig. 9 Pull-out force vs. upward displacement of H50 anchors installed in the sand and clay layers.

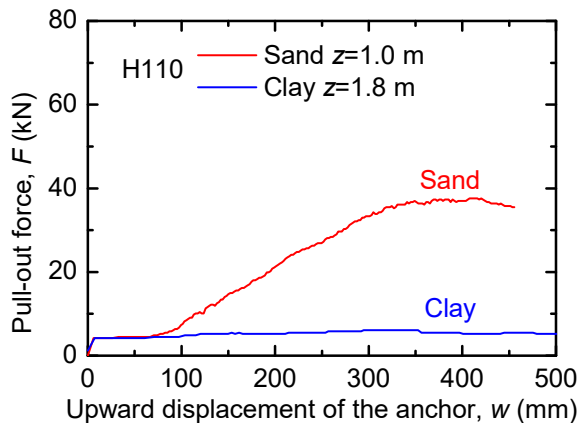


Fig. 10 Pull-out force vs. upward displacement of H110 anchors installed in the sand and clay layers.

For anchors in the sand layer, the pull-out forces began to increase again after this plateau and reached a peak value at a relatively large w of 400–500 mm. Therefore, the anchors in the sand layer were significantly influenced by the sand. By comparing Figs. 12 and 13, the pull-out force of the 440-mm long HG320 began to increase at about 50% of the displacement of the 340 mm long HG180 in the sand

layer. This is reasonable because HG320 had a smaller relative distance (the distance between the bottom of the overlying sand and anchor plate divided by the anchor length).

In clay, the anchors maintained a plateau from the early stage to the large upward displacement, as shown in Figs. 9 and 10 in which small-sized anchors were tested. As shown in Figs. 11 and 12, HG100 and HG180 anchors (length = 340 mm) required upward displacement equal to their anchor length until the pull-out forces began to increase again. Subsequently, with an additional pull-out displacement of around 100 mm, the anchors appeared to be fully open and reached their peak values in the clay layer.

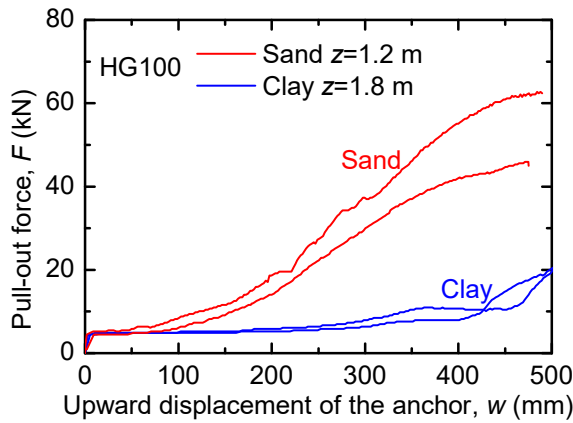


Fig. 11 Pull-out force vs. upward displacement of HG100 anchors installed in the sand and clay layers.

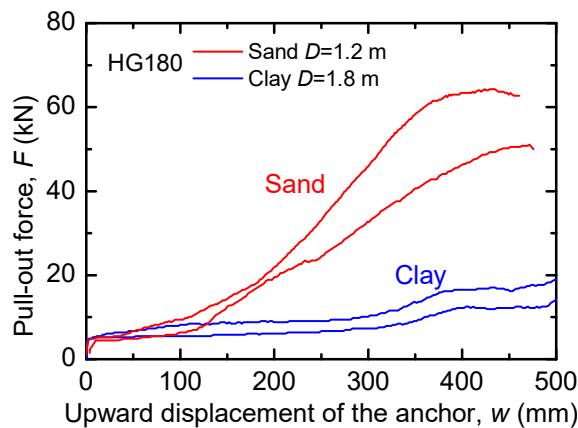


Fig. 12 Pull-out force vs. upward displacement of HG180 anchors installed in the sand and clay layers.

However, the pull-out forces in the clay layer did not increase similar to those in sand. As shown in Figs. 9–13, the anchors in the sand layer had significantly greater F values than their clay counterparts, although the overburden pressures on the anchors in the sand layer were less.

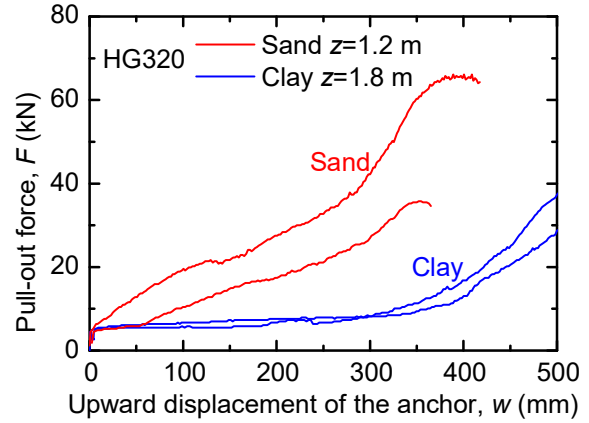


Fig. 13 Pull-out force vs. upward displacement of HG320 anchors installed in the sand and clay layers.

Therefore, if the anchors are installed in the clay layer below the sand layer, the effects of the top sand layer should be ignored in design of the pull-out forces when the anchors do not reach the sand layer.

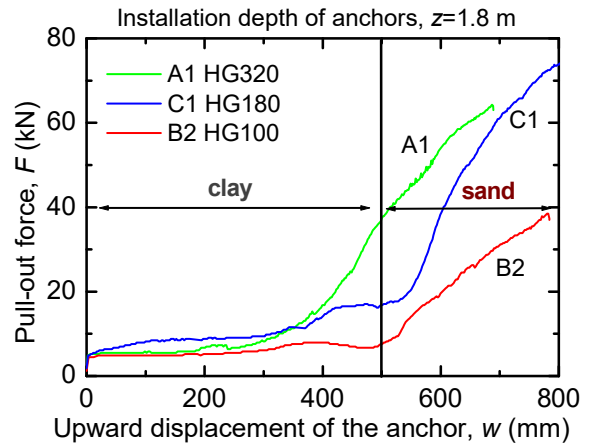


Fig. 14 Pull-out force vs. displacement of HG anchors installed in the clay layer through the sand layer.

Figure 14 shows the relation between F vs. w of the anchors installed at a depth of 1.8 m. The F values of HG180 and HG100 began to increase rapidly when the anchors reached the sand layer. In the sand layer, the larger the anchor, the greater the pull-out force. Figure 14 shows that when the anchors were pulled out of the clay layer, the pull-out forces were not affected by the overlying sand layer.

Figure 15 shows the relation between the pull-out pressure, $p = F/A$ (A = projected area of the flip anchors), and w of the HG anchors. In sandy ground conditions, plate anchors such as rectangular and circular anchors are well known to lift inverted trapezoidal soil wedges over the anchor plates [6–8, 19–21]. This ground failure mechanism usually decreases p as A increases. The measured trend of p

in the sand layer conformed to the above mechanism. However, the p values of HG100 and HG180 remained nearly constant, and their amplitudes were almost similar during pulling out in the clay layer. Thus, the p values of HG320 were smaller than the former two anchors. Because HG320 had approximately three times the area of HG100, a larger displacement was required to open it sufficiently. Therefore, at a displacement of 500 mm, the p values of HG320 were nearly equal to the p values of HG100 and HG180 at a 400 mm upward displacement. Therefore, in the clay layer, the p values of sufficiently opened anchors were nearly constant regardless of the size of the anchors.

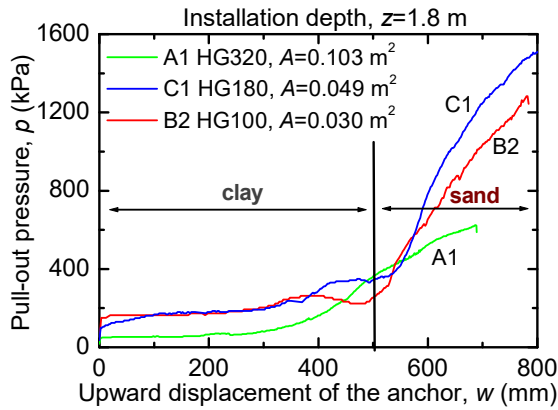


Fig. 15 Pull-out pressures vs. displacements of HG anchors installed in clay through sand layer.

Calculation Method of Pull-Out Resistance Force of Flip Anchors in Clay

Calculation methods for plate anchors in clay

First, the calculation methods for plate anchors other than flip anchors are reviewed. The calculation methods of the pull-out capacity for the square, rectangular, or circular anchors in clay have already been proposed. Das [11] proposed Eq. (1) and Merifield [17] proposed Eq. (2) for the ultimate pressure acting on the anchor plates:

$$q_0 = c_u F_c + \gamma H \quad (1)$$

$$q_u = Q_u / A = c_u N_c \quad (2)$$

where q_0 is the net ultimate loads per unit area, c_u is the undrained shear strength of soil, F_c and N_c are anchor breakout factors, γ is effective unit weight of soil, H is the embedment depth of the anchor, q_u is the average ultimate pressure, Q_u is the pull-out force; and A is the anchor area. The value of F_c or N_c is a function of embedment ratios, H/B or H/D (B = width of a plate anchor and D = diameter of a circular anchor), and overburden pressure [11, 17]. The values of F_c and N_c are functions of soil profile, anchor shape,

embedment ratios H/B or H/D , and overburden ratio, $\gamma H/c_u$. Several calculation steps are required to obtain the F_c and N_c values, hindering their practical use.

A calculation method for the flip anchors in clay

The T-bar penetration test is used to estimate the undrained shear strength c_u of clay ground. The c_u value is estimated using Eq. (3) [22] with the measured value of pressure p on the T-bar, regardless of the size of the T-bar:

$$c_u = p / N_b \quad (3)$$

where N_b is the bearing factor of T-bar. N_b ranges from 8.5 to 12.5 for various types of clay with an average value of 10.5 [23]. In this field experiment, the range of c_u values for the clay layer was estimated using the VSTs, as mentioned earlier. When estimating the c_u values from soil tests other than the T-bar test, the pressure of the anchor p can be estimated using Eq. (4):

$$p = N_b c_u \quad (4)$$

In Fig. 16, the range of the calculated values of p reasonably agrees with the measured values of p .

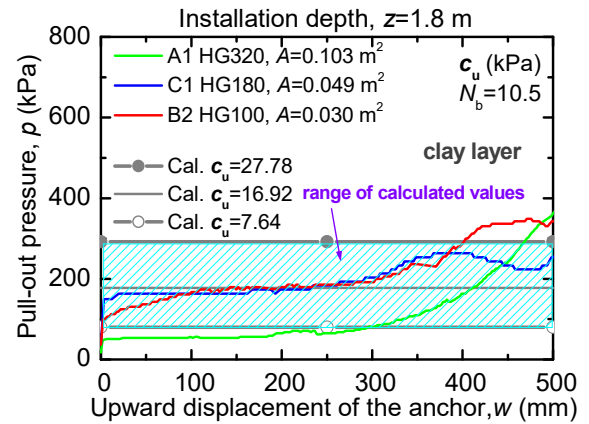


Fig. 16 Calculated p in clay vs. measured p .

Therefore, when performing a T-bar penetration test on site, the p values from the T-bar test can be used to directly estimate the approximate pressure on the flip anchor as Eq. (5).

$$F = pA \quad (5)$$

Currently, the T-bar penetration test is rarely used for site investigations in Japan. In practice, the c_u values are empirically estimated from the SPT- N values, VST, pressuremeter test, or unconfined compression test. Therefore, if the c_u value is obtained, the pressure on the anchor can be estimated using Eq. (4).

CONCLUSION

The pull-out experiments of the flip-type anchors were conducted in ground where a top sand layer covered a clay layer to investigate the pull-out mechanisms of flip anchors in clay. It was clearly shown that the pull-out mechanism of the anchor in clay was quite different from that in sand. As for the anchors being pulled out in clay, the pull-out force was not affected by the overburden pressure. It was proportional to the anchor size. This indicates that the pressure acting on the anchor head was constant regardless of the size of the anchor.

To predict the pull-out force of flip anchors in clay, the interpretation method of the T-bar penetration test was used. The predicted p range estimated from the c_u values of the VSTs and bearing factor of T-bar N_b of 10.5 agreed well with the measured p range. Therefore, this interpretation method can be promising for the prediction of the pull-out capacity of flip anchors in clay.

REFERENCES

- [1] Anchoring Rope and Rigging Pty Ltd., <https://hulkearthanchors.com>, 2019.
- [2] Dickin E.A. and Leung C.F., Evaluation of design methods for vertical anchor plates, *Journal of Geotechnical Engineering*, Vol. 111, Issue 4, 1985, pp. 500-520.
- [3] Dickin E.A., Uplift behavior of horizontal anchor plates in sand, *Journal of Geotechnical Engineering*, Vol. 114, Issue 11, 1988, pp. 1300-1317.
- [4] Dickin E.A. and Laman M., Uplift response of strip anchors in cohesionless soil, *Advances in Engineering Software*, Vol. 38, 2007, pp. 618-625.
- [5] Emirler B., Tolun M. and Laman M., Experimental investigation of the uplift capacity of group anchor plates embedded in sand, *Geomechanics and Engineering*, Vol. 11, Issue 5, 2016, pp. 691-711.
- [6] Liu J., Liu M. and Zhu Z., Sand deformation around an uplift plate anchor, *Journal of Geotechnical and Geoenvironmental Engineering*, Vol. 138, Issue 6, 2012.
- [7] Llamparuthi K., Dickin E.A. and Muthukrisnaiah K., Experimental investigation of the uplift behaviour of circular plate anchors embedded in sand, *Canadian Geotechnical Journal*, Vol. 39, Issue 3, 2002, pp. 648-664.
- [8] Merifield R.S., Lyamin A.V. and Sloan S.W., Three-dimensional lower-bound solutions for the stability of plate anchors in sand, *Géotechnique*, Vol. 56, Issue 2, 2006, pp. 123-132.
- [9] Merifield R.S. and Sloan S.W., The ultimate pullout capacity of anchors in frictional soils, *Canadian Geotechnical Journal*, Vol. 43, 2006, pp. 852-868.
- [10] Niroumand H., Kassim K.A. and Nazir R., Anchor plates in two-layered cohesion less soils, *American Journal of Applied Sciences*, Vol. 7, Issue 10, 2010, pp. 1396-1399.
- [11] Das B.M., Model tests for uplift capacity of foundations in clay, *Soils and Foundations*, Vol. 18, Issue 2, 1978, 17-24.
- [12] Das B.M., A procedure for estimation of ultimate uplift capacity of foundations in clay, *Soils and Foundations*, Vol. 20, Issue 1, 1980, pp. 77-82.
- [13] Das B.M., Moreno R. and Dallo K.F., Ultimate pullout capacity of shallow vertical anchors in clay, *Soils and Foundations*, Vol. 25, Issue 2, 1985, pp. 148-152.
- [14] Das B.M. and Puri V.K., Holding capacity of inclined square plate anchors in clay, *Soils and Foundations*, Vol. 29, Issue 3, 1989, pp. 138-144.
- [15] Han C., Wang D., Gaudin C., O'Loughlin C.D. and Cassidy M.J., Behaviour of vertically loaded plate anchors under sustained uplift, *Géotechnique*, Vol. 66, Issue 8, 2016, pp. 681-693.
- [16] Khatri V.N. and Kumar J., Vertical uplift resistance of circular plate anchors in clays under undrained condition, *Computers and Geotechnics*, Vol. 36, Issue 8, 2009, pp. 1352-1359.
- [17] Merifield R.S., Lyamin A.V., Sloan S.W. and Yu H.S., Three-dimensional lower bound solutions for stability of plate anchors in clay, *Journal of Geotechnical and Geoenvironmental Engineering*, Vol. 129, Issue 3, 2006, pp. 243-253.
- [18] Singh V., Maitra S. and Chatterjee S., Generalized design approach for inclined strip anchors in clay, *International journal of Geomechanics*, Vol. 17, Issue 6, 2017.
- [19] Tanaka T. and Sakai T., Progressive failure and scale effect of trap-door problems with granular materials, *Soils and Foundations*, Vol. 33, Issue 1, 1993, pp. 11-22.
- [20] Yoshida S., Komura K., Matsumoto T. and Yoshida T., Pull-out experiment of two-dimensional model flip-type ground anchors installed in dry sand ground, *Geotechnics for sustainable infrastructure development - Geotec Hanoi*, 2019, pp. 1245-1252.
- [21] Yoshida S., Matsumoto T., Komura K. and Yoshida T., Field pull-out experiments of flip-type ground anchors installed in dry sand ground, *Geomate proceedings*, 2019, pp. 569-574.
- [22] Almeida M.S.S., Oliveira J.R.M.S., Rammah K.I. and Trejo P.C., Investigation of bearing capacity factor of T-bar penetrometer at shallow depths in clayey soils, *Journal of Geo-Engineering Sciences*, Vol. 1, 2013, pp. 1-12.
- [23] Low H. E., Lunne T., Andersen K.H., Sjørsen M.A. and Randolph M. F., Estimation of intact and remoulded undrained shear strengths from penetration tests in soft clays, *Géotechnique*, Vol. 60, No. 11, 2010, pp. 843-859.

FINITE DIFFERENCE APPROXIMATION FOR SOLVING TRANSIENT HEAT CONDUCTION EQUATION OF THE CAST IRON

Dalal Adnan Maturi¹

¹Departement of Mathematics, Faculty of Science, King Abdulaziz University, P.O.Box 42664, Jeddah 21551,
Saudi Arabia

ABSTRACT

In this paper, finite differences for solving Transient heat conduction equation of the Cast iron by using the finite difference method using the MATLAB algorithm for the direct problem of calculating the value of temperature in different time quantities for a separate point required as well as checking the temperature field according to the time quantity as shown by Examples and Figures, the proposed method is still very accurate and since the cast iron is an important material and metal in mineral installations in various engineering fields through many bridges, tunnels, buildings, towers, sports facilities and industrial facilities and others. We note that the design standards that relate to structural stability, the length of endurance, fire resistance, and control of environmental pollution and cost have become more acute and decisive. These standards, in addition to the continuous decline in national resources, have resulted in heavy pressure on engineers to try to reduce the quantities of construction materials required for the construction process as they in turn require induction Technical methods and knowledge of the quality of minerals used for construction, it is evident from the examples and forms that we obtain, which shows the effectiveness of the method used to detect the quality of cast iron metal and the possibility of using it in making tools that are not subjected to shocks such as: water pipes or gas pipes or In a mother in the field of construction, it was limited to some simple structural elements to support the old stone and wooden buildings and help in the implementation of some of the roofs with a wider metaphor due to the property that it bears the extreme pressure and its low tolerance to tension.

Keywords: Finite Difference Method, Transient Heat Conduction Equation, Cast Iron, Matlab.

INTRODUCTION

Finite difference method is one of several techniques for obtaining numerical solution of partial differential equation. Finite difference method describes functions as discrete values across a grid and approximate their derivatives as differences between points on the grid. Knowing a little about how difference methods are formulated and in what regimes they are stable can help save a lot of time, both in the design of finite differencing algorithms, and in the time that they take to run, the finite difference approximations for derivatives are one of the simplest and of the oldest methods to solve differential equations.

We need a fast, realistic and reliable method to solve the heat conduction equation of the Cast Iron.

The exploitation and manufacture of iron began during the thousand years BC in Syria and in the country Hitter, and the history of the simplest types of iron dates back to the early BC. It is the twelfth century AD developed charcoal kilns in Europe and was able to provide the heat necessary to melt iron. The iron produced in this way was not amenable to road because of the high carbon content in it, so it was necessary to purify it, that is, to reduce the carbon content in it by burning it.

Benjamin Huntsman in England in 1740 managed to melt iron and prepare cast iron in crucible fashion. In 1811, Friedrich Kropp founded the first cast iron preparation plant in Essen. This gave a major breakthrough in iron production for the nineteenth century, and the emergence of several inventions that helped to increase its manufacture: steam machines provided to the steel industry strong labor, and coal mines provided the coal needed for its manufacture, railways and development, as well as steam ships, all of which use products Steel which is a popular market.

The steel industry in all countries was of great importance from an economic point of view and has political significance, as it was considered one of the pride of the state among nations. The importance of steel at the time appears in the construction of the Eiffel Tower, as it opened on the occasion of the International Exhibition in 1889 as one of the pillars of technological progress.

FINITE DIFFERENCE METHOD FOR HEAT CONDUCTION EQUATION

The linear second order partial differential equation

$$Au_{xx} + 2Bu_{xy} + Cu_{yy} + Du_x + Eu_y + Fu + G = 0$$

as a parabolic equation if $B^2 - AC = 0$. A parabolic equation holds in an open domain or in a semi-open domain.

The partial differential equation governing the flow of heat in the rod is given by the parabolic equation

$$u_t = c^2 u_{xx}, \quad 0 \leq x \leq l, \quad t > 0.$$

Where c^2 is a constant and depends on the material properties of the rod.

The heat conduction equation of the Cast Iron

$$\begin{aligned} u_t &= (0.12)u_{xx} \\ u(0, t) &= u(1, t) = 0, \quad \forall t \in (0, t_F) \\ u(x, 0) &= u_0(x), \quad \forall x \in [0, 1], \end{aligned}$$

Where t_F Denotes the terminal time for the model. Here without loss of generality, we assume that the spatial domain is $[0, 1]$.

At first divide the physical domain $(0, t_F) \times (0, 1)$ by $N \times J$ uniform grid points

$$\begin{aligned} t_n &= n\Delta t, \Delta t = \frac{t_F}{N}, n = 0, 1, \dots, N, \\ x_j &= j\Delta x, \Delta x = \frac{1}{J}, j = 0, 1, \dots, J. \end{aligned}$$

Then, we denote the approximate solution $u_j^n \approx u(x_j, t_n)$. At an arbitrary point (x_j, t_n) . To obtain a finite difference scheme, we need to approximate the derivatives in (1) by some finite differences. (Explicit scheme)

Substituting

$$\begin{aligned} u_t(x_j, t_n) &\approx (u_j^n - u_j^{n-1})/\Delta t, \\ u_{xx}(x_j, t_n) &\approx (u_{j+1}^n - 2u_j^n + u_{j-1}^n)/(\Delta x)^2, \end{aligned}$$

Into (1), another difference scheme for (1) can be constructed as:

$$\frac{u_j^n - u_j^{n-1}}{\Delta t} = \frac{u_{j+1}^n - 2u_j^n + u_{j-1}^n}{(\Delta x)^2}, \quad 1 \leq j \leq J-1, 1 \leq n \leq N.$$

SEVERALS EXAMPLES

(i) Example1. Find the solution of the heat conduction equation of the Cast Iron

$$\begin{aligned} u_t &= (0.12)u_{xx} \quad 0 < x < 1, \quad t > 0; \\ u(0, t) &= u(1, t) = 0, \quad t > 0; \\ u(x, 0) &= 2 \sin(\pi x/2) - \sin \pi x + 4 \sin 2\pi x, \\ &0 \leq x \leq 1. \end{aligned}$$

Applying the finite difference method using Matlab, then the result show as follows.

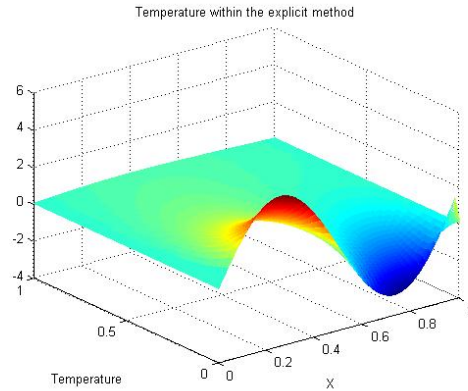
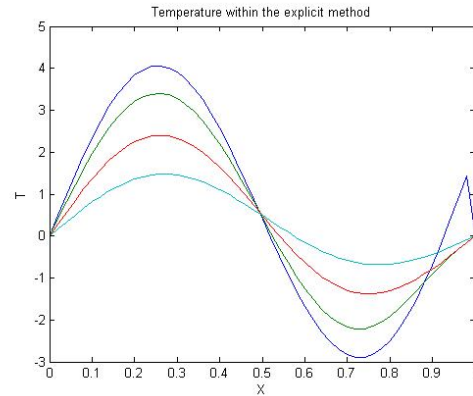
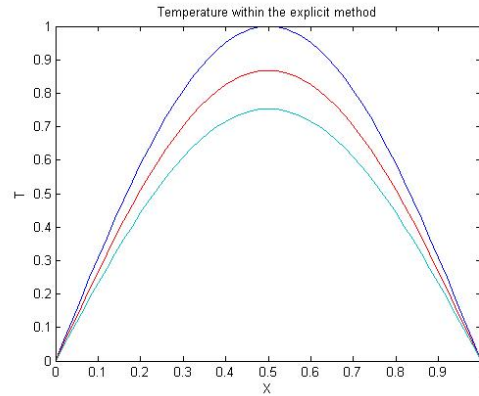


Fig.1 Temperature distributions at several times for the heat conduction of the Cast Iron for example 1.

(ii) Example2. Find the solution of the heat conduction equation of the Cast Iron

$$\begin{aligned} u_t &= (0.12)u_{xx} \quad 0 < x < 1, \quad t > 0; \\ u(0, t) &= u(1, t) = 0, \quad t > 0; \\ u(x, 0) &= \sin \pi x, \quad 0 \leq x \leq 1. \end{aligned}$$

Applying the finite difference method using Matlab, then the result show as follows.



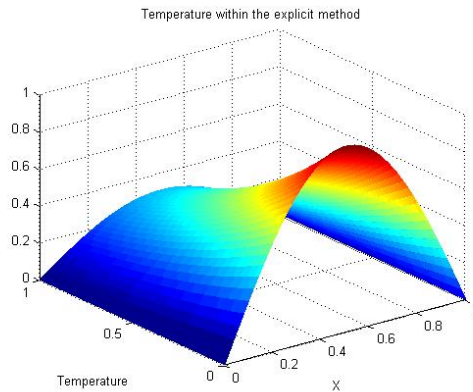


Fig.2 Temperature distributions at several times for the heat conduction of the Cast Iron for example 2.

(iii) Example3. Find the solution of the heat conduction equation of the Cast Iron

$$\begin{aligned} u_t &= (0.12)u_{xx} \quad 0 < x < 1, \quad t > 0; \\ u(0, t) &= u(1, t) = 0, \quad t > 0; \\ u(x, 0) &= \sin 2\pi x - \sin 5\pi x, \quad 0 \leq x \leq 1. \end{aligned}$$

Applying the finite difference method using Matlab, then the result show as follows.

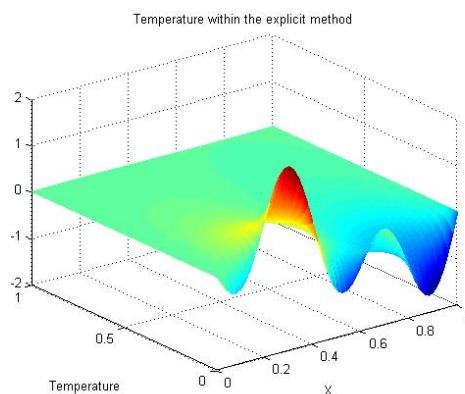
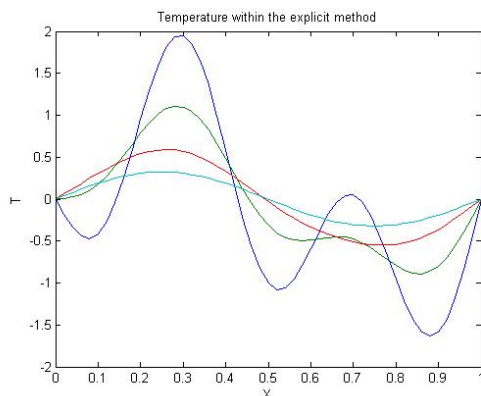


Fig.3 Temperature distributions at several times for the heat conduction of the Cast Iron for example 3.

CONCLUSION

In this paper, calculations are performed by the MATLAB Programming Program and Evolutionary Laws for a one-dimensional thermal conductivity equation using the finite difference method in solving the thermal conductivity equation for cast iron. All examples demonstrate that the finite difference method is a powerful mathematical tool for solving the cast iron thermal conductivity formula. The graphic shapes we provided to define a higher resolution and simplicity for the proposed method. In addition, it should be noted that the described method can easily be generalized to build more heat for different materials. This work focuses on cast iron because Gray cast iron is an alloy of cast iron with a graphite microscopic structure. It is called gray because it is the color that appears inside it when breaking, which indicates the presence of graphite. Gray cast iron is the most popular and widely used cast iron alloy. Gray cast iron is used in applications that are not progressively perceived, such as the internal combustion engine, pump bodies, funds, electrical boxes and cosmetic castings. Gray cast iron also has high thermal capacity and thermal conductivity, often used in some cookware.

ACKNOWLEDGMENTS

This paper was supported by the Deanship of Scientific Research (DSR), King Abdulaziz University, Jeddah.

REFERENCES

- [1] William F.A., Numerical Methods for Partial Differential Equations. Academic Press, New York, NY, 3rd edition, 1992.
- [2] Jim D., and H.H.R., On the numerical solution of heat conduction problems in two and three space variables. Trans. Amer. Math.Soc., 82: 1956, pp.421-439.
- [3] Mitchell A.R., and Griffiths D.F., The Finite Difference Method in Partial Differential Equations. John Wiley & Sons, Chichester, 1980.
- [4] Mitchell A.R., and Griffiths D.F., The Finite Difference Method in Partial Differential Equations. John Wiley & Sons, Chichester, 1980.
- [5] Dalal A.M, Amani Z.B., Badreah M.G., Numerical Solution of Volterra Integral Equation of Second Kind Using Implicit Trapezoidal, Journal of Advances In Mathematics, Vol8, No.2, 2014, pp.1540-1553.
- [6] Dalal A.M., Adomian Decomposition Method of Fredholm Integral Equation of the Second Kind Using Maple, Journal of Advances In Mathematics, Vol9, No.1, 2014, pp.1868-1875.
- [7] Dalal A.M., Application of Adomian Decomposition Method for Solving of Fredholm

- Integral Equation of the Second Kind, European Journal of Science and Engineering, Vol9, No.2, 2014, pp.1-9.
- [8] Dalal A.M., Adomian Decomposition Method for Solving of Fredholm Integral Equation of the Second Kind Using Matlab, International Journal of GEOMATE, Dec. 2016, Vol. 11, Issue 28, pp.2830-2833. Special Issue on Science, Engineering and Environment, ISSN: 2186-2990, Japan.
- [9] Dalal A.M., and Honida M.M., Numerical Solution of System of Three Nonlinear Volterra Integral Equation Using Implicit Trapezoidal, Journal of Mathematics Research, Vol.10, No. 1, February 2018, ISSN 1916-9795 E-ISSN 1916-9809.
- [10] Dalal A.M., Finite Difference Method for Solving Heat Conduction Equation of The Granite, International Journal of GEOMATE, Sept. 2019, Vol. 17, Issue 61, pp.135-140. Special Issue on Science, Engineering and Environment, ISSN: 2186-2982(P),2186-2990(O), Japan.
- [11] Dalal A.M., FINITE DIFFERENCE METHOD FOR SOLVING HEAT CONDUCTION EQUATION OF THE BRICK, International Journal of GEOMATE, April, 2020 Vol.18, Issue 68, pp.114-119.
- [12] Dalal A.M., Eman A., Simbawa M., THE MODIFIED DECOMPOSITION METHOD FOR SOLVING VOLTERRA FREDHOLM INTEGRO-DIFFERENTIAL EQUATION USING MAPLE, International Journal of GEOMATE, March, 2020 Vol.18, Issue 67, pp.84-89.

DEVELOPMENT OF ARTIFICIAL BEACHROCK USING WATERMELON SEEDS AS A SOURCE OF UREASE

Md. Al Imran¹, Kazunori Nakashima², Niki Evelpidou³ and Satoru Kawasaki⁴

¹ Graduate School of Engineering, Hokkaido University, Sapporo, Japan

^{2,4} Faculty of Engineering, Hokkaido University, Sapporo, Japan

³ Faculty of Geology and Geoenvironment, National and Kapodistrian University of Athens, Athens, Greece

ABSTRACT

In recent years, the formation of artificial beachrock and bio-cementation method has gained considerable attention as a sustainable alternative tool in the area of geotechnical and geo-environmental engineering field for soil improvement and construction materials. In general, earlier methods of soil improvement were mostly concentrated on microbes (Bacteria, Fungi, etc.) as a source of urease enzyme widely known as MICP method (Microbial Induced Carbonate Precipitation). To address some of the key limitations of MICP method this study focused on using crude enzyme (low cost, eco-friendly). Crude enzyme was extracted from watermelon seeds (*Citrullus lanatus*) considered as “food waste material” and the carbonate formation process known as EICP “Enzyme Induced Carbonate Precipitation.” Crushed and blended watermelon seeds (both dry and germinated) used as a source of urease enzyme. Subsequently, their urease activity was also investigated with various environmental parameters (Temperature, pH, etc.) and investigated the carbonate precipitation trend using calcium chloride (CaCl_2) and urea [$(\text{CO}(\text{NH}_2)_2$]. The form of carbonate (calcite, aragonite, vaterite, etc.) was also confirmed by XRD and SEM-EDX analysis. Finally, syringe ($d = 2.3 \text{ cm}$, $h = 7.1 \text{ cm}$) sand solidification test was conducted using commercially available “Mikawa sand” (mean diameter, $D_{50} = 870 \text{ mm}$) and successfully achieved unconfined compressive strength (UCS) of about 1.2 MPa at neutral pH (~ 7) and temperature condition (30°C) considering various curing days (14 days) and conditions. This study could be useful as an eco-friendly and sustainable method for numerous bio-geotechnical applications (for instance, ground improvement, liquefaction mitigation, artificial beach rock formations, coastal erosion protection, etc.) and the extracted crude urease from watermelon seeds could play as an alternative to replace commercially available urease for carbonate precipitation.

Keywords: EICP, Watermelon seeds, Bio-cementation, Urease enzyme, Crude extract, Artificial beachrock

INTRODUCTION

Recently bio-inspired techniques have been widely used for different geotechnical applications. The maintenance, management of all of these methods were expensive and not eco-friendly [1, 2, 3]. Therefore, a new alternative countermeasure was needed. One of the emerging alternative approach known as “Microbial Induced Carbonate Precipitation-MICP method,” learned from “natural beachrock.” A beach rock consisted of marine sediments that have been cemented in the intertidal layer mostly by CaCO_3 , and its deposition time was much shorter than that of other sedimentary rocks. The cemented portion of beachrock primarily made up of both calcium carbonate and silica.

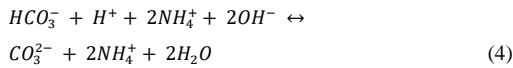
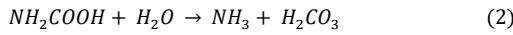
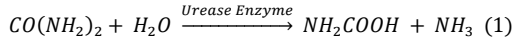
Several researchers have studied the beachrock formation mechanisms [3, 4]. However, some of the difficulties related to the current MICP method, have created requirements for alternative demand of solutions considering economic and ecological sustainability. For instance, the screening, isolation transportation, filtering, physical non-homogeneity, oxygen requirement, urease activity, viscosity, deep

penetration, microorganism strength, etc. marked this approach a complicated process. It challenged the use of MICP method in real field applications. Likewise, researchers around the world have tried to overcome some of these leading limitations, but yet, some unresolved issues related to MICP persisted. As an alternative technology, EICP (Enzyme Induced Carbonate Precipitation) has drawn considerable interest to the researcher for investigating the feasibility of using this method from laboratory scale to real field application.

The demand for using the EICP process may be fulfilled with commercially available urease enzyme, which is very costly because it has been manufactured for use in some specific applications in small amounts at high purity levels [5],[6],[7]. Therefore, it was essential to find an alternative source of urease enzyme to optimize the benefits through bio-inspired engineering applications and making artificial beachrock considering cost, environmental safety, and sustainability. This study focused on using crude urease extracted from watermelon (*Citrullus lanatus*) seeds as the source of urease enzyme considering waste utilization,

cost-effectiveness, availability of the material, and environmental safety.

During the CaCO_3 precipitation, the following reaction occurred in the presence of urea, urease enzyme, and calcium chloride, Eq. (1-5).



The primary objectives of this study were to find out investigate an effective extraction procedure of crude urease enzyme from watermelon seeds and to develop cemented samples towards making artificial beachrock. In this study series of test-tube experiments were conducted to identify the variations of precipitated crystals and their morphology considering their reaction rate with time. The precipitated crystals were analyzed with SEM (Scanning electron microscope) and XRD (X-Ray Diffraction) to confirm their morphology. Finally, the extracted crude enzyme was analyzed and compared with a pure commercial enzyme (Urease from Jack bean: Wako pure chemical industries, Ltd., Japan) for measuring urease activity.

Besides, syringe sand solidification tests were conducted using the extracted crude enzyme and successfully obtained the cemented sand specimen in a laboratory scale up to several MPa, which could be a mimic of natural beachrock. The findings of these studies could play a significant role in the development of bio-cemented sand (natural beachrock imitation) using low-cost plant-derived urease enzyme. Moreover, it could also be possible to recycle waste food waste materials like watermelon seeds.

METHODS

Extraction of crude urease

Finely crushed and blended watermelon seeds (0.5 g) using 10 mL of distilled water (concentration estimated 50 g / L) stirred at 600 rpm for around 1 h. The crude extract was collected after centrifugation and filtration. After centrifugation, the collected transparent supernatant and pellets were used to investigate the urease activity considering different environmental parameters (temperature, pH, etc.) followed by the indophenol method [8], [9]. The extraction procedure presented in Fig. 1. The urease activity of the enzyme (crude extracts) solution was calculated by dividing the slope of the initial linear part of the ammonium

corresponds to time curve. Finally, to validate the data, the urease activity was compared to available commercial urease enzymes (jack bean, Wako pure chemical industries, Ltd., Japan).

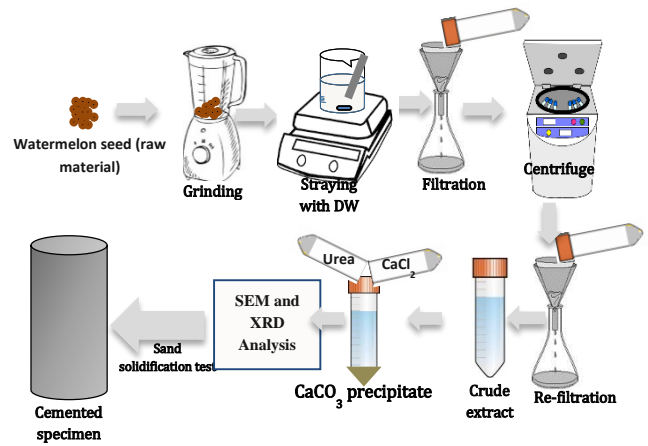


Fig. 1 Extraction procedure of crude enzyme for making artificial beachrock

CaCO_3 precipitation test

A series of experiments were conducted to confirm the morphology of CaCO_3 precipitation and its precipitation trend, by various combinations of CaCl_2 -urea and urease. The set of experiments conducted in transparent polypropylene tubes. 10 mL of equimolar solutions of CaCl_2 -urea was formulated as 0.3 mol/L, 0.5 M, and 0.7 M and adjusted the concentrated distinctly by adding crude extract solution from watermelon seed. The adjusted solution was then added to the test tube and kept in a shaker at 30 °C for 48 h. The obtained precipitation (CaCO_3) was separated from the solution using a filter paper (Whatman filter paper, grade 4) and kept in an oven drier for about 24 h at 100 °C. The crystal precipitation ratio (%) was calculated by the mass of the precipitated materials obtained from the test divided by the theoretical mass of CaCO_3 (g) crystals. The sand solidification testing conditions were shown in table 1.

Table 1: Testing conditions

Control				
Urea- CaCl_2 (M)	0.3/0.5/0.7 M	0.3	0.5	0.7
Enzyme Solution	No	Yes	Yes	Yes
Initial pH	7.5/7.6/7.6	7.6	7.7	7.6
Final pH	7.5/7.6/7.7	7.9	8.1	7.9

The hydrolysis rate was measured immediately after mixing of solutions with time, and a standard

curve was established using the obtained results after complete hydrolysis of several concentrations of urea. Finally, precipitated CaCO_3 weighed using a scale to calculate the total carbonate precipitate amount. Scanning Electron Microscope (SEM) and X-ray diffraction (XRD) analysis were also conducted to investigate the morphology of the precipitated carbonate.

Sand solidification (syringe) test

Commercially available dried “Mikawa” sand (Fig. 2) placed at 110 °C for 24 h and were then transferred (85 g) into a 50 mL syringe (diameter, $\phi=2.3$ cm, height $h=7.1$ cm) and compacted gently.

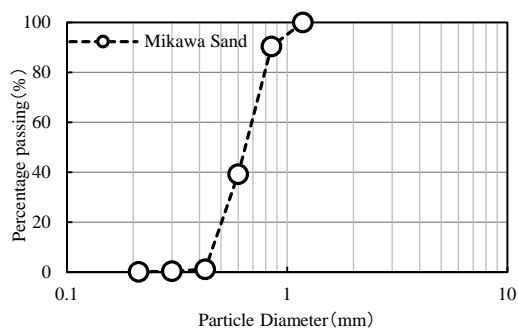


Fig. 2 Particle size distribution of Mikawa sand

The prepared samples were then placed in an incubator (30 °C). Subsequently, 26 mL of prepared urea- CaCl_2 -urease solution (crude extract) was added to the syringe and maintained the final level of the solution above the top surface of the sand sample. After 24 h, a new cementation solution (urea- CaCl_2) was injected into the samples with the same volume and concentration and drained the previously injected solution gradually (Fig. 3). The crude urease injection interval was 48 h. Different curing days were chosen for investigating the effect, variations, and distribution of precipitated calcium carbonate within the sand particles. The condition of the syringe solidification test outlined in Table 2.



Fig. 3 Status of sand solidification test using extracted crude enzyme

Table 2: Testing conditions

Cases	Crude urease	Crude urease Injection interval	Urea- CaCl_2 (M) (added everyday)	Temp (°C)	Curing days
1	No		Control sample		
2	Added	48 h	0.5	30	14
3	Added	48 h	0.5	30	21

RESULTS AND DISCUSSION

Results of urease extraction

A summary of urease activity (U/mL) of the extracted crude enzyme from watermelon seeds presented in Fig. 4. The urease activity was also compared with the commercially available urease enzyme made from jack bean (Wako pure chemical industries, Ltd., Japan). According to the results, the urease activity was highest for non-treated crude extract (around 10 U/mL) and gradually decreased with time (up to 07 days). For the treated sample, the urease activity was somewhat lower than the non-treated sample (8 U/mL) but almost constant with time (up to 07 days).

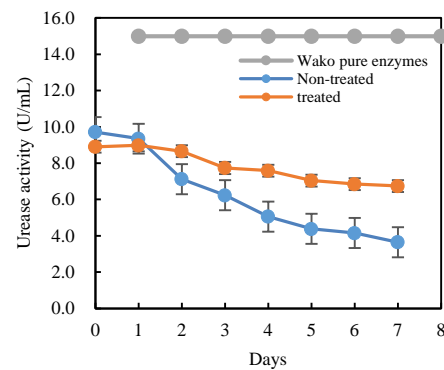


Fig. 4 Urease activity of the extracted solution

For the commercial jack bean urease, the urease activity was observed around 15 U/mL. The purification level of the extracted crude enzyme was around 60-70% (Table 3). The fluctuation of these purification level and urease activity of the crude enzyme to commercial enzyme was influenced by certain metabolic factors [10]-[11] of seeds, including some biological reactions and presence of specific organic compounds. The maximum urease activity was obtained from jack bean seeds, as reported previously [9]-[11]. However, from the findings of this study, the urease enzyme could be extracted up to a purity level of 60 percent, which could be sufficient to make bio-cemented for different geotechnical approaches.

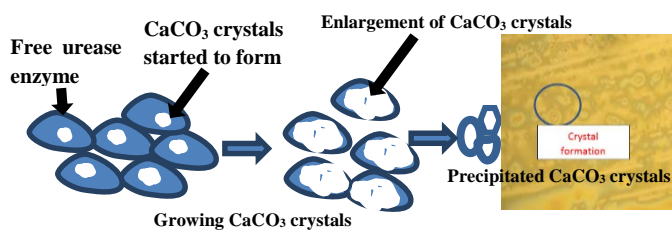
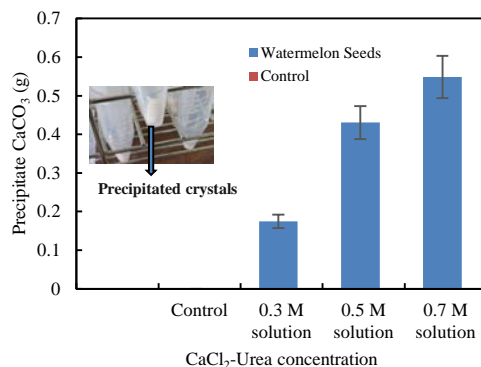
Table 3: Crude urease extraction results with their purification percentage

Product	Urease activity (U/mL)	Volume of extraction (mL)	Total Units (U)	Specific activity (U/mL)	Purification fold	Loss of enzyme (%)
Wako pure enzymes	15	100	150	10	0.67	0
Non-treated	10	100	100	10	1	33
Treated	8	100	80	10	1.25	47

* Loss of enzyme = [Sum of crude extract (U) – Total Units after treatment] / Sum of crude extract (U)]

CaCO₃ precipitation test

It is reported that, CaCO₃ acts as the main binding materials in between the sand particles to stabilize the soil for producing artificial beach rock and bio-cemented sand [12-15]. In EICP process, the crystal precipitation amount closely related with CaCl₂-urea concentration, and the CaCO₃ crystals started to form immediately because of the accessibility of free urease enzyme (Fig. 5), which was also reported by previous studies [16]. Fig. 5 showed the evidence of forming and enlargement of CaCO₃ crystals.

Fig. 5 Growing of CaCO₃ crystalsFig. 6 Trend of CaCO₃ precipitation

It was revealed that, the efficiency of bio-cemented samples depends on the type and structure of the precipitated CaCO₃ polymorphs (vaterite or calcite). When the crystals formed bridges between the existing sand/soil grains, they prevented the movement of the grains, which identified as a primary reason for improving the strength and stiffness of the material [16]. Fig. 6 indicated the trend of CaCO₃ precipitation at different CaCl₂-urea concentration. Results showed that, higher concentration of CaCl₂-urea leads to precipitate higher amount of CaCO₃ crystal.

In addition, from the SEM images it showed that that the precipitated crystals morphology (CaCO₃) is highly inconsistent in shape and size (Fig. 7). But the value for crystals precipitation depends on the concentration of urease enzyme and concentration of reactant solutions, which was also reported in previous studies [17]-[18]. The results of this study showed that, precipitated calcium carbonate crystals from crude extract enzyme may appear as highly disorder and amorphous due to presence or inheritance of different organic compounds confined to the raw materials (crude extract solution from watermelon seeds).

Furthermore, the results also indicated that the reaction rate of EICP process were very fast which leads to precipitated different crystalline phases of CaCO₃ crystals. However, the observation of this study could be considered as significant outcomes for various bio-geotechnical applications.

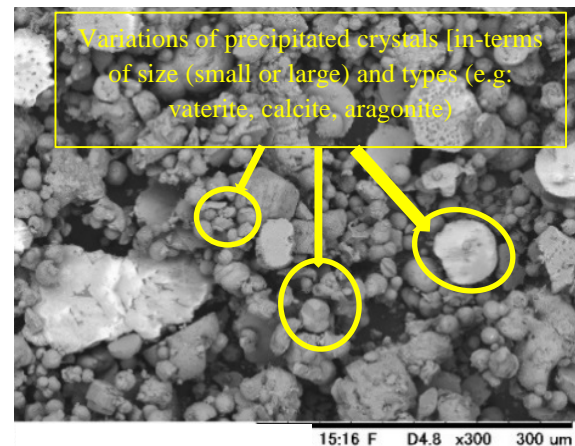


Fig. 7 SEM images of precipitated crystals

Sand solidification test (Small scale)

Mikawa sand was used for sand solidification using the extracted crude solutions from watermelon seeds. From the results, it showed that the higher UCS was obtained for the longest curing sample (case 2) compared with case 1. The variations of the UCS strength was also observed in

top, middle and bottom portions of the both specimens (case 1 and case 2). From the results, it was observed that, the bottom portion showed the higher UCS value compared to top and middle portions of the both treated samples (Fig. 8). The possible reason was the fast reaction rate of the urea hydrolysis and distribution variations of precipitated CaCO_3 within the specimens (case 1 and case 2). Because of the reaction rate, most of the precipitated CaCO_3 tends to deposit at the middle and bottom portion and increased the bonding capacity in between the sand particles at the bottom and middle portion and increased the strength (UCS) (for both case 1 and case 2). But it was also observed that, with increasing the curing time (21 days), the distribution of CaCO_3 precipitation was also fluctuate at the top, middle and bottom portion (case 2) and strength (UCS) was also increased. Further investigation is needed for obtaining homogenous strength of the sample by ensuring uniform distribution of CaCO_3 precipitation.

In addition, another reason could be higher solubility, lower viscosity, fast penetration and deposition at the bottom portion of the sand, which also supported by previous studies [19]-[20]. A higher UCS was also observed obtained (around 1.2 MPa) after continuous curing (21 days) at 2.5% of CaCO_3 for case 2. In case of 1, maximum UCS was obtained (below 1 MPa) with less than 2% of CaCO_3 content and the bottom portion bearing the highest strength Fig. 9. And Fig. 10 also showed the results of the precipitated crystal behaviour in between the cemented sand particles.

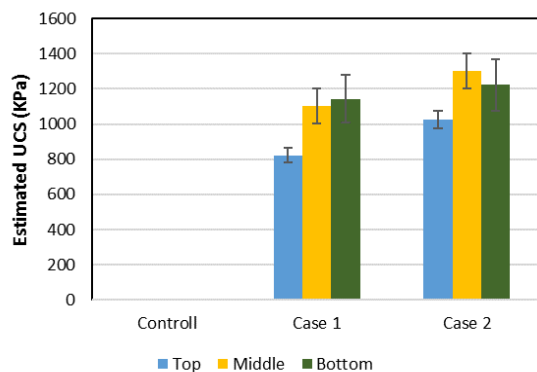


Fig. 8 Estimated UCS of the solidified sand with % of CaCO_3 content

Form the results, it showed that, CaCO_3 is the primary binding materials for improving the strength of sand particles which is an agreement of previous studies [21]. Another important observation was viscosity of the cementation solution could affect the crystal precipitation rate to form CaCO_3 and improving the sand strength to a most stable phase of calcium carbonate. However,

further investigation is needed to improve this methodology, which could be appropriate for field application.

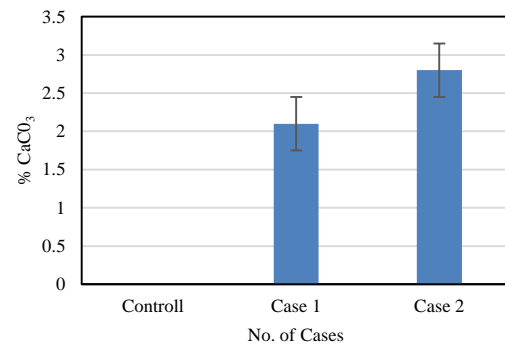


Fig. 9 Percentage (%) of CaCO_3 content of the cemented sand specimen

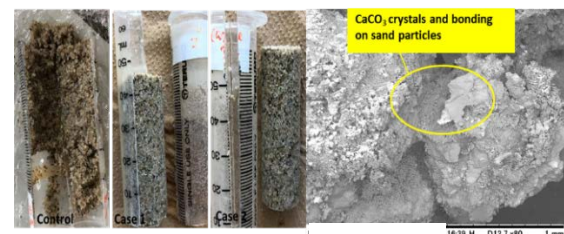


Fig. 10 Status of solidified sand (left images) and SEM images of solidified sand showing the CaCO_3 bonding in between the sand particles (right images)

CONCLUSIONS

The prospect of using the enzyme induced carbonate precipitation (EICP) method as an effective bio-inspired technique has been evaluated in this study using natural source of urease enzyme (watermelon seeds). The development of alternative sources for urease enzymes which are economical and easy to regulate in the natural world was a major problem in the feasibility of calcite Precipitations Strategies. Through extracting the enzyme from watermelon seeds (upto 60% purity level) in a sustainable, cost-effective, and eco-friendly way, this research successfully addressed these challenges. Furthermore, this study successfully obtained solidified sand sample upto 1.2 MPa using watermelon seeds as a source of urease enzyme and the results from this study clearly indicated that, plant derived urease enzymes could play a vital role for making artificial beachrock. However, still some major challenges for field implementations of this EICP method remained in this novel area. Nevertheless, the findings of these studies could play a substantial role for soil/sand stabilization, coastal erosion protection, ground improvement in deeper portion of the soil, improvement of piles and slope stability, to support foundation and

embankment, improvement soils liquefactions under the existing structures and other bio-geotechnical applications.

ACKNOWLEDGEMENTS

This work was partly supported by JSPS KAKENHI, grant number JP19H02229.

REFERENCES

- [1] Lee, Y.S.; Park, W. Current challenges and future directions for bacterial self-healing concrete. *Appl. Microbiol. Biotechnol.* 2018, 102, 3059–3070.
- [2] Dejong, J.T.; Soga, K.; Kavazanjian, E.; Burns, S.; Van Paassen, L.A.; Al Qabany, A.; Aydilek, A.; Bang, S.S.; Burbank, M.; Caslake, L.F.; et al. Biogeochemical processes and geotechnical applications: Progress, opportunities and challenges. In *Proceedings of the Bio- and Chemo-Mechanical Processes in Geotechnical Engineering - Geotechnique Symposium in Print 2013*, 51, 101-109.
- [3] Eberemu, K.J.O.A.O.; Yakubu, T.S.I.S.E.; Sani, E.W.G.J.E. Review of the use of microorganisms in geotechnical engineering applications. *SN Appl. Sci.* 2020, 2, 207–219.
- [4] Danjo, T.; Kawasaki, S. Formation Mechanisms of Beachrocks in Okinawa and Ishikawa, Japan, with a Focus on Cements. *Mater. Trans.* 2014, 55, 3, 493-500.
- [5] Dilrukshi, R.A.N.; Nakashima, K.; Kawasaki, S. Soil improvement using plant-derived urease-induced calcium carbonate precipitation. *Soils Found.* 2018, 58, 894–910.
- [6] El-Hefnawy, M.E.; Sakran, M.; Ismail, A.I.; Aboelfetoh, E.F. Extraction, purification, kinetic and thermodynamic properties of urease from germinating *Pisum Sativum* L. seeds. *BMC Biochem.* 2014, 15, 1–8.
- [7] Natarajan, K.R. Kinetic Study of the Enzyme Urease from *Dolichos biflorus*. *J. Chem. Educ.* 1995, 72, 556.
- [8] Weber, M.; Jones, M.J.; Ulrich, J. Optimisation of isolation and purification of the jack bean enzyme urease by extraction and subsequent crystallization. *Food Bioprod. Process.* 2008.
- [9] Prakash, O.; Bhushan, G. Isolation, purification and partial characterisation of urease from seeds of water melon (*Citrullus vulgaris*). *J. Plant Biochem. Biotechnol.* 1997, 6, 45–47.
- [10] Mendes, M.J.; Karmali, A.; Brown, P. One-step affinity purification of urease from jack beans. *Biochimie* 2003, 70, 1369–1372.
- [11] Fujita, M.; Nakashima, K.; Achal, V.; Kawasaki, S. Whole-cell evaluation of urease activity of *Pararhodobacter* sp. isolated from peripheral beachrock. *Biochem. Eng. J.* 2017, 124, 1–5.
- [12] Kappaun, K.; Piovesan, A.R.; Carlini, C.R.; Ligabue-Braun, R. Ureases: Historical aspects, catalytic, and non-catalytic properties – A review. *J. Adv. Res.* 2018, 3, 3-17.
- [13] Wani, A.A.; Sogi, D.S.; Singh, P.; Wani, I.A.; Shivhare, U.S. Characterisation and functional properties of watermelon (*Citrullus lanatus*) seed proteins. *J. Sci. Food Agric.* 2011, 91, 1, 113-121.
- [14] Mobley, H.L.T.; Hausinger, R.P. Microbial ureases: Significance, regulation, and molecular characterization. *Microbiol. Rev.* 1989, 53, 1, 85-108.
- [15] Dhami, N.K.; Reddy, M.S.; Mukherjee, M.S. Biomineralization of calcium carbonates and their engineered applications: A review. *Front. Microbiol.* 2013, 4, 1–13.
- [16] Baiq, H.S.; Yasuhara, H.; Kinoshita, N.; Putra, H.; Johan, E. Examination of calcite precipitation using plant-derived urease enzyme for soil improvement. *Int. J. GEOMATE* 2020, 19, 231–237.
- [17] Almajed, A.; Tirkolaei, H.K.; Kavazanjian, E. Baseline investigation on enzyme-induced calcium carbonate precipitation. *J. Geotech. Geoenvironmental Eng.* 2018, 144, 1–11.
- [18] Al-Thawadi, S.; Cord-Ruwisch, R. Calcium Carbonate Crystals Formation by Ureolytic Bacteria Isolated from Australian Soil and Sludge. *J. Adv. Sci. Eng. Res.* 2012, 2, 12–26.
- [19] Sun, X.; Miao, L.; Wu, L. Applicability and Theoretical Calculation of Enzymatic Calcium Carbonate Precipitation for Sand Improvement. *Geomicrobiol. J.* 2020, 0, 1–11.
- [20] Dilrukshi, R.A.N.; Kawasaki, S. Sand Cementation Using the pH Dependency of Calcium Phosphate Compounds and the Addition of Various Powders. *Geo-Chicago* 2016, 104–115.
- [21] Kavazanjian, E.; Hamdan, N. Enzyme induced carbonate precipitation (eicp) columns for ground improvement. In *Proceedings of the Geotechnical Special Publication*; 2015, 256, 2252–2261.

STUDY ON STRUCTURAL EFFECTIVENESS OF A BUILDINGS STRUCTURE BY USING A CFRTP

Yasuhide Mochida¹, Kouhei Kasahara²

¹Professor of Department of Architecture and Urban Design, Graduate School of Science and Engineering, Ritsumeikan University, Japan; ²Master Degree Student of Department of Architecture and Urban Design, Graduate School of Science and Engineering, Ritsumeikan University, Japan

ABSTRACT

At present, carbon-fiber reinforced plastics (CFRP) are not permitted to be used as structural members in the architectural field. Therefore, in order to popularize CFRP in the architectural field, this study aims to show the usefulness of CFRP (CFRTP) using thermoplastic resin, which is inexpensive to manufacture and excellent in recyclability among CFRP, and evaluates the effectiveness when CFRTP strand rods are used for bracing material. As a result of comparing by eigenvalue analysis using round steel, PC steel stranded wire, and CFRTP for braces, the long period was able to be confirmed by the use of the frame of CFRTP brace. Then, this paper carries out comparisons by time history response analysis between a seismic resistant model using a three-dimensional frame model and a seismic isolation brace model using a CFRTP brace and an oil damper in the lowest layer. As the result, it was proven that the isolation brace showed the reduction performance equivalent to the conventional isolation device for the input seismic motion.

Keywords: carbon fiber reinforced thermo plastics, strand rod, brace of isolation, seismic isolation layer

INTRODUCTION

Carbon-fiber reinforced plastics (Carbon Fiber Reinforced Plastics: CFRP) are materials utilized in various fields because of their excellent properties such as light weight, high strength, corrosion resistance, and non-magnetism. Among them, a CFRP using a thermoplastic resin (Carbon Fiber Reinforced Thermo Plastics: CFRTP) as a base resin can be produced at a lower cost than a CFRP using a thermosetting resin which is generally popular, is easy to carry, and is also excellent in recyclability because it can be separated by heating a base material and a carbon fiber. Therefore, it is a material which can also be expected to be popularized in the architectural field in the future. However, CFRP is currently used in the civil engineering field as a substitute for reinforcing bars and carbon-fiber sheet wrapping reinforcement method, etc., but its use for structural members is not permitted because it is not designated as a designated building material under Article 37 of the Building Standards Construction Law in the architectural field, and it has not generally become popular.

This study aims to evaluate the effectiveness of CFRTP strand rods for buildings when they are used as brace materials by referring to the use method of PC (Prestressed Concrete) steel materials, and to examine their application to the seismic isolation device "seismic isolation brace" (Fig. 1) of brace frames as an application method suitable for strand

rods, and to contribute to the popularization of CFRTP in the architectural field.

The structural analysis software midas iGen was used for the analysis of this study.

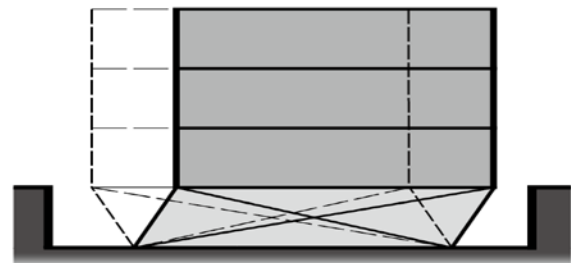


Fig. 1 Seismic isolation

STUDY ON TWISTING PERFORMANCE OF CFRTP

In the bonding method of CFRTP using the inner thread cutting steel pipe by previous studies, the adhesion force between the adhesive resin is increased by using a member obtained by adding twisting, it has been confirmed that the advantage that the tensile stiffness of the joint is increased can be obtained. Therefore, in this chapter, we derive the equation for evaluating the twist angle of CFRTP strand rods and the tensile stiffness and tensile strength of members, and clarify the relation between them. (1a), (1b) The equation is the 2) of the equation for evaluating the twist angle of the strand rope of the steel material.

$$E_w = E(\cos^3 \alpha - \nu \sin^2 \alpha \cos \alpha)(\cos^3 \beta - \nu \sin^2 \beta \cos \beta) \quad (1a)$$

$$P_w = m \cdot n \cdot EA(\cos^3 \alpha - \nu \sin^2 \alpha \cos \alpha)(\cos^3 \beta - \nu \sin^2 \beta \cos \beta) \varepsilon_z \quad (1b)$$

E_w : Young's modulus of member

P_w : Axial force of child wire (steel)

α : Strand angle of strand

β : Twist angle of child wire

E : Young's modulus of the child line

ν : Poisson's ratio of the child line

m, n : $m \times n$ strand ropes

When this equation is adapted to CFRTP strand rods, the equation for evaluating tensile stiffness and tensile strength is as follows.

$$E_c = E(\cos^3 \beta - \nu \sin^2 \beta \cos \beta) \quad (1c)$$

$$\sigma_{c \max} = \frac{\sigma_{s \max}}{\cos^3 \beta - \nu \sin^2 \beta \cos \beta} \quad (1d)$$

E_c : Young's modulus of CFRTP strand rod

$\sigma_{c \max}$: Breaking strength of CFRTP strand rods

$\sigma_{s \max}$: Breaking strength of the strands

(1c), (1d) From the equation, the relationship between the twist angle and Young's modulus using the physical properties in Table-1 and the breaking strength is shown in the graph as shown in Figure-2.

Table 1 Physical Properties of Strand Rod

Young's modulus of the child wire(kN/mm ²)	94
Breaking Strength of Wire(N/mm ²)	1644
Poisson's ratio	0.06

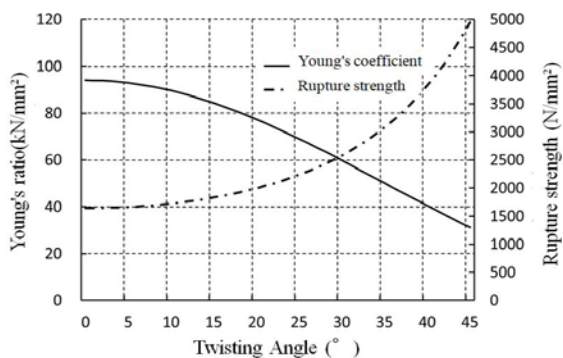


Fig. 2 Relationship between twist angle and physical properties

Young's modulus viewed the property of decreasing as the twist angle increases, the result that the strength increases as the twist angle increases conversely with respect to the breaking

strength.

Further, the value of the twist angle 14.7° obtained from the evaluation equation is a result which is not large difference even compared with the value of the experimental value measured from the test piece of the same twist angle, it was confirmed that the evaluation formula can be used roughly.

COMPARATIVE STUDY OF PRESTRESSING STEEL BY NUMERICAL ANALYSIS

Outline of the Analysis Model

The effect of prestressing steel and the change in deformation performance and natural period due to prestressing force are verified when CFRTP strand rods are used with braced members in Table-2 and when prestressing steel stranded wires or round steel are used for the steel frame validation model shown in Fig. 3 with a span of 8000mm and a height of 3500mm. Incidentally, since CFRTP is a material having a property of brittle fracture without plastic zone, this analysis is to consider only the elastic range, the braced section was set to stay in the elastic zone.

Table 2 Comparative brace member

Types of Braces (naming)	Young's coefficient (kN/mm ²)	Strength of yield point (N/mm ²)	Diameter (mm)	Tension force (kN)
Round steel (SS400)	205	235	27	0
PC steel wire (SWPR7B)	200	1583	10	0 61
CFRTP(24 K3P×7)	85	1629	10	0 61

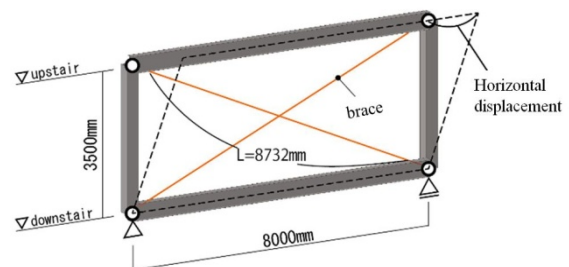


Fig. 3 Analysis model

Static Analysis

In the static analysis, the horizontal displacement was confirmed by applying a horizontal load of

100kN to the model upper beam. Figure 4 shows the results.

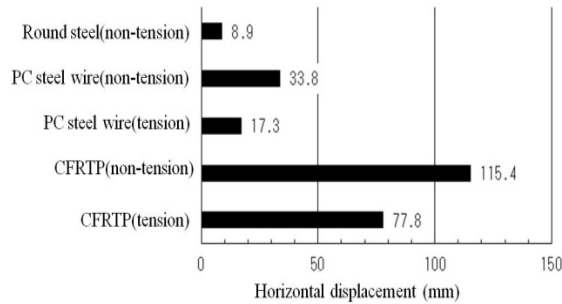


Fig. 4 Horizontal displacement of the model

As shown in Fig. 5, CFRTP with the smallest axial stiffness had the greatest displacement, and in the same member, the displacement became smaller because both the tension side and the compression side braces resisted the horizontal force by introducing the prestressing force.

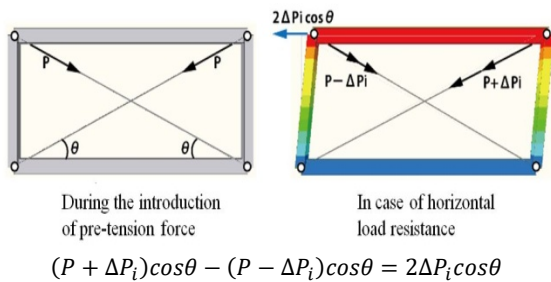


Fig. 5 Concept of Horizontal Resistance

Eigenvalue Analysis

As shown in Table-3, the natural period is longer in the order of CFRTP, PC-steel stranded wire, and round steel. In the case of the tensioned steel and the non-tensioned steel, the horizontal stiffness of the frame increases due to the introduction of tensioned force. Therefore, the natural period of the non-tensioned steel model is longer, and the natural period of CFRTP is 1.93s at the highest. From this, it was clarified that the long period of the frame could be attempted by the utilization as a bracing member in CFRTP of non-tension.

Table 3 Natural Period

Bracing member	Fixed cycle (s)
Round steel(non-tension)	0.46
PC steel wire(non-tension)	1.26
PC steel wire(tension)	0.89
CFRTP(non-tension)	1.93

CFRTP(tension)

1.37

EXAMINATION OF SEISMIC ISOLATION BRACES ALONE

Outline of Analysis

In this analysis, time calendar response analyses were carried out by changing three types of parameters such as span length (2000-6000mm in every 1000mm), brace cross section (9, 10, 16mm in diameter), and twist angle of brace (14.7°, 30°) of the framing model as shown in Fig. 3 to clarify the relationship between the critical horizontal displacement, brace proof stress usage rate, natural period, maximum acceleration of the upper beam, and horizontal stiffness, and to examine the shape of the brace frame suitable for seismic isolation braces. The time calendar response load used Tohoku1978 NS seismic waves as the maximal acceleration of 500gal.

Analysis Results

Span Length (Fig. 6, 7)

The critical horizontal displacement became comparatively large in the models of 2000mm span and 6000mm span. This increases the aspect ratio of the frame, especially in the case of short spans, and the horizontal displacement increased because the large effect of the brace deformation on the column. Also, if the span is long, the axial stiffness decreases due to the length of the brace and the amount of deformation increases. (Fig. 6)

For the bearing capacity utilization factor (= sectional force/breaking load) of the brace member, it was kept relatively small at 2000 and 6000mm spans, but no large difference between spans was observed. (Fig. 6)

Although the natural period is influenced by the aspect ratio of the frame and the axial stiffness of the brace, the natural period tends to be longer as the span becomes longer as a whole model comparison. Since the maximum acceleration of the upper beam is affected by the natural period, the longer the span and the longer the natural period, the smaller the maximum acceleration can be suppressed. The horizontal stiffness of the model became larger for the longer span, because the angle of the brace faced horizontally as the span became larger. (Fig. 7)

From the above, it is said that a frame with a long span is suitable, considering the appropriateness of the seismic isolation brace from

the viewpoint of the span length.

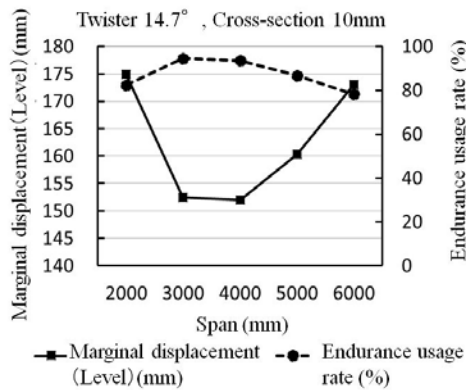


Fig. 6 Comparison result by span ①

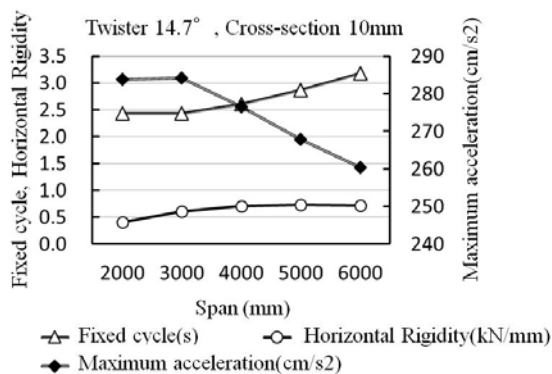


Fig. 7 Comparison result by span ②

Brace Section (Fig. 8)

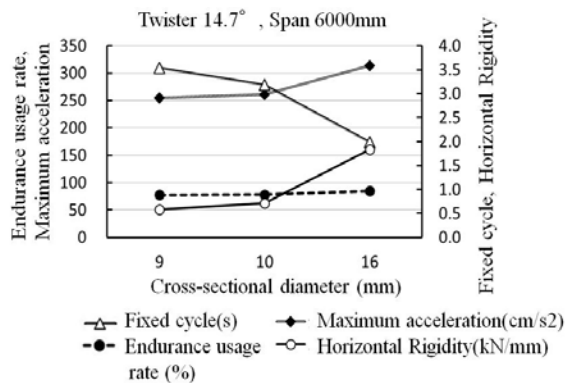


Fig. 8 Comparison results by cross section of brace

The larger the cross section, the higher the axial stiffness and the horizontal stiffness of the frame, and the shorter natural period was shown. On the other hand, the smaller the axial stiffness, the longer the natural period and the smaller the horizontal stiffness.

The maximum acceleration of the upper beam becomes smaller with the model of small section with longer natural period.

Though the proof stress utilization factor of the

brace member tends to increase slightly as the cross section increases, there was no big difference. The phenomenon in which the use rate is kept to the same level in each section is thin.

It is considered that the brace has a softer structure as the whole frame, and the axial force borne by the brace material is small. Therefore, the smaller the cross-section of the brace, the better its performance as a seismic isolation device.

Brace Twist Angle (Fig. 9)

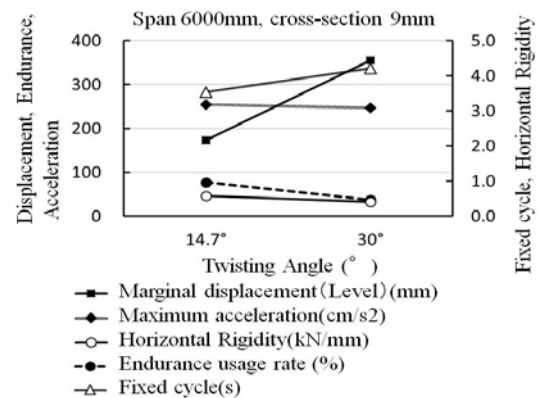


Fig. 9 Comparison Results by Twist Angle

As shown in Chapter 2, the strength of the member is increased by increasing the twist angle. It has been found that there are physical property changes of degree increase and rigidity decrease. Therefore, the critical horizontal displacement of the bracing material was higher at a twist angle of 30° with a lower Young's modulus and higher fracture strength, and the intrinsic period was longer, resulting in a lower strength utilization rate of the bracing material. And, the maximum acceleration was reduced by the longer natural period, and the horizontal stiffness lowered.

It can be said that using a strand rod with a large twist angle becomes a long period and is suitable for seismic isolation.

EXAMINATION IN STEREO FRAME MODEL

Outline of Analysis

In the five-story stereoscopic frame model, this paper carries out time calendar response analysis using a seismic resistant structural model of S pure rigid frame and a model incorporating a seismic isolation brace in the same model, and evaluates the performance as a seismic isolation device of seismic isolation brace from each response value.

A model of 3500,4500mm was set for the first floor height. Referring to the results of Chapter 4, which showed high seismic isolation performance, the span was set to 6000mm, and two CFRTP strand rods with a twist angle of 30° were used for the braces at 9mm and 10mm diameters. In addition, an oil damper is incorporated in the seismic isolation brace model, and the performance is shown in Tab.6.

There are a total of six types of analytical models according to the height of the first floor, the structure, and the diameter of the strand rod, as shown in Table-5.

Five types of El Centro1940 NS, Taft1952 EW, Hachinohe1968 NS, Tohoku1978 NS, JM-Kobe1995 NS seismic waves (Fig. 10) were adopted as time calendar response loads, and time history response analyses were carried out for each seismic wave. The seismic waves were used in the X - and Y - axis directions as the maximum acceleration of 500gal.

Table 4 Oil damper performance

Type	Oil damper
Company	Kayaba System Machinery, Inc
Product	BDS model 500kN stroke500-1400
Model number	BDS901400-L-4
Initial attenuation coefficient	0.25kN * s/mm
Spring rigidity	155kN/mm

Table 5 List of Analysis Models

Model symbol	Format	Brace section	Dam per
3.5-	earthquake-resistant	—	—
3.5-9d	seismic isolation braces	9 mm	○
3.5-10d	seismic isolation braces	10 mm	○
3.5-	earthquake-resistant	—	—
4.5-9d	seismic isolation braces	9 mm	○
4.5-10d	seismic isolation braces	10 mm	○

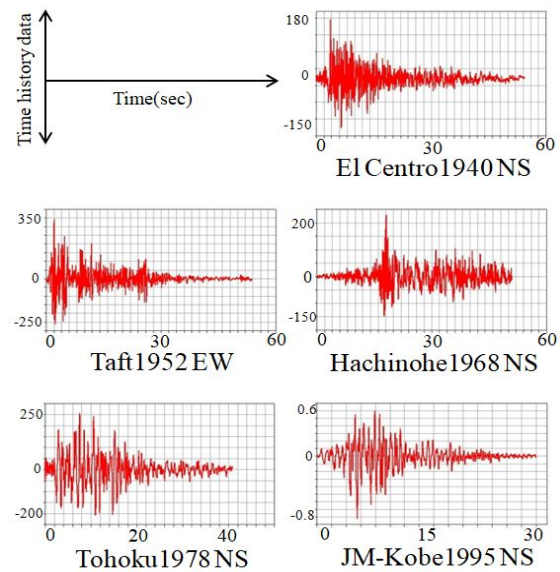


Fig. 10 Waveform of input seismic wave

Analysis Results

The natural period was lengthened to 3.7-4.6 s for the seismic isolation model, compared to 0.8-1.0 s for the seismic model (Fig.11). The maximum acceleration is also amplified in the upper floors of the seismic isolation model, whereas the maximum acceleration in the upper part of the seismic isolation bracing model is In terms of structure, it is possible to reduce the earthquake motion by 50-60% of the input motion, which is about the same as that of ordinary seismic isolation devices such as laminated rubber(Figs.12 and 13). The interlaminar deformation angle is more than 1/200 for the seismic structure model, while the seismic isolation brace model is more than 1/200. For each model, for the 2-5 floors above the seismic isolation layer, about 1/750 in the X-axis, 1/600 in the Y-axis It was reduced to the extent (Figs. 14 and 15).

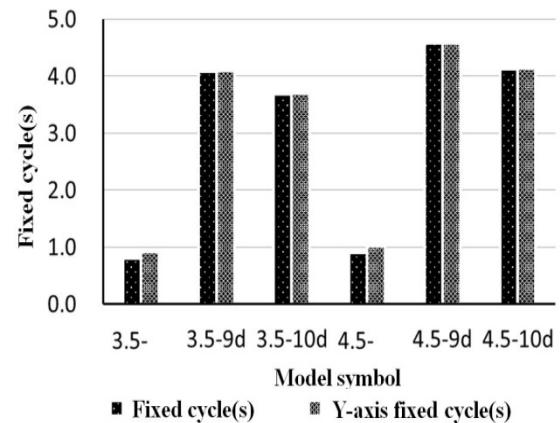


Fig.11 Eigenfrequency of each model

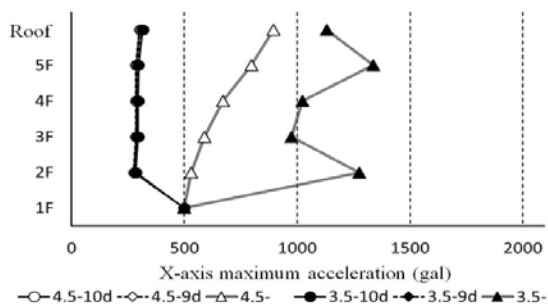


Fig.12 X-axis maximum acceleration

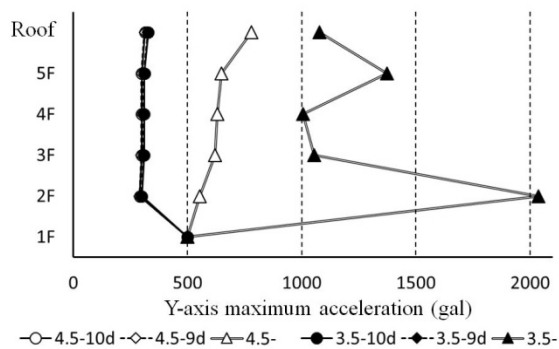


Fig.13 Y-axis maximum acceleration

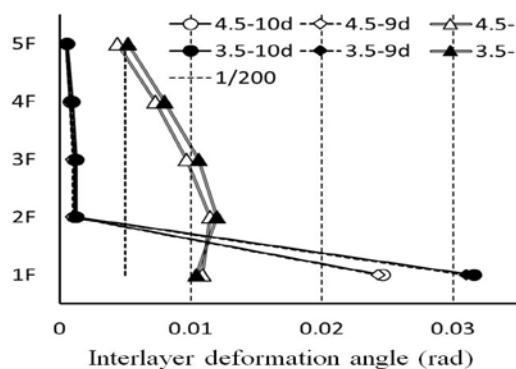


Fig.14 X-axis interlayer deformation angle

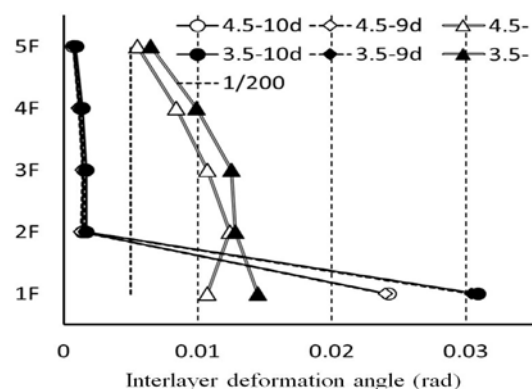


Fig.15 Y-axis interlayer deformation angle

SUMMARY AND CONCLUSIONS

In order to show the usefulness of CFRTP, this study examined the performance of CFRETP and evaluated the performance when CFRTP was used as bracing material.

The equation for evaluating Young's modulus and twist angle of CFRTP was derived, and it was proven that the Young's modulus decreased and the rupture strength increased as the twist angle increased for CFRTP strand rod.

When CFRTP was used for the brace frame, it was more rich in deformation performance than the steel material, and the natural period became comparatively long, and it came to the application as a seismic isolation brace.

By the examination in the seismic isolation brace single body model, the result was that the shape of the seismic isolation brace has the aspect ratio of 1 or less, the brace member is long and thin, and the seismic isolation performance is improved as the twist angle is bigger.

When a seismic isolation brace was incorporated into a three-dimensional model of a five-story S structure, it was possible to make a four-second seismic isolation in which the maximum acceleration was reduced to 50-60% of the vibration at the time of input, but the point that the deformation of the first layer, which is a seismic isolation layer, becomes larger than the seismic structure is a problem. And, it was proven that security of the floor height of the base isolation layer and small section of the member were effective in order to suppress the proof stress use rate of the brace material.

REFERENCES

- [1] Toyo Maeda, Kozo Kimura: Cutting-edge p213-216 of carbon fiber, 2007.1.
- [2] Shizuo Shimada: Deformation and Stress of Elastic Wires, Society of Civil Engineers, 1961, 72Appendix1, p. 1-16, 1961.
- [3] Naoaki Hamada: Construction of External Seismic Reinforcement Work for School Facilities Using Oblique PC Steel Materials, p.377-378, 2010.10.
- [4] Kunio Saito, Akira Okada: Challenges and Development of Cable Structure in Architecture, p1-4, September 1994
- [5] Hiroshi Sakata and Mikio Kodama: 8. Case Study (4): PC with Special Materials, p43-44

- [6] Naaki Hamada: Construction of external seismic reinforcement of school facilities using slanted PC steel, p.377-378, 2010.10
- [7] Tensile Test Results: Better Living, 2013.5, General Foundation
- [8] Architectural Society of Japan: Cable Structural Design Guidelines and Explanations, p85-87, June 1994.
- [9] Shizuo Shimada: Deformation and Stress of Elastic Wires, Society of Civil Engineers, 1961, 72Appendix1 p.1-16,1961
- [10] Shimadzu Test CSC News No. 270, 2007, Applied Technology Department, Analytical Measurement Division, Shimadzu Works.

UTILIZATION GGBFS AS CEMENT SUBSTITUTION TO REDUCE PRODUCTION COST OF CONSTRUCTION PROJECT

Ranti Hidayawanti¹, Yusnita Rahayu², Soetjipto Soewono³, Fahdun Ibnu Wachid⁴ and Rony Panca Adi Widodo⁵

^{1,2}Faculty of Territorial Science Engineering, Institut Teknologi PLN, Indonesia; ³Faculty of Electricity and Renewable Energy, Institute Technology PLN, Indonesia; ⁴PT PJB, Indonesia; ⁵Adhimix RMC, Indonesia

ABSTRACT

The development of construction is currently advancing rapidly, the positive and negative impacts of the construction of this construction can begin to be felt. One negative impact is the reduction in natural resources that can not be renewed as the main material for development, for example limestone as the material for cement. It is well known that concrete is a building material and as an effort to meet high quality concrete, a good compiler is also needed. Various kinds of research and experiments have been carried out to improve the quality of concrete. Starting from the addition of additives, concrete treatments, improving the quality of concrete materials and the utilization of industrial waste as a concrete reinforcement mixture. This study aims to utilize waste from burning iron, namely Grand Granulated Blast Furnace Slag (GGBFS) or cement slag. GGBFS can be used for concrete mixes because it has almost the same properties as cement, C_3S_2 which can increase the elasticity and reduce the heat of hydration in concrete. GGBFS is used to replace some of the fine aggregate in concrete that aims to determine the extent of its effect on compressive strength of the high quality of concrete. The composition of substitution of fine aggregate with GGBFS is 0%, 25%, 50%, 75% of the volume cement. The method be used is initial setting time, compressive strength, linear regression and slag activity index. Based on research result initial setting time increases with a variation of 75%, for the optimum compressive strength test GGBFS in this mixture of 75%, linear regression reaches a value of 0.9781 with a category of strong relationship and applicable as well as slag index activity values enter grades 100 and 120 approaching OPC 100. Beside that GGBFS is very good to be used as a substitute for some cement in concrete and can also reduce production cost 3% and environmentally friendly.

Keywords: GGBFS, Cement, Concrete, Compressive Strength, Production Cost

INTRODUCTION

In the development world of construction, most building compilers are concrete. For examples road infrastructure, buildings and many more and encourage us to be able to maintain the quality of the concrete. Concrete is very popular because the basic materials are easily obtained from natural resources and easy to use. Along with the development of concrete material needs, the need for cement which is becoming scarce and expensive is needed for innovation to develop technology including utilizing industrial waste. For examples GGBFS (ground granulated blast-furnace slag) or cement slag. GGBFS according to ACI 233R-95 [1], is a slag furnace of metal or iron with a temperature of about 1500° C. GGBFS is used to make strong and durable concrete structures that can be combined with ordinary Portland or other pozzolan materials. When cement is blended with slag, it modifies mineralogical distribution and surface electrical properties, increases tortuosity, and reduces porosity and threshold pore size to show high chloride resistance and better durability performance[2]. In developed countries the use of Concrete Slag has been used, but in Indonesia not all constructions have implemented

concrete slag waste. Utilization of industrial waste in the construction sector is used to improve the quality and compressive strength of concrete because it contributes to reducing the use of natural resources. 70% of construction materials are concrete [3]. With the utilization of concrete slag can reduce the potential loss or save money of construction companies [4]. The purpose of this research is to measure the utilization of GGBFS with variations of 0%, 25%, 50% and 75% in the quality of K200 - K700. From this variation, will be chosen the optimum one for Tokyo Apartment construction. From the laboratory test results, it is recommended to utilize GGBFS with a variation of 25% with the quality of the K400.



Fig.1 Tokyo Apartment Project using GGBFS

Figure 1 shows The Tokyo Tower Apartment construction project is owned by PT Agung Sedayu Group (ASG) and is carried out by PT Multikon, PT Rekaguna Teknik and PT Pulau Intan, with an implementation time of 356 (three hundred and fifty six) calendar days starting on 1 August 2019. The Tokyo Tower Apartment construction project was carried out by 6 towers in advance with 2 towers from each contractor, of which 5 towers will be carried out after the 3rd quarter of 2020. The land area of 35.000 m² and the volume of concrete for 6 towers 300.000 m³, foundation work 56.000 m³, has a contract value of 1.5 trillion rupiah. To minimize the need for cement which has a higher price, it is necessary to innovate to substitute cement with other materials without reducing quality.

In designing concrete used for high-rise buildings, good quality is needed to meet the specifications including the quality of the K200 - K700 concrete. This compressive strength calculation is supported by other formulations such as initial setting time (w/c), slag index activity and linear regression.

TOOLS AND MATERIALS

To support the fulfillment of concrete needs, the material used are as follows :

- GGBFS Slag : ex. PT. KSI
- Natural Sand : Ex Belitung
- Coarse aggregaten10-25mm : ex. Purwakarta
- Admixture Type F : Standard Adhimix
- Cement : Type 1 (OPC) and water : Concrete Standard



Fig. 2 Materials Research

Tools need that are used as follows :

- Mortar Mixer : 1 Unit
- Mortar Cube Mold 5x5x5 cm : 12 set @ 3 ea
- Mortar Flow Test : 1 Set
- Cylindrical Mold D15 X h30 cm : 40 ea
- Compressive Strength equipment



Fig. 3 Required Tools

Figure 3 shows some of the tools that used in the experiments of mortar and concrete specimens.

METHODOLOGY

Experiments carried out at the laboratory scale include mortar cube experiments and concrete experiments using a small mixer with a capacity of 100 liters. Variations in mortar experiments are with a mixture of GGBFS 0%, 25%, 50% and 75%. While the concrete experiment was carried out looking for the correlation w/c (cement water factor) to the percentage of GGBFS use is w/c K200 – K700.

To find out the quality of GBFS in addition to direct testing of the slag material both physical and chemical testing, a comparison method is also performed. By conducting laboratory scale experiments on cube compressive strength of 5x5x5 cm, which refers to ASTM-C 109 Standard Test Method for Compressive Strength of Hydraulic Cement Mortars [5]. As well as the compressive strength of concrete cylinders 15 x height 30 cm which refers to ASTM-C39 [6] Standard Test Method for Compressive Strength of Cylindrical Concrete Specimens. Furthermore, applying Slag index activity and linear regression.

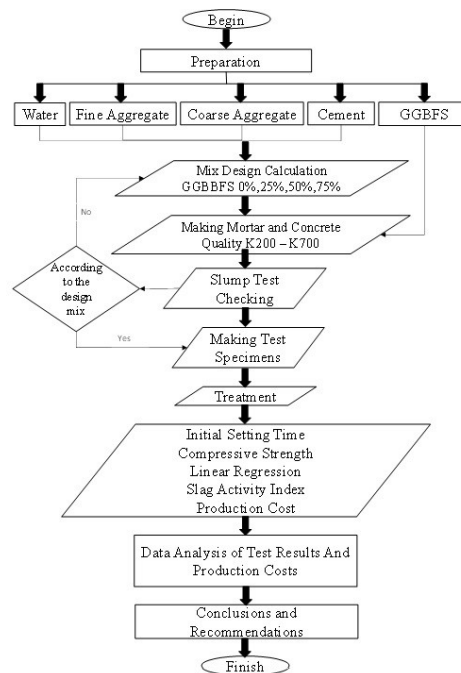


Fig. 4 Research Methodology

RESULT

Mortar Experiment

The results of mortar experiments conducted 3 (three) times obtained the following average data as follows :

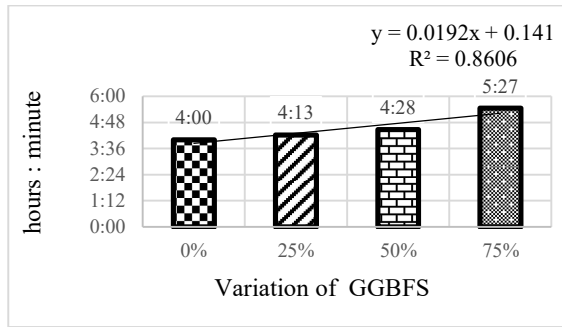


Fig. 5 Initial setting Time of Mortar

From figure 5 shows the addition of GGBFS has the effect of increasing the initial setting time, as the greater use of GGBFS the longer the initial setting time.

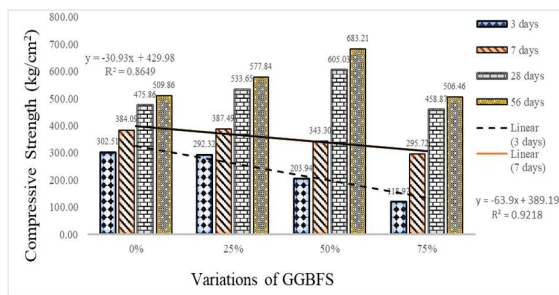


Fig. 6 Mortar Strength Mortar Comparison

Figure 6 shows, the greater the use of GGBFS, the compressive strength at the age of 3 and 7 days are resulting lower, but at the age of 28 days there was a significant increase can even exceed 100% OPC so that will influence the value of linear regression. At the age of 28 days and 56 days the need for water is greater so using slag is not recommended.

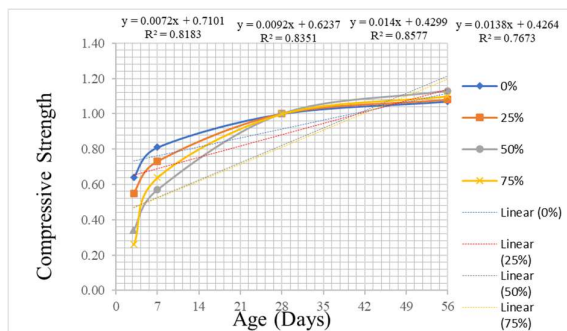


Fig. 7 Development of Mortar Strength

Figure 7 shows, The development of compressive strength using GGBFS at the age of 3 and 7 days is very slow compared to 100% OPC. With the development of a 50% variation the regression value reached 0.8577, meaning that the strong relationship between mortar age and compressive strength can be used. The linear regression formulation is as follows:

$$Y = a + bx \quad (1)$$

a = water requirement (ltr/m³)

b = w/c

determination coefficient of the correlation relationship is formulated:

$$r^2 = \frac{a(\sum y) + b(\sum xy) - n(\bar{y})^2}{(\sum y^2) - n(\bar{y})^2} \quad (2)$$

coefficient value of relations

0 = no relation

1 = perfect relation

Concrete Experiment

The results of concrete experiments using variations of GGBFS compared to 100% OPC are as follows:

$$\text{Compressive strength} = \frac{P}{A} \quad (3)$$

f'c = Concrete compressive strength (Mpa)

P = maximum load (N)

A = press area of test object (mm²)

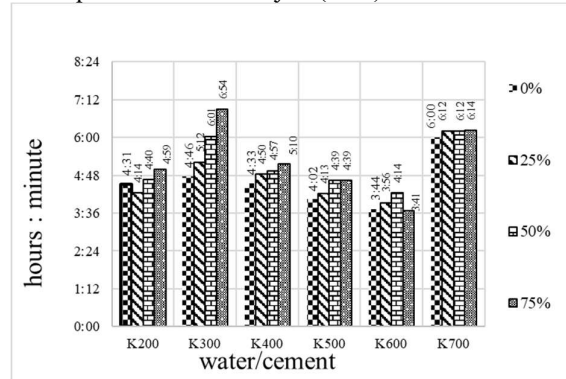


Fig. 8 Initial setting time of Concrete

Figure 8 shows, The use of GGBFS has a tendency that the initial concrete setting time will increase by an average of 30 minutes. Although the data does not show a clear pattern and some data shows the opposite, namely in w/c sample K200 for GGBFS 25% and w/c sample K600 GGBFS 75%. The greater the use of GGBS the smaller air needed to get the same working / slump ability. It can be seen that the greater quality of concrete the smaller initial setting time since the achievement of GGBFS is greater and the requisite for cement is smaller so that the binding time of concrete is lower.

From Fig. 8 for water per cement (W/C) is not too significant because the addition of water to cement for each constant quality is between 10-20 liters.

Before making a testing sample or printing a test sample on a cylindrical mold, a slump test is needed so that the researcher can find out how much water is needed in a concrete mixture. The effects of combinations of mineral admixtures in concrete on the performance-related properties under different aspect ratio are compared to conventional concrete[7]. The following are the results of water needs and slump tests:

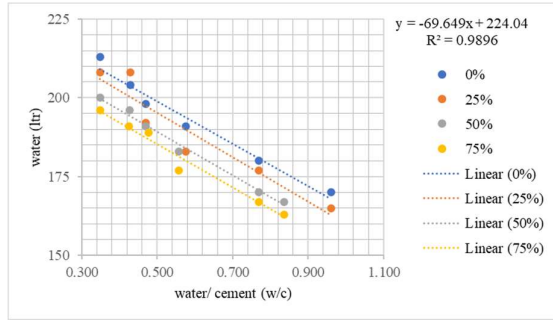


Fig. 9 Water requirements perm³, slump 12cm, size 25mm

Figure 9 shows, the greater the use of GGBFS the less water needs to get the same workability / slump. With the utilization of GGBFS 50%, the greater the water/cement used, the less water used and the results of the linear regression show the value of 0.9896 means that it has a strong relationship and can be used[8].

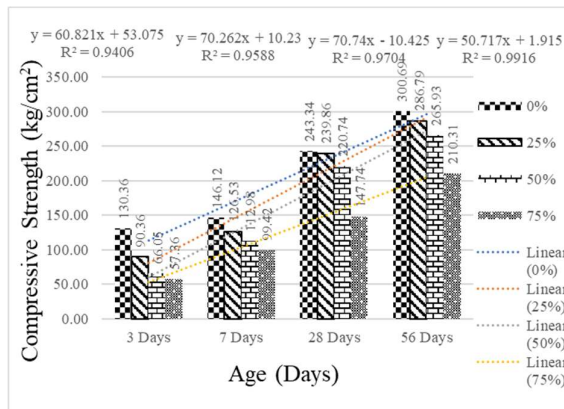


Fig.10 Quality of Compressive Strength (K200)

The greater the use of GGBFS, the compressive strength produced is lower, especially in the early age. But the development of compressive strength increases every time, this can be seen from the graph above. For K200 quality, the utilization of GGBFS can use a Slag mixture with a variation of 0%, 25% and 50%, a variation of 75% does not meet the compressive strength and does not reach the required compressive strength.

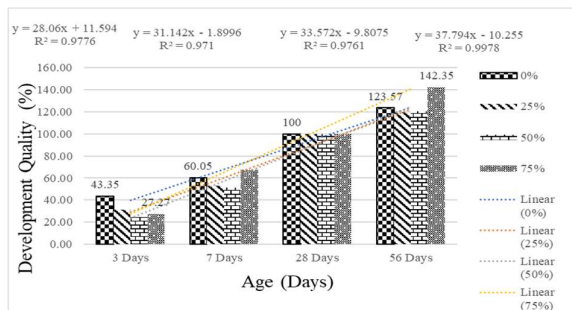


Fig. 11 Development of Quality Concrete (K-200)

Figure 11 shows, the percentage achievement of 28 days of age varies 0% -75% in accordance with the requirements for compressive strength but for 75% variation the use of slag is not recommended because the compressive strength does not meet the specifics even though the percentage is 100%.

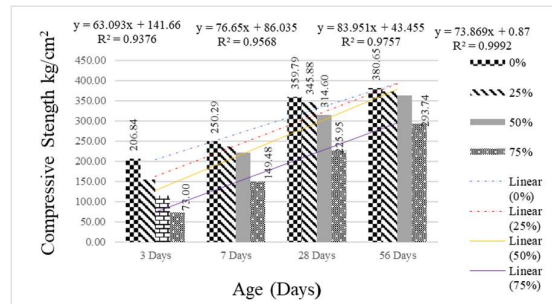


Fig.12 Quality of Compressive Strength (K300)

Based on the results of the compressive strength test of K-300 concrete quality, it can be seen that in each test 3 days, 7 days, 28 days and 56 days the compressive strength of concrete has decreased every additional variation in the percentage of GGBFS substitution for cement. At the age of 28 days, the quality of K300 using GGBFS can use a mixture of Slag with a variation of 0%, 25% and 50%, the variation of 75% does not meet the compressive strength and does not reach the required compressive strength. This can be seen at the age of 28 days, the compressive strength value of 0% variation is 359.79 kg / cm², GGBFS variation 25% = 345.88 kg / cm² and 50% GGBFS variation 314.60 kg / cm², while the 75% variation in compressive strength value decreases 225.95 kg/cm² and not included in the category required.

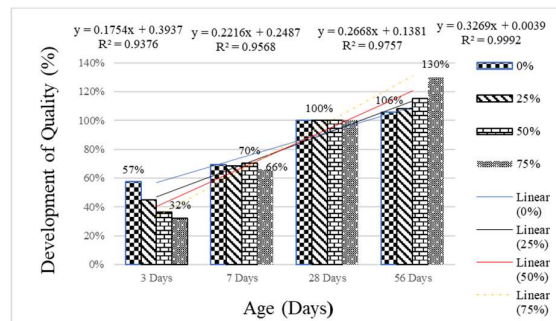


Fig.13 Development of Quality Concrete (K-300)

Figure 13 shows the development of compressive strength increases every time, this can be seen from the graph above. The achievement of the percentage of 28 days of variation 0% -50% meets the requirements for compressive strength but for variation of 75% is not recommended because the compressive strength does not meet specifications even though the percentage is 100%.

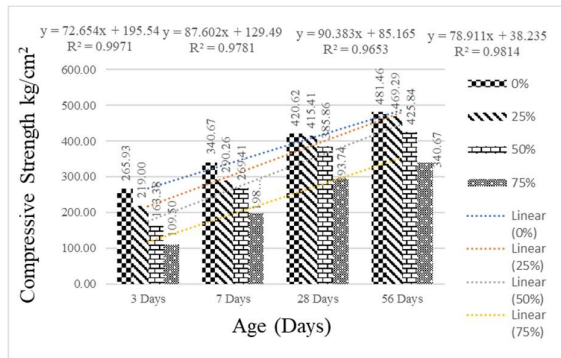


Fig. 14 Quality of Compressive Strength (K400)

Figure 14 shows, the results of the compressive strength test of K-400 concrete quality, at the age of 28 days the incoming variation is only 0% with a compressive strength of 420.62kg / cm² and 25% with a compressive strength of 415.41kg/cm².

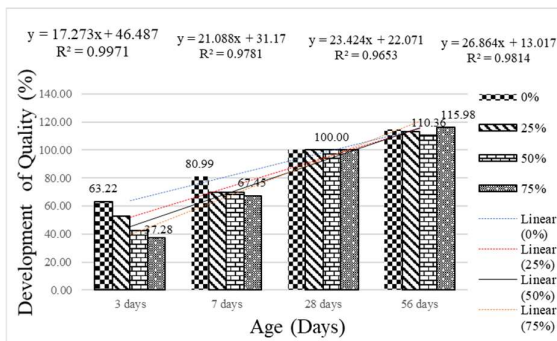


Fig.15 Development of Quality Concrete (K400)

Figure 15 shows compressive strength increases every time, this can be seen from the graph above. The achievement of the percentage of 28 days of variation 0%-25% meets the requirements for the compressive strength but for variations of 50% and 75% are not recommended because the compressive strength does not meet specifications even though the percentage is 100%.

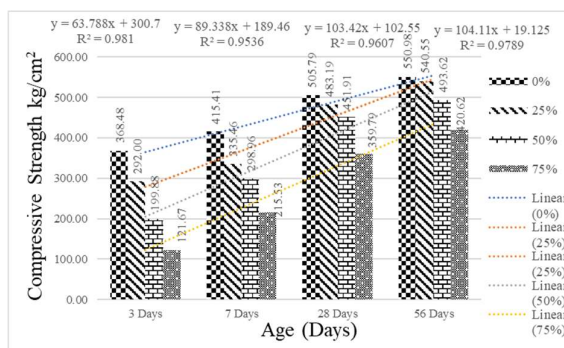


Fig.16 Quality of Compressive Strength (K500)

Figure 16 shows the compressive strength test of the K-500 concrete quality, it can be seen that the use of

GGBFS is not required because from the point of view of compressive strength still does not meet the requirements.

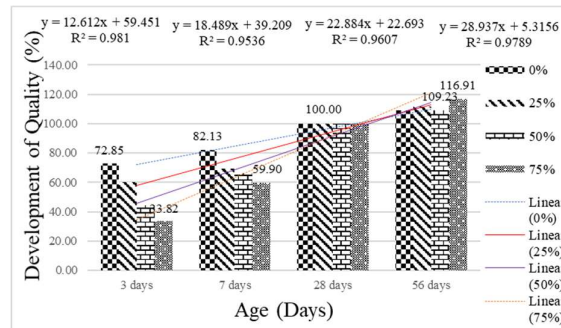


Fig.17 Development of Quality Concrete (K500)

Figure 17 shows, compressive strength increases every time, this can be seen from the graph above. The percentage of K 500 quality development increases every time, for example the age of 3 days with a variation of 72.85% at the age of 28 days to 100%.

Linear Regression Experiment

From the results of the compressive strength of the K200 – K400 quality taken samples for linear regression calculations, where the result is the higher the age of the concrete produced the higher the compressive strength. From the results of linear regression analysis it can be R = 0.9781 on variation of 25% with quality of K400 which means it approaches the value of 1 and the concrete on the construction project can be applied [8].

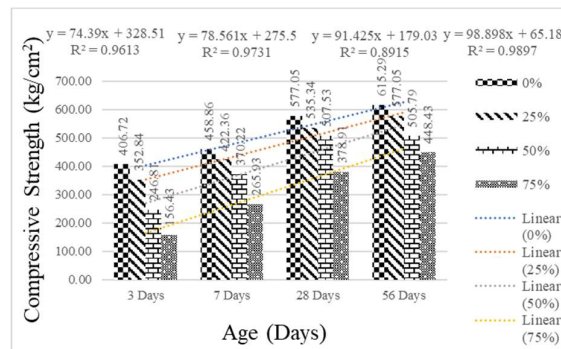


Fig.18 Quality of Compressive Strength (K600)

Figure 18 shows, the results of the compressive strength test of K-600 concrete quality, it can be seen that in each test 3 days, 7 days, 28 days and 56 days the compressive strength of concrete has decreased with each variation of the GGBFS substitution percentage variation for cement. For K600 quality is not required because the compressive strength for variation 0% = 577.05 kg / cm², 25% = 535.34 kg / cm², 50% = 451.91kg / cm² and 75% = 359.79 kg / cm², the result of all variations are below the standard even though the percentage values reaches 100% and the linear regression approaches 1.

The higher the quality of the concrete, the more cement is needed so that the use of GGBFS to achieve the compressive strength is not optimal since it is influenced by the quality of materials other than cement.

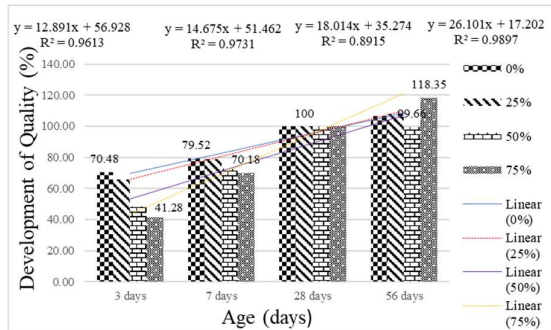


Fig.19 Development of Quality Concrete (K600)

Figure 19 shows, the percentage of K 600 quality development increases every time, for example the age of 7 days with a variation of 50% results 41.28% while the age of 28 days the quality of development rises to 100%. The use of the K600 is not recommended because it does not comply with the required standards.

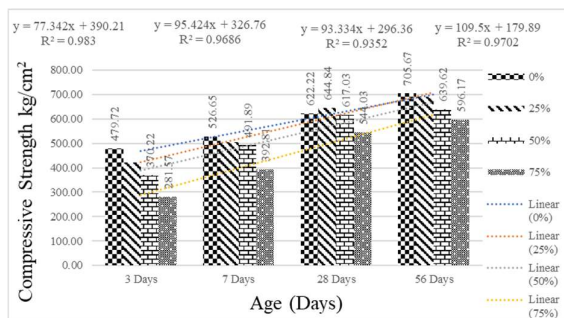


Fig.20 Quality of Compressive Strength (K700)

Figure 20 shows, the results of compressive strength testing of K-700 concrete quality, it can be seen that in each test at the age of 28 days does not meet the specifications because the compressive strength does not meet the required standards.

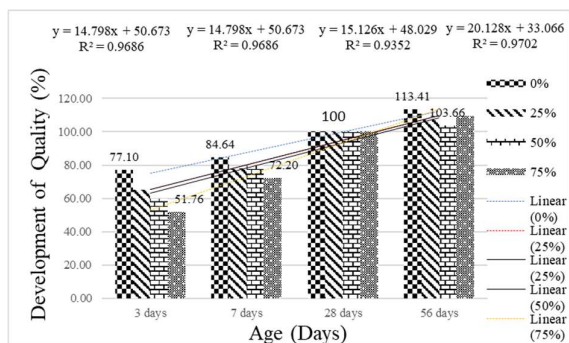


Fig.21 Quality of Compressive Strength (K700)

Figure 21 shows, the percentage of K 700 quality development increases every time, while the age of 28 days the quality development increases to 100%.

Slag Activity Index Experiment

$$\text{Slag Activity Index, \%} = \frac{SP}{P} \times 100\% \quad (4)$$

SP = average compressive strength of the slag-reference cement cubes

P = average compressive strength of the reference cement cubes

In this test, the compressive strength values of 7 days and 28 days [9] were compared by comparing samples with a 25%, 50%, 75% GBFS mixture divided by OPC cement with a sample that had a 100% OPC cement mixture. Following are the results of slag activity index testing:

Table 1. Slag Index Activity

Variation of GGBFS	Compressive Strength(kg/cm²)		Slag Index Activity		
	7 days	28 days	7 days	28 days	
0%	384.09	475.86			
25%	387.49	533.65	100.89	Grade 120	112.14
0%	384.09	475.86	89.38	Grade 100	127.14
50%	343.30	605.03			
0%	384.09	475.86	76.99	Grade 100	96.43
75%	295.72	458.87			

Production Cost

Production costs are all costs associated with the goods produced, in which there are elements of raw material costs, direct labor costs, and overhead costs. Based on [10] As production costs increase, it is necessary to find alternative solutions for the mix of raw materials for concrete production. Prices for concrete for K200 - K700 concrete for 2020 are as follows:

Table 2. Price of Concrete Quality 2020

Concrete Quality	Price per m³ (IDR)	
	GGBFS Concrete	Conventional Concrete
K200	700.000	720.000
K300	750.000	775.000
K400	800.000	830.000
K500	900.000	930.000
K600	1.000.000	1.030.000
K700	1.200.000	1.230.000

In implementing the Tokyo Apartment construction project used the K 400 concrete quality, with the utilization of slag, the resulting difference is:

$$\text{Cost} = \text{Volume} \times \text{Selling Price} \quad (4)$$

So, the calculation is as follows:

1. Utilization of Slag $300.000\text{m}^3 \times 900\text{k} = 270$ billion
2. With Conventional Concrete $300.000\text{m}^3 \times 930\text{k} = 279$ billion

From the difference generated for the sale price with the use of slag is 9 billion. The construction value of the construction can reduce the efficiency of materials or cost of production by 3%. The utilization of this slag has an impact to improve a friendly environment without reducing quality in the use of high quality of concrete.

CONCLUSIONS

In mortar experiments, the more levels of GGBFS content, the longer the initial time or the initial binding of concrete for 30 minutes.

Concrete compressive strength and the development of K200-K700 concrete quality at the age of concrete 3 days, 7 days, 28 days and 56 days on each variation will decrease in value. For examples variations of 0%, 25%, 50% and 75% in the age of concrete results will decrease. However, the compressive strength value of each variation will increase, for example 0% variation, 3,7,14 days and 28 days the value will increase. The use of Slag for over K500 quality is not recommended because it does not meet specifications even though the percentage is 100% and the linear regression is close to 1.

Slag index activity is categorized in grades 100 and 120 according to ASTM C989, Linear Regression generated from K500 concrete quality with a correlation of $R = 0.913$ can be used for high level quality of concrete.

The utilization of GGBFS can reduce the cost of production by 9 billion or 3% and it can also improve a healthy environment without reducing the quality of high quality concrete.

ACKNOWLEDGMENTS

The author would like to thank the Rector and the Institute for Community Service Research in internal grants for the Superior Research of the Civil Department of the PLN Institute of Technology No. SK:

0094.SK/2/A0/2020.

REFERENCES

- [1] ACI(American Concrete Institute), ACI 233R-03. Slag Cement in Concrete and Mortar. in ; American Concrete Institute, 2003, pp. 1–19.
- [2] Yogarajah E, Nawa T, Igarashi T, Physical, chemical, and mineralogical characteristics of blast furnace slag on durability of concrete. *MATEC Web Conf.*, vol. 147, p. 01007, 2018.
- [3] Hidayawanti R, Legino S, Harjanto D. Optimizing the Utilization Cement Slag and Fly Ash of Concrete Quality. in *The IIER International Conference*, 2018, March, pp. 14–18.
- [4] Hidayawanti R, Legino S, Sangadji I, Panca Adi Widodo R. The Efficiency of Fly Ash and Cement Slag to Development Building. *Geomate*, vol. 16, no. 57, pp. 95–100, 2019.
- [5] ASTM Committee. ASTM C109/C109M-02. Standard Test Method for Compressive Strength of Hydraulic Cement Mortars. in *Annual Book of ASTM Standards*. vol. 04, 2002, pp. 1–6.
- [6] ASTM C-39International, *Standard Test Method for Compressive Strength of Cylindrical Concrete Specimens*. no. C. 2010. p 1-7
- [7] Cleetus A, Shibu R, Paul VK, Jacob. B. Analysis and Study of the Effect of Ggbfs on Concrete Structures. *Irjet*, vol. 5, no. 3, pp. 3033–3037, 2018.
- [8] Hidayawanti R, Purnama DD, Iduwin T, Legino S, Wachid FI. The Impact Aggregate Quality Material as a Linear Regression. *GEOMATE*, vol. 18, no. 70, pp. 23–29, 2020.
- [9] ASTM C989. Standard Specification for Slag Cement for Use in Concrete and Mortars. in : *ASTM Standards*, vol. 44, no. 0, 2013, pp. 1–8.
- [10] Pourmahmoud N, Sadeghifar H, Torkavannejad A. International Journal of Heat and Mass Transfer A novel , state-of-the-art tubular architecture for polymer electrolyte membrane fuel cells : Performance enhancement , size and cost reduction. *Int. J. Heat Mass Transf.*, vol. 108, pp. 577–584, 2017.

POSSIBLE RECYCLING OF WASTE GLASS IN SUSTAINABLE FIRED CLAY BRICKS: A REVIEW

Yuecheng Xin, Abbas Mohajerani, Halenur Kurmus, John V. Smith

School of Engineering, RMIT University, Melbourne, Australia

ABSTRACT

The production of waste glass (WG) in Australia from 2016 to 2017 was about 1.1 million tonnes, and approximately 612 kilotonnes were recycled, while around 467 kilotonnes went to landfill. The current recycling techniques practiced for crushed waste glass (CWG) are limited, resulting in a growing environmental challenge. Therefore, there is an interest in the development of novel technologies to recycle WG. This paper provides a comprehensive review of the research conducted on recycling CWG in fired-clay bricks. The relationship between the firing temperature and the resulting physical/mechanical properties of bricks incorporating CWG is particularly examined. It was found that recycling CWG in bricks facilitates in reducing the global carbon footprint and improves the physical/mechanical properties of bricks. Therefore, incorporating CWG in fired clay bricks is a practical and feasible method to develop an environmentally friendly construction material and solve a growing waste issue. However, further research on the application of CWG in fired clay bricks is recommended.

Keywords: Waste glass, Recycling, Fired clay bricks, Physical and mechanical properties, Sustainability, Geomaterials.

INTRODUCTION

Bricks are a common construction material used widely around the world [1]. The production of fired clay bricks relies on extensive mining of natural resources and the use of non-renewable raw materials. Therefore, it is becoming vital to develop environmentally friendly and energy-efficient construction material by the addition of wastes. A number of studies have been conducted on recycling various wastes in fired clay bricks. Such wastes include cigarette butts [2], biosolids [1], microplastics [3], olive mill wastewater (OMW) [4], rice husk [5], foundry by-products [6] and marble powder [7]. Figure 1 illustrates the overall trend of documents published by year on recycling wastes and waste glass (WG) in fired clay bricks. An upward trend in the number of papers published on recycling WG in fired clay bricks can be seen to increase dramatically following the year 2015.

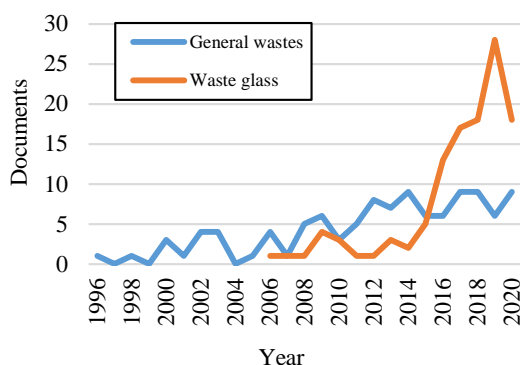


Fig.1 The number of documents published between 1996 to 2020 on recycling waste and WG in fired clay bricks.

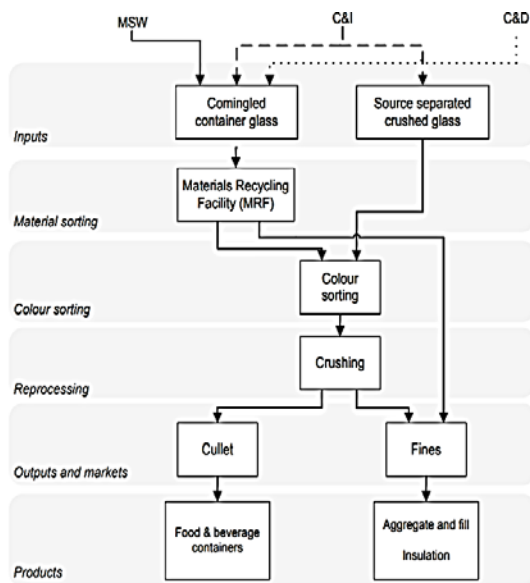
WG is a readily available domestic material, and around 11 million tonnes of glass containers are manufactured each year. Typically, WG is deposited in landfills. However, many countries are limited with space, and therefore landfills are facing a growing issue with the space available for WG [8]. For instance, the amount of waste generated per capita in Australia has gradually increased to an unprecedented level in the recent period. According to the Australia National Waste Report [9], a total of 1.1 million tonnes of WG was generated in the 2016 to 2017 period alone. 612 kilotonnes of WG were recycled, and landfills received the rest of 467 kilotonnes. Besides, the disposal of solid waste has an immense impact on the environment, economy, and health, which is a significant management issue that many countries are facing. Based on the statements from the World Wildlife Fund (WWF), recycling WG is a feasible method to reduce the space consumed in landfills. Likewise, because using recycled glass to produce glass products decreases the use of energy and raw materials, related air pollution and water pollution will be reduced by 20% and 50% respectively [10]. Evidently, using CWG as an additive in the making of fired clay bricks is becoming popular.

In Victoria, according to the fact sheet from Net Balance, each year, around 257,000 tonnes of glass waste is produced, and the majority was from glass packings such as beverage bottles, jars, beads, and

bowls. The remaining glass waste was from post-consumer glasses, flat glass (windows), and other sources. While 195,000 tonnes are recovered, only 124,000 tonnes are crushed into glass cullet for glass manufacturing. Victoria's recycled glass inventory is estimated to exceed 300,000 tonnes, mainly contaminated by ceramics, stoneware, Pyrex glass, and plastic. Besides, up to 62,000 tonnes of glass is expected to be sent to landfills each year [11].

Most glass packaging is collected from households or commercial sites (such as bars, clubs, sports venues, hotels, and restaurants) in mechanized, bin-based, fully commingled systems. Some glass is collected separately from other materials. On-site glass crushers are often used to reduce volume. The mixed materials are sorted from paper grads, plastics and metals by using the recycling facilities in the capital and regional centers. The glass is then sent to one of the beneficiation plants, including Visy, SKM, and Polytrade [12]. However, an issue has been indicated by many stakeholders that although the collection efficiency has been improved, mixed materials and compaction can cause cross-contamination and reduce the quality of the collected materials.

Figure 2 indicates the glass cullet and glass fines recovery process in Victoria.



Note: MSW: Municipal solid waste C&I: Commercial & Industrial C&D: Collection & Disposal

Fig. 2 The generic process for glass cullet and glass fines recovery in Victoria [11].

In addition to reusing glass packaging waste for packaging production, many other secondary markets can be used. The glass can be used for water quality projects as a filter medium. Similarly, CWG can also be used in various road base and sub-base

applications. The advantage is that it can accommodate large quantities of material [12]. As time progressed, the development of novel technology increased, including the addition of CWG in construction materials. According to a study [8], CWG is being added into concrete as a fine aggregate, in asphalt concrete, and in ultra-lightweight fibre reinforced concrete.

The objective of this paper is to collect and review major research studies on the recycling of CWG in fired clay bricks. Six CWG recycling proposals and practices are studied, including; type 1: 30% black dust and 70% superfine WG, type 2: recycled PC and TV WG, type 3: soda-lime glass powder WG, type 4: shop glazing window WG, type 5: thin-film transition liquid crystal display (TFT-LCD) WG powder and type 6: the combination of sludge and WG.

RESEARCH ON RECYCLING OF WASTE GLASS

Type 1: 30% Black Dust and 70% Superfine WG

Federico [13] studied the effects of CWG on the properties of fired clay bricks. Eleven sets were prepared with A (0% glass), B (5% glass), C (5% glass), D (10% glass), E (10% glass), F (15% glass), G (15% glass), L (0% glass), X (0% glass), FL (0% glass), and FX (0% glass). Each set contained 30 samples. Set A was categorized as the control group, and the remaining were test groups. B, D, and F contained different percentages of WG with the same glass mesh size. C, E, and G contained different percentages of WG with the same glass mesh size. As a result, the influence of the percentage of WG addition by mass, as well as the influence of WG particle size on the properties and durability of the bricks can be investigated. In addition, samples L, X, FL, and FX were prepared to investigate the influence of the methodology used and the firing temperatures on the bricks. Lignosulfonate (20 ml) was added to the water during the mixing process in order to increase the plasticity of the clay. The test results show that the percentage of WG has a significant effect on compressive strength. The maximum compressive strength was found to be 133.4 MPa for G (15% glass). Additionally, the particle size of the WG had a great effect on water absorption properties. A microstructural analysis was conducted, it was found the increase in WG reduced the porosity of the brick samples.

Type 2: Recycled PC and TV WG

According to a study, the disposal of PC monitors and TV sets is becoming a growing issue, approximately 25,000 m³ of PC monitors and TV sets are being produced in European countries per year [14]. Moreover, a high concentration of lead, barium,

and strontium exists in the funnel and panel of the cathode ray tube display, which results in the technical problem of re-using PC and TV glass to manufacture new glass. Therefore, the focus of this study is to add PC and TV glass into fired clay bricks. Three different mixture ratios of clay and glass are prepared: control sample without waste (C0), 2% and 5% by weight (wt.) funnel glass (CT2 and CT5), and 2% and 5% by wt. panel glass (CS2 and CS5). The samples were fired at three different temperatures 900°C, 950°C, and 1000°C. The firing shrinkage, bending strength, water absorption, open porosity, and bulk density were investigated. The results revealed bricks incorporating CWG result in higher bulk density, bending strength, and firing shrinkage and lower water absorption. The maximum bending strength (22.8 MPa) was found for bricks incorporating 5% screen glass, with a firing temperature of 950 °C.

Type 3: Soda-lime Glass Powder WG

Demir [15] investigated the effect of milled WG on the properties of fired clay bricks. The waste was added at a ratio of 0%, 2.5%, 5%, and 10% by wt. and the samples were fired at four different temperatures of 850°C, 950°C, and 1050°C. The results showed a linear relationship between shrinkage and the firing temperature. Shrinkage increased with an increase in temperature, while the increase in firing temperature resulted in a decrease in porosity and water absorption. The results additionally revealed higher firing temperature increases the mechanical strength, as shown in Table 1.

Table 1 Compressive strength test results [15].

Waste glass content	Compressive strength MPa		
	850 °C	950 °C	1050 °C
0%	16.45	19.50	20.37
2.5%	18.75	22.65	24.50
5%	20.15	25.13	27.15
10%	20.62	27.56	29.35

Another study discussed the effects on the physical-mechanical properties of fired clay bricks when incorporated with WG (soda-lime glass) [16]. The study aims to reduce the firing temperature of the brick in order to save energy. The study has been performed by utilizing different amounts of glass, including 0%, 5%, and 10% by wt., with a firing temperature within the range from 900°C to 1000°C. The glass additive contains sodium oxide (Na_2O) and has a Non-crystalline structure, which helps with reducing the required firing temperature, increasing the glassy phase in the brick to enhance the durability, and reducing the costs of manufacturing. In addition, the Na_2O assists in the vitrification of the bricks

resulting in higher density and lower water absorption and drying shrinkage.

In 2017, a study proved the firing temperature can successfully be decreased from 1050°C to 650°C for fired clay bricks with the addition of WG powder (borosilicate glass, colored glass, and soda-lime glass) [17]. The ratio of glass content used in the study included 0%, 20%, 35%, and 50% by wt. and the specimens were fired at 650°C, 850°C, and 1050°C. Besides, the results indicated that the bricks (35% soda-lime glass) have better compressive strength than others, as shown in Table 2.

Table 2 Compressive strength test results [17].

Waste glass content	Compressive strength MPa		
	650 °C	850 °C	1050 °C
0%	21.88	22.22	25.62
35% soda-lime glass	28.88	31.79	35.14
35% borosilicate glass	24.18	27.44	31.78
35% coloured glass	26.84	27.04	30.08

Furthermore, a study was performed on the addition of various sizes of glass cullet in red clay bricks with a focus on the subsequent physical and mechanical properties [18]. All specimens were air-dried at room temperature for 72 hr and later fired at 1000°C for 12 hr. The bricks with glass cullet incorporated demonstrated a lower water absorption compared to the controlled bricks. The compressive strength increased with the decrease in the particle size of the glass cullet brick samples. The results show that increasing the glass content and reducing the particle size of the glass can significantly improve the properties of the fired clay bricks for water absorption and compressive strength.

Type 4: Shop Glazing Window WG

Abdeen [19] studied the performance of fired clay bricks containing waste glazing window glass. The selected contents of waste glazing window glass included 0%, 10%, 20%, 30%, and 40% by wt. The firing temperatures for the fired clay bricks incorporated with glazing window glass were 900°C, 1000°C, and 1100°C. The result revealed the compressive strength of the fired clay bricks increased with the increase in glazing window glass content and firing temperature, as shown in Table 3.

Table 3 Compressive strength test results [19]

Waste glass content _%	Compressive strength MPa		
	900°C	1000 °C	1100 °C
0	18.61	21.33	28.82
10	22.91	30.67	47.45
20	20.41	32.34	77.75
30	21.91	42.75	96.37
40	17.88	43.17	55.98

Type 5: Thin-film Transition Liquid Crystal Display WG Powder

In 2018, Chao-Wei [20] investigated the addition of TFT-LCD WG in fired clay bricks. The ratio of TFT-LCD glass content used in this study were 0%, 10%, 20% and 30% by wt. The specimens were fired at 900°C, 950°C, 1000°C, and 1050°C. Several tests were conducted to evaluate the effects of adding TFT-LCD WG powder in fired clay bricks. The results displayed a decrease in water absorption and an increase in compressive strength with the increase in TFT-LCD WG content in the fired clay brick samples. The maximum compressive strength (48.2 MPa) was reached by adding 20% glass cullet into bricks and firing at 1050°C.

Type 6: The combination of Sludge and WG

Rahman et al. investigated the effects of adding WG in textile sludge-based bricks [21]. The bricks contained textile sludge, which increased the porosity, and as a result, reducing the mechanical properties of the fired clay bricks. However, the compressive strength and water absorption are known to increase with the addition of WG. Therefore, textile sludge and WG additions were combined and incorporated in fired clay bricks for the purpose of this investigation. Various percentages of sludge content were added in the production of bricks between 0% to 40% by wt., in addition to 5% and 10% by wt. WG. All specimens were fired at 1150°C. The results confirm the addition of WG to the textile sludge-based bricks improved the compressive strength, shrinkage, and water absorption properties. In addition, the bricks incorporating sludge and WG were tested for heavy metal leaching. The results revealed the leachate concentrations for heavy metals for bricks incorporating WG and sludge were below the standard regulatory limits. Therefore, recycling fabric sludge and WG in the production of fired clay bricks is an environmentally friendly solution to a growing pollution issue.

A group of researchers investigated the use of WG in addition to galvanized sludge in brick production to boost the immobilization of heavy metals [22]. Various contents of WG were studied, including 0%, 10%, 15%, 20%, 25%, and 30% by wt., while the galvanized sludge content studied was 10%. The firing temperatures were 850°C, 950°C and 1050°C

respectively. The experimental results revealed when more than 15% WG content was added, the concentration of heavy metals leached from bricks incorporating 10% galvanized sludge was found to be below the regulatory limits. Therefore, WG can be used as an enhancer in conjunction with hazardous wastes (galvanized sludge) in the production of fired clay bricks for the stabilization and solidification of heavy metals.

CONCLUSION

In conclusion, this study provides a review of the research conducted in utilizing various WG types in the production of fired clay bricks. The six CWG recycling proposals and practices studied were 30% black dust and 70% superfine WG, recycled PC and TV WG, soda-lime glass powder WG, shop glazing window WG, thin-film transition liquid crystal display (TFT-LCD), WG powder and the combination of sludge and WG. The effects of the WG particle size, WG content, firing temperature, and brick preparation process on the physical and mechanical properties of fired clay bricks were analyzed. The distinct procedures and sample types followed in recycling WG into fired clay bricks are summarized in Table 4.

It was found whether WG is added exclusively or with the addition of another waste, the addition of WG in fired clay bricks demonstrated encouraging physical and mechanical properties, particularly with the improvement in compressive strength. Moreover, the addition of WG assists in reducing the maximum desired firing temperature significantly and, consequently, the firing time. Therefore, it contributes to minimizing the world's carbon footprint. Besides, the reviewed research studies reveal and confirm the addition of WG in fired clay bricks is a feasible and effective approach to reduce the growing amount of WG in landfills worldwide. Furthermore, the partial replacement of clay with WG in brick production will assist in decreasing the consumption of natural materials.

RECOMMENDATIONS

Based on the review, the following research and developments are recommended for widespread industry adoption:

- Further study is recommended to determine the optimal ratio of WG content in fired clay bricks, in addition to the optimal firing temperature.
- A comprehensive study on the combination of WG with other waste additives is recommended with an emphasis on environmental implications.
- A life cycle assessment is recommended to evaluate the negative and positive environmental impacts of incorporating WG in fired clay bricks.

- A comprehensive and feasible manufacturing method is recommended to be developed for the incorporation of CWG in fired clay bricks.

Table 4 Summary of some of the research conducted in recycling various WG types in fired clay bricks

Glass sample type	Particle size	Waste glass by wt.	Drying process	Firing process	Ref.
Black dust and superfines	150 -300 μm 75-150 μm 45-75 μm	0%, 5%, 10% and 15%	Air dry for 24 hr Oven dry for 12 hr at 110 °C	Fired between 999.6°C and 1106 °C	[13]
Recycled PC and TV waste glass.	Passing 0.25 mm sieve	2% and 5%	Air dry for 48 hr Oven dry at 100°C overnight	Fired at 900°C, 950°C and 1000°C with 4 hr soak time	[14]
Crushed waste glass powder (bottle)	21 μm	0%, 2%, 2.5%, 5% and 10%	Air dry for 24 hr Oven dry at 110 °C	Fired at 850°C, 950°C, and 1050°C with a heating rate of 3°C/min and held for 2 hr	[15]
Soda-lime glass	Ball mill crushed (1 hr)	0%, 5% and 10%	Air dry for 24 hr Oven dry for 24 hr at 110 °C \pm 5°C	Fired at 900°C, 950°C and 1000°C and held for 1 hr	[16]
Sodalime glass, coloured glass, and borosilicate glass	0.85 mm	0%, 20%, 35%, and 50%	Air-dry overnight Oven dry at 110°C for 24 hr	Fired at 650°C, 850°C and 1050°C for 3 hr with a heating rate of 5°C /min and soaking period of 15 min	[17]
Crushed Glass Cullet	<500, <300, and <212 μm	0%, 20%, 25%, and 30%	Air dry for 72hr	Fired at 1000 °C for 12h	[18]
Shop Glazing windows	150 μm and <600 μm	0%, 10%, 20%, 30% and 40%	Air dry for 24 hr Oven dry at 45°C for 6 hr and then at 110°C for 24 h	Fired at 900°C, 1000°C and 1100°C with a heating rate of 2.5°C/min until 600°C reached, and then 5°C/min until 900°C reached, 1000°C and 1100°C	[19]
Thin-film transition liquid crystal display waste glass powder	Ball mill crushed	0%, 10%, 20%, and 30%	Set one: air dry for two days Set two: air dry one day Set three: Oven dry at 100°C for one day Set four: oven dry at 50°C for one day	Fired at 900°C, 950°C, 1000°C, and 1050 °C	[20]
Combination of sludge and waste glass (bottle)	<250 μm	5% and 10%	Air dry for one day and oven-dry overnight	Fired at 1150°C	[21]
	<74 μm	0%, 5%, 10%, 15%, 20%, 25% and 30%.	Oven dry for 24 hr at 110°C.	Fired at 850°C, 950°C, and 1050°C with a heating rate of 300°C/h for 3 hr until target temperature reached	[22]

ACKNOWLEDGMENT

This work is part of an ongoing study on recycling waste in construction materials. The authors would like to thank Visy industries Australia Pty Ltd and RMIT University for their financial and in-kind support.

REFERENCES

- [1] Mohajerani, A., Ukwatta, A., Jeffrey-Bailey, T., Swaney, M., Ahmed, M., Rodwell, G., Bartolo, S., Eshtiaghi, N., and Setunge, S.J.B. A Proposal for Recycling the World's Unused Stockpiles of Treated Wastewater Sludge (Biosolids) in Fired-Clay Bricks, 2019, 9(1), 14.
- [2] Kurmus, H. and Mohajerani, A.J.M. Recycling of Cigarette Butts in Fired Clay Bricks: A New Laboratory Investigation, 2020, 13(3), 790.
- [3] Mohajerani, A. and Karabatak, B.J.W.M. Microplastics and pollutants in biosolids have contaminated agricultural soils: An analytical study and a proposal to cease the use of biosolids in farmlands and utilise them in sustainable bricks, 2020, 107, 252-265.
- [4] Mekki, H., Anderson, M., Amar, E., Skerratt, G.R., BenZina, M.J.J.o.C.T., Biotechnology: International Research in Process, E., and Technology, C. Olive oil mill waste water as a replacement for fresh water in the manufacture of fired clay bricks, 2006, 81(8), 1419-1425.
- [5] Chiang, K.-Y., Chou, P.-H., Hua, C.-R., Chien, K.-L., and Cheeseman, C. Lightweight bricks manufactured from water treatment sludge and rice husks, *Journal of hazardous materials*. 2009, 171(1-3), 76-82.
- [6] Alonso-Santurde, R., Coz, A., Viguri, J., and Andrés, A. Recycling of foundry by-products in the ceramic industry: Green and core sand in clay bricks, *Construction and Building Materials*. 2012, 27(1), 97-106.
- [7] Munir, M.J., Abbas, S., Nehdi, M.L., Kazmi, S.M., and Khitab, A.J.J.o.M.i.C.E. Development of eco-friendly fired clay bricks incorporating recycled marble powder, 2018, 30(5), 04018069.
- [8] Mohajerani, A., Vajna, J., Cheung, T.H.H., Kurmus, H., Arulrajah, A., Horpibulsuk, S.J.C., and Materials, B. Practical recycling applications of crushed waste glass in construction materials: A review, 2017, 156, 443-467.
- [9] Dunnet, S.C. Current issues at the South Fremantle landfill site, Western Australia, *Rural Remote Environmental Health*. 2004, 3(1), 40-51.
- [10] WWF. 'Recycling Glass - How it helps environment', 2020. Viewed <https://www.panda.org/knowledge_hub/teacher_resources/project_ideas/recycling_glass.cfm>.
- [11] NetBalance. Market summary – recycled glass, 2014.
- [12] Allan, P. Assessment of Australia recycling infrastructure - Glass packing, 2018.
- [13] 13. Federico, L.M. 2006, Effects of Waste Glass Addition on the Properties of Fired Clay Brick (Doctoral dissertation).
- [14] 14. Dondi, M., Guarini, G., Raimondo, M., and Zanelli, C. Recycling PC and TV waste glass in clay bricks and roof tiles, *Waste management*. 2009, 29(6), 1945-1951.
- [15] 15. Demir, I. Reuse of waste glass in building brick production, *Waste management & research*. 2009, 27(6), 572-577.
- [16] 16. Phonphuak, N., Kanyakam, S., and Chindaprasirt, P.J.J.o.C.p. Utilization of waste glass to enhance physical-mechanical properties of fired clay brick, 2016, 112, 3057-3062.
- [17] 17. Sarmeen Akhtar, U., Moniruz Zaman, M., Islam, M.S., Nigar, F., and Hossain, M.K.J.T.o.t.I.C.S. Effect of different types of glasses as fluxing agent on the sintering temperature of bricks, 2017, 76(2), 128-132.
- [18] 18. Ponce Peña, P., González Lozano, M.A., Rodríguez Pulido, A., Lara Castro, R.H., Quiñones Jurado, Z.V., Pérez Medina, J.C., Poisot Vázquez, M.E., Villavicencio Torres, A.J.A.i.M.S., and Engineering. Effect of crushed glass cullet sizes on physical and mechanical properties of red clay bricks, 2016, 2016.
- [19] 19. Abdeen, H.H. Properties of Fired Clay Bricks Mixed with Waste Glass, *Journal of Scientific Research & Reports* 2016, 13(4).
- [20] 20. Tang, C.-W.J.S. Properties of fired bricks incorporating TFT-LCD waste glass powder with reservoir sediments, 2018, 10(7), 2503.
- [21] 21. Rahman, A., Urabe, T., Kishimoto, N., and Mizuhara, S.J.E.t. Effects of waste glass additions on quality of textile sludge-based bricks, 2015, 36(19), 2443-2450.
- [22] 22. Mao, L., Wu, Y., Zhang, W., and Huang, Q.J.J.o.e.m. The reuse of waste glass for enhancement of heavy metals immobilization during the introduction of galvanized sludge in brick manufacturing, 2019, 231, 780-787.

DYNAMIC PROPERTIES OF RIGID POLYURETHANE FOAM IN CYCLIC TRIAXIAL TESTS

Atsushi Koyama¹, Daisuke Suetsugu¹ and Yoshinori Fukubayashi¹

¹Faculty of Engineering, University of Miyazaki, Japan

ABSTRACT

The aim of this study is to clarify the dynamic properties of rigid polyurethane foam. A method for renovating a deteriorated bridge as a lightweight embankment was proposed. The space underneath a bridge is filled with polyurethane to support the upper structure. In this case, the upper structure of the bridge is considerably heavier than the polyurethane. Therefore, it is important to examine the seismic behavior of this new lightweight embankment. However, the dynamic deformation characteristics of polyurethane have not been clarified previously. In this study, stress-controlled cyclic triaxial tests based on JGS0542-2009 are used to evaluate the effect of the confining stress and the presence of a rigid layer on the dynamic properties of rigid polyurethane foam. As a result, the shear modulus of rigid polyurethane foam increases with increasing confining stress regardless of the absence of the rigid layer. The shear modulus of polyurethane with the rigid layer is lower than that of polyurethane without the rigid layer. The value of shear modulus of rigid polyurethane foam was measured in the range of approximately 1.6~3.2MPa. Moreover, the stiffness degradation and of rigid polyurethane foam are in good agreement with the Hardin-Drnevich model.

Keywords: Cyclic triaxial tests, Dynamic properties, Lightweight embankment, Rigid polyurethane

INTRODUCTION

There are approximately 720,000 bridges in Japan will be more than 50 years old within 10 years. Along with a decline in the number of civil engineers engaged in bridge maintenance work, local governments may not be able to adequately cover inspection costs. Therefore, measures against bridge deterioration must be undertaken to improve maintenance efficiency [1]. Solution achieve this, the aim of this study is to establish a method for renovating a deteriorated bridge as a lightweight embankment by filling the bridge's substructure space with polyurethane foam, which is a lightweight embankment material. This lightweight embankment method takes advantage of the low weight (36 kg/m³), adhesiveness, and foamability of polyurethane.

In this method, two types of rigid polyurethane foam stock solution are mixed and foamed at site. The volume increases by approximately 30 times because of the foaming, and a lightweight embankment of any shape can be formed to suit the topography and shape of the structure. Because the polyurethane is formed of closed cells, it is impermeable to water and air. In this study, this technology was applied to renovate deteriorated bridges as lightweight embankments by directly spraying/filling the substructure space and allowing the polyurethane to take the vertical load.

Figure 1 shows a schematic diagram of the method of renovation of a simple girder bridge to a lightweight embankment. Both dead and live loads

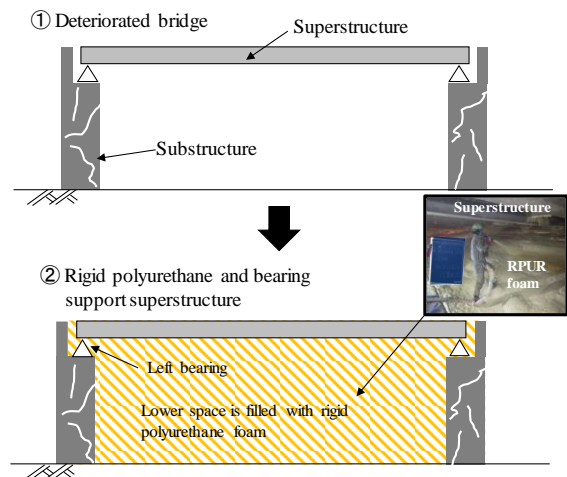


Fig. 1 Renovation of the deteriorated bridge to lightweight embankment.

are supported by spraying/filling the substructure space of the bridge with polyurethane. Owing to the adhesiveness of polyurethane, water/air is prevented from penetrating the bridge member in positions where the polyurethane adheres to the member, and this is expected to inhibit member deterioration. The design should be such that even if, after a long period of time, the bearing capacity of the support covered in polyurethane is reduced or lost because of deterioration and the condition cannot be confirmed visually, the dead and live loads are within a range that can be supported by the polyurethane.

In a situation where the vertical load is supported

Table 1 Properties of polyurethane

Name	Density ρ (kg/m ³)	Yield strength σ_y (kPa)	Allowable stress σ_a (kPa)	Poisson's ratio ν	Cell type
Rigid polyurethane	36	120	60	0.05	Closed
Golpazir et al.	31.3	68	—	0.02	Open

by the polyurethane, the embankment would be heavier at the top, and its seismic stability could decrease. However, the dynamic properties of polyurethane required to evaluate the seismic stability of an embankment have not been investigated [2]. The mechanical properties of expanded polystyrene (EPS), which is a lightweight polymeric material with properties similar to those of polyurethane, have been evaluated in static and dynamic shear tests. For example, the higher is the density of EPS, the greater is its compressive strength. Moreover, the shear modulus G also increases. The density is reported to have little influence on the damping ratio h [3]–[6]. Gatto et al. [7] investigated the dynamic properties of polyurethane using resonance tests. They reported that, in the micro-strain range, G and h were not affected by the changes in the confining pressure when the confining pressure was in the range 50–300 kPa. Golpazir et al. [8] used stress-controlled cyclic triaxial tests to show the influence of initial shear stress on the dynamic properties of one-liquid type polyurethane. Their results showed that, as the initial shear stress increases, G decreases. They also reported that, unlike typical soil materials, h of polyurethane decreases with increasing shear strain, and the viscoelasticity of polyurethane is considered to be the cause. A decrease in h with increasing shear strain was also reported for EPS [6].

Currently, there is limited research on the dynamic properties of polyurethane foam using cyclic triaxial tests, and data needs to be accumulated. The rigid polyurethane foam used in this study is foamed approximately every 10 cm, and polyurethane layers form inside the embankment. A rigid surface, called a “skin,” exists at the boundaries between layers (see Fig. 3). The influence of this skin on the dynamic properties has not been examined previously.

Therefore, the objective of this study was to examine the influence of the presence or absence of a skin and the differences in confining pressure on the dynamic properties of polyurethane using stress-controlled cyclic triaxial tests.

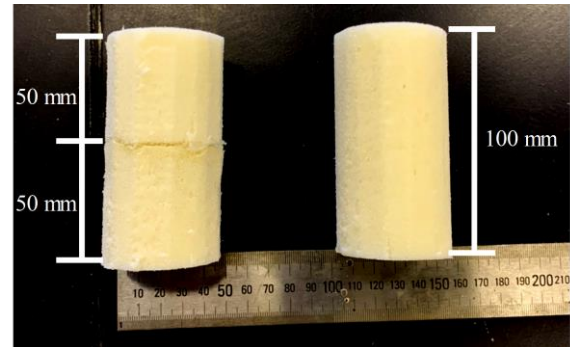


Fig. 2 Test specimens of polyurethane (left: two-layer sample; right: one-layer sample, $\phi=50$ mm).

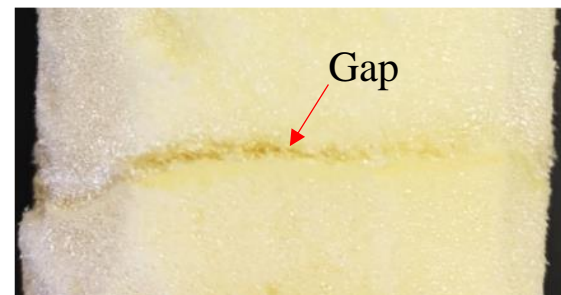


Fig. 3 Gap due to the rigid layer (skin) of two-layer specimen.



Fig. 4 Cyclic triaxial apparatus.

MATERIALS AND METHOD

Sample preparation

The rigid polyurethane foam used in this study is a two-liquid (polyol and isocyanate) mixed-type that is used in lightweight embankment construction methods. Table 1 shows the values of the physical properties of the rigid polyurethane foam. For comparison, Table 1 also shows the physical property values of the one-liquid type polyurethane used by Golpazir et al. [8]. The density of the rigid polyurethane foam used in this study is higher than that used by Golpazir et al. [8] and the yield strength is approximately double. Furthermore, the rigid polyurethane foam used in this study is a closed-cell type, whereas Golpazir et al. [8] used an open-cell type.

The time required since the spraying until the completion of foaming is approximately 1 min. When the foam hardens, more than 95% of the prescribed strength develops within 24 h. In this study, a sample in which polyurethane foam is foamed continuously to a height of 100 mm is called a “one-layer sample,” and a sample in which polyurethane foam is foamed to a height of 50 mm and a second layer is sprayed/foamed on top such that it has two layers and a skin is called a “two-layer sample” (Fig. 2). As shown in Fig. 3, an area where the density of the polyurethane is low occurs at the boundary in the samples with a skin.

Test procedure for cyclic triaxial shear tests

In this study, a stress-controlled cyclic triaxial test was performed to evaluate the effect of the confining stress and the presence or absence of a rigid layer on the dynamic properties, namely, the shear modulus and damping ratio of polyurethane.

Figure 4 shows the cyclic triaxial test apparatus. The cyclic triaxial test was performed in accordance with the Japanese Geotechnical Society standard 0542-2009 [9]. The sample was covered with a membrane and placed in the tester and an isotropic stress was applied until the prescribed confining pressure σ_c was reached. The sample was left to stand for 1 h, and then cyclic loading was started immediately. At each cyclic loading stage, a sinusoidal cyclic load at a frequency $f = 0.1$ Hz was applied for 11 cycles, under a prescribed deviator stress q . The deviator stress was increased in 15–17 stages. The load and axial displacement were measured during the cyclic loading. The axial displacement was measured using a gap sensor.

In the polyurethane lightweight embankment method, the allowable compressive stress of the polyurethane is established as 60 kPa. To minimize the creep deformation of the polyurethane when a bridge is renovated as a lightweight embankment,

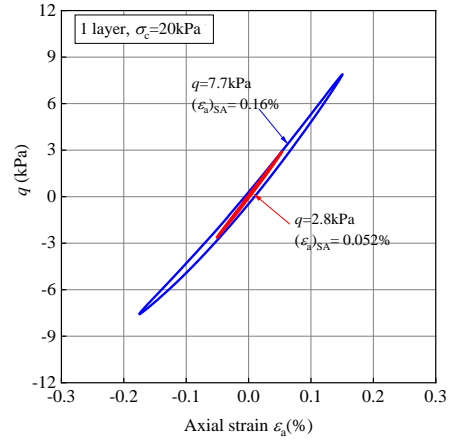


Fig. 5 Stress-strain hysteresis loops for rigid polyurethane samples with different deviator stress.

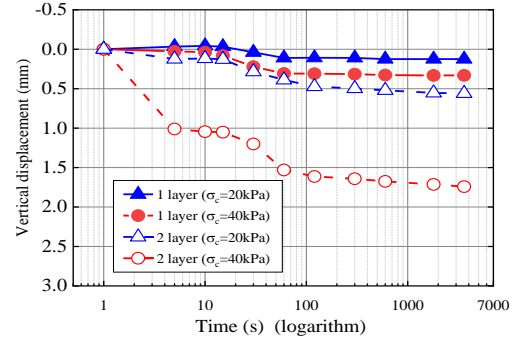


Fig. 6 Vertical displacement of polyurethane during isotropic compression.

the dead load acting on the polyurethane should be designed to be approximately 20 kPa. Therefore, σ_c was set at 20 kPa and 40 kPa in the cyclic triaxial test. These values of σ_c are within the elastic region of the rigid polyurethane foam. The one-layer and two-layer samples were tested with the two aforementioned values of σ_c .

The equivalent Young's modulus E_{eq} was obtained from the hysteresis loop using Eq. (1) and this was converted to the equivalent shear modulus G_{eq} using Eq. (2). Here, $\nu = 0.05$.

$$E_{eq} = \frac{\sigma_d}{(\varepsilon_a)_{SA}} \times \frac{1}{10} \quad (\text{MPa}) \quad (1)$$

where

σ_d : single amplitude cyclic deviator stress (kPa)
 $(\varepsilon_a)_{SA}$: single amplitude axial strain (%)

$$G_{eq} = \frac{E_{eq}}{2} \times (1 + \nu) \quad (\text{MPa}) \quad (2)$$

The hysteresis damping ratio h was determined using Eq. (3).

$$h = \frac{1}{2\pi} \cdot \frac{\Delta W}{W} \times 100 \quad (\%) \quad (3)$$

where

ΔW : area of the hysteresis curve ($N \cdot cm$)

W : equivalent elastic energy in that loading cycle

In this study, G_{eq} and h were calculated using data from the 10th cycle in each loading stage. Figure 5 is an example of hysteresis loops that show the relationship between q and $(\varepsilon_a)_{SA}$ for one-layer samples at $\sigma_c = 20$ kPa. It is evident from the figure that polyurethane deforms to the same extent in compression and extension. However, when $(\varepsilon_a)_{SA}$ exceeded approximately 0.4%, the extension deformation of the polyurethane did not follow the load on the extension side and pulled the membrane. Therefore, in this study, the test was stopped at approximately $(\varepsilon_a)_{SA} = 0.4\%$.

RESULTS AND DISCUSSION

Dynamic properties of rigid polyurethane foam

Figure 6 shows the relationship between the vertical displacement and time for one-layer and two-layer samples under each σ_c . As shown in the figure, the vertical displacement of each sample increased with an increase in σ_c . The amount of compression was greater in the two-layer samples at both the confining pressures. This is because the gap caused by the skin (Fig. 2) was filled when the sample was isotropically compressed. Two-layer samples have a gap between the bottom and top layer. It is probable that the density of polyurethane is low in this gap. In all the samples, the vertical displacement became constant after approximately 120 s from the initiation of loading. Therefore, isotropic compression was stopped at 1 h.

Figure 7 shows the relationship $G_{eq}-\gamma_{SA}$ and $h-\gamma_{SA}$ for the one-layer and two-layer samples, respectively. γ_{SA} is the single amplitude shear strain.

As shown in Fig. 7, the value of G_{eq} increases and the value of h decreases with increasing σ_c , regardless of the presence or absence of a skin. This is assumed to be because the higher the confining pressure, the harder the polyurethane becomes.

At either value of σ_c , h increased with increasing γ . This trend is opposite to that shown in the test results by Golpazir et al. [8]. Additionally, the value of h in this study was approximately one tenth of the value in their test results. The loading frequency of the cyclic load in tests performed by Golpazir et al. [8] was 0.02 Hz, whereas in this study it was 0.1 Hz.

However, Athanasopoulos et al. [4] reported that, in the case of EPS, the loading frequency has little effect on the dynamic properties. Therefore, it is assumed that the differences in the structure of the polyurethane, such as open and closed cells, and strength influence the test results, not the different test methods. Therefore, data must be collected from tests performed using several types of polyurethane with different physical properties.

Figure 8 shows the relationship $G_{eq}-\gamma_{SA}$ and $h-\gamma$ comparing the presence and absence of a skin. Regardless of the size of σ_c , G_{eq} was larger and h was smaller in the one-layer samples compared with the two-layer samples. G_{eq} was small in the two-layer samples because there was cyclic loading at the gap caused by the skin. The effect of the presence or absence of a skin on G_{eq} and h was smaller when $\sigma_c = 40$ kPa than when $\sigma_c = 20$ kPa. This is considered to be because, as shown in Fig. 6, the greater the value of σ_c , the more the gap caused by the skin was filled, and therefore the differences in G_{eq} and h between the one-layer and two-layer samples were smaller.

Degradation curves of rigid polyurethane foam

Figure 9 shows the relationship between G/G_0 , which is G_{eq} normalized by the initial shear modulus G_0 , and γ_{SA} . Figure 9 also shows the $G/G_0-\gamma_{SA}$ relationship approximated by the Hardin-Drnevich model (H-D model) [10], which is a nonlinear soil model represented by Eq. (4). The H-D model is a nonlinear formula that easily determines the related model parameters. Table 2 shows the parameters used in the H-D model.

$$\frac{G}{G_0} = \frac{1}{1 + \gamma/\gamma_r} \quad (4)$$

where

G_0 : shear modulus at minimum shear strain

γ_r : shear strain in $G/G_0=0.5$

In the cyclic triaxial test results, the relationship between G/G_0 and γ_{SA} can be expressed using σ_c , regardless of the presence or absence of a skin. It is evident from Fig. 9 that there is good agreement between the experimental values and the H-D model.

Figure 10 shows the relationship between h and γ_{SA} from the H-D model, calculated using Eq. (5), and the experimental values from the cyclic triaxial test.

$$h = h_{\max} \times \left(1 - \frac{G}{G_0}\right) \quad (5)$$

where

h_{\max} : maximum value of damping ratio

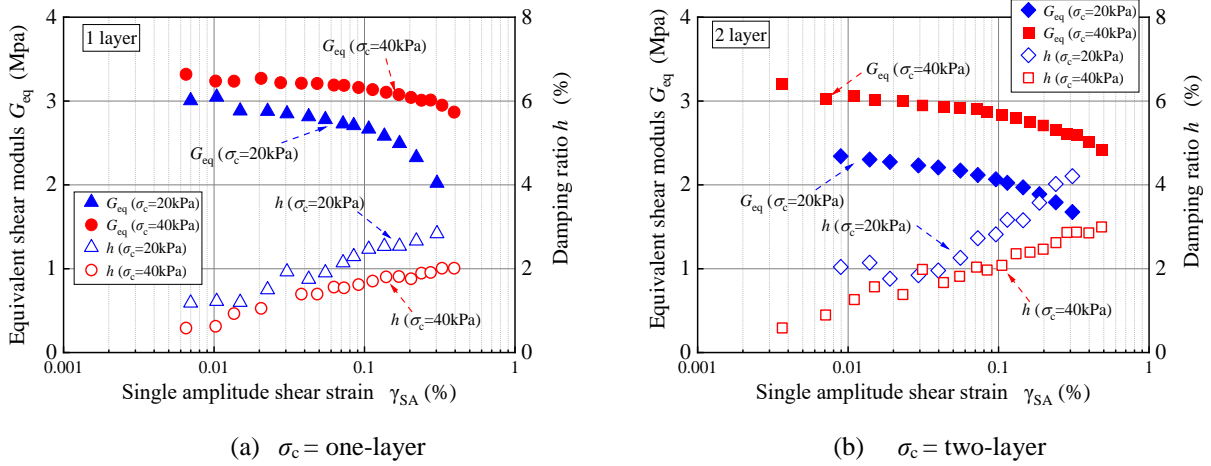
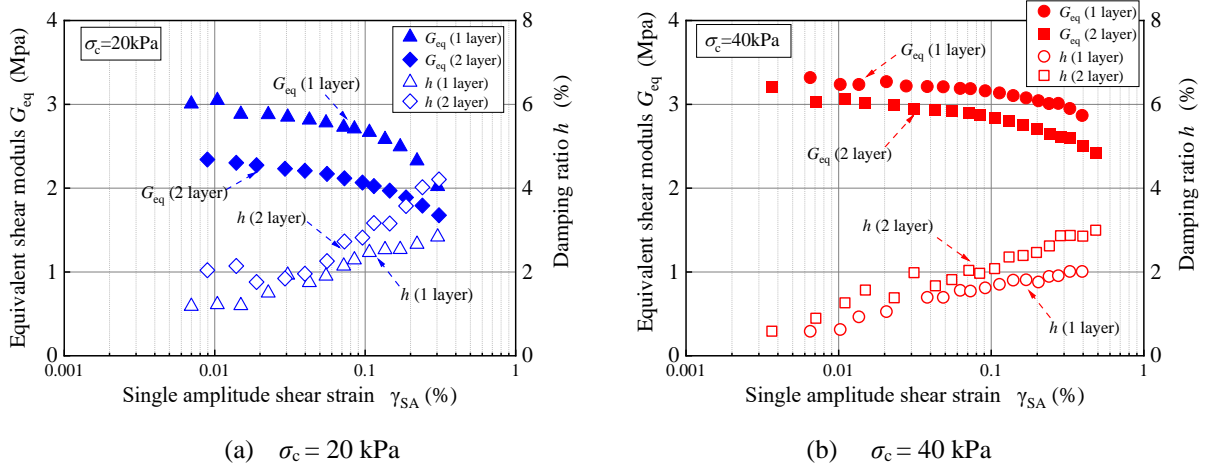

 Fig. 7 Relationship G_{eq} - γ_{SA} and h - γ_{SA} of rigid polyurethane foam with varying confining stress.

 Fig. 8 Relationship G_{eq} - γ_{SA} and h - γ_{SA} of rigid polyurethane foam with different type of specimens.

Figure 10 shows that there is a difference in the h - γ_{SA} relationship between the experimental values and the H-D model. Unlike the G/G_0 - γ_{SA} relationship, the h - γ_{SA} relationship differs depending on the presence or absence of a skin under both values of σ_c , particularly when $\gamma_{SA} = 0.02\%$ or more. Although not illustrated here, even when a different nonlinear model (the modified Ramberg-Osgood model [11]) was used, it was not possible to accurately approximate the h - γ_{SA} relationship. This means that the h - γ_{SA} relationship obtained using Masing's rule, as in the H-D model and the modified R-O model, might not be appropriate for the rigid polyurethane foam.

Figures 9 and 10 show the test results for marine clay (void ratio $e=1.391$) at $\sigma_c = 50 \text{ kPa}$. In marine clay, G/G_0 decreases and h increases with increasing γ_{SA} . In clay, G/G_0 decreases significantly after $\gamma_{SA} = 0.003\%$, whereas a striking decrease in G/G_0 is not observed in rigid polyurethane foam until $\gamma_{SA} = 0.1\%$. Furthermore, in clay, $G_0 = 15.6 \text{ MPa}$, which is

approximately three times greater than that in rigid polyurethane foam. Additionally, h of rigid polyurethane foam is substantially small compared with that of clay. Consequently, rigid polyurethane foam can be considered as a material with lower stiffness than soil materials, but one whose stiffness does not readily decrease.

CONCLUSIONS

- (1) For the rigid polyurethane foam used in this study, the value of G_{eq} increases and the value of h decreases with increasing confining pressure. This trend was not affected by the presence or absence of a skin.
- (2) In samples with a skin, there was cyclic loading at the gap caused by the skin; therefore, G_{eq} was smaller in two-layer samples than in one-layer samples. When σ_c increased, the gap caused by the skin was filled, and thus, the difference in the G_{eq} - γ_{SA} relationship between

the one-layer and two-layer samples became smaller.

- (3) When the H-D model representing the nonlinearity of soil was applied to the rigid polyurethane foam, there was good agreement with the experimental values for the G/G_0 - γ_{SA} relationship, but not for the h - γ_{SA} relationship. Therefore, the applicability of other nonlinear models and prediction formulas must be examined.

ACKNOWLEDGMENTS

This study was financially supported by the geoscience center foundation and RBH Research technical committee. We wish to offer our sincere gratitude.

REFERENCES

- [1] MLIT web page, <https://www.mlit.go.jp/en/index.html> (accessed 2020-07-02)
- [2] Nakamura H., Enomoto K., Aoki T. and Mitabe H., Full-scale shaking table tests on poured-in-place rigid polyurethane embankments, Tsuti to Kiso, Vol.51, No.4, 2003, pp.14-16 (in Japanese).
- [3] Chun S. B., Lim S. H., Sagong. M. and Kim K., Development of a hyperbolic constitutive model for expanded polystyrene (EPS) geofom under triaxial compression tests, Geotextiles and Geomembranes, Vol.22, 2004, pp.223-237.
- [4] Athanasopoulos A., Pelekis P.C. and Xenaki V.C, Dynamic properties of EPS geofom : an experimental investigation, Geosynthetics International, Vol.6, No.3, 1999, pp.171-194.
- [5] Ossa A. and Romo M.P., Dynamic characterization of EPS geofom, Geotextiles and Geomembranes, Vol.29, 2011, pp.40-50.
- [6] Trandafir A. C., Bartlett S. F. and Lingwall B. N., Behavior of EPS geofom in stress-controlled cyclic uniaxial tests, Geotextiles and Geomembranes, Vol.28, 2010, pp.514-524.
- [7] Gatto M. P. A., Montrasio L., Tsinaris A., Pitilakis D. and Anastasiadis A., The dynamic behaviour of polyurethane foams in geotechnical conditions, in Proc. 7th International Conference on Earthquake Geotechnical Engineering, 2019, pp.2566-2573.
- [8] Golpazir I., Ghalandarzadeh A., Jafari K. M. and Mahdavi M., Dynamic properties of polyurethane foam-sand mixtures using cyclic triaxial tests, Construction and Building Materials., Vol.118, 2016, pp.104-115.
- [9] JGS0542-2009, Method for cyclic triaxial tests to determine deformation properties of geomaterials, 2009, pp.751-767.
- [10] Hardin B. O. and Drnevich, V. P., Shear

Table 2 Parameters of H-D model

σ_c (kPa)	G_0 (MPa)	γ_r (%)	h_{max} (%)
20	3.1	0.65	4.5
40	3.4	1.8	3.5

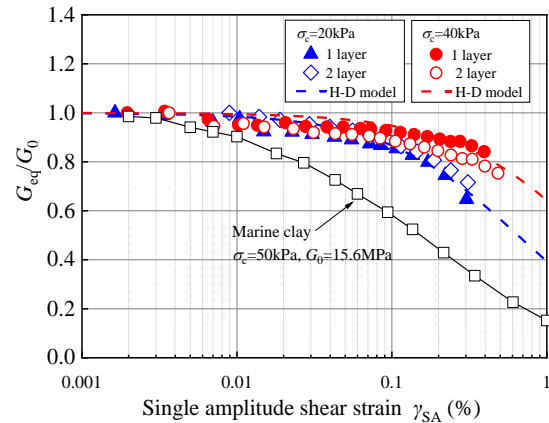


Fig. 9 Relationship between normalized shear modulus and shear strain of rigid polyurethane foam with H-D model.

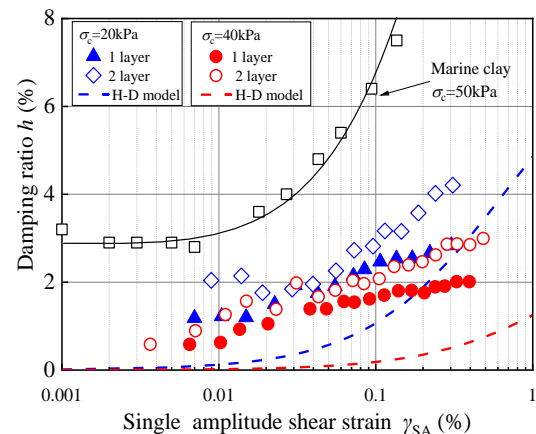


Fig. 10 Relationship between damping ratio and shear strain of rigid polyurethane foam with H-D model.

modulus and damping in soils: design equations and curves, in Proc. of the American Society of civil engineers, Vol.98, No.SM7, 1972, pp.667-692.

- [11] Tatsuoka F. and Fukushima S, Stress-strain relation of sand for irregular cyclic excitation (1), Seisan Kenkyu, Vol.30, No.9, 1978, pp.26-29.

EVALUATION OF FROST DAMAGE RESISTANCE OF LPC-FA COMBINED CONCRETE CURED FOR A LONG TIME

Shogo KAWAMORITA¹, Kazuhito NIWASE²

^{1,2}National Institute of Technology (KOSEN), Hachinohe College, JAPAN

ABSTRACT

In cold regions in the world, the deterioration of a concrete surface such as scaling and pop-out is caused by freezing and thawing action, which has a major influence on the durability and the appearance of the concrete structure. Deterioration resistance generally improves with densification. In this study, I evaluated the frost damage resistance of concrete using Low Heat Portland cement and fly ash (LPC-FA concrete). In long-term material, various tests were carried out using specimens that had been cured in water and exposure, focusing on the void structure and strength properties. In the strength properties, all mix proportions are around 50 N/mm², it was confirmed that it had a sufficient strength regardless of the W/B and Air. On the other hand, the exposed specimens are expected to have supplied less water. Therefore, it is considered that the densification of the structure by the pozzolanic reaction is insufficient. About the scaling test, the mix proportion of W/B 45% - Air 2.5% was 0.70 kg/m² when cured in water for 1 year, so resistance equal to or higher than that of general concrete was confirmed. However, in the exposed specimens, gravel peeling was observed in small proportions of Air. In this regard, considering the results of the air void spacing factor and the pore size distribution, it was suggested that a dense structure with a lot of fine voids less than 60nm that is difficult to freeze has high deterioration resistance.

Keywords: Air voids structure, Compressive strength, Fly ash, Frost damage, Low heat portland cement

INTRODUCTION

Concrete structure and concrete products are strictly controlled to use materials, mix proportions, curing, construction and the like so as to have predetermined quality and performance. However, in cold regions where the temperature is below freezing, surface deterioration such as scaling and pop-out is sometimes observed due to freezing and thawing action. Furthermore, the compounding with salt damage, carbonation and the like has a major influence on the durability and the appearance of the concrete structure [1].

Since these deteriorations progress from the surface, the degree of deterioration tends to be small if the strength property and the mass transfer resistance of the surface layer are favorable. The concrete surface layer has a role as a protective layer to prevent external deterioration factors entering the inside, and is a very important part for enhancing deterioration resistance.

In order to improve the resistance to deterioration of concrete, it is necessary to densify the surface layer. It is known that these concretes become very high resistance to deterioration by curing long term [2]. In particular, concrete using fly ash degrades in response to changes in void structure due to material age, such as the transition zone that becomes coarse voids with a diameter of 50nm several years resistance also changes [3]. Deterioration resistance generally improves with densification. However, the resistance of frost damage may be reduced in terms of expansion

pressure and osmotic pressure [4].

Therefore, in this study, I fabricated a specimen whose properties change significantly with age. At various ages, various tests such as scaling tests were performed, and the deterioration resistance at long-term age was examined from the viewpoint of strength characteristics and void structure.

EXPERIMENT OUTLINE

Materials used and mix proportion

Design policy

In this study, concrete using low heat portland cement and fly ash (LPC-FA concrete) was taken as a cement matrix with large changes in strength property and void structure on material age. The used materials and the mix proportions were designed in consideration of strength development, physical and chemical performance, suppression of cracks, and workability so that effects other than void structure change are minimized. The design principal of the materials used and the ingredients are shown in Table 1.

Materials used

As the binder, low heat portland cement and fly ash were added with super plasticizer and limestone fine

Table. 1 Design principal

Characteristic	Policy
Strength expression	Increase compressive strength
Physical and chemical performance	Reduce permeability and diffusivity
	Set appropriate congelation time
	Use chemically stable materials
	Reduce the large air voids and densify
Crack control	Suppression of heat of hydration
	Suppression of drying shrinkage
	Suppression of self-contraction
Workability	Increase flowability and material separation resistance

Table. 2 Outline of the materials

Material, Name	Code	Note
Low heat portland cement	LPC	Density=3.24g/cm ³ , Specific surface area=3730cm ² /g
Fly ash	FA	Density=2.17g/cm ³ , JIS type II, Specific surface area=3610cm ² /g
Limestone fine powder	LS	Density=2.70g/cm ³ , Specific surface area=5250cm ² /g
Sand : Lime crushed sand	S	Density=2.66g/cm ³ , FM=2.79 Hachinohe Matsudate Production
Gravel : Lime crushed stone	G	Density=2.69g/cm ³ , FM=6.63 Hachinohe Matsudate Production
Admixture : Air entraining and high range water reducing admixture, Air amount regulator	SP	Carboxyl group-containing polyether compound
	AS	Polyalkylene glycol derivative

Table. 3 Mix proportion

W/B (%)	Gmax (mm)	s/a (%)	Slump flow (cm)	Air (%)	Unit amount (kg/m ³)							
					W	Powder : P			S	G	SP	AS
						Binder : B		LS				
						LPC	FA					
45	20	53.4	65±5.0	2.5	160	249	107	178	883	780	0.95	
				5.0								0.060
				7.5								0.150
60				2.5	156	186	80	265	886			0.005※
				5.0								0.060
				7.5								0.030
75				2.5	155	148	64	318	887			
				5.0								0.015
				7.5								0.090

※ Defoamer

powder in consideration of self-filling property so that there was no difference in the quality of the specimens due to the factors at the concrete placing. Also, in order to eliminate the influence caused by the aggregate as much as possible, the materials other than the binder were unified with the materials based on chemically stable limestone. An outline of the materials used is shown in Table 2.

Mix proportion

The mix proportion was based on LPC-FA concrete with the water binder ratio of 45%, which has execution of workability test in previous studies [5] [6]. The water binder ratio was set to 60% and 75% to make a clear difference in pore structure. In addition, the unit amounts of water, powder and aggregate were adjusted so that the fresh property would not cause harmful materials separation, and the slump flow would have the same ratio within the range satisfying the standard. The mix proportion of the specimens is shown in Table 3.

Experimental method

Specimens

The concrete was mixed in a mixing amount of about 20 to 50 liters per batch and the mixing time for 120 seconds by a twin screw forced mixer. Each mix proportion was placing concrete in two batches of 100*100*400 mm, 100*500*400 mm, φ100*200mm.

The content of air was adjusted to be approximately 2.5%, 5.0%, 7.5% depending on the content of admixture added, and the slump flow was confirmed to be 65±5.0cm. The prepared specimens were demolded at 1 day of material age, and after curing water for 28 days, 91 days, 365 days in constant temperature curing tank (20°C) respectively, they were subjected to various tests. Figure 1 shows the exposed specimens.

The test sample for bubble measurement was 100*100*50 mm, and the test sample for scaling test was cut to 150*150*50 mm for the test. For the compressive strength test and the electrophoresis test, a specimen of φ100*200 mm was used, and the



Fig. 1 Exposed specimens

crushed specimen after the compressive strength test was used for the mercury injection method. As for exposed specimens, specimens of $\phi 50 \times 100$ mm and $\phi 100 \times 200$ mm were sampled by coring. The $\phi 50 \times 100$ mm specimen was subjected to the compressive strength test and the mercury injection method, and the $\phi 100 \times 200$ mm specimen was subjected to the scaling test.

Experimental item

In the experiment, the Compressive strength was measured to obtain a general indicator, and a Scaling test and Electrophoretic diffusion test based on deterioration in a chloride environment was performed. Moreover, in order to obtain the index of the air voids structure, manual linear traverse method was carried out. They based on various standards. The test items and methods are as follows.

- Scaling amount : Scaling test (RILEM-CDF method)
- Compressive strength : Compressive strength test (JIS R 5201)
- Air content and Air void spacing factor after curing : Manual linear traverse method (ASTM C 457)
- Pore size distribution : Mercury injection method
- Effective diffusion coefficient : Electrophoresis test (JSCE-G571)

TEST RESULTS AND DISCUSSION

Scaling test

The scaling amounts up to 50 cycles was measured under each mix proportions and material age. In the exposed specimens, when the air content was small, the coarse aggregate peeled and the surface layer was destroyed. Figure 2 shows the exposed specimen before and after the scaling test. The test results are shown in Figure 3.

At 28 days of age, it was confirmed that the larger the air content, the higher the resistance, and the

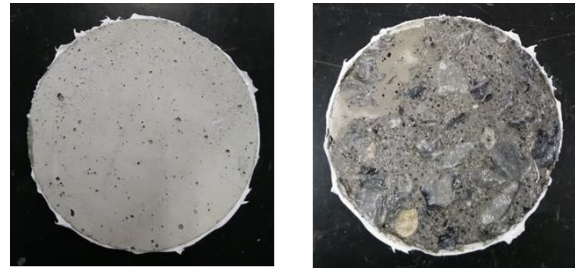


Fig. 2 Before and after the scaling test

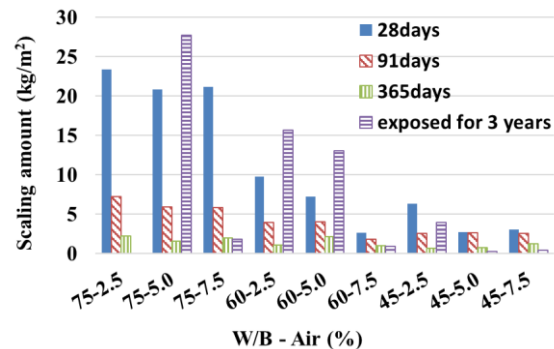


Fig. 3 Scaling amount

larger W/B, the lower the resistance regardless of the air content. However, at this point, even with a proportion of W/B 60% and air content 7.5%, 2.625 kg/m² was obtained, which is equivalent to that of general concrete. Furthermore, at 365 days of age, all the formulations were less than 2.5 kg/m², confirming a significant improvement in resistance with material age. In particular, it was 0.70 kg/m² at W/B 45% and air content 2.5%, and the result was that the scaling amount was extremely small even when the air content was small.

Then, I will compare the specimens that were aged 365 days in water and the specimens that were exposed for 3 years. In the case of a proportion with a small amount of air, the exposed specimen tends to greatly exceed the scaling amount. On the other hand, with the formulations with air content 7.5% and the formulation with W/B 45% air content 5.0%, the exposed specimen had a smaller scaling amount. Especially for W/B 45%, when the air content was 5.0% and 7.5%, the specimens cured in water were 0.789 kg/m² and 1.213 kg/m² respectively, but the exposed specimens were 0.237 kg/m² and 0.416 kg/m², which was about one-third the value of the exposed specimens for both formulations compared to the specimens cured in water. This is equivalent to or better than the commonly used concrete structures.

Compressive strength test

Figure 4 shows the compressive strength test results of the specimens that were aged in water for 1

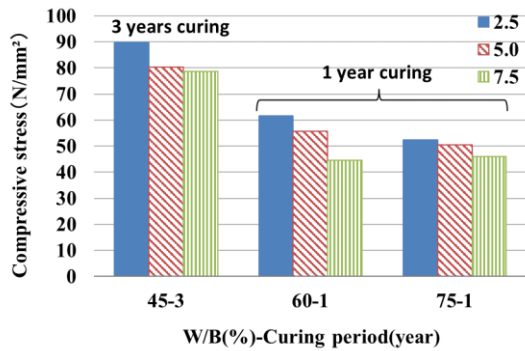


Fig. 4 Compressive strength (water curing)

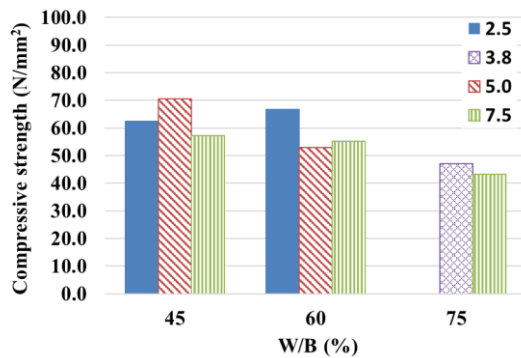


Fig. 5 Compressive strength (exposed specimens)

year and 3 years, and Figure 5 shows the compressive strength test results of the exposed specimens that were aged in air for 3 years. Regarding the exposed specimens, it was 3.8% and 7.5% due to the adjustment of the air volume. Moreover, cracks could not be confirmed visually.

As a result, the strength after 1 years underwater curing and 3 years in-air curing were close to each other, and there was not much difference due to the composition. At W/B 75%, the strength tends to be a little low, but still 40 to 50 N/mm² was secured. From Figure 5, the strength of W/B 45% and 60% are about 60 N/mm², which is about the same, and no correlation depending on the air content was seen.

Then, when the cumulative temperature at 1 years old age of the specimen cured in water is calculated, it becomes 10950°C. From the Japan Meteorological Agency data, the cumulative temperature of the exposed specimen was approximately 12580°C, and no clear difference was observed. And, the number of cycles that received the freeze-thaw action was about 330 times. In a previous study, in freeze-thaw tests, specimens that had been aged in water for 1 year tended to break at 150 cycles at a W/B 75% and an air content 2.5%. However, the exposed specimens had sufficient strength for all mix proportions [7]. In addition, it is estimated that about 50 m³ of water was supplied in three years from the rainfall. It can be seen that this is extremely small compared with the supply amount in underwater curing.

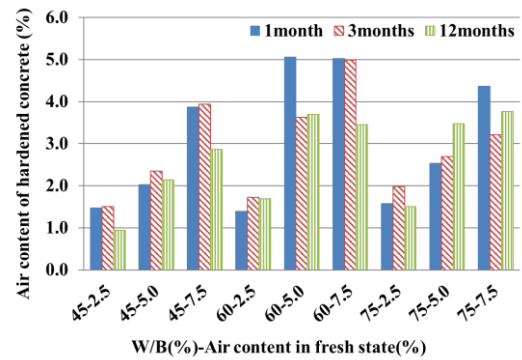


Fig. 6 Air content of hardened concrete

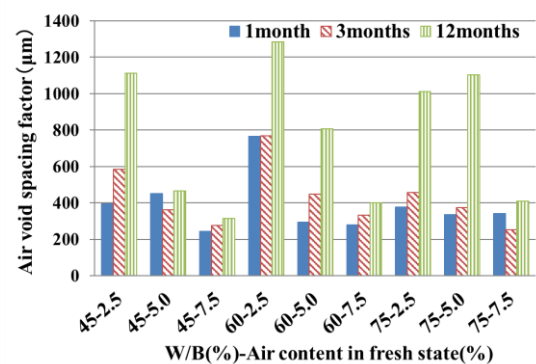


Fig. 7 Air void spacing factor

From these, it is considered that the difference due to the curing method is not due to the cumulative temperature or the freeze-thaw action, and is because the water supply necessary for the pozzolanic action is not sufficient. It is estimated that strength will develop with the supply of water due to precipitation in the future, so observation will continue until the material age of 5 years.

Air content after curing and air voids spacing factor

Air volume after curing

The content of air of each mix proportions measured using the linear traverse method is shown in Figure 6. The air content was about 2/3 of the air content of air at the time of freshness. In addition, the values were almost the same for each mix proportions regardless of the curing period. This is considered to be due to the fact that the influence of densification is not reflected, since the measurement of the content of air by the linear traverse method cannot measure the pore diameter of about 10μm or less.

Air voids spacing factor

Figure 7 shows the air voids spacing factor for each compounding condition measured using the linear traverse method.

The air voids spacing factor tended to double in the specimens with a relatively small content of air at 365 days of age. This is considered to be due to the fact that during the curing period of 365 days, the voids with minute bubble diameters became less than the bubble diameters that could be measured by the progress of the pozzolanic reaction, and the air voids spacing factor increased significantly. There was no change in the specimen with an air content of about 7.5% when fresh.

Here, based on the results of the scaling test, in the exposed specimens, the air voids spacing factor is about 800 to 1200 μm in all of the formulations in which the scaling amount was remarkably large. On the contrary, it can be confirmed that the mix proportions with good results is about 400 μm or less. Therefore, if the air voids spacing factor exceeds a certain value, it is considered that there is a high possibility that deterioration such as peeling of coarse aggregate will occur along with a significant decrease in scaling resistance.

Pore size distribution

Figure 8 shows the results of 365 days of the pore size distribution of each specimen obtained by the mercury injection method, and Figure 9 shows the results of the exposed specimen.

From Figure 8, it can be confirmed that in the 365 days old specimens, an extremely dense cement matrix was formed in all the mix proportions. It is known that the voids that affect freeze-thaw action are 100 to 1000 nm, and voids of 6 to 20 nm do not freeze up to -43°C [8]. Furthermore, the capillary voids (3 to 2000 nm) occupy about 2/3 of the voids in concrete. Based on this, it can be confirmed that the specimens cured in water for 365 days have a very small amounts of voids of 100 to 1000 nm, and most of them are fine voids of 30 to 40 nm or less that are hard to freeze. From this, it is considered that since the water in the voids does not freeze, a dense structure with high resistance that can relieve the expansion pressure and the osmotic pressure is formed.

On the other hand, as shown in Figure 9, the exposure specimens varied depending on the composition, and the correlation with the scaling test could not be confirmed. It is considered that this is because the densification of the tissue due to the hydration reaction and the pozzolan reaction was insufficient because it was not cured in water. In particular, in the case of W/B 60% air content 7.5% and W/B 75% proportions, there is a peak at about 100 nm, so there is concern about the effect of freeze-thaw action.

From these results, it is considered important to densify the voids, which are detrimental to the freeze-thaw action, in water for a certain period of time so that the voids do not freeze until they become dense.

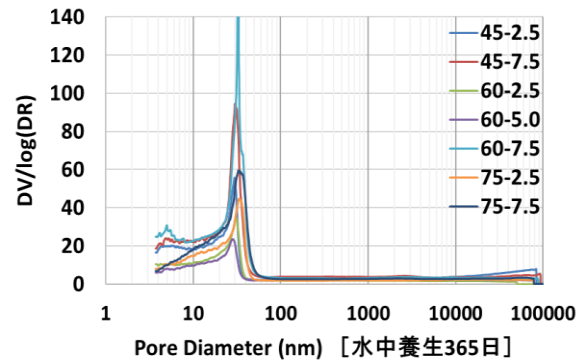


Fig. 8 Pore size distribution (water curing, 365 days)

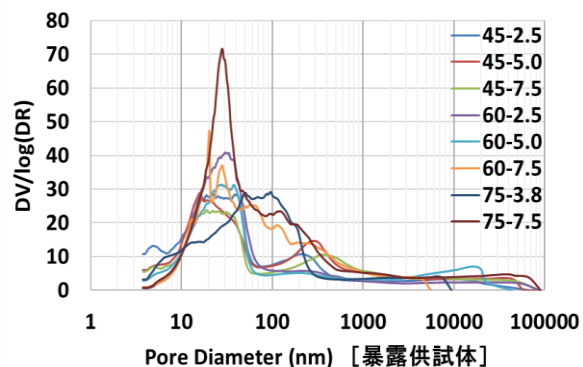


Fig. 9 Pore size distribution (exposed for 3 years)

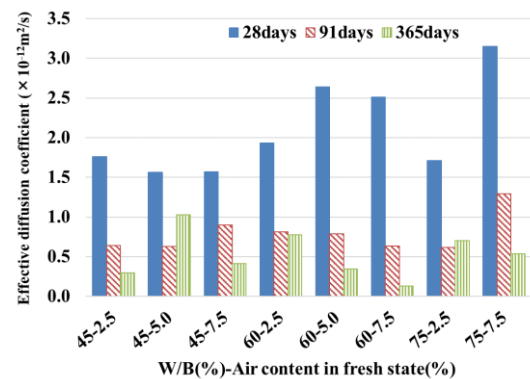


Fig. 10 Effective diffusion coefficient

As a result, deterioration resistance was able to be improved, so it is expected that the specimens at 365 days of age had good scaling resistance, although the bubble spacing coefficient was significantly large.

Effective diffusion coefficient

Figure 10 shows the effective diffusion coefficient of each mix proportions measured by the electrophoresis test.

Until 28 days of age, the effective diffusion coefficient was in the order of $10^{-12} \text{ m}^2/\text{s}$ in all cases. At 91 and 365 days of age, most of the mix proportions had small values on the order of 10^{-13} .

m²/s. The reason why the effective diffusion coefficient is large in any of the mix proportions is considered to be that the number of samples is one. However, very good results have been obtained in comparison with general concrete. From these results, the mass transfer resistance, which is important for complex deterioration such as salt damage and neutralization, was confirmed that is sufficiently small regardless of the mix proportions if good curing conditions are satisfied using LPC-FA combined concrete.

CONCLUSIONS

In this study, the deterioration resistance of LPC-FA concrete was evaluated from the viewpoint of strength characteristics and void structure.

In compressive strength, it was suggested that the water supply was low and the pozzolanic reaction did not proceed sufficiently in the exposed specimen. However, no difference due to W/B was observed, and it was confirmed that even W/B75% had sufficient strength, so it is considered that the strength characteristics are sufficient.

From the viewpoint of the void structure, it has been confirmed that the scaling deterioration resistance is significantly reduced when the air voids spacing factor exceeds a certain value. On the other hand, it was suggested from the results of the pore size distribution that it is important to perform underwater curing for an appropriate period to form a dense structure with many fine voids that are difficult to freeze. In this case, it is considered that the deterioration resistance may not decrease even if the air voids spacing factor is large.

From the result of the effective diffusion coefficient, the invasion of deterioration factors from the outside was found to be sufficiently small regardless of the mix proportions at the material age of 365 days.

From these, it is important to densify the structure to reduce the deterioration of frost damage under chloride environment, and it is necessary to sufficiently advance the pozzolanic reaction after an appropriate curing period. By satisfying these requirements, LPC-FA concrete is considered to have sufficient practicability.

In the future, I plan to conduct an electrophoresis test and voids measurement of exposed specimens at the material age of 3 years. Furthermore, I will continue to observe for 5 years of material age, and will carry out various tests such as compressive strength test, scaling test, mercury injection method, etc. to evaluate and examine changes in strength characteristics and voids structure.

ACKNOWLEDGMENT

Part of this research was conducted in response to a grant fund for research or activities related to the maintenance and maintenance of social capital in FY2019.

REFERENCES

- [1] M. Shoya and Y. Tsukinaga, "Frost Damage of Concrete Structure in Tohoku District," Concrete Journal, Vol.42, No.12, pp.3-8, 2004 (in Japanese)
- [2] K. Niwase, M. Hironaga and Y. Tsuji, "Design of the Concrete Used for Sub-surface LLW Disposal Facility," Concrete Journal, Vol. 44, No. 2, pp.3-8, 2006 (in Japanese)
- [3] H. Uchikawa, S. Hanehara and D. Sawaki, "Estimation of the Thickness of Transition Zone in Hardened Mortar and Concrete, and Investigation of the Relationship between their Thickness and Strength Development," Concrete Research and Technology, Vol. 4, No. 2, 1993 (in Japanese)
- [4] Powers, T.C., "Mechanisms of shrinkage and reversible creep of hardened cement paste," International Conference on the Structure of Concrete, Cement and Concrete Association, London, pp.319-344, 1968
- [5] K. Niwase, N. Sugihashi and Y. Tsuji, "Materials and Proportion's Design of Self-compacting Mortar Used for Low Diffusion Layer in Sub-surface Radioactive Waste Disposal Facility in Japan," Concrete Research and Technology, Vol. 21, No. 3, pp.43-51, 2010 (in Japanese)
- [6] K. Niwase, N. Sugihashi and Y. Tsuji, "Required Initial Performance of Low Diffusion Layer in Sub-surface Radioactive Waste Disposal Facilities After Carry in out a Full-size Model Test, Concrete Research and Technology," Vol. 21, No. 3, pp.53-62, 2010 (in Japanese)
- [7] H. Mawatari, K. Niwase, T. Sugawara and Y. Edamatsu, "Changes of Frost Damage Resistance and Air Voids Structure of LPC-FA Concrete According to Curing Periods," Our World in Concrete & Structures, August 2017 (in Japanese)
- [8] S. Hanehara, D. Sawaki, "Void structure and physical properties of hardened concrete," Gypsum & Lime, No.240, pp.32-34, 1992 (in Japanese)

IMPROVEMENT OF INITIAL STRENGTH OF LPC-FA CONCRETE BY USING C-S-H-TYPE ACCELERATOR

Takuya KUDO* and Kazuhito NIWASE*

¹National Institute of Technology, Hachinohe College (Tamonoki Hachinohe 039-1192, Japan)

ABSTRACT

Most social infrastructures in Japan have been aging rapidly because there were constructed during the high growth period. Moreover, the number of skilled workers with a lot of experience are decreasing. As a result, there is a concern about degradation of structure quality. That is why it is necessary to develop new materials that have excellent long-term durability and easy workability.

Owing to previous studies, it is known that concrete using low heat portland cement and fly ash (hereinafter, this is called "LPC-FA concrete") has excellent long-term durability, but there is a problem with low initial strength. Therefore, in this study, basic research was carried out to enhance the initial strength of LPC-FA concrete. The initial strength of LPC-FA concrete was tried to improve by using a combination of accelerating admixture (MXS) to accelerate the hydration reaction with C-S-H nanocrystals, air entraining and high-range water reducing admixture (ME). Two materials have been confirmed to be good combination by previous research.

In this study, the W/B were at 30% evaluated the initial strength and fluidity. In addition, the effective diffusion coefficient of chloride ions was measured as the mass transfer resistance of the deterioration factor from the surface.

From the test results, it was confirmed that the initial strength of LPC-FA concrete could be increased by combining ME and MXS, and an extremely dense cement matrix was formed.

INTRODUCTION

Most social infrastructures in Japan have been aging rapidly because there were constructed during the high growth period. Moreover, the number of skilled workers with a lot of experience are decreasing. As a result, there is a concern about degradation of structure quality. That is why it is necessary to develop new materials that have excellent long-term durability and easy workability.

In this study, we carried out basic research aimed at improving the initial strength of fly ash concrete (LPC-FA concrete) using low heat Portland cement. Owing to previous studies, it is known that concrete using low heat Portland cement and fly ash (hereinafter, this is called "LPC-FA concrete") has excellent long-term durability, but there is a problem with low initial strength. On the other hand, the development of chemical admixture technology has enabled us to obtain products with unprecedented results. Therefore, in this study, we tried to improve the initial strength of LPC-FA concrete by using air entraining and high-range water reducing admixture and accelerating admixture together. Also, by reducing W/B, voids can be reduced, and high initial strength and improved mass transfer resistance can be expected.

In the experiment, the initial strength and fluidity of LPC-FA concrete were confirmed by preliminary experiments using mortar. In addition, the effective diffusion coefficient of chloride ions was measured as

the penetration resistance of the deterioration factor from the surface.

EXAMINATION SUMMARY

Fluidity Evaluation

A slump flow test was performed to evaluate the fluidity. Fluidity evaluation was performed according to THE SLUMP FLOW TEST METHOD FOR CONCRETE (JIS A 1150). Assuming on-site construction for the construction time, after kneading for 0, 30, 60, 90 and 120 minutes, tests were conducted using mortar.

STRENGTH EVALUATION

The strength evaluation was performed according to THE COMPRESSIVE STRENGTH TEST METHOD FOR CONCRETE (JIS A 1108). The specimens were cured by underwater curing. Material age was 3, 7, 28 and 91 days.

MASS TRANSFER RESISTANCE EVALUATION

Evaluation of mass transfer resistance was conducted in accordance with the Society of Civil Engineers' Procedure "TEST METHOD FOR

EFFECTIVE DIFFUSION COEFFICIENT OF CHLORIDE ION CONCRETE BY MIGRATION" (JSCE-G 571-2003)¹⁾. As the specimen, a column specimen cut into a size of $\phi 100 \times h 50$ mm was used.

The diffusion cell used in this test is shown in Fig.1. This diffusion cell is taken into consideration so that the side of the specimen is made into the state shown in Fig.2 with the epoxy resin and the heat shrinkable rubber, and the cells on the NaCl solution side and the NaOH solution side are connected. As a result, chloride ion moves only in the specimen, and movement from the joint surface at the side of the specimen is blocked. Even when solution leakage occurs from a fine gap, there is no contact of the solution outside the specimen, so it has an advantage that is not reflected in the data.

MIX PROPORTIONS DESIGN

Mix Proportions of Viscosity Study by Adjusting the Substitution Rate of Limestone Fine Powder

The basic mix proportions were created based on the $W/B = 50\%$ mortar composition²⁾ of the previous study. We believe that fluidity will change significantly with changes in W/B , so we decided to adjust with substitution rate of limestone fine powder (LS)⁴⁾. It was set in three mix proportions of 10%, 20% and 30%. Below, LS10 indicates that the ratio of limestone fine powder to fine aggregate is 10%. The common condition is $W/B = 30\%$. Fly ash (FA) addition rate is 30%, and the addition amounts of

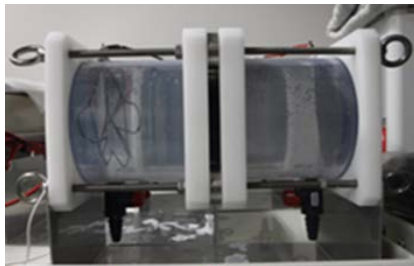


Fig.1 Diffusion cell

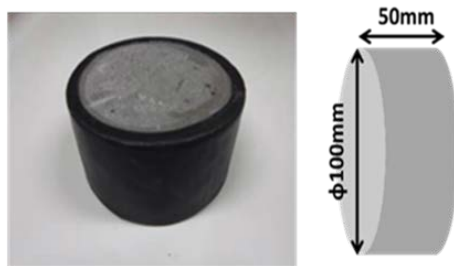


Fig.2 Specimen for electrophoretic method

ME and MXS are both $C \times 3\%$. Trial mixing was carried out with mix proportions shown in table.1. In LS10, the fluidity is high, but separation was

confirmed at the edge. It did not separate at 20% and became high flow. At 30%, the fluidity decreased and did not flow uniformly on the flow table. From this result, the substitution rate was determined to be 20%. There was no change in the LS substitution rate when $W/B = 50\%$. It is considered that this is because the unit cement amount and fly ash amount increased due to the change of W/B , and the chemical admixture amount also increased.

MIX PROPORTIONS DURING VARIOUS WITH MORTAR

Mix proportions of mortar were determined in table2. table.3 shows the materials used. Mix proportions are

Table1. Viscosity study mix proportions

Type	Unit volume weight (kg/m ³)						
	W	C	F	LS	S	ME	MXS
LS10	178	483	207	145	1304	14.5	14.5
LS20	178	483	207	290	1160	14.5	14.5
LS30	178	484	207	436	1016	14.5	14.5

Table2 mix proportions during various with mortar

Type	W/B	Unit volume weight (kg/m ³)						
		W	C	F	LS	S	ME	MXS
OPC-ME-MXS	30	178	483	207	290	1161	14.5	14.5
OPC-ME-MXS	50	211	322	138	322	1288	9.7	9.7
OPC-ME	30	193	483	207	290	1161	14.5	—
LPC-ME-MXS	30	179	483	208	291	1164	14.5	14.5

OPC : Ordinary Portland Cement, LPC : Low Heat Portland Cement, F : fly ash, LS : Limestone fine powder, ME : Air entraining and high-range water reducing admixture, MXS : Accelerating admixture

Table3. Using materials

Material	Abbreviation	Overview
Cement	OPC	Ordinary Portland Cement Density=3.160g/cm ³ Specific surface
	LPC	Low Heat Portland Cement Density=3.220g/cm ³ Specific surface
Fly ash	FA	JIS type II Density=2.190g/cm ³ Specific surface
Limestone fine powder	LS	Density=2.700g/cm ³
Air entraining and high-range water reducing admixture	ME	PAE, Amount to use=C×0.5~3.0%
Accelerating admixture	MXS	Amount to use = C×0.5 6.0%

OPC-ME which added only air entraining and high-range water reducing admixture to OPC and OPC-ME-MXS which added air entraining and high-range water reducing admixture and accelerating admixture to OPC, LPC-ME-MXS which added air entraining and high-range water reducing admixture and accelerating admixture to LPC, In three types. As a general condition, $W/B = 30\%$, FA replacement rate 30%. C and 3% were added to ME and MXS, and LS was 20% to fine aggregate.

FLUIDITY EVALUATION

Slump Flow Test Results

Fig.3 shows the decrease in viscosity with the three formulations ($W/B=30\%$). Fig.4 shows the $W/B = 50\%$ viscosity reduction obtained in the previous study ²⁾ and the $W/B = 30\%$ viscosity reduction obtained in this test. Fig.5 to 7 show the state of slump flow immediately after kneading the three types of mix proportions ($W/B = 30\%$). LPC-ME-MXS (30%) showed very high fluidity. As a result, it could not be measured because it did not fit in the 80 x 80 cm flow table. In addition, the measurement was performed from 2 hours after kneading, but no decrease in the flow value was observed. Both OPC-ME and OPC-ME-MXS showed very high fluidity immediately after kneading. Comparing the flow values of the two mix proportions, the flow value immediately after

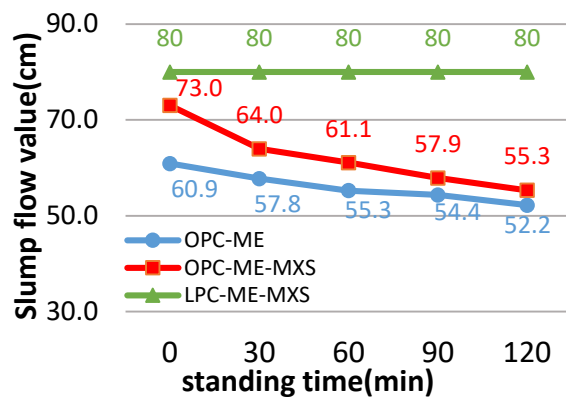


Fig.3 Slump flow test results

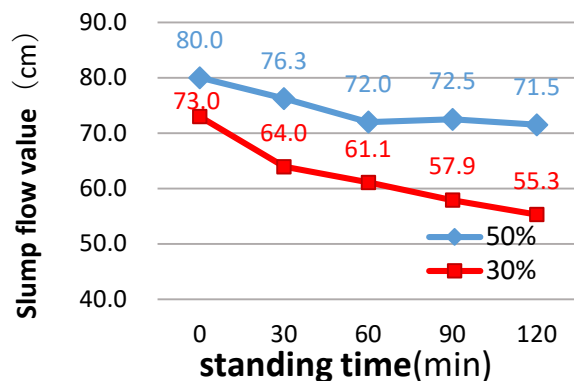


Fig.4 OPC-ME-MXS slump flow test results

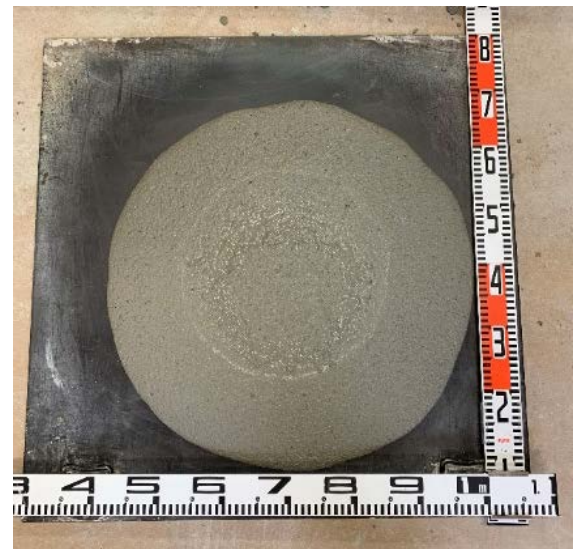


Fig.5 OPC-ME

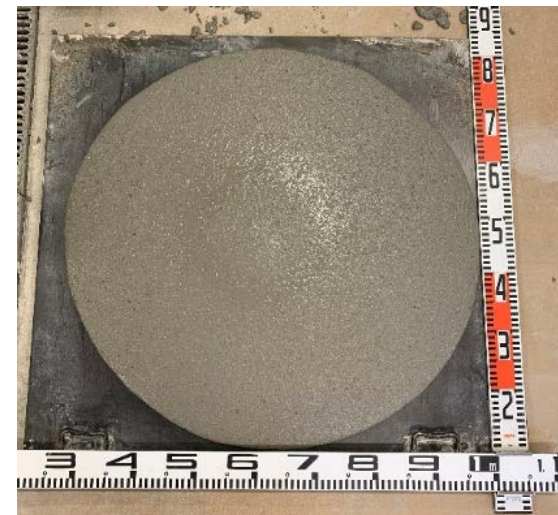


Fig.6 OPC-ME-MXS



Fig.7 LPC-ME-MXS

kneading was 60.9 cm for OPC-ME and 73.0 cm for OPC-ME-MXS, a difference of 12.1 cm. After that, the flow values of the two mix proportions decreased with time, and after 2 hours, OPC-ME was 52.2 cm and OPC-ME-MXS was 55.3 cm. The decrease in the flow value after the lapse of 2 hours was 8.7 cm for OPC-ME and 17.7 cm for OPC-ME-MXS. The OPC-ME-MXS has a larger decrease in the flow value over time.

The flow values immediately after kneading of OPC-ME-MXS and LPC-ME-MXS were much larger than those of OPC-ME without MXS added. However, after 2 hours, the LPC-ME-MXS kept a high flow, but the flow value of OPC-ME-MXS decreased to the same level as OPC-ME. Comparing OPC-ME-MXS with $W/B = 50\%$ and $W/B = 30\%$, 50% had a decrease in flow value of 8.5 cm after 2 hours, which was about half of 30%. By setting the W/B to 30%, the decrease in the flow value with the passage of time became large. Therefore, it is necessary to consider the deterioration of fluidity with the passage of time when constructing with a low water cement ratio.

SLUMP FLOW TEST CONSIDERATIONS

The result of the slump flow test of LPC was extremely large compared to the result of the OPC test. Also, there was a big difference in the tendency of viscosity decrease. This is probably because LPC has less interstitial phase that adsorbs the admixture more easily than OPC⁵⁾. Especially at low water cement ratios such as high strength concrete, low porosity and admixtures such as fly ash tend to be compatible. Therefore, it is considered that such a difference in the flow value appears. The results of the slump flow test of OPC-ME and OPC-ME-MXS show that the addition of MXS has a great influence on the fluidity. It is generally believed that addition of MXS accelerates curing and reduces the flow value. However, with this mix proportions, the flow value of OPC-ME-MXS and LPC-ME-MXS with MXS increased. From this, it is considered that chemical factors that have not been confirmed so far have occurred, such as MXS inhibiting the adsorption of ME. In the future, it is necessary to examine the chemical factors. Regarding the properties related to pumpability, all three mix proportions showed thixotropy, in which the viscosity decreased when the shear stress was continued and increased when it was stationary. Therefore, when applying it, it is necessary to confirm the pumpability in consideration of its workability. Then, in some cases, it is considered that the driving with the bucket may be suitable.

STRENGTH EVALUATION

Compressive Strength Test Results

Fig.8 shows the results of the compressive strength test. As a result, the 3-days strength was 20 N/mm² or more in all mix proportions, and sufficient strength could be obtained. Among them, OPC-ME-MXS was 61.1 N/mm², which was about 1.7 times stronger than OPC-ME. The lowest strength mix proportion was LPC-ME-MXS at 26.3 N / mm². However, the increase from 3 to 7 days intensity was the largest and increased by about 22N / mm². Therefore, it became the same level as OPC-ME.

Next, pay attention to the presence or absence of MXS and compare OPC-ME-MXS and OPC-ME. At 3-days strength, the difference in strength between the two mix proportions were 25.1 N/mm². After that, the strength of OPC-ME-MXS was higher than that of OPC-ME. From 28-days strength to 91-days strength, OPC-ME increased by about 12 N/mm², while OPC-ME-MXS increased by about 25 N/mm², which was about twice the increase of OPC-ME. It was confirmed that the effect of adding MXS was remarkable by the age of 3 days. It was found that the long-term strength increase was higher in the mix proportion containing MXS. It can be considered that MXS influenced the pozzolan reaction by FA.

The strength of the two OPC mix proportions continued to increase up to the 91-days age, while LPC decreased by 11.6 N/mm² from the 28-days strength to the 91-days strength. Fig.9 shows a 28-days strength comparison of LPC-ME-MXS with $W/B = 30\%$ and $W/B = 50\%$ obtained in a previous study²⁾. By lowering W/B , $W/B = 30\%$ was about 15 N / mm² higher than $W/B = 50\%$ at 3 days strength. Even in the strength after 3 days, the mix proportion of $W/B = 30\%$ was high. The increase from 3-days intensity to 28-days intensity was about 40 N / mm² for $W/B = 50\%$ and about 70 N / mm² for $W/B = 30\%$. Therefore, a large increase in strength could be confirmed in the long term.

COMPRESSIVE STRENGTH TEST CONSIDERATIONS

According to the compression test results of this mix proportions, a compression strength of over 20 N/mm² was obtained for all the mix proportions at the time of 3-days strength. This is considered to be because the W/B of this mix proportion was 30%, and the voids were reduced due to the very low water-cement ratio. In addition, the water-powder ratio was also extremely small at 20%, so it is considered that the specimen was a dense sample. OPC-ME-MXS has much higher compressive strength than OPC-ME. Among them, there was a remarkable difference in the amount of increase in strength up to 3 days. This is considered to be due to

the mechanism of hardening promotion by MXS shown in Fig. 10. MXS is accelerating admixture whose main component is calcium silicate hydrate (C-S-H) nanocrystals. This introduced C-S-H seed crystals into the liquid phase and accelerated hardening without waiting for C-S-H to form from the cement. It is considered that this improves the initial strength. Furthermore, the increase in OPC-ME-MXS from 28-days intensity to 91-days intensity was about double that of OPC-ME. It is considered that this is because the C-S-H structure was more compacted by the pozzolan reaction with FA.

LPC-ME-MXS was the smallest at 3-days intensity but the largest at 28-days intensity. This is considered to be due to the characteristic that the strength of LPC increases over a long period of time. The cause of the 91-days intensity decline has not been clarified at present. Fig.11 shows the condition of LPC-ME-MXS specimens after the 91-days-old compression. It is considered that the peeling observed on the side surface of the test piece after the compression test is one of the causes of the decrease in strength. It is known that there is a close

increases and the total length of cracks that occur until the destruction. That is, it is said that the smaller the size of the test piece, the shorter the elapsed time from the occurrence of local microcracks to the destruction of the entire system, so that the strength decreases. In the future, we will investigate the cause of the decrease in 91-days strength from the viewpoint of fracture mode and specimen size.

MASS TRANSFER RESISTANCE EVALUTION

Mass Transfer Resistance Results

Fig.12 shows the electrophoresis test results. All were below the order of $1.0 \times 10^{-12} \text{ m}^2 / \text{s}$ in this mix proportions. OPC-ME-MXS has a smaller value than OPC-ME, and LPC-ME-MXS has an even smaller value. The average value of LPC-ME-MXS was $1.0 \times 10^{-14} \text{ m}^2 / \text{s}$. There were also specimens of the order of $1.0 \times 10^{-14} \text{ m}^2 / \text{s}$ in OPC-ME-MXS. The average value of OPC-ME-MXS was less than half the average value of OPC-ME.

MASS TRANSFER RESISTANCE CONSIDERATION

The value of the effective diffusion coefficient shows that an extremely dense cement matrix was formed. This time, we were able to obtain very small values for all mix proportions. It is considered that because W / B was very low at 30%, the voids were reduced and the mortar became dense. The water/powder ratio was about 20%, and the amount

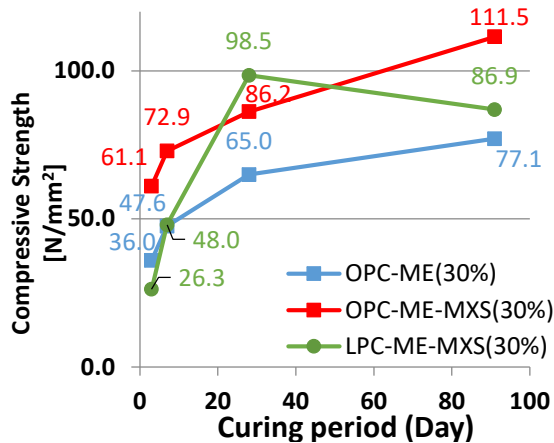


Fig.8 Compression test result

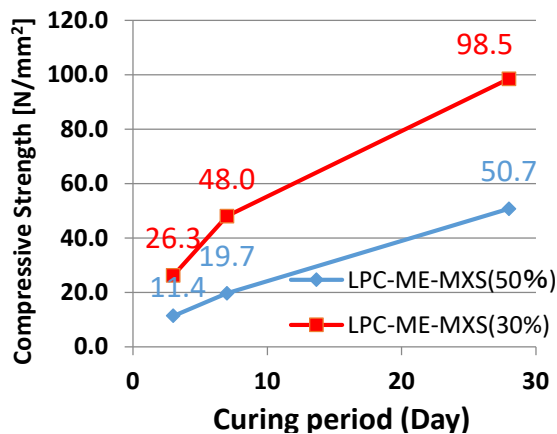


Fig.9 LPC-ME-MXS compression test results

strength increases as the size of the specimen

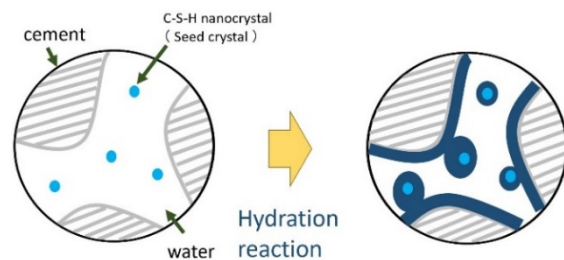


Fig.10 the mechanism of hardening promotion by MXS



Fig.11 LPC-ME-MXS specimens after the 91-days-old compression test.

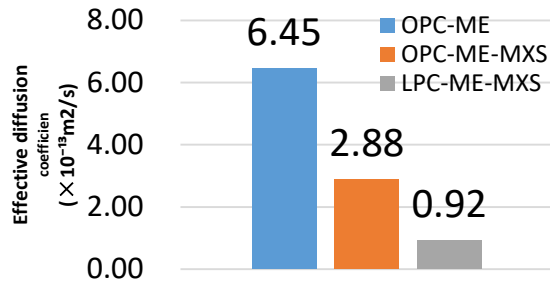


Fig.12. Mass transfer resistance results

of powder was very large. This is also considered to be one of the factors that reduced the effective diffusion coefficient.

OPC-ME-MXS was able to get a smaller value than OPC-ME. It is considered that this is due to the seed crystal of the above nanoparticles contained in MXS. From this, it is considered that the addition of MXS is effective in increasing the mass transfer resistance.

This mix proportions have extremely high mass transfer resistance even at 28 days of age, and it was found that the effect of MXS was much larger than expected. In the future, it is expected that the effective diffusion coefficient will be further reduced by the pozzolanic reaction due to the addition of fly ash.

CONCLUSION

The following findings have become clear from this study.

- 1) By using MXS and ME together, a large flow value could be obtained for mortar. Moreover, when MXS and ME are used together, LPC has a larger flow value than OPC.
- 2) By combining MXS and ME, it was confirmed that a high initial strength could be obtained in the LPC-FA mortar, and a very dense cement matrix was formed.
- 3) In mortar, LPC-ME-MXS had the highest compressive strength of 28-days-old specimens. However, the 91-days intensity was decreased only in LPC-ME-MXS.
- 4) By setting the W / B to 30%, the strength of all three mix proportions was higher than that of the previous study²⁾ where the W / B was 50%.
- 5) At the 3-days intensity, OPC-ME-MXS showed a marked increase. However, the increase in LPC-ME-MXS also increased at 7-days intensity.
- 6) An extremely small effective diffusion coefficient was obtained. This is probably because the W / B was 30% and the voids were reduced. Moreover, it is expected that the large amount of powder contributed to the compactness of the specimen. The effective diffusion coefficient was reduced by adding MXS, and the mass transfer resistance was improved. In the future, it is expected that the effective diffusion coefficient will be further

reduced by the pozzolanic reaction due to the addition of fly ash.

FUTURE TASKS

- 1) Examine the chemical basis for the factors of high workability, strength, and mass transfer resistance obtained by adding MXS.
- 2) Examine the factors that reduced the long-term strength of LPC-ME-MXS.
- 3) We will study the fluidity and initial strength when W / B is further reduced.
- 4) Considering economic efficiency, we will study the fluidity and initial strength when the addition rate of the chemical admixture is reduced.
- 5) The concrete mix proportion is decided based on the data of the preliminary experiment with mortar, and each test is conducted.

REFERENCE

- 1) TEST METHOD FOR EFFECTIVE DIFFUSION COEFFICIENT OF CHLORIDE ION CONCRETE BY MIGRATION (JSCE-G 571-2003) (in Japan)
- 2) Sora SUTO, Kazuhito NIWASE : Study on Improvement of Early Strength of Highly Durable Concrete by Combined Use of Chemical Admixtures, The 3rd International Conference on Structural and Civil Engineering(ICSCE2019),2019
- 3) Sora SUTO, Kazuhito NIWASE : Evaluation of effect on strength development by combined use of Air entraining and high-range water reducing admixture and Accelerating admixture, JSCE Hokkaido Branch Papers, Vol 75, Jan. 2019 (in Japan)
- 4) K.NIWASE,N,SUGIHASHI,Y,TSUJI:Mortar mix design of low diffusion layer for sub-surface radioactive waste disposal facilities in japan, The 7th International Symposium on Cement & Concrete (ISCC2010), The 11th International Conference on Advance in Concrete Technology and Sustainable Development,2010
- 5) Toyoharu NAWA: Current Status of Belite Rich Cement, Concrete Journal, Vol.34, No.12, pp16~25, Dec.1996
- 6) Taisei SAKAI, Kazuhito NIWASE : Basic Study of Cement Solidification Technology for Solidification of Cesium Adsorbed Zeolite Evaluation of Microscopic Structure of Cement Solidification , 8th Int. Conf. on Geotechnique, Construction Materials and Environment, pp.537-542,2018
- 7) Yasuo TANIGAWA, Kazuo YAMADA, On the size effect of compressive strength of concrete, Proceedings of Architectural Institute of Japan No. 262, December 1977 (in Japan)

POSSIBLE RECYCLING OPTIONS FOR WASTE MATERIALS IN CERAMIC TILES

Qibin Yuan, Abbas Mohajerani, Halenur Kurmus, John V. Smith

School of Engineering, RMIT University, Australia

ABSTRACT

Throughout the world, the generation of wastes is increasing in quantity and diversity at a rapid rate. To slow down the deterioration of our ecosystem, effective and efficient methods must be developed to dispose of and recycle the wastes produced. Besides, there is a need to reduce the resources utilised and lower the impact on our environment. In 2017, over 13.5 million square meters of tiles were produced globally, and the demand for ceramic tiles has escalated along with social development. There has been an increasing incentive to recycle waste materials in ceramic tiles due to the high heterogeneity of the raw materials in the composition of ceramics and the matrix for creating ceramic tiles being flexibly interchangeable. The objective of this paper is to review and discuss the various recycling options of waste materials in the production of ceramic tiles. Past experimentation includes the addition of glass, coal ash, municipal solid waste ash, and sewage sludge in the production of ceramic tiles. They were used as an additive or substitute of the key ingredient to the ceramic matrix. The results show that there are generally enhancements on the physical and mechanical properties with minor adverse effects of the tiles. Furthermore, the heavy metals found in toxic wastes were found to be immobilised during the firing process of tiles. Hence, the addition of wastes in tiles offers a sustainable solution in easing the necessity of managing wastes and decreasing the consumption of natural resources. Further research developments are essential.

Keywords: Waste Materials; Ceramic Tiles; Recycling; Sustainability; Geomaterials

INTRODUCTION

From the beginning of the industrialisation and the continued growth in the population of worldwide, how to deal with wastes has become a significant problem that can't be ignored [1]. In 2016, the annual global municipal solid waste generation reached 2.01 billion tonnes, and it will rise to 3.40 billion tonnes by 2050 if all conditions remain the same. The same report from the World Bank also indicates more than 33% of waste is mismanaged, and only 13.5% of waste has been recycled globally [2]. Moreover, the common uncontrolled disposal methods in developing and transition countries can cause severe heavy metal pollution to the ecosystem and have negative impacts on human society, such as economic sustainability and social inclusion [3]. As natural resources are depleting and climate change by gas emission and environmental contaminations are increasing, many researchers are focusing on reusing waste materials, and the outcomes indicate a prominent future for recycling.

Ceramic tiles are considered to be a feasible product for waste materials recycling. Technological innovations in the manufacturing cycle of the ceramic tile industry cause extreme changes in the range of raw materials and the development of novel ceramic products like porcelain tile. These novel ceramic products have significant advancement in technical performance and aesthetic appearance, but also have brought difficulties to the classification of ceramic

tiles due to the various formulations and wide selection of raw materials [4].

Research confirmed that modern ceramic products exhibit high tolerance in its compositional structure, which shows the potential to recycle waste materials without compensating the overall quality [5]. Furthermore, research reported that there are 13.552 million m² of ceramic tiles produced in 2017, with a compound annual growth rate of 5.2% [6]. Therefore, the ceramic tile industry has the capability to recycle a large amount of waste material while reducing the usage of natural raw materials. Utilising waste materials in the manufacturing process of ceramic tile can be a sustainable solution to ease the pressure on waste management.

USE OF WASTE MATERIALS

Waste glass, coal fly ash, coal bottom ash, municipal solid waste incineration (MSWI) fly ash, MSWI bottom ash, sewage sludge and sewage sludge incineration ash will be reviewed and discussed in this article.

Glass Waste

Glass is one of the most common materials in our life. Despite the superior properties of glass products, the popularity is because of its high recyclability, where recycled glass products have no apparent loss in purity and quality [7]. Due to the different chemical

compositions of different types of glass, it is essential to categorise glass wastes before the recycling process. Most glass wastes are soda-lime-silicate (SLS) glass, which can be found in containers and flat glasses of windows and doors. Other common glass types that will be reviewed include alkali-barium silicate from cathode ray tubes, sodium borosilicate from liquid crystal display and Pyrex, lead glass from crystal glassware and cathode-ray tubes, and alumino-borosilicate from glass fibres [8]. Due to the glass types, other than SLS, commonly being used for electronics and other purposes, it is necessary to sort before recycling as they might contain hazardous chemicals and heavy metals. However, recent studies show special treatment like washing with acid can increase the recovery rate [8, 9].

Incorporating high amounts (>60 wt.%) of end of life fluorescent lamp glass (FLG) and waste packing glass (PWG) into ceramic tiles have received promising experimental results. The final products achieve comparable mechanical properties to traditional ceramic tiles. Furthermore, FLG (<400 μm) tile passes the ISO requirement of BIA group of water absorption (<0.5%) and bending strength (>35MPa), which is equivalent to high sintered floor tiles. It is to be noted that these two types of glasses are close to typical SLS glass but contain different impurities and at different ratios of chemical components. The differences in the composition of these two glass wastes cause different characteristic temperatures, which further affect the properties of the final tiles (shown in table 1). Unfortunately, this experiment didn't carry out control sample tile and PLG (<100 μm) tile, so we can only assume that the finer particle size of PGW results in better performance, and the tiles with different waste glasses have noticeable performance gap [10].

Table 1 Properties of ceramic tiles with waste glass [10].

Sample type	Linear shrinkage (LS %)	Water absorption (WA %)	Bending strength (MPa)
PGW (<400 μm)	4.87	1.83	23.37
PGW (<100 μm)	5.46	0.29	30.6
FLG (<400 μm)	8.79	0.02	40.93

Note: Results are under the same manufacturing processes. Sintering 60 min at 1000 °C, and formed by pressing (40 MPa).

Another comprehensive review paper compared multiple research studies on recycling different types of glass into ceramic tiles. Overall, waste glass has the potential to be recycled into ceramic tiles and

enhance the properties. Water absorption will decrease with the increase of glass regardless of the types of glass waste, and bending strength will generally improve with a high amount of glass waste and higher temperatures [8]. It is worth mentioning that multiple studies have found that firing temperature is critical to the performance of the tiles. Firing shrinkage is found to increase with increasing firing temperature [11], but it will decrease if the firing temperature is beyond a certain range [12]. Firing temperature also has a similar effect on flexural strength. Flexural strength improves at higher temperature [13], but another study found flexural strength decreases if firing temperature rises beyond the range of 1120°C to 1140°C [14]. Besides, waste glass can increase the hardness of tile, but there is some controversy about the effects on abrasion resistance [11, 15].

Significantly, studies found tiles incorporating waste glass contain a high content of heavy metals; however, the leachate of heavy metals decreases after the firing process [16, 17]. Therefore, it can be considered safe to recycle hazardous glass waste into the ceramic tile as the firing process can destruct toxic organic compounds and encapsulated hazardous contaminants through immobilisation. Recycling waste glass into ceramic tiles can reduce natural resource usage, lower the mixing requirement, reduce energy usage on firing, and offers a possible recycling option for hazardous glass waste [8, 10].

Coal Ash

Many power plants generate electricity from coal combustion. The unburned solid residues are known as ash, and they can be classified as fly ash or bottom ash according to the location where it was captured [18]. Due to the enormous amount of coal ashes and potential impact on the ecosystem, such as leaching toxic or chemical substances and accumulation throughout the food chain [19], researchers put lots of effort into utilising coal ash [20].

Fly ash

Zimmer and Bergmann incorporated 20 – 80 wt.% of coal fly ash in their experiments on tile production. They have found 60% of fly ash is the maximum amount that satisfied the minimum flexural strength (green) requirement of handling under industrial conditions. The optimum sample tile, with 60% fly ash, passed the technical properties requirement with a flexural strength of 30 MPa, water absorption of 12%, and shrinkage of 7.5%. Moreover, with addition of limestone and feldspar into fly ash tiles can result in reducing total linear shrinkage and reduce porosity with flexural strength increase achieving the requirements for more versatile applications [21]. Another researcher achieved promising results on

recycling coal fly ash with borax solid waste to replace part of the potassium feldspar in the formula of ceramic wall tiles. The 10% fly ash tile showed an increase in flexural strength with other comparable properties to the control wall tiles, and the 10% fly ash and 5% borax waste tile have a significant improvement on its flexural and water absorption but slightly increase its firing shrinkage [22]. In the northwest of China, researchers incorporated 70 wt.% high alumina coal fly ash into ceramic tile to achieve 67 MPa flexural strength and apparent porosity of 0.13% [23], which have a massive potential to the ceramic industry and to reduce the quantity of wastes. However, coal fly ash usually contains toxic heavy metal, such as Pb, Cd and Cr, and even radioactive elements (^{238}U , ^{232}Th , ^{226}Ra , ^{40}K , etc.). Therefore, it is crucial to measure the level of leachability and radioactivity, and then apply proper mitigations on coal fly ash before reusing it [24].

Bottom ash

Coal bottom ash also can be used as a raw material for ceramic tiles. Namkane et al. [25] incorporated 20 - 80 wt.% of bottom coal ash into the clay body, and they have found all samples can be classified as BIIb group according to the ISO rules for water absorption under 1175°C except for a sample that contained 80% bottom ash. The optimal bottom ash tile is the tile with 40% of bottom ash and 60% of clay as they have the lowest linear shrinkage with the smallest deformation, and the flexural strength can reach 24.8 MPa, which is feasible for ceramic tile but lower than commercial products. Consequently, Namakane and his team continued their research with the addition of sand and leonardite, which are common wastes from coal mining, to enhance the plasticity of tiles, as bottom ash is a non-plastic material. The highest amount of waste content that achieved the properties required for ceramic tiles can reach up to 42.8 wt.% (21.4 wt.% of bottom coal ash and leonardite). Additionally, this tile can be used as a floor tile, as it satisfies the BIIa group of flexural strength (22-30 MPa) and UA group for chemical aggression resistance [26], and further proved the possibility to recycle bottom coal ash in ceramic tiles.

Municipal Solid Waste Incineration Ash

Fly ash

Municipal solid waste incineration (MSWI) ash is a type of hazardous waste, and significant quantities are generated daily all over the world. Researchers in China studied the recycling of untreated MSWI fly ash into ceramic tiles. They found that incorporating 20 wt.% of MSWI fly ash would be the ideal ratio for recycling the maximal amount of waste and creating tiles in line with the Chinese standards, which shows

in high compressive strength of 18.6 MPa and low water absorption of 7.4% after being sintered at 960°C. Also, the firing temperature above 1000°C can stabilise heavy metals. However, Cd, Hg, Pb, and Zn are still exceeding the limit when the leachability analysis was conducted on an unglazed tile. In contrast, the glazed tile can effectively encapsulate heavy metals in ceramic tiles to a lower amount of leaching, and even below the detection limit for the instruments used [27]. Another research also discovered that glaze could effectively stabilise fly ash, and only when used in a strongly acidic environment will cause the heavy metal leach out [28].

Bottom ash

Italian researchers also attempted to make porcelainised tiles with untreated MSWI bottom ash and vitrified bottom ash (50% MSWI bottom ash + 50% glass cullet). Results show all tiles with up to 15% of untreated or vitrified bottom ash can meet the requirements for floor tiles with the features of water absorption below 0.1%, bending strength around 45 to 53 MPa, and some improvement on linear shrinkage compare to the control tile. Besides, the vitrified bottom ash tile has more visible enhancement of properties and would be more suitable for ceramic tile making. However, bottom ash can cause noticeable deformation on the planarity [29]. Therefore, consideration should be taken on the amount of bottom ash used or maybe reformulate the recipe for better performance.

In another study, researchers used 2 – 5 wt.% untreated bottom ash and 5 – 10 wt.% vitrified bottom ash (with glass) to replace part of Na-feldspar sand to test the possibilities of making porcelain tiles and monoporosa tile. The result shows MSWI bottom ash is technically feasible for ceramic tile making. For porous single firing tile, with the addition of 5%, untreated bottom ash does not have many impacts on its water absorption and linear shrinkage. Vitrified bottom ash is not tested due to its not cost-effective to put in production. For porcelain stone tile, vitrified bottom ash tiles exhibit clear improvement on its water absorption and linear shrinkage compared with the control tile at a temperature above 1160°C. Additionally, MSWI bottom ash is classified as not dangerous waste, but it does release heavy metals and solubilisation of alkaline metals. Therefore, a leachability test was conducted. The result of the leaching test shows all fired tiles only release a small amount of leachate, and they are below the limit value for inert waste [30]. Similarly, another research result also shows that post-treated bottom ash does not have significant ecotoxicity impacts on the environment due to the sintering and vitrification process which can immobilise the heavy metals, alkali and anions [31]. Thus, there is an opportunity for recycling MSWI bottom ash into ceramic tiles.

Sewage Sludge

Sewage sludge is another high volume solid waste generated by human activities from wastewater treatment plants. Zhou et al. [32] used 50 - 65 wt.% untreated sewage sludge to replace the kaolin in the raw materials of tiles. The XRD pattern indicates the composition of sewage sludge is like natural clayey material, mainly composed of quartz, kaolinite, and a small amount of illite and albite. Hence, it would be a viable alternative to traditional raw materials. Furthermore, tiles with up to 60% of sewage sludge can achieve the tile requirements. Tiles with 60% of sewage sludge have water absorption of 1.14%, bending strength of 25.5 MPa, and linear sintering shrinkage around 12% under sintering temperature at 1210°C. To sum up the key findings, tiles with a high content (more than 60 wt.%) of sewage sludge and under high firing temperature (above 1210°C) easily have severe deformation defects. Tiles containing less than or equal to 60 wt.% sewage sludge satisfied the requirements of split tiles (bending strength > 23MPa & water absorption < 3%). The leachability of sewage sludge tiles are reduced significantly once they are fired, and the leaching is far below the regulatory limit [32]. However, in another research, the results are almost entirely different. Jordán et al. [33] tested the effects of adding 0 - 10 wt.% of three sources of sewage sludges into two types of ceramic clays in their experiments. The overall results show the amount of sewage sludge has no impacts to linear shrinkage (before and after firing), porosity and water absorption will increase with the increases in sewage sludge content, and bending strength will decrease while sewage sludge increases [33]. Differences in results might be caused by a different process of preparation, diverse raw materials selection, different firing temperatures etc. Besides, the methods of Jordán et al. [33] are not revealed in their report, and the processes and results of Zhou et al. [32] are shown in Fig.1.

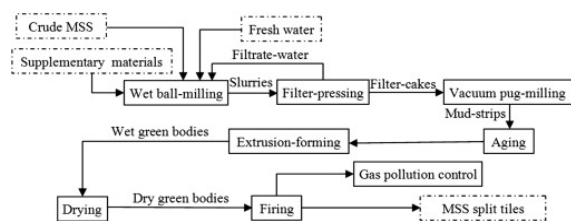


Fig.1 Flowchart of preparation process of municipal sewage sludge (MSS) [32].

Incinerated ash

Sewage sludge is also often incinerated, as this process can significantly reduce the mass, volume and hazardous components [34]. In a comprehensive review paper written by Lynn et al. [34], they

reviewed and summarised the main findings of various research studies. In general, recycling sewage sludge ash into glazed and unglazed tiles is a possible solution with no significant production issues. The water absorption of unglazed ceramic tiles often exceeds the required limit; however, it only has minor impacts on low ash content tiles and application of glaze can effectively reduce water absorption. Bending strength and abrasion limit fulfils the standards, but they will decrease with the increase of sewage sludge ash. Moreover, there is no impact on chemical resistance, no significant effects on firing shrinkage, and there is a reduction of loss on ignition due to organic matter having been burned off prior to the tile firing process [34]. Subsequently, research shows the overall performance can be improved by adding nano-SiO₂ additive into the tile recipe [35]. Thereupon, more in-depth studies on the manufacturing formula and processes need to be undertaken in order to recycle sewage sludge ash with high efficiency and high quality.

DISCUSSION AND CONCLUSION

As shown above, recycling of different wastes in ceramic tiles shows the ability to enhance some properties of ceramic tiles. Still, at the same time, the other properties might be compensated due to the addition of wastes. In addition, most studies did not apply glazing or use some fluxing agents like feldspar, which have shown the ability to improve the performance further, and they are commonly used in the industry. Moreover, many journal articles did not reveal the process of manufacture or did not set a control ceramic tile to compare with experimental tiles. This brought some difficulty compared with the properties of commercial tiles directly as the formula may not be able to produce qualified tiles.

Many research studies have discovered that some factors can influence the properties critically. One is the firing temperature; many studies show that waste samples appear to have better performance than the control samples with increasing the firing temperature. However, if the temperature is over or below the optimal temperature range, inferior performance will occur. A suitable range of firing temperature needs to be determined, such as using XRD to determine the composition of waste material. The second factor is the differences in materials. Waste materials or raw materials of ceramic tile may have different chemical or mineralogical compositions if the acquired location is different. Therefore, it is necessary to determine the composition of materials and test them locally before they are included in the manufacturing process. The third one is the variations in manufacturing techniques. Since there are many commercial methods for making ceramic tiles, the experimental methods may not be suitable, and the results may be

different. Hence, a suitable method in production needs to be selected and tested in trials in production conditions.

Ceramic tiles have proven their strong tolerance for recycling waste materials. The high heterogeneity and versatile uses create the possibility to use various wastes to make the most widely used products. Plus, tiles used for different purposes have different product standards, which further expand the feasibility of recycling. For future development, the tiles with waste need to achieve a balanced performance by finding the optimal formula ratio and production method. As most of the studies did not apply glazing, use fluxing agents, and such techniques, more in-depth experiments can test their effect on performance and properties. In the future, researchers can investigate recycling more different kinds of waste material into ceramic tiles.

ACKNOWLEDGMENTS

This work is part of an ongoing study on recycling waste in construction materials. The authors would like to thank Visy Industries Australia Pty Ltd, RMIT University and the Australian Government Research Training Program (RTP) scholarship for their financial and in-kind support.

REFERENCES

1. Nwachukwu, M.A., Ronald, M., and Feng, H. Global capacity, potentials and trends of solid waste research and management, *Waste Management & Research*. 2017, 35(9), 923-934.
2. Kaza, S., Yao, L., Bhada-Tata, P., and Van Woerden, F. *What a Waste 2.0: A Global Snapshot of Solid Waste Management To 2050*, World Bank Publications, Washington, D. C., UNITED STATES, 2018, <<http://ebookcentral.proquest.com/lib/rmit/detail.action?docID=5614550>>.
3. Ferronato, N. and Torretta, V. Waste Mismanagement in Developing Countries: A Review of Global Issues, *International journal of environmental research and public health*. 2019, 16(6), 1060.
4. Dondi, M., Raimondo, M., and Zanelli, C. Clays and bodies for ceramic tiles: Reappraisal and technological classification, *Applied Clay Science*. 2014, 96, 91-109.
5. Rahaman, M.N. *Ceramic Processing*, CRC Press LLC, Milton, UNITED KINGDOM, 2017, <<http://ebookcentral.proquest.com/lib/rmit/detail.action?docID=5477211>>.
6. World production and consumption of ceramic tiles, 2018. Viewed 28/04/2020, <http://www.mec-studies.com/filealbum/740_0.pdf>.
7. GPI. 'Benefits of Glass Packaging', 2020. Viewed 30/04, <<https://www.gpi.org/benefits-of-glass-packaging>>.
8. Silva, R.V., de Brito, J., Lye, C.Q., and Dhir, R.K. The role of glass waste in the production of ceramic-based products and other applications: A review, *Journal of Cleaner Production*. 2017, 167, 346-364.
9. Ling, T.-C. and Poon, C.-S. Utilisation of recycled glass derived from cathode ray tube glass as fine aggregate in cement mortar, *Journal of Hazardous Materials*. 2011, 192(2), 451-456.
10. Andreola, F., Barbieri, L., Lancellotti, I., Leonelli, C., and Manfredini, T. Recycling of industrial wastes in ceramic manufacturing: State of art and glass case studies, *Ceramics International*. 2016, 42(12), 13333-13338.
11. Lin, K.L. Use of thin film transistor liquid crystal display (TFT-LCD) waste glass in the production of ceramic tiles, *Journal of Hazardous Materials*. 2007, 148(1-2), 91-97.
12. Hwang, J.-Y., Huang, X., Garkida, A., and Hein, A. Waste colored glasses as sintering aid in ceramic tiles production, *JMMCE*. 2006, 5(5), 119-129.
13. Youssef, N.F., Abadir, M.F., and Shater, M.A.O. Utilisation of soda glass (cullet) in the manufacture of wall and floor tiles, *Journal of the European Ceramic Society*. 1998, 18(12), 1721-1727.
14. Matteucci, F., Dondi, M., and Guarini, G. Effect of soda-lime glass on sintering and technological properties of porcelain stoneware tiles, *Ceramics International*. 2002, 28(8), 873-880.
15. Lin, K.-L., Lee, T.-C., and Hwang, C.-L. Effects of sintering temperature on the characteristics of solar panel waste glass in the production of ceramic tiles, *Journal of Material Cycles and Waste Management*. 2015, 17(1), 194-200.
16. Raimondo, M., Zanelli, C., Matteucci, F., Guarini, G., Dondi, M., and Labrincha, J.A. Effect of waste glass (TV/PC cathodic tube and screen) on technological properties and sintering behaviour of porcelain stoneware tiles, *Ceramics International*. 2007, 33(4), 615-623.
17. Dondi, M., Guarini, G., Raimondo, M., and Zanelli, C. Recycling PC and TV waste glass in clay bricks and roof tiles, *Waste Management*. 2009, 29(6), 1945-1951.

18. Benavidez, E., Grasselli, C., and Quaranta, N. Densification of ashes from a thermal power plant, *Ceramics International*. 2003, 29(1), 61-68.
19. Carlson, C.L. and Adriano, D.C. Environmental impacts of coal combustion residues, *Journal of Environmental quality*. 1993, 22(2), 227-247.
20. Ahmaruzzaman, M. A review on the utilisation of fly ash, *Progress in Energy and Combustion Science*. 2010, 36(3), 327-363.
21. Zimmer, A. and Bergmann, C.P. Fly ash of mineral coal as ceramic tiles raw material, *Waste Management*. 2007, 27(1), 59-68.
22. Olgun, A., Erdogan, Y., Ayhan, Y., and Zeybek, B. Development of ceramic tiles from coal fly ash and tincal ore waste, *Ceramics International*. 2005, 31(1), 153-158.
23. Wang, H., Zhu, M., Sun, Y., Ji, R., Liu, L., and Wang, X. Synthesis of a ceramic tile base based on high-alumina fly ash, *Construction and Building Materials*. 2017, 155, 930-938.
24. Wang, N., Sun, X., Zhao, Q., Yang, Y., and Wang, P. Leachability and adverse effects of coal fly ash: A review, *Journal of Hazardous Materials*. 2020, 396, 122725.
25. Namkane, K., Naksata, W., Thiansem, S., Sooksamiti, P., and Arqueropanyo, O.-a. Utilisation of coal bottom ash as raw material for production of ceramic floor tiles, *Environmental Earth Sciences*. 2016, 75(5), 386.
26. Namkane, K., Naksata, W., Thiansem, S., Sooksamiti, P., and Arqueropanyo, O.-a. Utilisation of leonardite and coal bottom ash for production of ceramic floor tiles, *Environmental Earth Sciences*. 2017, 76(17), 628.
27. Haiying, Z., Youcai, Z., and Jingyu, Q. Study on use of MSWI fly ash in ceramic tile, *Journal of Hazardous Materials*. 2007, 141(1), 106-114.
28. Zhipeng, T., Bingru, Z., Chengjun, H., Rongzhi, T., Huangpu, Z., and Fengting, L. The physiochemical properties and heavy metal pollution of fly ash from municipal solid waste incineration, *Process Safety and Environmental Protection*. 2015, 98, 333-341.
29. Barbieri, L., Corradi, A., Lancellotti, I., and Manfredini, T. Use of municipal incinerator bottom ash as sintering promoter in industrial ceramics, *Waste Management*. 2002, 22(8), 859-863.
30. Rambaldi, E., Esposito, L., Andreola, F., Barbieri, L., Lancellotti, I., and Vassura, I. The recycling of MSWI bottom ash in silicate based ceramic, *Ceramics International*. 2010, 36(8), 2469-2476.
31. Andreola, F., Barbieri, L., Queiroz Soares, B., Karamanov, A., Schabbach, L.M., Bernardin, A.M., and Pich, C.T. Toxicological analysis of ceramic building materials – Tiles and glasses – Obtained from post-treated bottom ashes, *Waste Management*. 2019, 98, 50-57.
32. Zhou, J., Li, T., Zhang, Q., Wang, Y., and Shu, Z. Direct-utilization of sewage sludge to prepare split tiles, *Ceramics International*. 2013, 39(8), 9179-9186.
33. Jordán, M.M., Almendro-Candel, M.B., Romero, M., and Rincón, J.M. Application of sewage sludge in the manufacturing of ceramic tile bodies, *Applied Clay Science*. 2005, 30(3), 219-224.
34. Lynn, C.J., Dhir, R.K., Ghataora, G.S., and West, R.P. Sewage sludge ash characteristics and potential for use in concrete, *Construction and Building Materials*. 2015, 98, 767-779.
35. Chen, L. and Lin, D.F. Applications of sewage sludge ash and nano-SiO₂ to manufacture tile as construction material, *Construction and Building Materials*. 2009, 23(11), 3312-3320.

EFFECTS OF SIZE AND GRADING, TYPE AND QUALITY OF AGGREGATES ON MECHANICAL PROPERTIES OF UNBOUND ROADBED MATERIALS: A LITERATURE REVIEW

Hong Nam Thai¹, Akira Kato¹, Hoang Giang Nguyen², Tien Dung Nguyen², Ton Kien Tong²,
Van Tuan Nguyen², Taro Uchimura¹, Takeshi Maki¹, Ken Kawamoto^{1,2}

¹ Graduate School of Science and Engineering, Saitama University, Saitama, Japan; ² National University of
Civil Engineering, Hanoi, Vietnam.

ABSTRACT

Unbound graded aggregates are used to construct the base and subbase of the road pavement structure, and it is known that the mechanical properties of the unbound graded aggregates depend significantly on aggregate size and grading, especially on the maximum particle size and fines content (typically, particle size < 0.075 mm). In recent years, not only natural aggregates but also recycled aggregates from construction and demolition waste (CDW) have been used actively in the construction of road base and subbase. This paper investigated previous studies and reviewed results about effects of aggregate size and grading, type and quality of aggregates on the mechanical properties such as compaction, bearing capacity, resilient modulus, and shear strength for recycled aggregates from CDW and others including natural aggregates, and discuss how these properties affect their performance as unbound roadbed layers. The results collected from the literature indicated that the mechanical properties of most recycled materials and mixtures were comparable to natural aggregates and could be used to construct road base and subbase, except for reclaimed asphalt pavement and fine recycled glass.

Keywords: Road Base and Subbase, Aggregate Size and Grading, Construction and Demolition Waste, Mechanical Properties

INTRODUCTION

Nowadays, apart from materials crushed from natural stones, there are many kinds of materials used for unbound road base layers, in which the CDW are the most widely used materials. In several developed countries, the use of CDW instead of natural aggregate (NA) in road base construction has become popular. Specifically, in 2017 Spain had the percentage of CDW recycled was highest by 98%, followed by Japan, France, Germany at 96%, 93%, 85% respectively [1]-[2]. The use of CDW in road construction is one of the solutions to reduce the dumping of CDW, as well as the consumption of NA; however, there are some difficulties to recycle CDW because the types and quality of recycled aggregates affect significantly the mechanical properties of unbound roadbed materials.

Base and subbase layers are the important layers in pavement structure, they are required to have high rigidity and strength to bear the vertical load transmitted from surface layers. Besides, due to the low impact of horizontal load, the base and subbase layers of the pavement structure are usually made of unbound aggregates. For example, Yoder and Witczak [3] presented that the stability of unbound aggregate depends on some factors such as particle-size distribution, particle shape, relative density, internal friction, and cohesion. Among of the factors,

the size distribution of aggregate, particularly the proportion of fines was the most important. Xiao et al. [4] investigated the effect of particle size distribution on the mechanical properties, permeability, frost susceptibility, and susceptibility to erosion. Therefore, the size of the aggregate particles, grading, especially fines content (F_c , kg/kg in %) need to be controlled to meet the technical requirements, ensuring the ability to work properly during construction and improving the performance and longevity of the pavement structure.

This paper concentrated on reviewing previous studies to examine the effects of size and grading, type and quality of aggregates on the mechanical properties of unbound road base and subbase layers. The review working was done by comparing kinds of materials used, F_c , maximum particle size (D_{max} , mm) mixing proportion, test results of references selected and suggestion the future research.

METHODOLOGY

Based on the keywords such as unbound aggregate, road base and subbase, aggregate size, fines content, grading, and CDW materials, journal papers, books, and reports published in English after 1970's were searched in this study [e.g., Web of ScienceTM (Clarivate Analytics)]. The classification and detailed search were conducted to find the

conferences related to the effects of size and grading, type and quality of aggregates on mechanical properties such as compaction, bearing capacity, stiffness and shear strength of unbound aggregate for road base and subbase. A total of 33 references was selected to compare and summarize the data in this study.

A variety of materials were used in selected references, including NA, recycled aggregates (RA) such as recycled concrete (RC), recycled clay brick (RCB), reclaimed asphalt pavement (RAP), fine recycled glass (FRG), waste rock (WR) and mixed aggregate between them. These RA were classified with different properties as followed:

+ RC: has a minimum of 90%, by mass, of Portland cement-based fragments and NA [5].

+ RCB: is mainly contained brick rubble and also a high amount of adhered mortar and other impurities such as tile [6].

+ RAP: is more than 90% of composition composed of asphalt-based materials [5].

+ FRG: is the by-product of crushing mixed color bottles and other glass products collected from both municipal and industrial waste streams [7].

+ WR: is excavated during site preparation, they would have been disposed as waste [7].

There were two groups of materials classified according to D_{\max} of aggregates; $D_{\max} \leq 25\text{mm}$ for the road base and $D_{\max} > 25\text{mm}$ for the road subbase.

RESULTS AND DISCUSSION

Effects of Size and Grading, Type and Quality of Aggregates on the Compaction Characteristic

The maximum dry density (MDD) measured by the compaction test is one of the factors to evaluate the effects of aggregate size and grading, quality of aggregate on the compaction characteristic. Figure 1 shows the relationship between F_c and MDD. It can be noticed that most of NA had higher MDD than RA regardless of D_{\max} and F_c since NA has less porous in particle than RA [6]. In comparison among RAs, MDD tends to increase with increasing F_c without regard for the type of aggregate, while it seems that the opposite tendency was shown when $D_{\max} > 25\text{mm}$ from a comprehensive point of view. This is because fines fill the void of the mass of aggregate.

However, it could be assumed that fines fully occupy the void of the mass at lower F_c , which is around 3-10%, and assume a role as a framework of soil structure if F_c exceeds a certain value. As the occupation of fines in the mass increase, dry density therefore decreases. In addition, it might be assumed that MDD depends on intrinsic particle strength of NA, RC, and RCB [6], that is the reason why the larger particle and the breakable material was compacted, the lower MDDs of RC and RCB were obtained.

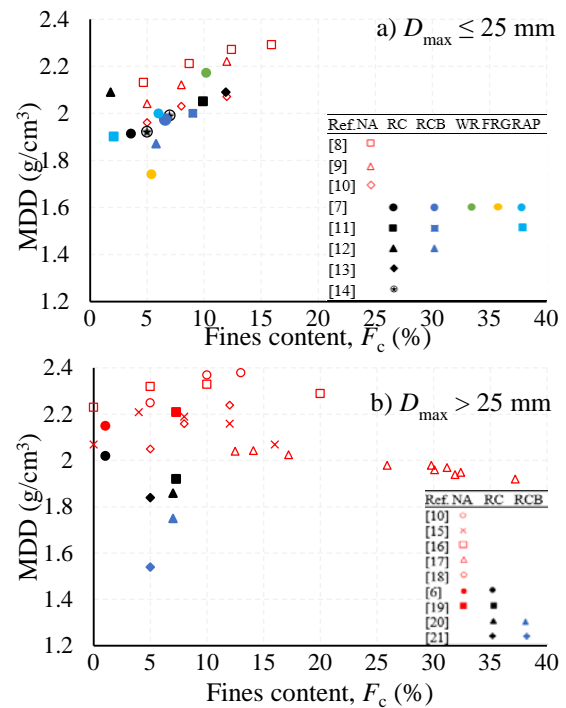


Fig.1 The effects of fines content and type of aggregates on MDD. (a) Samples with $D_{\max} \leq 25\text{mm}$, and (b) samples with $D_{\max} > 25\text{mm}$

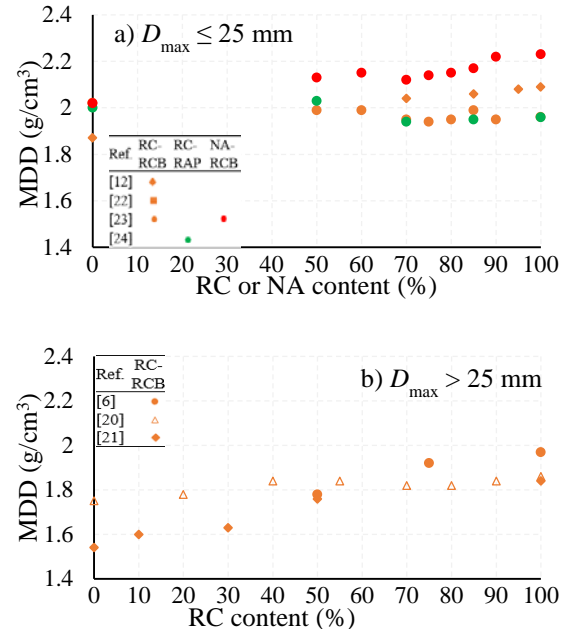


Fig. 2 The effects of mixing proportion on MDD. (a) Samples with $D_{\max} \leq 25\text{mm}$, and (b) samples with $D_{\max} > 25\text{mm}$

Figure 2 shows the relationship between mixing proportion of RC or NA to RCB or RAP. It seems that MDD gradually increases or is almost constant with increasing the mixing proportion of NA or RC

regardless of D_{\max} . Focusing on results of [12] and [23], differences between specific gravities of RCB and NA or RC might cause the tendency given that single-particle strength becomes high in proportion to the specific gravity, whereas specific gravities of RC and RCB in [23] are not much difference (Fig. 2a). An increase in coarse-grained fraction causes a reduction of MDD since the larger particle is more breakable during compaction (Fig. 2b).

Effects of Size and Grading, Type and Quality of Aggregates On Bearing Capacity

Figure 3 illustrates the effects of F_c and type, quality of aggregates on CBR. It can be mentioned that CBR of recycled materials is much higher than that of natural materials except for FRG and RAP regardless of D_{\max} . Fines contribute to increase in MDD for NA, while it cannot be clearly seen a tendency due to F_c for RA. As is the case with the compaction test results, the peak of CBR also appeared around 3-10% of F_c for all materials, and CBR gradually decreases with increasing F_c since fines bear the load as a main frame of soil structure.

With regard to the effect of the mixing proportion of RC or NA to RCB, CBR values exceed 100 % under all mixing conditions although a tendency due to mixing proportion did not appear, as shown in Fig. 4a. Whereas, CBR of RAP was improved mixing RC. On the other hand, the dependence of mixing proportion of RC to CBR is clearly shown increasing coarse-grains fraction. One possible reason might be that the amount of fine-grain fraction by breakage increases by breakage for RCB.

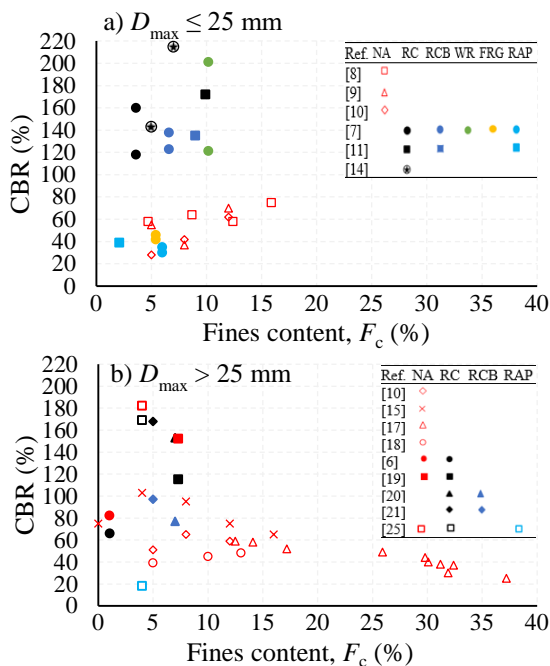


Fig. 3 The effects of fines content and type of aggregates on CBR. (a) Samples with $D_{\max} \leq 25$ mm, and (b) samples with $D_{\max} > 25$ mm

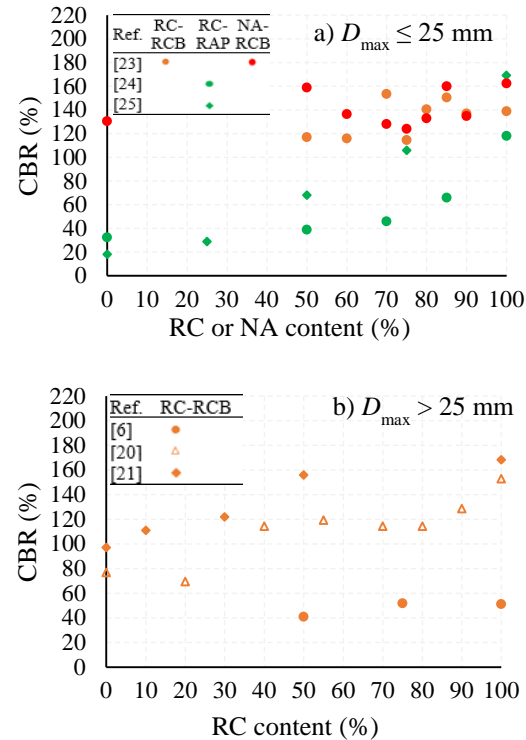


Fig. 4 The effects of the mixing proportion on CBR. (a) Samples with $D_{\max} \leq 25$ mm, and (b) samples with $D_{\max} > 25$ mm

Effects of Size and Grading, Type and Quality of Aggregates on Stiffness Characteristic

Resilient modulus (M_r) is a parameter representing the stiffness of the material and was used in most selected conferences. M_r is determined by the repeated load compression tests on test specimens. There were three trends of M_r with NA samples; M_r increased when F_c increased [26], M_r decreased when F_c increased [27], and M_r reached the highest value at a F_c value [16], [28] as shown in Table 1. Several researchers presented that M_r of RC was higher than M_r of NA, as in [29], [31], and satisfied to be greater than the minimum requirement of 300 MPa [31] (Australia standard). This can be explained that there was an amount of existing cement particles inside RC, when RC was mixed to water, these particles would be hydrated and contributed to increasing the strength of RC samples [5]. In the comparison among M_r of kinds of RA, RC had the highest M_r , followed by RCB and WR (Fig. 5). Turning to the mixtures, Arulrajah et al. [23] reported that CB-RC blends had the higher M_r values than CB-NA blends and most of the blends would perform satisfactorily as a subbase material. Arisha et al. [20] showed that M_r of RCB-RC blends reached highest with sample using 45% RCB, while Cameron et al.

[22] indicated that M_r of RCB-RC blends decreased when RCB content increased. M_r of NA-RAP

mixtures increased with the increase of RAP content (Fig. 6).

Table 1 The effects of size and grading, type and quality of aggregate on stiffness characteristic

Materials	Test conditions				Effects on M_r	Ref.
	Mixing proportion	Fines size (mm)	Range of F_c	D_{max} (mm)		
NA	*	<0.075	0 - 20%	31.75	M_r reached highest with 5% fines content and lowest with 10% fines content	[16]
RC, RCB	RC-RCB: 100-0, 90-10, 80-20, 70-30, 55-45, 40-60, 20-80, and 0-100	<0.075	*	37.5	M_r reached highest with sample using 45% RCB	[20]
RC, RCB	RC-RCB: 90-10, 80-20, 70-30	*	*	20	A decrease in M_r as the RCB content increased	[22]
RC, CB, NA	CB-RC/NA: 0-100, 15-85, 20-80, 25-75, 30-70, 40-60, and 50-50	<0.075	*	20	The CB-RC blends had higher M_r values than CB-NA blends.	[23]
NA	*	<0.075	7 - 12%	*	M_r increased with the increase of F_c	[26]
NA	*	<0.075	0 - 17.7%	25	M_r decreased when F_c increased	[27]
NA	*	<0.074	2 - 14%	38.1	M_r reached highest with $F_c = 6-10\%$	[28]
RC	*	<0.075	*	20	RC had higher M_r than NA	[29]
RC, CB, WR	*	<0.075	*	20	RC had the highest M_r value and WR had the lowest M_r value	[30]
RC, NA	*	<0.075	*	20	RC had higher M_r than NA and was greater than the minimum requirement of 300 MPa	[31]
RAP, NA	RAP-NA: 0-100, 25-75, 50-50, 75-25	<0.075	*	20	M_r increased as the RAP content increased	[32]

Note: * data not available

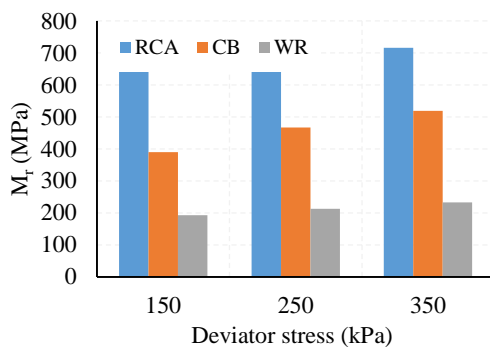


Fig.5 M_r of RA samples [30]

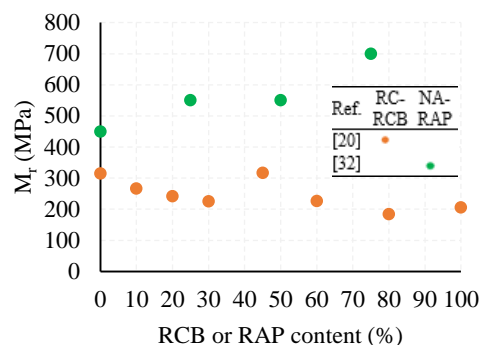


Fig.6 The effects of the mixing proportion on M_r

Effects of Size and Grading, Type and Quality of Aggregate on Shear Strength Characteristic

The shear strength properties are assessed via the cohesion (c), friction angle (ϕ) of materials determined by drawing Mohr circles for the confining pressures of the triaxial tests. Figure 7 shows the effects of F_c on c and ϕ of NA samples in [16], [33]. It can be seen that ϕ reached the highest value when $F_c = 5\%$, while c decreased when F_c from 0 to 5% and increased when F_c from 5% to 20%. Shear strength peaked highest with $F_c = 10\%$ and reduced with higher fines [16]. This can be explained in [3], [33]. Specifically, when samples contain little or no fines (Fig. 8a), shear strength is formed based on grain to grain contact. When samples contain sufficient fines (Fig. 8b), the fines fill the voids between the grains and bind them together. This combines grain to grain contact to increase the shear strength of samples. However, with samples contain high fines content (Fig. 8c), the grains are surrounded by fines, grain to grain contact will be reduced significantly, the shear strength decrease and depend on the shear strength of fines. However, Osouli et al.

[9] studied crushed stone aggregates of $D_{\max} = 25$ mm using two values of F_c (5 and 12 %), and presented that shear strength properties were not affected by

Figure 9 shows that RAP had the highest c by 53 kPa, followed by WR, RC, RCB (from 41 to 46 kPa) and FRG had the lowest c by 0 kPa. WR, RC, RCB had ϕ ranging from 49 to 51 degrees, whereas RAP and FRG had $\phi = 37$ degrees. Arulrajah et al. [23] showed that RCB–RC blends had c ranging from 41 to 80 kPa and ϕ ranging from 43 to 50 degrees, and RCB–NA blends had lower c by 41 to 62 kPa and higher ϕ by 46 to 51 degrees.

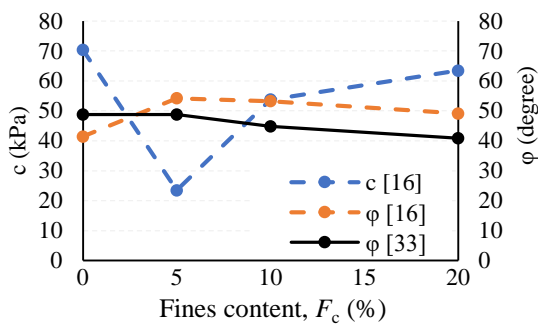


Fig.7 The effects of fines content on c and ϕ of NA samples

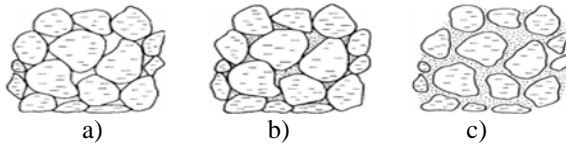


Fig. 8 Physical states of soil-aggregate mixtures (Adopted from [3])

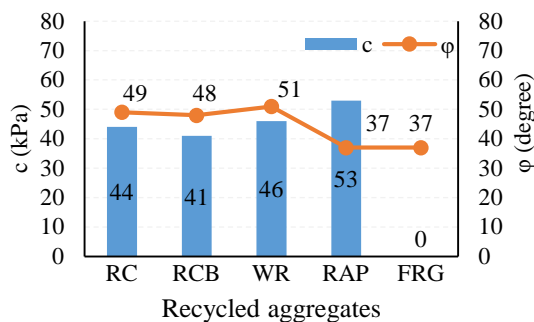


Fig.9 Cohesion and friction angle of RA samples [7]

CONCLUSIONS

Based on the results of series of experiments determined by many authors, some conclusions could be summarized below:

+ Size and grading of aggregates had the influence on mechanical properties of unbound aggregate roadbed layers, in which F_c and D_{\max} were the most influential. Nevertheless, there was little research on

quality of fines, $c = 70$ kPa and $\phi = 41$ degrees for both samples.

the effects of F_c and D_{\max} on mechanical properties of recycled aggregates which are becoming popular as substitutes for natural aggregates. Therefore, it is necessary to study the effects of F_c and D_{\max} on the mechanical properties of recycled aggregates in the future.

+ Samples with $D_{\max} \leq 25$ mm often have the higher MDD and CBR than that with $D_{\max} > 25$ mm.

+ RC, RCB, WR and RC-RCB mixtures had lower MDD than NA but their CBR are comparable to or higher than NA and satisfied to be greater than the requirement for road base and subbase. CBR of RAP, FRG was smallest and did not meet the technical requirement for road base and subbase.

+ Due to the hydration of the remaining unhydrated cement particles in RC, M_r values of RC, RC-RCB blends were higher than that of NA, NA-RCB blends respectively, and met the technical requirement for road base and subbase.

+ Most RA samples had lower cohesion and equivalent friction angle in comparison with NA samples.

ACKNOWLEDGMENTS

This research was supported by JST-JICA Science and Technology Research Partnership for Sustainable Development (SATREPS) project (No. JPMJSA1701).

REFERENCES

- [1] Deloitte, Resource Efficient Use of Mixed Wastes Improving management of construction and demolition waste, 2017.
- [2] MLIT, White paper on land, infrastructure, transport and tourism in Japan, 2017.
- [3] E. Yoder and M. W. Witczak, Principles of Pavement Design, Second Edition, 1975, pp. 1–711.
- [4] Y. Xiao, E. Tutumluer, Y. Qian, and J. Siekmeier, Gradation effects influencing mechanical properties of aggregate base-granular subbase materials in Minnesota, Transp. Res. Rec., no. 2267, 2012, pp. 14–26.
- [5] R. Cardoso, R. V. Silva, de J. Brito, and R. Dhir, Use of recycled aggregates from construction and demolition waste in geotechnical applications: A literature review, Waste Manag., vol. 49, 2016, pp. 131–145.
- [6] C. S. Poon and D. Chan, Feasible use of recycled concrete aggregates and crushed clay brick as unbound road sub-base, Constr. Build. Mater., vol. 20, no. 8, 2006, pp. 578–585.
- [7] A. Arulrajah, J. Piratheepan, M. M. Disfani, and M. W. Bo, Geotechnical and geoenvironmental

- properties of recycled construction and demolition materials in pavement subbase applications, *J. Mater. Civ. Eng.*, vol. 25, no. 8, 2013, pp. 1077–1088.
- [8] D. Mishra, E. Tutumluer, and A. A. Butt, Quantifying effects of particle shape and type and amount of fines on unbound aggregate performance through controlled gradation, *Transp. Res. Rec.*, no. 2167, 2010, pp. 61–71.
- [9] A. Osouli, S. Salam, and E. Tutumluer, Effect of plasticity index and dust ratio on moisture-density and strength characteristics of aggregates, *Transp. Geotech.*, vol. 9, 2016, pp. 69–79.
- [10] R. Chaulagai, A. Osouli, S. Salam, E. Tutumluer, S. Beshears, H. Shoup, M. Bay, Influence of maximum particle size, fines content, and dust ratio on the behavior of base and subbase coarse aggregates, *Transp. Res. Rec.*, vol. 2655, 2017, pp. 20–26.
- [11] M. A. Rahman, M. Imteaz, A. Arulrajah, and M. M. Disfani, Suitability of recycled construction and demolition aggregates as alternative pipe backfilling materials, *J. Clean. Prod.*, vol. 66, 2014, pp. 75–84.
- [12] M. Diagne, J. M. Tinjum, and K. Nokkaew, The effects of recycled clay brick content on the engineering properties, weathering durability, and resilient modulus of recycled concrete aggregate, *Transp. Geotech.*, vol. 3, 2015, pp. 15–23.
- [13] T. T. Kien, L. T. Thanh, and P. V Lu, Utilisation of construction demolition waste as stabilised materials for road base applications, *Int. Conf. on Sustainable Built Environment for Now and the Future*, 2013, pp. 285–293.
- [14] A. R. Gabr, K. G. Mills, and D. A. Cameron, Repeated Load Triaxial Testing of Recycled Concrete Aggregate for Pavement Base Construction, *Geotech. Geol. Eng.*, vol. 31, no. 1, 2013, pp. 119–132.
- [15] B. I. Siswosoebrotho, P. Widodo, and E. Augusta, The Influence of Fines Content and Plasticity on the Strength and Permeability of Aggregate Base Class A, *Proceedings of the Eastern Asia Society for Transp. Studies*, vol. 5, 2000, pp. 845–856.
- [16] J. A. Gandara, A. Kancherla, G. Alvarado, S. Nazarian, and T. Scullion, TX-0-4358-2 Impact of Aggregate Gradation on Base Material Performance, 2005, pp. 1–63.
- [17] I. I. I. Inan, W. K. Mampearachchi, and P. A. S. Udayanga, Effect of Fine Percentage on the Properties of Sub-base Material, *Eng. J. Inst. Eng. Sri Lanka*, vol. 49, no. 4, 2016, p. 15.
- [18] M. Y. Fattah, M. M. Hilal, and H. B. Flyeh, Effect of fine material on compaction characteristics of subbase material using the Superpave Gyratory Compactor, *Int. J. Civ. Eng. Technol.*, vol. 7, no. 5, 2016, pp. 466–476.
- [19] J. R. Jiménez, F. Agrela, J. Ayuso, and M. López, A comparative study of recycled aggregates from concrete and mixed debris as material for unbound road sub-base, *Mater. Constr.*, vol. 61, no. 302, 2011, pp. 289–302.
- [20] A. Arisha, A. Gabr, S. El-Badawy, and S. Shwally, Using Blends of Construction & Demolition Waste Materials and Recycled Clay Masonry Brick in Pavement, *Procedia Eng.*, vol. 143, 2016, pp. 1317–1324.
- [21] C. T. Viet, T. N. Van, G. N. Hoang, and K. Ken, Utilization of Construction and Demolition Waste (CDW) for Unbound Road Subbase in Hanoi, Vietnam, *Lect. Notes Civ. Eng.*, vol. 62, 2020, pp. 731–735.
- [22] D. A. Cameron, A. H. Azam, and M. M. Rahman, Recycled clay masonry and recycled concrete aggregate blends in pavement, *Geotech. Spec. Publ.*, no. 225 GSP, 2012, pp. 1532–1541.
- [23] A. Arulrajah, J. Piratheepan, M. W. Bo, and N. Sivakugan, Geotechnical characteristics of recycled crushed brick blends for pavement sub-base applications, *Can. Geotech. J.*, vol. 49, no. 7, 2012, pp. 796–811.
- [24] A. Arulrajah, J. Piratheepan, and M. M. Disfani, Reclaimed asphalt pavement and recycled concrete aggregate blends in pavement subbases: Laboratory and field evaluation, *J. Mater. Civ. Eng.*, vol. 26, no. 2, 2014, pp. 349–357.
- [25] T. A. Bennert and A. Maher, The use of recycled concrete aggregate in a dense graded aggregate base course, 2008, pp. 1–65.
- [26] W. E. I. Khogali and H. M. Elhussein, Novel approach for characterization of unbound materials, *Transp. Res. Rec.*, vol. 1874, 2004, pp. 38–46.
- [27] S. M. L. David N. Richardson, Resilient Moduli of Granular Base Materials Using a Modified Type 5 Gradation, 2009, pp. 1–40.
- [28] M. Hatipoglu, B. Cetin, and A. H. Aydilek, Effects of Fines Content on Hydraulic and Mechanical Performance of Unbound Granular Base Aggregates, *J. Transp. Eng. Part B Pavements*, vol. 146, no. 1, 2020, pp. 1–20.
- [29] A. Arulrajah, J. Piratheepan, M. M. Y. Ali, and M. W. Bo, Geotechnical properties of recycled concrete aggregate in pavement sub-base applications, *Geotech. Test. J.*, vol. 35, no. 5, 2012, pp. 1–9.
- [30] A. Arulrajah, J. Piratheepan, M. M. Disfani, and M. W. Bo, Resilient moduli response of recycled construction and demolition materials in pavement subbase applications, *J. Mater. Civ. Eng.*, vol. 25, no. 12, 2013, pp. 1920–1928.
- [31] A. R. Gabr and D. A. Cameron, Properties of Recycled Concrete Aggregate for Unbound Pavement Construction, *J. Mater. Civ. Eng.*, vol. 24, no. 6, 2012, pp. 754–764.
- [32] W. Kim, J. F. Labuz, and S. Dai, Resilient modulus of base course containing recycled

- asphalt pavement, Transp. Res. Rec., no. 2005, 2007, pp. 27–35.
- [33] X. Chen and J. Zhang, Effect of clay invasion on shear behavior and dilatancy of unbound aggregate subbase, Transp. Geotech., vol. 6, 2016, pp. 16–25.

RECYCLING OF CIGARETTE BUTTS IN STONE MASTIC ASPHALT

Md Tareq Rahman, Abbas Mohajerani and Filippo Giustozzi

School of Engineering, RMIT University, Melbourne, Australia

ABSTRACT

Trillions of cigarettes are produced every year around the globe, resulting in a large amount of mephitic waste cigarette butts (CBs) being dumped into the environment. Waste CBs take years to decompose with most containing a cellulose-acetate based filter, tar, nicotine, tobacco, and many highly toxic chemicals that leach into the soil and waterbodies thereby resulting in contamination and toxicity. In the area of asset management, the road and highway sector are the largest in the world. This research work has investigated the possible recycling of CBs in stone mastic asphalt. Waste CBs were processed and encapsulated with bitumen before the preparation of the mix. Modified stone mastic asphalt samples were prepared by replacing up to 2% of coarse aggregate with bitumen encapsulated CBs in accordance with the existing AASHTOO and Austroads guidelines. Laboratory tests were conducted on the CB modified asphalt samples and the results were compared with those of the standard control samples prepared without CBs. The preliminary results found are promising and show that recycling encapsulated CBs in asphalt concrete could contribute a solution to CB pollution around the world. This paper presents the experimental procedures and discusses some of the significant outcomes of the study.

Keywords: Cigarette butts; Stone mastic asphalt; Recycling; Waste Management; Flexible pavement

INTRODUCTION

Cigarette butt pollution

Around the world, approximately one billion people are cigarette smokers [1]. As reported by Euromonitor, during the year 2013, the total production of cigarettes was 5.7 trillion, 99% of which have a cellulose acetate (plastic based) filter. This production is expected to increase to 9 trillion by the year 2025 [2]-[4]. Hence, the ongoing concern about the recycling of waste cigarette butts. The 'Cigarette Butt Pollution Project' in the USA estimated that approximately one-third of the total production is littered in the environment [2], [5]. Cigarette butts contain toxic materials that spread into the environment slowly as cellulose acetate is photodegradable but not biodegradable [6]-[8]. In order to save the environment from the pollution caused by waste cigarette butts, efficient recycling methods are needed.

Cigarette butt waste clean-up is very costly, with a San Francisco litter audit study finding the cost to be more than \$7 million annually [5]. Furthermore, the incineration of waste cigarette butts creates hazardous fumes that are severely detrimental to public health and the environment [9], [10]. However, waste cigarette butts can be collected and processed for recycling in construction materials. Recent research at RMIT University has proved that waste cigarette butts can be used in the preparation of clay bricks [2], [11]. Mohajerani et al. (2017) developed a CB encapsulation method to incorporate CBs in dense asphalt for the first time [12]. Dense asphalt was prepared with bitumen C170 and C320 encapsulated

with bitumen and paraffin wax, consecutively [12], [13]. The results revealed the possibility of using encapsulated CBs in asphalt for light, medium, and heavy traffic conditions. The development of advanced materials incorporating waste cigarette butts will bring a new dimension to the construction materials.

Cigarette butt pollution exists all over the world. However, a sustainable technique to recycle waste CBs in asphalt concrete and bitumen can solve this problem. Previous studies have proved the prospect of recycling different waste materials in asphalt [14]-[16]. This study can contribute to the solution of CB pollution problem around the world and bring sustainability to the environment by introducing a new procedure to recycle CBs in asphalt concrete for flexible pavements. This research adds knowledge to the sector of waste management and the roads and highway industry.

Asphalt

Hot mix asphalt (HMA) can be dense or open graded. As the name suggests, dense-graded HMA has a lower void ratio compared to open grade HMA. Dense-graded HMA contains a large variety of particle sizes to spread through the asphalt concrete mix effectively. Furthermore, dense grade HMA suits all traffic condition types and is considered the most commonly used type of asphalt concrete around the world [17]. Open-graded HMA is typically used as a drainage layer due to the higher void ratio, which allows the mix to be more permeable [17], [18].

Stone mastic asphalt (SMA) is a gap graded asphalt that is commonly used throughout Europe

[18]. The aggregates used in SMA mixes are often of higher quality compared to the aggregates used for standard HMA mixes due to the superior physical and mechanical properties that are required for the stone-to-stone contact structure. The high content of coarse aggregates in SMA creates high rutting resistance and improves the longevity of the structure [19].

The comparative differences between HMA and SMA are illustrated in Table 1. Although the gradation may vary among the different types of asphalt, the basic ingredients are mostly the same. In the case of HMA, open-graded aggregates and bitumen are used, while gap-graded aggregate, fibers, and bitumen are used in SMA.

Table 1. Advantages and disadvantages of HMA and SMA [14]-[16].

Type of Asphalt	Advantages	Disadvantages
Hot Mix Asphalt (HMA)	Low cost	Lower rutting resistance
	Effective in all traffic conditions	Shorter service life
		Poorer quality aggregates used
Stone Mastic Asphalt (SMA)	Long service life	
	High resistance to deformation	Low skid resistance
	Increased fatigue testing life	High cost
	Noise-reductive properties	Increased risk of flat spots occurring due to SMA design procedure
	Decreased water spray when raining	

Use of waste materials in asphalt

According to the statistics, around 95% of the world's highways are flexible pavements that are constructed using asphalt concrete [15], [20]. The use of additives and modifiers can improve the properties and performance of asphalt concrete. Several research works have been carried out to investigate the use of waste materials in asphalt concrete, such as rice husk, fly ash, palm oil fruit ash, coffee grounds, waste cooking oil, waste rubber ground, steel slag, copper mine tailing, waste plastic, and crushed glass, etc. [21]-[26]. Waste cigarette butts can be a potential modifier in asphalt concrete and can introduce advanced asphalt concrete that will exhibit better

engineering properties in terms of the stability, resilient modulus, and flow of asphalt concrete.

RESEARCH DESIGN

This research was designed by following the industry standards. The materials were selected according to the Austroads and VicRoads guidelines. Stone mastic asphalt was selected for this part of the investigation. The research design diagram is shown in Fig. 1. In this research, asphalt samples were prepared with CBs by replacing coarse aggregates up to 2% by weight. Volumetric analysis and preliminary mechanical performance assessment were carried out for all samples, and the results were reviewed and compared with the control samples.

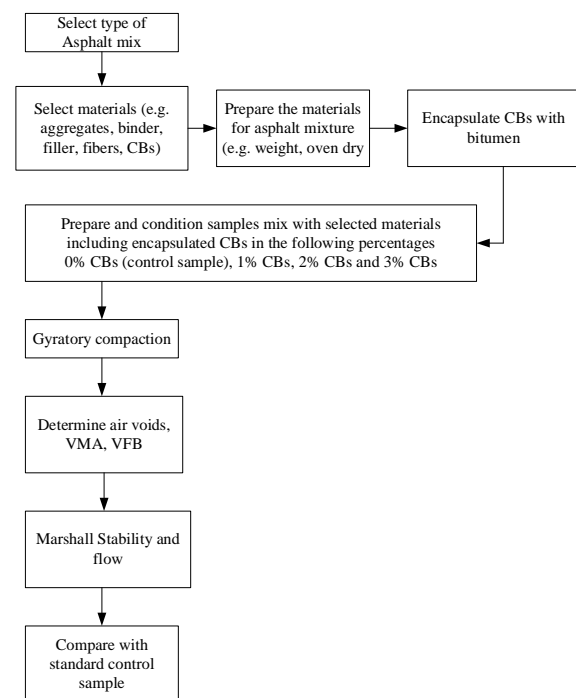


Fig. 1. Research design.

RESEARCH DESIGN

Pre-processing and encapsulation of CBs

Background of CB encapsulation

Bitumen encapsulated CBs were first developed and incorporated in dense asphalt by Mohajerani et al. (2017) [12]. Encapsulation was done by curing oven dried CBs with hot bitumen. Fig. 2. exhibits the bitumen encapsulated CBs and some of the dense asphalt samples prepared in this breakthrough research. The physical and mechanical performance of the samples were propitious and this work has widened the scope of research for recycling cigarette butts (CBs) in asphalt concrete [12], [27]. Asphalt

samples were prepared incorporating CBs 10 kg/m³, 15 kg/m³, and 25 kg/m³, and without CBs (control samples). The impacts of different quantities of CBs encapsulated with different classes of bitumen in terms of the Marshall Stability and Flow of dense asphalt samples are shown in Fig. 3.



Fig. 2. Encapsulated CBs and a few dense asphalt samples used in the research conducted by Mohajerani et al. in 2017 [12].

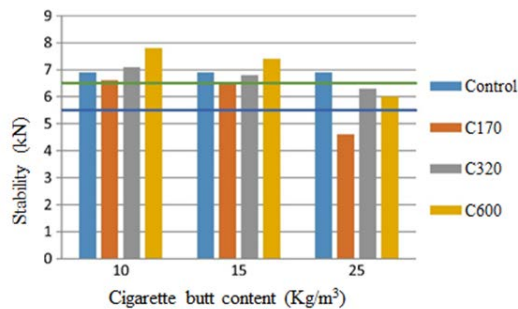


Fig. 3. Marshall Stability and Flow of asphalt prepared with different amounts of CBs, encapsulated with C170, C320, and C600 [12].

Mohajerani et al. (2017) assessed the resilient modulus of asphalt concrete prepared with CBs and found that all the samples met the standard range 2500-4000 MPa for bitumen class C170 [12]. The results are shown in Fig. 4.

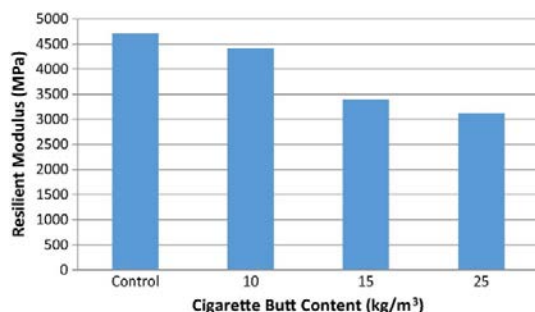


Fig. 4. Resilient Modulus of Asphalt Concrete prepared with different amounts of bitumen class C170 encapsulated CBs [12]

Preparation of bitumen encapsulated CBs for stone mastic asphalt

Cigarette butts were pre-processed by encapsulation with bitumen. Encapsulation was achieved by curing CBs in hot liquid bitumen. Fig. 5. and Fig. 6. show the condition of the CBs before and after encapsulation, consecutively.



Fig. 5. CBs before encapsulation. Waste CBs (left) and oven dried and cleaned CBs (right).



Fig. 6. Encapsulated CBs.

A few arbitrary encapsulated CBs were picked and cut into pieces to observe the sections. It was found that the CBs were encapsulated properly, and that all the pores of the CBs were filled with bitumen. The sections of the encapsulated CBs are shown in Fig. 7.



Fig. 7. Sections of Bitumen encapsulated CBs.

Asphalt sample preparation

The samples were prepared in the laboratory following the Austroads and VicRoads standards. The type of aggregate was granite, the gradation of which was adapted from VicRoads section 404; illustrated

in Table 2 [28]. The amount of materials used in the preparation of the sample is given in Table 3.

Table 2. Adapted gradation for the preparation of stone mastic asphalt.

Sieve retained (mm)	% Passing (Adapted for this research)	% Passing range according to VicRoads Standard
9.5	95.0	90-100
6.7	35.0	25-45
4.7	32.0	18-32
2.36	22.0	15-30
<2.36	0.0	13-24

The stone mastic asphalt mix was prepared using selected aggregates as per the gradation, 6% of mineral fillers, 0.3% of cellulose fibers, and 6.5% of bitumen PMB class A10E. The asphalt mix was prepared at 170°C. Compaction was done with a Gyratory Compactor. Pictures of some of the prepared stone mastic asphalt samples are shown in Fig. 8.

Table 3. Amount of materials in stone mastic asphalt sample

Aggregate Size (Retained)	% Measured for asphalt mix (by weight)
9.5 mm	4.36
6.7 mm	52.32
4.7 mm	2.62
2.36 mm	8.72
Fines	19.18
Filler (limestone)	6
Fiber	0.3
Bitumen	6.5



Fig. 8. Preparation of stone mastic asphalt sample. Mix without addition of bitumen (top left), Mixing process with bitumen (top right), compaction done with gyratory compactor (bottom left), and compacted stone mastic asphalt samples (bottom right)

LABORATORY TESTING

Preliminary laboratory investigation involved volumetric assessment and the Marshall Stability and Flow Test following AS/NZS 2891.5:2015 guideline. The stone mastic asphalt (SMA) samples were prepared following 4.8% - 5.2% air void according to VicRoads [28][29].

Results and discussion

After preparation of the control sample, the CB modified samples were prepared with bitumen encapsulated CBs by 1% and 2%. The aggregates retained in the 9.5 mm sieve were replaced with encapsulated CBs by weight. Volumetric analysis on the control sample and the Marshall stability and flow test were conducted for all the samples as a preliminary investigation. The results are shown in Table 4.

Table 4. Preliminary test results.

Type of Sample	Type of test	Test Results	Standard check with the range
Control Sample	Air void	5%	VicRoads and Austroads (4.8%-5.2%)
	VMA	19.1%	VicRoads and Austroads (13%-20%)
	VFA	73.8%	VicRoads and Austroads (65%-80%)
	Marshall Stability	13.6 KN	VicRoads and Austroads

Sample with 1% CBs	Flow	10.8 mm	(minimum 5.5KN) Asphalt Institute (8 mm-16 mm)
	Marshall Stability	13.9 KN	VicRoads and Austroads (minimum 5.5KN)
	Flow	9.2 mm	Asphalt Institute (8 mm-16 mm)
Samples with 2% CBs	Marshall Stability	15.1 KN	VicRoads and Austroads (minimum 5.5KN)
	Flow	10 mm	Asphalt Institute (8 mm-16 mm)

The results show an increase in the stability with the increase of CBs in the mix. Fig. 9. shows the change in stability of the samples before and after modification with encapsulated CBs. This shows that CB modified stone mastic asphalt can sustain under higher loading conditions. It has been observed that encapsulated CBs in stone mastic asphalt improves the strength. The flow value is within the range of 8-16 mm. Comparative analysis shows a better perspective of the results in Fig. 10.

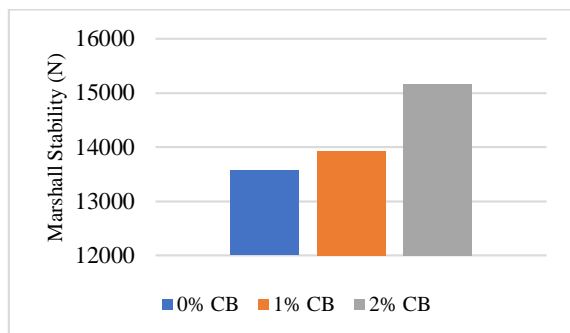


Fig. 9. Stability of the samples.

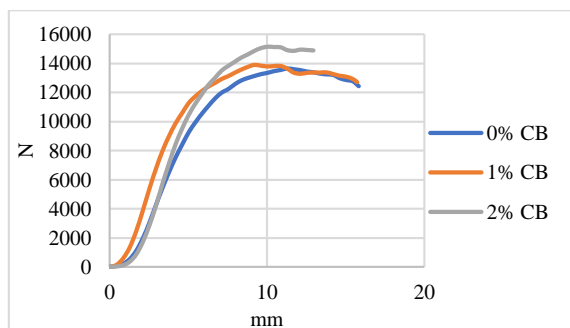


Fig. 10. Comparative analysis of Marshall stability and flow results.

The sustaining period of the samples was analyzed based on the Marshall stability and flow

results as shown in Fig. 11. It was found that the control sample with 0% CBs had a higher sustaining period, which is 13 seconds, however, this sample failed at a lower loading condition. Although the samples with 1% CBs and 2 % CBs failed quickly compared to the control sample, they can sustain higher loading conditions. The addition of 2% CB stone mastic asphalt presented a better sustaining period than the sample with 1% CBs under higher loading conditions.

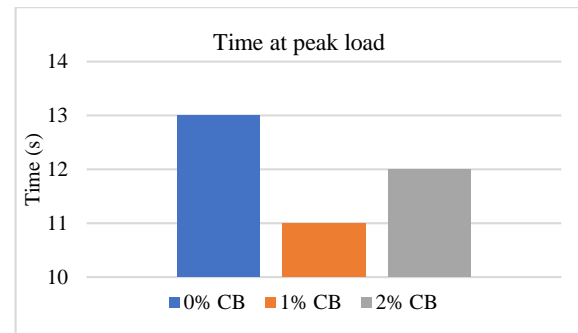


Fig. 11. Sustaining period of samples.

CONCLUSION

The aim of this study was to recycle waste CBs in asphalt. Stone mastic asphalt samples were prepared with bitumen encapsulated CBs in this research and the Marshall stability and flow test were performed to assess performance. The results from the laboratory investigation herald a new area to explore in the sector of advanced materials for flexible pavements. This paper has presented and discussed some of the results from a comprehensive study on recycling cigarette butts in asphalt. The results are promising, as incorporation of CBs enhanced the performance of asphalt. The outcomes were analyzed and compared with the control sample. This investigation reveals a possible sustainable method to recycle CBs in stone mastic asphalt. The results of this research provide evidence of the mechanical properties of this advanced material. This confirms the prospect of bitumen encapsulated CBs in asphalt concrete. This method can recycle up to 15kg CBs in each m³ of stone mastic asphalt. The improved method of encapsulation and mixing process was found suitable for heavy traffic conditions. This work contributes to the roads and highways sector in terms of adopting a sustainable approach in construction.

ACKNOWLEDGEMENTS

This work is part of an ongoing postgraduate study on recycling cigarette butts in asphalt concrete. The authors would like to thank Butt-Out Australia

Pty Ltd, RMIT University and the Australian Government Research Training Program (RTP) scholarship for their financial and in-kind support.

REFERENCES

- [1] World Health Organization, World health organization Tobacco fact sheet. 2014.
- [2] Mohajerani, A., A.A. Kadir, and L. Larobina, A practical proposal for solving the world's cigarette butt problem: Recycling in fired clay bricks. *Waste management*, 2016. 52: p. 228-244.
- [3] Novotny, T.E., K. Lum, E. Smith, V. Wang, and R. Barnes, Filtered cigarettes and the case for an environmental policy on cigarette waste. *Int. J. Environ. Res. Public Health*, 2009. 6: p. 1-14.
- [4] Euromonitor International, Global Tobacco: Key Findings Part 1 – Tobacco Overview, Cigarettes and the Future. 2014 [cited 2018 29 November]; Available from: <https://www.euromonitor.com/global-tobacco-key-findings-part-1-tobacco-overview-cigarettes-and-the-future/report>.
- [5] Cigarette Butt Pollution, The Environmental Impact of Cigarette Butt Waste: Just the Facts. 2013. Available from: <https://www.reefreelief.org/2013/02/the-environmental-impact-of-cigarette-butt-waste-just-the-facts/>
- [6] Kurmus, H., Mohajerani, A., The toxicity and valorization options of cigarette butts. *Waste Management*. 2020 Mar 1; 104:104-18.
- [7] Hon, N.S., Photodegradation of cellulose acetate fibers. *Journal of Polymer Science: Polymer Chemistry Edition*, 1977. 15(3): p. 725-744.
- [8] Rahman, M.T., Mohajerani, A., Giustozzi, F., Possible Recycling of Cigarette Butts as Fiber Modifier in Bitumen for Asphalt Concrete. *Materials*. 2020 Jan;13(3):734.
- [9] Knox, A., An overview of incineration and EFW technology as applied to the management of municipal solid waste (MSW). ONEIA Energy Subcommittee, 2005.
- [10] Mohajerani, A., A.A. Kadir, and L.J.W.m. Larobina, A practical proposal for solving the world's cigarette butt problem: Recycling in fired clay bricks. 2016. 52: p. 228-244.
- [11] Mohajerani, A., Y. Tanriverdi, B.T. Nguyen, K.K. Wong, H.N. Dissanayake, L. Johnson, D. Whitfield, G. Thomson, E. Alqattan, and A. Rezaei, Physico-mechanical properties of asphalt concrete incorporated with encapsulated cigarette butts. *Construction and Building Materials*, 2017. 153: p. 69-80.
- [12] Rahman MT, Mohajerani A, Giustozzi F. Recycling of Waste Materials for Asphalt Concrete and Bitumen: A Review. *Materials*. 2020 Jan;13(7):1495.
- [13] Rahman, M.T., M.R. Hainin, and W.A.W.A. Bakar, Use of waste cooking oil, tire rubber powder and palm oil fuel ash in partial replacement of bitumen. *Construction and Building Materials*, 2017. 150: p. 95-104.
- [14] Aziz, M.M.A., M.T. Rahman, M.R. Hainin, and W.A.W.A. Bakar, An overview on alternative binders for flexible pavement. *Construction and Building Materials*, 2015. 84: p. 315-319.
- [15] Putman, B.J., S.N.J.R. Amirkhanian, conservation, and recycling, Utilization of waste fibers in stone matrix asphalt mixtures. 2004. 42(3): p. 265-274.
- [16] Garcia, J. and K. Hansen, HMA pavement mix type selection guide. 2002: National Asphalt Pavement Association.
- [17] Pavement Interactive, HMA Pavement. 2012 [cited 2018 25/06]; Available from: <http://www.pavementinteractive.org/hma-pavement/>.
- [18] Blazejewski, K., Stone matrix asphalt: Theory and practice. 2016: CRC Press.
- [19] Shafabakhsh, G. and Y. Sajed, Investigation of dynamic behavior of hot mix asphalt containing waste materials; case study: Glass cullet. *Case Studies in Construction Materials*, 2014. 1: p. 96-103.
- [20] National Research Council, Highway Capacity Manual. 2000, Transportation Research Board (TRB): Washington, DC.
- [21] Waller, H.F. Use of waste materials in hot-mix asphalt. 1993. ASTM.
- [22] Rokade, S. Use of waste plastic and waste rubber tyres in flexible highway pavements. in International conference on future environment and energy, IPCBEE. 2012.
- [23] Fini, E.H., I.L. Al-Qadi, Z. You, B. Zada, and J. Mills-Beale, Partial replacement of asphalt binder with bio-binder: characterisation and modification. *International Journal of Pavement Engineering*, 2012. 13(6): p. 515-522.
- [24] Huang, S.-C., D. Salomon, and J.E. Haddock, Alternative Binders for Sustainable Asphalt Pavements: Papers from a Workshop. Workshop Introduction. Transportation Research E-Circular, 2012(E-C165).
- [25] Rusbintardjo, G., M.R. Hainin, M.A. Mubarak, and N.I.M. Yusoff, The performance characteristics of stone mastic asphalt mixtures using oil palm fruit ash-modified bitumen. *International Journal of Pavement Research and Technology*, 2014. 7(4): p. 227-236.
- [26] Oluwasola, E.A., M.R. Hainin, and M.M.A. Aziz, Evaluation of asphalt mixtures incorporating electric arc furnace steel slag and copper mine tailings for road construction. *Transportation Geotechnics*, 2015. 2: p. 47-55.
- [27] VicRoads, SECTION 404 - STONE MASTIC ASPHALT. 2012: Australia.
- [28] Rebbechi J, YEO R. Pavement surfacings trial: long term performance review. In Research into Practice: 22nd ARRB Conference ARRB 2006.

A STUDY ON COMPRESSIVE STRENGTH AND EFFECTIVE DIFFUSION COEFFICIENT OF SOLIDIFIED BODY WITH HIGH ZEOLITE MIXING RATE

Ryo Takano¹ and Kazuhito Niwase¹

National Institute of Technology, Hachinohe College (Tamonoki Hachinohe 039-1192, JAPAN)

ABSTRACT

The accident at the Fukushima Daiichi Nuclear Power Plant caused a large amount of high concentration of radioactive contaminated water due to groundwater flowing into the reactor building and core cooling. The radioactive contaminated water has been removed by adsorbing cesium, a major nuclide, on zeolite. Cement solidification technology is considered as one of the options as a solidification method for stabilizing cesium-adsorbed zeolite based on economics, manufacturability, and experience with low-level radioactive waste.

In previous studies on the development of cement solidification technology, we have studied zeolite mixing rates that can be solidified into good conditions from the viewpoint of fresh properties, physical stability, and nuclide containment performance. At present, it is possible to confirm the feasibility of zeolite mixing rate up to about 50% of the solidified body volume. In this study, we focused on further improvement of the volume reduction rate and prepared a specimen with a solidified body volume of 75 % and conducted the same study.

As a result, it was confirmed that production was possible and excellent strength development. In addition, as for the physical properties after curing, the hydration reaction and the pozzolanic reaction were promoted because the curing condition was sealed at 80 °C and the compressive strength and the effective diffusion coefficient showed a peak after 28 days of curing. When the curing period was 91 days, changes in the pore structure and the occurrence of microcracks were confirmed.

Keywords: Cesium adsorbed zeolite, Cement solidification, Disposal of low level radioactive waste, Effective diffusion coefficient

INTRODUCTION

On March 11, 2011, an accident at the Fukushima Daiichi Nuclear Power Plant during the Tohoku Pacific Ocean Earthquake caused a large amount of high concentrations of radioactive contaminated water caused by groundwater and core cooling that flowed into the reactor building. Currently, the radioactive contaminated water, by zeolite having a high cation exchange function, has been removed by adsorbing cesium is a major nuclide.

Zeolite adsorbed the cesium is assumed to be intermediate management until the radiation effect and heat generation is reduced, the current situation is stored as a secondary waste in the box culvert, continues to increase.

Therefore, it is urgent to establish an intermediate management method based on the final disposal. As required matters, as well as to suppress the leakage of radioactivity, and the production of the waste body in a high radiation environment, economic sand due to the reduction of the waste body based on the amount of occurrence is large it is required.

Cement solidification technology, from the results of the buried disposal of low-level radioactive waste, as a processing method that can

satisfy the requirements described above, it is one of the options. In the past study,[1] the relationship between thermal influence, mechanical stability, and nuclide confinement was evaluated for the purpose of feasibility study of cement solidification technology. As a result, in the formulation conditions of 50% of the solidified body volume zeolite, cement solidification technique of cesium adsorption zeolite could be determined to be feasible.

Furthermore, the main component of zeolite is silica and alumina, causing a reaction similar to the pozzolanic reaction, it was suggested that the zeolite itself is dense.

The purpose of this study is to study the maximum mixing rate of zeolite by focusing on improving the reduction rate in waste bodies from the viewpoint of fresh properties, mechanical stability, and nuclide confinement performance.

PRELIMINARY EXPERIMENT

In this study, A preliminary experiment was conducted on the formulation used in the test. The mixing ratio is shown in Table-1.

Blended with three types of zeolite mixing rate (75%, 80%,85%), water cement ratio (hereinafter,

Table 1 Mix proportion

ZV	W/C	Unit contents(kg/m ³)				
		W	OPC	Z	WZ	SP(ME) C × 6%
0.75	0.8	179	224	545	294	13.4
0.75	0.9	185	206	545	294	12.3
0.75	1.0	190	190	545	294	11.4
0.80	0.8	143	179	582	313	10.7
0.80	0.9	148	164	582	313	9.9
0.80	1.0	152	152	582	313	9.1
0.85	0.8	107	134	618	333	8.1
0.85	0.9	111	123	618	333	7.4
0.85	1.0	114	114	618	333	6.8

W/C) three (0.8,0.9,1.0), high-performance AE

reduction Water agent (hereinafter, SP) normal Portland cement (density: 3.16g / cm³, specific surface area: 3340cm² / g) (hereinafter, OPC) was adjusted to 6% of, a total of nine formulations were examined. Particle size of the natural zeolite used (mordenite type) is 0.5mm or less, and mixed in a dry state. Zeolite is porous, the water absorption from the cement paste, since the decrease in workability is concerned, apart from the unit water volume, was added water absorption content in the outer crack. [2] Kneading mixing was carried out in a Mortar mixer. The procedure is shown below.

- 1) Using a kneading machine, the kneading bowl and paddle were fixed in the mixing position. Then, the prescribed amount of water and afterward the cement were added.
- 2) Immediately start the kneading machine at a low speed.
- 3) After starting the kneading machine for 30 seconds, put the specified amount of zeolite in 30 seconds.
- 4) Speed up and continue kneading for 90 seconds.
- 5) Pause for 90 seconds and scrape off for the first 15 seconds of the pause.
- 6) After the pause, start again at high speed and mix for 60 seconds.

The table flow test was measured flow value of the formulation examined. The situation is shown in Fig.1and Fig.2.

By the previous study, if the flow value is obtained 150mm or more, [3]it was set the criteria that there is sufficient liquidity. The results are shown in Fig. 3. Those flow value satisfies 150 mm, zeolite mixing rate 75 % water cement ratio 80 %



Fig.1 ZV75%-0.8 flow test



Fig.2 ZV75%-0.9 flow test

(hereinafter, ZV75 %-0.8), zeolite mixing rate 75 % water cement ratio 90 % (hereinafter, ZV75 %-0.9) because it was two types, this formulation was the subject of study.

SPECIMEN PREPARATION

The kneading was carried out with a biaxial forced kneading mixer. In the past, we had considered a method of making cement paste by self-filling, but we thought that it is impossible to make it by self-filling because zeolite with a very small particle size of 0.5 mm or less is used. Therefore, the procedure is shown below.

- 1) Add cement to the twin screw forced kneading mixer.
- 2) Add one third of the total amount of water and mix for 30 seconds.
- 3) Add half the total amount of zeolite and mix for 90 seconds. At this time, add 1/3 of the total amount of water while mixing.
- 4) Add zeolite and water as in 3), and mix for 180 seconds.
- 5) After kneading, let stand for 5 minutes.
- 6) Place it in the formwork and let it stand in a constant temperature room (20°C) for 2 days.
- 7) After the curing period, cut and polish for each test.

This time, as the test piece, a cylindrical test piece was prepared. For the cylindrical specimen, a cylindrical plastic mold ($\phi=100$ mm, $h=200$ mm) and a steel cylindrical form ($\phi=50$ mm, $h=100$ mm) were used. The situation is shown in Fig.4 and Fig.5.

CURING METHOD

Curing method was sealed curing. Thus, by constant moisture inside the specimen, to block the effect of water from the external environment.

Zeolite adsorbed cesium in consideration that it has a heating property, it was carried out high temperature curing. As realistic concentration adjustment is performed through the half-life, curing temperature was set to 80°. Curing period is 7 days, 28 days, and 91 days. Fig. 6 shows the sealing process.

COMPRESSIVE STRENGTH TEST METHOD

Compressive strength test, in accordance with the compressive strength test method of concrete (JIS A 1108), was carried out.

ELECTROPHRESIS TEST METHOD

Electrophoresis test was carried out in accordance with the "TEST METHOD FOR EFFECTIVE DIFFUSION COEFFICIENT OF

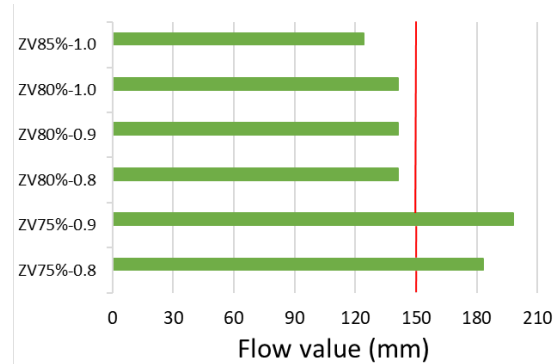


Fig.3 Flow Value



Fig.4 Cylindrical plastic mold ($\phi=100$ mm, $h=200$ mm)



Fig.5 Steel cylinder formwork ($\phi=50$ mm, $h=100$ mm)



Fig.6 Sealed state

CHLORIDE ION CONCRETE BY MIGRATION” (JSCE-G 571-2003)[4] Also, I show a photograph of the test in Fig. 7 This is a photograph of the diffusion cell originally developed in this experiment.

Unlike the conventional experimental system, cells of NaCl solution side and NaOH solution side are considered to be divided. Thus, chloride ions move only the specimen, movement from the test body side junction surface is blocked. By any chance from the fine gap, even if the solution leakage has occurred, since there is no contact of the solution outside the specimen, it has the advantage that it is not reflected in the data.

MERCURY POROSIMETRY METHOD

In relation to the effective diffusion coefficient, measured the pore size distribution. The cut cylindrical specimen was crushed to a particle size of 2.5-5.0 mm, subjected to acetone immersion and furnace drying treatment of 24 hours, and those that stopped hydration as a sample. The test was carried out using a mercury-press-fitting porosimeter, focusing on the peak of the pore size, to evaluate the denseness of the specimen.

In the mercury injection method, when mercury enters the void,

The pore size was calculated from the injection pressure and the amount of mercury injected, and the pore structure was calculated.

The relationship between the pressure at the time of mercury injection and the void diameter d is expressed by the Washburn equation (1) from the measured pressure p , the surface tension γ of mercury, and the contact angle θ between the mercury and the wall of the void. A schematic diagram is shown in Fig.8.[5]

$$d = -(4\gamma/p) \cos\theta \quad (1)$$

COMPRESSIVE STRENGTH TEST RESULT

Fig.9 shows the compressive strength test results. In the formulation of ZV75%-0.8, 7 days strength was 9.54 N/mm², 28 days strength was 8.00 N/mm², and 91 days strength was 3.72 N/mm². Strength was expected to improve over time, in this formulation, decrease trend was confirmed. Possible causes, by sealing during curing was not complete, drying shrinkage occurs, and a decrease in strength due to microcracks generated. In this experiment using a drying furnace that imparts a constant temperature of 80 degrees, by sealing the humidity, it was prevented a scatter of water. However, since the sealing was not complete, water will be released from the specimen, it is believed to have led to a change in pore structure from drying shrinkage. In addition, ZV75%-0.8 is poor filling

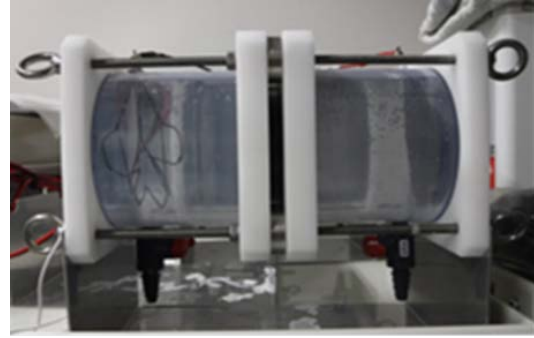


Fig.7 Diffusion cell

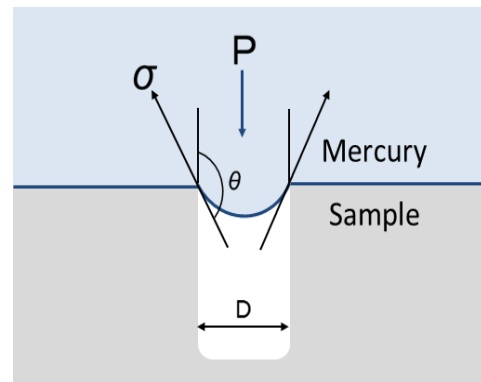


Fig.8 Schematic diagram of pore measurement

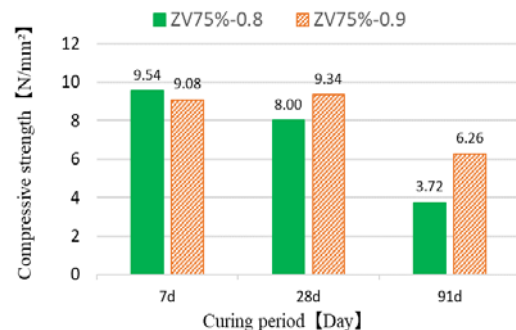


Fig.9 Compressive strength test result



Fig.10 ZV75%-0.8 specimen

property, it is also considered to be the cause of the strength reduction that was an individual with a lot of voids. The situation is shown in Fig.10. With respect to the decrease in strength, it shows a decrease in proportion to the passage of time. Therefore, at the stage of 91 days strength, but was greater than 1.5 N/mm² is the reference value of the waste body, since the possibility of showing a subsequent downward trend remains sufficiently, it is considered that it is necessary to review.

On the other hand, in the formulation of ZV75%-0.9, 7 days strength was 9.08 N/mm², 28 days strength was 9.34 N/mm², it can be seen that the strength is increased. Therefore, ZV75%-0.9, compared to ZV75%-0.8, more cement volume mixed, strength is considered to have improved even 28 days strength. 91 days strength was 6.26 N/mm². As with ZV75%-0.8, it can be confirmed that it has decreased significantly compared to 28 days strength. This is also the same as ZV75%-0.8, it is believed that the change in pore structure due to drying shrinkage has led to a decrease in strength.

Both formulations in 91 days, significant strength reduction was observed. However, since it exceeded 1.5N/mm² is a technical reference value of the waste body, mechanical stability at the 91 days strength time was determined to have been evaluated.[6] However, since there is a possibility that it will continue to show a declining trend after this, it is necessary to consider.

ELECTROPHRESIS TEST RESULT

Fig.11 shows the effective diffusion coefficient calculated by electrophoresis test. The vertical axis of the graph shows the value of the effective diffusion coefficient and is organized based on $1.0 \times 10^{-12} \text{ m}^2/\text{s}$. The horizontal axis shows the curing period, 7 days curing from the left, 28 days curing, and shows the 91 days curing. Focusing on ZV75%-0.8, the execution diffusion coefficient of $3.07 \times 10^{-12} \text{ m}^2/\text{s}$ was shown in 7 days curing. In the 28-day curing, it shows the effective diffusion coefficient of $1.88 \times 10^{-12} \text{ m}^2/\text{s}$, it can be seen that it is decreasing. This is believed to be due to densification of the specimen inside. However, in the 91 days curing, the effective diffusion coefficient of $3.68 \times 10^{-12} \text{ m}^2/\text{s}$ was shown, and an increase in the effective diffusion coefficient was confirmed.

On the other hand, the 7-day curing of ZV75%-0.9 showed the execution diffusion coefficient of $3.33 \times 10^{-12} \text{ m}^2/\text{s}$. In the 28-day curing, it shows the effective diffusion coefficient of $2.38 \times 10^{-12} \text{ m}^2/\text{s}$, it can be seen that it is decreasing. This is believed to be due to densification of the specimen inside. However, in the 91-day curing, the effective diffusion coefficient of $3.20 \times 10^{-12} \text{ m}^2/\text{s}$ was shown, and the increase of the effective diffusion

coefficient in 91-day curing was confirmed as well as ZV75%-0.8.

In both specimens, at the time of 28-day curing, the promotion of hydration reaction from 7 days curing to 28 days curing, densification of the internal structure occurs, over 91 days curing, by promoting the pozzolanic reaction by zeolite, it was expected to be further densified. However, the effective diffusion coefficient increased in the 91 days curing. Possible causes from this is a change in the pore structure due to long-term thermal history. Concrete as the heating temperature is high, chloride permeability and permeability is increased.[7] The long-term heat application, the temperature inside the concrete is increased, since the permeability of the chloride ions is increased, it is considered that the effective diffusion coefficient is increased. Further, the high temperature heat imparting, hydration reaction is promoted, at the time of 7-day curing is toward the end, in the 28-day strength, pozzolanic reaction by zeolite is considered to have been toward the end.

MERCURY POROSIMETRY RESULT

Fig.12 shows the pore size distribution of ZV75 %-0.8. Both specimens can be seen that there is a gap from 10 nm to 100 nm. This is believed to be those that the gap of the zeolite is reflected. In 7 days curing, but the first peak is at 30 nm, in the 28 days curing, the first peak is 20 nm. Similarly, the

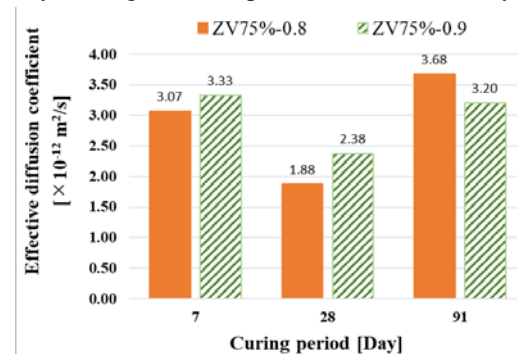


Fig.11 Effective diffusion coefficient

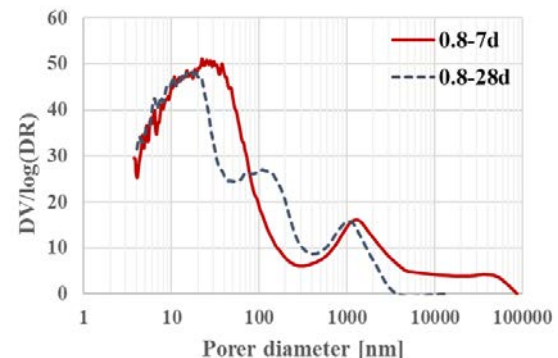


Fig.12 Pore size distribution ZV75 %-0.8

second peak that was present in the vicinity of 1000 nm of 7 days curing has a second peak in the vicinity of 100 nm of 28 days curing, the void of 100000 nm from 10000 nm of 7 days curing, it can be confirmed that it has become a third peak that is present in the vicinity of 1000 nm of 28 days curing. Therefore, ZV75%-0.8 from 7 days curing to 28 days curing, it was confirmed that it is densified. This pozzolanic reaction of hydration reaction and natural zeolite by cement is affected, it is considered to be those densified.

Fig.13 shows the pore size distribution of ZV75%-0.9. And Fig. 14 shows the pore size distribution of zeolite. ZV75%-0.8, it can be seen that there is a gap between 10 nm and 100 nm in both specimens. This is believed to be those that the gap of the zeolite is reflected. In 7days curing, the first peak has 80 nm from 10 nm, the second peak can be seen to be present in the vicinity of 1000 nm. In 28 days curing, it can be seen that the first peak is present in 40 nm from 10 nm. Further, the second peak is present in the vicinity of 100 nm. When comparing the 7 days curing and 28 days curing, almost unchanged, pore size distribution is consistent. Further, it can be confirmed that the data of the void structure from 10 nm to 50 nm is unstable.

CONCLUSION

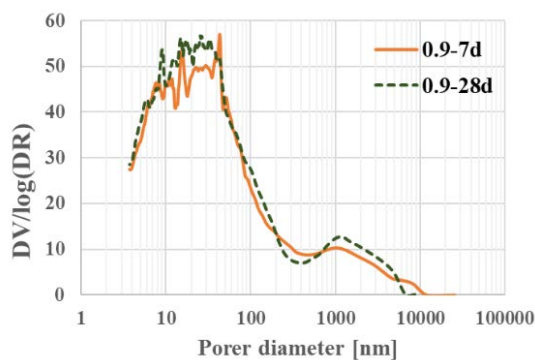


Fig.13 Pore size distribution ZV75%-0.9

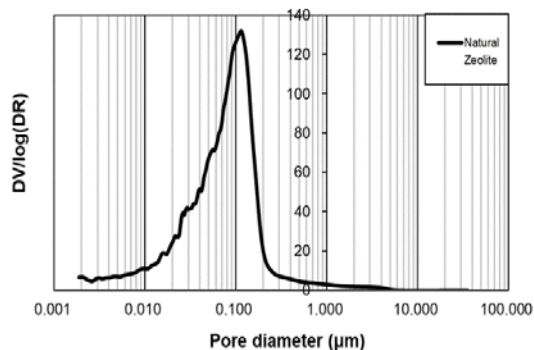


Fig.14 Zeolite pore size distribution

(1) In this study, a solidified body with a high mixing ratio, in which 75 % of the whole specimen was zeolite, could be prepared by the blending examination.[6]

(2) The compressive strength of all the specimens reached 1.5 N/mm², which is considered to be the technical standard for waste, and the mechanical stability could be evaluated. However, it is necessary to improve the fresh property, because the individual difference greatly appeared due to the voids caused by the poor filling property, especially in ZV75 %-0.8.

(3) The hydration reaction and the pozzolanic reaction were accelerated by the application of heat history, and the compressive strength and the effective diffusion coefficient showed peaks after 28 days of curing. However, structural changes and fine cracks will begin to occur on the 91 days, so there is room for further improvement in consideration of the amount of calcium hydroxide produced.

REFERENCES

- [1] K.Niwase,T.Sakai,H.mawatari: Basic Study on Design of Solidified Mixture of Zeolite for Cement Solidification Technology of Cesium Adsorbed Zeolite, Proceedings of Annual Meeting of Atomic Energy Society of Japan (CD-ROM),Mar.2018
- [2] H. Mawatari, K. Niwase and M.Satou, Evaluation of Physical Properties of Fast Ash Cement and Fly Ash Combination Type Filler in Cement Solidification Technique of Cesium Adsorbing Zeolite, Cement and Concrete Collected Papers, Vol.71, Mar. 2018 (in Japanese)
- [3] K.Niwase,A.Imabuchi:COMPRESSIVE STRENGTH OF CEMENT SOLID FORM MIXED WITH ZEOLITE FOR SOLIDIFICATION OF CESIUM ADSORBED ZEOLITE,43rd Conference on Our World in Concrete & Structures,30-31, August 2018.
- [4] Test method for effective diffusion coefficient of chloride ion in concrete by JSCE standard electrophoresis (draft) (JSCEG 571-2003)
- [5] Washburn E.V. : Dynamics of Capillary Flow, Physical Review, Vol. 17, pp.273-283 (1921).
- [6] Nuclear Regulatory Agency: Operational procedure for waste confirmation, Established February 26, 2014 Original pipe dismantling No. 1402262
- [7] Y.sugino, R.kamata, T.tanibe, M.Ozawa : Effect of surface impregnant on pore structure and resistance to substance intrusion of heated concrete, Taiheiyo Cement Research Report No. 174 (2008)

INVESTIGATING COMPRESSIVE, PULLOUT AND TENSILE STRENGTH OF CONCRETE CONTAINING POLYPROPYLENE

Md Jahidul Islam¹, Niaz Md Ashraful haque² and Anika Tahsin³

^{1,2,3}Department of Civil Engineering, Military Institute of Science and Technology, Bangladesh;

ABSTRACT

Every year a large number of plastic wastes are generated throughout the world which is a major threat to the environment due to its non-biodegradable nature where polypropylene consists of more than 35 percent of the total. These plastics need to be recycled and reused in an environment friendly way. On the other hand, for construction purposes an alternative of natural stones, whose reserve is depleting, must be sought. Therefore, aim of this study is to investigate the compressive, tensile and pull-out strength of concrete partially mixed with recycled waste polypropylene (PP) as a coarse aggregate. In order to evaluate the strength of concrete, twelve different mixes are considered where stone chips are replaced by PP at 10% and 20% (by volume) with four different water-cement ratios (0.35 and 0.4 with admixture; 0.45 and 0.5 without admixture) and compared with concrete with no PP aggregate. At 90 days, for concrete with 10% PP replacement compressive strength reduction was between 4% and 26%; whereas, tensile strength decreased from 7% to 11%. The results of pull out strength reveals that in most cases concrete with 10% PP replacement have higher pull out stress compare to concrete without PP. Finally, the use of 10% PP in concrete is safe and can generate strong structural elements.

Keywords: Polypropylene, Composite concrete, Compressive strength, Pull out strength, Split tensile strength

INTRODUCTION

Civilization has made the waste disposal and waste management a major natural concern worldwide. Now a day, the plastic products have become one of the most essential material of our civilized lifestyle; and thus the global plastic production has increased immensely during the past 50 years [1]. Among various waste materials, plastic-based waste materials are worst as they don't effectively debase or decayed [2]. Plastic is accessible nearly all over and its utilization around the world expanded from 5 million tons to almost 335 million tons amidst the year 1950–2016 [3]. Only around 7% of these produced plastics are recycled, and the rest are went to the landfill and polluting the earth. Hence, plastic wastes are considered to be a serious environmental problem universally. According to statistical report, around 34% of these huge plastic wastes are polypropylene found in municipal solid waste [4].

Currently, the global concrete consumption is estimated around 25 billion tons per year and annual coarse aggregate (stone) usage is more than 3.9 billion tones [5]. The use of waste product like plastics in concrete not only makes it economical but also helps in reducing the plastic waste disposal problems.

The use of polypropylene (PP), due to its low unit weight, reduces the unit weight of concrete which results in a reduction in the dead load of a structural concrete member of a building. Reducing a building's self-weight would help reduce the building's seismic

risk, as the earthquake forces are linearly dependent on the dead weight. Application of recycled PP as a partial substitute of coarse aggregate in concrete offers certain advantages, i.e. reduction in the usage of natural resources, low cost alternative to conventional aggregates, recycling of polymer waste, avoidance of contamination and energy savings.

Polypropylene (PP) is an affordable and plentiful thermoplastic used in a wide variety of applications including food packaging, textiles, laboratory equipment, vehicle parts, and banknotes. It is slightly harder, more heat resistant, mechanically rugged material; and has a high chemical resistance [6]. It is the second-most widely produced commodity plastic and can be used in making composite concrete for its excellent material property [7]. The melting point of polypropylene is exceptionally high compared to other plastics at 320°F (160°C).

Several studies have been carried out in recent years on specific types of composites such as concrete with PP fibers and PET aggregates, but not much with crushed PP aggregates and particularly with regard to pull out strength. Therefore, in the present study emphasize is given on finding out compressive strength, pull-out strength and tensile strength of concrete with polypropylene as partial replacement of coarse aggregates at various proportion.

MATERIALS

For the experimental work, stone aggregates and recycled waste PP were used as two different types of coarse aggregates. Specification of aggregate was

selected based on the ASTM C33 [8]. Ordinary Portland Cement (OPC) has been used as binding material for this research work. River (Lalakhali, Sylhet, Bangladesh) sand, as demonstrated in Fig. 1(a), has been collected and used as fine aggregates (FA). Coarse aggregate (CA) as crushed stones were purchased from local market according to required quantities and displayed in Fig. 1(b). Shredded PP aggregate, as shown in Fig. 2, was used as partial replacement of coarse aggregate. Polypropylene (PP) aggregate was prepared using a collection, washing, and scraping procedure. It had been melted and cooled into a certain shape after that. Such plastic cooled molds were then shredded into different sizes. This process made the surface of the concrete rough and little porous that could result in better bonding behavior in concrete.



Fig. 1 Aggregate: (a) coarse, and (b) fine.



Fig. 2 Processed polypropylene (PP) aggregates

The properties of materials were determined by conducting laboratory tests, such as aggregate sieve analysis (ASTM C 136) [9], specific gravity and absorption capacity of coarse and fine aggregate (ASTM C 127 and ASTM C 128) [10-11], unit weight (ASTM C 29) [12], aggregate impact value (AIV) (BS 812-112) [13], and aggregate crushing value (ACV) (BS 812-110) [14]. The properties of the materials are summarized in Table 1.

Water-reducing admixture following ASTM C 494 [15], to maintain uniform workability for lower water-cement ratios (0.35 and 0.40), was used for all combination of fresh concrete. The specific gravity of admixture was 1.21.

Table 1 Properties of coarse and fine aggregates

Description	Crushed Stone	Polypropylene (PP)	Sand
Maximum Size (mm)	19	12	-
Fineness Modulus	7.12	6.77	2.46
Specific Gravity	2.61	0.85	2.7
Water Absorption (%)	0.36	0.3	2.8
Compacted Unit Weight (kg/m ³)	1560	622	1604
AIV	20.3	0.47	-
ACV	21.85	3.6	-

METHODOLOGY

Using plastic waste as aggregate in construction is an economical and green concept of modern civil engineering [16]. To achieve the objectives of this study, a number of experiments have been conducted in the laboratories. The concrete samples were prepared with 0%, 10% and 20% replacement of PP as coarse aggregate with four different w/c ratios (0.35, 0.40, 0.45 and 0.50). Concrete cylinder samples, 100 mm x 200 mm, were prepared as per requirement of the test methods following ASTM C 192 [17]. The compressive strength was determined after 7 days, 28 days and 90 days. The splitting tensile strength was determined after 28 and 90 days. Moreover, a total of 36 concrete cylinders inserted with steel bars, as shown in Fig. 3, were casted for pull out strength determination at 28 days. All the specimen was cast in steel molds and compacted using an internal vibrator. After casting, the specimens were stored in a humid room for 24 hours then demolded. After demolding the specimens were cured in a water tank at controlled temperature ($23 \pm 2^\circ\text{C}$) condition for 28 days except for samples that were tested at 7 days.



Fig. 3 Specimen for pull out strength test.

Mix Design

(a) Five different concrete (b) cures were prepared for this study. Among them, six were prepared with admixtures and the other six were without admixtures. Mix design for the concrete specimens was proposed considering stone chips with three different partial replacement of PP (0%, 10% and 20% by volume) along with four different water cement ratios (0.35, 0.40, 0.45 and 0.50). Each mix design was designated with a unique name for ease in referencing within the text. Table 2 shows the mix proportion for 1 m³ of concrete.

Table 2 Mix design for 1m³ of concrete

Designation	Water (kg)	Cement (kg)	CA (kg)	PP (kg)	FA (kg)	Adm. (l)
WC3 5P0	206	589	977	-	487	1.85
WC4 0P0	206	514	975	-	552	1.23
WC4 5P0	205	456	972	-	605	-
WC5 0P0	205	410	972	-	643	-
WC3 5P10	206	589	879	39	474	1.85
WC4 0P10	206	514	877	39	539	1.23
WC4 5P10	205	456	875	39	592	-
WC5 0P10	205	410	875	39	630	-
WC3 5P20	206	589	781	78	461	1.85
WC4 0P20	206	514	780	78	526	1.23
WC4 5P20	205	456	778	77	579	-
WC5 0P20	205	410	778	77	617	-

Note: WCXPY, “X” stands for the water cement ratio and “Y” stands for percentage of PP replacement.

Testing Procedure

The compressive strength test, as shown in Fig. 4(a) was performed according to ASTM C 39 [18] and the loading rate was kept at 0.25 ± 0.05 MPa/sec. The splitting tensile strength was performed according to ASTM C 496 [19]. Pull out strength determination was conducted according to ASTM C 900 [20]. The test setup for different tests are shown in Fig. 4.

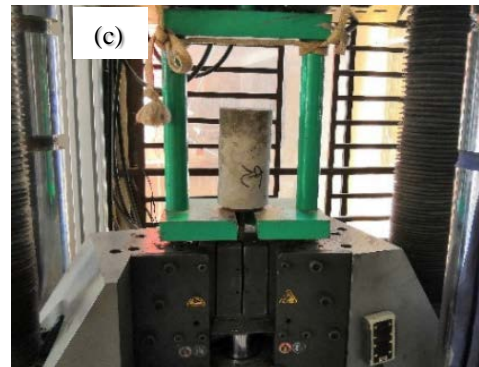


Fig. 4 Test setup (a) compressive strength test, (b) splitting tensile strength test, (c) Pull out strength test of concrete.

RESULTS AND DISCUSSIONS

The effect of using Polypropylene chips as a partial replacement of coarse aggregates on compressive strength, splitting tensile strength and pull out strength are presented in this section

Effect on Compressive strength

The compressive strengths at 7, 28 and 90 days after casting were measured for all type of concretes. Figure 5 represents some of the failed concrete cylinders under compressive force. In most cases, failure was limited to cone and shear failure. An illustrative comparison of compressive strength among various mixes are also shown in Fig. 6 and Fig. 7.

Overall, it is seen that the compressive strengths are increased almost 32% and 48% at 28 days and 90 days compared to 7 days. Based on the test data, it can be seen that, concrete with PP produces lower strength compared to regular concrete with no PP content. This is expected as synthetic PP does not bond well with the binding material used in concrete. However, with increase in concrete age interfacial transition zone between the aggregate and cement matrix gain strength. It is evident from the test results as variation in concrete compressive strength

becomes less at 90 days (4 to 26%) compare to the compressive strength variation at 28 days (14 to 27%). For concrete with w/c ratio of 0.4 and admixture, compressive strength at 90 days was 44.3 MPa compare to the control concrete with compressive strength of 46.2 MPa. However, with 20% PP concrete reduction was higher with 37.2 MPa compressive strength.

Adding admixtures at lower w/c ratios reduces the compressive strength variation for concrete with PP, especially for 10% replacement. As observed from the Fig. 6 and 7, at 90 days compressive strength variations are only 13% and 4% for concrete with admixture and w/c ratios of 0.35 and 0.40, respectively. On the other hand, compressive strength variations at 90 days are 16% and 14% for concrete no admixture and w/c ratios of 0.45 and 0.5, respectively. Replacing stone aggregate with PP aggregate reduces the compressive strength of concrete. However, the minimum strength is 27.2 MPa for concrete with 20% PP and w/c ratio of 0.50 which is still high enough to be used in structural concrete.



Fig. 5 Failure of concrete cylinder under compressive force.

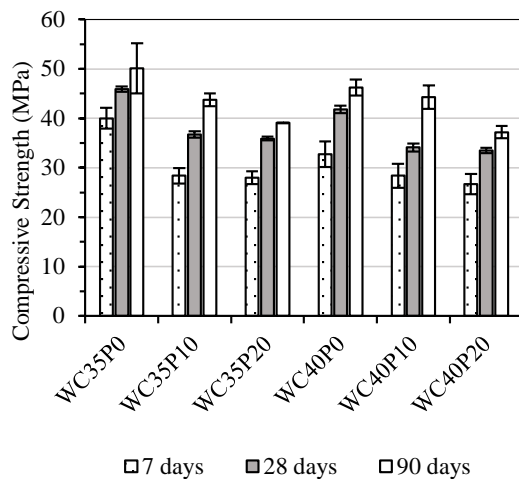


Fig. 6 Compressive strength comparison of

concrete samples with admixture and w/c ratio of 0.35 and 0.40

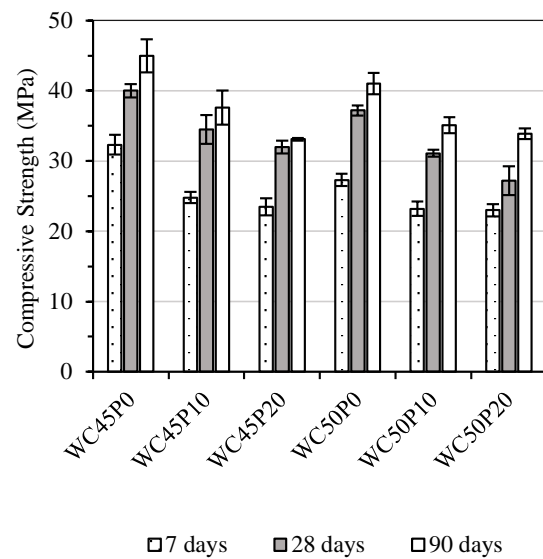


Fig. 7 Compressive strength comparison of concrete samples without admixture and w/c ratio of 0.35 and 0.40

Effect on Tensile Strength

The tensile strengths at 28 days and 90 days after casting were measured according to ASTM C496 for all type of concretes. Specimen after the tensile test is shown in Fig. 8. Comparison of tensile strength among various mixes are illustrated in Fig. 9 and Fig. 10. Based on the test data, it can be said that, concrete with PP produces little lower tensile strength compared to regular concrete with no PP content. The tensile strengths are decreased with increasing w/c ratio. Among all the w/c ratio at 28 days, for 10% PP replacement the relative reduction of strength was between 3% and 15% and the minimum strength was 3.2 MPa at the w/c ratio of 0.50. For 20% PP replacement the relative reduction was between 20% and 24% and minimum strength was 2.7 MPa. Similar trend is also seen for test results at 90 days.



Fig. 8 Specimen after split tensile test.

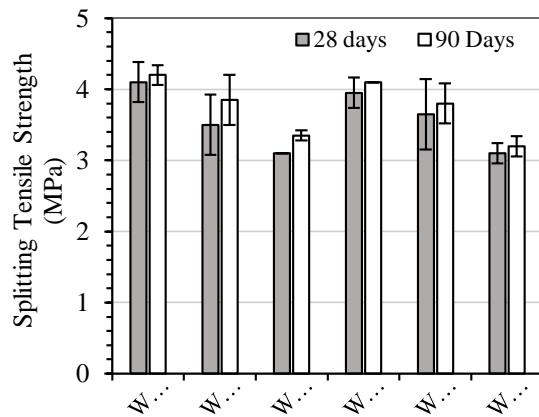


Fig. 9 Tensile strength comparison of concrete samples with admixture and w/c ratio of 0.35 and 0.40.

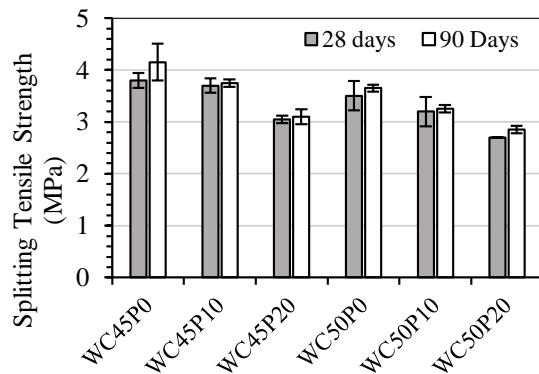


Fig. 10. Tensile strength comparison of concrete samples without admixture and w/c ratio of 0.35 and 0.40.

Relationship between Compressive and Tensile Strength

The relationship between the compressive and tensile strength for 0, 10 and 20% PP replaced concrete, as shown in Fig. 11, indicates that tensile strength increases with increasing compressive strength. Based on the test results an equation is proposed for tensile strength with moderate correlation ($R^2 = 0.775$). Babu et al. [21] used expanded polystyrene (EPS) in concrete and proposed an expression for splitting tensile strength. ACI 318 [22] also provides a guideline for calculating splitting tensile strength from the compressive strength. Both these equations along with the proposed equation is illustrated in Table 3 and Figure 11. As observed from Figure 11, equation proposed by Babu et al. overestimates the tensile strength. ACI 318 equation gives better prediction for compressive strength from 27 to 38 MPa only.

Table 3 Equations for split tensile strength

Designation	Equation	Aggregate type
Proposed Eqn.	$f_t = 0.212 f_c^{0.78}$	PP+NA
Babu et. al [21]	$f_t = 0.242 f_c^{0.79}$	EPS
ACI 318 [22]	$f_t = 0.556 f_c^{0.5}$	NA

Here: f_c = compressive strength at 28 days; f_t = splitting tensile strength at 28 days.

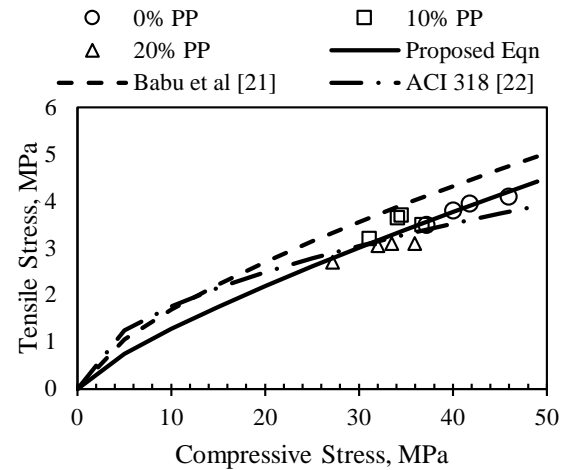


Fig. 11 Relationship between compressive and tensile strength

Effect on Pull out Strength

The pull out strength test was conducted according to ASTM C 900. In this test method, the strength was determined by pulling a cast in place insert rebar by means of a jack reacting against a bearing ring. The pull out strength was determined by measuring the maximum force to pull the inserted rebar from concrete mass. All the measured forces and corresponding pull out strengths for various combinations are demonstrated in Table 4.

Table 4 Pull out strength of concrete specimens

Designation	Pull out Force, (kN)	Pull Out Stress (MPa)
WC35P0	42.3	5.95
WC35P10	37.8	5.31
WC35P20	26.3	3.70
WC40P0	38.1	5.34
WC40P10	43.7	6.14
WC40P20	22.9	3.22
WC45P0	31.1	4.36
WC45P10	36.2	5.08
WC45P20	22.5	3.16
WC50P0	24.8	3.48
WC50P10	28.8	4.04
WC50P20	22.5	3.14



Fig. 12 Concrete conic frustum of cast in place rebar in pull out test.

From the pull out force data it can be observed that, for all four types of water cement ratios, with the increment of PP percentage the bonding strength between the concrete and rebar decreases. However, except for concrete with w/c ratio of 0.35, the 10% PP replaced concrete showed 14 – 17% higher bonding strength than the control sample with no PP concrete. Higher pull out strength indicates good bonding behavior between the rebar and concrete with 10% PP replacement.

CONCLUSION

Compared to regular concrete, PP concrete has the lower compressive strength as well as the lower tensile strength. It is to be expected as the synthetic nature of the PP provides lesser bonding with the cement mortar compare to the natural stone aggregate. Based on the experimental results following observations can be made:

- i. With increase in age interfacial transition zone of PP concrete improved and gave lower variation. For concrete with admixtures (w/c ratios of 0.35 and 0.4) and 10% PP replacement, variations in concrete strength at 28 days were 20% and 13%, respectively; whereas, variations at 90 days were 18% and 4%, respectively.
- ii. Compressive strength is reduced with PP percentage increase. However, concrete w/c ratios of 0.45 and 0.50, and 20% PP replacement still produced minimum of 33 MPa at 90 days.
- iii. Tensile strength of PP concrete showed better performances. Concrete with 10% PP replacement showed reduction up to 11% at 90 days for all w/c ratios.
- iv. Except for w/c ratio of 0.35, concrete with 10% PP replacement showed higher pull out strength compare to the concrete without PP.
- v. Therefore, it can be concluded that the recycled PP with an optimum percentage can be adopted as partial replacement of coarse aggregate in concrete used for structural purposes.

REFERENCES

- [1] Gu, Lei & Ozbakkaloglu, Togay. (2016). Use of Recycled Plastics in Concrete: A Critical Review. *Waste Management*. 51. 10.1016/j.wasman.2016.03.005.
- [2] Frigione, M. 2010. Recycling of PET bottles as fine aggregate in concrete. *Waste Management*, 30 (6): 1101–1106.
- [3] Statista, 2016. Global production of plastic since 1950. [online]. Available at: <https://www.statista.com/statistics/282732/global-production-of-plastics-since-1950>. [Accessed 12 October 2019].
- [4] Islam, Md, Sarwar, Navid and Al shafian, Sultan, Conference proceeding in International Conference on Recent Innovation in Civil Engineering for Sustainable Development (IICSD-2015), An Investigation of Concrete Properties with Polypropylene (PP) as Partial Replacement of Coarse Aggregate. pp. 1.
- [5] USGS Mineral Commodity Summaries, 2017. [online], <https://mineralsmakelife.org/wp-content/uploads/2017/04/Mineral-Commodity-Summaries-2017.pdf> [Accessed 12 June 2019]
- [6] Whiteley, K. S., Heggs, T. G., Koch, H., Mawer, R. L., & Immel, W. 2005. Polyolefins in Ullmann's Encyclopedia of Industrial Chemistry. Weinheim: Wiley-VCH Verlag GmbH & Co.
- [7] Bagherzadeh R., Pakravan, H. R., Sadeghi, A. H., Latifi, M., & Merati, A. A. 2012. An Investigation on Adding Polypropylene Fibers to Reinforce Lightweight Cement Composites (LWC). *Journal of Engineered Fabrics & Fibers (JEFF)*. 7 (4): 13-21.
- [8] ASTM C33 / C33M-18, Standard Specification for Concrete Aggregates, ASTM International, West Conshohocken, PA, 2018, www.astm.org
- [9] ASTM C136/C136M-14, Standard Test Method for Sieve Analysis of Fine and Coarse Aggregates, ASTM International, West Conshohocken, PA, 2014, www.astm.org.
- [10] ASTM C127-15, Standard Test Method for Relative Density (Specific Gravity), and Absorption of Coarse Aggregate, ASTM International, West Conshohocken, PA, 2015, www.astm.org.
- [11] ASTM C128-15, Standard Test Method for Relative Density (Specific Gravity), and Absorption of Fine Aggregate, ASTM International, West Conshohocken, PA, 2015, www.astm.org.
- [12] ASTM C29/C29M-09, Standard Test Method for Bulk Density ("Unit Weight") and Voids in Aggregate, ASTM International, West Conshohocken, PA, 2009, www.astm.org.
- [13] BS 812-112, Testing aggregates — Part 112: Methods for determination of aggregate impact

- value (AIV), 1990, BSI.
- [14] BS 812-110, Testing aggregates — Part 110: Methods for determination of aggregate crushing value (ACV), 1990, BSI.
 - [15] ASTM C494 / C494M-19, Standard Specification for Chemical Admixtures for Concrete, ASTM International, West Conshohocken, PA, 2019, www.astm.org
 - [16] Islam, M. J., Meherier, M. S., Islam, A. K., M. R. 2016. Effects of waste PET as coarse aggregate on the fresh and harden properties of concrete. *Construction and Building Materials*, 125,946-951.
 - [17] ASTM C192 / C192M-18, Standard Practice for Making and Curing Concrete Test Specimens in the Laboratory, ASTM International, West Conshohocken, PA, 2018, www.astm.org
 - [18] ASTM C39 / C39M-18, Standard Test Method for Compressive Strength of Cylindrical Concrete Specimens, ASTM International, West Conshohocken, PA, 2018, www.astm.org
 - [19] ASTM C496 / C496M-17, Standard Test Method for Splitting Tensile Strength of Cylindrical Concrete Specimens, ASTM International, West Conshohocken, PA, 2017, www.astm.org
 - [20] ASTM C900-19, Standard Test Method for Pullout Strength of Hardened Concrete, ASTM International, West Conshohocken, PA, 2019, www.astm.org
 - [21] Babu, D. S., Ganesh Babu, K., & Tiong-Huan, W. 2006. Effect of polystyrene aggregate size on strength and moisture migration characteristics of lightweight concrete. *Cement and Concrete Composites*, 28(6): 520-527.
 - [22] ACI Committee 318. Building Code Requirements for Structural Concrete: (ACI 318-95); and Commentary (ACI 318R-95). Farmington Hills, MI: American Concrete Institute, 1995.

SOLAR PANEL FOUNDATIONS ON SLOPING LAND AND OFFSHORE ~ A REVIEW

Alex Otieno Owino¹, Jamie Ure Ovia¹, Jim Shiau², Zakaria Hossain¹

¹Dept. of Environmental Science Graduate School of Bioresources, Mie University, Japan

²School of Civil Engineering and Surveying, University of Southern Queensland, Queensland, Australia

ABSTRACT

Renewable energy is rapidly becoming an alternative to fossil fuel-based energy generation. With new innovative advances in renewable energy technology more so solar energy, and the markets improving, solar panel prices have become more affordable. Currently, more and more countries are opting for solar power energy. Owing to urbanization and population increase on flat terrains, finding flat lands to accommodate this technology is becoming more difficult. This review hence provides an expert view on how to suit the emerging energy source by venturing ideas into solar panel installation techniques on sloping land and offshores to offer an alternative solution to this flat terrain land scarcity problem. Only a handful of companies handle the latest design and installation techniques of solar panels on slopes and offshores. These companies make use of engineering structures such as piles, cables, and anchors to achieve the best foundation capacities in these potential areas. This paper, therefore, aims to provide a review of a couple of designs that have been used to best suit the two suitable installation locations that act as the best alternatives to the flat land terrains. Furthermore, the potential effects of solar panel installation, such as slope instability, offshore wave fluctuations, photovoltaic shading, the factor of safety, ultimate foundation capacity and several foundation design considerations such as the seismic response, foundation geometry, lateral and pull-out capacities act as the primary considerations for the future research prospects.

Keywords: Solar energy, Sloping land, Offshore, Piles, Cables, Anchors.

INTRODUCTION

Recently, the demand for renewable energy has started to increase globally. A report published by the World Bank, within the last decade, shows there has been an increase in the levels of electrification. This electrification has seen an increase from 83% world population in 2010 to 89% world population in 2017 in most of the areas with abridged grid connectivity rates more so in the developing countries. With a 2030 target for 92% electrification globally and access to clean energy, the exertions have led to an increase in the number of researches on this field with more emphasis on the production of green energy concerning the goals towards low carbon emission. [1][2]

With the increase in electrification on the rise in some parts of the World, accessibility to electricity has had a tremendous sharp decline due to rising populations and economic factors. Some of the common challenges facing the energy sector include low electrification levels, high grid, and related system losses, persistent power interruptions and power shortages, high electricity prices, unstable power prices caused by volatile oil prices, the institutional governance and related operational challenges including lack of synergy and duplication. The global population without access to the electricity grid is, as shown in figure 1 below. [3]

The lack of access to the main electricity grids in the

regions affected contributes to the gap in access between the urban areas and the rural areas. As a result, there has been a hike in the installation of off-grid electricity supply systems, and the major contributor to the off-grid systems is electricity from renewable sources, more so, solar energy through Solar Home Systems, SHSs. [4]

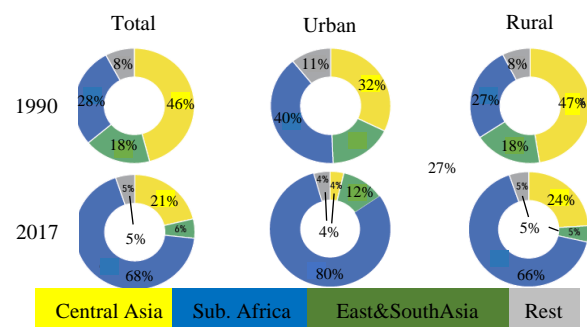


Fig. 1. Regional shares of the global energy access deficit, in total and along the urban/rural divide, 1990 and 2017, (Source: World Bank) [3]

The shifting to solar energy preference for the off-grid connectivity is on the boom since 2017, where to date, about 120 million of the global population had access to the basic electrification systems like solar lights below 11 watts. This off-grid connectivity is evident in countries like Kenya, Benin, Rwanda, Burkina Faso, Tanzania, Papua New Guinea, Fiji, Jordan, Samoa, and Vanuatu. Based on data from the

International Renewable Energy Agency (IRENA) on off-grid solar home systems installations, access to mini-grids increased by 16% between 2015 and 2017 in several countries more so in sub-Saharan Africa, Asia, and the Pacific regions as shown in Figure 2 [5]. With these rising trends and an indication of the advancement and maturity of off-grid and or mini-grids technology, there is potential to fully exploit all the ventures in engineering design and research for better suitable and economic systems to support the dream of solar energy provision in the developing countries. [6]

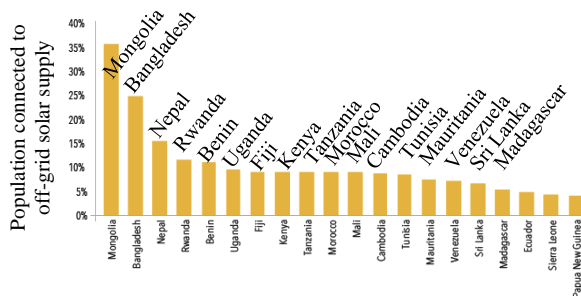


Fig. 2 Top 20 countries with the highest share of solar lighting systems 2017 (Source: IRENA, International Renewable Energy Agency). [5].

Solar energy tops the list when it comes to availability, cleanliness, and the abundance in most parts of the World. As for developing countries with low economies, solar energy is a viable solution to energy distribution because most of these countries have more than nine hours of sunshine per day. Figure 3 below is a burst of sunshine tracking record along the equator, northern hemisphere, and the southern hemisphere regions that experience at least nine hours of sunshine throughout the year [7].

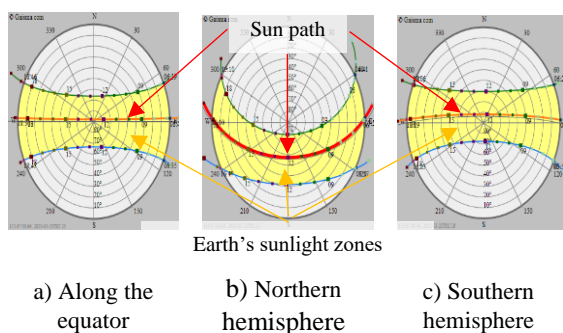


Fig. 3 World - Sunrise, sunset, dawn and dusk times, (Source of Sunrise, sunset, dawn and dusk times around the World, www.gaisma.com, Accessed 2020.03.25.) [7]

With the abundance of solar panels in the production line, comes another challenge of where to install them. Flat terrains are a huge attraction when it comes to the development of engineering projects. A question, therefore, arises that, what next, when the flat terrain landscape becomes scarce? An

exploration of the next available land terrains then becomes handy. This review paper focuses on two relatively new topographical conditions that have the potential to expand solar energy generation in many countries; slopes and offshore. The main areas under consideration are sloping lands with higher slope degrees, and offshore areas of islands, freshwater lakes, abandoned quarries, lagoons, water pans, irrigation canals, and salty water in oceans and seas. It is paramount importance to conduct this study as there is still a limited number of researches conducted on these locations, which could be new data assets for future research.

SLOPES

Engineering construction works such as the construction of photovoltaic systems have, for long, neglected sloping lands. However, with the depletion of the low terrain lands in most parts of the World, it leaves us with one option that is to explore the unused slopes. Another factor contributing to the utilization of the sloping land is the high prices associated with low terrain land, which in most countries are either allocated for agriculture or city expansion projects. With the increasing demands of energy by the enlarging cities, we, therefore, propose the utilization of the sloping lands for generating green energy through the installation of solar panels.

For the last decade, piles stabilized slopes and became one of the most commonly used slope reinforcement techniques in the construction industry, more so in the ground mount photovoltaic systems. Due to the unique stabilization setups of piles, analysis of the interaction of the piles with the surrounding soils have employed different methods, both numerically and analytically [8-12]. Some of these analyses include El Sawwaf (2006) and (2008) who use a series of shallow rigid piles to examine the influences generated in sandy sloping soils [13,14] while Chen & Martin (2001), conducted an analysis based on the finite element method to determine the effect generated by the installation of piles near the crest of slopes [15]. Besides, another study by Georgiadis & Georgiadis (2010), examined the effects of piles on sloping land under the undrained lateral loading conditions using FEM and concluded that the soil adhesion has a significant role to play on the pile-soil lateral capacity [16].

Concept of slope mounted photovoltaic systems

Developing any engineering structure on slopes is not a commonly practiced phenomenon due to the challenges involved and the complexities of the project design. Nevertheless, such locations can be made available by conducting thorough analysis and

understanding of the required slope parameters to support any structure imposed on them, including in this case the ground mount solar photovoltaic systems. Figure 4 represents a ground-mounted photovoltaic system on slopes.

This engineering concept involves the use of single piles to locate the solar panels on sloping land hence making use of somewhat an idle land. Since the slope is already at an angle to the sun, the amount of solar irradiance to the solar cells is improved, and higher energy tapping efficiencies achieved. This technology tackles two engineering problems, i.e., to use the installed piles to act as the ground stabilizers to curb ground slip and to provide green energy to the consumers nearby.

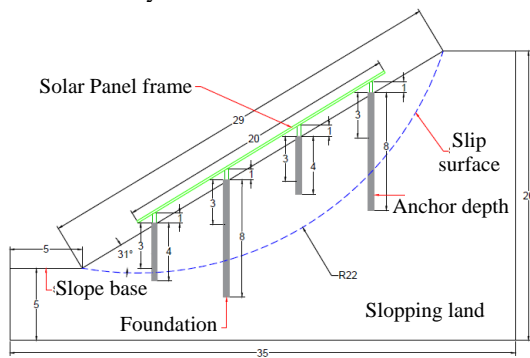


Fig. 4 Slope mounted photovoltaic support structures

Slope mount design components

Foundations

In this field of engineering construction, a few companies have been able to come up with solar farms on sloping lands due to numerous factors that arise into play when it comes to the viability and strength of the foundation. Hence a comprehensive evaluation based on the slope stability, ease of installation, and ultimate pile bearing capacity need to be done. All the previously stated researches, bring about an important parameter that needs more attention called lateral and axial capacity. The lateral and axial capacity of piles, both shallow and deep, requires an in-depth understanding of the interaction of the pile and the surrounding soils to be able to evaluate the ultimate bearing capacity [17-19]. To further understand the interaction of the piles and the surrounding soil medium, numerical solutions have also been used in past researches to illustrate how the ground mount photovoltaic support structures responded during both lateral and axial loading. A seamless example was the use of civil engineering software FLAC2D incorporating the Finite Difference Method to simulate the foundation response and the ultimate foundation bearing capacity [20,21].

Also, in this specific field of support structures in the solar industry, most of the foundations involved

were majorly targeting lands with low degrees of slope angle. Some of the support structures in use today include the driven piles, screw piles, concrete piles, and the ballasted piles. Their principal design considerations focused on the ability to support the structures above ground with minimum consideration to the ground response when it comes to extreme conditions such as those experienced in sloping lands. The flaws associated with such design led to the development of different types of foundations to be used in a single project, as witnessed in most solar farms. These assemblies of different support structure arrays have a higher risk of inducing an imbalance in the ground in-situ parameters hence failure more so if used in sloping land.

Photovoltaic mounting systems

The mounting systems component is very crucial for any photovoltaic installation. In most cases, the use of aluminum frames has been practiced due to lightweight and quality while ensuring strength. A quality mounting frame should attach easily to the foundation structure and should be able to hold a good number of the photovoltaic modules over the area specified. [22-27]

Solar photovoltaic modules

These are the main energy tapping components of the solar farm. The module consisting of photovoltaic cells use sunlight as the energy source to produce direct current. To this time, most of the photovoltaic modules consist of wafer-based crystalline silicon cells or thin-film cells. With the hiking progress on photovoltaic system developments, detailed researches on various kinds of modules depending on the prevailing environmental conditions such as shading, dust accumulation, heat dissipation, performance characterization, temperature dependence, to improve on efficiency have been carried out [28-33]. Non the less more evaluations have also been done considering the cost and performance criterion [34].

Cables, Batteries and Inverters

Once the solar photovoltaic modules are setup, cables need to be then connected to transfer the power to inverters and batteries. While the inverter housing can be built further away on the well-leveled ground, the cables from different photovoltaic arrays must be connected and aligned along the slope length to the inverter housing. Batteries, on the other hand, are used to store the direct energy generated for use in the absence of the sun.

Slope mount design aspects

Site topography

Before commencing the development of solar panel ground mount structures, survey procedures are necessary to establish the critical ground features for the design to be viable. Some of the features checked in this case include the slope angle, the slope orientation to the sun, and if the geometry of the proposed project area can accommodate the photovoltaic modules according to the projected power output.

Foundation depth and Pile length

To further understand the phenomenon of the pile and soil interaction, understanding of the pile element properties and the forces that are induced to the pile by soil movements is essential. The performance of a pile in a slope will be much dependent on the foundation depth and pile length. The interaction between these two parameters produces the soil induced driving forces, the earth pressures, and the reaction forces applied to the unstable sloping terrain. Hence a thorough design and analysis should be conducted to investigate their responses on sloping terrains.

Slope slip surface

The slips surface is the failure plane upon which the sloping bank is liable to fail when there is an imbalance on the forces imposed on it. In most instances, for extreme high slopes, the use of anchors is practiced to hold the different layers to the failure plane. Nevertheless, considering the soil strengths in some given projects, pile have been used to perform the same purpose when deeply rooted into the ground. Deep piles ensure the stability of the ground at higher slope angles without failure hence increased factor of safety of the sloping land as will be discussed in some of the existing structures later in this paper

Ground drainage patterns

Groundwater discharge capability is another imperative factor worth considering when undertaking construction on slopes to ensure proper water flow and liquidity. An increase in the water pressure in the soil is the number one contributor to slope failure. Besides, solar panel shadowing effects may induce the differences in the water retaining abilities of the soil as compared to the in-situ state due to the influence on zones for water infiltration. Therefore, in the design of solar panel farms, shadowing effects on-site drainage should be considered.

Loading patterns

In addition to the earth forces, most engineering structures exposed to outward forces that may experience detrimental effects on the structures if not adequately incorporated into the design loading calculations. These loadings include incidences such as strong winds (Typhoons), cyclones, and seismic forces from earthquakes and landslides. For this reason, slopes are susceptible areas, and a detailed analysis is essential to examine the static and dynamic response upon photovoltaic structure inclusion.

Existing solar farm on sloping land

As can be seen previously, constructing solar farms on sloping land is no easy feat. Nevertheless, there have been successful construction projects as investigated next. The first large-scale solar power plant, known as the Dream Solar Higuchi Nagasaki is in Togitsucho, Nishisonogi-gun, Nagasaki Prefecture, and constructions were completed on September 2015 by the Daiwa Lease Co Ltd (Fig.5)

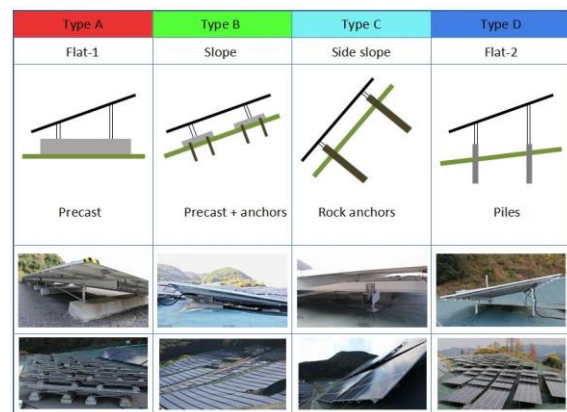


Fig. 5 Dream Solar Higuchi Nagasaki foundation designs (Source: Daiwa Lease/Daiwa House Industry, Nikkei B.P., Photos of Type B Daiwa Lease/Daiwa House Industry)

This solar power plant has an output of about 15MW and located on the southern slopes of a former hilly golf course. The initial planning of the solar power plant took into consideration the types of foundations needed for the solar panels. Since the mountain terrain was previously a golf course, the Daiwa Group optimized on the situation and did not do significant landscaping of the slope. Instead, the company only cut down a few trees on-site to array solar panels more evenly. Due to the undulating slope terrains, the company used four kinds of foundations to strengthen the solar array which includes, use of the precast concrete ballast blocks for the flat areas, precast blocks with ground anchors for areas with higher slope degrees, rock anchors for areas where the slope was even more than the later and piles. Ultimately a technique was used to hammer in the piles while crushing the bedrock to ensuring excellent grip at the soil pile interface. Subsequently, the panel

assemblies were attached to the foundations while maintaining the lowest possible eccentricity to dampen all the moments that may arise when acted upon by outward forces [35,36].

Next, taking a look into the Exeo Matsue Solar Farm, which was constructed by Kyowa Exeo Corp, provides us with an understanding of pile foundations construction. This solar farm has a capacity of 2.3 MW and is located in Matsue City, Shimane Prefecture, as shown in figure 6.



Fig. 6 Exeo Matsue Solar Farm H Pile foundations assembly (source: Kyowa Exeo)

The support structure consisted of a reinforced concrete pile inserted at a depth below the ground and used as a post above ground. The type of reinforced concrete pile used was called the H Pile, a Shinei Tech Co Limited concrete secondary pile product. Since the H pile could adapt quickly to the sloping terrain, the strength further improved by the inclusion of the mounting systems that allowed for ease of attachment of the solar panels above by anchorage into the concrete column. This installation was an efficient setup since the slope was facing the southern direction hence direct nominal irradiance and consisted of 1,900 concrete pile driven into the slope covering a rented area of about 25,000m² [37].

Also, Kanagawa prefectures largest solar plant, Ashigara Oi Solar Way is a perfect example of a solar plant located in a hilly environment. This plant covers a former testing ground site from Komatsu Limited. With an output of 13MW, the solar plant is a perfect example of how idle lands can be converted and made useful by setting up renewable energy power generation plants. The joint effort between Toko Electrical Construction, Kumagaigumi Co Limited, and Aizawa Concrete Corp (Tomakomai City, Hokkaido) came up with a strong foundation that would withstand the weight of the solar panel arrays and also taking care of the sloping ground challenges involved at such locations uphill, i.e., slope stability. As a result of the joint venture, a multipurpose high-intensity concrete H-shaped prestressed concrete piles were used as the foundation structure and as the laterals on which the mounting structures attached.

The H-shaped prestressed concrete piles were set up at equal intervals bellow the proposed array area then driven into the ground. Next, the lateral piles, set up to run parallel to each other, supported the mounting structures. For this foundation and superstructure set up, the tolerance was more robust because the lateral H-shaped piles were attached inside the ground by the longitudinal piles hence transmitting all the loads to the ground. The solar power plant location aerial view and a representation of the foundation set up are as shown in figure 7 [38].



Fig. 7 Ashigara Oi Solar Way H-shaped P.C. laterals and longitudinal piles (source: Japan Asia Group)



Fig. 8 Sakura-no-Sato Mega Power Plant (source: Toda Corp)

Besides, Figure 8 is a mega solar power plant that was constructed at the hills north of Nagasaki Fishing Port on a steep south-facing roadside slope by Sakuranosato Mega Power. This solar power plant has 2.141MW output and is known as the Sakuranosato Mega Power Plant, which started operations in October 2015. The main challenge when constructing this solar power system was the angle of the slope, which was 30°, a very steep slope. As a result of this steep slope, all construction works operated almost no heavy machinery. In the middle of the solar power plant, there was an access road that ran east-west, used by heavy trucks and crane vehicles needed to load or offload heavy materials. Furthermore, a monorail was set up from bottom to top to transfer construction materials. Due to the topography factor, a new type of mortar application method involved casting the mortar into a cubic frame

molded by the four corners of the driven steel frames. The array mounting structures were then bolted on top of the concrete cube foundations as shown in figure 9



Fig 9 Sakura-no-Sato MPP, Casted mortar foundations with steel mounting frame attachments (source: Toda Corp, Nikkei B.P.)

With such high slope angles, came an additional challenge when it comes to maintenance. To curb this challenge, the company opted to use a woven weed barrier to discourage weed growth on the site hence reduced weed management [39].

Ultimately, for all the power plants constructed on the slopes, water flow was given a significant priority to prevent the imbalance in the soil moisture content due to the added ground cover. To achieve natural water flow along the slope, drainage channels constructed downslope met with the area drainage network for efficient disposal. The next section of this review will focus on the installations of solar photovoltaic arrays offshore.

OFFSHORE

Most countries worldwide enjoy a vast availability of waterfronts through waterways, abandoned quarries, lagoons, lakes, rivers, and a long coastline with seas and oceans. Therefore, considering the communities living along these waterfronts, and the distances from the national electricity grid, the development of the offshore solar farms can be beneficial in tackling the energy challenges faced by the citizens by introducing mini-grids from the solar energy generated in such localizes areas. Another factor that makes the waterbodies highly reliable for the solar farm installation is the presence of vast areas without shadowing effects from nearby built environments hence the high direct nominal irradiance (DNI). Since these areas also experience high rates of solar radiation throughout the year, the shadowing effect created by the vast areas of the solar panels can also lead to water conservations on the water bodies by inhibiting the extra exposure to the direct heat from the sun hence reduced water loss through evaporation. i.e., concerning the water bodies that

need evaporation control measures since they may be supplying water for other purposes, for example, agriculture and household use. Locating the solar panels over the water bodies have also proven to improve the panel efficiencies due to the cooling effect in the immediate surrounding [40-42]. Also, another motivating factor is on the matter of land ownership and how it can be solved to avoid the usage of private land for the development of solar energy farms. Since land ownership in most parts of the World is considered personal property, the development of projects that need vast parcels of land in the populated zones always tends to halt due to the unreadiness of the landowners to give out their lands. Consequently, more focus away from the land area is needed, and preference developed for the installation of the power plants further offshore.

The vast areas offshore, with minimum shadowing, have also contributed to more focus on the methods essential to make the offshore farms more productive due to the increased sunshine hours. A study to analyze the effects of temperature on the performance of solar panels was first done by the National Institute of Advanced Science and Technology in Japan [43] and funded by the Japanese Ministry for the Environment [44]. As a relatively new field of research, further research should be conducted to ensure proper design, and show that these photovoltaic farms are economical and environmentally friendly.

Concept of offshore photovoltaic systems

Offshore installations of photovoltaic systems being a new venture in the solar energy industry, several installation methods are available to ensure the viability of the projects. One of the major contributing factors in offshore farm economics is the ability to keep the arrays further offshore without any potential damage incurred for the longest time possible. This durability concern, therefore, brings in the key challenges, i.e., superstructure foundation design, mounting structure design, and locating of the inverter housing. The new concept makes use of the buoyancy conditions created by the floats to keep the panels afloat and, in some cases, track the movements of the sun for efficient exposure of the panel surfaces. Another incentive of the offshore photovoltaic installations is the proper use of the vast areas available for power generation hence high energy yield capabilities.

Components of offshore photovoltaic systems

The figures 10a and 10b show the crucial components of the offshore photovoltaic systems which are;

The foundation - Also known as the mooring system

upon which the panels permanently attach to achieve the desired strength. The main aim of the foundation structure is to keep the structure afloat in a fixed position, never to be swayed away by the waves in the waterbody under consideration [45].

Buoyancy floats - These are the structures on which the photovoltaic arrays attach to keep them floating on the water surface, as the name depicts. They constitute high-density poly-ethylene blocks, and their arrangement on the water surface is mostly dependent on the array geometry and the power output required for a given project.

P.V. arrays and cables and inverter housing - These are the central energy tapping systems and power transmission equipment, respectively, as explained in the slope section above.

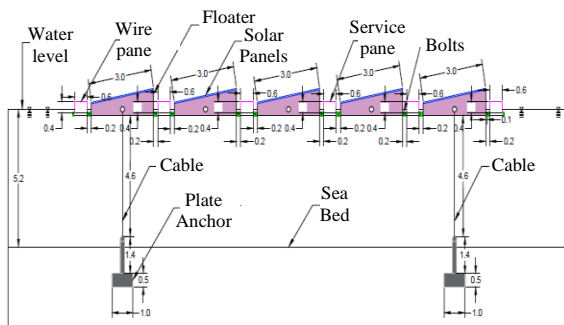


Fig. 10a A completely offshore solar farm components.

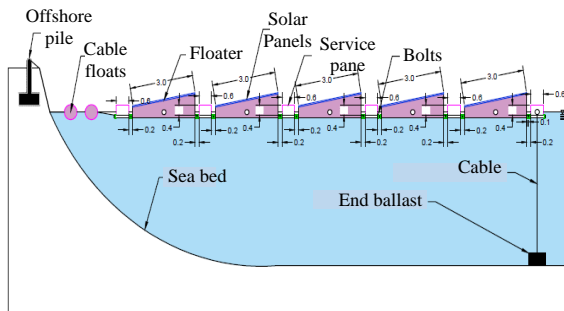


Fig. 10b Land-fixed offshore solar farm foundation components

Existing offshore foundation Design

Some of the existing offshore photovoltaic array foundations design include the following;

Bottom anchored foundations

In the construction field, a good number of the fixed bottom foundation structures are into practice. In this scenario, the review paper draws the focus on the use of the bottom anchoring system for the attachment of the solar panel arrays offshore. This foundation type consists of the assembly of a bottom anchor placed at a design depth below the seabed. The anchor dampens all the lateral forces subjected to the solar panel array at the water surface, more so

earthquakes and water waves. This new concept of solar arrays attachment is most suitable for all water depths. The mitigations factors put in place include the investigation of the effects of corrosion, durability of the floats, design ultimate capacity, projected electricity output, and the ease of installation. Since the offshore farms are developing rapidly, most developing bottom anchorage installations are evident in countries like Japan, Fig 11 [46], France Fig 12 [47], South Korea [48], United Kingdom [49], United States [50], with more recent construction works in the United Arab Emirates [51].

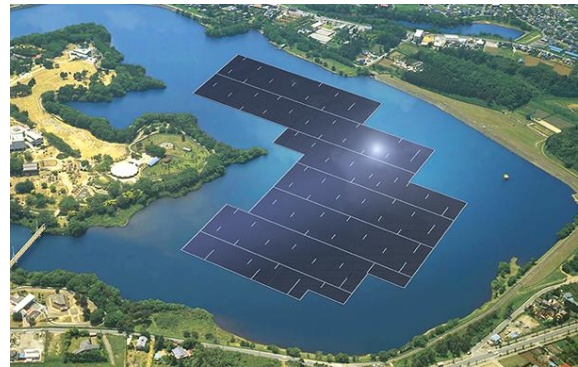


Fig 11 The Yamakura Dam plant (Source Kyocera Corp)



Fig. 12 Piolenc in Southern France. (Source AFP)

Land-fixed offshore solar farm foundation

This foundation concept involves the combination of a pile foundation onshore and a cable attachment to transfer the assembled solar panel arrays further offshore. Panels are assembled on land and moved offshore, depending on the required capacity. The cable system dominates this construction assembly due to its robust strength factors, and it allows for much less material usage in the foundation structure. Also, this combination employs the use of anti-tide ballasted floats for superstructure stability. The ballasted floats reduce the wave action on the panel area during the fluctuation in the wave strength and wave direction. An excellent example of such a foundation is in the construction of the 145 MW floating photovoltaic plant built on a 225ha section of the Cirata Reservoir in West Java, Indonesia. This method of land support utilizes the vast archipelago

present in the region. Thus, supporting foundation structures, as shown in figure 13 [52].



Fig. 13 145 MW of floating P.V. in Indonesia. (Source Hanwha Q Cells)

POWER TRANSMISSION AND STORAGE CONSIDERATIONS

With efforts to increase the area covered by the solar panels to tap the abundant energy source, the main challenge is energy storage in the night. The solar energy research field has led to the innovation of new ways to store energy in lithium batteries and through direct feed into the grid straight from the solar farm. A comprehensive assessment is necessary to determine which method of transmission suits best the end-user, more so if the energy generated is to be readily available to those parts that are isolated from the main grids. In the case energy produced exceeds the capacity of a given area, then a link to the primary grid should be included to supply the excess energy. As researchers in this field of renewable energy, this review is a solution-based projection analysis of the possible ways to curb energy demands. Figure 14 below illustrates an energy storage and distribution network that best suits the isolated grids to ensure round the clock energy provision to the target customers.

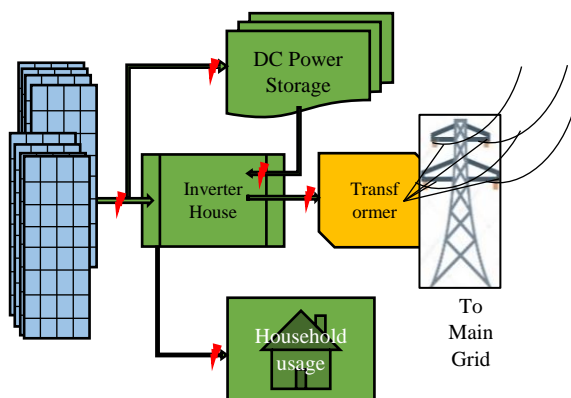


Fig. 14 The power transmission and storage network

CONCLUSION

From this review, it is evident that we have a variety

of cross-cutting techniques that have implemented to tap into solar energy at all locations, both on slopes and offshore. Furthermore, more research on design charts for photovoltaics installation on slopes is needed as well as to fully understand the effects that the solar panels have on overall stability to the slope. As for the offshore structures, the review paper shows that this new installation method is the right way of saving vast areas of land to be used for other purposes while also improving on the photovoltaic array efficiency due to the cooling effect from the surrounding waterfronts. For this reason, further research is called for when it comes to design if the overall efficiency in installation and electricity production needs to be realized, not forgetting the strength and durability of the structure. Since the technology readiness of solar energy is high and attractive now, scaling up its potential is indispensable

FURTHER RESEARCH GOALS

This review depicts a state that allows for knowledge expansion and for improving existing technologies when it comes to foundation design and the developments related to support structures of green energy sources. With the prices of solar panels reducing over time, the need to facilitate their installation is scaling in size, and alternative locations to develop the farms are necessary.

This paper brings to light that solar panels on slopes are a great way to use sloping land that would otherwise be left idle effectively. In addition to this, the offshore foundation design is necessary to make use of the vast areas with maximum direct nominal irradiance (DNI) as a result of zero shadowings and obstruction. After reviewing the current industry practices, several pieces of research questions were raised for an answer in the future regarding the effect of pile and plate anchor installation on the overall stability of the slope and offshore power projects, respectively. Also, the reduction of pile and plate anchor capacity to the lateral loading and pull-out force is the critical research items in the next stage of this research. This paper has also highlighted the need to bring industry partners and government bodies to join the research program to develop new measures when it comes to venturing into renewable energies without boundaries or any hindrance whatsoever. The research questions that this review paper aims at addressing and expounding on in the next stage of this research are;

- ✓ What are the best foundation types for solar panels on slopes?
- ✓ What are the best foundation types for solar panels on nearshore and further offshore?
- ✓ What is the maximum or optimum slope angle for solar panels on slopes?

- ✓ What is the optimum depth of anchors and cable assemblies required for efficient foundation stability?
- ✓ What are the influences of lateral capacity and pull-out capacity of the pile in slope and anchors in offshore scenarios, respectively?
- ✓ What is the factor of safety before and after the installation of solar panels on slope and plate anchors in offshore scenarios?
- ✓ What is the optimum embedded length of the pile as well as that of the plate anchor that would not bring in adverse reduction to the factor of safety, FoS?
- ✓ What are the responses to seismic forces on slope and seabed/ lakebed, with and without the solar panels installed? Is there a difference?
- ✓ Are the new proposed foundation designs economically viable when it comes to the construction costs and ease of installation?

Therefore, fundamental research is mandatory on these emerging support structures to evaluate their performance, efficiency, and design cost, as will be conceptualized and put into the design charts in the next task of this research process.

ACKNOWLEDGMENTS

The first author and second author would like to express their gratitude to the Japanese Government through MEXT and Japan International Cooperation Agency (JICA), respectively, for providing scholarships to study and research at Mie University, Japan. Much gratitude to the School of Civil Engineering and Surveying, University of Southern Queensland, Queensland, Australia, for the continued support in matters of research in the civil engineering field.

REFERENCES

- [1] ESMAP (Energy Sector Management Assistance Program). State of Electricity Access Report. Washington, DC: World Bank. 2017 <http://documents.worldbank.org/curated/en/364571494517675149/pdf/114841-REVISED-JUNE12-FINAL-SEAR-web-REV-optimized.pdf>.
- [2] ESMAP (Energy Sector Management Assistance Program), Policy Matters: Regulatory Indicators for Sustainable Energy. World Bank, Washington, DC, 2018d <https://openknowledge.worldbank.org/handle/10986/30970>.
- [3] ECOSOC (United Nations Economic and Social Council), (2018) “Ministerial Declaration of the High-Level Segment of the 2018 Session of the Economic and Social Council on the Annual Theme ‘From Global to Local: Supporting Sustainable and Resilient Societies in Urban and Rural Communities.’” August 1, 2018. http://www.un.org/ga/search/view_doc.asp?symbol=E/HLS/2018/1&Lang=E.
- [4] Sustainable Energy for All (SEforALL) and the Climate Policy Initiative (CPI), “Energizing Finance: Understanding the Landscape, (2018): Tracking Finance for Electricity and Clean Cooking Access in High-Impact Countries.” SEforALL and CPI, Washington, DC, 2018. <https://www.seforall.org/sites/default/files/EF-2018-SEforALL.pdf>
- [5] IRENA (International Renewable Energy Agency), “Measurement and Estimation of Off-Grid Solar, Hydro and Biogas Energy.” IRENA, Abu Dhabi, 2019
- [6] United Nations. Transforming our world: (September 2015) The 2030 Agenda for Sustainable Development. General Assembly Report on Sustainable Development Goals, A/RES/70/1, NewYor, 2015.
- [7] World - Sunrise, sunset, dawn and dusk times, Courtesy of Sunrise, sunset, dawn and dusk times around the World, <https://www.gaisma.com/en/dir/001-continent.html>
- [8] Ito T, Matsui T, Hong PW., “Design method for stabilizing piles against landslide – one row of piles”. Soils Found; Vol.21, No.1, 1981, pp. 21–37.
- [9] Poulos HG., “Design of reinforcing piles to increase slope stability”. Can Geotech J X, Vol.32, 1995, pp. 808–818.
- [10] Chen LT, Poulos HG., “Piles subjected to lateral soil movements”. J Geotech Geoenviron Eng ASCE, Vol.123, No.9, 1997, pp. 802–811.
- [11] Sanping, Z. and Robert, L., Stability analysis of drilled shafts reinforced slope. Soils and Foundations, Vol.42, No.2, 2002, pp.93-102.
- [12] Won, J., You, K., Jeong, S. and Kim, S., Coupled effects in stability analysis of pile–slope systems. Computers and Geotechnics, Vol.32 (4), 2005, pp.304-315.
- [13] El Sawwaf, M., Lateral behaviour of vertical pile group embedded in stabilized earth slope. Journal of Geotechnical and Geoenvironmental Engineering, Vol.134(7), 2008, pp. 1015-1020.
- [14] El Sawwaf, M., Lateral resistance of single pile located near a geosynthetic reinforced slope. Journal of Geotechnical and Geoenvironmental Engineering, Vol.132(10), 2006, pp. 1336-1345.
- [15] Chen, C.Y. & Martin, G.R., Effect of embankment slope on lateral response of piles. Proceedings of the International Conference on FLAC and Numerical Modeling in Geomechanics, Lyon, France, 2001, pp. 47-54.
- [16] Georgiadis, K. and Georgiadis, M., Undrained lateral pile response in sloping ground. Journal of geotechnical and geo-environmental engineering, 136(11), 2010, pp.1489-1500.

- [17] Zhao, H., Yin, P.B. and Li, X.B., Mechanical response of bridge piles in high-steep slopes and sensitivity study. *Journal of Central South University*, 22(10), 2015, pp. 4043-4048.
- [18] P. Yin, M. Zhao, C. Yang et al., Experimental study on bearing capacity of bridge piles in cross slopes under complex loads,” *China Civil Engineering Journal*, Vol. 47, No.5, 2014, pp. 110–117.
- [19] Ventura, Mark C., Stephen K. Cassens, and Scott James Rau. *Solar Array Foundation and Installation*. U.S. Patent Application 12/613,252, filed May 5, 2011.
- [20] Owino, A.O., Hossain, Z. and Shiau, J., Parametric study on the response of composite single piles to lateral load by numerical simulation (FDM). *European Journal of Engineering Research and Science* Vol.3, No. 10, 2018, pp.16-20.
- [21] Owino, A.O., Hossain, Z. and Shiau, J., Pull-out resistance of single piles and parametric study using the Finite Difference Method (FDM). *American Journal of Civil Engineering and Architecture* Vol.6, No. 5, 2018, pp. 193-198.
- [22] Barkaszi, S.F. and Dunlop, J.P., Discussion of strategies for mounting photovoltaic arrays on rooftops. In *International Solar Energy Conference*, Vol. 16702, pp. 333-338. American Society of Mechanical Engineers, 2001.
- [23] Baumann, T., Schär, D., Carigiet, F., Dreisiebner, A. and Baumgartner, F., Performance analysis of PV green roof systems. In *32nd European Photovoltaic Solar Energy Conference and Exhibition; 1618*, Vol. 1622, 2016.
- [24] Port, J., Solar panel mounting systems. U.S. Patent 7,814,899, issued October 19, 2010.
- [25] Lenox, C.J. and Johnson, K.M., PV module mounting method and mounting assembly. U.S. Patent 8,424,255, Issued April 23, 2013.
- [26] Harberts, J.H., Faust, A., Klinkman, J.E., Katt, R.P. and Raffler, D.W., Mounting systems for solar panels. U.S. Patent 8,413,944, issued April 9, 2013.
- [27] Frischknecht, R., Itten, R., Sinha, P., de Wild-Scholten, M., Zhang, J., Heath, G.A. and Olson, C., Life cycle inventories and life cycle assessments of photovoltaic systems. No. NREL/TP-6A20-73853. National Renewable Energy Lab. (NREL), Golden, CO (United States), 2015.
- [28] Ramabadrnan, R. and Mathur, B., Effect of shading on series and parallel connected solar PV modules, *Modern Applied Science* Vol.3, No. 10 2009, pp. 32-41.
- [29] Adinoyi, M.J. and Said, S.A., Effect of dust accumulation on the power outputs of solar photovoltaic modules. *Renewable energy* Vol.60, 2013, pp. 633-636.
- [30] Paudyal, B.R. and Shakya, S.R., Dust accumulation effects on efficiency of solar PV modules for off grid purpose: A case study of Kathmandu, *Solar Energy* Vol.135, 2016, pp.103-110.
- [31] Solanki, C.S., Sangani, C.S., Gunashekar, D. and Antony, G., Enhanced heat dissipation of V-trough PV modules for better performance, *Solar Energy Materials and Solar Cells* Vol.92, No. 12, 2008, pp.1634-1638.
- [32] Strevel, N., Trippel, L. and Gloeckler, M., Performance characterization and superior energy yield of First Solar PV power plants in high-temperature conditions, *Photovoltaics international* Vol.17, No. 3 (2012, pp.148-154.
- [33] Dubey, S., Sarvaiya, J.N. and Seshadri, B., Temperature dependent photovoltaic (PV) efficiency and its effect on PV production in the world—a review, *Energy Procedia*, Vol.33, 2013, pp.311-321.
- [34] Shah, A., Meier, J., Buechel, A., Kroll, U., Steinhäuser, J., Meillaud, F., Schade, H. and Dominé, D., Towards very low-cost mass production of thin-film silicon photovoltaic (PV) solar modules on glass, *Thin solid films* Vol.502, No.1-2 2006, pp.292-299.
- [35] Kato S., 4 Types of Foundations Adopted for 15MW Solar Plant, 2016, Retrieved from https://project.nikkeibp.co.jp/ms/atclen/news_en/15mk/021100369/?ST=msbe?ST=msbe&P=4, 2016/02/11)
- [36] Kato S., 2.1MW Solar Plant Built on Roadside Slope, 2015, Retrieved from *Solar Power Plant Business*: https://tech.nikkeibp.co.jp/dm/english/NEWS_EN/20150810/431534/?ST=msbe.
- [37] Solar Panels Arrayed in Accordance With Slopes Using New Construction Method https://project.nikkeibp.co.jp/ms/atclen/news_en/15mk/030300418/?ST=msbe?ST=msbe&P=1
- [38] Kanagawa Prefecture's Largest Solar Plant Rated 'A', "Ashigara Oi Solar Way", https://project.nikkeibp.co.jp/ms/english/NEWS_EN/20150217/404440/?ST=msbe?ST=msbe&P=1
- [39] Solar Power Generated in Nagasaki 'Consumed' at Facility in Ibaraki, <https://project.nikkeibp.co.jp/ms/atclen/19/00001/00328/?ST=msbe>
- [40] Gotmare, J.A. and Prayagi, S.V., Enhancing the performance of photovoltaic panels by stationary cooling, *Int J Sci Eng Technol*, Vol.2, No. 7, 2014, pp.1465-1468.
- [41] Dash, P.K. and Gupta, N.C., Effect of temperature on power output from different commercially available photovoltaic modules, *International Journal of Engineering Research and Applications*, Vol.5, No.1, 2015, pp.148-151.

- [42] Fesharaki, V.J., Dehghani, M., Fesharaki, J.J. and Tavasoli, H., The effect of temperature on photovoltaic cell efficiency, In Proceedings of the 1st International Conference on Emerging Trends in Energy Conservation–EETEC, Tehran, Iran, 2011, pp. 20-21.
- [43] Trapani, K. and Redón Santafé, M., A review of floating photovoltaic installations: 2007–2013, Progress in Photovoltaics: Research and Applications, Vol.23, No. 4 (2015, pp.524-532.
- [44] Ueda, Y., Sakurai, T., Tatebe, S., Itoh, A., Kurokawa, K., Performance Analysis of PV System on the Water, Proceedings of the 23rd European Photovoltaic Solar Energy Conference, Valencia, Spain, 2008, pp. 2670-2673.
- [45] Sharma, P., Muni, B. and Sen, D., Design parameters of 10 KW floating solar power plant, In Proceedings of the International Advanced Research Journal in Science, Engineering and Technology (IARJSET), National Conference on Renewable Energy and Environment (NCREE-2015), Ghaziabad, India, Vol.2, 2015.
- [46] Corporation, T. C. (2018). 13. 7MW plant on the Yamakura Dam reservoir and completion ceremony held at the project site (right). 27–29.
- [47] France's first floating solar power plant, <https://www.thelocal.fr/20191018/in-pictures-frances-first-floating-solar-power-plant>
- [48] Floating Solar Farm in Spotlight as S. Korea Goes Green Posted on November 16, 2018, by Korea Bizwire in Business, Energy & Green, Environment, Most Viewed, Policies and Regulation, <http://koreabizwire.com/floating-solar-farm-in-spotlight-as-s-korea-goes-green/127522>
- [49] Britain's first floating solar panel project installed <https://www.telegraph.co.uk/news/earth/energy/solarpower/11110547/Britains-first-floating-solar-panel-project-installed.html>
- [50] America's largest floating solar project completed, <https://pv-magazine.usa.com/2019/10/23/americas-largest-floating-solar-project-completed/>
- [51] UAE to launch the first floating solar plant, <https://www.arabianindustry.com/utilities/news/2020/feb/15/uae-to-launch-first-floating-solar-plant-6326788/>
- [52] Masdar to install 145 MW of floating PV in Indonesia, <https://www.pvmagazine.com/2020/01/16/masdar-to-build-145-mw-of-floating-pv-in-indonesia/>

Environment

THE DYNAMICS OF LAND COVER CHANGE AND CAUSAL FACTORS IN THE KURANJI WATERSHED

Teguh Haria Aditia Putra¹, Bambang Istijono², Aprisal³, Bujang Rusman⁴ and Taufika Ophiyandri⁵

¹ Doctoral Program in Agricultural Science, Andalas University, Indonesia

^{2,5} Department of Civil Engineering, Andalas University, Indonesia

^{3,4} Department of Soil Science, Andalas University, Indonesia

ABSTRACT

Land cover changes (LCC) are one indicator of an increase in population in a watershed area that demands the provision of housing locations, road infrastructure, and productive land to meet the needs of life. LCC can have a positive impact in the form of increased land use values and incomes, while also negative impacts in the form of erosion, landslides and floods. The watershed area should have a balance in its development. This research is important as a first step in overcoming changes in land cover that can threaten the sustainability and sustainability of the Kuranji watershed. This study details LCC in the Kuranji watershed from 1985 to 2018 and the factors causing these changes. The methodology used is descriptive qualitative with 60 respondents. Data were obtained by interviewing respondents. Respondents are those having agricultural land and working in the agricultural sector and this research was carried out in 2019. The results showed an increase in the type of land cover of settlements and mixed gardens, while forests, rice fields and shrubs have decreased. The main factor influencing changes in land cover is economic (59%), followed by social factors (25%) and politics (16%). It was also found that local wisdom of the Minangkabau culture was able to reduce LCC. The local wisdom of the Minangkabau culture explains that land owned by the community, which is a hereditary inheritance, should not be traded without very important reasons.

Keywords: LCC, ArcGIS, Descriptive qualitative

INTRODUCTION

Land cover in the watershed is always changing. This change is a major issue in controlling the sustainability of watershed areas. This change becomes very dangerous if it occurs in the upstream watershed, which is a protected area and conservation area. Changes in land cover have an influence on the carrying capacity of watershed areas if done on a large scale. Changes in land cover can cause landslides, floods and other hydrogeological disasters.

Land cover changes (LCC) with increasing population. The higher the population, the land needs are also increasing. The increasing need for land must be accompanied by soil and water conservation techniques so that the impact caused by changes in land cover can be minimized.

One of the watersheds undergoing land cover change is the Kuranji watershed. This watershed has an area of 22,469.55 hectare located in Padang City. Statistical data show there has been an increase in population in the Kuranji watershed, namely in the Districts of Kuranji, Pauh and Koto Tengah in the past five years. The increase was 60,441 people, with a population growth rate of 2.28 - 2.83% [1]. The high rate of population growth triggers land conversion that aims to meet the needs of life. Examples of these changes are forest area into agriculture, and agricultural area into a developed

area.

The change in the Kuranji watershed is very dynamic because it is in an urban area. LCC in the Kuranji watershed is also triggered by the growth of tertiary education areas. The development of this education area has triggered the community to provide infrastructure to support educational activities such as student boarding houses, food stalls, photocopy stalls and others. This makes the area around the tertiary education a satellite city.

LCC in the Kuranji watershed have increased quite rapidly in the past 10 years. This change is due to the occurrence of a large earthquake in Padang City on 30 September, 2009, having the potential for a tsunami. Since the earthquake, some people who lived on the coast have moved to the central Kuranji watershed, which is a tsunami safe zone. The move of coastal communities in the central part of the Kuranji watershed was also encouraged by the prediction of the Mentawai Megathrust earthquake accompanied by a tsunami.

LCC in the Kuranji watershed are very dangerous, especially in the upper and middle watersheds. This is because the Kuranji watershed has a steep topography of 54.66% of the watershed area. Judging from the shape of the watershed, the Kuranji watershed has a shape that extends near the moon in the upper reaches. This form explains that the Kuranji watershed has a great potential for flooding if vegetation cover is reduced and does not

function as a soil protector. More details about the slope of the Kuranji watershed can be seen in Fig. 1.

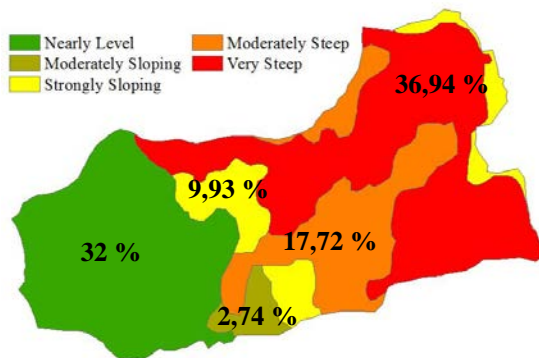


Fig. 1 Slope conditions in the Kuranji Watershed

The purpose of the study was to analyze LCC Kuranji watershed in the last 33 years as well knowing the factors causing changes in land cover.

MATERIALS AND METHOD

Materials

This research was conducted at the Kuranji watershed in Padang City, West Sumatra, Indonesia. It has a maximum height of 1860 meters above sea level with annual rainfall of more than 5,054 mm. Based on geographical position, the Kuranji watershed is located between 100°21'18,84" E - 100°33'52,87" E and 0°47'23,36" S - 0°56'13,71" S.

Determination of LCC was by using a 1985 topographic map with a scale of 1: 50,000 and SAS Planet (Arc-GIS Imagery) satellite imagery in 2018 with a spatial resolution of 20x20 meters. The tools used are GPS and ArcGIS 10.6. Information gathering factors that cause changes in land cover was by open interview techniques.

Method

The methodology used in determining land cover change is to perform interpretation and delineation analysis on each map year using ArcGIS 10.6. Then, an area value analysis is performed on the attribute table, so that, every year, the map will contain the value of each land cover and the factors that support changes in land cover determined using descriptive qualitative analysis methods.

This research was conducted from July 2019 to November 2019. Data were collected through interviews with respondents with a purposive sampling technique. Requirements to be a respondent are people who have agricultural land and people who work in the agricultural sector. The respondent sampling locations are people who live in the middle and upper Kuranji watersheds with 60

respondents.

In technical data collection, the researcher asks questions to the respondent related to the purpose of the study and the respondent answers them. Data needed from respondents are divided into three factors. 1). Economic factors, including community income, land value, development of education centers. 2). Social factors, including population growth, land ownership, environmental knowledge, agricultural land needs. 3). Political factors, including the high cost of living and weak law enforcement.

After obtaining research data, tabulation of the data is based on economic, social and political factors to obtain a percentage value. Then, a qualitative descriptive analysis is performed.

RESULT AND DISCUSSION

Land Cover in 1985

Land cover in the Kuranji watershed in 1985 was obtained by conducting spatial analysis using a topographic map in 1985. Land cover is grouped into five types. The land cover is classified into forests with an area of 13,242.54 hectare, settlements of 1,507.54 hectare, paddy fields 4,131.67 hectare, shrubs 2,064.41 hectare and mixed gardens 1,523.39 hectare. The complete land cover of the Kuranji watershed in 1985 can be seen in Fig. 2.

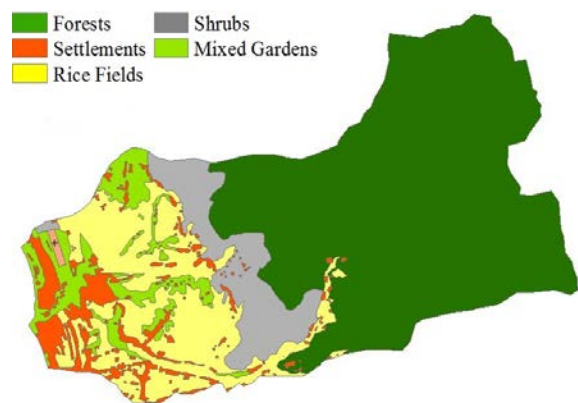


Fig. 2 Type of Land Cover 1985 in Kuranji Watershed

Land Cover in 2018

Based on the results of the interpretation of satellite imagery in 2018, land cover in the Kuranji watershed is grouped into five types. The land cover is a forest with an area of 12,114.12 hectare, settlement 4,084.62 hectare, rice fields 2,935.98 hectare, shrubs 747.61 hectare and mixed gardens 2,587.22 hectare. The land cover of the Kuranji watershed in 2018 can be seen in Fig. 3.

LCC in the Kuranji watershed that occurred in

1985 to 2018 were dominated by the reduction of forest area by 1,128.42 hectare. Forest areas turned into mixed gardens and shrubs. Paddy fields also experienced a reduction of 1,195.69 hectare. Most of the changes in rice fields were into settlements. Shrubs also experienced a reduction of 1,316.8 hectare, turning into mixed gardens, rice fields and settlements. Reducing forest areas or vegetation areas to other areas will have an impact on the environment, including erosion, flooding and reduced groundwater supplies.

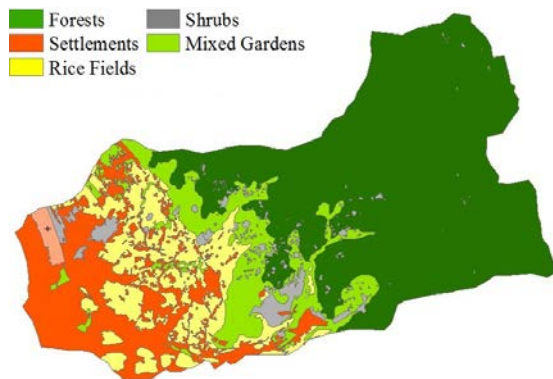


Fig. 3 Type of Land Cover 2018 in Kuranji Watershed

The impact caused by the reduction of forest area or vegetation area has also been conveyed by several experts. According to [2], the decrease in vegetation cover in the watershed area by 91% caused erosion of 7.2 to 7.7 tons / hectare / year. According to [3], an increase in forest area can increase the quality and quantity of water, while [4] added that forest areas were better able to increase water fill from ground level to aquifers compared to agricultural land.

Not only LCC, high and intensive agricultural activities in land management in the Kuranji watershed can reduce environmental quality. This was stated by [5] that intensively cultivated agricultural and horticultural land resulted in soil degradation. Based on the opinion of the experts above, it can be concluded that maintaining forest cover and vegetation cover can reduce erosion, surface runoff and flooding.

The fact that has occurred in the Kuranji watershed is that forest areas that are in protected and conservation areas have begun to decrease and settlement areas are increasing. Reduction of forest area results in low infiltration and high surface runoff resulting in flooding. [6] added that the Kuranji watershed often results in flooding due to low infiltration while [7] reported that changes in land cover from natural land use to anthropogenic have increased surface water. This has a big impact when accompanied by very high rainfall intensity. [8] stated that the reduction in vegetation had an

impact on the increase in flood inundation areas.

In addition to reducing land cover, several types of land cover in the Kuranji watershed have also increased. The increase was experienced by mixed garden land cover of 1,063.83 hectare and settlements of 2,577.08 hectare. The high change in land cover is due to the high rate of population growth. Changes in land cover in the Kuranji watershed have increased since 1985 and in 2009 after the earthquake that hit Padang City. More details on differences in LCC from 1985 - 2018 can be seen in Fig. 4.

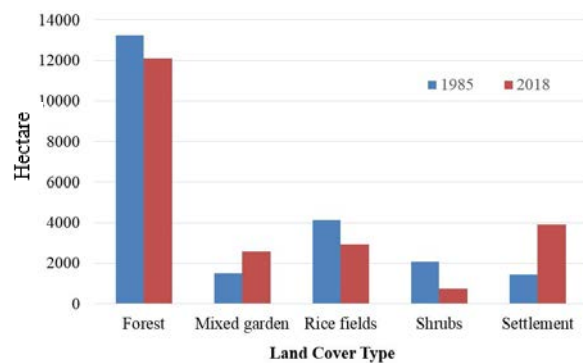


Fig. 4 LCC 1985-2018 in Kuranji Watershed

LCC to land that does or does not lack vegetation has an impact on the amount of erosion, surface runoff and flooding. [9] mentioned that changes in forest cover result in critical land and have an impact on landslides, especially on steep slopes and exceed 40%. [10] One such impact is caused by the loss of vegetation (plant roots) in protecting the soil from the danger of soil erosion. It was also added by [11] that changes in land use into built up areas would have an impact on changes in flow characteristics, flooding in the rainy season, decreasing river discharge and drought in the dry season.

The topography of the Kuranji watershed in the middle and upstream is quite steep. This area has changed forest cover through illegal logging. This type of forest land covers turns into shrubs, mixed gardens and agricultural crops. This area is a protected forest and conservation area and the protection of this area aims to maintain the quality of the watershed, such as physical land, water management and biodiversity. For more details on changes in types of forest land cover due to illegal logging in protected and conservation areas (Fig. 5).

Fig. 5 explains that land cover conversion converts forests into shrubs and agricultural crops. Protected forests have changed by 118.17 hectare (4.1%) and conservation areas by 16.74 hectare (0.18%). In other areas of use, there was a change in land cover of mixed estate gardens to become shrubs and agricultural crops by 63.1 hectare (0.6%).

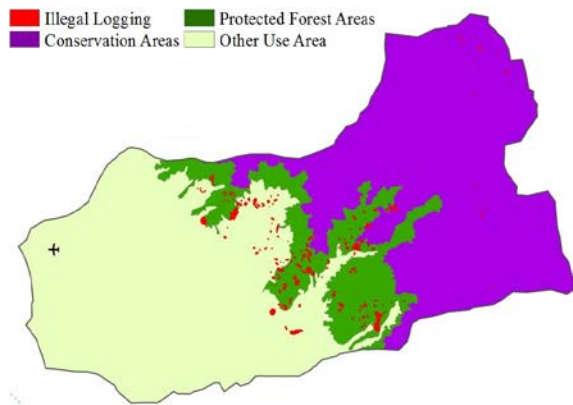


Fig. 5 Illegal Logging in Protected Forests and Conservation Areas

LCC have a major impact on soil erosion, surface runoff and flooding. This change becomes very dangerous if it occurs in steep sloped areas such as the Kuranji watershed. The steeper a slope, the faster the surface flow and the greater potential to wash away soil particles. It was also stated by [12] that the slope factor has a great influence on the high surface runoff and causes flooding.

Previous researchers also conveyed the impact caused by changes in land cover. [13] stated that changes in forest land cover to build up land and agriculture can increase flood discharge.

The Cause of LCC in the Kuranji Watershed

The condition of the Kuranji watershed area does have its own attraction in the occurrence of changes in land cover. This is because the Kuranji watershed is the largest in Padang City, where parts of the region have economic centers such as the area of higher education. The growth of economic centers will lead to the conversion of land into developed areas. On a large scale, it will disrupt the sustainability of the watershed. It was stated by [14] that the change of land cover into a residential area made the Kuranji watershed vulnerable to flooding. This is caused by damage to the physical properties of the soil and has an impact on reducing infiltration.

Based on the analysis of satellite imagery in 2018, changes in the type of land cover from forest vegetation to mixed plantations and shrubs continue to occur and threaten the sustainability of the upstream watershed. The change in land cover is in the middle Kuranji watershed and toward the upstream watershed. Generally located in protected areas and conservation areas.

The LCC explains that there is human activity in the area that must be protected and the ecosystems conserved. Thus, it is important to know what factors are driving the community to make changes in land cover. More clearly the cause of changes in land cover in the Kuranji watershed can be seen in

Fig. 6. The dominant factor causing changes in land cover in the Kuranji watershed is economic with a value of 57%. These economic factors explain that the level of income and the number of family dependents encourage the community to be even more active in meeting their daily needs. The method adopted by the community is to change the forest land cover into mixed gardens and paddy fields to settlements.

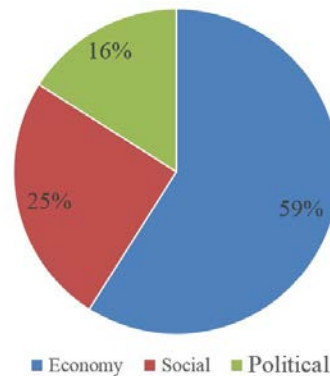


Fig. 6 Causative Factor LCC in Kuranji Watershed

The high value of land around the tertiary education area encourages people to sell land and increase land use value. So what was once planted agricultural land is converted into built land such as boarding houses, food stalls and shops. All these changes are intended for students and the local community in supporting education and other activities. The same thing was said by [15], [16], [17] that changes in land cover will be faster if an area changes from an agrarian area to an area that develops an economy in the service sector.

Previous researchers have also expressed their opinions about the factors that cause changes in land cover. As stated by [18], changes in land cover are strongly influenced by socioeconomic factors. [19] also stressed that the LCC was driven by economic development and the development of educational areas. [20] and [21] added that changes in land cover and increased built up land were influenced by economic factors, as apparent in the Kuranji watershed. This can be explained as that the Kuranji watershed's strategic location in the economic field, means it can increase the built area quickly.

The next factor affecting changes in land cover is the community social factor of 22%. The low level of income of the community as farmers who live in the middle part of the Kuranji watershed has led the community to begin to utilize the upstream watershed area. Small land tenure makes people change forest land cover in the upstream watershed with the goal is to increase the area of agricultural land and increase income.

Part of the forest cover is converted into mixed gardens with durian (*durio zibethinus*), mangosteen (*garcinia mangostana*), rambutan (*nephelium*

lappaceum), jengkol (*archidendron pauciflorum*), petai (*parkia speciosa*), cacao (*theobroma cacao*), pohon sirih (*areca catechu*), and pohon jati (*Tectona grandis*). In some places that are easily accessible, people plant serai (*cymbopogon citratus*), and lime musk (*lat. citrus amblycarpa*).

In the Kuranji watershed, the middle part of the paddy field is converted into a settlement. Shrubs become mixed settlements and gardens. Changes in land cover are also caused by the high rate of population growth in the Kuranji watershed, which ranges from 2.28% to 2.83%. In line with the opinion above, [22] added that the increase in agricultural land and population growth most determine the change in land cover. This explains that there is a high dependence on forest products in increasing community income.

The Kuranji watershed community is aware that changing forest cover can cause catastrophic floods and landslides. However, LCC are still being made with the aim that economic needs continue to be met. As long as the economic needs have not been met, the change in forest land cover will continue to occur. It was also stated by [23] that the change in land cover is strongly influenced by socioeconomic aspects.

High population growth in the Kuranji watershed also supports accelerating land cover changes. The change is related to the needs of the community for a place to live and to conduct economic activities. [24] states that an increase in population also has an impact on increasing changes in land cover.

An interesting factor of community attitudes toward changes in land cover is also influenced by Minangkabau culture. This culture explains that people who own customary land can only use it and it cannot be traded. Utilization is for agricultural land, community plantations, mixed gardens and a small portion for shelter. The strong culture of Minangkabau adopted by the community means changes in land cover are not so great. [25] explained that local culture can reduce access to forest areas. This has an impact on the reduced harvesting of forest wood, which causes changes in land cover.

Political factors also affect changes in land cover of the Kuranji watershed with a value of 15%. The high cost of living resulting from government policies drives people to try to increase income. One method is the use of forest areas for agriculture. [26] explained that government policies, population growth and socioeconomic impact had a large influence on changes in land cover. [27] also stated that national and international policies have the potential for changes in land cover in agriculture. Weak law enforcement also makes people uncontrollable in making changes to land cover.

CONCLUSIONS

LCC in the Kuranji watershed from 1985-2018 are very high. The biggest change was in residential land cover with an increase of 2,577.08 hectare (63.1%). Mixed gardens also increased by 1,063.83 hectare (41.12%). Reduction of forest land cover was by 1,128.42 hectare (8.52%), rice fields by 1,195.69 hectare (28.94%) and shrubs by 1,316.8 hectare (63.78%). LCC have occurred in protected and conservation areas. This area is a forest area that should not be disturbed. Disruption to this area is due to an increase in population and the necessities of people's lives. The factors causing LCC are influenced by economic (59%), social (25%) and political (16%) factors. Economic factors are influenced by low community income, the number of family dependents and high land values. Social factors are influenced by population growth, agricultural land needs, small land tenure and community knowledge and attitudes towards the environment. Political factors are influenced by the high cost of living and weak law enforcement. One important finding in this research is that the local wisdom of the Minangkabau culture adopted by the community can reduce land cover changes.

ACKNOWLEDGEMENTS

We want to express our sincere gratitude to the University of Andalas for the 2020 Research Grant.

REFERENCES

- [1] Badan Pusat Statistik Padang City, Padang in Numbers 2018 (Kota Padang Dalam Angka 2018). Padang: Badan Pusat Statistik Kota Padang, 2018.
- [2] L. Tadesse, K. V. Suryabhagavan, G. Sridhar, and G. Legesse, "Land use and land cover changes and Soil erosion in Yezat Watershed, North Western Ethiopia," *Int. Soil Water Conserv. Res.*, vol. 5, no. 2, pp. 85–94, 2017.
- [3] P. Ferreira, A. van Soesbergen, M. Mulligan, M. Freitas, and M. M. Vale, "Can Forests Buffer Negative Impacts Of Land-Use And Climate Changes On Water Ecosystem Services? The Case Of A Brazilian Megalopolis," *Sci. Total Environ.*, vol. 685, pp. 248–258, 2019.
- [4] Y. Ouyang, W. Jin, J. M. Grace, S. E. Obalum, W. C. Zipperer, and X. Huang, "Estimating Impact Of Forest Land On Groundwater Recharge In A Humid Subtropical Watershed Of The Lower Mississippi River Alluvial Valley," *J. Hydrol. Reg. Stud.*, vol. 26, no. September, p. 100631, 2019.
- [5] Aprisal, B. Istijono, Juniarti, and M. Harianti, "Soil Quality Index Analysis Under Horticultural

- Farming in Sumani Upper Watershed,” *Int. J. GEOMATE*, vol. 16, no. 56, pp. 191–196, 2019.
- [6] Aprisal, B. Istijono, T. Ophiyandri, and Nurhamidah, “A Study of The Quality of Soil Infiltration at The Downstream of Kuranji River, Padang City,” *Int. J. GEOMATE*, vol. 16, no. 56, pp. 16–20, 2019.
- [7] Y. Antomi, Ernawati, Triyatno, Ikhwan, and S. Fatimah, “The Dynamics of Land Use Change in Padang City for Hydrological Modeling,” *Int. J. GEOMATE*, vol. 17, no. 64, pp. 32–40, 2019.
- [8] P. T. Juwono, “The Effect Of Land Use Change to The Depth and Area Of Inundation in The Bang Sub Watershed Malang Indonesia,” *Int. J. GEOMATE*, vol. 16, no. 53, pp. 238–244, 2019.
- [9] B. Istijono, H. Abdul, and O. Taufika, “Landslide Hazard of Maninjau Area,” *Int. J. Disaster Resil. Built Environ.*, vol. 7, no. 3, pp. 302–312, Jan. 2016.
- [10] B. Istijono, A. Hakam, and T. Ophiyandri, “Investigation of The Effects of Plant Variety and Soil Sediment to The Coastal Abrasion in West Sumatra,” *Int. J. GEOMATE*, vol. 14, no. 44, pp. 52–57, 2018.
- [11] R. Permatasari, A. Sabar, D. K. Natakusumah, and H. Samaulah, “Effects Of Watershed Topography and Land Use on Baseflow Hydrology in Upstream Komering South Sumatera, Indonesia,” *Int. J. GEOMATE*, vol. 17, no. 59, pp. 28–33, 2019.
- [12] M. T. B. Dalu, C. M. Shackleton, and T. Dalu, “Influence of Land Cover, Proximity to Streams and Household Topographical Location on Flooding Impact in Informal Settlements in The Eastern Cape, South Africa,” *Int. J. Disaster Risk Reduct.*, vol. 28, pp. 481–490, Jun. 2018.
- [13] S. S. Sachro, S. Edhisono, W. Prasetyo, and V. Kurniawan, “Model Land Cover Index - Peak Discharge in Management of River Basin,” *Int. J. GEOMATE*, vol. 13, no. 40, pp. 93–100, 2017.
- [14] Aprisal, B. Istijono, T. Ophiyandri, and Nurhamidah, “The Effect of Flood to Quality Index of Soil Physical Properties at The Downstream of Kuranji River Watershed, Padang City,” *Int. J. GEOMATE*, vol. 16, no. 54, pp. 74–80, 2019.
- [15] F. O. Akinyemi and G. Mashame, “Analysis of Land Change in The Dryland Agricultural Landscapes of Eastern Botswana,” *Land Use Policy*, vol. 76, pp. 798–811, Jul. 2018.
- [16] P. Esposito, F. Patriarca, and L. Salvati, “Tertiarization and Land Use Change: The Case of Italy,” *Econ. Model.*, vol. 71, pp. 80–86, Apr. 2018.
- [17] J. Wang, T. He, and Y. Lin, “Changes in Ecological, Agricultural, and Urban Land Space in 1984–2012 in China: Land Policies and Regional Social-Economical Drivers,” *Habitat Int.*, vol. 71, pp. 1–13, Jan. 2018.
- [18] F. Xystrakis, T. Psarras, and N. Koutsias, “A Process-Based Land Use/Land Cover Change Assessment on A Mountainous Area of Greece During 1945–2009: Signs of Socio-Economic Drivers,” *Sci. Total Environ.*, vol. 587–588, pp. 360–370, 2017.
- [19] T. Van Ninh and C. Waisurasingha, “Land Use/Cover Change And Landscape Fragmentation Analyses In Khon Kaen City, Northeastern Thailand,” *Int. J. GEOMATE*, vol. 15, no. 47, pp. 201–208, 2018.
- [20] A. N. Dang and A. Kawasaki, “Integrating Biophysical And Socio-Economic Factors For Land-Use and Land-Cover Change Projection in Agricultural Economic Regions,” *Ecol. Modell.*, vol. 344, pp. 29–37, 2017.
- [21] D. Gounaridis, I. Chorianopoulos, E. Symeonakis, and S. Koukoulas, “A Random Forest-Cellular Automata Modelling Approach to Explore Future Land Use/Cover Change in Attica (Greece), Under Different Socio-Economic Realities And Scales,” *Sci. Total Environ.*, vol. 646, pp. 320–335, 2019.
- [22] F. Handavu, P. W. C. Chirwa, and S. Syampungani, “Socio-Economic Factors Influencing Land-Use and Land-Cover Changes in The Miombo Woodlands of The Copperbelt Province in Zambia,” *For. Policy Econ.*, vol. 100, no. October 2018, pp. 75–94, 2019.
- [23] T. Belay and D. A. Mengistu, “Land Use And Land Cover Dynamics and Drivers in The Muga Watershed, Upper Blue Nile Basin, Ethiopia,” *Remote Sens. Appl. Soc. Environ.*, vol. 15, no. July, p. 100249, 2019.
- [24] M. Acheampong, Q. Yu, L. D. Enomah, J. Anchang, and M. Edful, “Land Use/Cover Change in Ghana’s Oil City: Assessing The Impact of Neoliberal Economic Policies and Implications For Sustainable Fevelopment Goal Number One – A Remote Sensing And GIS Approach,” *Land use policy*, vol. 73, no. February, pp. 373–384, 2018.
- [25] Y. Dou, L. Zhen, X. Yu, M. Bakker, G. J. Carsjens, and Z. Xue, “Assessing The Influences of Ecological Restoration on Perceptions of Cultural Ecosystem Services By Residents of Agricultural Landscapes of Western China,” *Sci. Total Environ.*, vol. 646, pp. 685–695, 2019.
- [26] J. Bao, S. Gao, and J. Ge, “Dynamic Land Use and Its Policy in Response to Environmental and Social-economic Changes in China: A Case Study of The Jiangsu Coast (1750–2015),” *Land Use Policy*, vol. 82, no. December 2018, pp. 169–180, 2019.
- [27] M. Bonilla-Moheno and T. M. Aide, “Beyond Deforestation: Land Cover Transitions in Mexico,” *Agric. Syst.*, vol. 178, no. May 2019, p. 102734, 2020.

CONVERSION OF WASTE STONE-FINE SLURRY INTO GEOPOLYMER CEMENT WITH ADDITION OF COAL FLY ASH

Takaaki Wajima¹ and Say Buntan¹

¹Department of Urban Environment Systems, Chiba University, Japan

ABSTRACT

In the crushed stone production process, waste stone-fine slurry is generated as wastewater, and most of them are landfilled as dehydrated cake after some treatments. Recently, it is becoming difficult to secure landfill sites, and effective utilization of by-products, dehydrated cake, is desired. On the other hand, a large amount of coal fly ash was discharged from coal fired power plant, due to the operation suspension of nuclear power plants since the Fukushima nuclear accident occurs. In this study, we attempted to prepare geopolymer cement from waste stone-fine slurry with addition of coal fly ash. Waste stone-fine slurry used in this study was discharged from one of the quarries in Japan. NaOH solution was added into the slurry, and heated at 60 - 180 °C for 0 - 24 h to obtain the high Si solution for preparation of geopolymer cement. After heating, the slurry was cooled to room temperature by quenching with tap water, and various amounts of coal fly ash were added, mixed and cured at 80 °C for 24 h. The strength and water purification ability of the product were examined. The solution with high Si content to prepare the geopolymer can be obtained at 120 °C for 9 h in 4 - 8 M NaOH solution, and the products obtained from 6 - 8 M NaOH slurry solution with addition of 0.55 - 0.70 weight ratio of coal fly ash have higher strength than other products and Portland cement. The product indicates NH_4^+ removal ability for wastewater treatment.

Keywords: Waste stone-fine slurry, Coal fly ash, Geopolymer, NH_4^+ removal, Alkali reaction

INTRODUCTION

In the crushed stone production process, waste stone-fine slurry is generated as wastewater in large quantities from crushing, cutting, polishing and cleaning processes, and most of them are landfilled as dehydrated cake after some treatments, such as coagulation, sedimentation and filter press. Currently, it is becoming difficult to secure landfill sites due to the decrease of the landfill space, and the amount of dehydrated cake tends to increase. Therefore, further development of effective utilization of by-products, such as dehydrated cakes, is desired by laws in Japan, and there are some researches to reuse the dehydrated cake for improved soil, roadbed, greening, porous sintered compact, space filling and so on [1].

Coal as an energy source has an advantage in terms of abundant deposits, compared with the other energy sources. In 2012, the percentage of electric power generation in coal power plants in Japan occupies about 23.4 % to all amount of electric power [2]. By an increase in coal demand, the discharge amount of coal ash is estimated to be increased. According to the law relating recycling in Japan, the coal ash derived from thermal power plant is especially designated as specified by-product, and the effective usage of this coal ash is strongly required. Recently, the reuse and recycle of coal ash are tried to proceed aggressively, and the percentage and amount of effective usage in 2014 reach about 98 % and 9.4 million ton/year, respectively. However,

more than 0.2 million ton/year of coal ash must be deposited in landfill. Furthermore, since the Great East Japan Earthquake on March 11, 2011, the focus of energy production in Japan has shifted from nuclear power toward coal-generated power. The fly ash generated at coal-fired power plants was mostly wasted before the earthquake, more fly ash is expected to be generated, and the lack of landfill space is anticipated in Japan. New recycle technologies for consumption of a large amount of coal ash are desired to develop [3-6].

Geopolymer is three dimensional aluminosilicate based construction and building material, which is sustainable and environmental friendly due to low emission of carbon during their production and processing. Geopolymer cement is generally produced by mixing alkali activator (sodium silicate, sodium hydroxide, water) and various aluminosilicate precursors such as fly ash and bottom ash [7-12], clays [13-15], metakaolin [16,17], natural soil [18], glass [19], slags [20, 21], volcanic ashes and rice husk ash [22-26]. Ordinary Portland cement is mainly solidified by the formation of needle-like calcium silicate hydrate (C-S-H), while geopolymer cement is mainly solidified by the polymerization of silicate ions sparked by metal ions, such as Al^{3+} , Fe^{3+} and so on, which is similar to the reaction of zeolite synthesis [27,28], and geopolymer cement has high acid resistance, high fire resistance and ion exchange ability [29-34]. Therefore, geopolymer cement has attracted attention, and are associated with numerous

international patents as well as a number of commercial engineering project.

In our previous studies, zeolite can be synthesized from green tuff stone cake by NaOH reaction, with extracting high content of Si from the cake [35]. Furthermore, geopolymer cement can be prepared by mixing alkali fused stone dust, water and coal fly ash due to the reaction between soluble contents of Si and Al from the fused cake and coal fly ash [36]. There is the possibility to produce geopolymer cement from coal fly ash and the slurry by converting the slurry into alkali activator using alkali reaction.

In this study, we attempted to prepare geopolymer cement from the waste fine-stone slurry and coal fly ash. The alkali activator, sodium silicate solution, was prepared from the slurry by treating with NaOH, and the prepared activator was mixed with coal fly ash to form geopolymer cement. The conditions, such as NaOH concentration, heating temperature, heating time, and mixing ratio of coal fly ash, to prepare the geopolymer product with the hard structure were investigated and the water purification ability of the obtained geopolymer cement was evaluated.

EXPERIMENT

Sample

Waste fine-stone slurry generated from one of the domestic crushed stone companies in Japan was used for the experiment. Concentration of fine-stone in slurry is 928 g/L, and the diameter of fine stone is under 250 μm . Coal fly ash used in this study was commercially available fly ash type V. The chemical compositions and mineralogical compositions of the fine-stone in the slurry and coal fly ash are shown in Table 1 and Figure 1, respectively. The fine slurry mainly composed of SiO_2 (61.7 %), Al_2O_3 (19.6 %) and some minor elements in the form of quartz (SiO_2), calcite (CaCO_3), talc ($\text{Mg}_3\text{Si}_4\text{O}_{10}(\text{OH})_2$), albite ($\text{NaAlSi}_3\text{O}_8$), anorthite ($\text{CaAl}_2\text{Si}_2\text{O}_8$), muscovite ($\text{KAl}_3\text{Si}_3\text{O}_{10}(\text{OH})_2$), clinocllore ($(\text{Mg, Fe, Al})_6(\text{Si, Al})_4\text{O}_{10}(\text{OH})_8$) and so on. Coal fly ash also mainly composed of SiO_2 (55.0 %), Al_2O_3 (20.8 %) and some minor elements in the form of quartz (SiO_2) and mullite ($\text{Si}_2\text{Al}_6\text{O}_{13}$) with amorphous phases indicating the broad hump of 20 - 30 $^\circ$.

Table 1 Chemical compositions of fine stone in slurry and coal fly ash.

Contents (%)	Fine stone in slurry	Coal fly ash
SiO_2	61.7	55.0
Al_2O_3	19.6	20.8
CaO	2.1	5.1
MgO	1.4	0.2
Fe_2O_3	4.8	10.7

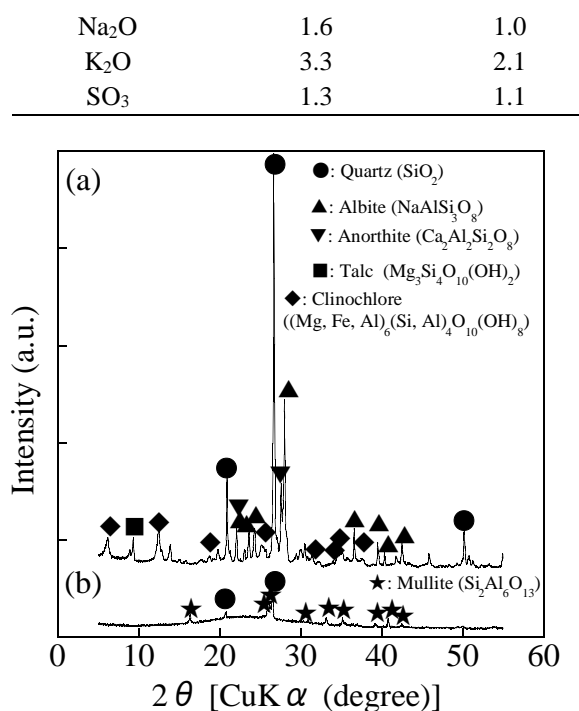


Fig. 1 XRD patterns of (a) fine stone in slurry and (b) coal fly ash.

Preparation

Silica solution

Sodium silicate solution for making geopolymer cement was prepared from the slurry with addition of NaOH. NaOH solution (5 mL) was added into the slurry (10 mL) to prepare 15 mL of the slurry with 2 - 8 M NaOH concentration in a 50 mL of pressure vessel, and heated at 60 - 180 $^\circ\text{C}$ for 0 - 24 h in electric furnace. It is noted that rising time to setting temperature is 30 min. After heating, the vessel was quenched with tap water, the solution was filtered, and the concentration of Si in the filtrate was measured using atomic absorption spectrometer (AAnalyst 200, Perkin Elmer).

Geopolymer cement

Geopolymer cement was prepared from the slurry treated with NaOH on various condition. Coal fly ash was mixed with the slurry obtained on various condition at the mixing weight ratio of ash / slurry = 0.25 - 0.75, poured into a mold ($\phi 25 \text{ mm} \times 5 \text{ mm}$), and set in an oven at 80 $^\circ\text{C}$ for 24 h. After heating, the hardness of the product was judged with a bamboo needle to insert into the product. The hardened products were subjected to strength tests using a strength tester (ZT series ZTA-500N, IMADA). The sharp point attachment (S-3) was inserted into the sample at a speed of 30 mm/min to measure the strength when the sample broke. Strength tests for the

ordinary Portland cement were carried out to compare strength. Portland cement was prepared at water-cement ratio (W/C) = 50 %, formed in a mold and cured at room temperature for 7 days.

NH₄⁺ Removal Test

The water purification ability of the product was estimated for NH₄⁺ removal test. The NH₄⁺ solution with 900 mg/L, which simulated piggery wastewater, was prepared using NH₄Cl (Wako). The product block was prepared with a mold of $\phi 25 \text{ mm} \times 5 \text{ mm}$ to remove the mold, and added into 200 mL of NH₄⁺ solution for 168 h. During the immersion of the product block, the concentration of NH₄⁺ in the solution was analyzed using thymol blue method for monitoring the NH₄⁺ removal.

RESULTS AND DISCUSSION

Silicate Solution from The Slurry

Fig.2 shows the Si concentration of the slurry treated with 2 - 8 M NaOH concentration at 60 - 180 °C for 24 h. It is noted that Si concentration for preparing geopolymer cement is set to 20 - 60 g/L [37]. With increasing the NaOH concentration and temperature, Si concentration in the obtained slurry increases. About 60 g/L of Si contains in the slurry treated with 6 - 8 M NaOH at 140 °C and 180 °C, while lower than 20 g/L of Si contains in the slurry treated at 60 °C and 100 °C regardless of NaOH concentration. In the case of 120 °C, with increasing the NaOH concentration, Si content increases from 22 g/L to 49 g/L, which are desired contents for preparing geopolymer cement [37]. Therefore, the temperature of slurry treatment is set to 120 °C in this study.

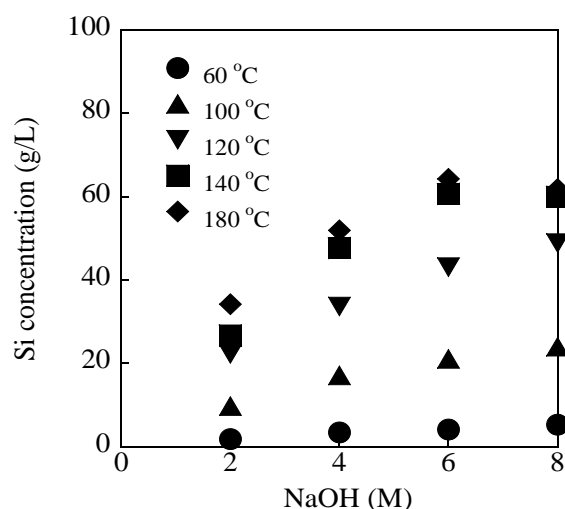


Fig. 2 Concentration of Si in the slurry treated with

2 - 8 M NaOH concentration at 60 - 180 °C for 24 h.

Figure 3 shows the Si concentration of the slurry treated with 2 - 8 M NaOH concentration at 120 °C for 0 - 18 h. With increasing the NaOH concentration and reaction time, Si concentration in the slurry increases, and the slurry treated with 4 - 8 M NaOH for 9 h contains 20 - 35 g/L of Si within 20 - 60 g/L of Si for preparing geopolymer cement [37].

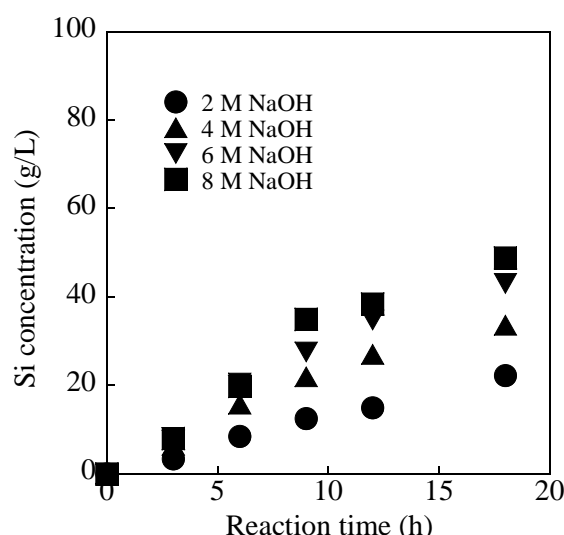


Fig. 3 Concentration of Si in the slurry treated with 2 - 8 M NaOH concentration at 120 °C for 0 - 18 h

Therefore, silicate solution for preparing geopolymer cement can be prepared from the slurry treated with 4 - 8 M NaOH at 120 °C for 9 h.

Geopolymer Formation

We attempted to form geopolymer product from the slurry treated with 4 - 8 M NaOH at 120 °C for 9 h. Figure 4 shows the condition for preparing hardened product with addition of coal fly ash to the slurry with various NaOH concentration. The horizontal axis indicates NaOH concentration in the slurry, the vertical axis indicates the mixing ratio of coal fly ash, and the plots indicate the condition to obtain the hardened product without sticking a bamboo needle into the product. The hardened product can be obtained when the mixing ratio of coal fly ash are 0.55 and 0.70 regardless of NaOH concentration, and from the slurry with 4 M NaOH concentration regardless of mixing ratio.

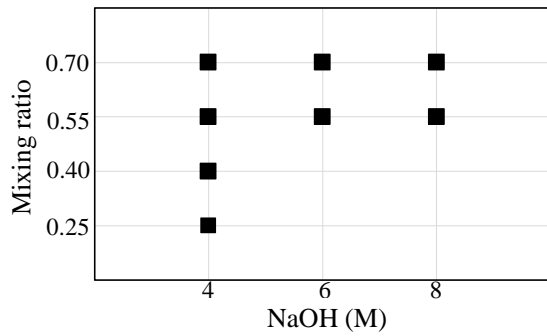


Fig. 4 Conditions for preparing hardened product with addition of coal fly ash to the slurry with various NaOH concentration.

Figure 5 shows the strength of the product from the slurry with 4 - 8 M NaOH concentration at various mixing ratio of coal fly ash. It is noted that the strength of Portland cement sample is 167 N using this measurement. The strengths of the product are higher than that of Portland cement and those of the product from the slurry with 6 - 8 M NaOH indicates 345 - 450 N when the mixing ratios are 0.55 and 0.70, while those are low (5 - 25 N) when the ratio are 0.25 and 0.40.

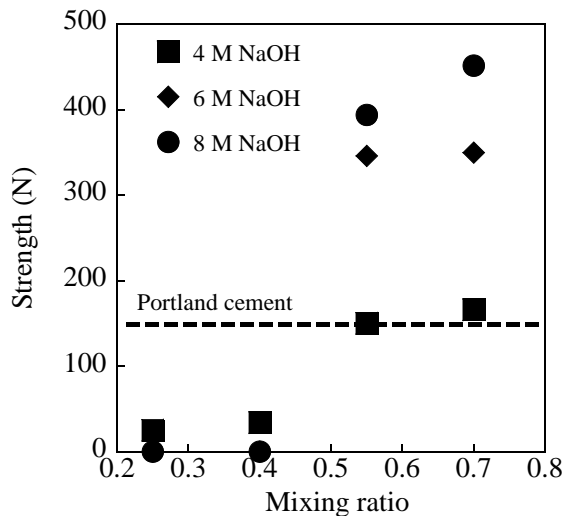


Fig. 5 The strength of the product from the slurry with 4 - 8 M NaOH concentration at various mixing ratio of coal fly ash

From these results, the geopolymer product with sufficient strength can be prepared from the mixture of the slurry treated with 4 - 8 M NaOH at 120 °C for 9 h and coal fly ash at the mixing weight ratio of coal fly ash to the slurry = 0.55 - 0.70.

Water Purification

Three product blocks were used for this removal test. Product-1 was prepared from the slurry with 6 M NaOH at the weight ratio of coal fly ash = 0.70, Product-2 from the slurry with 8 M NaOH at the weight ratio of ash = 0.70, and Product-3 from the slurry with 8 M NaOH at the ratio of ash = 0.55. Figure 6 shows the XRD patterns of the product. All products indicate almost same XRD patterns including quartz, mullite, albite and hydroxysodalite ($\text{Na}_6\text{Al}_6\text{Si}_6\text{O}_{24} \cdot 8\text{H}_2\text{O}$). Hydroxysodalite is formed by alkali treatment of the slurry, while quartz, mullite and albite are originated from fine-stone and coal fly ash.

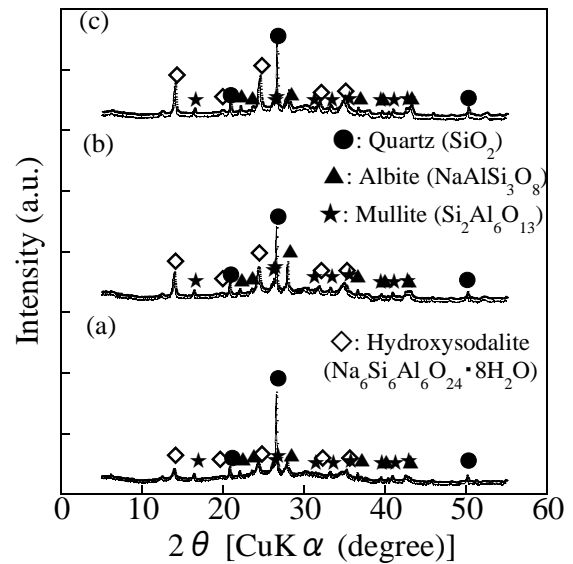


Fig. 6 XRD patterns of the products: (a) Product-1, (b) Product-2, (c) Product-3.

The water purification ability of the obtained geopolymer product was examined using NH_4^+ solution. Figure 7 shows the NH_4^+ concentration in the solution after immersion of the product block. All products indicate the NH_4^+ removal ability. In comparison with NH_4^+ removal of product when the mixing ratios of coal fly ash are same, Product-2 obtained from the slurry with 8 M NaOH indicates higher NH_4^+ removal than Product-1 from the slurry with 6 M NaOH. In comparison with NH_4^+ removal of the product from the slurry with the same concentration of NaOH, Product-3 obtained at the mixing ratio of 0.55 indicates higher NH_4^+ removal than Product-2 at the mixing ratio of 0.70. Product-3 can decrease NH_4^+ concentration from 900 mg/L to 540 mg/L for 7 days.

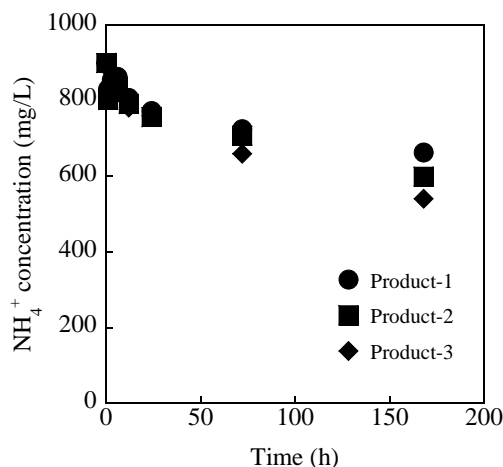


Fig. 7 NH_4^+ concentration in the solution after immersion of the product block.

CONCLUSIONS

We attempted to prepare geopolymer cement from the waste fine slurry and coal fly ash via alkali reaction. The silica solution for preparing geopolymer cement can be prepared from the slurry by treating with 4 - 8M NaOH at 120 °C for 9 h, and the hardened geopolymer product can be formed by mixing with coal fly ash (the mixing weight ratio = 0.55 - 0.70). The product obtained from the slurry treated with 6 - 8 M NaOH by mixing with coal fly ash (the mixing ratio = 0.55 - 0.70) indicates higher strength than ordinary Portland cement, and has the NH_4^+ removal ability. These results suggested that waste slurry can be converted into geopolymer cement with sufficient strength and water purification ability by alkali reaction and mixing with coal fly ash.

REFERENCES

- [1] Japan Institute of Aggregate Technology (JIAT), Aggregate Technology Handbook, JIAT, Tokyo, 2020.
- [2] Japan Fly Ash Association (JFAA), Coal Ash Handbook, 6th ed. JFAA, Tokyo, 2015.
- [3] Nhan C.T., Graydon J.W., and Kirk D.W., Utilizing Coal Fly Ash as a Landfill Barrier Mater. Waste Manage., Vol. 16, 1996, pp.587-595.
- [4] Chandra N., Sharma P., Pashkov G.L., Voskresenskaya E.N., Amritphale S.S., and Baghel N. S., Coal Fly Ash Utilization: Low Temperature Sintering of Wall Tiles, Waste Manage., Vol. 28, 2008, pp.1993-2002.
- [5] Ahmaruzzaman M., A Review on the Utilization of Fly Ash, Prog. Energy Combust. Sci., Vol. 36, 2010, pp.327-363.
- [6] Zacco A., Borgese L., Gianoncelli A., Struis R. W. J., Depero L. and Bontempi E., Review of Fly Ash Inertisation Treatments and Recycling, Environ. Chem. Lett., Vol. 12, 2014, pp.153-175.
- [7] Temuujin J., Riessen A., and MacKenzie K. J. D., Preparation and characterisation of fly ash based geopolymer mortars, Constr. Build. Mater., Vol. 24, 2010, pp.1906-1910.
- [8] Xu H., Li Q., Shen L., Wang W., and Zhai J., Synthesis of thermostable geopolymer from circulating fluidized bed combustion (CFBC) bottom ashes, J. Hazard. Mater., Vol. 175, 2010, pp. 198-204.
- [9] Khan M. Z. N., Ahmed Shaikh F., Hao Y., and Hao H., Synthesis of high strength ambient cured geopolymer composite by using low calcium fly ash, Constr. Build. Mater., Vol. 125, 2016, pp.809-820.
- [10] Freidin C., Cementless pressed blocks from waste products of coal-firing power station, Constr. Build. Mater., Vol. 21, 2007, pp.12-18.
- [11] Shehab H.K., Eisa A.S., and Wahba A.M., Mechanical properties of fly ash based geopolymer concrete with full and partial cement replacement, Constr. Build. Mater., Vol. 126, 2016, pp.560-565.
- [12] Haq E., Padmanabhan S.K., Licciulli A., Synthesis and characteristics of fly ash and bottom ash based geopolymers—a comparative study, Ceram. Int., Vol. 40, 2014, pp.2965-2971.
- [13] Longhi M.A., Rodríguez E.D., Bernal S.A., Provis J.L., and Kirchheim A.P., Valorisation of a kaolin mining waste for the production of geopolymers, J. Cleaner Prod., Vol. 115, 2016, pp.265-272.
- [14] Dikko B.B.K., Elimbi A., Cyr M., Manga J.D., and Kouamo H. T., Effect of the rate of calcination of kaolin on the properties of metakaolin-based geopolymers, J. Asian Ceram. Soc., Vol. 3, 2015, pp.130-138.
- [15] Burciaga-Diaz O., Escalante-Garcia J.I., and Gorokhovskiy A., Geopolymers based on a coarse low-purity kaolin mineral: mechanical strength as a function of the chemical composition and temperature, Cem. Concr. Compos., Vol. 34, 2012, pp.18-24.
- [16] Yuan J., He P., Jia D., Yang C., Zhang Y., Yan S., Yang Z., Duan X., Wang S., and Zhou Y., Effect of curing temperature and $\text{SiO}_2/\text{K}_2\text{O}$ molar ratio on the performance of metakaolin-based geopolymers, Ceram. Int., Vol. 42, 2016, pp.16184-16190.
- [17] He P., Wang M., Fu S., Jia D., Yan S., Yuan J.,

- Xu J., Wang P., and Zhou Y., Effects of Si/Al ratio on the structure and properties of metakaolin based geopolymer, *Ceram. Int.*, Vol. 42, 2016, pp.14416-14422.
- [18] Zaidi S.F.A., Haq E.U., Nur K., Ejaz N., Anisur-Rehman M., Zubair M., and Naveed M., Synthesis & characterization of natural soil based inorganic polymer foam for thermal insulations, *Constr. Build. Mater.*, Vol. 157, 2017, pp.994-1000.
- [19] Hajimohammadi A., Ngo T., and Kashani A., Sustainable one-part geopolymer foams with glass fines versus sand as aggregates, *Constr. Build. Mater.*, Vol. 171, 2018, pp.223-231.
- [20] Luukkonen T., Abdollahnejad Z., Yliniemi J., Kinnunen P., and Illikainen M., One-part alkali-activated materials: a review, *Cem. Concr. Res.*, Vol. 103, 2018, pp.21-34.
- [21] Hajimohammadi A., Ngo T., Mendis P., Kashani A., and Deventer J.S.J., Alkali activated slag foams: the effect of the alkali reaction on foam characteristics, *J. Cleaner Prod.*, Vol. 147, 2017, pp.330-339.
- [22] Kastiukas G., Zhou X., and Castro-Gomes J., Development and optimisation of phase change material-impregnated lightweight aggregates for geopolymer composites made from aluminosilicate rich mud and milled glass powder, *Constr. Build. Mater.*, Vol. 110, 2016, pp.201-210.
- [23] Huseien G.F., Mirza J., Ismail M., and Hussin M. W., Influence of different curing temperatures and alkali activators on properties of GBFS geopolymer mortars containing fly ash and palm-oil fuel ash, *Constr. Build. Mater.*, Vol. 125, 2016, pp.1229-1240.
- [24] Sore S.O., Messan A., Prud'homme E., Escadeillas G., and Tsobnang F., Synthesis and characterization of geopolymer binders based on local materials from Burkina Faso – Metakaolin and rice husk ash, *Constr. Build. Mater.*, Vol. 124, 2016, pp.301-311.
- [25] Gado R., Recycling and utilization assessment of waste fired clay bricks (Grog) with granulated blast-furnace slag for geopolymer production, *Process Saf. Environ. Prot.*, Vol. 103, 2016, pp.237-251.
- [26] El-Naggar M.R., and El-Dessouky M.I., Re-use of waste glass in improving properties of metakaolin-based geopolymers: mechanical and microstructure examinations, *Constr. Build. Mater.*, Vol. 132, 2017, pp.543-555.
- [27] Melkon T., Gunther M., and Stefan K.H., Relation of water adsorption capacities of zeolites with their structural properties, *Microporous Mesoporous Mater.*, Vol. 264, 2018, pp.70-75.
- [28] Habbib G., Oliver S., Yan M., and Philippe K., *The Reconstruction of Natural Zeolites*, Springer, pp.1-5.
- [29] Liew Y.M., Heah C.Y., Long-yuan L., Nur A.J., Mohd M.A.B.A., Tan S. J., and Kamarudin H., Characteristics of geopolymer and case examples of construction, *Construct. Build. Mater.*, Vol. 156, 2017, pp.9-18.
- [30] Singh N.B., Foamed geopolymer concrete, *Mater. Today, Proceedings 5*, 2018, pp.15243-15252.
- [31] Part W.K., Mahyuddin R., Cheah C.B., An overview on the influence of various factors on the properties of geopolymer concrete derived from industrial by-products, *Constr. Build. Mater.*, Vol. 77, 2015, pp.370-395.
- [32] Peng M.X., Wang Z.H., Shen S.H., Xiao Q.G., Li L.J., Tang Y.C., Hu L.L., Alkali fusion of bentonite to synthesize one-part geopolymeric cements cured at elevated temperature by comparison with two-part ones, *Constr. Build. Mater.*, Vol. 130, 2017, pp.103-112.
- [33] Piotr R., Magdalena K., and Włodzimierz M., Spectroscopic studies of fly ash-based geopolymers, *Spectrochimica Acta Part A: Molecular and Biomolecular Spectroscopy*, Vol. 198, 2018, pp.283-289.
- [34] Ankur M., and Rafat S., Sulfuric acid resistance of fly ash based geopolymer concrete, *Constr. Build. Mater.*, Vol. 146, 2017, pp.136-143.
- [35] Wajima T., Synthesis of zeolitic material from green tuff stone cake and its adsorption properties of silver (I) from aqueous solution, *Microporous Mesoporous Mater.*, Vol. 233, 2016, pp.154-162.
- [36] Sakamoto K., and Wajima T., Preparation of geopolymer cement from crushed stone by-product using alkali fusion, *Int. J. GEOMATE*, 2019, pp.17-22.
- [37] Agrawal U.S., Wanjari S.P., and Naresh D.N., Impact of replacement of natural river sand with geopolymer fly ash sand on hardened properties of concrete, *Constr. Build. Mater.*, Vol. 209, 2019, pp.499-507.

SALINITY PREDICTION USING DYNAMIC PARAMETER OF THAILAND'S BANG KRACHAO

Uma Seeboonruang¹, Pinit Tanachaichoksirikun¹ and Uba Sirikaew¹

¹Department of Civil Engineering, Faculty of Engineering, King Mongkut's Institute of Technology
Ladkrabang, Thailand

ABSTRACT

Insufficient fresh water is one of the many factors for domestic, agriculture, and environment problems. These problems are affected by seawater intrusion, increasing trend over the time. In the global scale, seawater intrusion, the uncertainty of climate, and water tide are the major problem of surface and ground water, especially, zone of delta. The natural factor is not the only factor, the human activity is also, for example, processing of hydraulic structure, land use and forcing of water for living, making salinity distribution. Then, monitoring of water quality provided and alert this information. Moreover, prediction of salinity can protect and conserve water quality. Here, A multiple regression with dynamic parameter was applied to predict salinity of water in the delta of Thailand. The calibration and verification provided a root mean square error (RMSE) < 5% (calibration) and < 7% (verification) with the high correlation coefficient (R^2). This showed a good model for salinity prediction. The results revealed a good prediction of salinity in one hour that enough for saline water prevention. So, the area could be improved salinity of water to protect water problem.

Keywords: Regression analysis, Climate Variable, Salinity Sensor, Salt Water, Seawater Intrusion

INTRODUCTION

Fresh water is one of the important factors for agriculture. Current shortage of fresh water in the Chao Phraya Basin is a problem that become much more intense as the seawater has intruded because of climate change [1]. According to the study of the Pak Phanang River in April 1994, the intrusion of seawater had an impact of 100 kilometers radius [2]. For the Tha Chin River, there was an encroachment of seawater into the main rivers and canals [3]. During the dry season, surface water level decreases, therefore, allowing the sea to rise and enter the basin.

Not only the natural factors mentioned cause the seawater encroachment problems, humans are also another factor in causing the problems. For example, opening and closing the floodgates, farming, forcing water for use, irrigation buildings, flood prevention, and changes in land use for shrimp farming or salt farming can cause salinity distribution problems [1]. The excessive use of fresh water for agriculture and the growing drainage of seawater into freshwater streams for shrimp farming also cause the fresh water, presenting in the soil and the soil surface cannot push the salinity out. [4].

Bang Krachao area is a large green area in the center of Bangkok (Latitude 13°N and Longitude 100°E) and is known as the green lung of Bangkok. [6]. This area has absorbed an average of 6,000 tons of carbon dioxide per year and has produced up to 6 million tons of oxygen per day [7]. This area is a protect area, controlled building by the Ministerial Regulations [8].

Surrounding water of Bang Krachao consists of seawater, fresh water, and brackish water [7]. Because this area is suitable for agriculture. Many fruits were cultivated in the area, such as Nam Dok Mai mango and Sapodilla, which can tolerate very little salinity (0.12 g/l) [9].

Bang Krachao has a floodgate, the Khlong Lat Pho floodgate, controlling the flow of water and preventing salinity intrusion into the area. However, the openings and closings of the floodgates have not a systematic management due to the fact that one cannot predict the level of salinity that will occur in the future. Sometimes during the dry season, the floodgate remains closed, causing water inside the Bang Krachao becoming sewage and having a higher concentrated salt in the water. When this water is transpired, it direct impact on the island's ecosystems and agricultural crops.

A prediction of the salinity is executed by using the MIKE11 simulation model, such as the salinity intrusion analysis in Tha Chin River [10], the real-time prediction of salinity research in the Mekong River Delta [11]. These were commonly used to predict the salinity in large rivers. However, MIKE11 simulation model still requires many variables such as river's cross section, river's slope, slope of friction, and distribution coefficient. Currently, there is no through survey throughout the river around Bang Krachao Island. Therefore, this study investigated the past and above information and focused on the salinity data in Bang Krachao area, in order to predict the salinity that will occur in the future and planning

water management and systematic openings and closings of the floodgates in Bang Krachao.

Predicting the salinity in advance in the Chao Phraya River can have a difference, as water can be managed and prevented saline water from entering Bang Krachao. If the salinity was a low level, the water gate will be opened to allow the water from the Chao Phraya River flow into the agricultural area. On the other hand, if the water in the Chao Phraya River was a high salinity value, floodgate will be closed to prevent salinity in the Chao Phraya River flowing into agricultural areas. The variables used in this research are hourly salinity values in the past. The Multiple Linear Regression method was analyzed because the analysis results in a short period of time can suggest opening or closing the floodgates. In addition, the hourly salinity values in each station for salinity quality measurement were heavily watered between each other with the current time from 0-6 hours of every station with SPSS program to find the most suitable variable and coefficient value in the amount of 1 hour in advance salinity prediction. In this amount of time, it should be enough for the openings and closings of the floodgates to have a lesser impact on agricultural crops.

STUDY AREA

Bang Krachao area was selected for this study due to 3 factors: i) Bang Krachao area is the largest green area of Bangkok ii) Bang Krachao area is the downstream area of the Chao Phraya River with an area connected to the Gulf of Thailand and iii) Bang Krachao area is an ecological diversity area, since it is a connection area between fresh water, brackish water, and saline water. Bang Krachao area is, therefore, a suitable place for the study of salinity forecasting to take place, ecologically, engineeringly, and economically.

General and Topography

Fig. 1 shows the location of Bang Krachao area. Bang Krachao locates in Phra Pradaeng, Samut Prakan (the south of Bangkok). It is an island with the Chao Phraya River, with 15 kilometers, covering an area of 18.9 square kilometers. The shape of the Chao Phraya River that flows through the Bang Ka Chao area resembles a stomach. An isthmus from upstream to downstream about 580 meters in Bang Krachao bend, covering an area of 6 sub-districts, namely, Bang Nam Phueng, Bang Yo, Bang Korbuac, Bang Kasob, Bang Krachao, and Song Khanong. There are boundaries adjacent to Bangkok in 3 directions, with the Chao Phraya River in the way, separating Bang Krachao and Bangkok. The south is connected to the Gulf of Thailand, which is the sea area of Thailand, causing the Bang Krachao area to be constantly influenced by encroachment of sea water [12].

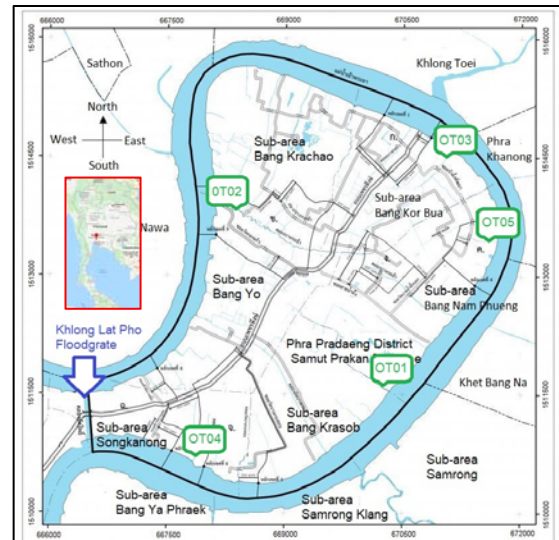


Fig. 1 Location and Monitoring of Bang Krachao

Geology

The Bang Krachao area is a floodplain basin, making a large wetland, caused by the accumulation of sediment in the river mouth. There is a unique ecosystem called “Three Water” which consists of fresh water, saline water, and brackish water. The rich fertility of the area is caused by the accumulation of river sediment, resulting in agricultural products with distinctive flavors, such as Nam Dok Mai mango and Nam Hom coconut. Terrain and ecology at the arch of the Chao Phraya River in Bang Krachao area helps slow down saline water and sedimentation from various soil conditions that are caused by sediment deposition at the delta of the Chao Phraya River, causing the area of Bang Krachao to have soil fertility, making it a place for resting water, and preventing flood from happening in the vicinity of Bangkok with an average ground level of 0.50-0.60 m above mean sea level. The soil in Bang Krachao consists of clay from sedimentation. Its salinity was changed according to the influence of the sea. The delta is influenced by brackish water during the high tide of the sea and the tide is a distribution from the mangrove forest. As for the low plains along the waterfront or the areas in which water is soaked during the rainy season and dried during the dry season, they originally were a freshwater swamp forest. Now it is changed, becoming a garden that has been dug to help drain water. As for the high upland in the middle of the bend was once covered by lowland forest which is now transformed into a garden and residential areas.

Water Level

The water level in Bang Krachao area from the survey showed that the average water level is at the mean sea level. The highest water level is +1.50 m.

(mean sea level) and the lowest water level is -2.00 m. (mean sea level) (Fig. 2). The station with the highest change in water level is OT01 which is the station that is the arch of Chao Phraya river that water has low velocity and most influenced by fluctuations in sea level.

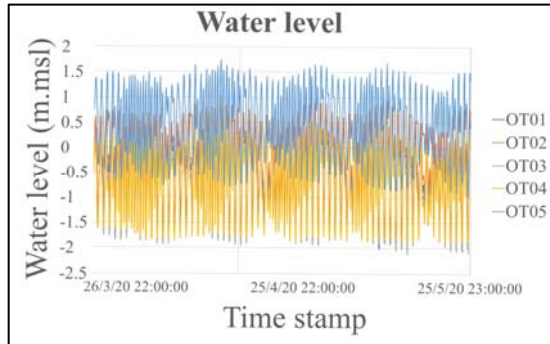


Fig. 2 Water Level of Bang Krachao

Salinity

In the survey data of this research, monitors were installed to measure the water level and salinity, as shown in Fig. 4, which consist of two main parts: the automatic long distance surface water quality measurement system and the automatic surface water quality database system for measuring water level and water quality, or salinity. After that, the monitors will send the data to the computer server. There are five stations: Khlong Ta Sak Station (OT01), Khlong Bang Krachao Nok Temple (OT02), Bang Nam Phueng Canal Floodgate Station (OT03), Khlong Yai Bai Floodgate Station (OT04), and Khlong Phae Floodgate Station (OT05), as shown in Fig. 1. The function principle of the salinity meter is that after the system measured salinity and water levels, it will send the measured data to the Remote Terminal Unit (RTU), a remote-control system will then transmit

data to the server via internet. The server then showed the survey results on the website and application.

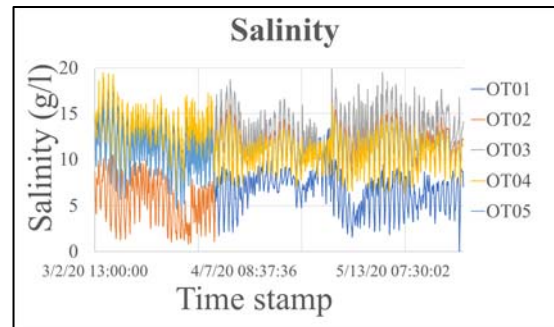


Fig. 3 Salinity of Bang Krachao

In Fig. 3 showed that the salinity values from the survey in Bang Krachao area. The salinity values were between 0.7 - 18.7 g/l. The station with the highest salinity is OT04, which is the last station before the water in the Chao Phraya River flowing into the Gulf of Thailand. The average salinity in Bang Krachao area was 10.65 g/l. This showed that the average salinity value in Bang Krachao was very high when compared to the allowed salinity of Nam Dok Mai mangoes and other plants in Bang Krachao area (0.12 g/l). The reasons of these stations have high salinity because the openings and closings of the floodgates were not suitable for salinity movement.

Salinity and Problem

The problem of intrusion of saline water occurred in Bang Krachao area because this area is the last area of the Chao Phraya River where the floodgates were closed to prevent the intrusion of saline water. Nowadays, the openings and closings of the floodgates were done all the periods of tides.

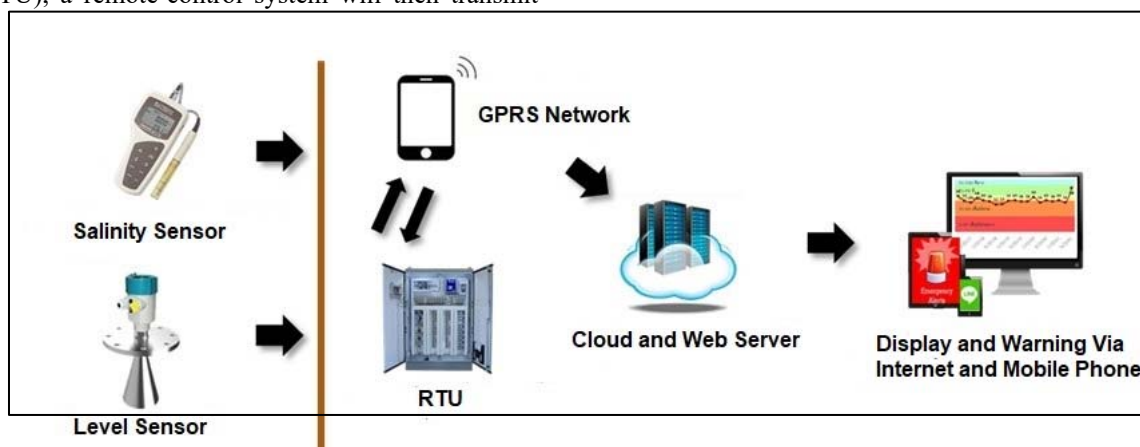


Fig. 4 Diagram of data collecting [13]

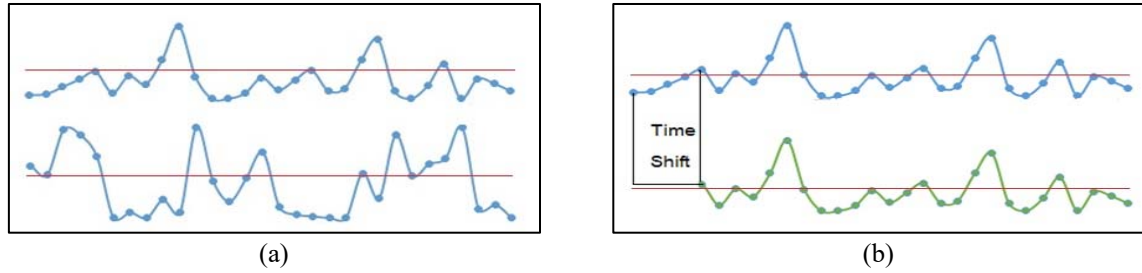


Fig. 5 Salinity data and auto-correlation process (a) Salinity data of two stations at the same time (b) Salinity data of two stations with auto-correlation

When floodgates were opened and closed only during periods of tides, there will not be openings and closings of floodgates during droughts to drive off the saline water. This results in salinity penetrating into the soil around the island. Higher concentration of salt in the soil causes the plants, especially famous plants like mangoes and Nam Hom coconut, low salt tolerance plants, and grow slower.

MODELING FRAMEWORK

The dynamics analysis of surface water flow was selected with Multiple Linear Regression and SPSS to help in the analyzing process because it is a program that is popular in statistical analysis. It can also analyze the relationships of various variables.

Multiple Regression Analysis

A multiple linear regression model was applied to study every linear relationship between one dependent variable (Y_i) and several of independent variable (X_i). The multiple regression equation is:

$$Y_i = b_0 + b_1 X_1 + b_2 X_2 + \dots + b_n X_n \quad (1)$$

where b_i are coefficient parameters.

When using this linear prediction, there is a limitation that both variables must be connected in a straight line or as close to a straight line as possible to be more accurate. In terms of how to use variables in this work, one can take the relationship between salinity values and water levels to create a prediction equation [14].

Autocorrelation

Correlation is the measurement of the similarity of two sets of data or signals, which is based on the product of multiplying the size of both sets of data at the same time period, then combining all the results together. If the data of both sets are identical, the result of multiplying both data together and adding them together will result in a positive and high value. But in the case where the two sets of data have different characteristics, as in Fig. 5(a) the result of

multiplication may be positive at some points and negative at some points, resulting in the result being either small or near zero.

The position of the time of the data was adjusted to overlap (Time Shift or Time Lag) until the two sets of data have the same phase, as in Fig. 5(b), of the sum of the products of the two data sets and ultimately have a positive value and possibly a high value. But if the two data sets overlap and the phases are not the same, the result of the sum of the multiplication of the products will be either small or near zero.

From the aspects of the overlapped times data showed the results for each time, as they overlap by considering the sum of the products from the same data set at the first time and the time that they overlap. This can be called autonomy (Auto-correlation), an examination of the relationships of data in different sequences in time series, where data at a distance of k apart with lag = k , the autocorrelation coefficient (Autocorrelation Coefficient) with Lag = k can be found from the equation:

$$r_k = \frac{\sum_{i=1}^{N-k} (x_i - \bar{x})(x_{i+k} - \bar{x})}{\sum_{i=1}^N (x_i - \bar{x})^2} \quad (2)$$

When taking the correlation coefficient to plot the graph, in general, a graph with a higher coefficient of time is zero and the less of the coefficient becomes zero when the time-lapse Gradually increase.

Dynamic Parameter

This analysis takes into account the shift time analysis, which is an analysis used to analyze areas, such as the prediction at the OT2 station in the future 1 hour ahead. It will use the dimensional data of the current time to the previous 6 hours and the length dimension data from OT1 station to OT5 station. It will then look for the relationship via SPSS program and find the equation to use for predicting salinity in the future. It has a total of 45,000 data. The variables in each station has the following values:

Y_{OTij} is the predicted salinity value at the OTj station in the future i hours.

X_{OTij} is the observed salinity value of the OTj station with i hours remaining.

Additionally, the data was separated to verify the model, receiving a total of 22,860 data.

Calibration Process

Calibrating a model is the most important step. It is to analyze the accuracy of the model before using it to predict the characteristics and behavior of salinity in the future. This study will use the correlation method between variables or Cross-Correlation to examine. This method considers the similarities between two different variable data [15]. The consideration of two variables is the series of x and y values when $i = 0, 1, 2, \dots, m$, and it will result as Correlation Coefficient (r_m) at Lag Time equals to m from the equation:

$$r_m = \frac{\sum (x_i - \bar{x})(y_{i-m} - \bar{y})}{\sqrt{\sum (x_i - \bar{x})^2 \sum (y_{i-m} - \bar{y})^2}} \quad (3)$$

Where r_m is the Correlation Coefficient at time overlapping m

Correlation Coefficient (R) indicates the two closely related variables [16]. Correlation Coefficient (R^2) obtained from the x and y series analysis in the direction of downward. The distribution of the data is that if the correlation coefficient is positive means when x is high and the value of y is also high. If the correlation coefficient is negative, it means that x is low and the value of y is also lower. If the correlation coefficient is 0, then the x and y values are not related at all.

Table 1 Correlation and relationship levels [17]

Correlation Coefficient (R^2)	Strength of Correlation
0.00 – 0.54	Low
0.55 – 0.69	Moderate
0.70 – 1.00	High

RESULTS AND DISCUSSTION

Results of Calibration

From the calibration procedure was showed in Table 2 that the error values and correlation values. The values of Y_{OT01} , Y_{OT02} , Y_{OT03} , Y_{OT04} , Y_{OT05} were influenced by each other. Each station has different

initial salinity variables used in the prediction. This is caused by the appropriate overlapping time period and the appropriate distance in each station. It can be observed from the model summary obtained from the program with the highest R^2 and the lowest standard error each and every model will always have salinity overlapping of one hour of the station used for the prediction.

Results of Salinity Prediction with Multiple Regression

The regression analysis shown in Fig. 6 shows that the model is highly correlated. It has an equation similar to $Y=X$. The results indicated the regression models appropriated for predicting the dependent variables. Regression model of Y_{OT01} , Y_{OT02} , Y_{OT03} , Y_{OT04} and Y_{OT05} were:

$$\begin{aligned} Y_{OT01} &= 0.442 + 2.081X_{OT13} - 0.974X_{OT11} - 0.169X_{OT22} \\ &+ 0.095X_{OT04} + 0.035X_{OT61} \\ Y_{OT02} &= -0.7 + 0.693X_{OT12} + 0.039X_{OT55} + 2.29X_{OT13} \\ &- 1.97X_{OT11} \\ Y_{OT03} &= 0.876 + 2.570X_{OT13} - 1.499X_{OT11} - 0.156X_{OT22} \\ &+ 0.048X_{OT21} - 0.017X_{OT61} \\ Y_{OT04} &= 1.161 + 0.777X_{OT14} - 1.355X_{OT11} + 1.702X_{OT13} \\ &- 0.189X_{OT22} \\ Y_{OT05} &= 0.577 + 0.448X_{OT15} - 1.541X_{OT11} + 2.155X_{OT13} \\ &- 0.094X_{OT22} \end{aligned}$$

Fig. 6 shows scattered plot between observed data and computed data. These plots show correlation coefficient (R^2) of 0.88 (OT01), 0.98 (OT02), 0.91 (OT03), 0.85 (OT04) and 0.94 (OT05). These are good comparable, and the root mean error were 0.71 (OT01), 0.25 (OT02), 0.57 (OT03), 0.87 (OT04) and 0.43 (OT05). They can be explained that the computed data close to the observed data and indicated that this model can predicabile.

Application

The salinity obtained from the predictions has a high accuracy when compared to the value obtained from the actual measurement. Therefore, multiple regression analysis using dynamic variables can be used to predict the salinity values of at least 1 hour in the future. Predicting just 1 hour of salinity is shown to result in giving an accurate salinity value. It can also be used to create a more systematic openings and

Table 2. Salinity Calibration

Station	Predictors	R^2	RMSE
Y_{OT01}	X_{OT13} , X_{OT11} , X_{OT22} , X_{OT34} , X_{OT61}	0.92	0.37
Y_{OT02}	X_{OT12} , X_{OT55} , X_{OT13} , X_{OT11}	0.98	0.08
Y_{OT03}	X_{OT13} , X_{OT11} , X_{OT22} , X_{OT21} , X_{OT61}	0.95	0.22
Y_{OT04}	X_{OT14} , X_{OT11} , X_{OT13} , X_{OT22}	0.89	0.54
Y_{OT05}	X_{OT15} , X_{OT11} , X_{OT13} , X_{OT22}	0.97	0.13

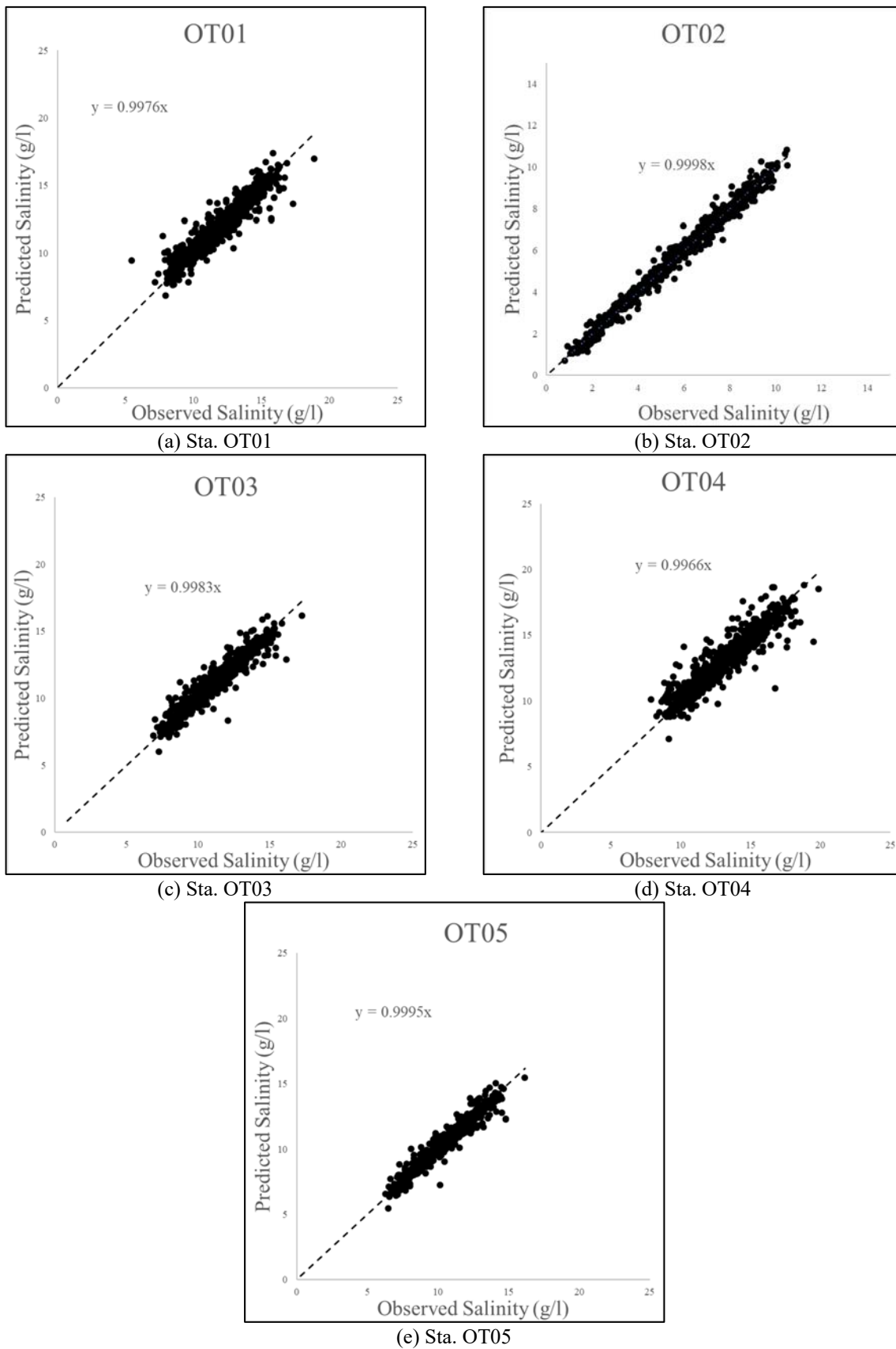


Fig. 6 Scatter plot between observed data and computed data.

closings of floodgates, especially the Khlong Lat Pho floodgate, so that salinity does not enter the Bang Krachao area.

CONCLUSIONS

This research has investigated the salinity of Bang Krachao, Thailand. To aid decision in saline water management, the values of salinity data for calibration were demonstrated, while also showing the strong correlation of shift time of salinity in each station, where simulated and measured values agree.

The calibrated process was showed that the salinity source variables in each station were related and verified the model by using the equations from the calibrate algorithm to analyze. The model is accurate and suitable, for predicting the salinity values for opening and closing floodgates.

In summary, the multiple regression analysis with dynamic variable can be used for planning to manage the gate operation in the surrounding canals. In addition, if you need additional research information, you can access the Website: <http://www.bangkachao-wateronline.com>

ACKNOWLEDGMENTS

We thank the Agricultural Research Development Agency Public Organization (ARDA) for funding. Special thanks to the Thai Royal Irrigation Development and Thai Meteorological Department for the data.

REFERENCES

- [1] Wongs S., and Sunaree S., The Preliminary Prediction Effects of Salinity Intrusion on Agriculture: The Case Study Assuming Using IPCC Data on Increasing of Sea Level Rise in Gulf of Thailand, Kasem Bundit Engineering Journal, Vol 7 No 1, 2017.
- [2] Wisuwatt T., Innovation in Irrigation Engineering for Remote Control of Irrigation Buildings and Water Management in Pak Phanang Upper Irrigation and Maintenance Project, In Special Book of Technology and innovation For Sustainable Education, Faculty of Science, Kamphaengsaen Kasetsart University, 2016, pp. 80-88.
- [3] Nuttawut I., and Wisuwatt T., A Study on Salinity Intrusion and Control Measure in the Thachin River, Journal of Research and Development, 2014.
- [4] Bureau of Water and Hydrology Management of Royal Irrigation Department, Summary of saltwater encroachment situations and mitigation measures, 2014. (in Thai)
- [5] Easey R., The Battle to Save Bangkok's Green Lung.
- [6] Marshall A., Best of Asia: Best Urban Oasis, Time, 2006.
- [7] Sri Nakhon Khuean Khan Garden, pptep (in Thai)
- [8] Ministerial Regulation, Requiring for Bang Krachao, Bang Nam Phueng, Bang Nam Phueng, Bang Yo, Bang Krak and Songkanong in Phra Pradaeng, Samut Prakarn: Is an Environmental Protection Area, Government Gazette, pp. 3-9.
- [9] Land Research and Development, Salty Tolerant Plants and Plants Like Salt, [Online]. Available: http://www.ldd.go.th/Lddwebsite/web_ord/Technical/pdf/P_Technical03001_3.pdf. [Accessed 24 May 2020].
- [10] Kornkanok A., Department of Water Resources Engineering, Faculty of Engineering, Kasetsart University 10th Thaacid National Symposium.
- [11] Lam N. T., Real-Time Prediction of Salinity in the Mekong River Delta, 10th International Conference on Asian and Pacific Coasts.
- [12] Department of Intellectual Property, Geographical Indication Registration Nam Dok Mai Mango Registration Number Sor Chor 57100064, 2014.
- [13] Seeboonruang, U., and Chulkaivalsucharit, V., Development of Automatic Warning System for Water Salinity in Bang Krachao, Thailand. Sensors and Materials, Vol. 32 Issue 20, 2020, pp. 587–597.
- [14] Nonglak W., Cross Correlation. Auto Correlation-2D Pattern Identification, 2010. (in Thai)
- [15] Higgins J., Introduction to Multiple Regression, The Radical Statistician. Vol.1, 2005, pp. 1-15.
- [16] Taweesin, K., Seeboonruang, U., and Saraphirom, P., The Influence of Climate Variability Effects on Groundwater Time Series in the Lower Central Plains of Thailand. Water, Vol. 290 Issue 10, 2018.

SOIL PARAMETERS IN DIFFERENT LAND USE TYPES IN CU LAO DUNG, VIETNAM

Duong Minh Truyen¹, Truong Hoang Dan², Duong Van Ni³ and Ly Van Loi⁴

¹College of Environment and Natural Resources, Cantho University, Vietnam;^{2,3,4}Cantho University, Vietnam

ABSTRACT

Cu Lao Dung is a land strip lying in the middle of Hau river, at the end of Cuu Long river, flowing into the East Sea. It is located in the marine economic region of Soc Trang province, Vietnam. This islet has great advantages with three ecological regions of freshwater, brackish and brine water. However, there are not many detailed studies on environmental indicators in the different land use types there, especially those in locations near the islet center. Therefore, the study of soil parameters across different agricultural land use types was carried out during the rainy season in 2019 to give an overview of the soil environment in the islet. The results showed that in the surveyed land use types, the amount of potassium fertilizer in the soil was higher than that of nitrogen and phosphorus. In Mango farm and Shrimp farm, pH and EC values collected outperform those in two other land use types, but still below 5. The main source of irrigation there was rainy water, so the amount of fertilizer accumulated in the soil was not washed out often. In general, although Cu Lao Dung is located in a favorable geographical location, but the people there do not have reasonable cultivation methods to improve the soil environment and still rely heavily on chemical fertilizers.

Keywords: Cu Lao Dung, soil, freshwater land use types

INTRODUCTION

Cu Lao Dung (CLD) is the largest islet of Hauriver, belonging to Soc Trang province (figure 1). The East borders to Dinh An estuary, the West borders to Hau river, the South borders to the East Sea and the North borders to another My Phuoc island in Soc Trang province [13].

Because CLD is located at the mouth of Hau river and connected to the East sea, its terrain is flat and the canal system is intertwined, therefore, water quality is varied from saline to fresh seasonally, however it is still favorable conditions for economic and agricultural development in centuries ago [7, 13]. Every year, the saline intrusion usually in late February and early March. Therefore, the amount of fresh water flowing from the upstream is insufficient, not enough to wash salinity in soil, thus affecting the quality of farmland. The fresh water mainly depends on rainwater [2, 7].

Depend on the present of saline, brackish and fresh water, the land use types in Cu Lao Dung is very diverse. The area that received fresh water from the Hau River, is suitable for perennial fruit trees such as Mango, Longan, Pomelo, Coconutfruits and the rest is dominate with cash crops. At the end of the islet bordering to the sea, this is saline water permanent then shrimp farming combine with exploitation of resources under forest canopy such as crested gibbons, sesarmid crabs, snails, etc.

Although there are studies on land uses at CLD, however the in-depth studies in soil characters in

relation to crops farming has not received much attention. Therefore, this survey on farming and soil characters were conducted to understand this dependences.

METHODS

The Participatory Rural Appraisal (PRA) social mapping [8] was applied to collect information relate to land use types, crop management in Cu Lao Dung. At the same time, other information relate to the different of natural conditions, ecosystems and soil quality in the study area. Soil sampling was conducted on 6 locations representing common land use types in the surveyed area.



Figure 1. Sampling location (source canthopromotion.vn; ontheworldmap.com).

At each land use type, 5 soil samples were collected in the top from 15 - 20cm. Soil samples

were sent to Can Tho University laboratory for analysis. The analysed characters were:

- + Conductivity (EC) (dSm^{-1})
- + pH
- + Nitrogen content (N) (%)
- + Potassium content (K) (%)
- + Phosphorus content (P) (%)

The soil characters of the study area was assessed by comparing between land use types and crops. The values of pH, nitrogen (N), phosphorus (P) and potassium levels in the soil were compared based on the Forest Sector Handbook chapter of Soil and Soil Nutrition [11, 12].

RESULTS AND DISCUSSION

EC values

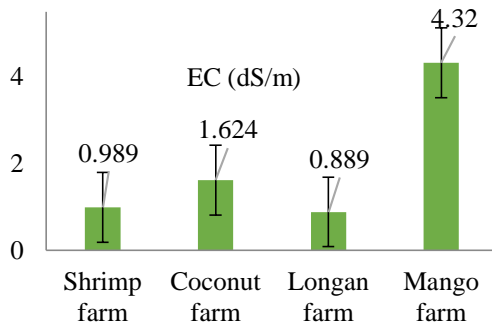


Figure 2. EC values obtained at four different land use types.

Six locations in freshwater zone with 4 different land use types has EC values varied from 0.889 to 4.32 dSm^{-1} (figure 2). The Mango farm had the highest EC value of 4.32 dSm^{-1} , followed by Coconut farm of 1.624 dSm^{-1} ; the lowest was obtained in the Longan farm at 0.889 dSm^{-1} . The average value of the EC on all land uses types was 1.956 dSm^{-1} , but EC value obtained in the Mango farm was different to all others as Shrimp, Coconut and Longan farms significantly.

Using standard measurement of salinity [1], the crop performances was presented below:

Table 1 Classification by salinity and effects on crops

Designation	EC in soil (dS/m)	Crop performances
Salt free	0 – 2	Salinity effects are mostly negligible
Slightly saline	2 – 4	The productivity of many plants may be limited
Slightly saline	4 – 8	The productivity of many crops is limited
Moderately saline	8 – 16	Some plants can tolerate

Strongly saline	>16	Only tolerant crops can tolerate
-----------------	-----	----------------------------------

Based on information in the table 1, Mango farm had an EC value of 4.32 dSm^{-1} ; considered as slightly saline soil. The EC values in other land use types fluctuated from 0 to 2 and be classified as salt free soil.

pH values

Based on the results of soil samples collected at 4 different land use types, the results were shown in the following chart:

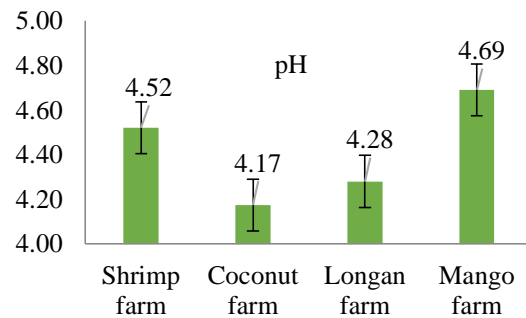


Figure 3. pH values observed at four different land use types.

From the chart, it illustrated that the highest pH value obtained in the Mango farm of 4.69. The lowest was at Coconut farm of 4.17.

pH, which represented for “power of hydrogen”, considered as a measure of how acidic or alkaline a solution was. Using the standard of pH values (table 2), with representing the soil characteristics [9, 11, 12, 14], it showed that the pH values of four different land use types ranged from 4.4 to 4.69. The results found that soil at Cu Lao Dung Islet was strongly acidic.

Table 2 pH scale

pH	Classification of soil
<3	Very strongly acid
3 – 4.5	Very strongly acid
4.5 – 5.5	Strongly acid
5.5 – 6.5	Medium acid
6.5 – 7.0	Slightly acid
7.0	Neutral
7.0 – 7.5	Slightly alkaline
7.5 – 8.0	Medium alkaline
8.0 – 9.0	Strongly alkaline
>9.0	Very strongly alkaline

According to the results of EC and pH values in 4 land use types in Cu Lao Dung Islet, it was clear that Mango could tolerate slightly saline (EC at 4.69 dSm^{-1}) and strongly acidic soil (pH of 4.69), while

Coconut and Longan only suffered salt free soil with EC values at 1.624 dSm^{-1} and 0.889 dSm^{-1} respectively, they could not suffer saline soil. However, these crops could endure very strongly acidic soil, pH ranging from 4.17 to 4.28.

Shrimp farm had salt free value at 0.989 dSm^{-1} and pH at 4.52 because farmers added freshwater in the beginning crops and the samples were taken at that time.

Many things can affect the conductivity of soil, including the irrigation [1, 5]. Natural rain will dilute the salt near the roots. This prevents the plant from being "burnt" by excess salts and nutrients, as plant roots are clogged with salt and nutrients. Plants cannot absorb salt, which can be stunted. If irrigation water is high in salt, salts can accumulate in the fields, increasing salinity and conductivity. For most plants, conductivity is considered good for the plant if it does not exceed 4 dSm^{-1} [16]. However, this number will vary, depending on the specific crop. In Cu Lao Dung, the irrigation depended on irregular rainwater, which caused the pH values of soil surface layer to be low due to less washout.

The total value of N - P - K

Cu Lao Dung district has transferred over 400 hectares of sugarcane to aquaculture, mainly Shrimp farming since July 2018. During the conversion of cultivation to Shrimp farming, the use of fertilizers to create a suitable water environment was an indispensable element. Fertilizers commonly used in the study area were nitrogen, phosphorus and potassium (N-P-K). The results of soil samples collected at 4 land use types in An Thanh I commune area were shown in the chart below.

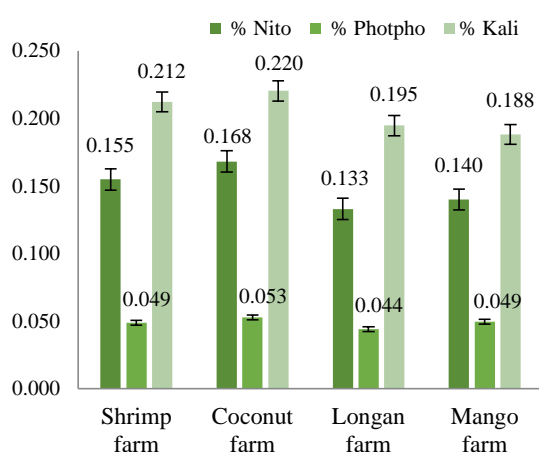


Figure 4. Total percentage of nitrogen, phosphorus, and potassium concentration collected in four land use types.

Four different land uses types in freshwater zone had varied values of total nitrogen, phosphorus and potassium, with figures of potassium supplied much significantly higher than that of nitrogen and

phosphorus. Coconut farm had the highest values of total N – P – K fertilizers applied than Shrimp, Mango and Longan farms.

Using the standard stress level of nitrogen, phosphorus, and potassium [3, 4, 6, 15, 17], the concentration of total N – P – K in cropland was performed in the table 3.

Table 3 Definition of nitrogen, phosphorus, and potassium stress levels.

Level	Nitrogen (N) stress level (%)	Nitrogen concentration in cropland
I	>0.30	Nitrogen sufficiency
II	0.15 – 0.30	No nitrogen stress
III	0.09 – 0.15	Nitrogen stress
IV	<0.09	Nitrogen scarcity
Level	Phosphorus (P) stress level (%)	Phosphorus concentration in cropland
I	> 0.15	Phosphorus sufficiency
II	0.10 – 0.15	No phosphorus stress
III	0.05 – 0.10	Phosphorus stress
IV	< 0.05	Phosphorus scarcity
Level	Potassium (K) stress level (%)	Potassium concentration in cropland
I	> 0.25	Potassium sufficiency
II	0.15 – 0.25	No Potassium stress
III	0.10 – 0.15	Potassium stress
IV	< 0.10	Potassium scarcity

According to the nitrogen (N) stress levels, Longan farm and Mango farm were in level III – nitrogen stress while those numbers in 2 other land use types, namely Shrimp farm and Coconut farm were in level II – no nitrogen stress. It means that the amount of nitrogen (N) applied was deficient in Longan and Mango farms.

Moving on phosphorus (P) fertilizer, three surveyed land use types, namely Shrimp, Longan and Mango farms were in level IV – phosphorus scarcity, while Coconut farm was in level III – phosphorus stress.

Although potassium (K) fertilizer was applied at the same time with nitrogen and phosphorus fertilizer, four different land use types had level II – no potassium stress in the table 3. Unlike nitrogen and phosphorus, potassium ions do not participate in permanent organic compounds in plants, but obviously exist in the form of inorganic salts and dissolved organic salts. Potassium content in soil usually varies from 0.5 to 3.0%. It is usually higher in arid, young, and black alluvial soil than red soil and weathered rock located in areas with higher precipitation [3, 10].

From the results, Mango farm could tolerate slightly alkaline soil. Therefore, it was needed to put down phosphorus (P) and potassium (K) fertilizer in Mango farm. Besides, Coconut and Longan farm could stand acidic soil and nitrogen (N) was suggested to add in these farms. On the other hand, Shrimp farm was significantly different because fertilizer applied depending on the farming time. Nevertheless, in Cu Lao Dung Islet, local farmers chose to put more potassium (K) fertilizer in the farms because this type of fertilizer could increase drought and salinity tolerance for crops.

CONCLUSIONS

In freshwater zone of Cu Lao Dung, the results in four surveyed land use types, namely Shrimp, Coconut, Longan and Mango farms were significantly different with Mango farm had salinity tolerance while acidity tolerance belonged to Coconut and Longan farms. To increase crops tolerance, potassium fertilizer was applied in farm much more than nitrogen and phosphorus fertilizer.

ACKNOWLEDGMENTS

The process of conducting research and results achieved through the ODA project, which funded by Can Tho University. Sincere thanks to the teachers, instructors, and local officers who assisted in providing the information to complete this article.

REFERENCE

- [1] Akpan UE, Okon AA, Ituen EE. Measurement of salinity and electrical conductivity of some soil samples of Uruan local government Area of Akwa Ibom State, Nigeria. *Global Journal of pure and applied sciences*. Vol. 8, Issue 3, 2002, pp 399-404.
- [2] An TD, Tsujimura M, Le Phu V, Kawachi A, Ha DT. Chemical characteristics of surface water and groundwater in coastal watershed, Mekong Delta, Vietnam. *Procedia Environmental Sciences*. Vol 20, 2014, pp 712-721.
- [3] Bidari BI, Hebsur NS. Potassium in relation to yield and quality of selected vegetable crops. *Karnataka Journal of Agricultural Sciences*. Vol 21, Issue 1, 2011.
- [4] Colwell JD. The estimation of the phosphorus fertilizer requirements of wheat in southern New South Wales by soil analysis. *Australian Journal of Experimental Agriculture*. Vol 3, Issue 10, 1963, pp 190-197.
- [5] Lenntech, B. V. Water conductivity. *Water Treatment*, 2016. Retrieved 6 May 2020.
- [6] Liu J, You L, Amini M, Obersteiner M, Herrero M, Zehnder AJ, Yang H. A high-resolution assessment on global nitrogen flows in cropland. *Proceedings of the National Academy of Sciences*. Vol 107, Issue 17, 2010, pp 8035-8040.
- [7] Mai NT, Kantoush SA, Sumi TE, Thang TD, Binh DV, Trung LV. The influences of tidal regime and morphology change on salinity intrusion in Hau River. In: *Proceedings of the 38th IAHR World Congress*, 2019, pp 1-6.
- [8] Map S. *Participatory Rural Appraisal (PRA)*, 1993.
- [9] Marion GM, Millero FJ, Camões MF, Spitzer P, Feistel R, Chen CT. pH of seawater. *Marine Chemistry*. Vol 126, Issue 1-4, 2011, pp 89-96.
- [10] Mc Lean EO, Watson ME. Soil measurements of plant-available potassium. *Potassium in agriculture*, 1985, pp 277-308.
- [11] McDonald RC, Isbell RF, Speight JG, Walker J, Hopkins MS. *Australian soil and land survey: field handbook*. CSIRO publishing, 1998.
- [12] Rengel Z, editor. *Handbook of soil acidity*. CRC Press; 2003.
- [13] Seung Kyu LE, Truong An DA. Assessment of Sugarcane Yield in the Cu Lao Dung Isles, Soc Trang Province of Vietnam in the Context of Water Scarcity. *Transylvanian Review*, Vol 1, Issue 5, 2019;
- [14] Spurway CH. Soil reaction (pH) preferences of plants. *Michigan State University Agricultural Experiment Station. Special Bulletin*, 1941, pp 306.
- [15] Talibudeen O. The Role of Potassium in Agriculture. VJ Kilmer, SE Younts, NC Brady (Eds.) *Madison, Wisconsin: American Society of Agronomy, etc., 1966*, pp. 523. *Experimental Agriculture*. Vol 5, Issue 4, 1969, pp 344.
- [16] Valdez-Aguilar LA, Grieve CM, Poss J. Salinity and alkaline pH in irrigation water affect marigold plants: I. Growth and shoot dry weight partitioning, 2009.
- [17] Wang SJ, Fox DG, Cherney DJ, Klausner SD, Bouldin DR. Impact of dairy farming on well water nitrate level and soil content of phosphorus and potassium. *Journal of dairy science*, Vol 82, Issue 10, 1999, pp 2164-2169.

PREPARATION OF FLUORIDE ADSORBENT FROM ZIRCON SAND USING MECHANOCHEMICAL TREATMENT, AND ITS APPLICATION FOR FLUORIDE REMOVAL

Nagisa Minami¹ and Takaaki Wajima¹

¹Department of Urban Environment Systems, Graduate School of Engineering, Chiba University, Japan;
1-33 Yayoi-cho, Inage-ku, Chiba, Japan

ABSTRACT

Removal of low-concentration fluoride in natural water is an important issue all over the world. Japan is a volcanic country to have many hot springs, and the removal of low-concentration fluoride from hot spring drainage is desired. In this study, we attempted to prepare a novel adsorbent with high selective removal ability of fluoride from zircon sand using mechanochemical treatment, and applied it for removing fluoride from hot spring water. Mechanochemical treatment of zircon sand was carried out using a planetary ball mill, and fluoride removal of the product was examined using fluoride aqueous solution and hot spring water. The hot spring water is collected from one of the hot spring in Japan, and a typical sulfic acid hot spring water pH 2 including high contents of SO_4^{2-} ($12000 \text{ mg} \cdot \text{L}^{-1}$) and Cl^- ($5000 \text{ mg} \cdot \text{L}^{-1}$) with $11 - 15 \text{ mg} \cdot \text{L}^{-1}$ of fluoride ion. Regardless of ball sizes, with increasing the mechanochemical treatment time to 10 min, the removal ability of the product for fluoride increases, and then be almost constant. With decreasing pH of the solution to 2, the adsorption amount increases, and then be almost constant. With increasing the temperature of the solution, the adsorption amount decreases, while the rate of adsorption increases and the amount increases. The adsorption isotherm at pH 2 follows much better Langmuir model than Freundlich model, and the calculated maximum adsorption amount is $0.09 \text{ mmol} \cdot \text{g}^{-1}$. Fluoride can be adsorbed selectively from hot spring water below Japanese effluent standard for fluoride ($8.0 \text{ mg} \cdot \text{L}^{-1}$).

Keywords: Zircon sand, Fluoride removal, Mechanochemical treatment, Hot spring water

INTRODUCTION

Fluorine is a dangerous anionic species, and excessive ingestion of fluorine causes fluorosis and neurological abnormalities in the human body. Therefore, removal of low concentrations of fluoride in natural water is an important issue all over the world. There are coagulation-sedimentation, reverse osmosis membrane, and adsorption as methods of removing fluoride in wastewater. However, coagulation-sedimentation method has a problem of sludge treatment, and reverse osmosis membrane method is a high equipment cost [1].

In Japan, there are many hot spring areas, and hot spring water contains fluoride coexisting with some cations and anions. Therefore, selective removal for low concentrations of fluoride in hot spring wastewater is desired, and simple on-site adsorption method for fluoride is focused on.

Zirconia (ZrO_2) attracts as an adsorbent having Zr-O-H on its surface, which has a selective adsorption capacity for fluorine [2]. However, the zirconia adsorbents are expensive because its manufacturing requires a multi-steps with a lot of energy [3]. In previous studies, zircon sand can be converted into the adsorbent with Zr-O-H using simple mechanochemical treatment, and phosphorus in seawater can be removed selectively [4][5].

In this study, we prepares a new adsorbent with

high selective fluoride adsorption ability from zircon sand by mechanochemical treatment, and applied it to remove fluoride from hot spring water.

EXPERIMENTAL

Sample

In this study, raw zircon sand (ZrSiO_4) (WAKO) was used, and hot spring water used was collected from one of hot spring water in Japan. The chemical composition of hot spring water is shown in Table 1, and the pH of hot spring water is about 2. This hot spring water is sulfic acid water with $12 \text{ mg} \cdot \text{g}^{-1}$ of F^- .

Table 1 Chemical composition of hot spring water.

Ion	Concentration [mg/L]
F^-	12
Cl^-	5101
SO_4^{2-}	12720
Na^{2+}	210
K^+	140
Mg^{2+}	103
Ca^{2+}	25
Fe^{2+}	149
Al^{3+}	122

Mechanochemical Treatment

A planetary ball mill (P-6, Fritsch) was used for mechanochemical treatment. Pots and balls were made of silicon nitride with high wear resistance. Treatment was carried out at rotation speed of 400 rpm for 1 to 60 min using three different diameter balls (ϕ 5, 10, 15 mm). The volume filling rate of the ball into the pot was about 30 %, and the number of balls with ϕ 5 mm, ϕ 10 mm and ϕ 15 mm were 180, 18 and 7, respectively.

The products obtained under each mechanochemical treatment condition for fluoride adsorption was estimated as follows. 0.1 g of the product after mechanochemical treatment was added into 10 mL of KF aqueous solution with $0.1 \text{ mmol} \cdot \text{L}^{-1}$ in 50 mL of the tube, and shaken with reciprocal shaker at room temperature for 12 h. After shaking, the tube was centrifuged, and a part of the supernatant was collected. The pH of the collected solution was measured with a pH meter (F-72, HORIBA), and the fluoride concentration in the collected solution was measured with a fluoride ion meter (TiN-5101, TOKO). The adsorption amount ($\text{mmol} \cdot \text{g}^{-1}$) and removal percent (%) for fluoride were calculated from the measured fluoride concentration using the following equations:

$$q = (C_0 - C) \cdot L \cdot W^{-1} \quad (1)$$

$$R = \{(C_0 - C) \cdot 100\} \cdot C_0^{-1} \quad (2)$$

where q is adsorption amount [$\text{mmol} \cdot \text{g}^{-1}$], C_0 is initial fluoride concentration [$\text{mmol} \cdot \text{L}^{-1}$], C is fluoride concentration after shaking [$\text{mmol} \cdot \text{L}^{-1}$], W is weight of sample [g], L is volume of solution [L] and R is the removal percentage of fluoride [%].

Fluoride Adsorption

The fluoride adsorption ability of the product obtained by mechanochemical treatment for 10 min using ϕ 5 mm balls was investigated.

The pH dependence of the fluoride adsorption for the product was investigated, in comparison with that of raw zircon sand. $0.1 \text{ mmol} \cdot \text{L}^{-1}$ KF solution with pH 1 - 7 was adjusted using HCl. 0.1 g of the raw sand or the product was added into the KF solution with different pHs, and shaken for 12 h at room temperature. After shaking, the mixture was centrifuged, the pH of the supernatant was measured with a pH meter, and the fluoride concentration in the

supernatant was measured by a fluoride ion meter to calculate the fluoride adsorption amount using the equations (1).

The amount of fluoride adsorption in diluted seawater was examined for fluoride selective adsorption of the product and raw sand. 0.1 g of the product or raw sand was added into 10 mL of diluted seawater, which diluted 10 – 1000 times, with $0.1 \text{ mmol} \cdot \text{L}^{-1} \text{F}^-$, and shaken for 12 h. After shaking, the mixture was centrifuged, the pH (equilibrium pH) of the supernatant was measured with a pH meter, and the fluoride concentration in the supernatant was measured by a fluoride ion meter to calculate the fluoride adsorption amount using equations (1).

Fluoride adsorption isotherm was examined using KF solution with pH 2, adjusted by HCl solution. 0.1 g of the product or raw zircon sand was added into $0.05 - 4.0 \text{ mmol} \cdot \text{L}^{-1}$ KF solution, and shaken for 12 h. After shaking, the mixture was centrifuged, the pH (equilibrium pH) of the supernatant was measured with a pH meter, and the fluoride concentration in the supernatant was measured by a fluoride ion meter to calculate the fluoride adsorption amount using equations (1).

Fluoride adsorption kinetics of the product in KF solution was examined. 1.0 g of the product was added into 200 mL of $0.1 \text{ mmol} \cdot \text{L}^{-1}$ KF solution, and was stirred for 1.5 h at 20, 30 and 40 °C. During stirring, a part of the solution (2 mL) was collected at each time, and was filtered using a membrane filter. The fluoride concentration in the filtrate was determined by a fluoride ion meter to calculate the fluoride adsorption amount using (1).

RESULTS AND DISCUSSION

Fluoride Adsorption Ability

The amount of fluoride adsorption of the product obtained by mechanochemical treatment is shown in Fig. 1. With increasing the mechanochemical treatment time to 10 minutes, the fluoride adsorption of the product increased, and then became almost constant, regardless of the ball diameter. The fluoride adsorption amount of the product after 10 minutes mechanochemical treatment is $0.004 \text{ mmol} \cdot \text{g}^{-1}$, which is almost 2 times as that of raw zircon sand ($0.002 \text{ mmol} \cdot \text{g}^{-1}$). The removal of fluoride was about 50%. It is noted that the amount of fluoride adsorption of the product was about 1/29 of the amount of fluoride adsorption of magnesite ($0.114 \text{ mmol} \cdot \text{g}^{-1}$) [6], and 1/250 of the amount of fluoride adsorption of zirconia ($1.0 \text{ mmol} \cdot \text{g}^{-1}$) [7].

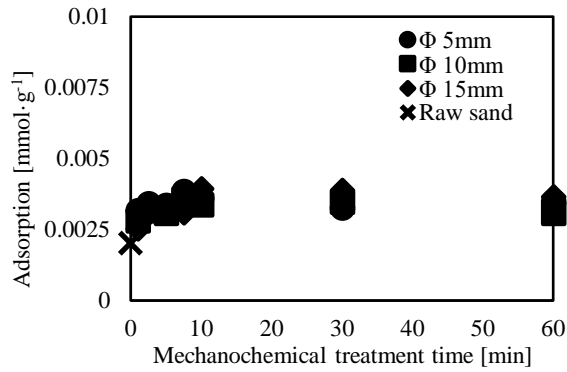


Fig. 1 Fluoride adsorption amount of the product after mechanochemical treatment using the ball with various diameter.

The pH dependence of the fluoride adsorption of the product and raw sand is shown in Fig. 2. The fluoride adsorption of the product increased with decreasing pH, and the adsorption amount at pH 3.5 was $0.008 \text{ mmol} \cdot \text{g}^{-1}$, which was about 2 times higher than that at pH 7, while adsorption of raw zircon sand at pH 3.2 was $0.007 \text{ mmol} \cdot \text{g}^{-1}$. It is reported that the fluoride adsorption amount of Zr adsorbent with Zr-OH on the surface increases as the pH decreases [8]. It is considered that Zr-O-H is increased on the surface of the product by mechanochemical treatment.

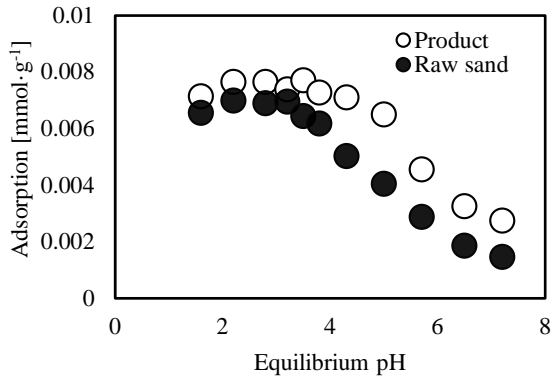


Fig. 2 Effect of pH on fluoride adsorption amount of the product.

The fluoride adsorption amounts of the product and zircon sand in diluted seawater were shown in Fig. 3. The product indicates higher fluoride adsorption than raw sand and almost same adsorption amount in 1/10 – 1/1000 diluted seawater as in distilled water. This result shows that product can selectively adsorb fluoride in high saline water.

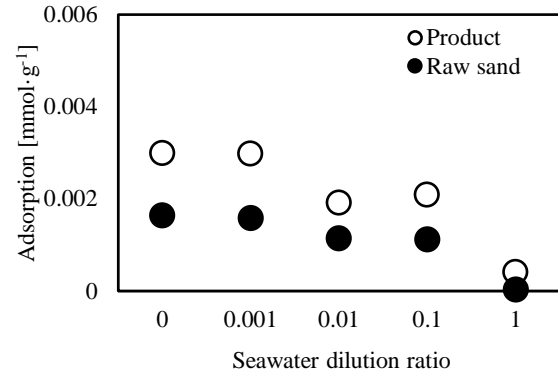


Fig. 3 Fluoride adsorption amount of the product and raw sand in seawater.

Fig. 4 shows the adsorption isotherms of the product and raw sand in fluoride solution at pH 2. As the equilibrium concentration increased, the fluoride adsorption increased sharply up to the equilibrium concentration of $0.09 \text{ mmol} \cdot \text{L}^{-1}$ and $0.06 \text{ mmol} \cdot \text{L}^{-1}$ for the product and raw sand, respectively, and then gradually increased.

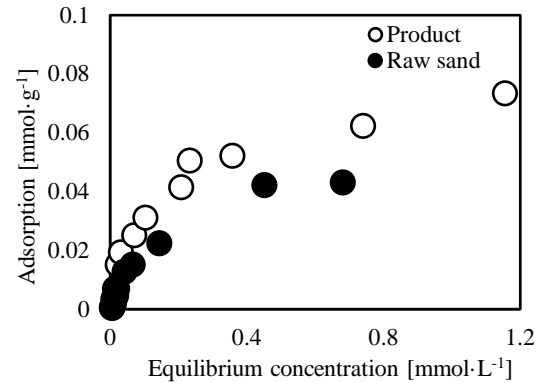


Fig. 4 Fluoride adsorption isotherm of the product at pH 2.

The experimental results obtained in Fig. 4 for the product and raw sand are analyzed using the Langmuir adsorption model and the Freundlich adsorption model to estimate the fluoride adsorption behavior of the product. The linear equations of Langmuir adsorption model and Freundlich adsorption model are as follow:

$$C \cdot q^{-1} = (q_{\max} \cdot K_L)^{-1} + C \cdot (q_{\max})^{-1} \quad (3)$$

$$\ln q = \ln K_F + n^{-1} \cdot \ln C \quad (4)$$

where q is adsorption amount [$\text{mmol} \cdot \text{g}^{-1}$], C is fluoride concentration [$\text{mmol} \cdot \text{L}^{-1}$], q_{\max} is the maximum adsorption amount [$\text{mmol} \cdot \text{g}^{-1}$], K_L is adsorption equilibrium constant of Langmuir, K_F and n are constant of Freundlich.

The results are shown in Table 2. According to the correlation coefficient, Langmuir equation (correlation coefficient: $R^2 = 0.98$) could be more realistic than that Freundlich's equation ($R^2 = 0.93$). The calculated maximum adsorption capacity of the product using Langmuir equation is $0.09 \text{ mmol} \cdot \text{g}^{-1}$.

Table 2 The results of parameter from adsorption isotherm of the product and raw sand.

	Langmuir			Freundlich		
	q_{\max}	K_L	R^2	n	K_F	R^2
Product	0.09	5.19	0.98	2.13	0.33	0.93
Raw sand	0.06	4.94	0.96	1.13	0.38	0.86

The important feature of the Langmuir isotherm can be written in form of a dimensionless quantity known as separator factor (R_L) which is given by (5).

$$R_L = (1 + K_L \cdot C_{0,\max})^{-1} \quad (5)$$

where K_L and $C_{0,\max}$ are the adsorption equilibrium constant of Langmuir model and maximum initial concentration, respectively.

The value of R_L determines nature of the isotherm shape. It can either be favorable ($0 < R_L < 1$), unfavorable adsorption ($R_L > 1$), liner ($R_L = 1$) or irreversible adsorption ($R_L = 0$). The obtained values of R_L to be 0.092 for fluoride adsorption by the product suggest that the process is favorable.

The value of the Freundlich constant (n) indicates the affinity between the adsorbent and the adsorbate. The adsorbate is easily adsorbed ($0.1 < n^{-1} < 0.5$), or difficulty adsorbed ($n^{-1} > 2$) [9]. The value of n^{-1} obtained to be 0.469 for fluoride adsorption by the product suggest that the process has affinity.

Figure 5 shows the fluoride adsorption of product after mechanochemical treatment in fluoride solution at various temperatures. As the stirring time increased, the fluoride adsorption increased, and then be almost constant. As the temperature decreased, the fluoride adsorption amount increased.

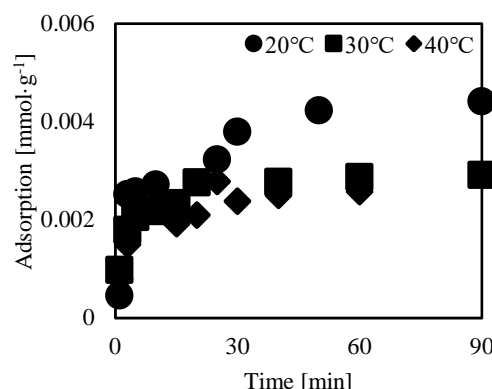


Fig. 5 Fluoride adsorption of the product at various temperatures.

The experimental results obtained in Fig. 5 were analyzed by pseudo-first-order and pseudo-second-order kinetics models to estimate the fluoride adsorption behavior of the product in fluoride solution. The linearized equations of pseudo-first-order and pseudo-second-order kinetics models are as follows;

$$\ln(q_e - q_t) = \ln q_e - k_1 \cdot t \quad (6)$$

$$t \cdot q_t^{-1} = (k_2 \cdot q_e^2)^{-1} + t \cdot q_e^{-1} \quad (7)$$

where q_e , q_t , k_1 , k_2 and t are the maximum adsorption amount ($\text{mmol} \cdot \text{g}^{-1}$), the adsorption amount at time ($\text{mmol} \cdot \text{g}^{-1}$), the pseudo-first-order adsorption kinetics constant (min^{-1}), the pseudo-second-order adsorption kinetics constant ($\text{g} \cdot \text{mmol}^{-1} \cdot \text{g}^{-1}$), and time (min), respectively.

The results analyzed are shown in Table 3. According to the correlation coefficient (R^2), the data fit much better to pseudo-second-order model than to pseudo-first-order model. It was found that the product has higher adsorption amount at lower temperature, while reaction rates decrease.

Table 3. The results of parameters from adsorption kinetics.

Temp.	Pseudo-first-order			Pseudo-second-order		
	q_e	k_1	R^2	q_e	k_2	R^2
20 °C	0.003	0.034	0.92	0.005	41	0.99
30 °C	0.002	0.025	0.83	0.004	72	0.98
40 °C	0.002	0.023	0.82	0.003	91	0.98

The activation energy for fluoride adsorption was calculated by the Arrhenius equation as follows;

$$k_2 = A \cdot \exp(-\Delta E \cdot (R \cdot T)^{-1}) \quad (8)$$

where ΔE is the activation energy [$\text{kJ} \cdot \text{mol}^{-1}$], A is the frequency factor, T is the absolute temperature [K], and R is the gas constant. From the plot of $\ln(k_2)$ vs. $1/T$ (Fig. 6), the activation energy for the adsorption of fluoride was found to be $7.53 \text{ kJ} \cdot \text{mol}^{-1}$.

The magnitude of ΔE indicates the type of adsorption, which can be physical or chemical. The physical adsorption process has lower ΔE values ($5 - 40 \text{ kJ} \cdot \text{mol}^{-1}$), while the chemical adsorption has higher ΔE values ($40 - 800 \text{ kJ} \cdot \text{mol}^{-1}$) [10]. It is noted that the activation energy of fluoride chemical adsorption of Mg-Al oxide was $73.3 \text{ kJ} \cdot \text{mol}^{-1}$ [11], and the activation energy of fluoride physical adsorption of tetrametallic oxide adsorbent (Fe-Al-Ce-Ni) was $1.1 \text{ kJ} \cdot \text{mol}^{-1}$ [10]. The activation energy of ordinary physical adsorption supports the high F^- affinity of the product and the feasibility of the reaction.

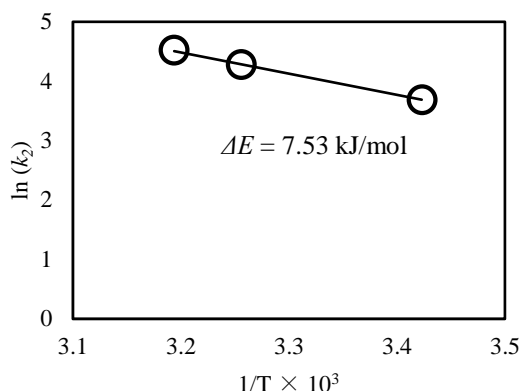


Fig. 6 Arrhenius plot for fluoride adsorption on the adsorbent.

Fluoride Adsorption From Hot Spring Water

Figure 7 shows the fluoride ion concentration and the fluoride removal from the hot spring water after treatment for 3 h by adding various amounts of the product. It is noted that the Japanese fluoride effluent standard value is 8.0 mg/L . With increasing the addition of the product, fluoride concentration decreases, and be lower than effluent standard. The removal was 34 % with more than 100 g/L addition.

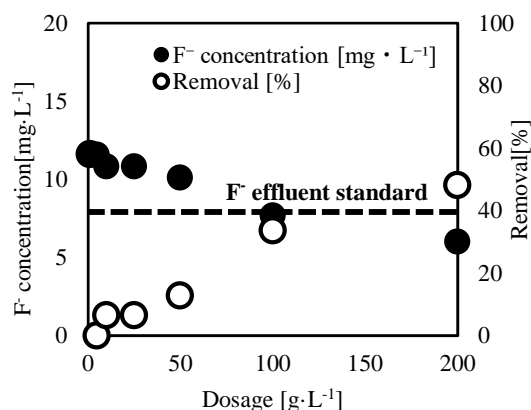


Fig. 7 Concentration and removal of fluoride from hot spring water.

Figure 8 shows the fluoride concentration and the fluoride removal at each shaking time when the product was added at $100 \text{ g} \cdot \text{L}^{-1}$. With increasing the reaction time, the fluoride concentration gradually decreased to Japanese effluent standard, and the removal reached to 49%, which indicates that fluoride in the hot spring water can be removed to below the effluent standard value by treating at $100 \text{ g} \cdot \text{L}^{-1}$ for 180 min.

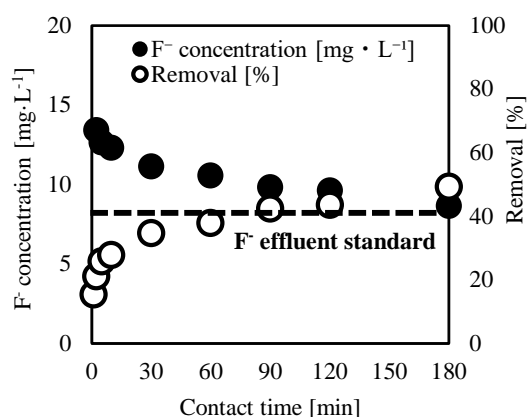


Fig. 8 Concentration and removal of fluoride during the treatment.

The chemical composition of hot spring water and treated water with $100 \text{ g} \cdot \text{L}^{-1}$ addition for 3 h is shown in Table 4. While 35 % of F^- was removed in the hot spring water after the treatment, other elements were removed less than 16 %. It suggests that fluoride in hot spring water can be selectively removed using mechanochemically treated zircon sand.

Table 4 pHs and chemical compositions of hot spring water and treated water.

	Hot spring water	Treated water
pH	1.6	1.7
F ⁻	11.6	7.6
Cl ⁻	5101	5167
SO ₄ ²⁻	12720	10739
Na ⁺	210	221
K ⁺	140	117
Mg ²⁺	103	105
Ca ²⁺	24.7	27.8
Fe ²⁺	149	151
Al ³⁺	122	125

CONCLUSIONS

Highly selective fluoride adsorbent was attempted to be prepared from zircon sand by mechanochemical treatment using a planetary ball mill, and the fluoride adsorption ability of the product, such as fluoride adsorption amount, pH dependence, fluoride adsorption isotherms and kinetics, was investigated. The results are as follows;

1. The amount of fluoride adsorption of zircon sand can be increased rapidly within 10 min of mechanochemical treatment.
2. The amount of fluoride adsorption of the product increased with decreasing pH.
3. The fluoride adsorption of the product in high saline water was higher than raw sand.
4. The adsorption isotherm at pH 2 was fitted to Langmuir model better than Freundlich model, and the calculated maximum adsorption amount is 0.09 mmol · g⁻¹.
5. The adsorption kinetics of the fluoride in the fluoride solution fit to pseudo-second-order model better than pseudo-first-order model. The product indicates higher adsorption amount at lower temperature, while the reaction kinetics decrease.
6. Fluoride can be adsorbed selectively from hot spring water below Japanese effluent standard for fluoride (8.0 mg · L⁻¹).

These results indicate that a novel product with high selective fluoride adsorption ability can be prepared by simple mechanochemical treatment, and can be applied to remove fluoride from hot spring water.

REFERENCES

- [1] NEC facilities Co., Ltd., Law and treatment technology for boron and fluorine in wastewater, Chemical Equipment, Industry Research Committee, Ed., 2010, pp. 68-79
- [2] Halla L., Velazquez J., Robert H., Juan M. and Jose R. R., Zirconium – Carbon Hybrid Sorbent for Removal of Fluoride from Water: Oxalic Acid Mediated Zr(IV) Assembly and Adsorption Mechanism, *Environmental Science Technology*, Vol. 48, No. 2, 2014, pp.1166 – 1174
- [3] Munemiya S., Manufacturing method and applications of zirconia grain, *Newsletter of the Japan Institute of Metals and Materials*, Vol. 23, No. 2, 1984, pp.97-103
- [4] Hirota K. and Wajima T., Preparation of Highly Selective Phosphorus Adsorbent From Zircon Sand by Mechanochemical Treatment, *J. Ion. Exch.*, Vol. 29, 2018, pp.158-162
- [5] Hirota K. and Wajima T., Selective Removal of Phosphorus from Seawater Using Mechanochemical Treated Zircon Sand, *International Journal of Environmental Science and Development*, Vol. 11, No. 5, pp. 263-267
- [6] Meenaksh S., Sundaran C. and Natrayasamy V., Defluoridation of Water using Magnesia/ Chitosan Composite, *Journal of Hazardous Materials*, Vol. 163, issue 2-3, 2008, pp.618-624
- [7] Blackwell A. and Carr P.M., Study of the Fluoride Adsorption Characteristics of Porous Microparticulate Zirconium Oxide, *Journal of Chromatography, A* 549, 1991, pp. 43-57
- [8] Shiomi H., Mukai H., Masui M., Hashidume Y. and Akita Y., Development of Phosphorous Adsorbent using Mechano-chemically Treated Calcium Silicate, *Journal of the Society of Material Science, Japan*, Vol. 53, No. 6, 2004, pp. 618-622
- [9] Ogata F., Tominaga H., Kangawa M., Inoue K. and Kawasaki N., Adsorption Capacity of Dye in the Presence of Dying Assistant Auxiliaries by Carbonaceous Material Produced from Cotton, *Journal of the Surface Science Society of Japan*, Vol. 32, No. 12, 2011, pp. 804-808
- [10] Raghav S. and Kumar D., Adsorption Equilibrium, Kinetics, and Thermodynamic Studies of Fluoride Adsorbed by Tetrametallic Oxide Adsorbent, *Journal of Chemical & Engineering data*, Vol. 63, 2018, pp. 1682-1697
- [11] Kameda T., Oba J. and Yoshioka T., Kinetics and Equilibrium Studies on Mg-Al Oxide for Removal of Fluoride in Aqueous Solution and its Use in Recycling, *Journal of Environmental Management*, Vol. 56, 2015, pp. 252-256

COMPARISON OF THE NATIONAL PARK MANAGEMENT SYSTEM IN THE UNITED STATES AND JAPAN

Takashi Kuchii, Atsushi Nakashima

PhD ABD, Faculty of Systems Engineering, Wakayama University, Japan
Professor, Faculty of Systems Engineering, Wakayama University, Japan

ABSTRACT

"National Parks" have been introduced in various countries since Yellowstone National Park was designated in the US in 1872 as the first National park. National Parks can be symbols of a country. In some developing regions, where institutional design and management for nature conservation are not matured and where the economy tends to take precedence over nature conservation, it is important for authorities to have a common understanding based on accurate information. The United States and Japan have leading examples of National parks and their management systems. Yellowstone area in the US and Yakushima area in Japan are iconic National Park areas. Each of those parks have different climate, geology, geography, fauna and flora. However, both have a state of the 'National Park management system' and something precious act human beings try to preserve. From data survey, interview survey, and comparison on both areas, the following has been revealed. (1) The management systems are different, (2) Differences between the two systems are related to land systems, history, etc. (3) There are other kinds of conservation systems, not only the National Parks system. Since each country has its own circumstances, it does not make sense to create 'uniform standards' or 'common systems'. Organize comparisons more along the lines of a Nature Conservation system to deepen our understanding deeper and accommodate National park diversity.

Keywords: National park, Yellow stone, Yakushima, Conservation and Utilization

INTRODUCTION

More than 150 countries have a National Park System [1]. The National Park System conserves many of the country's outstanding landscapes and precious nature. The Nepalese side of the world's highest mountain, Mt. Everest is designated as Sagarmatha National Park. Africa's highest mountain is in Kilimanjaro National Park. North America's is Denali National Park, Australia's is Kosciuszko National Park and Europe's highest mountain, Mt. El Brace is in Prielbrusye National Park.

The National Park system is different in each country. U.S. has 59 National Parks, Australia has more than 500. The first National park among Japan's 34 was designated in 1934. On the other hand, it was in 2016, Three River Source National Park was designated in China as their first National Park, 144 years after Yellowstone.

Also the management systems and management authorities vary.

National Park Management System in the world can be divided into 2 types; Non-Exclusive type and Exclusive type [2].

In the case of the Non-Exclusive type, the park authority doesn't have the land ownership or land management power directly. UK, Japan, Korea are among the countries who adopt this type. Here, the park authority needs to put more priority on

cooperating with some other stake holders to manage the park.

With the Exclusive type, the park authority has power to manage all or most of the land. U.S., Canada, Tanzania are among the countries with this type. The park authority has total control exclusive power to manage the park.

In this full paper, comparison is done between Yellowstone National Park in U.S. as 'Exclusive type' and Yakushima National Park in Japan as 'Non-Exclusive type'. Both National Parks are included in Man and the Biosphere site (MAB Biosphere Reserve) and registered on the World Heritage List as the first ones in their respective countries by UNESCO.

UNESCO designated 27 MAB Biosphere Reserve site as first ones in the US in 1976. Among the first 27, 14 were withdrawn and only 13 remain as MAB Biosphere Reserves at this moment. UNESCO designated 4 sites as the first in Japan in 1980. UNESCO registered Yellowstone as Natural World Heritage in 1978 as the only one in the US. UNESCO registered Yakushima as a first one in Japan in 1993. Both areas are considered important areas from the aspect of the world nature network.

Both National Parks and the irrespective regions have high reputations and are recognized as successful examples of nature conservation and park management.

MATERIAL AND METHOD

This comparison was focused on the park management systems of Yellowstone National Park and Yakushima National Park.

These researches have been done through visiting parks, hearing from park rangers, checking website, papers and books.

Yellowstone National Park and Management of U.S. National Park

Yellowstone National Park is located in the Rocky Mountains in the U.S. (Wyoming, Montana, Idaho states; Latitude 44.42, Longitude -110.58). It was designated on March 1, 1872 as the U.S. first National Park (Also the first National Park in the world). The area covers to 8,983 km², the number of visitors in 2017 was 4,116,000. In 1976 it was registered as MAB Biosphere reserve, then in 1978 as Natural World Heritage site both as first ones in U.S. by UNESCO. This park was also listed as 'World Heritage in Danger' during 1995-2003 because of increasing tourists and invasive species. The management authority of this park is the U.S. National Park Service.

Yellowstone National Park is surrounded by Grand Teton National Park, Jhon.D. Rockefeller ,Jr. Memorial Parkway, 6 National Forests (Gallatin, Custer, Beaverhead-Deerlodge, Caribou-Targhee, Bridger-Teton, Shoshone; managed by the U.S. National Forest Service), 3 National Wild Life Refuges (National Elk Refuge, Red Rock Lakes, Grays Lake; managed by the U.S. Fish and Wildlife Service) . In the western U.S., the Bureau of Land Management manages a vast area (one eighth of the U.S.'s land), but not around Yellowstone National Park.

Yellowstone National Park has some specific natural features. This is an active volcanic area, and half of World Geysers are in Yellowstone National Park. There is a Continental Divide, which divides the river to the Pacific and to the Gulf of Mexico. Wolves were reintroduced into this area. Bison are still living in the wild, but the number of bison has been controlled [3][4].

Park Rangers are on duty in National Parks for nature conservation, visitor protection, visitor interpretation, facility management and so on. In Yellowstone National Park, approximately 780 Park Rangers are employed. Among them, 190 park rangers have regular life time employment [5]. Some law enforcement Park Rangers carry guns and have not only the authority to arrest, but also authority to

refer to local court.

At National Park in U.S. there are entry point gates where visitors pay an entrance fee, so for visitors it is clear where the National Park begins. Throughout the park the main roads are paved for visitors and parking areas are set at viewpoints or trailheads.

In National Parks forestry, mining, hunting and private commercial business activities are principally not allowed.

Yakushima National Park and Management of Japan National Park

Yakushima National Park is located in Yaku Island, South West Japan (Kagoshima Prefecture; Latitude 30.20, Longitude 130.30).

National Park law was introduced in 1931 and 8 parks were designated in 1934 in Japan.

Yakushima was incorporated with Kirishima National Park in 1969 and designated as Yakushima National Park independently in 2012. The area covers 245.66 km², the number of visitors in 2017 was 169,000. In 1981 it was registered as an MAB Biosphere reserve, then in 1993 part of the park was registered as Natural World Heritage site, registrations by UNESCO were first for Japan.

The Ministry of Environment in Japan manages the National Park as the park authority.

Yakushima National Park occupies approximately 45% of the land area of Yaku island. More than 85% of the National Park land property is National Forest which is managed by the Forestry Agency of Japan. The Ministry of Environment in Japan designated Wilderness areas, Gensei-Shizen-Kankyo Hozen-Chiiki, just beside Yakushima National Park as a precious area to be preserved.

Yakushima National Park also has some specific natural features. It's a small island of 541 km², but has a 1935m peak, so it's called 'a high peak standing by the sea'. The island is in middle of the flow of the Kuroshio currents, one of the world's largest ocean currents and receives a high level of precipitation. At the sea side, there is 4,500mm of precipitation, and at the mountain side, 10,000mm per year. Mountain peaks are subarctic, on the other hand the sea side areas are subtropical. In this region cedar trees grow slowly and live long, some cedar lives more than 2,000 years [6][7] .

Park Rangers are on duty in National Parks for nature conservation, visitor protection, visitor interpretation, facility management and so on. In Yakushima National Park, approximately 7 Park

Rangers are employed. Among them, 5 park rangers are employed on a full time basis. They are government officers. However they don't have authority to arrest and prosecute.

At National Parks in Japan there are no entrance gates. Visitors don't pay an entrance fee, so for visitors it is not clear where the National Park begins. Some people are living in the National Park and some people own land inside the National Park. Roads are used by both visitors and local people every day. Many roads are managed by local government, not by the park authority.

In the National Parks, forestry and some other business activities are possible with permissions. The Forest Agency of Japan is established for forestry mainly.

There are many differences between U.S. and Japan National Parks.

Table.1 Comparison of Yellowstone National Park and Yakushima National Park

	Yellow Stone National Park	Yakushima National Park
Park Authority	U.S. National Park Service	Ministry of Environment
Land Authority	U.S. National Park Service	Forestry Agency, Prefecture, Private, etc.
Designated	1st March 1872 as US and the World first National Park by President Ulysses S. Grant	Incorporated to Kirishima National Park in 1969 and designated independently in 2012
Original management Act	1894 Park Protection Act	1931 Natural Park Act
Visitors 2017	4,116,000	169,000
Area	8983km ²	541km ²
Number of Rangers	780	7 in Park Authority (60 in related)
MAB	1976 a first in U.S.	1981 a first in Japan
World Heritage	1978 a first in U.S.	1993 a first in Japan
Other related system inside the Park		Forest Ecosystem Reserve (National Forest), Special Natural Monument, Prefectural Management Area
Other related system around the park	National Forest, National Wild Life Refuge, National Park Way, National Park, Wilderness Area	Wilderness Area
Zoning in park	No	Yes

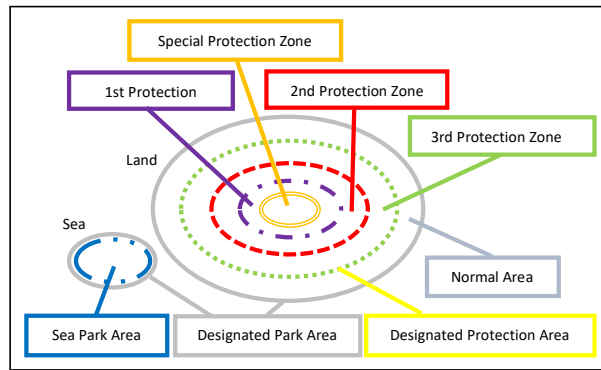


Fig.1 Concept of zoning system of National Park in Japan

Japan National Parks have a zoning system for the land area of the National Park System. The zones are Special Protection Zone, 1st Protection Zone, 2nd Protection Zone, 3rd Protection Zone and Normal Zone. Special Protection Zone is the core area where no one can do commercial activities.

Fig.1 shows the image of zoning system of National park in Japan. Special protection Zone and 1st Protection zone are often treated as the core area.

RESULTS

Comparison between Yellowstone National Park and Yakushima National Park from the prospective of park management revealed differences below.

Firstly, U.S. National Parks have only one authority for land and park management. Japan National Parks have some authority for land management and some authority for specific objective management inside the park.

Secondly, Japan National Parks have a small number of Park Rangers. However, National Parks are managed not only by the National Park authority in Japan. In Yakushima's case, the Forestry agency, Kagoshima Prefecture, Yaku Town and the Ministry of Environment are managing Yakushima National Park cooperatively. Total number of public officers who work for Yakushima National Park area is around 60 [8].

Thirdly, Japan National Park has the zoning system in National Park areas. The U.S. National Parks don't have such designated zoning system inside National Parks. However, this doesn't mean the U.S. Nature conservation system doesn't apply the concept of Core Zone and Buffer Zone.

The U.S. Nature Conservation system often regards National Park areas or National Monument areas as core preservation area. Additionally, National Forest, National Wild Life Refuge,

National Grass Land, National Conservation Area, National Sea Shore, National Lake Shore, State Park and some other management areas usually play a role as a buffer zone to protect the core zones. (Fig.2)

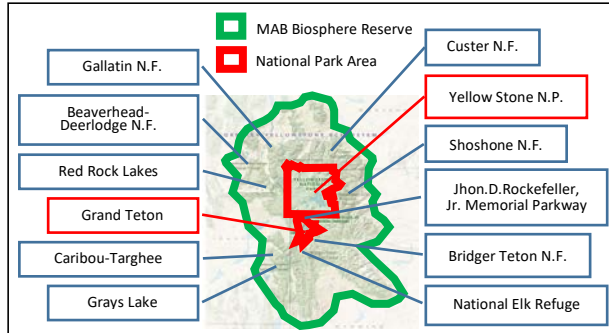


Fig2. Yellowstone National Park is surrounded by National Forests and National Wild Life Refuges.

Japan has Wilderness Areas designated by the Ministry of Environment under the Nature Conservation Act. In Japan, Wilderness areas are preserved more strictly than National Parks. U.S. also has Wilderness Area designated by the United States Congress under the Wilderness Act. Wilderness Areas are designated over National Forests, National Wild Life Refuges, National Monuments, lands managed by the Bureau of Land Management and some National Parks etc to encourage the management authority to prioritize preservation rather than utilization. The term Wilderness Area in U.S. and in Japan have a different meaning.

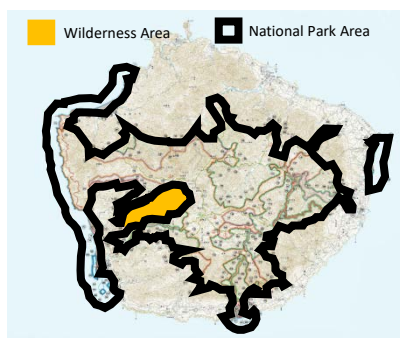


Fig.3 National Park Area and Wilderness Area in Yaku island.

The following charts show the difference of Management Authority and Management system of Yellowstone National Park area (Fig.4) and Yakushima National Park area (Fig.5).

Yellowstone Management system looks simple. One authority for one land. USFWS manage National Wild Life Refuge area. U.S. Forest Service manages National Forest area. National Park Service

manages National Park and Park Way area. These areas do not overlap

On the other hand, Yakushima Management System is multi layered and overlapping.

A place is preserved or managed as Special Natural Monument by the Ministry of Education, Culture, Sports, Science and Technology (MEXT), as Forest Ecosystem Reserve by the Forestry Agency and as National Park by the Ministry of Environment. Three Authorities for one land.

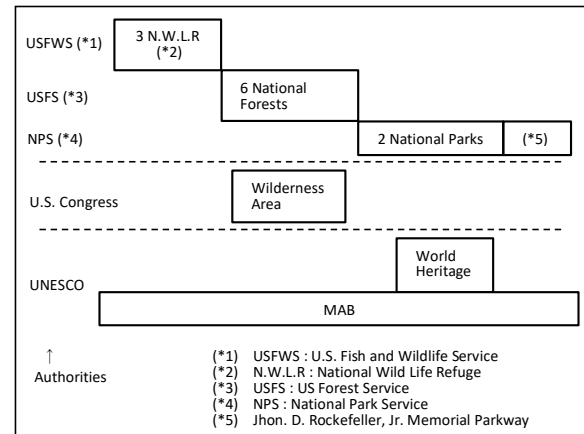


Fig.4 Yellowstone Management Authority and Management system

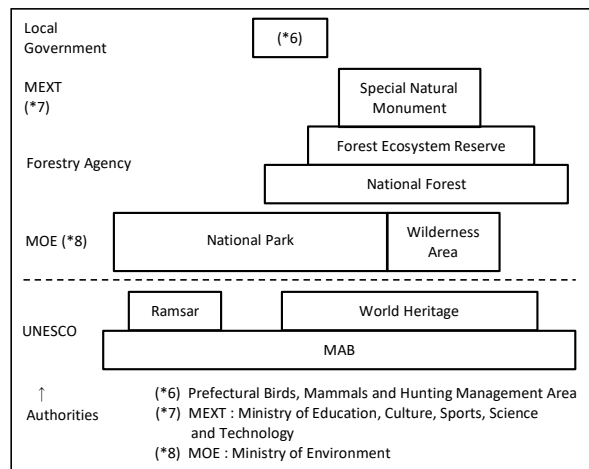


Fig.5 Yakushima Management Authority and Management system

DISCUSSION

The concept of National Park system was invented in U.S. and Japanese government imported National Park system from U.S. Where do the differences come from?

History of Yellowstone National Park

Before deepening discussion, following show some background by reviewing the history regarding management of both National Parks.

11000 years ago Native Americans began to hunt and fish in the region
 1848 Gold Rush started in West coast of U.S.
 1862 Home Stead Act by Abraham Lincoln
 1860s Explorations started
 1871 Ferdinand V. Hayden explored and wrote comprehensive reports
 1872 President Ulysses S. Grant sign 'The Act of Dedication' which created Yellow Stone National Park' as pleasure ground
 1870s-1880s Native American excluded from National Park
 1886 U.S. Army built Camp Sheridan at Mammoth Hot Spring -1916 Army management
 1894 Park Protection Act (6 important people including Theodore Roosevelt)
 1900 Lacy Act (Prosecute poachers)
 1916 U.S. National Park Service is created
 1917 National Park Service took over the management from Army
 1929 The first Park Area designation
 1929-1930s Great Depression
 1933-1942 CCC New Deal relief Agency made facilities in the Park
 1976 Registered UNESCO MAB Reserve
 1978 Registered UNESCO World Heritage site
 [3][4][5][10][11]

At the early stage in governance of the area, Yellowstone became a National Park and Native Americans who might have some right or claim to the land have been excluded from the area. Only the US Army and National Park Service have been the main authority in this area.

Yellowstone was designated for the purpose of being pleasure ground at the beginning. Civilian Conservation Corp (CCC) constructed park facilities such as tourist roads and visitor centers after the great depression.



Fig.6 Buffalos in Yellowstone National Park

History of Yakushima National Park

Small numbers of local people were resident in the area
 1595 Shimazu Clan direct management started
 1642 Forestry industry boomed in Yakushima
 1879 Land become a National property by the Land Tax Reform at Meiji Restoration
 1891 The Forest Management Force was established and prohibited local people from cutting trees
 1904-1920 Local people challenged in court, and lost
 1921 Yakushima Constitutional declaration. Local people are allowed to use Yakushima forest in a specific ways
 1931 Natural Park Act is established. (Yakushima is not National Park yet)
 1957 The Forestry Agency made management plan of Yakushima forestry. Then commercial forestry boomed again
 1964 Yakushima is incorporated into Kirishima National Park and Park is managed by Ministry of Health and Welfare. Land management controlled by the Forestry Agency.
 1966 The peak of forestry activity.
 1971 The Environment Agency is established and park management transferred.
 1975 Designated as Wilderness area
 1981 Registered on MAB Reserves
 1992 The Forest Agency designated Forest Ecosystem Reserve
 1993 Registered on World Nature Heritage
 2001 Ministry of Environment established.
 2005 Registered as a Ramsar Site (Nagata hama)
 2012 Independently the Ministry of Environment designated as Yakushima National Park
 [7][8] [9]

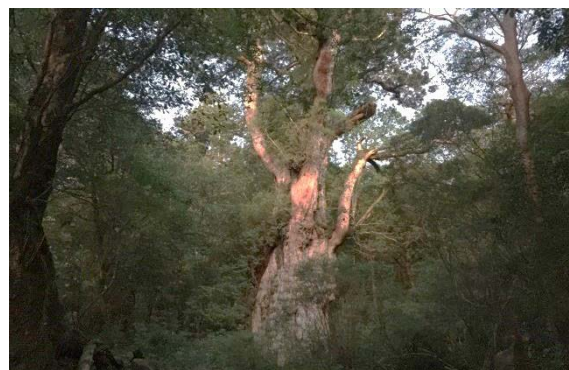


Fig.7 Joumon Sugi, Yaku Cider in Yakushima National Park

From the beginning in Japan, the National Park Authorities didn't have power over land management. The Forestry Agency had land management power and rights to timber. The management plan was made by the Forestry Agency originally in 1957.

And also local people had rights to use the forests based on 'Yakushima Constitutional declaration' of 1921.

Yakushima was incorporated into National park in 1964 after many things were confirmed. The Agency of Environment was established after the land use for forestry boomed.

Japan is small and populated, so there have been intensive utilization of land. Rights on land become complicated. For example, In Japan's Civil Code, 10 types of land rights are prescribed. Land occupying right, land ownership right, land cultivating right, land collateral right and so on.

Difference of National Park Management System

Japan introduced a National Park System from the U.S. and developed it along with Japanese society. Even though Japan's Park Authority didn't have direct management right on the land, they developed their own system and build a cooperate system from different aspects of preservation, conservation or utilization on a land. It leads to multi-layered system. And the park authority was faced with the necessity of having a zoning system in National Parks.

The power of authorities of U.S. National Parks and other nature conservation systems are mainly based on land management power. So at the National Parks, authorities can preserve without compromise core.

However, recently the different type of movement is occurring in U.S. National Park. Gateway Arch National Park was designated in 2018. The main attraction of the park is an artificial arch in St. Louis city in MISSOURI.

The system can be changed by the respective country's policy. It will be interesting to watch closely the future developments in U.S. National Parks.

CONCLUSION

This research made clear the difference of National Park Management System between U.S. and Japan.

(1) The National Park management systems of U.S. and Japan are different. U.S. National parks are managed by U.S. National Park Service. In Japan, management authorities are multi layered on a land

to conserve, so sometimes the decision makings take time and sometimes the authority can't decide without compromise.

(2) Differences between the two systems are related to land systems, history, etc. Intensive utilization of land in Japan invented zoning system over National Park management system.

(3) There are other kinds of conservation systems, not only the National Parks system. Both countries have Wilderness area, but they are different systems.

Conclusive Remarks

Authority of National Park management in U.S. is the National Park Service. The National Park Service manages the park based on land management power and laws. Outside of Parks in U.S., there are some other systems which conserve and utilize nature, such as National forest, National grass land, and so on. All systems are based on land management power. 4 major authorities are managing public land for Nature conservation and utilization at the federal level. These 4 authorities are U.S. National Park Service, U.S. National Forest Service, U.S. Fish and Wildlife Service and Bureau of Land Management.

Authorities of National Park in Japan are multi layered. The responsibilities are divided into multiple authorities and these authorities cooperate with each other to manage the park areas together.

Important decisions regarding park management in Japan can take time, more than U.S. National Parks. When the authorities have different interests on the same assets, conflict occurs. Often it is not clear who has the final decision power regarding the area or the issues.

However, sometimes the fact that time takes for decision making can work to prevent rapid developing. It can also allow impact of damage to be greater.

Comparisons between Yellowstone National Park and Yakushima National Park revealed differences and these differences are derived from history and land management power.

To manage a park, it's better for park authority to have exclusive power to manage. However, different from U.S. management, Japan has a complicated land right system and the governor's policy was for forestry for a long time. So currently the park authority doesn't have exclusive power to manage.

UK, Japan, Korea or some other counties adopt Non-Exclusive Park Management system. However,

their histories are also different, so comparison research including them can be meaningful.

A simple comparison of National Park Management Systems was not enough to comprehensively realize the difference of Management system regarding Nature Conservation and Utilization in both countries. Organizing comparisons focused more in the field of Nature Conservation systems will make our understanding deeper. Since each country has its own circumstances, it does not make sense to create 'uniform standards' or 'common systems'.

It is important for park authorities and stakeholders in some developing regions, where institutional design and management for nature conservation are not matured, and where the economy tends to take precedence over nature conservation, to have a common understanding based on accurate information.

ACKNOWLEDGEMENTS

We thank all the people of the Graduate School of Systems Engineering, Wakayama University, Mr. Tsutomu Asoshina, Ex-Manager of Nagano Nature Conservation Office and Mrs. Hiroko Kuchii, the president of Kailash Co., Ltd. for assistance in this survey.

REFERENCES

- [1] Hiroshi ONODERA, Munehiro ABE, Tsunao WATANABE, Keiji NAKAJIMA, Toshio TORII, Katsuji BANSO, Tamaki NOMURA, Michiharu KONO, Yuuki IWASA, Mitsuyuki OKAMOTO, Kei OSADA, Katsumi UEMATSU, Toshinori TANAKA, Kokuritsu Kouen Ron - Kokuritsu kouen no hachijuunen wo tou-Professionals Discussion on National Parks - review of 80 years history of National Park in Japan-, Nanpou Shinsha, Issue 2017, pp14
- [2] Toshinori TANAKA, National Park System in Japan as non-exclusive management, Yowai Chiikisei to shiten no nihon no kokuritu kouen seido, Hokkaido Journal of New Global Law and Policy, July 2012, pp6
- [3] Yellowstone Resources and Issues Handbook, U.S. Department of the Interior, National Park Service, Yellowstone National Park, pp.1-p104
- [4] Foundation Document Yellowstone National Park, U.S. Department of the Interior, National Park Service, 2014, pp.1-81
- [5] U.S. National Service, Yellow Stone National Park Website, <https://www.nps.gov/yell/index.htm>, 4th June 2020
- [6] Hisae TOKUMARU, Nature Conservation on Yakushima Island: Kagoshima Prefecture's Efforts, Global Environmental Research of Association of International Research Initiatives for Environmental Studies Vol.7 No.1, Issue 2003, pp.103-111
- [7] Yakusugi Museum, Yakusima Yakusugi Monogatari, Yaku Island Cedar Story, Yakusugi Museun, 2000, pp44-45
- [8] Masashi NORIHISA, 20 years of Yakushima the World Heritage, Report for a meeting by Kagoshima Prefecture, 2012, pp.3-9,21,26 <http://www.env.go.jp/nature/isan/kento/conf02/03/mat02.pdf>
- [9] Ministry of Environment, Yakushima Website, <http://www.env.go.jp/park/yakushima/>, 4th June 2020,
- [10] Shigeyuki OKAJIMA, Nature Conservation Movement in U.S., Amerika no Kankyou Hogo Undou, Iwanami Shinsho, Issue 1990, pp1-212
- [11] Alfred Runte, NATIONAL PARKS, TAYLOR TRADE PUBLISHING, 1947, pp29-41

DIVERSITY OF NATURE CONSERVATION SYSTEM IN EACH REGION AND CHALLENGE OF CREATING GLOBAL NATURE CONSERVATION SYSTEM

Takashi Kuchii¹, Hiroko Kuchii² and Atsushi Nakashima³

¹PhD ABD, Faculty of Systems Engineering, Wakayama University, Japan,

²President, Kailash Co., Ltd, Japan

³Professor, Faculty of Systems Engineering, Wakayama University, Japan

ABSTRACT

The National Park system is one of the oldest of a variety of Nature Conservation Systems or International Nature designation. Over 150 [1] countries have National Parks and the first National Park was born in 1872. National Parks are popular tourist attractions all over the world. Authorities of National Parks try to balance nature conservation with utilization. In some countries such as Tanzania, Nepal and Ecuador where Nature conservation systems are developing, the countermeasures to an increasing number of visitors has also become an urgent matter. They need to utilize such assets for their daily life. From experience and information by visiting, interviewing and reading books and full papers, this research makes points clear, such as differences among 'National Parks' in 10 countries and their related systems. Efforts have been made to grasp the National park from a global prospective by International organizations, but it requires more research and trials. Nature Conservation Systems including the National Park System are new to humans. We currently stand at the entrance of Nature Conservation from a Global view. Mutual international cooperation is necessary. It is also important to prioritize economic aspects creating a global standard for National Parks and Nature Conservation.

Keywords: National Park, IUCN Categories, Conservation and Utilization, Nature Conservation

INTRODUCTION

National Parks are popular tourist's attraction all over the world.

Kilimanjaro National Park is in Tanzania. Climbing Mt. Kilimanjaro is an interesting tour. On the way down from the top of Africa, a guide proposed to go on Safari for big cat hunting.

Galapagos National Park is in Ecuador. It is well known Darwin's theory of evolution. Endemic species such as Galápagos giant tortoise, Galapagos penguin, finches and more can be seen easily. To enter the Island, visitors must get 20USD permission before they leave for the Galapagos Islands and need to pay 100USD at the airport. Visitors must be clear of invasive species and pass through a disinfection mat on entry. Visitors can't look around the National Park without official guides.

Brijuni National Park in Croatia was a residence of Josip Broz Tito, the President of the Socialist Federal Republic of Yugoslavia. He welcomed many country leaders to the Brijuni and accepted many gifts of endangered animals and raised them in the island. Brijuni is a very beautiful island and good tourist attraction, but has no primeval nature.

Yellowstone National park was the only place in the U.S. where wild bison existed. Recently the authorities have controlled the numbers of bison. Yellowstone is popular as the first National Park in the world, which was designated in 1872.

China, a world leader in many ways, designated their first National Park in 2016. Beijing Great Wall National Park is popular tourist place and registered as World Cultural Heritage. Rapa Nui, Easter Island is designated as Chilean National Park and is also registered as World Cultural Heritage.

National Park systems vary in each country. Some try to preserve primitive nature and some try to protect monuments. Some National Parks put priority on nature preservation, some on visitor control and some on utilization for the tourist industry.

Annapurna range in Nepal is very significant place which has beautiful landscape. However, the Nepalese government conserves it not as 'National Park' but as 'Conservation Area'.

Mt. Aconcagua, the tallest in South America stands in Argentina and was designated as 'Provincial Park', not as 'National Park'.

In Australia they designate more than 600 National Parks and managed by local governments, not by National government.

Standards for designation of National Parks look different in each country.

National Park system is a system to balance conservation and utilization. However, each country has different National Park system and standards. International organization such as IUCN and other Conventions are trying to categorize or standardize regulation of National Parks and Nature

Conservation.

The overall objective of this paper is to grasp the existence of difference among 'National Parks' and present the issue regarding international designation and the necessity for more research and cooperation to categorize and make standards for National Parks, which are widely accepted in the world as the main system of Nature Conservation.

MATERIAL AND METHOD

Among National Parks which we actually visited and did some researches, we selected 10 National Parks from 10 countries, 3 from Asia, 1 from North America, 2 from South America, 1 from Oceania, 2 from Europe and 1 from Africa. Studies have been done by interview, book, papers and website research.

Many National Parks are registered or designated by international organizations. How international Organizations are trying to categorize, recognize and create definitions on National Parks is stated in following section.

Protected Area Categories

IUCN protected area management categories classify protected areas according to their management objectives. The categories are recognized by international bodies such as the United Nations and by many national governments as the global standard for defining and recording protected areas and as such are increasingly being incorporated into government legislation.

Category Ia: Strict Nature Reserve

To conserve regionally, nationally or globally outstanding ecosystems, species (occurrences or aggregations) and/or geodiversity features: these attributes will have been formed mostly or entirely by non-human forces and will be degraded or destroyed when subjected to all but very light human impact.

Category Ib: Wilderness Area

To protect the long-term ecological integrity of natural areas that are undisturbed by significant human activity, free of modern infrastructure and where natural forces and processes predominate, so that current and future generations have the opportunity to experience such areas.

Category II: National Park

To protect natural biodiversity along with its underlying ecological structure and supporting environmental processes, and to promote education and recreation.

Category III: Natural Monument or Feature

To protect specific outstanding natural features and their associated biodiversity and habitats.

Category IV: Habitat/Species Management Area

To maintain, conserve and restore species and habitats.

Category V: Protected Landscape/Seascape

To protect and sustain important landscapes/seascapes and the associated nature conservation and other values created by interactions with humans through traditional management practices.

Category VI: Protected area with sustainable use of natural resources

To protect natural ecosystems and use natural resources sustainably, when conservation and sustainable use can be mutually beneficial. [2]

World Natural Heritage

The United Nations Educational, Scientific and Cultural Organization (UNESCO) seek to encourage the identification, protection and preservation of cultural and natural heritage around the world considered to be of outstanding value to humanity. This is embodied in an international treaty called the Convention concerning the Protection of the World Cultural and Natural Heritage, adopted by UNESCO in 1972. 1121 properties are listed including 218 Nature Heritages and 39 mixed, as of June 2020. [3]

World Network of Biosphere Reserves

The World Network of Biosphere Reserves of the MAB Programme was launched in 1971 by UNESCO. The Network is one of the main international tools to develop and implement sustainable development approaches in a wide array of contexts. There are 701 biosphere reserves in 124 countries, including 21 trans-boundary sites. [4]

The Convention on Wetlands in Ramsar

The Convention on Wetlands is the intergovernmental treaty that provides the framework for the conservation and wise use of wetlands and their resources. The Convention was adopted in the Iranian city of Ramsar in 1971 and came into force in 1975. There are 2,331 Ramsar Sites in 170 countries, covering over 2,100,000 square kilometers. [5]

UNESCO Global Geoparks

UNESCO Global Geoparks (UGGp) began in 2001. They are single, unified geographical areas where sites and landscapes of international geological significance are managed with a holistic concept of protection, education and sustainable development. There are 147 UNESCO Global Geoparks within 41 Member States, covering a total area of 288,000 km². [6]

RESULTS AND DISCUSSION

This research on 10 National Parks was focused not only on 'Nature' but on international designation

and nature conservation systems.

In some countries, the National Park System is the main one to conserve nature. And in some countries, there are a range of conservation systems other than National Park.

Information as for the National Parks in developed countries was easier to obtain rather than in the case of developing countries.

Table.1 shows comparison among 10 National Parks in 10 countries. These National Parks are popular National Parks in each country and are big tourist attractions. They are designated not only as National Parks, but also as World Heritage, MAB or Ramsar. All 10 National Parks are assigned IUCN Categories. Some parks charge expensive entrance fees, and some are free of charge.

Table.1 Comparison of 10 National Parks in 10 countries

Park Name	Country	IUCN Categories	Designation Year	Entrance Fee	World Natural Heritage	MAB Reserve	Ramsar Site	Geoparks	Area	Visitor (Year)
Shiretoko	Japan	Ia	1964	Free	2005	-	-	-	386km ²	1,760,000 (2017)
Komodo	Indonesia	II	1980	18USD	1991	1977	-	-	1817km ²	45,000 (2010)
Chitwan	Nepal	II	1976	18USD	1984	-	2003	-	952km ²	37,097 (2016)
Lake district	U.K.	V	1951	Free	2017	-	1991	-	2362km ²	19,380,000 (2018)
Torransuo	Finland	II	1990	Free	-	-	2004	-	30km ²	17,900 (2013)
Kilimanjaro	Tanzania	II	1974	100USD over	1987	-	-	-	1,668km ²	52,000
Denali	U.S.	V	1917	15USD	-	1976	-	-	19,185.79 km ²	594,660 (2018)
Galapagos	Ecuador	II	1959	100USD	1979	1984	2002	-	7,970km ²	275000 (2018)
Los Glaciers	Argentina	II	1937	22USD	1981	-	-	-	7,269km ²	542,794 (2015)
Francois Peron	Australia	II	1993	Free	1991	-	-	-	525km ²	

Table.2 International designation and conservation system in 10 countries *() is heritage in danger

country	National Parks	World Nature Heritage	MAB Reserve	Ramsar site	Geoparks	Park Authority	First National Park	Other Nature Conservation system
Japan	34	4	10	52	9	Ministry of Environment	1934	Wilderness Area, Quasi-National Parks, Prefectural Natural Parks, Forest Ecosystem Reserve and so on.
Indonesia	54	4(1)	16	7	4	Ministry of Environment and Forestry	1980	3 Nature Reserves and over 100 Marine protected areas.
Nepal	12	2	0	10	0	Ministry of Forests and Environment	1973	1 Wildlife Reserve, 1 Hunting Reserve, 6 Conservation Areas, and 13 Buffer Zones, covering 23.39 % of the total country's land.
U.K.	15	6	7	175	7	15 own authority	1951	Area of Outstanding Natural Beauty (AONB) and some other protected area from aspects such as Biodiversity value, Geo diversity value or Scenic value.
Finland	40	1	2	49	1	Metsähallitus	1956	19 Strict nature reserves and 12 Wilderness Area.
Tanzania	22	4(1)	5	4	1	Tanzania National Parks (TANAPA)	1951	1 Conservation Area, 2 Game reserves, 2 Marine Park, 12 Forest Nature Reserves.
U.S.	62	13(1)	28	40	0	National Park Service	1872	Variety kinds of Nature Conservation system in Federal. Every State also has its own conservation systems.
Ecuador	11	2	7	19	1	Ministerio del Ambiente y Agua	1959	5 Nature Reserves of Ecological, Forest and Biological.
Argentina	37	5	15	23	0	Administración de Parques Nacionales	1934	Provincial protected area.
Australia	685	16	9	66	0	6 by National, others by states government	1879	Antarctic Specially Protected Areas, Commonwealth Marine reserves and many states managed reserves.

Table.2 shows nature conservation systems in the 10 countries. In 9 of these countries, the National Park Authority is National Governments. In Australia, the State Governments are in control.

The number of Ramsar sites in UK is the largest in the world. And the number of National Park in Australia is the largest in the world. The second oldest National Park in the world is the Royal National Park in Australia. All countries have their own nature conservation system.

Through this study, we found some interesting points. 10 National Parks are all categorized with IUCN categories. And IUCN Categories have a category II National Park, but some National Parks are categorized in Ib and V, not II. In some National Parks visitors need to pay to enter the park. Developing countries have tendency to charge the entry fees of National Parks. The U.S. has a wide range of nature conservation systems. So it seems the U.S. is passionate about nature conservation, but interestingly they don't have Geoparks as of June 2020.

Simplicity is important for global standards

These IUCN categories are decided based on application from authorities in each country. So categories can be strongly influenced by how they described the park on the application form. The Category Assessment is re-applicable. [7]

Among these 10 researched National parks, some National Parks are categorized in Ib and V, not II. The Denali National Park and The Lake District National Park are both categorized in V. However, comparing the visit experience, The Denali National Park and The Lake District National Park were very different.



Fig.1 Denali N.P.: IUCN Category V

Perhaps it would be better for IUCN to review the categories system so that National Parks can have multiple-categories. That multiple-category system is already adopted by UNESCO the World Natural Heritage adopted. Another option would be

to change the name of category II from 'National Park'.



Fig. 2 Lake District N.P.: IUCN Category V

If the Global standards or Systems are not simple, confusion can easily occur. IUCN have been playing and will play big roles in leading nature conservation in the world. So IUCN has responsibility to make their efforts easily understandable.

Local Economy and National Parks

In Tanzania, adjacent to National Parks, there are Game Reserves where recreational hunting occurs. Visitors can shoot a lion with rifles if they pay 10,000 USD. There are no fences between National Parks and Game Reserves. This is a surprising fact in 2020. They call Buffalos, leopards, lions, elephants and rhinoceros are promoted as the Big Five of hunting. Entrance fees and Activity fees are very important income especially for developing countries. It's easy to say for outsiders 'Don't kill wild animals', but things are not so easy.

The guides who proposed me big cat hunting said that he didn't want to kill lions but it was such big income and if he was successful he wouldn't have to work for some years.

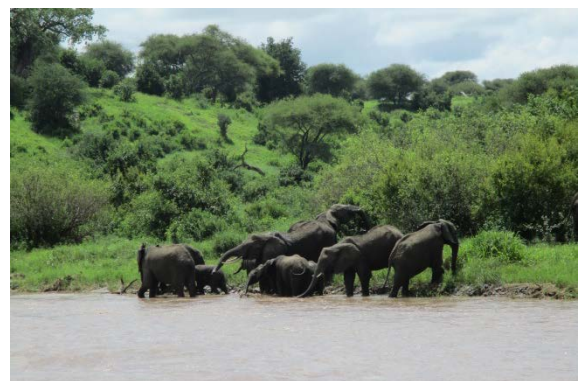


Fig. 3 Elephants in Tanzania Safari

To climb Mt. Kilimanjaro in Tanzania, a climber pays the park authority 810 USD for 6 nights 7 days climbing. Climbers need to pay for guides, porters, tent, food, etc, totally over 2,000USD + tips.

Tanzania's GDP per person is 1,029USD in 2018. A climber pays almost double the amount of one person's yearly income only for 7days. To climb Mt. Annapurna South in Nepal, visitors pay over 6,000 USD. The trek to the Annapurna Base Camp cost over 800 USD. Nepal's GDP per person is 1,034USD in 2018/ 2019.

For these countries, tourism is quite a large industry. For reference, GDP per person in U.S. is 59,531USD and in Japan is 39,303USD. [8]

International standards to conserve nature should pay attention to their local life.



Fig. 4 Annapurna Conservation Area

National Park spread widely

The first National Park was created in 1887 and spread over more than 150 countries. It spread very fast all over the world.

The Table.3 shows the number of countries which introduce National Park in each 10 years. (113 countries information were found through website research.)

It is less than 150 years since 'National Park' spread to 150 countries after the first designation in 1872. In the 1930s National Parks became popular. The World War II interrupted this. Many countries introduce National Parks between the 1950s and the 1980s. In recent years the IUCN hosts 'The World Parks Congress' to gather information and wisdom.

In the 1970s pollution and in the 1990s climate change became big issues for humans all over the world. National Park system was established before these issues. However, National Park is still a new concept in human history.

International organizations are trying to involve many bodies in Nature Conservation activity. However, usually the decision maker is each country

or national authority. Geoparks have 147 sites around the world. There are no Geoparks in The United States, former Soviet Union territory, India or Australia. The largest number of Geoparks is China's 33 out of the total 147. China designated their first National Park in 2016. There might be some special reason for this, not scientific reasons.

Table.3 First National Park Designation in Each Country

1870s	2	United States, Australia
1880s	2	Canada, New Zealand
1890s		
1900s	2	Namibia, Sweden
1910s	3	Switzerland, Mexico, Spain
1920s	7	Italy, Zambia, South Africa, Zimbabwe, Iceland, Algeria, Guyana
1930s	16	Chile, Argentina, Netherlands, Ireland, Poland, Burundi, Japan, Romania, India, Brazil, Uruguay, Venezuela, Sri Lanka, Greece, Belarus, Bolivia
1940s	7	Morocco, Kenya, Georgia, North Macedonia, Paraguay, Croatia, Slovakia
1950s	15	Tanzania, United Kingdom, Uganda, Montenegro, Côte d'Ivoire, Burkina Faso, Niger, Costa Rica, Guatemala, Finland, Dominican Republic, Madagascar, Turkey, Ethiopia, Ecuador
1960s	18	Mozambique, Serbia, Colombia, Thailand, Slovenia, Peru, Vietnam, Norway, Chad, Bulgaria, Czech Republic, France, Israel, Bosnia and Herzegovina, Malawi, Albania, South Korea, Botswana
1970s	18	Germany, Ghana, Estonia, Portugal, Pakistan, Hungary, Seychelles, Nepal, Latvia, Denmark, Iran, Lithuania, Dominica, Kyrgyzstan, Panama, Gambia, Nigeria, Nicaragua
1980s	14	Tunisia, Indonesia, Ukraine, Austria, Myanmar, Egypt, Russia, Haiti, Taiwan, Kazakhstan, Sierra Leone, Kosovo, Belize, Fiji
1990s	3	Tonga, Cambodia, Mauritius
2000s	5	Belgium, Gabon, Azerbaijan, Malta, Afghanistan
2010s	1	China

CONCLUSION

Rights of autonomy must be respected. However, Nature doesn't have a national border. Some Wild animals move around. They are trans-boundary. Forest fire in Australia in 2019 changed the surface color of Glaciers in New Zealand. Yellow sands from the Chinese deserts fly to Japan every year. Asian garbage drifted to seashore in America. All human beings are under the effect of global climate change.

At this moment, Nature Conservation is

dependent on each country's policy. When wild fires occurred in Brazil in 2019, many countries or bodies proposed support to the Brazil government. However, they were rejected. No one outside Brazil can force the Brazilian government to do something in Brazil. Recently it became more possible than before to pressure governments by gathering public opinion through SNS or other internet tools.

There is a definite necessity to cooperate over borders for the Nature Conservation. International organizations and nations are struggling. The history of International Nature Conservation is not old. Geoparks started in 2001, Ramsar in 1975, World Heritage in 1972, MAB programme in 1971 and National Park in 1872. IUCN organization was established in 1948 and UNESCO organization was established in 1946.

Human beings are at the beginning of Global Nature Conservation. It's better to make simple systems or standards for mutual understanding to involve many bodies.

To unite to one Nature Conservation system is impossible. Diversity is very highly valued when it comes to nature conservation. However, showing a simple standard or definition can be possible. Especially in the way of minimum standard regulations or mandatory standard regulations should be discussed and shared all over the world quickly. We all expect IUCN to play this important role in global society.

In the developing countries, there is a priority more on economic development or the tourism industry rather than Nature Conservation. Their daily life is important and Nature Conservation is also important. It's ideal to categorize or to make standards for Nature based on scientific knowledge. Developing countries need to utilize their national assets to create benefit as their countries developed. So it may be best to show some economic benefits of a global standard or global categorization for Nature Conservation alongside scientific knowledge.

It must be remembered that in the U.S. Yellowstone National Park was designated in 1872 as a pleasure ground. In Japan, there was an era when local governments wanted to have National Parks in their jurisdiction as tourism attractions, so in the 1940s Japan created Quasi-National Parks and Prefectural Nature Parks. Lions are hunted in Tanzania and Bison numbers are controlled in

Yellowstone.

Human beings stand at the entrance of Nature Conservation from Global view. More research should be done and more supporters should be involved, and systems and categories should be simple so that everyone can understand and comprehend.

ACKNOWLEDGEMENTS

We thank all the people of the Graduate School of Systems Engineering, Wakayama University for assistance in this survey.

REFERENCES

- [1] Hiroshi ONODERA, Munehiro ABE, Tsunao WATANABE, Keiji NAKAJIMA, Toshio TORII, Katsuji BANSHO, Tamaki NOMURA, Michiharu KONO, Yuuki IWASA, Mitsuyuki OKAMOTO, Kei OSADA, Katsumi UEMATSU, Toshinori TANAKA, Kokuritsu Kouen Ron - Kokuritsu kouen no hachijuunen wo tou- Professionals Discussion on National Parks - review of 80 years history of National Park in Japan-, Nanpou Shinsha, Issue 2017, pp14
- [2] IUCN, Protected Areas Website, <https://www.iucn.org/theme/protected-areas/about/protected-area-categories>, 12th June 2020
- [3] UNESCO, World Heritage Website, <https://whc.unesco.org/en/about/>, 12th June 2020
- [4] UNESCO, Biosphere Reserves Website, <https://en.unesco.org/biosphere/wnbr>, 12th June 2020
- [5] Ramsar Convention, Ramsar Website, <https://www.ramsar.org/>, 12th June 2020
- [6] UNESCO, UNESCO Global Geoparks Website, <http://www.unesco.org/new/en/natural-sciences/environment/earth-sciences/unesco-global-geoparks/>, 12th June 2020
- [7] Dudley Nigel, Shadie Peter, Stolton Sue, IUCN Guidelines for applying protected area management categories, IUCN, 2013, pp.1-31
- [8] Ministry of Foreign Affairs, World Area Website, <https://www.mofa.go.jp/mofaj/area/index.html>, 12th June 2020

THE ENVIRONMENTAL PARAMETERS CONTROLLING THE HABITAT OF INVASIVE ALIEN SPECIES, *SPARTINA* *ALTERNIFLORA* IDENTIFIED BY PREDICTIVE MODELING

Michiko Masuda¹, Testuya Morioka² and Fumitake Nishimura³

^{1,2}Faculty of Engineering, Nagoya Institute of Technology, Japan; ³ Faculty of Technology, Kyoto University, Japan

ABSTRACT

Spartina alterniflora introduced worldwide has impacted local Japanese ecosystems. Then the management methods of the species are seriously required. In 2019, the invasion of the species was reported at Aichi Prefecture, Japan. The vegetation of the species was grown up to 449 m² for 5 years. However, the relationship between the habitation of the species and environmental factors remains unclear. Therefore, we made a habitat prediction model using GLM (general linear model) to define the environment of the *S. alterniflora* habitat of Aichi Pref., incorporating data in 2019. That measured population density, location, ignition loss of physical environmental data, pH, NaCl concentration and altitude over the sea level by us. Our analysis showed that the standardization parameter altitude over the sea level was the main effect in the predictive model (estimate 4.158) and had the greatest absolute value. And the Wald value is significantly large (42.426). Secondary the reciprocal relationship expression between the altitude and pH was high value, 1.007. The species likes the habitat that altitude is high and pH is 7.1-7.3. For the GLM, we made the distribution for the species, the reappearance is well done. Then the avoidance of the species expansion, the bank of the tidal area should erase the higher riverbed.

Keywords: General Linear Model, Habitation, Invasive species, Management of Invasive Species

INTRODUCTION

Smooth cordgrass, *Spartina alterniflora* was ordinarily distributed at seashore at North America and the Gulf Coast of the Mexico. The species is a perennial plant at salt marsh and estuary. They occupied rapidly into the tidal zone and the environmental condition of the tidal zone has been changed by the species [1]. The vegetation of the species reduces the energy of the sea wave and helps stop the coastal erosion. In China and other countries planted the species that grew up in North Carolina, Georgia and Florida for the controlling the sea erosion [2]-[5]. An S. Q. *et al.* (2007) showed that introduced *S. alterniflora* in China was approximately 2.6 km² until 1985, and that it has increased more than 430 times after 15 years (1120 km²), in 2000 [6].

Thus, rapid invasion showed significant adverse impacts on natural ecosystems, this species listed by Lows *et al.* (2000) among the 100 most hazardous invasive species in the world [7]. In 2008, the species was detected at Aichi Prefecture, Japan and next year at Kumamoto Prefecture. The rapid expansion of the species changed the tidal area, salt marsh and creek area in Aichi Prefecture. About 3 years later the creek was filled by the plant and the water stream was prevented and the creek is almost dry land. The Ministry of the Environment declared the species an invasive alien species (LAS) on the Invasive Alien Species Act of Japan in 2014 [8]. In Aichi Prefecture,

the Ministry of Land, Infrastructure, Transport and Tourism, many companies and many volunteers removed the species from the salt marsh and creek from 2011 to 2013, then all the plant removed from this area. In 2018 the species was detected 50 km away from where *S. alterniflora* was previously discovered in Aichi Pref. From the Street View at Google map the invasion of the species was observed at the map in 2013. For 5 years the vegetation of the species has been widespread until 2018.

In order to prevent the invasion, it is necessary to monitor the invasion of the species, but it is impossible to do it because of the necessity to monitor a vast area along seashore. To conserve the local natural ecosystems we must detect rapidly in order to remove them with low cost. We, therefore, made a habitat prediction model using GLM (General linear models) to further define the environment of *S. alterniflora* habitat. The area of the invasion prediction is defined, we can easily find out the invasion of the species. In a protection plan of the salt marsh and tidal area ecosystem, analysis using GLM is carried out for relation about habitation density and environmental factors [9][10]. In this analysis, we considered the habitation restriction factors of the *S. alterniflora* in Japan.

MATERIALS AND METHODS

Study site

The place of the investigation was Horikawa river, located in center of Japan at Pacific Ocean side (Fig. 1). The creek is 1.08km for the agriculture drain. It has the gate to prevent sea water flood about 500m from the mouth of the river. The banks of the river are made of concrete brock that have higher river bed.

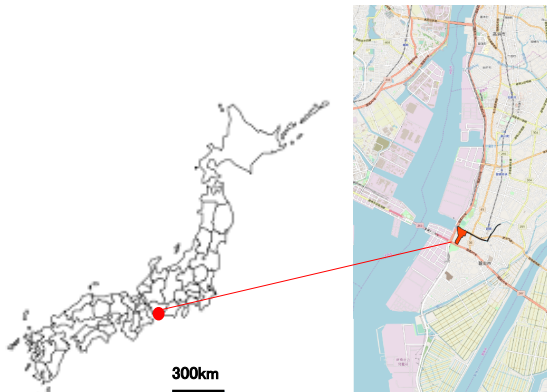


Fig. 1 Map of research locality

Study Plant

Spartina alterniflora commonly known as smooth cordgrass or oyster grass, is a salt-tolerant perennial grass native to the Atlantic Coast of North America. It is also found on the Pacific Coast of the United States, where it is considered an invasive species. *Spartina* species are among the few salt marshes plants that have been introduced outside their native range for erosion control due to their abilities to colonize open areas, stabilize eroding shorelines, and reclaim land.

The species displays considerable genetic and genotypic diversity, which affects growth and morphology, and ecological functions [11]. In the low intertidal zone, *S. alterniflora* is often the dominant species because of its high tolerance of frequently flooding and hypoxia conditions. Very few species can survive the ecological challenge of high salt and too little oxygen. Even though salt marsh productivity is very high, species diversity is very low. Salt marsh communities are dominated by a few species of halophytes, plants, that are adapted for growth and reproduction in a saline environment. The height of the species ranges from 100 to 200 cm along the creek banks. Recent evidence suggests that the commonly observed tall and short forms may be genetically distinct, numerous studies have demonstrated that the difference in productivity between forms is a function of environmental variables [12] [13].

Distribution Research

In order to know the distribution of the species in Horikawa river, we mapped the species using the 50m measure and GPS (Garmin) in 9th April, 2019, through the river. When we detect the species, we

made the quadrat (1m x 1m) and measured the vegetation cover percentage by photographs. And the reproduction of seeds was counted on 20th Sep. 2019. We set the quadrat (1m x 1m), and harvest all the reproduction stems. After harvest, all stems put into polyester bags with ethanol not to help expansion of the species. The number of seeds at each stems was counted at laboratory.

Environmental Factor Measurements

For the measurement of environmental factors, we set 130 plots (2m x 2m) in Fig. 2 for the distribution of the species is edge of the river. The water vein is right side. The samplings and measurement were carried out on 130 plots in summer (2nd Aug. to 20th Sep. in 2019). The four environmental parameters, altitude from sea level (*h*), pH (*ph*), loss on ignition (*IL*) and NaCl (*psu*) concentration were measured in each plot. The altitude from sea level was measured using measure pole for leveling. The water pH was measured pH meter (TOA DDK). Loss on ignition was measured by sampling mud (core sampling 5cm diameter 5 cm depth). After sampling the mud was into the incubator at 120°C for 2days in order to loss the water. After pretreatment, the weight was measured and they were burned in the muffle furnace (800°C 4days) to measure loss on ignition.

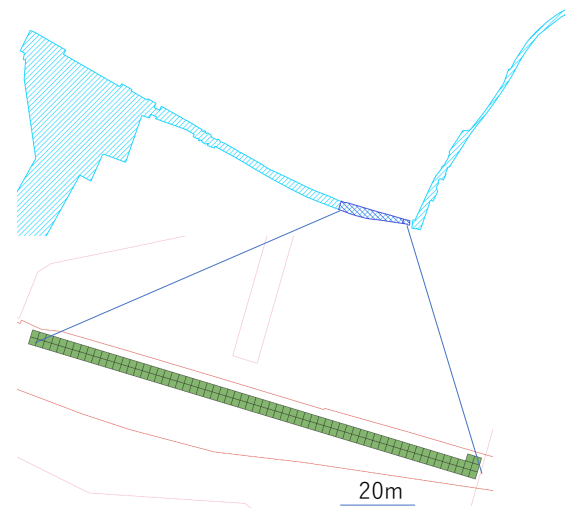


Fig. 2 Location of each plots.

Statistical Analysis

We performed analysis using GLM (using quick-R: correspondence analysis program) to elucidate habitation density of the *S. alterniflora* and its relationship to environmental factors. The Environmental parameters used in this study assumes four kinds of measurement data. The population of *S. alterniflora* at each plot was used the distribution research data.

In this study, the response is the population

density of *S. alterniflora*. Thus, we supposed that the probability distribution of the response obeyed negative binomial distribution. To explain the distribution of density, our model assumes the main effect term (when a factor acts alone) and an interaction term (when two factors interact). In the case of interaction terms, we performed centration for 2 variables beforehand and incorporated it as an explanatory variable. In total, the model assumes 6 variables of interaction between 2 factors as explanation variables, in addition to the main effect variable (4 variables). As a standard to evaluate the good model, we used by Akaike's information criterion (AIC).

RESULTS

Distribution

Distribution of *S. alterniflora* was shown in Fig. 3. The total area was 499 m², 93 populations were detected. The population was not always linked, 430m distant was observed between two next populations.

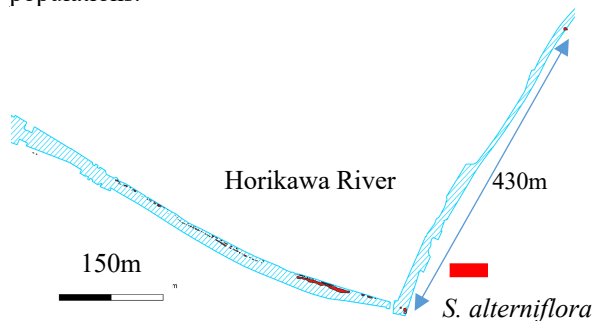


Fig. 3 Distribution of *S. alterniflora* in Horikawa River.

The number of seed reproduction at each shoot was shown in Fig. 4. There were 4 times differences about seed production at each shoot. The mean seed production was 19908/m².

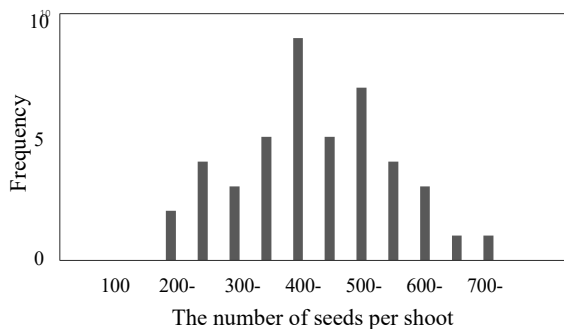


Fig. 4 The histogram of seed production at each shoot

Field Census

Fig. 5 showed the population density of the species. The unit of the range is vegetation cover area

percentage. The census was carried out from 0-100% vegetation cover at 130 plots.

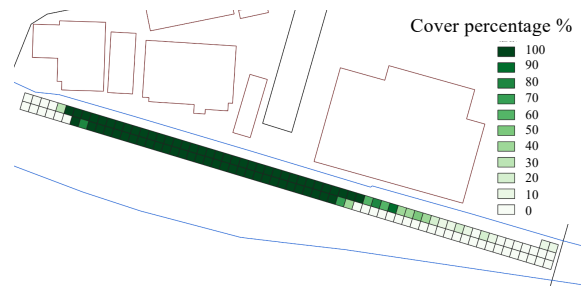


Fig. 5 Population density of *S. alterniflora* at modeling area in Horikawa River.

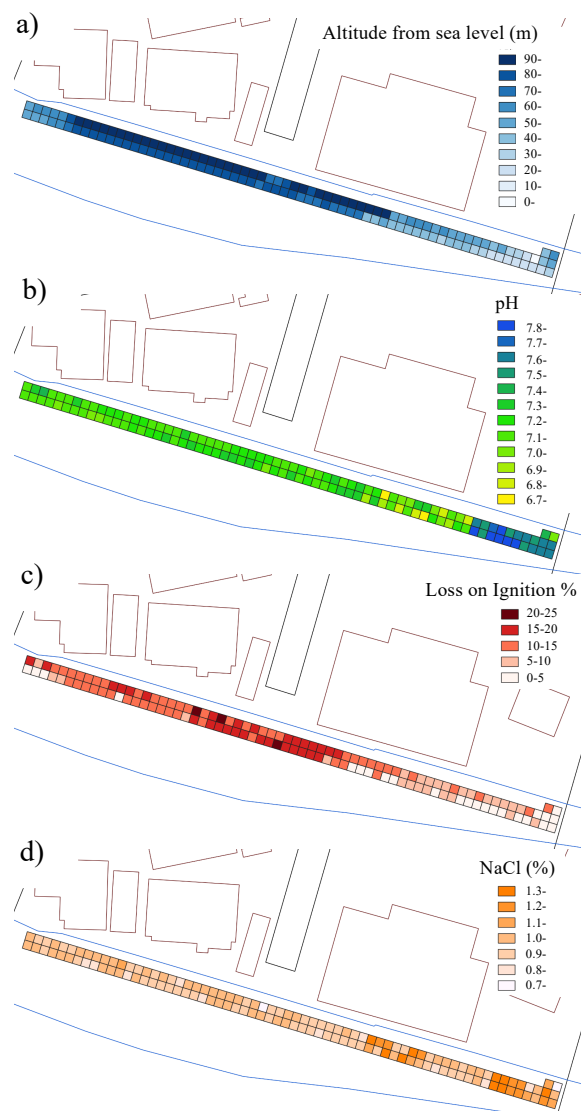


Fig. 6 Population density of *S. alterniflora* at modeling area in Horikawa River, a) The altitude from sea level, b) pH, c) The loss of ignition, d) NaCl percentage of water

Fig. 6 shows the environmental descriptors of

environmental factors in census area. The altitude from sea level is 0 to 102m. The edge of the river is higher because of higher river bed. The pH is ranged from 6.8 to 7.9. The higher level is observed the right side of the Fig. 6-b. The loss on ignition showed distributions at the center of the research areas (in Fig. 6-c). The distribution of NaCl ranges from 0.7% to 1.4%, the NaCl level is lower than sea water.

Fig. 7 showed the relationships between the vegetation percentage of the species and four parameters. Clear relationships between the vegetation cover percentage and four parameters were not observed.

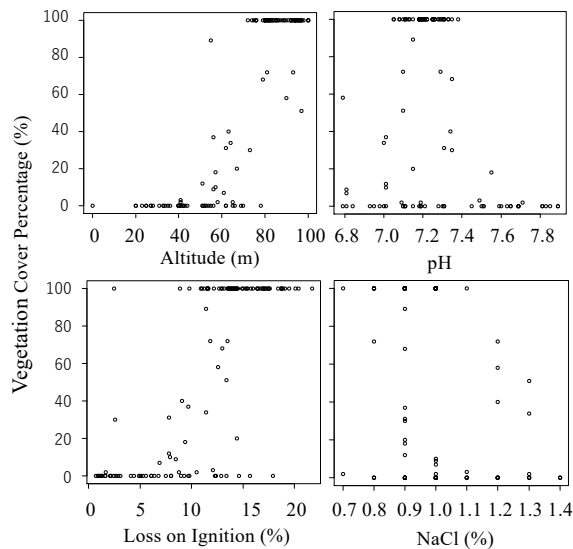


Fig. 7 The relationships between the vegetation cover percentage and four environmental parameters

The Habitation Model

A newly created *S. alterniflora* habitation model of this area found the main relationship effect variable on population density to be the standardization parameter the altitude from sea level, with a value of 4.158. This was the biggest value by the absolute value of all effects calculated. The Wald statistic value was 42.426 indicating significance. Secondary the standardized pH value was also high, 0.925. The Wald statistic value was 16.924. The statistics value of the model was shown in Table 1.

Fig. 8 shows the habitation model from the general linear model. The habitation model was made of parameters shown in Table 1, that is altitude from sea level (h), pH (ph), the loss of ignition (IL) and NaCl concentration (psu), the relationships parameters $h:ph$, $h:psu$, $ph:IL$, $ph:psu$ and $IL:psu$. Large parts of the calculated habitation model agree with the observed distribution data. Form the data the census and the expectation model, Fig. 9 shows there was a relationship between expected density and the observed density. In 92% of the plots the difference of the vegetation cover percentage is under 20

percentage.

Table 1 The new model analysis parameters by new general linear model

parameter	β	SE	Wald z value	P value
α	0.005	0.047	0.038	0.97
h	4.158	0.098	42.426	0.016***
ph	0.925	0.055	16.902	0.016***
IL	-0.446	0.071	-6.307	0.000***
psu	-0.772	0.062	-12.49	0.016***
$h:ph$	1.007	0.12	9.831	0.016***
$h:psu$	-0.554	0.090	-6.144	0.000***
$ph:IL$	-0.865	0.088	-9.790	0.016***
$ph:psu$	0.208	0.051	4.64	0.000***
$IL:psu$	-0.691	0.085	-8.116	0.000***

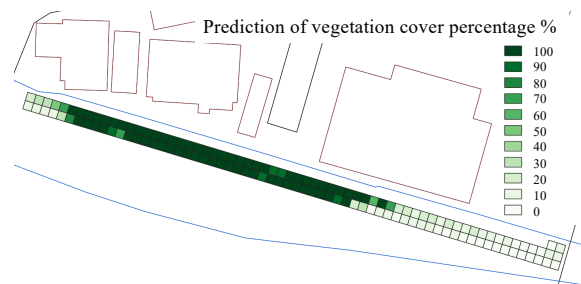


Fig. 8 Suitable habitation model of *S. alterniflora* predicted density. The unit of the range is percentage of vegetation cover

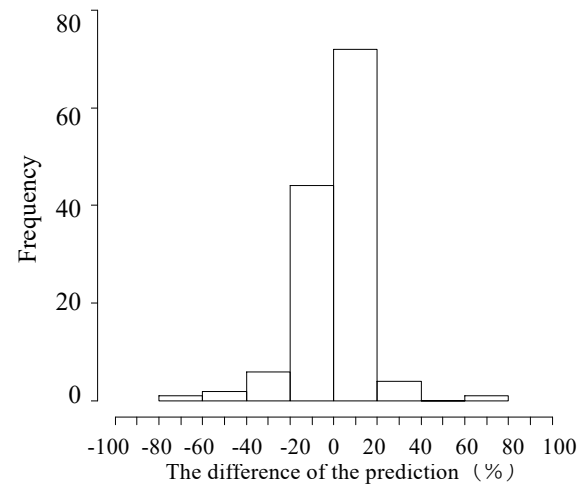


Fig. 9 The histogram is the differences of the population between the predicted value and the observation value.

DISCUSSION

From the data of Horikawa River, the area of *S. alterniflora* was dredged for stinking ooze in 2013. It

is expected the invasion of the species is almost 10 years ago. Then the species has been widespread in Aichi Pref. before 2013. The production of the seeds expected 5176 seeds/m² by our data, the total seed production of the area would be over 2500000 seeds. Hayasaka (2020) reported the percentage of the seeds is almost 60% then 1300000 seeds dispersed in 2020. The invasive ability is serious problems [14]. In 2016 5 km away from this area, single population was observed in Agui River, near sea shore. The population may be connected the Horikawa River population.

The Agui River population was easily removed because of the short time invasion, it was very lucky occasion. In Toyohashi City the cost of the removal was almost over 30 million yen. It is very important that we find out the population as soon as the invasion occurrence of the species for the cost reduction. Our Japanese land has long seashore line and over 40000 rivers. To find out the invasion rapidly, it is necessary to monitor rivers.

In this study we performed analysis based on four environmental parameters and the 6 relationships between two factors. Some studies used the GLM models and predicted the habitation of each species [15]-[18]. Each model used many environmental factors from 8 to 10. But our environmental factors were not so much, and the prediction was suite to the observation distribution. The most impact factor is the altitude from sea levels, secondary pH value. Both the parameters can be easily measured, so we can easily expect the invasion area of the species. The altitude from sea level is 1m and concrete bank is easily invaded by the species.

Though our model explains well the distribution, there are some problems about the environmental factor fluctuation. It was reported that *S. alterniflora* changes a tideland into the grassy plain and it has a big influence on a native species [19][20]. In our study site, five years have already passed after *S. alterniflora* invasion, and environmental condition may change. The sand and mud were gathered at the root of the plants and the height from sea level was changed. After the invasion, it is necessary to investigate the environmental factors at once. Now, the removal of the vegetation of the species and sludge was finished at October in 2019. The environmental factors are changed and the seeds was dispersed in 2018, maybe the invasion will be repeat again. For the improvement of our model, the investigation of the environmental parameters at early invasion stage is needed.

CONCLUSION

The following conclusions are drawn from the study.

- 1) General linear model is effective to more fully understand the habitation area of *S.*

alterniflora, invasive plant in sea shore area.

- 2) However, the species changed the environmental conditions, so more precise investigation needed in order to understand the invasion of the species.
- 3) From the predictive model, we were able to predict an invasive condition for the environmental factors of the future.

Then our monitoring site should be done below the site,

- 1) The altitude from the sea level is 0 to 1m and concrete banks should be monitored once a year.
- 2) Because of the different ecotypes, we should research another area using the general linear model.

ACKNOWLEDGMENTS

We send thanks to Prof. K. Serizawa who which cooperated with the research. We also thank to Mr. T. Hanai who helped us about field census. And we thank the member of our laboratory about the help the research.

REFERENCES

- [1] Barkworth M.E., Flora of North America North of Mexico, Vol. 25, Barkworth *et. al.* eds. Oxford University Press, 2003, pp. 240-250.
- [2] Xu H., Created environments voluntarily colonized by *Spartina alterniflora* in coastal Louisiana. Master's thesis of LSU 2230, 2006, https://digitalcommons.lsu.edu/gradschool_theses/2230/.
- [3] Wan S., Qin P., Liu J. and Zhou H., The positive and negative effects of exotic *Spartina alterniflora* in China. Ecological Engineering, Vol. 35, Issue 4, 2009, pp. 444-452.
- [4] Zhang R.S., Shen Y.M., Lu S.G., Wang Y.H., Li J.L. and Zhang Z.L., Formation of *Spartina alterniflora* salt marshes on the coast of Jiangsu Province, China. Ecological Engineering, Vol. 23, Issue 2, 2004, pp. 95-105.
- [5] Feng J., Shou J., Cui X., Ning C. Wu H., Zhu X. and Lin G., Effect of short-term invasion of *Spartina alterniflora* and the subsequent restoration of native mangroves on the soil organic carbon, nitrogen and phosphorus stock. Chemosphere, Vol. 184, 2017, pp. 774-783.
- [6] An S.Q., Gu B.H., Zhou C. and Wang Z., *Spartina* invasion in China: Implications for invasive species management and future research. Weed Research, Vol. 47, Issue 3, 2007, pp. 183-191.
- [7] Lowe S. Browne M. and Boudjelas S., 100 of the world's invasive alien species. Alien, Vol. 12, 2000, pp. 1-12.
- [8] Ministry of the Environment, List of regulated

- living organisms under the Invasive Alien Species Act, 2005, https://www.env.go.jp/nature/intro/2outline/list/fuka_plant.pdf
- [9] Christophe J., and Antoine G., Modelling the distribution of bats in relation to landscape structure in a temperate mountain environment. *Journal of Applied Ecology*, Vol. 38, Issue 6, 2001, pp.1169-1181.
- [10] Sugiyama Y., Nakamura M., Senda S., Masuda M., Environmental parameters controlling the habitat of the blackish water clam *Corbicula japonica* identified by the predictive modelling. *International Journal of GEOMATE*, Vol. 17, Issue 59, 2019, 68-73.
- [11] Proffitt C.E., Travis S.E. and Edwards K.R., genotype and elevation influence on *Spartina alterniflora* colonization and growth in a created salt marsh. *Ecological Applications*, Vol. 13, Issue 1, 2003, 180-192.
- [12] Mendelssohn I. A., and MacKEE K.L., *Spartina alterniflora* die-back in Louisiana time-course investigation of soil waterlogging effects. *Journal of Ecology*, Vol. 76, Issue 3, 1988, pp. 509-521.
- [13] Boyer K.E. and Zedler J. B., Nitrogen addition could shift plant community composition in a restored California salt marsh. *Restoration Ecology*, Vol. 7, Issue 1, 1999, pp.74-85.
- [14] Hayasaka D., Nakagawa M., Maebara Y., Kurazono T. and Hashimoto K., Seed germination characteristics of invasive *Spartina alterniflora* Loisel in Japan: implications for its effective management. *Scientific Reports* ISSN 2045-2322, Vol. 10, 2020, article number 2116.
- [15] Christophe J., and Antoine G., Modelling the distribution of bats in relation to landscape structure in a temperate mountain environment. *Journal of Applied Ecology*, Vol. 38, Issue 6, 2001, pp.1169-1181.
- [16] Minami N., Cleridy E. L., The Analysis of Data with Much Zero: Excessive Estimate of The Tendency by The Negative Clause 2 Regression Model. *Proceedings of the Institute of Statistical Mathematics*, Vol. 61, Issue 2, 2013, pp.271-287.
- [17] Zeileis A., Kleiber C., Jackman S., Regression Models for Count Data in R. *Journal of Statistical Software*, Vol. 27, Issue 8, 2008.
- [18] Silveira T.C.L., Gama A.M.S., Alves T.P. and Fontoura, N.F., Modeling habitat suitability of the invasive clam *Corbicula fluminea* in a Neotropical shallow lagoon, southern Brazil. *Braz. J. Biol.*, Vol. 76, No. 3, 2016, pp. 718-725.
- [19] Mooring M.T., Cooper A.W. and Seneca E.D., Seed germination response and evidence for height ecophenes in *Spartina alterniflora* from North Carolina. *American Journal of Botany*, Vol 58, Issue 1, 1971, pp.48-55.
- [20] Lindau C.W. and Hossener L.R., Substrate characterization of an experimental marsh and three natural marshes. *Soil Science Society of America Proceedings*, Vol. 45, Issue 3, 1981, pp. 1171-1176.

PARADIGM SHIFT IN NATURAL RESOURCES AND ENERGY POLICIES

Hisatoshi Tanaka¹, Atsushi Nakashima² and Nabil Maghrebi³

¹Graduate School of Systems Engineering, Wakayama University, Japan

²Wakayama University, Japan

³Wakayama University, Japan

ABSTRACT

Looking back at Japan's period of rapid economic growth (1955-1973), it is clear that it has much in common with the current situation in emerging and developing countries. In particular, natural resources and energy policies, which are essential for social and economic development, seem to be lacking in many developing countries, in very similar way to what Japan experienced before its shift toward economic modernization and industrialization without natural resources. It is clear that resources management and energy policy require the existence of long-term strategies. The issues of resource and energy security, economic efficiency and environmental protection are not necessarily mutually exclusive. However, it is a fundamental trilemma that is usually faced by many resource and energy policymakers. Japan's economy has already plunged into a steady-state economy and it seems to be entangled in more than three decades of prolonged stagnation. This paper examines some aspects of the trilemma based on energy related research and policy materials. It is argued that a paradigm shift is important because future resources and energy policies may be unsustainable for industry and society if allowed to be pursued along uncertain and risky paths.

Keywords: Paradigm shift, Energy policies, Energy security, Economic efficiency, Environmental protection

INTRODUCTION

Today, the dramatic changes in the global environment, especially the problem of global warming and its solutions, are a common global challenge. It is undeniable that the background to this is deeply related to the resource and energy policies of emerging and developing countries that aim to catch up with the developed world. Meanwhile, developed countries, which have been degrading the global environment, are beginning to review their resource and energy policies to redesign their economic growth strategies to achieve a sustainable society [1].

After World War II, Japan, as a latecomer to industry, pushed forward to catch up with the developed nations and succeeded in economic growth [2]. The image of Japan then overlaps with that of today's emerging nations. On the contrary, today Japan, as one of the most developed countries, is being forced to work towards the realization of a sustainable society.

At the same time as shifting resource and energy policies, it is necessary to recognize that energy security, economics and environmental protection are three interrelated issues when considering the potential impact of the energy system on the environment [3]-[4]. This is a basic trilemma that many energies policymakers face on a regular basis. Therefore, there is an urgent need to redefine the

critical role of the public and private sectors in promoting basic research and applied technologies to meet the needs of society, including improving energy efficiency and raising awareness of energy education [5].

The purpose of this study is to re-examine the state of Japanese society during the period of rapid economic growth, and to redefine energy policy and identify issues to be addressed in order to promote technological innovation in an environmentally friendly manner. It is hoped that the results of this study will help emerging and developing countries to consider policies related to economic growth.

JAPANESE HIGH ECONOMIC GROWTH

Japan lost much of the country's economic base in World War II [6]. During the post-war reconstruction period, American-style capitalism was adopted in many fields in an effort to build a new industrial society [7]. As a result, many Japanese companies have converted their management methods, which they learned and developed from Germany after the Meiji era, to the American style. And a mass consumer society without initiative was born against the background of mass production, mass consumption and disposable culture [8].

During the period of rapid economic growth (1955-1973), when the foundations of Japan were laid, the country grew as an export-led economy using

cheap labor and a single exchange rate of ¥360 to the dollar as two weapons of international competitiveness [9]. In the process, the Japanese state also promoted an aggressive industrial promotion policy [10]–[11]. It could be described as a kind of trickle-down economy, where the wealth of the developed Western countries, the customers of Japanese companies, was the starting point for increasing the income of domestic workers through the circulation of capital and goods [12].

These were (1) strengthening the economic base by investing in modern capital equipment in key industries, (2) promoting exports, and (3) reinvesting profits back into the country [13]. The acquisition of valuable foreign currency has also enabled the country to import cheap oil from the Middle East and to change its main energy source from coal to oil [14]. This optimistic "use lots of cheap oil" energy policy lasted until the 1973 oil crisis [15].

As shown in Figure 1, the 1973 oil crisis was a turning point in energy conservation, especially in the industrial sector, and became. This promoted economic growth while reducing energy

consumption [16]. Meanwhile, energy consumption in the transport, household, business and other sectors is rising slowly. In the 1990s, energy-saving measures were implemented in the transportation sector and the effects of these measures can be clearly seen [17]–[18].

The household sector has remained largely unchanged since the beginning of the 21st century, mainly due to the increased energy efficiency of home appliances [19]. In addition, the downward trend since fiscal 2011 has been driven by the energy-saving orientation after the Great East Japan Earthquake (i.e., widespread use of LED light bulbs and the speed of change (such as the spread of energy-appliances) is accelerating. The growth in business and other sectors continued through 2007, with the tertiary sector showing significant growth. In addition, the global financial crisis has led to a noticeable decline since fiscal 2007. The sharp increase in the business and other sectors in 1990 was due to a change in the calculation method of the Comprehensive Energy Statistics.

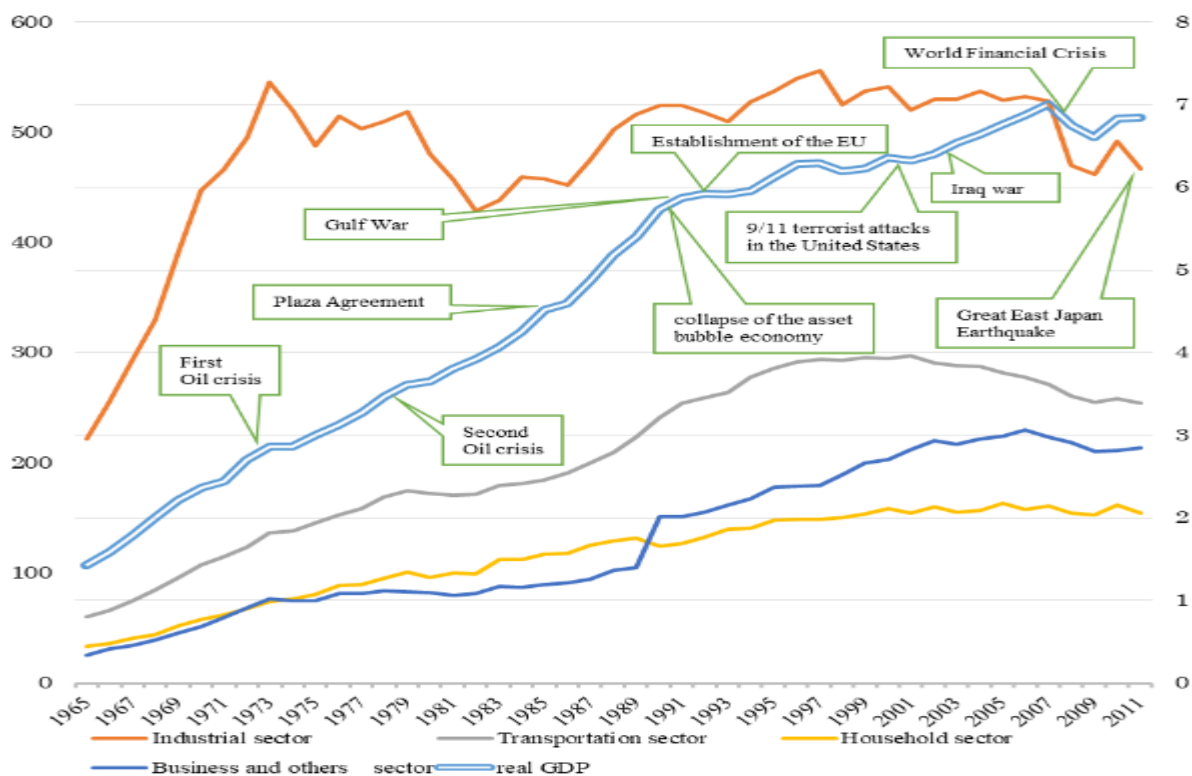


Fig. 1 Final energy consumption and real GDP

• Left-hand axis: Real GDP (unit: trillions of yen) • Right-hand axis: Magnitude of energy (unit: 10^{18} J)

Source: Compiled by the author based on data from the Agency for Natural Resources and Energy's Aggregate Energy Statistics, the Cabinet Office's National Accounts, and the Institute of Energy Economics, Japan (IEEJ) Energy and Economic Statistics Handbook.

Note: The method of calculation of "General Energy Statistics" has been changed since 1990.

The rapid economic growth of the 1960s, sparked

by the technological innovations of the post-1955 era,

led to two mainstream trends in the Japanese government and business community [20]-[21].

There are two main types of public-private partnerships: (1) centralization of power and (2) organization. This system of public-private partnerships will create an affluent and egalitarian image of the "100 million middle class" in Japanese society and It has become an escape route for the Japanese style management society and has narrowed the choices of the people, which is the essence of the times [22]. As a result, despite the fact that "there is a human life and there is an economy", "there is an economy and there is a human life" a reversed idea of "there is" has been created.

The essence of rapid economic growth is that the entire population is working towards the goal of creating "prosperity" as envisioned by the government. It was a matter of pushing forward. On the one hand, the occurrence of external diseconomies was noted early on, but any criticism was rather silenced for the sake of economic prosperity [23].

EXTERNAL DISECONOMIES

From the 1960s to the 1970s, a number of social contradictions erupted in Japan, including the problem of pollution [24]. This was the result of a national policy that prioritized industrial growth above all else as a latecomer to capitalism, a stove-piped administration that wanted to protect the interests of ministries and agencies, and a value system that emphasized the pursuit of corporate profits and the disposable income of the people [25].

Resource and energy policies, which are essential for economic growth, are strongly influenced by the nature of a country's administration. In other words, in a democracy where the people can choose their own government, we have a serious problem of environmental destruction. Based on this, the way in which people choose to solve social, economic and environmental problems depends on which government they choose.

The Ministry of International Trade and Industry (now the Ministry of Economy, Trade and Industry) provided administrative guidance for the economic growth at that time. The Ministry of Trade and Industry (MITI) guided the Japanese economy with policies that were appropriate to the economic conditions of the time. At the same time, the existence of an intermediary organization (industrial association) that links the ministry and business community facilitated energy policy implementation.

For example, the Ministry of International Trade and Industry (now the Ministry of Economy, Trade and Industry) enacted a law to promote the automotive parts industry as an important industry development measure. However, because environmental considerations are reflected in market

competitiveness and market prices, there has been little awareness of the importance of investing in the environment. It was not until the end of the period of high economic growth that the failure to take care of the environment and manage the crisis had a serious impact on the structure of the industry and market value, which would bounce back on the survival of the company [26].

JAPAN'S NATURAL RESOURCES PROBLEMS

Japan faces significant resource problems as the natural result of the fact that it is almost impossible to acquire energy resources domestically. The reason for this is that both coal and oil reserves are small and unprofitable. There have been "self-developed oil fields" overseas in the past, in which Japanese oil development companies and trading companies have acquired concessions in overseas concessions and developed them. However, the small scale of investment has prevented it from taking the lead in acquiring resources, and as a result, many other countries As well as, it has always been at the mercy of American trends. As a result, because energy policy does not allow for the free drawing up of a long-term vision, the resources on the market are mainly purchased at spot prices, which tend to reflect demand, and are subject to changes in international conditions [27].

In 1955, at the beginning of Japan's rapid economic growth, hydroelectric power was the main source of electricity in Japan [28]. However, in order to meet the increasing demand for electricity in conjunction with economic growth, it was necessary to switch to thermal power generation. At the time, the lack of foreign currency prevented the importation of sufficient oil, and coal, which was less efficient at generating electricity [29].

As a result, there was a movement to take advantage of the "peaceful use of nuclear power" boom created by the United States to use nuclear power first before oil-fired power. Japan's nuclear power program began with the submission of a budget for nuclear research and development to the Diet in 1954 [30]. The Atomic Energy Basic Law was enacted as early as December 19 of the following year, in order to regulate the use of nuclear power [31]. As a result, the introduction of nuclear power generation in Japan was approved for the purpose of providing a stable and inexpensive supply of industrial power.

Meanwhile, at the end of the 1950s, most of Japan's local governments were absorbed in the long phase of economic growth and waves of labour migration toward urban cities that continued to drain local populations. The rate of modernization of local industries remained low, and some municipalities sought to attract a new industry to replace the

declining coal industry. In 1974, when Japan's research and development of nuclear power generation under the guidance of the United States progressed, the "Three Laws on Power Sources" were enacted. This has created a mechanism to subsidize municipalities that attract nuclear power plants. As a result, depopulated and financially strapped municipalities have become more aggressive in attracting nuclear power plants, including the Fukushima Daiichi nuclear power plant, which suffered an accident in March 2011 [32]. At the time, the slogan of the town of Futaba in Fukushima Prefecture, which invited the plant, was "Nuclear Power: Energy for a Brighter Future."

ENVIRONMENTAL INVESTMENT

Environmental issues are very much an economic issue. For example, in emissions trading, the environment is perceived as a market value and is material to trade. In other words, the environment itself began to form part of the value of the product. It is not the resources that are destroying the environment, but the economic behavior of the people who use them.

Within the current elemental technologies and measures, unless the mass-production and mass-consumption economy is changed, the resource neither the problem nor the environmental problem can be fundamentally solved. Moreover, it is impossible to solve environmental problems through economic rationality alone. This is because the economy is not just about productivity; there is also an economy in consumption. In order to solve environmental problems, there is a need to reform the consumer market and consumer awareness at the same time.

Figure 2 compares indicators of GDP production and energy consumption (supply) with major countries in 2018. Taking Japan as the base value of 1, we can look at the GDP production efficiency of other countries. A smaller value indicates a country's energy use and value creation efficiency. In order to balance the challenges of global economic growth and energy conservation, one option is to not only demand reductions from more efficient countries, but also to strongly demand improvements from less efficient countries.

When environmental issues are examined from a managerial perspective, it is possible to realize that there are indeed many environmental business opportunities. In the past, investment in environmental measures has been an economic burden for companies, but investment from technological innovation has it is a business opportunity. Today, environmental issues have become the basis for evaluating the SDGs and ESGs being considered in financial markets. It has become one of the most important management issues for

companies.

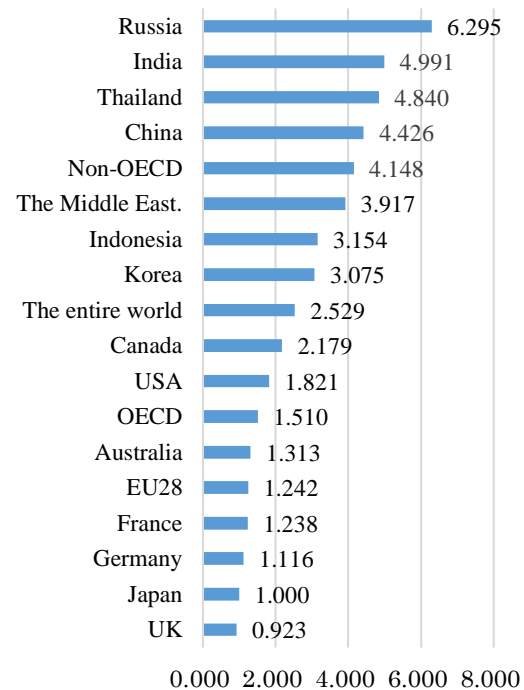


Fig. 2 Major countries in primary energy consumption per real GDP

Source: "Energy White Paper 2019" by the Ministry of Economy, Trade and Industry and the Agency for Natural Resources and Energy (June 7, 2019)

CONCLUSION

Japan has prospered for more than half a century since it became the world's second largest economy in 1968 [33]. But it has been slow to change its resource and energy policies, and fiscal conditions may only be part of the explanation. There has been rather little willingness to address the major international challenges, including the global environmental problems that the world is currently facing.

There is a fundamental trilemma in formulating an effective energy policy given the potential tradeoffs between energy security, environmental protection, and sustainable economic development. Rebuilding a sustainable society will require however a paradigm shift from high to sustainable economic growth, from unlimited greed to limited wants, and from environmentally harmful energy sources to new and renewable energy.

Thus, it is imperative to strengthen basic and applied research, and achieve technology advances in the energy sector in line with social policies, economic orientations, environmental initiatives. There is an urgent need to raise consumer awareness through better energy education, and redefine the

critical role of the public and private sectors in promoting responsible investment. Japan can then take the lead in simultaneously addressing the fundamental energy challenges, global environmental problems and sustainable social and economic development.

REFERENCES

- [1] Agency for Natural Resources and Energy, Energy Policies of Major Countries, Recent Developments and Challenges Faced, 2019.
- [2] Cabinet Office, Government of Japan, Economic White Paper, 1954-1973, 2019.
- [3] Agency for Natural Resources and Energy., Japan's Energy Problem, 2019.
- [4] G20 Ministerial Meeting on Energy Transition for Sustainable Growth and Global Environment.
- [5] Keidanren, Considering Energy, 2019.
- [6] Haruhito Takeda., Japanese Economic History, Yuhikaku, 2019.
- [7] Takahide Nakamura., A History of Showa Economy, Iwanami Seminar Books 17, 1986.
- [8] Modern Japanese Economy, The Second Term, Mass Consumption Society as History, What Was High Growth?, Keio University Press, 2019.
- [9] Takenori Inoki., A Postwar World Economic History from the Perspective of Freedom and Equality, Chuko Shinsho, 2009.
- [10] National Archives, The Development of High Growth Policy, 2020.
- [11] Tomotaka Kuwabara., Economic and Industrial Policy Bureau, Ministry of Economy, Trade and Industry, Changes in economic and industrial policy, 2015.
- [12] Edited by Keiji Fukao., Takashi Nakamura., and Masayuki Nakabayashi., Iwanami Koza, History of the Japanese Economy 5, Contemporary 1, From the Sino-Japanese War Period to the Period of Rapid Growth 1937-1972, 2018.
- [13] Shibata Shinya., Foundations of Political Economy, Sompusha, 2011, pp.25-131.
- [14] Agency for Natural Resources and Energy., Japan's 150-year history of energy, 2020.
- [15] Agency for Natural Resources and Energy and National Life and Economic Activity, 2019.
- [16] Agency for Natural Resources and Energy, What happens when the oil stops? ~Learning from History, A Risk to Japan's Energy Supply?, 2019.
- [17] Energy Efficiency. and Conservation Division., Agency for Natural Resources and Energy, on energy efficiency and conservation measures in the transportation sector, 2020.
- [18] Ministry of Land, Infrastructure, Transport and Tourism (MLIT Japan), Environment. carbon dioxide emissions in the transport sector, 2020.
- [19] JXTG Nippon Oil & Energy Corporation., Oil handbook, 2019.
- [20] Takenori Inoki., Japan's Modern Era.7, The Fruits of Economic Growth 1955-1972, Chuokoron Shinsha, 2002.
- [21] Haruto Takeda., A Reading of the National Income Doubling Plan, Japan Economic Review, 2014.
- [22] Haruto Takeda., The Japanese Economy in High Growth Period. What are the Conditions for High Growth?, Monozukuri Management Research Series, The University of Tokyo, 2011.
- [23] Environmental Restoration and Conservation Agency (ERCA). Air Pollution in the First Half of High Economic Growth 1945-1964, 2019.
- [24] Environmental Restoration and Conservation Agency (ERCA)., Rapid Economic Growth and the Intensification of Pollution 1965-1974,
- [25] Akio Watanabe., Japanese Modernity 8. Great Power Japan's Fluctuations 1972-, Chuo Koron Shinsha, 2000.
- [26] Environmental Restoration and Conservation Agency (ERCA)., Air Pollution after the Oil Crisis and Period of Stable Economic Growth, 1975-1984, 2019.
- [27] Agency for Natural Resources and Energy, Department of Natural Resources and Fuels. Efforts to acquire resources from overseas and develop domestic resources, 2019.
- [28] Agency for Natural Resources and Energy., Japan's 150-year history of energy, 2019.
- [29] JXTG Nippon Oil & Energy Corporation, Petroleum Handbook, 2019.
- [30] Agency for Natural Resources and Energy, Nuclear Power Generation, 2019.
- [31] Ministry of Internal Affairs and Communications, Nuclear Regulation Authority The Fundamental Law of Atomic Energy, 2019.
- [32] The Federation Electric Power Companies of Japan, Atomic Energy and Regional Societies, and the Three Methods of Power Supply Payment System, 2019.
- [33] Agency for Natural Resources and Energy., Japan's 150-year history of energy

TECHNOLOGICAL INNOVATION AND ESG INVESTMENT IN THE JAPANESE ENERGY SECTOR

Hisatoshi Tanaka¹, Atsushi Nakashima² and Nabil Maghrebi³

¹Graduate School of Systems Engineering, Wakayama University, Japan;

²Graduate School of Systems Engineering, Wakayama University, Japan;

³Graduate School of Economics, Wakayama University, Japan

ABSTRACT

In recent years, the global assessment of the economic activities of companies has become more severe. This is due to the existence of agreements on global warming measures such as the Kyoto Protocol of COP3 in 1997 and the Paris Agreement of COP21 in 2015, as well as the global sharing of the concept of the Sustainable Development Goals (SDGs) adopted at the UN Summit in 2015. In international financial markets, the term "sustainable finance" has become widespread in order to realize a sustainable society, and there is a gradual shift away from "investments solely for profit" toward "ESG investments for social contribution." In Japan as well there is a growing emphasis in the energy sector on renewable energy using natural resources. At the same time, the construction of energy technological systems that enable a virtuous cycle of "what is gained from nature is returned to nature" is underway. The objective of this paper is to identify and examine issues related to ESG investment in the energy sector, analyze some relevant data, and provide some recommendations for the future of ESG in Japan. The analytical evidence based on macroeconomic data related to the energy sector indicates that new ESG investment is essential for technological innovation in response to the environmental needs of future generations.

Keywords: Market economy, SDGs, ESG, TCFD

INTRODUCTION

The market economy aims at economic growth and social development through the functioning of the marketplace of supply and demand [1]. There is a mechanism in place to allocate resources to more productive industries [2]. An important part of that is preventing the waste of resources [3]. In addition, the decision on which type of resources to consume is essentially left to the free and voluntary actions of economic agents including households and companies [4].

In a market economy, it is the consumer who decides the actual allocation of resources, but it is there that the actions of individual economic agents are aggregated and lead to the allocation of resources in the economy as a whole [5]. On the other hand, while market economies adapt quickly to shocks, there is always a degree of instability built into them [6].

The real economy and society have grown significantly on a global scale. As a result, instability within existing market mechanisms has become apparent [7]. Stability has broken down in the industrial sector, especially in the developed economies, and one of the problems has been the negative impact on the environment that could not be solved by the market economy [8].

In Japan, coal-fired power plants are operating as one of the main energy infrastructures that support the

industrial society [9], [10]. However, with the realization of a low-carbon society and the emphasis on renewable and natural energy becoming an international trend, Japanese energy companies are being asked to adopt the SDGs and ESG perspectives as part of their management strategies [11], [12].

The purpose of this study is to identify and discuss issues related to ESG investment in the energy sector, analyze some relevant data, and provide some recommendations for the future of ESG in Japan. It is hoped that the evidence will be helpful to companies and investors who are considering the introduction of ESG in the future.

SDGS AND ESG CONCEPTS

Although the concepts of SDGs and ESG are similar, their perspectives are different [13]. The SDGs are global environmental and social goals adopted by the United Nations. The SDGs consist of 17 goals and 169 targets, each of which has an environmental it has a policy of alleviating social problems. For this reason, the SDGs are not a way of thinking that is confined to the company's profit opportunities or risk management. Pursuing a positive impact outside the company is in line with the purposes of the SDGs.

ESG stands for Environment, Social and Governance. The key to this is the consideration of the stakeholders surrounding the company.

Stakeholders include not only shareholders and investors, but also customers, employees, business partners, competitors, local communities and the environment.

Japanese companies have traditionally applied the SDGs framework to explain their CSR activities. Similarly, the SDGs have been incorporated into ESG activities and have become entrenched due to their affinity. ESG activities mean that a company can avoid conflict with its stakeholders as much as possible, while at the same time, it can help them to understand the interrelated social, economic and environmental challenges. It is an activity to meet the demands and expectations of the company. Therefore, companies that were actively engaged in the SDGs were inevitably considered to have taken ESG considerations into account in their economic activities. As a result, investors viewed companies working to solve environmental and social problems as more socially aligned than those that simply emphasized financial attractiveness, and they expected to see stability in earnings. However, given the original purpose of the SDGs, it is likely to be of limited application.

ESG INVESTMENT STRATEGIES

In today's corporate management, investors (mainly institutional investors) are looking to the SDGs and ESGs as "non-financial indicators" to measure corporate value [14]. As a result, companies cannot ignore these trends in their economic activities; rather, they are required to be actively involved [15].

Some companies, especially multinational corporations, are proactively incorporating the SDGs into both their business goals and management issues. There has been an emergence of a mindset that is trying to be embraced. In other words, companies involved in the SDGs have created opportunities to improve their position in the global market and to enter new markets by placing the SDGs at the center of their business models, rather than just as a social contribution. At the same time, ESG-conscious management is being incorporated into management strategies, as it would otherwise put firms at a disadvantage in market competition.

From the international perspective, data from the Global Sustainable Investment Alliance (GSIA) show that the share of ESG investment in global investment is increasing every year. Figure 1 shows ESG investment as a percentage of total investment in 2016. This shows that in the European region and Australia, ESG investment already accounts for more than 50% of total assets. Even in the U.S., where public opinion on the environment is rather divided, ESG investment accounts for more than 20% of the total. It is only when the US and Canada are put together that the aggregate ESG investment can

approach the level in Europe. On the other hand, there is a large gap of just over 3% in Japan, and investors in Japan are less interested in ESG than in Europe and the United States. There are indications that ESG investment is still in its infancy.

ESG FROM INVESTORS' PERSPECTIVE

Traditional investments have been profit-driven. However, after the global economic crisis of 2008, ESG has become more important, especially for institutional investors who manage pension funds [16]. ESG investment is a method of capital management that aims to reduce negative social externalities through "non-financial information" related to ESG as well as "financial information" such as profits, dividends and tangible assets [17].

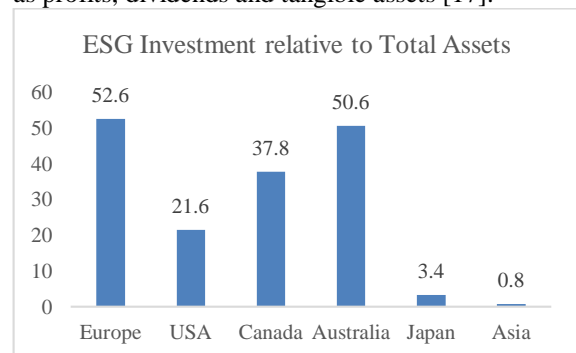


Fig. 1 ESG investment as a percentage of total assets (2016)

Source: data from GSIA Review 2016, prepared by the authors.

This may encourage behavioral changes in companies and investors. For example, diminishing long-term risks with environmental issues in mind, job opportunities through new revenue generation for companies increase, etc. As a result, it has the potential to enhance sustainable growth and broaden its contribution to society.

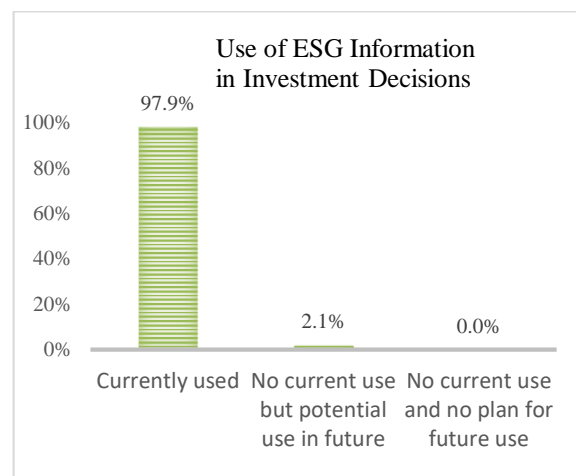


Fig.2 Use of ESG information in investment decisions

Source: Compiled by the author based on data from the Environmental Economics Office, Industrial Science and Technology Policy and Environment Bureau, Ministry of Economy, Trade and Industry.

Japan's Ministry of Economy, Trade and Industry (METI) issued in December 2019 a "Survey for Management Institutions on ESG Investment." It is possible to assess the efforts by managers and investors toward ESG investment based on the results of the survey. As shown in Figure 2, a large proportion (98%) of the sample of Japanese investment management institutions (48 respondent companies with a total of approximately ¥3988 trillion under management) do indeed use ESG information in their investment decisions.



Fig. 3 Japanese ESG Investment Standards

Source: Compiled by the authors based on data from the Environmental Economics Office, Industrial Science and Technology Policy and Environment Bureau, Ministry of Economy, Trade and Industry.

Figure 3 shows the ESG investment decisions in Japan. When using ESG information to make investment decisions, 93.8% of asset managers said they would use the Task Force for Climate-related Financial Disclosures (TCFD). Other international initiatives include the UN Principles for Responsible Investment (PRI) and the SDGs.

Figure 4 shows the number of institutions supporting TCFD. It is noted that Japan has the highest number of institutions in the world that support TCFD. With reference to Figure 5, the evidence suggests that only about 40% of the institutions regard TCFD as relevant for ESG investment purposes. In the future, the number of support organizations should be increased, and the information should be made public and its content enhanced.

CORPORATE ESG-PERSPECTIVES

In the era of globalization since 1990, the capitalist economy in the era of globalization has added the conditions of "energy and information" to the prerequisites of "people, money and goods," and it is a system that cannot function without these conditions constantly circulating [18]. As a result, the challenge for corporate management is how to get closer to the corporate value that stakeholders seek.

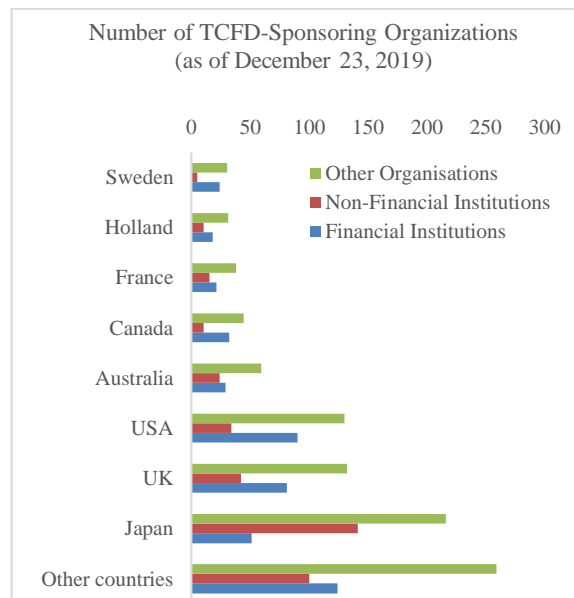


Fig. 4 Number of institutions supporting TCFD

Source: Compiled by the authors based on data from the Environmental Economics Office, Industrial Science and Technology Policy and Environment Bureau, Ministry of Economy, Trade and Industry.

For companies, a focus on ESG is an opportunity to be evaluated on the non-financial aspects of the future. Until now, companies have not considered environmental measures because they are not marketable [19]. However, environmental care and social contributions are now one of the most important business strategies, as they enhance a company's reputation and lead to increased corporate value and sustainable growth [20].

There is no denying that the impact of ESG valuations on corporate value is directly reflected in the share price of companies, which in turn has had a significant impact on the liquidity of direct funds available to them [21]. Investment markets are increasingly emphasizing the existence of social value and assessing firm performance from an ethical perspective [22].

ESG investors evaluate a company's ability to strengthen its operating base for sustainable growth. However, it is not the ultimate goal for companies to incorporate ESG indicators and ESG ratings. It's only

about long-term growth expectations and gaining profits.

In order for Japanese companies to be properly evaluated on a global scale, they need to simply disclose information and obtain an ESG rating. Companies need to show investors that they have long-term growth potential and that they can generate new profits.

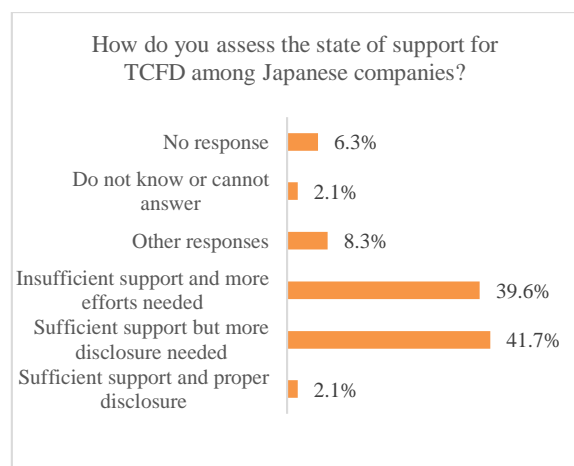


Fig. 5 Evaluation of Japanese companies' support for TCFD

Source: Compiled by the authors based on data from the Environmental Economics Office, Industrial Science and Technology Policy and Environment Bureau, Ministry of Economy, Trade and Industry.

In order for companies to use ESG information for further development of their sustainability management initiatives and for information disclosure, it is important to consider the essential significance of their ESG initiatives, clarify their priorities, and indicate their intentions. In doing so, it would be more effective if it could be streamlined with data-driven analysis and scoring possible.

Even if companies are making progress on ESG initiatives, the impact is not immediately apparent. However, if a company's unique risk factors surface, it could cause significant damage to the company's value. The company needs to pay attention to investor relations (IR), ESG compliance, and other information disclosure.

Until now, ESG measures have tended to be viewed as an extension of corporate social responsibility (CSR) activities [23]. In the future, corporate managers will need to consider ESG measures as a more important management issue.

ESG ASSESSMENT

Each evaluation organization uses its own indicators to assess a company's ESG efforts. For example, of the four ESG indicators designated by Japan's GPIF, the comprehensive ESG indicator FTSE Blossom Japan Index (FTSE) and MSCI Japan

ESG the Select Leaders Index (MSIC) has different evaluation criteria. What they have in common is the adoption of uniform standards worldwide.

Table 1 shows some of the items assessed by FTSE and MSIC. For example, the themes themselves are different in the assessment items on environment and governance. This has led to a discrepancy between the FTSE and MSCI ratings.

Table 1 Environment and Governance Assessment

ESG criteria	Assessment items	FTSE	MSCI
Environment	Climate Change	✓	✓
	Natural Resources		✓
	Pollution and Waste		✓
	Environmental Market		✓
	Opportunities		
	Biodiversity	✓	
	Pollution and Resource Use	✓	
	Water Security	✓	
	Supply Chain	✓	
	Corporate Governance	✓	✓
Governance	Corporate Behavior		✓
	Tax Transparency	✓	
	Risk Management	✓	
	Prevention of Decay	✓	

Source: prepared by the authors from FTSE and MSCI references. The checkmark symbol denotes the applicability of environmental or governance assessment criteria for the stock market indices.

Different ESG assessment bodies have different ESG assessment criteria, which means there is room for companies to get in that's what it means. Therefore, companies that desire to enhance their ESG evaluation should check in advance the items required by the evaluation organization and make sure that they make the appropriate efforts to disclose relevant information. There are no legal issues with this type of action, and it is not fraudulent. However, the company is required to be honest and accountable to investors and the market. Therefore, it is likely to take some time for many investors to change their perceptions about ESG.

CONCLUSION

As Japan has entered a steady-state economy, it is difficult to determine whether the ESG initiatives of Japanese firms are the manifest of transitory effects of competition or the result of structural changes in Japanese firms. Companies are free to evaluate the SDGs and ESGs in any way they wish. However, the choice between remaining in the existing investment market or entering the new ESG investment market is

already made by companies on behalf of investors and for the interest of investors.

In fact, ESG investment is gaining popularity among institutional investors around the world because the focus on the SDGs and ESGs by portfolio managers reduces the risk of deterioration in future corporate performance or business discontinuity, and it improves also long-term risk-adjusted returns. In promoting the SDGs and ESGs, international organizations and governments provide frameworks and guidelines for information disclosure. Particularly on the environmental front, with the adoption of the Paris Agreement, it is expected that the assessment of inadequate companies will become more severe.

As volatility is bound to rise in global equity markets in 2020 given the increased economic uncertainty, the SDGs and ESG, which are the focus of institutional investors, such as insurance companies and pension funds, who invest for the long term, can help them to have a consistent investment policy even in a rapidly changing market environment. ESG is no longer a merely ethical issue for companies but has become an important issue that cannot be ignored for the firm's business continuity and sustainable growth.

REFERENCES

- [1] Kikuo Iwata., *Studying Economics*, Chikuma Shobo, 1994, pp.27.
- [2] Kikuo Iwata., *Studying Economics*, Chikuma Shobo, 1994, pp.229.
- [3] Kikuo Iwata., *Studying Economics*, Chikuma Shobo, 1994, pp.229.
- [4] Iwao Nakatani., *Economics*, Shueisha, 2002, pp.178.
- [5] Motoshige Ito., *Hajimete no Keizaigaku*, Nihon Keizai Shimbun Publications Inc, Part I, 2004, pp.30.
- [6] Nihon Keizai Shimbun (ed.), *Easy Economics*, Nihon Keizai Shimbun, 2001, pp.20.
- [7] Asahi Noguchi. and Hideomi Tanaka., *Structural Reform Theory Misunderstood*, Toyo Keizai Shinpo Sha, 2001, pp.32.
- [8] Takeshi Nakano. and Keita Shibayama., *The True Story of Global Depression*, 2011, pp.85-88, pp.189ff.
- [9] Agency for Natural Resources and Energy, *Are we continuing to utilize coal-fired power generation? ~Energy Mix and Efforts to Achieve CO2 Reduction in FY2030*,
- [10] Agency for Natural Resources and Energy, *Basic Energy Plan*, 2019, pp. 26ff.
- [11] Cabinet Public Relations Office., *SDGs Action PLAN 2018 - Aiming to transmit Japan's SDG model in 2019 ~*,
- [12] Keidanren., *Achieving the SDGs through the Realization of Society 5.0*, 2018,
- [13] Mizuguchi Tsuyoshi., *ESG Investment. The Shape of New Capitalism*, in *Nihon Keizai Shimbun Publishing*, 2017.
- [14] Kenji Sawami., *The Latest Trends in Non-Financial Information Disclosure*, Information Sensor, Vol. 64, 2011, pp. 16-17.
- [15] Matsuo Takami., *Introduction System and Issues of Non-Financial Indicators in Performance Evaluation System of Strategic Thinking*, *Journal of National Economy*. 194.4, 2006, pp. 73-89.
- [16] Lukasz Mamica., *Pasquale Tridico., Economic Policy and the Financial Crisis*, Routledge, 2014, pp.6.
- [17] Bank of Japan., *Recent trends in ESG investment*, *Bank of Japan Review*, 2019, pp. 1-6.
- [18] Shinya Shibata., *Foundations of Political Economy*, Sompusha, 2011, pp.25-131.
- [19] Ministry of Economy, Trade and Industry (METI)., *Circulation and Economy Vision 2020*, pp. 5-43,
- [20] Ministry of the Environment., *Environment and Management*,
- [21] Daiwa Institute of Research Holdings Ltd., *Does an improved ESG rating affect stock prices?*, 2019, pp.1-9.
- [22] Daisuke Okamoto., Mitsuhiro Umezu., *Corporate Evaluation + Corporate Ethics Approach to CSR*, Keio University Press, 2006, 253pp.
- [23] Ministry of Internal Affairs and Communications, *Changes brought about by the spread of social media*, pp. 199- 214.

DESALINATION BEHAVIOR OF NATURAL ZEOLITE IN SEAWATER

* Fumika Sekihata¹, and Takaaki Wajima¹

¹ Department of Urban Environment Systems, Chiba University, Japan

ABSTRACT

In recent years, it has been considered to secure water and food using seawater desalination technology, and a new simple desalination material for reducing high concentration sodium chloride in seawater is required. In this study, desalting agents were prepared from natural zeolite with addition of calcined Ca-Fe type layered double hydroxide (LDH) to desalinate seawater for agricultural use. Mordenite type natural zeolite from Fukushima, Japan was used. The salinity and pH of seawater used in this study were 3.61% and 8.0, respectively. When more than 250 g/L of natural zeolite was added, the salinity decreased from about 3.56% to about 2.92% (reduction : about 18.0%) after stirring for 1 h. With higher dosage of calcined Ca-Fe LDH, the reduction time of salinity and the increase of pH became faster, while the reduction rate of salinity was almost same and pH value increased. When the mixture was used at the mixing ratio of natural zeolite and calcined Ca-Fe LDH was 5:4, the salinity decreased to 1.0% (reduction : about 70.0%) after stirring for 1 h, and the pH of the solution increased to 9.0 - 9.7. Radish sprouts could be harvested using seawater treated with a mixture of natural zeolite and calcined Ca-Fe LDH (5 : 4), while it was not possible to harvest using seawater and seawater treated with natural zeolite with lower addition of calcined Ca-Fe LDH.

Keywords: Natural Zeolite, Calcined Ca-Fe LDH, Desalination, Radish Sprouts

INTRODUCTION

In recent years, the demand for water has been increasing due to the increase of the world population, the improvement of economy and living standard. The total amount of water resources on the earth is about 1.3 billion km³. In water resources, seawater is about 97.5%, freshwater is about 2.5%, and human beings can only use about 0.01% of the total water resources due to the most freshwater present as glacier, cloud, vapor and so on. About 70% of fresh water for utilization of human being is used for agriculture. Therefore, the development of technology for obtaining agricultural water from high-salinity water, such as seawater, is under consideration to secure food. The main seawater desalination technologies are the multi-stage flash evaporation method and the reverse osmosis membrane method, which are methods for producing high-purity water used for securing drinking water or industrial water. Therefore, the production of agricultural water using these methods is expensive, and a simple new desalination method is desired. In previous studies, seawater was treated with calcined Mg-Al layered double hydroxide (LDH) and natural zeolite in two steps to obtain a solution that can be used for germination of radish sprouts from seawater [1-3] and we have succeeded in cultivating radish sprouts using seawater shaken for 5 h with a mixture of mordenite-type natural zeolite (produced in Iizaka, Fukushima Prefecture, Japan) and calcined Ca-Fe LDH (calcination at 500 °C) (mixing ratio of zeolite to LDH = 5 : 4) [4]. There is a possibility to

develop a new desalination material that reduces the high concentration of sodium chloride in seawater, causing salt damage to a level where crops can grow, using natural zeolite with calcined LDH. However, little information can be available on the desalination behaviors of natural zeolite with calcined Ca-Fe LDH.

In this study, the desalination behaviors of natural zeolite, calcined Ca-Fe LDH and the mixture of these were examined to produce the solution for plant growth from seawater.

EXPERIMENTAL

Samples

Mordenite-type natural zeolite obtained from Iizaka mine, Fukushima Prefecture, Japan was used as a natural zeolite sample. The exchangeable cations and cation exchange capacity of natural zeolite were shown in Table 1 [5,6].

Table 1 Exchangeable cations and cation exchange capacity of natural zeolite

Exchangeable cations (mmol/g)				Cation exchange capacity (mmol/g)
Na ⁺	K ⁺	Mg ²⁺	Ca ²⁺	
0.50	0.20	0.02	0.19	1.82

The calcined Ca-Fe LDH was prepared as follows. A mixed solution of Ca²⁺ and Fe³⁺ (Ca/Fe = 2) (200

mL) was prepared from 0.2 M CaCl_2 solution and 0.1 M FeCl_3 solution, and dropwise to 0.3 M NaCl solution (100 mL) at 4 mL/min. The stirring was carried out for 1 h while bubbling nitrogen gas, and the pH of the NaCl solution was maintained at 12.5 by dropping NaOH solution during the stirring. After stirring, the mixture was filtered, dried, and calcined in an electric furnace at 500°C for 1 h to obtain calcined Ca-Fe LDH. The mineralogical compositions of natural zeolite and calcined Ca-Fe LDH were shown in Fig.1.

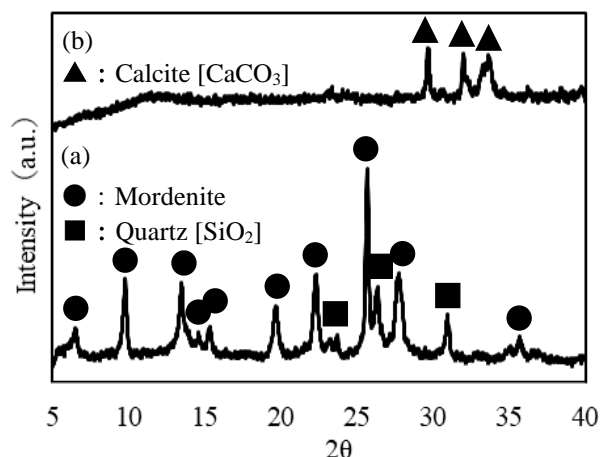


Fig. 1 XRD pattern of (a) natural zeolite and (b) calcined Ca-Fe LDH

Seawater used in this study was collected from the surface layer of Imari Bay, Saga prefecture, Japan. Chemical composition, salinity and pH of seawater were shown in Table 2.

Table 2 Chemical composition, salinity and pH of seawater

	Value
Content (mmol/L)	
SO_4^{2-}	34
Cl^-	805
Na^+	475
K^+	11
Mg^{2+}	71
Ca^{2+}	10
Fe^{3+}	0
Salinity(%)	3.46
pH	8.0

Desalination Ability

The desalting ability was evaluated as follows. Raw natural zeolite was added to 40 mL of seawater, and stirred for 0 - 2 h. Calcined Ca-Fe LDH was added to 40 mL of seawater, and shaken for 0 - 2 h.

The mixtures of natural zeolite (15 g) and calcined Ca-Fe LDH (1, 6, 12 g) were added to 40 mL of seawater, and stirring for a 0 - 24 h. After stirring or shaking, the solution is filtered, the pH of the filtrate is measured by pH meter (Horiba, F-72), salinity is measured by salinity meter (LAQUAact, ES-71), the concentrations of SO_4^{2-} , Cl^- , Na^+ , K^+ , Mg^{2+} and Ca^{2+} in the filtrate were measured with an ion chromatograph (Tosho, IC-2010) and Fe^{3+} content in the filtrate was determined using an atomic absorption spectrophotometer (Perkin Elmer, AAnalyst 200). The reduction rate of each ion in seawater after treatment was calculated using equation (1).

$$R = \frac{C_0 - C}{C_0} \times 100 \quad (1)$$

where R is reduction rate (%), C_0 is each ion concentration in initial solution (mg/L), and C is each ion concentration in the solution after treatment (mg/L). The residue was dried, and the structure was confirmed by a powder X-ray diffraction apparatus (Rigaku, MiniFlex 600).

Growth Test

Radish sprouts (30 seeds) were used for 10 days growth test. Seawater or seawater treated with the mixtures of natural zeolite and calcined Ca-Fe LDH (5 : 2, 5 : 4) was given by a spray every day, and germinations of radish sprouts were observed.

RESULT AND DISCUSSION

Seawater Desalination with Natural Zeolites

Figure 2 shows the salinity and pH of seawater during natural zeolite treatment with various dosages. When 250 - 500 g/L of natural zeolite was added, the salinity rapidly decreased within 15 minutes, and then be almost constant to about 3.0 % (R : about 15.5 - 19.1%). When 50 - 125 g/L of natural zeolite was added, the salinity gradually decreased to 3.11 - 3.16% for 60 minutes, and then be almost constant (R : 11.2 - 12.6%). The pH decreased from 8.0 of seawater to 5.0 - 7.5 in 60 minutes, and became almost constant. With increasing the dosage of natural zeolite, the decrease of pH was larger.

From the above results, when more than 250 g/L of natural zeolite was added, the reduction of salinity was almost same after stirring for 1 h. Therefore, 375 g/L of natural zeolite was used for the subsequent experimental condition.

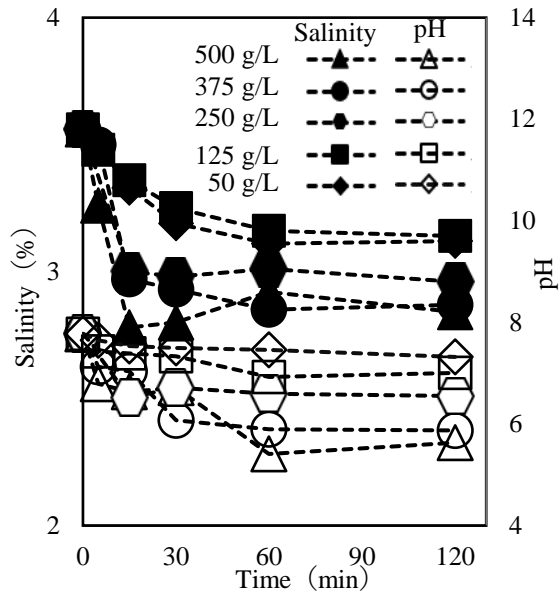


Fig. 2 Salinity and pH of seawater after treatment of natural zeolite

Figure 3 shows amounts of each ion in seawater during natural zeolite treatment. For 30 minutes-stirring, the Na^+ concentration decreased from 475 mmol/L to 274 mmol/L, and then became almost constant (R : about 40%), while the Ca^{2+} concentration increased from 10 mmol/L to 71 mmol/L for 30-minutes stirring. For 60-minutes stirring, Cl^- decreased from 805 mmol/L to 500 mmol/L, and then be almost constant (R : about 27%). The decrease of SO_4^{2-} , K^+ , and Mg^{2+} concentration and the increase of Fe^{3+} concentration were confirmed, and those amounts were very small compared with those of Cl^- , Na^+ and Ca^{2+} concentration. The reduction of SO_4^{2-} , K^+ and Mg^{2+} , were 37%, 50% and 37%, respectively.

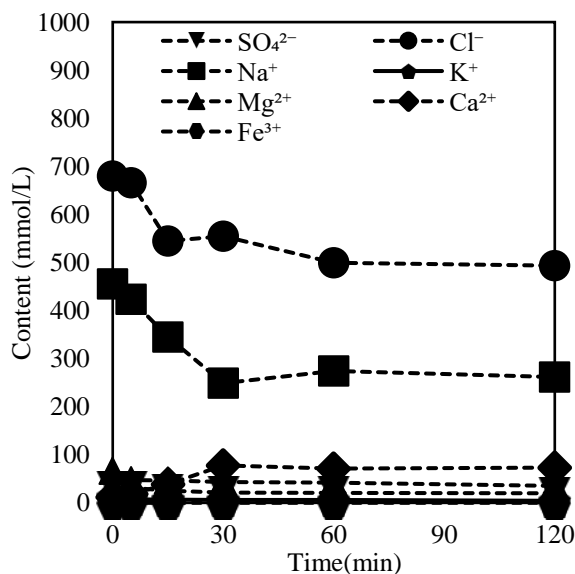


Fig. 3 Concentrations of each content in seawater after treatment of natural zeolite

Seawater Desalination with Calcined Ca-Fe LDH

Figure 4 shows the salinity and pH of seawater after calcined Ca-Fe LDH treatment. When 300 g/L of calcined Ca-Fe LDH was added, the salinity rapidly decreased from 3.61% to 3.26% (R : about 10%) in 10 minutes, then gradually increased to 3.49%, the pH increased from 8.0 to 10 in 5 minutes and then be almost constant. When 30 g/L of calcined Ca-Fe LDH was added, the salinity decreased to 3.2% after 30 minutes, then gradually increased, the pH increased from 8.0 to 8.8 in 30 minutes and then be almost constant. With higher dosage, the reduction time of salinity decreased and increase of pH became faster, while the reduction rate of salinity was almost same and pH value increased.

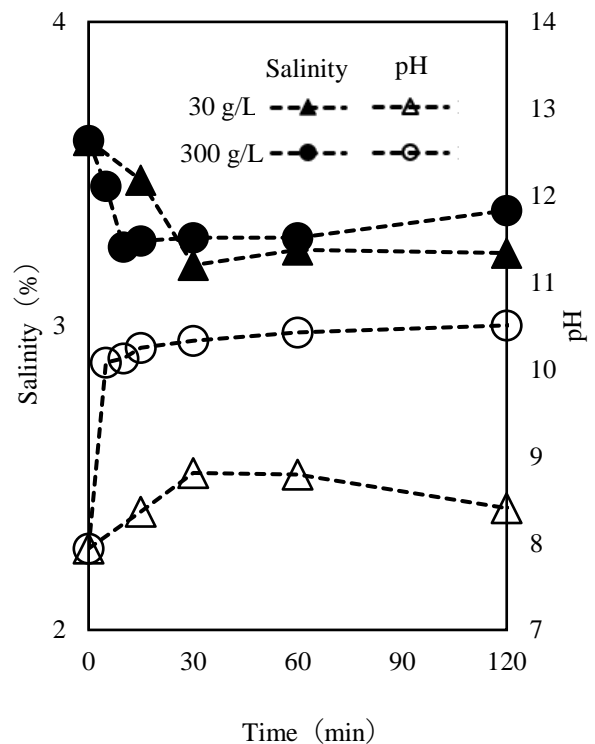


Fig. 4 Salinity and pH of seawater after treatment of calcined Ca-Fe LDH

Figure 5 shows amounts of each ion in seawater during treatment at 300 g/L dosage. The Na^+ concentration decreased from 475 mmol/L to 365 mmol/L in 10 minutes (R : about 23%), and became constant. The Cl^- concentration decreased from 805 mmol/L to 644 mmol/L in 10 minutes (R : about 9%), then was almost constant for 1 h and increased after 1 h. It is considered that Cl^- was captured in the calcined Ca-Fe LDH due to the reconstruction of Ca-Fe LDH (checked by XRD) and Ca-Fe LDH released the captured Cl^- as weak anion by ion exchange reaction of other anions, such as carbonate ion in the solution. The reduction rates of SO_4^{2-} , Mg^{2+} and K^+ in

the solution were about 26%, 24% and 17%, respectively. The Ca^{2+} concentration increased from 10 mmol/L to 333 mmol/L after 1-h treatment, and then became constant. The concentration of Fe^{3+} increased to 0.649 mmol/L within 1-h stirring. It is considered that Ca^{2+} and Fe^{3+} forming calcined Ca-Fe LDH were dissolved into seawater within 1 h.

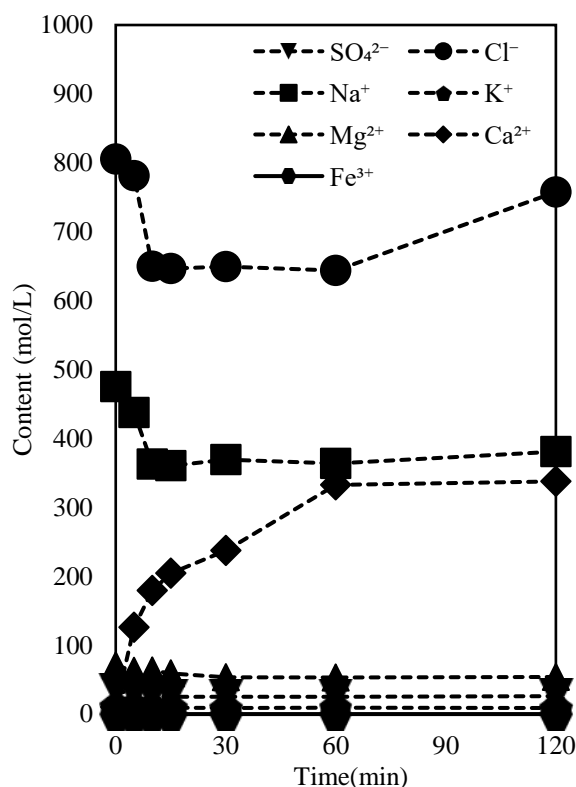


Fig. 5 Concentrations of each content in seawater after treatment of calcined Ca-Fe LDH

Seawater Desalination with a Mixture of Natural Zeolite and Calcined Ca-Fe LDH

In order to determine the effect of adding ratio of calcined Ca-Fe LDH to natural zeolite on seawater desalination, the mixtures of natural zeolite (15 g) and calcined Ca-Fe LDH (1, 6, 12 g) were prepared, and their desalination behaviors were investigated.

Figure 6 shows the salinity and pH of seawater during the treatment by each mixture. For all mixtures the salinity reduced within 1 h, and then be almost constant. The mixture of natural zeolite and calcined Ca-Fe LDH (1 g) reduced the salinity to about 2.46% (R : about 32%) and pH became 8.1 after 1-h treatment. The mixture of natural zeolite and calcined Ca-Fe LDH (6 g) reduced the salinity to about 2.1% (R : about 42%) and pH became 9.3 after 1-h treatment. When a mixture of natural zeolite and calcined Ca-Fe LDH (12 g) was added, the salinity decreased to about 1.0% (R : about 70%) after 1 h treatment, then remained constant thereafter, and the pH after the treatment was 9.7. From these results, the

salinity was reduced to less than 1 % at which the plant could be cultivated using the mixture of natural zeolite and calcined Ca-Fe LDH at the mixing ratio of natural zeolite to LDH = 5 : 4.

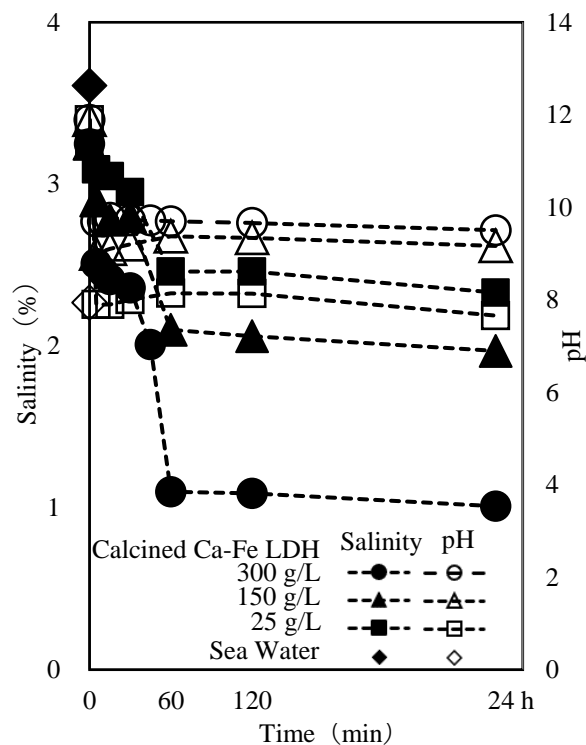


Fig. 6 Salinity and pH of seawater after treatment of the mixture of natural zeolite and calcined Ca-Fe LDH

Concentrations SO_4^{2-} , Cl^- , Na^+ , K^+ , Mg^{2+} , Ca^{2+} and Fe^{3+} in seawater after treatment with a mixture of 15 g of natural zeolite and various amounts of calcined Ca-Fe LDH were examined. The addition amount of calcined Ca-Fe LDH to seawater is (a) 1.0 g, (b) 6.0 g, and (c) 12.0 g.

Figure 7 shows amounts of each ion in seawater during the treatment using each mixture. In all cases, Cl^- and Na^+ were significantly reduced, SO_4^{2-} , K^+ and Mg^{2+} , which were much lower concentrations in seawater than Cl^- and Na^+ , were also reduced, and Ca^{2+} and Fe^{3+} increased. The concentrations of all ions became constant after 1 h stirring regardless of mixing ratio.

In the case of 1.0 g and 6.0 g, Na^+ and Cl^- decreased rapidly for 5 minutes and gradually decreased for 1 h. After 1 h, the concentrations of Cl^- and Na^+ were 441 mmol/L and 280 mmol/L at 1.0 g, and those were 366 mmol/L and 181 mmol/L at 6.0 g, respectively. At 12.0 g, the Cl^- and Na^+ concentrations decreased sharply for 5 minutes, and then gradually decreased to 226 mmol/L and 60 mmol/L, respectively. The concentration of Ca^{2+} in the solution after 1-h increased with increasing the LDH addition.

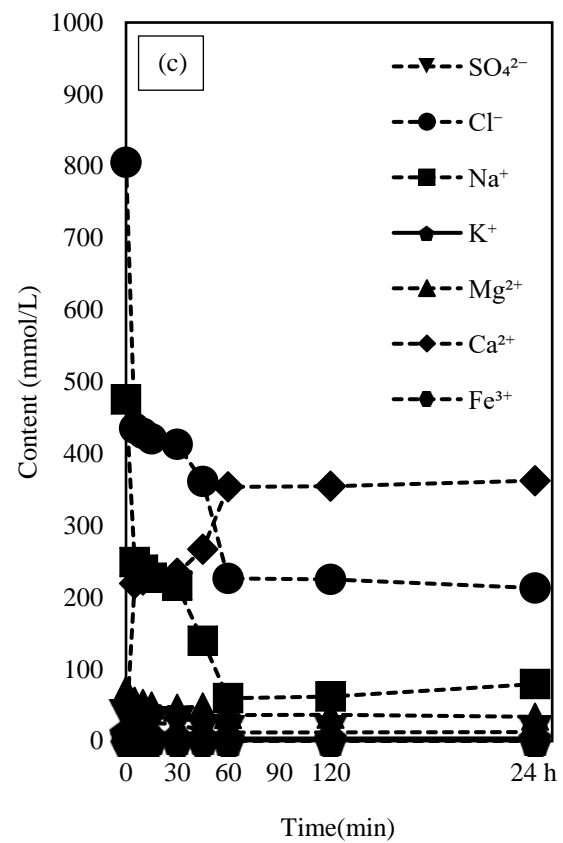
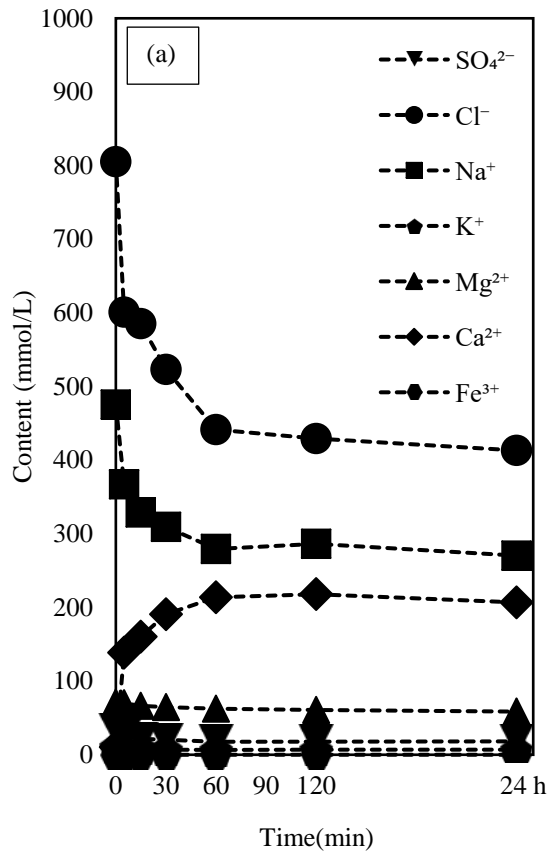
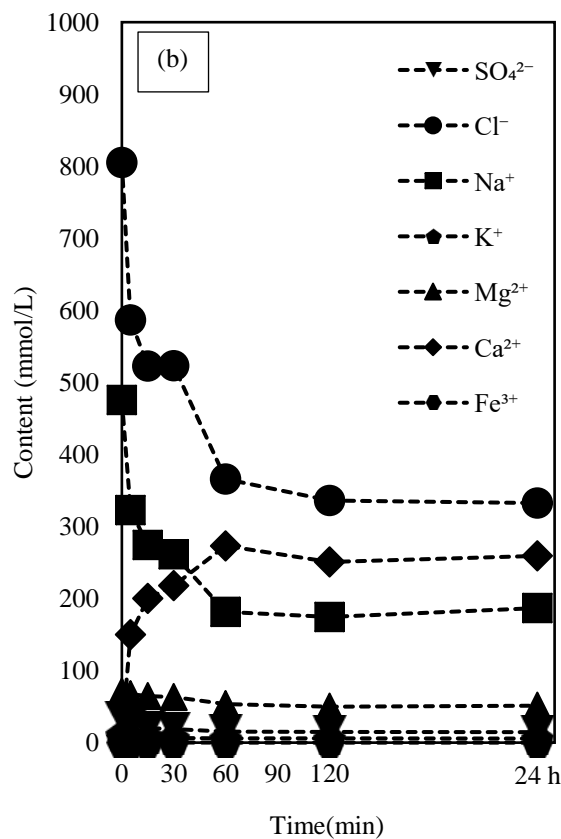


Fig. 7 Concentrations of each content in seawater after treatment of the mixture of natural zeolite and calcined Ca-Fe LDH of (a) 1.0 g, (b) 6.0 g and (c) 12.0g



When desalting seawater with natural zeolite and calcined Ca-Fe LDH, the concentrations of SO_4^{2-} , Cl^- , Na^+ , K^+ , Mg^{2+} decreased, and Ca^{2+} and Fe^{3+} increased. With increasing the LDH addition, these change is larger and the salinity of seawater decreases.

Cultivation of Radish Sprouts

Table 3 shows the ion contents, salinity and pH of (a) seawater, (b) seawater treated with the mixture of natural zeolite (15 g) and calcined Ca-Fe LDH (6 g) and (c) seawater treated with the mixture of natural zeolite (15 g) and calcined Ca-Fe LDH (12 g). It is noted that treatment time is 1 h.

By desalting with a mixture of natural zeolite and calcined Ca-Fe LDH, Cl^- and Na^+ were significantly reduced from seawater concentrations. In addition, the decrease rate increased as the amount of calcined Ca-Fe LDH added increased. The concentration of Ca^{2+} in the treated seawater increased as the amount of calcined Ca-Fe LDH added increased. Other SO_4^{2-} , K^+ and Mg^{2+} were much smaller than those of Cl^- and Na^+ , and with increasing calcined Ca-Fe LDH addition these contents decreased. Fe^{3+} concentration were zero regardless of the treatment.

Table. 3 Each ion concentration, salinity and pH of (a) the seawater and (b) the seawater after treatment of the mixture of the mixture of natural zeolite (15 g) and Calcined Ca-Fe LDH (6 g) and (c) the seawater after treatment of the mixture of natural zeolite (15 g) and calcined Ca-Fe LDH (12 g)

Sample	(a)	(b)	(c)
Content (mmol/L)			
SO ₄ ²⁻	34	15	12
Cl ⁻	805	333	226
Na ⁺	475	187	60
K ⁺	11	6	4
Mg ²⁺	71	51	36
Ca ²⁺	10	259	354
Fe ³⁺	0	0	0
Salinity(%)	3.61	2.10	1.10
pH	8.0	9.3	9.7

Figure 8 shows observation of radish sprouts after 10 day growth using (a) seawater, (b) the seawater treated with the mixture of natural zeolite (15 g) and calcined Ca-Fe LDH (6 g), and (c) the seawater treated with the mixture of natural zeolite (15 g) and calcined Ca-Fe LDH (12 g). The germination of radish sprouts could be confirmed in seawater treated with a mixture of natural zeolite (15 g) and calcined Ca-Fe LDH (12 g), while radish sprouts cannot be germinated in seawater and seawater treated with a mixture of natural zeolite (15 g) and calcined Ca-Fe LDH (6 g).

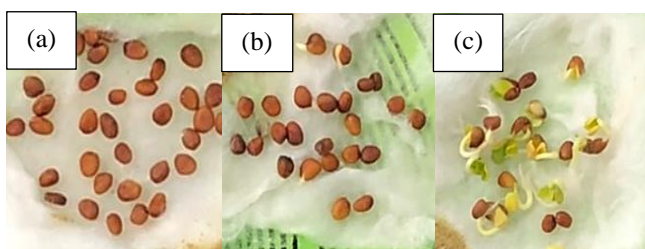


Fig. 8 Observation of radish sprouts after 10 day growth using (a) seawater, and (b) the seawater treated with the mixture of natural zeolite (15 g) and calcined Ca-Fe LDH (6 g) and (c) the seawater treated with the mixture of natural zeolite (15 g) and calcined Ca-Fe LDH (12 g)

CONCLUSION

Mordenite type natural zeolite mixed with calcined Ca-Fe LDH were used for desalination of

seawater. By investigating the desalination behavior of these, we attempted to develop desalination materials to obtain the solution for agriculture from seawater in order to stably supply agriculture water resources.

When 250 - 500 g/L of natural zeolite was added, the salinity rapidly decreased within 15 minutes to about 3.0% (*R* : about 15.5-19.1%). When 300 g/L of calcined Ca-Fe LDH was added, the salinity rapidly decreased from 3.61% to 3.26% (*R* : about 10%) in 10 minutes, then gradually increased to 3.49%, the pH increased from 8.0 to 10 in 5 minutes and then almost constant. With higher dosage, the reduction time of salinity and increase of pH became faster while the reduction rate of salinity was almost same and pH value increased. When a mixture of natural zeolite (375 g/L) and calcined Ca-Fe LDH (300 g/L) was added, the salinity decreased to about 1.0% (*R* : about 70%) after 1 h treatment, then remained constant thereafter, and the pH after the treatment was 9.7. Germination of radish sprouts was confirmed in seawater treated with a mixture of mordenite type natural zeolite (375 g/L) and calcined Ca-Fe LDH (300 g/L) for 1-h. From these results, the salinity was reduced to less than 1 % at which the plant could be cultivated using the mixture of natural zeolite and calcined Ca-Fe LDH.

REFERENCES

- [1] Wajima, T., Shimizu, T., Yamamoto, T. and Ikegami, Y., Simple two-step process for making agricultural cultivation solution from seawater using calcined hydrotalcite and natural zeolite. *Clay Sci.*, Vol.14, 2008, pp.7-12.
- [2] Wajima, T., Shimizu, T. and Ikegami, Y., New simple proceed of making agricultural cultivation solution from seawater. *Bull. Soc. Sea water Sci.*, Vol.60, 2006, pp.201-202.
- [3] Wajima, T., Desalination behavior of calcined hydrotalcite from seawater for preparation of agricultural cultivation solution using natural zeolite. *Energy Environ. Res.*, Vol.4, 2014, pp.3-10.
- [4] Sekihata, F. and Wajima, T., Desalination behavior of natural zeolite in seawater. *Int. J. GEOMATE*, Vol. 19, 2020, pp.123-129.
- [5] Wajima, T., Shimizu, T. and Ikegami, Y., Ion exchange properties of natural zeolite in the preparation of an agricultural cultivation solution from seawater. *J. Ion. Exch.*, Vol. 18, 2007, pp.201-202.
- [6] Wajima, T., Ion exchange properties of Japanese natural zeolite in seawater. *Anal. Sci.*, Vol. 29, 2013, pp.139-141.

ESTUARY ZONATION BOUNDARY BASED ON SEA SURFACE SALINITY DISTRIBUTION IN CILETUH BAY, WEST JAVA

S. Supriatna¹, Iqbal Putut Ash Shidiq¹, Dennisa M. Tunjung¹

¹Department of Geography, Faculty Mathematics & Natural Sciences, University of Indonesia

ABSTRACT

Estuary is the area where there is a mixing of the seawater with fresh water from the mainland. The estuary region is unique because the mixing of the seawater with freshwater makes the formation of brackish water with fluctuating salinity. The estuary region is very dynamic because there is always a process of changing in the physical and biological environments. The estuary region has a salinity ranging from 0,5-30 ‰ or ppt (part per thousand). This research aims to analyze the Ciletuh estuary zonation based on surface water salinity and to know the relationship of salinity with variables of rainfall (seasons), river discharge, and tides. The salinity value is obtained from Sentinel 2A, through image processing using the salinity estimation algorithms. The statistical analysis is carried out to get the algorithm calculation model, where spatial analysis conducted to obtain zonation waters. The results show that the mapping of the salinity distribution is forming the estuary boundary, and the variables of rainfall, river discharge, and tides are affecting the salinity value.

Keywords: Algorithm, Estuary, Salinity, Sentinel 2A, Zonation

INTRODUCTION

The estuary area is the meeting area between land and sea, which is an important component of the river basin in the complex and dynamic coastal area [1]. This region is very dynamic because there is always a process of changing in the physical or biological environment. The mixing of seawater with freshwater makes the estuaries uniquely forming the brackish water with a fluctuating salinity [2]. The tides and the season influence the changes that occurred in the salinity. The process of water movement due to tidal currents in transporting minerals, organic materials, and sediment and the presence of freshwater flows that occur continuously from the upstream of the river is a basic material that supports the productivity of the waters in the region that exceeds the high marine productivity and freshwater water [1]. Therefore, the estuarine region becomes the most productive area, so it becomes exciting to be studied [3]. The increase of rainfall in tropical areas related to global climate change can affect the dynamics of metabolism on the surface of water estuary [4]. Changes in seawater will cause negative ecological consequences, while the presence of reclamation water has an adverse impact on ecology for the estuary environment [5]. Estuaries in temperate and tropical regions were influenced by the source of CDOM (Cromophic Dissolved Organic Matter), which streams mixed with seawater signifying a negative connection between the CDOM and its degree of saltiness [6]. Estuarine waters have lower salinity than oceans and higher than freshwater. The range is 5-30 ppt [3].

Seawater salinity levels can be identified by remote sensing technology. This remote sensing sensor can provide spatial and temporal data in various resolutions as well as the scope required for coastal identification and analysis, and also data with temporal and high spatial diversity. Not only that, but the remote sensing technology is also the most effective approach to observe coastal formations and seafront [7]. Remote sensing satellite techniques can be applied to monitor salinity in coastal environments. That freshwater discharge not only affects the level of salinity and patterns in normal conditions but is also very important in restoring the salinity pattern to normal conditions after a storm disorder [8]. The results of distant sensing imagery on seasonal climate change in the Chesapeake, Delaware, and Mid-Atlantic regions were based on better models of results in the determination of salinity levels [9]. It also found the right symptoms in the Mid-Atlantic region over a period of six years. The process of mapping estuary in different water areas has been previously done in the north and south coast of Java Island using remote sensing techniques. The locations were in Cilamaya [10] and Cimandiri [2]. Those previous studies also created regression models between the observed sea surface salinity and remote sensing spectral bands. Models resulted from those studies were applied in this study for identifying the estuary zone in Ciletuh Bay. Hopefully, the determination of the estuary zone can help the local government and society in managing the estuary region.

This research was conducted in the waters of estuaries in Ciletuh Bay, West Java. It is located on

the southern coast of Java island. The purpose of this research is to create a map of the estuary zone based on a rainy and dry season with a remote sensing approach. The waters of Ciletuh are the estuary of three streams, namely Ciletuh river, Cikanteh river, and Cimarunjung river. Ciletuh itself is a productive area because it has a wealth of marine resources that are quite high. One of the dominant fish commodities is the production of Sidat fish. Sidat fish is a type of fish that mostly live in tropical areas [11, 12]. The estuary zone firstly needed to be determined before calculating its potential productivity. Determination of the zoning of the estuaries can be done by analyzing the sea surface salinity distribution [3].

METHODS

This research was conducted in Ciletuh Bay, Sukabumi Regency, West Java. This research refers to the geographic approach using remote sensing, which is the interpretation of the Sentinel 2A imageries. The Sentinel-2A imagery used was level 1C acquired on March 26th, 2019 and August 23rd, 2019. In this research, image processing is employing two algorithms from previous studies in Cimandiri [2] and Cilamaya [10].

Cimandiri Algorithm

Cimandiri algorithm is an algorithm to model the sea surface salinity distribution in Indonesia. It was made from research on the utilization of remote sensing technology through the use of multi-temporal data of LANDSAT 8 OLI-TIRS satellite imagery to map the sea surface salinity of Pelabuhan Ratu Bay (south coast of Java Island). The formula is as follows [2]:

$$S = 29,983 + (165,047 * Blue) - (260,77 * Green) + (2,609 * Red) \dots\dots\dots (1)$$

Where S is the salinity (ppt), $Blue$ is the blue spectral band, $Green$ is the green spectral band, and Red is the red spectral band.

Cilamaya Algorithm

Cilamaya algorithm is an estimator algorithm of salinity distribution in Indonesia made from research on the utilization of remote sensing technology through the use of multi-temporal data of Sentinel 2A satellite imagery to map the salinity distribution of Cilamaya estuaries (north coast of Java Island). The formula is as follows [10]:

$$S = 139,566970 + (86,21318 * \ln Blue) - (24,62518 * \ln Red) \dots\dots\dots (2)$$

Where S is the salinity (ppt), \ln is the natural log, $Blue$ is the blue spectral band, and Red is the red spectral band.

The determination of zoning in the estuary will be based on the salinity value of image processing results. Salinity value of less than 0,5 ‰ will be classified as the freshwater or limnetic zone. Salinity 0,5 to 5 ‰ will be classified as the mexo-oligohaline, where 5 to 18 ‰ will be included in the mexo-mesohaline class. Meanwhile, 18 to 30 ‰ will be placed in the mexo-polyhaline class, and 30 to 40 ‰ will be classified as the euryhaline. Lastly, salinity with more than 40 ‰ will be included in the hypersaline class [13].

Estuary zoning areas in this study were analyzed based on the rainy season and the dry season. The determination of the season is based on Oldeman's classification, which states that the wet month is the month with high rainfall (more than 200 mm/month), and the dry month is the month with low rainfall (less than 100 mm/month) [2, 10].

Tides and ocean currents (direction and velocity) also influence salinity concentrations in estuary waters. The fluctuation of the salinity is affected by the tides and the ocean currents [2, 14].

RESULT AND DISCUSSIONS

The monthly average rainfall in Ciletuh estuary showed typical rainy months from January until May in 2019. The average rainfall during January-May 2019 is more than 200 mm/month. In contrast, June until September 2019 is showing typical dry months, with average rainfall below 100 mm/month [15]. This condition signifies that the Ciletuh estuary area was experiencing the dry season during the period. The transition period between the dry and rainy months occurred in May, October, and November 2019 (Figure 1).

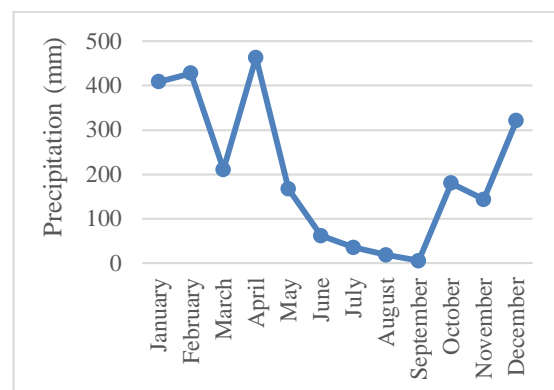


Fig 1. Graph of average monthly rainfall in 2019.

The tidal data of seawater at Ciletuh station in the rainy season of 2019 showed an average of 0,51 meters. Meanwhile, the tide of seawater at Ciletuh station in the dry season of 2019 was 0,33 meters. The

tides of the seawater in Ciletuh is higher in the dry months (Table 1).

Table 1 Rainfall and tidal data [16]

Date	Precipitation (mm)	Tides (m)
March 26 th 2019 (rainy month)	210,8	-0,38
August 23 rd 2019 (dry month)	18,8	-0,28

The sea surface salinity can be modeled using the relationship between the observed salinity value towards remote sensing spectral. Previous studies showed that Landsat 7 ETM+ imageries could be used to estimate the concentration of chlorophyll-a, turbidity, and salinity [12, 17].

The algorithms of Cimandiri and Cilamaya are applied to determine the distribution of salinity of the sea surfaces during the rainy months (March 26th, 2019) and dry months (August 23rd, 2019) in the Ciletuh estuary. The statistical methods have been tested, and it could accurately predict sea surface salinity through its combination with the remote sensing approach, especially in the physical and ecological applications [18]. Spatio-temporal changes of the sea surface salinity on the ocean are influenced by the freshwater flow and river discharge, which have been studied using Meris, MODIS imagery, and river discharge data [19].

Sea Surface Salinity from Cimandiri Algorithm

The distribution of sea surface salinity values in the Ciletuh estuary, calculated using the Cimandiri algorithm model, can be seen in Figure 2.

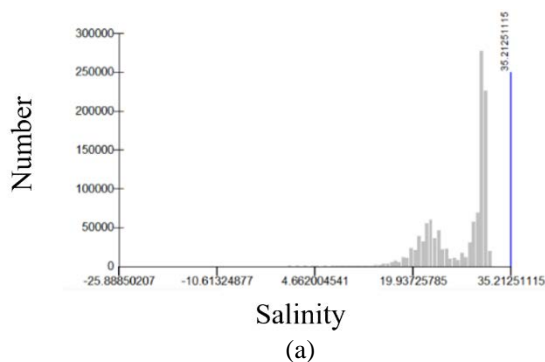


Fig. 2 Graphic distribution of sea surface salinity of Ciletuh estuary from the Cimandiri algorithm. (a)

The sea surface salinity distribution from Sentinel 2A imageries with the Cimandiri algorithm is shown in Figure 3 below. From the figure, it is known that the

salinity value ranged between 13 to 32 ppt, especially in the rainy months of 2019. The low

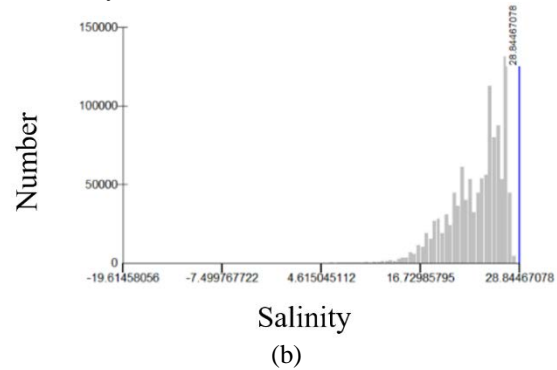


Fig2. March 26th, 2019 (rainy month), and (b) August 23rd, 2019 (dry month).

salinity level is found on the shore of Ciletuh (Fig. 3a). On the other hand, the sea surface salinity ranged between 9 to 28 ppt, especially in the dry months of 2019, and it spread more towards the offshore (Fig. 3b). Based on the results, it is known that the lowest salinity value occurred in August 2019, with the lowest salinity found at nine ppt.

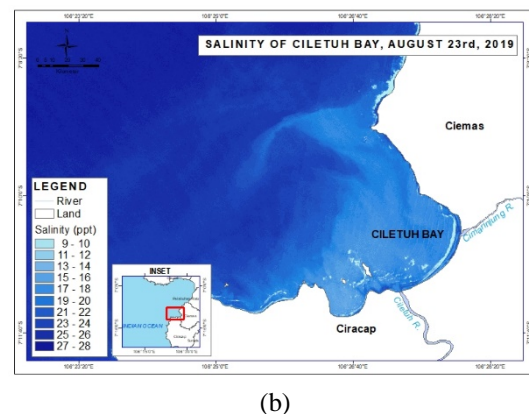
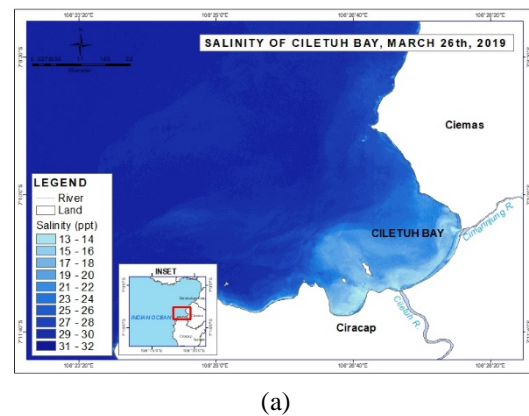
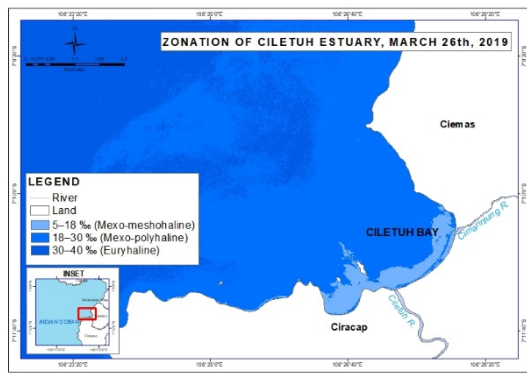
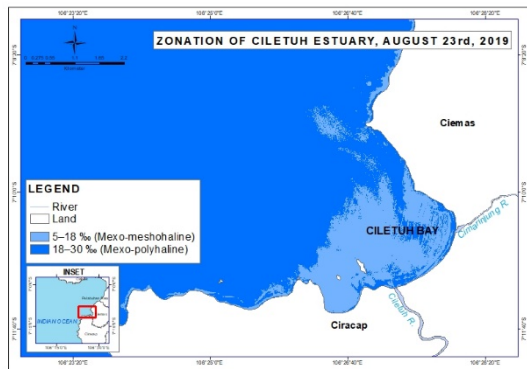


Fig. 3 Distribution of Ciletuh Bay salinity based from the Cimandiri algorithm. (a) March 26th, 2019 (rainy month), and (b) August 23rd, 2019 (dry month).



(a)



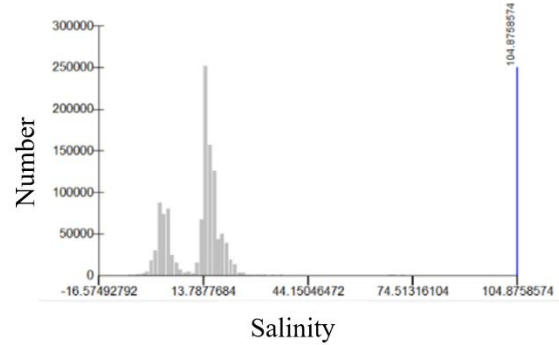
(b)

Fig. 4 Zoning of Ciletuh Bay estuary based on Cimandiri Algorithm on (a) March 26th, 2019 (rainy month), and (b) August 23rd, 2019 (dry month).

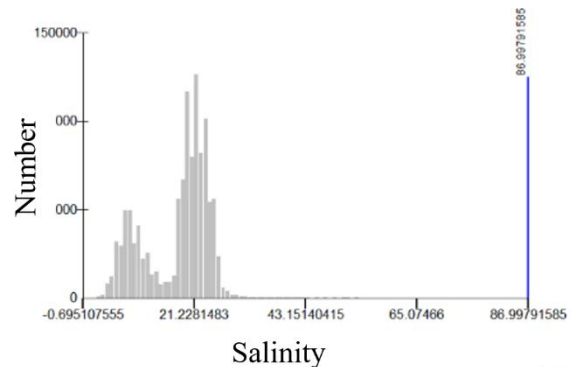
Based on the determination of the estuary zoning, March 2019 has three classes [13], which are the mexo-meshohaline (163,2 hectares), mexo-polyhaline (2661,7 hectares), and euryhaline (1888,7 hectares). In August 2019, there were two classes, which the mexo-meshohaline (592 hectares) and mexo-polyhaline (3121,6 hectares). Based on the process using the Cimandiri algorithm, the zoning classes that formed during the rainy and dry season are not having much different because the amount of rainfall in March 2019 is lower than other rainy months in 2019 (Fig. 1). In August 2019 the euryhaline class is formed (Fig. 4).

Sea Surface Salinity from Cilamaya Algorithm

The distribution of sea surface salinity values in the Ciletuh estuary, calculated using the Cilamaya algorithm model, can be seen in Figure 5.



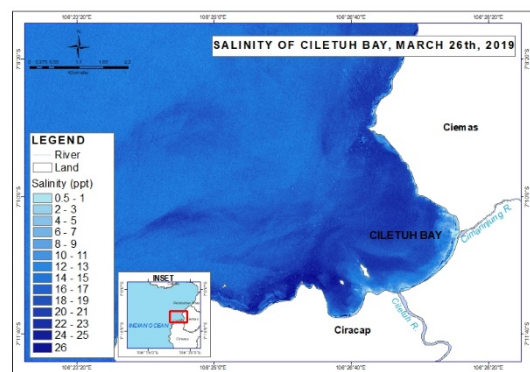
(a)



(b)

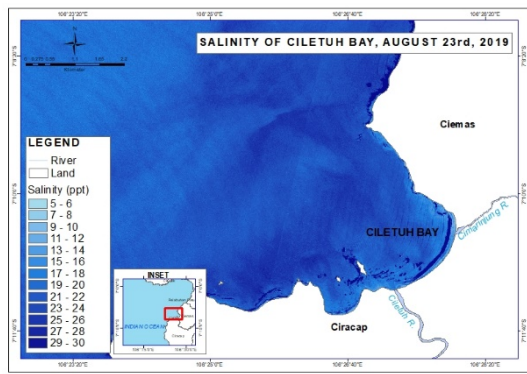
Fig. 5 Graphic distribution of sea surface salinity of Ciletuh Estuary with Cilamaya Algorithm (a) March 26th, 2019 (rainy month) and (b) August 23rd, 2019 (dry month).

The sea surface salinity distribution from Sentinel 2A imageries with the Cilamaya algorithm is shown in Figure 6 below. From the figure, it is known that the salinity value ranged between 0,5 to 26 ppt, especially in the rainy months of 2019 (Fig. 6a). On the other hand, the sea surface salinity ranged between 5 to 30 ppt, especially in the dry months of 2019 (Fig. 6b). Based on the results, it is known that the lowest salinity value occurred in March 2019, with the lowest salinity found at 0,5 ppt.



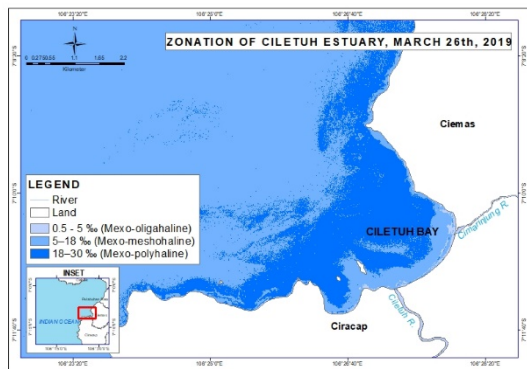
(a)

Fig. 6 Distribution of Ciletuh Bay salinity based on Cilamaya Algorithm on (a)

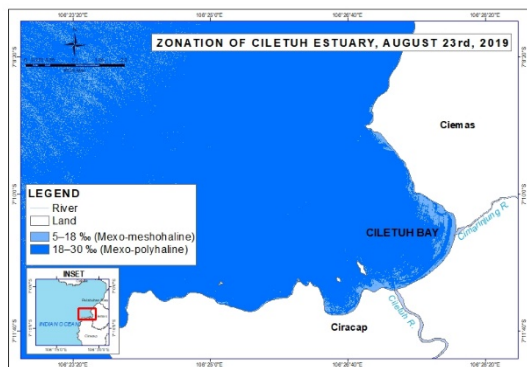


(b)

Fig.6 March 26th, 2019 (rainy month), (b) August 23rd, 2019 (dry month).



(a)



(b)

Fig. 7 Zoning Salinity of Ciletuh Bay Based on Cilamaya Algorithm on (a) March 26th, 2019 (rainy month), (b) August 23rd, 2019 (dry month).

Based on the determination of the estuary zoning, March 2019 has three classes [13], which are the Mexo-oligohaline (17,7 hectares), Mexo-meshohaline (3618,7 hectares), and Mexo-polyhaline (1077 hectares). While, August 2019 had two classes, with the Mexo-meshohaline (148,6 hectares), and Mexo-polyhaline (4565 hectares). In rainy month the Mexo-oligohaline zone is formed and the Mexo-meshohaline zone is formed more broadly. Tides in

March 2019 is -0,38 m, while in August 2019 is -0,28. The tide of seawater can affect the amount of freshwater and seawater mixed in the estuarine zone [10]. These results are temporally similar to the results of [20] research at the mouth of the Ganges showing a variation of salinity in Estuari Hooghly.

There are differences in the results of estuaries zoning by using Cimandiri algorithm and Cilamaya algorithm. Zones formed using the Cimandiri algorithm are dominated by the Mexo-polyhaline zone, while using the Cilamaya algorithm the Mexo-meshohaline zone is more dominant.

Differences in distribution of salinity and zoning at Ciletuh Bay Estuary are influenced by the season. March is a wet month and is included in the rainy season, so the amount of rainfall in this month is higher than the month of August which is a dry month or included in the dry season. The rainfall affects the fluctuations between salt water and fresh water. The rainfall also affects the discharge of river water entering the estuary. The region with maximum turbidity in the region of the estuaries has been examined by [21], here more tidal cycles play an important role in the maximum turbidity meter zone (MTZ) change rather than the seasonal cycle of estuaries. In his research [22] said that increased salinity in coastal waters could protect vegetation species. The results of the study of the zone of Estuary Ciletuh based on the results of the analysis of [23], the salinity value is carried out by using a remote sensing system and the results of the salinity measuring algorithm, Muara Cimadur based on the salinity classification zone is at a distance of about 3-4 km from the river mouth in the wet month, while 1-2 km from the river mouth in the dry month.

CONCLUSION

Based on the analysis in this research, there are differences in results obtained from the use of the Cimandiri and the Cilamaya algorithms. Differences distribution of salinity at Ciletuh Bay Estuary are influenced by the season. In the rainy months, the water area has a low salinity level (0,5-5 ppt and 5-18 ppt), and it is wider than the dry season. The area with low salinity based on the results of the Cilamaya algorithm occurred in March 2019. Meanwhile, a low salinity area from the Cimandiri algorithm was found in August 2019. The low salinity area (0,5-5 ppt, 5-18 ppt, and 18-30 ppt) is the area of Ciletuh Bay.

ACKNOWLEDGMENTS

Thanks are due to Directorate Research and Community Services (DRPM) Universitas Indonesia, which has supported and funded this PUTI grant research in 2020.

REFERENCES

- [1] A.K.M. Azad Hossain, Yafei Jia, Xiaobo Chao, and Mustafa Altinaka., Application of Advanced Remote Sensing Techniques to Improve Modeling Estuary Water Quality. Charles W. Finkl & Christopher Makowski. (Editors). In book: Remote Sensing and Modeling Advances in Coastal and Marine Resources, Springer International Publishing Switzerland, 2014, pp. 295-313.
- [2] Supriatna L., Supriatna J., Koestoer R. H., & Takarina N. D., Algorithm model for the determination of Cimandiri Estuarine boundary using remote sensing, AIP Conference Proceedings, 1729, 2016, 020079.
- [3] Supriadi I., Dinamika estuary tropik, Oseana, XXXVI (4), 2001, pp. 1-11.
- [4] Mead L.H. & Wiegner T.N., Surface Water Metabolism Potential in a Tropical Estuary, Hilo Bay, Hawai'i, USA, During Storm and Non-storm Conditions. Journal of Estuaries and Coasts, 33, 2010, pp. 1.099-1.112
- [5] Su Q., Qin H., Fu G., Environmental and ecological impacts of water supplement schemes in a heavily polluted estuary, Journal of Science of the Total Environment, 472, 2014, pp. 704-711.
- [6] Catala T.S., Mladenov N., Echevarria F., Reche I., Positive trends between salinity and chromophoric and fluorescent dissolved organic matter in a seasonally inverse estuary, Journal of Estuarine, Coastal and Shelf Science, 133, 2013, pp. 206-216.
- [7] Klemas, V., Remote Sensing of Coastal Plumes and Ocean Fronts: Overview and Case Study. Journal of Coastal Research, 28 1A, 2012, pp. 1-7
- [8] Wang F., & Xu Y.J., Development and application of a remote sensing-based salinity prediction model for a large estuarine lake in the US Gulf of Mexico coast. Journal of Hydrology, 360, 2008, pp. 184-194
- [9] Geiger E.F., Grossi M.D., Trembanis A.C., Kohut J.T., Oliver M.J., Satellite-derived coastal ocean and estuarine salinity in the Mid-Atlantic. Journal of Continental Shelf Research, 63, 2013, pp. 235-242.
- [10] S. Kaffah S., Supriatna, & A. Damayanti., Cilamaya estuary zonation based on sea surface salinity with 2 Sentinel-2A satellite imagery. IOP Conference Series: Earth and Environmental Science, 481(1), 2020, 012071.
- [11] M. Faqihuddin, S. Supriatna and T. G. Pin., The Distribution of Fish Larvae based on Salinity Values at South Coast by Sukabumi Regency, West Java, Indonesia. AIP Conference Proceedings, 2023, 2018, 020187.
- [12] F Firdaus, T G Pin, and Supriatna., Distribution of phytoplankton using remote sensing in Cimandiri Estuary, Sukabumi, West Java. IOP Conf. Series: Earth and Environmental Science 481, 2020, 012066.
- [13] Taupp T. & Wetzel M. A., Leaving the beaten track-Approaches beyond the Venice System to classify estuarine waters according to salinity, Estuarine, Coastal and Shelf Science, 148. 2014. Pp. 27-35.
- [14] Lenkopane M., Werner A.D., Lockington D.A., Li L., Influence of variable salinity conditions in a tidal creek on riparian groundwater flow and salinity dynamics, Journal of Hydrology, 375, 2009, pp. 536-545.
- [15] The Meteorological, Climatological and Geophysical Agency of Indonesia, Data Curah Hujan Bulanan 2019 & 2020, <http://dataonline.bmkg.go.id>.
- [16] The Geospatial Information Agency of Indonesia., Data Pasang Surut 2019 & 2020. <http://tides.big.go.id/pasut/>
- [17] Mantas V.M., Pereira A.J.S.C., Neto J., Patrício J., Marques J.C., Monitoring estuarine water quality using satellite imagery: The Mondego river estuary (Portugal) as a case study, Journal of Ocean & Coastal Management, 72, 2013, pp. 13-21.
- [18] Urquhart E.A., Zaitchik B.F., Hoffman M.J., Guikema S.D., Geiger E.F., Remotely sensed estimates of surface salinity in the Chesapeake Bay: A statistical approach, Journal of Remote Sensing of Environment, 123, 2012, pp. 522-531.
- [19] Qing, S., Zhang, J., Cui, T., Bao, Y. , Retrieval of sea surface salinity with MERIS and MODIS data in the Bohai Sea. Journal of Remote Sensing of Environment, 136, 2013, pp. 117-125.
- [20] Ghosh P., Chakrabarti R., Bhattacharya S.K., Short- and long-term temporal variations in salinity and the oxygen, carbon and hydrogen isotopic compositions of the Hooghly Estuary water, India, Journal of Chemical Geology, 335, 2013, pp. 118-127.
- [21] Jiang X., Lu B., He Y., Response of the turbidity maximum zone to fluctuations in sediment discharge from river to estuary in the Changjiang Estuary (China), Journal of Estuarine, Coastal and Shelf Science, 131, 2013, pp. 24-30.
- [22] Malcangio D. & Petrillo A.F., Modelling of brine outfall at the planning stage of desalination plants. Journal of Desalination, 254, 2010, pp. 114-125.
- [23] S. Supriatna, M. P. Tambunan, H. F. Azzahra., Estuary area and fish larvae cathing location in Cimadur, Bayah, Banten, Indonesia, AIP Conference Proceedings 2023, 2018, 020182.

EFFECTS OF RIPARIAN WORKS ON ICHTHYOFAUNA IN THE NACHI RIVER, JAPAN

Taiki Mizumachi¹, Kentarou Hirashima² and Atsushi Nakashima³

¹Graduate School of Systems Engineering, Wakayama University, Japan;

²Wakayama Prefectural Museum of Natural History, Japan;

³Faculty of Systems Engineering, Wakayama University, Japan

ABSTRACT

Many studies on the effects of artificial river environment modification on fish have been conducted before and after river environment modification, and few studies have been conducted during river environment modification. In this study, the flood was caused by the passage of the typhoon Talas in 2011, and the Nachi River in the southern part of the Kii Peninsula, Japan where long-term riparian works are being carried out was selected as the study site. We investigated the effects of riparian works on fish inhabiting rivers. From September 2013 to November 2015, fish were collected from three points in the Nachi River. From April 2017 to November 2019, fish were collected from four points in the Nachi River. We collected fish using a hand net (2 mm mesh) at each survey point at night and also collected fish by fishing. During the survey period, 25 species were identified, and 1707 individuals were collected. As a result, the number and population of diadromous fish species increased over time. Many fish species could be identified even when the turbidity caused by riparian works was strong. On the other hand, after a large-scale terrain change due to riparian works, some fish species could not be identified, and other species could be newly identified. From this, it is thought that topographical changes due to riparian works affect ichthyofauna more than turbidity.

Keywords: Ichthyofauna, Riparian works, Turbid water, Riverbed topography, Nachi River

INTRODUCTION

Turbidity of rivers and changes in river topography due to natural disasters and artificial changes in the river environment is said to directly affect fish and their habitat, or indirectly through food resources. Various studies have been conducted on the damage to the living body, repellent behavior, growth rate, etc [1]-[3]. For example, large-scale flood disturbance is known to reduce fish population density [4]. According to Keizo Watanabe et al., the accumulation of suspended solids on the riverbed due to riparian works reduces boulders and loose stone and adversely affects benthic fish [5]. However, in most cases, research on natural disasters and artificial changes in the river environment is a comparison of before and after an alteration of the river environment, and few studies have been conducted during the alteration of the river environment. Understanding the response of fish communities to riparian works is important not only for the protection and conservation of fish but also as an indicator of the degree of recovery of fish populations from damage caused by environmental changes.

Therefore, in this study, we investigated the effect of riparian works on the fauna of fish in the Nachi River, where major flood damage caused by typhoon Talas occurred in 2011 and long-term riparian works were carried out.

MATERIALS AND METHODS

Survey Sites Overview

Japan is located in East Asia and is a region with high rainfall. Also, Japan has many mountains and a few plains, so it is a steep slope river compared to foreign rivers. The Nachi River (estuary position: 33° 38' N, 135° 56' E) surveyed in this study is a river originating from the Nachi Mountains in Wakayama Prefecture, Japan. The basin area of 24.5 km² and an extension of the trunk river of about 8.5 km. The climate is affected by the Kuroshio Current, and the annual average temperature is about 17 °C, which is warm throughout the year, and the average annual rainfall is about 3,500 mm, which is the region with a lot of precipitation in Japan. The typhoon Talas that occurred at the end of August 2011 washed away riverbed structures and bedrock of the Nachi River. In addition, after the flood damage, large-scale riparian works have been carried out at multiple locations from the estuary to the upstream, and the river topography and riverbed materials have changed significantly. The riparian works caused turbidity in the daytime, but the turbidity was mostly resolved at night. The survey period is from September 2013 to November 2015 and from April 2017 to November 2019. In this study, a total of 39 surveys were conducted.

Survey Methods

This study collected fish from three points on the Nachi River from September 2013 to November 2015 and collected fish from four points on the Nachi River from April 2017 to November 2019. Four survey points were set at intervals of 1 to 2 km from the mouth of the Nachi River, and St. 1, St. 2, St. 3, and St. 4 were set from the downstream side (Fig. 1). At each point, fish were collected by using a hand net (mesh size 2 mm), and fish were also collected by fishing at St. 2 and St. 3. The bait used for fishing was mainly crustaceans captured at the survey point, and only when the bait could not be captured, commercially available bait was used for fishing. The survey time was 45 minutes at each point. The number of fish and the total length of the fish collected were recorded for each species. After recording the number and total length of the collected fish species, some fish were re-released at the collection point except for others. Individuals who could not identify the species at the site were brought home and the species were identified in the laboratory. The identification of fishes followed Nakabo (2013) [6]. A part of the sample brought back was used as a registered sample (WMNH) of the Wakayama Prefectural Museum of Natural History. In 2013, when the survey started, the river water became cloudy due to the riparian works, and the daytime survey could only be conducted in limited places. For this reason, all surveys were conducted at night.

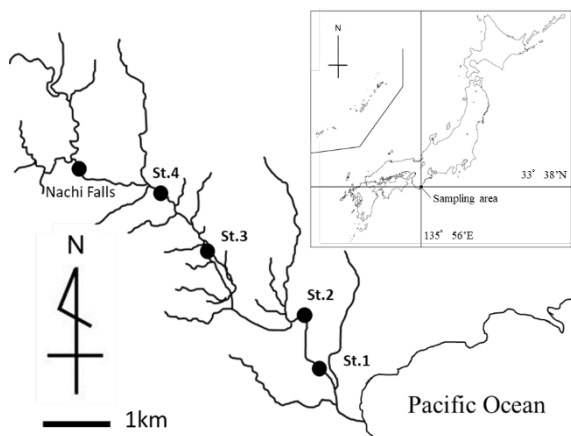


Fig. 1 Map of study sites. Locations of the Nachi Falls and four survey points (St. 1 - St. 4) are indicated. Water flows from the upper left to the lower right.

RESULT

Environmental Conditions at Each Survey Point

Fig. 2 shows the changes in the environment at each survey point. At each survey point, changes in the riverbed topography due to riparian works were observed at least once.

Since St. 1 is located in the downstream area when riparian works were carried out in the upstream area, it was always under the influence of turbidity. The depth of water in April 2017 when the survey started was about 10 to 50 cm, and there were places where the flow was slow and places where the flow was fast. However, in January 2019, due to riparian works, the riverbed topography and riverbed material became uniform, the water depth was almost constant and about 10 to 20 cm, and the flow velocity increased. In St. 1 from September 2017 to April 2018, loose stones in the riverbed decreased due to the inflow and accumulation of sediment due to riparian works, and most of the riverbed material changed to sand and mud. After September 2018, the riverbed was renewed by flood, and the riverbed material became sand and gravel.

St. 2 was the survey site that was most affected by the riparian works. From March 2014 to February 2015, construction on the left bank was performed, and the river water was always muddy during the day. Sand and mud were deposited on the riverbed, and loose stones were reduced, but no significant change was observed in the river topography. However, when the construction of the right bank started after July 2015, the pool disappeared, the water surface width became extremely narrow, the riverbed topography changed to rapids, and the riverbed material was gravel and boulders. In 2017, the riverbed topography was riffle and the water depth remained shallow, but after April 2018, a pool was gradually formed in the same place as before.

St. 3 had a dam, and the area directly below it was a pool with a depth of 1 to 1.5 m. From December 2013 to January of the following year, the river topography about 40m downstream of the dam changed from rapid to riffle due to the riparian works. In October 2014, the river topography returned to rapids, but after September 2018, the river surface was extremely narrowed due to the riparian works. Until May 2019, the riparian works were ongoing. After the construction, part of the riverbed was changed to concrete and a dam was installed.

Most of the riverbed materials in St. 4 were boulders. In October 2014, the removal of sediment and boulders that had accumulated on the dam was confirmed, but the change in river topography was minor. The removal of boulders in the river channel was confirmed in March 2015, and part of the rapid changed to riffle. In addition, riverbed material became sand and gravel, but two months later it became gravel and boulders. Around March 2018, due to the riparian works, the riverbed material was only boulders, the water surface width became narrow, and the water depth increased. Around September 2018, the river topography became riffle and rapid again due to the riparian works, and the riverbed material became sand, gravel, and boulders.

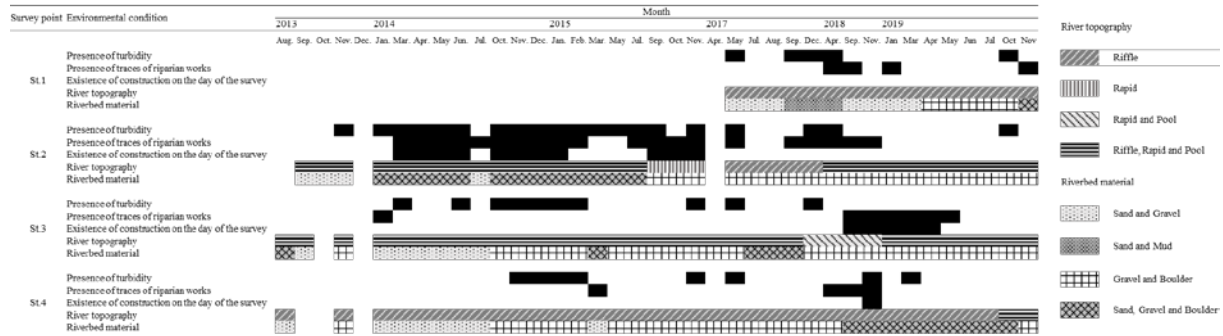


Fig. 2 Changes over time in conditions at each survey point on the Nachi River.

Ichthyofauna confirmed in the Nachi River

Table 1 shows a list of fish confirmed in the Nachi River during the survey period. During the survey period, 25 species were confirmed and 1707 individuals were collected. Many fish could be confirmed at each point even if turbidity occurred due to the riparian works. The number of fish species and the number of individuals that have been confirmed have increased year by year since the start of the study.

In St. 1, 18 species were confirmed and 205 individuals were collected. In St. 1, much amphidromous fish such as Barcheek Goby (*Rhinogobius similis*) were confirmed, and also peripheral fish such as Striped Mullet (*Mugil cephalus*) and Grass Puffer (*Takifugu alboplumbeus*) were confirmed. A Grass Puffer could not be confirmed after the water became shallow and the flow became fast. In July and September 2017, it was confirmed that large Giant Mottled Eel (*Anguilla marmorata*) inhabited, and the Giant Mottled Eel was active at night. After the river depth became shallow due to the riparian works, small individuals were only confirmed in the gap between the boulder and the riverbed. From December 2018 to January 2019, the riverbed topography became monotonous due to riparian works, the water depth became shallow, and sand on the riverbed decreased. After that, Yellowfin Goby (*Acanthogobius flavimanus*) was not confirmed. Moreover, after the water became shallow, we could not confirm Grass Puffer and Striped Mullet over 100 mm. Only in January 2019, Ayu (*Plecoglossus altivelis altivelis*) with a total length of more than 100 mm were confirmed. Ayu is known as an annual fish and dies after the spawning season (October to November) [7]. In general, individuals with a total length of around 100 mm are often seen during the run-up period from the sea, from May to June. Therefore, it was different from the time when it originally appeared.

In St. 2, 16 species were confirmed and 1076 individuals were collected. In St. 2, there were a pool where the tetrapod sank and a pool formed of boulders and bedrock. Giant Mottled Eel and Catfish (*Silurus*

asotus), which are large fish, were inhabited only in that pool. We also confirmed the inhabitation of freshwater fish Dark Chub (*Nipponocypris temminckii*) and Chinese Minnow (*Phoxinus oxycephalus*), but Chinese Minnow was only larvae and juveniles than 30 mm. Ayu was also confirmed to inhabit after April, which is the time of the run-up period, but most of the confirmed individuals were small. From March 2014 to February 2015, due to the construction on the left bank, many fishes including Giant Mottled Eel could be confirmed even after turbidity occurred in the daytime river. On the other hand, Barcheek Goby could not be confirmed during the construction period. Also, due to the construction of the right bank after July 2015, the pool disappeared and the river topography changed. Floating Goby (*Gymnogobius petchiliensis*) was the only fish species that could be confirmed thereafter, and the number of individuals that could be visually confirmed was very small. In 2017, the riverbed topography was monotonous as in St. 1, and the water depth was uniform. However, we were able to reconfirm the habitat of many fish, including benthic fish, which had not been confirmed since July 2015. Also, as time passed, a pool was formed. In the pool, we could once again confirm the inhabitation of Giant Mottled Eel and Catfish, which are large fish. In addition, after 2019, when the river topography from the estuary to St. 2 became monotonous, many Striped Mullet larvae and juveniles (total length of 30-40 mm) have been confirmed. In St. 2, the river was still turbid during the survey, but even in that case, it was possible to confirm the inhabitation of Giant Mottled Eel, catfish, and benthic fish.

In St. 3, 15 species were confirmed and 154 individuals were collected. The benthic fishes Monk Goby (*Sicyopterus japonicus*), Floating Goby, and Common Freshwater Goby (*Rhinogobius nagoyae*) have appeared stably, and Ayu was confirmed to inhabit during the run-up period from April to September. In addition, after May 2015, it was confirmed that Catfish, a large fish, lived in the pool under the dam, and after July 2015 that Giant Mottled Eel lived. A large amount of benthic fish was confirmed in riffle, and freshwater fish such as Dark

Table 1 The fishes appeared in Nachi River. The number indicates the collected number of individuals. Black circles indicate visual observations.

St.1	Family	Scientific name	Month																Collected number	Size range(mm)					
			2017				2018				2019														
			Apr.	May	Jul.	Aug.	Sep.	Dec.	Apr.	Sep.	Nov.	Jan.	Mar.	Apr.	May	Jun.	Jul.	Oct.			Nov.				
Anguillidae	<i>Anguilla japonica</i>				•																				
	<i>Anguilla marmorata</i>																							•	
Cyprinidae	<i>Candidia temminckii</i>																								10
	<i>Tribolodon hakonensis</i>																								
Plecoglossidae	<i>Plecoglossus altivelis altivelis</i>																								47 - 115
Mugilidae	<i>Mugil cephalus cephalus</i>																								24 - 125
Sparidae	<i>Acanthopagrus schlegelii</i>																								
Kuhliidae	<i>Kuhlia marginata</i>																								31
Gobiidae	<i>Sicyopterus japonicus</i>																								36 - 75
	<i>Gymnogobius petschiliensis</i>																								31 - 109
	<i>Gymnogobius breunigii</i>																								44 - 53
	<i>Acanthogobius flavimanus</i>																								56 - 152
	<i>Rhinogobius similis</i>																								27 - 98
	<i>Rhinogobius nagoyae</i>																								27 - 65
	<i>Rhinogobius mizunoi</i>																								82
	<i>Tridentiger brevispinis</i>																								49 - 98
	<i>Tridentiger obscurus</i>																								33 - 61
Tetraodontidae	<i>Takifugu alboplumbus</i>																								108 - 169
	18 Species																								total 205

St.2	Family	Scientific name	Month																Collected number	Size range(mm)								
			2013				2014				2015				2017						2018				2019			
			Aug.	Sep.	Oct.	Nov.	Dec.	Jan.	Mar.	Apr.	May	Jun.	Jul.	Oct.	Nov.	Dec.	Jan.	Mar.			Apr.	May	Jun.	Jul.	Oct.	Nov.		
Anguillidae	<i>Anguilla marmorata</i>																								675 - 1090			
Cyprinidae	<i>Cyprinus carpio</i>																								450			
	<i>Candidia temminckii</i>																								31 - 108			
	<i>Phoxinus oxycephalus jousi</i>																								20 - 24			
	<i>Tribolodon hakonensis</i>																								157			
Siluridae	<i>Silurus asotus</i>																								552 - 585			
Plecoglossidae	<i>Plecoglossus altivelis altivelis</i>																								47 - 85			
Mugilidae	<i>Mugil cephalus cephalus</i>																								17 - 52			
Kuhliidae	<i>Kuhlia marginata</i>																								34			
Gobiidae	<i>Sicyopterus japonicus</i>																								46 - 103			
	<i>Gymnogobius petschiliensis</i>																								32 - 108			
	<i>Rhinogobius similis</i>																								25 - 90			
	<i>Rhinogobius nagoyae</i>																								26 - 54			
	<i>Rhinogobius mizunoi</i>																								41			
	<i>Tridentiger brevispinis</i>																								42 - 85			
	<i>Tridentiger obscurus</i>																								37			
	16 Species																								total 1076			

St.3	Family	Scientific name	Month																Collected number	Size range(mm)					
			2013				2014				2015				2019										
			Aug.	Sep.	Oct.	Nov.	Dec.	Jan.	Mar.	Apr.	May	Jun.	Jul.	Oct.	Nov.	Dec.	Jan.	Mar.			Apr.	May	Jun.	Jul.	Oct.
Anguillidae	<i>Anguilla japonica</i>																								860
	<i>Anguilla marmorata</i>																								24 - 162
Cyprinidae	<i>Candidia temminckii</i>																								22 - 36
	<i>Phoxinus oxycephalus jousi</i>																								
	<i>Tribolodon hakonensis</i>																								
Siluridae	<i>Silurus asotus</i>																								31
Plecoglossidae	<i>Plecoglossus altivelis altivelis</i>																								
Adrianichthyidae	<i>Oryzias latipes</i>																								
Gobiidae	<i>Sicyopterus japonicus</i>																								42 - 84
	<i>Gymnogobius petschiliensis</i>																								40 - 109
	<i>Rhinogobius similis</i>																								
	<i>Rhinogobius nagoyae</i>																								32 - 96
	<i>Rhinogobius fluviatilis</i>																								
	<i>Rhinogobius mizunoi</i>																								65 - 83
	<i>Tridentiger brevispinis</i>																								64 - 87
	15 Species																								total 154

St.4	Family	Scientific name	Month																Collected number	Size range(mm)								
			2013				2014				2015				2017						2018				2019			
			Aug.	Sep.	Oct.	Nov.	Dec.	Jan.	Mar.	Apr.	May	Jun.	Jul.	Oct.	Nov.	Dec.	Jan.	Mar.			Apr.	May	Jun.	Jul.	Oct.	Nov.		
Anguillidae	<i>Anguilla japonica</i>																											
Cyprinidae	<i>Candidia temminckii</i>																								33 - 156			
	<i>Phoxinus oxycephalus jousi</i>																								7 - 134			
Salmonidae	<i>Oncorhynchus masou ishikawae</i>																											
Gobiidae	<i>Sicyopterus japonicus</i>																								47 - 75			
	<i>Gymnogobius petschiliensis</i>																											
	<i>Rhinogobius nagoyae</i>																								42 - 95			
	<i>Rhinogobius fluviatilis</i>																								67 - 114			
	<i>Rhinogobius mizunoi</i>																								62 - 107			
	<i>Rhinogobius brunneus</i>																								94			
	10 Species																								total 272			

Chub and Chinese Minnow were confirmed in the pool and a place where the flow was gentle. In addition, while the confirmed Chinese Minnow was a small individual of less than 30 mm, Dark Chub was confirmed from a small individual to a large individual exceeding 100 mm. The number of fish species that could be confirmed decreased after December 2017 when the river topography changed significantly due to the flood, but many fish species could be confirmed again after April 2019.

In St. 4, 10 species were confirmed and 272 individuals were collected. There has been little change over time since the survey started. In St. 4, many Dark Chub and Chinese Minnow were confirmed in comparison with other survey points, and much large freshwater fish was confirmed in comparison with other points. On the other hand, the number of fish species confirmed in St. 4 was smaller than in other survey points.

DISCUSSION

Since 19 of the 25 species confirmed in this survey were amphidromous fish and peripheral fish, it was speculated that a large number of invaders from the sea were inhabited. Even in the place where construction was done during the daytime and the place that was strongly affected by turbidity, it was confirmed that many fish species such as Giant Mottled Eel, Dark Chub, and Floating Goby, were observed at night. Therefore, it became clear that many fish species inhabit the river even during the riparian works. In addition, the presence of many fish was confirmed even before the turbidity of the river subsided, suggesting that the habitat was present even during the strong turbidity of the river during the daytime. Inhabitation of Ayu, which is said to be weak against turbidity, was also confirmed [8], but most of them were small. Ayu, an annual fish, generally lays eggs and dies from October to November [7]. However, St. 1 confirmed Ayu with a total length of over 100 mm in January 2019. Although it is suggested that these individuals were immature during the spawning season, it was not possible to clarify whether they were due to the riparian works due to the small number of confirmed individuals. However, since it is known that the sedimentation of fine-grained soil due to riparian works reduces the production of attached algae [9], it is fully possible that riparian works hindered the growth of Ayu through bait resources. In addition, since sedimentation of riverbed decreases loose stones, which are the spawning grounds for fish, it is considered that riparian works may hinder the recovery of fish populations.

At St. 1, the closest distance from the river mouth, more amphidromous fish and peripheral fish were confirmed during the survey period than at other

survey points. From this, it became clear that many invading individuals from the sea live or are temporarily used. In St. 2, many fishes could be confirmed when the physical environment of the channel before the riparian works was complicated and diverse. On the other hand, after the river topography became monotonous due to the riparian works, the number of fish species and the number of fish that could be confirmed clearly decreased. This suggests that changes in river topography have a significant impact on fish. However, after returning to the original diverse river topography, many fishes such as Giant Mottled Eel could be confirmed again. Therefore, by making the river topography complicated and diversified, the population of many fish species could be increased. It was suggested that the recovery would occur in a relatively short period of time. This has supported the existing study [10]. In St. 3, large Giant Mottled Eel and Catfish were confirmed after the riparian works were started in St. 2. This suggests that large fish such as Giant Mottled Eel may have moved to seek suitable habitat due to riparian works. In recent years, rivers are often divided by artificial structures such as dams. In such rivers, the movement of fish is restricted by the structures [11], and the impact of riparian works on fish may become more prominent. In St. 4, there was no significant change in the fish species that appeared compared to the other survey points. From this, it was suggested that the impact on fish is minor when the riparian works are short-term and the topographical changes are small.

In this study, it was clarified that abrupt changes in river topography have more direct and short-term effects on fish than turbidity associated with riparian works. Rivers in Japan are often more transparent than rivers in the world and are in a rare river condition in the world called rapids [12]. Among them, the speciation of fish inhabiting Japan has become established. Due to the high transparency of rivers, studies on river turbidity have been actively conducted in Japan [3]. However, the related species of fish that live in the muddy water rivers of the Asian also inhabit Japan [13]. From this, it was considered that the complicated river topography created by the rapid stream is more important than the transparent water quality. On the other hand, in this study, we confirmed that Ayu lived at a time different from the original appearance time and that freshwater fish that lived in the downstream region were mostly smaller. From these facts, it could not be denied that the cloudiness of rivers could impede the growth of fish. In addition, the Nachi River that we surveyed this time was a small-scale river, and it was a river where turbidity could easily subside. In addition, floods occurred in

the summer due to typhoons, and the riverbed was renewed. From these facts, it is unlikely that a sufficient reaction appeared for all fishes. It is expected that turbidity caused by riparian works and long-term sediment accumulation on the riverbed will cause great damage to fish with loose stones as spawning sites. Therefore, it is necessary to continue the investigation in order to clarify the impact of the inflow of suspended solids into the river due to the riparian works.

ACKNOWLEDGMENTS

We thank all the members of the Graduate School of Systems Engineering, Wakayama University for assistance in the field survey.

REFERENCES

- [1] Berg, L. and T.G. Northcote, Changes in Territorial, Gill-flaring, and Feeding Behavior in Juvenile Coho Salmon (*Oncorhynchus kisutch*) following Short-term Pulses of Suspended Sediment, *Can. J. Fish Aquat. Sci.*, Vol.42, 1985, pp.1410-1417.
- [2] Bunt, C. M., S. J. Cooke, J. F. Schreer and D. P. Philipp, Effects of incremental increases in silt load on the cardiovascular performance of riverine and lacustrine rock bass, *Ambloplites rupestris*, *Environmental Pollution*, Vol.128, 2004, pp. 437-444.
- [3] Sutherland, A. B. and J. L. Meyer, Effects of increased suspended sediment on growth rate and gill condition of two southern Appalachian minnows, *Environ. Biol. Fish.*, Vol.80, 2007, pp. 389-403.
- [4] Kousuke Sumida, Yo Miyake, Yuya Watanabe, and Mikio Inoue, Responses of stream invertebrate and fish assemblages to an extreme flood event in the Shigenobu River, southwestern Japan, *Ecol. Civil Eng.*, Vol.22, No.1, 2019, pp. 35-49.
- [5] Keizo Watanabe, Futoshi Nakamura, Kunishige Kamura, Hiroyuki Yamada, Yasuharu Watanabe, and Susumu Tsuchiya, Influence of stream alteration on the abundance and distribution of benthic fish, *Ecol. Civil Eng.*, Vol.4, No.2, 2001, pp. 133-146.
- [6] Nakabo, T. (ed.), *Fishers of Japan with Pictorial Keys to the Species*. Third Edition., Tokyo:Tokai University Press., 2013, pp. 1-2428.
- [7] Rikizo Ishida, On The Spawning of the Ayu, *Plecoglossus altivelis* T. & S.- I . Structure of The Spawning Shoal and Spawning Behavior, *Bulletin of the Japanese Society of Scientific Fisheries*, Vol.25, No.4, 1959, pp. 259-268.
- [8] Satoshi Awata, Hirohiko Takeshima, Tetsuya Tsuruta, Takashi Yamada, and Kei'ichiro Iguchi, Stress Hormone Response to Long-or Short-time Exposure to Suspended Solids in Ayu *Plecoglossus altivelis*, *Aquaculture Sci.*, Vol.58, No.3, 2010, pp. 425-427.
- [9] Graham. A. A, Siltation of stone-surface periphyton in rivers by clay-sized particiles from low concentrations in suspension, *Hydrobiologia*, Vol.199, 1990, pp. 107-115.
- [10] Teruo Toyoshima, Shigeru Nakano, Mikio Inoue, Yugo Ono, Yoshimasa Kurashige, Fish population responses to stream habitat improvement in a concrete-lined channel, *Japanese Journal of Ecology*, Vol.46, 1996, pp. 9-20.
- [11] Shugo Kikuchi, and Mikio Inoue, Population fragmentation of a stream-resident salmonid by dams: downstream progress of extinctions from headwaters, *Ecol. Civil Eng.*, Vol.17, No.1, 2014, pp. 17-28.
- [12] Yoshimasa Kurashige, and Takeshi Takenaka, Visual Water Clarity and Suspended Substance under Baseflow Conditions in the Nishibetsu River, Japan, *Jpn.J.Limnol*, Vol.56, No.3, 1995, pp. 195-203.
- [13] Atsushi Doi, A review of taxonomic studies of cypriniform fishes in South-east Asia, *Japan J. Ichthyol.*, Vol.44, No.1, 1997, pp. 1-33.

EARLY FOREST RESTORATION ON THE CLOSED SKI SLOPE IS ENHANCED BY NATURAL REGENERATION AND ARTIFICIAL THINNING

Tetsuoh Shiota¹, Chizuru Iwasaki¹, Tetsuo Okano¹, and Shinjiro Oya²

¹Faculty of Agriculture, Shinshu University, Japan; ²Nagano Prefecture Forestry Research Center, Japan

ABSTRACT

Recently, there are many ski resorts that have been closed due to management difficulties in Japan. Forest restoration on the abandoned ski slope is necessary from the viewpoints of landscape management, prevention of avalanche, and one of the landslide disasters. However, it is difficult to establish forests due to poor nutrients by topsoil removals at the time of ski slope development. In this study, we evaluate the effect of thinning to ease competition for nutrients. The study site is in Mt. Tateshina, central Japan. The ski slope was closed in 1997. Natural regeneration of larch was observed in 1998 and the artificial thinning was done in 2003. Two thinned and nine un-thinned quadrat plots were set. DBH with the height of all living and dead trees were measured. To clarify the growth process, nine sample trees were selected and their tree ring at 1 m interval in height was analyzed. The un-thinned plot was characterized by high density, small tree size, and many dead trees, suggesting that severe competition has occurred. On the contrary, the thinned plot was characterized by the small density, large tree size, and less dead trees. According to the tree ring analysis, the size-order of individuals in the un-thinned plot was determined at 5-year-old, while one of them in the thinned plot was changed after thinning. It was concluded that the artificial thinning of natural forest on the ski slope is useful to accelerate tree growth and early forest development.

Keywords: Abandoned ski slope, Forest restoration, Topsoil disturbance, Lessening of competition

INTRODUCTION

Ski resorts facilities have been developed in the mountainous regions of the world. The ski slope is usually constructed on forest area in Japan, whereas on pastureland and heathland in European Alps [1]. This causes that the Japanese civil engineering work of the ski slope is accompanied by a drastic change in landscape: the forest ecosystems was separated by the grass and dwarf shrub ecosystem [1,2].

In the ski slope development process, all of trees were harvested and their stumps and large rocks were pull off. Furthermore, huge amount of topsoil was removed to smooth ski slope [2-4]. In many case, the exotic or local meadow species were introduced and controlled. According to the previous research in Japan, the following characteristics are common on the ski slope vegetation: the existence of the introduced exotic grasses, the development of un-vegetated patches, and the restriction of woody plant establishments [1,2]. These vegetation characteristics are thought to be the results of the civil engineering works and the artificial maintenances of the ski slopes.

Recently, there are many Japanese ski resorts which have been closed due to management difficulties [5]. The ski slopes are left derelict because these ski resorts companies lack adequate capital. These abandoned ski slopes continue to separate the forest ecosystems and deteriorate the landscape quality. Additionally, they increase the risk of

avalanche, topsoil erosion, and landslide disasters [2,4].

The early forest restoration on the abandoned ski slope is necessary from the viewpoints of the conservation of ecosystem services. However, artificial reforestation is impractical due to the low capital strength. The natural regeneration is possible but entail uncertainty [6]. The amount of seeds supply is directly affected by the masting event in surrounding forests. In some cases, the patches of large herbaceous perennial plant or of shrub species inhibit the regeneration and development of tree species [4,7,8]. In another cases, the topsoil removals cause the insufficient of nutrients and the limitation of initial growth of trees [3,4,9].

In this study, we evaluate the effects of artificial thinning on the topsoil removed ski slope. In this site, the natural regeneration of Japanese larch was succeeded [4]. Because number of saplings was enough, it would be difficult to avoid their competition in poor nutrient condition. We examined the hypothesis that artificial thinning will ease the competition among trees and accelerate their growth.

STUDY SITE AND METHODS

Study Site

Study site was located on the north facing slope (36.1216 N, 138.3405 E, alt. 1,800 m) of Mt.

Tateshina, Nagano prefecture, central Japan (Figure 1). The closed Tateshina Associates Ski Resorts has borrowed this area from National Forest until 1997.

The ski slope was surrounded by the artificial forests of Japanese larch (*Larix kaempferi*). There was the long step surface with from 1 to 2 m height between the ski slope and the surrounding larch forests. This step suggests that the civil engineering work to construct ski slope was severe.

Just after the close of the ski resorts, the first natural regeneration of larch has occurred in 1998. In 2002, the density of larch was 70,000 trees/ha and of broad-leaved pioneer tree species (e.g. *Betula platyphylla*, *Alnus filma*, *Alnus masumurae*, and *Salix sachalinensis*) was 20,000 trees/ha (Dr. Y.Koyama, personal communication). In 2003, when trees were 5-year-old, the National Forest thinned them to 3,000 trees/ha. The National Forest assumed that the severe competition causes the growth stunting.

In 2016, we found small un-thinned larch patches, which age is 18-, 11-, and 6-year-old. The 18-year-old patch was located in the middle of the slope. This rectangle patch had 10 m and 15m sides and was surrounded by thinned larch and broad-leaved tree stand. We also found another 18-year-old un-thinned patch nearby the road in the lower part of the ski slope. In this patch, the density of larch was smaller due to the coverage of dwarf bamboo (*Sasa senanensis*). The 11-year-old patches were near the top of the ski slope. To construct the starting terraces, the topsoil of this position was removed until about 3 m depth. On the other hand, the 6-year-old patches were established beside the parking place for construction vehicles, which surface was tamped down.

Quadrat plots

To discuss the developmental stage using the chronosequence method, we set eleven quadrat plots in the patches that were different in age (Table 1). The

size of the quadrat plot was determined considering the patch size and the stand density.

Two 18-year-old thinned (T18-1, T18-2) and un-thinned plots (C18-1, C18-2) were set on the constructed ski slope. In addition, an un-thinned plot was set nearby road (S18-1).

Additionally, three un-thinned 11- year-old (C11-1, C11-2, and C11-3) and 6- year-old (C6-1, C6-2, and C6-3) plots, which were 2 m and 1 m squares, respectively, were set. There was no coverage vegetation in 11-year- old plots, whereas herbaceous plants covered the 6-year-old plots.

Measurements

For each plot, tree height and diameter at breast height (DBH) of every tree were measured with species identification. The tree height was measured by the height meter (Measurement Pole, SK Co. or Vertex IV, Haglov Co.). DBH was measured by steel tape.



Fig. 1 The studied abandoned ski slope covered by larch trees.

Table 1 Outline of quadrat plots

Plot	Treatment	Regeneration	Age	Size [m ²]	Location on slope	Vegetation of ground surface	Dead tree	Thinned stump
T18-1 T18-2	Thinned	1998	18	10 x 10	Middle	Meadow	-	Many
C18-1 C18-2	Un-thinned	1998	18	5 x 5	Middle	-	Many	-
S18-1	Un-thinned	1998	18	10 x 10	Bottom	Dwarf bamboo	Few	-
C11-1 C11-2 C11-3	Un-thinned	2005	11	2 x 3	Top	-	Many	-
C6-1 C6-2 C6-3	Un-thinned	2010	6	1 x 1	Bottom	Herbaceous plants	-	-

To trace the growing process, the tree rings of stem were analyzed. The disk samples from 1 m interval cross-section of the stem of nine trees were collected in thinned (T18-1) and un-thinned (C18-1) plots, respectively. These sample trees were selected considering size classification in each plot. The annual ring width on disk samples was analyzed through four radial directions.

RESULTS

Stand Structure

Stand density of each plot was shown in Figure 2. Stand density of T18 (Triangle), S18 (Solid circle), and C18 (Open circle) plots were about 3,000, 6,000, and 12,000 tree/ha, respectively. On the other hand, those of C6 and C11 (Open circle) was ranged from 30,000 to 80,000 and from 27,000 to 60,000 tree/ha, respectively.

The canopy height of each plot was represented in Figure 3. The dashed line represents a height growth curve for the lowest-grade site index. We calculated this curve by referring to the growth curve in the fifth-grade site of Nagano prefecture [10]. The canopy height of un-thinned plots (C6, C11, and C18, Open circle) was lower than those of the fifth-grade site index. On the other hand, those of S18 (Solid circle) and T18 (Triangle) plots were close to those of the fifth-grade site index. The average DBH represents large value in T18 (Triangle) and S18 (Solid circle) plots, and small value in C18 plots (Open circle).

The relationship between average D2H and stand density was represented in Figure 4. The power function was found in the data of C11, C18, and S18 plots, in which the power was approximately -1.5 ($\ln Y = 18.49 - 1.411 \ln X$, $r^2 = 0.931$). The values of C6 plots were obviously under this power function, whereas the values of T18 plots were closely situated.

The height frequency of living (Open bar) and dead (Solid bar) trees in each plot were represented in Figure 5. In C6 plots, the concentrated or unimodal distribution patterns were found. In C11 plots, the bimodal distribution pattern was found and the small trees were died. In C18 plots, the bimodal distribution with positive skewness was observed, and the small size trees were died. In S18 and T18 plots, unimodal distribution with negative skewness was observed, however, there were few dead trees.

Reconstructed Stem Growth

Based on the tree ring analysis, height growth was reconstructed (Figure 6). In both plots, bimodal size-classification were found before thinning. But the growth of lower size class trees represented the quick growth in the thinned plot. Finally, the height range of lower trees expanded in the thinned plot (T18-1).

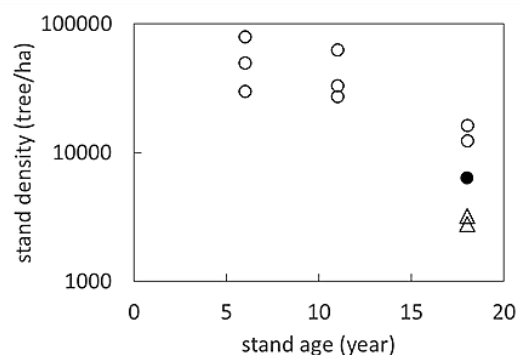


Fig. 2 Stand density of each quadrat plot.

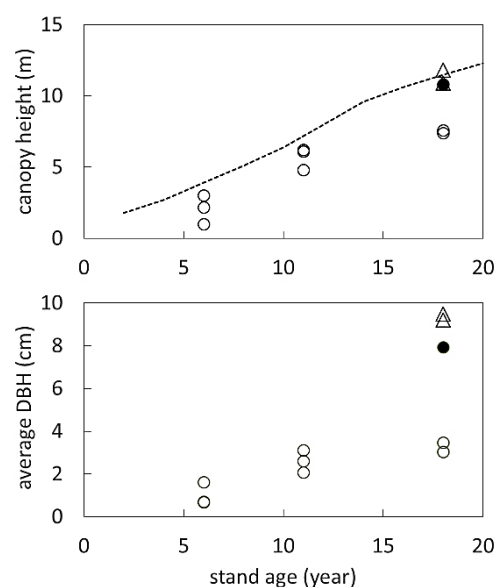


Fig. 3 Canopy height and average DBH of each quadrat plot.

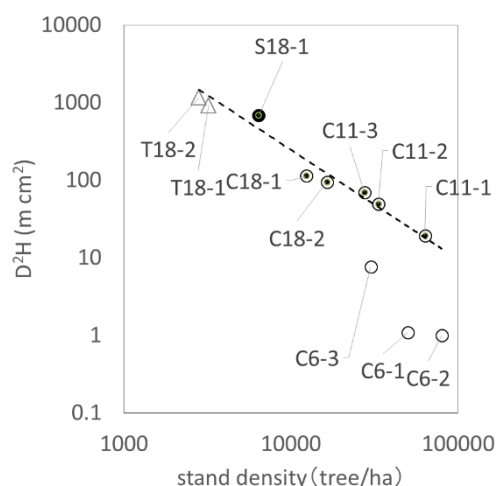


Fig. 4 Relationship between average D^2H and stand density.

DISCUSSIONS

Natural Regeneration and Self-Thinning

The natural regeneration of larch was succeeding at this site in 1998, 2005, and 2010 (Table 1). This interval supports that the masting cycle of Japanese larch is from five to eight years. This long interval also suggests that the masting year is a valuable opportunity for larch forest establishment.

The un-thinned plot was characterized by high density. The initial stand density is evaluated from 60,000 to 80,000 tree/ha based on the first and third regeneration (Figure 2, C6 plots). These values were enough high for the natural establishment of forests. However, the previous study reports that the stand density of 4- to 7-year-old Japanese larch was from 60,000 to 280,000 tree/ha in natural regeneration [6]. The density of this study is relatively lower than in the previous study.

The high stand density in un-thinned plots causes severe competition among trees which are characterized by many small tree sizes and by dead trees (Figure 6). In C11, C18, and S18 plots, the dead trees were found (Figure 6). The power function between density and tree size in these plots suggests that the self-thinning [11] has occurred (Figure 5). Oppositely, the competition in C6 plots is not thought to be severe, because of without dead trees by the self-thinning and of unimodal height distribution (Figure 5, 6).

Additionally, the un-thinned plots were characterized by a low growth rate in height and diameter. Comparing to the lowest growth curve in Nagano prefecture [10], their heights were smaller. Usually, topsoil removal affects the vegetation and inhibits tree growth [3, 4, 9]. The more intense competition might be occurred not only for light but also for underground resources. The heavy competition with topsoil removal should be one of the reasons why the height growth was limited.

Effects of Artificial Thinning

Thinning release the competition for light and underground resources among trees. In fact, trees in thinned plots were larger than those of un-thinned plots (Figures 2 and 3). Similar effects were found in S-plot, where dwarf-bamboo decreased the larch tree density. In this plot, small density eases the competition and accelerates tree growth until the local lowest height growth curve [10].

Additionally, thinning affects the size structure. The change of skewness from positive to negative represents that the larger trees were increased in the population (Figure 5). The growth of the lower-class trees was improved by thinning, although size-classification was occurred before thinning. This

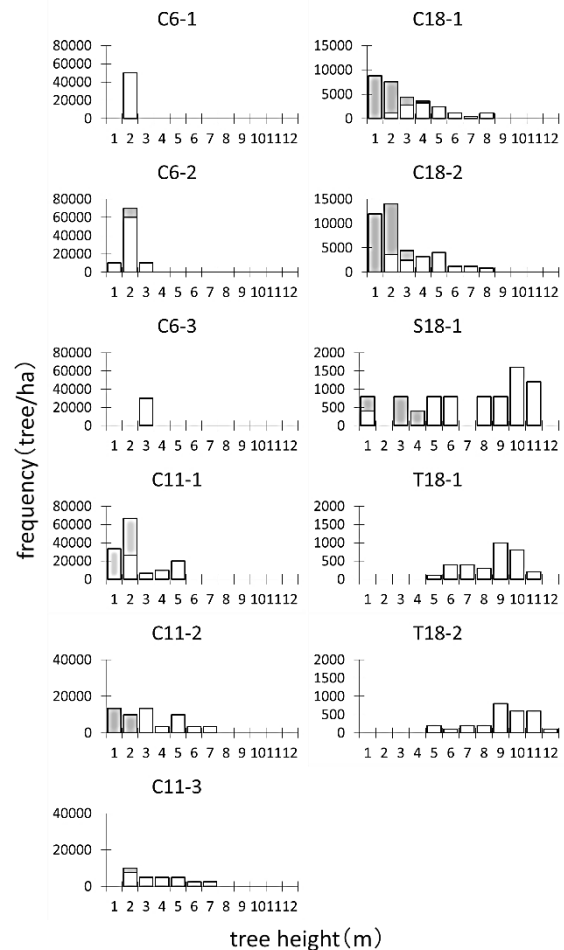


Fig. 5 Size structure of each quadrat plot.

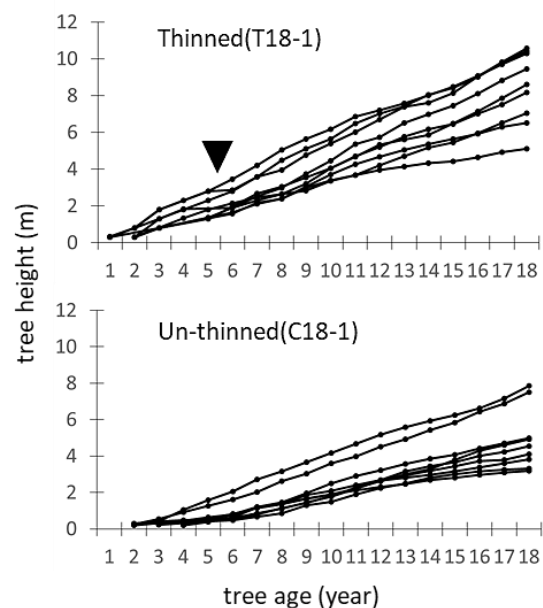


Fig. 6 Reconstructed height growth of nine trees in thinned and un-thinned plot.

results that the smaller trees, which were stunted in the un-thinned plot, could survive by their growth and resource acquisition in the thinned plot (Figure 6).

The artificial thinning contribute the improving mortality and initial growth in a natural regenerated dense stand. This effect may be more enhanced in the poor soil condition such as the constructed ski slope. However, we also should pay attention to the limitation of this effects. At first, from the view of control the competition, the thinning should be planed before a severe competition stage. On the second, the effects may be limited in the severer soil condition. The release effects of the thinning are based on the existence of a certain amount of resources. If there are no or little resources, it will be difficult to expect the improvement effects.

CONCLUSION

In some cases, the civil engineering work on ski slope has affects for long time including the reforestation stage. However, the parts of them are possible to be improved by the adequate stand density control, not only by the natural regeneration.

ACKNOWLEDGMENTS

We thank Toshin Forest Station and Chubu Regional Forest Office for their support to our using the study site. We also thank Dr. Yasuhiro Koyama for his helpful suggestions and the previous study data on this site. This work is partly supported by grants from the Ministry of Education, Science, and Culture of Japan (KAKENHI No. 26450222).

REFERENCES

- [1] Titus H.J. and Tsuyuzaki S. Ski Slope Vegetation at Snoqualmie Pass, Washington State, USA, and a Comparison with Ski Slope Vegetation in Temperate Coniferous Forest Zones. *Ecol. Res.* Vol.13, 1998, pp.97-104.
- [2] Tsuyuzaki S., Environmental Deterioration Resulting from Ski-Resort Construction in Japan. *Environmental Conservation*, Vol.21, 1994, pp.121-125.
- [3] Nakamura T., Human Impacts on Vegetation and Soil of Skiing Area: I. A Case Study in Teine Skiing Area, Hokkaido, Japan. *J. Japan. Grassl. Sci.*, 29, 1984, pp.331-340. (In Japanese with English Summary)
- [4] Koyama Y., and Koyama K., Vegetation Change for 20-Year Period at Abandoned Ski Slopes in Northern Nagano Prefecture, Central Japan. *Bull. Inst. Natur. Edu. Shiga Heights, Shinshu Univ.* Vol.39, 2002, pp.1-6. (In Japanese with English Summary)
- [5] Kureha, M., Changing ski tourism in Japan: From mass tourism to ecotourism? *Global Environmental Research*, Vol.12, 2008, pp.137-144.
- [6] Igarashi T., Yajima T., Matsuda K., Natsume S., Takikawa S., Natural Regeneration in the Japanese Larch Plantation, *Bull. Exp. For. Hokkaido Univ.*, Vol.44, 1987, pp.1019-1040. (In Japanese with English Summary)
- [7] Saito I.T., *Miscanthus sinensis* Community as an Indicator for Forecasting Tree Regeneration on Abandoned Skislope in the Lowland of Hokkaido, Northern Japan. *Vege. Sci.* Vol.29, 2012, 41-48.
- [8] Iwasaki C., Shiota T., Okano T., Oya S. A Difficulty of Ski Slope Reforestation with the Tall Glass Community. *Bull. Shinshu Univ. AFC.* Vol.17, 2019, pp.26-36. (In Japanese with English Summary)
- [9] Nakagawa M., Hasui H., Ishihara N., Takiya M., Ohno Y., and Yasama M., Effects of Top Soil Removal for Natural Regeneration on Growth of Japanese Larch – A Case Study in Higashikagura Town-. *Boreal Forest Research* Vol.60, 2012, pp.117-119. (In Japanese)
- [10] Katakura M., Yamauchi M., and Furukawa H., A Study on Long-Harvesting-Cycled Management of Japanese Cypress and Japanese Larch. *Bulletin of Nagano Prefecture Forest Research Center*, Vol. 19, 2005, pp.1-16. (In Japanese)
- [11] Yoda, K., Kira, T., Ogawa, H. & Hozumi, K., Self-thinning in Overcrowded Pure Stands under Cultivated and Natural Conditions: Intraspecific Competition among Higher Plants XI. *J. Biol. Osaka City Univ.* Vol.14, 1963, pp.107-129.

THE ADEQUACY OF HOUSEHOLDS SANITATION LEVEL IN THE CITY OF JAKARTA: A MICRODATA ANALYSIS FROM SUSENAS 2017

Noviyati Valentina Sidabutar¹ and Chotib²

^{1,2}School of Strategic and Global Studies, University of Indonesia, Indonesia

ABSTRACT

As a metropolitan city, Jakarta faces the problems of uncontrolled migrant populations and limited housing availability. This results in the uncontrolled growth of organic settlements with a lack of adequate sanitation facilities. Furthermore, open defecation in public spaces is still practiced in some areas. Using the multinomial logistic regression method, this research aims to identify the adequacy of household sanitation in Jakarta, focusing on human waste disposal facilities in households. The dependent variable (adequacy of sanitation facilities) is divided into three categories; adequate private sanitation (used by one household), adequate shared sanitation (used by multiple households), and inadequate sanitation. This research also aims to identify the correlation of household characteristics as predisposition factors towards the trends in the sanitation adequacy. The household characteristics analyzed in this study are income, employment status, level of education, marital status, gender, number of household members, and migrant status. This research uses microdata from the 2017 National Socio-Economic Survey. It was found that 85.64% of the household sanitation sampled in the research is adequate (of which 68.81% are adequate private sanitation and 16.83% adequate shared sanitation), and 14.36% were classified as inadequate. Sanitation adequacy is highly correlated with long term residency, high education, household members ≥ 4 people, unemployed, married, female-headed household, and high expenditure. The government can utilize those predisposing factors in planning the design policies and interventions on sanitation to lower the percentage of households with inadequate sanitation.

Keywords: Adequacy level, Households, Sanitation, Jakarta.

INTRODUCTION

Jakarta as a megapolitan city has a massive physical development that is a very strong magnet for migrants seeking a better life in this city. Therefore, Jakarta's population growth is strongly influenced by the influx of migrants. According to the 2019 statistic [1], the average population of Jakarta in the last two years has increased by 247 people every day or equal to 10 people every hour. This data illustrates the exponential population growth of Jakarta, which increases housing needs. As a result of the housing scarcity, some low-income migrant resorts to organic settlements. These organic settlements, with dense and slum characteristics, and also poverty, are often labeled as an urban-diseases.

Most households in Jakarta still use traditional latrines in their sanitation facilities. However, Jakarta's Health Office reported that in January of 2019, there are 115,185 households who are still practicing open defecation [2], or latrines that dump feces directly to the environment.

Lack of sanitation facilities and the practice of open defecation are strongly related to human and environmental health. It can cause water and land pollution, and increase the infection rate of various diseases such as diarrhea. On the other hand, this also results in increased economic burden for cities to address public health problems.

These sanitation issues, have been declared as one

of the strategic issues in development in Indonesia [4]. Until now, Indonesia is still struggling to achieve the universal access to sanitation as mandated by the United Nation's 6th Sustainable Development Goals (SDGs). Nevertheless, Jakarta targeted 100% proper and safe sanitation by the year of 2024 [5], even when there are a variety of obstacles to be faced with.

The main objective of this research paper is to map the adequacy of household sanitation in Jakarta, in order to achieve the SDG's target as well as the regional targets. This research also aims to identify the influence of household characteristics on the adequacy of household sanitation. This study focuses on household sanitation facilities for feces disposal in Jakarta, using microdata from the 2017 National Socio-Economic Survey.

LITERATUR REVIEW

Human beings can only be healthy in a healthy environment [6]. Dahlgren and Whitehead argued that environmental health is an important component of public health, where the individual lifestyle to the socio-economic and cultural environment takes part as major determinants [6]. It covers all aspects of human behavior in relation to the living environment, with the aim of improving and maintaining the highest level of human health by modifying social and environmental factors. On the other hand, environmental health is in actuality a byproduct of

human activities. Therefore, human activities are keys to the public health.

According to Lawrence Blum, there are four factors that influence public health: 1) environmental factors (physical, biological and socio-cultural), 2) behavioral factors (attitudes and lifestyles), 3) health service factors, and 4) heredity. Green divided the determinants of health behavior into three main factors consisting of predisposing factors, enabling factors, and reinforcing factors [7].

One of physical component that supports the environmental health is the availability of adequate sanitation in households. According to WHO-Unicef Joint Monitoring Program (JMP), the criteria for global measurement of sanitation services known as the sanitation ladders consists of safely managed sanitation, basic sanitation, shared sanitation, unimproved sanitation, and open defecation [3]. The sanitation service refers to the management of excreta from facilities including emptying and transporting process of the excreta from the facilities. This sanitation issues have been declared as The United Nation's 6th Sustainable Development Goal. The goal targets to achieve universal access to basic sanitation services and progressively improving sanitation to safely managed sanitation by the year of 2030. The target can be achieved if all levels of society have healthy sanitation behavior.

According to the theory of Thoughts and Feeling by WHO [8], there are four main factors that shape a person's behavior, one of which is a resource reason which includes facilities, money, time, energy. Resources can have a positive or negative effect on human behavior. On the other hand, the availability of resources is strongly influenced by three reasons: 1) the level of understanding and consideration (the presence of knowledge, beliefs, and attitudes), 2) influence from important people in their lives, and 3) culture. These factors shape the way of life in urban communities.

The Function theory expressed by Katz [8], considers that changes in individual behavior can occur when individuals feel a need. The need revealed the ability of individuals to deal with the surrounding environment. On the other hand, individual behavior also depends on the individual's character, which is shaped in the household.

From the theories explained above, we can further hypothesize that an individual's decision to provide adequate sanitation is influenced by the individual's resources (especially financial), knowledge, and need.

Household income illustrates the economic condition and welfare of the household, the ability to fulfill all basic and non-basic needs, and the ability to maintain their standard of living. Household welfare can be assumed to be in line with the proportion of household expenditure which is spent on non-food needs [9].

Household income is also an important predictor

in determining the ability of households to adopt an adequate sanitation facility. There have been numerous research that found a positive correlation between latrine ownership and high socio-economic status [10,11]. Those research found that rich households have a strong will to build their own latrines, even a latent demand for improving sanitation comes from them [12]. In addition, poor households tend to prioritize the fulfillment of basic needs above the procurement of adequate sanitation facilities [13,14]. Poverty has also been proven to reduce the demand for sanitation [15-17], and that individuals with low-income tend to not use latrines [18].

Migration status has a potential correlation in improving household welfare [21] and social status [20]. Most migration is done to increase the current value of the expected lifetime income [22]. Migrants in the new urban environment have better working conditions and quality of life. They are usually women, well educated, older, living in longer migration periods [23], unmarried, and have informal jobs [20].

Education and employment status of a household are reliable indicators for household welfare [19]. Employment provides opportunities to gain income, while education is a way to develop knowledge and get better employment. However, individuals with informal employment status in Jakarta has been found to have higher welfare level due to migration [20].

Education has a significant influence on the use of household latrines [18,16]. Household heads with higher education have more knowledge of healthy living [14]. A better understanding of the health impact of poor sanitation is a driving factor for investment in adequate sanitation, which declines the trend in open defecation [27].

Gender also influences sanitation preferences. Numerous research has shown that females tend to have high preferences for the health and non-health benefits of sanitation such as hygiene and privacy [10,25-27]. Research shows that women have an important role in determining sanitation choices and are able to persuade their partners to invest in adequate sanitation facilities [25].

Household size also determines the needs for sanitation facilities, especially the size of a septic tank. Commonly, households with four or more household members have a higher chance of having a latrine [28].

Efforts to improve access to sanitation facilities at the household level is expected to reduce the environmental and economic burden of a city. Indirectly, it can improve welfare, helps reduce poverty levels by reducing health costs, productivity gains associate morbidity and mortality, increase gender equality, environmental sustainability, and water resource [12,30]. Ultimately, sanitation adequacy can improve health and save lives.

METHODS

This research uses the microdata from the 2017 National Socio-Economic Survey which is conducted by The Indonesia's Central Bureau of Statistics. The survey, also known as *Susenas*, do annual collection of data relating to the socio-economic conditions of the community, including health, education, fertility, family planning, housing and other socio-economic conditions in all provinces in Indonesia. Data and indicators from *Susenas* have been widely used and are seen as important pieces of evidence useful for planning, monitoring, and evaluating government development programs. The 2017 survey sampled 3,483 households spread in six regions in Jakarta.

This research uses a quantitative approach to fulfill the research aims. Descriptive analysis is performed for data analysis using a cross-tabulation method, to map the adequacy of household sanitation in Jakarta. While the inferential analysis is performed using a multinomial logistic regression method, to identify the influence of household characteristics on the adequacy of household sanitation.

The research begins with examining the influence of resources (illustrated by the level of income and employment status of households) on sanitation adequacy. The research then examines the level of understanding (illustrated by the level of education), as well as other variables (marital status, gender, household size and migration status of households) and their correlation to sanitation adequacy.

The dependent variable in this research is the adequacy of household sanitation, adopted from sanitation ladder of The JMP [3]. The sanitation ladder was simplified into three categories: (1) level 0: inadequate sanitation (unimproved sanitation and open defecation), (2) level 1: adequate shared sanitation (shared sanitation), (3) level 2: adequate private sanitation (safely managed sanitation dan basic sanitation).

The independent variables are the predisposing factors that consist of household income (measured by expenditure per-capita (*exp_cap*)), employment status (*workstat*), education (*educ*), marital status (*maritalstat*), gender (*gend*), number of household member (*art*), and migration status (*risenmig* and *lifetimemig*). Pearson correlation method is used to define the correlation between each of independent variables. The result indicates that there is no multicollinearity between the independent variables.

Research Model

The dependent variables are treated in multinomial forms with three categories that do not have a natural sequence. The level labeled 0 ($Y=0$) set as the reference category that forms the basis of the logit function to compare other categories ($Y=1$ and $Y=2$) against $Y=0$. Modification of the variables

results in statistical modeling as follows:

$$\ln\left(\frac{P_{shared}}{P_{inadequate}}\right) = \beta_0 + \beta_1 exp_cap + \beta_2 workstat + \beta_3 educ + \beta_4 maritalstat + \beta_5 gend + \beta_6 art + \beta_7 risenmig + \beta_8 lifetimemig + \epsilon$$

$$\ln\left(\frac{P_{private}}{P_{inadequate}}\right) = \beta_0 + \beta_1 exp_cap + \beta_2 workstat + \beta_3 educ + \beta_4 maritalstat + \beta_5 gend + \beta_6 art + \beta_7 risenmig + \beta_8 lifetimemig + \epsilon$$

with:

$P_{inadequate}$ = opportunity for inadequate sanitation category

P_{shared} = opportunity for adequate shared sanitation category

$P_{private}$ = opportunity for adequate private sanitation category

Iteration log shows how fast the model is converged. The log likelihood value (-2.546,679), Chi-square likelihood ratio of 674.84 with p-value <0.0001, prob>chi2 value <0.05, Pseudo R2 value of 11.7%, and a large sample size shows that the model describes the quality of household sanitation facilities adequately. Partial effect was used in this research, which estimated by the Average Marginal Effect (AME), to obtain additional probabilities in each dependent variable.

RESULT

In this research, 85.64% of the sampled households in Jakarta owned adequate sanitation, of which 68.81% are private sanitation and 16.83% are shared sanitation. The rest of the households (14.36%) owned inadequate sanitation. Figure 1 shows the distribution of household sanitation adequacy in six regions of Jakarta. East Jakarta has the highest percentage of adequate private sanitation (78.95%), Central Jakarta has the highest percentage of adequate shared sanitation (34.43%), and the Thousand Islands has the highest percentage of inadequate sanitation (38.03%).

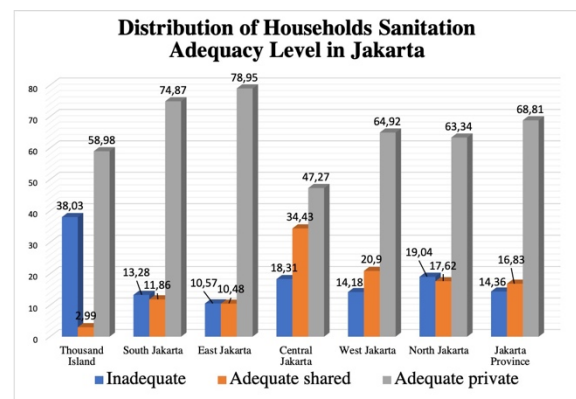


Fig.1 Distribution of Households Sanitation Adequacy Level in Jakarta

This research found that households in East Jakarta tend to have the longest duration of stay, have a private home, with better financial ability. The households in Central Jakarta have a higher percentage of migrant households who live in rental houses. On the other hand, households in Thousand Islands district tend to have a longer duration of stay, have a private home, but have a lower financial ability.

Table 1 Summary of Descriptive Statistic

Dependent Independent	Adequacy level of sanitation facilities in households				
	Inadequate	Adq. Shared	Adq. Private	Total %	n
Gender					
Female	11,86	15,72	72,42	100	328.619
Male	14,88	17,06	68,06	100	1.565.697
Number of household member					
<4 person	16	27,1	56,9	100	865.327
≥4 person	12,97	8,19	78,83	100	1.028.989
Marital status					
Not married	13,44	22,84	63,72	100	506.461
Married	14,69	14,64	70,67	100	1.387.855
Education					
Uneducated	20,36	18,67	60,98	100	148.999
Primary	21,4	19,08	59,52	100	330.771
Middle sch.	13,89	18,78	67,33	100	1.077.312
Univ.	6,27	7,60	86,13	100	337.234
Employment status					
Unemployed	9,28	8,76	81,96	100	392.172
Informal	15,68	17,32	67,00	100	613.269
Formal	15,68	20,05	64,26	100	888.875
Expenditure per capita (Rp 100.000)	16,232	18,035	24,725	-	-
Recent migrant					
Non-migrant	14,02	15,2	70,78	100	1.811.487
Migrant	21,8	52,45	25,74	100	82.829
Lifetime migrant					
Non-migrant	13,22	11,87	74,91	100	826.159
Migrant	15,24	20,67	64,1	100	1.068.157

Table 1 shows the summary of the descriptive statistics in this research. It provides some initial insight into the household characteristics and its correlation to the quality of sanitation. The independent variables with a strong influence on the private sanitation adequacy are (1) female (72,42%), (2) household member ≥4 people (78,83%), (3) married (70,67%), (4) college education (86,13%), (5) unemployed (81,96%), (6) high expenditure, (7) non-migrant recent (70,78%), and (8) non-migrant lifetime (74,91%). While the inadequate sanitation is strongly related with (1) male (14,88%), (2) household member <4 people (16%), (3) married (14,69%), (4) low education (primary) (21,4%), (5) informal and formal sector (15,68%), (6) low expenditure, (7) recent migrant (21,8), (8) lifetime migrant (15,24%).

Table 2 shows the inferential analysis results of the significant relationship between research variables and the comparison within the adequacy of household sanitation. The results of the inferential analysis are in line with the descriptive results. The comparison result can be summarized in two point:

1. the variables which significantly influence the increase from inadequate to adequate shared

sanitation category are household members <4 people (14,6%), formal employment status (11,2%), not married (9,6%), migrant lifetime (4,4%), and junior/senior high school education (0,7%). While gender, expenditure, and recent migrant status show no significant effect.

2. The variables which significantly influence the increase from inadequate to adequate private sanitation category are non-migrant recent (26,2%), higher level of education/university (19,7%), unemployment (17,9%), household members ≥4 people (16,4%), married (11,4%), female-headed (8,6%), and high expenditure (0,6%). The lifetime migrant status shows no significant effect.

Table 2 Multinomial Logistic Regression Analysis

Independent Variables	Adequate Shared sanitation			Adequate Private sanitation		
	Coef.	Std. err.	Part. effect	Coef.	Std. err.	Part. effect
Gender (0 = Female, 1 = Male)	0,17	0,23	0,06	-0,40**	0,21	-0,09
Number of household member (0 = <4 person, 1 = ≥4 person)	-0,90***	0,14	-0,15	0,48***	0,11	0,16
Marital status (0 = not married, 1 = married)	-0,54***	0,20	-0,10	0,37**	0,18	0,12
Education primary (0 = uneducated, 1 = primary)	0,03	0,23	-0,00	0,04	0,18	0,01
Mid.school (0 = uneducated, 1 = mid.sch)	0,56***	0,22	0,01	0,68***	0,17	0,08
Univ. (0 = uneducated, 1 = univ.)	0,50	0,32	-0,06	1,38***	0,25	0,20
Employment status Informal (0 = unemployment, 1 = informal)	0,10	0,20	0,07	-0,75***	0,16	-0,13
Formal (0 = unemployment, 1 = formal)	0,34*	0,20	0,11	-0,89***	0,16	-0,18
Expenditure per capita (Rp.100.000)	-0,01	0,01	-0,00	0,03***	0,00	0,01
Recent migrant (0 = non-mig, 1 = migrant)	0,33	0,27	0,15	-1,30***	0,29	-0,26
Lifetime migrant (0 = non-mig, 1 = migrant)	0,35***	0,13	0,04	-0,04	0,10	-0,04
_cons	0,03	0,27		0,97***	0,21	
Number of obs	3.483					
LR chi2(22)	674,84					
Prob > chi2	0,000					
Pseudo R2	0,117					
Log likelihood	-2.546,6791					

Note : *) significant at 10%; **) significant at 5%; ***) significant at 1%

DISCUSSION

This research found a statistical correlation between household characteristics with sanitation quality. In this research, longer duration of stay, a higher level of education, and unemployment status

have a significant correlation with the high percentage of marginal effect to the adequate private sanitation category. When households have been living longer in Jakarta, it can be assumed that they can adapt to the urban environment and improve their standards of living. On the other hand, education (formal and informal) can catalyze this process of behavior change, especially in increasing the knowledge on the importance of adequate sanitation, as well as improving the chance to have a better job opportunity. On the other hand, the unemployment status does not describe poor financial status. The samples tend to have a good financial ability even though they are unemployed.

From further descriptive investigation, this research found a statistical correlation between some variables:

1. female-headed households tend to have a higher correlation to adequate sanitation, with characteristics of not married, unemployed, and live in their own house together with children/son-in-law/grandchildren.
2. male-headed households tend to have a higher correlation to inadequate sanitation, with characteristics of not married, working in the informal sector, living alone in a rental house with uninhabitable condition.

The operational definition of not married status in this research is divided into three categories: single, widowed by law, and widowed by death. There are two possibilities why females who are not married tend to have adequate sanitation; (1) the female is an elder in her house at the time of the survey, and indirectly appointed as the head of the family, and (2) the females who are widowed have sufficient monthly living expenses or have inheritance so that they are financially capable even though they are unemployed.

On the other hand, the inadequate category indicates a correlation with the status of recent migrants, who live in rental houses, with uninhabitable conditions. Some of the migrants who come to Jakarta may have limited resources or financial ability. They try to survive by settling temporarily in a densely populated area. Many of them are from villages. They may still carry traits and habits that they develop while living in their previous dwelling. The transition between traditional rural culture to modern urban culture can create problems in their daily life, such as continually practicing open defecation [31]. According to research, these household characteristics found in Central Jakarta area. As for the Thousand Islands, our conjecture is related to low education and low welfare.

The other variables that also have a significant correlation to the adequate private sanitation category are being married, household members of ≥ 4 people, and female-headed households. Females tend to have a high preference for private defecation facilities in the household due to privacy needs, hygiene, and

safety factors. Even, the rate of open defecation is lower in female than in male [21].

Jakarta is targeted to achieve 100% access to proper and safe sanitation by 2024 [4]. Eradicating 14.36% of the inadequate category is a heavy task. The biggest challenge is presented by the practice of open defecation, inadequate sanitation facility in households, and inadequate clean water and sanitation service coverage. *Susenas* data show that the coverage of clean water services in 2017 is only 60% [5]. It can be ascertained that the remaining 40% still uses ground water sources to fulfill their water needs. Besides that, the coverage of wastewater management services in 2017 is 24.33% [12], and only targeted to be 35% by 2022 [29]. The lack of access to water resources may have influenced the household sanitation adequacy. Heads of households need strong reasons for the importance of adequate sanitation to decide to adopt adequate sanitation.

CONCLUSION

Research findings shows that 85.64% of household sanitation facilities in Jakarta have adequate sanitation (68.81% are adequate private sanitation and 16.83% adequate shared sanitation, while 14.36% are inadequate. The household characteristics of inadequate sanitations are male-headed household, household members < 4 people, married, with low education and income, working in informal sector, migrant (recent migrant and lifetime migrant), and living rented house in low living condition. The household characteristics that significantly influence the change from inadequate to adequate private sanitation are non-migrant recent, university education, household members ≥ 4 people, unemployed, married, female-headed household, and high expenditure. The problem of low-quality sanitation in households in Jakarta can be overcome by incorporating these correlated household characteristics in the policymaking process, especially to lower the percentage of inadequate sanitation.

Limitations of the Study

The analysis in this study is dependent on the availability of variables in the *Susenas* data. A comprehensive analysis conducting a household survey specifically to study the feasibility of disposal facilities at the household level in Jakarta is strongly recommended. It will strongly support the analysis results.

Acknowledgments

This paper is part of the University of Indonesia Research Grant 2020: Social-Humanities International Indexed Publications (Q4).

REFERENCES

- [1] Jakarta Provincial Statistics Board, Regional Statistics of DKI Jakarta Province 2019.
- [2] Jakarta Provincial Health Office, Presentation: Cross Convergence Community-Based Total Sanitation Program, 2019.
- [3] WHO and Unicef, Progress on Household Drinking Water, Sanitation and Hygiene 2000-2017: Special focus on inequalities, New York, 2019.
- [4] Republic of Indonesia, Presidential Regulation No. 18 of 2020 concerning National Medium-Term Development Plan for 2020-2024.
- [5] Regional Regulation of Jakarta Province No. 1 of 2018 concerning Regional Medium-Term Development Plan 2017-2022.
- [6] Stephen B., Clay's Handbook of Environmental Health, 21 Ed., Routledge, 2017, pp. 23-24.
- [7] Soekidjo N., Promosi Kesehatan: Teori dan Aplikasi, Rineka Cipta, 2010, hal. 59-60.
- [8] Soekidjo N., Ilmu Perilaku Kesehatan, Rineka Cipta, 2014, hal.75-82.
- [9] Jakarta Provincial Statistics Board, People's Welfare Indicator 2019.
- [10] Christine van Wijk-Sijbesma, Gender in Water Resources Management, Water Supply and Sanitation, IRC International Water and Sanitation Centre, Netherland, 1998, pp. 99-123.
- [11] Adam B., Marion W.J., P. Dabrase, I. Bhagwat, Patterns And Determinants Of Communal Latrine Usage in Urban Poverty Pockets in Bhopal, India, J. Tropical Medicine and Intl. Health, Vol.16,no.7, 2011, pp. 854–862.
- [12] William, F.V., and Jessica A.P., Unbundling household preferences for improved sanitation: A choice experiment from an urban settlement in Nicaragua, J. of Environmental Management 218, 2018, pp. 477-485.
- [13] Josef, N., Jana K., and Helena H., The Role of Perceived Social Norms in Rural Sanitation: An Explorative Study from Infrastructure-Restricted Settings of South Ethiopia, Int. J. Environmental Research and Public Health, 14, 794, 2017.
- [14] Anne T., Margaret K., Afullo A., Factors Influencing Latrine Coverage among the Maasai of Ildamat Location Kajiado District, J. Developing Country Studies,6,11,2016,pp.22-27.
- [15] Elena G., and Isabel G., Why do Household Invest In Sanitation In Rural Benin: Health, Wealth, or Prestige?, J. Water Resource. Res., 50, 2014, pp. 8314-8329.
- [16] Josef N., Frantisek F., Joseph K.W.H, Anant K., Social Determinants of Environmental Health: A Case of Sanitation in Rural Jharkhand. J. Science of the Total Environment 643, 2018, pp. 762–774.
- [17] Marion W.J., and Val Curtis, Achieving the “Good Life”: Why Some People Want Laterines in Rural Benin, J. Social Science & Medicine 61 (11), 2005, pp. 2446-2459.
- [18] Laeli A., Bagoes W., and Budi L., Factors that Influence the Utilization of Family Latrines in Jatibarang District, Brebes. J. Indonesian Health Promotion, Vol.14, No.1, 2019, pp.1-14.
- [19] Stephen M.S., and Martin, E.P.S., Pursuit Of Pleasure, Engagement, and Meaning: Relationships to Subjective and Objective Measures of Well-Being. J. Positive Psychology, 5(4), 2010, pp. 253-263.
- [20] Chotib and Beti N., Are Migrant Workers in DKI Jakarta More Welfare than Non Migrants? A Data Analysis of National Social and Economic Survey (Susenas) 2013, J. Strategic and Global Studies. Vol.1, No.1, 2018, pp.15-28.
- [21] Nanda M., and Chotib, Level of Well-Being among Migrants in Indonesia, Pertanika J. Soc. Sci. & Hum. 27 (3), 2019, pp. 2153 – 2167.
- [22] John K., and James R.W., Wages, Welfare Benefits and Migration, J. of Econometrics, 156, 2010, pp. 229–238.
- [23] Loc D.N., Katharina R. and Ulrike G., Rural–Urban Migration, Household Vulnerability, and Welfare in Vietnam. J. of World Development Vol. 71, 2013, pp. 79–93, 2015.
- [24] Ismaila R.A., Access to Sanitation Facilities among Nigerian Households: Determinants and Sustainability Implications. J. of Sustainability, 9, 2017, pp. 547-564.
- [25] Monica S.F., Wendy W., and Anjana B., Toolkit on Gender in Water and Sanitation, Gender Toolkit Series No.2, Washington D.C.: The World Bank, 1996, pp. 17-19.
- [26] O.O.Aluko, E.O.Oloruntoba, U.A.Chukwunye, E.U.Henry, E.Ojogun, The Dynamics and Determinants of Household Shared Sanitation Cleanliness in A Heterogeneous Urban Settlement in Southwest Nigeria, J. The Royal Society for Public Health, 165, 2018, pp. 125-135.
- [27] Kasnodiharjo and Elsa Elsi, Description of Environmental Sanitation, Maternal Behavior, and Child Health, J. National Public Health, Vol. 7, No. 9, 2013, pp. 415-420.
- [28] Abate B.B., Mesele B.A., Z.A. Gebrezgi, and Dejen Y.T., Availability and Utilization of Sanitation facilities in Enderta district, Tigray, Ethiopia, J. of Preventive Medicine And Hygiene, 2018, pp. E219-E225.
- [29] Regional Regulation of Jakarta Province No. 41 of 2016 concerning Master Plan for the Development of Domestic Wastewater Management Infrastructure and Facilities.
- [30] Hoang V.M., and Nguyen V.H., Economic Aspect of Sanitation in Developing Country, J. Environmental Health Insights, 5, 2011. pp.63-70
- [31] Parsudi S., Urban Society and Culture, YPKIK Publisher, 2004, pp.30.

SPATIAL PATTERN OF EARTHQUAKE PRONE AREAS OF BANTUL REGENCY, INDONESIA

Susiloningtyas, D¹, Della Ayu Lestari¹, Hengki Tasman², Tuty Handayani¹, Annacletus Ari Dartoyo³

¹Geography Department, Faculty of Mathematics and Natural Science, Universitas Indonesia, Indonesia

²Mathematics Department, Faculty of Mathematics and Natural Science, Universitas Indonesia

³Geospatial Information Agency, Indonesia

ABSTRACT

Bantul Regency is located around the subduction zone between the Indo-Australian Plate and is passed by the Opak Fault making it an earthquake-prone region. Earthquake disaster is a disaster that cannot be predicted so that an earthquake disaster mitigation effort is needed by studying the historical earthquake that occurred. The purpose of this study was to analyze Peak Ground Acceleration (PGA) both the average and maximum values in Bantul District based on earthquakes that occurred from 1900 to 2017. calculations using the Gutenberg - Richter method with the Richter formula combined with the intensity attenuation formula Subardjo-Prih Harjadi which is a function of magnitude, epicenter distance, and earthquake intensit. The PGA was then analyzed using the overlapping method with the built-up area. Based on the PGA average PGA distribution, the lowest average PGA value is 33.81 gals and the highest is 36.23 gals. Whereas based on the maximum PGA, the highest PGA distribution is in the northwest and southeast regions of Bantul Regency with the lowest maximum PGA value of 223.58 gals and the highest of 248.42 gals. The PGA value has the potential for an enormous risk of damage is on the VII MMI Scale. Pajangan Subdistrict, Bambanglipuro Subdistrict and Pundong Subdistrict are on average high PGA and maximum PGA, so these sub-districts have a higher risk potential than other sub-districts.

Keywords: Earthquake, Magnitude, Peak Ground Acceleration (PGA), vulnerability

INTRODUCTION

Indonesia-based on its geographical location is one of the regions prone to natural disasters. One of the natural disasters that often happens is an earthquake. Data shows that Indonesia is a country that is has a top level of seismicity in the world, over ten times as much seismicity in the United States [5]. Indonesia geographically located between 6° North Latitude-11° South Latitude and 95° East Longitude - 141° East Longitude are three places the world's major plates are the Indo-Australian Plate, the Eurasian Plate and the Pacific Plate. The activity of the three plates causes good soil movement small earthquakes that are only detected by seismographs, quakes that can be felt an average of about 70-100 times per year, and a quake cause damage between 1-2 times per year [5]

Yogyakarta Province and its surroundings are on two active plates, Indo Australia and Eurasia, which stretches from the western hemisphere of Sumatra to the southern hemisphere of Nusa Tenggara. This causes the Yogyakarta region and its surroundings very prone to tectonic earthquakes [4]. The source of the earthquake in this region is located in the sea from the subduction zone and on land from an active fault. In addition, there is an earthquake distribution at the top of the subduction zone or also known as the inter-plate zone, the accretionary prism zone. This earthquake is characterized by the epicenter of position in the sea but with shallow depth. The source

of the earthquake from the Benioff zone sometimes also occurs in this area. The source of the earthquake on land has been identified as coming from the Opak Fault. This is a fault that is considered causing the 2006 Yogyakarta earthquake. Based on the earthquake distribution, there may be other active faults besides the Opak fault. The maximum magnitude of the earthquake originating from the subduction zone was 8.1 Mw, while the Opak fault was 6.8 Mw [4].

One of the most damaging earthquake evidences occurred on Saturday, May 27, 2006 at 05.53 WIB obtained from the Meteorological, Climatological, and Geophysical Agency of Indonesia station, United States Geological Survey (USGS), and the station owned by the Volcano Technology Research and Development Center, Yogyakarta. Data from the Volcano Technology Research and Development Center is then analyzed by the Geological Agency Emergency Response Team. USGS noted that the epicenter was located at coordinates 8.01° South Latitude & 110.29° East Longitude at a depth of 17.2 km, strength of 6.2 Mw, and intensity of damage to VII MMI. According to BMKG, the earthquake centered at 7.89° South Latitude & 110.37° East Longitude and a depth of 40 km, with a magnitude of 6.2 Mw, and an intensity of VII MMI. While according to Meteorological, Climatological, and Geophysical Agency of Indonesia, the earthquake was centered at 8.08° South Latitude & 110.31° East Longitude, depth of 33 km, with a magnitude of 5.8

SR and intensity scale VII-IX MMI [4].

Over 5,000 people die, huge property losses, and a lot of environmental damage. Several cracks in the ground, liquefaction, and landslides occurred in the Yogyakarta region, which showed that the earthquake shocks were strong. The Bantul region experienced the worst disaster, so that the May 27, 2006 earthquake can also be referred to as the “Bantul’s Earthquake”. The 2006 Yogyakarta earthquake was one of the earthquakes with the most casualties in Indonesia since 1612 [4].

This earthquake has made us aware of the importance of mitigation efforts, both structural or physical and non-structural or non-physical mitigation [7] [10] [11]. Mitigation efforts must be carried out to minimize the risk of earthquake and tsunami disasters in the Yogyakarta region, which may be repeated in the future. Including non-physical mitigation efforts, delivery of data and information about the danger and impact of the earthquake so that people can prepare for disasters. Various attempts were made to reduce the impact that occurs when an earthquake occurs. One of them is by knowing the Peak Ground Acceleration (PGA) both the average value and the maximum value in Bantul Regency based on earthquakes that occurred from 1900 to 2020 [1] [3]. The PGA was then analyzed using the overlapping method with the built-up area of Bantul Regency. I expect the results of this study can be used as a reference in disaster mitigation efforts and disaster risk management plans.

METHODS

Earthquake wave vibration parameters recorded by seismographs generally the velocity deviation or velocity in units of kine (cm/s). Besides velocity, other parameters such as displacement (deviation in micrometer units) and acceleration (acceleration in gal units or cm/s^2) can also be specified. Seismic or frequent wave acceleration parameters called the acceleration of the ground is one of the important parameters in science seismology [8]. Acceleration is the parameter that states changes in speed from rest to a certain speed. Peak Ground Acceleration is the value of the greatest ground vibration acceleration that ever happened somewhere caused by earthquake waves [6]. In this study, calculations using the Gutenberg-Richter method with the Richter formula combined with the intensity attenuation formula Subardjo-Prih Harjadi which is a function of magnitude, epicenter distance, and earthquake intensity. The greater the PGA that occurs, the greater the risk. PGA data which is a parameter of the source of damage caused by an earthquake, obtained through functions of magnitude, epicenter distance, and earthquake intensity earth (Ibrahim & Subardjo, 2005). The PGA calculation value is carried out the

steps as follows [5] [9]:

- a. Calculate epicenter distance

The epicenter distance is determined by calculating the distance from the epicenter to the point X, using the formula:

$$\cos \Delta = \cos L_e \cos L_x + \sin L_e \sin L_x \cos (\lambda E - \lambda X) \quad (1)$$

Information:

$\cos \Delta$: Epicenter distance to point X
 L_x : The geographical latitude of the point X, for which the PGA value will be calculated;
 λx : Geographic longitude of point X, for which the PGA value will be calculated;
 L_e : Epicenter geographical latitude,
 λe : Epicenter geographical longitude
 Δ : Distance between points E and X in degrees
 Δ° : converted to kilometers, diverting 111.11 Km for every 1°

- b. Calculate the intensity in the hypocenter with the formula;

$$I_o = 1.5 (M - 0.5) \quad (2)$$

Information

I_o : Intensity at the source;
 M : Magnitude of body wave (Richter Scale)

- c. Calculate the intensity at point X with the formula of the attenuation constant of Prih Haryadi and Subardjo:

$$I = (I_o \cdot \exp -b \cdot \Delta) \quad (3)$$

Information:

I : Surface intensity
 I_o : Intensity at the source
 Δ : Distance to the source of the earthquake (epicenter)
 b : The attenuation constant (energy decay), worth 0.0021
 \exp : Natural number, worth 2,786

- d. Calculate the PGA value at point X with the formula;

$$\log \alpha = (I / 3) - 0.5 \quad (4)$$

Information:

α : Peak Ground Acceleration (PGA) in gal (cm / second)
 I : Surface intensity on the MMI scale and the numbers 3 and 0.5 are constants.

The point of the earthquake taken in this study was that an earthquake that had occurred in the Special Region of Yogyakarta with a coordinate limit of $7^\circ 32' 30''$ LS to $8^\circ 12' 20''$ LS and $110^\circ 0' 10''$ BT

to 110 ° 50' 5" BT sourced from Earthquake USGS and BMKG. Determination of the reference point is done by making the center of gravity. Determination of the emphasis is done on each village in the city of Bengkulu, as many as 75 reference points. In one earthquake event, the PGA value was calculated at each center of gravity so that at each point a PGA value was obtained, then the PGA value was calculated for all reference points from the PGA values, a maximum PGA value is sought at each point. After getting the maximum PGA value in each village in Bengkulu City, then the same point value will be calculated and will form a contour-like line using the interpolation method. In this study earthquake data was divided into two groups, i.e. maximum PGA and average PGA. The division of these two groups is based on different patterns and levels of earthquake risk. Then from the minimum and maximum values of each group are categorized into three classes with the equal interval method each class has the same interval in the interpolation's division class.

DISCUSSIONS

Distribution of Earthquakes in Yogyakarta

The frequency of earthquakes in Yogyakarta is not really high but destructive earthquakes, in the period of 120 years, i.e. the period 1900 to 2020 there were 34 earthquakes with a magnitude of 3.7 SR to 6.3 SR with a depth of less than 100 km (Fig 1). Earthquakes with a magnitude of less than 4 SR occurred three times, earthquakes with a magnitude of 4 SR up to 5 SR occurred 26 times and earthquakes with a strength of over 5 SR occurred three times. Significant and destructive earthquake occurred on March 13, 1981 with the intensity in Yogyakarta VII MMI with the resulting impact of the cracked walls of the Ambarukmo Hotel. On 25 May 2001 with magnitude 6.3 SR depth of 143 km and intensity in Yogyakarta V MMI and minor damage in Yogyakarta. On May 27 2006, with magnitude 5.9 SR 33 km and intensity VII MMI. This is characterized by: shocks felt by everyone, including those inside the vehicle; crockery falling and breaking; old buildings and buildings that are designed not to withstand earthquake shocks collapse and are damaged; liquefaction, land cracks, and landslides occur; turbid community wells, gutters and irrigation channels damaged; and the ceiling and the top of the building are broken.

Geologically, Bantul Regency is bypassed by the Opak Fault. Based on historical records of destructive earthquake events from Supartoyo et al. (2014) coupled with the events of 2015, the Yogyakarta area has experienced at least seven destructive earthquake events. One incident is thought to have caused a tsunami, namely the earthquake in 1840. The

destructive earthquake events in 1943, 2006 and 2010 were estimated to originate from the Opak fault. In addition, Bantul Regency is located in the collision's vicinity zone (subduction zone) between the Indo-Australian Plate which is moving northward to the Eurasian Continent Plate at a speed of $\pm 7\text{ cm / year}$. This zone is about 200 - 250 km from the South Coast of Java and has the potential to cause an earthquake. The earthquake that occurred in the collision zone was one of the prime causes of local tsunamis, which in a quick time had the potential to impact the South Coast of Java, including the beaches in Bantul Regency.

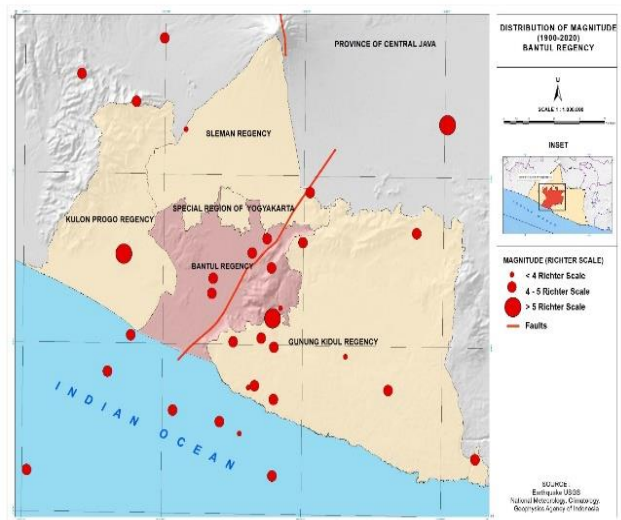


Fig. 1 Distribution of Magnitude (1900-2020) Bantul Regency.

Based on these conditions, the May 27, 2008 earthquake had a very significant impact on Bantul District with 4,143 fatalities, then 71,763 houses were damaged, 71,372 houses were severely / moderately damaged and 73,679 houses were lightly damaged. For Bantul Regency itself the most severe damage occurred in Jetis sub-district in 143 people, then 71,763 houses were damaged, 71,372 houses were severely damaged / moderately damaged and 73,679 houses were lightly damaged. For Bantul Regency itself the most severe damage occurred in Jetis sub-district in 143 people, then 71,763 houses were damaged, 71,372 houses were severely damaged / moderately damaged and 73,679 houses were lightly damaged. For Bantul Regency itself the most severe damage occurred in Jetis sub-district in where 11,356 houses were totally damaged. Damage data in every district is complete can be seen in Table 1. The earthquake also caused Adi Sutjipto Airport to be temporarily closed due communication disruptions, building damage and cracks on the runway, so that air transportation was diverted to Semarang and Achmad Yani Airport Adisumarmo, Solo Airport.

Spatial Pattern of the Average of Peak Ground Acceleration, Year 1900 to 2020

If assessed based on the PGA, the average PGA distribution in Bantul Regency shows in Figure 2 with the lowest average PGA value of 33.81 gals and the highest of 36.23 gals. Based on [2] with an average PGA value is in the class of 25-50 gals, the resulting risk level is small. This average PGA distribution has a pattern further north, so the average PGA is getting lower (Fig.2). The average low PGA area (<34 gals) is in the north of the Regency with an area of 5638.98 Ha or 11.03% of the Bantul Regency area is in the sub-districts of Sedayu Sub-district, part of the Kasihan Sub-district, part of the Banguntapan Sub-District and part of the Pinyungan Sub-District. The average PGA area (34-35 gals) is in the north of Bantul Regency with an area of 11,133 hectares or 21, 78% of the Bantul Regency area is in some areas of Sedayu District, Pajangan District, Kasihan District, Sewon District, Banguntapan District, Pleret District and Pinyungan District. Then for the PGA region the average high (> 35 gals) is in the middle to the south of Bantul Regency with an area of 34,346, 65 Ha or 67.19% of the Bantul Regency area.

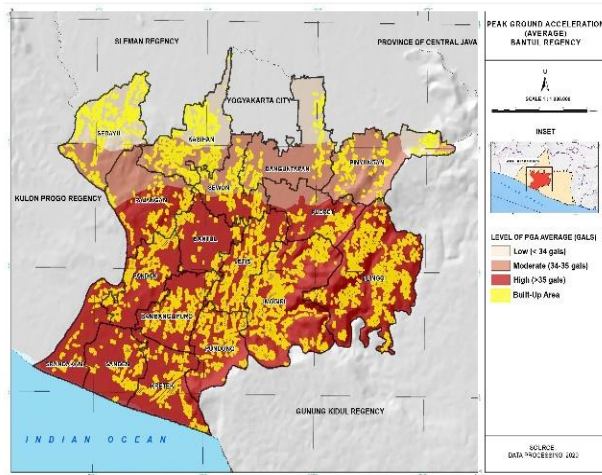


Fig. 2 Peak Ground Accelarton (Average) Bantul Regency

Table 1. shows the area of built-up area that is in each average PGA class. The lowest risk districts are in Sedayu District which has an area of 634.27 Ha with 537.47 Ha including the low class and 96.80 Ha including the moderate class. Conversely, it can also be seen that several sub-districts that are on a high average PGA with the entire area included in the class. Such as Bambanglipuro Subdistrict, Imogiri Subdistrict, Jetis Subdistrict, Jetis Subdistrict, Kretek Subdistrict, Pandak Subdistrict, Pandak Subdistrict, Pudonhm Subdistrict, Sanden Subdistrict and Srambat Subdistrict. These sub-districts have a higher risk potential than other sub-districts, so efforts are

needed to mitigate disasters so that they can recover quickly in the event of an earthquake.

Table 1. Distribution of Built-up Area in each class of PGA Average

District Name	Built-up Area (Ha)			Total
	Low PGA	Moderate PGA	High PGA	
Bambanglipuro			452.78	452.78
Banguntapan	79.72	184.42	6.48	270.61
Bantul		3.11	179.54	182.65
Dlingo		3.26	965.57	968.83
Imogiri			1077.99	1077.99
Jetis			657.23	657.23
Pity	376.91	390.78		767.70
Clove			373.28	373.28
Display		37.57	251.54	289.10
Pandak			451.95	451.95
Piyungan	67.51	200.95		268.45
Pleret		10.72	183.80	194.52
Pudong			411.62	411.62
Sanden			220.30	220.30
Sedayu	537.47	96.80		634.27
Sewon		232.27	142.01	374.28
Srambat			122.66	122.66
Total of Built-up Area				7718.22

Spatial Pattern of the Maximum of Peak Ground Acceleration, Year 1900 to 2020

If assessed based on the maximum PGA, PGA's distribution in Bantul Regency shows in Figure 3 with the lowest maximum PGA value of 223.58 gals and the highest of 248.42 gals. Based on Fauzi, 2000 with a maximum PGA value which is in the class 200-300 gals with a high level of risk. This is indicated from the earthquake on May 27, 2006 which has intensity VII MMI. This is characterized by: shocks felt by everyone, including those inside the vehicle; crockery falling and breaking; old buildings and buildings that are designed not to withstand earthquake shocks collapse and are heavily damaged; liquefaction, land cracks, and landslides occur; turbid community wells, gutters and irrigation channels damaged; and it breaks the ceiling and the top of the building.

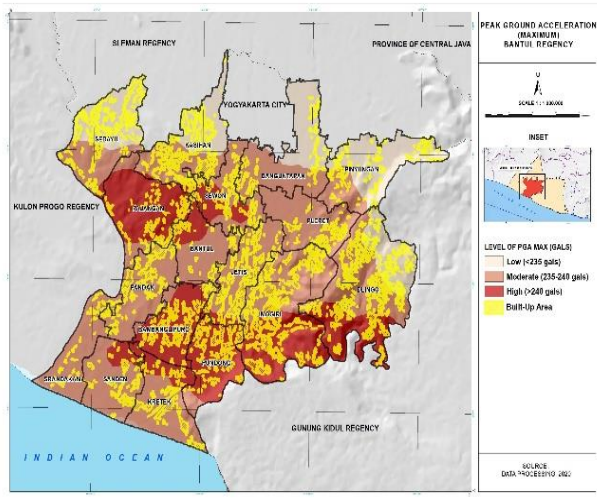


Fig. 3 Peak Ground Acceleration (Average) Bantul Regency

In general, this maximum PGA distribution has a pattern going further north, the average PGA getting lower. However, specifically for the maximum PGA which is in the high class spread in the northwest and southeastern areas of Bantul Regency. This happened because of the magnitude of the influence of the earthquake on May 25, 2001, with magnitude 6.3 SR depth of 143 km which has an epicenter point in the western part of Yogyakarta that affects the northwest region of Bantul Regency. Then the earthquake on May 27, 2006, with a magnitude of 5.9 SR depth of 33 km which has an epicenter point in the southeastern Bantul Regency.

Table 2. shows the area of developed land is in each of the maximum PGA classes. The district with the lowest risk is in Pinyungan District which has an area of 268.45 Ha with 203.39 Ha including the low class and 65.06 Ha including the moderate class. Conversely, it can also be seen that some sub-districts that are at the maximum PGA that are in the high class with almost the entire area of the area included in the class, such as Pleret District, Bambanglipuro District and Pundong District. These districts have a higher risk potential than other districts. This is in line with the earthquake damage data of May 27, 2006, in the sub-district which was damaged. The total damaged houses in Pundong District were 6,793 houses, Pleret District as many as 1,228 houses and Bambanglipuro District 6,587 houses. These sub-districts also need more attention as a disaster mitigation effort.

Table 2. Distribution of Built-up Area in each class of PGA Maximum

District Name	Built-up Area (Ha)			Total
	Low PGA	Moderate PGA	High PGA	
Bambanglipuro		49.51	403.26	452.78
Banguntapan	117.59	150.77	2.20	270.61
Bantul		109.11	73.54	182.65
Dlingo	205.55	531.67	231.61	968.83
Imogiri		564.46	513.53	1077.99
Jetis		602.30	54.93	657.23
Pity	369.80	377.53	20.26	767.70
Clove		301.62	71.66	373.28
Display		57.49	231.62	289.10
Pandak		448.16	3.79	451.95
Piyungan	203.39	65.06		268.45
Pleret		194.52		194.52
Pudong		1.04	410.57	411.62
Sanden		180.43	39.87	220.30
Sedayu	506.02	120.18	8.29	634.27
Sewon		261.49	112.78	374.28
Srambat		122.66		122.66
Total of Built-up Area				7718.22

CONCLUSION

The frequency of earthquakes in Yogyakarta is high, in the period of 43 years, namely the period 1974 to 2017 there were 34 earthquakes with a magnitude of 3.7 SR to 6.3 SR with a depth of less than 100 km. Based on the PGA, the average PGA distribution has a pattern that the further north the average PGA is lower with an average PGA value of 33.81 gals and the highest of 36.23 gals. Based on the maximum PGA, the highest PGA distribution is in the northwest and southeast regions of Bantul Regency with the lowest maximum PGA value of 223.58 gals and the highest of 248.42 gals. The PGA value has the potential for a large risk of damage which is on the VII MMI Scale. Pajangan Subdistrict, Bambanglipuro Subdistrict and Pundong Subdistrict are on average high PGA and maximum PGA as well, so these sub-districts have a higher risk potential than other sub-districts. More attention is needed to these sub-districts to mitigate disasters.

REFERENCES

- [1] Emad G.S.M., Sarah L.G., Application of GMPEs to Estimate the Minimum Magnitude and Peak Ground Acceleration of Prehistoric Earthquakes at Hollywood, *Journal of Engineering Geology*, vol.214, 2016, pp.60-66
- [2] Fauzi, "Geographic Information System for Natural Disaster Map in Indonesia". 2000.
- [3] Gandomi M., Soltanpour M., Zolfaghari M.R., Gandomi A.H., Prediction of Peak Ground Acceleration of Iran's Tectonic Regions Using a Hybrid Soft Computing Technique, *Journal of Geoscience Frontiers*, vol.7, 2016, pp.75-82
- [4] Geological Agency of Mineral Resources of the Republic of Indonesia., 10 Years from the Yogyakarta Earthquake, *GEOMAGZ*, Vol.6, No.2. The Ministry of Energy and Mineral Resources of the Republic of Indonesia, 2016, pp.18-29
- [5] Ibrahim, G and Subardjo, *Pengetahuan Seismologi. Jakarta: Badan Meteorologi dan Geofisika*. 2005
- [6] Mase L.Z., Likitlersuang S., Tobita Tetsuo., Analysis of Seismic Ground Response Caused During Strong Earthquake in Northern Thailand, *Journal of Soil Dynamics and Earthquake Engineering*, Vol.114, 2018, pp.126
- [7] Rahpeyma S., Halldorsson B., Hraskelsson B., Green R.A., Jonsson S., Site Effect Estimation on Two Icelandic Strong-Motion Arrays Using a Bayesian Hierarchical Model for the Spatial Distribution of Earthquake Peak Ground Acceleration, *Journal of Soil Dynamics and Earthquake Engineering*, vol.120, 2019, pp.369-385
- [8] Silacheva N.V., Kulbayeva U.K., Kravchenko N.A., Probabilistic Seismic Hazard Assessment of Kazakhstan and Almaty City in Peak Ground Accelerations, *Journal of Geodesy and Geodynamics*, Vol.9, 2018, pp.131-141
- [9] Supriatna, Samedi, J.M., & Nurmala, C., Peak Ground Acceleration (PGA) of Destructive Earthquake in Cimandiri Fault, Sukabumi, West Java. Paper Reference Number 17. Depok: Department of Geography, Faculty of Mathematics and Natural Science University of Indonesia. 2010
- [10] Wegener T., Goda K., Erdik M., Daniell J., Wenzel F., A Spatial Correlation Model of Peak Ground Acceleration and Response Spectra Based on Data of the Istanbul Earthquake Rapid Response and Early Warning System. *Journal of Soil Dynamics and Earthquake Engineering*, vol.85, 2016, pp.166-178
- [11] Zeng Z., Shuanggen J., and Lihong J., *Co-seismic Deformation Following the 2007 Bengkulu Earthquake Constrained by GRACE and GPS Observations*. *Journal of the Earth and Planetary Interiors*, vol. 280, 2018, pp. 20-31

INFLUENCE OF LIGHT ON MICROBIAL RIVER WATER ECOSYSTEM AND ITS SELF-PURIFICATION POTENTIAL

Fumitake Nishimura¹, Yuki Koike² and Michiko Masuda³

¹ Department of Environmental Engineering, Kyoto University, Japan; ² Department of Civil and Environmental Engineering, Ehime University, Japan; ³ Department of Civil Engineering, Nagoya Institute of Technology, Japan

ABSTRACT

Self-purification at rivers is mainly conducted by microorganisms attached on river bed. In order to enhance the self-purification capacity, several process or technologies have been proposed for improvement of river water quality and preservation of bio-diversity. From the viewpoints of environmental engineering, finding influential parameters and their effective control are effective to improve river water quality. However, there are a lot of parameters affecting self-purification capacity at rivers, and quantitative evaluation of these parameters have not been completed. In this study, influence of light on both microbial river water ecosystem and its self-purification capacity are investigated. There are several type of water purification facilities incorporated in rivers in order to improve river water quality and maintain bio-diversity. Most of the cases, light (sun light) is not blocked, and the light might affect microbial community and structure by photo synthesis.

Lab-scale experimental facilities (artificial river) are set, and artificial contaminated river water are introduced to the system. Light irradiation stimulates algal activity and affects the composition of the other microorganisms such as bacteria and zooplankton. By mass balance analysis of carbon, it is made clear that amount of organic carbon accumulated in the river under lighting condition becomes almost double compared with the case under dark condition. It is suggested that clean river water condition can be affected by light more than contaminated river water condition because of the large relative intensity of organic carbon loading by photo synthesis.

Keywords: self-purification, river ecosystem, mass balance analysis, photosynthesis

INTRODUCTION

In order to preserve water environment in both urban section and the catchment area around the section, sewerage is important facilities and plays important roles. However, sewerage development requires not only huge cost but also long time. For example, it takes 38 years to increase its coverage from 30% (at the end of FY1980) to 79% (at the end of FY2018) in Japan [1]. In the areas of where the sewerage system has not been developed, the ratio of domestic contaminants to total contaminants load into enclosed water areas such as lakes and inner bays is higher [2]. It is difficult to reduce the discharge amount of contaminants by individual households, therefore, direct purification in rivers, channels, lakes and bays is being conducted in order to reduce the loading rate until the sewerage system development is completed [3], [4]. Among the direct purification methods, the contact oxidation process has been attracting attention and it is adopted in many places because it enhances the natural purification function and seems to be environment-friendly. has high hydrophilicity [5]. However, good results are not always obtained because proper design and operating factors have not been sufficiently clarified. Operational and design parameters in the system are inlet water quality, water flow rate, HRT, DO, the

water temperature, and so on. Light irradiation is one of them. In the direct purification process to the river, it is practically not designed to block sunlight. There are some cases where light irradiation was studied as a design factor in the design of direct purification [6], [7], [8], but few cases, and studies including treatment processes have not been sufficiently conducted. However, the effects of light (mainly visible light) on the treatment results should be fully considered taking into account photosynthesis.

In this study, the effects of light irradiation on the biota, which is the main component of purification, during the treatment process was investigated using a laboratory-scale contact oxidation system. The amount and number of microorganisms in the treatment process, their activity, dissolved oxygen, and the concentration of organic and inorganic substances in the treated water were monitored and evaluated the effects of light.

MATERIALS AND METHODS

The schematic diagram of the experimental equipment is shown in Fig. 1. The experimental water channel was made of acrylic and the width, height and length of the channel are 1 cm, 4 cm, 200 cm, respectively. In the water channel, a fiber carrier (made by Chisso Filter Co., Ltd., Japan, material:

polyethylene/polypropylene mixture, fiber length 64 mm, specific gravity 0.90 to 0.96, that is easy to fix for retaining biota) is packed. The thickness of the incorporated fiber carrier is 1 cm, and attached to the channel bottom. The packing density of the fiber carrier becomes 0.031 g/cm³. Organisms used in this study was collected from Okawa, Miyamae River, and irrigation channels in Matsuyama City, Ehime Prefecture, Japan, and they were inoculated at 25 cm intervals from the upstream to the downstream. Three experimental channels were prepared, and two of them were set under the light conditions, (hereinafter referred to as case L-1 and case L-2) and the other was set under dark condition. (hereinafter referred to as case D). These three channels were installed on the same shelf, and the entire shelf was surrounded by a blackout curtain. Under light conditions, white fluorescent lamps were used to irradiate the upper part of the channel with an illumination intensity of 3000 Lux every 12 hours. Under dark conditions, the water channels were covered with aluminum foil to block the light. The water temperature in the water channel was set to 25°C by contacting silicon tubes on both sides of the water channel (inner diameter: 8 mm× outer diameter: 1 mm) and circulating water at 30°C inside the tube. The composition of the artificial wastewater used in these experiments was shown in Table 1. The wastewater was continuously flowed into the experimental channels with a flowrate of 100 mL/h. The DOC of the artificial wastewater was set to 20 mgC/L, assuming a small-to-medium-

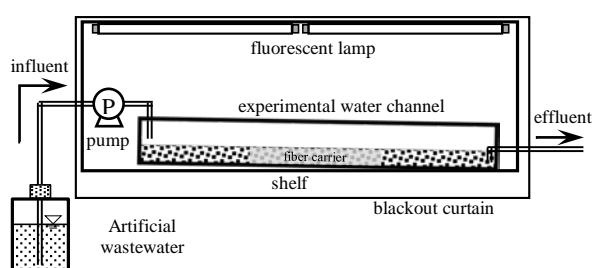


Fig.1 Schematic diagram of experimental setup

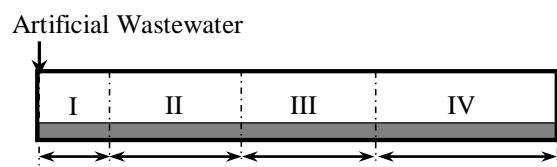


Fig.2 Section of the waterway (Unit:cm)

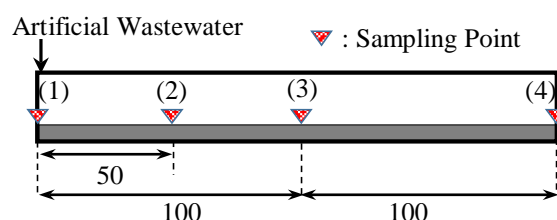


Fig.3 Points of sampling (Unit:cm)

sized river in a city where sewerage development is delayed. The hydraulic retention time was estimated 188 minutes as a result of the tracer experiment using NaCl, that means average water level of the channel was 1.56cm. The experimental equipment was operated for 90 days in winter season.

DOC was measured as the amount of dissolved organic matter in each channel, and the number of viable and total bacteria was measured as the amount of biomass over time. Then, on the 90th day, in order to grasp the condition inside the channel in detail, the channel was divided into four sections I to IV shown in Fig. 2 from the artificial wastewater inflow section. For the division of the sections, visual observation of both the algae green density and water depth in the channel on day 73 were considered. SS, viable cell count, total cell count, zooplankton population, Chl-*a* concentration, and total dehydrogenase activity of each category were measured. For the measurement of the number of bacteria and the number of zooplankton population, the sampling points shown in Fig. 3 were provided in each compartment. Syringe was used for the sampling. Samples mixed with dissolved and suspended matters from both the fiber carrier and the channel wall were collected and used for the measurement of SS, Chl-*a* concentration and total dehydrogenase activity.

Table 1 Composition of artificial wastewater

Substrate	concentration	Substrate	concentration
NaCl	1.32mg/L	NaHCO ₃	38.3mg/L
KH ₂ PO ₄	3.72mg/L	MgSO ₄ · 7H ₂ O	1.64mg/L
KCl	2.68mg/L	Dextrin	15.2mg/L
NH ₄ Cl	19.1mg/L	Bacto peptone	32.7mg/L

RESULTS DISCUSSION

Removal capacity of organic matter and accumulated materials in channels

Fig. 4 shows the daily change of DOC in the inflow and outflow water of each case. From the 3rd day after the start of the experiment, it was almost in the range of 3 to 6 mgC/L, and there was no difference in the removal efficiency of organic substances in the entire channel resulting from the effect of light irradiation.

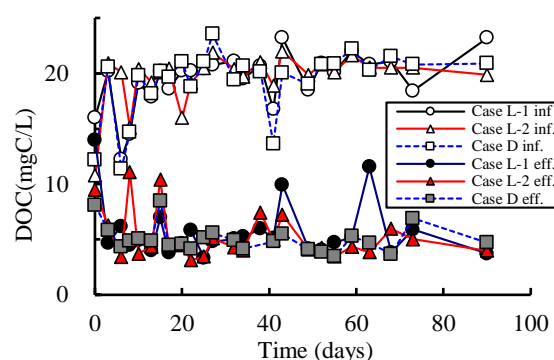


Fig.4 Time course of DOC in influent and effluent

Fig. 5 shows the SS and its composition in each section. Under dark conditions, SS increased slightly in section II but decreased as it flowed down. In the cases of light conditions, it did not decrease as much as in dark condition, and in some section it increased to the same level or in sections III-IV. The amount of accumulated organic matter in the entire canal was 120 to 130 mgC in the two cases under the light condition, whereas the amount in the dark condition is 50 to 60 mgC which was about 50% or less of the light condition. It is suggested that organic matter is easy to accumulate under light conditions due to photosynthesis.

Biota in the channel

Fig. 6 shows the total and viable cell counts at each section. There was no difference in total and viable cell counts under both dark and light conditions, and the numbers decreased as they flowed down. Between section I and section IV, the number of viable cells decreased by one order and the total number of cells decreased by two orders. In section I, where the loading rate of organic matter load is higher, the environment became anaerobic, and under light conditions, the presence of purple bacteria were observed.

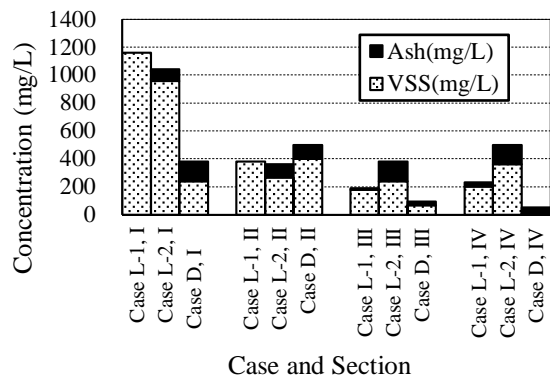


Fig.5 SS and its composition at each section

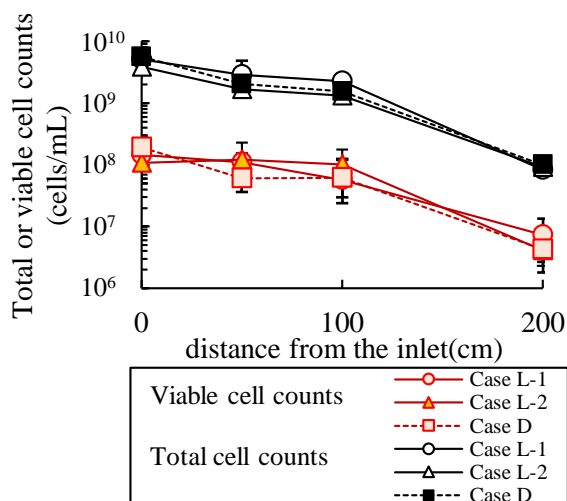


Fig.6 Total and viable cell counts at each point

Fig. 7 shows the population of zooplankton. In Section I, the population tended to be small in all cases. It is considered that it was difficult for zooplankton to live in Section I because of its anaerobic condition. The proportion of metazoans increased as they flowed under both light and dark conditions.

The Chl-*a* concentration at each division is shown in Fig. 8. More number of algae was confirmed in section IV where the organic matter load was low. The algae inoculated at the beginning of the experiment remained in sections II to IV. It is considered that the main component of SS in section I and IV was microbial communities and algae, respectively.

The total dehydrogenase activity in each section is shown in Fig. 9. The activity tended to be higher in light conditions, and the difference in the sections III and IV was obvious.

Carbon balance in the channel

Considering these experimental results, it can be concluded that the treated water quality was not different between light and dark condition, however, the organic carbon amount accumulated in the channel was higher in light conditions than in dark condition due to photosynthesis. In particular, it was suggested that the effect of light cannot be ignored

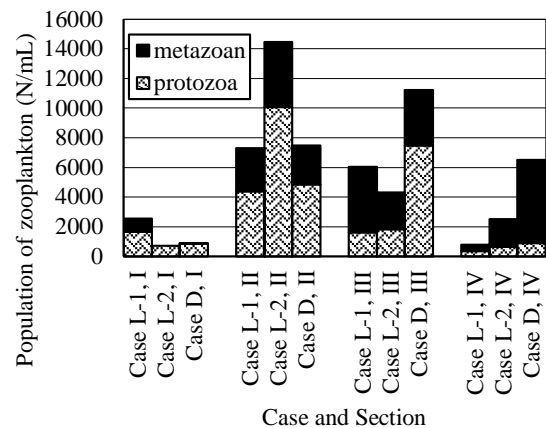


Fig.7 Population of zooplankton at each section

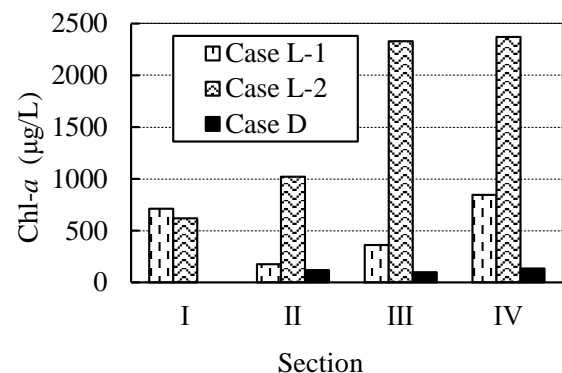


Fig.8 Concentration of Chl-*a* at each section

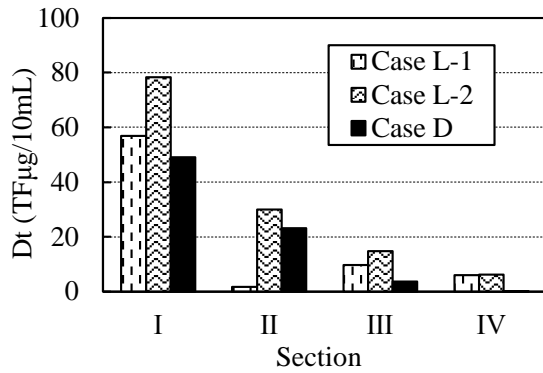


Fig.9 Dehydrogenase activity at each division

Table 2 Expression of carbon conversion of standing crop

Symbol	Item	Equation
C_P	Algae	$C_P = b \cdot (P/1000) \cdot (V/1000)$
C_B	Bacteria	$C_B = B \cdot a \cdot w_B \cdot V$
C_{Z1}	Protozoa	$C_{Z1} = Z_1 \cdot a^* \cdot w_{Z1} \cdot V$
C_{Z2}	metazoan	$C_{Z2} = Z_2 \cdot a^* \cdot w_{Z2} \cdot V$
C_O	Abiotic organic matter	$C_O = D_1 \cdot (V/1000)$

*: (C/protozoan dry weight), (C/bacterial dry weight) were used for (C/metazoan dry weight)

Table 3 Carbon transfer process and the expression

Process	Equations
Death of bacteria	$R_1 = k_B \cdot w_B \cdot a \cdot B$
Death of algae	$R_2 = k_P \cdot (P/1000) \cdot (V/1000) \cdot b$
Death of protozoa	$R_{3-1} = k_{Z1} \cdot w_{Z1} \cdot a \cdot Z_1 \cdot V$
Death of metazoan	$R_{3-2} = k_{Z2} \cdot w_{Z2} \cdot a \cdot Z_2 \cdot V$
Degradation of abiotic organic matter by bacteria	$R_4 = B \cdot r_1 \cdot V$ (assuming 1 cell = 1 CFU)
Predation of algae by metazoans	$R_5 = a \cdot r_2 \cdot Z_2 \cdot w_{Z2} \cdot V$ In case $R_5 > C_P$, $R_5 = A \cdot r_3 \cdot (V/1000)$
Primary production by algae	$R_6 = r_4 \cdot c \cdot (P/1000) \cdot (V/1000)$
Bacterial predation by zooplankton	$R_7 = r_5 \cdot a \cdot Z \cdot V$
Inflow into the section	$R_8 = D_1 \cdot (Q/1000) \cdot 24$
Outflow to the outside	$R_9 = D_2 \cdot (Q/1000) \cdot 24$

A: Algal biomass/algal biomass (literature value)(= C_P/e)

D_1 : DOC at the previous section (mgC/L)

D_2 : DOC in the effluent (mgC/L)

P : Chl- a (μ g/L)

B : viable bacteria count (CFU/mL)

Z_1 : Protozoa population (N/mL)

Z_2 : Metazoan population (N/mL)

Z : Zooplankton population (N/mL) (= $Z_1 + Z_2$)

V : Volume of the section (mL)

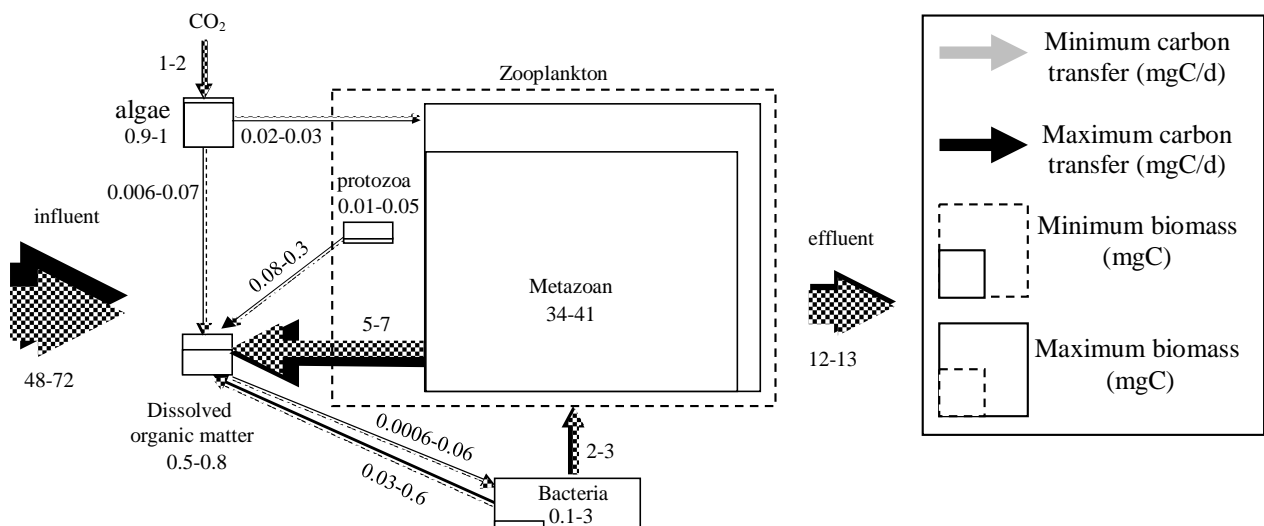
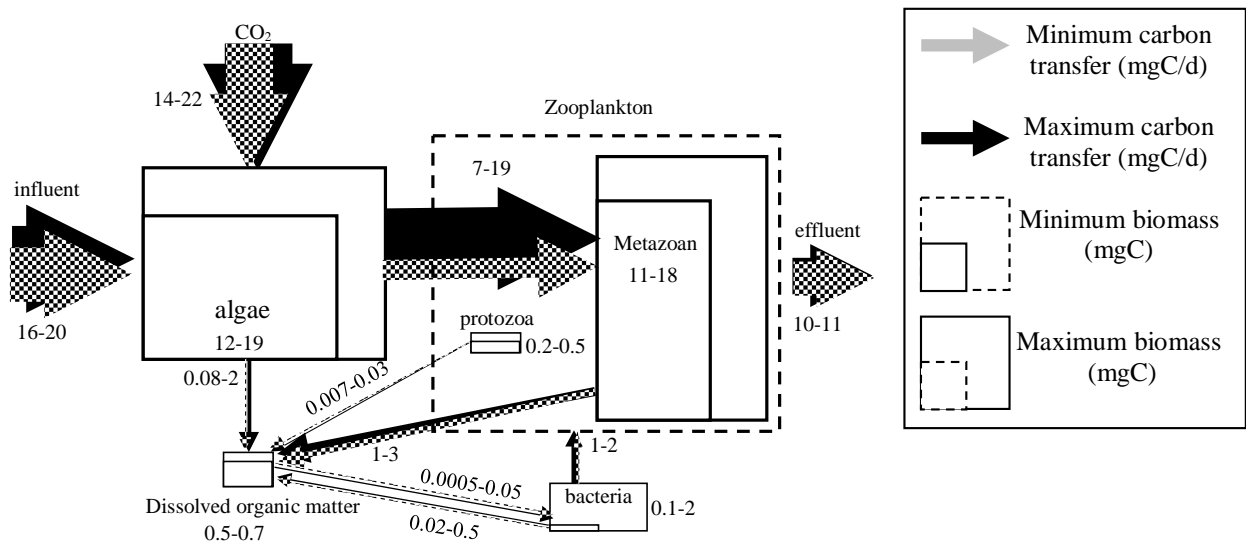
Q : flow rate (mL/h)

when the amount of inflowing organic matter is small and the load due to photosynthesis is large.

Fig. 10 and **11** show the carbon balances of case L-2 and Case D in section IV, respectively. Boxes indicate living organisms and abiotic organic matter that compose the ecosystem, and arrows show carbon transfer rate. The numbers attached to the arrows and boxes indicate the ranges of quantity in each process or state valuables. The box size and the thickness of the arrow are based on each quantity. The extant amount was calculated using the carbon conversion formula shown in Table 2 based on the measured value. The inflow and outflow amounts were actually measured values. The amount of carbon transfer was calculated using the formula shown in Table 3 based on each existing amount. Table 4 shows the literature values used to determine each quantity.

Table 4 Literature values for the calculation of carbon transfer and storage

Symbol	Content	Values	reference
k_B	Rate constant of self decomposition (Bacteria)	0.25(1/d)	[9]
k_P	Rate constant of self decomposition (Algae)	0.007-0.07(1/d)	[9], [10]
k_{Z1}	Rate constant of self decomposition(protozoa: Ciliata)	0.15(1/d)	[12]
k_{Z2}	Rate constant of self decomposition(metazoan : Rotatoria)	0.15(1/d)	[12]
r_1	Intake activity of organic compounds by bacteria	1.2-7.7 ($\times 10^{-12}$ mgC/(cell·d))	[13]
r_2	Filtration rate of rotifer	0.6~1.5 (1/(mgDW·d))	[14]
r_3	Carbon transfer rate with intake of algae by zooplankton	0.000045 (mgC/d)	[15]
r_4	Primary production rate	53.0 (mg-carbohydrate/(mgChl- a ·d))	[16]
r_5	Predation rate of bacteria by zooplankton	0.000012 (mgBacteria/(N-zooplankton·d))	[17]
w_B	Dry weight of bacteria (<i>Escherichia coli</i>)	4.0×10^{-10} (mg/cell)	[18]
w_{Z1}	Dry weight of protozoa (<i>Alcaligenes faecalis</i>)	5.56×10^{-10} (mg/cell)	[18]
	(Ciliata)	1.20×10^{-6} (mg/N)	
	(<i>Colpoda steinii</i>)	1.39×10^{-6} (mg/N)	
	(<i>Tetrahymena pyriformis</i>)	1.60×10^{-6} (mg/N)	
	(<i>Colpidium campylum</i>)	3.85×10^{-6} (mg/N)	
	(<i>Vorticella microstoma</i>)		
w_{Z2}	Dry weight of protozoa (Ciliata)	8.9×10^{-5} (mg/N)	[19]
	(<i>Brachionus angularis</i>)		
a	C/(Dry weight of bacteria)	0.531	[20]
b	C/Chl- a	49	[21]
c	C/carbohydrate	1.1	[21]
e	Algal amount	0.0009(mgC/L)	[15]



The abundance of algae was about 10 times larger under light conditions than the dark condition. In terms of carbon transfer, the primary production was about 10 times, the predation of algae was 100-1000 times, and the death of algae was 10-1000 times larger under light conditions than the dark condition.

It was suggested that light irradiation activates the primary production by algae and increases the existing amount. And the algae predation amount of zooplankton and the production of abiotic organic matter due to algae death increase accordingly.

CONCLUSIONS

In this study, the influence of light irradiation on the

carbon balance in the process of contact oxidation treatment for wastewater containing organic matter was discussed. The results obtained in this study are shown as follows;

- 1) There were not clear effects of light irradiation on the organic matter removal capacity of the entire channel, but the amount of accumulated organic matter in the channel under light condition was almost double compared to that of dark condition.
- 2) Light irradiation had an effect on the biota in the channels, including the presence of photosynthetic bacteria and the number of algae, but no effect on the number of bacteria.
- 3) According to the carbon balance analysis in the channel, it was suggested that the light irradiation

increases the load of organic compounds due to photosynthesis 10 times greater compared to the dark conditions, and the effect of light irradiation cannot be ignored when the inflow amount of organic compounds is relatively small. In the case nutrients such as nitrogen and phosphorus exist in the water, internal production by algae gives

ACKNOWLEDGEMENTS

We wish to thank staff and students in laboratory of Ecology, Faculty of Science, Ehime University for their assistance of conducting the experiment.

REFERENCES

- [1] Ministry of Land, Infrastructure, Transport and Tourism, Japan.
<http://www1.mlit.go.jp/common/001273126.pdf> (in Japanese)
- [2] Ministry of the Environment, Japan.
<https://www.env.go.jp/council/09water/y0917-01/mat05.pdf> (in Japanese)
- [3] C. Junjun, M. Jian, J. Wei, C. Jinqian, L. Xuan, J. Bohua, W. Haiming: Treatment of heavily polluted river water by tidal-operated biofilters with organic/inorganic media: Evaluation of performance and bacterial community, *Bioresource Technology*, Vol. 279, pp.34-42, 2019.
- [4] Y. Sheng, Y. Qu, C. Ding, Q. Sun, R.J. Mortimer: A combined application of different engineering and biological techniques to remediate a heavily polluted river, *Ecol. Eng.*, vol. 57, pp.1-7, 2013.
- [5] Jibo Xiao, Shuyi Chu, Guangming Tian, Ronald W. Thring, Lingzhou Cui: An Eco-tank system containing microbes and different aquatic plant species for the bioremediation of N,N-dimethylformamide polluted river waters, *Journal of Hazardous Materials*, Vol.320, pp.564-570, 2016.
- [6] R.J. Craggs, A. Zwart, J.W. Nagels, R.J. Davies-Colley: Modelling sunlight disinfection in a high rate pond: *Ecological Engineering*, Vol.22, No.2, pp.113-122, 2004.
- [7] C. Schultz-Fademrecht, M. Wichern, H. Horn: The impact of sunlight on inactivation of indicator microorganisms both in river water and benthic biofilms, *Water Research*, Vol.42, No.19, pp.4771-4779, 2008.
- [8] Chawalit Chaiwong, Thammarat Koottatep, Chongrak Polprasert: Comparative study on attached-growth photobioreactors under blue and red lights for treatment of septic tank effluent, *Journal of Environmental Management*, Vol.260, No.15, 110134, 2020.
- [9] Eckenfelder jr., W. W., and O'Connor, D. J.: *Biological Waste Treatment*. Pergamon Press, Oxford- London- New York- Paris, pp.22-42, 1961.
- [10] DePinto, J.V. and Verhoff, F.H.: Nutrient regeneration from aerobic decomposition of green algae, *Environmental Science and Technology*, 11, pp.371-377, 1977.
- [11] Takuya OKUBO, Mitsumasa, Akihiko MURAKAMI: Characteristics of purification in Small channels, *Journal of Japan Society of Water Environment*, Vol.16, No.4, pp.261-269, 1993
- [12] Shigeo FUJII, Isao SOMIYA and Toshiyuki SHIRAKI: Studies on the Effect of Phytoplankton and Zooplankton on Self-Purification in Eutrophicated Water, *Journal of Japan Society of Water Environment*, Vol.15, No.6, p.347, 1992.
- [13] Edited by Isao Somiya: Purification mechanism of nature(Shizen no Joka Kiko, in Japanese), p.127, Gihodo Shuppan, 1995.
- [14] Edited by Yoshiro Iwasa: Engineering limnology, p.318, Sankaido publishing, ISBN: 9784381008121 (in Japanese).
- [15] Shigeo FUJII, Isao SOMIYA and Toshiyuki SHIRAKI: Studies on the Effect of Phytoplankton and Zooplankton on Self-Purification in Eutrophicated Water, *Journal of Japan Society of Water Environment*, Vol.15, No.6, p.397, 1992. (in Japanese)
- [16] Edited by Yoshiro Iwasa: Engineering limnology, p.322, Sankaido publishing, ISBN: 9784381008121 (in Japanese)
- [17] Ryuichi sudo: Biology for wastewater treatment(Haisui syori no seibutu gaku, in Japanese), p.180, The Industrial Water Institute
- [18] Ryuichi sudo: Biology for wastewater treatment(Haisui syori no seibutu gaku, in Japanese), p.180, The Industrial Water Institute, 1977.
- [19] Jurgens et al: Effect of metazoan and protozoan predation on the distribution of bacterial biomass in microcosms, *Journal of water and waste*, Vol.39, No.10, p.85, 1997.
- [20] Edited by Isao Somiya: Purification mechanism of nature(Shizen no Joka Kiko, in Japanese), p.19, Gihodo Shuppan, 1995.
- [21] Edited by Yoshiro Iwasa: Engineering limnology, p.320, Sankaido publishing, ISBN: 9784381008121. (in Japanese)

ABILITY AND WILLINGNESS TO PAY FOR WASTE WATER MANAGEMENT MAINTENANCE SERVICES (IPAL)

**Marselina Djayasinga, Tsra Subianto, Tri Joko Prasetyo*

Economic and Business Faculty, University of Lampung, Indonesia

ABSTRACT: Infrastructure sustainability must be maintained through public participation payment for the utilization of these public facilities. However, it is difficult to determine the appropriate tariff of public utilization. Ability and Willingness to Pay (ATP and WTP) are used to get it. This study aims to estimate ATP and WTP of beneficiary of waste water management maintenance services (IPAL). Using a purposive random sampling and cluster technique from 300 RT, there are 153 are selected as samples. There are 3 classification of household: household native inhabitants, household comers without experience with PDAMs, and household comers with experience PDAM. PDAM is another alternative of water supply produced by government. The results of this study are, the highest ATP is household inhabitants compared to the other 2 household categories. The WTP for IPAL is 30% higher than the rate set by the government initially. Increasing WTP is affected by the level of education, reference cognition, level of income and satisfaction. Continuous improvement in technology of water treatment, socialization to the community and use of tariffs based on volume of usage must be carried out for the continuity of infrastructure.

Keywords: Willingness to pay, Ability to pay, Waste water management services

1. INTRODUCTION

Lack of public awareness of waste water treatment has caused some areas to become a crisis of clean water and polluted the environment. Recently, waste water management maintenance services is becoming an important issue in the water protection in Indonesia. According to Hua (2010) the increasing population and reduced water resources have caused the need for clean water to be a very pressing problem in almost all parts of the world and lack of awareness of proper waste water.. This habit is driven by the low charge even free of charge of this services. As a public good, waste water management maintenance services IPAL) in Indonesia, is not on market mechanism. The tariff cannot be determine because no one can express their preference. So, it is needed the method to get the tariff which reflect the ability and willingness to pay of beneficiaries in order to maintenance this public facilities sustain for long time and arose awareness community to protect the water. Community is expected to respond for this public facilities by expected to be willing to participate through pay some cost to maintain the sustainability of this public infrastructure.

Langkapura Baru Sub district, in Bandar Lampung City is one of the worst sanitation areas, where domestic waste water, both black water and gray water, is thrown into the environment without any prior treatment, thus polluting surrounding groundwater and often experiencing drought. Now,

the village is being built a Waste Water Treatment Plant, we called IPAL and immediately operating precisely at RT. 05 LK.II Langkapura Baru. The total population of households who will use the service is 350 families.

The IPAL program aims to overcome the problems of clean water and sanitation through the provision of assistance to Low-Income Communities by building communal IPAL. This public facility will treat household black water and gray water waste so that treated wastewater can be returned safely to household and environment in accordance with environmental quality standards. This processed wastewater will be the next source of clean water. The regional government cooperating with the Islamic Development Bank (IDB) only build the IPAL infrastructure, meanwhile for operational and maintenance costs are expected to come from community participation. So that the amount of the tariff is needed to cover this operational and maintenance costs of the IPAL, which will be charged to the community, especially the beneficiaries, which is in accordance with the ATP and WTP beneficiary households

Now, the city government has set a tariff for Communal IPAL in the Langkapura Baru Village for operation and maintenance of this public infrastructure by IDR 100,000 / month / household. This tariff is set by the city government with the consideration that the government will provide a subsidy of IDR 50,000 / household, and honestly this subsidy can build the same

infrastructure in other regions if burden to community. Allen Consulting Group (2003) states that one source of financing for public goods can come from fees in the form of tariffs, where the levy rates are influenced by the ability to pay (Ability to Pay) and Willingness to Pay. Based on this background, it is a technique for estimating tariffs that cover operational and maintenance costs and encourage environmental awareness. One of the methods to estimate is the Ability to Pay (ATP) and Willing to Pay (WTP).

ATP is the ability to pay for public services received based on income that is considered ideal. According to Rubiani (2004), ATP is the amount of money that can be paid by the community to replace the service costs it receives While Russel (1995) states that ATP is a consideration in spending his income / expenditure to buy goods or other services. ATP is related to the limitations of household income, where household need make priorities economically in choosing maximum satisfaction. ATP is the rest of income after deducted by essential expenditure, non-food expenditure, non-essential expenditure.

According [14] one form of participation of community can be seen from their willingness to pay. WTP according to Wedgwood. A (2003) is the maximum amount of an individual's status for willingness to pay for an item or service, Mankiw (2004) defines WTP as the highest price that each beneficiary is willing to pay using the consumer surplus approach of the demand curve. The consumer surplus is the willingness of a person to pay an economic value less the value actually paid by him. Economists, psychologists, and marketing researchers rely on measures of consumers' willingness to pay (WTP) in estimating demand for private and public goods and in designing optimal price schedules [22] and customers pay what they bid (s) so they must bid less than their true WTP if they want to obtain surplus from the transaction.. Using WTP to avoid the problem of free-riders in the determination of tariffs for public goods services [3].

2. OBJECTIVES

This study aims (1) to calculate the ability and willingness to pay off household to waste water management maintenance services (IPAL) in order to get the tariff in which is resulting which cover operational and maintenance cost and arouse the awareness of households to be more responsible in water protection, (2) to investigate the relationship between respondent's characteristic with their WTP. This study is expected to provide policy to set tariff in which keep infrastructure sustainable and community awareness.

3. LITERATURE REVIEW

Public participation is essential and may lead to enormous benefits for sustainability development [5, 22] agree that public goods are build by the government should be managed by the community which requires active community involvement. Involvement, participation and some characteristic of household determine their choices in WTP. WTP is a technique to know the willingness of individuals to pay for public goods benefit in which the price of it cannot be determined by market mechanism because of the lack of information or preferences. Some experts also define WTP is the maximum price beneficiaries willing to pay for a given quantity of product or services [21]. WTP as a way of calculating the ability of each individual on an aggregate basis to pay in order to improve environmental conditions to conform to desired standards. Economic valuation is an attempt to provide a quantitative value to goods and services produced by natural resources and environment regardless of whether the market value is available or not [17] and. CVM is done by asking directly to benefit about the value of benefits of public goods includes resources and environment. [12] found that almost 85% of respondents are willing to pay a higher tariff and this WTP is effected by the level of education, family income This result also supported by [11] that the average WTP of consumers on waste treatment services is higher than the tariffs paid.

WTP is based on the user's perception of the public services. To get user perception, it can be used the Contingent Valuation Method (CVM). According to [7] CVM is one technique to analyze the valuation function that can provide qualitative information that is difficult to identify using other conventional valuation techniques. CVM is conducted because people is unable to express its preference for economic, such as for tourism hunting services, dumping tariffs, pollution, waste management, utilizing wildlife, environmental quality, etc. CVM is a method of measuring someone's preference [8]. CVM is measuring WTP by eliciting stated user preferences through direct surveys. The user is directly asked about their WTP by using open-ended questions [17]. In these surveys, household or beneficiaries are offered some alternative services or condition with varying attributes. WTP is inferred indirectly from their ranking or ratings of these alternative services.

Some characteristics of community such as education level, gender, age, lines of class, race, ethnicity, house type, house distance, income and service quality, awareness, perception and household satisfaction level toward the benefits of

public goods in correlating with WTP [4, 13]. Effects on WTP is high when they are interactions with each other.. Community awareness of the environment is influenced by the level of education and knowledge about the environment [7]. According to [17] household concerning will affect WTP and it increases along with improving the quality of services. Income inequalities can influence environmental degradation. Inequalities may affect the overall extent of environmental quality so that the higher income the higher WTP .High level of awareness and knowledge and positive attitude will increase environmental protection [2].

4. METHODOLOGY

The location of IPAL construction is in the RT. 05 .LK II Langkapura Baru, City of Bandar Lampung. There are 350 households will receive direct benefits from this infrastructure are 350 families. With a quota purposive sampling technique with the cluster method, 158 respondents were selected. Through structured questionnaires and interview techniques, to determine the amount of tariff for operational and maintenance services based on their ATP and WTP. The Contingent Valuation Method (CVM) method with game bidding techniques are conducted by giving repeated questions about the desire to pay for wastewater management maintenance services with a number of services. The frequency of water flowed into the household is service scenario. At the starting point, tariffs are used and the service promised by the government is IDR 100,000 / month / RT and water is supplied to household twice a week. The 7 scenarios are designed as follows:

Table 1. 7 Scenarios of Services IPAL

Scenarios	Services	Tariff/ month
Scenario A	Water will be flowed to household once a week	90.000
Scenario B (starting point)	Water will be flowed to household 2 times a week	100.000
Scenario C	Water will be flowed to household 3 times a week	110.000
Scenario D	Water will be flowed to household 4 times a week	120.000
Scenario E	Water treatment will be flowed 5 times a week	130.000
Scenario F	Water treatment will	140.000

be flowed times a week
Scenario G Water treatment will 150.000
be flowed every day
(7x a week)

The starting point of IPAL services scenario at B, in which wastewater treatment will be flowed to household 2 times a week with tariff IDR 100.000. IPAL services is decreased or increased by flowing water to household once a week, Increased scenario using IDR 10.000 every stage .If most respondents answer to one scenario selected, then his scenario is the actual WTP desired mostly

4.1.Hypothesis Development

To answer the second objective that the relationship between the characteristics of the respondent with their WTP, correlation technique and crosstab analysis techniques are used. The respondent's characteristic consists of 5 elements, namely the number of family members, the level of education, reference cognition. Level of income and satisfaction of the services. The hypothesis developed as follows:

- Ha (1):Numbers of Family has a positive correlation with WTP.
- Ha (2):Level of education has a positive correlation with their WTP
- Ha(3):The reference cognition has a positive relationship with WTP.
- Ha(4):Level of income level has a positive relationship with WTP.
- Ha(5):The level of satisfaction of respondents has a positive relationship with WTP.

5. RESULT

Descriptive Respondent

Questioner distributed to 350 households. There are 158 households that returned and responded the questioner or 45%. The purpose of the household classified is to prove the correlation between reference cognition with their WTP. It may be correlated between perceptions of RTs who have no reference at all about clean water management, and households that have already felt clean water management services such as IPAL, namely PDAM

Table 2. Family Categories of Respondent

Family Categories	KK	Percentage
Household stay formerly	78	49%
Household comers without experience with PDAM service.	43	27%
Household comers with experience with PDAM service.	37	24%

The original RT was obtained by 78 households, namely the RTs that settled in that location and had never moved. During this time they have experience in the difficulty of obtaining water, especially during the dry season. The second is 43 newcomer RT groups, namely RTs who moved to that location and have settled in that location and this household has never experienced water treatment services like the previous PDAM. PDAM is a water treatment service that is managed by the city government where the source of the spring is from a river or mountain or other source, then it is channeled to RT. Third, namely immigrant households that live in that location but already have experience in experiencing PDAM services. They already know a little about the quality of PDAM water, the tariff, the frequency of the water flowing to the previous household. The characteristics of respondents based on the number of family members and the level of education obtained the following results.

Table 3. Descriptive of Respondents

	A	B	C
Family member :			
< 5 person	40 %	65%	60%
≥ 5 person	60%	35%	40%
Level of Education			
< 9 years	40%	20%	15%
9 ≤ x < 12 years	25%	25%	20%
≥ 12 years	35%	55%	65%

Note: A is household stay formerly and never move to other location, B is household comers without PDAM service experience, C is household comers with PDAM experience

Households which stay formerly in that location have a greater number of family members than household comers with relatively lower levels of education than comers. On the other hand, household comers is dominated by small family. They have a family members less than 5 people, but they have with a relatively higher level of education than formerly household.

ATP dan WTP

The Ability to Pay for household stay formerly on average, is lower than to ATP in household comers, but their willingness to pay (WTP) is highest than to the other 2 categories of households. This is presumably because the former households have experience having difficulty obtaining water so they highly value water and realize how difficult it is to obtain clean water. While ATP for household comers with experience using PDAM services is the highest compared to the other two household categories, but they have the lowest WTP compared to the other two household categories. Household comers with PDAM experience have had references to the quality and quantity of clean water provided by the city government so far with cheaper rates because PDAM tariffs have been subsidized by the government.

Table 4. ATP and WTP IPAL (IDR ,000)

Family Category	ATP	WTP
Household stay formerly	295	125
Household comers without experience with PDAM	305	115
Household comers with experience with PDAM	315	95

Based on the questionnaire, the average tariff for PDAM water services, ranges from IDR 100,000 - 300,000 / month with water can be used not only for bathing and MCK but for drinking and cooking. Household comers consider that wastewater management from IPAL are still unsure about the quality of water produced. This condition happen because of the source of wastewater from IPAL is come from black and gray water. Whether it is hygienic or not to be consumed, the use of waste water that has been processed by IPAL is still bog question. Based on the IPAL experience, water is usage only limited for non-eating, drinking purposes such as washing clothes, flush for toilet, washing vehicles, flushing plants. Household who stay formerly do not really care about wastewater quality. The important for them is, that water supply is always there regularly every day. For this condition and they want to pay higher because of the benefits of water and water difficulties so far.

WTP

Of the 158 respondents who were filled with the questionnaire, respondents were dominantly chosen scenario F, by 35,7%. They desired the wastewater management services working 6 times a week to flow the water. They agreed to pay IDR140.000 charged per month. If it compares with government tariff which is IDR 100.000, this WTP can increases 40%. A total of 31,4 % of respondents are willing to pay IDR 110.000 or scenario D, in which wastewater treatment is flowed to the household by four times a week, A, B, C, E, F. The respondent's choice is shown in

Table 5. Validity of WTP of IPAL (IDR)

Scenario	Tarif WTP	Valid (%)
A	90.000	10,5%
B	100.000	26,3%
C	110.000	30,8%
D	120.000	31,4%
E	130.000	24,2%
F	140.000	35,7 %
G	150.000	20,8%

The actual WTP is that it is willing to pay IDR 140,000 a month or increase 40% as long as the quality of water treatment is improved, by increasing the flow of water to household 6 times a day. This result is higher than what [7] found in WTP of water supply in Nigeria. It 's mean that the WTP can be pushed to increase if their satisfaction of public services is increased.

5.1 Correlation Between the Characteristics of Respondent with Their WTP of IPAL

The relationship of some characteristics of respondents with their WTP used Pearson Product Moment Test. Characteristics of respondents consist of 5 elements, namely family members, the level of education, reference recognition, the level of income and satisfaction. The result on

5.1 Correlation Between the Characteristics of Respondent with Their WTP of IPAL

Relationship of some characteristics of respondents with WTP used Pearson Product Moment Test. Characteristics of respondents consist of 5 elements, namely family members, the level of education, reference recognition, the level of income and satisfaction. The result on

Table 6. Correlation Between Characteristics of

Respondents with Their WTP

Characteristic Respondent	coefficient	Sign
The family member	0,593	0,230
Level Education	0,786	0,036*
Reference Cognition	0,155	0,025*
Level of Income	0,733	0,090**
Level of Satisfaction	0,740	0,010*

*) significant on 95%

**) significant on 0,1%

From 5 characteristics of respondent, only the family members has no correlation with their WTP of IPAL, others such as level of education, level of income, reference cognition and satisfaction of IPAL services have correlation positively. The more the number of families is not relevant to the more their WTP. The family members has no correlation with WTP because IPAL tariff setting initially, is fixed cost, does not depend on the number of usage. Wastewater treatment by IPAL is not equipped with a meter or water volume meter distributed such PDAM's did. Increasing WTP is also supported by level of education and awareness of wastewater treatment with coefficient correlation equal to 78,6%. The higher level of education, the higher their WTP of IPAL. With higher levels of education and knowledge, household tend to wish and better understand about water protection. The more knowledge about environmental, the higher their WTP. Respondents who have good knowledge about the benefits and damage of the environment, they will tend to be more likely to be willing to pay [15]. Level of income is also correlated with WTP with 73.3%. It means that if the household has more income, the family has more WTP, with a coefficient correlation of 56.8%.

Reference cognition is used as a variable because of past experiences either satisfied or unsatisfied of the services, has a big influence on their WTP. For formerly household who often difficult to get clean water especially in the dry season, they have highest appreciate with wastewater treatment, whatever its form. He [6] shows that experience is positively correlated with environmental awareness. People who have environmental experiences are willing to pay higher. Respondents will have more knowledge that will not be environmentally damaging and

are likely to be willing to make conservation efforts environment.

Level satisfaction of household from IPAL services, affects their WTP. Comes households who had experienced the benefits of other water sources, especially those provided by the government, such as the PDAM, The satisfaction of household increases if the quality of water treatment by implementing new technology will increase the quality of wastewater treatment. He [10] shows that more services are added, more WTP increases. Management service in Kampala City, Uganda can be improved by improving the quality of waste services [3].

Level of income does not have a significant effect with degree of freedom 5%, but significant on its 10%. For households, water is a vital goods, requirement and is determined by the government in a fixed rate. So whatever the tariff is charged to household, it will still to pays it unaffected by its income.

6. CONCLUSIONS

- (1) The ATP of household which stay formerly on the location, , on average is lower than others the ATP from other household classification, but their WTP is relatively higher than the 2 other categories of households, because they highly value water and know how difficult it is to obtain clean water when dry season arrives;
- (2) The average ATP of household comes who have never had the experience of using PDAM services is relatively highest compared to the other two categories of household, but on average, their WTPs are medium, because they feel the importance of water and feel the quality of wastewater quality treats IPAL is quality standard;
- (3) Household comes that have had experience using PDAM services, their ATP is medium, but their WTP are lowest, compared to 2 sample categories of household. They have had experience enjoying water supplied by the government that has better quality and this household is still unsure, is the quality of wastewater of IPAL to be supplied is high such as PDAM did;
- (4) Reference cognitive is positively correlated with their WTP because previous references are mainly on experiences with PDAMs with better quality and with tariffs so far;
- (5) The city government needs to improve continually wastewater treatment by IPAL using high technology so that the quality of wastewater is quality standards, at least the

same with other drinking water and government promote it;

- (6) Tariff per household, should be determination as a variable costs or a number of uses.

7. REFERENCES

- [1] Altaf MA, Haroon J, Whittington D. 1992. Willingness to Pay for Water for Rural Punjab. Pakistan. World Bank Water and Sanitation Programme.
- [2] Afroz R, Using a Contingent Valuation Approach for Improved Solid Waste Management Facility. Journal Elsevier Waste Management, Vol.31,2011,pp.800-808.
- [3] Meinrad Z, Sharifah ZB, Sayed ZASH, Mahyar Sakari., Relationship Between Awareness, Knowledge and Attitudes Towards Environmental Education Among Secondary School Students in Malaysia, World Applied Sciences Journal, 22 (9),2013, pp. 1326-1333.
- [4] Banga, Margaret, Households Willingness to Pay for Improved Solid Waste Collection Services in Kampala City, Uganda. The Journal of Environment and Development, 2011.
- [5] Brahim, Djemaci, Using a Contingent Valuation Approach for Improved Household Solid Waste Management in Algeria. Munich Personal. 2015.
- [6] Chutarat Chompunth, Role of Public Participation in Environmental Impact Assessment in Thailand, International Journal of GEOMATE, Volume 12, Issue 33, 2017.
- [7] Finger, M, From Knowledge to Action? Exploring the Relationship Between Environmental Experiences, Learning, and Behavior, Journal of Social Issues 50(3), 1994, pp.141-160.
- [8] Fonta. W. Metall. Using a Contingent Valuation Approach for Improved Solid Waste Management Facility: Evidence from Enugu State Nigeria. Journal of African Economics. 2008.
- [9] Ghanem Samar Khairy, The Relationship Between Population and The Environment and Its Impact on Sustainable Development in Egypt Using a MultiEquation Model ,Environment, Development And Sustainability, Vol.20,2018, Issue 1pp. 305-340. Hagos, Households Willingness To Pay for Improved Urban Waste Management in Mekelle City, Ethiopia, Discussion Paper Series, 2012, EfDDP12-06

- [10]Hua Wang. Water pricing with household surveys: A study of acceptability and willingness to pay in Chongqing, China. *China Economic Review*. 21(1):136-149 · March. 2010
- [11]James K. Boyce., Inequality and Environmental Protection. Paper, Political Economy Research Institute MIT, 2003.Ladiyance,Sand Yuliana, L., Variable Effected Willingness To Pay Household at Bidaracina Jatinegara, East Jakarta, *Widya Journal*.Vol 2.No 2., 2014.
- [12]Marselina, Djayasinga., Ria Virsa. Willingness to Pay (WTP) By Contingent Valuation Method (Case Study: Waste Management Services. *Journal of GEOMATE*, Vol 17, Issue 62, pp 59-64.2019.
- [13]Steven Russel. Julian Fox Rusbhi. Dina Arhin.. Ability to Pay for Health Care: Concepts and Evidence. *Health Policy and Planning*, 1996; 11(3):219-37
- [14]Takehisa Kumakawa, Altruism,and Willingness to Pay for Environmental Goods: A Contingent valuation study, *Journal of Geoscience and Environment Protection*, 5, 63-68, 2017.
- [15]Tolulope J. Akeju. Gbenga J. Oladehinde and Kasali Abubakar, An Analysis of Willingness to Pay (WTP) for Improved Water Supply in Owo Local Government, Ondo State, Nigeria, *Asian Research Journal of Arts & Social Sciences* 5(3): 1-15, 2018.
- [16]Whittington D, Briscoe J, Mu X, Barron W. 1990.Estimating the willingness to pay for water services in developing countries: A case study of the use of contingent valuation surveys in Southern Haiti. *Economic Development and Cultural Change*38 (2):293-312.
- [17]WASH (Water and Sanitation for Health). 1988. Guidelines for Conducting Willingness-To-Pay Studies for Improved Water Services in Developing Countries. WASH Field Report No. 306, October 1988.Washington DC: USAID.

LIFE CYCLE ASSESSMENT APPROACH FOR PREDICTING GREENHOUSE GAS EMISSION FROM COLUMN, BEAM AND PLATE IN A REAL ESTATE CONSTRUCTION

Yatnanta Padma Devia¹, Indradi Wijatmiko¹, Bernadus Martino¹, and Annisa Nur Rakhmawati

¹Faculty of Engineering, Brawijaya University, Indonesia

ABSTRACT

Buildings and their construction together contribute annually 36% of global energy use and 39% of energy-related carbon dioxide emissions. In energy use per m², buildings sector energy intensity constantly to improve at an annual average rate of around 1.5%. Building growth in ASEAN countries, include Indonesia, are predicted rapid to double by 2040. Indonesia, is committing to 29% reduction in greenhouse gas (GHG) emissions by applying the Intended Nationally Determined Contribution (INDC). Emission reduction in many sector should be contributed, include construction sector. This study estimates the GHG emission of the use of column, beam and plate in a real estate project in Malang – Indonesia, based on their life cycle assessment (LCA). The stages of LCA consist of goal and scope definition, life cycle inventory, life cycle impact assessment, and interpretation of the result. Each an individual construction material of column, beam and plate plus transport and electricity related to project is analyzed by using software tools SimaPro 9.0 and GaBi. Then, an individual construction material that contributes most significant to GHG emission is discussed. It is shown that the individual material of column and beam in a conventional process namely cement, reinforced bar, and sand contribute $\pm 50\%$, 26-44%, and $\pm 10\%$ GHG emission, respectively. In a ready mix process, the highest GHG emission for two sub-structural materials (beam and plate) are ready mix concrete, reinforced bar, and wooden board. The dimension and quantities of aforementioned sub-structural material also make in impact to GHG emission.

Keywords: Beam, Column, Greenhouse Gas (GHG) emission, Life Cycle Assessment (LCA), Plate

INTRODUCTION

According to the United Nations Environment Program [1], buildings and their construction together contribute annually 36% of global energy use and 39% of energy-related carbon dioxide emissions. CO₂ emissions from buildings construction increase continually, from 3.1 Gt CO₂ in 2010 to around 3.7 Gt CO₂ in 2016 [1]. Buildings sector energy intensity (in terms of energy use per m²) constantly to improve at an annual average rate of around 1.5% [1]. Building growth in ASEAN country, include Indonesia, is expected rapid to double by 2040. The environmental impact of building growth should be investigated.

Many investigations were conducted to mitigate greenhouse gas (GHG) emission or environmental impacts in the buildings and construction industries. Ragheb [2] determined which life cycle phase (manufacturing of materials, construction, use, maintenance, and demolition) contributes the most to the total impact and investigated key assembly systems (foundation, structure, walls, floors, roofs) affect its environmental impact in Michigan. Their study resulted that the use phase of the building has the highest total impact (more than 90%). For building assembly system, especially structure system (beams and column) has the highest contribution to fossil fuel consumption and to eutrophication, namely 31% and 56%, respectively

[2]. Rey and Yepes [3] by their literature review, mentioned that concrete structures using steel frames had a greater impact when compared to wooden frames and bamboo frames. Moreover, the frame materials manufacturing caused greater energy and emission impact than the construction process. For different construction units, it was observed that the greater environmental impact related to concrete slab [3]. The three construction materials that produced the largest percentages of carbon dioxide emissions were cement, ceramics and steel in 30.3%, 20.3% and 18.75 per m² of building, respectively [4]. According to Basbagill et.al. [5], the impacts for each building component especially column and beams was 0.27% (minimum) until 19.18% (maximum) of total impact. The environmental impacts of conventional reinforced concrete, with production as critical stage, were 3.5 times more damage to ecosystem, 32% more extraction of natural resources, and 53% effect to the human health [6].

Indonesia, is committing to 29% reduction in GHG emissions by applying Intended Nationally Determined Contribution (INDC). Emission reduction in many sector should be contributed, include construction sector. Indonesia government has a blue print Indonesia Construction 2030 as a grand design and grand strategy in construction sector. In the document stated that Indonesia must be oriented not to contribute to environmental

damage, but instead became a pioneer in the improvement of environmental quality in the entire habitat of Indonesia inhabited by humans and all other creatures in a symbiotic mutualism. However, there are still lack numbers of research in Indonesia that investigated GHG emission of construction material and assembly process in detail from its life cycle especially at early design stages. Hendra [7] investigated an average carbon emission in the small housing cluster construction was below threshold environmental balance (314 ppm) with the ratio of simultaneously construction: gradually construction was 2.1:1.7. Saputele et.al. [8], using cradle to cradle in a small laboratory scope, has confirmed relation of higher cement consumption will produce higher carbon dioxide emission for laboratory concrete waste. Prior research in Indonesia has not includes the most environmental impact in Life Cycle Assessment (LCA) of material or process construction. The sensitivity analysis has also neglected in previous research in Indonesia.

Some methods for estimating GHG emission are LCA [5] [6], Strategic Environmental Assessment (SEA), Environment Impact Assessment (EIA), Environmental Risk Assessment (ERA), Cost Benefit Analysis (CBA), Material Flow Analysis (MFA), Ecological Footprint and Carbon Footprint [9], supply chain method that applied actual corporate and published data [10]. Some researchers have integrated LCA with Building Information Modeling (BIM), energy analysis, cost, embodied energy and sensitivity analysis [4] [5]. According to Hermawan et.al. [11], the advantage of LCA are a tool in the construction industry manufacturing where this LCA can describe the needs and environmental impacts resulting from each stage and help in making environmental impact reduction decisions. A number of software tools have also been used such as DProfiler for Building Information Model, eQuest for energy simulation, SimaPro and Athena Ecocalculator for operational CO₂eq [5], LCA Manager 1.3 and database Ecoinvent 2.0 [6], and Gabi. In this research, SimaPro 9.0 and Gabi will be used. The strength of SimaPro 9.0 compared to previous version are new and update data in Ecoinvent 3.5 and in method especially ReCiPe 2016 that implemented a regionalized water consumption category (in endpoint), inclusion of normalization (endpoint and midpoint) and weighting set (endpoint). The LCA community recommended the ReCiPe method for several impact categories and promoted consistency the midpoint and the endpoint methods [12].

This study purpose is to estimate environmental impact of the use of column, beam and plate at real estate project in Malang City, East Java Province, Indonesia. Based on LCA, the environmental impacts are measured in GHG emissions that the sum of the emission during raw material procurement,

construction material production, the transportation and on site construction using SimaPro 9.0 and Gabi software.

METHODS

A typical house 216 m² is used in this research. The location is in Malang City, East Java, Indonesia. It is a two-storey house with four types column and beam which detail information are presented in Table 1 and Table 2, respectively. All columns and lintel beam were constructed by conventional methods, while ready mix concrete were utilized for other type of beams and plate. All of data collected by learning the design and visiting site project.

Table 1 Details information of the column

Column dimension			Number of column	Quantity Volume (m ³)
Length (cm)	Width (cm)	Height (m)		
25	25	4	7	1.75
20	20	4	6	0.96
15	20	4	12	91.44
15	15	4	73	6.57

Table 2 Detail information of the beam

Beam dimension			Quantity Volume (m ³)
Length (cm)	Width (cm)	Height (m)	
25	50	30.80	3.85
15	30	98.40	4.43
15	15	5.05	0.11
15	15	13.26	0.33*

Note: *lintel beam

To estimate GHG emission, the detail information of LCA of column, beam and plate plus transport and electricity related to project were analyzed by using software tools SimaPro 9.0 and GaBi.

RESULT AND DISCUSSION

Goal and Scope Definition

The first goal is to estimate construction material impact, related with greenhouse gas emission in the term of global warming potential. The parameter is carbon dioxide equivalents (CO₂-eq) using the relevant 100-year global warming potential, which measure the sum of the emission during raw material procurement, construction material production, transportation, and on site construction. Furthermore, the following goal is to determine which stage of construction material contributes most significantly

to environmental impact.

The scope of LCA that applied in this research is *cradle to grave*, which means life cycle from the raw material to the operation process. This scope consists of raw material procurement, construction material production, transportation, and on site construction. Figure 1 schematically represents the life cycle of a typical house.

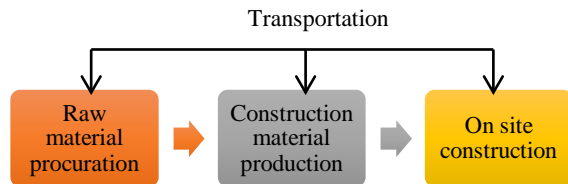


Fig 1. House project life cycle stages for estimating impact of early phase designs.

Life Cycle Inventory

The second phase of life cycle assessment is making an inventory of input and output related to the study scope. At the input stage, each column and beam is divided into several sub materials resources need and its transportation. Those resources need defined into process, product stages and system description. The resources need and transportation will map into emission rate that described as the output. Materials input in each column, beam and plate are shown in Table 3, Table 4, and Table 5 respectively.

Table 3 Material in each column

Type Column	Material	Quantity	Unit
25 x 25	Multiplex	12.99	sheet
	Wooden board	1.48	m ³
	Wooden block	0.56	m ³
	Concrete wire	7.42	kg
	Cement	973.88	kg
	Sand	1.36	m ³
	Gravel	1.40	m ³
	Reinforced bar $\phi 8$	17.43	bar
	Reinforced bar $\phi 12$	6.30	bar
	Reinforced bar $\phi 13$	18.90	bar
20 x 20	Multiplex	8.90	sheet
	Wooden board	1.02	m ³
	Wooden block	0.38	m ³
	Concrete wire	5.09	kg
	Cement	667.80	kg
	Sand	0.93	m ³
	Gravel	1.40	m ³
	Reinforced bar $\phi 8$	8.82	bar
	Reinforced bar $\phi 13$	8.40	bar

15 x 20	Multiplex	4.60	sheet
	Wooden board	0.9	m ³
	Wooden block	0.19	m ³
	Concrete wire	4.01	kg
	Cement	489.72	kg
	Sand	0.70	m ³
	Gravel	1.02	m ³
	Reinforced bar $\phi 8$	13.60	bar
15 x 15	Reinforced bar $\phi 12$	15.40	bar
	Wooden block	1.14	m ³
	Concrete wire	23.92	kg
	Cement	2,922.92	kg
	Sand	4.18	m ³
	Gravel	6.07	m ³
	Reinforced bar $\phi 8$	49.02	bar
	Reinforced bar $\phi 10$	68.40	bar

Table 4 Material in each beam

Type Beam	Material	Quantity	Unit
25 x 50	Multiplex	12.41	sheet
	Wooden block	20.22	m ³
	Concrete wire	13.30	kg
	Ready mix	3.85	m ³
	Reinforced bar $\phi 8$	27.19	bar
	Reinforced bar $\phi 12$	12.27	bar
	Reinforced bar $\phi 13$	27.60	bar
15 x 30	Multiplex	11.78	sheet
	Wooden block	18.14	m ³
	Concrete wire	9.47	kg
	Ready mix	4.43	m ³
	Reinforced bar $\phi 8$	32.55	bar
	Reinforced bar $\phi 10$	13.38	bar
	Reinforced bar $\phi 12$	26.75	bar
15 x 15	Multiplex	3.29	sheet
	Wooden block	5.07	m ³
	Concrete wire	2.64	kg
	Ready mix	0.11	m ³
	Reinforced bar $\phi 8$	31.03	bar
	Reinforced bar $\phi 10$	43.29	bar
15 x 15 (lintel beam)	Multiplex	50.20	sheet
	Wooden block	3.77	m ³
	Concrete wire	40.34	kg
	Cement	5,791.41	kg
	Sand	9.32	m ³
	Gravel	13.99	m ³
	Reinforced bar $\phi 8$	4.00	bar
	Reinforced bar $\phi 10$	4.70	bar

Table 5 Material in plate

Material	Quantity	Unit
Scaffolding (bamboo)	26.90	m ³
Wooden block	2.40	m ³
Multiplex	54.00	sheet
Reinforced bar	604.00	bar
Concrete wire	29.30	kg
Ready mix	17.3	m ³
Vibrator electricity	11,268.60	kWh

The calculation of quantity of materials used to build columns, beam and plate are considering 16 kg/sheet for multiplex and wooden board, 600 kg/m³ for wooden block, 500 kg/m³ for bamboo, 1,800 kg/m³ for sand, 1,400 kg/m³ for gravel and 2,330 kg/m³ for ready mix. To calculate weight of reinforced bar, the weight of each bar are used, which 4.74 kg/bar, 7.4 kg/bar, 10.66 kg/bar, and 12.48 kg/bar for reinforced bar ϕ 8, ϕ 10, ϕ 12, and ϕ 13, respectively. The results of quantities in kg were converted to kg CO₂-eq using conversion emission factor.

The other emission source that should be considered is transportation. Table 6 shows the distance between raw material place and project location. The distances in km were changed to kg CO₂-eq.

Table 6 Distances from raw material place to project for calculating transportation emission

Material	Distance (km)
Multiplex	5.00
Wooden board	8.80
Wooden block	8.80
Concrete wire	5.30
Nail	5.3
Cement	1.10
Sand	17.00
Gravel	17.00
Reinforced bar ϕ 8	6.60
Reinforced bar ϕ 10	6.60
Reinforced bar ϕ 12	6.60
Reinforced bar ϕ 13	6.60
Ready Mix	11.00
Bamboo	8.80

Life Cycle Impact Assessment

In this phase, the life cycle inventory result are evaluated their impact potency. Then, the impact results are interpreted in the final phase. In this research, ReCipe 2016 Midpoint with characterization impact assessment is selected in SimaPro software.

Each column and beam is classified into 4 types

dimensions with different quantities and methods. The dimensions of column are 25 x 50, 20 x 20, 15 x 20, and 15 x 15, while beam are categorized 25 x 50, 15 x 30, 15 x 15, and lintel beam 15 x 15. While in this research also separate nine individual material categories for column, beam and plate: multiplex/wooden board, wooden block, concrete wire, cement, sand, gravel, and reinforced bar (ϕ 8, ϕ 10, ϕ 12, and ϕ 13), ready mix concrete and bamboo plus transport to project.

In this phase of impact assessment, the individual materials were analyzed in network flow and table for each type column, beam and plate. Moreover, the impact assessment for general column, beam and plate were also calculated. Table 7 show the impact assessment in the form of greenhouse gas of individual materials for each type column, beam and plate, as indicator of global warming impact.

Table 7 Greenhouse gas as global warming impact for each type column, beam and plate

Type	Material	Greenhouse gas (kg CO ₂ -eq)
Column 25 x 25	Multiplex	-96.20
	Wooden block	65.90
	Concrete wire	16.90
	Cement	932.00
	Sand	201.00
	Gravel	68.30
	Reinforced bar	753
Column 20 x 20	Multiplex	-66.00
	Wooden block	45.20
	Concrete wire	11.60
	Cement	639.00
	Sand	138.00
	Gravel	46.80
	Reinforced bar	286.00
Column 15 x 20	Multiplex	-55.50
	Wooden block	18.80
	Concrete wire	9.14
	Cement	469.00
	Sand	104.00
	Gravel	34.00
	Reinforced bar	447.00
Column 15 x 15	Wooden block	112.00
	Concrete wire	54.50
	Cement	2,800.00
	Sand	618.00
	Gravel	203.00
	Reinforced bar	1,440.00
Beam 25 x 50	Multiplex	-10.70
	Wooden block	2,390.00
	Concrete wire	30.30

Type	Material	Greenhouse gas (kg CO ₂ -eq)
Beam 15 x 30	Ready mix	1,020.00
	Reinforced bar	1,180.00
	Multiplex	-10.20
	Wooden block	2,150.00
	Concrete wire	21.60
Beam 15 x 15	Ready mix	1,170.00
	Reinforced bar	1,050.00
	Multiplex	-2.85
	Wooden block	600.00
	Concrete wire	6.03
Lintel 15 x 15	Ready mix	30.00
	Reinforced bar	913.00
	Multiplex	-0.94
	Wooden block	9.64
	Concrete wire	1.99
Plate	Cement	120.00
	Sand	29.90
	Gravel	10.10
	Reinforced bar	283.00
	Scaffolding	23.30
	Wooden block	1.54 x 10 ⁵
	Multiplex	-1,740.00
	Reinforced bar	8,800.00
	Concrete wire	66.80
	Ready mix	1.01 x 10 ⁷
	Vibrator elect.	2.38 x 10 ⁴

Multiplex, as shown as Table 7, gives a negative greenhouse gas emission. Multiplex material does not have an impact on the environment because this material can be recycled. In network flow, the red

arrow indicates the emissions from each material or process, while the green arrow indicates recyclable material or no negative impact on the environment. Fig. 2, Fig. 3 and Fig. 4 show the network flow to calculate GHG emission as the global warming impact for whole column, beam and plate, respectively.

Interpretation

By using SimaPro 9.0, the dominant GHGs almost came from unvaried materials from each types of column due to the same conventional construction method. Based on Table 7, three materials that produce highest GHGs on four types column came from cement 469 kg CO₂-eq – 2,800 kg CO₂-eq (45% - 58%), reinforced bar 28 kg CO₂-eq - 753 kg CO₂-eq (26% - 44%) and sand 104 kg CO₂-eq - 618 kg CO₂-eq (10% - 13%). Similarly, on the conventional beam construction (lintel beam 15 x 15), the highest GHGs produced from cement 5,420 kg CO₂-eq (58.80%), gravel 1,400 kg CO₂-eq (15.20%) and sand 1,380 kg CO₂-eq (15%). The reinforced bar on lintel beam which installed above doors and windows, do not give high GHG due to dimension and quantities.

On the contrary, the three highest GHG emissions on ready mix process for beam and plate are varied sources depend on dimension and quantities. Ready mix concrete on beam and plate produced GHG on 983 kg CO₂-eq – 1,130 kg CO₂-eq (20% - 45%) and 4,570 kg CO₂-eq (87.30%), respectively. Reinforced bar contribute GHG 913 kg CO₂-eq – 1,180 kg CO₂-eq (25% - 58%) on beam construction and 440.90 kg CO₂-eq (8.43%) on plate process.

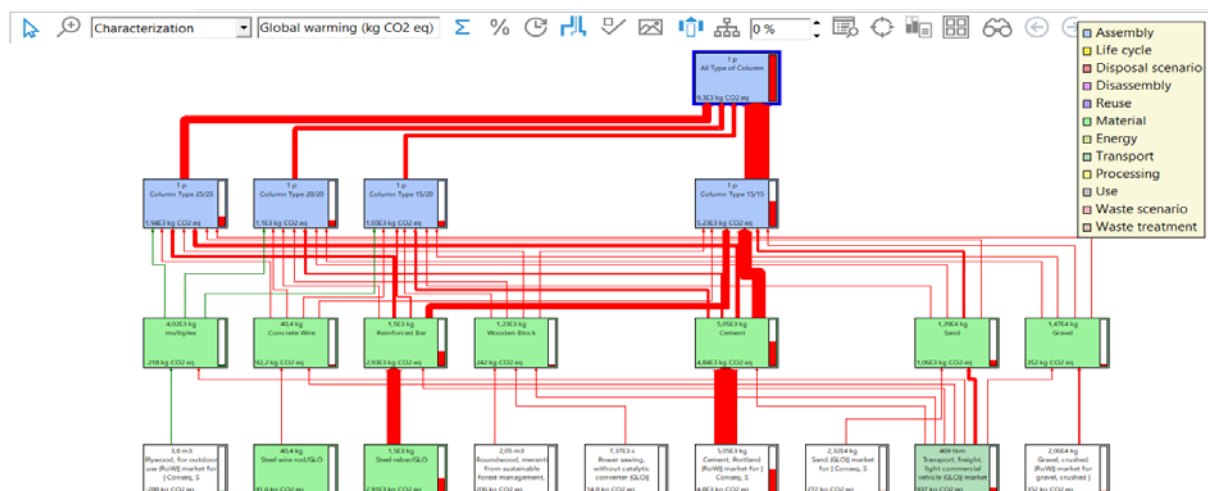


Fig 2. Network flow and emission GHG of all column type

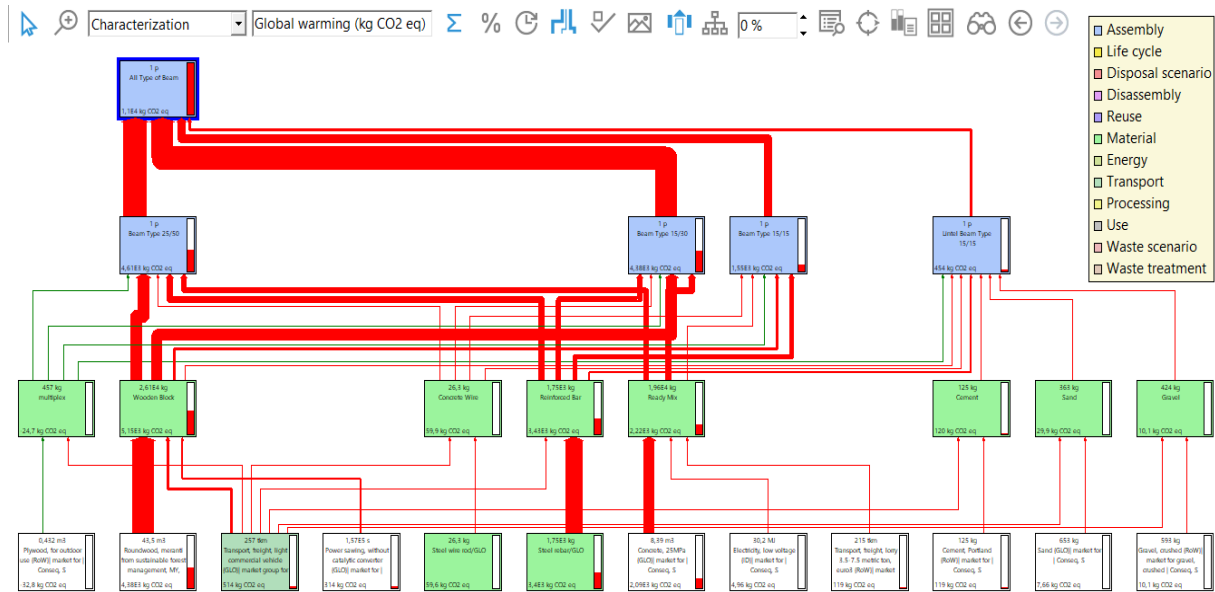


Fig 3. Network flow and emission GHG of all beam type

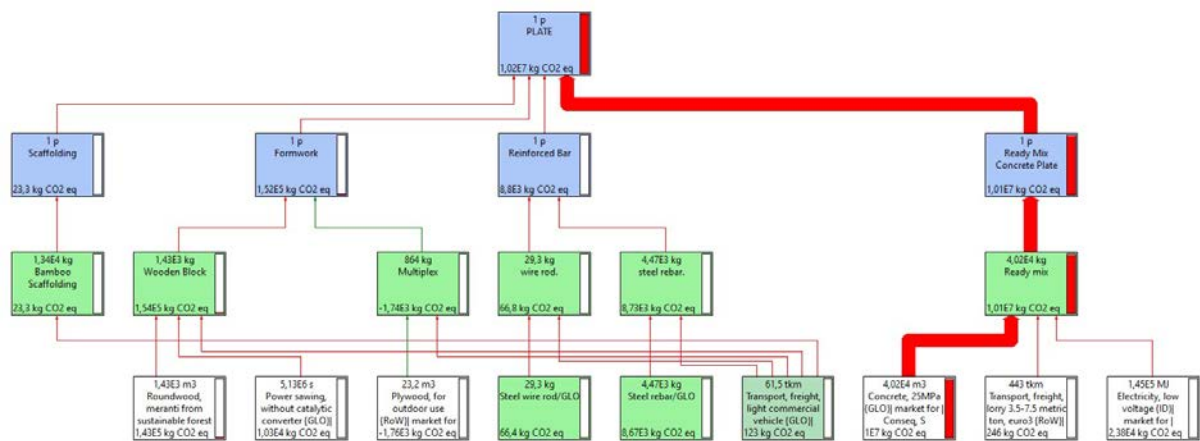


Fig 4. Network flow and emission GHG of plate

According to column network flow analysis (Fig. 2), it seen clearly that cement, reinforced bar, and sand emitted three highest GHG as global warming emission at 4,840 kg CO₂-eq (52%), 2,926 kg CO₂-eq (31.50%), and 1,061 kg CO₂-eq (11.40%), respectively. A high emission from cement could be explained by cement production and transportation. It originated from fuel combustion and from the calcination reaction. The rest of CO₂ emissions emerge from grinding and transport [13].

Meanwhile, the beam works consist of two method, a conventional process and ready mix process. As a consequence, beam network flow analysis (Fig. 3) resulted not only cement (120 kg CO₂-eq, 1.09%) and reinforced bar (3,426 kg CO₂-eq, 31.20%) produced GHG emission, but also ready mix concrete at 2,200 kg CO₂-eq (20.20%) and wooden block 5,150 kg CO₂-eq (46.90%). Fig.

4 shows plate network flow analysis that dominated by emission from ready mix concrete at 1.01 x 10⁷ kg CO₂-eq (98.40%). This emission included emission from transportation and electricity.

Furthermore, in comparison to SimaPro 9.0, the impact assessment also calculated using GaBi software. The calculation indicates that there is no significant difference in both of software result, especially on GHG as global warming indicator.

CONCLUSIONS

The emission of GHGs from conventional process of column and beam in a real estate construction derived from cement, reinforced bar, and sand at $\pm 50\%$, 26-44%, and $\pm 10\%$ GHG emission, respectively. In a ready mix process, the highest GHG emission for beam and plate are ready mix concrete, reinforced bar, and wooden board.

The varied sources that contribute dominant GHG depend on dimension and quantities of structural material.

ACKNOWLEDGMENTS

We would like to acknowledge the Faculty of Engineering, Brawijaya University for supporting financial grant for this research.

REFERENCES

- [1] UNEP, Global Status Report 2017, Towards a zero emission, efficient, and resilient buildings and construction sector, 2017.
- [2] Ragheb A.F., Towards Environmental Profiling for Office Buildings Using Life Cycle Assessment (LCA), Dissertation University Michigan, 2011.
- [3] Rey J.G., Yepes V., Environmental Assessment of Concrete Structures, *International Journal of Construction Engineering and Management* 1 (3), 2012, pp. 33-41, DOI: 10.5923/j.ijcem.20120103.04
- [4] Bribian I.Z., Capilla A.V., Uson A.A., Life Cycle Assessment of Building Materials: Comparative Analysis of Energy and Environmental Impacts and Evaluation of the Eco-efficiency Improvement Potential. *Building and Environment* 46(5), 2011, pp. 1133-40.
- [5] Basbagill J., Flager F., Lepech M., Fischer M., Application of Life-Cycle Assessment to Early Stage Building Design for Reduced Embodied Environmental Impacts, *Building and Environment* 60, 2013, pp. 81 – 92.
- [6] Carolina G.G.D., Manuel G.S.J., Ramon C.H., Luis A.S.J., Consolacion G.S.M., LCA as Comparative Tool for Concrete Columns and Glulam Columns, *Journal of Sustainable Architecture and Civil Engineering* 2 (11), 2015, pp. 21-31. DOI 10.5755/j01.sace.11.2.10291
- [7] Hendra F.H., Pembangunan Perumahan Rendah Emisi Karbon di Surabaya Timur (in Bahasa), Seminar Nasional Sains dan Teknologi Terapan IV, Institut Teknologi Adhi Tama Surabaya, 2016
- [8] Sapulete C.A., Lie H.A., Priastiwi Y.A., Sustainability Beton Metode Life Cycle Assessment Studi Kasus: Limbah Beton Laboratorium Bahan dan Konstruksi Departemen Teknik Sipil Universitas Diponegoro Semarang (in Bahasa). *Media Komunikasi Teknik Sipil*, Vol 24, No 2, 2018, pp.140-147.
- [9] Finnveden et. al., Recent Developments in Life Cycle Assessment, *Journal of Environmental Management* 91, 2009, pp. 1-21.
- [10] Akan M.O.A., Dhavale D.G., Sarkis J., Greenhouse Gas Emissions in The Construction Industry: An Analysis and Evaluation of A Concrete Supply Chain, 2017.
- [11] Hermawan, Marzuki P.F., Abduh M., Driejana R., Peran Life Cycle Analysis (LCA) pada Material Konstruksi Dalam Upaya Menurunkan Dampak Emisi Karbon Dioksida pada Efek Gas Rumah Kaca. *Konferensi Nasional Teknik Sipil 7 UNS*, 2013.
- [12] Emami N., Heinonen J., Marteinsson B., Saynajoki A., Junnonen J.M., Laine J., Junnila S., A Life Cycle Assessment of Two Residential Buildings Using Two Different LCA Database-Software Combinations: Recognizing Uniformities and Inconsistencies. *Building* 9, 20, 2019.
- [13] IPCC, AR5 Climate Change 2014: Mitigation of Climate Change, 2014

TRENDS IN THE USE OF STREET TREES IN JAPAN

Masaaki Furuno ¹, Taizo Uchida ², Daisuke Hayasaka ³, Xue Jun Huan ⁴ and Teruo Arase ⁵

¹ Graduate School of Engineering, Kyusyu Sangyo University, Japan; ² Faculty of Architecture and Civil Engineering, Kyusyu Sangyo University, Japan; ³ Faculty of Agriculture, Kindai University, Japan; ⁴ Faculty of Landscape Engineering, Suzhou Polytechnic Institute of Agriculture, China; ⁵ Faculty of Agriculture, Shinshu University, Japan;

ABSTRACT

Street trees are one of the important components of green infrastructure in urban area. This study surveyed trends in the introduction of street trees across Japan. The results showed that Japanese street trees tended to be mainly broad-leaved rather than coniferous, and many of these were native species. In addition, we found that street trees not only fulfill the roles of disaster prevention and disaster reduction, but also contribute to citizen welfare and recreation because a relatively large number were flowering trees such as sakura, camellia and dogwood. On the other hand, species composition of street trees was not monotonous across Japanese, which were broadly categorized into four groups, and each group had species such as *Picea glehnii*, *Quercus acuta*, *Aucuba japonica* and *Planchonella obovata* that were unique to that group. Each group had correlation with latitude, longitude, Kira's Warmth Index, annual precipitation, etc. Also, there were only five species that were common to all groups: Rosaceae sp., Lythraceae sp., Theaceae sp., *Juniperus chinensis*, Fabaceae sp. It was suggested that these five species are the street trees that represent Japan. Incidentally, weeds which invade the narrow soil beds at the base of high trees were managed by installation of shrubs, garden plants such as flowers and artificial cover such as concrete in addition to weeding in Japan.

Keywords: Street trees, Green infrastructure, Trend in Japan, Management

INTRODUCTION

Urban areas are facing big problems such as the heat island phenomenon, air pollution, and increased risk of disasters due to climate change [1]–[10], [23], [24]. Green infrastructure in urban areas has recently attracted attention as a way to combat some of these problems [11]–[14], [20], [22]. Green infrastructure is a nature-based solution that contributes to disaster prevention and reduction by incorporating the natural environment into normal infrastructure [11]–[14], [20], [22]. Trees planted along streets (street trees) are one example of green infrastructure that is actively introduced because they fulfill the roles of preventing the spread of fires and reducing earthquake damage [15], [16]. It is difficult to introduce new large green infrastructure such as parks in urban areas because of limited space and the high costs associated with construction and maintenance; however, more street trees are expected to be introduced in the future because they are smaller and cheaper than full parks.

Although there are various reports on the use of street trees in various prefectures and urban areas in Japan, there is no clear study on trends in the introduction of street trees across Japan (e.g. native species ratio) [17]–[19], [25], [26]. Clarifying this tendency would be useful for promoting green infrastructure in the future. Therefore, this study analyzed trends in the introduction of street trees across Japan based on a collection of reports on street tree use in various parts of Japan.

MATERIALS AND METHODS

In this study, the top 50 high tree species in number planted in each Japanese prefectures (47 prefectures × 50 species = 2350 species) were targeted. Information on species planted was obtained from “The Roadside Trees of Japan VIII” issued by the National Institute for Land and Infrastructure Management Ministry of Land, Infrastructure, Transport and Tourism, Japan [17]. We tallied the ratio of native species, evergreen broad-leaved, deciduous broad-leaved, coniferous, flowering (i.e. trees that are generally grown for the enjoyment of their flowers such as sakura, camellia and dogwood) and edible (i.e. trees with generally edible fruits such as ginkgo, olive and orange) trees. We also determined in what areas these street trees were used from the classification of prefectures by Two Way Indicator Species Analysis (TWINSPAN), and Detrended Correspondence Analysis (DCA).

In addition, we examined street tree management from a survey of 1629 high trees randomly selected in Fukuoka City, Fukuoka Prefecture, and located in western Japan and one of the five biggest cities in Japan. Street tree management was inferred by examining the narrow soil beds at the base of high

trees planted along the sidewalk.

TWINSPAN and DCA were analyzed using PC-ORD Ver.4.25 (MjM Software Design). Also, relationship between the stand scores extracted from DCA and environmental variables (latitude, longitude, Kira's Warmth Index, annual precipitation, daylight hours and snowfall of each prefecture [21]) were analyzed by Pearson's correlation test.

RESULTS

Trends in street trees used in Japan

Native species accounted for 57.1% of street trees in this study (Fig.1). 46.0% of street trees were deciduous broad-leaved, 40.1% were evergreen broad-leaved, 13.9% were coniferous, 24.6% were flowering and 5.6% were edible (Fig.1).

Japanese prefectures were broadly categorized into four groups (A, B, C and D) based on the species composition of street trees by TWINSPAN (Fig.2 and Table 1). Group A included four prefectures and had

96 species of street trees, Group B included 20 prefectures and had 141 species of street trees, Group C included 22 prefectures and had 155 species of street trees, and Group D included 1 prefecture and had 50 species of street trees. There was a significant difference in the rate of evergreen broad-leaved, deciduous broad-leaved and coniferous trees among these groups. Group A had the most deciduous broad-leaved and coniferous trees, followed by Group B, Group C, and Group D, respectively (Table 1).

Each group had its own unique street trees that were used only in that group (Appendix 1). Group A had 27 unique species such as *Picea glehnii*, *Abies sachalinensis* and *Populus suaveolens*, Group B had 21 unique species such as *Quercus acuta*, *Chamaecyparis obtusa* and *Larix kaempferi*, Group C had 44 unique species such as *Aucuba japonica*, *Aphananthe aspera* and *Cinnamomum daphnoides*, and Group D had unique 29 species such as *Planchonella obovata*, *Satakentia liukiensis* and *Millettia pinnatas*. Incidentally, there were also five species that were common to all groups: Rosaceae sp.,

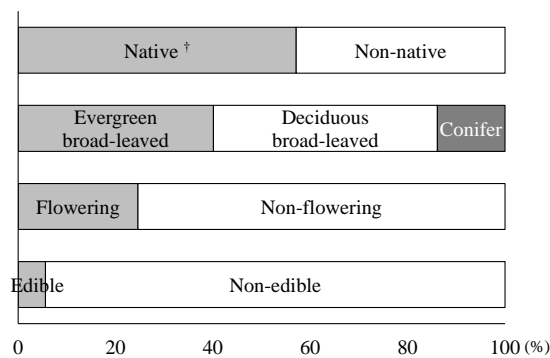


Fig. 1 Trends in Japanese street trees. 252 species were analyzed, excluding duplicates from 2350 species in the research target.
†Varieties were included.

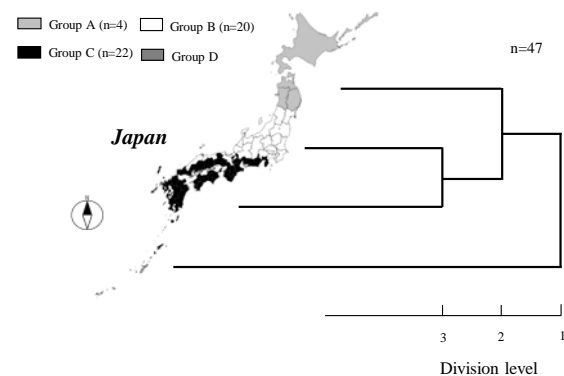


Fig. 2 Classification of prefectures by TWINSPAN. Top 50 high tree plant species in number used in each Japanese prefectures and the number of each planted was set as a variable.

Table 1 Tendencies in street trees for each group.

	Group				P-value ‡
	A (n=4)	B (n=20)	C (n=22)	D (n=1)	
Total number of species	96	141	155	50	-
Native (%) †	56.3	64.5	61.3	52.0	.360
Evergreen broad-leaved (%)	7.3	30.4	49.0	68.0	.000
Deciduous broad-leaved (%)	71.9	54.6	42.6	24.0	.000
Coniferous (%)	20.8	14.8	8.4	8.0	.022
Flowering (%)	25.0	24.1	23.2	34.0	.481
Edible (%)	5.2	5.0	5.8	6.0	.986

†Varieties were included.

‡Pearson's χ^2

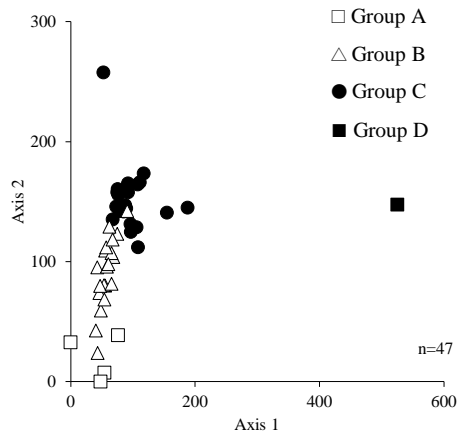


Fig. 3 Ranking of Japanese prefectures by DCA.

Lythraceae sp., Theaceae sp., *Juniperus chinensis*, Fabaceae sp. (Appendix 1).

Each group was ranked on two axes by DCA (“after-the-fact coefficient of determination” was 0.536) (Fig.3). Each group was arranged in the order of Group A, B, C, D on the left side (i.e. the first axis). Each group had a high positive correlation with Kira’s Warmth Index and annual precipitation, and a negative correlation with latitude and longitude on the first axis (Table 2). Namely, it was suggested Group A had higher latitude, colder temperatures and lower annual precipitation followed by Group B, C, and D, respectively. For the second axis, each group was arranged in the order of Group A, B, C, and D along the bottom side. Each group had a high positive correlation with Kira’s Warmth Index and daylight hours, and a negative correlation with latitude, snowfall and longitude on the second axis (Table 2). The groups had same tendency as the first axis, and Group A had high snowfall and low daylight hours followed by Group B, C, and D, respectively.

Street tree management

Results of the survey of the narrow soil beds at the base of high trees showed the following five types of management: no installation (n=614), installation of artificial cover such as concrete and iron (n=322), installation of garden plants such as flowers (n=177), installation of shrubs (n=341) and others (n=175) (Fig.4 and Photo 1). No installation was defined as nothing installed on the narrow soil beds at the base of high trees. Signal devices, garbage cans, road signs, billboards, etc. were included in “Others” (Photo 1).

DISCUSSION

Trends in street trees used in Japan

There are various reports on street trees used in

Table 2 Correlation between DCA stand scores and environmental variables.

	Axis 1 †	Axis 2 ‡
Latitude	-0.760**	-0.697**
Longitude	-0.614**	-0.634**
Kira’s Warmth Index †	0.793**	0.668**
Annual precipitation †	0.379**	0.278
Daylight hours (h) †	-0.090	0.344*
Snowfall (cm) †	-0.282	-0.685**

†Data were obtained from the Automated Meteorological Data Acquisition System (2009-2018).

‡Pearson’s correlation coefficient.

* $p < 0.05$, ** $p < 0.01$.

Japanese prefectures and urban areas [17]–[19], [25], [26]. However, there is no clear summary of trends in street tree use across Japan. This study collected and analyzed information on street tree trends across Japan. Results showed that evergreen broad-leaved and deciduous broad-leaved species accounted for nearly 90% of street trees in Japan and that many street trees were native species (Fig.1). Therefore, we considered that Japanese street trees tended to consist of mainly broad-leaved and native species. In addition, we found that street trees as a green infrastructure not only fulfill the roles of disaster prevention and disaster reduction, but also contribute to citizen welfare and recreation because a relatively large number were flowering trees (Fig.1). Since few edible street trees were found, it was suggested that the role of street trees as edible was small (Fig.1).

Although there were some similarities, species composition of street trees was not monotonous across Japanese prefectures, which were broadly categorized into four groups (Fig.2). Group A tended to have the most deciduous broad-leaved and coniferous trees, and few evergreen broad-leaved trees, followed by Group B, C, and D, respectively (Table 1). Also, it was suggested that Group A had high latitude, cold temperatures, heavy snowfall, low annual precipitation and low daylight hours followed by Group B, C, and D, respectively (Fig.3 and Table 2). On the other hand, each group had species that were unique to that group (Appendix 1). From above results, it was suggested that Japanese street trees have different species composition based on the latitude, temperature and annual precipitation of each area.

On the other hand, each group had also five species (Rosaceae sp., Lythraceae sp., Theaceae sp., *Juniperus chinensis*, and Fabaceae sp.) that were common to all Groups regardless of latitude, temperature and annual precipitation (Appendix 1), it was suggested that these five species are the street trees that represent Japan.

Street tree management

This study inferred street tree management by examining the narrow soil beds at the base of high trees. The results showed that Japanese street tree had five patterns of no installation, installation of garden plants such as flowers, installation of artificial cover such as concrete and iron, installation of shrubs, and others (Fig.4 and Photo 1). “No installation” accounted for 37.7% of street tree. In “No installation”, weeds often invaded (the authors frequently observe this) (Photo 1). Therefore, it was suggested that weeds are allowed to invade the narrow soil beds at the base of high trees and are then managed by weeding in japan. In addition, we

consider that Japanese street tree management tends also to prevent invasion of weeds by installation of shrubs, garden plants and artificial cover, because they accounted for 51.2% of street tree management. Incidentally, it was suggested that “Installation of garden plants” fulfilled also the role of recreation for citizens and improving the urban landscape. Overall, weeds which invade the narrow soil beds at the base of high trees were managed by installation of shrubs, garden plants such as flowers and artificial cover such as concrete in addition to weeding in japan.

REFERENCES

- [1] Logaraj R., Nasrin A., Chng S.F., Amirhosein G., Ali G., Li P.W., Norhaslina H. and Nik M.S., A critical review of Urban Heat Island phenomenon in the context of Greater Kuala Lumpur, Malaysia, Sustainable Cities and Society, Vol. 39, 2018, pp.99-113.
- [2] LÍgia T.S., Fernando F., Maria P. and Bruno M., SAUS: A tool for preserving urban green areas from air pollution, Urban Forestry & Urban Greening, Vol. 46, 2019, Article 126440.
- [3] Junyan Y., Beixiang S., Yi S., Simon M., Yi Z and Geyang X., Air pollution dispersal in high density urban areas: Research on the triadic relation of wind, air pollution, and urban form, Sustainable Cities and Society, Vol. 54, 2020, Article 101941

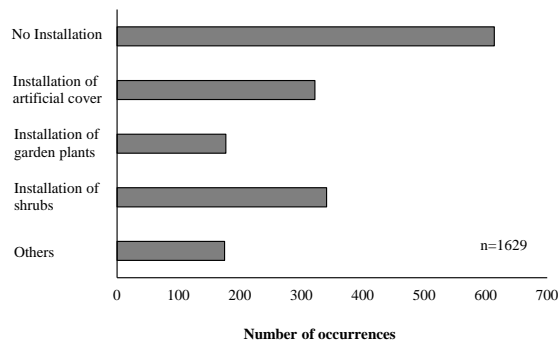


Fig. 4 Street tree management.

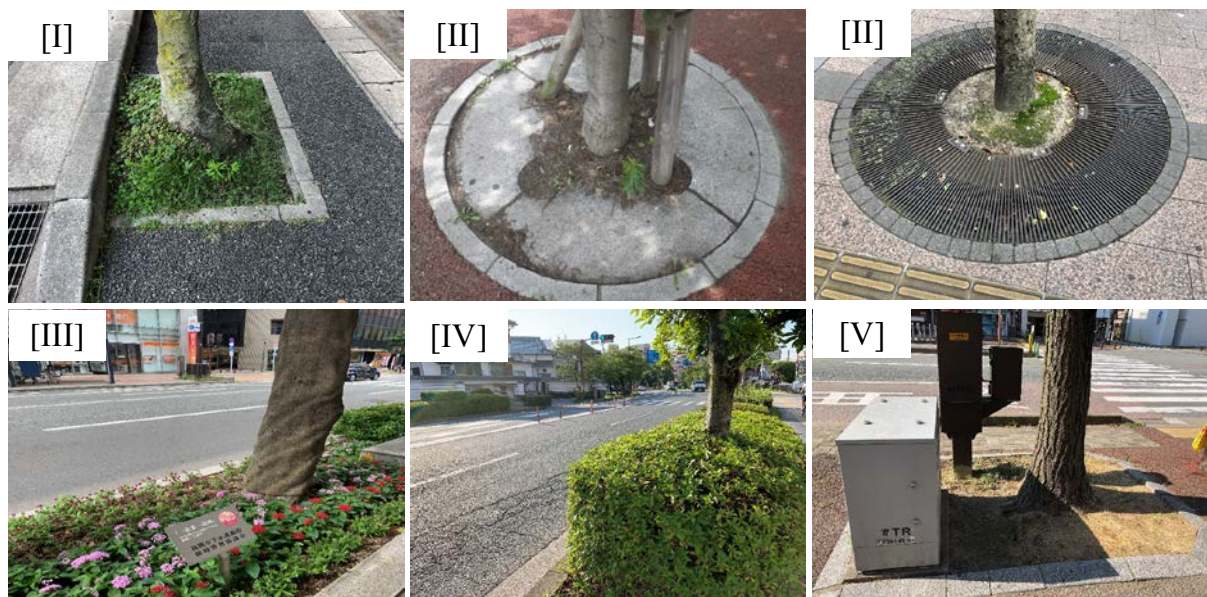


Photo 1 Street tree management patterns.

[I] No management, [II] Introducing garden plants such as flowers, [III] Installation of artificial cover such as concrete and iron, [IV] Introducing shrubs, [V] Other

- [4] Rathphum P., Kasem C., Surat B., Physical characteristics of Bangkok and its urban heat island phenomenon, *Building and Environment*, Vol. 143, 2018, pp. 561-569.
- [5] Xuefan Z. and Hong C., Impact of urbanization-related land use land cover changes and urban morphology changes on the urban heat island phenomenon, Vol. 635, 2018, pp. 1467-1476.
- [6] Young K.Y, In S.K., Min H.C., Sumin K. and Jin C.P., Effect of PCM cool roof system on the reduction in urban heat island phenomenon, *Building and Environment*, Vol. 122, 2017, pp. 411-421.
- [7] Mohsen S., Sami G.A.-G., Climate change impacts on critical urban infrastructure and urban resiliency strategies for the Middle East, *Sustainable Cities and Society*, Vol. 54, 2020, Article 101948.
- [8] Vidhee A. and Amit G., Implications of land use transitions and climate change on local flooding in urban areas: An assessment of 42 Indian cities, *Land Use Policy*, Vol.95, 2020, Article 104571
- [9] Abbas R., Parichehreh B. and Alireza M.B., Analysis of performance criteria and sustainability index in urban stormwater systems under the impacts of climate change, *Journal of Cleaner Production*, Vol.271, 2020, Article 122727
- [10] Xin D., Linkun J., Siyu Z., Ru G. and Yani Z., Vulnerability of urban water infrastructures to climate change at city level, *Resources, Conservation and Recycling*, Vol. 161, 2020, Article 104918.
- [11] Vidya V., Aaron I.P., Daniel R.P., Denise L., David J.M., Robert I.M., William M.M. and Sera L.Y., A systematic review of the human health and social well-being outcomes of green infrastructure for stormwater and flood management, *Journal of Environmental Management*, Vol. 246, 2019, pp. 868-880.
- [12] Angela R.M., Daniel J.B., Erin P.M., Kristina G.H., Sarah L. and Erin C., Seasonal drivers of chemical and hydrological patterns in roadside infiltration-based green infrastructure, *Science of The Total Environment*, Vol. 714, 2020, Article 136503.
- [13] Federica M., Elisabetta S., Alessandro S., Lina F. and Fausto M., Regulating Ecosystem Services and Green Infrastructure: assessment of Urban Heat Island effect mitigation in the municipality of Rome, Italy, *Ecological Modelling*, Vol. 392, 2019, pp. 92-102.
- [14] HP of European Commission: https://ec.europa.eu/environment/nature/ecosystems/index_en.htm, Referenced in 2020.6.30
- [15] Kida Y. and Kaniwa M., Urban disaster prevention: "Especially about disaster prevention ability of trees and their maintenance and management": About disaster prevention ability of trees and the method to maintain and diagnose them, *Journal of the Japanese Society of Revegetation Technology*, Vol. 44, Issue 3, 2019, pp. 433.
- [16] HP of Kyoto city: <https://www.city.kyoto.lg.jp/kensetu/page/0000079886.html>, Referenced in 2020.6.30
- [17] National Institute for Land and Infrastructure Management Ministry of Land, Infrastructure, Transport and Tourism, Japan., *The Roadside Trees of Japan VIII, TECHNICAL NOTE of National Institute for Land and Infrastructure Management*, No.1050, 2018
- [18] Fukuoka T., Takahashi A and Fuse S., A Report on the Examination of Roadside Trees in Sanda City, Hyogo Prefecture, *Humans and Nature*, Vol. 17, 2007, pp. 35-41.
- [19] Fujisaki K. and Yamauchi Y., Current situation of street trees in Yokohama city and consideration for future, *Journal of the Japanese Society of Revegetation Technology*, Vol. 44, Issue 1, 2018, pp. 217-220.
- [20] Fukuoka T. and Kato S., Toward the Implementation of Green Infrastructure in Japan through the Examination of City of Portland's Green Infrastructure Projects, *Journal of the Japanese Institute of Landscape Architecture*, Vol. 78, Issue 5, 2015, pp. 777-782.
- [21] HP of Japan Meteorological Agency: <https://www.jma.go.jp/jma/index.html>, Referenced in 2020.6.30
- [22] Yoshida T., Green Infrastructure and Ecosystem-based Disaster Risk Reduction Bring about Resilience, *Journal of Rural Planning Association*, Vol. 36, Issue 3, 2017, pp. 430-434.
- [23] Zening W., Yanxia S., Huiliang W. and Meimei W., Urban flood disaster risk evaluation based on ontology and Bayesian Network, *Journal of Hydrology*, Vol. 583, 2020, Article 124596.
- [24] Gül Ö., Nanco D., Helge B., Hans B., Kris L. and Mike B., Urban water management and climate change adaptation: A self-assessment study by seven midsize cities in the North Sea Region, *Sustainable Cities and Society*, Vol. 55, 2020, Article 102066.
- [25] Shoda T., Imanishi J. and Shibata S., Measurement of above-ground biomass of a *Zelkova serrata* (Thunb.) Makino. and two *Ginkgo biloba* L. street trees in Kyoto City, Japan, *Journal of the Japanese Society of Revegetation Technology*, Vol. 45, Issue 1, 2019, pp. 192-195.
- [26] Hioki Y. and Takada M., Present status on *Ailanthus altissima* (Mill.) Swingle escaped from national road route 9, which planted as street tree and evaluation of its invasiveness, *Journal of the Japanese Society of Revegetation Technology*, Vol. 40, Issue 2, 2014, pp. 302-314.

Appendix 1 Street trees present in each group.

Species	Family	Group				Native	Flowering	Edible
		A (n=4)	B (n=20)	C (n=22)	D (n=1)			
Rosaceae sp (<i>Cerasus x yedoensis</i>) ‡	Rosaceae	V	V	V	V	●	●	
Lythraceae sp (<i>Lagerstroemia indica</i>) ‡	Lythraceae	IV	V	V	V		●	
Theaceae sp (<i>Camellia japonica</i>) †	Theaceae	III	V	V	V	●	●	
<i>Juniperus chinensis</i> *	Cupressaceae	IV	IV	V	V	●		
Fabaceae sp (<i>Acacia dealbata</i>) †	Fabaceae	III	II	II	V		●	
<i>Picea glehnii</i> *	Pinaceae	III				●		
<i>Aria alnifolia</i> ‡	Rosaceae	III				●	●	
<i>Malus prunifolia</i> ‡	Rosaceae	III					●	●
<i>Abies homolepis</i> *	Pinaceae	III				●		
<i>Quercus dentata</i> ‡	Fagaceae	III				●		
Bignoniaceae sp (<i>Catalpa ovata</i>) ‡	Bignoniaceae	III						
<i>Populus alba</i> ‡	Salicaceae	III						
<i>Abies sachalinensis</i> *	Pinaceae	III				●		
<i>Picea pungens</i> *	Pinaceae	III						
Others	-	(18 species)				(8 species)	(3 species)	(1 species)
<i>Quercus acuta</i> †	Fagaceae		I			●		
<i>Aesculus x carnea</i> ‡	Sapindaceae		I					
Linnaeaceae sp (<i>Abelia x grandiflora</i>) †	Linnaeaceae		I				●	
<i>Carpinus tschonoskii</i> ‡	Betulaceae		I			●		
<i>Deutzia crenata</i> ‡	Hydrangeaceae		I			●		
<i>Ilex serrata</i> ‡	Aquifoliaceae		I			●	●	
<i>Chamaecyparis pisifera</i> *	Cupressaceae		I					
<i>Chamaecyparis obtusa</i> *	Cupressaceae		I			●		
<i>Larix kaempferi</i> *	Pinaceae		I			●		
Others	-	(12 species)				(6 species)	(3 species)	-
<i>Erythrina crista-galli</i> ‡	Fabaceae			II			●	
Juglandaceae sp (<i>Pterocarya rhoifolia</i>) ‡	Juglandaceae			II		●		
Arecaceae sp (<i>Phoenix dactylifera</i>) †	Arecaceae			II				●
<i>Podocarpus macrophyllus</i> *	Podocarpaceae			II				
Aucubaceae sp (<i>Aucuba japonica</i>) †	Aucubaceae			I		●		
<i>Ficus superba</i> †	Moraceae			I		●		
<i>Malvaviscus penduliflorus</i> †	Malvaceae			I			●	
<i>Olea europaea</i> †	Oleaceae			I				●
<i>Dendropanax trifidus</i> †	Fabaceae			I		●		
Others	-		(35 species)			(17 species)	(7 species)	(1 species)
<i>Planchonella obovata</i> †	Sapotaceae				V	●		
<i>Palaquium formosanum</i> †	Sapotaceae				V			
<i>Hibiscus tiliaceus</i> †	Malvaceae				V	●	●	
<i>Tabebuia rosea</i> ‡	Bignoniaceae				V		●	
<i>Bombax ceiba</i> ‡	Malvaceae				V		●	
<i>Millettia pinnata</i> †	Fabaceae				V	●		
<i>Cocos nucifera</i> †	Arecaceae				V			●
<i>Araucaria heterophylla</i> *	Araucariaceae				V			
<i>Thespesia populnea</i> †	Malvaceae				V	●	●	
Others	-			(20 species)		(8 species)	(8 species)	(1 species)
<i>Firmiana simplex</i> ‡	Sterculiaceae	III	III	III		●		
<i>Fraxinus lanuginosa</i> ‡	Oleaceae	II	I			●		
<i>Bischofia javanica</i> †	Euphorbiaceae			I	V	●		
<i>Carpinus laxiflora</i> ‡	Betulaceae	II	II	I		●		
Pinaceae sp (<i>Pinus densiflora</i>) *	Pinaceae	V	V	V		●		
<i>Ulmus parvifolia</i> ‡	Ulmaceae		V	IV		●		
<i>Thujaopsis dolabrata</i> *	Cupressaceae	IV	II			●		
<i>Pieris japonica</i> †	Ericaceae		I	I		●	●	
<i>Acer rubrum</i> ‡	Aceraceae	II	I					
Others (117 species)	-	-	-	-	-	(75 species)	(26 species)	(7 species)

Occurrence frequency: I, <20; II, <40; III, <60; IV, <80; V, ≤100

†Evergreen broad-leaved.

‡Deciduous broad-leaved.

*Coniferous.

THE RELATIONSHIP BETWEEN LAND USE AND TRANSPORT PERFORMANCE: A CASE STUDY OF PADANG, INDONESIA

Aleksander Purba¹, Nikko Yulianda², Shahnaz Nabila Fuady³

¹Faculty of Engineering, Lampung University, Indonesia; ^{2,3}Urban and Regional Planning Department,
Insitut Teknologi Sumatera, Indonesia

ABSTRACT

Padang on the west coast of Indonesia is one of the oldest cities with a history of more than a century. As the west gate of Indonesia from the direction of the Indian ocean, its existence is known as a port city with the main function as warehousing and logistics center. After continuing to develop as a city of trade and services, Padang is now considered as one of the most congested cities in Indonesia. A series of secondary data has been collected including satellite imagery and both qualitative and quantitative methods were used simultaneously. The pattern of urban space has not changed significantly for decades, even though the number of trips has continued to increase. The population of close to 1 million and land use with more diverse functions results in the road network being overwhelmed to serve vehicle flow. Uncontrolled on-street parking contributes to reducing transport performance. Case study found the degree of saturation and wide road occupied for parking variables, and the speed and number of warehouse building variables are having strong correlation each other.

Keywords: Land use, transport, relationship, Padang, Indonesia

INTRODUCTION

City paradigm in Indonesia according to Law No. 26/2007 governing Spatial Planning emphasizes that cities are areas with denser population concentrations compared to surrounding areas due to functional centralization related to the activities of the population for work, commerce, social, culture, recreation and education. It must be acknowledged that the model of city growth in developing countries is not by design as is common in developed countries, for example Eindhoven, the Netherland [1], and Wellington, New Zealand [2], but develops naturally, sporadically and spreads irregularly beyond administrative boundaries. Daily activities and residences are also further apart, because owning a house in the city center is not affordable for most city residents. Rapid city growth and high dependence of auto ultimately triggered new urban problems in the form of imbalance between land use from the demand side and the ability of the transportation system from the supply side to accommodate the movement of people and goods and services as experienced by Shanghai [3]. The situation in almost all cities in Indonesia is increasingly worrisome because the authority is still focused on approaching the supply side by building flyovers, underpasses, LRT and even the metro and is still very limited in steps related to reducing demand side. Lack of reference to best practices in the region as conducted by Denver in the USA [4], loose and out of date regulations and the absence of the role of civil society have triggered the city of more suffering, marked by, among others, the

continuing depletion of green space. The same problem is also experienced by Lop Buri province, Thailand [5] and even Georgia (USA) due to the development of interstate highway [6], though 10% increase in a city's initial stock of highway causes about 1.5% increase in its employment over a 20-year period in the USA [7].

This paper evaluates the long experience of one of the oldest cities in Indonesia; Padang city based on the National Spatial Planning document is directed to become a National Activity Center and will be developed into the PALAPA (PADang-Lubuk Alung-PARIaman) Metropolitan Core City. As the capital of west Sumatera province the largest city on the west coast of Sumatra is the west gate of Indonesia from Indian ocean. With a land area of almost 700 km² and a population of nearly 1 million, Padang, which was hit by a major tsunami disaster at the end of 2009, is now ranked fourth as the most congested city in Indonesia according to the INRIX 2017 Global Traffic Scorecard [8]. Integrated of land use and transport is still a big challenge in the operational agency settings and integrating it with transport systems [9], tension between bottom up and top down [10], [11], and the need to bridge the gap between the proliferation of activity-based travel demand and their integration with operational models in practice [12]; the challenges became more complex if the city sustainability issue is associated with energy scarcity and climate change [13]. The more advanced approaches using a relatively new database (LEHD) to explore land-use-transportation relationships conducted by Horner and Schleith [14], usage of

mobile phones to indicate the social function of land use in Singapore [15], and applying a spatial composite index to portray an overview of the sustainability performance [16].

MATERIAL AND METHOD

Study Area

Initially the city consisted of 3 districts with 15 villages. In its current development Padang covers 11 districts with elevations varying from 25 m to 1,853

m (Lubuk Kilangan) and coastal areas with elevations from 0 to 8 m (Padang Barat). Administratively, this city besides dealing directly with Indian ocean in the west is flanked by three regencies, each of Padang Pariaman in the north, Solok in the east and Pesisir Selatan in the south as shown in Fig. 1. Based on regulations, the city of Padang is classified as a large city with a population of 927,168 (2017); with an average growth of 1.53% annually the population is predicted to reach 1 million in 2022 and will position it as a metropolitan city.

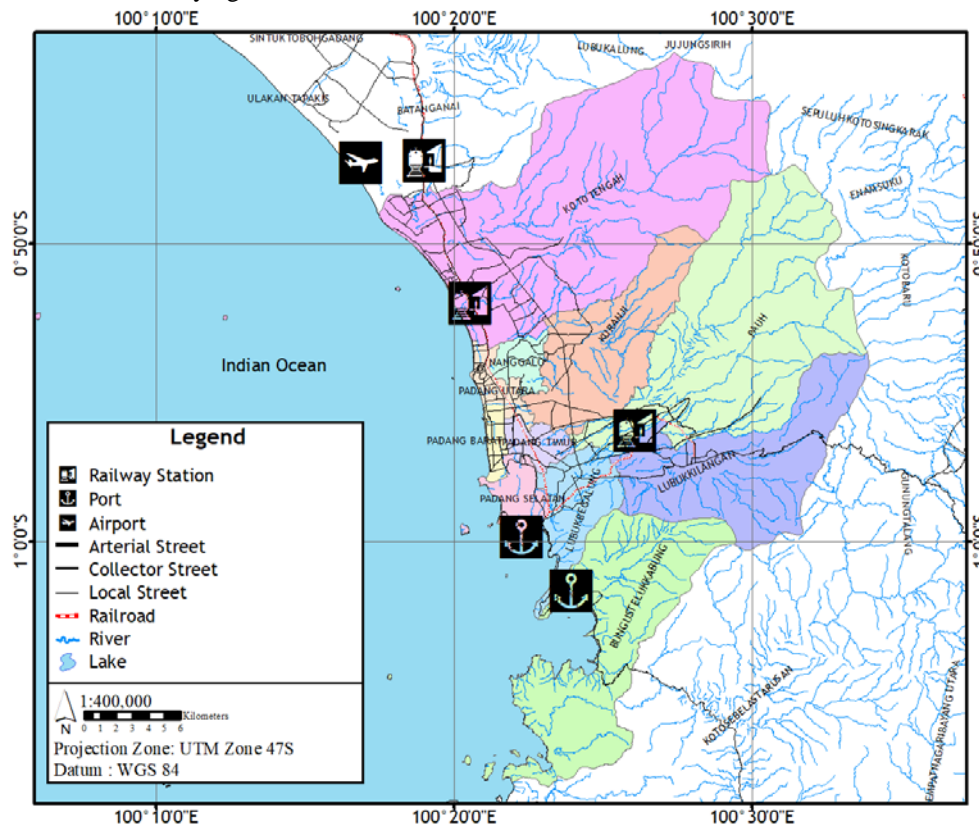


Fig. 1 Administrative map of Padang city

Interestingly, the population distribution is also diverse; Koto Tengah district has a density rate of 817 people/km² and Padang Timur is much denser at 9,751 people/km² with land use dominated by education center and middle class housing complex and closer to the central business district despite the area including in the tsunami alert zone. Based on population structure data, productive age with a range of 15-55 years dominates with a percentage of 62% indicating more than half of the population has the potential to travel and daily urban activities such as education, shopping, leisure, economic and financial activity, social, and culture. City economic structure is supported by wholesale and retail trade, car and motorcycle repair and transportation, and warehousing, respectively. While the number of registered vehicles tends to be constant and even

decreases during the 2013-2017 period as shown in Fig. 2. As with other cities in Indonesia public transportation service is dominated by paratransit with capacity 12 people as many as 1,979 units covering 40 routes.

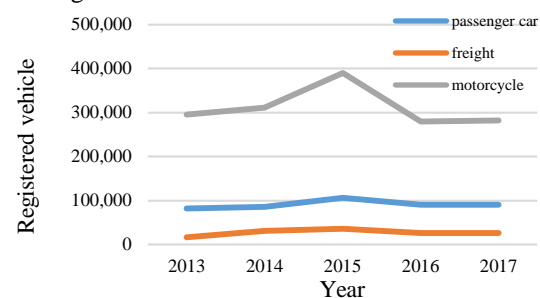


Fig. 2 Number of motorized vehicle 2013-2017

New bus service named Trans Padang with a capacity of 40 people serving two routes began to operate since the last two years. At almost the same time, downtown Padang is also connected by train to the Minangkabau international airport initiated by the central government. The first train departs from Padang station on 06:30 a.m. and the last one would depart on 06:00 p.m. with totally six trips daily and 45 minutes' travel time. Although the transport supply available varies, the facts in the field indicate the opposite condition. Based on the results of INRIX research, Padang ranks fourth as the most congested city in Indonesia as shown in Fig. 3 below. Based on Fig. 3 on average the city residents of Padang lost 45 hours annually due to congestion and delay.

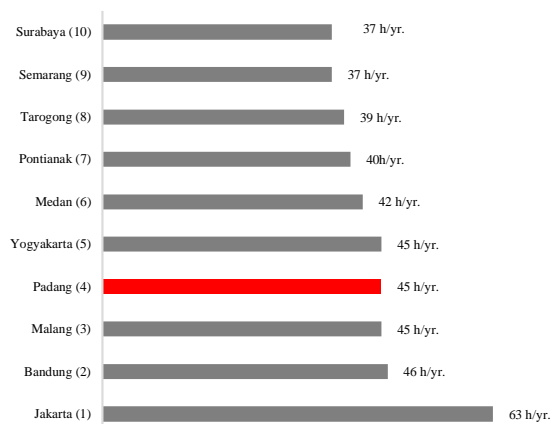


Fig. 3 Indonesia most congested cities (hours/year)

Data Sources

Primary data related to land use was conducted by classified building function along the study corridor based on regulation (Regulation of the Minister of Agrarian Affairs and Spatial Planning / Head of National Land Agency No 16/2018 concerning Guidelines for Compiling Detailed Spatial Planning and Zoning Regulation of Regency/City). According to its regulation the building function to be classified is a building that has conformity with definition, purpose of determination and zone perform criterion of housing, trade and services, offices, industries, public service entities, tourism, and others.

In order to understand road performance, the whole information related to road section characteristics is needed. Road characteristic data was collected in a number of standard field form survey for urban road i.e. geometric form, traffic flow, and road side activity. Geometric itself covering road section type, lane number and lane width, section length, curb, shoulder, median, and pedestrian facility. Hence, the way the traffic controlled was conducted including parking management, split, and flow distribution. Moving car observer method has been used to count the traffic flow, velocity, and density for sixteen road section entire research area.

A series of secondary data has been collected including satellite imagery, population, registered vehicle, road class, and road information, spatial plans, transport master plan, and traffic and road transport master plan. Both qualitative and quantitative methods were used simultaneously in order to get convergent findings.

RESULT AND FINDINGS

Land use development

The area that focuses on this study is Kampung Pondok district; the historical development of this region began since 1915 and after more than a century the spatial patterns almost resemble actual current conditions. According to Topographische Inrichting, Batavia map (1915) Kampung Pondok was clearly directed to support the commercial system of the city which at that time was functioning as a port. Its vital function was triggered by the growth of the city and was proven by permanent buildings that lined the estuary of the Batang Arau river as shown in Fig. 4.

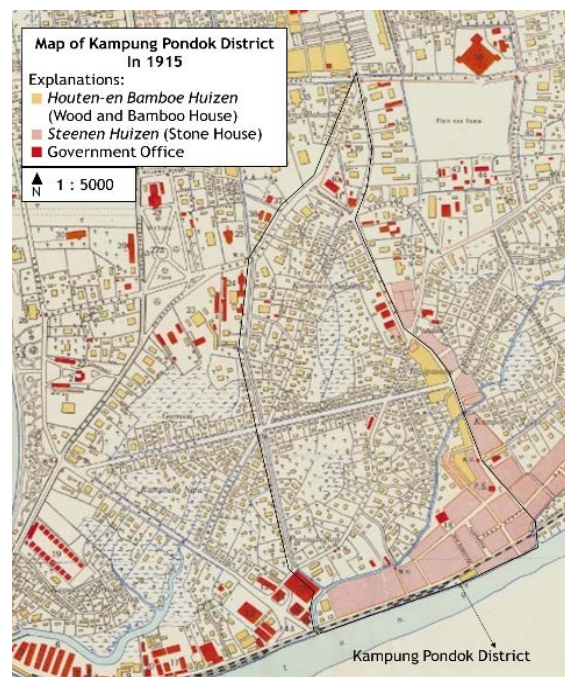


Fig. 4 Topographische Inrichting Map (1915)

Refer to the map permanent buildings associated with function perform as government offices, rock houses and wood and bamboo houses. It is clearly seen in the map that railway line has been available direct to the port indicating an advance transport system.

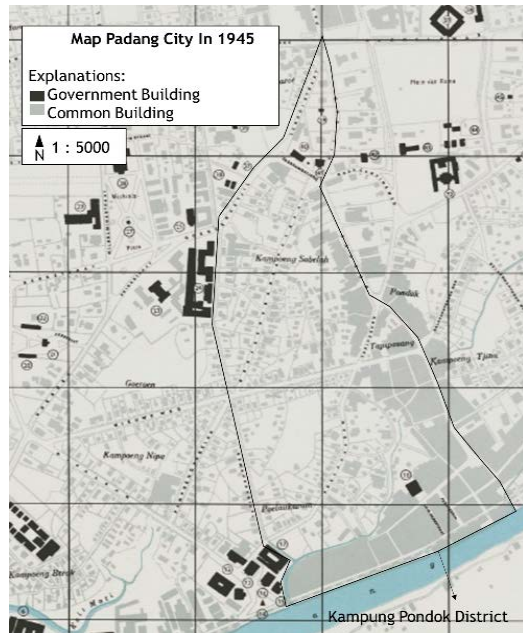


Fig. 5 Map of Kampung Pondok district (1945)

Rapid urban activity around river estuary and its surrounding coast encourage the growth of buildings supporting port activities such as warehousing and logistics centers. Hence, the existence of the port and its supporting facilities shows that the Kampung

Pondok region performs a strategic function on the growth of urban areas at the time.

In 1945 the area was remapped to understand the development of urban land use after four centuries of interacting with various urban activities. As can be seen in Fig. 5 the built up area continues to grow along the river estuary and looks more concentrated in the southern part of the city. Non-government buildings are also seen beginning to fill the area that was previously green space, indicating the presence of the port has an important contribution in driving the development of land use towards the north of the city

But the delta along the Batang Arau river is still seen as a major trading area through its building function characteristics, especially warehousing, logistics centers, banks, and markets. Along with the echoes of Indonesia's independence, cities are developing more rapidly including Padang city. The city reform at that time was more focused on improving the road network to accommodate the development of land use and increasing population, which implies an increase in travel demand. Based on the comparison of maps in 1915 and 1945 with current conditions, it shows that the road sections in Kampung Pondok district have not changed significantly.

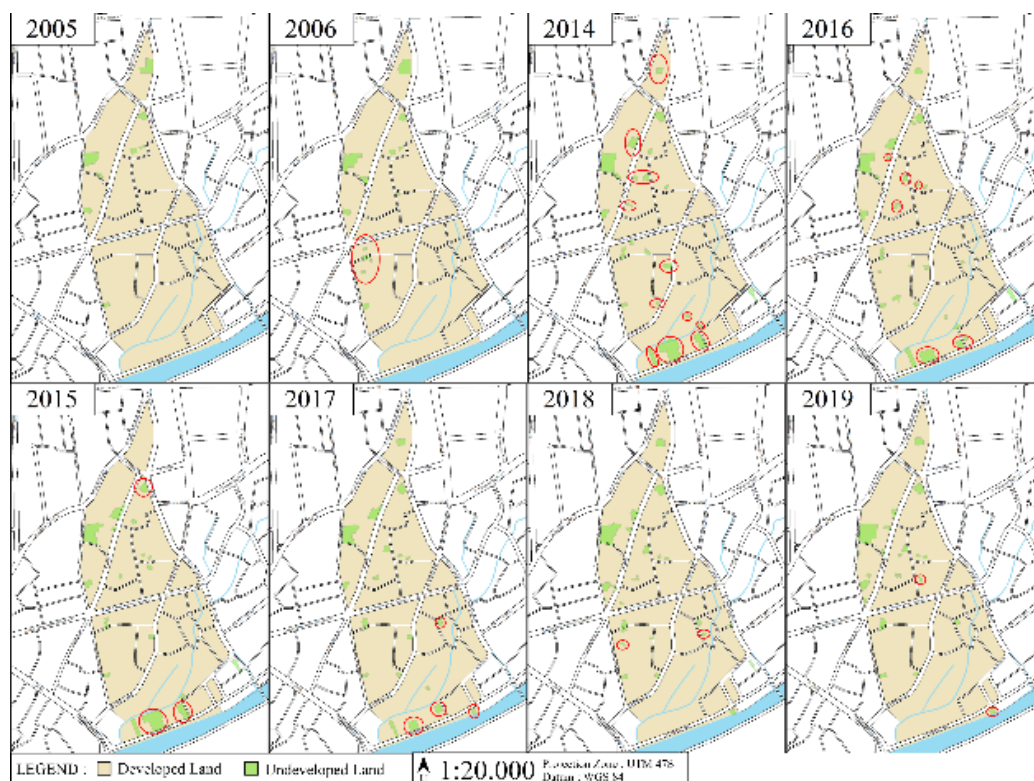


Fig. 6 Open space of Kampung Pondok (2005-2019)

This indicates that the development of the region has maintained a spatial pattern over the last century dominated by commercial support activities in the

form of warehousing, logistic centers, plus trade centers and office buildings as markers of city modernization. In order to identify the latest spatial

patterns and future plans in Kampung Pondok district, the authors elaborated the city spatial planning 2010-2030 period which stated that the west Padang district will focus on a strategic area for the development of trade and services. Furthermore, more detailed identification is done based on Ministry Spatial Planning Act No 16/2018 enacted guidelines for preparation of detailed spatial planning and the regency/city zoning regulations. As can be seen at this time along the study corridor dominated by buildings that functioned as trade centers and mixed functions, in addition to part of the space functioned for reduced green space. Hence, analyses focusing on average travel speed, density, and level of service analysis according to Indonesian Highway Capacity

education, religion and military. But the growth of land use in the current condition is no longer stimulated by the existence of ports; the area develops because of the function directed as the CBD. Figure 6 shows changes in land use around Kampung Pondok district over the past few years. The existence of small roads seems to contribute to the degradation of the region with increasing population and has an impact on increasing demand for housing and roads. The next figure shows more clearly the changes in the Kampung Pondok district over the past decade. The high demand for various urban activities, resulting in

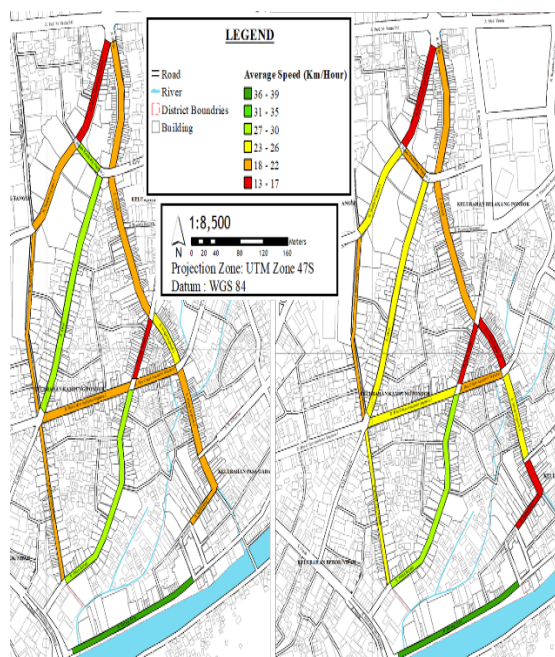


Fig. 7a (left) and Fig. 7b (right) show average speed during 12-2 and 4-6

Manual (1997) [17]. There were sixteen road sections observed in April 2019 during 12–2 and 4–6. Average travel speed in the two observation periods is shown in Fig. 7a and Fig. 7b, respectively. The next Fig. 8a and Fig. 8b express level of density (pcu/km) in the same period. Almost the same with speed motion, level of density getting worse during 4-6 period.

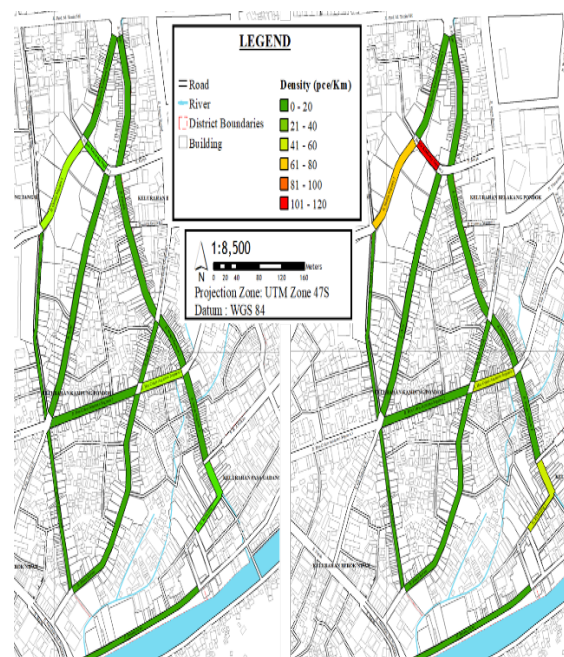


Fig. 8a (left) and Fig. 8b (right) show density level during 12-2 and 4-6

Analysis result related to the level of service as the ratio of volume to capacity can be seen in Fig. 9. As the CBD growing more excessive to northern part of entire city the level of service of road network was more suffering compare to southern part.

Relationship between activity and road performance

This section elaborated correlation between activity entire surrounding area and road performance in order to identify whether the land use and road network influence each other. In this case the identification of connectedness is done by the relationship between level of service of road network variables and land use variables.

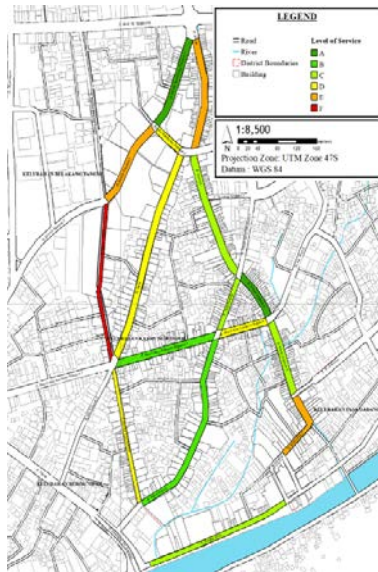


Fig. 9 Level of service of road network

Table 2 Relationship between speed and land use function

No	Variable	Coeff. of correlation	Sig.	Sig. level
1	Speed vs no. of local scale of trade and services building	-0.085	0.754	N/S
2	Speed vs no. of district scale of trade and services building	0.189	0.483	N/S
3	Speed vs no. of regional scale of trade and services building	-0.143	0.598	N/S
4	Speed vs no. of public facilities bldg.	-0.24	0.370	N/S
5	Speed vs no. of residential building	0.221	0.411	N/S
6	Speed vs no. of warehouse building	0.672	0.004	S
7	Speed vs wide road	0.007	0.980	N/S
8	Speed vs wide road occupied for parking	-0.083	0.759	N/S
9	Speed vs no. of lane	0.132	0.626	N/S
10	Speed vs no. of traffic direction	0.423	0.103	N/S

CONCLUSION

In this research the authors explore and find that Kampung Pondok district plays an important role in the historical development of Padang city during a decade as a center of trade and services. In the current condition the region is supported by the number of local, district and regional scale trade buildings and building services which are denser compare to other areas within the city. Growing populations and land use activities that continue to grow increase the number and intensity of travel in the region. As the icon of city, Kampung Pondok district experiencing pressure in the form of high vehicle movement while the ability of the road network to flow has not changed significantly for the last few decades. Most roads show the level of service of D and E indicating the flow rate is almost reaching capacity level or unstable flow. Average travel speed was less than 18 km/hour far below the standard average travel speed in urban areas of 40 km/hour. Interesting to note the density pattern that was shown in Fig. 8a and Fig. 8b; both figures expressed the density level varies from 20 to 60 pcu/km, which are classified as normal cases

Table 1 shows the relationship between degree of saturation (DS) and land use function and Table 2 shows the relationship between speed and land use function.

Table 1 Relationship between DS and land use function

No	Variable	Coeff. of correlation	Sig.	Sig. level
1	DS vs no. of local scale of trade and services building	-0.253	0.334	N/S
2	DS vs no. of district scale of trade and services building	-0.337	0.202	N/S
3	DS vs no. of regional scale of trade and services building	0.177	0.512	N/S
4	DS vs no. of public facilities building	0.349	0.185	N/S
5	DS vs no. of residential building	0.252	0.346	N/S
6	DS vs no. of warehouse building	-0.085	0.754	N/S
7	DS vs wide road	-0.172	0.525	N/S
8	DS vs wide road occupied for parking	-0.535	0.033	S
9	DS vs no. of lane	0.026	0.925	N/S
10	DS vs no. of traffic direction	0.606	0.013	S

except two road sections in northern part as can be seen in Fig. 8b. According to field observation a combination of the low travel speed and a normal counted of density pattern was due to the part of wide road occupied for parking since there is no off street parking available within surrounding of the district. This fact is in-line with the findings expressed in Table 1 and Table 2, where the degree of saturation and wide road occupied for parking variables, and the speed and number of warehouse building variables are having strong correlation each other.

REFERENCES

- [1] Wang, Z., Han, Q., and de Vries, B., Land Use/Land Cover and Accessibility: Implications of the Correlations for Land Use and Transport Planning, *J. of Appl. Spatial Analysis*, Vol. 12, 2019, pp. 923–940.
- [2] Witten, K., Pearce, J., and Day, P., Neighbourhood destination accessibility index: A GIS tool for measuring infrastructure support for neighbourhood physical activity, *J. of Environment and Planning A*, Vol. 43, No. 1, 2011, pp. 205–223.
- [3] Tian, L., Ge, B., and Li, Y., Impacts of state-led and bottom-up urbanization on land use change in the peri-urban areas of Shanghai: Planned growth or uncontrolled sprawl? *J. of Cities*, Vol. 60, 2017, pp. 476–486.
- [4] Ratner, K. A., and Goetz, A. R., The reshaping of land use and urban form in Denver through transit-oriented development, *J. of Cities*, Vol. 30, 2013, pp. 31–46.
- [5] Patarasuk, R., Road network connectivity and land-cover dynamics in Lop Buri province, Thailand, *J. of Transport Geography*, Vol. 28, 2013, pp. 111–123.
- [6] Mothorpe, C., Hanson, A., and Schnier, K., The impact of interstate highways on land use

- conversion, *The Annals of Regional Science*, Vol. 51, No. 3, 2013, pp. 833–870.
- [7] Duranton, G., and Turner, M. A., Urban growth and transportation *J. of Review of Economic Studies*, Vol. 79, No. 4, 2012, pp. 1407–1440.
- [8] INRIX Global Traffic Scorecard, 2017. Retrieved from <https://english.kontan.co.id/news/jakartas-traffic-worsens-in-2017-survey>
- [9] Waddell, P., Integrated land use and transportation planning and modelling: Addressing challenges in research and practice, *J. of Transport Reviews*, Vol. 31, No. 2, 2011, pp. 209–229.
- [10] Batty, M., and Marshall, S., Thinking organic, acting civic: The paradox of planning for cities in evolution, *J. of Landscape and Urban Planning*, Vol. 166, 2017, pp. 4–14.
- [11] Chaudhuri, G., and Clarke, K. C., On the spatiotemporal dynamics of the coupling between land use and road networks: Does political history matter? *J. of Environment and Planning. B, Planning & Design*, Vol. 42, No. 1, 2015, pp. 133–156.
- [12] Acheampong, R. A., and Silva, E. A., Land use–transport interaction modeling: A review of the literature and future research directions. *J. of Transport and Land Use*, Vol. 8, No. 3, 2015, pp. 11–38.
- [13] Simmonds, D., Waddell, P., and Wegener, M., Equilibrium versus dynamics in urban modelling. *J. of Environment and Planning. B, Planning & Design*, Vol. 40, No. 6, 2013, pp. 1051–1070.
- [14] Horner, M. W., and Schleith, D., Analyzing temporal changes in land-use–transportation relationships: A LEHD-based approach. *J. of Applied Geography*, Vol. 35, No. 1–2, 2012, pp. 491–498.
- [15] Pei, T., Sobolevsky, S., Ratti, C., Shaw, S. L., Li, T., and Zhou, C., A new insight into land use classification based on aggregated mobile phone data. *International J. of Geographical Information Science*, Vol. 28, No. 9, 2014, pp. 1988–2007.
- [16] Dur, F., and Yigitcanlar, T., Assessing land-use and transport integration via a spatial composite indexing model, *J. of Environmental Science and Technology*, Vol. 12, No. 3, 2015, pp. 803–816.
- [17] Ministry of Public Works, Indonesian Highway Capacity Manual, Jakarta, 1997, pp. 1-564.

THE UTILIZATION OF BIOGAS SLUDGE TO LEAD ZERO WASTE SYSTEM IN BIOGAS IMPLEMENTATION: THE EFFECT OF VOLUME ON CARBON DIOXIDE AND METHANE CONTENT

Ambar Pertiwiningrum¹, Margaretha Arnita Wuri², Widyawati Luhur Pambudi³ and Lies Mira⁴

^{1,3,4}Faculty of Animal Science, Gadjah Mada University, Indonesia; ^{1,2}Centre for Development of Sustainable Region (CDSR), Indonesia

ABSTRACT

Biogas is a solution to slow the effects of global warming by converting and trapping methane of manure to energy. To make biogas cleaner and more environmentally friendly, residue from biogas also should be treated. The strategy is recycling biogas sludge to be an adsorbent for biogas purification because it will reduce waste generation. It means the utilization of sludge leads to a zero waste biogas system. The study was to investigate the use of biochar from biogas sludge and find the optimal condition for biogas purification. Five treatment of biochar based biogas sludge were conducted, every column of adsorption filled with 100% of the volume zeolite, 50% of the volume zeolite and biochar, 25% of the volume zeolite and 75% of the volume of biochar, and the last 100% of the volume biochar. The results showed that 5 treatment of biochar reduced carbon dioxide (impurity gas in biogas) and the largest reduction of carbon dioxide presented by 100% of the volume biochar. The decrease in carbon dioxide by 100% volume of zeolite is almost the same as the decrease in carbon dioxide by 100% volume of biochar. But the system also decreased the methane content in proportion to the decrease in carbon dioxide. The reduction in carbon dioxide also affected the temperature of biogas combustion and calorific value. We agree that using 100% of the volume biochar from sludge can replace zeolite in biogas purification but further modification is also needed to increase the value of methane.

Keywords: Biogas, Sludge, Biochar, Zero Waste, Methane

INTRODUCTION

Biogas is one of many solutions to slow the effects of global warming by converting and trapping methane of manure to energy. The implementation of biogas technology reduces dependency on fossil fuel energies for cooking or electricity in rural or urban areas [1]. By utilization waste or manure from livestock, biogas becomes cheap energy sources. In a rural area, adopting biogas technology improves energy access, reduces cost for purchasing firewood or fossil fuel, reduces the workload of women for looking for firewood, and diminishes manure smells [2]-[3]. It's more beneficial if the dissemination of biogas applies the bio-cycle system [4]. For example, biogas also generates waste, bio-slurry, that it's usually used as organic fertilizer [5]-[6].

Bio-cycle is the cycle through which energy and essential substances transferred among species and between the biotic and abiotic parts of the environment. Recycling of biogas sludge as organic fertilizer gives benefit not only to reduce biogas waste but also to enhance soil productivity [7]. But utilization biogas sludge as biochar for biogas purification in biogas system is rare. Whereas with the use of sludge generated from biogas production for biogas purification leads to a zero waste

management in biogas implementation. The use of biogas sludge as biochar also drives a circular economy because biochar is not only can use in biogas purification but also in agriculture, energy, and waste management sectors. In a circular economy system, biogas sludge can be utilized and recycled as a valuable product in the biogas system [8].

Biochar is carbon-based material that is from agricultural residue, animal waste, or forestry waste, that have carbon content [9]. Biochar has been utilized for the removal of heavy metal from wastewater, soil enrichment, and gas separation. Many studies are reported that biochar can use for carbon dioxide adsorption in biogas purification [10]-[12]. It's also claimed to be comparable to other commercial porous materials like zeolite and activated carbon. Pore structures in biochar, like in zeolite or activated carbon, play an important role in carbon dioxide adsorption [13]. However, most of these commercial adsorbents are too expensive because some rural areas don't have access to the distribution of commercial adsorbents. According to Minh-Viet et al. [11], biochar has advantages of relatively low cost, easy regeneration, and stable cyclic performance. It can be concluded that biochar is a green adsorbent. There is a need to develop local-based potential resources of biochar to

minimize the cost distribution of adsorbent. Moreover, local potential sources that are came from biogas production lead to the bio-cycle system in biogas and a zero waste biogas management [12]. Our previous study has been investigated the capability of carbon dioxide adsorption from biogas sludge-based biochar for biogas adsorption [8]. In Ambar et al. [8] biogas sludge-based biochar was combined with zeolite in each mass of 40 grams every column. But we evaluated that utilization each 40 grams mass of biogas sludge-based biochar and zeolite is not to be comparable because both of them have different specific mass. So in this study we evaluated the utilization mass of adsorbents with volume ratio.

METHODOLOGY

The carbon dioxide adsorption column was made from stainless steel material and completed with two flowmeters with measurement specification in a range of 25 LPM (liter per minute) at outlet and inlet pipes, and the compressor. The inlet and outlet pipes of column adsorption were connected with biogas holder that holding of raw biogas (biogas from biodigester) and purified biogas (biogas from column adsorption) respectively. The biochar was produced from biogas sludge that collected from biogas production of dairy cattle manure in the Center of Agro Technology Innovation, Universitas Gadjah Mada.

Biogas Sludge-Based Biochar Synthesis

Biogas sludge-based biochar was produced by the pyrolysis process. Before the pyrolysis process, biogas sludge was dried under sunlight for four days to reduce water content. The pyrolysis process was going for four hours at the temperature of 255°C. The heat from pyrolysis induced the oxidation of carbon and then formed stable carbon of biochar. Biochar was characterized by a surface area analyzer to identified the surface area, volume, and diameter of pores. Surface area analysis used a nitrogen adsorption method at 77 K.

Biogas Purification: Carbon Dioxide Adsorption

Carbon dioxide adsorption is conducted at room temperature. Each of column adsorption contained a volume of zeolite and biochar. There were six formulations of adsorbents that presented in Table 1. The first step of biogas purification is biogas filled in adsorption column by the compressor with a pressure range of 5-7 bar. Biogas that after through adsorption column was held in purified biogas holder to analyze the composition. Samples of biogas before and after carbon dioxide adsorption were analyzed by Gas Chromatography (GC) to be

identified the composition of methane and carbon dioxide.

Table 1 Formulations of the adsorbents in a column adsorption

Biogas Samples	% volume of zeolite	% volume of biogas sludge-based biochar
P0	0	0
P1	0	100
P2	75	25
P3	50	50
P4	25	75
P5	100	0

RESULTS AND DISCUSSION

Before and after biogas purification, biogas samples are analyzed its composition, especially methane and carbon dioxide because it's the largest composition in biogas. Biogas composition was analyzed and calculated by gas chromatography. The relation of the capability of carbon dioxide adsorption and surface area was investigated in this study.

Surface Area Analysis

The feature of carbon-based material is having many pores on its surface like biochar and zeolite. The porous structure of biochar and zeolite was determined from a nitrogen adsorption-desorption isotherm method at low temperature (77 K). Pore volume, pore size, and specific surface area were evaluated and showed in Table 3.

Table 3 Specific surface area, volume and pore size of natural zeolite and biogas sludge-based biochar

Porous Material	Specific surface area (m ² /g)	Mean pore size (nm)	Total pore volume (cc/g)	Micro-pore volume (cc/g)	Meso-pore volume (cc/g)
Zeolite	47.66	47.41	0.11	0.017	0.093
Biochar	34.06	39.15	0.067	0.013	0.054

These results showed that zeolite has a higher specific surface area, pore volume, dan size compared to biochar. Both zeolite and biogas sludge biochar-based biochar has a dominant pore size in the mesopore zone (pore size range of 2 - 50 nm) according to the International Union of Pure and Applied Chemistry (IUPAC). These results were also strengthened by the bigger mesopore volume of

zeolite and biochar compared to micropore volume. The relation between pore characteristics and the capability to adsorb carbon dioxide was investigated in this study.

Carbon Dioxide Composition

Carbon dioxide is the main impurity gas in biogas, which range of 20-40% [14]. These results of carbon dioxide analysis raw and purified biogas are shown in Table 2. The capability of zeolite and biochar to adsorb carbon dioxide has been proven. The results showed that all formulation of adsorbents capable to reduce carbon dioxide composition in biogas. The use of 100% volume of biochar reduced 26.54% carbon dioxide. The carbon dioxide reduction performed by 100% volume of zeolite was 26.65%. These results indicated that biogas sludge-based biochar has the same capability in carbon dioxide capturing as zeolite. The features in pore structure and mineral contents such as K, Na, Ca, Mg in biochar facilitate carbon dioxide adsorption. The existence of mineral content is able to increase alkalinity condition on biochar's surface and has implication to increase adsorbent affinity to carbon dioxide that plays as acidic molecules [15]. Although this results show the ability of zeolite for capturing carbon dioxide is better than biochar, the value is not significant. It's caused by zeolite is not activated to expand pore structures.

Table 2 The carbon dioxide reduction (%) after biogas purification

Sampling	P1	P2	P3	P4	P5
1st	36.61	0.07	16.99	1.04	26.39
2nd	29.48	30.79	20.10	3.25	24.40
3rd	11.00	20.86	22.66	10.40	29.16
Average	25.70	17.24	19.92	4.89	26.65

Methane Composition

Methane is the main component in biogas that produces energy for cooking or electricity. By carbon dioxide adsorption, methane in biogas should be increase. But the study showed different results. After biogas purification, methane composition in biogas went down. The reduction of methane was presented in Table 4.

The decrease in methane composition looked directly proportional to the decrease in carbon dioxide composition. The highest methane reduction performed by 100% volume of zeolite, the same as with carbon dioxide reduction. These results can be explained. The physical characteristic of adsorbents that are represented by specific surface area contributes to the capability to carbon dioxide adsorption [16]. The greater specific surface area

resulted not only in the greater the capability in carbon dioxide adsorption but also in the methane reduction in biogas. It can be explained that dominant pores in biochar and zeolite, mesopore (see Table 3), played an important role in methane adsorption. It's happened due to methane molecules are easier adsorbed in mesopore areas than micropore areas [17].

Table 4 The methane reduction (%) after biogas purification

Sampling	P1	P2	P3	P4	P5
1st	25.67	6.53	16.90	14.22	25.65
2nd	20.10	15.44	17.86	17.58	23.67
3rd	30.08	2.67	19.14	12.28	29.45
Average	25.70	8.43	17.97	14.69	26.26

Based on surface area analysis, either zeolite or biochar was included in mesopore-based material [18]. Mesopore size is capable to adsorb large size molecule effectively like methane molecules [17]. Mesopore volume of zeolite or biochar can adsorb not only carbon dioxide but also carbon dioxide, which has a molecule size of 0.32 and 0.4 nm respectively. Although there is methane reduction, the value are still smaller than carbon dioxide reduction because carbon dioxide molecules are more reactive to interact with pore structures in biochar.

CONCLUSIONS

From these results we concluded that biogas sludge-based biochar can be an alternative adsorbent of natural zeolite in biogas purification. Further research is required to improve the carbon dioxide adsorption and methane enrichment capabilities. Activation of adsorbent is recommended to enhance micropore size in adsorbents so that increasing carbon dioxide adsorption in biogas.

ACKNOWLEDGMENTS

We gratefully acknowledge the support from BRIN - Ristek Grant through Research Directorate of Universitas Gadjah Mada with a contract number of 2921/UN1.DITLIT/DIT-LIT/PT/2020. We also thank for the Center of Agro Technology Innovation for helpful for this research.

REFERENCES

- [1] Florence L., Johnny M., Peter N. W., Jo Smith, and Bedru B., Dis-adoption of Household Biogas in Central Uganda. *Energy for Sustainable Development*, Vol. 37, 2017, pp.124-132.
- [2] Debadayita R., Pinakeswar M., and Michele L.

- C., The Implementation of Decentralised Biogas Plants in Assam, NE India: The Impact and Effectiveness of The National Biogas and Manure Management Programme. *Energy Policy*, Vol. 68, 2014, pp.80-91.
- [3] Liu Y., Kuang Y., Huang N., Wu Z., and Xu L., Popularizing Household-Scale Biogas Digester for Rural Sustainable Energy Development and Greenhouse Gas Mitigation. *Renewable Energy*, Vol. 33, pp.2027-2035.
- [4] Cahyono A., Bambang H. S., Bambang S., Ambar P., Wiratni, Iwan S., and Dibyo P., Bio-cycles Farming System for Production of Biogas through Gama Digester, Gama Purification and Gama Compressing. *Journal of the Japan of Energy*, Vol. 90, 2011, pp.1085-1089.
- [5] Ambar P., Margaretha A. W., Dina S., Rachmawan B., Cahyono A. D. K., and Misri G., Improving Nutrients in Cattle Manure by Converting It Into Biogas Sludge and Compost, in *Proc. 2019 Int. Conf. on Resources and Environment Series*, 2019, pp. 1-6.
- [6] Ambar P., Ngesti H., and Siti S., The Use of Sludge from Cow Manure Biodigester as Fertilizer and Carrier of *Cordyceps sp.* For White Grub Pest Control. *Journal of Agricultural Science and Technology A*, Vol. 6, Issue 3, 2016, pp.149-153.
- [7] J. Lehmann, and S. Joseph. *Biochar for Environmental Management: An Introduction*, Biochar for Environmental Management, 1st ed. Earthscan, 2009, pp.1-9.
- [8] Ambar P., Andang W. H., Margaretha A. W., Adam G., Rachmawan B., and Misri G., Organic Cycle System: The Recycling of Biogas Sludge of Cow Manure as Biochar for Biogas Purification., Vol. 9, Issue 72, 2020.
- [9] Hashim A. A. and Can B. A., Life Cycle Environmental and Economic Performance of Biochar Compared with Activated Carbon: A Meta-Analysis. *Resources. Conservation and Recycling*, Vol. 118, 2017, pp.13-26.
- [10] Shou-Heng L. and Yi-Yang H., Valorization of Coffee Grounds to Biochar-Derived Adsorbents for CO₂ Adsorption. Vol. 175, 2018, pp.354-360.
- [11] Minh-Viet N. and Byeong-Kyu L., A Novel Removal of CO₂ using Nitrogen Doped Biochar Beads as A Green Adsorbent. *Process Safety and Environmental Protection*, Vol. 104, 2016, pp.490-498.
- [12] Ambar P., Margaretha A. W., Andang W. H., Rachmawan B., and Misri G., Heating Value Enhancement by Biogas Purification Using Natural Zeolite and Rice Straw-Based Biochar. *International Journal of GEOMATE*, Vol. 16, Issue 55, 2019, pp.80-85.
- [13] Zhang X., Zhang S., Yang H., Shi T., Chen Y., and Chen H., Influence of NH₃/CO₂ Modification on Characteristic of Biochar and The CO₂ Capture. *Bioenergy Resources*, Vol. 6, 2013, pp.1147-1153.
- [14] Peter J. J., *Digisource*, 2009, pp.1-36.
- [15] Danielle B., Mourad K., Patrick N., Murielle M., and Robert H., Advances in Principal Factors Influencing Carbon Dioxide Adsorption on Zeolites. *Science and Technology of Advanced Materials*, Vol. 9, 2008, pp.1-7.
- [16] Xiaoyun X., Yue K., Ling Z., and Xinde C., Chemical Transformation of CO₂ during Its Capture by Waste Biomass Derived Biochars. *Environmental Pollution*, Vol. 213, 2016, pp.533-540.
- [17] Deneb P., Imen G., Cecile H., Camelia M. G., Mejdi J., and David B., CO₂ and CH₄ Adsorption Behavior of Biomass Based Activated Carbons. *Energies*, Vol. 11, 2018, pp.1-10.
- [18] Nani H., Purwanto and Istadi, Study of Activated Carbon and Zeolite Integrated Application on Biomethane Production Based on Biogas. *Journal of Industrial Research*, Vol. 8, 2014, pp:65-72

ENVIRONMENTAL IMPACT ANALYSIS IN HOTEL SECTOR: A CASE STUDY IN THAILAND

Jarotwan Koiwanit¹ and Viachaslau Filimonau²

¹Faculty of Engineering, King Mongkut's Institute of Technology Ladkrabang, Bangkok 10520, Thailand; ²Faculty of Management, Bournemouth University, Talbot Campus, Fern Barrow, BH12 5BB, Poole

ABSTRACT:

Climate change is a major environmental impact. With its 5% share, the tourism industry is an important contributor to global greenhouse gas (GHG) emissions. To reduce this contribution, the tourism industry has started looking into the measures of carbon footprint mitigation. In order to develop such measures, the environmental performance of tourism enterprises should first be accurately assessed. Accurate assessments of the environmental significance of tourism enterprises, such as tourist accommodation facilities, are however rare which is due to data availability and immaturity of appraisal approaches. This paper contributes to knowledge with a case study of one of the largest hotels in Thailand, King Paradise (Koh Phayam, Ranong) whose environmental impacts have been comprehensively appraised by applying the method of life cycle impact assessment (LCIA). The results showed that food waste composting, single-use shower toiletry bottles switching and applying electric vehicles to Koh Phayam community can substantially decrease the environmental impacts. The adoption of electric vehicles showed the greatest carbon reduction potential although food waste composting was cheapest for implementation. By integrating these environmental innovations into its operations, King Paradise can minimise its emissions and waste and become a more environmentally sustainable company.

Keywords: Tourism, Hotel, Greenhouse gas emissions, Energy efficiency, Waste reduction, Life Cycle Assessment (LCA)

INTRODUCTION

Despite a number of socio-economic benefits, tourism generates significant environmental externalities, such as carbon footprint [1]. However, the carbon footprint of tourism has not been sufficiently researched, especially in the context of developing and transitional economies, such as Thailand, where international and domestic tourism is on the rise [2]. More studies are necessary to quantify the carbon impacts of tourism and its particular sectors, such as hotels, in this country to promote a sustainable low-carbon tourism industry in Thailand.

This study will assess the carbon footprint of one of the largest hotels in Thailand, King Paradise (Koh Phayam, Ranong), by applying the method of Life Cycle Assessment (LCA). The potential of LCA to provide accurate, yet holistic, assessments of environmental impacts of hotels has long been recognised [3], but it has never been applied in the context of Thailand. This study will therefore partially plug an important knowledge gap in sustainable tourism research.

KING PARADISE'S BACKGROUND AND ITS ENVIRONMENTAL PERFORMANCE

King Paradise is located in Koh Phayam, Ranong, Thailand. Koh Phayam is surrounded by natural environment with sandy beaches and clear blue sea and is the undiscovered pearl of the Andaman Sea. Given that the Koh Phayam island is located circa 35 km from Ranong (Fig. 1) [4], most visitors arrive by boat or speed boat. They subsequently travel to the King Paradise hotel by motorcycle or faint, depending on the size of the group. The hotel is located 5 km away from the boat terminal.



Fig. 1 Koh Phayam map [5]

At King Paradise, there are 40 rooms which include 2 types of rooms: 1) bungalows (maximum with 2 guests) and 2) houses (4 guests). Most of the guests are from European countries (70-80% of total) while the rest are normally from Asian countries. In high season (November – May), the hotel has approximately 100 customers per day while there are around 40 customers per day during low season (June – October). As a result, there are approximately 27,000 guests per year.

In terms of King Paradise's environmental performance, King Paradise has mostly focused on waste reduction and they have been taking different actions to manage and reduce solid waste, a large fraction of which is represented by food waste. Examples of actions/campaigns for waste reduction are shown as follows:

Food Waste Reduction

The hotel is trying to reduce food waste by not buying a lot of food at one time even though the food will be a lot of cheaper when bought in Ranong instead of buying in Koh Phayam. In this way, the hotel will not produce a lot of food waste.

Solid Waste Management

The hotel together with their customers works hard to clear the plastic debris and create a waste-free zone on its premises. In addition, the hotel runs a zero waste campaign to alter attitudes, values and behaviors of the King Paradise community in regards to proper waste disposal habits. These can help the hotel to conserve and protect the environment.

Recycling Program

There are a lot of recyclable wastes, for examples water bottles, cans, beer bottles, etc. and to reduce wastes, the hotel collects all of them and sells to recycling company. However, in order to become more environmentally friendly, there are some other areas the hotel can also focus on such as energy efficiency, green transportation, etc.

SUGGESTIONS FOR IMPROVEMENT

King Paradise has put an effort in improving in their environmental performance; however, during an inspection visit to the hotel, there are also some rooms for improvement and the suggestions were analyzed based on criteria on the follow and the description of each criterion can be found in [6]. The five suggestions for improvement in this study are shown in Table 1.

As can be seen from Table 1, the first three suggestions are the most reliable, cheap, and easy for an implementation and thus these are explained in more details in Results and discussion section.

RESEARCH METHOD

In this study, the survey collected data for the 2020 year of King Paradise' operations in January – March 2020. In addition, the hotel owners were further interviewed to rectify any data gaps and clarify any data inconsistencies identified in the survey as well as represent the 'business-as-usual' operational performance of the studied hotel in the reference year of 2019. As a result, the interview refined the survey results and confirmed that the collected data were representative of the hotel' business-as-usual operations.

RESULTS AND DISCUSSION

The environmental impacts of each suggestion presented in this section will be evaluated using the life cycle assessment (LCA) methodology. LCA is a methodology that identifies the whole life cycle of a product, often called the cradle-to-grave approach, in which complex systems are broken down into elementary flows. The GaBi software system together with CML 2001, a life cycle impact assessment (LCIA) methodology, was applied in this study. In this study, suggestions are used to interpret the outcome as a comparative study which helps to identify important unit processes that affect the most of the results to further improve their processes.

No Food Waste at the Consumption Stage → Composting

Food waste is continually to be the main issues of concern globally. Food waste cause serious environmental consequence as public outrage over food waste grow. There are 1.3 billion tonnes of a third of the world's food is lost or waste each year while hungers account for almost a billion [7]. The increasing attention has been paid to food waste issues mainly due to its negative environmental, social, and economic impacts [8,9]. In Thailand, many hotels have begun to launch many campaigns to reduce food waste and, in meantime, enlarge its benefits. King Paradise which is considered as the leading hotel in Koh Phayam, has also put more concerns on reductions in GHG emissions.

However, most of food waste end up in landfill and emits GHG emissions once it is broken down or in the best case, it can be utilized to produce animal feed or recover energy (e.g. anaerobic digestion) [13]. Therefore, in this study, composting is one way of suggestions required in the transformation

of the express to help in reducing overall food wastage problems. The functional unit used in this study is 1 year of food waste collected from King Paradise's restaurant. The observed results showed that there was 2.07×10^3 kg CO₂ eq. of GWP from food waste for disposal. As the GHG emissions of landfilling food waste are, on average, 2 times larger than the GHG emissions of composting [14] the GHG emissions of composting were 1.035×10^3 kg CO₂ eq. The environmental concerns were significantly decreased and this helps King Paradise to be more environmentally responsible and reduce the company's impact on the environment.

working on reducing mini bottles of shampoo and other toiletries to reduce plastic waste [15-17]. Instead of using tiny, single-use shower toiletry bottles, this study offers King Paradise's guests a recyclable pump-designed dispenser which is one of the favorable [18,19].

These include toiletry bottles of shampoo, conditioner and bath gel. By this design and which uses an average of 13,500 bathroom miniatures every year in which the average person uses a half of bottle per night. This study assumed that one bottle generates 19 g of plastic waste [20] and this produces approximately 256.5 kg of plastic waste per year or 777 kg CO₂ eq. of GWP per year.

Table 1 Analysis of Suggestion for Improvement

Suggestion points	Reliability	Applicability	Cost	Knowledge	Time to adopt	Parties involved	Public perception	Ease of implementation	Capacity to reduce emissions	Administrative simplicity
No food waste at the consumption stage	High	High	Low	High	Now	-King Paradise	High	High	Medium	Easy
Motion Sensor Light Installation	High	High	Medium	Medium	1 week	-King Paradise -Construction company	High	Medium	High	Medium
Single-use shower toiletry bottles switching	High	High	Low	High	1 week	-King Paradise	Medium	High	Medium	Easy
Solar Cells Installation	High	Medium	High	Medium	1 year	-King Paradise -Construction company	High	Medium	High	Medium
Electric Motorcycles	High	Medium	High	Medium	2-3 years	Motorcycle rental companies -Koh Phayam	High	Medium	High	Medium

Single-Use Shower Toiletry Bottles Switching

Since packaging usually ends up as waste, the packaging of a product is also a very important factor to consider when it comes to environmental impact. Many hotel companies (e.g. InterContinental Hotels Group, Marriott International, Holiday Inn, Kimpton, Six Senses, Crowne Plaza, Staybridge Suites) have been

Switching single-use shower toiletry bottles to pump dispensers does not require time and too much cost. It could take only up to a month before the pump dispensers are implemented. Therefore, this is considered as a long term suggestion for King Paradise to improve their environmental performance. As this transition is a big step in the right direction, the public perception of this transition will be medium because there are some

who like to take them home and giving a complaint at the first step of changing. This could be solved by education to the public. For a 0.4L refillable liquid dispenser, it produces 0.3 kg per dispenser [21]. There are 40 rooms at King Paradise and it is estimated that King Paradise will produce 24 kg of plastic waste in total. This study assumes that the dispenser will last as long as the hotel does [22]. As a result, this study assumed that it will last 50 years. This shows that King Paradise will produce 0.48 kg of plastic waste in total per year or 1.45 kg CO₂ eq. of GWP per year. This can reduce GWP by 775.55 kg CO₂ eq. per year compared to using bathroom miniatures.

Another suggestion for King Paradise to reduce the environmental impact of the single used containers is that the hotel could have any unused items to homeless shelters so all the containers can be used and this helps the hotel to be able to reduce their waste and time to dispose them [23]. In addition, the hotel may provide the smallest practical amount in recyclable containers and donate amenities left behind.

However, the more up-to-date innovative concept of SOAPBOTTLE designed by Jonna Breitenhuber is the packaging-free products in which the product itself is turning to its own packaging [24]. The packaging is made from a traditional piece of soap that has been hollowed out. On the top of the packaging, there is a reusable metal to allow users to open the top and pour out the soap [25]. This concept can avoid waste as the soap is made from natural resources and is biodegradable. In addition, the packaging is slowly dissolved as hand soap [26].

Electric Motorcycles

In Thailand, transportation was ranged as the second largest contributor to CO₂ emissions [27, 28]. Not only does road transportation contribute to the high costs of fuel consumption, but it will also lead to high GHG emissions and other environmental impacts. To cope with this problem, an electric vehicle is a part of alternative transportation mode which has recently experienced considerable growth and the use of electric vehicle has become an important approach in ensuring lower emissions [29,30]. As electric vehicles services continue to rise, this study aims to evaluate the environmental impacts of electric motorcycles compared to conventional motorcycles use using the Life Cycle Assessment (LCA) methodology.

During visit and from the interview, as most of tourists coming to the hotel as a small group, motorbicycle is preferably considered as the most convenient commuter transport to drive their customers way from King Paradise to Coastal rather than faint or bicycle. The energy use for the

motorbicycle is from the combustion of gasoline refined from crude oil [31]. In general, the average number of passengers per riding is no more than two in at any given time. Based on the interviews, the study assumed that each consumer will be driving the vehicle one time per day for around 20 km around the island. In this study, the baseline of the comparisons is the car-renting use and the number of passenger per riding is assumed to be 2. By these assumptions, it is estimated that the driving distance from all the consumers will be 270,000 km per year. According to The Sustainable City IX: Urban Regeneration and Sustainability, the total GHG emissions per km of a motorcycle are estimated to 78.5 g CO₂ eq. [32]. Based on The Sustainable City IX: Urban Regeneration and Sustainability, this shows that motorcycles in this study produce 21,195 kg CO₂ eq. per year [32].

However, the GHG impacts from an electric vehicle (EV) in use phase were investigated and compared with its conventional motorcycle in this study. The operating parameters taken from several literature reviews are shown in Table 2.

Table 2 Main operating parameters of an electric motorcycle

Parameter	Value	Unit	Ref./ comment
- Driving behavior	-	-	Cautious
- Type of road	-	-	City
- Slope of the road	-	-	Flat
-Acceleration	0	m/s ²	
- Total weight (kg)	150.7	kg	[33]
-Rolling friction of the tires	0.015	-	[34]
-Temperature at time of the travel	35	°C	Expert's estimate
-Density of air at 35 °C	1.15	kg.m ⁻³	[35]
-Aerodynamic drag coefficient	0.65		[36]
-Frontal area of the vehicle	1.057 × 0.699	m × m	[33]
-Velocity	16.7	m/s	Expert's estimate

In this study, the GWP is 16690 kg CO₂ eq. in gasoline and electric vehicles, respectively. The results show that the GHG environmental impact can be decreased up to 78.7% in the electric motorcycle compared to the conventional motorcycle. Though these vehicles are operated by

external providers, the hotel can work closely to the communities to cope with an environmental issue.

CONCLUSION

Over the years, hotels have been undergoing changes to become more environmentally friendly. King Paradise has set to create a positive impact in the community being socially responsible by respecting the environment. They strive to reduce their environmental externalities by investing into food waste reduction, solid waste management, and recycling program, which reduces GHG emissions. This generates significant cost savings and consequently provides high returns on investment. In this study, the energy efficiency and environmental performance of King Paradise have been analyzed. It can be shown that King Paradise has put in a lot of effort to enhance their environmental performance.

However, there are some areas of improvement and this study has presented five suggestions for King Paradise's further improvement while the three of them were selected as case studies. This study paid a visit to the King Paradise to inspect the applicability of our suggestions. The results showed that the option that is the most reliable, cheap, and easy for an implementation is the food waste composting. However, transportation sector is one of the main emitters of large quantities of pollutions to the atmosphere and an electric vehicle is showing highest reduction in GHG emissions, it becomes an important option for Koh Phayam community to be considered. The sensitivity analysis can be obtained as a future work to identify important parameters that affect the most of the results in each suggestion.

ACKNOWLEDGEMENT

We are grateful for the required information from King Paradise for this project. This work was supported by King Mongkut's Institute of Technology Ladkrabang Academic Melting Pot [KREF206226].

REFERENCES

- [1] Lenzen M., Sun Y., Faturay F., Ting Y., Geschke A., and Malik A., The Carbon Footprint of Global Tourism, *Nature Climate Change*, Vol. 8, Issue 6, 2018, pp. 522-528.
- [2] Manomaivibool P., Wasteful Tourism in DevelopingE? A Present Situation and Sustainable Scenarios, *Resources Conservation & Recycling*, Vol. 103, 2015, pp. 69-76.
- [3] Kuo N. and Chen P., Quantifying Energy Use, Carbon Dioxide Emission, and other Environmental Loads from Island Tourism Based on a Life Cycle Assessment Approach, *Journal of Cleaner Production*, Vol. 17, Issue 15, 2019, pp.1324-1330.
- [4] Kohphayam, Kohpharam Island, Ranong, Thailand, 2020. Retrieved from <http://kohphayam.org/> (Accessed 20 May 2020)
- [5] Thaitropic, Koh Phayam, 2017. Retrieved from <https://www.thaitropic.com/koh-phayam/> (Accessed 18 May 2020)
- [6] Koiwanit, J., A comparative Assessment of Life-Cycle Greenhouse Gas Emissions from Hypothetical Electric Airport Transportation Services in Thailand, *Conference proceedings, in IOP Conference Series: Earth and Environmental Science*, 8th International Conference on Future Environment and Energy (ICFEE 2018), 2018, pp.1-8.
- [7] Food and Agriculture Organization of the United Nations, Food Loss and Food Waste. Retrieved from <http://www.fao.org/food-loss-and-food-waste/en/> (Accessed 18 March 2020)
- [8] Papargyropoulou E., Lozano R., Steinberger J. K., Wright N., and Ujang, Z.B, The Food Waste Hierarchy as a Framework for the Management of Food Surplus and Food Waste. *Journal of Cleaner Production*, Vol.76, 2004, pp. 106-115.
- [9] Salomone R., Saija G., Mondello G., Giannetto A., Fasulo S., and Savastano D., Environmental Impact of Food Waste Bioconversion by Insects: Application of Life Cycle Assessment to Process Using *Hermetia Illucens*, *Journal of Cleaner Production*, Vol. 140, 2017, pp. 890-905.
- [10] Corrado, S., Caldeira, C., Eriksson, M., Hanssen, O. J., Hauser, H., van Holsteijn, F., Liu, G., Östergren, K., Parry, A. and Secondi, L., Food waste accounting methodologies: Challenges, opportunities, and further advancements, *Glob. Food Sec.*, Vol. 20, 2019.
- [11] Parfitt J., Barthel M., and Macnaughton S., Food Waste within Food Supply Chains: Quantification and Potential for Change to 2050. *Philosophical Transactions of the Royal Society B*, Vol. 365, 2010, pp. 3065-3081.
- [12] Galanakis C.M., Emerging Technologies for the Production of Nutraceuticals from Agricultural By-Products: A Viewpoint of Opportunities and Challenges, *Food and Bioproducts Processing*, Vol. 91, Issue. 4, 2013, pp.575-579.
- [13] Cristóbal S. and Ramon J., Multi Criteria Analysis in the Renewable Energy Industry, *Springer Science & Business Media*, London, 2012, pp. 1-103.
- [14] Eriksson M., Strid I., and Hansson P.-A., Carbon Footprint of Food Waste Management Options in the Waste Hierarchy – a Swedish Case Study, *Journal of Cleaner Production*, Vol. 93, 2015, pp.115-125.
- [15] Golgowski N., Those Tiny Hotel Shampoo

- Bottles May Soon Be a Thing of the Past, Huffpost, 2019. Retrieved from https://www.huffpost.com/entry/ihg-hotel-shampoo-bottles-plastic-waste_n_5d41d2d2e4b0db8affb27022?guccounter=1&guce_referrer=aHR0cHM6Ly93d3cuZ29vZ2xLLmNvbS8&guce_referrer_sig=AQAAANZgjKWwaQN1Fb_DTcc4moq2Q8wqvLH2LpgqaW0p67HcHcS Zy6_UfpzSxIXqhHxUTT7Qqr35Qk5cWjy-5qOi7oIQ1cLKLch6FHNpHlwzYrGeObRxIdc82tkaFnrdx-D-Ylbqj8HZISOu4qYX4_tIvDET_fYI_pmTU6UtaWyBKeO2 (Accessed 12 April 2020)
- [16] Bethesda M.D., Marriott International to eliminate single-used shower toiletry Bottles from properties worldwide, expanding successful 2018 initiative, Marriott international, 2019. Retrieved from <https://news.marriott.com/news/2019/08/28/marriott-international-to-eliminate-single-use-shower-toiletry-bottles-from-properties-worldwide-expanding-successful-2018-initiative> (Accessed 1 January 2020)
- [17] Associated Press, Holiday Inn to eliminate mini bottles of shampoo and other toiletries, MarketWatch, 2019. Retrieved from <https://www.marketwatch.com/story/holiday-inn-to-eliminate-mini-bottles-of-shampoo-and-other-toiletries-2019-07-30> (Accessed 27 Feb 2020)
- [18] TUI group sustainable development, Plastic reduction guidelines for hotels, TUI group sustainable development sustainability, 2019. Retrieved from https://www.tuigroup.com/damfiles/default/downloads/plastic_reduction_guide.pdf-2f4f4f0e2278382fcd50d9a530985b84.pdf (Accessed 18 December 2019)
- [19] Green Hotel, Membership conservation guidelines and ideas, 2010. Retrieved from <http://greenhotels.com/memship.php>
- [20] Wastecare Corporation, PET – Plastic Water/ Soda Bottles – By Bale Weights, Size and Recycling Equipment, Wastecare Corporation, Georgia, US, 2013. Retrieved from <https://www.wastecare.com/usefulinfo/PET-Plastic-Water-Soda-Bottles-Bale-Weights.htm> (Accessed 9 March 2020)
- [21] Jay R., Soap and Paper Dispensers, 2018. Retrieved from https://www.richardjay.com.au/wp-content/uploads/2019/05/Catalogue_Brightwell_Washroom-range_RJ_v20180807.pdf (Accessed 12 April 2020)
- [22] Carter J., 10 Best Soap Dispensers (Review) in 2020, Gearhungry, 2020. Retrieved from <https://www.gearhungry.com/best-soap-dispenser/> (Accessed 12 May 2020)
- [23] Eco Rooms, 2010. Retrieved from <http://www.ecorooms.com/criteria.html> (Accessed 21 December 2019)
- [24] Breitenhuber J., Jonna Breitenhuber design, 2020. Retrieved from <http://jonnabreitenhuber.de/> (Accessed 12 May 2020)
- [25] Segrán E., The Future of Packaging could be as Simple as a Bar of Soap: One Designer's Water-Soluble Vision for Replacing all Those Plastic Shampoo Bottles, Fast Company, 2019. Retrieved from <https://www.fastcompany.com/90412294/the-future-of-packaging-could-be-as-simple-as-a-bar-of-soap>. (Accessed 21 April 2020)
- [26] Designboom, Soap Bottle by Jonna Breitenhuber is a Liquid Hygiene Product Packaging Made from Soap, 2020. Retrieved from <https://www.designboom.com/design/soapbottle-jonna-packaging-made-from-soap-10-01-2019> (Accessed 19 January 2020)
- [27] Department of Alternative Energy Development and Efficiency, Energy in Thailand Facts & Figures, Ministry of Energy, Bangkok, 2013.
- [28] Energy Policy and Planning Office, Energy statistics of Thailand, Ministry of Energy, Bangkok, 2003.
- [29] Ellingsen L.A., Singh B., and Strømman A.H., The Size and Range Effect: Lifecycle Greenhouse Gas Emissions of Electric Vehicles, Environmental Research Letters, Vol. 11, Issue 5, 2016.
- [30] Chen T.D. and Kockelman K.M., Carsharing's Life-Cycle Impacts on Energy Use and Greenhouse Gas Emissions, Transportation Research Part D Transport and Environment, Vol. 47, 2016, pp. 276-284.
- [31] Pugliaresi L. and Pyziur M., Gasoline Blending an EPRINC Primer, 2015. Retrieved from <https://eprinc.org/wp-content/uploads/2015/06/Updated-Gasoline-Primer-2015.pdf> (Accessed 19 January 2020)
- [32] Marchettini N., Brebbia C.A., Pulselli R., and Bastianoni S., The Sustainable City IX: Urban Regeneration and Sustainability, WIT Transaction on Ecology and The Environment, WIT Press, Southampton, UK, 2014.
- [33] Ultimatespecs, Hondawave 100 Specs, 2013. Retrieved from <https://www.ultimatespecs.com/motorcycles-specs/um/honda-wave-100-2013> (Accessed 8 December 2019)
- [34] Nguyen V.-T. and Hwang P., Study of a Novel Hybrid Powertrain system for Honda Wave 110cc Motorcycle with Rear Wheel Electric Motor, International Journal of Innovative Studies in Sciences and Engineering Technology (IJISSET), Vol. 5, Issue 4, 2019, pp. 43-46.
- [35] Engineering Student, 2018. Retrieved from <http://www.engineerstudent.co.uk> (Accessed 8 April 2020)
- [36] Cossalter, V., Motorcycle Dynamics. 2nd Ed, 2006. Retrieved from https://books.google.co.th/books/about/Motorcycle_Dynamics.html?id=rJTQxITnkbGc&redir_esc=y&hl=en (Accessed 13 February 2020)

TOWARD SUSTAINABLE COMMUNITIES: A COMPREHENSIVE ENVIRONMENTAL IMPACT ASSESSMENT OF BUILDING

Nantamol Limphitakphong^{1,2} and Orathai Chavalparit^{2,3}

¹ Interdisciplinary Program of Environment, Development and Sustainability Program, Chulalongkorn University, Thailand; ² Research Unit of Environmental Management and Sustainable Industry, Chulalongkorn University, Thailand; ³ Department of Environmental Engineering, Chulalongkorn University, Thailand

ABSTRACT

Coupling with the changing of climate naturally, an occurrence of excessive artificial environment has caused many severe impacts widely. To cope with such emerging instability, sustainable city was presented as one of the most important actions among sustainable development goals because of a rapid growth of population and urbanization. Several attempts have been made to alleviate such issue substantially focusing on construction industry since it consumes numerous resources and effects various kinds of environment impact. Based on life cycle assessment approach, this study therefore was aimed to assess the comprehensive environmental impacts of building by considering “cradle-to-grave” system boundary throughout its service life of 50 years. The results demonstrated that majority of impact categories associated with all stages of building life involved global warming, natural resource depletion, eutrophication, smog, water intake, human health - criteria air pollutants, and ecotoxicity. Hotspot of such impacts was found during the operation phase of building rather than construction and demolition phases. Of what findings, appropriate strategies for minimizing the environmental impacts and increasing an effective use of the natural resources will consequently be suggested for designing sustainable low carbon building in the future pertinently.

Keywords: Environmental impact; Educational building; Life cycle assessment; Global warming; Sustainability

NOMENCLATURE

A.Eng	-	Architectural Engineering
CP	-	Construction Phase
DP	-	Demolition Phase
EB	-	Educational Building
HVAC	-	Heating, Ventilation and Air Conditioning Engineering
OP	-	Operation Phase
S.Eng	-	Structural Engineering
SFPE	-	Sanitary and Fire Protection Engineering
TEI	-	Total Environmental Impacts

INTRODUCTION

Globally, the changing of climate both naturally and artificially has caused several impacts severely. In 2015, with agreement of all parties in the United Nations to protect the planet from these economic, social and environmental challenges, a blueprint of 17 sustainable development goals which intended to be achieved by 2030 has been established. Because of the rapid urbanization, sustainable city is prioritized for making cities inclusive, safe, resilient and sustainable [1]. Since construction industry plays important role in leading the growth of the country, either developed or developing countries have put several attempts to ease and to solve such issue substantially as it consumes numerous resources and

effects various kinds of environment impact.

Evidently, buildings consumed 40% of either global energy consumption or raw materials, and 12% of global potable water consumption, whilst emitted 1/3 of global greenhouse gas emissions and generated 4/10 of waste to landfill [2]. The nature resources depletion and environment degradation had brought the awareness to finding the methods to reduce its consequent effects unceasingly. Kofoworola and Gheewala [3] had analyzed the life cycle energy of a typical office building and emphasized importance of considering embodied energy coupling with operating energy for incorporation into the existing energy code. Anastaselos [4] had evaluated the environmental performance of energy systems used in residential buildings and emphasized the higher annual impact savings in buildings using a natural gas boiler for floor heating and applying poly-Si PV. Moschetti [5] had explored the most influential aspects for transition from zero-energy to zero-emission building and concluded that besides renewable energy, the materials' embodied energy and emissions should be focused on for a full compensation of life cycle emission of building. Thaipradit [6] had demonstrated the energy and environment performances of educational buildings and revealed that autoclaved aerated concrete block, cellulose wall insulation and triple glazing were of importance in reducing life cycle energy and carbon

of building located in tropical country. Yim [7] had analyzed buildings' life cycle greenhouse gas emissions in high-density cities and found that 85% of the life cycle GHG emission of the building case study occurred from the operating energy.

Nevertheless, most of previous studies focused only on one aspect of environmental impacts individually; for instance, primary energy consumption, global warming potential. To pursue sustainable development, all environmental impact categories should be integrated into consideration. This study, therefore, was aimed to explore solutions for sustainable building transition regarding all relevant environmental impacts using life cycle assessment as a tool. An educational building of Chulalongkorn University was selected as a case study to demonstrating a good practice as well as enhancing capacity building with knowledge transfer for communities and interested parties. The findings of this study will be useful for building owner/developer in designing sustainable low carbon building pertinently.

RESEARCH METHODOLOGY

Building Description

Table 1 describes characteristics of educational building of Chulalongkorn University. The case study building is located in the heart of Bangkok at 13.92 latitudes and 100.6 longitudes with a range of dry-bulb temperature of 19.0 – 37.2 °C and humidity ratio of 11.2 – 28.7 gw/kgda throughout the year [8]. For indoor air temperature, air-conditioners are primarily set at 25 °C as recommended by the Ministry of energy.

Table 1 Characteristics of case study educational building.

Parameters	Specifications
Building floors	12 floors above ground
Gross floor area	20,000 m ²
Structure	Concrete
Envelope	Brick and curtain wall combination (aluminium/clear flat glass)
Window-to-wall ratio	0.169
Floors	Cast-in place concrete
Roof	Flat roof, concrete
Solar PV installation	25 kW

Life Cycle Assessment (LCA)

Building life cycle could be roughly classified into three main phases namely construction, operation, and demolition. To estimate environmental performances of building throughout its life cycle,

four steps of life cycle assessment procedure as presented in ISO14040-44:2006 [9]-[10] were applied in this study using SimaPro V.8.2 program with Building for Environmental and Economic Sustainability (BEES+) method [11].

Goal and scope

To moving towards sustainability, comprehensive understanding of key points effecting environmental challenges is necessary in order to alleviating and/or preventing such damage that might be occurred pertinently. In this study, goals of using LCA approach were to quantify the level of environmental performances of educational building demonstrating through a study of Chulalongkorn University and to identify hotspots causing each category of environmental impacts.

As presented in Fig. 1, a scope of this study involved three phases of building life cycle including building construction (cradle), building operation with a life span of 50 years (gate) and building demolition (grave). Due to a complexity of materials used throughout building service life, however, transportation occurred within and between each phase was omitted.

To simplify an understand about environmental performance related to this building case study as a whole, either dataset of building inventory or impact was referred an educational building with a gross floor area of 20,000 m² and a reference study period of 50 years as a functional unit [12].

Life cycle inventory analysis

Based on data availability, firstly, a secondary data recorded both type and quantity of construction materials obtained from building owner was accessed to build an inventory of building material. Following a class of construction work, the inventory of CP was classified into four groups including S.Eng, A.Eng, HVAC, and SFPE. In total, 20 different types of building material represented a majority of mass intensity and embodied energy [13] were selected to demonstrate a level of environmental impacts during building construction phase.

Secondly, an inventory of OP was built upon a primary data of resources consumption and waste/wastewater generation on a monthly basis. The log sheet obtained from building manager provided five dataset including electricity from grid, electricity generated from rooftop PV system, tap water, wastewater, and solid waste as illustrated in fig. 1.

Lastly, an inventory of DP was formulated either in accordance to an interview with demolition worker or literature reviews [14]-[15]. Building demolition waste were classified based on methods of waste management namely reuse, recycle, and final disposal (landfill).

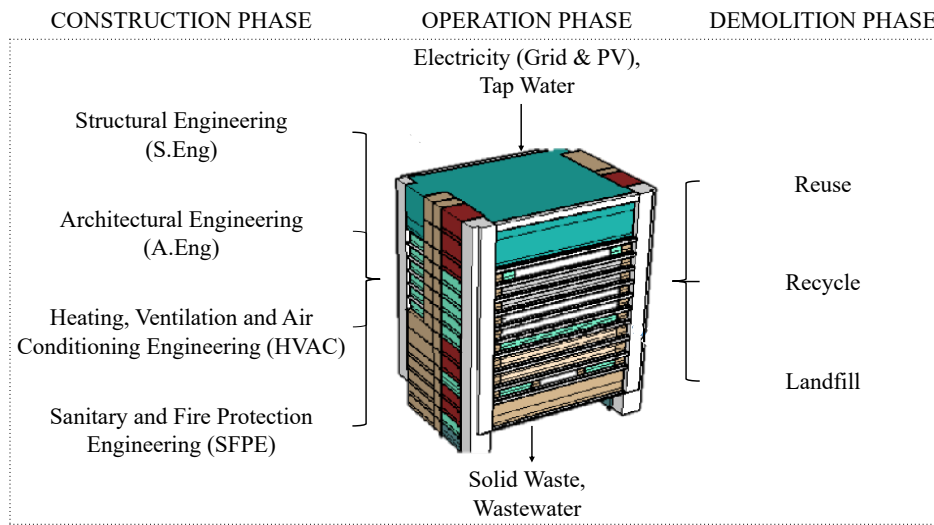


Fig 1. System boundary of this case study.

Life cycle impact assessment

The impact assessment was performed through SimaPro V.8.2 using BEES+ method with stakeholder panel weighting to support environmentally preferable purchasing [16]. A single score accounting from weighting results of all environmental performances throughout building life cycle were performed to emphasize the overall impact as a whole. Moreover, a contribution of eleven impact categories including global warming, acidification, human health – cancer, human health – non cancer, human health - criteria air pollutants, eutrophication, ecotoxicity, smog, nature resource depletion, water intake, and ozone depletion in each phase of building life was quantify to reveal a major effect related to building.

Interpretation

Hotspots of environmental performances was discussed in this procedure. Equation (1) is used to estimate the total amount of environmental impacts for an entire service life of educational building case study. Of what findings, appropriate strategies in the context of educational building for reducing the environmental impact and increasing the natural resources consumption were proposed.

$$TEI_{EB} = \sum_{i=1}^4 TEI_{CP} + 50 \sum_{j=1}^5 AEI_{OP} + \sum_{k=1}^3 TEI_{DP} \quad (1)$$

Where TEI_{EB} is total environmental impacts of educational building throughout its life cycle (Pt), while TEI_{CP} and TEI_{DP} are total environmental impacts of educational building during construction and demolition phase (Pt). AEI_{OP} represents environmental impacts of educational building during

operation phase annually (Pt). 50 indicates a number of building service life, while i, j and k refer four classes of building materials used for building construction, five datasets of input and output during building operation, and three types of waste management for building demolition respectively.

RESULTS AND DISCUSSION

Environmental Impact of Building During Construction Phase

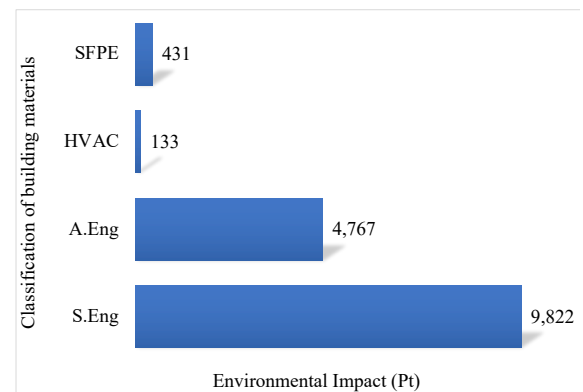


Fig 2. Level of environment impacts during building construction phase.

Figure 2 illustrates scores of TEI_{CP} classified by building construction components with total score of 15,153 Pt. Undoubtedly, building materials used for a purpose of S.Eng was the dominant contribution in this activity, followed by a group of materials used for A.Eng, SFPE and HVAC respectively.

Within S.Eng group, more than 90% of TEI_{CP} contributed to concrete and reinforcing steel. It was difficult to decrease the amount of materials used for S.Eng due to a concern of safety. Shams [17]

suggested to use fly-ash or blast furnace slag for new building construction instead of using virgin cement, mortar, or concrete to reduce environmental impact from structural materials. Autoclaved aerated concrete block was recommended by Thaipradit [6] to replacing conventional concrete block even an embodied carbon of the former was greater than the latter, but for a long run throughout building service life it helped reduce a huge amount of operational energy, resulting in minimizing TEI as a consequence.

Whilst a majority of TEI_{CP} within the A.Eng group involved window frame – aluminium, gypsum fibreboard, alkyd paint for primer and top coat, brick, and cement mortar. Unlike the S.Eng group, several rooms were feasible for minimizing the impacts generated by A.Eng materials. For instance, to get closer to neutral impact, loft style had been encouraged. According to the results of this study, about 10% of TEI_{CP} from A.Eng would be reduced if no painting applied.

Environmental Impact of Building During Operation Phase

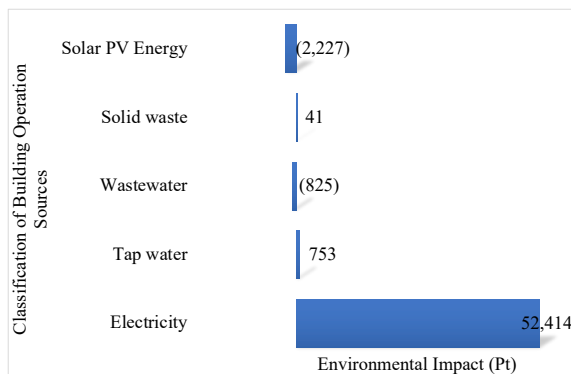


Fig 3. Level of environment impacts during building operation phase.

Figure 3 illustrates scores of TEI_{OP} classified by type of input-output resources with total score of 50,156 Pt. Unlike CP, either positive or negative impacts were found in this phase. Noticeably, a main cause affecting TEI_{OP} was consumption of electricity. The strongest recommendation for minimizing TEI_{OP}, therefore, was relying rather on green energy either from on-site or off-site.

In addition, building energy management measure was recommended since it had the largest potential in reducing energy consumption and GHG emission [18]. Installation of external wall insulations was also suggested as it helped reduce a requirement of energy consumption compared to the case with no insulation installation [13].

Environmental Impact of Building During Demolition Phase

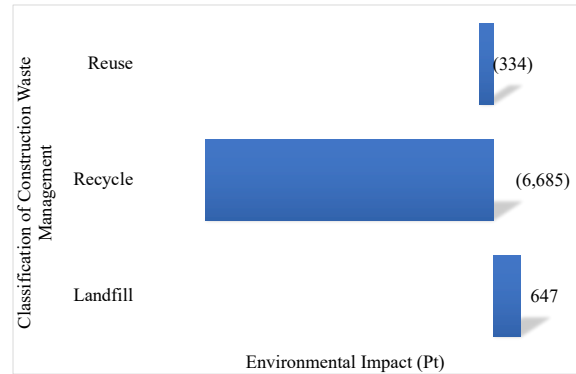


Fig 4. Level of environment impacts during building demolition phase.

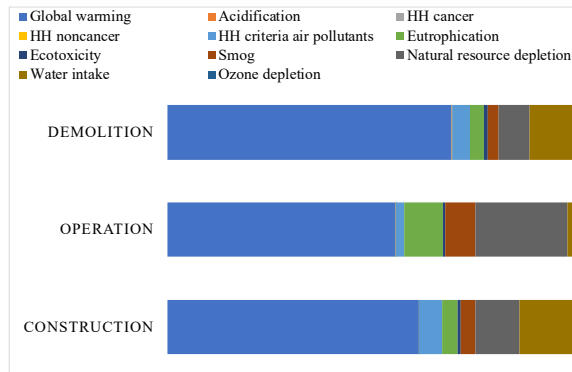
Figure 4 illustrates scores of TEI_{DP} classified by construction waste management with total score of -6,372 Pt. The negative value reflected benefits gained from using used materials instead of the virgin one for a new cycle. The avoided impacts of construction and demolition waste management from steel, glass and plastic was highlighted by [19]. Whilst 100% recycling of ferrous and non-ferrous metals, cardboard, plastic and glass were suggested for maximizing both environmental and economic benefits [20]. In this study, a concept of zero waste to landfill was introduced in this phase, however, there were still leftovers, yet to find better solutions for disposal. Among that some can be used for backfilling/land reclamation, reducing the TEI_{DP} occurred from direct landfill.

Life Cycle Environmental Impacts of Educational Building

To sum up, the results of this study demonstrated that the level of TEI_{EB} was 58,937 Pt. The biggest contribution to TEI_{EB} occurred during building operation phase (85%) followed by building construction phase (26%), while the activity of building demolition phase helped compensate about 11% of the total impact. It emphasized that all phase of building life cycle was necessary for taking into account to understand its life cycle impact comprehensively. The positive impacts occurred from demolition waste management could be traded off for the negative impacts generated from construction materials, whereas the negative impacts contributed to using non-green energy could be minimized by fully operating on green energy.

As illustrated in fig. 5, considering a contribution of environmental performances on each phase of building life cycle, global warming was the dominant concern in every phases because it currently is a biggest challenge mentioned in every stage domestically and internationally, followed by water intake and natural resources depletion for CP and DP, and by natural resources depletion, eutrophication

and smog for OP. Water intake was not a major concern during building operation phase because besides the consumption of tap water, re-using treated wastewater was taking into account as presented the positive impacts in Fig. 3.



Note: construction and operation phases presented a contribution of total negative impacts, while a contribution of total positive impacts was presented for demolition phase.

Fig 5. Contribution of environmental performances throughout building life cycle.

As a whole, the environmental impact categories of educational building could be classified into 4 main groups depending on a degree of damage as super severe impacts – $TEI \geq 50\%$ (global warming), severe impacts – $20\% \leq TEI < 50\%$ (natural resources depletion), moderate impacts – $5\% \leq TEI < 20\%$ (eutrophication, smog, water intake), and mild impacts – $TEI < 5\%$ (human health - criteria air pollutants and ecotoxicity). To reduce the TEI_{EB} , global warming and natural resources depletion should be prioritized.

In addition, to reduce the impact of global warming, coupling with using low embodied carbon materials [6], [13] or recycled materials [17], innovation on green construction materials was needed exceptionally. Water harvesting was also recommended to minimize the impact of water intake as well as natural resources depletion as a consequence [21]. The impact of natural resources depletion was merely possible to relieve since it was related to the amount of materials used which could not be deducted to preventing building collapse. Using recycled materials instead of the virgin one [6], [17], building on loft design, and applying building energy management [18] were strongly recommended for consuming least natural resources as possible. In a case that all measures mentioned above had been implementing, this case study building will become a zero-carbon building, referring the definition firstly defined by the UK government [22] with TEI_{EB} reduction of 89% approximately. A variety of green innovation/knowledge, however, is still purposefully needed to demonstrate a case of sustainable building successfully.

CONCLUSIONS

To moving towards sustainability, a case study of educational building of Chulalongkorn University was assessed to quantify the level of environmental impacts throughout building life cycle using life cycle assessment approach and was analyzed to pinpoint pathways for building sustainable building in the future.

The results revealed that throughout building life cycle, operation phase had contributed the highest negative impacts (causing by a huge consumption of non-green energy), followed by construction phase (mainly generating from a use of structural engineering materials). Whilst the positive impacts were occurred during demolition phase from reusing and recycling materials for a new cycle, which could be a trade-off for construction materials used in construction phase. For a full compensation of life cycle impacts of building, building management strategies was strongly suggested to focus on low embodied impacts materials for construction phase coupling with using green energy/resources for operation phase and applying zero-waste to landfill approach for demolition phase.

ACKNOWLEDGMENTS

Financial support from Thailand Research Fund through the Royal Golden Jubilee Ph.D. Program (Grant No. PHD/0071/2559) is acknowledged.

REFERENCES

- [1] United Nations, Cities – United Nations Sustainable Development Actin 2015, UN Web Services Section, Department of Public Information, 2015, <http://www.un.org/sustainable-development/cities/>.
- [2] Intergovernmental Panel on Climate Change (IPCC), Climate Change 2014: Synthesis Report, Contribution of Working Groups I, II and III to the Fifth Assessment Report of the Intergovernmental Panel on Climate Change, Geneva, Switzerland, 2014, 151 pp.
- [3] Oyeshola F.K. and Shabbir H.G, Life cycle energy assessment of a typical office building in Thailand, Energy and Buildings, Vol. 41, Issue 10, 2009, pp. 1076-1083.
- [4] Anastaselos D., Oxizidis S., Manoudis A. and Papadopoulos A.M., Environmental Performance of Energy Systems of Residential Buildings: Toward Sustainable Communities, Sustainable Cities and Society, Vol. 20, 2016, pp.96-108.
- [5] Moschetti R., Brattebø H. and Sparrevik, M., Exploring the Pathway from Zero- energy to Zero-emission Building Solutions: A Case Study of a Norwegian Office Building, Energy and Buildings, Vol. 188-189, 2019, pp.84-97.

- [6] Thaipradit P., Limphitakphong N., Kanchanapiya P., Tantisattayakul T. and Chavalparit O., The Influence of Building Envelop Materials on Its Life Cycle Performance: A Case Study of Educational Building in Thailand, *Key Engineering Materials*, Vol. 780, 2018, pp.74-79.
- [7] Yim S.Y.C., Ng S.T., Hossain M.U. and Wong J.M.W., Comprehensive Evaluation of Carbon Emissions for the Development of High-Rise Residential Building, *Buildings*, Vol. 8, 2018, pp.1-19.
- [8] Energy Plus, Weather Data, 2018, <https://energyplus.net/weather>
- [9] International Organisation for Standardisation, “ISO 14040 (2006): Environmental Management - Life Cycle Assessment - Principles and Framework”, 2006, pp. 1-20.
- [10] International Organisation for Standardisation, “ISO 14044 (2006): Environmental Management - Life Cycle Assessment – Requirements and Guidelines”, 2006, pp. 1-46.
- [11] PRé Consultant, “SimaPro Database Manual – Methods”, 2018, pp. 1-70.
- [12] European Commission. Model for Life Cycle Assessment (LCA) of Buildings, EUR 29123 EN, 2018, pp. 1-107.
- [13] Limphitakphong N., Thaipradit P., Kanchanapiya P., Tantisattayakul T. and Chavalparit O., Embodied Carbon Emissions of Construction Materials: A Case Study of Buildings in Thailand, *International Journal of GEOMATE*, Vol. 18, Issue 68, 2020, pp. 187-193.
- [14] European Environment Agency (EEA), Construction and Demolition Waste: Challenges and Opportunities in A Circular Economy, 2020, pp. 1-8.
- [15] Kubba S., Green Construction Project Management and Cost Oversight, Chapter 6 - Choosing Materials and Products, 2010, pp. 221-266.
- [16] Gloria T.P., Lippiatt B.C., and Cooper J., Life Cycle Impact Assessment Weights to Support Environmentally Preferable Purchasing in the United States, *Environmental Science and Technology*, Vol. 41, Issue 21, 2007, pp. 7551-7557.
- [17] Shams S., Mahmud K. and Al-Amin M., A Comparative Analysis of Building Materials for Sustainable Construction with Emphasis on CO₂ Reduction, *International Journal of Environment and Sustainable Development*, Vol. 10, Issue 4, 2011, pp. 364 – 374.
- [18] Phupadtong A., Limphitakphong N., Kanchanapiya P., Tantisattayakul T. and Chavalparit O., The Assessment of The Environmental and Economic Performances for Improving Existing Educational Building: A Case Study of Bangkok, Thailand, *International Journal of Sustainable Energy Development*, Vol. 9, 2018, pp.208-212.
- [19] Rosado L.P, Vitale P., Pentecado C.S.G., Arena U., Life Cycle Assessment of Construction and Demolition Waste Management in A Large Area of São Paulo State, Brazil, *Waste Management*, Vol. 85, 2019, pp. 477-489.
- [20] Kucukvar M., Egilmez G. and Tatari O., Life Cycle Assessment and Optimization-Based Decision Analysis of Construction Waste Recycling for A LEED-Certified University Building, *Sustainability*, Vol. 8, Issue 89, 2016, pp. 1-13.
- [21] Monjaiang P., Limphitakphong N., Kanchanapiya P., Tantisattayakul T. and Chavalparit O., Assessing Potential of Rainwater Harvesting: Case Study Building in Bangkok, *International Journal of Sustainable Energy Development*, Vol. 9, 2018, pp.222-225.
- [22] The UK Government, Building a Greener Future: Policy Statement, Department for Communities and Local Government: London, 2007, pp.1-25.

EXPERIMENTAL INVESTIGATION OF PHYSICAL PROPERTIES OF PEATS IN WESTERN PROVINCE, SRI LANKA

A.M.Z. Zimar¹, M.C.M. Nasvi², D. Robert^{3*}, S.Jayakody⁴, J.R.R.N.Jayarathne⁵ and John V. Smith⁶

^{1,3,6}School of Civil and Infrastructure Engineering, RMIT University, Australia

^{1,4,5}Faculty of Engineering, South Eastern University of Sri Lanka

²Faculty of Engineering, University of Peradeniya, Sri Lanka

*Corresponding Author

ABSTRACT

Peat soils are extremely soft soils that exhibit high compressibility, low shear strength, and low bearing capacity. There are about 2500 hectares of peatland in Sri Lanka, and a larger part is in the western coastal region of the island. The soft quality of peat soils was a major challenge for the recently completed expressway constructions where many ground improvement techniques were applied. Understanding the physical properties and developing correlations among easily identifiable physical properties of the peat will be helpful for future construction works in this region. This study describes the properties of Muthurajawela peats on the western coast of Sri Lanka. Peat soil samples were collected from the Muthurajawela region, and physical properties were determined. Results revealed that the Muthurajawela peats are fibric and hemic peats with high acidity. Also, the applicability of existing correlations was assessed and calibrated against the tested properties obtained from the current study. Outcomes from this study are helpful in identifying design parameters and suitable correlations that are required for evaluating the local peat soils, which will form the foundations for many planned upcoming infrastructure developments in this region.

Keywords: Peat, Fiber content, Organic content, Hemic peats, Fibric peats

INTRODUCTION

Peat occurs in over 4.5% of the total land coverage in the world [1]. In Sri Lanka, peat covers around 25,000 hectares [2], and Muthurajawela is the most significant peat area on the island. The Southern Highway is Sri Lanka's first E Class (expressway) highway that links the capital of Sri Lanka, Colombo and Matara, a major city in the south of the island. Many stretches of the highway went through flood plains and wetlands such as the flood plains of Welipenna river, Bentota river, and Gingaga river areas, which consist of very soft peats [3]. Similarly, the Colombo - Katunayake Expressway (E03) was the second E Class highway in Sri Lanka, which was opened in October 2013. The proposed alignment was laid on marshy lands starting from the brink of Kelani River. It traverses the flood plains of the Kelani River and the marshy areas of Peliyagoda and Muthurajawela before it reaches the Negombo lagoon area. Soft peat was found down to 12 m depth in certain areas of the alignment, and several ground improvements such as traditional preloading techniques, prefabricated vertical drains, sand compaction piles, driven piles, and stone columns were carried out during the construction [3].

Peat soils form in the wetlands under suitable climatic and topographic conditions. Peat contains fragmented organic materials and partly decomposed plants such as leaves and stems, which have been chemically changed and fossilized from vegetation

[4]. Peat soils are classified according to physical, chemical and physico-chemical properties such as texture, organic content, ash content, fiber content, pH, colour, water content, and degree of decomposition.

Peats are problematic soil due to the low shear strength, high compressibility, and high water content. It exhibits distinctive mechanical properties compared to clay and sandy soils. The water saturated environment within the peat deposits generates anaerobic conditions and limits the decomposition of fresh plant litter. Peatlands are divided into fens/topogeneous and bogs/ombrogenous. Fens are areas where groundwater is fed or surface water is fed by runoff from marginal sites, whereas bogs are areas where water is fed only by rainwater. The formation of fen peat happens when plants die and accumulates at the bottom of a lake. Generally, fen peat is underlain by very soft organic mud. Bog peats are typically fibric (fibrous) and acidic [5].

The previous practice was to remove the peat by excavation or any displacement method when it was encountered during construction. Nowadays, this trend has been changed, and the knowledge of peat soil behaviour has improved among engineers. Several techniques such as surface reinforcement, preloading and preloading with vertical drains, stone columns, dynamic replacement, thermal pre-compression, deep stabilization, and chemical stabilization are widely used for the peat soil improvement in the world [1, 6].

However, peat soil should be well studied before designing appropriate ground improvement methods. There are many ongoing construction activities around the Muthurajwela area, in the western province of Sri Lanka. However, no major studies have focused on the properties of peats in Muthurajwela region. Hence, this research aims to characterize peats in the Muthurajwela region by investigating their physical properties and checking whether the existing correlations reported in the literature are applicable to predict the properties of peats in the Muthurajwela region. The outcomes of this study will be useful for engineering designers to understand the characteristics of local peats in Western Province, Sri Lanka.

EXPERIMENTAL METHODS

Physical Properties

Peat samples were collected from six locations in the Muthurajwela area and designated as L1 to L6, as shown in Fig. 1. The minimum distance between two sampling locations was maintained as 800 m, and samples were transported in sealed boxes to the laboratory to maintain the in-situ moisture contents.

Physical properties such as natural moisture content, specific gravity, bulk density, organic content, and fiber content were investigated at the laboratory. Each index property test was conducted for five samples in order to ensure reproducibility for all the physical properties investigated.

Field moisture content, organic content and ash content of peat soils were determined as per ASTM D2974-14 [7]. Oven-dried peat specimens were used to find the organic content and ash content.

Specimens were placed inside a muffle furnace, and the temperature was gradually raised to 440°C until the samples were completely ignited. Then, remaining ash was cooled in a desiccator, and the

mass of ash content was weighed. Organic matter content of peat is represented by loss on ignition (%) and derived using the Eqs. (1) and (2).

$$\text{Ash Content (\%)} = (M_a \times 100) / M_d \quad (1)$$

Where M_a is the mass of ash, and M_d is oven-dried mass.

$$\text{Organic content (\%)} = 100 - \text{Ash content (\%)} \quad (2)$$

Fiber content of the peat was determined using ASTM D1997-91[8]. The test required 500 g of peat sample to soak in 5% of Sodium-Hexametaphosphate for about 15 hours. The soaked sample was washed by applying a gentle flow of water through a 150 μ m sieve, and the retained mass on the sieve was oven-dried at a temperature of 105°C until a constant mass was achieved. Fiber content was calculated using Eq. (3).

$$\text{Fiber content (\%)} = M_f / M_s \times 100 \quad (3)$$

Where M_f is dry mass of fibers and M_s is the initial dry mass of soil.

Specific gravity and bulk density of the samples were determined in accordance with ASTM D854-02 [9] and ASTM D4531-86 [10] respectively. The pH values of peat soils were measured in the laboratory using a pH meter according to ASTM D2976-71 [11].

Classification of Peats

Peat was initially classified using the Von Post classification and Munsell colour system at the site. In the Von Post Classification, peat can be categorized from H1 to H10 where H1 is considered as fully undecomposed fibric peat, and H10 is for completely decomposed amorphous peat (sapric peat). In this method, a handful of peat was taken and gently squeezed to drain the water out. The condition of the

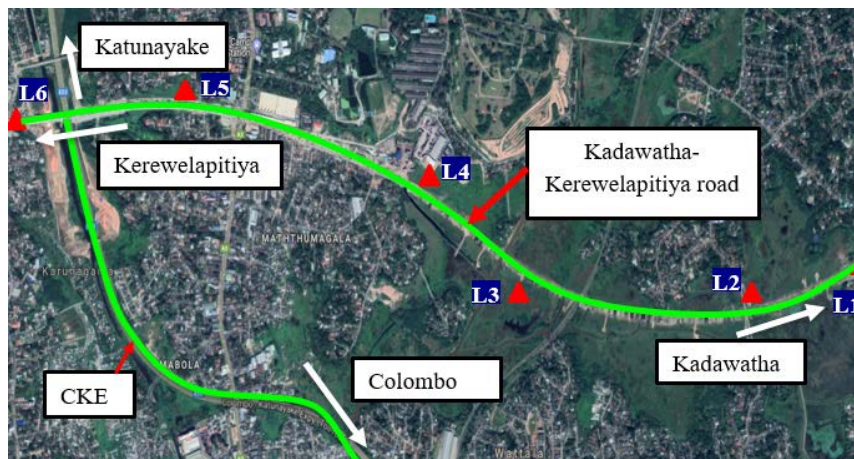


Fig. 1 Peat sample locations.

squeezed peat was carefully observed and compared with the Munsell colour system for classification. The Munsell colour system specifies colours based on three colour dimensions: hue, value (lightness), and chroma (colour purity). Colour of the peat was compared with the colour range given in the standard Munsell colour chart.

The American Society for Testing and Materials (ASTM) Standards classifies peat based on fiber content, ash content, and acidity of soil, as shown in Table 1.

Table 1. Classification of peat based on ASTM standard

Fiber content [8]	Fibric: Peat with greater than 67% fibers.
	Hemic: Peat with between 33% and 67% fibers.
	Sapric: Peat with less than 33% fibers.
Ash content [7]	Low ash: Peat with less than 5% ash.
	Medium ash: Peat with between 5% and 15% ash.
	High ash: Peat with more than 15% ash.
Acidity [11]	Highly acidic: Peat with a pH less than 4.5.
	Moderate acidic: Peat with a pH between 4.5 and 5.5.
	Slightly acidic: Peat with a pH greater than 5.5 and less than 7.
	Basic: Peat with a pH equal or greater than 7.

RESULTS AND DISCUSSION

Physical Properties

Table 2 shows the physical properties of six different peat samples collected from locations L1 to L6. The moisture content of the specimens varied from 200% to 370%. while specific gravity values ranged between 1.86 to 2.19. Both field moisture content and specific gravity values are within the range that was reported for Sri Lankan peat [12]. The observed higher specific gravity values imply higher decomposition of peats under the prevalent environment. Bulk density of peat varied from 1025 to 1240 kg/m³, which was lower compared to other soils due to the inertial gases present either in macropores or in the micropores [13].

The average organic content of the peats from locations L3, L5, and L6 are 48.4%, 50.6%, and 53.8% respectively, while the other locations show values less than 30%. The organic content of the peat increases with the presence of perforated and porous

lightweight fibers, which results in low specific gravity values [14].

The fiber contents of peat samples varies from 55% to 82%, and it has been found that there is irregular structure of fibers and organic matter in peat in Muthurajawela, Sri Lanka [15]. The highest fiber content was observed at location L4 while location L5 showed the least, which results in lower specific gravity value compared to other locations. Based on the acidity test, it was concluded that the Muthurajawela peat is highly acidic.

Classification of Muthurajawela Peat

Peat samples were classified by Von Post scale method, which is a primary method of peat classification used in the field by observing the degree of humification. Dark brown muddy water was observed when the peat was squeezed at location L1 to L4, and plant structures were not easily recognizable.

Therefore, peats from location L1 to L4 were classified as H4. Peat structure was easily identifiable, and yellowish water was observed during squeezing at location L1 and L2 which belongs to category H2 in the Von Post classification.

In addition, the colour of the peat soil samples was observed for classification as per the Munsell colour system, as shown in Table 3. Colour of the peat of locations L1, L2, L4 and L6 were black while locations L3 and L5 showed very dark grey and very dark brown respectively.

Fiber content, ash content and pH values were used to categorize the peat soil according to the ASTM standards, as shown in Table 1. Fiber content tests of the peat samples from locations L1 to L4 indicate 33% to 67% of fibers, while the locations L5 and L6 showed more than 67% of fibers. Therefore, peats from locations L1 to L4 were considered as Hemic while peat samples from L5 and L6 were Fibric. This clearly means that the decomposition process is being continued and conversion into the form of Sapric peats is expected with time.

Fibric and Hemic peats have higher water holding capacity, permeability and compressibility compared to Sapric peats. Therefore, the identified peat types in Muthurajawela reflect high susceptibility to greater settlement under the structural load. Ash content of the peats from all six locations were more than 15%, and the pH value was less than 4.5. Hence, Muthurajawela peat is highly acidic with high ash content.

Correlations Between Index Properties of Muthurajawela Peat

Correlations are useful to predict complex engineering properties from the physical properties

Table 2. Physical properties of peat soil in the Western province of Sri Lanka

Parameter	Samples location					
	L1	L2	L3	L4	L5	L6
Moisture content (%)	370	320	202	211	244	264
Specific gravity (G_s)	2.19	2.05	1.99	2.17	1.89	1.86
Ash content (%)	77.3	72.3	51.6	77	49.4	46.2
Organic content (%)	22.7	27.7	48.4	23	50.6	53.8
pH value	3.3	1.6	3.9	3.8	3.1	3.3
Dry density (kg/m^3)	263	275	411	376	312	282
Bulk density (kg/m^3)	1236	1151	1241	1168	1074	1026
Fiber content (%)	64.8	66.8	64.5	54.8	82.3	73.5

Table 3. Classification of peat soil samples in the Muthurajawela region in the Western province of Sri Lanka

Classification Parameter	Locations					
	L1	L2	L3	L4	L5	L6
Color (Munsell chart)	Black	Black	Very dark grey	Black	Very dark brown	Black
Von post scale	H4	H4	H4	H4	H2	H2
Fiber content	Hemic	Hemic	Hemic	Hemic	Fibric	Fibric
Ash content	High ash	High ash	High ash	High ash	High ash	High ash
Acidity	Highly acidic	Highly acidic	Highly acidic	Highly acidic	Highly acidic	Highly acidic

which could be easily be determined from laboratory tests. The applicability of previously developed correlations by Al-Raziqi et al., [16] and Kazeiman et al., [17] were assessed by plotting the experimental values against the computed results using the empirical Eqs. (4), (5) and (6). The analyses were conducted for dry density, specific gravity and organic content of Muthurajawela peat and are discussed below;

Moisture content $[w]$ vs. dry density $[\rho_d]$

Figure 2 illustrates the in-situ dry density (ρ_d) and in-situ moisture content (w) relationship for the Muthurajawela peats.

The experimental dry density values are compared with the curve using the empirical Eq. (4) developed by Al-Raziqi et al. [17] for Malaysian and New Zealand peats. Both experimental and calculated results show a reasonable match between the results; hence, Eq. (4) can be applicable to estimate the dry

density of Muthurajawela peat based on in-situ moisture content.

$$\rho_d = 0.872 (w + 0.317)^{-0.982} \quad (4)$$

Organic content (OC) vs specific gravity $[G_s]$

Figure 3 shows the relation between specific gravity and organic content (loss on ignition). Muthurajawela peats satisfy the equation proposed by Kazemian & Huat [17]. The close alignment between the results illustrates the applicability of the Eq. (5) for the prediction of the specific gravity of Muthurajawela peat by OC.

$$G_s = 5.26(OC)^{-0.285} \quad (5)$$

Bulk density $[\rho_b]$ vs organic content $[OC]$

Figure 4 shows the relationship between bulk density $[\rho_b]$ and organic content $[OC]$. The organic content versus bulk density of the Muthurajawela peat follows the equation proposed by Kazemian & Huat

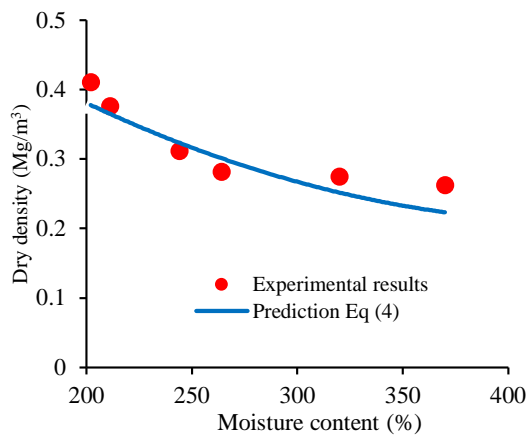


Fig. 2 Dry density as a function of moisture content.

[17] for the same relationship for peat in West Malaysia, as shown in Eq. (6). Hence, Eq. (6) can be used to predict the organic content of peat in Muthurajawela region.

$$OC = 59.836 \times \rho_b^{-4.64} \quad (6)$$

CONCLUSIONS

An experimental study was conducted to determine the physical properties of Muthurajawela peat and to evaluate the applicability of the existing correlations reported in the literature to predict the properties of Muthurajawela peat. The following conclusions were drawn from the findings of this study.

- Muthurajawela peat is categorized in the range of H2 to H4 based on the Von Post classification.
- The moisture content of the Muthurajawela peat ranges from 200% to 370% while the bulk density ranges from 1026 - 1241 kg/m³.
- Peats in this region belong to hemic and fibric type with high acidity and ash content.
- The available correlations in the literature were reasonable fits for the peats of Muthurajawela when predicting the physical properties such that dry/bulk density and specific gravity using in-situ measures of moisture content and organic content, respectively.

This study will improve the knowledge on characteristics of peat soil in Muthurajawela region which could be used to understand the behavior of peat and to propose possible ground improvement practices for future construction works.

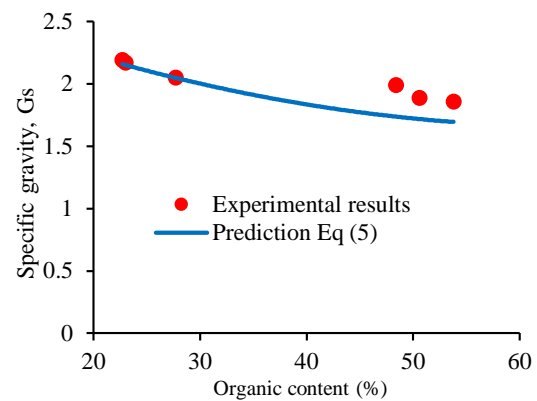


Fig. 3 Specific gravity as a function of organic content

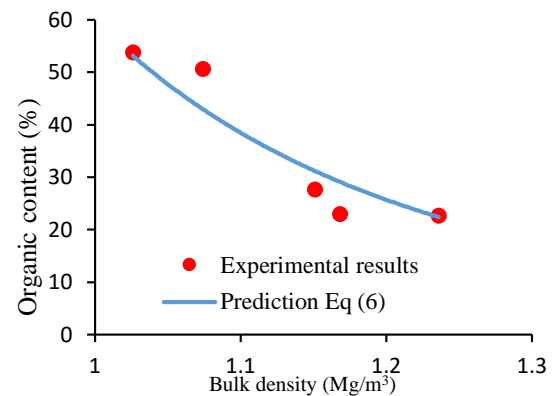


Fig. 4 Organic content as a function of bulk density

ACKNOWLEDGEMENT

The authors acknowledge South Eastern University of Sri Lanka (SEUSL) for the support provided under the University Research Grant scheme to conduct this research study. Also, our gratitude goes to the National Building Research Organization (NBRO), Sri Lanka for their assistance in obtaining peat samples in Muthurajawela region

REFERENCES

- [1] Mesri, G., M.J.J.o.G. Ajlouni, and G. Engineering, Engineering properties of fibrous peats. *Journal of Geotechnical Geoenvironmental Engineering* 2007. 133(7): p. 850-866.
- [2] Cooray, P., The geology of Sri Lanka, National Museum of Sri Lanka Publ. 1984, Colombo.
- [3] Karunawardena, A. and Toki M. Performance of Highway Embankments Constructed Over Sri Lankan Peaty Soils. *International Journal of Integrated Engineering*. 2014. 6(2).

- [4] Dhowian, A. and Edil AW, Consolidation behavior of peats. 1980. *Geotechnical Testing Journal*. 3(3): p. 105-114.
- [5] Ovenden, L., Peat accumulation in northern wetlands. *J Quaternary research*, 1990. 33(3): p. 377-386.
- [6] Edil, T. Recent advances in geotechnical characterization and construction over peats and organic soils. in *Proceedings 2nd International Conference on Advances in Soft Soil Engineering and Technology*.(Eds). Huat et al. Malaysia: Putrajaya. 2003.
- [7] ASTM D2974-14. Standard Test Methods for Moisture, Ash, and Organic Matter of Peat and Other Organic Soils. 2014: West Conshohocken, PA.
- [8] ASTM D1997-91. Standard Test Method for Laboratory Determination of the Fiber Content of Peat Samples by Dry Mass. . 2008: West Conshohocken, PA.
- [9] ASTM D854 -02. Standard test methods for specific gravity of soil solids by water pycnometer. 2002: West Conshohocken, PA.
- [10] ASTM D4531-86. Standard Test Methods for Bulk Density of Peat and Peat Products. 1999: West Conshohocken, PA.
- [11] ASTM D 2976-71(R98). Standard Test Method for pH of Peat Materials. 1998: West Conshohocken, PA.
- [12] Karunawardena, W.A., Consolidation analysis of Sri Lankan peaty clay using elasto-viscoplastic theory. 2007.
- [13] Huang, J., J.J.G. Han, and Geomembranes, 3D coupled mechanical and hydraulic modeling of a geosynthetic-reinforced deep mixed column-supported embankment. 2009. 27(4): p. 272-280.
- [14] Kaniraj, S.R. and R.R. Joseph. Geotechnical behavior of organic soils of North Sarawak. in *Fourth Int Conference on Soft Soil Engineering*. Vancouver, Canada. 2006.
- [15] Zimar, A.M.Z, Nasvi, M.C.M., Jayakody., S. Geotechnical Characterization of Peats in Muthurajawela Region in the Western Coast of Sri Lanka. *Geotechnical and Geological Engineering* 2020: p. 1-15.
- [16] Al-Raziqi, A., B. Huat, and H. Munzir. Index properties of some tropical peat and organic soils. in *Proc 2nd int conference on advances in soft soil engineering and technology*, Putrajaya. University Putra Malaysia Press, Malaysia. 2003.
- [17] Kazemian, S. and B.B.J.E.J.o.G.E. Huat, Compressibility characteristics of fibrous tr tropical peat reinforced with cement column. 2009. 14: p. 1-13.

SPATIAL MODELLING OF LARVA GLASS EEL AT CILETUH BAY, WEST JAVA, INDONESIA

Illa Annisa, S. Supriatna, and Iqbal Putut Ash Shidiq

Department of Geography, Faculty Mathematics & Natural Sciences, University of Indonesia, Indonesia

ABSTRACT

Eel larva or *Leptocephalus* is the larval stage of the eel, one of the fish species which naturally grow at the river freshwater into the brackish area such as bay or estuary, thus making the bay a potential area for the habitat. The study located in Ciletuh Bay, south coast of the West Java province. The coastline is directly facing the Indian Ocean, and it is one of the famous places for the eel catching spots. Eel is one of the essential and valuable commodities in the area, which are being caught and traded by the local communities. The abundant amount of the glass eel and the eel larva (*Leptocephalus*) influenced by the local condition and the characteristics of the bay environment, specifically the dynamics of the water transition. The study aims to identify the spatio-temporal dynamics of the eel larva potential habitat within the area of Ciletuh Bay. The spatio-temporal distribution of the eel larva is being identified with some of the oceanographic parameters, like the seasonal sea surface salinity and tides, water depth, and distance from the coastline. The sea surface salinity generated from a previously developed algorithm, which is employing Sentinel 2A imagery. The result shows that the habitat of eel larva is at a depth of five meters, with a radius of one kilometer to the northwest, extends to two kilometers to the northeast. An estuary with a type of sandy beach becomes a suitable area for the spawning the eel so that on the sandy estuary, the amount of larva glass eel in this area is very high. Furthermore, the spatial model for the habitat of the eel larva is required to optimize the cultivation and conservation of the bay area and to achieve a sustainable rearing for the species.

Keywords: Ciletuh Bay, Larva Glass Eel, Remote Sensing, Spatio-temporal.

INTRODUCTION

Eel (*Anguilla spp.*) is an elongated type of fish species that live in an estuary region. Particularly in Indonesia, the eel mostly spreads within the Indian Ocean, specifically from the west coast of the Sumatra waters to the southern part of Java sea [1]. It is a high-value commodity and profitable for the local community. One of the unique characteristics of eel is their habitat, from freshwater to saltwater and in the brackish water, which is known as estuary. Their habitat ideally influenced by the level of sea surface salinity, tides, oxygen, seawater current, waves, freshwater disorders, and water depth. The unique life cycle of eel starts with their mass migration from freshwater to the ocean. From there, they produce a larva, which will grow and evolve into glass eel and migrate back into the estuary [2]. Those life cycles are associated with the nature of the coastal ecosystem in the tropical region, where the abundance of fish in the river delta with low surface salinity [3].

Eel is known to be a nomadic organism. In order to survive, eel moves from a particular place to a more suitable place, by adjusting on the environmental conditions of the area. Their habitat is heavily influenced by oceanographic parameters such as sea surface temperature (SST) and sea surface salinity. Sea surface salinity can be used to estimate the level

of sediment and chlorophyll. It is also influencing the nature of saltwater, horizontally and vertically, as we saw in the tidal phenomenon [4].

As mentioned before, the estuary is a transitional zone between freshwater and saltwater with significant salinity differences. Nevertheless, biological productivity in the estuarine region tends to be higher. The area is rich in nutrients that are beneficial for the fish larvae [5].

The process of eel larva migration into the estuary area is influenced by the local oceanic-hydrological and climatic factors [6]. The dynamics of the water transitions are affected by local conditions and the environmental characteristics of the bay, which also determine the abundance and distribution of eel larvae. These species can tolerate the significant environmental differences between freshwater and saltwater in the estuary region. Other factors that affect the abundance of the eel larvae are the seasonal sea surface salinity, tide, and water temperature, and also water depth [7]. Harrison et al. [8] stated that in order to identify eel through their life cycle, the most important thing to be concerned about is their spatio-temporal dynamics on a local scale.

Ciletuh Bay is the estuary of two rivers, Ciletuh and Cimarunjung. They are located on the south coast of West Java Province and directly facing the Indian Ocean. Ciletuh Bay is a dynamic estuary, where there

are much freshwater going into the waters of the bay. The estuary of the river is one of the places where the species are reproducing. The estuary is an area of water with the highest level of productivity in the world that supports the natural ecological system between seas and rivers. As a transitional area, the estuary of the river is well-protected natural zoning and is also a habitat for the many species of living creatures that have different characteristics. Fish is an essential component of the estuaries that utilize the estuary as a habitat for its life cycle [9].

METHODS

The study is located at Ciletuh Bay. This study selects two specific sites located in Ciemas and Ciracap sub-districts, Sukabumi, in southern West Java (Figure 1). The absolute location is in the 7° 11' 0" South and 106° 27' 0" East, and it is about 30 kilometers from the Pelabuhanratu Bay [10].

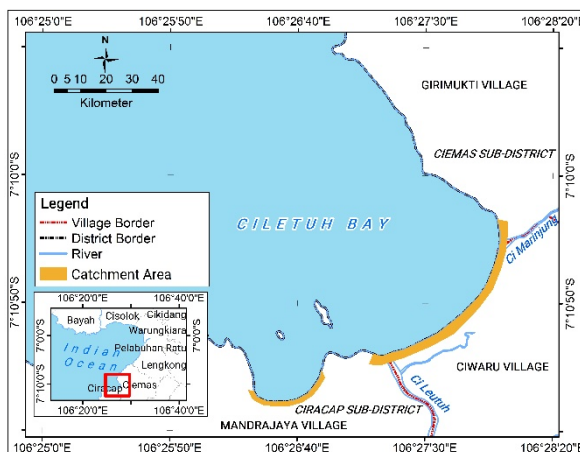


Fig. 1 Location of the study area.

Data Collection and Data Processing

The study includes data from 2018, 2019, and 2020 to perform the temporal analysis. The samples were taken in-situ in two zones, intertidal and subtidal. The samples were randomly distributed in three different clusters. The clusters were placed in a measured distance (1, 2, and 5 kilometers) from the shore. Samples from the river were also taken, specifically in the river body 500 meters from the intertidal zone. The seasonal condition is also considered here; thus, data from the dry and wet months were collected in this study. These conditions are influencing the spawning process of the fish. The egg is transported to the shallow water, and it will hatch into the larvae [11].

Sea surface salinity

In this study, the sea surface salinity extracted from Sentinel 2A imageries. In order to map the distribution of sea surface salinity, this study used a previously developed algorithm employing spectral value from satellite imageries. The estimation of the sea surface salinity refers to the following equation [12]:

$$\text{Salinity (ppt)} = 29.938 + (165.047 * \text{Blue}) - (26.277 * \text{Green}) + (2.609 * \text{Red}) \quad (1)$$

where Blue, Green, and Red are the spectral bands of the Sentinel 2A. Furthermore, the sea surface salinity is being employed to delineate the boundary of the estuary zone.

Water depth

Information on water depth was extracted from national bathymetry data. The national bathymetry data or BATNAS were generated from the data inversion of the gravity anomaly resulted from the combination of altimetry and echo-sounding data. The information were readily collected from www.batnas.big.go.id.

Meteorological, oceanographic, and primary data

The climate data were obtained from the Meteorological Climatological and Geophysical Agency (BMKG). The data contains the annual rainfall information (2018-2020). As the supporting data, the information of daily highest and lowest tidal were obtained from the local authority in the Ciletuh area. Lastly, primary data regarding the eel larva catching spot, including fishing period and the amount of production, were gathered from the field via a questionnaire-based interview with the fishermen around Ciletuh Bay.

RESULT AND DISCUSSION

Ciletuh Bay has a unique geological condition. The beach-side is controlled by the activity of the Eurasian and the Indian-Australian plate. This geological activity makes Ciletuh Bay have some varieties of rocks with different characteristics. Besides that, it is also in the estuary zone of Ciletuh and Cimarunjung rivers, which are affecting the physical and chemical condition of Ciletuh Bay.

Ciletuh Bay is one of the coastal waters in the southern part of West Java, which has the potential for the eel habitat (including their migration). The eel

and eel larva fishing sites are in the estuary, which points to the downstream portion of the river that connects directly to the sea [13].

The eel fish and eel larva collectors are the local community residing at a radius of three to four kilometers from the edge of the Ciletuh and Cimarunjung river. The usual fishing time of the larvae was at night to dawn (Figure 2). The eel larvae that have been collected are mostly sold to collectors who will then be marketed to Japan and South Korea. Some the collectors are doing the fish farming by cultivating the eel and marketed them at the Ciletuh Geopark, in the form of fresh food. Some of the fishermen can sell the eel larvae for one million rupiahs for 6,000 tails [14].

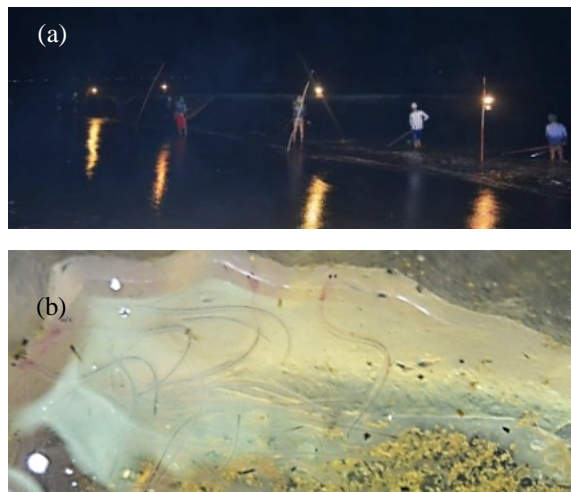


Fig. 2 The process of eel larva fishing in the study area. (a) the night fishing and (b) the glass eel larva captured around Ciletuh Bay.

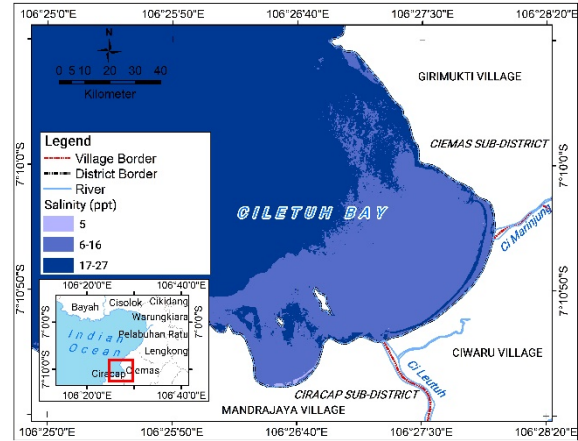
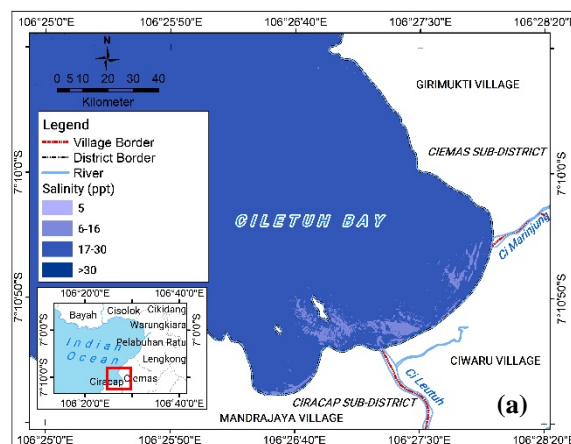


Fig. 3 The sea surface salinity for the dry months. (a) 27 September 2018 (b) 22 October 2019.

Based on the previously developed algorithm or the Cimandiri algorithm [12], this study has been able to map the sea surface salinity (Figure 3 and 4). As mentioned before, the estimation of the sea surface salinity is differentiated based on the dry and wet months. The classifications are shown in Table 1. The value can be used to determine the boundary of the estuary.

Table 1 The image acquisition date for the dry and wet months

Classification	Image acquisition date
Dry months	27 September 2018
	22 October 2019
Wet months	19 February 2018
	5 January 2019
	19 April 2020

Remote sensing-based studies and observations on sea surface salinity in the tropical region have been done previously [15]–[17]. Based on those studies, it is known that the values of salinity are dynamically formed against time and influenced by monsoons, ocean currents, freshwater coming from rivers, and sea waves.

Based on the results (Figure 3 and 4), the sea surface salinity in the dry and wet months are ranging from 5 to 16 ppt. It will further group as the mesohaline zone [18]. In the estuary of the Ciletuh river, the salinity ranges from 5 to 16 ppt, whereas in the estuary of Cimarunjung river salinity ranges from 6 to 16 ppt. It is assumed that the bigger size of the Ciletuh river will bring more sediments to the estuary and decreasing the salinity of the water.

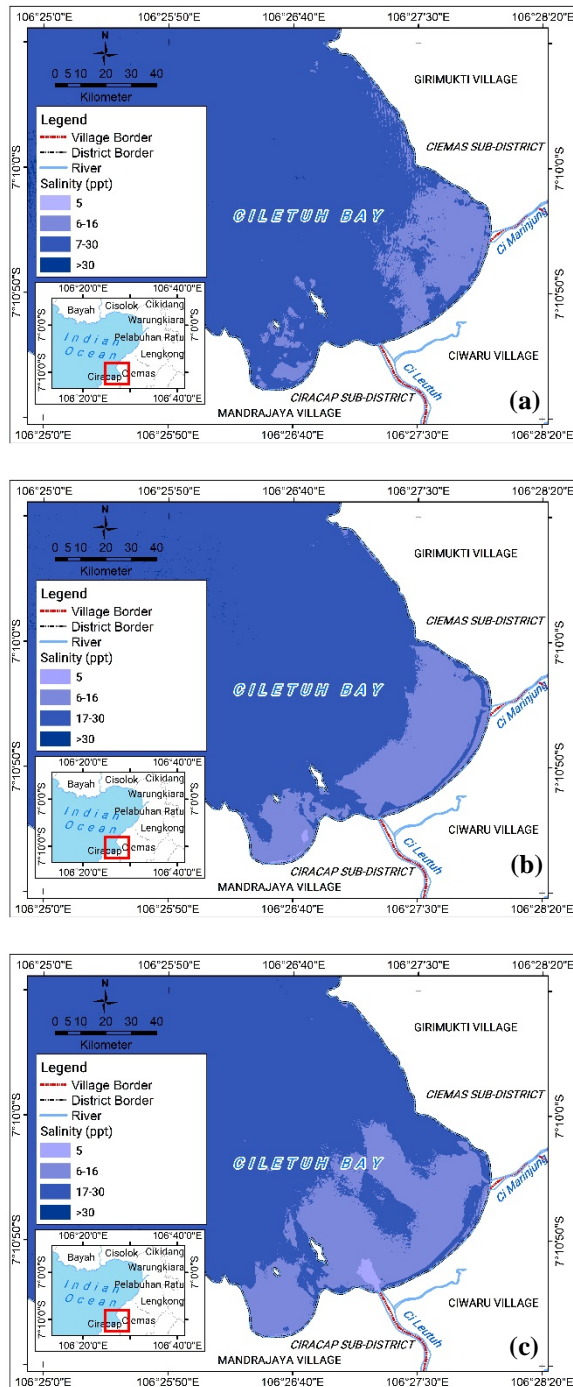


Fig. 4 The sea surface salinity for the wet months. (a) 19 February 2018, (b) 5 January 2019, and (c) 19 April 2020.

As this study observed the annual rainfall data, it is known that during the last three years, the dry month has an average rainfall of 19 mm, wherein the wet months the average rainfall is 419.65 mm (Figure 5). Rainfall will affects the discharge to the river. High rainfall is enlarging the probability of the streamflow so that the mixture of freshwater (from rainwater) will further neutralize the salinity of the seawater. The intensity of high rainfall will bring

more freshwater to the river estuary, mixing the water in the estuary and finally dominated water in the estuary.

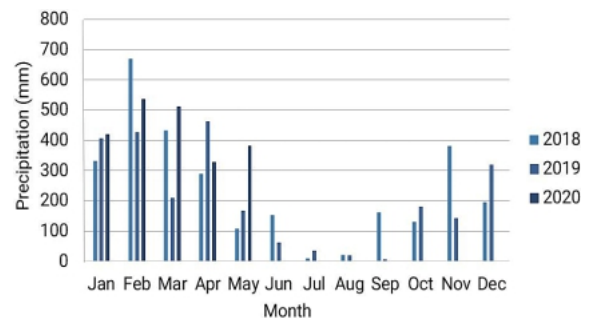


Fig. 5 Annual rainfall (mm) in 2018-2020 around Ciletuh Bay

Freshwater flows play an important role in the hydrodynamic process [19]. It can be seen that in wet months the salinity value will be less because of the high rainfall when the rainfall decreases, the salinity increases.

The tidal factors also influence the mixture of freshwater and salty water in the estuary. Not only that, but the tide of the seawater will also influence the eel larvae migration to the estuary. Then, it will settle in the area and occupy it as the proper habitat. The tidal wave phenomenon is one of the factors of coastal hydraulics, which is affecting the character of the flow in the estuary [17]. The tidal data is associating with the image acquisition date in dry and wet months. The high tides will result in the greater water mass that enters the river estuary so that the mixing of salinity highly increases, causing a higher sea surface salinity in the river estuary. In contrast, at times of low tides, waves are followed by the low salinity value in the estuary.

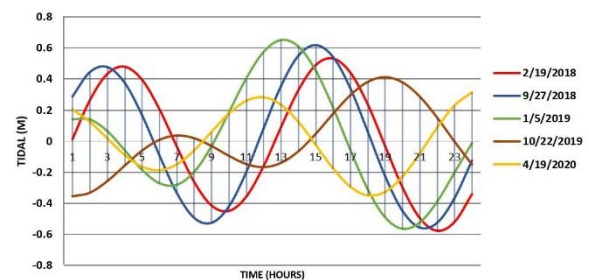


Fig. 6 Hourly tidal dynamics in 1 day (meter) at around Ciletuh Bay.

Based on Figure 6, it is known that the highest tides occurred on 5 January 2019 (0.653 m), while the lowest tides occurred on 19 February 2018 (-0.575 m). The highest tide occurred at 13:00 (1:00 pm), and the lowest ebb occurred at night (19:00 or 7:00 pm). On 22 October 2019, tidal patterns differ by an average of 0.3-0.4 meters and at a wave height of 0 meters. However, there are no significant differences in the

daily ups and downs of the tides during 2018-2020.

The eel larva migrates from the sea to the river at night, which it utilizes the currents brought by the sea breeze. The sea waves generated by the wind are bringing the seawater to the bay. At night the sea breeze evokes waves until early morning. Based on the tidal wave above (Figure 6), at night (21:00 or 9:00 pm) towards the morning (04:00 or 4:00 pm), the formed waves start to move up, so that fishers or collectors of eel larva will fishing in that the early morning.

The presence of chlorophyll strongly influences the life cycle of eel. Around the area of Pelabuhanratu Bay, which is a large bay around Ciletuh Bay, the chlorophyll-a, surface salinity, and suspended solids are tend to increase towards the west direction and decrease towards the southwest or moving away from Ciletuh Bay, especially in the rainy season. Apart from that, the sea surface temperature has the highest value along the coastline, including Ciletuh Bay, but this variable does not affect the chlorophyll content [20].

Based on the interview with fishers, the fishing spots are usually located on Cimandiri estuary, which 10 kilometers from Ciletuh Bay. The fishing activities starts at night (in between 7:00 pm to 5:00 am) because it is easier to spot the glass eel and eel larva with minimum lighting. The average amount of catch is about 0.7 ounces per day. In the dry months, the average amount ranges from 1 to 1.2 ounces per day, while in the wet months, the average daily amount is 0.5 ounces [21].

The underwater topography around Ciletuh Bay is being observed using bathymetry data. The seafloor around the coastal area dominated by flat and slightly steep terrains that extend from the estuary towards the west direction to the ocean. Figure 7 displays variations of water depth around Ciletuh Bay. The depth is ranging from five to 30 meters below the water.

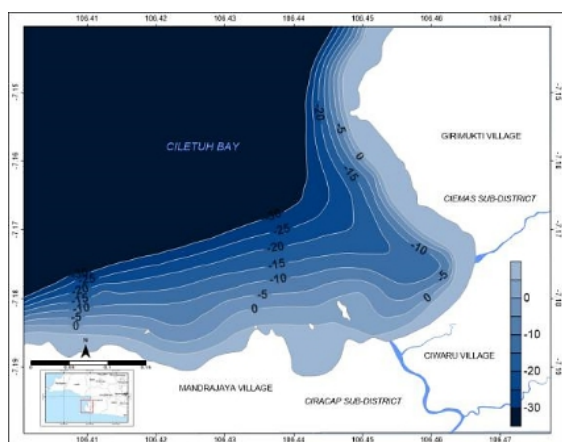


Fig. 7 Bathymetry of the Ciletuh Bay.

Seawater with less salinity was found at 5 meters depth. The salinity level of the bay is mostly found from zero up to five ppt. Nevertheless, a higher range of salinity was found at the end of the river (from 5 up to 16 ppt). As the water gets deeper, the salinity increase. The study found salinity at six up to 16 ppt in the depth of 10 to 15 meters. Lastly, the highest salinity was found at a depth greater than 15 meters (more than 16 ppt).

It is found that Ciletuh estuary has high sea surface salinity because it is mostly located in the deeper water. Regarding the seasonal aspect, the salinity of the wet months were less than 30 ppt, and it was found at 5-20 meters depth. The excess of freshwater from the precipitation is dropping the salinity, as can be seen from the wet month of 19 April 2020, where the lowest salinity (0-5 ppt) were found in the depth of five meters. In the other rainy months, it is found that the water with 0-16 ppt of salinity was extended towards the ocean until the depth of 20 meters. Salinity value in the dry month increases with the value higher than 16 ppt, and it was extended towards the bay and mouth of the river. For example, on 27 September 2018, most of the water was saline with a value of 17-30 ppt.

Figure 8 is showing a cross-section of the seafloor, and temporal salinity value at 0-meter depth. From the figure, it is known that even in the same depth, salinity might be different each month. From the figure, it also suggested that distance from the shoreline is also varying the salinity value.

On 19 February 2018, most of the catchment area at Cimarunjung river have high salinity (12 ppt). As the distance is getting far from the end of the river, the number of fishing spots decrease, while salinity increase to 25-30 ppt. On 18 September 2018, the fishing area got smaller because of the zone dominated by very saline water (29-30 ppt). On 5 January 2019, the fishing ground extended as the salinity dropped to 11 ppt.

Similar patterns were found in the dry months. On 22 October 2019, the fishing ground has medium saline water (15 ppt), but as it is getting far from the estuary, the salinity increase to 30-32 ppt. On 19 April 2020, salinity in the estuary found at five ppt. As it is getting far from the estuary, the salinity increases to 16-46 ppt (Figure 8).

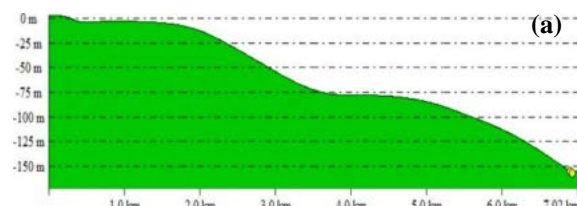


Fig. 8 Cross-section and temporal sea surface salinity of Ciletuh Bay. (a)

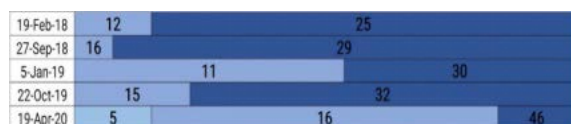


Fig. 8 Cross-section of the seafloor and (b) temporal sea surface salinity in 0-meter depth.

Based on the analysis, it can be said that the habitat of the eel and eel larva is at five-meter depth and in the radius of one kilometer to the northwest and two kilometers to the northeast. An estuary with sandy-type each becomes a suitable breeding area for the eel so that there is an abundance amount of eel in this area. A gravelly substrate with 81.4-100% sandy fraction is mostly found in the sediments around Ciletuh Bay [22].

The abundance of eel can be seen from the area flooded at the highest tide [23]. The presence of eel and glass eel influenced by topographical factors, and the river's technology, as well as the physical and chemical properties of river waters. It is also influenced by waste disposal from activities surrounding the river, including agriculture, plantation, and settlements.

Lastly, the Ciletuh estuaries are potential as eel habitat. Therefore it is vital to maintain environmental sustainability and the culture process as a livelihood for the people around, for the supply of cultivation activities, and also as a tourist attraction. A reasonable management effort with the monitoring of rivers will improve Ciletuh Bay as the preservation of the eel habitat.

CONCLUSIONS

Based on the results of the analysis, the eel larva habitat in Ciletuh Bay is influenced by natural conditions (dry and wet months). Different amounts of rainfall between those months are affecting sea surface temperature and salinity, as it is also proven by results from remote sensing data. The study also found a similar characteristic of tides between those months. The potential habitat of the eel and eel larva has been found between 5 to 20-meter depth. The abundance of the eel and eel larva was found at nighttime with the production peak at the wet months (December-May), where less saline water is available.

ACKNOWLEDGMENTS

This study is supported and funded by the Directorate Research and Community Services (DPRM), University of Indonesia under the Publikasi Terindeks International (PUTI) 2020 research grant. The authors also express their greatest gratitude and the highest appreciation to Department of Geography,

Faculty of Mathematics and Natural Science, University of Indonesia which has facilitated the research activities.

REFERENCES

- [1] Arai, T., Do we protect freshwater eels or do we drive them to extinction. Springer Plus, 2014, 3:534.
- [2] Linton E.D., Jonsson B., Noakes D.L.G. Effects of water temperature on the swimming and climbing behavior of glass eels, *Anguilla* sp. *Environmental Biology of Fishes*, 2007, pp. 78:189-192.
- [3] York J.K., G.B. McManus, W.J. Kimmerer, A.M. Slaughter, and T.R. Ignoffo., Trophic links in the plankton in the low salinity zone of a large temperate estuary: top-down effects of introduced copepods. *Estuaries and Coasts* 37, 2014, pp. 576-588.
- [4] Kang X., Xia M., Joseph P. S., & Chingbu P., Dynamics of water and salt exchange at Maryland Coastal Bays. *Estuarine, Coastal and Shelf Science*, 189, 2017, pp. 1-16.
- [5] G. A. Knox and T. Miyabara. *Coastal Zone Resource Development and Conservation in Southeast Asia, with Special Reference to Indonesia* (East-West Center Resources Systems Institute, Honolulu, Hawaii), 1983.
- [6] Arribas C, Fernández-Delgado C, Oliva-Paterna FJ, Drake P. Oceanic and local environmental conditions as forcing mechanisms of the glass eel recruitment to the southernmost European estuary. *Estuar. Coast. Shelf Sci*, 2012, pp. 107:46–57
- [7] Guo, Hongyi, Xuguang Zhang, Ya Zhang, Wenqiao Tang, and Jiamin Wu. Effects of Environmental Variables on Recruitment of *Anguilla japonica* Glass Eels in the Yangtze Estuary, China. *Fisheries Science*, 2017, pp. 333–410.
- [8] Harrison Andrew J., Alan M. Walker, Adrian C. Pinder, Cédric Briand, and Miran W. Aprahamian. A Review of Glass Eel Migratory Behaviour, Sampling Techniques and Abundance Estimates in Estuaries: Implications for Assessing Recruitment, Local Production and Exploitation. *Reviews in Fish Biology and Fisheries*, 2014, pp. 967–83
- [9] Santos R. V., Ramos S., & Bonecker A. C., Environmental control on larval stages of fish subject to specific salinity range in tropical estuaries. *Regional Studies in Marine Science*, 13, 2017, pp. 42-53
- [10] Global/Trans-national services. GeoHack-Teluk Ciletuh, 2020.
- [11] Machando I., Calliari D., Denicola A., & Grana L. R., Coupling suitable prey field to in situ fish larval condition and abundance in a subtropical estuary. *Estuarine, Coastal and Shelf Science*, 187,

- 2017, pp. 31-42
- [12] Supriatna L., Supriatna J., Koestoer R. H., & Takarina N. D., Algorithm model for the determination of Cimandiri Estuarine boundary using remote sensing, AIP Conference Proceedings, 1729, 2016, 020079.
- [13] Triatmodjo, B. Teknik Pantai, second edition, 1999.
- [14] Taufik., Menjaga Denyut Teluk Ciletuh Lewat Konservasi dan Budidaya. Media: CNN Indonesia, 2018.
- [15] Wang Y., Hua J., Pan H., Li S., Failler P., An integrated model for marine fishery management in the Pearl River Estuary: Linking socio-economic systems and ecosystems. Journal of Marine Policy, 64, 2016, pp. 135–147.
- [16] Geiger E.F., Grossi M.D., Trembanis A.C., Kohut J.T., Oliver M.J., Satellite-derived coastal ocean and estuarine salinity in the Mid-Atlantic. Journal of Continental Shelf Research, 63, 2013, pp. 235-242.
- [17] Min J.E., Ryu J.H., Lee S., Son S.H., Monitoring of suspended sediment variation using Landsat and MODIS in the Saemangeum coastal area of Korea. Marine Pollution Bulletin, 64, 2012, pp. 382-390.
- [18] Taupp T. & Wetzel M. A., Leaving the beaten track-Approaches beyond the Venice System to classify estuarine waters according to salinity, Estuarine, Coastal and Shelf Science, 148, 2014, pp. 27-35
- [19] Trinugroho, Muchamad Wahyu, Binod Bhatta, and Muhammad Babur. The Seawater Intrusion under Dam Failure in the Cimanuk River Estuary, Indonesia, Regional Studies in Marine Science, 2020, 36: 101267.
- [20] D S Irianto, Supriatna, and Tjiong Giok Pin., Distribution of glass eel by the water surface salinity using landsat TM at Pelabuhanratu Bay, West Java, IOP Conference Series: Earth and Environmental, 47, 2016, 012016.
- [21] Suhanda, D, Yuniarti, Ihsan, YN., Harahap, SA., Nutrient Concentration and Population of Macrozoobenthos in Ciletuh Bay, Sukabumi District, West Java, IOP Conference Series: Earth and Environmental, 406, 2014, 012014.
- [22] Sriarti, Telaah struktur dan kelimpahan populasi benih ikan sidat, *Anguilla bicolor bicolor* di muara Sungai Cimandiri, Pelabuhan Ratu, Jawa Barat, 1998.

NUMERICAL SIMULATION OF THREE-DIMENSIONAL FLOW AND LOCAL SCOUR AROUND A CYLINDER INDUCED BY TSUNAMI RUN-UP

Yuki Kajikawa¹ and Masamitsu Kuroiwa²
^{1,2}Faculty of Engineering, Tottori University, Japan

ABSTRACT

In this paper, we have presented a numerical model of a fully three-dimensional flow and topography change to predict local scour around cylindrical structures induced by a tsunami run-up. In the numerical model, the three-dimensional Reynolds-averaged Navier–Stokes equations with the renormalization group theory k - ε turbulence model using the Cartesian coordinate system was adopted. Moreover, the fractional area/volume obstacle representation method was introduced into the governing equations such that the model could be applied to complex topography. Furthermore, non-equilibrium bed-load and suspended-load transport were considered for the topography change calculation. To validate this model, it was applied to a large-scale laboratory experiment with a cylinder. Comparison between the calculated and experimental results showed that the model accurately replicated the time variations of water levels and scour depths in the offshore side of the cylinder and next to it. However, the model could not replicate the local scour on the land side of the cylinder. It was suggested that introducing the effect of curling up of bed load and seepage of tsunami run-up flow into the model is necessary to predict the local scour more accurately.

Keywords: Tsunami run-up, Cylindrical structure, Local scour, Numerical simulation, Three-dimensional model

INTRODUCTION

When a tsunami strikes a shore area, local scour is induced around cylindrical structures, such as an oil tank and a wind power plant constructed in the area, owing to a tsunami run-up. The local scour not only decreases the stability of the structures, but also collapses the structures in a worst-case scenario. Therefore, it is extremely important to quantitatively evaluate the topography change including the local scour around cylindrical structures due to the tsunami run-up, in advance.

Several studies on local scour around a cylinder have been carried out experimentally [1], [2] and numerically [3]–[6]. In particular, local scour in a steady flow has been investigated over the past few decades, mainly in the field of river engineering. It can be predicted extremely accurately using a numerical model consisting of fully three-dimensional (3D) flow and non-equilibrium bed-load transport [3]. Moreover, several numerical models predicting local scour due to tsunamis [4], [5] and waves [6] have also been proposed in recent years, and these models have been validated by comparing the results with those of the experimental models.

Although several numerical models concerning the local scour around a cylinder have been proposed, there are extremely few models concerning the local scour due to the run-up and downflow of tsunamis. This is because the local scour due to the run-up and downflow of tsunamis is

an extremely complex phenomenon as there is a significant change in flow and sediment transport in time and space. Furthermore, the prediction becomes more difficult owing to an upward flow development, resulting in a strong non equilibrium sediment transport behind a cylinder [1], [4]. However, the development of a numerical model that can predict this phenomenon with high accuracy is urgently needed to prepare for tsunami disasters in the future.

In this paper, the authors present a numerical model that can estimate a fully 3D flow and topography change to predict the local scour around a cylinder caused by the tsunami run-up flow. In this model, the renormalization group theory (RNG) k - ε turbulence model is adopted, and both non-equilibrium bed-load and suspended-load transport are considered for the calculation of change in topography. The model was validated with the experimental data obtained from the local scour around a cylinder using a large-scale tank [1].

NUMERICAL MODEL

Governing Equations for Tsunami Flow

In the tsunami flow model, the 3D Reynolds-averaged Navier–Stokes (RANS) equations using the Cartesian coordinate system was adopted. Further, the fractional area/volume obstacle representation (FAVOR) method [7], which has the ability to smoothly impose boundary conditions at complex boundaries, was introduced into the

governing equations. Moreover, the RNG k - ε turbulence model [8] was adopted to accurately estimate the separation flows behind a cylinder as follows:

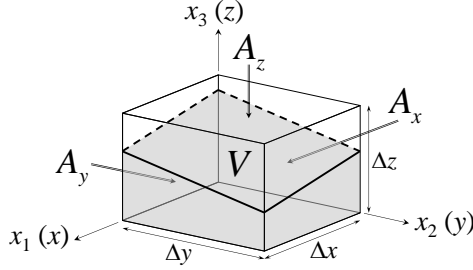


Fig. 1 Definition directions of each fractional area rate (A_x , A_y , A_z) for 3D flow. Δx , Δy , and Δz are the grid sizes in the x , y , and z directions, respectively.

$$\frac{\partial}{\partial x_j} \{A_{(j)} u_j\} = 0 \quad (1)$$

$$\begin{aligned} \frac{\partial u_i}{\partial t} + \frac{1}{V} \left\{ \frac{\partial A_{(j)} u_j u_i}{\partial x_j} \right\} = & -g \delta_{3i} - \frac{1}{\rho} \frac{\partial P}{\partial x_i} \\ & + \frac{1}{V} \frac{\partial}{\partial x_j} \left\{ A_{(j)} (\nu + \nu_t) \left(\frac{\partial u_i}{\partial x_j} + \frac{\partial u_j}{\partial x_i} \right) \right\} \end{aligned} \quad (2)$$

$$\begin{aligned} \frac{\partial k}{\partial t} + \frac{1}{V} \left\{ \frac{\partial A_{(j)} u_j k}{\partial x_j} \right\} = & \frac{1}{V} \frac{\partial}{\partial x_j} \left\{ A_{(j)} \left(\nu + \frac{\nu_t}{\sigma_k} \right) \frac{\partial k}{\partial x_j} \right\} \\ & + \nu_t \frac{\partial u_i}{\partial x_j} \left(\frac{\partial u_i}{\partial x_j} + \frac{\partial u_j}{\partial x_i} \right) - \varepsilon \end{aligned} \quad (3)$$

$$\begin{aligned} \frac{\partial \varepsilon}{\partial t} + \frac{1}{V} \left\{ \frac{\partial A_{(j)} u_j \varepsilon}{\partial x_j} \right\} = & \frac{1}{V} \frac{\partial}{\partial x_j} \left\{ A_{(j)} \left(\nu + \frac{\nu_t}{\sigma_\varepsilon} \right) \frac{\partial \varepsilon}{\partial x_j} \right\} \\ & + C_{\varepsilon 1}^* \frac{\varepsilon}{k} \nu_t \frac{\partial u_i}{\partial x_j} \left(\frac{\partial u_i}{\partial x_j} + \frac{\partial u_j}{\partial x_i} \right) - C_{\varepsilon 2} \frac{\varepsilon^2}{k} \end{aligned} \quad (4a)$$

$$C_{\varepsilon 1}^* = C_{\varepsilon 1} - \frac{\eta(1-\eta/\eta_0)}{1+\beta\eta^3}; \quad \eta = \frac{k}{\varepsilon} \sqrt{\frac{\partial u_i}{\partial x_j} \frac{\partial u_i}{\partial x_j} + \frac{\partial u_j}{\partial x_i} \frac{\partial u_i}{\partial x_j}} \quad (4b)$$

$$\nu_t = C_\mu \frac{k^2}{\varepsilon} \quad (5)$$

where t is time; $i = 1, 2, 3$; $j = 1, 2, 3$; $(x_1, x_2, x_3) = (x, y, z)$ in the Cartesian coordinates (x , y , and z denote the horizontal, cross, and vertical coordinates, respectively); u_j is the velocity in the x_j direction [$(u_1, u_2, u_3) = (u, v, w)$]; V is the fractional volume rate; $A_{(j)}$ is the fractional area rate in the x_j direction shown in Fig. 1 [$(A_{(1)}, A_{(2)}, A_{(3)}) = (A_x, A_y, A_z)$]; g is the gravitational acceleration; δ is the Kronecker's delta; ρ is the fluid density; $P = p + 2/3k$; p is the pressure; ν is the kinematic viscosity of fluid; k is

the turbulent kinetic energy; ε is the turbulent dissipation rate; and ν_t is the eddy viscosity coefficient.

The following standard values were used for each constant in the RNG k - ε turbulence model [8]:

$$\begin{aligned} C_\mu = 0.0845, \quad \sigma_k = 1/1.39, \quad \sigma_\varepsilon = 1/1.39 \\ C_{\varepsilon 1} = 1.42, \quad C_{\varepsilon 2} = 1.68, \quad \eta_0 = 4.38, \quad \beta = 0.012 \end{aligned} \quad (6)$$

Governing Equations for Topography Change

In the topography change model, both the bed-load and suspended-load transport were considered. The bed-load transport rate was estimated from the following non-equilibrium bed-load transport model proposed by Uchida and Fukuoka [9]:

$$\begin{aligned} \frac{\partial q_{Bi}}{\partial t} + \frac{1}{S} \left\{ \frac{\partial L_{(j)} u_{Bj} q_{Bi}}{\partial x_j} \right\} \\ = \frac{q_{Be} u_{Bei}}{\zeta_e} - \frac{q_{B^*} u_{Bi}}{\zeta} + m^* h_B (\gamma_{ei} - \gamma_i) \end{aligned} \quad (7a)$$

$$\begin{cases} u_B / \sqrt{sgd} = 3.3(q_{B^*})^{1/3}, u_{Be} / \sqrt{sgd} = 3.3(q_{Be^*})^{1/3} \\ h_B / d = 0.3(q_{B^*})^{2/3} \\ \zeta_e / d = 600(q_{Be^*})^{2/3}, \zeta / d = 600 \max(q_{Be^*}, q_{B^*})^{2/3} \end{cases} \quad (7b)$$

where q_{Bi} is the bed-load transport rate in the x_i direction ($q_B^2 = q_{Bi} q_{Bi}$); S is the movable bed area rate on two-dimensional horizontal (2DH) bed-plane; $L_{(j)}$ is the fractional line rate in the x_j direction shown in Fig. 2; u_{Bj} is the sediment particle velocity of bed load in the x_j direction ($u_B^2 = u_{Bj} u_{Bj}$); q_{Be} is the equilibrium bed-load transport rate; ζ is the spatial lag distance; ζ_e and u_{Bei} are the ζ and u_{Bi} for equilibrium condition, respectively; $m^* = \mu_k s g \cos \theta_b / (s + 1 + C_M)$; μ_k is the dynamic friction coefficient of sediment; s is the specific gravity of sediment in water ($= \sigma/\rho - 1$, σ is the density of sediment); θ_b is the maximum bed angle; C_M is the coefficient of added mass ($= 0.5$); $h_B = q_B u_B$; $\gamma_i = q_{Bi}/q_B$; $\gamma_{ei} = q_{Bei}/q_{Be}$; $q_B^* = q_B/(sgd^3)^{0.5}$; $q_{Be^*} = q_{Be}/(sgd^3)^{0.5}$; and d is the sediment diameter.

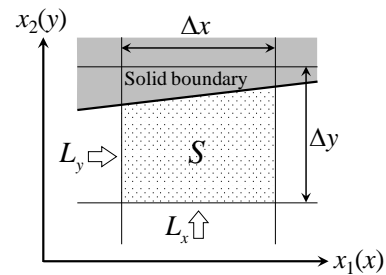


Fig. 2 Definition directions of each fractional line rate (L_x , L_y) on 2DH bed-plane.

The equilibrium bed-load transport rate q_{Be} in Eq. (7a) was calculated using the following formula given by Ashida and Michiue [10]:

$$\frac{q_{Be}}{\sqrt{sgd^3}} = 17\tau_*^{3/2} \left(1 - \frac{K_c \tau_{*c}}{\tau_*}\right) \left(1 - \sqrt{\frac{K_c \tau_{*c}}{\tau_*}}\right) \quad (8)$$

where τ_* and τ_{*c} are the non-dimensional bed tractive and critical bed tractive forces [11], respectively; and K_c is the correction factor attributed to the influence of bed inclination on sediment motion [12].

The suspended-load transport rate per unit area q_{su} was defined using the following formula proposed by Itakura and Kishi [13]:

$$q_{su} = K \left(\alpha_* \frac{\sigma - \rho}{\sigma} \frac{gd}{u_*} \Omega - w_f \right) \quad (9a)$$

$$\Omega = \frac{\tau_*}{B_*} \frac{\int_{\alpha'}^{\infty} \xi \frac{1}{\sqrt{\pi}} \exp(-\xi^2) d\xi}{\int_{\alpha'}^{\infty} \frac{1}{\sqrt{\pi}} \exp(-\xi^2) d\xi} + 2 \frac{\tau_*}{B_*} - 1 \quad (9b)$$

where w_f is the settling velocity of the sediment given by Rubey [14]; $\alpha' = B_*/\tau_* - 2$; $\alpha_* = 0.14$; $K = 0.008$; and $B_* = 0.143$.

The advection and diffusion processes of the suspended load were calculated using the following suspended-sediment transport equation, into which the FAVOR method was introduced:

$$\frac{\partial c}{\partial t} + \frac{1}{V} \left\{ \frac{\partial A_{(j)} u_j c}{\partial x_j} - \frac{\partial A_{(3)} w_f c}{\partial x_3} \right\} = \frac{1}{V} \frac{\partial}{\partial x_j} \left\{ A_{(j)} D_t \frac{\partial c}{\partial x_j} \right\} \quad (10)$$

where c is the concentration of the suspended load; D_t is the eddy diffusion coefficient ($= \nu_t/\sigma_t$); and σ_t is the turbulent Schmidt number ($= 0.8$).

The topography change was calculated using the following continuity equation of sediment transport into which the FAVOR method was introduced:

$$\frac{\partial z_b}{\partial t} + \frac{1}{S(1-\lambda)} \left\{ \frac{\partial L_{(j)} q_{Bj}}{\partial x_j} + S(q_{su} - w_f c_b) \right\} = 0 \quad (11)$$

where z_b is the bed elevation; λ is the porosity of the bed material; and c_b is the near-bed concentration of the suspended load.

Numerical Method

The governing equations were discretized using the finite-volume method on a collocated grid system. To satisfy local continuity and solve pressures, the highly simplified mark-and-cell (HSMAC) method was adopted in this model. The convective terms and diffusion terms in Eq. (2) were

discretized employing the fifth-order weighted essentially non-oscillatory (WENO) scheme [15] and central differencing scheme, respectively. The Adams-Bashforth method was used for time integration. Moreover, the hybrid scheme [16] was adopted to discretize Eqs. (3), (4), and (10) to avoid numerical oscillations.

As the boundary conditions, the time variation of the wave profile set in the experiment was provided at the offshore boundary. According to the logarithmic velocity distribution and assumption of local equilibrium of turbulence, the wall function was imposed at the solid wall. The free-slip condition was applied to the amount of velocities and turbulence at the water surface. Moreover, regarding the suspended load, the vertical flux was zero at the water surface, and it was equal to the suspended-load transport rate per unit area of the bed.

MODEL APPLICATION AND DISCUSSION

Model Application

A numerical simulation was performed using experimental data of change in topography with the local scour around a cylinder induced by the tsunami run-up [1]. The elevated view and top view of the experiment are shown in Fig. 3 and 4, respectively.

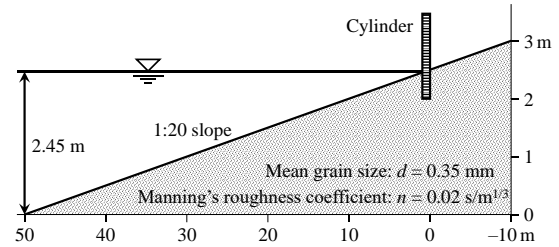


Fig. 3 Elevated view of the experiment.

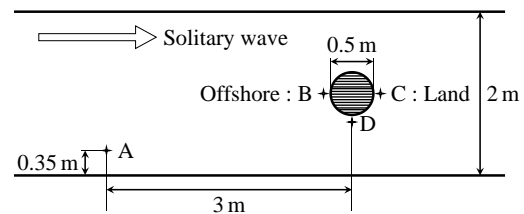


Fig. 4 Top view of the experiment: stations A, B, and C indicate the locations of the wave gauges. Stations B, C, and D indicate the locations of the scour depth recorders.

A large-scale sediment tank 135 m long, 2 m wide, and 5 m deep was used in the experiment [1]. A beach with a 1:20 slope was constructed using well-graded sand (mean grain size 0.35 mm) and a cylinder having 0.5 m diameter was vertically

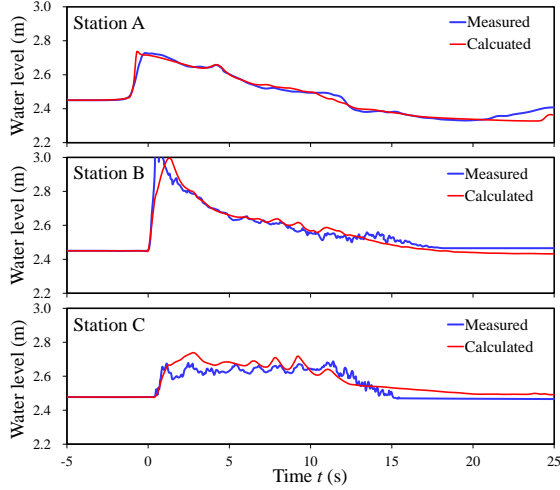


Fig. 6 Comparison of calculated and measured water levels at various stations.

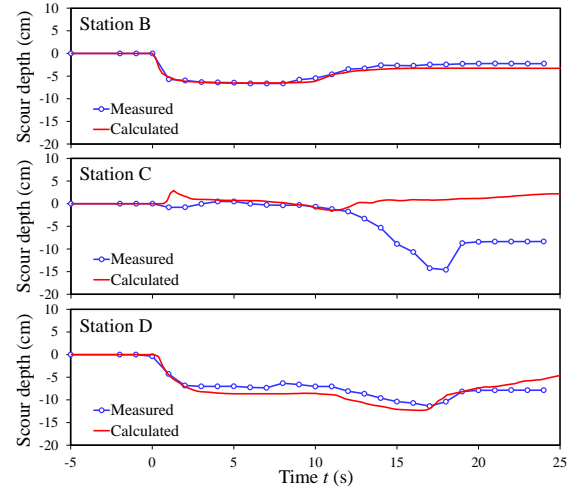


Fig. 7 Comparison of calculated and measured scour depths at various stations.

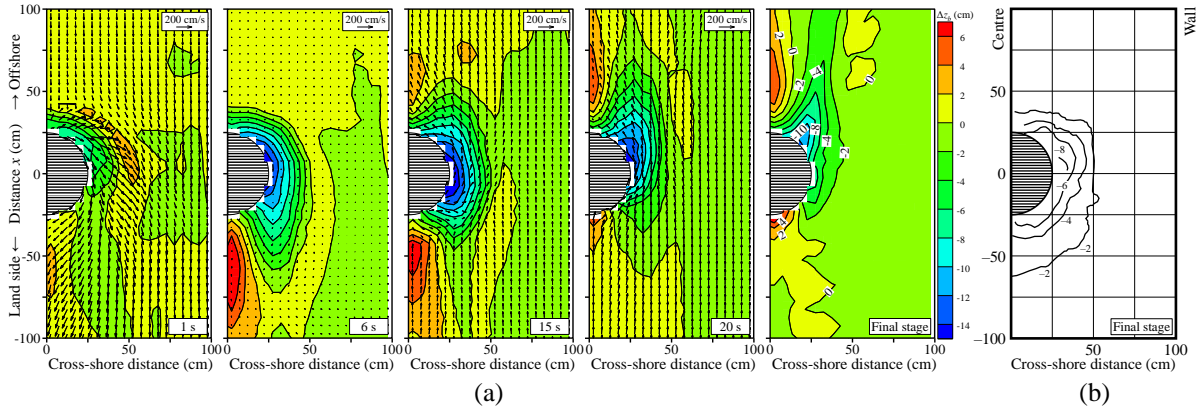


Fig. 8 Comparison of bed variation contour: (a) Calculated bed variation contour with near-bed flow velocity vectors and (b) measured bed variation contour at the final stage.

installed at the center of the beach. A solitary wave was generated at the offshore end of the tank. The experiments were carried out by systematically changing the water depth within a range of 2.25–2.65 m and wave height within a range of 0.10–0.30 m. In this study, we tried to achieve the experimental condition values of 2.45 m water depth and 0.22 m wave height as shown in Fig. 5.

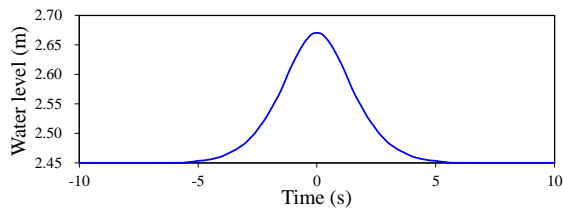


Fig. 5 Wave profile at the offshore boundary

The horizontal grid sizes (Δx and Δy) and vertical grid size (Δz) were set to 0.05 and 0.0125 m as the calculation conditions, respectively. The

calculation time step Δt was set to 0.002 s, and Manning's roughness coefficient n was set to 0.02 s/m^{1/3}.

Comparison of Water Level and Scour Depth

Figure 6 shows a comparison of calculated and measured water levels at Station (St.) A, B, and C indicated in Fig. 4. Here, $t = 0$ s indicates the time when the wave front arrived at St. B. The water level increases sharply when the wave front arrives, and it decreases gradually once the wave front passes. The calculated results are in good agreement with the measured values.

Figure 7 shows a comparison of the calculated and measured scour depths at St. B, C, and D, the locations of which are indicated in Fig. 4. The presented numerical model was found to accurately reproduce the time variations of scour depths in the offshore side of the cylinder (St. B) and next to it (St. D). However, the model could not reproduce the scour depth on the land side (St. C). Although

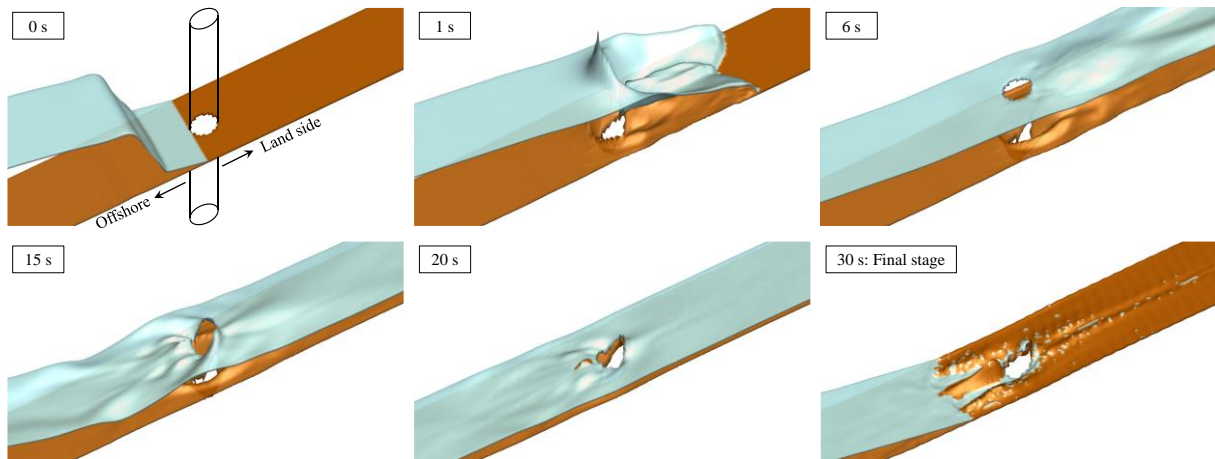


Fig. 9 Time variations from a bird's-eye view of calculated topography and water surface.

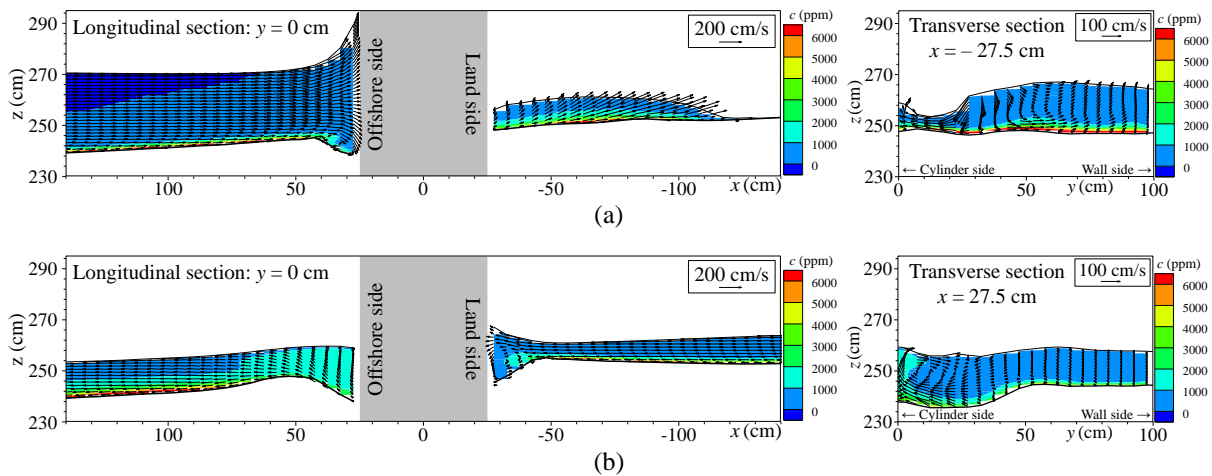


Fig. 10 Calculated 3D flow velocity vectors in the longitudinal and the transversal sections: (a) run-up of tsunami ($t = 1$ s) and (b) downflow of tsunami ($t = 15$ s).

erosion occurred on the land side of the cylinder in the experiment, sediment deposition occurred in the calculation.

The calculated bed variation contour with near-bed flow velocity vectors and measured bed variation contour at the final stage are shown in Figure 8(a) and 8(b), respectively. As shown in Fig. 8(a), at the time of the tsunami run-up ($t = 1-6$ s), reverse flows occur on the offshore side of the cylinder due to the development of horseshoe vortices, and the scour hole is formed concentrically. Moreover, a sediment deposition area is formed simultaneously on the land side. At the time of the tsunami backflow ($t = 15-20$ s), the sediment deposition flows into the scour hole. This is because the scour depth at St. C could not be reproduced, as shown in Fig. 7. The calculated bed variation contours at $t = 15-20$ s are relatively similar to the measured one shown in Fig. 8(b). However, the calculated bed variation contour at the final stage differs from the measured contour as explained above. The authors tried to calculate the bed

variation using various suspended-load transport rate formulas to reproduce this local scour, nevertheless failed to reproduce it.

Three-Dimensional Flow around Cylinder

Figure 9 illustrates the time variations from a bird's-eye view of the calculated topography and water surface. It can be seen that the model can adequately calculate the flooding and drying bed in the subcritical and supercritical flow fields caused by the tsunami run-up and downflow.

The calculated 3D flow velocity vectors in the longitudinal and transverse sections at the time of the tsunami run-up and downflow were shown in Fig. 10(a) and (b), respectively. The suspended-load concentration contours were also indicated in these figures. Here, the land side of the cylinder is focused on, where the local scour could not be reproduced by the presented model. As shown in the longitudinal section of Fig. 10(a), an upward flow that induces curling up of the bed-load is reproduced at the time

of the tsunami run-up. This flow situation can also be seen in the transverse section of Fig. 10(a). Moreover, a horseshoe vortex that expedites the formation of the local scour is reproduced at the time of the tsunami downflow shown in the longitudinal section of Fig. 10(b). In other words, the presented model can reproduce the flows, which have already been confirmed [1], on the land side of the cylinder, and there is a possibility that the model can reproduce the phenomenon more accurately by considering the mechanism of the curling up of the bed-load. Furthermore, the seepage of the tsunami run-up flow into the beach was not considered in this model. Therefore, a calculation considering seepage flows is also needed to improve the prediction accuracy.

CONCLUSIONS

In this study, we have proposed a fully 3D flow and topography change model considering the non-equilibrium bed-load and suspended-load transports with the final goal of a highly accurate prediction of local scour around cylindrical structures induced by tsunami run-up. The model was applied to a large-scale laboratory experiment using a cylinder that is installed on a uniform slope beach. Moreover, comparisons between the calculated and experimental data were carried out. Consequently, the proposed numerical model was found to accurately reproduce the time variations of water levels and scour depths on the offshore side of the cylinder and next to it. However, the model could not reproduce the local scour on the land side of the cylinder. In our next work, we intend to perform the calculations by incorporating the curling up of bed load and the seepage of tsunami run-up flow into the topography change model.

REFERENCES

- [1] Tonkin S., Yeh H., Kato F., and Sato S., Tsunami scour around a cylinder, *J. Fluid Mech.*, Vol. 496, 2003, pp.165-192.
- [2] Larsen B. E., Arbøll L. K., Kristoffersen S. F., Carstensen S., and Furhrman D. R., Experimental study of tsunami-induced scour around a monopile foundation, *Coast. Eng.*, Vol. 138, 2018, pp.9-21.
- [3] Nagata N., Hosoda T., Nakato T., and Muramoto Y., Three-dimensional numerical model for flow and bed deformation around river hydraulic structures, *J. Hydraul. Eng.*, Vol. 131, 2005, pp.1074-1087.
- [4] Pan C. and Huang W., Numerical modeling of tsunami wave run-up and effects on sediment scour around a cylindrical pier, *J. Eng. Mech.*, Vol. 138, No. 10, 2012, pp.1224-1235.
- [5] Larsen B. E., Fuhrman D. R., Baykal C., and Sumer B. M., Tsunami-induced scour around monopile foundations, *Coast. Eng.*, Vol. 129, 2017, pp.36-49.
- [6] Quezada M., Tamburrino A., and Niño Y., Numerical simulation of scour around circular piles due to unsteady currents and oscillatory flows, *Eng. Appl. Comput. Fluid Mech.*, Vol. 12, No. 1, 2018, pp.354-374.
- [7] Hirt C. W. and Sicilian J. M., A porosity technique for the definition obstacle in rectangular cell meshes, *Proc. 4th Int. Conf. on Ship Hydrodynamics*, Washington, DC, 1985.
- [8] Yakhot V., Orszag S. A., Thangam S., Gatski T. B., and Speziale C. G., Development of turbulence models for shear flows by a double expansion technique, *Phys. Fluid. A: Fluid Dynam.*, Vol. 4, No. 7, 1992, pp.1510-1520.
- [9] Uchida T. and Fukuoka S., Numerical calculation for bed variation in compound-meandering channel using depth integrated model without assumption of shallow water flow, *Adv. Water Resour.*, Vol. 72, 2014, pp.45-56.
- [10] Ashida K. and Michiue M., Study on hydraulic resistance and bed-load transport rate in alluvial stream, *Proc. Japan Soc. Civil Eng.*, Vol. 206, 1972, pp.59-69.
- [11] Iwagaki Y., Fundamental study on critical tractive force (I) Hydrodynamical study on critical tractive force, *Trans. Japan Soc. Civil Eng.*, Vol. 41, 1956, pp.1-17.
- [12] Takebayashi H. and Okabe T., Geometric characteristics of braided channel on non-uniform sediment bed, *The Int. Cong. INTERPRAVENT 2002 in the Pacific Rim*, Congress publication, 1, 2002, pp.79-89.
- [13] Itakura T. and Kishi T., Open channel flow with suspended sediments, *J. Hydraulic Division, ASCE*, Vol. 106 (HY8), 1980, pp.1325-1343.
- [14] Rubey W. W., Settling velocity of gravel, sand and silt particles, *Amer. J. Sci.*, Vol. 25, 1933, pp.325-338.
- [15] Liu X.-D., Osher S., and Chan, T., Weighted essentially non-oscillatory scheme, *J. Comput. Phys.*, Vol. 115, 1994, pp.200-212.
- [16] Spalding D. B., A novel finite difference formulation for differential expressions involving both first and second derivatives, *Int. J. Num. Methods Eng.*, Vol. 4, 1972, pp.551-559.

ON RELATIONSHIP BETWEEN MONUMENT AND THE STATION BUILDING

Kaho HASEGAWA¹, Kazunari TANAKA¹

¹Graduate Course in Architecture, Civil Engineering and Urban Design, Graduate School of Engineering Osaka
Institute of Technology, 5-16-1 Asahi-ku Osaka Japan

ABSTRACT

The relationship in this paper is an important element that shows not only the scale of a city, but also the image it is trying to project. The structure acts as a gateway to the culture, history and industry of a town. In recent years, by installing monuments in a public square, it has increased people's opportunity to be exposed to art in everyday life. Whereby, growing people's interest in art. Furthermore, a monument can be a symbol of a station. However, it can conversely be a factor that disrupts the view of the station square. Therefore, planners need to think about aspects such as location, position, size etc., of the monument. Previous studies have arranged the characteristics and constitution of the surroundings of monuments. The purpose of this study is to clear the characteristics of the monuments in front of the stations. We have not had methods to determine placement of monument. We conducted psychological evaluation surveys and we found the relationship between monuments and buildings show psychological elements of impression. These results are very promising and show that monuments can be an important factor of station squares without disturbing views.

Keywords: monument, psychological evaluation, symbol, landscape

INTRODUCTION

The square in front of the station is the entrance to the city and the symbol of the town. The monuments there are one of the symbols, but they also have an effect on the cityscape. The space in front of the station forms the daily lives of local residents and gives the tourist an image of the city. It is indispensable to focus attention on people's consciousness to find a characteristic station square with a monument.

PURPOSE AND METHOD

The purpose of this study is to clarify the characteristics of the monuments in front of the stations. Up to now, we have not had a standard method for the various decisions that need to be made when placing a monument at a station. The results of the research will show the possibility of standardizing the design of station buildings and public squares in front of them.

The method of research here is collect the squares in front of the stations where the following monuments are located and group them. Next, an impression evaluation experiment is conducted for the station squares with similar characteristics. From the results, we can grasp how the station space is influenced by the monuments.

SELECT THE STATION SQUARES



Fig1. Classification of monuments

In this research, we target two lines in the suburbs of Osaka (JR Kobe / Kyoto line, Hankyu Kobe / Kyoto main line). Then, we conducted principal component analysis using the indicators of the monument and the surrounding environment. Next, we classified the monuments by cluster analysis based on the three axes up to the extracted eigenvalue of 1.19 and cumulative contribution rate of 53.3%.

The 10 stations (Table2:A~J) were the subject of psychological evaluation, centering on the monuments that are strongly connected with the surrounding environment.

Table2. Select Stations

A	St.Koshienguchi	B	St.Nnishinomiya
C	St.Rokkomichi	D	St.Mukomachi
E	St.Nagaokakyo	F	St.Minase
G	St.Katura	H	St.Ibarakishi
I	St.Nada	J	St.Kobe

PSYCHOLOGICAL EVALUATIONS



Fig2.Photos used in the experiment (the upper :with monument, the lower: without monument)

Next, from these initial evaluations, I made questionnaires with the Semantic Differential method for the pictures of the station squares. I carried out a 5-step evaluation questionnaire for 14 pairs of adjectives. The adjective pairs used are as shown in Table4. The collected questionnaire data was analyzed with factor analysis to survey the impression of the images.

Table3. Difference of factors with and without the monument

No	1	2	3	4
A	-1.19	-2.20	0.05	-1.08
B	2.05	2.57	0.82	1.88
C	-1.35	-2.72	-0.93	-0.90
D	-1.13	-1.71	-0.17	-0.44
E	-0.33	-0.59	-0.71	-0.04
F	0.12	-0.31	0.30	0.00
G	-0.53	-0.97	0.75	-0.33
H	1.44	1.62	0.55	-0.27
I	-1.09	-1.68	-0.70	-0.99
J	1.48	2.73	2.55	2.37

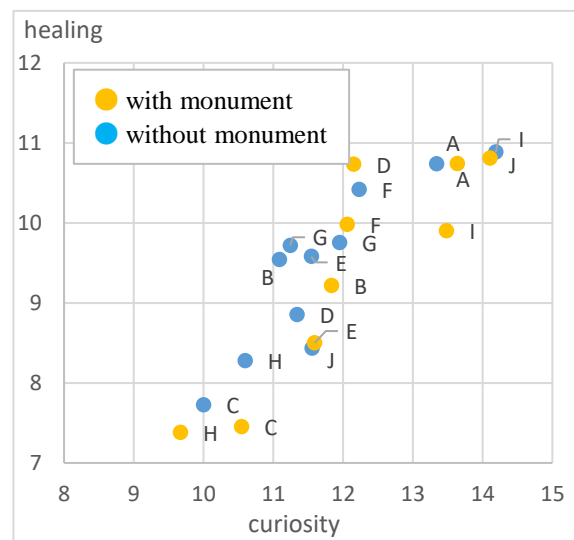


Fig3. Factor score for each station (comfort-neatness)

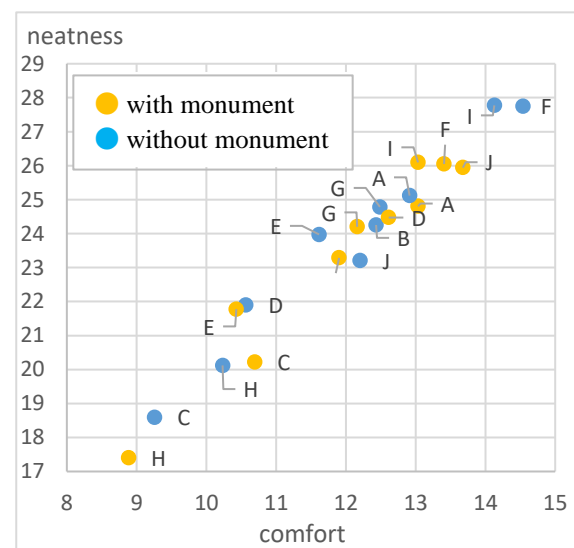


Fig4. Factor score for each station (curiosity-healing)

Table4. Adjective pairs used in the experiment
Difference of factors with and without the monument

frustrating	refreshing
overwhelm	exciting
ordinary	special
hate	favorite
dirty	clear
closed	open
cool	warm
simple	complicated
noisy	quiet
heavy	light
hard	soft
cramped	free
dangerous	safe
scattered	tidy

Based on the results of the questionnaire, a factor analysis was performed using the main factor method, and factors up to a cumulative contribution ratio of 49.4% and an eigenvalue of 1.35 were adopted. Each factor was evaluated in order of neatness, comfort, curiosity, and healing; and the factor score of each station was calculated. The category score of each station is shown in Fig 3,4.

RESULT AND DISCUSSION

First off, we focus on the difference between the presence and absence of monuments in the target station square. There was a big difference in the impressions depending on the presence or absence of monuments in the target station square. Furthermore, we pay attention to how impressions differ depending on the presence or absence of monuments. Then, there is a difference in impression depending on ones that give a positive impression

to the entire station square (which are regarded as highly symbolic monuments), and ones that give a negative impression (regarded as discordant monuments). On the other hand, those with no effect on impression can be regarded as inconspicuous monuments. We named the groups 1, 2, 3 in the order of monuments with high symbolism, the discordant monuments, and the inconspicuous monuments.



Fig5. Monument group example

CONCLUSIONS

In this study, we grasped the current situation by positioning monuments, and surveying and organizing target stations. In addition, we extracted the elements composing the target monuments and the installation environment, and performed classification using principal component analysis. Therefore, the monuments that affect the installation environment were extracted, and the landscape evaluation of those monuments and the station space was extracted from the psychological impression by the questionnaire. The results indicate that this study should be classified into four groups from the two indicators of symbolism and harmony. As a future task, it is necessary to understand the physical elements related to these groups in the station space.

REFERENCES

- [1] Yukiko Yamamoto, Shinji Ikaruga: Landscape Characteristics of Installation Space from the Open-Air Sculpture Installation Project Process, *J. Archit. Plan., AIJ* Vol. 75 No. 653, 1697-1706, 2010.7
- [2] Katunori Mizushima, Fumika Anbo, Yoshio Itoi: A Basic Study on The Expression Structure of Monuments in Station Squares, *J. Archit. Plan., AIJ* No. 585, 133~140
- [3] Tetsunobu Yoshitake, Kohta Yoshimoto, Chikashi Deguchi: A Study on Municipal Guidance and Permission System for Private Monuments, *Journal of the City Planning Institute of Japan* No. 45-3, 45~43, 2010.10
- [4] Takanori Ito, Sho Taira, Kosuke Narita: Utilization of the City Symbol for Creating Place Brandings, *Journal of the Science of Design*, 133~140, 2004.11
- [5] Shunsuke Saikai, Suguru Mori: A Basic Study of Transition on the Orientation of Public Arts in Hokkaido, *Proceedings of AIJ Hokkaido Architectural Research Conference*, 351~354, 2012.6

STUDY ON THE MEANING OF “QUAINT” SPACE

Yoshiki Shirafuji, Kenta Aoki, Koji Inoue, Dr. Kazunari Tanaka

Department of Civil Engineering and Urban Design, Osaka Institute of Technology, Japan

ABSTRACT

Since ancient times, there is a word “quaint” which represents a sense of beauty in Japan. Although there are studies on the architectural history, on the aging of facade and on the quality of calmness of houses, there is no study on the sense of “quaint” regarding spaces. We clarify what kind of impression “quaint” gives by using statistical analysis methods. It would be useful to clarify the concept of “quaint”. The research method consisted of a SD method and Image experiment. The adjectives are 5 steps each in the SD method, and the Image experiment was a picture questionnaire with 6 figures. The figures are brightness-edited parts of a standard picture. The method is based on the statistical data obtained from experiments. The analysis consisted of the Distribution Probability, Co-occurrence Network, and Factor Analysis. As a result, it appears there is difference from the Distribution Probability between the forms of the spaces. From the Co-occurrence Network Analysis, it was clear that the dark parts (or direction) and the bright parts (or direction) in spaces have an influence of feeling quaint. The two factors of “fresh feeling” and “stylish atmosphere” by the Factor Analysis have a possibility to explain the feeling of “quaint”.

Keywords: Aji, Quaint, Distribution probability, Co-occurrence network, Factor analysis

INTRODUCTION

The evaluation on authorizing it as engineering works inheritance establishes weight in beauty and friendly feeling particularly a technical aspect and the rarity and evaluates it[1]. I bring about the new viewpoint and sense of values for maintenance, the protection of the engineering works structure or a plan and the design by adopting the evaluation from an angle unlike these and think that how to catch may change.

BASIC RESEARCH

Using a dictionary and the Internet, we extracted expression of the Aji (quaint) to define the meaning of *quaint* in this study and performed a questionnaire survey for this with 73 subjects. As a result, Aji means a thing that brings back pleasant feelings or memories. We investigated this using the KJ method on 13 people to grasp what kind of object people felt quaint with.

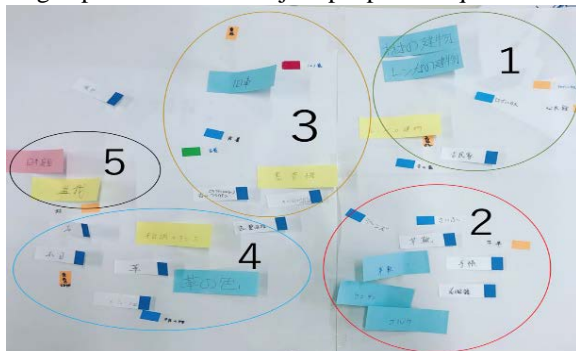


Figure 1 KJ method

The quaintness things could be grouped into 5 groups like figure.1 from KJ method. The targets were mostly in a room, that's why we choose space in a room.

NONFIGURATIVE QUAINT RESEARCH

We carried out the questionnaire survey by SD method on an imagined space for about 76 people who gave their impression on a space imagined freely by a subject. For statistical data, we performed analysis with probability distribution, factor analysis and co-occurrence network analysis. From the probability distribution, right and left came out symmetric which validated the data for all adjective. Showing an example table 1. A difference appeared in the space that felt quaint when we did probability distribution for each form of the room. Showing an example table 2.

Table 1 probability distribution

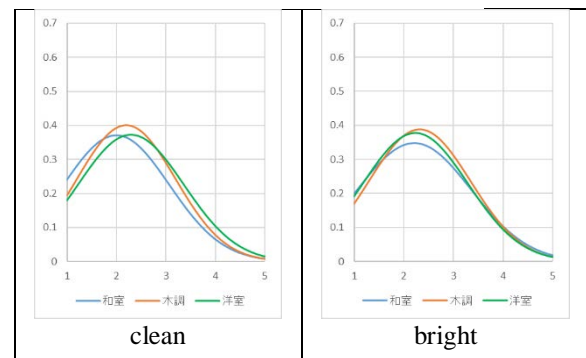
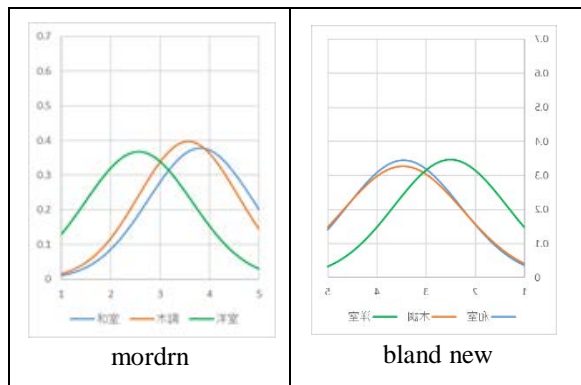


Table 2 Differences of probability distribution



An object and the relation of the form of the room were analyzed with co-occurrence network analysis. The relations with the object are the thinnest, and the Japanese-style room is considered to have an impression of being tidied up. This had the most number of the groups, and there were few strong ties. The Western-style room had least number of groups, and the ties in each group were stronger.

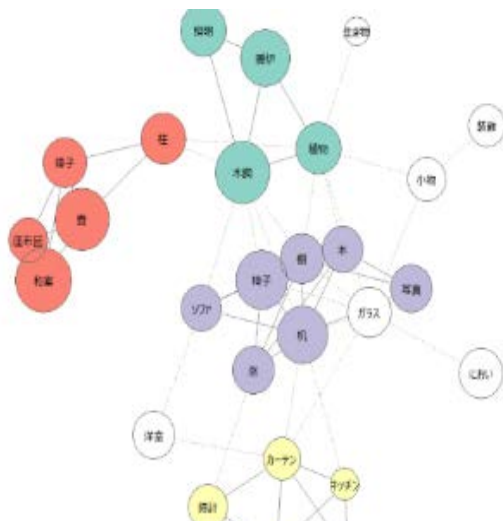


Figure 2 co-occurrence network

For the factor analysis, we got 4 factors to show in table 2. We interpret it as factor 1 and factor 2 are considered to be relatively easy to explain. Factor 1 interpreted as "refreshing" and "new construction", and factor 2 as "united feeling", "atmosphere that looked good". From the result of these analyses, we supposed imagined space. In this study we ignored the point less than 0.500.

Table 3 Factor Analysis

Factor	Adjective	point
Factor 1	Modern	0.610
	Brand new	0.651
	Bright	0.536
Factor 2	Clean	0.838
	Coherence	0.640
	Messy	0.677
Factor 3	Interesting	0.735
	Showy	0.412
	Unique	0.676
Factor 4	Comfortable	0.751
	Quietly	0.569
	Messy	0.406

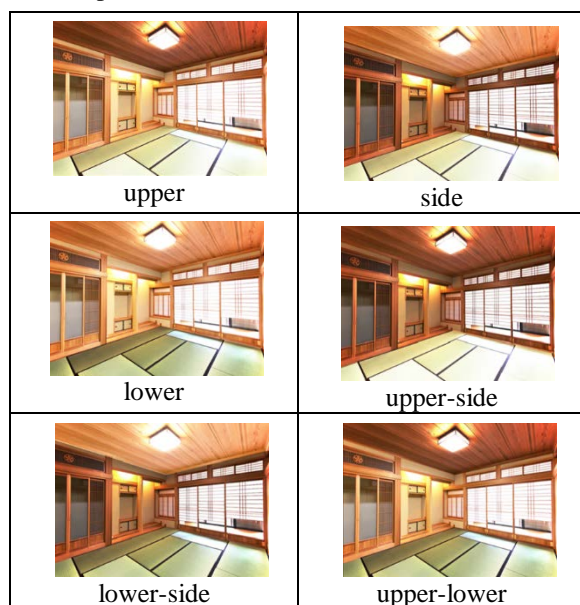
VISUALLY QUIANT RESEARCH

We evaluated the visually "quaint" feeling with nonfigurative research. We carried out two kinds of questionnaire surveys. One was evaluation by the pair comparison using four pictures (Table 4 pictures 1) where brightness and warmth were altered for 98 people. It turned out the picture that was made darker and warmer was considered the most quaint. The other evaluation was the six pictures method which altered the upper, lower, upper-side, lower-side etc., parts of a picture to warmer and/or darker (Table 5 pictures 2) [2]. As a result, a picture with many points that were edited were considered more quaint. Next, we examined the rank of the results, and it was revealed that the spot which ranked the highest was the upper-side part.

Table 4 pictures 1



Table 5 pictures 2



SUMMARY

From basic research, Aji means a thing that brings back pleasant feelings or memories. But in KJ method, no one mention feelings or memories. Everyone mentions a thing. We guess that they mention a thing with a itself background like a worn-out wallet.

From nonfigurative quaint research, In all adjectives that we used, we got the accuracy of data. In co-occurrence network, By the type of the rooms, a difference was greatly reflected on the relations with the thing. In the factor analysis, we got a factor of the abstract quaint.

From visually quaint research in that pictures, warmly-darkly is the best to feel quaint. Making a radar chart with the ranking and score. And make a line between 'upper-lower' and 'side' on figure 3. Left side of the line is easy to feel quaint. Right side is not important to feel quaint.

FUTURE ISSUE

In this study, we analyzed many aspects about "quaintness" and grasped the big picture regarding the what makes an image quaint. The object of the questionnaire is about 20 generations, and a result may change by the generation. Some disagreement occurred between *visually quaint* and *nonfigurative quaint* from the questionnaire. for example, figure 4 is showing probability distribution of "bright" and "warm". In this data, when people feel quaint, the space should be brightly and warmly. But compare with a result of visually quaint research, there is a disagreement about "bright". An imaged quaint space is bright. but darkly space is better than brightly space

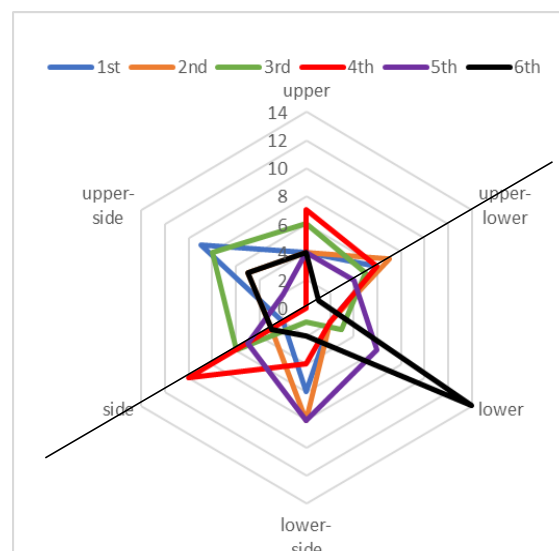


Figure 3 Rader chart

to feel quaint. We believe this is because we didn't quantify it. In addition, it is necessary to spread to municipal facilities, community spaces, and to investigate objects based on these results.

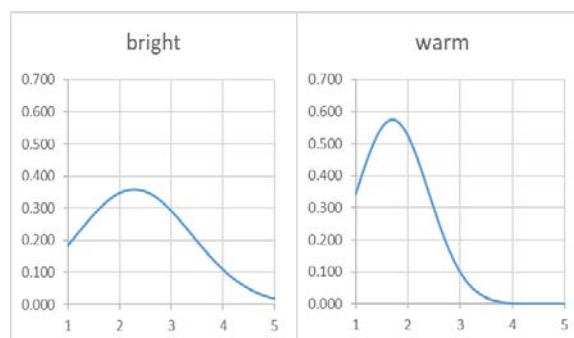


Figure 4 probability distribution

REFERENCE

- [1] 土木学会土木史研究委員会, 『日本の近代土木遺産(改定版)―現存する重要な土木構造物2800選』, 土木学会, 2005
- [2] P.シール, 船津孝行訳編『環境心理学6 環境研究の方法』誠信書房, 1975

SPATIAL CHARACTERISTICS OF FACTORS INFLUENCING THE OCCURRENCE AND SCALE OF MULTIPLE SLOPE FAILURES

Takashi Wada¹, Ryo Kodani², Hiroshi Miwa¹

¹ Department of Social Systems and Civil Engineering, Tottori University, Japan;

² Tottori City Office, Japan

ABSTRACT

In this study, we investigated the spatial characteristics of the factors influencing the occurrence and scale of multiple slope failures in areas with smaller grid sized than the unit size for the current emergency alert system for sediment disasters in Japan. We used high-resolution data for the spatial distribution of topography and rainfall. The study areas were located in southern Hiroshima Prefecture and southeastern Ehime Prefecture of Japan, where multiple slope failures occurred due to heavy rainfall in July 2018. With an increase in slope gradient, the frequency of smaller-scale slope failures increased significantly in southeastern Ehime Prefecture, whereas this tendency was not as noticeable in southern Hiroshima Prefecture. Larger-scale slope failures occurred at the same frequency on the area of mild (< 30 degree) and steep (≥ 30 degree) slope gradients. The reason for this is that the wide ranges of these slope failures expand to mild slopes closer to the mountain ridges. Total precipitation (i.e., long-term rainfall index) influenced the frequency of the occurrence of slope failure in southern Hiroshima Prefecture. Whereas, Maximum hourly precipitation (i.e., short-term rainfall index) related to the occurrence of slope failure in both study areas. Furthermore, we were able to estimate with a high possibility the occurrence of slope failure using a smaller grid size than the unit size for the current system, by combining the topographic indices (e.g., slope gradient) and rainfall indices (e.g., short- and long-term rainfall indices).

Keywords: Multiple slope failures, Slope gradient, Hourly precipitation, Total precipitation, GIS data

INTRODUCTION

Recently, the multiple sediment disasters, such as the disaster caused by the heavy rainfall due to the seasonal rain front and Typhoon Prapiroon in July 2018, have increased in Japan. Since the heavy rainfall occurred intensely and widely, and led to total precipitation of over 400 mm, it caused the serious sediment disasters in most part of Hiroshima and Ehime Prefectures [1], [2]. The unit size of the current emergency alert system for sediment disasters in Japan is too large (mainly a grid of 5 km) so that local inhabitants have difficulties in perceiving an increased possibility of nearby slope failure and sediment runoff by the emergency alert. Moreover, this unit size is not precise enough to consider local conditions of surface topography and precipitation, which may influence the occurrence of slope failures.

Considering the above-mentioned facts, it is necessary to establish an emergency alert system for sediment disasters on a smaller scale than that of the current system. Before a new system is implemented, it is necessary to investigate the spatial characteristics of local land factors (e.g., surface topography, geological features, land use conditions) and meteorological triggers (e.g., short- and long-term rainfall indices, wind direction), which can influence the occurrence and scale of slope failures on a smaller grid scale.

Iwahashi *et al.* [3] investigated the spatial

characteristics of long-term rainfall indices (e.g., total precipitation, daily precipitation) and local land factors in the areas with multiple slope failures in Japan using GIS data and aerial photographs. Their results indicated that the occurrence of slope failure and a slope gradients had a positive correlation. In addition, the occurrence of slope failure and long-term rainfall indices were also positively correlated. However, factors influencing the scale of slope failure have hardly been investigated in the previous studies.

It is widely accepted that high intensity and high duration rainfall events are the common important meteorological trigger for slope failures worldwide [4]. As such, in recent decades, several researchers have attempted to establish a rainfall-based alert system for sediment disasters [5]. In Japan, a rainfall-based alert system for sediment disasters in Japan uses a short-term rainfall index (e.g., hourly precipitation) and a long-term rainfall index (e.g., antecedent rainfall, precipitation for several days, soil water index) to determine the threshold for the occurrence of slope failure, the so-called critical line (CL) [6]. However, since these systems use the rainfall data obtained at the sparse observation points spatially, the space resolution of the rainfall data is low. Therefore, it is difficult to investigate the local relationships between the rainfall indices and the factors influencing an occurrence of a slope failure for small watersheds and districts. In addition, the

local land factors are not considered to determine the critical line (CL) for the occurrence of slope failure in these systems.

Herein, we investigate the spatial characteristics of the factors influencing the occurrence and scale of multiple slope failures caused by the heavy rainfall in July 2018. We scrutinize the characteristics on a smaller grid range than the one for the topographic and rainfall data used in the previous studies and the current alert system. For the study, the 10-m grid Digital Elevation Model (DEM) data provided by the Geospatial Information Authority of Japan and the 250-m grid rainfall data from the extended radar information network (XRAIN) in Japan were utilized. These data were converted to the 15-m grid DEM data and the 350-m grid rainfall data by averaging spatially these data.

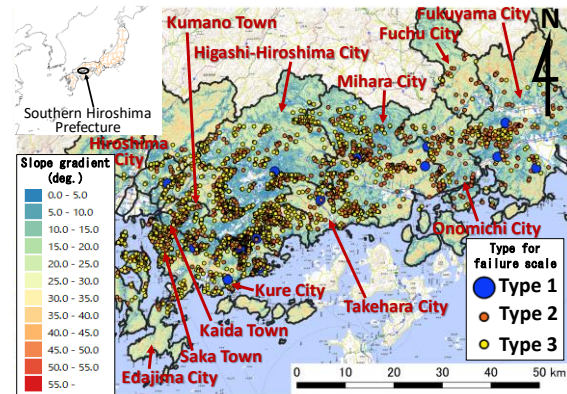
STUDY AREAS AND METHODS

Study area locations

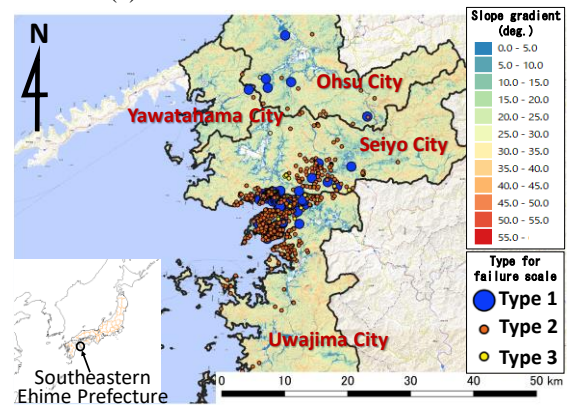
Southern Hiroshima Prefecture and southeastern Ehime Prefecture were selected as study areas. These areas are characterized by multiple slope failures that occurred by the heavy rainfall in July 2018 and led to the serious sediment disasters with many human damages. Fig. 1 shows the spatial distribution of slope failures obtained by the location data of them from the Geospatial Information Authority of Japan and slope gradients calculated by the 15-m grid DEM data in both study areas. The slope failures were classified using the methodology described below.

Classification of slope failures

We classified the slope failures surveyed by Sasahara *et al.* [2] (a total of 73 failures) into three scale types: large-scale failure (Type 1), small-scale failure (Type 2), and erosion of a mountain stream bed (Type 3). Table 1 shows a comparison of the field survey results with the estimated results obtained using the aerial photographs by the Geospatial Information Authority of Japan for each scale type of slope failure. The slope failures classification was based on the estimated failure volume, that is, a failure with over 1,000 m³ of the volume was classified as Type 1, a failure with under 1,000 m³ of the volume was classified as Type 2, and a sediment runoff with a negligible failure area at its upstream end was classified as Type 3. By investigating the scale and area of slope failure using the aerial photographs, it was estimated that they were positively correlated. On basis of the investigating results, the areas of slope failures of Types 1, 2 and 3 were defined as over 1,000 m², 100–1,000 m² and under 100 m², respectively. Therefore, we classified the other slope failures into three scale types with no field survey on basis of their failure areas estimated



(a) Southern Hiroshima Prefecture



(b) Southeastern Ehime Prefecture

Fig. 1 Spatial distribution of various slope failures caused by the heavy rainfall in July 2018 in two study areas.

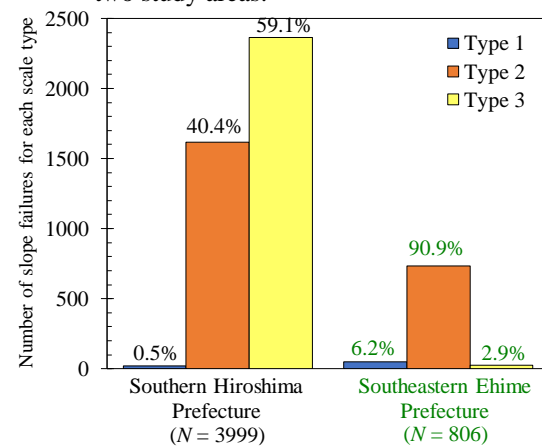

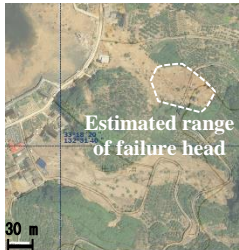

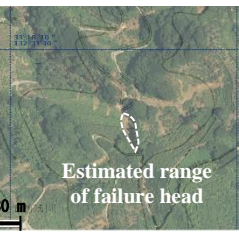

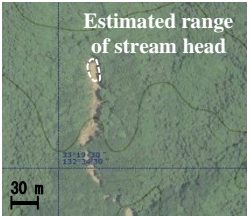


Fig. 2 Number and percentage of slope failures per each slope failure scale type.

by the aerial photographs in both study areas.

Fig. 1 shows the spatial distribution of all slope failure scale types in both study areas based on the classification method described above. Fig. 2 shows the number and percentage of slope failures for each scale type and study area. The failures of Type 3 were almost absent in southeastern Ehime Prefecture, whereas they were founded in abundance in southern Hiroshima Prefecture. The percentage of Type 1 failures to all other types of failures was higher in southeastern Ehime Prefecture than in southern

Table 1 An example of a comparison of the field survey results with the aerial photograph results for each slope failure scale type in southeastern Ehime Prefecture, Japan.

Scale type of slope failure	Field survey results by Sasahara <i>et al.</i> [2]	Estimated results by the aerial photographs after the disaster
Type 1 Large scale failure	<ul style="list-style-type: none"> · Failure depth; About 7.8 m · Failure width; About 45 m · Length of failure surface; About 75.5 m · Failure volume; About 26500 m³ 	<ul style="list-style-type: none"> · Failure head area; About 2200 m² 
Type 2 Small scale failure	<ul style="list-style-type: none"> · Failure depth; About 1.5 m · Failure width; About 5 m · Length of failure surface; About 40 m · Failure volume; About 300 m³ 	<ul style="list-style-type: none"> · Failure head area; About 100 m² 
Type 3 Erosion of mountain stream bed	<ul style="list-style-type: none"> · Erosion depth; About 2.5 m 	<ul style="list-style-type: none"> · Failure head area; About 80 m² 

Hiroshima Prefecture. These results indicate that various scale types of slope failures are predominant in some regions and are almost absent in other regions, despite being triggered by the same heavy rainfall. One possible reason for this is that their local land factors are different. As such, we investigated the spatial characteristics of topographic and rainfall indices, which influence the occurrence of these slope failures, and compared them between the study areas. Herein, the topographic indices were the slope gradient and slope-facing direction. The rainfall indices were the total precipitation and maximum hourly precipitation. Geological features, land use conditions and wind directions were not considered in this study because it was difficult to compare their influence on the occurrence of slope failures between two study areas by great difference between the characteristics of these factors in two study areas.

In order to investigate the effect of these indices on slope failure, considering the frequency of the index appearance in the study areas, we define the spatial frequency of slope failures for factor (F) using the following equation:

$$F = \sum A_f / \sum A \quad (1)$$

where, $\sum A_f$ is the total area of the target grids including slope failures; $\sum A$ is the total area of the target grids in the target range, including all of the municipalities where the slope failures occurred in July 2018. F_{gr} , F_{di} , F_{tp} and F_{hp} are the spatial

frequencies of slope failure for the slope gradient, slope-facing direction, total precipitation and maximum hourly precipitation, respectively.

RESULTS AND DISCUSSION

Occurrence and scale of slope failures vs. topographic indices

Fig. 3 shows the spatial frequency of slope failure for slope gradient F_{gr} for all slope failure scale types based on the 15-m grid-sized area. As slope gradient increases, the frequency of the Type 2 and 3 slope failure increases significantly in southeastern Ehime Prefecture, whereas this tendency is not as evident in southern Hiroshima Prefecture. We concluded that other indices, such as the geological feature (strongly weathered granite) and large total precipitation, influence the occurrence of slope failure in southern Hiroshima Prefecture. Larger-scale slope failures occurred at the same frequency on the area of mild (< 30 degree) and steep (≥ 30 degree) slope gradients. The reason for this is that the wide ranges of these slope failures expand to mild slopes closer to the mountain ridges. Accordingly, it is not necessarily to positively correlate a slope gradient to the occurrence of slope failure because this relationship is likely influenced by other factors (e.g., geological features, total precipitation). Therefore, we conducted an investigation on the spatial characteristics of the

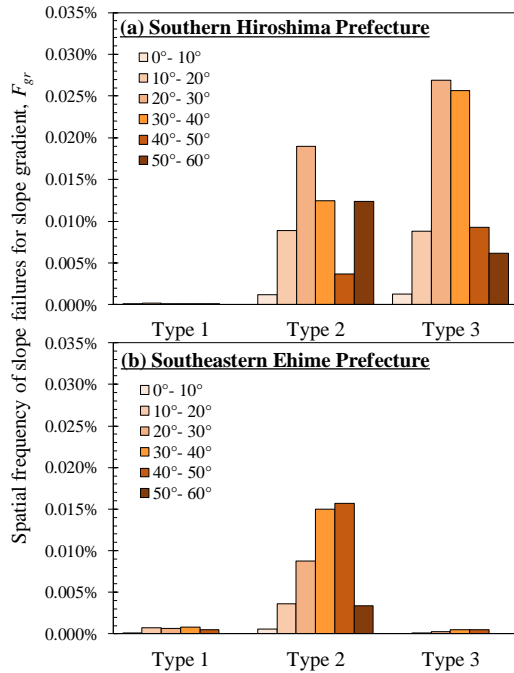


Fig. 3 Spatial frequency of slope failures for slope gradient (F_{gr}) for each slope failure scale type based on the 15-m grid-sized area.

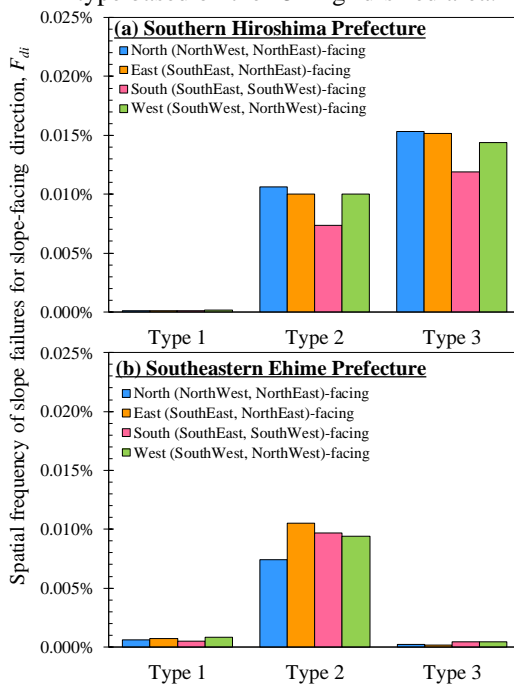


Fig. 4 Spatial frequency of slope failures for slope-facing direction (F_{di}) for each slope failure scale type based on the 15-m grid-sized area.

combined indices of local land factors and meteorological triggers, which influence the occurrence and scale of slope failures.

Fig. 4 shows the spatial frequency of slope failure for slope-facing direction F_{di} for each slope failure scale types based on the 15-m grid-sized area. F_{di} for all slope failure scale types are almost equal and the remarkable difference of F_{di} for each scale type is not

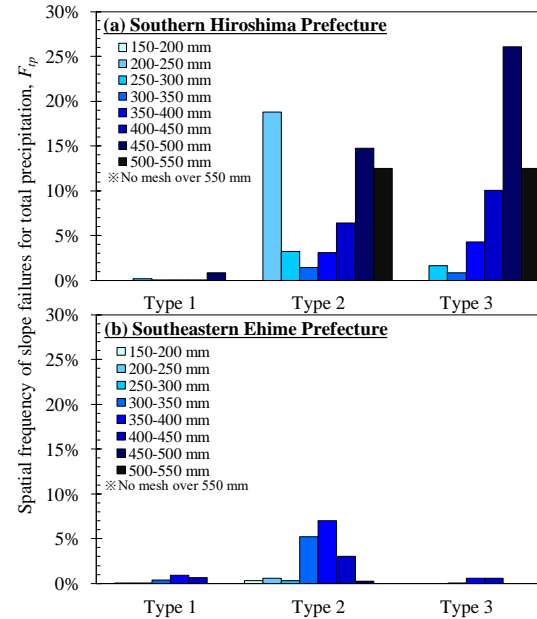


Fig. 5 Spatial frequency of slope failures for total precipitation (F_{tp}) for each slope failure scale type based on the 350-m grid-sized area.

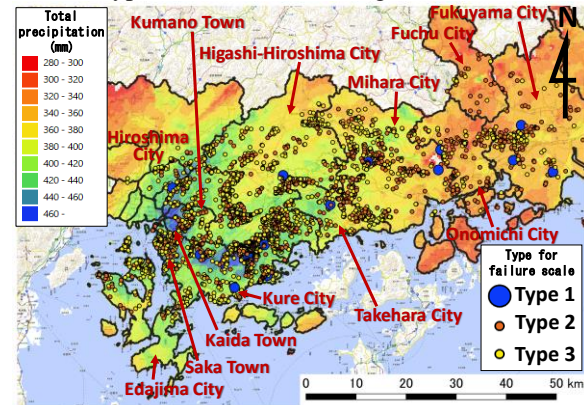


Fig. 6 Spatial distribution of slope failures for each slope failure scale type and total precipitation in southern Hiroshima Prefecture.

seen in each study area. This indicates that the occurrence of slope failure is unrelated to a slope-facing direction.

Occurrence and scale of slope failures vs. rainfall indices

Fig. 5 shows the spatial frequency of slope failures for total precipitation F_{tp} for all slope failure scale types based on the 350-m grid-sized area. In southern Hiroshima Prefecture, as total precipitation increases, the frequency of slope failure increases significantly. However, the frequency of slope failure for total precipitation range of 200–250 mm is relatively high due to the occurrence of slope failure in the limited small area of 200–250 mm of total precipitation. The special local land factor in this area may influence their occurrence and should be

investigated in future works. The frequency of slope failure is high ($> 10\%$) when total precipitation exceeds 450 mm, except the range of 200–250 mm. This is confirmed by overlapping of the high-density area of slope failure with the high total precipitation area in southern Hiroshima Prefecture (Fig. 6). However, in southeastern Ehime Prefecture, total precipitation and the frequency of slope failure are not correlated relatively.

Fig. 7 shows the spatial frequency of slope failure for maximum hourly precipitation F_{hp} for each slope failure scale type based on the 350-m grid-sized area. As maximum hourly precipitation increases, the frequency of slope failures increases in both study areas. Especially in southeastern Ehime Prefecture, the frequency of slope failures is high ($> 20\%$) when maximum hourly precipitation exceeds 80 mm/hr. This is confirmed by overlapping of the high-density area of slope failure with the high maximum hourly precipitation area in southeastern Ehime Prefecture (Fig. 8).

These results indicate that the occurrence and scale of typical slope failures depend on the rainfall indices with a different manner in each study area. Total precipitation (i.e., long-term rainfall index) is predominantly responsible for slope failure in southern Hiroshima Prefecture, whereas maximum hourly precipitation (i.e., short-term rainfall index) affects slope failure in both study areas. The study results also show that the 350-m grid-sized XRAIN data for the rainfall index lead to a high possibility of estimating the occurrence of slope failure in the grid-sized area.

Occurrence of slope failures and combined indices of local land factors and meteorological triggers

Table 2 shows the spatial frequency matrix of slope failures for all slope failure scale types and the combined indices of local land factors and meteorological triggers based on the 15-m grid-sized area. Using all 15-m grid DEM data without narrowing by any rainfall indices, the spatial frequencies of slope failures for various slope gradients (F_{gr}) in both study areas equal only 0.046% and 0.017% at most, respectively. However, as the maximum hourly precipitation and the total precipitation increase, F_{gr} for all slope gradients increases more in both study areas. As mentioned above, the rainfall indices that influence F_{gr} remarkably are different in each study area. In southern Hiroshima Prefecture, when a slope gradient ranges between 30° and 40° and total precipitation is over 450 mm, F_{gr} equals 0.249%, which is approximately 6.5 times higher than that without narrowing by any rainfall indices. In southeastern area Ehime Prefecture, when the slope gradient ranges between 30° and 40° and maximum hourly precipitation is over 90 mm/hr, F_{gr} equals 0.306%,

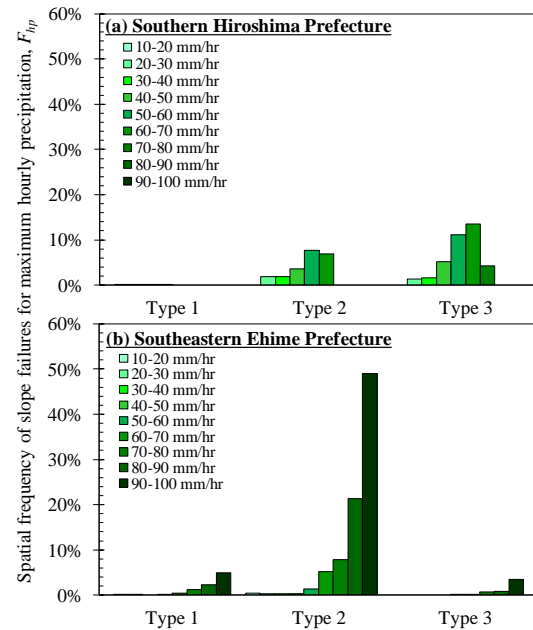


Fig. 7 Spatial frequency of slope failures for maximum hourly precipitation (F_{hp}) for each slope failure scale type based on the 350-m grid-sized area.

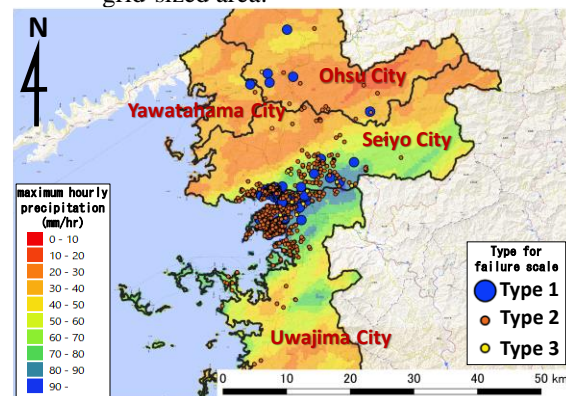


Fig. 8 Spatial distribution of slope failures for each slope failure scale type and maximum hourly precipitation in southeastern Ehime Prefecture.

which is approximately 18 times higher than that without narrowing by any rainfall indices. As a result, by combining the topographic and rainfall indices, we may be able to estimate with a high possibility the occurrence of slope failure using a smaller grid size than the unit size for the current system.

CONCLUSIONS

In this study, we used high-resolution data obtained from two areas in Japan to reveal the spatial characteristics of the topographic and rainfall indices influencing the occurrence and scale of multiple slope failures caused by the heavy rainfall in July 2018 in areas with smaller grid sized than the unit size for the current emergency alert system for sediment disasters in Japan.

Table 2 Spatial frequency matrix of slope failures for all slope failure scale types for a slope gradient and rainfall indices. The purple, red, orange, yellow and cream cell colors equal $> 0.3\%$, $> 0.2\%$, $> 0.1\%$, $> 0.05\%$ and $> 0.01\%$.

Slope gradient Rainfall index		Southern Hiroshima Prefecture						Southeastern Ehime Prefecture					
		0°- 10°	10°- 20°	20°- 30°	30°- 40°	40°- 50°	50°- 60°	0°- 10°	10°- 20°	20°- 30°	30°- 40°	40°- 50°	50°- 60°
Total precipitation	All data (Over 0 mm)	0.0026%	0.0179%	0.0459%	0.0382%	0.0131%	0.0186%	0.0007%	0.0045%	0.0096%	0.0163%	0.0167%	0.0034%
	Over 300 mm	0.0026%	0.0180%	0.0465%	0.0386%	0.0132%	0.0189%	0.0011%	0.0082%	0.0182%	0.0297%	0.0297%	0.0071%
	Over 400 mm	0.0037%	0.0404%	0.1027%	0.1002%	0.0512%	0.0565%	0.0014%	0.0032%	0.0075%	0.0102%	0.0133%	0.0000%
	Over 450 mm	0.0043%	0.0732%	0.1888%	0.2490%	0.1928%	0.0000%	0.0000%	0.0000%	0.0010%	0.0000%	0.0000%	0.0000%
Maximum hourly precipitation	All data (Over 0 mm/hr)	0.0026%	0.0179%	0.0459%	0.0382%	0.0131%	0.0186%	0.0007%	0.0045%	0.0096%	0.0163%	0.0167%	0.0034%
	Over 30 mm/hr	0.0029%	0.0214%	0.0561%	0.0489%	0.0181%	0.0203%	0.0031%	0.0184%	0.0389%	0.0629%	0.0602%	0.0127%
	Over 60 mm/hr	0.0032%	0.0369%	0.0859%	0.1203%	0.0824%	0.1057%	0.0050%	0.0426%	0.1122%	0.1969%	0.1961%	0.0473%
	Over 90 mm/hr	No rainfall data						0.0186%	0.1392%	0.2255%	0.3060%	0.1517%	0.0000%

The occurrence and scale of typical slope failures depend on a slope gradient and total precipitation (i.e., long-term rainfall index) with a different manner in each study area and can be influenced by other factors, such as geological features. Whereas maximum hourly precipitation (i.e., short-term rainfall index) affects slope failure in both study areas.

We investigated the spatial frequency of slope failure for all slope failure scale types by combining the topographic and rainfall indices, which influence the occurrence and scale of slope failure. The results indicate that there is a high possibility to estimate the occurrence of slope failure by combining these indices using a smaller grid size than the unit size for the current system.

Geological features and land use conditions were not considered herein. Therefore, it is necessary to evaluate the spatial frequency of slope failure based on these indices in both study areas in a future project. It is also essential to estimate temporal changes in the short-term and long-term rainfall indices for each topographic index in areas with the smaller grid than the unit size for the current system, in order to estimate the occurrence and scale of slope failure spatially and time-variably. Furthermore, the proposed methodology has to be verified by applying it in areas with other multiple slope failures.

ACKNOWLEDGMENTS

The field survey results used in our study is provided by the survey group of Japan Society of Erosion Control Engineering for the sediment disaster in Shikoku region caused by “Heavy Rain Event of July 2018”. The XRAIN dataset used in our study is provided by the Ministry of Land, Infrastructure, Transport and Tourism (MLIT) of Japan, and this dataset is archived and provided under the framework of the Data Integration and Analysis System (DIAS) funded by Ministry of Education, Culture, Sports, Science and Technology (MEXT) of Japan.

REFERENCES

- [1] Kaibori M., Hasegawa Y., Yamashita Y., Sakida H., Nakai S., Kuwada S., Hiramatsu S., Jitousono T., Irasawa M., Shimizu O., Imaizumi F., Nakatani K., Kashiwabara Y., Kato N., Torita E., Hirakawa Y., Yoshinaga S., Tanaka K. and Hayashi S., Sediment related disaster due to heavy rainfall in Hiroshima Prefecture in July, 2018, Journal of the Japan Society of Erosion Control Engineering, Vol.71, No.4, 2018, pp. 49–60. (in Japanese with English abstract)
- [2] Sasahara K., Ikeda T., Iwai Y., Kakuta K., Kanazawa A., Gonda Y., Saitou Y., Shuin Y., Tagata S., Fujita M., Miyata S., Miwa H., Murata I., Yamanoi K. and Wada T., Sediment Disasters in Shikoku Region in July, 2018, Journal of the Japan Society of Erosion Control Engineering, Vol.71, No.5, 2019, pp. 43–53. (in Japanese with English abstract)
- [3] Iwahashi J., Yamagishi H., Kamiya I. and Sato H., Discriminant Analysis for Landslides Caused by the 2004 Niigata Heavy Rainfall in July and the Mid Niigata Prefecture Earthquake in October, Journal of the Japan Landslide Society, Vol.45, No.1, 2008, pp. 1–12. (in Japanese with English abstract)
- [4] Wieczorek G. F., Landslides triggering mechanisms, In: Turner K. and Schuster R. L. (Eds.), Landslides: Investigation and Mitigation, National Research Council, Transportation Research Board, Washington, 1996, pp. 76–90.
- [5] Wieczorek G. F. and Glade T., Climatic Factors Influencing Occurrence of Debris Flows, In: Jakob, M. and Hunger, O. (Eds.), Debris-flow Hazards and Related Phenomena, Praxis, Springer, Berlin, 2005, pp. 325–362.
- [6] Osanai, N., Shimizu, T., Kuramoto, K., Kojima, S., and Noro, T. (2010): Japanese early-warning for debris flows and slope failures using rainfall indices with Radial Basis Function Network, Landslides, Vol. 7, pp. 325–338.

SPATIAL ENTRAPMENT OF WOMEN WORKERS IN METROPOLITAN AREAS

Putri Halimah¹, Chotib²

^{1,2}School of Strategic and Global Studies, University of Indonesia, Indonesia

ABSTRACT

Intercity integration in a metropolitan area forms a unified city that is interconnected like a mutualism symbiosis. Metropolitan areas provide opportunities for people between regions or between cities to connect with each other by doing non-permanent mobility. The purpose of this study is to identify how much potentially women are trapped spatially than men in some metropolitan areas in Indonesia. Spatial Entrapment is a condition that is more common in women who trip in shorter distance and times during commuting between place of residence and place of work. This study uses micro data from the 2018 National Labor Force Survey (SAKERNAS), which the survey was conducted by Indonesian Central Bureau of Statistics (BPS). The research approach is quantitative by using descriptive analysis to see the relationship between the independent variable and the dependent variable through bivariate cross tabulation analysis and graphics. Then, inferential analysis is used to determine the effect of independent variables on dependent variables inferentially. The inferential analysis model used in this study is multinomial logistics regression.

Keywords: Spatial entrapment, work trip, job mobility, gender gap, women workers

INTRODUCTION

In many developing countries, migration from rural areas to urban areas because of the necessity to improve better life. Urban areas offer classier education, better social services, also better jobs. Gradually, urban areas are transformed into metropolitan areas. Within metropolitan areas, human mobility in terms of work happens quickly and easily which is supported by infrastructure progress. It increases of women labor market and advances dual career household. Naturally, this condition changes the social theory in the traditional society about men-breadwinner and women-homemaker [1].

This paper analyzes spatial entrapment of women's work trip in a household. Spatial entrapment is a condition where women's work trip shorter than men in distance and time [2]. Women tend to experience unwell-being in job mobility, because they prefer to get low wages than having travel further [3]. Spatial entrapment can prevent workers from getting jobs better, or limit them at lower paying jobs [4].

Another approaches argues that women's shorter work trip because of their role as a mother [2], [5]. The presence of children in the household also contributes to the reduction in income from trips attended by women [6], and also reduce a women's work trip but not a man's [7]. Some researchers find that occupational or industrial segmentation is a reason why women's work trip shorter. In metropolitan cities, labor market competition is fierce, for entering labor market women's skill are needed [8]. It means, high educated women are more wanted. Then, work trip cost becomes an increasing expenditure for them [9].

Based on that urban phenomenon, we research in three metropolitan areas in Sumatera Island, Indonesia. They are Mebidangro (Medan, Binjai, Deliserdang, Karo); Palapa (Padang, Lubuk Alung, Pariaman); and Patung Raya Agung (Palembang, Banyuasin, Ogan Ilir, Ogan Komering Ilir). This paper highlights the problem of spatial entrapment on dual career households with dependent variables are distance and time work trip. While, independent variables are income, age, education, working status, and transportation. To examine spatial entrapment, we use multinomial logit regression by SPSS 26. Data for the study is derived from raw data of National Labor Force Survey (SAKERNAS) 2018, Central Bureau of Statistics. The advantage of this study is knowing the factors that influence the movement of women workers. So, in the future, stake holder will be able to plan urban development in terms of transportation, wages and labor policies that provide more comfortable, safe and fair space for women workers. The limitations of this study are limited in the metropolitan area of the Sumatra Island, and the variables used are also still limited.

LITERATURE REVIEW

Research on gender relations and spatial space has provided important information about the mobility of women workers. Research continues to develop in highlighting it so that a "spatial entrapment" thesis emerges. The thesis shows the limitations of the labor market and women's journey to work. Since the 1970s, researchers have found various case related to the relationship between travel behavior and gender.

Women have shorter distance and time of travel [10]. The differences of gender show that work trip depends on where women work and live [3]. This difference is due to the activities carried out by women, their dual roles as mothers and money-earners. They are segmented in local labor markets [11]. Women have no choice to get better job away from home, or women's experiences are limited in a work career compared to his male counterparts in the industries.

On the other hand, because the labor market is indeed limited. when women try to enter the labor market and fix things that give disadvantages for women economically. First, it is about wages that discriminate against women. The discriminatory wage structure is triggered by the demand for labor in the company is smaller, but the more offer by women workers in certain sectors [12]. Although, workers are homogeneous theoretically, many industries hypothesize that women and men workers are totally different. Some industries provide low-wage, predominately female-dominated jobs. They hire women workers around the residents with a preference for women in mobility and limited skills have shown the entrapment of working by segmentation of local labor market.

Women workers reduce the time of work trip because of their household responsibilities and the concentration of jobs in suburban areas [7]. Wheatley [5] describes about school-age children reflect the time or schedule of school will be entrapping women spatially, even highly skilled. The presence of children was significant for entrapping women worker. McQuaid and Chen [6] explain that women with two or three children will have work trip shorter. The age of the youngest child influences it, where the older the child, the less of traveling 30 min or more. Rapino [2] shows gender roles are significant in women's spatial entrapment. For married women, decreased of work trip time about 3% if having children under the age of five, decreased of work trip time about 11.5% if having children having children more than the age of five, and decreased of work trip about 5% if having no children in comparison with married men. Madden [3] explains that work trip lengths would be longer if women had the same job tenure, same wages, and same work hours.

Men have higher mobility in each marital status, single or married. Interestingly, married men will have higher mobility compared to unmarried women [13]. In the United Kingdom, Spain, and Australia, the proportion of total work time in mobility is twice

more than women. While women do not experience spatial entrapment in Finland [14]. Other studies show there are no systematic differences between men and women moving towards larger companies when looking at potential experience, years of work, education, and working status, and only a few minor differences for some sectors, company age and part-time status [15]. Another study indicates that gender equality in work hours and in wage will make as long as work trip between women and men, or women's will be longer [3]. Gender work trip gap based on the differences in jobs status and wage, where bigger household responsibility does not indicate women's length of the work trip become shorter [16]. It supports another study that female workers have a relatively long work trip and that the presence of adults or other children in the household does not reduce women's work trip [17].

Gender also influence to work trip time and accessibility of workers. According to the study, women tend to spend more time on their commuting and have a more limited spatial range in urban areas compared to men. Mostly, women depend on public transportation as the main mode of transportation [18], [19]. Transportation has the largest direct effect on the time of workers' trip so that people with private transportation (drive own cars) has significantly shorter work trip times than those who use public transportation. There is reducing the gender difference in work trip time because men and women equally use public transportation. On the other hand, in the suburbs where transit hub design that connects people to the place practically does not exist. It causes workers to have to drive for work, and women do not have access to it [20].

METHODS

This research uses a quantitative approach to identify spatial entrapment of women worker mobility in a household. We present descriptive analyses by cross tabulation method, and inferential analysis by multinomial logistic regression method. This study uses the micro data from National Labor Force Survey (SAKERNAS) 2018, Central Bureau of Statistics. We research in three metropolitan areas in Sumatera Island, Indonesia. They are Mebidangro (Medan, Binjai, Deliserdang, Karo); Palapa (Padang, Lubuk Alung, Pariaman);, and Patung Raya Agung (Palembang, Banyuasin, Ogan Ilir, Ogan Komering Ilir). The number of samples represented was 3.637 households. Dependent variables and independent variables category are below.

Table 1 The Category of Dependent Variables and Independent Variables

Dependent Variables	Category
Distance (dist)	1. Men > Women 2. Men < Women 3. Men = Women
Time (time)	1. Men > Women 2. Men < Women 3. Men = Women
Independent Variables	Category
Income (inc)	1. Men > Women 2. Men < Women 3. Men = Women
Education (educ)	1. Men > Women 2. Men < Women 3. Men = Women
Age (age)	1. Men > Women 2. Men < Women 3. Men = Women
Women work status (workstat)	1. Formal 2. Informal
Women Mode of transportation (trasnp)	1. Public transportation 3. Private transportation 4. Others

Research Model

Multinomial logistic regression analysis method is an analysis method that represents the relationship between qualitative or categorical response variables (more than 2 categories) with one or several independent variables. Research using this analytical method because the independent variables and the categorical independent variables are very suitable to be used to see the independent variables on the accepted variables. The model used in this study is as follows. Logit function from the differences of distance and time work trip between men and women consists of:

i. Logit function for $Y = 1$ relative to logit function for $Y = 3$

$$\ln \left[\frac{P(Y=1|x)}{P(Y=3|x)} \right] = \beta_{10} + \beta_{11} \text{inc1} + \beta_{12} \text{inc2} + \beta_{13} \text{age1} + \beta_{14} \text{age2} + \beta_{15} \text{educ1} + \beta_{16} \text{educ2} + \beta_{17} \text{workstat1} + \beta_{18} \text{transp1} + \beta_{19} \text{transp2} + \varepsilon \quad (1)$$

ii. Logit function for $Y = 2$ relative to logit function for $Y = 3$

$$\ln \left[\frac{P(Y=2|x)}{P(Y=3|x)} \right] = \beta_{20} + \beta_{21} \text{inc1} + \beta_{22} \text{inc2} + \beta_{23} \text{age1} + \beta_{24} \text{age2} + \beta_{25} \text{educ1} + \beta_{26} \text{educ2} + \beta_{27} \text{workstat1} + \beta_{28} \text{transp1} + \beta_{29} \text{transp2} + \varepsilon \quad (2)$$

Category $Y=3$ is the comparison. The value of probability is obtained from the logistic function of the logit model of the dichotomy above. Thus the probability values for each category are:

$p_1 = pr(Y=1 / x) = \left[\frac{e^{z_1}}{1 + e^{z_1} + e^{z_2}} \right]$; probability of man's distance and time are more than women

$p_2 = pr(Y=2 / x) = \left[\frac{e^{z_2}}{1 + e^{z_1} + e^{z_2}} \right]$; probability of man's distance and time are less than women

$p_3 = pr(Y=3 / x) = \left[\frac{1}{1 + e^{z_1} + e^{z_2}} \right]$; probability of men's and women's are equal

RESULTS

In the model significance test, the value of the final intercept is 0.00, meaning that at least one independent variable influences the dependent variable significantly. Partial test results show that income, women work status, and mode of transportation significantly influence the distance and time of work of women. In the R^2 coefficient, Nagelkerke's value is 0.638 for distance and 0.625 for time, meaning that the variability of the independent variable explains 63.8% of the distance variable, and 62,5% of the time variable.

Table 2 in below shows the descriptive analysis results of relationship between independent variable and dependent variable (distances). We can see that men's wage more than women's trigger men's work trip distance longer 66,1%. While, when women's wage more than men's wage only 34,9% cause women's work trip distance longer. Then, when there is an equality wages between women and men conclude an equality distance about 76,4%.

Table 2 Descriptive Analysis Results between Independent Variables and Dependent Variable (Distances)

Independent Variable		Men > Women	Men < Women	Men = Women
Income	Men > Women	66,1%	4,6%	29,3%
	Men < Women	23,8%	34,9%	41,3%
	Men = Women	19,6%	4,0%	76,4%
Education	Men > Women	49,2%	6,3%	44,5%
	Men < Women	41,1%	12,6%	46,3%
	Men = Women	46,9%	7,4%	45,8%
Age	Men > Women	46,2%	8,0%	45,8%
	Men < Women	44,9%	10,8%	44,4%
	Men = Women	47,5%	7,6%	44,9%
Women's work status	Formal	22,6%	29,7%	47,7%
	Informal	50,9%	4,0%	45,2%
Women's mode transportation	Public	6,7%	80,5%	12,9%
	Private	2,0%	21,3%	2,7%
	Others	2,4%	42,8%	12,1%

In education we can see that the higher women's education will make the higher distance (12,6%) or same distance (46,3%) of women's work trip. On the other hand, there is not significantly different about age for women's work trip distance. Informal work status for women make a gender gap for distance, it is about 50,9%. Then, formal work status gives the longer distance for women about 29,7%. The last is about mode of transportation. Mostly, women workers use public transportation for going through longer distance.

Table 3 Descriptive Analysis Results between Independent Variables and Dependent Variable (Times)

Independent Variable		Men > Women n	Men < Women n	Men = Women n
Income	Men > Women	65,3%	4,6%	30,0%
	Men < Women	23,6%	33,0%	43,4%
	Men = Women	19,4%	4,4%	76,2%
	Men > Women	48,3%	6,6%	45,1%
Education	Men < Women	40,8%	12,4%	46,8%
	Men = Women	46,4%	7,1%	46,5%
	Men > Women	45,7%	7,8%	46,5%
	Men < Women	44,1%	10,5%	45,4%
Age	Men = Women	47,9%	8,0%	44,1%
	Formal	22,1%	27,9%	50,0%
	Informal	50,4%	4,2%	45,5%
	Public	6,6%	80,3%	13,1%
Women's mode transportation	Private	1,7%	20,0%	3,1%
	Others	2,6%	43,5%	11,8%

Based on table 3 we can see how independent variables influence dependent variables (times). Income, work status, and mode of transportation present significantly value. Women's work trip times will be longer than men are caused by getting more income (33%), formal work status (27,9%), and public transportation (80,3%). Although the higher education women have able to increase the times of working (12,4%), but men's time still longer (40,8%). Likewise, the age shows less effect for women times.

Table 4 in below shows the results of multinomial logistic regression analysis for the distances. The tendency of women with higher incomes to travel farther is 6,280 times greater. That is, when men's income is higher in the household, women are 3.473 times more likely to be spatially trapped in distance. Then, formal work is also able to provide encouragement to women to make further

work trips by 13,345 times. While other variables with significant influence do not show too high a gap.

Table 4 Multinomial Logistic Regression Analysis (Distances)

Parameter Estimates						
Distance	Men > Women			Men < Women		
	B	Std. Error	Exp(B)	B	Std. Error	Exp(B)
Income						
Men > Women	1,922	0,118	6,836***	0,808	0,219	2,244***
men < women	1,245	0,179	3,472***	1,837	0,225	6,280***
Education						
Men > Women	0,074	0,116	1,077	-0,271	0,202	0,762
men < women	-0,109	0,119	0,897	0,07	0,183	1,073
Age						
Men > Women	0,06	0,181	1,062	0,048	0,307	1,049
men < women	-0,066	0,223	0,936	-0,038	0,372	0,962
Women's work status						
Formal	-2,194	0,135	0,111***	2,591	0,244	13,345***
Women's mode of transportation						
Public	0,639	0,241	1,895**	0,634	0,614	1,885
Private	0,438	0,126	1,550***	0,097	0,424	1,102

) significant at 5% * significant at 1%

Table 5 Multinomial Logistic Regression Analysis (Times)

Parameter Estimates						
Times	Men > Women			Men < Women		
	B	Std. Error	Exp(B)	B	Std. Error	Exp(B)
Income						
men > women	1,851	0,116	6,368***	0,716	0,214	2,047***
men < women	1,202	0,178	3,326***	1,694	0,221	5,443***
Education						
men > women	0,040	0,115	1,041	-	0,195	0,887
men < women	-0,092	0,118	0,912	0,154	0,181	1,167
Age						
men > women	-0,009	0,181	0,991	-	0,295	0,929
men < women	-0,151	0,222	0,860	-	0,361	0,884
Women's worker status						
Formal	-2,220	0,135	0,109***	2,310	0,229	10,070***
Women's mode of transportation						
Public	0,511	0,238	1,666**	0,201	0,619	1,223
Private	0,351	0,126	1,421**	-	0,402	0,819
				0,199		

) significant at 5% * significant at 1%

Table 5 in above shows the results of multinomial logistic regression analysis for the time. The result shows the similarity to the previous one. Income or wage influence women's work trip in time. The higher income, the longer time of women's work trip.

Even so, women with higher incomes will still be trapped in travel time. Because, when a man's income rises, he has 6,368 times the opportunity to increase his travel time, and women is 5,443 times. Likewise, with formal employment status can increase women's travel time 10,070 times longer. While other variables do not provide a significant difference in numbers.

DISCUSSION

The city center becomes a magnet for people in the surrounding area to come to cities with the aim of improving the economy, because in the city center there are various industries, offices, businesses and trade. The location theory pioneered by Von Thunen states that the main factor that determines location selection (land use) is the land rent / purchase price. This urban transformation will form a pattern of the existence of a core city as a center of urban activity in the economic, administrative, political, and the existence of satellite cities as a buffer in providing space for abundance of activities in the core city, such as more affordable housing [21].

Movement of people from villages to cities or between cities is common today. Progress in the construction of facilities and infrastructure that support the need for transportation causes the pattern of human movement to be faster and integrated. Mobility or human movement that occurs continuously is a modern phenomenon that occurs in urban areas, especially in metropolitan cities, industrial sites, offices, and businesses are concentrated there. The large number of industries and businesses makes the demand in the labor market increase, thus attracting individuals to do work by commuting, not only from villages to cities but also to travel long distances between cities [22].

Various theories regarding the development of urban structures which state that the city center or central business district (CBD) will experience development until it reaches the periphery that converts agricultural land into residential land for workers. The CBD area offers broader employment opportunities with higher incomes, and the sub-urban area offers the availability of settlements at affordable prices. The existence of cohesiveness between urban areas will certainly affect the pattern of movement of travel (mobility) of the community, because there will be workers from suburban areas who come to do job mobility. Demographic, social and economic characteristics have an influence on a person's mobility patterns. The demographic characteristics of the sexes show that compared to men, women tend to

experience inequality in mobility, because they prefer to get wages below the average, rather than choosing to travel further [6].

According to the results in this study, independent variables such as income or wages, women's work status, and mode of transportation influence the pattern of women's mobility significantly. The higher wages, formal work status, and using public transportation increase women's work trip in distance and time. However, women workers are not used to using private transportation because of limitation of ability in having own cars and drive it. In Indonesia, car have a similarity price with house. This research support previous research that state women more trapped spatially than men in distance and also time of working trip. Others independent variables, age and education does not influence significantly for women's worker mobility.

It shows that metropolitan areas in Sumatera Island describe a gender gap, inequality for participate in labor market. Gap of wages between men and women has a domino effect on the economy indirectly. women with low wages are unable to compete with male workers. even though they are able to increase company productivity. dependence on public transportation makes women trapped in work that only has access to the transit hub. they cannot work for long distances and long periods of time if there is no access to public transportation. therefore, transportation facilities in metropolitan cities need to be improved, such as the use of LRT. However, Palembang Cities has LRT transportation in in the city, but the transportation network has not been connected to the suburbs. Mostly, workers use traditional transportation such as tugboat to down the river, or buses to get to where they work.

CONCLUSIONS

Research findings show spatial entrapment in women workers are caused by income, women work status, and mode of transportation. Men's wage more than women's trigger men's work trip distance longer 66,1%. While, when women's wage more than men's wage only 34,9% cause women's work trip distance longer. Then, when there is an equality wages between women and men conclude an equality distance about 76,4%. Women's informal work status causes 50,9% men's distance work trip be longer. And 80,5% using for public transportation cause women's work trip in distance longer. Same as the length of work trip, wages, work status, and mode transportation influence how far women's go to work.

To overcome spatial entrapment in metropolitan areas in Sumatera Island, it needs cooperation from various sectors, such as governments, companies, and other stakeholders in determining wage eligibility for women workers, increasing transit hubs for public transportation networks, and a labor market that is wide open and fair for women.

ACKNOWLEDGMENTS

This paper is part of University of Indonesia Research Grant 2020: Social-Humanities International Indexed Publications (Q4).

REFERENCES

- [1] Lewis, J. (2001) The decline of the male breadwinner model: the implications for work and care. *Social Politics*, 8,2,152–70.
- [2] Rapino, M. A. (2008). Gender Roles and Spatial Entrapment. A Dissertation Doctor of Philosophy at the University of Connecticut.
- [3] Madden, Janice F. 1981. Why women work closer to home. *Urban Studies* 18, 2: 181-94.
- [4] Castree, N., Kitchin, R. & Rogers, A. (Eds.). (2013). *A Dictionary of Human Geography*. Oxford, United Kingdom: Oxford University Press.
- [5] Wheatley, D. (2013). Location, Vocation, Location? Spatial Entrapment among Women in Dual Career Households. *Gender, Work & Organization*, n/a-n/a. doi:10.1111/gwao.12005
- [6] McQuaid, Ronald W dan Tao Chen. (2019) . Commuting times: The Role of Gender, Children and Part-Time Work. *Research in Transportation Economics*, 34, 66-73
- [7] Singell, Larry D. and Jane H. Lilleydahl. 1986. "An empirical analysis of the commute to work patterns of males and females in two-earner households." *Urban Studies* 2: 119-129.
- [8] Hanson, S. and G. Pratt. 1992. Dynamic dependencies: a geographic investigation of local labor markets. *Economic Geography* 68: 373-405.
- [9] MacDonald, Heather and Alan Peters. 1994a. "Rural women in a restructuring economy: work and commuting in Eastern Iowa." *Economic Development Quarterly* 8: 171-185.
- [10] White, M.J. (1977), "A model of residential location choice and commuting by men and women workers", *Journal of Regional Science*, Vol. 17, pp. 41–52.
- [11] Hanson, S. and G. Pratt. 1988. "Reconceptualizing the Link Between Home and Work in Urban Geography", *Economic Geography*, 4: 299-321.
- [12] Jonung, C. (1998). Women's work and wages : A selection of papers from the 15th arne ryde symposium on economics of gender and family in honor of anna bugge and knut wicksell.
- [13] Warsida, R. Y., Adioetomo, S. M., & Pardede, E. L. (2013). The Effect of Socio-Demographic Variables on Commuting in Jabodetabek. *Jpournal of Economics and Development Indonesia*, 13, 159-176.
- [14] Craig, L., & van Tienoven, T. P. (2019). Gender, mobility and parental shares of daily travel with and for children: a cross-national time use comparison. *Journal of Transport Geography*, 76, 93-102.
- [15] Del Bono, E., & Vuri, D. (2011). Job mobility and the gender wage gap in Italy. *Labour Economics*, 18(1), 130-142.
- [16] Kimbrough, G. (2016). What Drives Gender Differences in Commuting. Unpublished Manuscript
- [17] England, K. V. L. (1993). Suburban Pink Collar Ghettos: The Spatial Entrapment of Women? *Annals of the Association of American Geographers*, 83, 225-242.
- [18] Kwan, M.-P. (1999). Gender and Individual Access to Urban Opportunities: A Study Using Space–Time Measures. *The Professional Geographer*, 51(2), 211-227.
- [19] Ng, W.-S., & Acker, A. (2018). Understanding Urban Travel Behaviour by Gender for Efficient and Equitable Transport Policies. *International Transport Forum*.
- [20] Preston, V., & McLafferty, S. (1993). Gender Differences in Commuting at Suburban and Central Locations. *Canadian Journal of Regional Science*, 16, 237-259.
- [21] Lee, Everett S. A Theory of Migration. *Demography*, Vol. 3, No. 1. (1966), pp. 47-57. Published by Population Association of America
- [22] Sharma, A., Chandrasekhar, S., 2014. Growth of the urban shadow, spatial distribution of economic activities, and commuting by workers in rural and urban India. *World Dev.* 61, 154–166.

DAMAGE PREDICTION OF THE STEEL GIRDER ARCH BRIDGE MODEL BASED ON ARTIFICIAL NEURAL NETWORK METHOD

Widya Apriani¹, Reni Suryanita^{2*}, Yohannes Firzal², and Fadrizal Lubis¹

^{1,4}Departement of Civil Engineering, Lancang Kuning University, Indonesia; ^{2,3}Departement of Civil Engineering, University of Riau ^{2,3}, Indonesia

ABSTRACT

Disasters due to the collapse of bridge structures that cannot be predicted in advance require enormous rehabilitation costs. This is caused by a decrease in ability or damage that cannot be identified earlier. The difficulty of directly predicting the conditions of the bridge structure is caused by the limitations of the test equipment testing conditions. Therefore, the study aims to analyse the damage location and severity identification which are critical structural components on the steel girder arch bridge. This research used parametric of steel girder arch bridge for training and testing data in Artificial Neural Networks. Simply supported girder is selected as the numerical model. The 146 data required for the ANNs, as the stiffness of element 10th is assumed to drop 10%, 20%, 30%, and 40% of whole the elements. The ANNs parameters used are epoch 500 value. Learning rate value 0.01-0.09, architecture 3 neuron input layer, 5 hidden layer neurons and 1 output. Simulation of the amount of training data and test data used are 90:10, 80:20, 70:30; and 50:50. ANNs are capable of producing outputs in terms of damage severity using the stiffness reduction cases with damage index methods. Therefore, the results show that ANNs trained to have a reliable potential 98% for structural damage identification. The results confirm the feasibility of the method and its application in preventing structural failure.

Keywords: Artificial Neural Network, Damage Assessment, Damage Index, Reduction Stiffness

INTRODUCTION

Deterioration of the bridge structure during service will cause damage and even collapse. This can be caused by vehicle load overloading, fatigue on these structural elements, earthquake occurrences outside of planned predictions, and large wind loads. In Riau province, several bridges have deteriorated. Based on the assessment carried out by the Bridge Management System (BMS) method on several bridges that have critical values, the Merangin Bridge, S. Jangkang Bridge, Parak Suak Buaya Bridge, and the Darauf Parit Bridge are most critical in the upper structure. Meanwhile, the Siak II Bridge condition is severely damaged, consisting of severely damaged building, heavily damaged floor, slightly damaged lower part of the building, and the watershed is slightly damaged. Of the 114 bridges that exist, this bridge requires handling in the form of rehabilitation and repair [1].

To prevent deterioration, a method of monitoring a bridge is needed that can predict the condition of a bridge at any time so that maintenance can be done early and prevent sudden collapse. There are several methods developed for bridge condition assessments such as BMS and Fracture Critical Member (FCM)[2]. However, the method has not shown satisfactory results because the real conditions of bridge structure behavior cannot be monitored in

detail. In recent times, Artificial Neural Network (ANN) method is one way that has been ascertained to be able to monitor bridge behavior directly.

ANN is an excellent tool for recognizing patterns in data[3]. This method can predict and evaluate the condition of the bridge structure due to various factors. Damage can be expressed by several parameters and by several aspects such as tenacity, lost hysteretic energy, stiffness [4].

Research shows good results where neural networks with one hidden layer can help predict stability and health conditions at certain times[4],[5]and[6]. Research on the application of ANN on the box girder concrete bridge has been carried out[7]. The level of success of the research conducted on the various bridge models above, it is necessary to develop the use of this ANN method on other bridges such as the type of curved steel frame in this study. So that the proposed health monitoring of curved steel structure bridges in a disaster early warning system attempt to be able to reduce casualties.

This paper develops a damage index procedure for predicting the location and the severity of the steel beam by making a scenario that is a failure made for several points along the block. So that the maximum degradation scenario can be reflected at all. In this study, stiffness reduction,

displacement and location is considered as the parameter that is influenced the most.

LITERATURE REVIEW

Damage Index

There are various DI methods proposed by many researchers. There have been many Damage Index methods used by researchers. Based on the available literature, it was found that the global damage index method uses multiple response parameters that are suitable for overall evaluation[8]. The type of damage depends on various factors, including tension strength, reduction of stiffness reduction. However, damage assessment with multiples factor, associates in estimation of reliable damage. The type of damage depends on different factors such as displacement, tensile stress. In this study, the expression of damage has been proposed by considering the top parameters in the bridge structure, namely displacement.

Structural damage reduces stiffness and alters the structure's modal strain energy[9]. The damage index β_{ji} for the 'j'th element and 'i'th mode of the beam is provided in Eq. (1):

$$\beta_{ji} = \frac{\left(\int_j [\phi_i''(x)]^2 dx + \int_0^L [\phi_i''(x)]^2 dx \right) \int_0^L [\phi_i''(x)]^2 dx}{\left(\int_j [\phi_i''(x)]^2 dx + \int_0^L [\phi_i''(x)]^2 dx \right) \int_0^L [\phi_i''(x)]^2 dx} \quad (1)$$

Or can be written as eq (2):

$$\beta_{ji} = \frac{[(\phi_{ji}'')^2 + \Sigma(\phi_{ji}'')^2][\Sigma(\phi_{ji}'')^2]}{[(\phi_{ji}'')^2 + \Sigma(\phi_{ji}'')^2][\Sigma(\phi_{ji}'')^2]} \quad (2)$$

where ϕ'' is the mode shape curvature, superscript * refers to the damaged state and L is the beam length.

Artificial Neural Network

Artificial neural networks (ANN) are derivatives of the biological nervous system. This method is one that has reliability if used to complement Structural Health Monitoring System (SHMS)[10]. With ANN, predictions of structural health conditions can be done quickly, because in the process ANN the workings of the human brain. The image below shows a typical network of 3 perceptron layers:

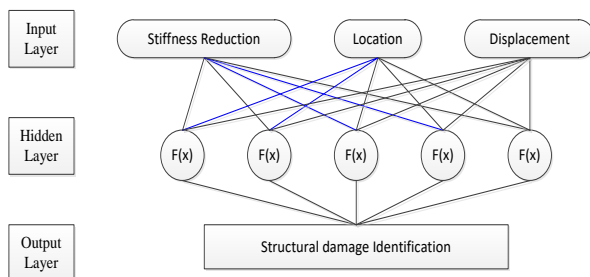


Fig 1. Architectural Layer of Artificial Neural Network

Architectural neural network layer that uses many layers with backpropagation type. Information processing consists of interconnected elements (neurons) that work simultaneously (fig 1). These neurons consist of input layers, hidden layers, output layers. The pattern of neo-neurons in the network, connecting weights such as training algorithms and activation functions is a determinant of the reliability of an ANN[11].

The training process is used to improve memorization and generalization capabilities, namely the ability of an ANN architecture design to absorb the amount of input data and take the patterns that have been learned. While the ability to generalize is the ability of ANN to make similar patterns that have been learned.

A good model of artificial neural networks will be shown by the results of a small error rate. To find out the accuracy of damage predictions, it uses the Mean Square Error (MSE), which shows a value close to zero is an accurate prediction. MSE can be calculated refer to Eq. (3) [12]:

$$RMSE = \sqrt{\frac{\sum (X-Y)^2}{n}} \quad (3)$$

With:

N = Amount of data

X = Observation Value

Y = Prediction Value

Correlation Coefficient (R) is a comparison of actual values with predictive values. The value of R can be calculated refer to "Eq. (4) [12]:

$$R = \frac{\sum xy}{\sqrt{\sum x^2 \sum y^2}} \quad (4)$$

By:

X = X - X'

Y = Y - Y'

X = Value of observation

Y = Prediction Value

X' = Average X value

Y' = Average Y value

Methods

METHODOLOGY

This research consists of the stages of diagnosis, analysis, and verification. The diagnosis and analysis phase is done by entering input data (modeling of structure) into the finite element program to then be used as input data on artificial neural networks with the help of a computer program called Matlab and Lusas. The model used is Siak III bridge in Pekanbaru, Indonesia with a steel arch bridge with a length of 168 m. Bridge structure elements consist of arch rib

frame (1200x800tw24mm), hanger (100 mm, $f_y = 490\text{MPa}$), tie beam (600x600 mm, $t_w = 24\text{mm}$), floor beam (400x400 mm, concrete).

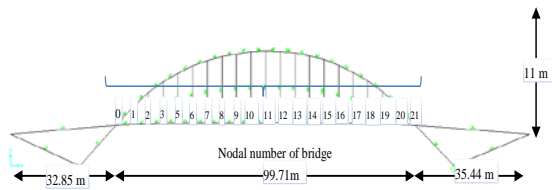


Fig 2. Longitudinal Cross Section of the Bridge

The design has been carried out utilizing the analytical method (NLTHA) has been carried out in SAP2000. Then the data is propagated forward towards the training target through an artificial neural network architecture that was previously designed. The earthquake load used is a record of the Pekanbaru data Modified with Kobe earthquake responses from Seismosoft Earthquake Engineering Software[13]. Design use mechanical properties of the steel girder arch bridge (Table 1).

Table 1. Mechanical properties of the Steel Girder Arch Bridge

Type of structural	JIS G 3106 SM YB
Stress yield (f_y)	295 MPa
Ultimate strength (f_u)	490 MPa
Modulus of elasticity (existing condition)	200,000 MPa
Specific gravity	78.5 kN/m ³

Experimental testing is needed to determine the behavior of the bridge girder if the Girder load is modeled into a simple supported I beam miniscaled with a ratio of 1: 5. Span length of 1100 mm, depth of 150 mm. The yield load of the steel beam was recorded at 60 kN in the experimental testing form. The experimental model is used to estimate lateral force displacement relationships (stiffness) at different loads using the LVDT tool. Girder is subjected to pushover loads based on FEMA 356. Tests of experimental work at the Structure Laboratory in Riau. The load is applied through the loading plate as pressure on the beam as shown in Figure. 3

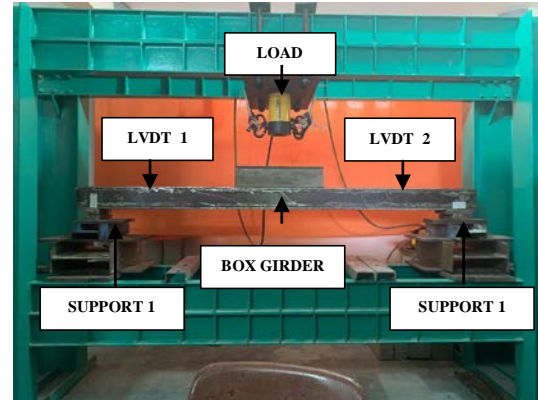


Fig 3 . Schematic diagram of the laboratory girder of arch bridge model.

Girder behavior analyzed through LUSAS is based on the theory of similitude laws. This finite element model simulation is useful for determining load tests. the type of element used is C3D8R (8-node linear brick, reduced integration). This is done to obtain the value of stiffness reduction which is the limit in the analysis of the collapse with ANN.

Damage assessment

The procedure for detecting the level of damage in steel beams is by considering stiffness reduction every 10% of stiffness deficiency to yielding limits. The damage scenario by simulating a proportional stiffness reduction of up to 40% in results and as shown in Table 3. The ANNs parameters used are epoch 500 values. Learning rate value 0.01-0.09, architecture 3 neuron input layer, 5 hidden layer neurons and 1 output. Simulation of the amount of training data and test data used are 90:10, 80:20, 70:30; and 50:50. Greater damage (or greater stiffness reduction) will provide greater structural deformation.

Validated FE models from simple beams were used and 21 partitions were simulated in the beams at a distance of 4.73 m apart, not including support, damage locations were 4.72 m, 9.45 m, 14.18 m, 18.91 m, 23.64 m, 28.37 m, 33.1 m, 37.83 m, 42.56 m and 47.29 m which coincide with the center of the 11 mm partition. Because the beams are symmetrical, four different severities of damage (10%, 20%, 30% and 40%) are introduced in the 21 left partitions to produce a single damage scenario. For some damage scenarios, only the smallest damage severity (10%) and greatest damage severity (40%) were introduced at 2 different locations.

All possible combinations were considered and 105 samples were produced for analysis using ANN. The input matrix consists of 21 rows (indicating the location of damage) and 102 columns (showing β at each location for the 105 samples produced) while the output matrix consists of 21 rows (showing damage locations) and 102 columns (showing the severity of damage at each location for 102 sample). The

Levenberg-Marquardt backpropagation method available from the NN tool in MATLAB R2015b is used to train the network. Sixty four of the 105 samples were randomly selected as training data sets while the samples were used in the testing phase and the remaining 41 samples were used in the validation phase. Training samples are used in the network for training purposes and the network is adjusted according to their mistakes; Validation samples are used to measure network generalizations and to stop training when generalizations do not show improvement anymore; Test samples are used to test network performance during and after training.

RESULT AND DISCUSSIONS

Displacements and Experimentally Measured Deflection.

Load variations compared to the displacement results with finite element analysis and experimental are shown in table 1. During the middle span testing ie point 11 damaged at 39 kN load and the experimental results stated a greater value compared to FEM as shown in table 2.

Table 2 Comparison of FE Displacements and experimentally measured deflection.

Load (kN)	Displacement 0,25 L(mm) (LVDT 1)		Displacement 0,25 L(mm) (LVDT 2)		Difference
	Lusas (FEM) mm	Measured mm	Lusas (FEM) mm	Measured mm	
10	1,015	1,780	1,528	2,260	-0,377
20	2,031	3,320	3,056	4,300	-0,339
30	3,046	4,820	4,585	6,460	-0,329
40	4,061	6,480	6,113	8,880	-0,342
50	5,076	8,480	7,642	11,920	-0,380
60	6,493	11,56	9,913	16,660	0,400

During the test, the beam was damaged in the middle span when the load was 11.92 kN and the resulting experimental test value was higher than the FEM results as shown in the table above. Loads range from 10 to 60 kN. The average percentage difference between experimental and FEM is 0.365%. When the load value is 40 kN, the percentage difference changes to + 0,400%. This shows that at 40 kN, the beam has already been yielded.

When the beam is loaded in the range of 10 kN to 60 kN, the average percentage difference between the experimental measured deflection and the deflection produced by FEM is 0.365%. Observation of reduction of stiffness is based on testing where the

first time it yields, when it is lowered by 40%. The other damage scenarios are simulated with proportional stiffness reductions with respect to the 40% stiffness reduction at yield and are as shown in Table 3.

Table 3 Damage scenarios of steel Hollow Beam

Damage Case	Stiffness reduction, (%)	Young Modulus (MPa)
1	10	180000
2	20	160000
3	30	140000
4	40	120000

Damage expression in the form of displacement, velocity, and acceleration is obtained at each planned damage point. Using the Park _ Ang equation, the Damage index value of the simulated damage point is shown in Figure 4.

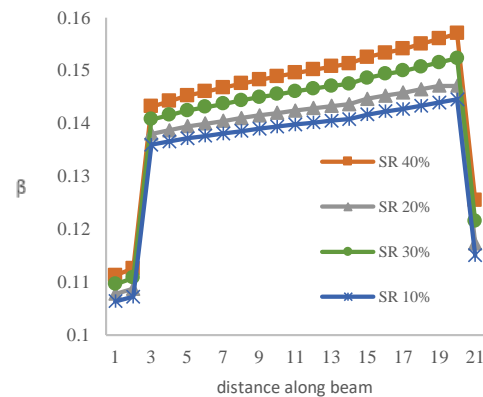


Fig 4. Plot of β vs distance along beam

The level of damage index (β) along the block is shown in fig. 4 for the 21 locations of the gusset bridge grder points. The highest level (β) indicates the location that experienced the greatest failure that is found at the location of point 20 for all severity reduction (SR).

After the location of the damage is first determined from the plot β versus the distance along the beam (fig 4). If several damage scenarios are observed from the β plot, the β values calculated along the beam can be input to trained ANNs to obtain the severity of the damage in terms of reducing stiffness at different damage locations along the beam.

In this research, the input layer-output layer and the curve were obtained from MATLAB R2015 with the ANN training method. The input layer consist of β at 21 locations (excluding supports) a total of 105 samples were fed into the input layer. Target layer consist of stiffness reduction. During the training of

ANN, each input vector would generate an output vector. The difference between the target vector and the output vector is an error and will propagate through the network in a backward manner. In this way, the mean square error (MSE) can be reduced so that the output vector can be as close as possible to the target vector. Simulation of the amount of training data and test data used are 90:10, 80:20, 70:30; and 50:50

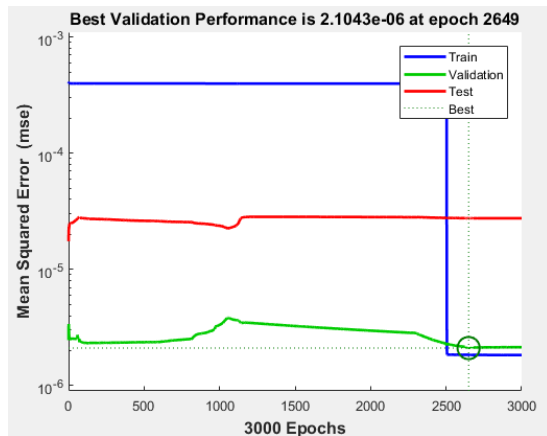


Fig 5. Error value: Best Validation Performance vs Mean Square Error (MSE)

From the figure 5, it is known that the results of training and testing data using ANN have produced the best error value (Mean Squared Error, MSE) of 2.1043×10^{-6} . ANN will be of good value if the MSE value is close to 1.

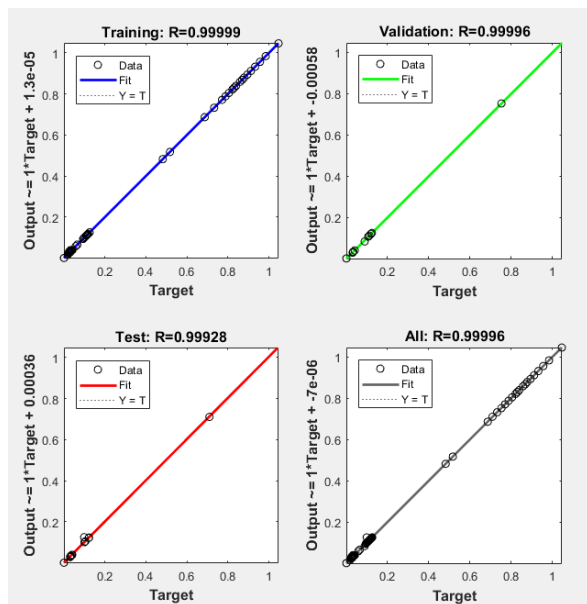


Fig 6. Training Process in Matlab

From figure 6, The number of neurons used in the hidden layer Aff MSE and the R value where the

R value measures the correlation between output and target, this R value varies from 0, which means random relationship to 1, which means close relationship. Neurons were used in the hidden layer for this study because they gave high R values as shown in Figure 6. Trained ANNs predict the severity of damage in terms of stiffness reduction with very low errors of 2.10×10^{-6} for training sets, 9.05×10^{-6} for validation sets and 3.85×10^{-5} for testing sets.

CONCLUSIONS

This paper has presented techniques for predicting damage to steel beams. This technique uses damage capital based on the damage index β and Artificial Neural Network (ANN) Variable β is used to measure the severity of the damage. The procedure for using ANN is practical because only the mode shape of the first bending mode is required and this can be easily obtained from measurements. The finite element model can then be easily validated to create databases for different damage scenarios. Therefore, the results show that ANNs are trained to have a reliable potential of 98% for structural damage identification. The results confirm the feasibility of the method and its application in preventing structural failure.

ACKNOWLEDGEMENTS

Gratitude to the Ministry of Research, Technology and Higher Education of Indonesia Grant for Higher Education Cooperation Year 2019–2020, Ministry of Public Works and Public Housing Indonesia and Civil Engineering Study Program at Lancang Kuning University.

REFERENCES

- [1] W. Apriani *et al.*, “Penilaian Kondisi Jembatan Rangka Baja di Riau,” vol. 4, no. 2, pp. 103–110, 2018.
- [2] W. Apriani and S. W. Megasari, “The Comparison of Condition Evaluation of Siak II Steel Frame Bridge between the FCM Method and the Bridge Management System,” *IOP Conf. Ser. Earth Environ. Sci.*, vol. 469, no. 1, 2020, doi: 10.1088/1755-1315/469/1/012049.
- [3] Mardiyono, R. Suryanita, and A. Adnan, “Intelligent monitoring system on prediction of building damage index using neural-network,” *TELKOMNIKA (Telecommunication Comput. Electron. Control.*, vol. 10, no. 1, pp. 155–164, 2012.
- [4] P. Hait, A. Sil, and S. Choudhury, “Seismic damage assessment and prediction using artificial neural network of RC building considering irregularities,” *J. Struct. Integr.*

- Maint.*, vol. 5, no. 1, pp. 51–69, 2020, doi: 10.1080/24705314.2019.1692167.
- [5] K. J. T. Elevado, J. G. Galupino, and R. S. Gallardo, “Artificial Neural Network (ANN) modelling of concrete mixed with waste ceramic tiles and fly ash,” *Int. J. GEOMATE*, vol. 15, no. 51, pp. 154–159, 2018, doi: 10.21660/2018.51.58567.
- [6] T. You, P. Gardoni, and S. Hurlebaus, “Iterative damage index method for structural health monitoring,” *Struct. Monit. Maint.*, vol. 1, no. 1, pp. 89–110, 2014, doi: 10.12989/smm.2014.1.1.089.
- [7] R. Suryanita and A. Adnan, “Application of Neural Networks in Bridge Health Prediction based on Acceleration and Displacement Data Domain Application of Neural Networks in Bridge Health Prediction based on Acceleration and Displacement Data Domain,” vol. I, no. February 2016, pp. 4–9, 2013, doi: 10.13140/RG.2.1.2384.0802.
- [8] Z. X. Tan, D. P. Thambiratnam, T. H. T. Chan, and H. Abdul Razak, “Detecting damage in steel beams using modal strain energy based damage index and Artificial Neural Network,” *Eng. Fail. Anal.*, vol. 79, no. January, pp. 253–262, 2017, doi: 10.1016/j.engfailanal.2017.04.035.
- [9] S. Park, N. Stubbs, R. Bolton, S. Choi, and C. Sikorsky, “Field verification of the damage index method in a concrete box-girder bridge via visual inspection,” *Comput. Civ. Infrastruct. Eng.*, vol. 16, no. 1, pp. 58–70, 2001, doi: 10.1111/0885-9507.00213.
- [10] S. Asmarani, J. I. Rastandi, B. O. Bangkit Sentosa, and M. Orientilize, “Damage assessment of moment resisting frame structures using correlation between damage index and natural frequency,” *IOP Conf. Ser. Earth Environ. Sci.*, vol. 426, no. 1, 2020, doi: 10.1088/1755-1315/426/1/012033.
- [11] A. C. Neves, I. González, J. Leander, and R. Karoumi, “Structural health monitoring of bridges: a model-free ANN-based approach to damage detection,” *J. Civ. Struct. Heal. Monit.*, vol. 7, no. 5, pp. 689–702, Nov. 2017, doi: 10.1007/s13349-017-0252-5.
- [12] M. Zulfakar, R. Suryanita, and E. Yuniarto, “Prediksi tingkat kerusakan struktur bangunan beton bertulang berdasarkan riwayat waktu gempa dengan metode jaringan saraf tiruan,” *Jom FTEKNIK*, vol. 3, no. 2, pp. 1–15, 2016.
- [13] Seismosoft, “SeismoSignal – A computer program for signal processing of strong-motion data.” 2014.

OPTIMUM LOCATION OF LAST-MINED STOPE IN SILL PILLAR RECOVERY WITH INFLUENCE OF BACKFILLING: A CASE STUDY

Huawei Xu, Derek B. Apel
Faculty of Engineering, University of Alberta, Canada

ABSTRACT

In order to extract steeply dipping orebodies, many mines in Canada have adopted sublevel a stoping method or one of its variations, such as blasthole stoping (BHS) and sublevel longhole retreat (SLR). In such methods, sill pillars are initially kept in place to support the great weight of the overburden in underground mining. After the mining is complete, the stope voids will be backfilled with cemented rockfill (CRF). The strength of the CRF affects the stability of the adjacent stopes in the sill pillar recovery excavation scheme. As the basic excavation element, stope plays a significant role not only in sill pillar recovery but also in the entire mining process. Sill pillar recovery may result in prolonged failure, fatality, and equipment loss. Choosing a rational location of the last mined stope in sill pillar recovery can effectively eliminate the instability of the recovery process. This paper uses the Finite Element Method (FEM), to present a comparison of sidewall swellings, floor heaves and the roof subsidence of the crossing cuts in each stope of different last mined stope location scenarios. It also presents the optimum location of the last mined stope in the sill pillar recovery process.

Keywords: Sill pillar recovery, Crossing cuts, Cemented rockfill(CRF), Stope location

INTRODUCTION

Pillar recovery is the practice of forming a series of pillars and then partially or totally extracting some or all of the pillars [1]. Pillar recovery is considered the most hazardous form of underground mining and is thought to be an art as much as a science [2]. Sill pillars are initially left in place to support the great weight of the overburden in underground mining. Pillar recovery is an important step in mining operations, specifically in the area of maximizing resource recovery. During the process of pillar recovery, it is possible to induce risks, such as overlaying rock subsidence, stope failure and pillar failure. Researchers initiated and proposed empirical, analytical theories and numerical technical methods to assess the stability and guarantee the safety of miners and mining equipment. Hudyma [3][4] studied microseismics, conventional ground control instruments, numerical modelling and visual observations to understand the mechanisms of pillar failures. Mark [1] and Iannacchione [5] analyzed the strengths and weaknesses of MHRA techniques, and assessed the major hazard risks to evaluate sill pillar recovery in two room-and-pillar mines. Zhukova [6] used monitored underground seismic registrations and mathematical models to improve the safety operations in pillar recovery. Langston [7] designed the stope layout, extraction procedure and ground support, which were applied to successively recover a pillar. Ghasemi [8][9] assessed the risk of pillar recovery operations and classified that risk into four categories by using indicators. Beruar [10] developed proper stope sequencing to avoid the highly stressed

area during pillar recovery. Valley [11] optimized the mining sequence, and suggested new directions for the different methods and the potential shortcomings. Townend [12] proposed five mitigation strategies to mitigate the high stress concentration while mining sill pillars.

Sill pillar recovery in the blasthole stoping (BHS) mining method, has not been widely discussed. BHS mining includes two sublevels. The one at the top of the stope is for drilling (overcut), and the other at the bottom is for production (undercut). For most hard rock mines in Canada, orebody blocks are usually steeply inclined and the BHS method is widely used.

BACKGROUND

The strength of the backfilled cemented rockfill (CRF) affects the displacement/subsidence of the open pit benches which determines the stability of the whole mine site, especially for the underground mines transferred from open pit to underground mining. For the recovery of sill pillars, most current research focuses on the room-and-pillar mining method. In these studies, the stress movement was mainly triggered by the layers above the mining level. Most of the studies did not take the backfilling into account. The relationship between the influence of the backfilled CRF and the stress redistribution and ground displacement in the process of sill pillar recovery has not been widely discussed. Sill pillars play a key role in maintaining the safety of the mining area above their location and below it. They can prevent mining-induced stresses from moving from one block to another. Recovering the sill pillar safely

can make the most use of the minerals. However, it can also trigger catastrophic problems. Then the stope sequences in the sill pillar recovery become significant. When the backfilled CRF is involved, the rational location of the last mined stope in the recovery process also becomes more significant.

Establishing the Numerical Modelling

The mine in this study was initially operated as an open-pit mine. Once the open-pit mining was complete, the operation shifted to underground mining. Under the open pit are two mineral zones: MZ#1 and MZ#2. First, we created a 3D numerical model. Next, the mining-induced redistributed stress field of the researched sill pillar was extracted and applied to the 2D sill pillar model. As shown in Fig. 1, there are seven levels. The sill pillar is located in the middle of the mining pipe in MZ#2. The sill pillar is 25m high and contains 21 stopes. The heights of the stope in each level and sill pillar are the same, 25 m, and the width is 7 m. As for the overcuts and undercuts in the stope in the sill pillar, the height is 5m and the width is same as that of the stope. The sill

pillar is located between level N1504 and level N1505.

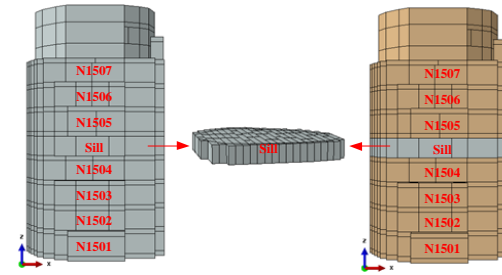


Fig. 1 Modelled pipe and sill pillar

Mechanical Properties of Modelled Rock and Backfilling CRF

Table-1 shows the rock mechanical properties applied in the model. Here, E is the elastic Young's modulus, ν is the Poisson's ratio, γ is the unit weight, ϕ is the angle of friction, C is the cohesive strength, σ_c is the maximum uniaxial compressive strength and σ_t is the tensile strength.

Table-1 Material properties

Rock Mass	E (GPa)	ν	γ (MN/m ³)	ϕ (°)	C (MPa)	σ_c (MPa)	σ_t (MPa)
MZ#1	18.7	0.26	0.024	26.4	4.2	66	3.4
MZ#2	19.6	0.24	0.024	28.1	4.7	79	3.7
Granite	24	0.3	0.026	45	9.3	130	0
CRF	2	0.3	0.022	35	1.2	1.5	0

Fig. 2 shows three examples of stope locations in the sill pillar. SCN#1 means that the last mined stope in the sill pillar is at the very left side of the sill pillar. SCN#21 means the last mined stope is at the very right side of the sill pillar. During the simulation process, the location of the last mined stope in the sill pillar changes from SCN#1 to SCN#21. The void areas in the figure are the overcuts and undercuts, the dark green is the sill pillar and the white is the backfilled CRF.

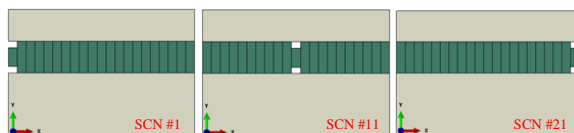


Fig. 2 Example stope location layout of sill pillar

RESULTS AND DISCUSSION

In order to compare the displacements of different locations in different stope location scenarios, eight

locations are numbered in the undercuts and overcuts, as shown in Fig.3. Node 1 and Node 3 are the two top corners, while Node 2 and Node 6 lie in the middle of the roof and floor respectively. Node 4 and Node 8 are in the middle of sidewalls, and Node 5 and Node 7 are the two floor corners. The stability of these locations is an external indicator of the overcuts and undercuts.

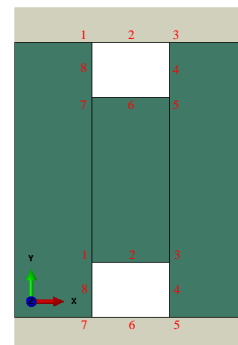


Fig. 3 Numbered location for comparison

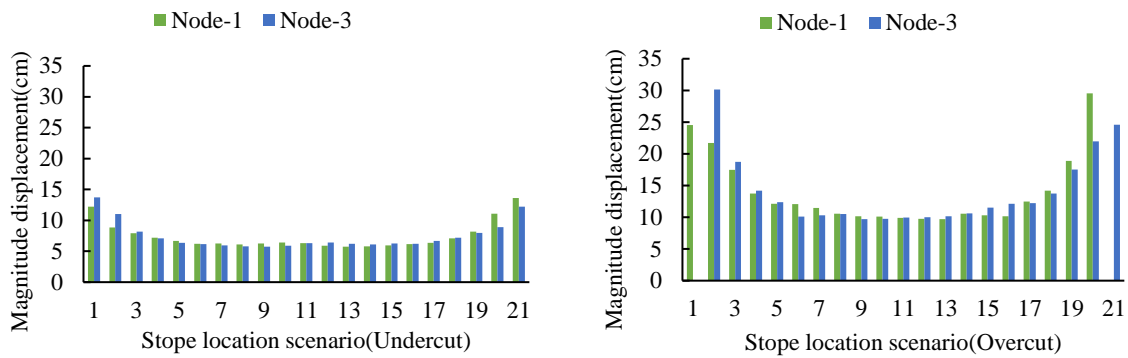


Fig. 4 Displacement at Node-1, Node-3 in both undercut and overcut

As shown in Fig. 4, compared with the displacement of the roof corners in the overcut, the displacement in the undercut is much smaller. For the undercut, except for the locations far from the sill pillar center, there is almost no difference between different stope location scenarios. For most of the displacements, at the same location number, the

overcut is about two times that of the undercut. At each location scenario, the two roof corners have almost the same displacement. There is a significant possibility that the roof corners in the overcut will fail at the two edges of the sill pillar if the last stope is located at the two edges of the sill pillar.

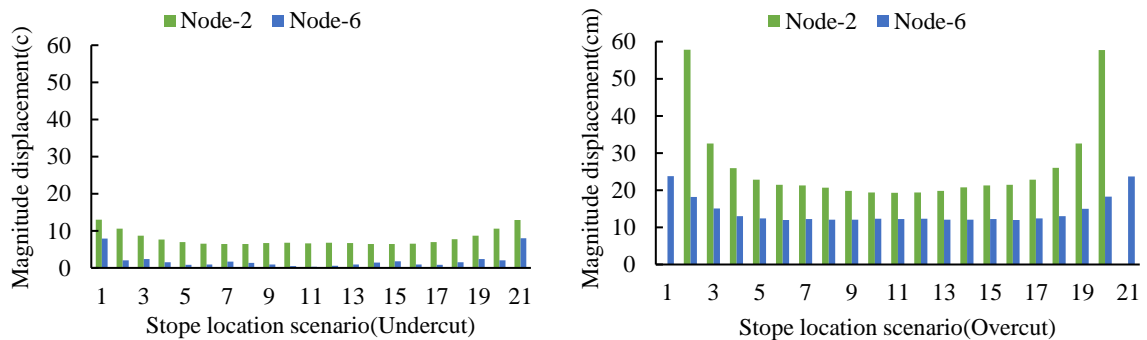


Fig. 5 Displacement at Node-2, Node-6 in both undercut and overcut

Figure 5 shows the roof displacement and floor heave in both the undercut and overcut. Unlike the roof corners displacement in Fig. 4, the roof displacement in both the undercut and overcut is larger than the floor heave. Similar to the roof corners, the roof displacement and floor heave in the overcut are much larger than those in the undercut. In the undercut, there is almost no floor heave, and the roof

displacement is negligible. The roof displacement in the overcut shows a slight difference except for the two edge location scenarios, while for the floor heave in the overcut, the edge location scenarios are almost the same at various locations. For the sake of safety, more supports should be installed in the roof and floor in the overcut.

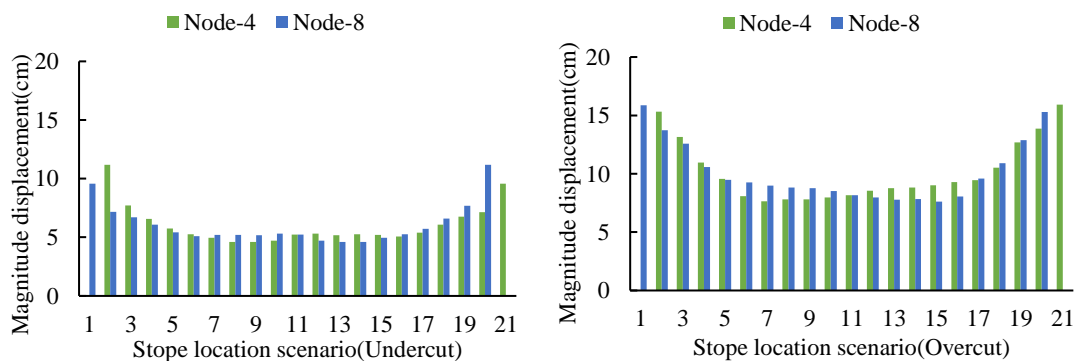


Fig. 6 Displacement at Node-4, Node-8 in both undercut and overcut

Figure 6 shows the configuration of the sidewall swellings. Similar to the roof corners displacement, the swellings show a gradual changing trend from the edge of the sill pillar to the center of the sill pillar. In the undercut, the sidewall swellings are almost the same at same stope location scenarios, and the

swellings are considerably lower, while the sidewall swellings in the overcut are almost twice the size of those in the undercut at the same stope location scenarios. More attention should be paid on the safety of sidewalls in the overcut.

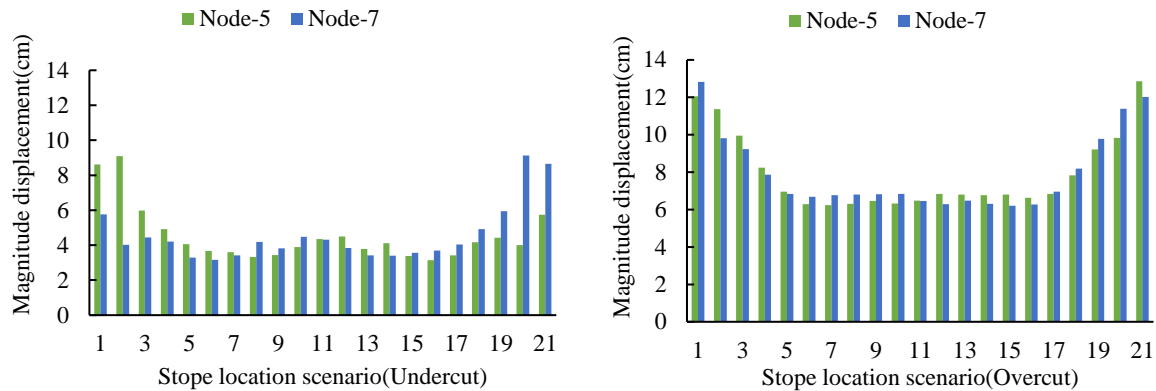


Fig. 7 Displacement at Node-5, Node-7 in both undercut and overcut

Floor heave is an important indicator of roadway safety in mining engineering. Figure 7 shows the heave of the two floor corners. The heave of the two floor corners at the same stope location in the sill pillar is almost the same. Most of the heaves are less than 10 cm for the undercut. For the overcut, the floor corners are in the granite; and for the undercut, the floor corners are in the backfilled CRF. The floor corner heave in the overcut is much larger than that in the undercut, which means the sill pillar takes most of the redistributed stresses and plays a key role in maintaining the safety in the mining process both above and underneath the blocks.

CONCLUSIONS

The following conclusions can be reached regarding the comparison of roof displacements, floor heaves and sidewall swellings of different locations in the undercuts and overcuts in various stope location scenarios.

From the roof displacements, floor heaves and sidewall swellings in both undercuts and overcuts, the sill pillar in this hard rock mine plays a key role in maintaining the safety of the mine throughout the mining and backfilling processes.

In the same stope location scenario, compared with overcut, the displacement of the roof corners in undercut is smaller, and most of the roof corner displacements in undercuts are less than 10 cm, while in the overcuts, all the displacements in roof corners are over 10 cm, which means the roof in the undercut is more stable than that in the overcut, and more protective measures should be taken in the roof of the overcut.

The floor heave in the undercut is tiny, and the values of the floor heave in the overcuts are more than 7 times of that in the undercuts, which means the floor in the undercut is more stable than the floor in the overcut. Also the roof displacements in the overcuts are more than 2 times of that in the undercuts. The sidewall swellings in the undercuts are about half of that in the overcuts at the same location scenario.

Roofs in the overcuts and floors in the undercuts are the backfilled CRF. The strength of the CRF is lower than the sill pillar hard rock, then the roof displacement in overcuts is much larger than that in undercuts. In both undercuts and overcuts, more attention should be paid to the supports on the roof than on the floor.

Based on the above conclusions, for the optimum location of the last mined stope in sill pillar recovery, the last mined stope can be any location between No.5 to No.17 in the sill pillar.

REFERENCE

- [1] C. Mark, F. Chase, and D. Pappas, "Reducing the Risk of Ground Falls During Pillar Recovery," *Trans Soc Min Eng*, pp. 153–160, 2003.
- [2] M. Christopher and G. Michael, "Preventing Roof Fall Fatalities During Pillar Recovery : A Ground Control Success Story," *Int. J. Min. Sci. Technol.*, vol. 27, no. 1, pp. 107–113, 2017.
- [3] M. R. Hudyma and B. Mining, "Geomechanics of Sill Pillar Mining," *Proceeding 1st North Am. Rock Mech. Symp.*, pp. 969–976, 1994.
- [4] Y. Potvin and M. Hudyma, "Open Stope Mining in Canada," *Proc. MassMin2000, Brisbane.*, no. January 2000, 2000.

- [5] A. T. Iannacchione, "Major Hazard Risk Assessment Applied to Pillar Recovery Operations," *Proc. 28th Int. Conf. Gr. Control mining. Morgantown, West Virginia Univ. USA; 2009*, pp. 261–270, 2009.
- [6] S. Zhukova, P. Korchak, A. Streshnev, and I. Salnikov, "Geodynamic Rock Condition , Mine Workings Stabilization During Pillar Recovery at the Level + 320 m of the Yukspor Deposit of the Khibiny Massif," *VII Int. Sci. Conf. "Problems Complex Dev. Georesources,"* vol. 02022, 2018.
- [7] R. B. Langston, H. A. D. Kirsten, E. A. Niemi, and J. A. Marjerison, "Extraction of a Remnant Sill Pillar Under Challenging Ground Conditions at the Stillwater Mine , Nye , Mt .," *ARMA*, 2006.
- [8] E. Ghasemi, K. Shahriar, and M. Sharifzadeh, "A New Method for Risk Assessment of Pillar Recovery Operation," *Saf. Sci.*, vol. 48, no. 10, pp. 1304–1312, 2010.
- [9] E. Ghasemi, M. Ataei, K. Shahriar, F. Sereshki, and S. Esmacil, "Assessment of Roof Fall Risk During Retreat Mining in Room and Pillar Coal Mines," *Int. J. Rock Mech. Min. Sci.*, vol. 54, pp. 80–89, 2012.
- [10] O. Beruar, A. S. Forsythe, and M. Yao, "Sill Pillar Mining in the Main Orebody at Vale ' s Coleman Mine," *ARMA*, vol. 9300, no. 3830 L, pp. 1–7, 2011.
- [11] B. Valley, W. Pun, D. J. Hutchinson, and B. Madjdabadi, "Rock Mass Change Monitoring in a Sill Pillar at Vale ' s Coleman Mine (Sudbury , Canada)," *Can. RM Conf.*, no. January, 2012.
- [12] S. Townend and A. Sampson-Forsythe, "Mitigation Strategies for Mining in High Stress Sill Pillars at Coleman Mine – A Case Study," *Aust. Cent. Geomech.*, pp. 65–78, 2014.

MEASURING ACCESS TO SUSTAINABLE TRANSPORT OPTIONS FOR THE ELDERLY

Kaniz Fatima¹, Sara Moridpour¹, Chris De Gruyter² and Tayebbeh Saghapour²

¹ Civil and Infrastructure Engineering Discipline, School of Engineering
RMIT University, Australia, ² School of Global, Urban and Social Studies, RMIT University, Australia

ABSTRACT

The elderly population is a major part of the total population all over the world. The public transport access for the elderly is not easy. A connected and accessible public transport system is a key requirement for a better quality of everyday life. Meanwhile, walking is a sustainable mode for short distances to reach desired destinations. Many researchers have focused on elderly transport accessibility. Accessibility index is one of the popular methods to measure the transport accessibility. This paper identifies public transport as well as walking accessibility indices for elderly considering the travel from the centre of one specific Statistical Area level one (SA1) to various destinations. According to the Victorian Integrated Survey of Travel and Activity (VISTA) data, the greater Melbourne region is classified into three home sub-regions including Melbourne Central Business District (CBD), inner Melbourne and outer Melbourne. The previous studies have mainly considered the distance as a measure of transport accessibility. However, total travel time and population have not been considered in accessibility analysis. This paper also analyses the elderly public transport and walking access in Melbourne metropolitan area using time-based accessibility indices to identify the elderly access level. The paper also compares the elderly public transport and walking access among the three different home sub-regions. The results from this research can be used by the planners to identify inaccessible areas for the elderly in an urban region.

Keywords: Public transport; Walking; Elderly; Accessibility

INTRODUCTION

The elderly population is increasing all over the world. The growth of the older population varies upon the country's characteristics such as size and growth. According to the [1], the projection shows by 2050 one in six people in the world will be aged 65 years or over. Reduced birth rate and increased expectation for a better lifestyle is another reason for the rapid growth of the elderly population.

A proper urban region should have easy public transport and walking access to all major necessity. Specifically, the group of the increased elderly population needs special attention when comes to mobility. Mobility is a major part of everyday life. It is a bridge between social welfare, mental health, physical health and daily needs. For the elderly group of the population need more time for planning to reach destinations, more walk time and more physical support. Public transport (PT) and walking are considered a sustainable mode of transport. But for the elderly, it is always not accessible. The most popular destinations may not be within PT and walking accessibility range. If reaching to the destination place need transport mode change, the PT system can be more complicated for the elderly. Also, for a walking trip, most of the elderly take longer time to reach a destination.

Many researchers focused on public transport and walking accessibility. However, a few types of

research conducted elderly time-based measures. The main contribution of this study uses time-based accessibility indices to calculate the elderly (65 and over) accessibility for three home sub-region of greater Melbourne (inner, middle and outer). This paper identifies and compare the elderly public transport and walking accessibility level for these three homes sub-region.

The next heading of the paper discusses the previous research related to elderly transport accessibility. This is followed by the data collection, index calculation procedures and the methodology. Then the results and discussion are highlighted. The key recommendation and conclusion remarks in the last section.

BACKGROUND

Mobility difficulties increase with age. According to [2], mobility difficulties increases to 17% for those aged 60–69 and to 39% for those aged 70 and over. Many elderlies prefer to stay in the same place/home after retirement. The living style is known as “Aging in place”. To support “Ageing in place” easy access to the destinations are necessary. Several research studies are related to elderly health, social and accessibility issues. Analyse the walking, private and public transport access is very important to understand elderly travel difficulties. Accessibility measures indicate elderly travel quality.

Public Transport (PT) Accessibility Study

Public transport trip can be included as a walk to the PT stop, boarding on the bus/tram/train, finding a seat, coping with interchanges as necessary and completing the journey to the destination. The traveller needs to be self-assured to make this journey. For the elderly maintaining, this information can be complicated sometimes. Using PT is more hassle if they have not habituated in it a regular basis. Table 1 represents the summary of previous time-based studies related to public transport accessibility. From Table 1 summary it is identified that travel time is one of the main elements for calculating public transport accessibility.

Table 1 Public Transport Accessibility Index Study (Time-Based)

Index & References	Definition
Time-Based Transit Service Area Tool (TTSAT) [3]	This measure considers transit service area based on users' travel time.
Person-based measures [4]	Person-based measures each person within a given time frame.
Local index of transit availability (LITA) [5]	A study of LITA used three main time variables for calculation.
Gravity-based measures [6], [7], [8]	The gravity model is followed by Newton's theory of gravity. This model considers that the trips produced at an origin and attracted to a destination are directly proportional to the total trip productions at the origin and the total attractions at the destination.
The elderly population and time-based index [9], [10]	A recent study introduced the elderly time-based accessibility.

Walking Accessibility Index Study

Walking is encouraged by many health professional and researchers [11], [12], [13]. Physical activity decreases the chance of getting a chronic disease [14]. Walking is one of the most recommended physical activity. Walkability study

measures walking access from the individual's place of origin to destinations. The proportion of the elderly physical activity is contrariwise with the increase of the elderly population growth [15]. However, similar to PT accessibility index very limited research considers the elderly walk time. Table 2 represents an overview of previous studies related to walking accessibility. From table 2 summary, it is observed that spatial distribution and closest walking time/distance are mostly used to calculate walking accessibility index.

Table 2 Walking Accessibility Study

Index & References	Definition
Gravity-based accessibility [13]	This measure based on the spatial distribution of residence & travels time/cost between zones.
Topological or Infrastructure based [13]	It considers an analysis of network connectivity and/or the characteristics of the walking infrastructures.
Walkability/walk score-type measures [13]	This measure considers build-in-environment and accessibility from an origin to a destination
Walk Score [16]	Walk Score considers the distance to the closest destination in each land use category. It is based on the gravity-based model
Walkability Index (WI) [17], [18]	The WI is calculated from the sum of the z-scores of the four mentioned urban form measures.

STUDY AREA AND DATASETS

The Greater Melbourne geographical area is considered as a case study to analyse access for the elderly.

Study area

According to the Victorian Integrated Survey of Travel and Activity (VISTA), the greater Melbourne region is divided into three home-region as inner, middle and outer Melbourne [19]. Figure 1 illustrates the three home sub-region for Greater Melbourne. The home-regions are also divided into statistical area level one (SA1). SA1 is known as the second smallest geographic area after mesh block. In Melbourne, there are around 10,290 SA1s. Most of the census datasets are collected based on SA1s. In this study, both public transport index and the walkability index

is calculated based on the SA1s. Table 3 summarized the number of SA1s, PT coverage and elderly population for each home sub-region. The datasets are analysed and extracted using VISTA data and ArcMap. From table 3 greater Melbourne outer region contains around 50% of the total SA1s. Public transport coverage is higher in inner and middle Melbourne than outer Melbourne region. Furthermore, the outer region elderly population is greater compare to the middle and inner region.

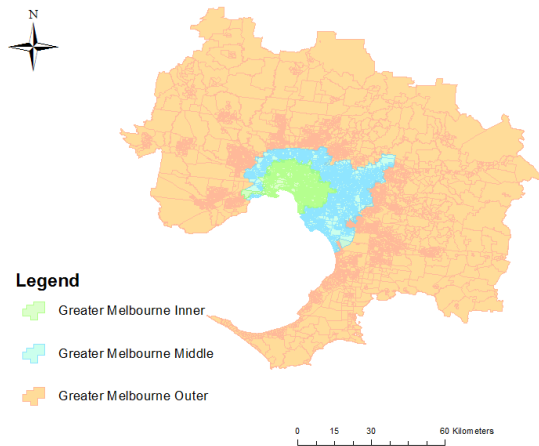


Figure 1: Greater Melbourne Home Sub-region.

Table 3 Home Sub-Region SA1 Summary

Home Sub Region	% of total SA1s	% of PT Coverage	% of Elderly Population
Melbourne Inner	21.10	41.19	36.66
Melbourne Middle	30.74	32.50	39.78
Melbourne Outer	48.16	26.31	23.56

Datasets

The datasets are collected from various available sources. All the datasets are analysed using a statistical analysis software package SPSS. The datasets analysed for this study are presented as follows.

VISTA Data

VISTA data is a detailed household data (2016) related to single-day travel [19]. This travel data collected throughout across greater Melbourne for a year. This dataset helps to identify the travel pattern and travel behaviour. Around 46,563 travel responses for weekdays and weekend are documented. Among these responses, 6,975 responses are from the elderly population[9], [10]. Most of the elderly details for

travel mode are not documented.

Point of Interest

A detailed point of interest (POI) datasets for greater Melbourne is extracted from the Australian Urban Research Infrastructure Network (AURIN) [20]. These points of interests are considered as the destination. According to the VISTA data, four major elderly popular destinations are considered to develop elderly PT and walkability indices [9].

Population

The population density is a major indicator of PT and walking accessibility measure [21]. Most of the elderly accessibility index did not consider population.

Travel Time

Melbourne public transport system is a combination of bus, train and train. Greater Melbourne timetable for these three modes is collected from different open datasets such as Public Transport Victoria (PTV) and Yarra tram.

Road Network

The road network datasets are analysed using ArcMap Network Analyst Extension. Arc Map network analysis tools provide spatial analysis using road network data, travel directions data, closest destination/PT stop analysis data and service area analysis data.

Street connectivity

The street network is used to calculate the number of intersections act as a proxy to show the potential mobility of pedestrians within the neighbourhood. Street connectivity datasets are analysed by using AURIN walkability tools.

Safety

Pedestrians are at greater risk of traffic-related injury than motor vehicle users. The elderly experience higher severity of pedestrian injuries than younger adults [22]. Accident rates datasets are extracted and analysed from VicRoads' crash database.

METHODOLOGY

The study contains two main parts. The first part is the public transport accessibility index calculation. The last part is related to walking accessibility index calculation. Both indices are measured based on SA1s

centroid towards specific destinations.

Methodology Calculation Procedure

The closest facility from each SA1 centroid is identified. For both indices' calculation, ArcMap network analyst tools are used to identify the closest facility and the closest public transport stop/station. The Public transport accessibility index and walking index classified into five different categories starting from very poor, poor, moderate, good and excellent. The Natural Breaks (Jenks) classification method is used to categorize the indices [23].

The methods for public transport and walking accessibility measure can be explained as follows:

- Calculate and identify the number of SA1 for each home-region for greater Melbourne.
- Calculate the public transport stop coverage (bus, tram and train) for all the SA1s and separate them as per home sub-region.
- Calculate and analyse the POIs coverage (four most travelled POI used by elderly) for each home sub-region area.
- Calculate and analyse the index classification from very poor to excellent for all SA1s.
- Calculate and analyse the accessibility percentage of PT and walking accessibility for all three home sub-region.

Elderly Public Transport Accessibility Index (EPTAI) Calculation

The time-based elderly PT accessibility index is presented in equation 1. The total travel time for public transport considered as the summation of walk time, average waiting time and in-vehicle time for a mode of transport.

$$EPTAI_{SA1} = \sum_{j=1}^4 (P_{ratio} * 10 * TTT_{ratioPOI}) \quad (1)$$

Where, P_{ratio} = Population ratio, $TTT_{ratioPOI}$ is the total travel time ratio for a specific POI.

TTT = Walk time (WT) to nearest PT stop/station + In-vehicle time (In VT) + Average waiting time (AvWT) + WT to nearest stop/station of POI + WT to POI,

TTT = WT to nearest PT stop/station + In VT + AvWT + WT to POI (if WT to nearest stop/station of POI = 0)

Elderly Walking accessibility Index (EWAI) Calculation

The elderly walking accessibility index considers the walk time to the destination, population, street connectivity, pedestrian safety/accident rates and land mix use. Each component for both indices is calculated using the statistical Z-score method. The Z

score calculated separately for all SA1s. The elderly walking accessibility index is presented in equation 2.

$$EWAI_{SA1} = (Z_{ScoreWalkTime}) + (Z_{scoreLUMIX}) + (Z_{ScoreStreetConnectivity}) + (Z_{ScorePratton}) + (Z_{ScoreSafety}) \quad (2)$$

$$LUMIX = -1 \sum_{j=1}^n (Pi * \ln(Pi) / \ln(n)) \quad (3)$$

Where, LUMIX = land use mix score, Pi = the proportion of the area covered by land use j , n = the total number of land-use types.

RESULTS AND DISCUSSION

This study compares the public transport and walking accessibility for the elderly among the Melbourne inner, middle and outer home sub-region.

Elderly Public Transport Accessibility Comparison

The PT accessibility is measured for shopping centres, health care centres, medical centres and recreation centres. Table 4 represents the summary of PT accessibility comparison. The POIs coverage is analysed using ArcMap.

From table 4 it can be observed, more than 70% of SA1s are categorized as a good and excellent category considering shopping centre PT access in Melbourne inner region. Only around 11% SA1s are observed as the very poor and poor category for the elderly shopping centre access in Melbourne inner region. On the other side, the Melbourne outer region shows complete opposite results. Around 65% of Melbourne outer SA1s are identified as a very poor and poor category for the elderly shopping centre PT access. But only around 17% SA1s are observed as good to the excellent category for the elderly PT access. The reason can be overall shopping centres are established a bit far away from the centroid of SA1s. Major shopping centres generally covers several SA1s. From some SA1s' shopping centres can be reached easily using one mode of transport. But from other SA1s' reaching to a shopping centre, requires mode change. Also, some shopping centres situated close to public transport stops. Furthermore, some shopping centres are not within the elderly walking limit which takes a longer time to reach using the PT mode. A typical shopping centre travel includes walk time to a nearby public transport stop, wait time, in-vehicle travel time and again walk time after reaching the destination (shopping centre nearby stop).

Likewise, effects can be observed for health care centres, education centres and recreation centres. The outer region is covered with less public transport accessibility for the elderly than the inner and middle region.

Table 4 Summary of Elderly PT Accessibility Comparison

	Melbourne Elderly PT Access (%)				
	Very Low	Low	Moderate	Good	Excellent
Shopping Centre (Shopping centre coverage: Inner 26.58%, Middle 34.17%, Outer 39.25%)					
Melbourne Inner	5.60	5.70	16.00	46.00	26.70
Melbourne Middle	9.80	10.56	23.00	33.00	23.64
Melbourne Outer	41.16	23.33	18.75	11.70	5.06
Health Care Centre (Health care centre coverage: Inner 30.07%, Middle 28.91%, Outer 41.02%)					
Melbourne Inner	4.33	6.65	13.66	37.88	37.48
Melbourne Middle	8.66	9.78	5.77	44.04	31.75
Melbourne Outer	31.93	28.55	17.00	11.67	10.85
Education Centre (Education centre coverage: Inner 21.25%, Middle 32.22%, Outer 46.53%)					
Melbourne Inner	4.46	5.66	15.66	35.77	38.45
Melbourne Middle	3.45	3.85	19.56	31.56	41.58
Melbourne Outer	24.56	17.73	16.78	21.65	19.28
Recreation Centre (Recreation centre coverage: Inner 26.74%, Middle 28.83%, Outer 44.43%)					
Melbourne Inner	4.36	8.64	16.74	25.83	44.43
Melbourne Middle	13.36	8.71	10.87	29.34	47.72
Melbourne Outer	28.19	24.95	18.86	16.77	11.23

Around 40% of health care centres are covered by the Melbourne outer region while the inner region covers around 30% and the middle region 29%. But the elderly PT accessibility is poor and very poor onto most of the outer region. Sometime to reach the closest facilities elderly required to change bus services twice. However, for education centres and recreation centres, the access level is slightly better in Melbourne outer region. The reason is the number of these two POIs coverage higher than the shopping centres and health care centres.

Elderly Walking Accessibility

Walking accessibility for the elderly is calculated using equation 2 for all three home-sub regions. For the elderly, education centres and recreation are within the walkable distance for some SA1s. But most of the shopping centres and health care centres are not accessible through walking for elderly. Table 5 summarised the elderly walking accessibility comparison. From table 5 it can be observed walking accessibility is higher in Melbourne inner region than Melbourne middle and outer region. Inner Melbourne region has more walking access to the destination compared to the other two home sub-regions. More than 76% of SA1s are categorized as a good and

excellent level of elderly walking access. Although the outer region identifies the opposite results. Around 45% of outer region SA1s assessed as very poor and poor level walking access for the elderly.

Table 5 Summary of Walking Accessibility Comparison

Access Level	Melbourne Elderly Walking Accessibility (%)		
	Inner	Middle	Outer
Very Poor	3.29	4.56	23.27
Poor	8.64	5.71	21.57
Moderate	11.74	9.87	15.86
Good	31.93	29.34	16.77
Excellent	44.40	50.52	22.53

CONCLUSIONS AND FUTURE RESEARCH DIRECTIONS

This study compares the level of the elderly public transport and walking accessibility within the greater Melbourne home sub-regions. The study conducted a network analysis using a time-based accessibility indices calculation. This study provides elderly accessibility level measure overview for three greater Melbourne home sub-region considering four specific destinations. Moreover, the study specifies

that public transport and walking accessibility level is more frequent in the greater Melbourne inner sub-region than the outer and middle region.

The technical approach of this index can be applied to other cities or larger geographic regions. The analysis results can be used to identify the most inaccessible region for the elderly group of people. The EPTAI and EWAI can be calculated for other POIs or destinations. Future research can consider this for elderly travel. These results can be used to implement further development of elderly sustainable transport access. The time-based accessibility measures can lead future planners to identify/modify various accessibility aspects. For instance, the PT route /stop and POIs distribution considering elderly travel specifically newly built outer regions in future.

REFERENCES

- [1] World Population Prospects, United Nations, Department of Economic and Social Affairs, Population Division, 2019.
- [2] Mackett, R., Improving accessibility for older people – Investing in a valuable asset, *Journal of Transport & Health*, 2015, Vol. 2, Pp. 5-13.
- [3] Cheng, CL. and Agrawal, AW., TTSAT: A New Approach to Mapping Transit Accessibility, *Journal of Public Transportation*, 2010, Vol. 13, Pp. 55-72.
- [4] Kim HM. and Kwan MP., Space-time accessibility measures: A geo-computational algorithm with a focus on the feasible opportunity set and possible activity duration, *Journal of Geographical Systems*, 2003, Vol. 5, Pp.71-91.
- [5] Cheng, CL. and Agrawal, AW., TTSAT: A New Approach to Mapping Transit Accessibility. *Journal of Public Transportation*, 2010, Vol. 13, Pp. 55-72.
- [6] Hanson, WG., How Accessibility Shapes Land Use, *Journal of the American Institute of Planners*, 1959, Vol. 35, Pp. 73-76.
- [7] Kwan, P., Spacetime and integral measures of individual accessibility: A comparative analysis using a point-based framework, *Geographical analysis*, 1998, Vol. 30, Pp. 191- 216.
- [8] Papa, E. and Coppola, P., Gravity-Based Accessibility measures for Integrated Transport-land Use Planning (GraBAM), *Dipartimento di Pianificazione e Scienza del Territorio DiPiST, Università degli Studi di Napoli“Federico II”*, 2013..
- [9] Fatima, K. and Moridpour, S., Measuring Public transport Accessibility for Elderly, *The 6th International Conference on Traffic and Logistic Engineering (ICTLE)*, Bangkok, Thailand, Pp. 1-6, 2018.
- [10] Fatima, K., Moridpour, S., Saghapour, T. and Gruyter, C.D., A Case Study of Elderly Public Transport Accessibility, *APCIM & ICTTE 2018 Proceedings of the Asia-Pacific Conference on Intelligent Medical 2018 & International Conference on Transportation and Traffic Engineering*, Pp. 253-257.
- [11] Maghelal, P. and Capp, C.J., Walkability: A Review of Existing Pedestrian Indices, *Journal of URISA*, 2011, Vol. 23, Issue 2, Pp. 5-19.
- [12] Notthoff, N. and Carstensen, L. L., Promoting walking in older adults: Perceived neighborhood walkability influences the effectiveness of motivational messages, *Journal of Health Psychology* 2015, Vol. 22, Issue 7, Pp. 834-843.
- [13] Vale, D.S., Saraiva, M. and Pereira, M., Active accessibility: a review of operational measures of walking and cycling accessibility, *Journal of Transport and Land Use*, 2016 Vol. 9, Issue 1, Pp 1-27.
- [14] Physical Activity Guidelines Advisory Committee Scientific Report, 2008. Washington, DC: U.S. Department of Health and Human Services.
- [15] Groot, LC. DE., Verheijden, MW., Henaau, St. De. Schroll, M. and Staveren, WA. VAN., Lifestyle, Nutritional status, health, and mortality in elderly people across Europe: A review of the longitudinal results of the SENECA study, *Journals Of Gerontology Series A-Biological Sciences And Medical Sciences*, 2004, Vol. 59, Issue 12, Pp. 1277-1284
- [16] Koschinsky, J., Talen, E., Alfonzo, M. and Lee, S., How walkable is Walker’s paradise?, *Environment and Planning B: Urban Analytics and City Science*, Vol 44, Issue 2, 2017.
- [17] Sundquist, K., Eriksson, U., Kawakami, N., Skog, L., Ohlsson, H. and Arvidsson, D., Neighborhood Walkability, Physical Activity, and Walking Behavior: The Swedish Neighborhood and Physical Activity (SNAP) Study, *Social Science and Medicine*, 2011, Vol. 72, Issue 8, Pp. 1266–1273.
- [18] Giles-Corti, B., Macaulay, G., Middleton, N., Boruff, V., Bull, F., Butterworth, I., Badland, H., Mavoa, S., Roberts, R. and Christian, H., Developing a Research and Practice Tool to Measure Walkability: A Demonstration Project, *Health Promotion Journal of Australia*, 2014, Vol. 25, Issue 3, Pp. 160–166.
- [19] Victorian Integrated Survey of Travel and Activity (VISTA), Department of Transport, Melbourne, Victoria, Australia, 2016. <http://www5.transport.vic.gov.au/>.
- [20] Australian Urban Research Infrastructure Network (AURIN) (<https://aurin.org.au/>).
- [21] Habibian, M. and Hosseinzadeh, A., Walkability index across trip purposes. *Sustainable Cities and Society*, 2018, Vol. 42, pp216-225.
- [22] Garrard, J., Senior Victorians and walking: Obstacles and opportunities. Final Report, 2013.
- [23] Brewer, AC. and Pickle, L., Evaluation of Methods for Classifying Epidemiological Data on Choropleth Maps in Series. *Annals of the Association of American Geographers*, 2002, Vol. 92, Pp. 662-681.

QUANTIFICATION OF SLOPE DEFORMATION USING LASER POINT CLOUD DATA BY MOBILE MAPPING SYSTEM

Naoto Samori¹, Satoshi Nishiyama², Koki Sakita³, Michinari Fuziki⁴ and Naoya Ono⁵

^{1,2,3}Graduate school of environmental and life science, Okayama University, Japan,

^{4,5}Kokusai Kogyo Co.,Ltd, Japan,

ABSTRACT

There exist many slopes in Japan, most of which were created during the period of high economic growth. It has been 50 years since they were constructed, and they are now aging. To judge the degree of deterioration, it is necessary to understand their deformation. The examination is currently performed by close-up visual inspection. However, the problem is that the results may vary depending on the inspector, and thus, uniform conclusions cannot be obtained. Therefore, in order to detect the slope deformation quantitatively, we proposed a survey method using a mobile measurement vehicle (mobile mapping system or MMS) and a differential analysis (method applying iterative closest point) approach considered to be capable of detecting the slope deformation using a point cloud. Point cloud is a set of points data that have position information of three-dimensional coordinates, namely X, Y, Z(H), and color information. We carried out three separate verification steps corresponding to MMS point cloud acquisition accuracy, deformation discriminability, and deformation extraction accuracy, and verified the detection of bulging, which is a sign of a landslide, on slopes that were assumed to cause visual landslide. It was confirmed that the target slope, which was assumed not to be deformed at the total station, was determined as not deformed even by our proposed detection method.

Keywords: Road slope, MMS, ICP, Difference analysis

BACKGROUND AND PURPOSE

Japan occupied about 70% of its land area in mountains and hills [1]. Slopes were constructed during the period of high economic growth, which was attained about 50 years ago. These mountains were cut, and slope protection was incorporated to develop the road transportation network. However, as years past, the slope protection was weathered by rain and wind, and due to aging effects, deformation of the slope, such as peeling of mortar and breakage of the legal frame, has occurred. Therefore, it is necessary to understand the deformations to prevent the slope from collapsing and causing damage to the surrounding area. However, the slope inspection method uses nondestructive examination approaches, including palpation and tapping, mainly for close-up visual inspection, and the results largely depend on the experience and skill of the engineer. Therefore, as the inspection outcome varies depending on the individual inspector, obtaining uniform results is impossible.

In recent years, surveying using a laser scanner, which can obtain point cloud data capable of quantitatively evaluating the shape of a structure, has received extensive attention. Point cloud data (Fig. 1) is a set of points that have position information of three-dimensional coordinates, namely X, Y, Z(H), and color information (RGB) obtained from camera image data. By rotating the point cloud of the object

and segmenting out only the region of interest by enlarging/reducing, the height and width of the object and the point cloud obtained by the laser scanner can be used to evaluate the degree of reflection. Since these points are all three-dimensional coordinates, RGB values, and quantitative data, it is possible to express the deformation quantitatively. A surveying method known as mobile mapping system (MMS) uses a mobile measurement vehicle equipped with a laser scanner that can acquire such point cloud and a sensor that acquires self-position information.

In this study, the slope is measured by an MMS survey, and the detection accuracy of deformation appearing on the slope using the evaluation of the measured data is verified. In addition, to detect the deformation, we introduced a difference analysis method by superimposing two separate point clouds. We performed three different verifications corresponding to the point cloud acquisition accuracy of the MMS survey, the deformation discriminability of the acquired point cloud, and the extraction accuracy of the deformation obtained by the difference analysis method. Based on these results, we forecast that a landslide would occur. The ability of the present method to detect the protrusion of deformation, which is a sign of landslide against the known slope, is also confirmed. Moreover, we investigated whether the point cloud obtained by MMS can extract the deformation through the difference analysis method.

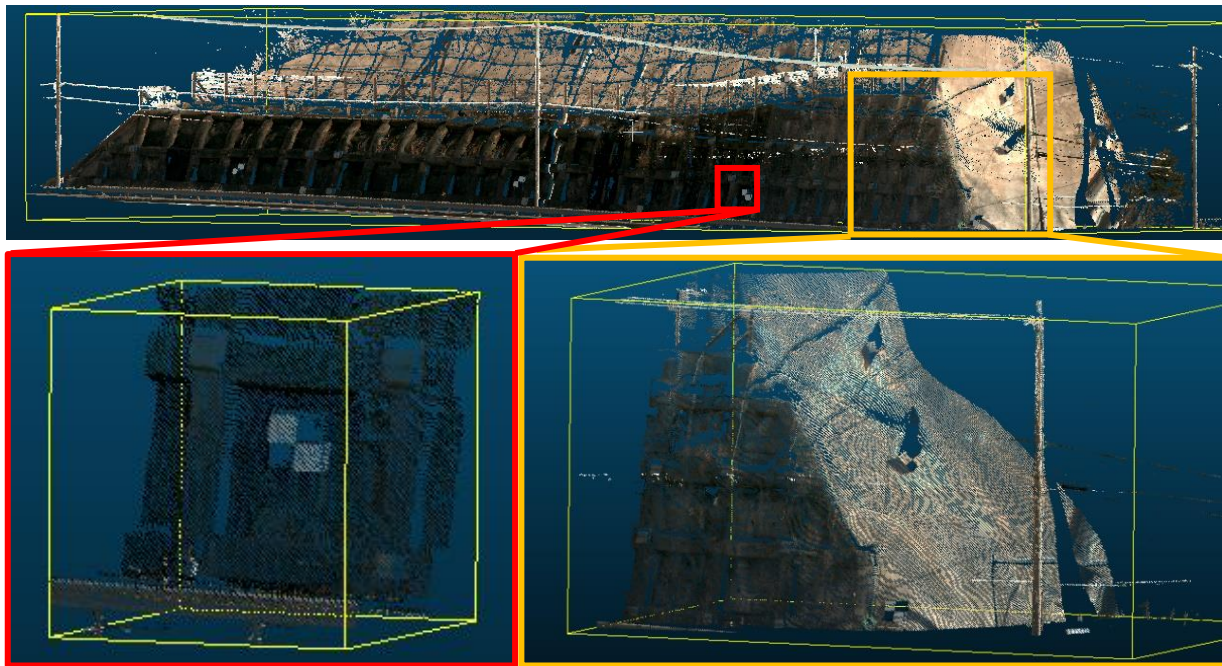


Fig. 1 Point cloud data on slope
(left: target in grating crib, right: side of slope)

VERIFICATION METHOD

In this chapter, we describe the verification approach to be used, MMS survey and difference analysis method, the slope to be verified, and the outline of the target installed on the slope.

MMS surveying is a method that can efficiently and two-dimensionally acquire three-dimensional position information about the terrain and features around the road during normal driving of a vehicle equipped with the necessary equipment in Fig. 2. When the road slope is measured three-dimensionally, the point cloud is usually obstructed by the influence of two-way traffic and pedestrians. On the other hand, the point cloud can be lost because the MMS performs its mobile acquisition while moving. However, it is possible to measure few places without such data loss. The vehicle used in this study is equipped with a laser scanner that scans 1 million points per second, a global navigation satellite system (GNSS) receiver, an inertial measurement device, an odometer, a camera, and other sensors that acquire self-position and orientation. MMS surveys are actively used in the management assistance of roads [2] and rivers [3] in effective.

The ICP associates the closest points in the two different point clouds and optimizes the position (rotational and parallel movements) for the entire point cloud. The matching and optimization are repeated, and the algorithm is terminated once these point clouds are the closest in the terms of distance. In the difference analysis method, as shown in Fig. 3,

the situation of the point cloud at the end of iterative closest point (ICP) is applied, and the detection of deformation amount of the points is considered to be by a vector through comparing the coordinate values of the points associated with the two point clouds.

The target slope to be measured had approximately a length of 70 m and a height of 10 m along the National Highway 9 and was suspected to have caused a landslide by visual inspection in Fig. 4. This slope was cut in 1987 during road widening, and its cross section was sloped by the ground anchor method with a frame. Then, on May 1, 2016, the anchor head protection concrete fell and an accident occurred where the concrete pieces had fallen on the roadway. Subsequently, various investigations and



Fig. 2 MMS surveying on the slope
(Devices are marked by the red rectangle)

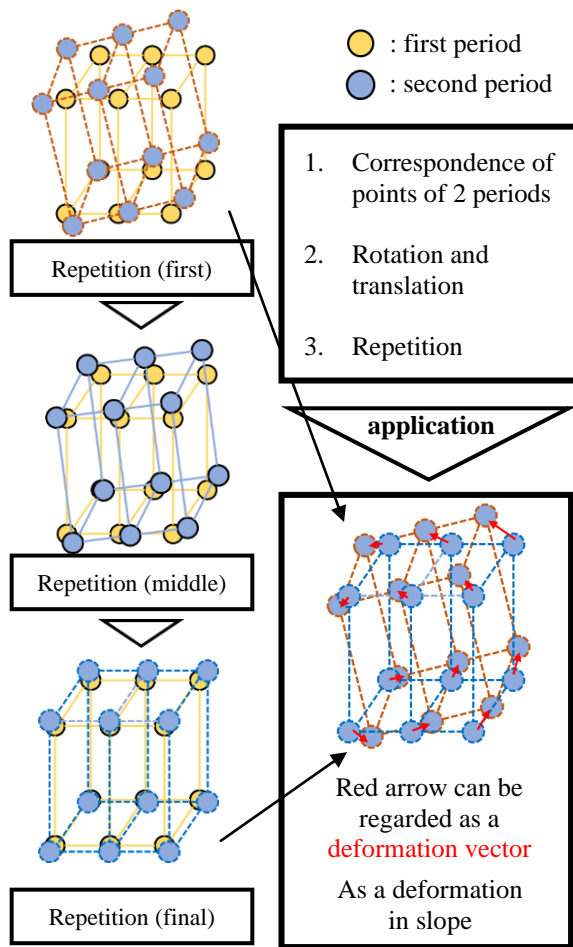


Fig. 3 Difference analysis algorithm

observations were carried out, and the slopes around the anchor rupture site were assumed to have a variation mode, causing them to be displaced toward the starting point side, although no visually significant deformation was observed. Therefore, in this study, the required deformation is defined as bulging, and this has been verified. In addition, targets, 0.7 m square, was installed on the slope as a reference point for adjustment, 8 points surrounding the entire slope and 6 points on the side of the starting point where fluctuations are expected. The first measurement period was January 13, 2018, that is, the second period was May 28, 2018, and the measurement was performed over a period of about 4 months. The MMS vehicle traveled in lane2 with a distance of approximately 12 m from the target slope at 50 km/h and acquired the point cloud of the slope in Fig. 5.

VERIFICATION

We describe verifications on three different parameters: the point cloud acquisition accuracy of the MMS survey, the deformation discriminability of

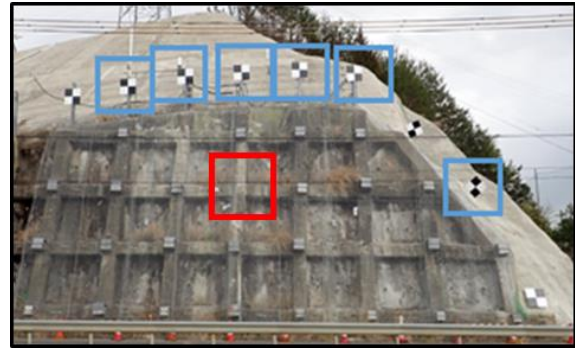


Fig. 4 Target slope
(red rectangle indicates the region where anchor head protection concrete fell, blue rectangles are reference points for verification)

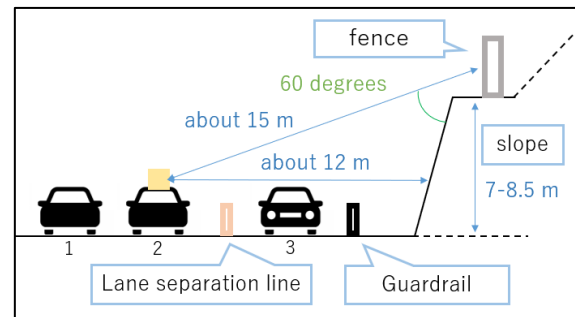


Fig. 5 Measurement conditions
(when measuring the slope, a distance of approximately 12 m vertically, when measuring the fence, a distance of approximately 15 m at 60 degrees)

the acquired point cloud, and the extraction accuracy of deformation obtained through the difference analysis method.

MMS Point Cloud Acquisition Accuracy

In this chapter, the verification of the point cloud acquisition accuracy of the MMS is presented.

The point closest to the center of the target in the point cloud acquired by the MMS was set as the center coordinate of the target acquired by the MMS survey. In addition, its true value was assumed to be a second-class A total station (TS) and was measured. The comparison results of the points acquired by the MMS and TS are expressed as the mean difference and RMS error (root mean squared error). The compared targets are the targets that surround the slope where fluctuations are expected. Note that CloudCompare [4], which is a software for point cloud analysis, was used to acquire the center coordinates of the target. The mean difference indicates the difference between the coordinates obtained by TS and MMS, and the RMS error indicates the variation with the difference in each of

the X, Y, and Z directions of the point group as the most probable value. In this study, we compared the XY plane, which is a horizontal plane with the ground, and the Z direction, which is the height direction of the slope. The mean difference of the MMS and RMS error (root mean squared error) are expressed by the following equations:

$$DIS = OBS - TV \quad (1)$$

$$\overline{DIS} = \frac{\sum DIS}{n} \quad (2)$$

$$RMS = \sqrt{\frac{\sum DIS^2}{n}} \quad (3)$$

where, DIS is the difference, OBS is the observed value, TV is the true value, \overline{DIS} is the average value of the difference, n is the verification score, RMS is the root mean squared error of the MMS survey.

It was observed that the average range was less than 20 mm for ΔXY and less than 30 mm for ΔZ in Fig. 6, while the errors were less than 20 mm and 25 mm, respectively. The average differences of the MMS data calculated using the adjustment reference points were 25 mm for ΔXY and less than 30 mm for ΔZ in Fig. 7, while the errors were less than 20 mm and 25 mm, respectively. The adjustment calculation data is obtained by superimposing the coordinates of the adjustment reference points acquired by the MMS surveying on the data acquired by the TS. The point cloud data acquired by the MMS survey satisfy the map information level of 0.70 m horizontally and less than 0.33 m vertically, both with and without adjustment calculation, and therefore, exhibit good accuracy. It can be said that the data of was obtained.

Distinguishability of the MMS

A simulated deformed specimen is placed on the slope to verify the scale of the deformed points acquired by the MMS.

The goal is to verify whether the data acquired by the MMS survey is reproduced as a deformation by using a simulated deformation specimen. The test specimen was installed near the toe of the slope, and faced the laser scanner. As shown in Fig. 8, two simulated specimens were installed (5, 10, 20, 30, 50, and 100 mm), and three simulated steps, a total of five. As a result, the point density of the data was measured as 967 (points/m²) on the target with a side of 0.7 m. Next, the acquired point cloud near the specimen is cut into a strip with a width of about 0.5 m and the cross section is displayed. It can be easily observed from the cross-sectional view in Fig. 9 that the schematic shape of the specimen is clearly expressed. From the results of 1 and 2 shown below, a simulated crack in the horizontal direction of approximately 20 mm and in the vertical direction of approximately 10 mm can be visually detected. It was also confirmed

from the results of 4 to 8 that the simulated step can be detected if the deformation is 10 mm or more.

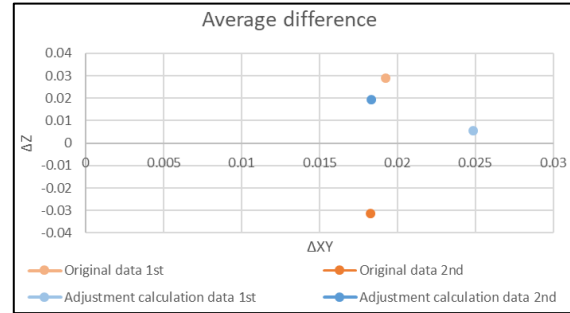


Fig. 6 Average difference result (unit: m)

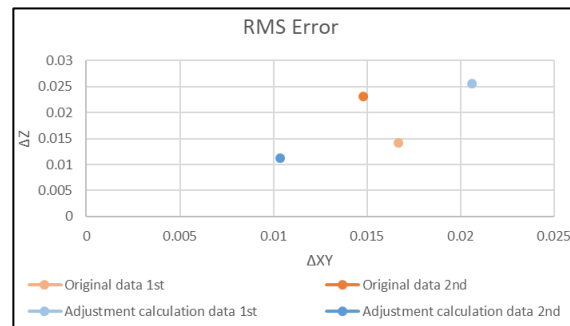


Fig. 7 RMS Error result (unit: m)

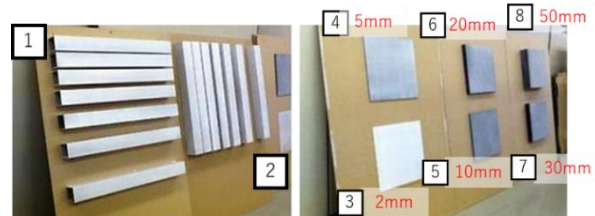


Fig. 8 Simulated deformation specimen

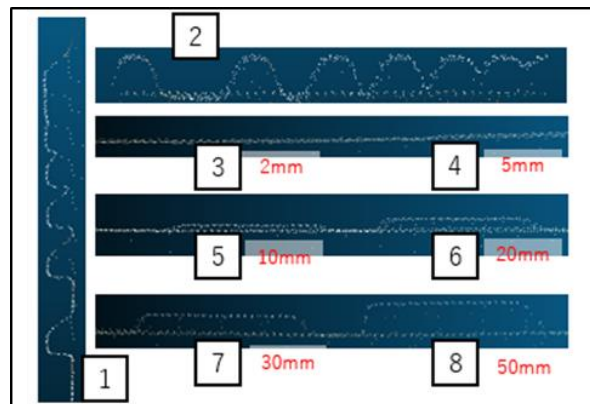


Fig. 9 Point cloud cross section of simulated deformed specimen

Deformation Accuracy of Difference Analysis

In this section, we investigate the detection accuracy of the deformation of the difference analysis method. We installed a sheet that could introduce a certain amount of deformation to the four law frames and could be scraped off (simulated deformation). The deformation is applied not in the first period, however, in the second period, followed by the calculation of the deformation between the two periods. As shown in Fig. 10, in the second period, law frame 1 did not exhibit any deformation, while in law frame 2, part of the concrete was shaved and a maximum of approximately 40 mm was scraped off. Sheets of 10 and 20 mm were installed in the legal frames 3 and 4, respectively. We also examined

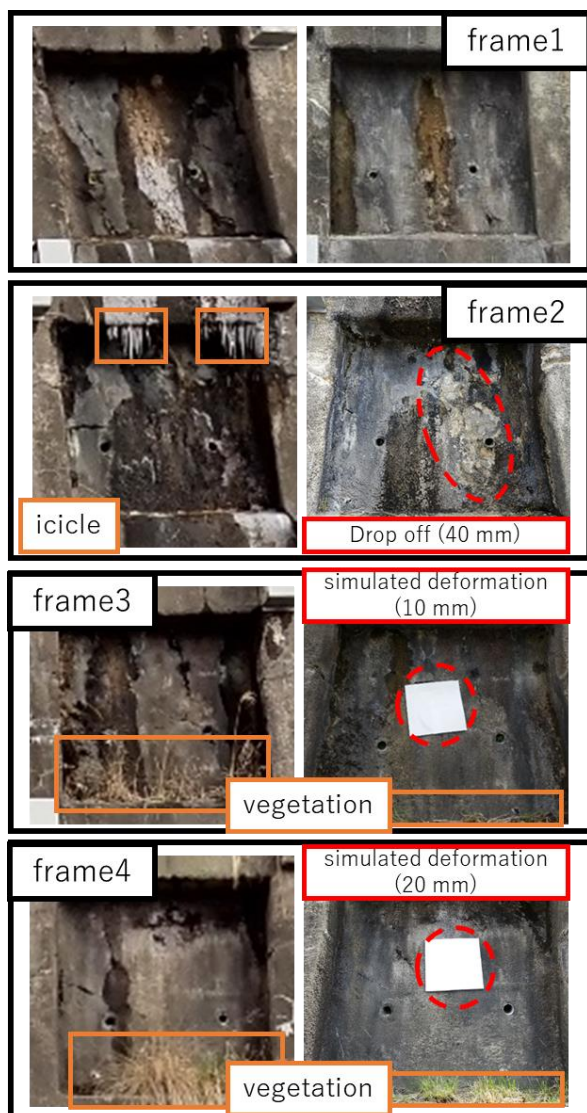


Fig. 10 Two stages of simulated deformation given to the slope
(1: no deformation, 2: drop off (40 mm),
3, 4: Simulated deformation (10 mm, 20 mm))

whether the analysis results shown in Fig. 11 could be obtained using this simulated transformation. For that, no deformation was applied to 1, so that deformation was absent. As a result, 2 was hanging down about 40 mm, so that the deformation was indented in the depth direction of the slope, while 3 and 4 were protrusions. With these parameters, we verified if the deformation was of 10 mm or 20 mm. The result is a cross-sectional view of the slope, where the numerical values shown in Fig. 12 represent the deformation quantity, while the arrows represent the direction of it. All the results from 1 to 4 were as expected, where 1 shows no deformation, 2 shows the displacement that moves towards the back of the slope, and 3 and 4 show the amount of deformation to be obtained clearly. Although it was not considered possible, we were able to detect a deformation that would extend to the front of the slope. Thus, it was found that the protrusion greater than 10 mm and lack of approximately 40 mm could be confirmed as deformation.

VERIFICATION THE ENTIRE SLOPE

Based on the previously obtained results, verification using the proposed method for the target slope is described in this section. The point cloud was acquired by MMS for the target slope, and the changes that occurred during the 2 o'clock period after about 4 months were extracted using the

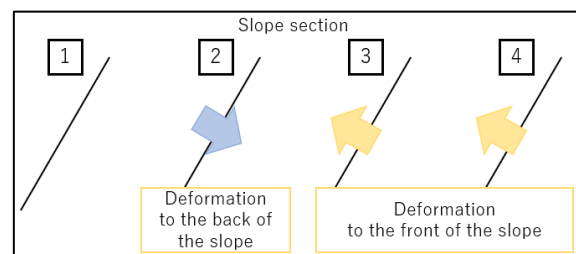


Fig. 11 Expected analysis result
(1: no deformation, 2: deformation to the back of the slope, 3, 4: deformation to the front of the slope)

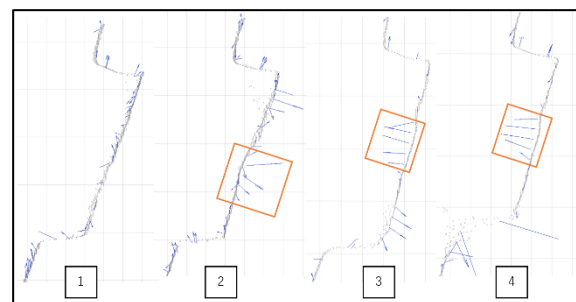


Fig. 12 Analysis result of slope with simulated deformation

difference analysis method. As a result of measuring the center coordinate of the reference point in this range by the TS, the average differences between the two periods are 2 mm and -1 mm in the plane and elevation directions, respectively, while the RMS error is 1 mm. Because the error of was about the mechanical error, there was no change in this slope. Therefore, it is confirmed that the deformation (outflow) is not extracted on the target slope through MMS and the difference analysis method. Fig. 13 shows the result of analyzing the point cloud data of two periods. The deformation direction is indicated by the arrow, while its size is expressed by a numerical value. When this slope actually causes protrusion, the deformation will be expected to appear in a wide area as shown in Fig. 14. The analysis results of the slope reveal that the errors of the entire point cloud and MMS survey are mainly due to the absence of vegetation and icicles in the first period, but not in the second period. However, it can be confirmed that there exists no deformation in a wide area. Therefore, it can be stated that a deformation such as a protrusion can be obtained using this method.

CONCLUSION

In this study, three different types of verifications were performed for detecting the change in the slope

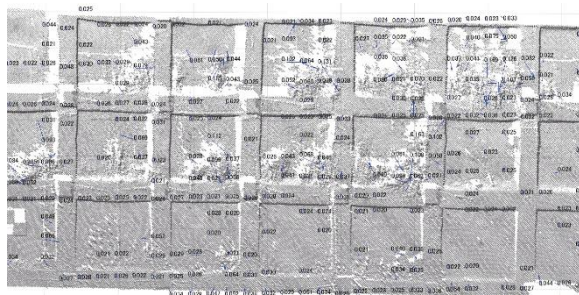


Fig. 13 Analysis results of slopes suspected to be landslides

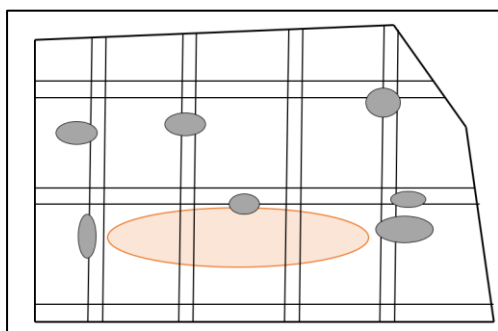


Fig. 14 If a landslide actually occurs, the expected deformation

between two time periods through the MMS and difference analysis method. The error of the adjustment calculation data in the MMS survey was less than 25 mm and 30 mm in the horizontal and vertical directions, respectively. If the error was about 10 mm, it was possible to obtain a point cloud that could identify a deformation such as a protrusion. In addition, cracks in the horizontal direction can be identified by approximately 20 mm, and those in the vertical direction by approximately 10 mm. The detection accuracy of the deformation obtained by the difference analysis method was approximately 10 mm, while the deformation imitating the protrusion and deformation imitating the lack of about 40 mm could be detected. From these verification results, together with the fact that target slope did not change, it can be deduced that similar results can be obtained through the difference analysis method for the point cloud acquired by MMS. In other words, it was confirmed that this method can detect the protrusion, which is a sign of landslide.

Meanwhile, although it was found that the presence or absence of the slope deformation can be obtained, the accuracy of the deformation amount was unclear. Confirming the deformation state will contribute to the prevention of the slope from collapsing. In the future, there is room to verify that it is not affected by noise such as vegetation and that the error of MMS survey and the correction by adjustment calculation are improved. Future work may include verification of noise effect on the deformation, such as vegetation, as well as improving the MMS survey error and the correction by adjustment calculation. Therefore, these noises must be removed, and verification must be performed.

ACKNOWLEDGMENTS

We would like to thank Editage (www.editage.com) for English language editing.

REFERENCES

- [1] Japan Institute of Country-ology and Engineering, JICE, 2020
- [2] Koichi Sakai, Takeshi Oishi, Shintaro Ono, Yasuhide Okamoto and Takayuki Hirasawa, Study of support for road maintenance work using omnidirectional video, product research, Vol.70, Issue 2, 2018, pp. 51-56.
- [3] Kikuo Tachibana, Koji Mano, Hideki Shimanura and Satoshi Nishiyama, The application of Mobile Mapping System to river embankment measurement, Photogrammetry and remote sensing, Vol.54, Issue 4, 2015, pp.166-177.
- [4] CloudCompare project, 2020

MEASURING THE ACCESSIBILITY TO TRANSIT STATION: A CASE STUDY OF TANJUNG KARANG, LAMPUNG INDONESIA

Aleksander Purba¹, Diti Artanti Utami Putri², Rahayu Sulistyorini³, Shahnaz Nabila Fuady⁴, and Lusmeilia Afriani⁵

^{1,3,5}Faculty of Engineering, Lampung University, Indonesia; ^{2,3,4}Urban and Regional Planning Study Program, Institut Teknologi Sumatera, Indonesia

ABSTRACT

Tanjung Karang station in the center of the capital city of Lampung province is the largest transit station within the city and has been in operation for decades. In addition to serving long-distance passengers between Lampung and South Sumatera provinces, the transit station is also connected to a number of districts in the northern part of the province where most of the users are commuter passengers. Analysis is conducted by using the scoring method against a number of variables that are considered the most decisive to indicate the level of accessibility. They are travel distance, travel time, travel cost, road network conditions, and public transport, respectively. The score of each variable is 2.55; 2.63; 2.74; 1.53; and 0.96, respectively, and the final score results is 2.08 meaning that the accessibility level of the study area to Tanjung Karang station is categorized as moderate. The lowest score regarding public transport indicates more effort is needed to make the city bus more attractive to citizens to use the bus to reach railway transit station.

Keywords: accessibility, transit station, public transport, Tanjung Karang, Indonesia

INTRODUCTION

Accessibility refers to people's ability to reach goods, services and activities, which is the ultimate goal of most transport activity. Many factors affect accessibility, including mobility (physical movement), the quality and affordability of transport options, transport system connectivity, mobility substitutes, and land use patterns. More comprehensive analysis of accessibility in planning expands the scope of potential solutions to transport problems [1]. Other researcher defining accessibility is the measure of the capacity of a location to be reached by, or to reach different locations. Therefore, the capacity and the arrangement of transport infrastructure are key elements in the determination of accessibility [2]. In other words, people who are in locations that are more accessible will be able to reach activities and destinations faster than those in inaccessible locations. The latter will be unable to reach the same amount of locations in a certain period of time. Accessibility determines equal access and opportunity. The public transport accessibility level (PTAL) in the United Kingdom, for example, is a method of transport planning that determines the access level of geographical locations in regards to public transportation [3]. In other European part, in order to rank certain place is conducted by measuring the levels of sustainable accessibility by travel mode at each geographical location in the study area as

illustrated for the city of Galway, Ireland [4]. Otherwise, it is often claimed that a modal shift from private to public transport (particularly rail) would generate positive feedback effects, including reductions in car travel and CO₂ emissions, as well as increases in walking and cycling. It would also create opportunities for urban development, especially near railway stations. Conversely, mixed land-use developments near railway stations would improve accessibility for people to live, work and play close to home with access to transit station. Analysis is conducted by using the scoring method against a number of variables that are considered the most decisive to indicate the level of accessibility.

CASE STUDY AND DATA

Bandar Lampung is the capital city of Lampung province in the south of Sumatra island, Indonesia. This city is the main gate to enter Sumatra, which becomes the main route for land transportation and logistics distribution activities from Java to Sumatra, and vice versa. Bandar Lampung has a strong role in the growing economy of Sumatra, also becomes the center of economy activities in Lampung region. The city's area is about 169.21 km², with an estimated population of 1,015,910 as of 2017. Tanjung Karang Station in Bandar Lampung is the terminus of the railway service from Palembang, Baturaja, Blambangan Umpu and Kotabumi. Figure 1 shows the transit station and surrounding areas.

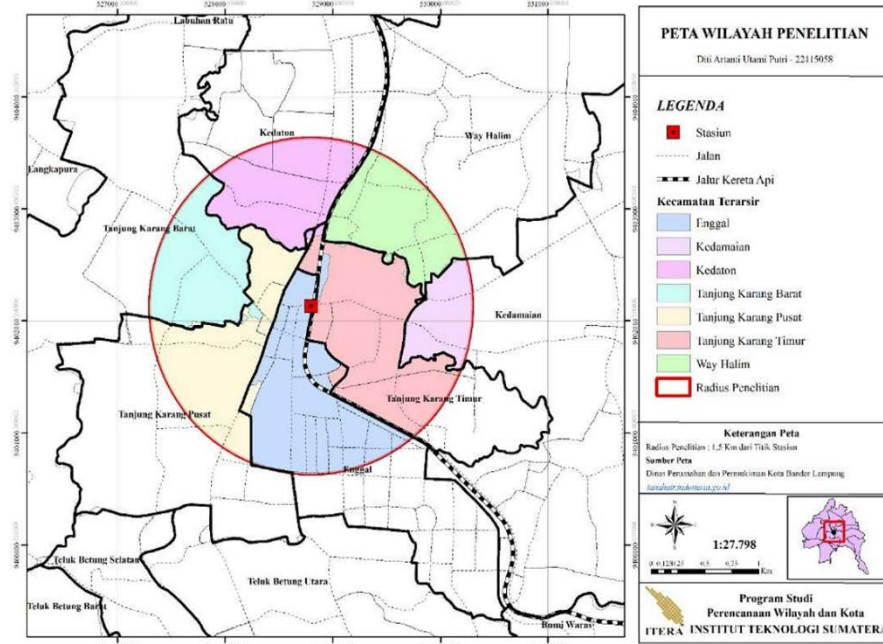


Fig. 1 Bandar Lampung city map

Passenger Statistics

The passenger traffic departing from Tanjung Karang railway station during fiscal year 2017-2018 presents in following Fig. 2. Number of the highest departure passenger in 2017 was recorded as 71,074 in October and as many as 92,820 in 2018 occurred on December.

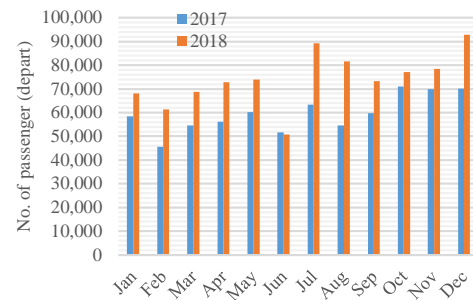


Fig. 2 Monthly depart passenger, 2017-2018

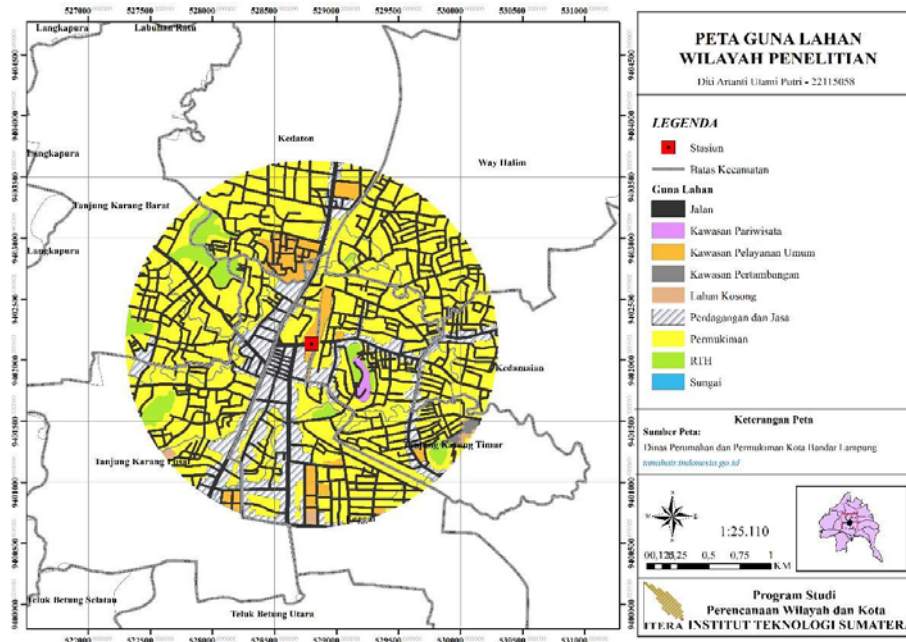


Fig. 3 Land use within study area

The average number of passengers per month during 2017 is 59,610 and an average of 72,281 people

during 2018 or there was a 21% increase in the number of departing passenger.

Characteristics of the Study Area

According to such literatures the most frequently used buffer sizes in the literature (700 and 800 m) were adopted, together with a larger buffer of 3000 m in line with the increasing body of TOD literature focusing on (electric) bicycles as feeder modes to railway stations.) [6], while other researchers emphasize the classification of railway stations. The structures of a station influence the functions it can fulfil – a common topic in e.g. ecology, where stability and reactions to disturbances are dealt with. Spatial planning and transport policy then discuss where which functions should be fulfilled, and railway stations generally form part of the context of other systems. The systematic description of these interrelations also illustrates why the interests of so many actors must be integrated in railway station operation and development [7]. The scope of this study is a residential area within ± 1.5 m radius of the station with a wide coverage of ± 7 km² and covers seven administrative districts as shown in Fig.3. According to Fig 3, most of the land are designated for residential (yellow), commercial (white), support facilities (orange) and open space (green).

RESULT AND DISCUSSION

A 160 respondents in the study area were surveyed and their responses related to the variable of travel distance, travel time, and travel cost are described below.

Travel Distance

The distance from the residence to railway station varies between 0.5 km to 4 km, with an average distance of 1.64 km. The graph related to travel distance based on grade level is shown in Fig. 4 below.

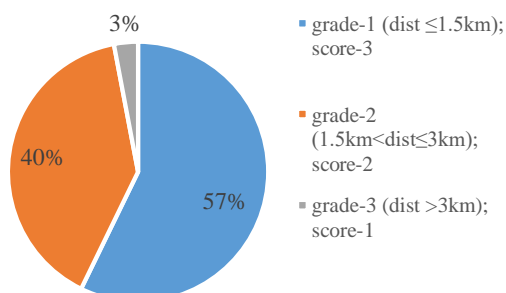


Fig. 4 Travel distance heading railway station

As many as 57% of 160 respondents reside less than 1.5 km from the station and 40% of them live between 1.5 km and 3 km. Referring to these finding,

the result of the travel distance variable score is 2.55 of 3.0.

Travel Time

Almost the same as the travel distance variable, the travel time records the time taken by the respondent from the residence to the railway station. The fastest time is recorded in 2 minutes and the longest time is 30 minutes. Graphically, the travel time required towards railway station based on three grades is presented in Fig. 5.

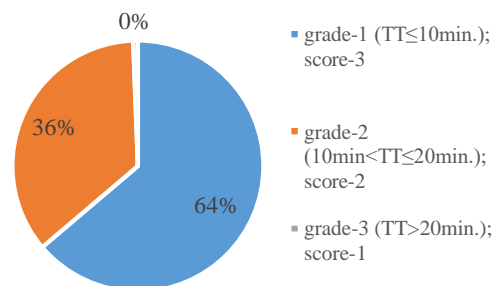


Fig. 5 Travel time heading to railway station

Nearly 64% of respondents take time about 10 minutes to reach railway station from home and the rest are needed the time between 10 minutes to 20 minutes. Since most of the respondents take time nearly to 10 minutes to reach railway station, a final score of 2.63 of 3.0 is obtained in terms of travel time variable.

Travel Cost

Travel costs vary from Rp0 to Rp15,000, indicating there are a number of respondents on foot or non-motorized transportation to reach the railway station and some of them have changed modes several times. Figure 6 shows the travel cost of respondents according to each grade.

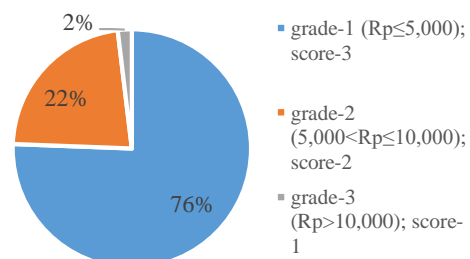


Fig. 6 Travel cost needed to reach station

As shown in Fig. 6, as many as 76% of 160 respondents paid Rp5,000 from the house to the railway station indicating the group used only one trip

and one mode of transportation since Rp5,000 was the average fare for a single trip by bus or para-transit mode. Based on the overall calculation result, the final score of travel cost variable is 2.74 of 3.0.

Road network Conditions

Scores related to road network conditions are calculated after field observations are made. Some decisive assessment components are the road surface, road markings, availability of sidewalks, and side friction.

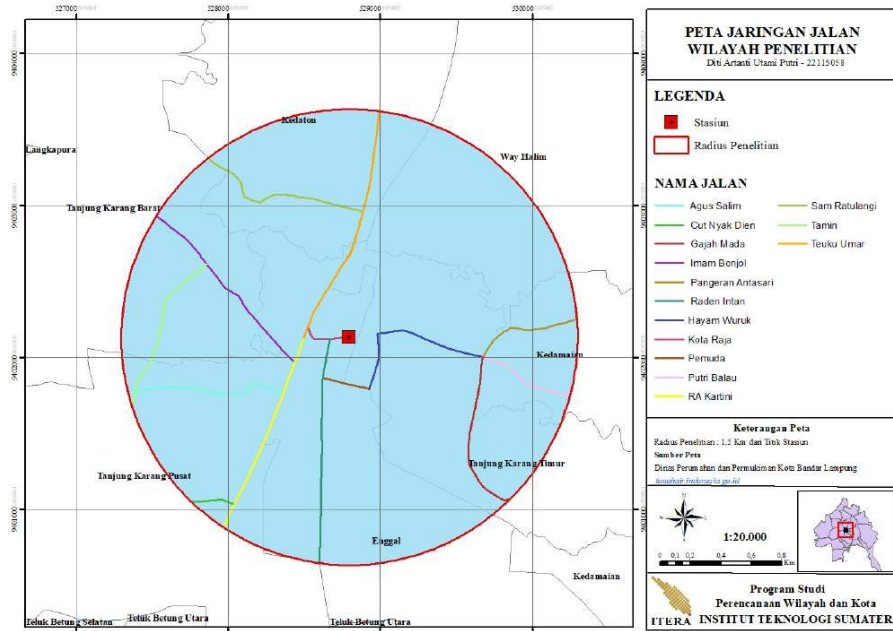


Fig. 7 Road network within study area

In this case, there are 14 road sections that were observed with several levels of function hierarchy, namely secondary arterials, primary collectors and secondary collectors referring to Indonesian urban road classification. Road network within study area and its surrounding presents in Fig. 7 and Table 1.

Table 1 Road network assessment score

Road section	Assessment score					Ave. score
	Surface	Shoulder	Marking	Side walk	Side friction	
Raden Intan	3	2	1	2	1	1.80
RA Kartini	3	1	3	2	1	2.00
Teuku Umar	3	1	3	3	1	2.20
Kota Raja	3	2	1	3	0	1.80
Imam Bonjol	3	1	2	1	0	1.40
Gajah Mada	3	1	1	3	0	1.60
Pemuda	2	0	0	0	0	0.40
Hayam Wuruk	3	2	2	1	0	1.60
Antasari	3	1	1	1	1	1.40
Putri Balau	3	1	2	0	2	1.60
Agus Salim	3	1	2	0	1	1.40
Tamin	3	1	2	0	3	1.80
Cut Nyak Din	3	0	1	0	2	1.20
Sam Ratulangi	3	1	1	0	1	1.20
Final score						1.53

Note: 3: excellent; 2: good; 1: moderate; 0: poor

Table 1 shows the variables that contributed the highest score to the assessment were road surfaces. This indicates that almost all of the 14 road sections observed were in excellent condition. Whereas the side friction variable contributes to the lowest value expressed by on street parking, entry-exit vehicles to land-use and street vendor activities within surrounding areas.

Public Transport Availability

In this section, the assessment is carried out related to the availability of public transport services (city buses and para-transit) on the fourteen road networks within the study area and the availability of bus stops along the network. Detailed assessment results are shown in Table 2. Based on observations, most of the road networks within the study area are serviced by para-transit, and only the main roads with the function of secondary arterial are served by city buses. City bus and para-transit services are fully carried out by private companies and almost without control by the city government regarding service quality. Resolving this issue has been stated as for the vast majority of station areas, the transportation supply is not enough to match the potential demand created by the existent land uses around the stations [8].

Table 2 PT and bus stop assessment score

Road section	Function	Assessment score		Ave. score
		PT availability	Bus stop	
Raden Intan	Secondary arterial	3	3	3.0
RA Kartini	Secondary arterial	2	1	1.5
Teuku Umar	Secondary arterial	2	0	1.0
Kota Raja	Secondary arterial	3	0	1.5
Imam Bonjol	Primary collector	1	0	0.5
Gajah Mada	Secondary collector	1	0	0.5
Pemuda	Secondary collector	3	0	1.5
Hayam Wuruk	Secondary collector	1	0	0.5
Antasari	Secondary collector	1	0	0.5
Putri Balau	Secondary collector	9	0	0.0
Agus Salim	Secondary collector	1	0	0.5
Tamin	Secondary collector	2	0	1.0
Cut Nyak Din	Secondary collector	2	0	1.0
Sam Ratulangi	Secondary collector	1	0	0.5
Final score				0.96

Note: 3: service & bus stops available; 2: unregularly service & rare bus stops; 1: sometimes service & no bus stops available; 0: both no available

Based on Japan experiences, typically, two actors are involved in the development of railway corridors in Tokyo. They are the local governments and the private railway operators. Local governments in Japan are two-tiered consisting of prefectures serving wider areas and municipalities serving local areas. In particular, the prefecture, in Tokyo called the Tokyo Metropolitan Government (TMG), plays an important role in the development of railway corridors. The role of the TMG mainly concerns conditioning and facilitating land use developments [9]. Station area projects in Europe suggested Both technological change (development of high-speed and urban-regional railway networks, transfer of distribution and manufacturing activities away from station areas) and institutional change (privatization of railway companies) play a role, and are compounded by two different strands of public policies: promoting the attractiveness of urban neighbourhoods and cities and promoting sustainable development [10].

Final Results of Accessibility Level

The classification for determining the level of accessibility of the study area is determined qualitatively as follows: poor accessibility (score: 0.00~1.20), moderate accessibility (score: 1.20~2.40), and good accessibility (score: 2.41~3.00). Hence, the final results of the assessment of accessibility level within the study area can be seen in Table 3.

Table 3 Final score of assessment

No	Variable	Score	Accessibility level
1	Travel distance	2.55	good
2	Travel time	2.63	good
3	Travel cost	2.74	good
4	Road network	1.53	moderate
5	Public transport	0.96	poor
Final score		2.08	moderate

Variables related to travel cost seem to give the highest value to the final score, while the public transport availability variable contributes to the smallest score. The final results of 2.08 meaning that the accessibility level of the study area to Tanjung Karang station is categorized as moderate

CONCLUSION

This paper develops a relatively simple way to determine the level of accessibility to reach a railway station and the end result is not so surprising since the best practices in developing cities within developing countries are still very limited in the practical order. The involvement of the main actors in the context of land-use transport interaction still requires more efforts, especially from the central and local government, railway companies, land developers and transport operators in order to create sustainable development. Experience clearly demonstrated that knowledge sharing is an essential element for integrated land use and transport planning to take place, but just bringing together under the same roof practitioners from the two fields of expertise will not make this form of integrated planning to occur (on the contrary, it might aggravate personal differences) [11]. In a dense urbanized area, where the dwelling market is saturated, it is necessary to take explicitly into consideration the interactions among the different urban agents, and the effects of such interactions on the dwelling price, in order to correctly forecast the evolution of the land use pattern, as stated by Coppola and Nuzzolo [12]. More advanced, a resilient city can generally be summarized as the dimensions of economic resilience, social resilience, ecological resilience, and infrastructure resilience. The results demonstrate the

cross-linkage between development and urban resilience, which is in nature a resilience in development. However, improving urban resilience to climate change requires a systematic, long-term, and local based approach. Urban development cannot autonomously lead to a more resilient city, it's often on the opposite [13]. Variables related to public transport availability which have the lowest score on the assessment of accessibility level is one of the most difficult big challenges since the city mayor of Bandar Lampung more pay attention to build flyovers and widening roads to overcome increasing travel demand. The steps to deal with rapid motorization through transport demand management manners and strategies to develop the non-motorized transport have not been seen at all. Several cities have jumped several steps ahead related to the issue of sustainable transport, and this issue is closely related to path walkability. As stated by Park et. al. [14], the path walkability is defined as the quality of physical walking environment that can be measured objectively based on the micro-level physical characteristics of a street and its adjacent intermediary space between the outer edge of the sidewalk and the façade of nearby buildings. Based on finding results the score of each variable i.e. travel distance, travel time, travel cost, road network conditions, and public transport is 2.55; 2.63; 2.74; 1.53; and 0.96, respectively, and the final score results is 2.08 meaning that the accessibility level is categorized as moderate. More efforts are needed to make Bandar Lampung to become more accessible for their citizens particularly the public transport performances.

REFERENCES

- [1] Litman, T., Evaluating Accessibility for Transport Planning Measuring People's Ability to Reach Desired Goods and Activities, Victoria Transport Policy Institute, 2020, pp. 1-64.
- [2] Rodrigue, J. P., The Geography of Transport Systems, Routledge, New York, 2020, pp.1-456.
- [3] Rosenberg, M., Defining Accessibility and Mobility in Transportation and Geography, 2020, thoughtco.com/accessibility-definition-geography-1434629.
- [4] Vega, A., Using Place Rank to measure sustainable accessibility, J. of Transport Geography, Vol. 24, 2012, pp. 411–418.
- [5] Duffhues, J., Mayer, I. S., Nefs, M., and van der Vliet, M., Breaking Barriers to Transit-Oriented Development: Insights from the Serious Game SPRINTCITY, J of Environment and Planning B: Planning and Design, Vol. 41, No. 5, 2014, pp. 770–791.
- [6] Caset, F., Vale, D. S., and Viana, C. M., Measuring the accessibility of railway stations in the Brussels regional express network: a node-place modeling approach, J. of NETWORKS & SPATIAL ECONOMICS, Vol. 18, No. 3, 2018, pp. 495–530.
- [7] Zemp, S., Stauffacher, M., Lang, D. J., and Scholz, R. W., Classifying railway stations for strategic transport and land use planning: Context matters! J. of Transport Geography, Vol. 19, No. 4, 2011, pp. 670–679.
- [8] Vale, D. S., Transit-oriented development, integration of land use and transport, and pedestrian accessibility: Combining node-place model with pedestrian shed ratio to evaluate and classify station areas in Lisbon, J. of Transport Geography, Vol. 45, 2015, pp. 70–80.
- [9] Chorus, P., and Bertolini, L., Developing transit-oriented corridors: Insights from Tokyo, International J. of Sustainable Transportation, Vol. 10, No. 2, 2014, pp. 86–95.
- [10] Bertolini, L., Curtis, C., and Renne, J., Station Area projects in Europe and Beyond: Towards Transit Oriented Development? J. of Built Environment, Vol. 38, No. 1, 2012, pp. 31–50.
- [11] Papa, E., Coppola, P., Angiello, G., and Carpentieri, G., The learning process of accessibility instrument developers: Testing the tools in planning practice, J. of Transportation Research Part A: Policy and Practice, Vol. 104, 2017, pp. 108–120.
- [12] Coppola, P., and Nuzzolo, A., Changing accessibility, dwelling price and the spatial distribution of socio-economic activities, J. of Research in Transportation Economics, Vol. 31, No. 1, 2011, pp. 63–71.
- [13] Yan, Zheng., Xin-Lu, Xie., Chen-Zhen, Lin., Mou, Wang., & Xiao-Jia, H., Development as adaptation: Framing and measuring urban resilience in Beijing, J. of Advances in Climate Change Research, Vol. 9, 2018, pp. 234–242.
- [14] Park, S., Choi, K., and Lee, J. S., To Walk or Not to Walk: Testing the Effect of Path Walkability on Transit Users' Access Mode Choices to the Station, International J. of Sustainable Transportation, Vol. 9, No. 8, 2014, pp. 529–541.

SEISMIC RESPONSE OF ABUTMENTS IN A REAL BRIDGE MODEL

Desy Setyowulan¹, Toshitaka Yamao², Eko Andi Suryo³, Eva Arifi⁴, and Devi Nuralinah⁵

^{1,3,4,5}Engineering, Universitas Brawijaya, Indonesia;

²Center for Water Cycle, Marine Environment and Disaster Management, Kumamoto University, Japan

ABSTRACT

Abutment performance suggestively impacts the seismic response of bridge constructions. This research aims to observe the seismic performance of abutments in the actual bridge construction with the consequence of the wing wall and movement constraint. Analytical model of concrete box girder bridge was implemented from the actual bridge in Japan, with the numerical model was performed by three-dimensional finite element model in ABAQUS software. Four distinct abutment modelling approaches were carried out including Type 1, Type 2 (ordinary form in Japan), Type 3, and Type 4 (the proposed design). The results confirmed that all types of abutments have a capability in resisting the shear stress. Nevertheless, the overall effects of seismic ground acceleration without liquefaction effect were insignificant on the displacement and the shear stress at the surface of abutments. Furthermore, further research is needed to determine the effect of liquefaction on the seismic behavior of abutment.

Keywords: ABAQUS, Abutment, Seismic Response, Real Bridge Model

INTRODUCTION

Abutment has an important function on the performance of bridge structure, because its behavior has been found to significantly impact the response of whole bridge due to high intensity of seismic excitation [1]. According to the previous experiences, many abutments collapsed in Japan due to the large stress on the surface of abutment and pounding between superstructure and substructure.

After 1995 Hyogo-ken Nanbu Earthquake, the consideration of 10 cm gap which has been used in the actual bridge in Japan was revised due to numerous damages on bridges suffered by collision phenomenon. Furthermore, necessary gap between two adjacent girder or among girder and abutments have to be taken into design of the superstructure for avoiding any damage of the bridge triggered by collision.

The substantial effect of parapet-unified wing walls of abutment subjected to horizontal loads through unseating prevention structure of bridge was studied [2]. According to this analysis, it was found that bending moment at base of parapet affected by the wing walls. In order to prove the result of numerical analysis, an experimental model of reinforced concrete parapet wall of abutment without wing wall subjected to incremental horizontal load was inspected previously [3]. From this model, it was found that crack developed on the bottom of parapet wall and propagate along this wall.

Recent study on cost analysis of proposed reinforcement method for abutment due to girder's collision was developed, which was modeled by 3D-Finite Element Method [4]. According to this

research, it could be confirmed that the proposed seismic reinforcement method is very effective to be compared with the current method of reinforcement.

METHODS

The modelling simulation of reinforced concrete abutments were developed by using three dimensional solid elements, which was performed with ABAQUS software [5]. The discretization of abutment's geometry, material properties for concrete and steel, applied load, and boundary condition for the structure were addressed.

Finite Element Modeling

Analytical model of concrete box girder bridge was assumed from the real bridge in Japan, which was conducted previously [6, 7] shown in Fig. 1. The total length of two span superstructures was 80 m with pier as its center and abutment in its edges. Four different abutment modelling approaches shown in Fig. 2 were used as the main parameter of this research. These approaches including Type 1 as abutment without wing wall, Type 2 as ordinary model in Japan, Type 3 as abutment with full wing wall, and Type 4 as a new type of abutment which is proposed in this research.

The dimensional configurations of the total height, width, and thickness of the wing wall and parapet wall were 8.0 m, 6.0 m and 0.5 m, respectively, with length of the wing wall was 4.0 m. The gap between superstructures were set to be 10 cm and 20 cm. The

bearing supports were assumed as fixed and roller bearings for pier and abutment, respectively. Additionally, the friction coefficient was set to be 0.1.

In this non-linear simulation, the material properties for concrete are shown in Fig. 3(a), with the ultimate strength of 29.4 MPa and 50% of the linear elastic range. The Poisson's ratio and modulus of elasticity were 0.2 and 20.6 GPa, respectively. The compression and tension damaged variables, d_c and d_t , were defined and plotted in Figs. 3(b) 3(c), respectively. In addition, the reinforcing bars was assumed as steel with Young's modulus, Poisson's ratio, density, and tensile strength of 206 GPa, 0.3, 7850 kg/m³, and 294 MPa.

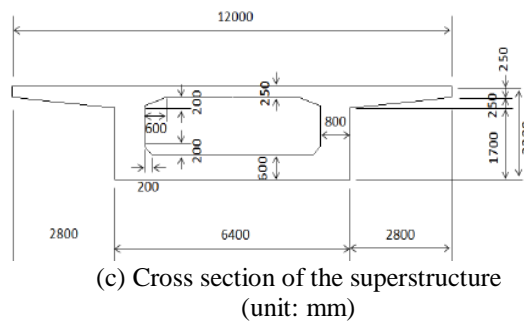
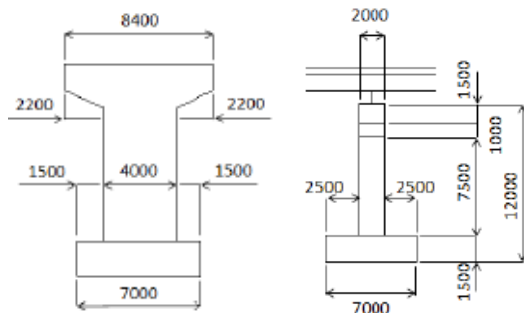
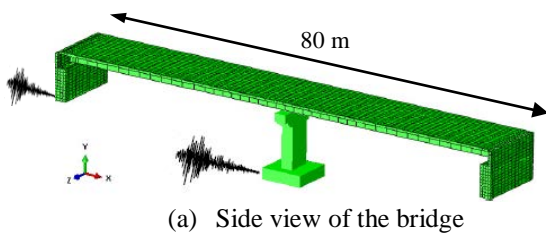


Fig. 1 Three-dimensional finite element models of concrete girder bridges in ABAQUS with the view of pier and cross section of superstructure [6, 7]

The method of Concrete Damaged Plasticity was selected due to its superiority in damage simulation. The concrete material of abutment was formed with C3D8R element, which is known as eight-node solid (brick) elements. The concrete materials for column and box girder were idealized by beam element and shell element, respectively. While the reinforcing bar

was idealized by 3D truss elements, identified as T3D2. In addition, the embedded method was applied to constraint the two-node truss element (reinforcing bar) into solid element (concrete) with the purpose of creating a proper bond action [8].

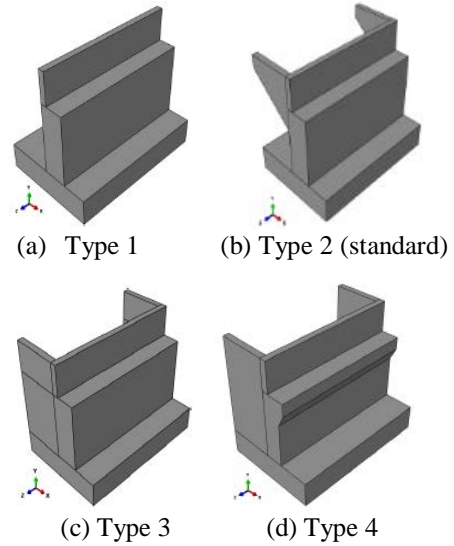


Fig. 2 Theoretical models of abutments in ABAQUS

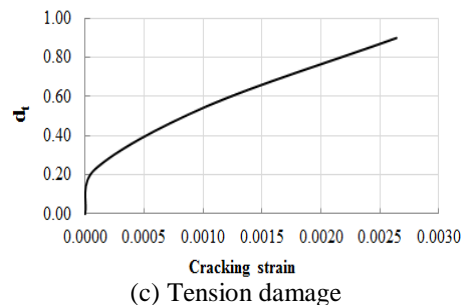
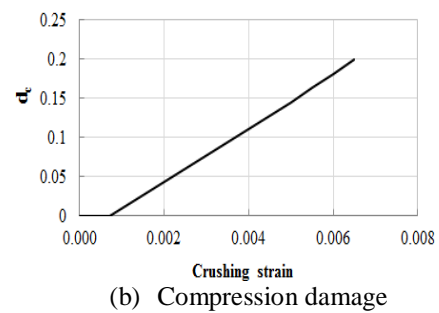
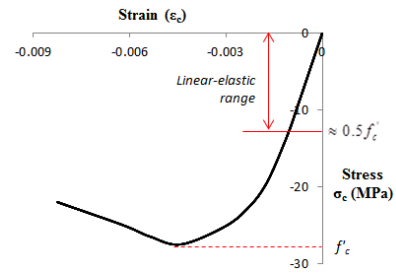


Fig.3 Material properties of the concrete

Input Seismic Wave

Level 2 Type 2 with ground Type I earthquake ground motion with accelerations type were applied horizontally at the lowest part of substructures. It is known as an inland direct strike type earthquake with low probability of occurrence, which is represents with strong accelerations and shorter duration. Three input seismic waves shown in Fig. 4. L2T2G1 depicted as Level 2, Type 2 and ground (soil) type 1. Furthermore, it was assumed that no liquefaction occurred.

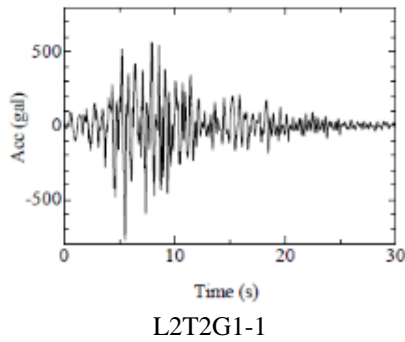


Fig.4 Input seismic wave (L2T2G1-1) from JSHB seismic waves [9].

Loading

The loading condition for abutment under earthquake should be designed with the combination of dead loads, earth pressure and seismic effect [9]. Calculation of the earth pressure was assumed as a distributed load acting on the backfill of abutment. The soil properties were determined previously by Yamao et al., 2012. Monobe-Okabe Method was used to calculate an active pressure strength during an earthquake, as determined in Eqs. (1) and (2). PEA and KEA were determined as strength of an active earth pressure (kN/m²) at depth x (m) and coefficient of active earth pressure, respectively.

$$P_{EA} = r K_{EA} + q' K_{EA} \quad (1)$$

$$K_{EA} = \frac{\cos^2(\phi - \theta_o - \theta)}{\cos \theta_o \cos^2 \theta \cos(\theta + \theta_o + \delta_E) \left(1 + \sqrt{\frac{\sin(\phi + \delta_E) \sin(\phi - \alpha - \theta_o)}{\cos(\theta + \theta_o + \delta_E) \cos(\theta - \alpha)}} \right)^2}$$

Proposal of the Damage Assessment

The determination of damage in abutment was examined by using an allowable stress of concrete [9], as shown in Table 1. An allowable stress for four different design strength of concrete are specified. Therefore, allowable shear stresses as the maximum

elastic limit and allowable compressive stresses with flexural types were defined as 1.9 MPa and 10.0 MPa.

Table 1. Allowable stresses of concrete [9]

Design strengths of concrete (MPa)		21	24	27	30
Type of stress					
Compressive stresses (MPa)	Flexural compressive stresses	7.0	8.0	9.0	10.0
	Axial compressive stresses	5.5	6.5	7.5	8.5
	When only concrete carries shear forces (τ_{o1})	0.22	0.23	0.24	0.25
Shear stresses (MPa)	When concrete and diagonal tensile reinforcement jointly carry (τ_{o2})	1.6	1.7	1.8	1.9
	Punching shear stresses (τ_{o3})	0.85	0.90	0.95	1.00

RESULTS AND DISCUSSIONS

Previous studies have reported that the areas subjected to high stress is frequently observed during the investigation of abutment's failure. Furthermore, evaluating the response stress, shear stress and displacement at abutments are useful in order to control the damage of abutments.

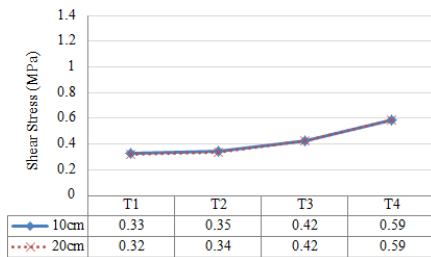
Eigenvalue Analysis

The dynamic characteristics for box-girder bridge structure in this study were explicitly portrayed through modal analysis procedures by eigenvalue analysis in previous research [7]. From this analysis, it was found the predominant mode was in equal position for bridge with different gap of 10 cm and 20 cm. Otherwise; installation of four different abutment modelling approaches had a significant effect on its predominant mode, due to effect of the wing wall. The possibility of bridge with abutment Type 4 to vibrate sympathetically was at the 9th mode in X-direction, 10th mode in Y and Z-direction.

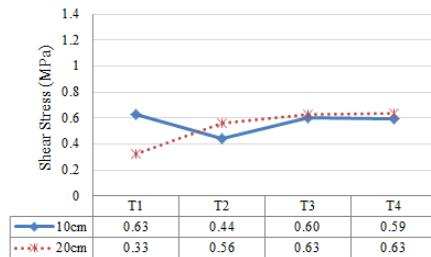
Shear Stresses of Abutments

In this numerical simulation, the maximum shear stress occurred in all abutments with different gap were analyzed, as shown in Figs. 5(a) through Figure 5(f). A1 and A2 denote the position of abutments in

the left and right side, respectively. According to these figures, it can be seen that installation of abutment Type 4 in concrete girder bridge generally increases the shear stress on vertical wall, when it is compared to Type 2. However, the maximum result is less than the maximum elastic limit of 1.9 MPa. It corresponds that abutments have a capability in resisting the shear load occurs in bridge due to the input seismic motion.



(a) A1 (L2T2G1-1)

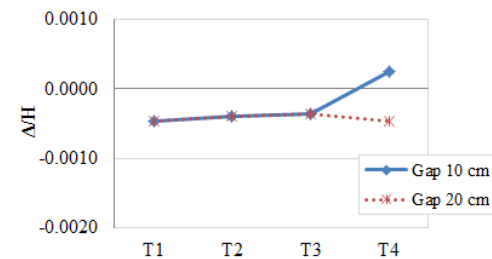


(b) A2 (L2T2G1-1)

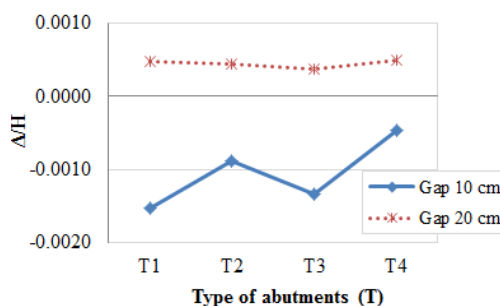
Fig.5 Maximum shear stress of abutments

Horizontal displacement of abutments

Figs. 7(a) through Figure 7(d) show the maximum horizontal displacement at the top of parapet wall with the ratio between displacements at the top of abutment (Δ) to the height of abutment (H), Δ/H .



(a) A1 (L2T2G1-1)



(b) A2 (L2T2G1-1)

(b) A2 (L2T2G1-1)

Fig. 6 Maximum horizontal displacement at top of abutments

The small and large displacements are determined by the ratio of 0.009 and 0.025, respectively [10]. Displacement to the left and right side of abutments are figured out by positive and negative values. From those simulations, it can be clarified that effect of input seismic motion is small on its horizontal displacement. This condition is possibly due to the ground motion which is applied at all support of the bridge, including of pier and abutments.

CONCLUSIONS

The seismic responses of abutments in a real bridge model were investigated. The conclusions of this research are given below.

1. Installation of different abutment modelling approaches have a significant effect on its predominant mode.
2. All types of abutments have a capability in resisting the shear stress occurs in bridge due to the input seismic motion.
3. Effect of input seismic motion is small on its horizontal displacement and the shear stress at the surface of abutments. It is possibly due to the position of the applied ground motion at all supports without any consideration on liquefaction.

ACKNOWLEDGMENTS

The authors greatly indebt to “DIKTI” (Directorate General of Higher Education) for providing financial support through this research. Special thanks to the Civil Engineering Department, Universitas Brawijaya for supporting this opportunity.

REFERENCE

- [1]. Aviram, A.; Mackie, K.R.; and Stojadinovic, B. (2008). Effect of abutment modeling on the seismic response of bridge structures. *Earth Eng & Eng Vib*, 7(4), 395-402.
- [2]. Yamao, T.; Kawachi, A.; and Tsutsui, M. (2012). Static and dynamic behaviour of a parapet wall of the abutment. *Proceeding of the 11th International Conference on Steel, Space and Composite Structures*. Qigdao, China.
- [3]. Susanti, L.; Setyowulan, D.; and Wijaya, M. N. (2018). An experimental investigation on behavior of RC parapet wall of abutment under collision. *International Journal of Civil Engineering and Technology (IJCIET)*, 9(9), 1831-1838.

- [4]. Hamamoto, T., Yamao, T., Setyowulan, D. (2020). Analytical Study on Seismic Response Reduction for PC Bridge: Effects of Cost on a Proposed Seismic Reinforcement Method Due to Collision. *Journal of Civil, Construction and Environmental Engineering (JCEE)*, 5(3), 57-66.
- [5]. Dassault Systems Simulia Corp. (2011). ABAQUS/CAE User's Manual 6.11.
- [6]. Setyowulan, D.; Hamamoto, T.; and Yamao, T. (2014). Elasto-plastic behavior of 3-dimensional reinforced concrete abutments considering the effect of the wing wall. *International Journal of Civil Engineering and Technology (IJCIET)*, 5(11), 97-113.
- [7]. Setyowulan, D.; Yamao, T.; Yamamoto, K.; and Hamamoto, T. (2016). Investigation of seismic response on girder bridges: the effect of displacement restriction and wing wall types. *Procedia-Social and Behavioral Sciences*, 218, 104-117.
- [8]. Mokhatar, S.N.; and Abdullah, R. (2012). Computational analysis of reinforced concrete slabs subjected to impact loads. *International Journal of Integrated Engineering*, 4(2), 70-76.
- [9]. Japan Road Association. (2002). Specifications for Highway Bridges Part V: Seismic design.
- [10]. Ahmed, A. (2014). Modeling of a reinforced concrete beam subjected to impact vibration using ABAQUS. *International Journal of Civil and Structural Engineering*, 4(3), 227-236.

PREDICTION OF AERODYNAMIC COEFFICIENTS FOR OFFSHORE TURBINE BLADE UNDER THE VARIATION OF WIND VELOCITIES

Eaindra Soe¹, Yasothorn Sapsathiarn¹ and Jetsadaporn Priyadumkol^{2*}

¹Department of Civil and Environmental Engineering, Faculty of Engineering, Mahidol University, Thailand

²Department of Mechanical Engineering, Faculty of Engineering, Mahidol University, Thailand

*Corresponding author: jetsadaporn.pri@mahidol.edu

ABSTRACT

Offshore wind turbine is an environmentally friendly and sustainable technology for generating electrical energy from wind energy at sea. Research in aerodynamics is crucial for the development of offshore wind energy technology to improve wind turbine blade design for maximum efficiency. In this study, numerical studies for the S809 airfoil aerodynamic performances under the wind speed of 7, 17.5, and 29 m/s are presented using the computational fluid dynamics ANSYS Fluent program. A two-dimensional model is developed in the presented study based on k- ω SST turbulence model. The turbulence model is validated with experimental results presented in the literature. The simulation results including lift coefficient (C_L) and drag coefficient, (C_D) obtained from the numerical study with the AOA range from -10° to 15° are presented. In addition, the effects of aerodynamic coefficients are also presented and discussed. Numerical results show that the sliding ratio is highest for the case of 6° AOA, in which the sliding ratios are 33.23, 41.90 and 45.87 at Reynolds numbers of 479211, 1198027 and 1882614, respectively.

Keywords: Offshore Wind Turbine Blade, Computational Fluid Dynamics (CFD), Aerodynamics Coefficients, Sliding Ratio, Angle of Attack (AOA)

INTRODUCTION

Energy demands have been significantly increasing day by day because of not only the expansion of populations but also the development of industrial sectors. Wind power becomes one of the main sustainable facility in comparison with other energy technologies like solar and hydropower because it can be found everywhere [1]. In order to make power from the wind, wind turbines are essential technology because it can operate with air and capture piece of its thermal energy, then discharge it into electricity [2].

Wind power has shifted from onshore to offshore locations in an attempt to exploit the accelerated and more stable wind speed. While shifting offshore wind, the tendency is to improve the sizes of the wind turbine blades so that more of this consistent wind can be taken, conclusively reducing the expense of energy [3]. At the present time, manufactures have been discussed the state of the art of offshore wind turbines massive of 7.5-12MW with rotor diameters of up to 200m [4].

The study of aerodynamic behavior of airfoils is essential for the design of practical wind turbine blades. The computational fluid dynamics, CFD is the further suitable way to analyze the aerodynamic loads of wind turbines with the rising computational capacity [5].

Many researchers have investigated the aerodynamics performances of various airfoils by employing CFD approach [6]-[10]. The blade profiles S809 and S816 were carried out by using two-dimensional CFD simulations to study lift and drag forces over the angle of attack (AOA) range of $\pm 180^\circ$ with wind velocity 11m/s at low Reynolds numbers [6]. Five different popular airfoil sections which were S8xx, FFA and AH series were analyzed by using CFD method to present the best airfoil profile for the optimum aerodynamic performance [7].

The flow and aerodynamic features of sharp trailing edged flat plate airfoil was systematically compared with NACA 0012 airfoil at three various Reynolds numbers by using CFD simulations [8]. The influences of rain on flow separation and aerodynamic performance of the single element and slatted NACA0012 airfoils through a mathematical model which was developed by the commercial CFD solver ANSYS FLUENT was investigated in [9]. The analysis of the 2D sub-sonic flow over NACA0012 airfoil at various AOAs and operating at a Reynolds number of 3×10^6 was presented in [10] to validate through the comparison of the predictions and the free field experimental measurements for the selected airfoil.

In this paper, S809 airfoil profile, developed by the NREL, is considered for analysis of wind turbine blade at different angles of attack from -10° to 15° .

Numerical results of simulations using Commercial Computational Fluid Dynamics (CFD) program are presented. Parameters including lift and drag coefficient are carried out by considering sliding ratio compared with three different velocities which are 7, 17.5 and 29 m/s (with Reynolds numbers of 479211, 1198027 and 1882614, respectively). The effects of aerodynamic coefficients are discussed.

HORIZONTAL AXIS WIND TURBINE (HAWT)

Modern HAWT blades have been consistently designed using well tested airfoils. National Renewable Energy Laboratory (NREL) and other agencies have developed several airfoil families especially for HAWT blades [6]. Before wind turbine energy production are designed, aerodynamic related to airfoils need to be determined.

In order to measure the aerodynamic loads, lift and drag coefficients are needed to investigate first because these coefficients could vary with AOA, α and the shape of the airfoil. The AOA plays a vital role in the wind turbine performance because the lift coefficient decreases when the AOA increases beyond a certain value which is call a stall point [11].

The lift and drag force on airfoil have been averaged and used for calculating lift coefficient and drag coefficient. Lift is defined as the force on the body in a direction normal to the flow direction. The drag on a body in an oncoming flow is defined as the force on the body in a direction parallel to the flow direction [11]. Moreover, sliding ratio is one of the predominant aerodynamic parameters of the airfoil as well. As a consequence of this, power output would be reduced when the sliding ratio is small. Similarly, the airfoil is designed, the sliding ratio should be maximized [12]. They can be defined as follows:

$$C_L = \frac{L}{\frac{1}{2} \rho V^2 c} \quad (1)$$

$$C_D = \frac{D}{\frac{1}{2} \rho V^2 c} \quad (2)$$

$$\epsilon = \frac{C_L}{C_D} = \frac{L}{D} \quad (3)$$

where, ρ is air density (kg/m^3), c is chord length (m), L is lift force (N/m), D is drag force (N/m), V is wind velocity (m/s), C_L is lift coefficient, C_D is drag coefficient and ϵ is sliding ratio.

NUMERICAL SIMULATION

The study and investigation of the S809 airfoil developed by NREL are conducted using a commercial computational fluid dynamics (CFD) package, ANSYS Fluent. The S809 airfoil is analyzed

as depicted in Fig. 1. This profile is a 21% thick with a sharp trailing edge and especially designed for HAWT blade. NREL simulated this profile by wind tunnel test with special quality. Then, the aerodynamic data of this airfoil could be attained in the technical report in [13]. The chord length of S809 airfoil is normalized equal to 1m in this simulation.

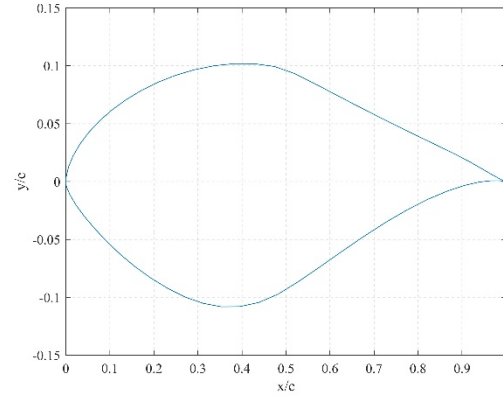


Fig. 1 S809 Airfoil Profile.

The dimension of domain and boundary condition are mainly influenced to forecast the aerodynamic flow field of airfoil. In this simulation, the computational domain is a C-type grid topology and it is extended to 12.5 chord lengths of airfoil in all direction as shown in Fig. 2. Hence, the boundary condition is applied as inlets, outlets and wall to all areas of domain as presented in Fig. 2. Thus, the inlet turbulence is considered with three variable wind velocity which are 7, 17.5 and 29m/s according to the Beaufort scales [14] at a medium range intensity 5%. At the outlet boundary, the pressure condition is set to the 0 Pa and the airfoil surface is considered as no-slip wall boundary condition. The convergence accuracy is set 10^{-5} for the absolute residuals variables equation in order to get highest precisions.

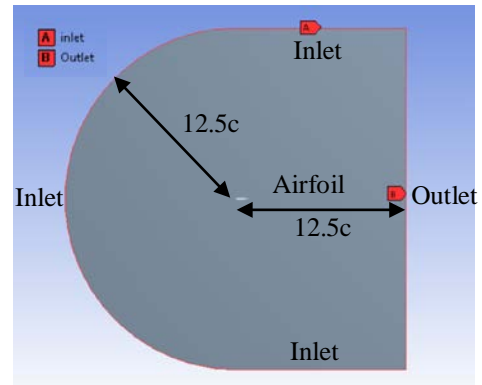


Fig. 2 The C-type domain for S809 airfoil simulation.

In this simulation, Fluent solver based a finite volume method is applied to solve the Reynolds-Averaged Navier-Stokes (RANS) equations. Thus, pressure-based solver SIMPLE is assigned as the pressure-velocity coupling algorithm. The air flow is set to be steady, incompressible and turbulent. In the previous studied [5], [15], [16] they suggested that K-Omega SST model was suitable for airfoil simulation. For this turbulence model, second order upwind is used in order to control and reduce the numerical solution errors. All these parameters are given in table 1.

Table 1 Input Parameters

Turbulence model	K-Omega SST
Fluid	Air, incompressible
Density, ρ	1.225 kg/m ³
Dynamic viscosity, μ	1.7894 x 10 ⁻⁵
Chord length, c	1 m
Discretization scheme	Pressure (second order upwind) Momentum (second order upwind)
CFD algorithm	Simple

The numerical precision especially relies on the computational grid. Basically, there are many kinds of mesh refinement patterns in CFD simulations. Figure 3 presents that the domain is discretized with the unstructured quadrilateral mesh. In addition, inflation is applied on the airfoil surface in order to capture the effect of the boundary layer as illustrated in Fig. 3.

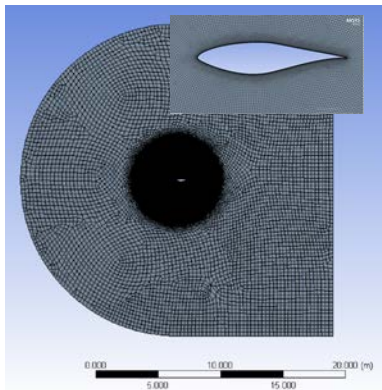


Fig. 3 The grid generated for the flow domain.

However, generating extra nodes and elements can cause the required computer memory and computational time. Therefore, the suitable number of elements should be determined until the further mesh refinement could not change the results. Figure 4 shows the convergent drag coefficient determined by relative graphs between number of element and drag coefficient at three different AOAs which are 0°,

1.02° and 5.13° respectively. This study focused on six cases of grid independent which are 17944, 42761, 110001, 185521, 319305 and 400302. The results reveal that the trends start constant at number of elements of 185521. Thus, this element number could be established as a good grid independent solution.

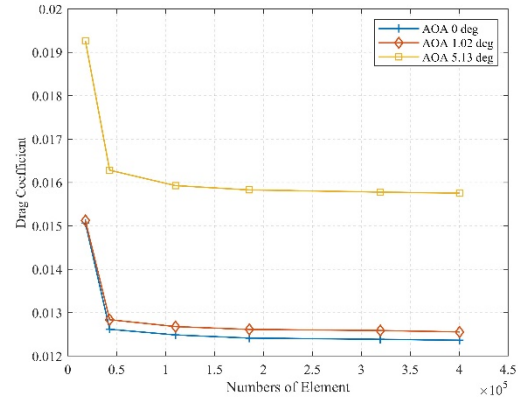


Fig. 4 The drag coefficient regarding on variable numbers of cells.

VALIDATION

The simulation results are compared with those obtained from experimental results [13] at three variable AOAs which are 0°, 1.02° and 5.13° for validation. Table 2 shows the lift coefficients of S809 airfoil at Reynolds number 2 million. It is found that the errors are less than 10% of all AOAs. Therefore, using this model can predict a phenomenon of turbulence flows in S809 airfoil correctly.

Table 2 Comparison of lift coefficients between numerical and experimental results

AOA	Numerical results	Experimental results [13]	Error (%)
0	0.1349	0.1469	8.17
1.02	0.2512	0.2716	7.51
5.13	0.7088	0.7609	6.85

RESULTS AND DISCUSSION

The results of the predicted CFD simulation at various conditions are reported in Figs 5, 6 and 7. Drag coefficient, lift coefficient and sliding ratio with the range of AOAs between -10° and 15° for three different wind speeds are discussed.

Drag Coefficient

The plot of drag coefficients and AOAs is obtained as shown in Fig. 5. The plot compares the predicted effects for various AOAs. The results show that the AOA at the minimum drag coefficients are 0 degrees which are 0.017, 0.014 and 0.012 at 7, 17.5 and 29m/s, respectively. At AOAs greater than 0 degree, the drag coefficients increase. In addition, there are notable rising trends from 5° to 15°.

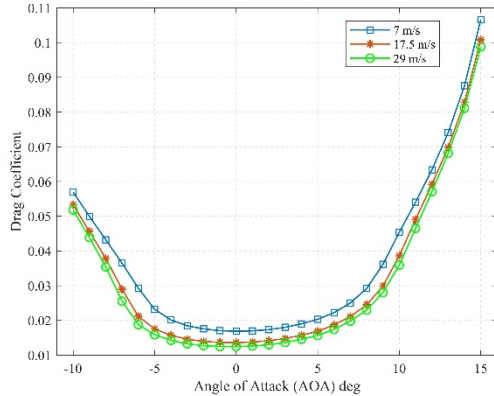


Fig. 5 Drag Coefficient Distribution between -10° to 15° for three different wind velocities.

Lift Coefficient

Lift coefficients at various velocities obtained from using the proposed model are plotted in Figs. 6. It is found that all results are similarly raising with a very significant slope in the AOA range from -5° to 10° for three velocities. At the AOA 6°, lift coefficients are 0.739, 0.783, 0.798 at 7, 17.5 and 29 m/s, respectively. While, it is found that the maximum lift coefficient raises to hit the critical AOA which is called stall point before reaching AOA 15°. In this study, the critical or stall angle of attack is around 9° - 15° for three velocities. After the lift coefficient has peaked at the critical AOA, the trend of this decreases noticeably again. The result shows a peak of 0.920, 0.990, 1.026 at AOAs of 13, 9, 10 degrees which corresponds to a wind speed of 7, 17.5 and 29 m/s, respectively.

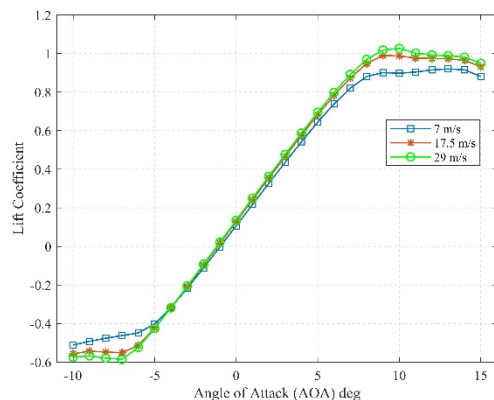


Fig. 6 Lift Coefficient Distribution between -10° to 15°

to 15° for three different wind velocities.

Sliding Ratio/ Lift to Drag Ratio

The sliding ratio for the simulation results are reported by graphs in Fig. 7. Figure 7 shows that the lowest sliding ratio is -17.32 at AOA of -5° for 7m/s wind velocity. While, at AOA -6°, the fewest sliding ratios are -24.26 and -27.91 at the velocities of 17.5 and 29 m/s, respectively. In contrast, the AOA at the maximum sliding ratios are equally at 6° which are 33.23, 41.90 and 45.87 at 7, 17.5 and 29 m/s, respectively. It is obvious that the airfoil has a maximum sliding ratio of 45.87 at AOA of 6°, which corresponds to a wind velocity of 29 m/s. Therefore, the higher wind velocity yields the best sliding ratio. In addition, it is claimed that AOA of 6 degrees is the best condition to operate a HAWT with S809 airfoil profile with all three velocities.

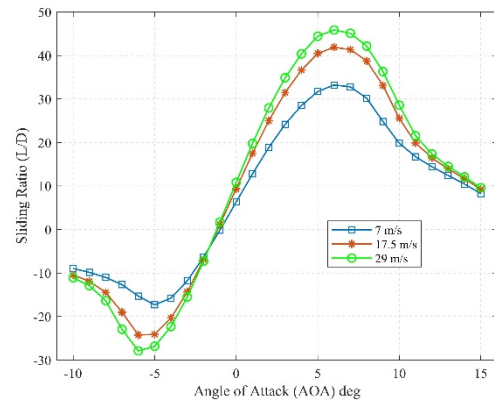


Fig. 7 Sliding Ratio Distribution between -10° to 15° for three different wind velocities.

CFD Simulation

The predictions of pressure contours and velocity streamlines in the flow domain at a velocity of 17.5 m/s are shown in Fig.8. Figure 8 shows the distribution of the pressure contours and velocity streamlines at the AOA of 0°, 6° and 12°.

From Fig.8a, the results demonstrate clearly that the pressure on the lower surface of the geometry is larger than that of the upper part increasing AOAs. Therefore, the under part of airfoil pressure at AOA 12° is greater than that side of its at AOA 0°. It is shown that the geometry is pushed to the upward movement as a result of airflow direction.

The velocity streamlines show significantly different among three AOAs as shown in Fig.8b. The simulation results illustrated the streamlines are formed to be a vortex on the trailing edge at the AOA of 12 degrees. There is a noticeable vortex effects of trailing part of profile at AOA of 12° comparing other two AOAs 0° and 6°. The vortex os expanded and

strongly separated flow above the stall angle of attack. As a result of this, the lift coefficient would decrease.

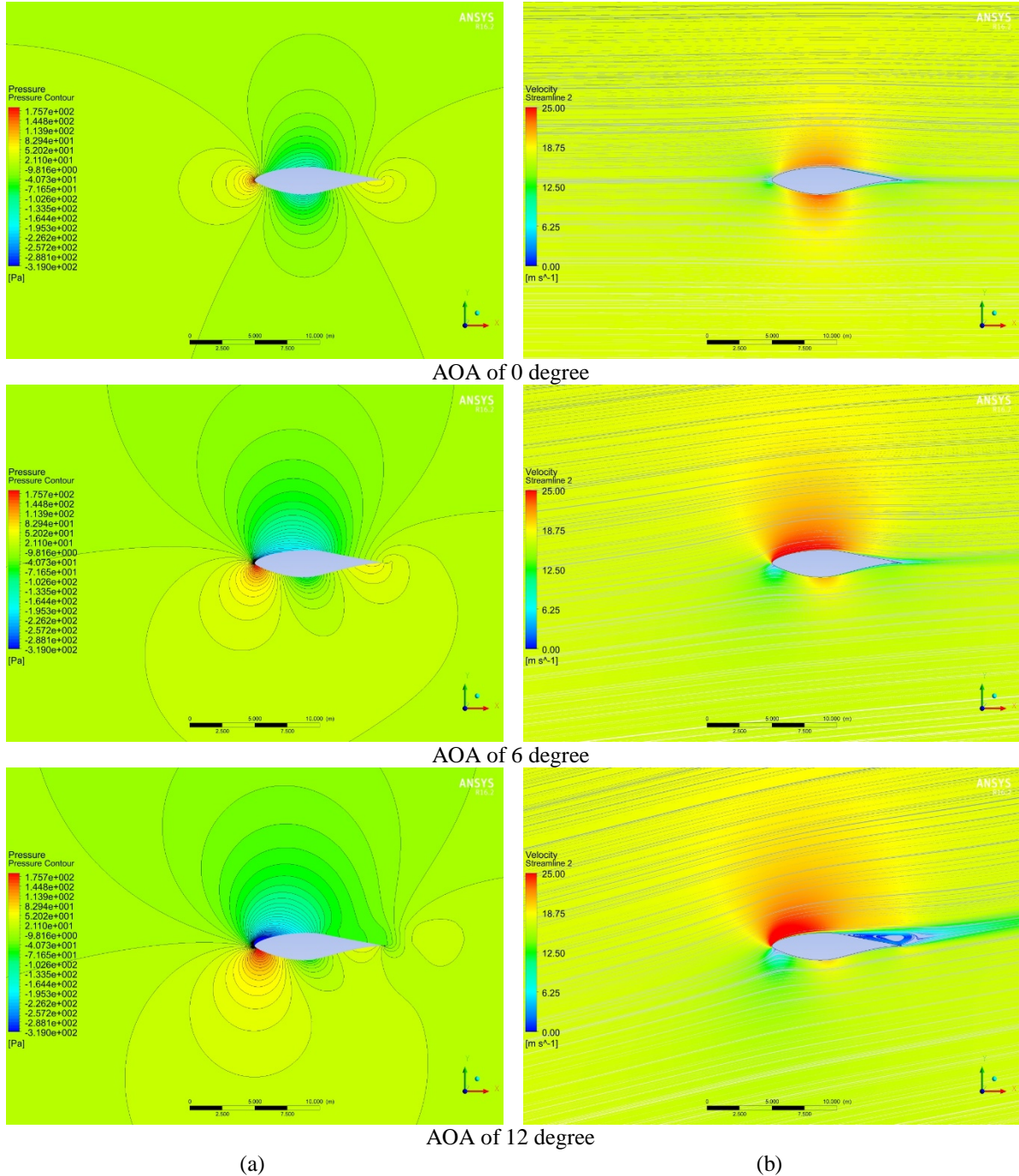


Fig. 8 Pressure contours (a) and velocity streamlines (b) in three different AOAs at 17.5 m/s

Conclusion

In this paper, S809 airfoil profile is studied with different angles of attack between -10° and 15° for different wind velocities. A two-dimensional model is developed in the presented study based on the $k-\omega$ SST turbulence model. Various parameters including lift and drag coefficients and lift-to-drag ratio. The lift

coefficients of the critical AOA at 13, 9 and 10 degrees corresponds to a wind speed of 7, 17.5 and 29 m/s, respectively. The simulation results show small different stall angle of attack because many airfoils [17] are typically around 15° to 20° . While, numerical study of the S809 shows that the maximum lift-to-drag ratio is achieved at AOA of 6° for three velocities at 7, 17.5 and 29 m/s respectively. Aerodynamic

analysis of wind turbine blades for a suitable angle of attack is crucial to improve the design of wind turbine blades for maximum efficiency.

ACKNOWLEDGMENTS

This work was supported by Faculty of Engineering, Mahidol University, EU Marie Curie RISE project RESET (H2020-MSCA-RISE-2016, reference no. 730888) and Graduate Studies of Mahidol University Alumni Association, Mahidol University.

REFERENCES

- [1] Khazem E. A., Abdullah O. I., and Sabri L. A., Steady-State and Vibration Analysis of a WindPACT 1.5-MW Turbine Blade. *FME Transactions*, Vol. 47, Issue 1, 2019, pp. 195-201.
- [2] Sayed M. A., Kandil H. A., and Morgan E. I., Aerodynamic Analysis of Different Wind Turbine Blade Profiles using Finite Volume Method. *Energy Conversion and Management*, Vol. 64, 2012, pp. 541-550.
- [3] Cox K., Echtermeyer A., Structural Design and Analysis of a 10MW Wind Turbine Blade. *Energy Procedia*, Vol. 24, 2012, pp. 194-201.
- [4] Otero A. D., Ponta F. L., Structural Analysis of Wind Turbine Blades by a Generalized Timoshenko Beam Model. *Journal of Solar Energy Engineering*, Vol. 132, Issue 1, 2010, pp.
- [5] Khchine Y. E., Sriti M., Boundary Layer and Amplified Grid Effects on Aerodynamic Performances of S809 Airfoil for Horizontal Axis Wind Turbine (HAWT). *Journal of Engineering Science and Technology*, Vol. 12, Issue 11, 2017, pp.3011-3022.
- [6] Sayed M. A., Kandil H. A., and Morgan E. I., Computational Fluid Dynamics Study of Wind Turbine Blade Profiles at Low Reynolds Numbers for Various Angle of Attack. *Journal of Renewable and Sustainable Energy*, Vol. 1440, Issue 1, 2012, pp. 467-479.
- [7] Abbaspour M., Radmanesh A. R., and Soltani M. R., Unsteady Floe over Offshore Wind Turbine Airfoils and Aerodynamic Loads with Computational Fluid Dynamic Simulations. *International Journal of Environmental Science and Technology*, Vol. 13, Issue 6, 2016, pp. 1525-1540.
- [8] Jha S. K., Gautam U., Pawar P., Narayanan S., and Kumaraswamidhas L. A., Investigations of Flow Phenomena Over a Flat Plate and NACA0012 Airfoil at High Angles of Attack. *Iranian Journal of Science and Technology, Transactions of Mechanical Engineering*. 2019, pp. 1-2.
- [9] Fatahian H., Salarian H., Nimvari ME., and Khaleghinia J., CFD Simulation of Aerodynamic Performance and Flow Separation of Single Element and Slatted Airfoils under Rain Condition. *Applied Mathematical Modelling*, 2020.
- [10] Douvi E., and Margaris D. P., Evaluation of the Turbulence Models for the Simulation of the Flow over a National Advisory Committee for Aeronautics (NACA) 0012 airfoil. *Journal of Mechanical Engineering Research*, Vol. 4, Issue 3, 2012, pp. 100-111.
- [11] Hansen M. O., *Aerodynamics of Wind Turbines*. 2015, pp. 8-10.
- [12] Hau E., *Wind Turbines: Fundamentals, Technologies, Application, Economics*. Springer Science and Business Media, 2013, pp. 120-134
- [13] Somers D. M., *Design and Experimental Results for the S809 Airfoil*. National Renewable Energy Laboratory, 1997.
- [14] Salvação N., and Soares C. G., Offshore Wind Energy Assessment for the Iberian Coast with a Regional Atmospheric Model. *Renewable Energies Offshore*, 2015, pp. 219-228.
- [15] Rocha, P. A. C., Rocha B. H. H., Carneiro F. O. M., and Silva M. E. V. D, and Bueno A. V., A Case Study on the Calibration of the $k-\omega$ SST (Shear Stress Transport) Turbulence Model for Small Scale Wind Turbines Designed with cambered and Symmetrical Airfoils. *Energy*, Vol. 65, 2016, pp. 144-150.
- [16] Rocha, P. A. C., Rocha B. H. H., Carneiro F. O. M., and Silva M. E. V. D, and Bueno A. V., $k-\omega$ SST (Shear Stress Transport) Turbulence Model Calibration: A Case Study on a Small-Scale Horizontal Wind Turbine. *Energy*, Vol. 65, 2016, pp. 412-418.
- [17] Karbasian, H. R., Moshizi S. A., and Maghrebi M. J., Dynamic Stall Analysis of S809 Pitching Airfoil in Unsteady Free Stream Velocity. *Journal of Mechanics*, Vol. 32, Issue 2, 2015, pp. 227-235.

NUMERICAL ANALYSIS OF INVASION PATTERNS DURING DRAINAGE PROCESS IN A SIMPLIFIED PORE NETWORK MODEL

Yuto Takeuchi¹, Junichiro Takeuchi² and Masayuki Fujihara³

^{1,2,3}Graduate School of Agriculture, Kyoto University, Japan

ABSTRACT

Immiscible two-phase flows in porous media concern various problems such as underground water pollution by non-aqueous phase liquid and enhanced oil recovery. It is well known that the drainage process of two-phase flows within porous media takes several patterns depending on the conditions, namely from a stable displacement, viscous fingering flow to capillary fingering flow. However, the physical mechanism of infiltration and critical conditions for varied invasion patterns have not been evident. This study employed numerical two-phase flow simulation using the Color Gradient Lattice Boltzmann Method (CG-LBM) in a simplified pore network model with different capillary number and viscosity ratio between the two fluids. The CG-LBM is superior in implementation of boundary conditions and specification of fluid parameters such as viscosity and interfacial force, and therefore suitable for two-phase flow simulation in porous media. Simulation results confirm that low capillary number flows produce the preferential flow for pore throats with large width, which is correspondent to the capillary fingering flow. In addition, the retreat of the invading fluid caused by Haines jump is seen. When capillary number is higher, these two phenomena did not apparently take place. Higher capillary number flows lead the invading fluid to simultaneously displacing different throats when its viscosity is higher than that of the invaded fluid (stable displacement), and the viscous fingering flow happens otherwise. These findings suggest that the conditions of capillary number and viscosity ratio, and occurrence of the preferential flow and Haines jump are key factors for different invasion patterns.

Keywords: Fingering flow, Lattice Boltzmann Method, Drainage process, Capillary number

INTRODUCTION

Immiscible two-phase flows in porous media concern various problems such as underground water pollution by non-aqueous phase liquid, enhanced oil recovery, and carbon capture and storage. The drainage process within porous media exhibits various patterns depending on conditions namely from stable displacement, a viscous fingering flow to a capillary fingering flow. Although the critical conditions determining these invasion patterns have been widely researched both physically [1]–[3] and numerically [4]–[6], there have been no universally accepted criteria about transition among the different invasion patterns. In addition, detailed physical mechanism during the fluid displacement in porous media has not been explicitly identified.

One of the most influential works about drainage process in porous media is by [7]. They numerically simulated displacement behavior by a capillary network model and classified the invasion patterns based on the saturation when breakthrough occurs. The result is compiled as a phase diagram plotting the types of invasion patterns on the coordinate whose x-axis is viscosity ratio M and y-axis is capillary number Ca . Although their work successfully reproduced different invasion patterns and classified them, it is reported that the threshold of the diagram is not universally fixed [1], [3], [5]. Also, it lacks

analyses of detailed process during displacement since it assumes simple capillary network fluid dynamics.

This paper numerically simulates the drainage process within a simplified pore network model using the Color Gradient Lattice Boltzmann Method (CG-LBM) with different conditions of Ca and M . The numerical results confirmed the three invasion patterns depending on the conditions, and the two notable fluid dynamic phenomena of a preferential flow and Haines jump are seen, which are concluded as key factors for different invasion patterns.

MATERIAL AND METHODS

Numerical Scheme

The Lattice Boltzmann Method (LBM) is a mesoscopic-based computational fluid method and treats a fluid as a collection of particles which can have finite number of lattice velocities. The probability of particles along a certain direction at a node is described by the particle distribution function. Fluid properties such as density, pressure and velocity are derived by zeroth and first moment of the particle distribution function. The computational procedure of the standard LBM consists of two steps: a collision step and streaming step. The simple iteration of these two steps develops the particle distribution functions

and computation of the moments of the particle distribution functions yields macroscopic variables at each node in a way that it recovers the incompressible Navier-Stokes equation within the limit of second order accuracy and low Mach number [8].

The CG-LBM is one of the multiphase LBM models, and good at explicit specification of fluids' properties such as viscosity ratio and interfacial tension. We implemented a computational method mainly based on [9], where multiphase features of interfacial tension and immiscibility are incorporated by adding a perturbation step and recoloring step to the standard LBM procedure, respectively. On the other hand, the wettability of fluids is modelled by assigning contact angle directly without considering contact angle hysteresis [10].

As boundary conditions, the standard bounce-back condition is applied at the walls of the pore model as a no-slip boundary condition, and the non-equilibrium bounce back method [11] is imposed at the inlet and outlet as a Dirichlet boundary condition.

The computer code we used was verified beforehand by simulating basic multiphase flow problems of droplet formation and contact angle test (not shown), and satisfying results were obtained. Throughout the simulations in this research, the contact angle of the wetting fluid against the nonwetting fluid is set to be 60 degrees.

Simulation Outline

Considering the high computational cost of the CG-LBM, a simplified pore network model is chosen as a simulated medium. The simulated porous model shown in Fig. 1 is composed of the four round pore bodies with the same size, four rectangular throats connecting them having different widths, and inlet and outlet throats. The width w of the pore throats and diameter d of the pore bodies are presented in Table 1 in a form of dimensionless lattice unit (lu). Note that all the values are nondimensionalized using lattice unit (lu), mass unit (mu), and time step (ts) for length, mass, and time unit, respectively in the rest of the paper. A constant velocity is imposed at the inlet. The inlet boundary nodes are assumed to be nonwetting nodes, and the outlet boundary nodes are treated as wetting nodes. The inlet velocity drives the nonwetting fluid colored red in Fig. 1 to invade the pores and the blue wetting fluid is drained from the outlet.

The key parameters of the simulation are capillary number $Ca = \mu_n u_n / \sigma$ and viscosity ratio $M = \mu_n / \mu_w$. Note that μ_n is the dynamic viscosity of the nonwetting fluid, u_n is the inlet velocity of the nonwetting fluid, σ is the interfacial tension, and μ_w is the dynamic viscosity of the wetting fluid. Several works about drainage process in porous media [1], [3], [5], [7] showed that the stable displacement occurs when both Ca and M are

higher, the viscous fingering flow takes place when Ca is higher and M is lower, and capillary fingering flow happens when Ca is lower. However, the threshold of the transition among those invasion patterns are different among different researches, and hence a universal criterion has not been available. In addition, the physical mechanism of the different invasion patterns has not been adequately researched because of the complicatedness of porous media.

We change the two parameters of Ca and M by appropriately choosing the kinematic viscosity, fluid density, interfacial tension, and inlet velocity from simulation to simulation while keeping the LBM specific error due to large velocity and kinematic viscosity small. Indeed, the maximum inlet velocity allowed is set to be 0.009 and that of kinematic viscosity to be 0.6. We realized the capillary number ranged from $Ca = 5.0 \times 10^{-5}$ to 7.2×10^{-2} and the viscosity ratio $M = 9.000$ and 0.111 . The simulation is stopped when the invading fluid reaches the outlet of the medium, i.e., when breakthrough occurs. The simulation results exhibited different invasion patterns each of which corresponds to the stable displacement, viscous fingering flow and capillary fingering flow. The physical mechanism of the variant displacement processes and their transitional values are analyzed in the next section.

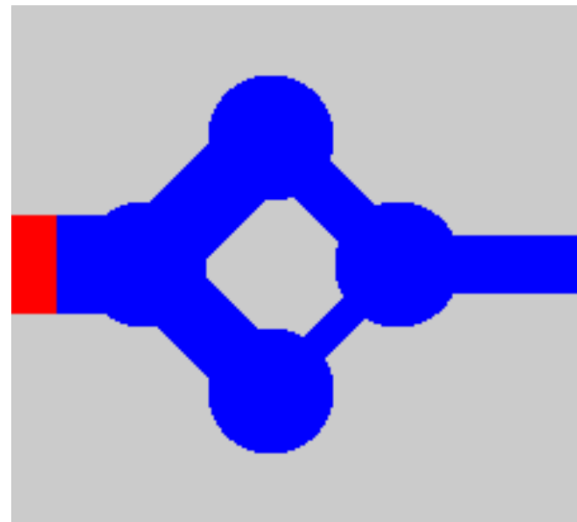


Fig. 1 The simulated porous model. The red region is occupied by an invading fluid and the blue region is occupied by an invaded fluid.

Table 1 Widths w of the pore throats and radius d of the pore bodies in the simulated porous model

w_{BL}	w_{TL}	w_{BR}	w_{TR}	d_B	w_I	w_O
28	32	12	20	50	40	24

Note: BL: Bottom-Left, TL: Top-Left, BR: Bottom-Right, TR: Top-Right, B: Body, I: Inlet, O: Outlet. The unit is lattice unit (lu).

RESULTS AND DISCUSSION

Capillary Fingering Flow

The representative flow development of capillary fingering regime is shown in Fig. 2. This regime assumes lower capillary number, and therefore the flow is dominated by capillary force while viscous force is neglectable.

The first notable characteristic is the preferential flow to larger pore throats. Referring to Fig. 2a, the invading fluid preferentially penetrates the top left throat without getting into the bottom left throat. This phenomenon is caused by variant threshold pressures of pore throats. The threshold pressure of a throat is defined as the pressure difference between the two fluids needed for the invading fluid to penetrate the throat. In drainage process, according to the Laplace law, the threshold pressure P^{th} is written as

$$P^{th} = \frac{2\sigma \cos \theta}{w}, \quad (1)$$

where θ is the contact angle. Since the contact angle and interfacial tension are constants throughout the domain, larger throats always hold smaller threshold pressure, leading the invading fluid to penetrate larger throats preferentially. While the fluid invades the pore throat with the largest throat width, the pressure difference between the invading and invaded fluid is fixed to the threshold pressure of that throat which is inevitably lower than the threshold pressure of the other pore throat. Hence, the invading fluid is not able to penetrate the other throat, waiting at the entrance of the throat (Fig. 2a). In addition, another preferential pattern between a pore body and throat is noticeable. From Fig. 2a to Fig. 2b, the invading fluid prefers the bottom left throat rather than the top body. The threshold pressure into a pore body with diameter d from a throat with width w is

$$P^{th} = -\frac{2\sigma \cos[\max(\alpha + \theta, 180^\circ)]}{w}, \quad (2)$$

where $\cos \alpha = -w/d$ and $90^\circ < \alpha < 180^\circ$. The threshold pressure into the top body from the top left throat is thus $P^{th} = 2\sigma \cos(\alpha + \theta) / 32 \approx 0.062\sigma$, which is higher than the threshold pressure into the bottom left throat $P^{th} = 2\sigma \cos 60^\circ / 28 \approx 0.036\sigma$. Hence, the invading fluid prefers the bottom left throat to the top body (Fig. 2b). Then, the invading fluid selects the top body rather than the bottom body, following Eq. (2) (Fig. 2c). During the invasion of the top body, the second characteristic, or the retreat of the invading fluid from the throat due to Haines jump [12] occurs. Haines jump is a jump of a fluid interface and abrupt pressure drop accompanying it [12]. When the invading fluid penetrates the top body from the top left throat, the invading fluid experiences the sudden change of the geometry and accompanying sudden drop of the capillary pressure. This makes the pressure of the invading fluid lower than the pressure needed to stay in the bottom left throat. Hence, the invading fluid in the bottom left throat retreats and the redistribution of the fluid occurs. The difference between average pressure of the invading and invaded fluids, and the average x-velocity before and during invasion of the top pore body are plotted in Fig. 3 for the same condition as Fig. 2. During the period (A), the invading fluid penetrates the bottom left throat, keeping the constant pressure. Then, during period (B), the pressure starts to increase by growing menisci while the interfaces stick to the critical points of the top left throat and top body, and the bottom left throat and bottom body. Finally it releases the pressure during the period (C) while penetrating the top body. Accompanying to the sharp pressure decline, the invading fluid retreats from the bottom left throat from (D) to (E). Also, the average x-velocity experiences the abrupt increase and the following

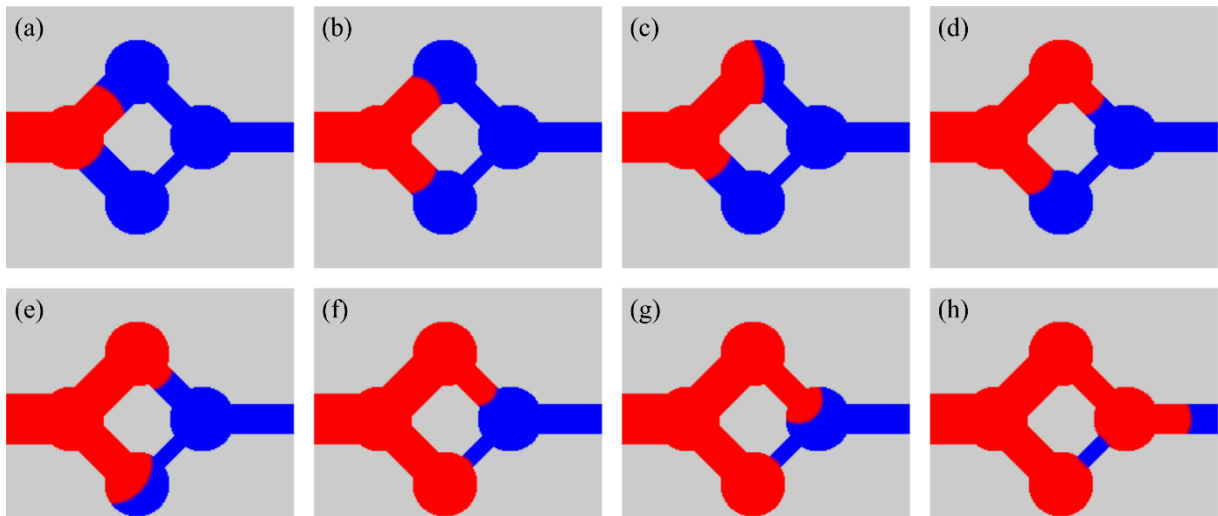


Fig. 2 The representative flow development in capillary fingering regime ($Ca = 3.6 \times 10^{-4}$, $M = 9.000$).

abrupt decrease during the retreat. This jump and retreat happen in a short period compared to the initial invasion of the bottom left throat: the invasion took around 160,000 time steps while the retreat occurred in 40,000 time steps. The change of average x-velocity shown in Fig. 3 also identifies the rapidness of the jump and retreat. This whole process is typical in the Haines jump phenomenon: accumulation of pressure, abrupt exchange of pressure into velocity, and the fluid redistribution.

After refilling the bottom left throat according to Eq. (1), the invading fluid penetrates the top right throat in the manner of comparison between Eq. (1) for the top right throat and Eq. (2) for the bottom body (Fig. 2d). Then, the bottom body is invaded while the Haines jump occurs (Fig. 2e) after which the top right throat is refilled (Fig. 2f). The threshold pressure into the right body $P^h = -2\sigma \cos(180^\circ) / 20 = \sigma / 10$ is higher than that into the bottom right throat $P^h = 2\sigma \cos 60^\circ / 12 = \sigma / 12$. However, Fig. 2g manifests the opposite selection, i.e., the right body is invaded. This discrepancy may be caused by an inertial effect. Indeed, the local Reynolds number at the fluid interface, $Re_{TR} = Uw_{TR} / \nu_n$, where U is the magnitude of velocity and ν_n is the kinematic viscosity of the invading fluid, during the invasion of the border between the top right throat and the right body reached $O(1)$, which can be large enough to exert an inertial effect. The local velocity of the interface was one or two order larger than the inlet velocity, which caused the local increase in Reynolds number compared to bulk Reynolds number. Since “inertia can influence the selection of the next pore to be invaded” [13], this apparently unreasonable preference can be caused by an inertial effect. In fact, detailed observation of the results revealed that the invading fluid once invaded the bottom right throat but retreated immediately. This suggests that although capillarity prefers the bottom right throat, inertia overcomes it and makes the invading fluid relax into the right body.

Stable Displacement

The representative flow development of stable displacement regime is shown in Fig. 4. In this regime, the capillary number is higher, and the viscosity ratio is larger. Hence, viscous force of the invading fluid is dominant. In this regime the preferential flow and Haines jump referred to in the capillary fingering regime do not apparently occur. On the contrary, the invading fluid simultaneously penetrates the bottom left throat and the top left throat (Fig. 4a). In this case, the dominant viscous force of the invading fluid virtually neglects the local capillary effect due to interfacial tension, i.e., the capillary pressure of a throat does not affect the propagation of the meniscus lying in the other throat. The retreat of the invading fluid due to the Haines jump does not take place for the same reason: during the displacement of a large pore body, the invading fluid is still be able to displace the invaded fluid, propelled by the viscous force (Fig. 4b, c, d, e).

Viscous Fingering Flow

The representative flow development of viscous fingering flow regime is shown in Fig. 5. This regime represents higher capillary number and smaller viscosity ratio. Hence, the flow is dominated by the viscous force of the invaded fluid. In this flow type, the finger-like interface is confirmed. In the same way as the stable displacement pattern, the flow is driven by bulk pressure difference between the inlet and outlet, and therefore capillarity of throats does not affect the fluid dynamics. Observing the state at breakthrough (Fig. 5d), the seemingly preferential path to the upper pores is evident, which is not by the capillarity but rather by the channeling effect [14], [15]. In the viscous fingering pattern, since bulk pressure difference is much larger than the local capillary pressure difference, the selection of an invaded pore does not occur pore by pore unlike the capillary fingering pattern. Instead, the overall viscous resistance through the series of pores from the

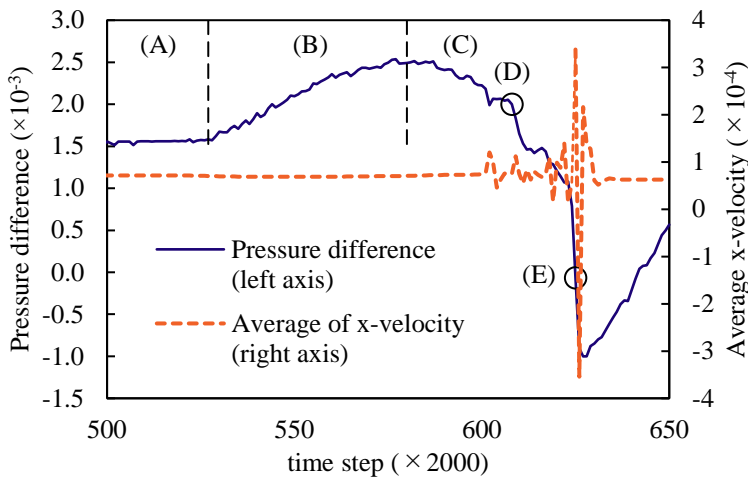


Fig. 3 Pressure difference and average x-velocity about invasion of top body.

- (A) Penetrate bottom left throat
- (B) Accumulate pressure by growing menisci while sticking to critical points
- (C) Penetrate top body while releasing pressure
- (D) Start to retreat from bottom left throat
- (E) Retreat completely to reach left body

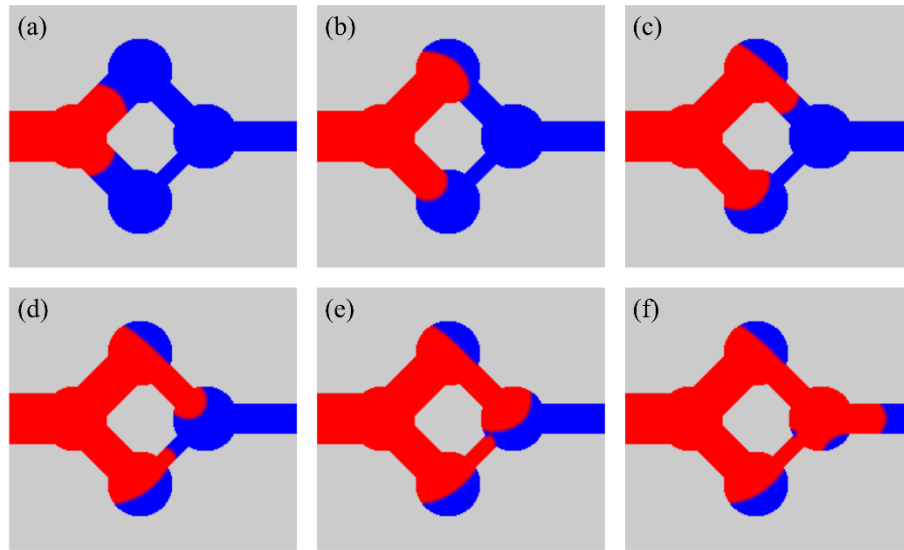


Fig. 4 The representative flow development in stable displacement regime ($Ca = 7.2 \times 10^{-2}$, $M = 9.000$).

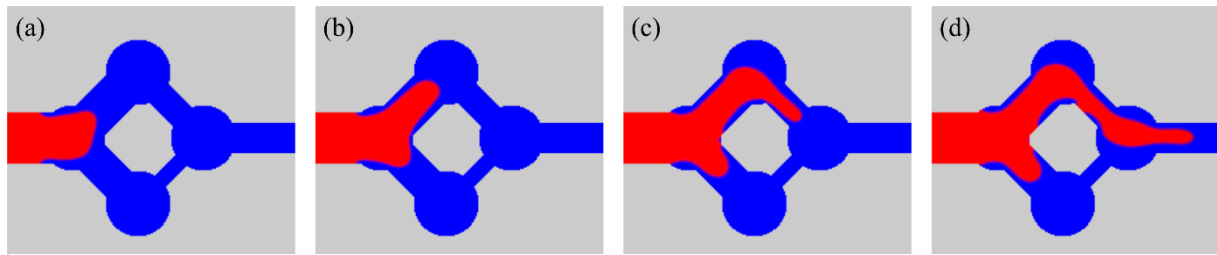


Fig. 5 The representative flow development in viscous fingering regime ($Ca = 7.2 \times 10^{-2}$, $M = 0.111$).

inlet to the outlet determines the flow path. In this manner, the upper series of pores is preferable for the invading fluid compared to the lower one. In other words, the upper channel is more permeable than the lower channel.

Critical Values For Transition

The critical values for the transition among the three invasion patterns are of interest from an engineering viewpoint since the different invasion patterns significantly alter efficiency of the operation. Table 2 and 3 show the presence and absence of the noted phenomena in capillary fingering regime, the preferential flow and retreat of the invading fluid due to Haines jump, for different viscosity ratios. From Table 2, the capillary fingering flow would transition to the stable displacement in $Ca = O(10^{-2})$, which roughly corresponds to [3] and [7]. Table 3 suggests that the transition from the capillary fingering to the viscous fingering would occur in $Ca = O(10^{-3})$, which is considerably higher than some of the literature [1], [3]. Since the domain size influences invasion patterns significantly, simulation on larger realistic porous media is needed instead of the simulated minimal porous model for further analyses.

CONCLUSIONS

In this paper, the drainage process in a simplified pore network model was numerically simulated using the CG-LBM, and the three different invasion patterns were obtained. These patterns correspond to a capillary fingering flow, stable displacement, and a viscous fingering flow, respectively. The two notable characteristics, namely the preferential flow to wider pore throats and the retreat of the invading fluid due to the Haines jump were observed for the low capillary number flows. During the Haines jump, the sudden release of pressure and abrupt change in mean velocity were confirmed. On the other hand, the preferential flow and Haines jump did not apparently happen for higher capillary number flows. When $Ca > O(10^{-2})$ and $\mu_n / \mu_w = 9.000$, the pore throats were simultaneously displaced, which is correspondent to the stable displacement. When $Ca > O(10^{-3})$ and $\mu_n / \mu_w = 0.111$, the viscous fingering flow developed, where the finger-like interface was observed. These findings suggest that the conditions of capillary number and viscosity ratio, and occurrence of the preferential flow and Haines jump are key factors for different invasion patterns.

Table 2 Presence and absence of preferential flow and retreat by Haines jump when $M = 9.000$

Ca	5.0×10^{-5}	1.0×10^{-4}	3.6×10^{-4}	3.6×10^{-3}	7.2×10^{-3}	1.0×10^{-2}	2.0×10^{-2}	3.6×10^{-2}	7.2×10^{-2}
logCa	-4.30	-4.00	-3.44	-2.44	-2.14	-2.00	-1.70	-1.44	-1.14
Preferential flow	Present	Present	Present	Present	Intermediate	Intermediate	Absent	Absent	Absent
Retreat by Haines jump	Present	Present	Present	Present	Present	Present	Intermediate	Absent	Absent

Table 3 Presence and absence of preferential flow and retreat by Haines jump when $M = 0.111$

Ca	5.0×10^{-5}	1.0×10^{-4}	3.6×10^{-4}	7.2×10^{-4}	3.6×10^{-3}	7.2×10^{-3}	1.0×10^{-2}	3.6×10^{-2}	7.2×10^{-2}
logCa	-4.30	-4.00	-3.44	-3.14	-2.44	-2.14	-2.00	-1.44	-1.14
Preferential flow	Present	Present	Intermediate	Absent	Absent	Absent	Absent	Absent	Absent
Retreat by Haines jump	Present	Present	Present	Present	Intermediate	Absent	Absent	Absent	Absent

REFERENCES

- [1] Chen Y. F., Wu D. S., Fang S., and Hu R., Experimental study on two-phase flow in rough fracture: Phase diagram and localized flow channel. *International Journal of Heat and Mass Transfer*, Vol. 122, 2018, pp.1298-1307.
- [2] Ferer M., Ji C., Bromhal G. S., Cook J., Ahmadi G., and Smith D. H., Crossover from capillary fingering to viscous fingering for immiscible unstable flow: Experiment and modeling. *Physical Review E*, Vol. 70, Issue 1, 2004, 016303.
- [3] Zhang C., Oostrom M., Wietsma, T. W., Grate J. W., and Warner, M. G., Influence of viscous and capillary forces on immiscible fluid displacement: Pore-scale experimental study in a water-wet micromodel demonstrating viscous and capillary fingering. *Energy & Fuels*, Vol. 25, Issue 8, 2011, pp.3493-3505.
- [4] Chen Y., Li Y., Valocchi A. J., and Christensen K. T., Lattice Boltzmann simulations of liquid CO₂ displacing water in a 2D heterogeneous micromodel at reservoir pressure conditions. *Journal of Contaminant Hydrology*, Vol. 212, 2018, pp.14-27.
- [5] Liu H., Zhang Y., and Valocchi A. J., Lattice Boltzmann simulation of immiscible fluid displacement in porous media: Homogeneous versus heterogeneous pore network. *Physics of Fluids*, Vol. 27, Issue 5, 2015, 052103.
- [6] Tsuji T., Jiang F., and Christensen K. T., Characterization of immiscible fluid displacement processes with various capillary numbers and viscosity ratios in 3D natural sandstone. *Advances in Water Resources*, Vol. 95, 2016, pp.3-15.
- [7] Lenormand R., Touboul E., and Zarcone C., Numerical models and experiments on immiscible displacements in porous media. *Journal of Fluid Mechanics*, Vol. 189, 1988, pp.165-187.
- [8] Krüger T., Kusumaatmaja H., Kuzmin A., Shardt O., Silva G., and Viggen E. M., The lattice Boltzmann method. Springer International Publishing, 2017.
- [9] Leclaire S., Pellerin N., Reggio M., and Trépanier J. Y., Enhanced equilibrium distribution functions for simulating immiscible multiphase flows with variable density ratios in a class of lattice Boltzmann models. *International Journal of Multiphase Flow*, Vol. 57, 2013, pp.159-168.
- [10] Xu Z., Liu H., and Valocchi A. J., Lattice Boltzmann simulation of immiscible two-phase flow with capillary valve effect in porous media. *Water Resources Research*, Vol. 53, Issue 5, 2017, pp.3770-3790.
- [11] Zou Q., and He X., On pressure and velocity boundary conditions for the lattice Boltzmann BGK model. *Physics of Fluids*, Vol. 9, Issue 6, 1997, pp.1591-1598.
- [12] Sun Z., and Santamarina J. C., Haines jumps: Pore scale mechanisms. *Physical Review E*, Vol. 100, Issue 2, 2019, 023115.
- [13] Ferrari A., and Lunati I., Inertial effects during irreversible meniscus reconfiguration in angular pores. *Advances in Water Resources*, Vol. 74, 2014, pp.1-13.
- [14] Tsang C. F., and Neretnieks I., Flow channeling in heterogeneous fractured rocks. *Reviews of Geophysics*, Vol. 36, Issue 2, 1998, pp.275-298.
- [15] Tang Y. B., Li M., Bernabé Y., and Zhao J. Z., Viscous Fingering and Preferential Flow Paths in Heterogeneous Porous Media. *Journal of Geophysical Research: Solid Earth*, Vol. 125, Issue 3, 2020, e2019JB019

A US\$6.07 BILLION JAKARTA - BANDUNG HIGH - SPEED RAIL: CHALLENGES AMID COVID-19 PANDEMIC

Aleksander Purba

Engineering Faculty, University of Lampung, Indonesia 35145

ABSTRACT

The Jakarta-Bandung high-speed railway project is one of the government's national strategic projects in the transportation sector and is expected to require a total investment of US\$6.07 billion. The railway project will serve four main stations: Halim in Jakarta, Karawang in West Java and Walini and Tegalar in Bandung regency. A total of 80 km of the railway will be elevated, while a further 16.9 km will be in tunnels. The trains will travel at 350 km per hour, cutting travel time between Jakarta and Bandung to 45 minutes, faster than the approximately three hours and a half on the Parahyangan existing train. Railway developer PT Kereta Cepat Indonesia China (KCIC), a joint venture between Indonesian and Chinese railway companies, initially planned to finish the project and start operations in December 2021. Unfortunately, development of the project would depend on the situation of the coronavirus outbreak in the country. In order to curb the outbreak, the Jakarta government called on the public in mid-March to implement social distancing measures by studying, working and praying at home. Hence Chinese workers wanting to return to work on the Jakarta-Bandung high-speed railway project should abide by the health and safety protocols. In late March a regulation offering an exemption for foreigners working on national strategic projects from the temporary ban on foreign arrivals and transits. The ban is set to last until the government declares an end to the outbreak. In order to speed-up the progress, the consortium have made a number of breakthroughs in building tunnels, railway bridges and stations to pursue the remaining progress of 56 percent over the next 18 months.

Keywords: *High-speed railway, Jakarta-Bandung, National strategic project, COVID-19*

INTRODUCTION

PT KCIC is established based on deed No. 86 dated October 16, 2015 and project Jakarta-Bandung high-speed railways (HSR) designated as one of the government's National Strategic Projects in Presidential Regulation No. 3 of 2016 concerning the Acceleration of National Strategic Projects. Having a length of 142.3 km stretching from Jakarta to Bandung, the HSR line has four halting stations, Halim, Karawang, Walini, and Tegalluar with one depot located in Tegalluar. The construction was carried out on a massive scale to pursue operational targets in 2021. Of the total length of the fast train track, more than 80 km of them have elevated structures while the remainder are 13 tunnels and sub-grades. Otherwise, the project construction has been facing challenges regarding land procurement as the main problem that needed to be solved after the issuance of the construction permit. And since the coronavirus is going global, Chinese workers wanting to return to work on the Jakarta-Bandung high-speed railway project should abide by the health and safety protocols. Hence, these situations cause and effect of delay of project delivery. The Indonesian government

has begun discussions on possible Japanese participation in a planned high-speed railway between Jakarta and Bandung, hoping to spur progress on the delayed Chinese-led project as costs mount. Meanwhile, the latest information indicates that the new proposal would combine that rail link with a Japanese-Indonesian project upgrading an existing 750 km connection between Jakarta and Surabaya. Discussions have begun on extending the high-speed Jakarta-Bandung railway to Surabaya and whether it would be possible to include Japan in the consortium. Many in the Indonesian government have argued that a single railway running through Bandung to Surabaya would be more efficient than separate routes going east and southeast from the capital. Cost overruns on the Bandung-Jakarta HSR project have given a boost to this view. The project was originally scheduled to be completed in 2019 at an estimated cost of US\$5.5 billion. However, the project expected to be completed in December 2021 at a cost of over US\$6.07 billion. In mid-May 2020, construction progress reaches 48.3% and has worked again and follow physical distancing although the Covid-19 pandemic is not yet over. This paper identifies the challenges to complete the HSR project successfully.

The previous paper related to the Jakarta-Bandung HSR can be found in Purba et. al. [1], and Purba [2].

PROJECT HIGHLIGHTS

Originally approved in May 2017 following the signing of a US\$4.5 billion loan agreement between the two countries, the project initially experienced a number of lengthy delays, largely on account of protracted land-rights negotiations. KCIC as HSR developer such optimism, however, went to the wall as soon as the unprecedented extent of the Covid-19 outbreak – and its wider implications – became apparent, with countries across Asia and beyond locking down flights and barring port entry. As in many other countries, a number of Chinese project directors, managers, engineers and consultants for the HSR project, who had returned home for the spring festival period, were unable to resume their roles. The map and brief data of Jakarta-Bandung HSR line are shown in Fig. 1 and Table 1, respectively. HSR Jakarta-Bandung comes with the latest type, CR400AF, which is equipped with modern and reliable technology. Combined with the concept of transit oriented development (TOD), HSR station ensures an integrated system with a wide choice of integrated transportation modes, a variety of culinary delights, facilities and other privileges [3].

As of September 2019, in line with the progress on physical infrastructure development, the Jakarta-Bandung HSR project in parallel is also preparing an operating system and maintenance of facilities and infrastructure. The contractor is preparing the need for human resources ranging from the organizational structure to the number of personnel for operational after the project completion. KCIC is targeting to involve 1,700 personnel for the train operation. In this regard, KCIC has been partnering with PT MRT Jakarta, a pioneer of modern railroad facilities in Indonesia operating the mass rapid train in Jakarta. The two companies agreed to transfer knowledge to each other in connection with the maintenance and operation, which include human resources development as well as innovation and strategies for developing Transit Oriented Development (TOD) and the other line of non-train businesses. Jakarta-Bandung HSR is an advanced-technology but risky mega project. The risk largely is sourced from the real demand of the train connecting the two big cities. Indeed, a lot of people commuting from Jakarta to Bandung, and in another way around.



Fig. 1 The proposed of HSR line

Table 1. Brief data of Jakarta-Bandung HSR line [4]

Element	Data
Termini	Halim (Jakarta) ~ Tegalluar (Bandung)
Intermediate station	Karawang and Walini (West Java)
Route length	Approximately 143 km
Schedule train frequency	Every 35 min (first year operation)
Job opportunity	39,000 jobs-HSR construction 20,000 jobs-TOD construction 28,000-HSR and TOD operation
Payback period of investment	40.2 years-without TOD 23.74 years-with TOD
Ticket price	IDR 225,000 (US\$16)
Speed	Maximum operating speed 350 km/h
Estimated journey time	Between Halim and Tegalluar:45 min
Revenue from ticket sales	US\$ 168 million (2020)
Commencement date	2020
Estimated completion date	2020
Passenger flow volume (2020)	About 29,000 passengers per day
Project costs	US\$ 5.135 billion-without TOD US\$ 5.294 billion-with TOD
Terms of loan (40 years loans period)	60% in US\$ with interest 2%/year 40% in RMB with interest 3.46%/year
Concession period	50 years (31 May 2019 ~ 31 May 2069)

FACTORS RELATED TO RIDERSHIP

Still, it does not guarantee that the commuters are interested to regularly take the HSR as a preferable transportation mode. While, the train can significantly cut the travel time more than half, the ticket price would also be taken into consideration. The more expensive the ticket price, the less appetite of people to take the HSR as a regular transportation mode. Therefore, TOD in areas surrounding the railway of bullet train is very important to pursue to enable smaller towns grow as the places of living. Shorter trip using HSR connecting the towns in affordable costs could increase the number of passengers [5]. Issue related to the number of passenger to be attracted by the HRS line has also been discussed in one of the most reputable colleges. Private car is still the main choice of transportation for Jakarta - Bandung road trip. At least 127,133 trips are made per day by private car, followed by public transportations which carry 13,000-14,000 passengers per day, a

large bus carries fewer than 1,000 passengers per day, and Argo Parahyangan train carries 2,000-2,500 passengers daily. As to meet the investment value which is Rp72,5 trillion, the minimum number of passengers per day should reach at least 21,134 people. The figure is considered unrealistic to be achieved. In addition, the ticket price is rather expensive which is Rp200,000 [6]. Otherwise, rail ridership in Indonesia has risen substantially in recent years, making decades of underinvestment and growing urban congestion important considerations for transport stakeholders as they upgrade and construct new lines. Statistics Indonesia (BPS) reports that total rail passengers rose from 199 million in 2011 to 202 million in 2012, 216 million in 2013, 277 million in 2014 and 325 million in 2015. The average length of a passenger journey has

simultaneously fallen from 95 km to 68 km, while the country's rail network remains limited to Java and Sumatra, with 22,296 km of total line operational in 2015. The Medium-Term Development Plan 2015-2019 includes an infrastructure development agenda that outlines projects such as having 3,258 km of newly built or rehabilitated rail lines, made up of 2,159 km of intercity railways and 1,099 km of urban railway, and boosting rail cargo volumes to 1.5 million twenty-foot equivalent units annually. Urban rail lines, including a planned light rail transit (LRT) system in Jakarta, are also expected to help reduce congestion and transport costs, which have become the highest in South-east Asia. It was forecast that the new line would attract around 10 million passengers per year in first year of operation, as shown in Fig. 2.

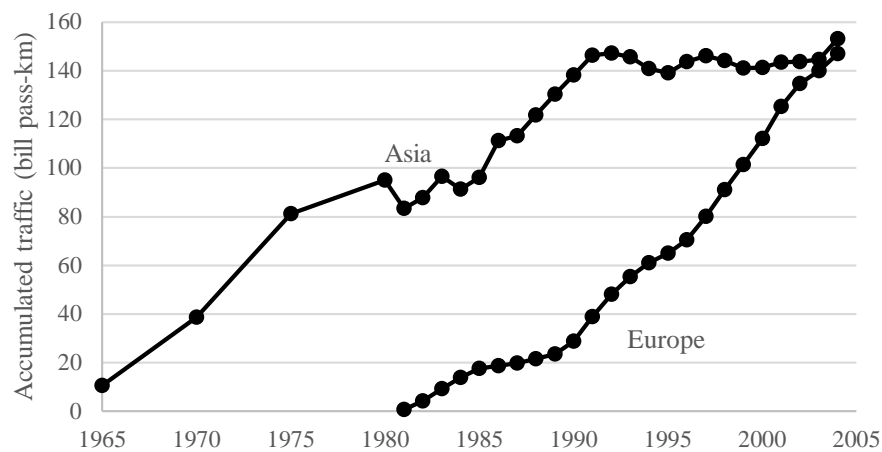


Fig. 2 Accumulated HSR traffic [7]

For twenty years, Shinkansen services in Japan enjoyed a sustained traffic, it gained 100 billion passengers-kilometer. From 1994 to 2004, within the next 20-years interval, the demand halved, because only 50 billion additional passengers-kilometer used HSR. When compared with most European HSR projects which are still in their first 20-year period, it is natural to expect high growth rates as expressed by Fig. 2. Based on passenger traffic data obtained from Europe and Asia, the first HSR line constructed in Indonesia is expected to gain considerable amounts of demand.

COVID-19 CHALLENGE

KCIC initially aimed to finish the project and begin operation by December 2021, a two-year delay from its original target. Currently KCIC is working on 13 tunnels, while the progress of land acquisition has

reached 99.96 percent. Meanwhile, construction on the HSR project is expected to be delayed amid the COVID-19 pandemic. Hence, the target must be rescheduled because the construction is suspended. To curb the outbreak, the central government called on the public to implement physical distancing measures by studying, working and praying at home. The provincial administration in Jakarta, which has become the national epicenter of the outbreak, recently introduced large-scale social restrictions that have suspended school, office, religious and public activities for 14 days. About 300 out of the 2000-strong Chinese workforce engaged on the project including senior managers travelled to China in February for the Lunar new year but were unable to return due to travel restrictions to prevent the spread of the COVID-19. The supply of materials from China has also been interrupted, although this should

resume as Chinese industry restarts after the COVID-19 lock-down. More trouble is caused by the fact that nearly 50% of materials, including pipes, waterproofing and signaling equipment are made in China. In late March a regulation offering an exemption for foreigners working on national strategic projects from the temporary ban on foreign arrivals and transits. Chinese workers wanting to return to work on the project should abide by the health and safety protocols. Previously, abnormal rainfall in the Jakarta area on January 2020 caused flash floods followed by repeated heavy rainfall and flooding into February which delayed the project. The ministry's construction safety committee found unmanaged debris from the HSR project had clogged the drainage system on the adjacent Jakarta-Cikampek toll road, causing some parts of the toll road to be flooded during heavy rains. KCIC had identified risks surrounding the project area to take action against potential disruption and environment damage. Apart from recovery measures, the contractors under the PT KCIC consortium (Table 2), which include China's Sinohydro, China Railway Engineering Corp (CREC) and state-owned builder PT Wijaya Karya, swept through a number of landslide and flood-prone areas, monitoring river and water gates across project locations to ensure they function normally.

Table 2 Shareholders in PT KCIC

Indonesia (60%)	
PT Wijaya Karya	22.8%
PT Kereta Api Indonesia	15%
PT Perkebunan Nusantara VIII	15%
PT Jasa Marga	7.2%
China (40%)	
China Railway International Co	2%
China Railway Engineering Corp	12%
Sinohydro	12%
CRRC	4.8%
China Railway Signal & Communication Co	9.2%

All such optimism, however, went to the wall as soon as the unprecedented extent of the COVID-19 outbreak. Recently, in order to speed up progress, some measures are being taken by the consortium to protect employees working on the project from the COVID-19, and communications between all parties has been stepped up. The construction of the HSR project is currently focusing on its tunnels, including the main tunnel in Halim, east Jakarta which is 1,885 meters long. The project will have 13 tunnels, 7 of which have started their excavation phase. Walini in west Java was another critical spot for the project because the developer had to construct three tunnels with a total length of 7.44 km. The project had been divided into 115 development points, and 32 of which

were elevated projects, including bridges in Bekasi, west Java. Currently, 42 points were under construction, including 7 tunnels and a train depot in Tegalluar, Bandung. To date, the progress of the HSR project has reached 44% and as for land acquisition alone, it has reached 99.96% [8]. The central government through the Transport Ministry was maintaining that the project had only actually been shut down for two weeks, with a December 2021 completion date still a possibility.

Technical Challenge

At the technical level, the challenges mainly arise from the local topography and geological conditions, such as land subsidence or sudden earthquake disasters. The topography along the HSR line is quite complicated, which might require special attention and methods for solving. Firstly, the topography along the line is diverse and complex which includes steep slopes which may be the cause of concern for the operation of HSR [9]. Referring to The Ministry of Economy, Trade and Industry [10] the steepest slope can be up to 30%, and may continue to increase because of the land subsidence, as a result of the overuse of underground water. The land subsidence itself can also be a problem, because it makes the rail uneven. In order to overcome the issue, the China Rail High-speed (CRH) is increasingly replacing the railroad by the viaduct bridge, which can be 58% of the total length of the HSR. However, these challenges may potentially be mitigated by the expertise of CRH which reportedly owns some of the world's longest high-speed railway networks with high operating speed, and low occurrence of accidents. As for the variety of constructive and operational environment, CRH have faced similar or more severe problems comparing with Jakarta-Bandung HSR project, such as the land subsidence, high temperature, and the tunnels and bridges.

New Normal

The Public Works and Public Housing (PUPR) Ministry is preparing a protocol to carry out construction services amid the new normal. The new normal construction protocol is designed to address several packages delayed due to COVID-19. The PUPR ministry suggest that the consortium will still operate with COVID-19 protocols under the new normal scenario, e.g. maintaining physical distancing practices (limited workers in one area) and limiting extra working hours for construction workers. The PUPR ministry also believes that land acquisitions, which require direct contact with a large number of people (land owners), would remain slower than normal. Undeniable, infrastructure development is one of the keys to boost economic recovery post-COVID-19 as it absorbs a large number of workers. According to Ministry of PUPR's rule of thumb,

every Rp1trillion worth of construction work could employ 14,000 workers. Overall, the government estimates that its strategic national project developments, included HSR project, could employ some 4 million workers per year, which in aggregate could employ 19 million workers in 2020-2024.

Meanwhile, the most common indicator is the number of passengers handled, but as stated by Shatkin [11], the Indonesian government has sought out investment aimed at integrating Indonesia more tightly into global flows of investment and trade, and part of that strategy has included the improvement of logistics. Referring to Chinese experience as study case, with the development of economic and social, many migrant workers began to accept high-speed rail which the price is relative high in traffic tools. In these migrant workers, mostly are under the age of 35. Along with the modernization of city, population flow more frequently. For the younger generation of office workers, the speed, punctuality and higher service

level of high-speed rail have a great attraction to them. Under normal circumstances, a business travel is urgent, and need to arrive on time. In previously of high-speed rail appearing, air travel is likely to attract most of this group. Because of the high-speed, punctuality, and less sensitive to weather conditions, high speed railway can compete with civil aviation [12]. In the wider context, Mittal et. al. [13] stated that the factors like population, income, travel speed and land-use development patterns would have a significant influence on the passenger transport demand. Along Java island itself, railway passenger services experienced a *renaissance* in the 1995-1999 period, with the introduction of many new passenger express services (Fig. 3). With the advent of cheap airplane tickets, operator PT Kereta Api has experienced a downturn in the number of passengers carried, though the number has stabilized and most trains remain at more than 50% occupancy rate.



Fig. 3 Conventional rail services along Java island

CONCLUSION

The Jakarta-Bandung high-speed railway project is one of the government's national strategic projects in the transportation sector and is expected to require a total investment of US\$6.07 billion. Three years after the ground breaking, the construction of the high-speed railway has faltered because of various technical and financial challenges, exacerbated by the COVID-19 pandemic. In mid-February 2020, construction progress reaches 44 percent and land acquisitions reach 99.96 percent. Due to the COVID-19 pandemic, work of the project has been halted temporarily, resulting in the delay of the targeted finish of construction and start of the operation. In mid-May 2020, construction progress reaches 48.3 percent and the construction has worked again and follow social/physical distancing, although the COVID-19 pandemic is not yet over. In order to speed-up the progress, the consortium have made a

number of breakthroughs in building tunnels, railway bridges and stations to pursue the remaining progress of 56 percent over the next 18 months through consolidation of manpower, equipment and advanced technology. Otherwise, referring to the new normal protocol's, the project's management team should to set a goal of zero infection for all employees and the consortium raised disinfection level and frequency, and tightened disease prevention in working areas such as offices and construction sites. The consortium should be conduct strict measures and made emergency response plans to prevent cases infected from outside of HSR project.

ACKNOWLEDGEMENT

I would like to express my special thanks of gratitude to my colleagues at PS PPI of Engineering Faculty of Lampung University as well as the Sustainable

Development Goals (SDGs) center who gave me the opportunity to do this project and provide funds for attending GEOMATE Conference in Melbourne, Australia, 11-13 November 2020.

REFERENCES

- [1] Purba, A., Nakamura, F., Niken, C., Jafri, M., and Pratomo, P., A current review of high speed railways experiences in Asia and Europe, AIP Conference Proceedings, 1903, 2017, pp. 060004-1-060004-8.
- [2] Purba, A., THE CHALLENGE OF DEVELOPING HIGH-SPEED RAIL PROJECTS: RECENT EVIDENCE FROM DEVELOPING COUNTRIES, International Journal of GEOMATE, Vol.18, Issue 70, 2020, pp. 99-105.
- [3] Retrieved from: <https://kcic.co.id/en/>
- [4] PT Kereta Cepat Indonesia China. High Speed Railway (HSR) Jakarta - Bandung, the Acceleration of Infrastructure in West Java. Rapat Kerja Kementerian Perhubungan (Ministry of Transportation), 2016, Jakarta.
- [5] Retrieved from: <https://www.trade-off.id/2019/09/12/construction-for-jakarta-bandung-bullet-train-is-in-progress/>
- [6] UGM Students Win Potential Analysis Competition of High Speed Rail. Available at <https://ugm.ac.id/en/newsPdf/12339-ugm-students-win-potential-analysis-competition-of-high-speed-rail>
- [7] International Union of Railways (UIC). Estimation des ressources et des activités économiques liées à la grande vitesse. Prepared by CENIT (Center for Innovation in Transport, Universitat Politècnica de Catalunya), 2005.
- [8] Retrieved from: <https://setkab.go.id/en/jakarta-bandung-high-speed-railway-project-to-be-completed-by-2021-transport-minister/>
- [9] Siddhartha, N., and Gusti, R., An Assessment of Economic and Financial Impacts of Jakarta-Bandung High-Speed Railway Project, Journal of Business and Political Economy, Vol.2, No.1, 2020, pp. 45-55.
- [10] The Ministry of Economy, Trade and Industry, Feasibility Study for Promotion of International Infrastructure Projects in FY2011, Study on the High Speed Railway Project (Jakarta-Bandung Section), Republic of Indonesia, Prepared by Yachiyo Engineering Co., Ltd and Japan International Consultants for Transportation Co., Ltd, 2012, pp. 1-20.
- [11] Shatkin, G., Financial sector actors, the state, and the rescaling of Jakarta's extended urban region, Land Use Policy, 2019, 104159.
- [12] Huang, Y., Song, H., and Jia, C. Y., Analysis on the Main Factors Influencing the High-Speed Railway Passenger Flow, Advanced Materials Research, 919-921, 2014, pp. 1085–1090.
- [13] Mittal, S., Dai, H., Fujimori, S., Hanaoka, T., and Zhang, R., Key factors influencing the global passenger transport dynamics using the AIM/transport model, Transportation Research Part D: Transport and Environment, Vol.55, 2017, pp. 373–388.

APPLYING DECENTRALIZED CONSENSUS: A CASE STUDY OF CARBON TRADING

Pasu Poonpakdee¹ and Jarotwan Koiwanit¹

¹Department of Industrial Engineering, Faculty of Engineering, King Mongkut's Institute of Technology
Ladkrabang, Bangkok 10520, Thailand

ABSTRACT

There has been a growing pressure in limiting global warming potential (GWP) because of human activities causing increased concentrations of greenhouse gas (GHG) emissions. The increase of average global temperatures causes impact on the environment, societies, and economies. As a result, early action is necessary to reduce GHG emissions at reasonable levels to mitigate the future global warming. Carbon markets are one of the early exchanging solutions aiming at the achievement of an environmental objective for low carbon business developers. However, all trading protocols are still having some rooms for improvement regarding how verification should be conducted and who should be responsible for this verification. Epidemic Protocol (Gossip Protocol) is focused on this study to offer new transaction platforms allowing parties to do carbon credit transactions without approval from any third parties by applying the transaction exchanging concept of Blockchain technology to the algorithm. The results show that the protocol can provide a consensus mechanism without global communication which supports carbon trading in the decentralized network.

Keywords: Epidemic Algorithms, Distributed Consensus, Carbon Trading

INTRODUCTION

Environmental changes influence all global communities. Each tonne of GHG emitted mostly is the carbon dioxide (CO₂) contributing to further climate change [1]. To cope with the reduction of the GHG emission in an attempt to mitigate the future climate change, one of the options directly controls the emissions permitted is carbon trading through carbon markets [2]. Carbon permit trading works by a cap fixed by the regulator in which emitters included in the system will be able to buy or sell carbon credits from or to other participants, respectively in order to cover their emissions by a quantitative limit on emissions produced [3]. To transfer carbon credit with trust and without any third parties, the concept of Blockchain technology has been introduced to transform transactional processes [4]–[6]. In addition, epidemic protocols have also been applied in this study in order to present the preliminary carbon trading work to show on how to improve the efficiency of a distributed consensus.

The paper is organized as follows. Section 2 provides works related to this study. Section 3 proposes the algorithm used in this study. Section 4 presents the simulation configuration while Section 5 provides experimental results. Finally, the conclusions and future work are presented in Section 6.

RELATED WORKS

Carbon Trading

As early action is necessary for reducing GHG emissions, a carbon markets has now become a “cap-and-trade” regime allowing for an efficient GHG emission sharing among emitters to limits the emissions below an established standard [7]. Companies are making strategies to buy or sell carbon credits with other companies having less pollution to avoid legislative restrictions. However, the third-party organizations to verify carbon trading is one of the major issues in carbon trading. Even though a centralized verification in the regulator allows for standardization and consistency, it requires resources, time, and a heavy monetary burden [8].

Blockchain Technology

Blockchain is a type of block structure holding a complete list of transaction records without any banks or any intermediaries [9]. In public blockchain, all transactions are visible to the public in the consensus process while private blockchain only allows nodes coming from one specific organization to join the consensus processes [10].

One of the greatest examples that shows how Blockchain is implemented in the real world, is Bitcoin. Bitcoin introduces the decentralized network

by announcing the transactions. Then the transactions need to be agreed by the member in the system [7].

Epidemic Protocols

An epidemic protocol is a distributed communication and computation paradigm tending to be used in an extreme-scale network system [11]-[12]. In this model, decentralized system has been adopted as a basis in which new information received can be randomly chosen peers. The protocols are scalable, easy to robust, deploy, and resilient to failure [13].

Local Convergence Detection

In practical carbon trading applications, a local convergence detection will be beneficial and helpful in which this can be used to terminate the protocol iterations [14]. Though epidemic aggregation protocols have some weaknesses, especially on its execution time, locally detection can help to minimize the execution time [14]. In addition, local convergence detection can be used to locally detect the time the information can be fully spread over the system. The study results showed the approval of the local convergence detection which can be represented the information fully distributed to the system.

THE PROPOSED ALGORITHM

In this work, the proposed algorithm was implemented based on gossip-based communication paradigm. The algorithm is designed based on the concepts of Blockchain, epidemic protocols and local convergence detection mechanism to develop a distributed network of institutions and regulators to execute the trading process successfully. The related functions to technologies can be organized as follows:

- Blockchain has a role in transaction exchanging and distributed ledger to maintain the carbon credits.
- Epidemic protocol has a role in communication pattern.
- Local convergence detection mechanism has a role in consensus mechanism.

Each node has the list of transactions contained in the transaction cache. At each cycle, the node (sender) will send its transaction cache to a group of randomly selected nodes (receivers) via push messages (line 11-12) in order to exchange the local information. Once the receiver receives the push messages, receiver merges its transaction cache with

the cache in the message (line 15), then the pull messages will also be sent to the sender (line 16). After that, the senders will merge its transaction caches with the caches from the pull messages (line 19).

In order to detect that the information is fully distributed to the network, the local convergence detection mechanism is adopted to the algorithm. After the sender receives every pull message, the sender will compare the transaction caches from every message including its transaction cache. If all the transactions in the caches are the same, the sender will start counting the round until it confirms. The counting round is to avoid the situation that the node misjudges the consensus status. If the number of rounds has reached the acceptance, the sender will consider that the information is fully distributed to the network system and it will stop sending the push messages to exchange the information in transaction cache (line 2 - 8).

Algorithm 1 The Proposed Algorithm

```

1: procedure CHECKCONSENSUS
2:   if the collected caches from different nodes are the same then
3:      $count \leftarrow ++$ 
4:   else
5:      $count \leftarrow 0$ 
6:   if  $count$  has reached the consensus acceptance (is equal to  $h$ ) then
7:      $c_i \leftarrow true$  (the status of node is consensus)
8:   end if
9: procedure SENDPUSHMESSAGE
10:  while  $c_i$  is equal to  $false$  (the status of node is NOT consensus) do
11:     $j_{1...p} \leftarrow \text{get } p \text{ random nodes}$ 
12:    send a push message to  $j_{1...p} : m_{\rightarrow} (i, Q_i)$ 
13:  end while
14: procedure RECEIVEPUSHMESSAGE( message  $m_{\rightarrow}$  )
15:   $Q_i \leftarrow Q_i \cup m_{\rightarrow}.Q_s$ 
16:  send a pull message to  $m_{\rightarrow}.s : m_{\leftarrow} (i, Q_i)$ 
17: end procedure
18: procedure RECEIVEPULLMESSAGE( message  $m_{\leftarrow}$  )
19:   $Q_i \leftarrow Q_i \cup m_{\leftarrow}.Q_d$ 
    
```

The scenario of the proposed algorithm is presented in Fig. 1.

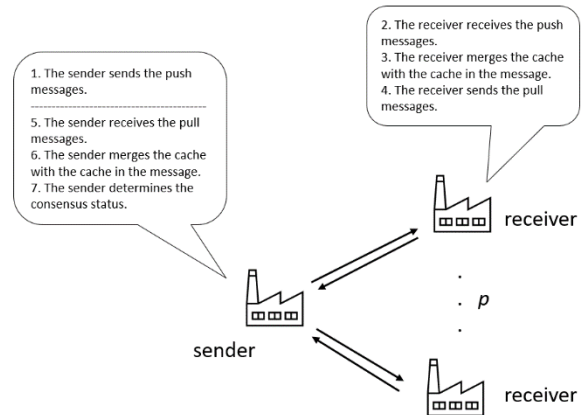


Fig. 1 The scenario of information distribution in the proposed algorithm

Table 1 describes the notation adopted in the proposed algorithms. Algorithm 1 shows the pseudocode of the proposed algorithm.

Table 1 Notation Adopted in the Pseudocode.

Parameters	Description
i	a node in the network, $i \in V$, where V is the set of nodes
p	number of sending messages in each cycle
h	number of cycles required to consensus
c_i	consensus status of node i
Q_i	local cache at node i
$m \rightarrow$	push message: - s , node originating the push - Q_s , main cache at s
$m \leftarrow$	pull message: - d , node originating the pull - Q_d , main cache at node d

SIMULATION CONFIGURATION

This section presents the configuration of simulation used in this study. In terms of the technical configuration, the initial topology is a regular random graph in which each node has 5 links to other nodes. The graph rewiring mechanism is performed by the epidemic membership protocol, called EMP+ [15]. The network size is assumed to be 100 nodes which refer as companies and each of them has the carbon credits which are randomly selected between -100 to 200. A negative number represents carbon credits a company emits less than its capped limit and the credits can be sold to another company exceeding its limit. In terms of a positive number, this represents carbon credits a company has above the permitted limit. Any companies can buy carbon credits to lower their GHG emissions on a voluntary basis.

The simulation was run for 100 cycles. The cycle length of the simulation is set to 40,200 and the network latency is randomized between 0 to 10,000. In the first cycle, every node will distribute the information in its local cache to other nodes. After 50 cycles, the simulation emulates the situation when a selected node transfers the carbon credits to another node.

The algorithm setting is shown as follows.

- the number of sending messages (p): 3
- the number of cycles for consensus (h): 4, 5, 6, 7

There are 3 objectives of the simulation in this study. The first objective is to capture the state that the node can detect that every node has received the information which is detected by the number of nodes that the consensus status is true. The second objective is to evaluate the correctness of the local information, and the last objective is to monitor the total number of messages overhead in the system.

EXPERIMENTAL RESULTS & DISCUSSION

The experimental results can be categorized in 3 sets. The first is the number of consensus nodes. The second is the correctness of the local information. Finally, it is the total number of messages overhead in the system.

Fig. 2 shows how the node determines the local consensus status. Y-axis presents the number of consensus nodes, while X-axis present the number of cycles. At the first cycle, every node will distribute their local information on how much carbon credits they trade with others. After several cycles, all nodes are set the status to consensus. According to the figures, the speed of consensus mechanism is directly related to parameter h . At cycle 50th, a node transfers some of its carbon credits to another. As a result, the new transactions are created, and the information is distributed.

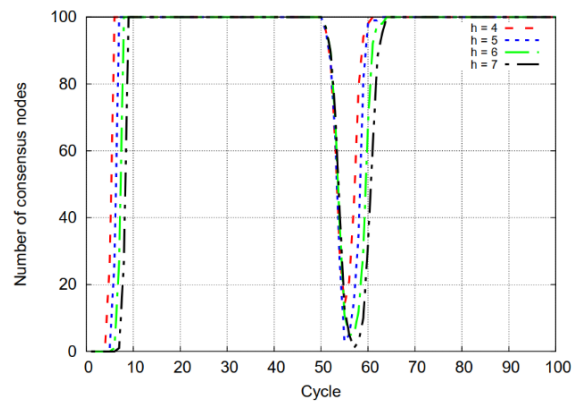


Fig. 2 Number of consensus nodes

Fig. 3 shows the correctness of the local information. Y-axis presents the standard deviation of the information cache size in the network, while X-axis presents the number of cycles. The result shows the accuracy of the algorithm when the parameter is changed. At the first cycle, every node starts to distribute the information and the information is fully distributed after several cycles. The effect of the parameter h can be noticed at cycle 50th when the

carbon credit is transferred. When parameter h is 4, the result shows that some nodes are not being able to receive the information because more effort is required to switch the consensus status and distribute the information. So the parameter h has to be set with the condition to provide the enough time for the information distribution.

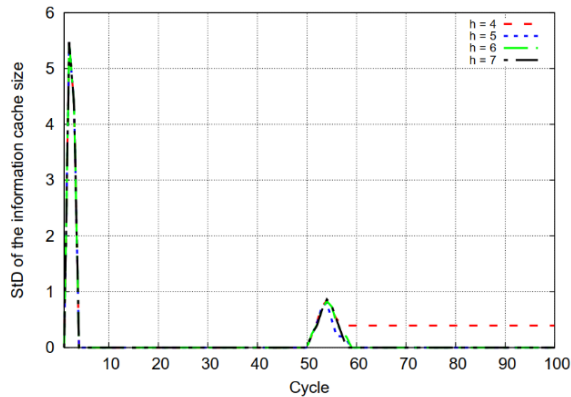


Fig. 3 Correctness of the local information

Table 2 shows the number of messages overhead in the network. The results show that parameter h has a strong relation with messages overhead. The higher number of h , the higher messages overhead.

Table 2 Message Overhead

Setting of parameter h	Message overhead
$h = 4$	4512
$h = 5$	5784
$h = 6$	6960
$h = 7$	8190

CONCLUSION & FUTURE WORKS

Though the use of carbon trading to trim out GHG emissions, understanding the maximization of the profitability of the carbon trading project was an objective of this study. This study demonstrates the blockchain technology together with epidemic protocols as a smart carbon transaction platform.

Blockchain technology has recently gained popularity as a potentially effective solution for financial transactions. In an epidemic algorithm, the reliability of carbon trading information delivery will then be proved by participants included in the carbon market system without any third parties. In other words, each participant can interact or transfer carbon credit through the blockchain technology with a

generated address in which users do not need to reveal their real identity. In addition, regulators who are approving or controlling the carbon trading are no longer needed in blockchain.

In general, it can be concluded that blockchain technology together with epidemic protocols provide the innovative solution for the carbon trading over the present forms of “cap-and-trade” system. The protocol with different network conditions should be considered and recommended for future work. The evaluation of the proposed algorithm with other consensus algorithms is one of the interesting challenges in this work.

REFERENCES

- [1] Moghal A. A. B., Dafalla M. A., Elkady T. Y., and Al-Shamrani M.A., Lime Leachability Studies on Stabilized Expansive Semi-Arid Soil. *International Journal of GEOMATE*, Vol. 9, Issue 18, 2015, pp.1467-1471.
- [2] J. Koiwanit, A. Manuilova, C. Chan, M. Wilson, and P. Tontiwachwuthikul, “A life cycle assessment study of a hypothetical Canadian oxyfuel combustion carbon dioxide capture process,” *Int. J. GHG Control*, vol. 28, pp. 257-274, 2014.
- [3] International Criminal Police Organisation (Interpol). “Guide to carbon trading crime” US, 2013.
- [4] V. Birla, G. Singhal, R. Birla and V. G. Gupta, “Carbon trading-the future money venture for india,” *Int. J. Scientific Research Engineering & Technology (IJSRET)*, Vol. 1, pp. 019-029, 2012.
- [5] P. Poonpakdee, J. Koiwanit, C. Yuangyai, and W. Chatwiriya. “Applying Epidemic Algorithm for Financial Service Based on Blockchain Technology,” *Int. Conference on Engineering, Applied Sciences and Technology (ICEAST2018)*, pp. 1-4, 2018.
- [6] A. Kosba, A. Miller, E. Shi, Z. Wen and C. Papamanthou, “Hawk: The Blockchain Model of Cryptography and Privacy-Preserving Smart Contracts”, *IEEE Symposium on Security and Privacy (SP)*, San Jose, CA, 2016, pp. 839-858, 2016
- [7] S. Nakamoto, “Bitcoin: A peer-to-peer electronic cash system,” 2008.
- [8] N. Nazir, “Carbon trading: Capital market challenges and regulatory reforms for Islamic finance,” *Academic Research International*, vol. 3, no. 3, 2012.
- [9] J. Rohleder, “The role of third-party verification in emissions trading systems: Developing best practices,” *Sustainable Dev.L.& Pol’y*, vol. 6, no. 26, 2005.
- [10] D. L. K. Chuen, “Handbook of digital currency:

- Bitcoin, innovation, financial instruments, and big data” Academic Press, 2015.
- [11] Z. Zheng, S. Xie, H. Dai, X. Chen, and H. Wang, “An overview of blockchain technology: Architecture, consensus, and future trends,” *IEEE International Congress on*, pp. 557-564, 2017.
 - [12] A. Montresor, and M. Jelasity, “PeerSim: A scalable P2P simulator”, in *Proc. of the 9th Int. Conference on Peer-to-Peer (P2P09)*, pp. 99 - 100, 2009.
 - [13] P. Poonpakdee, J. Koiwanit and C. Yuangyai, “Decentralized Network Building Change in Large Manufacturing Companies towards Industry 4.0” *Int. Conference on Mobile Systems and Pervasive Computing (MobiSPC 2017)*, vol. 110, pp. 46 - 53, 2017.
 - [14] P. T. Eugster, R. Guerraoui, A. Kermarrec, and L. Massoulie, “Epidemic information dissemination in distributed systems,” *Computer*, vol. 37, no. 5, pp. 60-67, 2004.
 - [15] P. Poonpakdee, N. G. Orhon, , and G. Di Fatta, “Convergence Detection in Epidemic Aggregation”, in *Euro-Par Workshops*, Springer, pp. 292 - 300, 2013.
 - [16] P. Poonpakdee, and G. Di Fatta, “Robust and efficient membership management in large-scale dynamic networks,” *Future Gener. Comput. Syst.*, vol. 75, pp. 85 - 93, 2017.

EVALUATING EFFECTS OF MIXING PROPORTION ON WATER RETENTION CURVE AND PORE SIZE DISTRIBUTION OF RECYCLED CONCRETE AGGREGATES BLENDED WITH AUTOCLAVED AERATED CONCRETE GRAINS

PHAM Van Nam¹, Akira KATO¹, NGUYEN Hoang Giang², NGUYEN Van Tuan², PHAN Quang Minh²,
and Ken KAWAMOTO^{1,2}

¹Graduate School of Science and Engineering, Saitama University, Japan.

²National University of Civil Engineering, Vietnam.

ABSTRACT

Due to rapid urbanization in developing countries, the generation of construction and demolition waste (CDW) and industrial by-products (IBPs) are increasing. In this study, we aimed to utilize the recycled materials from CDW and IBPs as the road base materials for improving the water retention capacity of the pavement structure especially for the water retentive pavement system, which can be expected to contribute to the mitigation of urban heat island (UHI), reducing the road surface temperature due to subsequent water evaporation. In order to improve the water retention capacity, testing samples graded recycled concrete aggregates (RC) from CDW blended with autoclaved aerated concrete (AAC) grains (size: 0.106-2 mm) made from AAC scrap at different proportions, i.e., RC 100%, RC 80%+AAC 20%, RC 60%+AAC 40%, and AAC 100%, were prepared. The water retention curves (WRCs), which represent the relationship between volumetric water content and matric potential were measured using a combination of hanging water, pressure chamber, and potentiometer methods in the laboratory. The measured WRCs were fitted by either sigmoidal or bimodal water retention model and the equivalent pore size distribution (PSDs) of tested samples were compared. The results showed a significant improvement of water retention capacity was found by blending AAC grains and the saturated volumetric water contents for 20 and 40% AAC blended RC samples increased approximately 1.8 to 2.2 times compared to that of RC 100%. Based on the results from estimated PSDs, the blending of AAC grains increased significantly fine pores ranging from 0.03 to 1 μm .

Keywords: Construction and Demolition Waste, Autoclaved Aerated Concrete, Water Retention, Pore Size Distribution

INTRODUCTION

It is well known that the urban heat island (UHI) effect is one of crucial issues in urban areas because of the generation of a large amount of heat from building environments and solar reflectance of paved surfaces. Water retentive pavements have been developed to mitigate UHI effect and reduce the temperature of the paved surface using water evaporation due to the heat energy from the sun [1][2][3][4] and its application in the road construction is becoming popular these days and industrial by-products (IBPs) have been recycled as water retentive materials [5][6][7]. Kinoshita et al [8] and Misaka et al [9] pointed out that the surface temperature of water retentive material decreases with increasing of evaporation efficiency and water retention. Therefore, if a long-term drought event occurs by continuous sunny weather especially during the summer period, water retention capacity is needed much more. Kato et al [10] used road base

materials made from graded recycled concrete aggregates (RC) blended with autoclaved aerated concrete (AAC) grains to improve the water retentive property. They reported that AAC grains themselves had high water retention capacity because of meso and micro-pores of AAC, and improved water retentive property of RC. However, it is required to collect more data for applying the developed materials to the road construction works.

On the background of recycling of IBPs and construction and demolition waste (CDW), the generation of IBPs and CDW have been increasing worldwide, especially in developing countries due to rapid urbanization and population explosion, a few researchers attempt to utilize the recycled materials from IBPs and CDW to develop road pavement and base materials [5][6][7][11]. However, most of the studies are mainly examining the hydraulic and mechanical properties of testing materials and very limited studies have been done to improve the water retention capacity of testing materials. Compared to

developed countries, the recycling rate of CDW and IBPs is very small in most of developing countries including Vietnam [12][13]. In order to promote the recycling of CDW and effective use of IBPs, therefore, we aimed to develop the road base materials utilizing both recycled materials from CDW and IBPs, especially targeting Vietnam in this study. A series of laboratory measurements to determine water retention curves for graded RC blended with AAC grains at different mixing proportions were carried out using the materials taken from Vietnam. Then, the effects of blending of AAC grains on the water retention capacity and pore size distribution were examined based on the measured water retention curves.

MATERIALS AND METHODS

Materials

Types of materials collected in Hanoi, Vietnam were used in this study. Graded recycled concrete aggregates made from CDW masonry which was recovered from the CDW dumping site in Hanoi (20° 59' 21.6" N, 105° 53' 58.1" E), Vietnam and crushed in Japan (Jaw crusher machine), and the graded RC (size: 0.075-25 mm) were blended with AAC grains (size: 0.106-2 mm), which was from Viglacera Joint Stock Company in Bac Ninh province (21°11'50.8"N, 106°00'42.8"E), Vietnam as shown in Figs. 1a and 1b. The basic physical and chemical properties of RC and AAC were measured in the laboratory as outlined in Table 1. As shown in Table 1 AAC grains have not only a higher water content at air-dried condition but also a higher water absorption than those of RC, indicating that AAC grains are beneficial to water retention capacity. RC was first sieved with a 25-mm sieve according to Vietnamese standard TCVN 8859-2011 [14], while AAC was sieved with a 2-mm sieve. Particle size distributions of tested materials are shown in Fig. 2. RC was used as base material, and AAC was mixed with RC as water retentive material to be 40% and 20% of mixing proportion. There were total of 4 tested samples: RC 100%, RC 60% +AAC 40%, RC 80% + AAC 20%, and AAC 100% in this study.

Table 1 Basic physical and chemical properties of RC and AAC samples used in this study

Test samples	G_s	W_{AD}	W_{abs} (%)		pH	EC
			<4.75 mm	>4.75 mm		
RC	2.63	0.9	8.5	5.2	11.0	4.8
AAC	2.51	2.1	61.4		9.0	0.9

G_s : Specific gravity, W_{AD} : Water content at air-dried condition, W_{abs} : Water absorption, and EC: Electric conductivity.

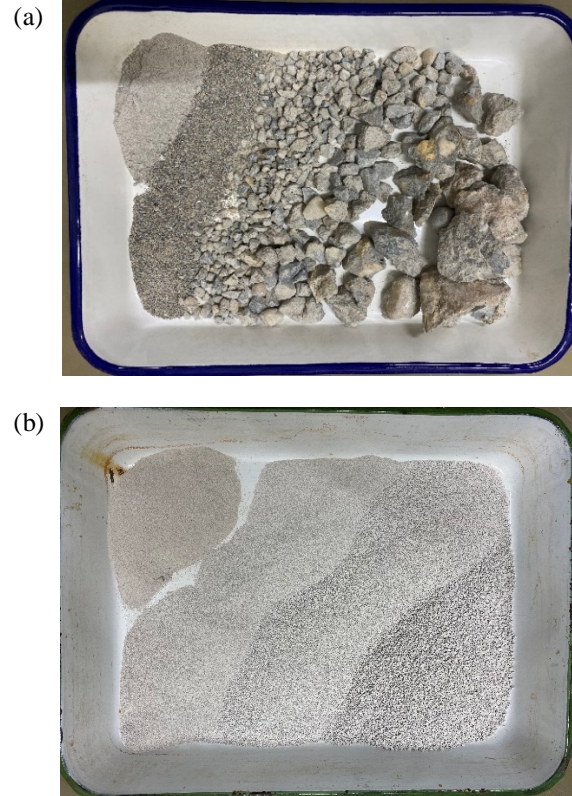


Fig. 1 Tested materials (a) Graded recycled concrete aggregate (RC), and (b) Autoclaved aerated concrete (AAC) grains.

Compaction test (ASTM D1557-2012 [15], TCN 333-06 [16]), California bearing ratio test (CBR) (JIS A 1211, 2009 [17], TCN 332-06 [18]), and constant head permeability test (ASTM D2434 – 68 (Reapproved 2006) [19], JIS A1211-2009 [20]) were carried out to assess maximum dry density (MDD), CBR value, and saturated hydraulic conductivity (K_s). The tested results were summarized in Table 2. CBR values increased with increasing of MDD. Inversely, the measure K_s decreased with increasing of MDD as discussed in [21].

Table 2 Mechanical and hydraulic properties

Test samples	MDD	CBR (K98)	K_s
	g.cm ³	%	cm/s
AAC 100%	0.73	31	1.14×10^{-3}
RC60%+ AAC 40%	1.21	55	1.85×10^{-4}
RC 80%+AAC 20%	1.52	113	8.78×10^{-5}
RC 100%	1.96	173	2.80×10^{-6}
Reference	>1.78 ^a	>100 ^b	> 3×10^{-3} ^c

CBR(K98): California bearing ratio value at dry density of 98% degree of compaction.

References: [22]^a, [18]^b, and [23]^c.

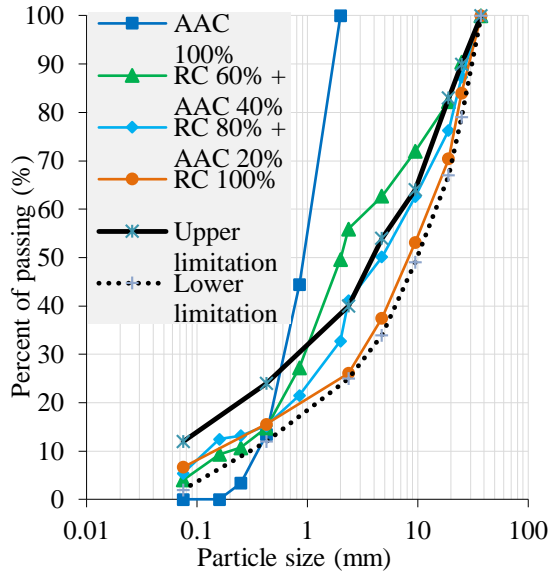


Fig. 2 Particle size distributions of tested materials

Measurement of the water retention curve and pore size distribution

First, the water content of the tested sample was adjusted to become at optimum water content mixed with distilled water. Then, the water adjusted sample was compacted in a stainless mold (120 mm height, 150 mm inner diameter based on [15][16]. The compacted sample was soaked subsequently in water for 1 week to saturate before draining to the desired water matrix potential (ψ , -cm H₂O) values using by a hanging-water column method (0 to - 60 cm H₂O), a pressure chamber method (-100 to -10000 cm H₂O). The ψ value for the air-dried sample was measure by a dewpoint potential meter (WP4-T, Decagon Devices Inc., WA, USA).

The measured water retention curves (WRCs) were fitted by the Durner model [24] based on the van Genuchten model [25] as the following equation:

$$\frac{\theta - \theta_r}{\theta - \theta_s} = \sum_{i=1}^k w_i \left[\frac{1}{1 + (\alpha_i |\psi|)^{n_i}} \right]^{m_i} \quad (1)$$

where θ (cm³/cm³), θ_r (cm³/cm³), θ_s (cm³/cm³) are the volumetric water content, residual volumetric water content, and the saturated volumetric water content, k is the number of the peak of pore-size density or subsystems which form the total pore size distribution (in this study is 2), w_i are the subcurves weighting factors, α_i , n_i , and m_i are the parameters of the subcurves ($m_i = 1 - 1/n_i$) indicate fitted parameters.

The equivalent pore size distributions (PSDs) of tested samples were obtained by using the following equation, which was defined by

$$\frac{d\theta(r)}{d \log r} = \frac{d\psi}{d \log |\psi|} \frac{d\theta(\psi)}{d|\psi|} = [\ln(10)] |\psi| C^* \quad (2)$$

where r is equivalent pore radius (μ m), C^* is specific moisture capacity ($r = 1500/|\psi|$ [26]). The equivalent pore radius can be calculated from the water retained capacity ($\theta_s - \theta_r$) in this study.

RESULTS AND DISCUSSION

The measured WRCs and estimated PSDs are shown in Figs. 4a and 4b. The fitted parameters for WRCs were summarized in Table 3.

The WRCs showed clearly that measured θ_s increased with increasing of mixing proportion of AAC grains. The θ_s values for 20% and 40% AAC blended samples became approximately 1.8 to 2.2 times higher than that for RC 100%, indicating the water retention capacity of RC was improved by blending AAC grains. The θ decreased unimodally with increasing water matrix potential for RC 100%, on the other hand, the θ of AAC 100% and AAC blended samples decreased bimodally with two different fields of water retention. Especially, a sharp drop in θ (water drainage) at around $\psi = -1.0 \times 10^4$ cm H₂O was observed in WRCs for AAC 100% and AAC blended samples.

As shown in Fig 4b, the blending of AAC grains had a great effect on PSDs of tested samples. By blending AAC grains, not only fine pores (micro to meso-pores) ranging from 0.03 to 1 μ m but also large pores (macro-pore) ranging from 5 to 300 μ m increased compared to RC 100%. The observed results in this study fairly related to the reported study in Lam et al. (2018) [27]. They characterized the PSDs of AAC samples using a mercury intrusion porosimetry and reported that the main peak of pores for AAC samples ranged from 0.02 to 0.08 μ m and the second peak ranged around 40 μ m.

Table 3 Fitting parameters for WRCs

Tested materials	AAC 100%	RC 60% + AAC 40%	RC 80% + AAC 20%	RC 100%
θ_s	0.70	0.52	0.42	0.24
θ_r	0.15	0.14	0.11	0.09
α_1	0.07	0.11	0.36	0.06
n_1	1.20	1.33	1.23	1.20
w_1	0.70	0.61	0.57	
α_2	9.0×10^{-5}	1.3×10^{-4}	3.1×10^{-4}	
n_2	4.01	3.22	2.41	
w_2	0.30	0.39	0.48	
R ²	0.98	0.97	0.99	0.93

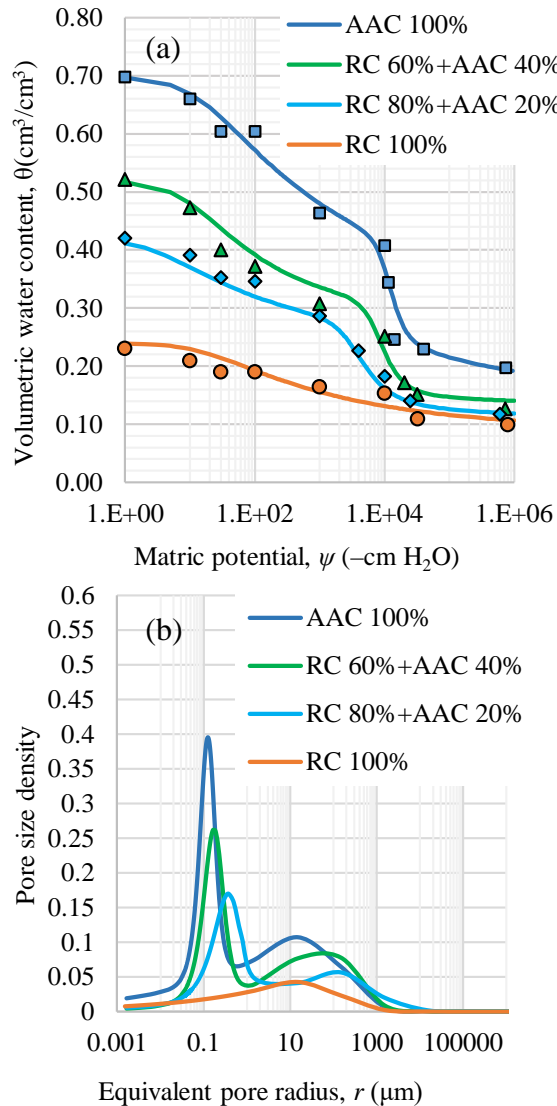


Fig. 4 (a) WRCs as a function of ψ , and (b) pore size density as a function of equivalent pore radius, r .

CONCLUSIONS

The laboratory experiments were carried out to evaluate water retention curves and pore size distributions for RC blended with AAC grains. The blending of AAC grains improved clearly the water retention capacity of RC and corresponding pore size distributions. Especially, it was observed that the blending of AAC grains gave a significant increase in both fine (ranging from 0.03 to 1 μm) and large pores (ranging from 5 to 300 μm), implying that the AAC grains have a high potential for developing water retentive pavements. However, the blending of AAC grains simultaneously causes a reduction in CBR (typically, AAC blending with $\geq 40\%$). Therefore, further studies are needed to improve both water retention and mechanical property to satisfy technical requirements for road base materials.

ACKNOWLEDGMENTS

This research was supported by JST-JICA Science and Technology Research Partnership for Sustainable Development (SATREPS) project (No. JPMJSA1701).

REFERENCES

- [1] Y. Qin., Y. He., J. E. Hiller., and G. Mei., A new water-retaining paver block for reducing runoff and cooling pavement, *J. Clean. Prod.*, Vol. 199, 2018, pp. 948-956.
- [2] M. Santamouris., Using cool pavements as a mitigation strategy to fight urban heat island - A review of the actual developments, *Renew. Sustain. Energy Rev.*, Vol. 26, 2013, pp. 224-240.
- [3] H. Yamagata., M. Nasu., M. Yoshizawa., A. Miyamoto., and M. Minamiyama., Heat island mitigation using water retentive pavement sprinkled with reclaimed wastewater, *Water Sci. Technol.*, Vol. 57, No. 5, 2008, pp. 763-771.
- [4] R. Kim., J. Bin Park., M. Jung-Soo., and L. Jung-Hun., Reduction effects of urban heat island by water-retentive pavement, *Mater. Sci. Forum*, Vol. 724, 2012, pp. 147-150.
- [5] K. Takahashi and K. Yabuta., Road temperature mitigation effect of 'road cool,' a water-retentive material using blast furnace slag, *JFE Tech. Rep.*, Vol. 13, 2009, pp. 58-62.
- [6] C. F. Lin., C. H. Wu., and H. M. Ho., Recovery of municipal waste incineration bottom ash and water treatment sludge to water permeable pavement materials, *Waste Manag.*, Vol. 26, No. 9, 2006, pp. 970-978.
- [7] J. Bin Park., S. Lee, C. S. Gee., and H. B. Pyun., Experimental study of non-sintering block for reducing surface temperature using recycling bottom ash, *Mater. Sci. Forum*, Vol. 620-622, 2009, pp. 105-108.
- [8] S. Kinoshita., A. Yoshida., and N. Okuno., Evaporation Performance Analysis for Water-Retentive Material , Based on Outdoor Heat-Budget and Transport Properties, *J. Heat Isl. Inst. Int.*, Vol. 7, No. 2, 2012, pp. 222-230.
- [9] I. Misaka., K. Narita., and H. Yokoyama., Evaluation of Evaporation Ability of the System for Mitigating Urban Heat Island, 7th Int. Conf. Urban Clim., 2009, pp. 2-5.
- [10] A. Kato., R. Ito., A. Matsuno., T. Uchimura., N.V. Tuan., N.H. Giang., and K. Kawamoto., Water Retention and Gas Transport Characteristics of Recycled Graded Roadbed Materials Blended With AAC Grains, 17th International waste management and landfill symposium., Proceedings SARDINIA 2019.
- [11] A. Arulrajah., A. Mohammadinia., S. Horpibulsuk., and W. Samingthong., Influence of class F fly ash and curing temperature on strength

- development of fly ash-recycled concrete aggregate blends, *Constr. Build. Mater.*, Vol. 127, 2016, pp. 743-750.
- [12] N. V. Tuan., T. T. Kien., D. T. T. Huyen., T. T. V. Nga., N. H. Giang., N. T. Dung., Y. Isobe., T. Ishigaki., and K. Kawamoto., Current status of construction and demolition waste management in Vietnam: Challenges and opportunities, *Int. J. GEOMATE*, Vol. 15, No. 52, 2018, pp. 23-29.
- [13] T. T. Kien., L. T. Thanh., and P. V. Lu., Recycling construction demolition waste in the world and in Vietnam, *Int. Conf. Sustain. Built Environ. Now Futur.*, 2013 pp. 247-256.
- [14] TCVN 8859-2011., Graded Aggregate Bases and Subbases Pavement - Specification for Construction and Acceptance. Ministry of Technology and Science of Viet Nam., 2011.
- [15] ASTM, D1557-12., Standard Test Methods for Laboratory Compaction Characteristics of Soil Using Modified Effort. ASTM International, West Conshohocken, 2012.
- [16] 22TCN 333-06., The standard method used related compaction of the material in a series of layers in a fixed mould (in Vietnamese). Ministry of Transport of Vietnam, 2006.
- [17] JIS A 1211-2009., Test Methods for the California Bearing Ratio of Soils in Laboratory. Japanese Standards Association, 2009.
- [18] TCN 332-06., Process to determine CBR value of soil, gravel in laboratory (in Vietnamese). Ministry of Transport of Vietnam, 2006.
- [19] ASTM D2434-68., Standard Test Method for Permeability of Granular Soils (Constant Head), Reapproved, 2006.
- [20] JIS A1218-2009., Test Methods For Permeability Of Saturated Soils. Japanese Standards Association ,2009.
- [21] R. D. Rafaela Cardoso., Rui Vasco Silva., and Jorge de Brito., Use of recycled aggregates from construction and demolition waste in geotechnical applications: A literature review, *Waste Manag.*, Vol. 49, 2016, pp. 131-145.
- [22] A. Arulrajah., M. M. Disfani., S. Horpibulsuk., C. Suksiripattanapong., and N. Prongmanee., Physical properties and shear strength responses of recycled construction and demolition materials in unbound pavement base/subbase applications, *Constr. Build. Mater.*, Vol. 58, 2014, pp. 245-257.
- [23] Method of on-site test for water permeability of porous pavement. Manual of Pavement Unvestigation and Testing Methods, Part 1 (in Japanese), pp. 122-126, 2007.
- [24] W. Durner., Hydraulic conductivity estimation for soils with heterogeneous pore structure, *Water Resour. Res.*, Vol. 30, No. 2, 1994, pp. 211-223.
- [25] van Genuchten., A closed-form equation for predicting the hydraulic conductivity of unsaturated soils, *Soil Sci. Soc. Am. J.*, Vol. 44, No. 5, 1980, pp. 892-898.
- [26] Brutsaert., Probability Laws For Pore-Size Distributions, *Soil Sci.*, Vol. 101, No. 2, 1966, pp. 85-92.
- [27] N. T. Lam., S. Asamoto., and K. Matsui., Microstructure and shrinkage behavior of Autoclaved Aerated Concrete (AAC) - Comparison of Vietnamese and Japanese AACs-, *J. Adv. Concr. Technol.*, Vol. 16, 2018, pp. 333-342.

A COMPARATIVE STUDY OF CONVENTIONAL EXTENDED AERATION AND MODERN MEMBRANE BIOREACTOR METHODS OF SEWAGE TREATMENT FROM THE ENVIRONMENTAL AND FINANCIAL PERSPECTIVES

Mohamed Fetouh¹, Rabee Rustum² and Adebayo J. Adelaye³

^{1,2}Department of Civil Engineering, Heriot-Watt University, United Arab Emirates; ³Department of Civil Engineering, Heriot-Watt University, United Kingdom

ABSTRACT

The conventional extended aeration (EA) method and its modifications have been considered as a routine, user-friendly method in wastewater treatment plants around the world. The membrane bioreactor (MBR) method has been promoted by membrane manufacturers over the past decade as the most efficient treatment method in the industry. Research has shown the higher quality of MBR effluent compared with that of EA, but the comparison has seldom included the financial aspects. If the quality of the effluent from both methods is acceptable for a given reuse application, then a major consideration in adopting either method must be financial (i.e., the capital expenditure (CAPEX) and operating expenses (OPEX) involved in their deployment). Simulation of both methods is conducted for domestic wastewater treatment plants using the biological and financial models of CAPDETWorks™. The CAPEX and OPEX findings from the simulation are interpreted to their present unit values by employing global market price indices as of October 2019. Hydraulic loads from 500 to 5,000 m³/d were considered for three influent strengths: weak, medium and strong. It is found that the EA method is less costly in meeting the effluent-quality requirements of certain reuse applications, while the MBR is recommended for the extra strong-strength influent especially for units smaller than 500 m³/d, due to both effluent quality and lifetime cost.

Keywords: Wastewater treatment, Extended aeration, Membrane bioreactor, Capital expenditure (CAPEX), Operating expenses (OPEX).

INTRODUCTION

In recent decades, engineered wastewater treatment methods have been progressively developed for various environmental aspects of reuse, such as agricultural, industrial, urban, groundwater-recharge, etc. [1], [2]. These treatment methods could be tailored, modelled and simulated to achieve the required level of quality for both effluent-water and solid-waste for a given influent with the help of proven, reliable Computer Aided Design programs. The process of selecting a method to be implemented and the adaptations required in order to comply with a certain environmental criterion of reuse has a commercial impact from the CAPEX and OPEX perspectives that needs to be considered, as well, which is the aim of this paper.

Environmental Aspect

Current advances in membrane manufacturing technology make the membrane-based methods increasingly attractive solutions for wastewater reuse applications [3], [4]. Mohammadi, Sabzali, Gholami, Dehghanifard, and Mirzaei [5] compared the performance of the EA and MBR methods for the treatment of high-strength wastewater under similar influent conditions, as COD was adjusted in the range

of 500 to 2700 and 500 to 5000 mg/L, respectively. The results showed that in the addition to the better effluent quality in terms of COD, BOD₅, and TSS of the MBR method than that of the EA, despite the higher organic load, the BOD₅/COD ratio of the effluent was 0.708 ± 0.18 and 0.537 ± 0.106 , respectively. This means that more stabilized effluent could also be a benefit of the MBR method of treatment. Meanwhile, the study recommended that special attention be given to cleaning the periodical scaling and biofouling on the MBR membrane due to the high influent strength.

Hatami, Nadali, Roshanaei, and Shokoohi [6] evaluated the possibility of reuse of the treated effluent from the EA wastewater treatment plant of Bojnourd City, Iran, for the agricultural applications. The results showed that the removal efficiency of BOD₅ and COD was 88% and 89%, respectively, with an average residual concentration of 27.0 and 61.0mg/L, respectively; while Chloride and Sodium Adsorption Ratio (SAR) residual values were 3.89 milliequivalents per liter (meq/L) and 221 milligrams per liter (mg/L), respectively. It was concluded that the said effluent could be valuable for agricultural applications, but due to its high chloride concentration, it has been recommended for semi-sensitive plants only.

Commercial Aspect

As it could be captured from the cited literature, in addition to other published papers, the relevant CAPEX and OPEX of the same were have not been addressed. Some of the literature has addressed the power consumption per unit flow rate of treated influent, but only very limited commercial comparative studies between the MBR wastewater treatment method and other conventional activated sludge methods, including EA, have been conducted.

Iglesias, Simón, Moragas, Arce, and Rodriguez-Roda [7] compiled the documented data from the public wastewater management institutions in Catalonia and Murcia (ACA and ESAMUR), Spain for fourteen full scale MBR units and compared them with those installed conventional activated sludge plants. Iglesias, Simón, Moragas, Arce, and Rodriguez-Roda [7] reported that Spain has one of the highest numbers of MBR-based municipal wastewater treatment plants (WWTPs) in Europe. The results showed that the CAPEX for the treatment plants of a conventional secondary treatment followed by a tertiary treatment of physical, chemical, sand-filtration and disinfection is approximately 30% less than those plants adapted MBR method; but, if the said tertiary treatment is replaced with an advanced membrane filtration (e.g. an ultra-filtration membrane followed by a disinfection unit) to achieve the same quality of the MBR effluent, the CAPEX is approximately 10% higher than that of the MBR plants for capacities less than 10,000 m³/d. In terms of the OPEX, the study showed that OPEX are similar for both systems, within the limitations of the study.

There are some limitations of the cited commercial comparative study. It did not consider the geographical difference in the cost of the equipment and construction material, nor the monetary value of the land, which represents a significant weight of the CAPEX of both methods, as MBR always requires a smaller foot-print than EA; while the OPEX did not consider the membrane replacement.

Aim and Method of the Study

On the trail to address the said limitations and help select the best option from the subject methods, especially for decentralized wastewater treatment plants of 500 m³/d to 5,000 m³/d hydraulic load, the following pages reveal an environmental and financial comparative study for the same. The environmental aspect is presented by the efficiency-of-treatment for each method in terms of characteristics of the treated effluent, while the financial aspect is presented by the method economics in terms of the equivalent CAPEX and OPEX for the same in USD, considering the updated global market price as of October 2019. The said study is conducted sequentially for three types of

organic loads: weak, medium and strong, to cover the potential loads from both developed and developing communities.

The method was selected to be of a proven, commercially available nature for the sake of ease replication of the study. Specialized software developers, such as Hydromantis Environmental Software Solutions Inc. (Hydromantis), EnviroSim Associated LTD (EnviroSim), AQUIFAS, etc. have produced powerful mathematical engines capable of running the most sophisticated, implicit mathematical models of wastewater treatment with minimal discernible error. The same have been presented in the form of software packages (e.g. GPSXTM and BioWinTM of Hydromantis and EnviroSim, respectively) that come with various features such as steady state and dynamic simulations, estimation of chemical and power consumption, etc. Hydromantis has further produced CAPDETWorksTM, a software package for the simulation of wastewater treatment plant performance while predicting the life-cycle cost of the same. CAPDETWorksTM version 04 2018 is used as a methodological, experimental tool for the subject study. The mathematical models used for both performance simulation and cost estimation are elaborated under 'METHOD'.

METHOD

Performance Modelling

Henze, Gujer, Mino, and Loosdrecht [8] have developed the Activated Sludge Model No. 1 (ASM1) which is a dynamic wastewater treatment model. ASM1 is adopted by most of the simulation programs (e.g. GPS-XTM & BioWinTM) in their library of models. According to Hydromantis CAPDETWorksTM version 04–User's Guide [9], the relevant adapted mode is based on the University of Cape Town (UCT) algorithm and is consistent with ASM1. For proper replication, the Solids Retention Time (SRT) shall be substituted with a sufficient time to allow for both biological oxygen removal and nitrification, considering the recommended operating SRT range for both EA and MBR methods, as well as the actual winter temperature and the recommended operating range of the Mixed Liquor Suspended Solids (MLSS). The said model is an accurate preliminary design tool, while for a more detailed design and consideration of dynamic simulation over an extended period of time, GPS-XTM, BioWinTM, AQUIFASTM etc., should be used. The 2018 CAPDETWorksTM version 04 is used as a computer-based simulation tool for the performance modelling. Details of the algorithm for the influent speciation, nitrifier growth/decay rates, minimum aerobic SRT, reactor solid mass, effluent BOD, etc. are elaborated at the Hydromantis CAPDETWorksTM version 04–Supplemental Technical Reference [10].

CAPEX and OPEX Modelling

In 1973, the Environmental Engineering Division of the U.S. Army prepared a cost estimation model for wastewater treatment systems for benefit of the U.S. Environmental Protection Agency (EPA). The algorithm was called CAPDET, which stands for 'process design and estimating algorithms for the Computer Assisted Procedure for Design and Evaluation of wastewater Treatment systems'. It was revised in 1982 to overcome the original version's limitation of not reflecting the regional cost differences or accommodating site-specific design requirements [11], [12]. Hydromantis has since developed the model further and presented it to the market in a user-friendly software package called CAPDETWorks™. The 2018 version 04 is used as a computer-based cost estimation tool for life-cycle modelling.

The default unit rate cost of the program's library can be overridden with available local prices, or updated in consideration of globally recognized cost indices that are regularly published in the relevant trade publications, such as Marshall And Swift (MAS), Engineering News Record (ENR), or Chemical Engineering Magazine (CEM). Further, Hydromantis has developed a compilation of cost indices called HECI, HCCI and HPCI (Hydromantis Equipment Cost Index, Hydromantis Construction Cost Index and Hydromantis Pipe Cost Index, respectively). For an easy global replication of the study, the local Dubai market prices are not considered, and the compiled cost indices of Hydromantis are considered instead. The same is updated to October 2019 and kept in USD. Table 1 shows the considered financial modelling assumptions that shall be revisited on a case-by-case basis. The OPEX over the plant lifetime is converted to its present value and added to the relevant CAPEX, the sum is divided by the plant capacity to calculate the unit lifetime cost in (\$/m³).

Table 1 Financial modelling assumptions

Items	Assumed Value
Interest rate	8.0%
Construction period	3 years
Operating life of the plant	40 years
Electricity	0.1 USD/kWh
Land cost	20,000 USD/acre
Design and engineering fees	15%
Technical fees	2%
Administration/legal fees	2%
Inspection fees	2%
Miscellaneous	5%
Contingency reserve	10%
Profit and overhead	15%

Simulation Procedures

Extended aeration method

On the trail to simulate the actual operation of an EA bioreactor, the reactor is placed in a complete plant that treats solid-waste as well, as illustrated in Fig.1. The process flow diagram is summarized as follows:

- 1-Preliminary Treatment: coarse mechanical bar screen followed by a grit and FOG (Fat, Oil & Grease) removal chamber.
- 2-Primary Treatment: a primary clarifier.
- 3-Secondary Treatment: an EA bioreactor followed by a secondary clarifier with Return Activated Sludge (RAS) and Waste Activated Sludge (WAS) streams to adjust the operating SRT and MLSS.
- 4-Tertiary Treatment: a multilayer sand filter.
- 5-Solids Treatment: a gravity thickener followed by an aerobic digester, then a belt-filter press.

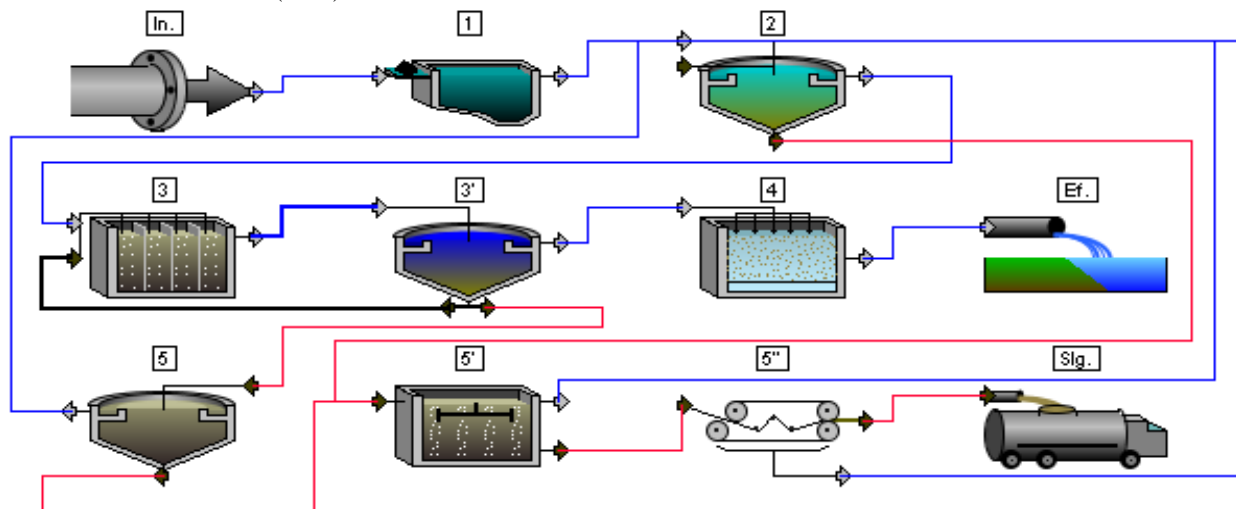


Fig. 1 Process flow diagram for EA plant

Membrane Bioreactor (MBR) method

In case of the MBR, both the aerated bioreactor and the secondary clarifier of the secondary treatment stage are replaced with an aerated membrane bioreactor. For the sake of equivalent comparison, the preliminary, tertiary, and solids treatments considered for EA plant are kept without change in the MBR plant; while the primary treatment was modified to an equalization tank followed by a fine screen to comply with the recommendations of membrane manufacturers.

Design Factors and Operating Parameters

For the sake of a traceable replication, the default, design factors and operating parameters at CAPDETWorks™ database library are used without change. The same can be overridden as needed.

RESULTS

Weak-Strength Influent Case

An influent of 500 m³/d is considered as a typical hydrological load for both plants. Table 2 shows higher removal efficiency of the EA method for the biological load in the form of BOD₅ and COD, in addition to better nitrification of the ammonia-nitrogen (NH₃-N) than the MBR method, and vice versa for the influent total suspended solids (TSS). Both reactors demonstrated high concentrations of nitrate-nitrogen (NO₃-N), as the process design did not address denitrification. It worth saying that for proper replication of the study, the actual local environmental conditions, such relative humidity, temperature, etc. shall be revisited.

Table 2 Performance comparison in terms of effluent quality (Eff.) for weak-strength influent (Inf.)

Items	Inf. (mg/L)	EA Eff. (mg/L)	MBR Eff. (mg/L)
BOD ₅	110	0.979	2.2
COD	250	1.47	4.13
TSS	100	8	1
TKN	20	0.095	1.21
NH ₃ -N	12	0.095	1.13
NO ₃ -N	0	15.5	9.1

A sensitivity analysis was conducted for a change in hydraulic-load from 500 m³/d to 5000 m³/d for the same weak-strength influent; two main findings were observed, as shown in Table 3: the dramatic decrease in the cubic meter cost as the plant capacity increases,

and the dramatic increase in the difference in the cubic meter cost as the plant capacity increases. Table 3 Lifetime cost comparison in terms of (\$/m³) for weak-strength influent (Inf.)

Influent Flow (m ³ /d)	EA Lifetime Cost (\$/m ³)	MBR Lifetime Cost (\$/m ³)	Difference in Lifetime Cost (%)
500	24,600	28,000	14%
1,000	13,500	16,200	20%
1,500	9,933	11,933	20%
2,000	8,050	9,850	22%
2,500	6,800	8,480	25%
3,000	5,933	7,567	28%
3,500	5,371	6,943	29%
4,000	4,925	6,625	35%
4,500	4,556	6,178	36%
5,000	4,260	5,920	39%

Attention should be given to the process design itself, as various installed EA plants have reported acceptable performance without primary clarifier, while both the tertiary and solids treatments vary from one plant to another to maintain the required level of compliance with local regulations.

Medium-Strength Influent Case

Like the weak-strength influent case, Table 4 shows that the EA method has a higher reduction in the biological load along with better nitrification, while the MBR method shows better removal of the TSS.

Table 4 Performance comparison in terms of effluent quality (Eff.) for medium-strength influent (Inf.)

Items	Inf. (mg/L)	EA Eff. (mg/L)	MBR Eff. (mg/L)
BOD ₅	220	0.979	2.2
COD	500	1.47	4.13
TSS	220	8	1
TKN	40	0.095	1.21
NH ₃ -N	25	0.095	1.13
NO ₃ -N	0	30.7	19.2

The same findings for the weak-strength influent case are noticed with the medium-strength influent case, but with smaller differences in the unit lifetime cost between the two methods, as shown in Table 5.

Table 5 Lifetime cost comparison in terms of (\$/m³) for medium-strength influent (Inf.).

Influent Flow (m ³ /d)	EA Lifetime Cost (\$/m ³)	MBR Lifetime Cost (\$/m ³)	Difference in Lifetime Cost (%)
500	24,800	28,400	15%
1,000	14,300	16,200	13%
1,500	10,400	11,933	15%
2,000	8,550	10,150	19%
2,500	7,360	8,960	22%
3,000	6,467	7,967	23%
3,500	6,029	7,286	21%
4,000	5,575	6,900	24%
4,500	5,156	6,444	25%
5,000	4,860	6,140	26%

Strong-Strength Influent Case

Results were like the weak and medium-strength influent, while the sensitivity analysis shows a much smaller difference in lifetime cost between the two methods, as illustrated in Tables 6 and 7 respectively.

Table 6 Performance comparison in terms of effluent quality (Eff.) for strong-strength influent (Inf.).

Items	Inf. (mg/L)	EA Eff. (mg/L)	MBR Eff. (mg/L)
BOD ₅	400	0.979	2.2
COD	1000	1.47	4.13
TSS	350	8	1
TKN	85	0.095	1.21
NH ₃ -N	50	0.095	1.13
NO ₃ -N	0	68	43.3

Table 7 Lifetime cost comparison in terms of (\$/m³) for strong-strength influent (Inf.).

Influent Flow (m ³ /d)	EA Lifetime Cost (\$/m ³)	MBR Lifetime Cost (\$/m ³)	Difference in Lifetime Cost (%)
500	26,600	28,400	7%
1,000	15,400	17,000	10%
1,500	11,467	12,933	13%
2,000	9,800	10,900	11%
2,500	8,520	9,520	12%
3,000	7,600	8,633	14%
3,500	6,943	7,829	13%

4,000	6,600	7,525	14%
4,500	6,178	7,000	13%
5,000	5,860	6,780	16%

The results of sensitivity analysis for difference in lifetime cost (%) between the EA and MBR of the three cases are represented in Fig. 2.

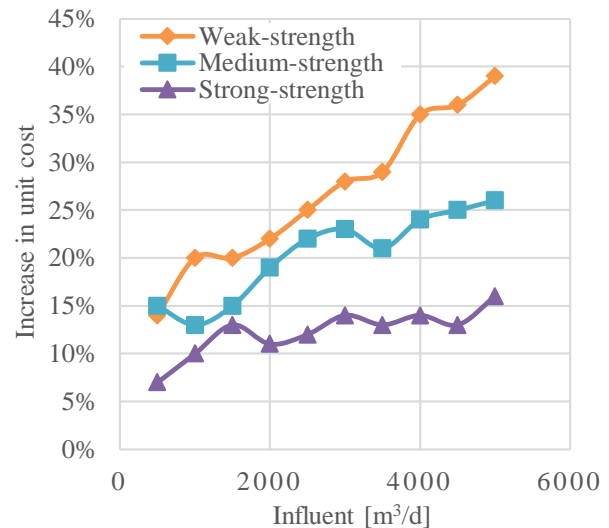


Fig. 2 Difference in unit lifetime cost for all strengths

DISCUSSION

Environmental Findings

The results show that the MBR method yields a much better effluent quality in terms of suspended solids (1.0 mg/L) compared to 8.0 mg/L from the EA method, due to the inherent filtration nature of its structure, a key merit introduced the MBR method to several areas of reuse-applications, as highlighted in [3]. Meanwhile, the EA method demonstrates a relatively higher removal efficiency for the BOD₅ and COD, and better nitrification than the MBR method, due to the higher SRT of 25.0 days compared to 10.0 days, respectively. The results that make the study in [6] appreciated in the use of EA effluent for the irrigation application for semi-sensitive plants. It is reasonable to find that the results agree with the study in [5] from the point of efficient removal of both methods for the biological load being treated, while not from the point of percentage of removal, as the said study was dedicated to the extra strong-strength influent that encountered in special applications where the COD ranges from 500 mg/L to 5000 mg/L with a corresponding SRT of 13 to 34 days, while the subject study considered the usual municipal influent ranges from 250 to 1000 mg/L with a corresponding SRT of only 10 days. Although we can benefit from the inherent advantage of the MBR method of maintaining a high operational MLSS in the bioreactor with minor limitation from the relevant

Hydraulic Retention Time (HRT), attention should be given to the disadvantage of the associated production of non-filterable inorganic compounds that could harm the microbial population and/or the membrane structure, as illustrated in [13].

Financial Findings

The results could be financially interpreted as follows:

- A dramatic decrease in the unit cost as the plant capacity increases for both methods, as expected.
- A dramatic increase in the difference in the unit cost as the plant capacity increases as in [7].
- The said observed difference in the lifetime unit cost decreases as the influent strength increases, shown in Fig.2, which makes the MBR method more attractive for strong-strength influent, especially for units smaller than 500 m³/d, leading to the conclusion that the MBR method is not only recommended for the extra-strong influent as concluded in [5], but it is also more cost competitive than other conventional methods of biological treatment, including the EA method.

CONCLUSION AND RECOMMENDATIONS

The MBR method of municipal wastewater treatment should not generally be specified for any development project, as the EA method is still an optimum solution economically, which complies with the effluent quality required for some reuse applications, such as irrigation of non-sensitive plants and landscapes. If MBR effluent quality is required for a specific area of application, the financial impact of the same should be addressed from the perspective of both CAPEX and OPEX. The MBR method is found to be more attractive for the strong-strength influent, especially for units smaller than 500m³/d, and is recommended for the extra strong-strength influent due to both effluent quality and lifetime cost.

For replication of the study, it is recommended that the following points be addressed:

- The local environmental conditions (relative humidity, temperature, etc.) shall be considered.
- If a pilot plant or lab model can be furnished, the actual values of the biological reaction(s) shall be verified accordingly.
- High consideration should be given to the process design (train of treatment) that varies from one plant to another to maintain the required level of compliance with local regulations.
- Globally updated unit prices are considered to widen the scope of benefit from the study; however, for the sake of accurate local monetary values, the local unit prices shall be considered instead.
- The financial modelling assumption should be revisited against the market and project conditions.

REFERENCES

- [1] Metcalf & Eddy, Inc., Tchobanoglous G., Burton F. L., and Stensel H. D., Wastewater Engineering: Treatment and Reuse, 4th ed., McGraw-Hill, Inc., ed 2004.
- [2] Asano T., Burton F. L., Leverenz H. L., Tsuchihashi R., and Tchobanoglous G., Water Reuse: Issues, Technologies, and Applications, Metcalf & Eddy, Inc./ McGraw-Hill, Inc, 2007.
- [3] Judd S., and Judd C., The MBR Book: Principles and Applications of Membrane Bioreactors for Water and Wastewater Treatment, 2nd ed., Elsevier/Butterworth Heinemann, ed 2011.
- [4] US Environmental Protection Agency, Guidelines for Water Reuse, EPA, 2012.
- [5] Mohammadi H., Sabzali A., Gholami M., Dehghanifard E., and Mirzaei R., Comparative Study of SBR and Extended Aeration Activated Sludge Processes in Treatment of High-Strength Wastewater. Desalination Journal, Vol. 287, 2012, pp. 109-115.
- [6] Hatami T., Nadali A., Roshanaei Gh., and Shokoohi R., Feasibility of Reuse of Effluent from the Extended Aeration Process of Wastewater Treatment Plant in the Bojnourd City for Agricultural and Irrigation Uses. Pajouhan Scientific Journal, Vol. 16, Issue 3, 2018, pp. 20-28.
- [7] Iglesias R., Simón P., Moragas L., Arce A., and Rodriguez-Roda I., Cost Comparison of Full-Scale Water Reclamation Technologies with an Emphasis on Membrane Bioreactors. Water Science & Technology Journal, Vol. 75, Issue 11, 2017, pp. 2562-2570.
- [8] Henze M., Gujer W., Mino T., and Loosdrecht M. V., Activated Sludge Models: ASM1, ASM2, ASM2d and ASM3, IWA, ed 2002.
- [9] Hydromantis CAPDETWorks™ ver. 04, User's Guide, 2018.
- [10] Hydromantis CAPDETWorks™ ver. 04 Supplemental Technical Reference, 2018.
- [11] Harris R. W., Cullinane M. J., and Sun P. T., Process Design and Estimating Algorithms for the Computer Assisted Procedure for Design and Evaluation of Wastewater Treatment Systems (CAPDET), EPA, 1982.
- [12] McGhee T., Mojgani P., and Vicidomina F., Use of EPA CAPDET Program for the Evaluation of Wastewater Treatment Alternatives. Water Pollution Control Federation Journal, Vol. 55, Issue 1, 1983, pp. 35-43.
- [13] Mohammed T A., Birima A. H., Noor M. J. M. M., Muyibi S., Muyibi S. A., and Idris A., Evaluation of Using Membrane Bioreactor for Treating Municipal Wastewater at Different Operating Conditions. Desalination Journal, Vol.221, Issue 1, 2008, pp. 502-510.

RESEARCH ON HOUSING RESTORATION COSTS AND DISASTER RISK MANAGEMENT FOR URBAN EARTHQUAKES

Norikazu Sakaba¹, Harumi Yashiro²

¹Tokio Marine & Nichido Risk Consulting Co., Ltd., Japan, ²National Defense Academy, Japan

ABSTRACT

A damage estimation by the Cabinet Office of the Japanese Government examines an earthquake directly beneath the Tokyo Metropolis as an earthquake disaster that will cause enormous damage. The economic losses are made clear in this damage estimation; however, the effects of financial support systems such as housing restoration funds, support grants for reconstructing the livelihoods of disaster victims, and earthquake insurance payments, which are insufficient throughout the region, are not clarified. In an urban structure such as Tokyo, where there are many apartment buildings, various financial support systems that were established according to lessons learned from previous disasters may not be effective. Therefore, this research performed a stochastic seismic analysis of the Tokyo Metropolis, and clarified trends in necessary restoration costs and various financial support funds for each category of damage (from partial destruction to complete destruction) according to the housing category. The AAL and VaR for the necessary restoration costs after a disaster were also estimated. To this end, individual building and households were modeled and a damage simulation was performed in order to understand the restoration costs required in the entire disaster area and to examine the effects of various financial support systems for procuring restoration costs. By showing AAL and VaR respectively, the costs required routinely and the costs needed when a major earthquake occurs were clarified. This research also showed quantitatively the extent to which these costs and support funds can be reduced by the ex-ante measure of making buildings earthquake proof.

Keywords: Disaster risk management, Housing restoration costs, Earthquakes in Japan, Stochastic seismic analysis, Ex-post compensation

INTRODUCTION

In recent years, numerous earthquakes caused by inland active faults have occurred in Japan, including the Kumamoto Earthquakes in April 2016, the Northern Osaka Prefecture Earthquake in June 2018, and the Hokkaido Eastern Ibari Earthquake in September 2018. These earthquakes caused serious damage to buildings, and many victims were forced to live as evacuees because they were unable to procure housing restoration costs. Even more households are expected to suffer damage as a result of an earthquake predicted to occur directly beneath the Tokyo Metropolis. For rapid restoration, it is necessary to understand the housing restoration costs and implement measures in advance. To address this issue, the national and local governments in Japan have conducted damage estimations to understand the building property damage and economic damage and taken disaster prevention/mitigation measures accordingly. However, there is also an economic loss due to the physical damage of completely or partially destroyed buildings that is not included in the cost required to restore them. These damage estimations are not considered to fully comprehend the restoration costs required in a disaster area. Considering past earthquake damage, in some cases, buildings judged to be completely destroyed were repaired, while in

other cases buildings judged to be partially destroyed were reconstructed. Therefore, the cost of the damage is not necessarily consistent with the restoration cost.

Housing restoration is an important component that supports livelihoods, and thus greatly influences the recovery and reconstruction of a disaster area. To plan rapid post-disaster recovery and reconstruction, it is important to understand the housing restoration costs in the entire disaster area and to implement measures on how these costs should be procured.

Among previous research on restoration costs for rebuilding housing in disaster areas, Okada (2012) [1] stated that the funds provided through systems of support for reconstructing the livelihoods of disaster victims are insufficient compared to the costs of newly constructing or repairing housing. Okada (2012) conducted an earthquake damage estimation in the city of Sapporo and showed that, if the Sapporo City Government were to cover the shortfall in the amount of money required for housing reconstruction, a considerable reserve fund far exceeding the finances of the local government would be required. In addition, Inui (2012) [2] compiled housing damage and rebuilding support in Ibaraki Prefecture after the Great East Japan Earthquake. The ratio of the support funds relative to the housing restoration costs was less than 20% for 41.2% of households, showing that the benefits under the current system are extremely

inadequate for rebuilding homes. This study suggested that the support funds provided by the various financial support measures are inadequate relative to the necessary restoration costs. However, the targets of this study were the city of Sapporo and one area of Ibaraki Prefecture, as well as that the numbers of households that suffered damage were not high. More households will suffer damage as a consequence of the predicted earthquake directly beneath the Tokyo Metropolis because it is a densely populated area. Accordingly, the necessary restoration costs and financial support systems are expected to be different.

Regarding previous research on restoration costs and measures, Okada et al. (2016) [3] and Nakashima et al. (2018) [4] identified as an issue the fact that the current framework of housing reconstruction support is uniform throughout the country. By performing damage estimations taking account of regional differences in home rebuilding costs and annual incomes, they showed quantitatively that the difficulty of reconstruction and the economic burden on households differ greatly across regions. They stated that a system of economic assistance that considers regional inequalities will reduce household debt after an earthquake disaster and improve the speed and quality of reconstruction. Nagamatsu et al. (2003) [5] presented the problem that all of the housing restoration costs cannot be procured under existing ex-post compensation systems. They proposed linking ex-ante damage mitigation measures and ex-post compensation systems and suggested that reducing housing restoration costs will lead to improved support. These findings are useful as examinations of financial support systems relative to necessary restoration costs. However, in an urban structure such as that of Tokyo, where there are many apartment buildings, existing financial support systems may not be sufficiently effective. Future measures must be implemented after clarifying trends in restoration costs by housing category (apartment, detached house, among others) and damage category.

In Tokyo, seismic retrofitting plans have been drawn up as efforts towards earthquake disaster prevention/mitigation [5]. As of 2003, the earthquake proofing rate was approximately 75%, while as of 2018 this had increased to approximately 80% [3]. However, the question of how to cover the cost, which ranges between several hundred thousand and several million Japanese yen per house, is a major issue. Considering the life of a housing unit of between 30 and 50 years, it is not inevitable that a large earthquake will occur during that time. Therefore, earthquake proofing is not likely to be profitable for many households. Earthquake proofing that is left to the autonomy of households may not progress. In contrast, the US National Flood Insurance Program (NFIP) can be cited as an example of promotion of aggressive ex-ante measures. A

characteristic of this program is that it integrates aid for the victims of flood damage and mitigation of flood damage. In addition, by taking ex-ante measures, it reduces destabilization of insurance when a major disaster happens (large insurance payouts leading to destabilization/collapse of the insurance system). Promoting ex-ante measures also makes it possible to reduce compensation amounts and allows a portion of the surplus funds that arise in the ex-post compensation to be invested in ex-ante measures. To implement this type of system linking ex-ante measures and ex-post measures, it is necessary to understand quantitatively the effects of the ex-ante measures. In particular, a quantitative evaluation of the extent to which promoting earthquake proofing will reduce restoration costs and support funds or stabilize support systems is desired.

To address this issue, this study conducts a stochastic seismic analysis of the Tokyo Metropolis and estimates expected values and Value at Risk (VaR) for the necessary restoration costs after a disaster. Trends in necessary restoration costs and various financial support funds are clarified for each category of damage (from partial destruction to complete destruction) according to the housing category (apartment, detached house, among others). By showing the Average Annual Loss (AAL) and VaR, respectively, this study clarifies the costs required routinely and the costs needed when a major earthquake occurs. This study also shows quantitatively the extent to which these costs and support funds can be reduced by the ex-ante measure of making buildings earthquake proof.

METHODS: DISASTER RISK MANAGEMENT

With the aim of integrating ex-ante measures and ex-post compensation, this study evaluates the extent to which ex-post compensation can be reduced when the ex-ante measure has been taken. Assuming that housing units are made earthquake proof to a performance equivalent to the standard since 1981, the analysis is performed with the earthquake proofing rate at the current level (apartments 82%, detached houses 71%), 85%, and 95%. AAL and VaR are compared for the necessary restoration costs and various financial support systems at each earthquake proofing rate. The funds required per year can be understood from AAL, and the funds required after a small to medium earthquake and a major earthquake can be understood from VaR. The surplus funds that can be used for ex-ante measures are determined from the extent to which each fund has been reduced compared to the current situation. The following equation is used as an indicator of stabilization of the financial support system.

$$\text{ROR} = \frac{\text{AAL}}{\text{Risk Amount}} = \frac{\text{AAL}}{99\% \text{VaR} - \text{AAL}} \quad (1)$$

Here, ROR represents “return on risk,” and it is an indicator showing the extent to which an annual reserve fund has been maintained relative to the risk amount. The risk amount shows the amount in excess of the annual reserve fund. A higher ROR indicates a more stable system.

METHODS: EVALUATION METHOD FOR RECOVERY COST ANALYSIS

To understand the restoration costs required in the entire disaster area and to examine the effects of various financial support systems for procuring restoration costs, individual building and households are modeled and a damage simulation is performed. By accumulating the restoration costs of each household and various financial support funds, trends in restoration costs and various financial support funds are evaluated quantitatively for each category of damage (from partial destruction to complete destruction) and each housing category (apartment, detached house, among others).

The damage simulation used in this study is divided into the following evaluation processes: exposure model evaluation, seismic hazard evaluation, damage function evaluation, and building asset evaluation. The results of the estimation of restoration costs in the entire disaster area are uncertain because there are evaluation errors in each process. However, this study verified the method with property damage caused by the Kumamoto earthquakes [6] and confirmed that the model's predicted values and the actual damage values show good correspondence. The Kumamoto earthquakes differ from the earthquake directly beneath Tokyo that is considered in this study, and the target regions also differ. However, the accuracy is considered sufficient for examining future measures. The following paragraphs describe each of the evaluation methods in the damage simulation.

Exposure Model Evaluation

An exposure model is created taking the Tokyo Metropolis as the target evaluation area [6]. Here, the exposure model shows households and buildings exposed to the seismic hazard. First, using census mesh data, data on the number of households by housing type and structure are created in 500-m mesh units. Next, the data on the number of households are divided proportionally based on Japan's Housing and Land Survey data on the number of housing units by housing type and construction period according to prefecture or municipal district, in order to create data on the number of households by housing type, structure, and age in 500-m mesh units.

Fig. 1 show the distributions of households by housing type that were created. Apartments are concentrated in the eastern part of Tokyo, while

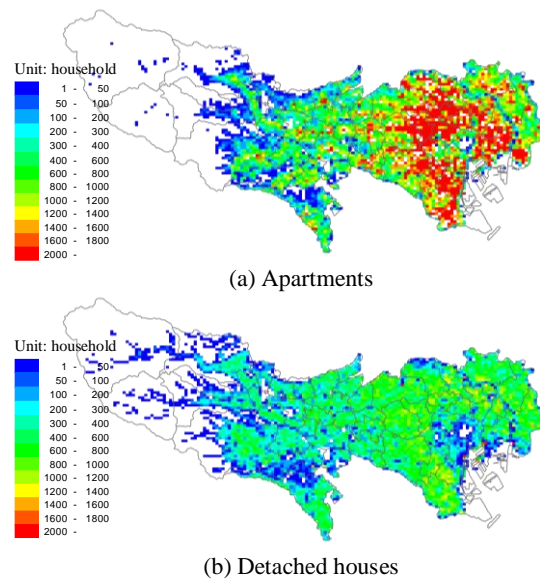


Fig. 1 Distribution of Households

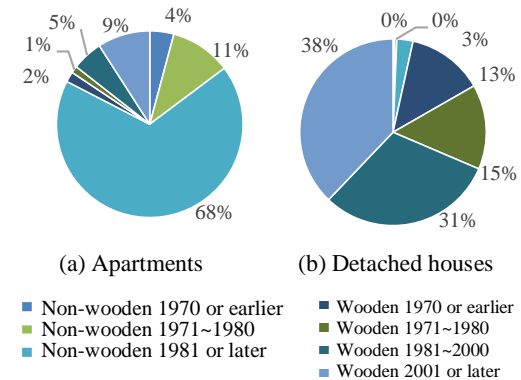


Fig. 2 Proportion of households by building age, and construction material

detached houses are distributed evenly across Tokyo. Next, Fig. 2 shows the proportions of households by structure and construction period according to housing type that were created. Sixty-eight percent of the apartments are non-wooden structures built from 1981 onwards, while 69% of the detached houses are wooden structures built between 1981–2000 and from 2001 onwards. Apartments are typified by non-wooden structures and detached houses by wooden structures, and, in both cases, many households reside in buildings with strengths equivalent to new earthquake proofing standards.

Seismic Hazard Evaluation

The Source model was based on published data from the HARP 2014 [7]. In this study, only inland earthquakes are included in the map. The earthquake prediction equation is adopted from Morikawa and Fujiwara (2013) [8]. The shallow and deep geotechnical structures are based on the data available

in J-SHIS [9]). The distribution of seismic intensity by return period is shown in Fig. 3.

Damage Function Evaluation for Housing Restoration

Since this study aims to estimate building restoration costs rather than the economic damage to buildings, the necessary housing restoration costs are calculated using the damage function proposed by the authors [10]. This damage function is defined as seismic intensity on the horizontal axis and necessary restoration cost ratio (ratio of restoration cost to replacement cost) on the vertical axis. Fig. 4 shows the damage function used in the analysis. This damage function is categorized into apartments and detached houses, and into wooden and non-wooden structures. The construction period is divided into 1970 or earlier, 1971–1980, and 1981 or later. Wooden structures built in 1981 or later are further divided into 1981–2001 and 2002 or later.

Building Asset Evaluation

To calculate the cost of restoration, building assets are set using new values rather than market values. The building assets of each household are calculated following Japan's National Tax Agency's "Reasonable Method of Calculating Losses" [11] by multiplying the construction cost per floor area according to structure by the total area of exclusive space per household [12]. However, apartment building assets include both common and exclusive space. Since there is no data available on the total area of common space per household, this is calculated based on the proportion of assets in exclusive and common spaces. Generally, fire insurance for condominium management associations takes the assessed value of common spaces as between 40% and 60% of the building's total assessed value. In this study, the standard that uses the inner (painted) surface of walls, ceilings, and similar construction elements to determine boundaries between exclusive and common spaces is adopted, and asset value is estimated taking exclusive space as 40% and common space as 60%. On this basis, the total area of common space per household is calculated by multiplying the ratio of assets in exclusive and common spaces by the area of exclusive space. Table 1 shows the value of building assets for each household, and Table 2 shows the total value of building assets in Tokyo. The table reveals that the apartments account for the majority of building assets in Tokyo.

Evaluation of the financial support system for housing rehabilitation

Housing Reconstruction Assistance Program

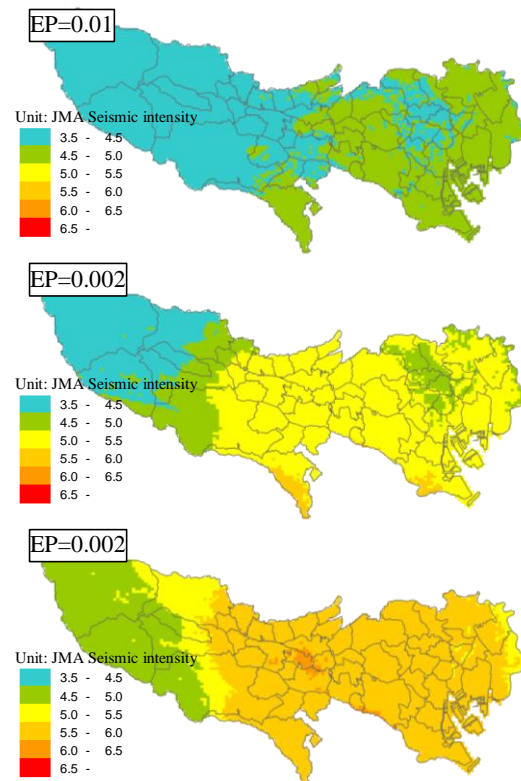


Fig. 3 Distribution of Seismic intensity by EP

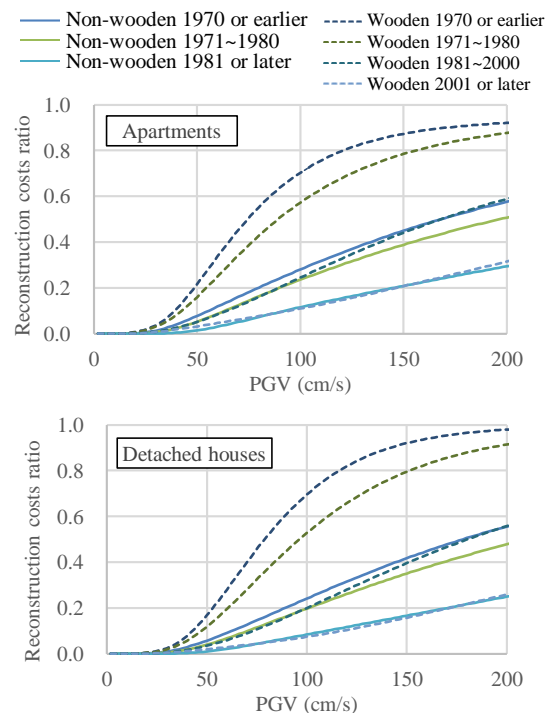


Fig. 4 Damage function of restoration cost

Housing reconstruction support programs provide funds to those whose livelihoods have been severely damaged by a natural disaster to help them rebuild their lives. They use funds contributed by the national

Table 1 Building assets per household

Category		Construction area	Construction cost	Building assets
Apartments	Non-wooden	51+77m ²	220K JPY / m ²	28,050K JPY
	Wooden	39+59m ²	174K JPY / m ²	16,965K JPY
Detached houses	Non-wooden	126m ²	220K JPY / m ²	27,720K JPY
	Wooden	107m ²	174K JPY / m ²	18,618K JPY

Table 2 Building assets in Tokyo

Category		Non-Wooden	Wooden	Total
Apartments	Pre 1980	100,727,746	12,855,517	113,583,264
	Post 1981	100,727,746	12,855,517	113,583,264
Detached houses	Pre 1980	1,837,420	34,418,929	36,256,349
	Post 1981	1,837,420	34,418,929	36,256,349
Total		102,565,167	47,274,446	149,839,613

Table 3 Settings disaster victims' life reconstruction funds

Damage State	Reconstruction	Base support	Additional support	Total
Completely destroyed	Rebuilding	1,000	2,000	3,000
	Rehabilitation	1,000	1,000	2,000
Largely destroyed	Rebuilding	1,000	2,000	3,000
	Rehabilitation	500	1,000	1,500
Half destroyed	Rebuilding	1,000	2,000	3,000

Table 4 Settings earthquake insurance

Damage State	Insurance amount	Payment rate	Total
Completely destroyed	50% of building assets	100%	50%
Largely destroyed		60%	30%
Half destroyed		30%	15%
Partial destroyed		5%	2.5%

and prefectural governments from the perspective of mutual aid. The funds set in this study are shown in Table 3.

Earthquake insurance system

Earthquake insurance is a type of non-life insurance that compensates for losses caused by disasters, such as earthquakes, volcanic eruptions, and tsunamis. It is operated jointly by the government and private non-life insurance companies. Earthquake insurance is purchased together with fire insurance, and the insurance amount is specified as between 30% and 50% of the amount of fire insurance. In 2014, some changes were made to the system, and partial destruction was divided into the two categories of small-scale partial destruction and large-scale partial destruction. The earthquake insurance money set in this study is shown in Table 4. Next, the earthquake insurance take-up rate for each household is set. Here, the take-up rate is the proportion of all households that have earthquake insurance. The earthquake

insurance take-up rate for detached houses and exclusive space in apartments is set at 36.7% [13]. Since no data is available for the earthquake insurance take-up rate for common space in apartments, this is set using the attachment rate shown in [14]. Here, the attachment rate represents the percentage of households with earthquake insurance attached to their fire insurance contracted during the relevant financial year. By multiplying the ratio of the attachment rate for exclusive space (71.9%) to the attachment rate for common space (38.1%) in 2015 by the earthquake insurance take-up rate for exclusive space, the earthquake insurance take-up rate for common space is set at 18.2%.

RESULTS AND DISCUSSION

Analysis of the Subject of Evaluation

First, the left-hand side of Fig. 5 shows the necessary restoration costs for each earthquake proofing rate and each return period. The respective

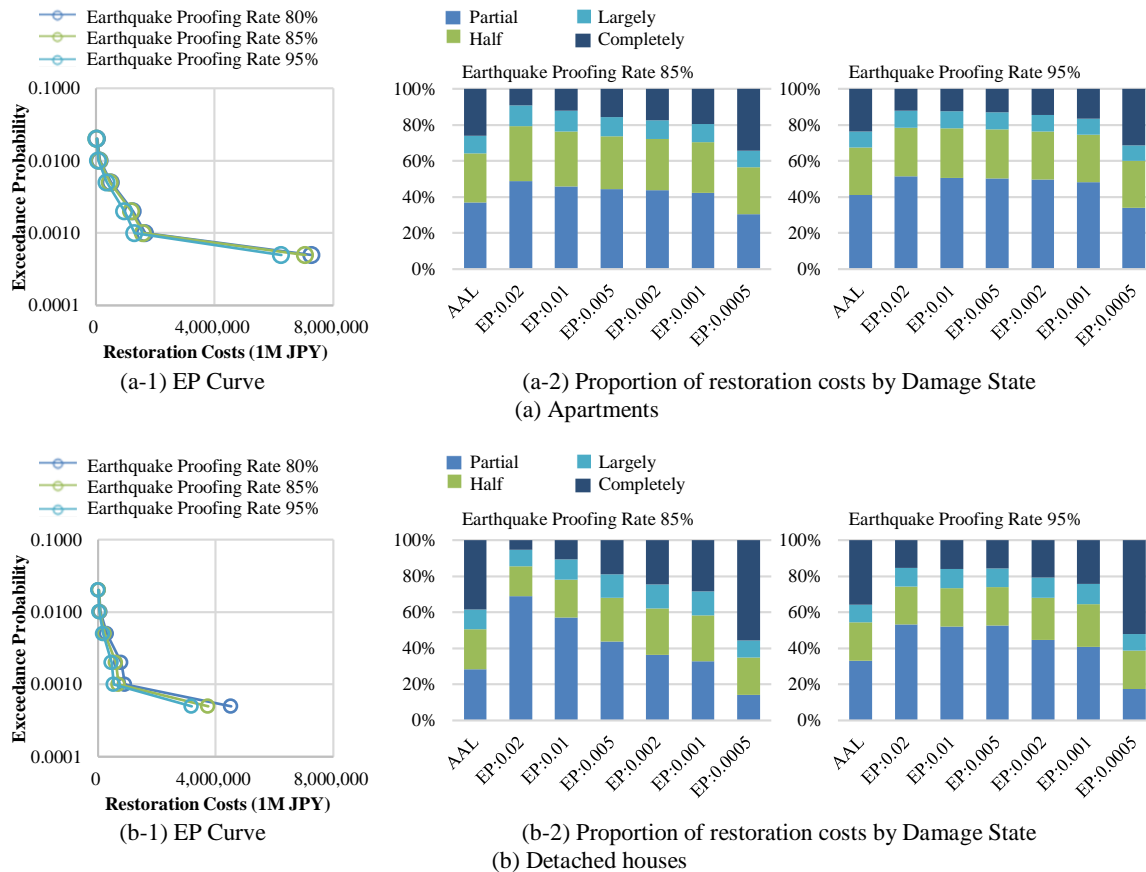


Fig. 5 Necessary restoration costs

graphs show the results for apartments and detached houses. The figure reveals that the necessary restoration costs were reduced at all return periods as a result of promoting earthquake proofing. By promoting the earthquake proofing rate from 80% to 95%, the necessary restoration costs for apartments at a return period of 2,000 years were reduced by approximately 1,019,997 million Japanese yen (from 7,273,176 million to 6,253,180 million Japanese yen). For detached houses, the costs were reduced by approximately 1,350,551 million Japanese yen (from 4,532,159 million to 3,181,608 million Japanese yen). The current earthquake proofing rate for detached houses is low, and therefore there was a large reduction in the necessary restoration costs when earthquake proofing was promoted. Next, the center and right-hand side of Fig. 5 show breakdowns of the extent of damage by return period. The figure reveals that the restoration costs differ for each return period and each damage extent. The shorter the return period, the greater the percentage of partial destruction and the smaller the percentage of total loss. The fact that the damaged households requiring restoration funds differ greatly with each return period suggests that the form of the financial support system will also differ depending on the focused return period.

Effectiveness of earthquake-resistance for

necessary restoration costs: the financial support system

In the next section, we evaluate the extent to which the ex-post compensation could be reduced by proceeding with the ex-ante measures. Table 5 shows the results of AAL, 99% VaR, and ROR of various financial support programs, as well as the cost of recovery from the earthquake disaster. It can be seen that the amount of financial assistance provided by the disaster relief and reconstruction assistance and earthquake insurance both decreased as a result of seismic retrofitting. AAL decreases by about 19-24% for both multifamily and single-family dwellings when seismic retrofitting is increased from 85% to 95%. 99% VaR decreases by about 29-36% for multifamily dwellings and 21-27% for single-family dwellings. The impact of seismic retrofitting is greater for VaR than for AAL than for the reduction in aid contributed in the event of a disaster. The effect of seismic retrofitting is to reduce the amount of aid paid out in the event of severe damage. In particular, the Livelihood Reconstruction Assistance Program will reduce the amount of aid paid out in comparison to the earthquake insurance program. The Life Reconstruction Assistance Program for disaster victims includes payments to households that are at least half destroyed, so the number of households

Table 5 AAL, 99% VaR, ROR by Earthquake Proofing rate

Unit: 1M JPY						
	Category	Earthquake Proofing rate	AAL	99% VaR	Risk Value	ROR
Apartments	Necessary restoration costs	82%	13,235	136,214	122,979	10.76%
		85%	12,686	127,117	114,432	11.09%
		95%	10,638	90,676	80,037	13.29%
	Support money from victims' life reconstruction costs	82%	831	6,741	5,910	14.06%
		85%	784	6,157	5,373	14.60%
		95%	605	3,944	3,339	18.12%
	Support money from earthquake insurance	82%	1,293	12,279	10,987	11.77%
		85%	1,234	11,412	10,178	12.12%
		95%	1,015	8,076	7,060	14.38%
Unit: 1M JPY						
	Category	Earthquake Proofing rate	AAL	99% VaR	Risk Value	ROR
Detachedhouses	Necessary restoration costs	71%	8,044	90,979	82,935	9.70%
		85%	6,360	68,014	61,654	10.32%
		95%	5,129	53,970	48,841	10.50%
	Support money from victims' life reconstruction costs	71%	656	3,359	2,703	24.26%
		85%	512	2,486	1,974	25.92%
		95%	389	1,814	1,425	27.29%
	Support money from earthquake insurance	71%	1,476	16,695	15,219	9.70%
		85%	1,167	12,481	11,313	10.32%
		95%	941	9,903	8,962	10.50%

whose houses are at least half destroyed is expected to decrease as a result of seismic retrofitting.

Next, promoting earthquake proofing from 85% to 95% increases ROR by between approximately 19% and 24% for apartments and between approximately 2% and 5% for detached houses. ROR is an indicator showing the extent to which an annual reserve fund has been maintained relative to the risk amount, and a higher ROR indicates a more stable support system. In this discussion, earthquake proofing results in a large decrease in 99% VaR. This means that the expenditure after a major disaster is stable relative to the reserve fund. The ROR shows that the system of support for reconstructing the livelihoods of disaster victims and the earthquake insurance system became more sustainable.

CONCLUSIONS

With the aim of integrating ex-ante measures and ex-post compensation, this study evaluated the extent to which restoration costs and financial support system funds can be reduced when the ex-ante measure of earthquake proofing has been taken. The study revealed that restoration costs and financial support system funds can be reduced by promoting earthquake proofing. The fund reducing effect was particularly noticeable for major earthquakes, such as 99% VaR, and was shown to contribute significantly to improving ROR. The results of this research will

be used to in developing a social system for disaster prevention that combines disaster prevention measures such as seismic retrofitting, systems of support for rebuilding the lives of disaster victims, and financial support measures such as earthquake insurance.

REFERENCES

- [1] Shigeyuki Okada, Estimation of earthquake risk financing of local governments necessary for reconstruction of victims' lives, Summary of Architectural Institute of Japan, 2012
- [2] Yasuyo Inui, The Feature of Housing Damage and the Supporting Subject of Housing Rebuilding in Ibaraki pref. after the Great Eastern Japan Earthquake, Journal of the City Planning Institute of Japan, 2012
- [3] Shigeyuki Okada, Tadayoshi Nakashima, Regional Disparities of Self-Payment Cost for Seismic Destroyed House Restoration, The Seismological Society of Japan, 2106, Fall Meeting
- [4] Tadayoshi Nakashima, Shigeyuki Okada, Financial Imbalances in Regional Disaster Recovery Following Earthquakes - Case Study Concerning Housing- Cost Expenditures in Japan, Sustainability, 10(9), 3225, 1-23
- [5] Tokyo earthquake-resilient Portal website

- <https://www.taishin.metro.tokyo.jp/tokyo/topic01.html>
- [6] Norikazu SAKABA, Harumi YASHIRO et al., Verification of earthquake damage estimation method of local government for 2016 Kumamoto earthquake
 - [7] Headquarters for Earthquake Research Promotion, National Seismic Hazard Maps 2014
 - [8] Morikawa and Fujiwara, A new ground motion prediction equation for Japan applicable up to M9 mega-earthquake, Journal of Disaster Research, 2013
 - [9] National Research Institute for Earth Science and Disaster Resilience, J-SHIS Earthquake Hazard Station (2020.1.10)
<http://www.j-shis.bosai.go.jp/>
 - [10] Norikazu SAKABA, Harumi YASHIRO, Economic Damage Analysis on Housing Reconstruction by The Tokyo Near-Field Earthquake, The Ninth Japan Conference on Structural Safety and Reliability, 2019
 - [11] National Tax Agency "Reasonable calculation method of loss amount" in miscellaneous loss deduction (2020.1.10)
<https://www.nta.go.jp/about/organization/tokyo/topics/sonshitsu/index.htm>
 - [12] Statistics Bureau, Ministry of Internal Affairs and Communications, Housing and Land Statistics Survey, 2018
 - [13] Non-Life Insurance Rating Organization of Japan, Changes in the participation rate of earthquake insurance by prefecture, 2018
http://www.sonpo.or.jp/news/statistics/syumoku/pdf/kanyu_jishin.pdf
 - [14] Non-Life Insurance Rating Organization of Japan, Changes in the participation rate of earthquake insurance by prefecture, 2018

INVESTIGATION OF THE INFLUENCE OF RECYCLED RUBBER PARTICLES ON CEMENT PASTE PROPERTIES

Mohamed Atef¹, Nahed A. Azab¹, Mohamed Hazem Abdellatif¹ and Ghada Bassioni^{2*}

¹Mechanical Engineering Department, Faculty of Engineering, Ain Shams University, Egypt, ² Chemistry Division, Faculty of Engineering, Ain Shams University

ABSTRACT

Egypt is one of the most consuming markets for tires all over the world. There is an urgent need to get rid of them by an economic and environmental way since it is considered as a harmful waste if burnt. The worldwide trend is directed towards development of new techniques to transform the rubber into useful products to maximize the benefit of recycling. This research deals with development of novel techniques for rubber powder recycling for various purposes in robust construction. Recycled rubber particles (RRP) treated by two different types of chemical treatment and mixed with cement pastes (CP) using different water to binder ratio (w/b) with water to cement ratio (w/c) kept constant at 0.3. The Fourier transform – infrared (FT-IR) spectra measured for untreated and treated rubberized cement pastes. The compressive strength investigated for the treated and untreated samples for 1, 3, 7, 14 and 28 days. The results aimed to enhance the compressive strength of rubberized cement pastes through improving the bonding strength between RRP and CP. Maintaining the compressive strength in the highest levels with different RRP percentages in addition to vibrational damping property of RRP give rubberized cement pastes the advantage to replace ordinary concrete in most of construction applications.

Keywords: rubber particles, Waste management, cement paste, mechanical Properties

INTRODUCTION

At the end of the 20th century, sustainable development and environmental protection became key goals of modern society. Civil engineering, especially the construction materials industry, has an important role in the sustainable development of buildings, in the reduction of pollution, and in conservation of natural resources and energy savings. In this context, the main problems that industry of construction materials faces are mainly related to high consumption of Portland cement and the associated high emission of carbon dioxide. With reference to the first point, concrete has been for decades the most used construction material in the world, and the global production of concrete has reached a value of more than 1 ton of concrete per person on the planet. Overall, cement companies are producing nearly 3 billion tons/year [1]. This led to the emission of almost 2 billion tons of CO₂ (6-7% of global CO₂ emissions) in the process [2, 3]. In order to reduce the greenhouse effect of cement production, several studies have identified the improvement of process efficiency and the increase in the use of various waste materials as a cement replacement.

According to a recent report, tire marketplace in Egypt is anticipated to cross USD 1 billion through 2020. Egypt automotive marketplace is one of the conspicuous markets in African mainland because of its huge market size and its geological area which is spanned to Asia. In 2013, Egypt was the third biggest vehicle creating market in Africa, after South Africa

and Morocco[4]. The possible increase by 2030 in the Egyptian tires market for different kinds of vehicles is illustrated in Figure 1. Egypt produces 20 million waste tires/ year and barely 10% of those are recycled [5].

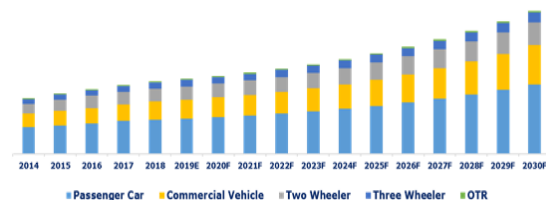


Figure 1 Egypt Tire Market Size, By vehicle type, By Volume [5]

Utilization and disposal of used tires represent an enormous challenge to industrialized countries worldwide because of their three dimensional-crosslinked structure which renders them nonbiodegradable, raising serious disposal concerns [6, 7]. The most obvious hazard associated with the uncontrolled disposal and accumulation of a large number of tires is the potential for large fires which are extremely detrimental to the environment. The environmental issues from the global disposal of these tires have led to increasing interest in economic recycling of tire rubber [8-10]. The rubber in tires is vulcanized and cannot be melted or dissolved, which makes recycling challenging [11, 12]. As a result, a

large number of used, worn out tires are ground for the benefits of expanding their applications [13, 14]. The application related to the ground or powdered tire rubber includes outdoor flooring and pavements, sports tracks, road construction, etc., which fall into the sectors with limited demanding and added value. Various construction industries have used rubber elements as a fundamental part of structure. This material has been used in the construction of concert halls as an acoustic absorber, in the construction of bridges (buffer), among others as waterproofing and filling in roads [15]. Research to date on the so-called Rubcrete has provided contradictory findings. There are some properties that are enhanced in Rubcrete compared with conventional concrete, including damping ratio, ductility, energy dissipation, impact resistance and toughness [16-18]. Conversely, the key mechanical properties of compressive strength, modulus of elasticity, and tensile strength are reduced [19, 20]. While there are many ways of recycling tires, in the structural materials area, a significant amount of research has recently focused on using crumb rubber from recycled tires as partial replacement of coarse aggregates. It is determined that a waste material like worn out tires may enhance the basic properties of concrete. The data presented in this research showed that there is great potential for the utilization of tires as aggregates. It was considered that used tires would provide much greater opportunities for value adding and cost recovery, as it could be used as a replacement for more expensive material such as rock aggregates. Rubber had great capability of becoming a permanent member of the concrete family because of its wide variety of decent properties like better flexibility, light weight and easy availability. Using rubber aggregates decreased the workability of the resultant mix, but this problem can be dealt with the use of the certain plasticizers [21]. The effect of partial replacement of coarse aggregates in concrete is studied by untreated tire rubber aggregates. It was observed that the specific gravity and bulk density of rubber aggregates are less as compared to natural coarse aggregates. The concrete density decreases when utilization of rubber aggregates in concrete increased. Due to this the lightweight concrete was acquired which assists to decrease the weight of structure. Using rubber aggregates in concrete resulted in decreasing the compressive strength but increasing toughness of concrete. It was found that optimum percentage of replacement of rubber aggregates can be up to 15%. It was observed that such type of concrete cannot be used in structural elements where high strength is required [22]. When the properties of concrete are evaluated with crumb rubber replacing fine aggregates, the results showed that up to 15 % of fine aggregates can be replaced with an equal volume of crumb rubber with a slight improvement of the concrete workability. The crumb rubber improved the

compressive strength by over 5 %. The splitting tensile strength decreased with an increase in the quantity of crumb rubber, and the modulus of rupture was decreased by an average of 12 %. However, increased strain at failure, good energy absorption, improved modulus of toughness, and ductility were observed in rubberized concrete [23]. It is studied that the partial effect of particle size of crumb tire as a fine aggregate replacement on compressive strength and time dependent deformations of structural concrete. Based on the compressive and preliminary time-dependent results, rubberized concrete had lower compressive strength than the control concrete mix for all crumb rubber sizes. Crumb rubber size has an effect on the strength of concrete, as the crumb rubber became smaller compressive strength decreased [24]. As mentioned before most of researches used rubber particles in form of fine or coarse aggregates. In some cases it was used as an additive in concrete application but was limited to be used as replacement of cement percentage in a mix design. The novelty of this work is studying the effect of using fine rubber particles as partial replacement of cement on compressive strength of different hardened cement pastes at different water to binder ratio (W/B ratio = 0.3 and 0.4). This was coupled by an extensive ESEM micrographic study

EXPERIMENTAL WORK

MATERIALS AND ITS CHARACTERIZATIONS

The materials used in sample preparation were: (i) Ordinary Portland Cement (OPC) (Type 42.5N) was provided by Torah Co., Helwan, Egypt and (ii) the untreated recycled rubber particles (RRP) which was delivered from Egypt local market and extracted from car tires by grinding then sieving. The chemical composition of OPC was determined by elemental analysis using wavelength dispersive X-Ray Spectrometry (standard less) as shown in Table 1. Particle Size Distribution tests (PSD) for both OPC and RRP were performed by laser diffraction technique using volume-based results of Malvern Mastersizer 2000 (Dry method). As shown in Figure 3, the volume weighted Mean of the OPC and RRP are 55.9 and 944.5 μm respectively.

FTIR test was performed for RRP by PerkinElmer instruments spectrum one. As Figure 2 indicates, the various transmittance peaks observed in the spectrum are related to specific functional groups; stretching vibration band of C-H bond at 2820 – 2970 cm^{-1} and C = C at 1540 – 1690 cm^{-1} . Also, at 960- 1190 cm^{-1} , the peak is assigned to C-S bond resulted from presence of Sulfur which is used in the vulcanization process of rubber.

Table 1 Chemical composition of Ordinary Portland Cement (OPC)

Constituents	SiO ₂	TiO ₂	Al ₂ O ₃	Fe ₂ O ₃ ^{tot.}	MgO	CaO	Na ₂ O	K ₂ O	P ₂ O ₅	MnO	Cl	LOI
Constituents (wt %)	13.4	0.46	2.95	4.08	1.57	64.2	0.574	0.275	0.191	0.075	0.202	5.01

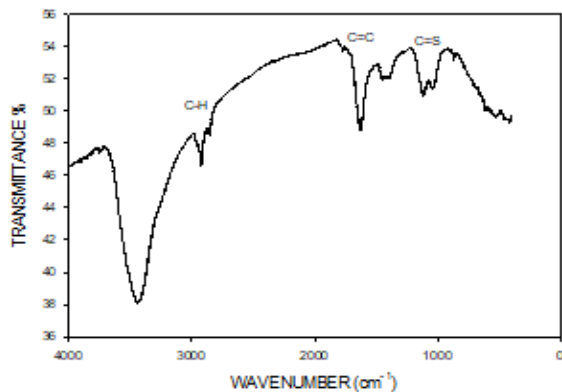
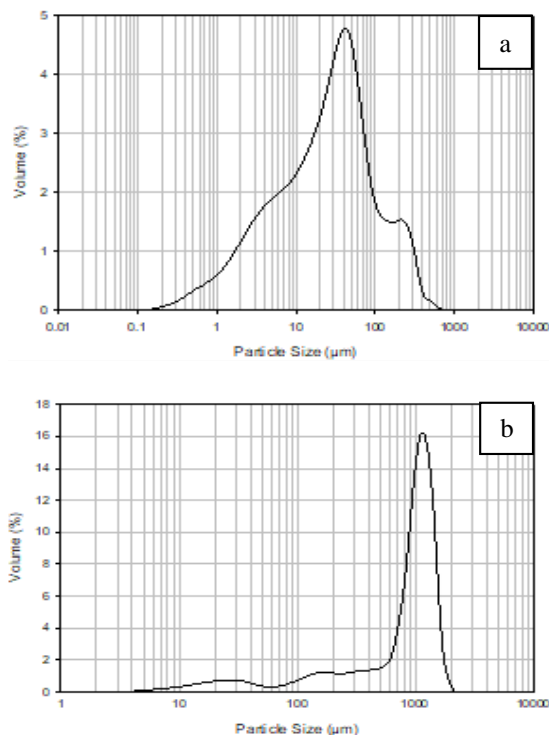


Figure 2 FTIR spectra for RRP

Figure 3 Particle size distribution (PSD) for a) OPC
b) RRP

Methods of investigation

Dry mixing

Firstly, OPC and RRP at different weight ratios (100/0, 95/5, 85/15, and 75/25 OPC/RRP) were carefully dry blended using a mechanical stirring for 30 min, to assure complete homogeneity,

Preparation of cement paste

The different cement pastes were made by mixing the rubberized cement with tap water. The water consistency of each paste should be in a reasonable

level to get the optimum properties. Each paste was stirred continuously for three minutes by electric mixer and assuring the homogeneity of the mixture by visual inspection. The dosage of recycled rubber particles (RRP) were 0 %, 5%, 15%, 25% by the weight of cement.

The resulting mixes were designated as shown in Table 2. The control samples are C-0.3 and C-0.4 for the cement pastes free from the RRP mixed at different w/b ratio 0.3 and 0.4 respectively. The rubberized cement mixtures are defined as “R5-0.3, R15-0.3 and R25-0.3” for the cement pastes containing 5, 15 and 25% by weight of cement and w/b = 0.3 and also in the same way for w/b = 0.4.

Table 2 Mix design of the prepared rubberized cement mixtures

Sample	w/b ratio	OPC Wt. (gm)	RRP Wt. (gm)	Water Wt. (gm)
C-0.3	0.3	3250	0	975
R5-0.3	0.3	3087.5	162.5	975
R15-0.3	0.3	2762.5	487.5	975
R25-0.3	0.3	2437.5	812.5	975
C-0.4	0.4	3250	0	1300
R5-0.4	0.4	3087.5	162.5	1300
R25-0.4	0.4	2437.5	812.5	1300

Molding

The pastes were molded immediately after the mixing was finished in 2” inch or 50 mm cubic steel mold according to ASTM Designation: C-109/C 109M-07 [25]. Each cube was filled gradually then compacted using a mechanically vibrating machine for two minutes to remove any air bubbles in order to achieve better impaction of the paste.

Curing

According to BS EN 4551-1 [26] immediately after molding, the mold was cured in a humid chamber during the first 24 hours at room temperature and then demolded. The demolded cubes were immersed in a container filled with tap water for the required curing periods of 1, 3, 7, 14 and 28 days.

Mechanical properties

Compressive strength measurements were carried out on the hardened cement paste using 30 Ton compressive machine manufactured by Lloyd Instruments Ltd, United Kingdom.

Three cubes were tested for compressive strength measurements at the various ages of hydration 1, 3, 7,

14 and 28 days and for different w/b ratio at 0.3 and 0.4.

Stopping of hydration

The stopping of hydration of all the pastes was performed on the crushed paste cubes after the compressive strength determination.

This process was performed by rinsing about 20 grams of the grounded cement pastes from the core of the specimen with about 150 ml of a mixture of acetone and methanol (1:1 by volume) using a magnetic stirrer for at least one hour. The solvent mixture was then removed by decantation and filtration. Finally, the sample was dried at 80°C in the drier overnight to remove the moisture.

ESEM Study

The morphology and microstructure of hardened cement pastes (0% and 25% RRP by weight of cement) prepared by two different w/b ratios (0.3 and 0.4) at 28 days curing time were investigated using environmental scanning electron microscopy (ESEM). Surface images were recorded using Quanta FEG 250 scanning electron microscope (FEI Company, USA) available at EDRC, DRC, Cairo. Samples were mounted onto SEM stubs. Applied SEM conditions were a 10.1 mm working distance, with in-lens detector with an excitation voltage of 20 kV.

RESULTS AND DISCUSSION

Compressive behavior of Untreated Rubberized Cement Paste

The hydration process after one day is characterized by two stages as shown in Figure 4. The first stage has a sharp increase in the strength due to the presence of pores which can accumulate the formed hydration products. This stage followed by a slight increase in the strength due to the limited pores available for new hydration precipitates.

Generally, it is observed that the compressive strength increases with increasing curing time as shown in Figure 4&Figure 5 and Table 3. This is mainly due to the increase in the amount of tobermorite like gel (calcium silicate hydrates “CSH”) and calcium aluminate hydrate (CAH) which accumulated in the open pores leading to a decrease in the porosity of the pastes [27, 28].

Also, it is indicated that the rate of hydration of the Rubberized cement pastes is lower than the control sample. This is attributed to dilution of cement by RRP which resulted in decreasing the amount of CSH responsible for gaining strength. As graphically represented in Figure 5, increasing the w/b ratio from 0.3 to 0.4 leads to decreasing compressive strength by 46.9% and 36.2% in case of control and 25% of RRP replacement, respectively. This can be explained by the fact that when the w/b

ratio increases, the initial porosity increases and then the compressive strength decreases.

Interestingly, in case of R25-0.3 and R25-0.4 the specimen gains about 83% of its full strength at the first stage of hydration up to 7 days rather than gaining only about 17% at the later stage. This means that most of unreacted cement is already hydrated in the first stage due to further dilution as illustrated above.

The strength results seem to be dependent on the nature and the physical state of the hydration products formed within the pore system of the hardened cement pastes; this achievement will receive further support from the results of the microstructure of the formed hydrates as will be discussed later in this investigation.

Table 3 Compressive strength of the control and Rubberized cement mixtures samples

Curing Days	Control		Rubberized			
	C-0.3	C-0.4	R5-0.3	R15-0.3	R25-0.3	R25-0.4
0	0.0	0.0	0.0	0.0	0.0	0.0
1	6.6	5.7	5.5	2.1	1.4	0.4
3	26.9	7.7	17.6	8.4	4.0	2.0
7	40.9	17.3	24.1	9.2	5.9	4.0
14	44.5	19.0	31.2	11.6	5.0	3.0
28	47.8	25.4	33.2	14.2	7.1	4.5

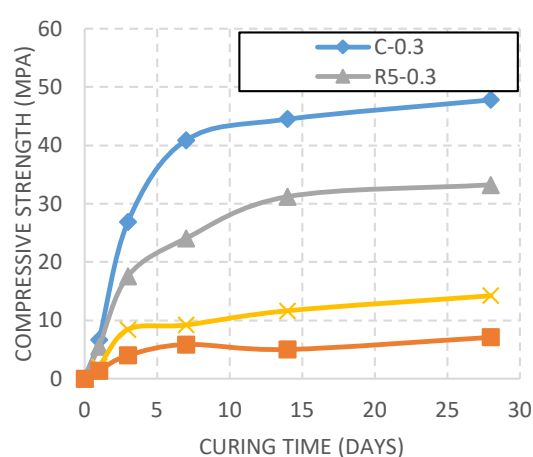


Figure 4 Compressive strength values of the hardened cement pastes containing different percentages of RRP at W/B = 0.3 versus curing times

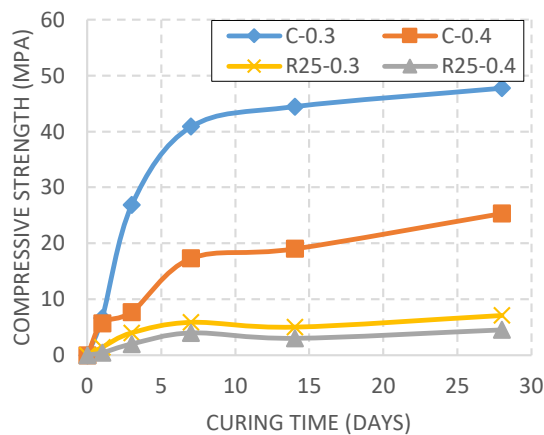


Figure 5 Effect of w/b ratio on the compressive strength of hardened cement pastes

Environmental scanning electron microscope (ESEM)

The ESEM micrographs obtained for the control and rubberized cement pastes are shown in Figure 6 (a-d) obtained after 28 days of hydration. The micrographs for the pastes displayed the formation of both microcrystalline and fibrous crystals of cement hydration products, mainly as calcium silicate hydrates (CSH), calcium hydroxide and calcium aluminate hydrate [29, 30]. These hydrates are formed around and in-between the cement grains and appears as clear binders between the partly hydrated cement grains. A denser structure of the formed hydrates could be clearly distinguished in C-0.3 than C-0.4, as a high w/b ratio leads to high porosity then lower strength.

The role of RRP as a filler appears clearly in case of R25-0.3 and R25-0.4 micrographs. The high reduction in the strength by 25 Wt. % RRP replacement resulted from decreasing the amount of hydration product and the agglomeration of RRP as illustrated in Figure 6 (b&d).

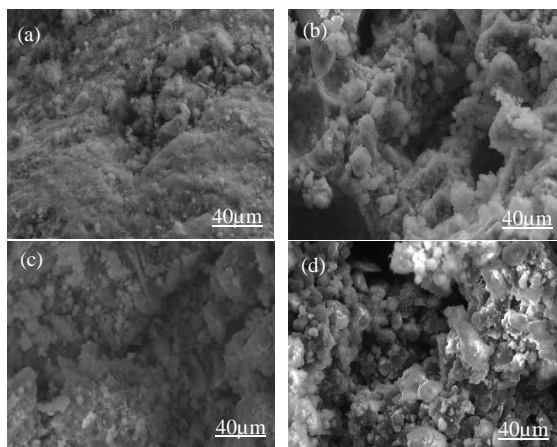


Figure 6 ESEM micrographs for hardened cement mixtures after 28 days: a) C-0.3 b) R25-0.3 c) C-0.4 d) R25-0.4

CONCLUSIONS

It is concluded from this study that the cement replacement with RRP causes deterioration in the strength. However the new rubberized cement mixture (R5-0.3) can be used in different applications instead of cement type 32.5N. As the w/b ratio decreases, the initial porosity decreases then compressive strength increases. Through utilizing non-biodegradable and recycled materials like rubber as a cement replacement a new approach is developed to produce a sustainable construction material.

REFERENCES

- [1] E. L. Bray, "US geological survey, mineral commodity summaries," ed, 2010.
- [2] G. P. Peters, G. Marland, C. Le Quéré, T. Boden, J. G. Canadell, and M. R. Raupach, "Rapid growth in CO₂ emissions after the 2008–2009 global financial crisis," *Nature climate change*, vol. 2, no. 1, pp. 2–4, 2012.
- [3] G. Bassioni, "A study towards "greener" construction," *Applied energy*, vol. 93, p. 132–137, 2012.
- [4] TECHSCI RESEARCH. (2020). *Egypt Tyre Market Forecast and Opportunities*, .
- [5] TECHSCI RESEARCH, " "Egypt Tire Market, By Vehicle Type (Passenger Car, Commercial Vehicle, OTR, Two-Wheeler & Three-Wheeler), By Demand Category (Replacement & OEM), By Radial Vs Bias, Competition, Forecast & Opportunities, 2030", " 2019.
- [6] X. Guo, D. Xiang, G. Duan, and P. Mou, "A review of mechanochemistry applications in waste management," *Waste management*, vol. 30, no. 1, pp. 4–10, 2010.
- [7] K. Reschner, "Scrap tire recycling: A summary of prevalent disposal and recycling methods," *EnTire Engineering, Berlin, Germany*, 2008.
- [8] A. Awad, R. El-gamasy, A. A. A. El-Wahab, and M. H. Abdellatif, "Mechanical behavior of PP reinforced with marble dust," *Construction and Building Materials*, vol. 228, p. 116766, 2019.
- [9] K. F. A. Elenien, A. Abdel-Wahab, R. ElGamsy, and M. H. Abdellatif, "Assessment of the properties of PP composite with addition of recycled tire rubber," *Ain Shams Engineering Journal*, vol. 9, no. 4, pp. 3271–3276, 2018.
- [10] A. Awad and M. H. Abdellatif, "Assessment of mechanical and physical properties of LDPE reinforced with marble dust," *Composites Part B: Engineering*, vol. 173, p. 106948, 2019.
- [11] R. Sonnier, E. Leroy, L. Clerc, A. Bergeret, and J. Lopez-Cuesta, "Compatibilisation of polyethylene/ground tyre rubber blends by γ irradiation," *Polymer degradation and stability*, vol. 91, no. 10, pp. 2375–2379, 2006.

- [12]M. Sienkiewicz, J. Kucinska-Lipka, H. Janik, and A. Balas, "Progress in used tyres management in the European Union: A review," *Waste management*, vol. 32, no. 10, pp. 1742-1751, 2012.
- [13]C. R. Kumar, I. Fuhrmann, and J. Karger-Kocsis, "LDPE-based thermoplastic elastomers containing ground tire rubber with and without dynamic curing," *Polymer Degradation and Stability*, vol. 76, no. 1, pp. 137-144, 2002.
- [14]Z. Wang, Y. Zhang, F. Du, and X. Wang, "Thermoplastic elastomer based on high impact polystyrene/ethylene-vinyl acetate copolymer/waste ground rubber tire powder composites compatibilized by styrene-butadiene-styrene block copolymer," *Materials Chemistry and Physics*, vol. 136, no. 2-3, pp. 1124-1129, 2012.
- [15]V. Stankevičius, G. Skripkiunas, A. Grinys, and K. Miškinis, "Acoustical Characteristics and physical-Mechanical Properties of Plaster with Rubber Waste Additives," *Material Science*, vol. 13, 01/07 2007.
- [16]R. Hassanli, O. Youssf, and J. E. Mills, "Experimental investigations of reinforced rubberized concrete structural members," *Journal of Building Engineering*, vol. 10, pp. 149-165, 2017.
- [17]O. Youssf, M. A. ElGawady, and J. E. Mills, "Experimental investigation of crumb rubber concrete columns under seismic loading," in *Structures*, 2015, vol. 3: Elsevier, pp. 13-27.
- [18]O. Youssf, M. A. ElGawady, and J. E. Mills, "Static cyclic behaviour of FRP-confined crumb rubber concrete columns," *Engineering Structures*, vol. 113, pp. 371-387, 2016.
- [19]B. S. Thomas, R. C. Gupta, and V. J. Panicker, "Experimental and modelling studies on high strength concrete containing waste tire rubber," *Sustainable Cities and Society*, vol. 19, pp. 68-73, 2015.
- [20]R. Hassanli, O. Youssf, and J. E. Mills, "Seismic performance of precast posttensioned segmental FRP-confined and unconfined crumb rubber concrete columns," *Journal of Composites for Construction*, vol. 21, no. 4, p. 04017006, 2017.
- [21]S. R. Tarry, "Effect of partial replacement of coarse aggregates in concrete by untreated and treated tyre rubber aggregates," *International Journal of Advanced Science and Research*, vol. 3, no. 1, pp. 65-69, 2018.
- [22]P. Asutkar, S. Shinde, and R. Patel, "Study on the behaviour of rubber aggregates concrete beams using analytical approach," *Engineering Science and Technology, an International Journal*, vol. 20, no. 1, pp. 151-159, 2017.
- [23]G. M. Siringi, A. Abolmaali, and P. B. Aswath, "Properties of concrete with crumb rubber replacing fine aggregates (Sand)," *Advances in Civil Engineering Materials*, vol. 2, no. 1, pp. 218-232, 2013.
- [24]K. Mushunje, M. Otieno, and Y. Ballim, "Partial replacement of conventional fine aggregate with crumb tyre rubber in structural concrete—effect of particle size on compressive strength and time dependent deformations," in *MATEC Web of Conferences*, 2018, vol. 199: EDP Sciences, p. 11002.
- [25]A. International, "C 109/C 109M-07. Standard test method for compressive strength of hydraulic cement mortars (using 2-in. or [50-mm] Cube Specimens)," ed.
- [26]B. BS, "4551: Part 1: 1998," *Methods of testing mortars, screeds and plasters*. London: British Standards Institution, 1998.
- [27]Y. Al Wahedi, J. Awayes and G. Bassioni, "Influence of classical and modern superplasticisers on the chemical and rheological behaviour of oil well cement: a comparative study," *Advances in cement research*, vol. 23 (4), pp. 175-184, 2011.
- [28]G. Bassioni and M. M. Ali, "Studying the physico-chemical properties of commercially available oil-well cement additives using calorimetry," *Journal of thermal analysis and calorimetry*, vol. 111 (1), pp. 295-303, 2013.
- [29]G. Bassioni and M. M. Ali, "The effect of counterion in lignosulfonates as oil-well cement retarders," *Advances in cement research*, vol. 25 (5), pp. 245-253, 2013.
- [30]C.-Y. Chen and M.-T. Lee, "Application of crumb rubber in cement-matrix composite," *Materials*, vol. 12, no. 3, p. 529, 2019.

IMPROVEMENT OF SOIL STRENGTH USING RICE HUSK ASH

Jamie Ure Ovia¹, Najmun Nahar¹, Alex Otieno Owino¹, Noma Tamaki² and Zakaria Hossain¹

¹Dept. of Environmental Science Graduate School of Bioresources, Mie University, Japan

²Make Integrated Technology Company Ltd., Osaka, Japan

ABSTRACT

Rice husk is considered an agricultural waste in most countries, but recently studies have shown that by burning this waste product in a controlled environment can produce rice husk ash (RHA), which is a very useful product due to its high SO₂ percentage. Because of the high SO₂ percentage, RHA has great potential to improve soil properties. In this paper three types of RHA ratio additive mixtures is investigated, 5%, 10% and 15% in comparison with the control soil. The strength of each of the RHA mixtures is determined by conducting the California Bearing Capacity (CBR) test for all the mixtures with curing periods of 1 and 7 days. The objective of the paper is to determine the optimum RHA ratio in which sandy soil reaches its peak bearing capacity.

Keywords: Rice husk ash; Ground improvement; Optimum moisture content; California Bearing Capacity

INTRODUCTION

Soil ground improvement is the alteration of soil to enhance its physical properties. Altering the properties can increase shear strength of a soil and improve load bearing capacity of a subgrade to support structures. Various innovative techniques have been investigated by geotechnical engineers over the years. An example is the influence of using lime piles on improvement of bearing capacity and failing slope stabilization of clay soils was investigated by Rogers and Glendinning [1]. Investigators Gidley and Sack proposed several methods for utilizing some industrial wastes in engineering construction [2].

Rice husks in many countries is considered to be agricultural waste and is unnecessarily dumped or burned in open heap areas [3]. According to recent study in 2014 the amount of rice husk generated globally was estimated to be 1.482×10^8 tons [4][5]. Rice husks if utilized correctly has immense potential to create many different products such as utilization for bioenergy as well as various industries that will use the amorphous silica (i.e. ceramics, glass making, steel production. Pharmaceuticals, rubber, etc.).[6]

The rice plant has the unique ability to take silica content from soil and eventually the silica accumulates into its structure as it grows [7]. The part of the plant with the highest silica content is the rice husk. When burned at high temperatures within an enclosed chamber, rice husk ash is produced. Rice husk ash has high percentage of siliceous minerals and so it has potential pozzolanic properties. Pozzolanas are siliceous and/or aluminous materials [8]. Pozzolanas have little or no cementitious value, but which will in finely divided form and in the presence of moisture, chemically reacts with calcium hydroxide liberated during the hydration of Portland cement to produce stable, insoluble cementitious compound which can be used to stabilize soils[9][10].

This paper aims to investigate the bearing capacity of soil when mixed only with RHA at different percentages. The reaction of the amorphous silica within the RHA is observed as it reacts with water and soil both for 1 and 7 days. Ultimately, the optimum RHA mixture that gives the highest bearing capacity is determined.

MATERIALS AND METHODS

Materials

Soil

The soil used for this paper was collected from the Handa area, Tsu City, Mie Prefecture. The physical properties of the soil are shown in Table 1. According to the graph of particle size distribution curve in Fig. 1 it was determined that the coefficient of gradation (C_u) and the coefficient of curvature (C_c) are 9.275 and 0.906 respectively. Moreover, in regulation with the United Classification of Sand soil by ASTM D-2487, the soil was classified to be well-graded sand with silt (SW-SM).

Table 1. Physical properties of soil

Parameters	Values
Specific gravity	2.74 g/cm ³
Maximum dry density	1.696 g/cm ³
Optimum moisture content	17.50%
Liquid limit, LL	37.52%
Plastic limit, PL	28.87%
Plasticity index, PI	8.55%
Sand (75 μ m - 2 mm)	89%
Silt (5 - 75 μ m)	9%
Clay < 5 μ m	2%

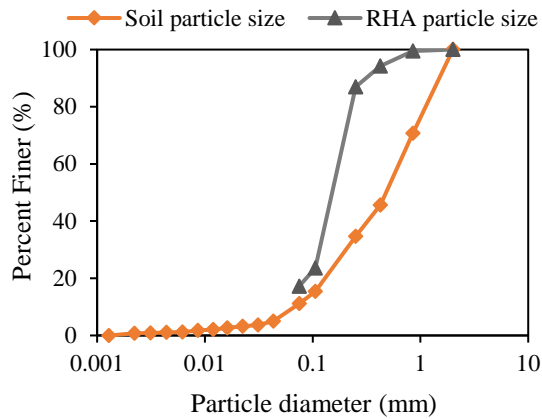


Figure 1. Particle size distribution curve for soil and RHA

Rice husk ash (RHA)

The RHA used was provided by Make Integrated Technology (MIT) Co., Ltd, Osaka Japan. By burning rice husks, itself at high temperature within an enclosed industrial machine, MIT company has been able to successfully convert high amounts of rice husks into a valuable material. The RHA used had SO₂ percentage of generally 85-90% as certified by Japanese Agricultural Standards (JAS). The chemical composition of the RHA is shown below in Table 2. The RHA also had a loss ignition of 85% and general composition of particle sizes ranging from 0.1-0.3µm, refer to Fig.1.

Table 2. Chemical composition of RHA

Element compound	Mass percentage
SiO ₂	91.1013
CO ₂	4.3490
K ₂ O	2.4031
CaO	0.5723
P ₂ O ₅	0.5178
SO ₃	0.3784
Cl	0.1867
MgO	0.1646
MnO	0.1414
Na ₂ O	0.0696
Fe ₂ O ₃	0.0536
Al ₂ O ₃	0.0350
ZnO	0.0172
Rb ₂ O	0.0072
SrO	0.0016
Br	0.0015

Laboratory Test

California Bearing Ratio (CBR) Test

The California Bearing Ratio (CBR) test was conducted in accordance with Japanese Industrial Standards (JIS A1211). The test used a standard CBR testing machine with a 5.08cm piston that penetrated the soil sample at a velocity of 1.27mm/min by means of a screw jack. Recordings were then taken at penetration depths of 0.5mm, 1mm, 1.5mm, 2mm, 2.5mm, 3mm, 4mm, 5mm, 7.5mm, 10mm and 12.5mm.

After three separate recordings were taken for sample, each data was then plotted on a load-penetration graph, but first load was needed to be calculated by taking into account the conversion factor of the CBR machine and multiplying it with each of recordings to get the loads. The best graph showing an accurate curve that runs convexly upwards was then chosen. If

The final step is to calculate the CBR percentage value by using Eq. (1). The load strength obtained from 5mm penetration was divided by the standard load strength of 5mm which is 19.9kN and then multiplied by 100 to get the final CBR value in percent.

$$CBR \text{ Value (\%)} = \frac{\text{Load Strength}}{\text{Standard Load Strength}} \times 100 \quad (1)$$

Rice husk ash mixtures and curing period

The soil mixture types and Optimum Moisture Content (OMC) of these mixtures are given in Table 3. Three types of RHA mixes were used; 5%, 10% and 15%. The control or regular soil was also tested to have a baseline to determine whether RHA additives change the composition of the soil mixture. The samples were prepared first by mixing in of RHA to the soil and water was added. The amount of water added was 1% below the OMC of each individual sample. Afterwards, the specimen was placed into a CBR mold and compacted with an automated hammer. The CBR mold was wrapped airtight and placed to cure for 24 hours and 7 days. The CBR molds were then tested on each of their respective days. Note that each soil mixture was tested three times and the most accurate data was collected from the three tests.

Table 3. All the soil mixtures tested

Mixture sample	RHA	OMC	Symbol
Control	0%	17.5%	-
1	5%	21.0%	5R
2	10%	25.0%	10R
3	15%	29.0%	15R

RESULTS AND DISCUSSION

Penetration Curve

The Fig.2 shows the penetration curve after 1 day of curing. It was observed that there was significant increase in applied load once the RHA was added to the soil. But as the RHA ratio increased over 5%, the applied load started to decrease.

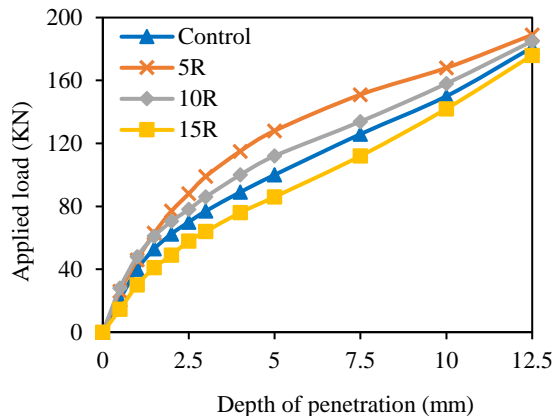


Fig. 2. Penetration curve for 1-day curing

From Fig.3 after 7 days of curing, the penetration-load curve increased to some degree when comparing to 1-day curing period. The trend is of the ratio percentages was still maintained with 5% RHA has the highest applied load.

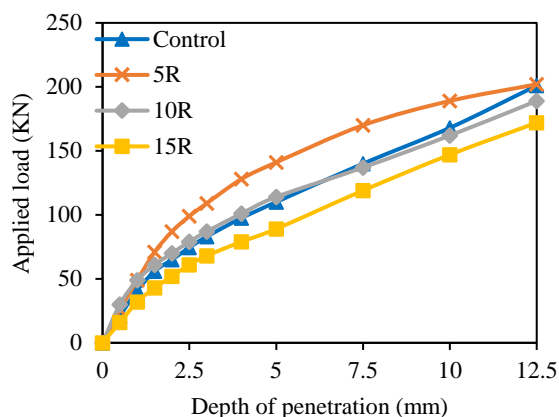


Fig. 3. Penetration curve for 7-day curing

CBR value

The CBR values obtained for both 1 and 7 days are shown in Fig.4. The 5% RHA showed highest CBR value out of all the mixtures, with the lowest being 15% RHA which was even lower CBR value than the soil control. The initial increase of CBR value with 5% RHA mixture may be because the ratio between soil and RHA gives a good plasticity index, but as RHA is added to the soil the plasticity index

increases thereby decreasing the CBR values. Also, this approves that RHA has little to no cementitious value and is not suitable to be a soil stabilizer alone.

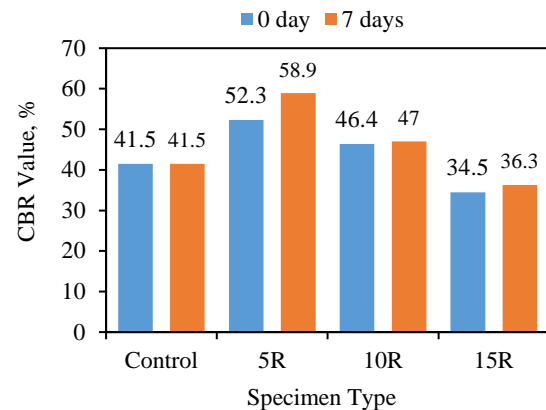


Fig. 4. CBR values for each specimen type both 1-day and 7-day

CONCLUSION

In summary, when working with RHA it is good maintain the mixture to be around 5% which will give the best bearing capacity for sandy soils. Additionally, excess of RHA within a sample will only worsen its properties and make the soil unsuitable. To conclude, I recommend in the future further work be done investigating the pozzolanic reaction between RHA and Portland cement to find out a suitable mix ratio for Geotechnical engineering purposes, and how the amount of time affects the soil mixtures properties.

ACKNOWLEDGMENTS

The first author would like to express gratitude to Japan International Cooperation Agency (JICA) for granting scholarship to study at Mie University.

REFERENCES

- [1] Rogers C D F, Glendinning S (1997). Improvement of clay soils in situ using lime piles, UK. *Journal of Engineering Geology*, 47(3): 243–257
- [2] Gidley JS, Sack WS. Environmental aspects of waste utilization in construction. *J Environ Eng ASCE* 1984;110(6):1117–33.
- [3] Ogbuagu N.J. (2018) Evaluation of rice husk ash and Portland cement reinforced clay for use as road subgrade using the CBR test, *Journal of Bioresources and Bioproducts*. 2018, 3(2) 65-70
- [4] FAO Statistical Yearbook. (2013) World food and agriculture. Rome: Food and Agriculture

- Organization of the United Nations; ISBN 978-92-5-1073964
- [5] FAO Rice Market Monitor (RMM). April 2015; 18(1): p. 1-14
- [6] Pote R., (2016). Potential application of rice husk ash waste from rice husk biomass power plant, *Renewable and Sustainable Energy Reviews* 53, 1468-1485.
- [7] R.G. Smith and G.A. Kamwanja, (1986) The use of rice husk for making a cementitious material, *Proc. Joint Symposium on the Use of Vegetable Plants and their Fibers as Building Material*.
- [8] Sima, J. (1974). Portland-Pozzolona Cement: Need for a Better Application. *Indian Concrete J.* 48: 33-34.
- [9] Saad, S.A (2015). Pozzolanic Reaction Mechanism of Rice Husk Ash in Concrete – A Review, *Applied Mechanics and Materials Vols. 773-774* (2015) pp 1143-1147
- [10] V.G. Papadakis, and S. Tsimas. (2002) Supplementary cementing materials in concrete: Part I: efficiency and design, *Cement and Concrete Research*, Vol. 32 (10), pp. 1525-1532.

SURFACE SHAPE MEASUREMENT AND EVALUATION OF MECHANICAL STABILITY BY DEM SIMULATION FOR DAMAGED TRADITIONAL STONEWALLS

Satoshi Sugimoto¹, Maho Yamaguchi¹ and Minoru Yamanaka²

¹Faculty of Engineering, Nagasaki University, Japan; ²Faculty of Engineering, Kagawa University, Japan

ABSTRACT

Kumamoto Castle has constructed about 400 years ago, and now the Cultural Affairs Agency of Japan treats it as an important historical spot. The 2016 Kumamoto Earthquake was damaged a lot of stone walls of this castle. Authors continue to investigate the deformation of unstable stonewalls by high accuracy laser module for measuring distance. And these stonewalls should be monitored continuously for evaluation of mechanical stability, so we developed and established the wireless network system for measuring the changing angle of some stonewalls surface in this castle. When installing this system in the future, the results of shape measurement of the surface of these stone walls will be important in identifying the locations to be installed and setting priorities.

The authors also carried out making a simulation model and calculation for evaluation of stonewalls stability by the distinct element method under the several conditions of stonewall shape and interface of materials. The failure area of stone walls and backfill are estimated by these results of DEM simulation, and it is discussed that these areas should be reinforced under the repair of damaged stonewalls.

Keywords: Damaged stone wall, Stability, Wireless sensor network, Monitoring and DEM simulation

INTRODUCTION

The 2016 Kumamoto earthquake caused enormous damage to ground structures such as buildings and stone walls at Kumamoto Castle. Besides, many stone walls in Kumamoto Castle collapsed and overturned, and tensile cracks occurred in the back of the embankment. The 2016 Kumamoto earthquake is characterized by the fact that Kumamoto Castle was damaged by a foreshock with a seismic intensity of 5+ and the main shock of 6+. Although the stonewalls of Kumamoto Castle escaped deformation during the foreshock, many cases were found to have been deformed or collapsed due to the mainshock (S.Sugimoto *et al.*, 2018 & 2017). And the stone walls that have undergone deformation will be examined for restoration work and appropriate management in the future. However, it is very difficult to distinguish whether the stone wall originally had a deformation or if the deformation was caused by the earthquake. Therefore, when considering the priority of restoration from the degree of deformation, it is required for the administrator to perform simple measurements daily. Besides, it is necessary to elucidate the mechanism of the stone wall collapse so that similar damage will never occur again in the future when another large-scale earthquake will occur. In this study, we used a simple method to quantitatively measure the deformation of the stonewall and used data collection and the distinct element method (analysis code: UDEC) to support the selection of remote monitoring points (Y. Katsuda *et al.*, 2018 & 2017). Based on the

research, we will build a model of stone walls. Then, numerical analysis of dynamic behavior was carried out, and factors affecting the stone wall were examined by comparing the collapse patterns under various conditions.

TYPE OF STONEWALL STRUCTURE

The stone walls of Kumamoto Castle can be roughly divided into three types according to the internal structure of the stone walls. In this study, the three types of shapes were named "stone base type", "half stone base type", and "stoneless base type" by adding the distance to the literature. Figure 1 shows the three types of internal structure, shape characteristics, and constituent materials. The stone base type is a stone wall with a low height, so many are made around the gate. The half stone base type is often made in the stone walls around the moat or the main enclosure. Since the northwestern part is not along the mountains, it is thought that many stone walls on this side were made of soil embankments and rubble. Many stoneless base types are made from south to southeast of Kumamoto Castle. This is probably because it was possible to pile up stonewalls on a steep slope. After all, the southeast side is along Mt. Chausu.

MEASUREMENT WITH A PORTABLE LASER RANGEFINDER

The Leica Geosystem's DISTO D510 is a portable

laser rangefinder that is mainly used to measure the shape of land plots and buildings. As shown in Figure 2, it is easy to measure linear distances and elevation angles. This instrument has an accuracy of 1.0 mm per 10 m and is available at a measuring distance of up to 200 m. Furthermore, it has been shown that there is a variation of about 0.3% when the angle between the measuring instrument and the horizontal plane exceeds 45 degrees. Therefore, in this study, it is necessary to fix the portable laser range finder (DISTO D510) to a tripod, measure the vertical distance and the horizontal distance, and to measure the shape within the range of 45 degrees. The condition was set.

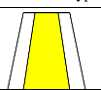





Type name	Stone base type	Half stone base type	Stoneless base type
Style			
State at the time of collapse			
Materials	Stone Cobblestone	Stone Cobblestone Embankment	Stone Embankment
Height	Low	A little high	High
Slope	steep	A little lenient	A little lenient

Fig. 1 Shape features of each stonewall.

Measuring method

The measurement was performed according to the following procedure. Install a measure parallel to the surface of the stone wall to be measured. At this time, either the left or right end is set as the measurement origin. A marker is set at the point set as the origin so that it can be easily compared in future measurements. Determine the distance between survey lines according to the length and size of the stone wall. After determining the measuring line, install the measure so that it intersects with the measure installed parallel to the stone wall. Install a portable laser range finder (DISTO D510) on the tripod and measure the measurement point. At this time, one point will be measured for each stone wall on the survey line, and the center of the stone wall will be measured.

There are two ways to organize the data in the measured stone wall cross-section: top reference and bottom reference.

The top reference is the uppermost stonewall as the origin of the X-axis and the Y-axis, and the bottom reference is the measured data with the lowermost stone wall as the X-axis and the Y-axis origin. By setting a standard, it is easy to judge the characteristics of the deformation and collapse of the stone wall when the surface shape of the stone wall changes. Moreover, based on the bottom of the stone

wall, the measured lateral position, height, and depth were input into the graph drawing software to create a shape distribution map. As shown in Fig. 2, a laser range finder fixed on a tripod is installed in front of the target stonewall, and the distance and angle of each stone wall are measured in the vertical direction. After the measurement, find the vertical and horizontal coordinates of each stone wall based on the distance and angle and plot the cross-section. If the ground where the stone wall is built inclines, it is difficult to create an accurate surface shape distribution map if measured normally. Therefore, when performing the measurement, we decided to use the bottom of the slope as the origin of the coordinate axis and use the two poles to measure the step. The distance between poles can be found by using two poles. Therefore, by adding the vertical distance between poles to each survey line, the standard can be unified and a surface shape distribution map can be created. Photo 1 shows the measurement using a pole.

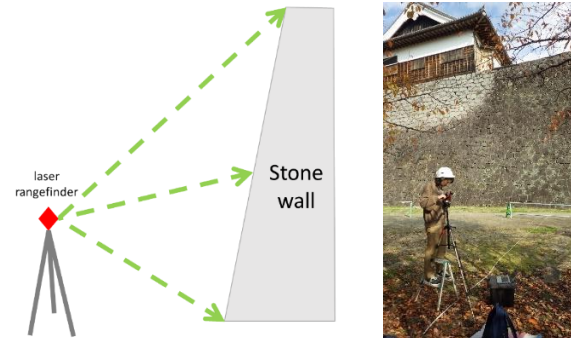


Fig. 2 Measurement schematic diagram and photo.



Photo 1 State of pole installation.

SURFACE SHAPE MEASUREMENT

A portable laser range finder was installed in front of the target stone wall, and the distance and angle of each stone wall were measured in the vertical direction. After the measurement, the vertical and horizontal coordinates of each stone wall were calculated based on the distance and angle, and the cross-section was plotted. This time, the measured data of 1984 and 2018 were used for comparison. The

1984 data is the newest data measured by Prof. Kuwahara (1984) before the Kumamoto earthquake. In selecting the measurement points, in addition to the points measured in the past, we newly measured the points with large deformation. Up to now, the measurement has been performed in 8 steps, and a total of 150 points have been measured as shown in Fig. 3.

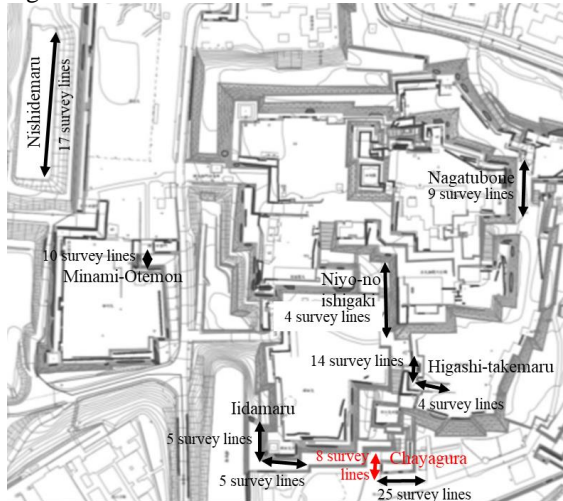


Fig. 3 Overall view of measurement points.

One case of the measurement result

STONEWALL OF "CHAYAGURA" TRACE

It is a stone wall located on the south side of Kumamoto Castle. Photo 2 is a panoramic view of the western surface of the stone wall at "Chayagura" trace. A total of 8 lines were measured at 1m intervals. Figure 4 shows the surface shape distribution map of the western surface of the stonewall. At around 5m, the surface shape is protruding. The possible reason for this is considered to be a phenomenon caused by the reduction of the gap between the stones, which is caused by the movement of the stones accumulated in the rear part of the stone wall due to the influence of external force such as vibration. It was confirmed at the site that the deformed parts were the same with this figure. This deformation seems to reflect the result of active earth pressure in the central part of the stone wall during the earthquake.



Photo 2 Stonewall of "Chayagura" trace.

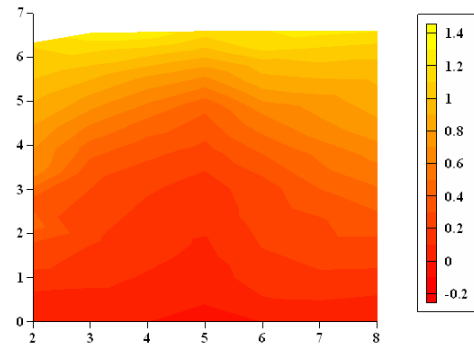


Fig. 4 Surface shape distribution map. (unit: m)

DYNAMIC ANALYSIS BY DISTINCT ELEMENT METHOD

The stone base type among the three types of stone walls was modeled by the distinct element method program (analysis code: UDEC) and the dynamic analysis was performed. In this research, the distinct element method (analysis code: UDEC), which is suitable for analyzing discontinuous structures such as stone walls and stone bridges, is used to reproduce individual movements of stone walls and stones. The stone base type consists only of chestnut stone and stone wall stone, and the damage was the largest of the three types, and more than half of the total collapsed, so this paper describes the results of this type.

Analysis model

Figure 5 shows a "stone base type" analytical model with a stonewall slope of 70° . Since the stone base type is built in a place where there is no background, stones were piled up on the left and right, and the inside was packed with a quarry stone block, as in the previous literature. The sandy ground represented by elasto-plastic elements was installed under the stone wall, and in the actual stone wall, the lower stone wall was buried in the ground, so the lower three steps were fixed as the foundation.

Boundary condition

In this study, the boundary conditions shown in Fig. 5 were set to properly reproduce the transmission of seismic waves from deep underground. A dashpot was provided on the boundary surface of the sandy ground at the bottom of the individual element model to make the bottom viscous boundary. The bottom viscous boundary is a boundary condition that evaluates the semi-infinite ground below the model bottom, and it is possible to absorb the wave energy dissipated at the bottom boundary and input only the rising wave component of the seismic wave. As a result, the transmission characteristics of seismic waves from deep underground can be satisfied. A free rock mass region was set up on both boundary

surfaces on the side of the distinct element method model as energy transfer boundaries. The energy transfer boundaries allow wave energy to be dissipated laterally in the model and absorbed in the free rock region. As a result, the lateral boundary can be evaluated as a semi-infinite ground area, and the actual foundation rock area can be reproduced.

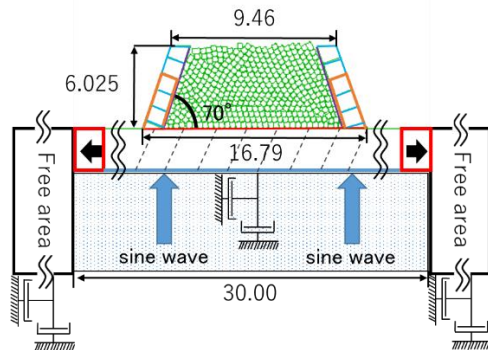


Fig. 5 Cross-section of the analysis model. (unit: m)

Input parameter

Table 1 shows the characteristic values of the surface of each block, and Table 2 shows the characteristic values of each joint. In this study, we focused on the stone base type that caused the most damage. To compare with the existing literature, the characteristic value was analyzed with the same value as the previous research. And the density of stones and cobblestones are applied each 2.5 kg/cm³ and 2.2 kg/cm³.

Model creation

Figure 6 shows a drawing of the stone base type with a stonewall slope of 70°. The left figure is a model before cutting the stone. We made two blocks inside the stonewall and one block above the stone wall and cut the block into 40 cm square. Since it is harder to create a gap when dropping one block than dropping it separately, we created blocks separately. In order to get closer to the actual construction procedure, rubble stones were made at a certain height and allowed to fall freely and packed inside the stonewall. Based on the reflections of previous studies, a gap was created in the corner of the stonewall just by free fall, so acceleration was applied in any direction to the model with the stone wall and the base fixed. From this, as shown in Fig. 8, it can be confirmed that the stones are sufficiently clogged.

Earthquake motion input

The input ground motion is given to the bottom of the individual element model. The input waveform had a frequency of 10 Hz, an amplitude of 1 m/sec, and an excitation time of 2 seconds, after which the gravity analysis was performed for 1 second.

Table 1 Characteristic value of block surface.

	Case 1	Case 2
Normal stiffness (N/mm)	3000	3000
Shear stiffness (N/mm)	3000	3000
Cohesion (kN/m ²)	0	0
Shear resistance angle (deg)	15	30

Table 2 Shear resistance angle value between different materials.

Stones and cobblestones (deg)	Stones and sandy ground (deg)	Cobblestones and sandy ground (deg)
15	15	15

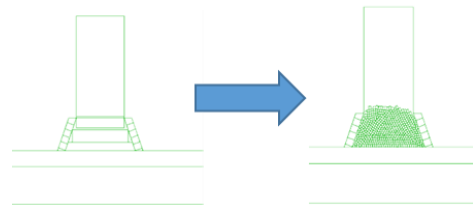


Fig. 6 Schematic diagram of the stone base type model creation.

Relationship between stone wall height and collapse range

In order to clarify the relationship between the height of the stone wall and the collapse range, the condition of the physical properties of each block was not changed, and only the height was set to half the value of the previous studies. The height of the stonewall used in the previous research is 12.0 m, and the height of the stone wall used in this research is 6.0 m. Figure 7 shows the analytical model of 12.0m and 6.0 m with a shear resistance angle of 15° on the surface of each block with a stone wall slope of 70°.

Figure 8 shows the displacement vectors of the 12.0 m high model and 6.0 m high model during deformation. As the height of the stone wall became lower, a difference appeared in how it collapsed under the same conditions. The slope of the slip surface varies depending on the height of the stone wall. This is because when the height is 12.0 m, the earth wall pressure is relatively small and the earth cover pressure is relatively small. Therefore, the horizontal force acting by the inertial force of the seismic motion is larger than the earth's cover pressure. It is considered that the surface inclination is steep. When the height is 6.0 m, the height of the stone wall is low, so the force exerted by the overburden pressure does not change much depending on the place, and the horizontal force acting by the earthquake motion is

larger than the overburden pressure. It is considered that the slope of the slip surface is gentle.

Figure 9 shows a comparison of the horizontal displacement of the stone wall at the top of the crown when a ground motion is applied, based on the height. When the height was 12 m, the horizontal displacement was larger than that when the height was 6 m. In both cases, although the stone wall has collapsed, the height of the stone wall is higher than that of the lower stone because it is taller, and it is thought that the stone wall was more susceptible to the influence of the stone. In addition, it is considered that the movement of the upper area also differs depending on how the clogs are clogged.

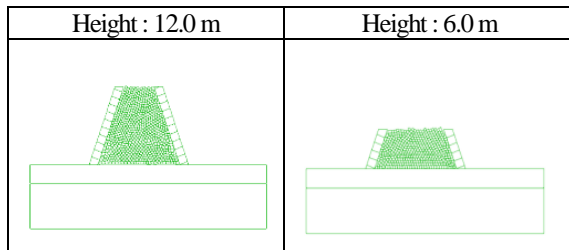


Fig. 7 Two kinds of models of stonewalls.

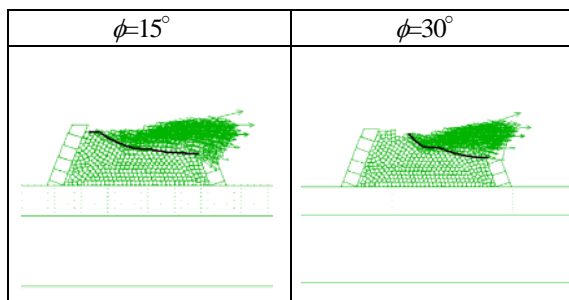


Fig. 8 Displacement vector diagram after the start of earthquake motion.

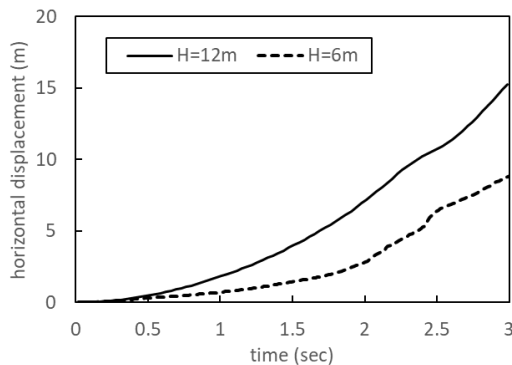


Fig. 9 Horizontal displacement of the top of the stonewall compared with height.

Relationship between shear resistance angle and collapse range

In order to clarify the effect of the size of the shear resistance angle on the cobblestone surface on the collapse of the stone wall, the other parameters were constant, the stone wall slope was 70°, the height was

6.0 m, and the shear resistance value of each block was The calculation was performed under the conditions of 30° and 15°. The results are shown in Figure 10. When Case 1 and Case 2 are compared, the inclination of the slip surface is significantly different because the shear resistance angle is different even if the height is the same. The distinct element method was used to express that the larger the shear resistance angle, the more difficult the stone wall is to collapse.

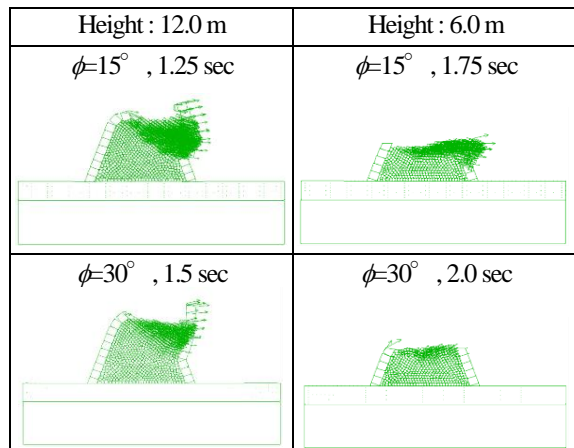


Fig. 10 Slip surface compared with each shear resistance angle.

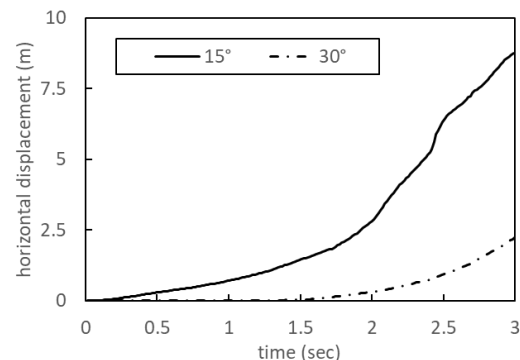


Fig. 11 The horizontal displacement of the top of the stonewall is compared with the shear resistance angle.

Figure 11 shows a comparison of the horizontal displacement of the stonewall at the top of the crown when a ground motion is applied, based on the value of the shear resistance angle. When the shear resistance angle is 15°, the upper stone wall is displaced from 0.25 seconds after the start of vibration, whereas when the shear resistance angle is 30°, the vibration is observed from 1.75 seconds after the start of vibration. It is considered that the larger the shear resistance angle is, the larger the force to resist when the earthquake motion is applied becomes, and it becomes difficult to transmit the force to the upper stone wall.

CONCLUSIONS

In this study, the simple method is used to quantitatively measure the deformation of the stone

wall, data collection and stone base type stone wall are used as the basis for the selection of the remote monitoring target, and the distinct element method (A dynamic analysis was performed using the analysis code: UDEC) to reproduce the collapse behavior of the stone wall. The results and considerations obtained in this study are described below.

1) Using a portable laser rangefinder, the surface shape of stone walls at various places in Kumamoto Castle was measured easily. In the stone wall with a height of about 5 m, many deformations were observed, which seemed to be extruded by the stones on the back. It is highly probable that a temporary active earth pressure condition was caused by the earthquake motion. Although it is necessary to verify the consistency with the 3D measurement results, it is a simple measurement method, but it is possible to quantitatively grasp the characteristics of the surface shape.

2) The damage situation at each height of the stone wall was collapsed in all cases when the height was 12 m. On the other hand, when the height was halved to 6 m, no collapse occurred when the shear resistance angle of the stonewall and the stone was 30° . From this, it can be confirmed that not only the slope of the stone wall but also the height of the stone wall contribute to the collapse.

3) It was found that the higher the height of the stone wall, the greater the depth of the stone, and the lower the height, the gentler the slope of the slip surface.

4) It was found that the stone-base type collapse factor in which the stone is composed is the active earth pressure generated when the stone is destroyed by the earthquake. However, it was confirmed that if the shear resistance angle of the stones exceeds a certain value, the active earth pressure is not generated enough to collapse the stone wall.

5) Even with the same height model, if the shear resistance angle is different, the displacement of the stone wall in the upper stage when vibration is applied is different. It is thought that this is because the larger the shear resistance angle, the greater the force that tries to resist when an earthquake motion is applied, and the more difficult it is to reach the upper stonewall.

ACKNOWLEDGMENTS

The authors gratefully appreciate a lot of support and understanding for this investigation from all officers of Kumamoto Castle Survey and Research Center after shortly after the 2016 Kumamoto earthquake. And our gratitude extends to all cooperators of this investigation with several

instruments and information.

REFERENCES

- [1] S. Sugimoto., M. Yamanaka., H. Maeda., N. Fukuda., Y. Katsuda.: Research of damaged condition by the 2016 Kumamoto Earthquake and ground investigation on stone walls and earth structures in Kumamoto Castle, International Journal of GEOMATE, Vol.14, Issue 45, 2018, pp.66-72.
- [2] S. Sugimoto., M. Yamanaka.: Reports of damaged earth structures in Kumamoto Castle, Proceedings of 54th Natural disaster and science symposium, 2017, pp.45-51. (in Japanese)
- [3] Y. Katsuda., Y.Jiang., K. Omine., S.Sugimoto.: Research of damaged stone structures in Kumamoto Castle by the 2016 Kumamoto Earthquake, Proceedings of 72th JSCE Conference (CD-ROM), 2017, pp.479-480. (in Japanese)
- [4] Y. Katsuda., S. Sugimoto., M. Yamanaka.: Reports of a survey on damaged stonewalls in Kumamoto Castle by the 2016 Kumamoto Earthquake, Proceedings of the Japan National Conference on Geotechnical Engineering, 2018. (in Japanese)
- [5] H. Yamamoto, T. Nishigata, S. Yao, K. Nishida, H. Kasa, I. Wada.: Study on Friction Characteristics of Stones and Effect of Packing in Castle Stone Wall, Proceedings of the National Symposium on Ground Improvement, 2008, pp.127-132. (in Japanese)
- [6] T. Nishimura, Y. Noma, H. Kasa, H. Yamamoto, T. Nishigata: Examination of deformation behavior of shaking table test by stability analysis of castle wall using distinct element method, Proceedings of 66th JSCE Conference (CD-ROM), 2011, pp.325-326. (in Japanese)
- [7] H. Kasa, H. Yamamoto, T. Awatani, K. Nishida, T. Nishigata, Y. Wada: Experimental study on stability improvement effect of boulder stone in the castle wall, Proceedings of 62th JSCE Conference (CD-ROM), 2007, pp.467-468. (in Japanese)
- [8] F. Kuwahara.: The gradient of the stone walls in Kumamoto Castle, Report of researches / Nippon Institute of Technology, 14-2, 1984, pp.59-74. (in Japanese)
- [9] I. Fujii., L. Yang., Y. Jiang., S. Li., T. Tanahashi.: Evaluation of the dynamic behaviors of the bedrock containing discontinuities under important buildings based on numerical simulations, Proceedings of 2011 JSCE west conference (CD-ROM), 2011, pp.411-422(in Japanese)

GEOMATE 2021

The Eleventh International Conference on Geotechnique, Construction Materials & Environment

3 - 5 November 2021

Kyoto, Japan

- The "International Journal of GEOMATE" is a Scientific Journal of the GEOMATE International Society that encompasses a broad area in Geotechnique, Construction Materials and Environment.
- The key objective of this journal is to promote interdisciplinary research from various regions of the globe.
- The editorial board of the journal is comprised of extensively qualified researchers, academicians, scientists from Japan and other countries of the world.
- It is peer-reviewed Journal that is published quarterly till 2015 and now monthly. All articles published in this journal are available on line.
- Contributors may download the manuscript preparation template for submitting paper or contact to the Editors-in-Chief

[editor@geomatejournal.com].

ISSN: 2186-2982 (Print) 2186-2990 (Online)



Scopus

EBSCO

CENGAGE Learning



GIF₂
GLOBAL IMPACT FACTOR



VOLUME
Issue
Month, Year

International Journal of GEOMATE

(Geotechnique, Construction Materials and Environment)



Tsu, Japan

THE GEOMATE INTERNATIONAL SOCIETY

<https://www.geomatejournal.com/>